

PROCEEDINGS OF

**The 58th Conference on
Simulation and Modelling
(SIMS 58)**

September 25th – 27th, 2017
Reykjavik, Iceland



Editor: Magnus Thor Jonsson

The conference is organized by University of Iceland, National Energy Authority in cooperation with the Scandinavian Simulation Society (SIMS)

Proceedings of the 58th Conference on Simulation and Modelling (SIMS 58) Reykjavik,
Iceland, September 25th – 27th, 2017

Editor:

Magnus Thor Jonsson

Published by:

Scandinavian Simulation Society and Linköping University Electronic Press

ISBN: 978-91-7685-417-4

Series: Linköping Electronic Conference Proceedings, No. 138

ISSN: 1650-3686

eISSN: 1650-3740

DOI: 10.3384/ecp17138

Organized by:

University of Iceland,

School of Engineering and Natural Science

Faculty of Ind. Eng., Mech. Eng. and Computer Science

and

National Energy Authority

Orkugarður

Grensasvegur 9

108 Reykjavik, Iceland

in co-operation with,

Scandinavian Simulation Society

c/o Esko Juuso, Department of Process and Environmental Engineering

P.O Box 4300

FIN-90014 University of Oulu

Finland

WELCOME TO SIMS 58

Welcome to the 58th Conference on Simulation Modelling and Optimization in Reykjavik, Iceland. Reykjavik is the northernmost and one of the smallest capital cities in the world. Although small for a capital, it is the country's largest and most populated city and with the urban area population of around 200000, it is the home of the vast majority of Iceland's people. The city is pioneer in the use of geothermal energy to provide low-cost heating and electricity. Iceland's energy consumption per capita is among the highest in the world, and the proportion of this consumption provided by renewable energy sources exceeds most other countries. The electricity is produced almost entirely from renewable energy sources, hydroelectric (70%) and geothermal (30%) and simulation, modelling and optimization are the key elements to utilize the renewable energy more efficiently.

The SIMS 58 will cover broad aspects of simulation, modelling and optimization and be a technical forum for participants to further their knowledge by being exposed to diverse topics, and exchange opinions and ideas both from industry and academia in a variety of topics related to simulation, modelling and optimization. The ambition is to bring the field of applied modelling and simulation techniques of energy systems to the general public as a contributing technology for efficient and sustainable energy systems. This year, the conference program contains two keynote speakers, 53 research papers and presentations organized into 14 sessions and an excursion to a geothermal park.

The focus of the conference is on simulation, modelling and optimization in a variety of applied contexts including topics such as geothermal, hydro and bio energy, oil production, automotive industry and methodology and technologies for simulation, modelling and optimization.

A key component of the SIMS conference is the opportunity to socialize and make new connections. The conference offers several possibilities such as a conference dinner at Bryggjan Brugghús (Bistro and Brewery), an excursion to the Reykjanes GEOPARK and last but not least some coffee and lunch breaks.

SIMS stands for the Scandinavia Simulation Society with members from five Nordic countries, Denmark, Finland, Norway, Sweden and Iceland. The goal of SIMS is to develop further the science and practice of modelling and simulation in all application areas and to be a forum for information interchange between professionals and non-professionals in the Nordic countries.

Thanks to all participants, authors, keynote speakers and presenters for their contribution to this conference. I also want to acknowledge the support I have received from the conference board, program committee and the SIMS board. The support from the National energy authority, Iceland is gratefully acknowledged.

Welcome, I hope you will enjoy the conference and the interactions with your colleagues and other presenter here.

Magnus Thor Jonsson

Organizer:

Program Chair

Magnus Thor Jonsson, University of Iceland

International Program Committee

Magnus Thor Jonsson, University of Iceland

Jónas Ketilsson, Orkustofnun/National energy authority, Iceland

Erik Dahlquist, Mälardalens Högskola, Sweden

Brian Elmegaard, DTU, Denmark

Lars Eriksson, Linköping University, Sweden

Britt Halvorsen, Høgskolen i Telemark, Norway

Kaj Juslin, VTT, Finland

Esko Juuso, University of Oulu, Finland

Magnus Komperød, Nexans Norway AS, Norway

Tiina Komulainen, Oslo and Akershus University College of Applied, Norway

Bernt Lie, Høgskolen i Telemark, Norway

Gerhard Nygaard, University of Stavanger, Norway

Adrian Pop, Linköping University, Sweden

Bernhard Thiele, Linköping University, Sweden

Tommi Karhela, VTT, Finland

Nikolaos Papakonstantinou, VTT, Finland

Kim Sørensen, Aalborg University, Denmark

Peter Ylén, VTT, Finland

Lena Buffoni, Linköping University, Sweden

National Organizing Committee

Magnus Thor Jonsson, University of Iceland

Baldur Petursson, National Energy Authority

Silja Ran Sigurdardottir, National Energy Authority

Jonas Ketilsson, National Energy Authority

Contents:

Session V11	13
Numerical investigation of conjugate heat transfer and flow performance of a fin and tube heat exchanger with vortex generators.....	13
Comparison of elastic vs. inelastic penstock model using OpenModelica.....	20
Computational fluid dynamics study of flow depth in an open Venturi channel for Newtonian fluid.....	29
A Deepened iTOUGH2 Model of Reykjanes for IDDP.....	35
Session A11	41
Modeling N/S ratio and temperature effects in simultaneous biological denitrification and sulfide oxidation.....	41
Microalgae Activated Sludge: Process Modelling and Optimization.....	48
Analysis of the effect of steam-to-biomass ratio in fluidized bed gasification with multiphase particle-in-cell CFD Simulation.....	54
Analyzing the effects of particle density, size, size distribution and shape for minimum fluidization velocity with Eulerian-Lagrangian CFD simulation.....	60
Session V12	66
Simulation of Starting and Stopping Vortices of an Airfoil.....	66
Validation of results from Barracuda® CFD modelling to predict the minimum fluidization velocity and the pressure drop of Geldart A particles.....	76
Numerical modeling of the calcination process in a cement kiln system.....	83
Use of Orthogonal Collocation Method for a Dynamic Model of the Flow in a Prismatic Open Channel: For Estimation Purposes.....	90
Session A12	97
Evaluation of drag models for CFD simulation of fluidized bed biomass gasification.....	97
Passivity-based analysis of biochemical networks displaying homeostasis.....	108
Methane from Syngas by Anaerobic Digestion.....	114
Effect of natural convection and radiation inside of a hollow beam in a standard fire.....	121
Session V13	128
Study of Fluidization Regimes using OpenFOAM Computational Fluid Dynamics.....	128
CFD Study of Particle Flow Patterns in a Rotating Cylinder Applying OpenFOAM and Fluent...	137
Model uncertainty of interfacial area and mass transfer coefficients in absorption column packings.....	144
Comparison of the influence of drag models in CFD simulation of particle mixing and segregation in a rotating cylinder.....	151
Session A13	157
Simulation of burning velocities in gases vented from thermal run-a-way lithium ion batteries....	157
Detonation propagation in stratified reactant layers.....	162
Using Image Processing for Flame Diagnostics.....	168
Open active contour model for front tracking of detonation waves.....	174
Session V21	180
Modeling and simulation of light oil production using inflow control devices.....	180
Simulation of Oil Production from Homogenous North Sea Reservoirs with Inflow Control using OLGA/Rocx.....	188
Simulation of Oil Production from Heterogeneous North Sea Reservoirs with Inflow Control using OLGA/Rocx.....	196

Session A21	203
Towards Effective Automatic Feedback for Simulator Training.....	203
Augmented and Virtual Reality for Engineering Education.....	209
Smart Integration of Energy Production.....	220
Session V22	227
Euler-Granular approach for modelling of dilute phase pneumatic conveying in a vertical pipe...	227
Concrete thermal energy storage for steam generation: A numerical investigation.....	234
Dynamic Modeling and Simulation of an Offshore Combined Heat and Power (CHP) Plant.....	241
Thermodynamic Optimization of an Organic Rankine Cycle for Power Generation From a Low Temperature Geothermal Heat Source.....	251
Session A22	263
Electrical Power System Modelling in Modelica – Comparing Open-source Library Options.....	263
Comparison of control strategies for a 2 DOF helicopter.....	271
Covering the Gap Between Advanced Control Theory Design and Real Time Implementation Using Simulink.....	280
Physiological based modeling and control of an industrial tank process.....	284
Session V23	292
Optimization of gas velocity and pressure drop in CO ₂ absorption column.....	292
Simulation and Economic Optimization of Vapour Recompression Configuration for Partial CO ₂ capture.....	298
Modelling and Validation of Hybrid Heavy Duty Vehicles with Exhaust Aftertreatment Systems.....	304
Optimal Control of Wastegate Throttle and Fuel Injection for a Heavy-Duty Turbocharged Diesel Engine During Tip-In.....	317
Session A23	326
Wave Front Tracking using Template Matching and Segmented Regression.....	326
A multi-period optimization model for the design of new LNG supply chains.....	332
The impact of signalling kinetics on controller motif performance.....	343
Data-driven Modeling of Ship Motion Prediction Based on Support Vector Regression.....	350
Session V24	355
Transient stability of fault ride through capability of a transmission system of a distributed hydropower system.....	355
Flood Control of Lake Toke: Model Development and Model Fitting.....	360
Hydropower Systems: Comparison of Mechanistic and Table Look-up Turbine Models.....	368
Session A24	374
Numerical Calculation of Stresses in Helical Cable Elements subject to Cable Bending and Twisting.....	374
Online Drilling Fluid Flowmetering in Open Channels with Ultrasonic Level Sensors using Critical Depths.....	385
Structural Analysis of the Casings in Deep Geothermal Wells.....	391
Modeling and simulation in the design process of a prosthetic foot.....	398

Conference location:

National Energy Authority, Orkugarður, Grensasvegur 9, 108 Reykjavik, Iceland

Opening ceremony and plenary session:

The conference opens on Monday, September 25th, at 08:30.

Conference opening speech:

Prof. Sigurður Magnús Garðarsson, Dean of School of Engineering and Sciences, University of Iceland.

Keynote 1:**Taming of the supercritical shrew**

Prof. Guðni A. Jóhannesson, Director General National Energy Authority

Keynote 2:**Model-Based Development - The Prosperous Life, Evolution, & Impact of a Diesel Engine Model**

Prof. Lars Eriksson, Vehicular Systems, Linköping University

Excursion:

The conference excursion will be on Wednesday, September 27th, at 10:00.

Resource Park in the Reykjanes peninsula**Svartsengi Geothermal Powerplant****Social program:**

The conference dinner will be on Tuesday, September 26th, at 19:30.

Bryggjan Brugghús, Bruggsalurinn

Author Index:

Alexander Z. Gjerset	360	Knut Vaagsaether	29, 128, 157, 162
Alice Bittante	332	Kristian D. Kvam	360
Amila C. Kahawalage	83	Kristian Thorsen	108, 284
Andre V. Gaathaug	174, 168, 162	Kristoffer Ekberg	317
Anis Yazidi	203	Kwangsu Park	292
Asanthi Jinasena	90	Lars Erik Øi	144, 292, 298
Åsmund Hasaas	360	Lars Eriksson	304, 317
Beathe Furenes	360	Lars O. Nord	241, 251
Bernt Lie	20, 29, 128, 360, 368	Lars-Andre Tokheim	137, 83, 151, 76
Bikram Kawan	350	Laura Marcano	203
Britt M. E. Moldestad	180, 128, 54, 60, 188 196, 76	Lilja Magnusdottir	35
Carlos Dinamarca	41	Liubomyr Vytvytskyi	20, 368
Carlos F. Pfeiffer	271, 280	Luca Riboldi	241
Chameera Jayarathna	76	Magnus Komperød	374
Christophe Lecompte	398	Magnus S. Hansen	188, 196
Cornelius Agu	97	Magnus Thor Jonsson	35, 391
Dag A. Eimer	144	Marianne Sørflaten Eikeland	54, 60
Dag Bjerketvedt	157, 162	Marius Lysaker	326
Daniel Myklatun Tveit	108	Mathias Henriksen	157, 168
Dietmar Winkler	263	Mexhid Ferati	203
Eirik Siljan	326	Michal Sposob	41
Emma Nehrenheim	48	Morten C Melaaen	83, 227
Erik Sundbø	298	Nils-Olav Skeie	360
Esko K. Juuso	220	Nora C. I. Furuviik	180, 196, 188
Felix Starker	398	Ola Marius Lysaker	174
Fjóla Jónsdóttir	398	Ole Kristian Vøllestad	188, 196
Frank Pettersson	332	Olov Holmer	317, 304
Geir Risvoll	343	Prasanna Welahettige	29, 128, 227
George Anthony Giannoumis	209	Ramesh Timsina	180
Glenn-Ole Kaasa	90	Reidar Kristoffersen	66
Gunnar Skúlason Kaldal	391	Roberto Agromayor	66, 251
Gunne J. Hegglid	355	Roshan Sharma	90, 271, 280
Guoyuan Li	350	Rubén M. Montañés	241
Håkon Viumdal	385	Rune Bakke	41, 114
Halldór Pálsson	391	Saba Mylvaganam	385
Hao Wang	350	Samee Maharjan	174
Hassan Ali	298	Sami Pajunen	121
Heimir Tryggvason	398	Sanjay Shah	114
Henrik Saxén	332	Shobhana Singh	13, 234
Inés Encabo Cáceres	251	Sigrún Nanna Karlsdóttir	391
J. Manjula Edirisinghe V.P.	355	Singh Shobhana	121
Jairo Rúa	66, 241	Sumudu S. Karunarathne	137, 144, 151
Janitha Chandimal Bandara	54, 60	Susantha Dissanayake	137
Jaroslav Cibulka	209	Svein Håvard Stokka	284
Jesús Zambrano	48	Sveinung Sund M.	188, 196
Joachim Lundberg	137, 157, 162, 168	Thomas Berg Iversen	188, 196
Jolanta Baczkiewicz	121	Thomas Øyvang	355
Jonathan Johnsplass	157	Tiina Komulainen	203
Jørgen Bohlin	188, 196	Tormod Drengstig	284, 343
Khim Chhantyal	385, 350	Turo Välikangas	121
Kim André Jakobsen	284	Valentyna Splavska	368
Kim Sørensen	13, 121, 234	Viktor Leek	317
Kjell-Arne Solli	97	W.K. Hiromi Ariyaratne	227
		Wenche Hennie Bergland	114

Numerical investigation of conjugate heat transfer and flow performance of a fin and tube heat exchanger with vortex generators

Shobhana Singh Kim Sørensen

Department of Energy Technology, Aalborg University, Pontoppidanstræde 111, 9022, Aalborg, Denmark,
{ssi,kso}@et.aau.dk

Abstract

Vortex generator is considered as an effective device for augmentation of the thermal-hydraulic performance of a heat exchanger. The aim of present study is to examine the influence of vortex generators on a double fin and tube heat exchanger performance. Vortex generator of rectangular winglet type is chosen and investigated at different angles of attack 0° , -10° and -20° with the flow direction. Three-dimensional numerical model is developed and simulations are performed for a Reynolds number range $5000 \leq Re \leq 11000$ taking conjugate heat transfer into account. The heat transfer and pressure loss characteristics are determined and analyzed for an in-line configuration of a fin and tube heat exchanger. In order to evaluate the enhancement in the performance on an equitable basis, the heat exchanger with plain fin surface is considered as a reference design. Results show that the angle of attack of a vortex generator has a significant impact on the volume goodness factor, and enhance the thermal performance of a fin and tube heat exchanger in comparison to the design with plain fin. The vortex generator at an angle of attack -10° is found to perform superior over the Reynolds number range studied. At $Re = 5000$, the vortex generator with an angle of attack -10° increases the volume goodness factor by 32% with respect to the baseline heat exchanger design.

Keywords: Fin and tube heat exchanger, vortex generator, conjugate heat transfer, volume goodness factor

1 Introduction

Fin and tube heat exchangers are one of the most commonly used thermal engineering systems due to the larger heat transfer area provided by the extended surface integrated tubes. In the process industry, vortex generators (VGs) are being increasingly incorporated in modern multi-functional heat exchangers to enhance heat and mass transfer and to increase energy efficiency (Ghanem et al. , 2013). The enhancement by vortex generators shows a great promise in reducing the size of heat exchangers (Biswas et al. , 1994). They are integrated into a surface by means of embossing, stamping, punching, or by other attachment processes.

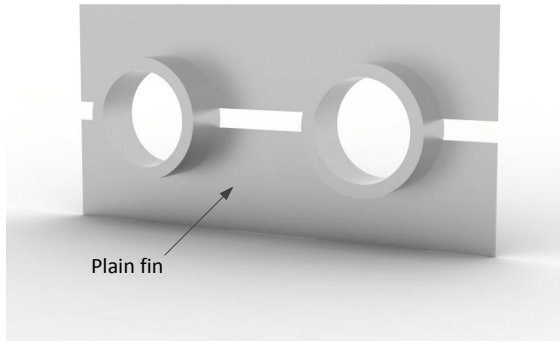
Wide range of application and design flexibility have made vortex generators an effective mode of performance enhancement. In fin and tube heat exchanger often negligible heat transfer takes place in the downstream of the circular tube due to a low velocity fluid which can be enhanced by several hundred percent by placing VG in the wake region behind the tubes (Biswas et al. , 1994; Joardar and Jacobi , 2008). Several experimental and numerical studies on different configurations of VGs have been carried out over the last two decades (Turk and Junkhan , 1986; Joardar and Jacobi , 2008; Tiggelbeck et al. , 1992, 1993; Jacobi and Shah , 1995; Jang et al. , 2013) including fin and tube heat exchangers (Fiebig , 1995; Fiebig et al. , 1994, 1993). However, most of the studies are commonly based on convective heat transfer analysis.

In majority of engineering applications, for example, waste heat recovery, heating and cooling, aerospace engineering etc., physical phenomena usually combines both heat transfer in solid and fluids. For accurate predictions of improved performance for a given application, numerical simulations with coupled temperature fields in solids and fluids are essential. It is pragmatic in testing different design configurations with vortex generators. Due to the lack of sufficient data on the impact of VGs on doubled fin and tube heat exchangers, present study work aims to investigate the effect of VGs with different angles of attack (α) on the heat transfer and pressure loss characteristics. The analysis is performed by developing a three-dimensional (3D) numerical model that includes conjugate heat transfer in solid and fluid domains simultaneously.

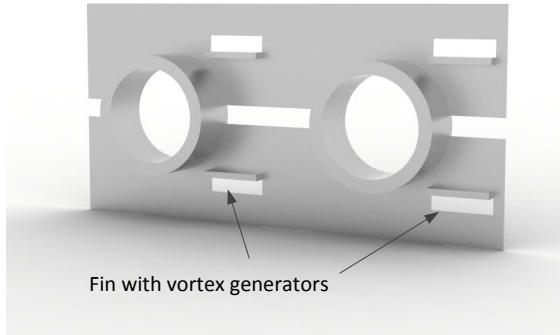
2 Numerical Model

2.1 Computational Geometry: Fin and Tube Heat Exchanger with Vortex Generators

Figure 1a shows a double fin and tube heat exchanger with plain fin and with VGs as investigated in the present study. The double fin and tube heat exchanger is generally designed for a wide range of applications such as marine exhaust gas boilers for waste heat recovery from coal-fired boilers (Singh et al., 2016a,b, 2017) due



(a) Plain fin



(b) Fin with vortex generator

Figure 1. Illustration of fin and tube heat exchanger design

to good anti-wear and anti-fouling performance, compact design, stability (Chen and Lai, 2012; Jin et al., 2013, 2016). To investigate the effectiveness of VGs, rectangular winglet vortex generator (RWVG) are selected considering their heat transfer enhancement performance better than delta winglets (Li et al., 2015). Two pairs of RWVGs each of height 0.004 m and length 0.019 m are placed longitudinally on the fin surface in the direction of the flow. The rectangular winglets can be easily manufactured by punching out off the fin surface at an angle of 90° as shown in Fig.1b. Figure 2 illustrates the design details of the rectangular vortex generator at an angles of attack α with the incoming flow direction. Table 1 lists the design parameters of the heat exchanger considered in the study.

2.2 Governing Equations

Based on flow velocity and Reynolds number (≥ 5000), Shear Stress Transport (SST) turbulence model is adopted to simulate the fluid flow in the domains of interest (Menter, 1994; Menter et al., 2003; Woelke, 2007).

The governing equations of mass, momentum, and

Table 1. Dimensions of the computational geometry simulated in the present study

Parameter	Value
Length of the fin, L_f	0.145 m
Width of the fin, W_f	0.032 m
Thickness of the fin base, δ_f	0.002 m
Width of the gap between fins, d_f	0.006 m
Fin pitch, p_f	0.015 m
Inner diameter of the tube, D_i	0.030 m
Outer diameter of the tube, D_o	0.038 m
Tube pitch, p_t	0.075 m
Length of the gas domain, L_g	0.150 m
Width of the gas domain, W_g	0.075 m
Thickness of the gas domain, $\frac{p_f}{2}$	0.0075 m
Length of RWVG, l_{VG}	0.019 m
Height of RWVG, h_{VG}	0.004 m
Thickness of RWVG, δ_{VG}	0.002 m
Angle of attack of RWVG, α	$0^\circ, -10^\circ, -20^\circ$

energy conservation can be written as:

$$\frac{\partial \rho}{\partial t} + \nabla(\rho \mathbf{U}) = 0 \quad (1)$$

$$\frac{\partial(\rho \mathbf{U})}{\partial t} + \nabla(\rho \mathbf{U} \otimes \mathbf{U}) - \nabla(\mu_{eff} - \nabla \mathbf{U}) = -\nabla p + \nabla(\mu_{eff} - \nabla \mathbf{U})^T + \mathbf{F} \quad (2)$$

where \mathbf{U} is the averaged flow velocity field [m/s], ρ is the density [kg/m^3], \otimes is the outer vector product, p is the pressure [Pa], \mathbf{F} is the total body force [N/m^3], μ_{eff} is the effective viscosity coefficient [$Pa.s$].

$$\frac{\partial(\rho C_p T)}{\partial t} + \nabla(\rho C_p \mathbf{U})T = -\nabla(\mathbf{q}) + \tau : \nabla \mathbf{U} - p \nabla \mathbf{U} + \mathbf{Q} \quad (3)$$

$$\frac{\partial(\rho C_p T)}{\partial t} = -\nabla(\mathbf{q}) + \mathbf{Q} \quad (4)$$

where C_p is the specific heat capacity at constant pressure [J/kgK], \mathbf{q} is the heat flux by conduction [W/m^2], $\tau : \nabla \mathbf{U}$ is the viscous heating term and is assumed negligible, \mathbf{Q} is the heat source [W/m^3].

The transport equations of SST model in terms of k and ω can be written as:

$$\frac{\partial(\rho \omega)}{\partial t} + \nabla(\rho \omega \mathbf{U}) = \nabla \left[\left(\mu + \frac{\mu_t}{\sigma_{\omega,1}} \right) \nabla(\omega) \right] + \gamma_2 \left[2\rho S_{ij} S_{ij} - \frac{2}{3} \rho \omega \frac{\partial U_i}{\partial x_j} \delta_{ij} \right] - \beta_2 \rho \omega^2 + 2 \frac{\rho}{\sigma_{\omega,2} \omega} \frac{\partial k}{\partial x_k} \frac{\partial \omega}{\partial x_k} \quad (5)$$

where ω is the turbulent frequency [$1/s$] and $\mu_t = \frac{\rho k}{\omega}$ is the eddy viscosity.

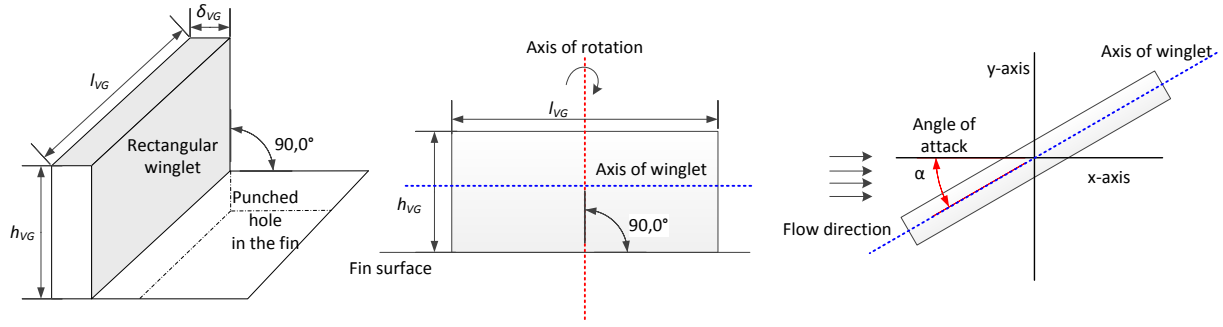


Figure 2. Schematic illustration of rectangular winglet vortex generator

$$\frac{\partial(\rho k)}{\partial t} + \nabla(\rho k \mathbf{U}) = \nabla \left[\left(\mu + \frac{\mu_t}{\sigma_k} \right) \nabla(k) \right] + P_k - \beta^* \rho k \omega \quad (6)$$

where k is the rate of turbulent kinetic energy [m^2/s^2].

The rate of production of turbulent kinetic energy which is given as:

$$P_k = \left(2\mu_t S_{ij} \cdot S_{ij} - \frac{2}{3} \rho k \frac{\partial U_i}{\partial x_j} \delta_{ij} \right) \quad (7)$$

2.3 Solution Procedure

In most of the numerical problems, Computational Fluid Dynamics (CFD) based tool solves the governing transport equations faster under specified conditions and predicts the physical processes such as fluid flow, heat transfer etc. with reliable accuracy. In the present work, Ansys CFX v.17.1.(Ansys, 2017) is used to develop the finite volume model and simulate steady state flow with coupled conjugate heat transfer. Control surface approach is used to perform the coupling between the fluid and solid grid interface. To gain the time savings and reduced computational power, symmetric boundary conditions are employed as shown in the Fig.3. The computational geometry has faces set as a plane of symmetry and periodic inlet and outlet. The boundary conditions at different faces of the computational domain are described in Table 2. Due to a high complexity design including VGs, unstructured mesh is generated with a fine boundary layers. Meshes with ≈ 7000000 and ≈ 13000000 average number of grid elements are selected for plain fin and fin with VG to achieve the reliable numerical solution, respectively. The convergence is obtained when the maximum residual of objective variables (i.e. temperature, pressure and velocity components) accomplished 10^{-4} .

2.4 Model Validation

In order to validate the model, the Nusselt number and Euler number values from the correlations of Chen et al.

Table 2. Boundary conditions used to solve the numerical model

Boundary	Conditions
Periodic	$m = \dot{m}_{in}$
Wall	$\mathbf{U} \cdot \mathbf{n} = 0; k = 0;$ $[\lim_{\omega \rightarrow 0} \omega = \frac{6\mu}{\rho \beta l_{w,2}}]$
Symmetry	$\mathbf{U} \cdot \mathbf{n} = 0; \nabla \cdot k = 0; \nabla \cdot \omega = 0$
Inner tube wall	$T = T_w$
Operating	Conditions
Gas temperature, T_{in}	573.15 K
Inner tube wall temperature, T_w	453.15 K

(2014) are compared with the present numerical results as shown in Fig.4. The standard deviation of predicted values of Nusselt and Euler numbers from the values obtained from the correlations values vary from 0.004 to 5.150, respectively. The deviation can be justified by the assumptions made in model parameters in addition to the experimental error in developing the correlations. The lower standard deviation in the numerical values indicates the reliability and validity of the computational model under given operating conditions.

3 Data Analysis and Performance Evaluation

In this section, the heat transfer and flow characteristics are defined to evaluate the performance enhancement in the fin and tube heat exchanger by RWVGs.

Reynolds number in the present study is determined as:

$$Re = \frac{u_{in} D_o}{\nu} \quad (8)$$

where Re is the Reynolds number [-], u_{in} is the inlet flow velocity [m/s], D_o is the outer tube diameter [m] and ν is the kinematic viscosity of the air [m^2/s].

The overall average heat transfer coefficient of the fin and tube heat exchanger is calculated as:

$$\bar{h} = \frac{Q}{A_t \Delta T_{lm}} \quad (9)$$

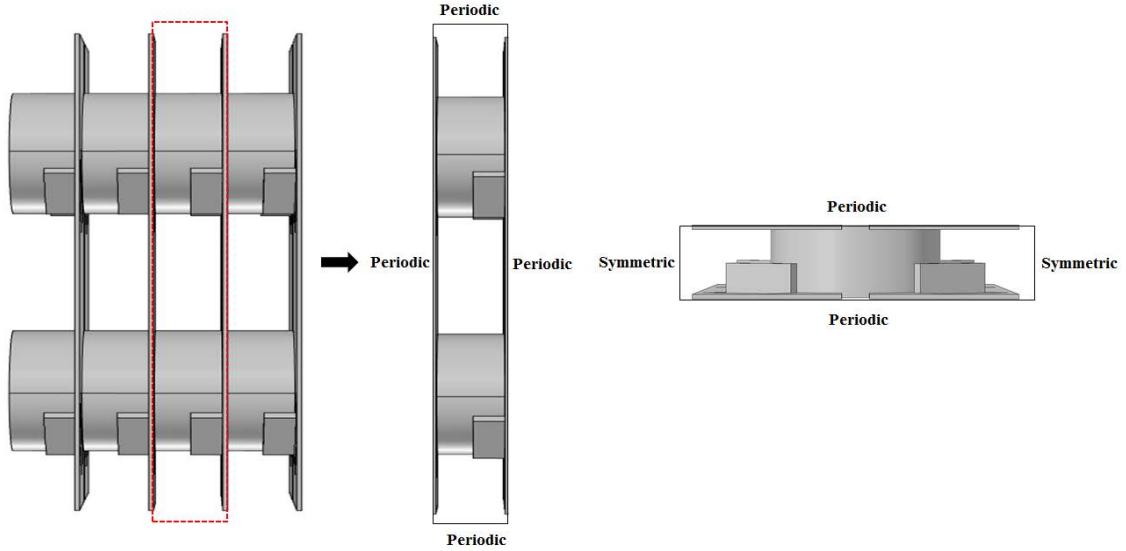


Figure 3. Computational geometry simulated in the present study

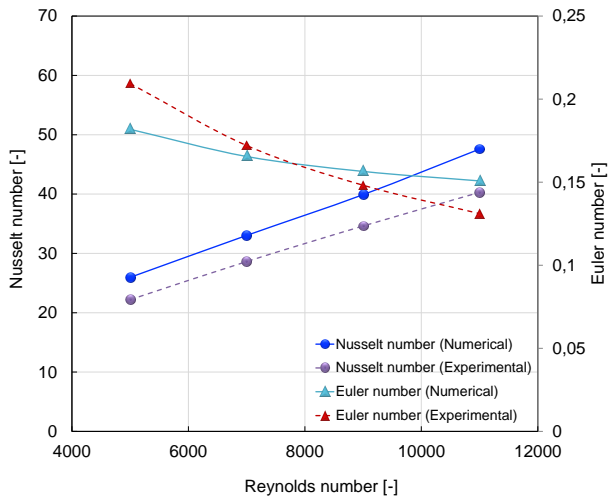


Figure 4. Numerical model validation based Nusselt number and Euler number correlations

where \bar{h} is the overall heat transfer coefficient [$W/m^2 \cdot K$], A_t is the total heat transfer area [m^2], and Q is the total heat transferred calculated as:

$$Q = \dot{m}C_p(T_{in} - T_{out}) \quad (10)$$

where \dot{m} is the mass flow rate [kg/s], C_p is the specific heat capacity [$J/kg \cdot K$], T_{in} and T_{out} are the mass averaged air temperature at the inlet and outlet [K]. ΔT_{lm} is the logarithmic mean temperature difference which is calculated as:

$$\Delta T_{lm} = \frac{(T_{in} - T_w) - (T_{out} - T_w)}{\ln\left(\frac{T_{in} - T_w}{T_{out} - T_w}\right)} \quad (11)$$

where T_w is the inner tube wall temperature [K].

In order to determine heat transfer characteristic, average Nusselt number which is calculated as:

$$\overline{Nu} = \frac{\bar{h}D_o}{k} \quad (12)$$

Colburn- j factor is calculated based on average Nusselt number and is expressed as:

$$j = \frac{\overline{Nu}}{RePr^{1/3}} \quad (13)$$

where ρ is the density of the fluid [kg/m^3], Pr is the Prandtl number [-], and \overline{Nu} is the

In addition to the heat transfer characteristics, pressure losses are evaluated using the Euler number, Eu and the friction factor, f as:

$$Eu = \frac{\Delta p}{\frac{1}{2}\rho u_{max}^2} \quad (14)$$

$$f = \frac{\Delta p}{\frac{1}{2}\rho u_{in}^2} \times \frac{D_o}{L_g} \quad (15)$$

where, Δp is the pressure loss [Pa] and L_g is the length of the gas domain in the computational geometry [m]

Due to a number of possible enhancement methods, operating conditions and available designs, comparison of performance on equitable basis can be challenging. In the present study, a factor called *Volume goodness factor* as proposed by Kays and London (1998) is utilized to predict the overall performance. It considers simultaneous effect of heat transfer and pressure loss and, therefore, useful in several practical applications.

$$\frac{j}{f^{1/3}} = \frac{\frac{\overline{Nu}}{RePr^{1/3}}}{\left(\frac{\Delta p}{\frac{1}{2}\rho u_{in}^2} \times \frac{D_o}{L_g}\right)^{1/3}} \quad (16)$$

4 Results and Discussion

4.1 Heat Transfer Enhancement

The influence of angle of attack (α) on Nusselt number can be seen in Fig.5a. It is clear that heat exchanger with RWVG has higher Nusselt number than that of baseline plain fin surface which increases with a increase in Reynolds number at a given α . VGs induce stronger vortical fluid flow due to which heat transfer coefficient becomes higher, thereby, augments the heat transfer between the fluid and surface. It is observed that Nusselt number increases as α varies from 0° to -20° , however, the increment becomes insignificant as α goes higher than 0° .

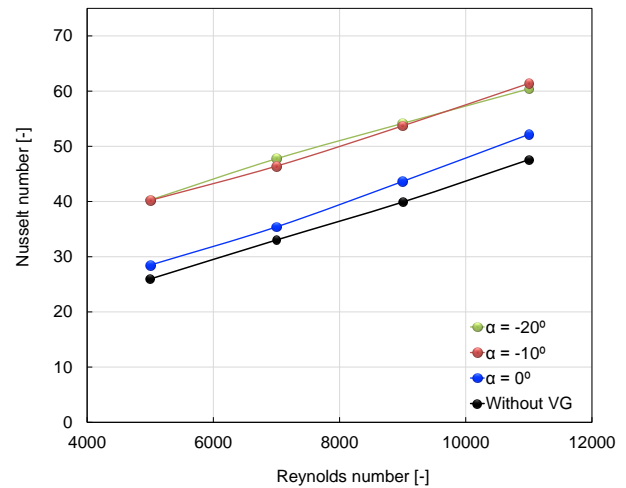
To make a rational comparison between the heat transfer performance at different α , Colburn- j factor normalized with the baseline plain fin value is plotted in Fig.5b. It can be seen that adding RWVG can enhance the heat transfer by up to 55% at a given Reynolds number. Moreover, it is interesting to note that Colburn- j factor ratio of fins with RWVG at $\alpha = -10^\circ$ and $\alpha = -20^\circ$ decreases as the Reynolds number increases while remains more or less constant at $\alpha = 0^\circ$ over the Reynolds number range. The results indicate that RWVGs in double fin and tube heat exchanger tend to loose their advantage relative to baseline plain fin at higher Reynolds number.

4.2 Induced Flow Loss

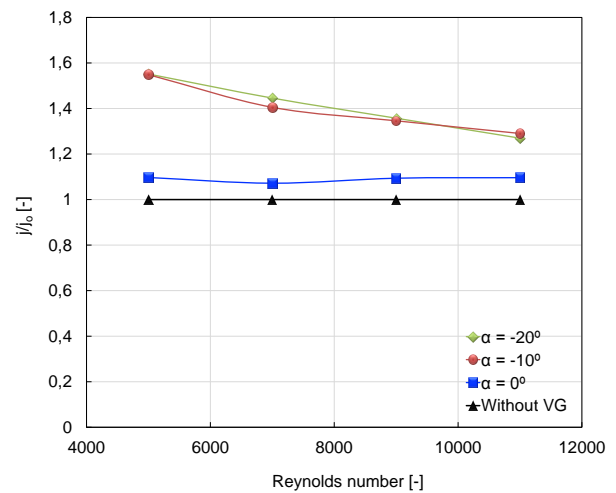
Enhancement in heat transfer in most of the applications is accompanied with a penalty of pressure loss. To account for this penalty, the Euler number with a different angle of attack is plotted against Reynolds number in Fig. 6a. The figure shows that Euler number increases as α vary from 0° to -20° . At $\alpha = -20^\circ$, Euler number is the highest which is due to the increased fluid velocity and consequently large pressure loss. The RWVG with $\alpha = 0^\circ$ performs nearly similar to the baseline plain fin design.

Another factor called friction factor (f) is evaluated using Eq.15. Figure 6b compares the normalized friction factor at different angles of attack to the baseline plain fin design. It can be seen that friction factor ratio remains nearly constant over the entire range of Reynolds number, however, fins with RWVGs have higher friction factor than baseline plain fin and the highest at $\alpha = -20^\circ$. At $\alpha = -20^\circ$ and $Re = 11000$, friction factor is 20% higher than that of baseline plain fin design. It is demonstrated by the results that adding RWVG to the fin surface increases the pressure loss which certainly is a disadvantage to the overall performance.

It is clear from the results that the angle of attack of RWVG has a significant impact on thermal and pressure loss characteristics of a fin and tube heat exchanger. It is, therefore, essential to analyze both characteristics together. In the present study, the overall performance is evaluated using Volume goodness factor from Eq.16.



(a) Nusselt number

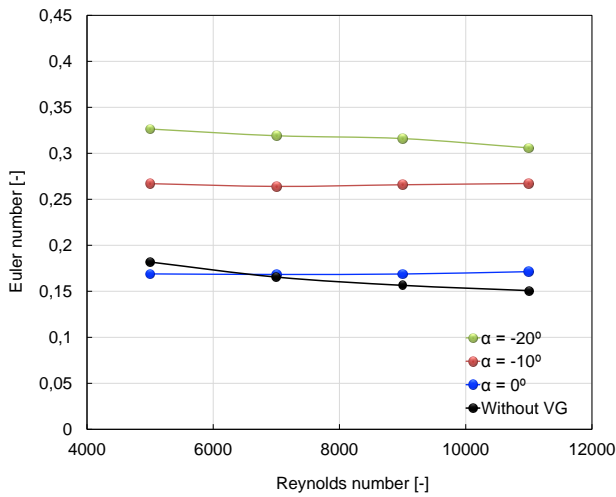


(b) Colburn j factor

Figure 5. Heat transfer characteristics with RWVG at different angle of attack

Figure 7 compares the factor with the plain fin factor as a reference. it is found that RWVG at $\alpha = -10^\circ$ has higher volume goodness factor followed by $\alpha = -20^\circ$ over the entire range of Reynolds number in this study which indicates that $\alpha = -10^\circ$ performs better in comparison to RWVG at other angles of attack when both heat transfer and pressure losses are considered together. The RWVG at $\alpha = -10^\circ$ and $Re = 5000$ has 32% higher volume goodness factor than that of conventional plain fin surface.

It is important to emphasize that the overall performance of the heat exchanger with RWVG at $\alpha = -20^\circ$ and $\alpha = -10^\circ$ decreases as the Reynolds number increases which indicate that the advantage of



(a) Euler number

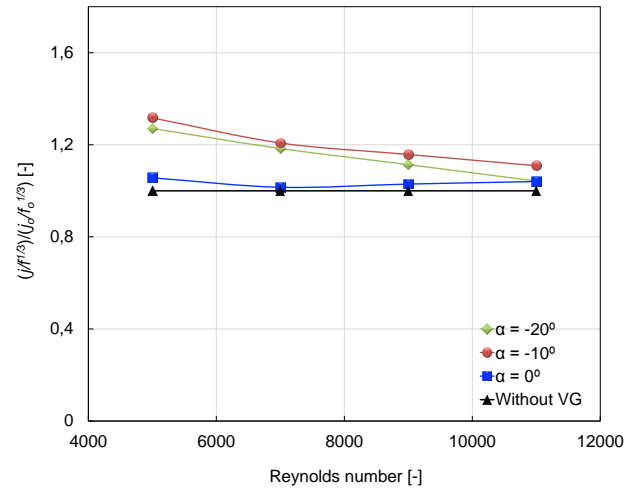
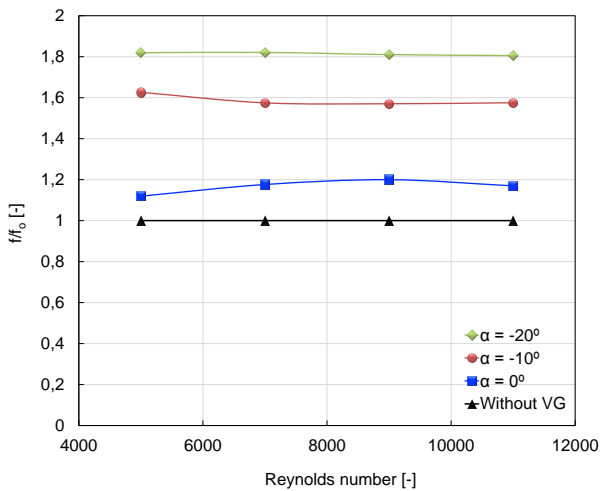


Figure 7. Overall performance comparison RWVG at different angle of attack



(b) Friction factor

Figure 6. Pressure loss evaluation with RWVG at different angle of attack

using RWVG at these angles of attack becomes less useful for higher Reynolds number. This is due to relatively lower heat transfer and higher pressure loss at higher Reynolds number (Figs.5b and 6b). On the other hand, performance improvement by RWVG at $\alpha = 0^\circ$ is noticed insignificant and nearly constant at all Reynolds numbers.

A larger value of *Volume goodness factor* leads to reduced heat exchanger volume and weight which is desirable in most of the practical applications. Adding RWVG at $\alpha = -10^\circ$ in the double fin and tube heat exchanger can not only increase the overall performance but also fulfills the light weight heat exchanger demands in a number of applications.

5 Conclusion

Performance enhancement using RWVGs in the double fin and tube heat exchanger is investigated numerically in the present study. The influence of different angles of attack of RWVG on heat transfer and pressure loss characteristics in relation to baseline plain fin design is demonstrated and discussed. The study can be concluded with following outcomes:

- The RWVGs significantly influence the thermal performance over the investigated range of Reynolds number i.e. $5000 \leq Re \leq 11000$. In reference to the reference design with plain fin, thermal performance is enhanced by up to 55% by RWVG with an angle of attack at $\alpha = -20^\circ$.
- It is interesting to note that beyond $\alpha = -10^\circ$, the angle of attack does not show significant improvement in thermal performance and performs similarly to $\alpha = -10^\circ$.
- As the angle of attack of RWVG varies from 0° to -20° , the pressure loss also increases. However, the trend remains more or less same over the entire range of Reynolds number studied.
- The overall performance enhancement is evaluated by comparing the volume goodness factor. Under the given operating conditions, the vortex generator at an angle of attack -10° is found to enhance the overall performance by up to 32%, thus furnishes the best performed double fin and tube heat exchanger design.
- The present investigation is useful not only in enhancing the overall performance of a double fin

and tube heat exchanger but also directs the future studies to limit the range of angle of attack of VGs while focusing on the VG location and other design parameters.

References

- G. Biswas, N.K. Mitra, M. Fiebig. Heat transfer enhancement in fin-tube heat exchangers by winglet type vortex generators, *International Journal of Heat and Mass Transfer*, Volume 37, Issue 2, January 1994, Pages 283-291
- A. Ghanem, C. Habchi, T. Lemenand, D. Della Valle, H. Peerhossaini, "Energy efficiency in process industry — High-efficiency vortex (HEV) multifunctional heat exchanger", *Renewable Energy*, vol. 56, pp. 96-104, 2013.
- A. Joardar, A.M. Jacobi, Heat transfer enhancement by winglet-type vortex generator arrays in compact plain-fin-and-tube heat exchangers, *International Journal of Refrigeration*, Volume 31, Issue 1, January 2008, Pages 87-97.
- S. Tiggelbeck, N.K. Mitra, M. Fiebig, "Flow Structure and Heat Transfer in a Channel with Multiple Longitudinal Vortex Generators", *Experimental Thermal and Fluid Science*, vol. 5, pp. 425-436, 1992.
- S.T. Tiggelbeck, N.K. Mitra, M. Fiebig, Experimental investigations of heat transfer enhancement and flow losses in a channel with double rows of longitudinal vortex generators, *Int. J. Heat Mass Transfer* 36 (1993) 2327–2337.
- A.M. Jacobi, R.K. Shah, Heat transfer surface enhancement through the use of longitudinal vortices: a review of recent progress, *Exp. Therm. Fluid Sci.* 11 (1995) 295–309.
- Jiin-Yuh Jang, Ling-Fang Hsu, Jin-Sheng Leu. Optimization of the span angle and location of vortex generators in a plate-fin and tube heat exchanger. *International Journal of Heat and Mass Transfer* 67 (2013) 432–444.
- M. Fiebig. Embedded vortices in internal flow: heat transfer and pressure loss enhancement”, *International Journal of Heat and Fluid Flow* 1995; 16: 376–388.
- M. Fiebig, A. Valencia, N.K. Mitra. Local heat transfer and flow losses in fin-and-tube heat exchangers with vortex generators: A comparison of round and flat tubes, *Experimental Thermal and Fluid Science* 1994; 8(1): 35-45.
- M. Fiebig, A. Valencia, N.K. Mitra. Wing-type vortex generators for fin-and-tube heat exchangers, *Exp. Therm. Fluid Sci.* 1993; 7: 287–295.
- Chen HT and Lai JR. Study of heat-transfer characteristics on the fin of two-row plate finned-tube heat exchangers. *International Journal of Heat and Mass Transfer* 2012; 55: 4088-4095.
- Jin Y, Tang GH, He YL and Tao WQ. Parametric study and field synergy principle analysis of H-type finned tube bank with 10 rows. *International Journal of Heat Mass Transfer* 2013; 60: 241-251.
- Jin Y, Yu ZQ, Tang GH, He YL and Tao WQ. Parametric study and multiple correlations of an H-type finned tube bank in a fully developed region. *Numerical Heat Transfer, Part A: Applications* 2016; 70(1): 64-78.
- A.Y. Turk, and G.H. Junkhan, “Heat Transfer Enhancement Downstream of Vortex Generators on a Flat Plate”, *Proceedings of the Eighth International Heat Transfer Conference*, 6, pp. 2903–2908, (1986).
- Chen H, Wang Y, Zhao Q, Ma H, Li Y and Chen Z. Experimental Investigation of Heat Transfer and Pressure Drop Characteristics of H-type Finned Tube Banks. *Energies* 2014; 7: 7094-7104.
- Kays, W. M., London, A. L., *Compact Heat Exchangers*, Reprint 3rd ed., Krieger Publishing Company, Malabar, Fla., USA, 1998.
- Li, L.; Du, X.; Zhang, Y.; Yang, L.; yang, Y. Numerical simulation on flow and heat transfer of fin-and-tube heat exchanger with longitudinal vortex generators. *Int. J. Thermal Sci.* 2015, 92, 85–96.
- Menter FR. Two-Equation Eddy-Viscosity Turbulence Models for Engineering Applications. *AIAA Journal* 1994; 38(8): 1598-1605.
- Menter FR, Kuntz M and Langtry R. Ten years of industrial experience with the SST Turbulence Model. *Turbulence Heat and Mass Transfer* 2003; 4.
- Woelke M. Eddy Viscosity Turbulence Models employed by Computational Fluid Dynamic. *Prace Instytutu Lotnictwa* 2007; 92-113.
- Singh S., Sørensen K., Condra T.J. Influence of the degree of thermal contact in fin and tube heat exchanger: A numerical analysis. *Applied Thermal Engineering* 2016; 107(25): 612–624.
- Singh S., Sørensen K., Condra T.J. Parametric CFD Analysis to Study the Influence of Fin Geometry on the Performance of a Fin and Tube Heat Exchanger. The 9th Eurosim Congress on Modelling and Simulation. EUROSIM 2016, 12 - 16 September 2016, Oulu Finland.
- Singh S., Sørensen K., Condra, T.J. 2017. Implications of fin profiles on overall performance and weight reduction of a fin and tube heat exchanger. *App. Therm. Eng.* 2017; 115: 962–976.
- ANSYS CFX, Inc. High-performance computational fluid dynamics (CFD) software tool, <http://www.ansys.com/products/fluids/ansys-cfx>.

Comparison of elastic vs. inelastic penstock model using OpenModelica

Vytvytskyi Liubomyr Lie Bernt

Department of Electrical engineering, Information Technology and Cybernetics, University College of Southeast Norway, Porsgrunn, Norway, {Liubomyr.Vytvytskyi, Bernt.Lie}@usn.no

Abstract

The possibility for modelling and simulating hydropower systems as accurately as possible take an important role in order to develop a control structure and to make efficient analysis tools for testing a designed controller for stability and performance in different operating regimes. Both the simulation time for such models as well as the accuracy are important.

A high head hydropower system is considered for this study. The pipe with the main part of the height drop is known as pressure shaft or penstock, and it can be modeled with two levels of accuracy which have been compared in this studying. A simple model with one nonlinear ODE considers inelastic walls of the penstock and incompressible water. A more realistic model for large pressure variations assumes a penstock with elastic walls and compressible water column in the penstock. This more detailed model of a penstock is described with two nonlinear PDEs which have been solved using the Kurganov-Petrova scheme.

Comparing results from these two models it can be concluded that the simple ODE model shows by and large the same results as the PDE model with just slightly smoothed dynamics. Obviously, the simulation time for the inelastic penstock model is considerably smaller. Both models show reasonable results and can be further used for control synthesis and analysis. In cases where the time consumption is most important, the simple ODE model for the penstock is preferred. On the other hand, for more accurate studies the elastic/compressible model for the penstock or even for other waterway units, such as conduit, is more useful.

The modeling part for both cases was done in OpenModelica using our own hydropower library, where all models for different units of the hydropower system have been developed and collected.

Keywords: high head hydropower, penstock/pressure shaft, Kurganov-Petrova scheme, OpenModelica

1 Introduction

1.1 Background

A transition towards more renewable energy sources is currently happening in Europe and all over the world, with increasing use of flexible hydropower plants to compensate for the highly changing production from intermittent energy sources such as wind and solar irradiation. Flexible hydropower plants involves pumping water up into reservoirs during surplus of intermittent power, and high head storage is the most efficient way to store such surplus power.

Around 96% of generated electricity (138 GWh) in Norway is produced by hydropower systems, which have a total capacity over 30 GW; over 1500 hydropower plants are operated¹. With these values, Norway occupies the 7th place among the hydropower producers in the world². Among the power plants, the high head hydropower plants generate more than 75% of all electricity produced from hydropower in Norway³.

In addition to hydropower plants, the number of wind power plants in Norway increase from year to year (13.4% increase in 2015 with respect to 2014⁴) due to this technology becoming cheaper and more mature. With long coast line, wind power has a huge potential for producing power in Norway⁵. On the other hand, this renewable energy source is intermittent and create considerable disturbances in the power grid. From this perspective, hydropower can be used to compensate for disturbances from the wind power.

To optimize the combination of intermittent power and stored power, the possibilities for modelling and simulating the hydropower system as accurately as possible take an important role in order to make an efficient analysis tool for testing a designed controller for stability and performance in different operating regimes (Sharefi, 2011).

¹ <http://lvk.no/LVK/Fagomrader/Vannkraftproduksjon/Nokkeltall---Oversikt-over-konsesjonssystemet-for>

² <https://snl.no/vannkraft>

³ https://no.wikipedia.org/wiki/Liste_over_vannkraftverk_i_Norge

⁴ <http://www.ssb.no/en/energi-og-industri/statistikker/elektrisitet/aar>

⁵ <http://www.vindportalen.no/Vindportalen/Vindkraft/Vindkraft-i-Norge>

1.2 Previous work

High head plants typically collect and store water in reservoirs in the mountains, with tunnels leading the relatively small flow of water down a considerable height difference to the aggregated turbine and generator. A dynamic model for such a hydropower system has been developed and studied in a previous work (Sharefi, 2011), where the Staggered grid scheme was used for discretization of a part of the model with partial differential equations (PDEs). Another scheme for discretization is the Kurganov-Petrova (KP) scheme, described in (Sharma, 2015; Kurganov & Petrova, 2007). The comparison of this KP scheme with Staggered grid for an open channel model using Matlab was done in (Vytvytskyi, et al., 2015). In (Saldamli, 2006) a Modelica extension for modeling with partial differential equations, PDEModelica, was proposed. An updated version of PDEModelica with implementation for OpenModelica was recently presented in (Silar, et al., 2017); this extension is not fully completed, though. In addition, a commercial Modelica library for hydropower system exists (Hydro Power Library from Modelon AB⁶), and has been used for modeling a high head hydropower plant in (Winkler, et al., 2011).

1.3 Overview of paper

In this work, a simple model of a hydropower system described with ordinary differential equations (ODEs) is compared with a more realistic model described with PDEs in order to find what accuracy level is needed in control synthesis. The current work uses the semi-discrete KP scheme implemented in Modelica for

solving the hyperbolic PDEs, which is a novelty compared to the commercial Hydro Power Library.

The paper is structured as follows: Section 2 gives a system description of the high head hydropower system. Section 3 consists of formulation and discretization of the model. Then simulation with validation and comparison of the different model complexities are described in Section 4. Finally, discussion and conclusions are given in Section 5.

2 System description

A typical structure for the high head hydropower plant is depicted in Figure 1⁷. Here, the water is transported from a reservoir, where it is stored, through a tunnel known as intake race / conduit / headrace closer to the powerhouse where the turbine and generator is installed. The conduit can have considerable length, normally with a small slope.

After the conduit, the water flows down with a steep slope and a relatively small flow rate to the turbine through a pipe known as the penstock or pressure shaft. There is large pressure change in this pipe due to the big height difference. At the point where the penstock is connected to the intake race, a surge tank may be installed to reduce the water hammer pressure variation and keep the mass oscillation within limits. This surge tank can be constructed as a pipe and is then denoted a surge shaft, but can also be variations such as an open or closed reservoir.

After the turbine, the water can flow directly to a downstream lake or river, often denoted tail water, or the

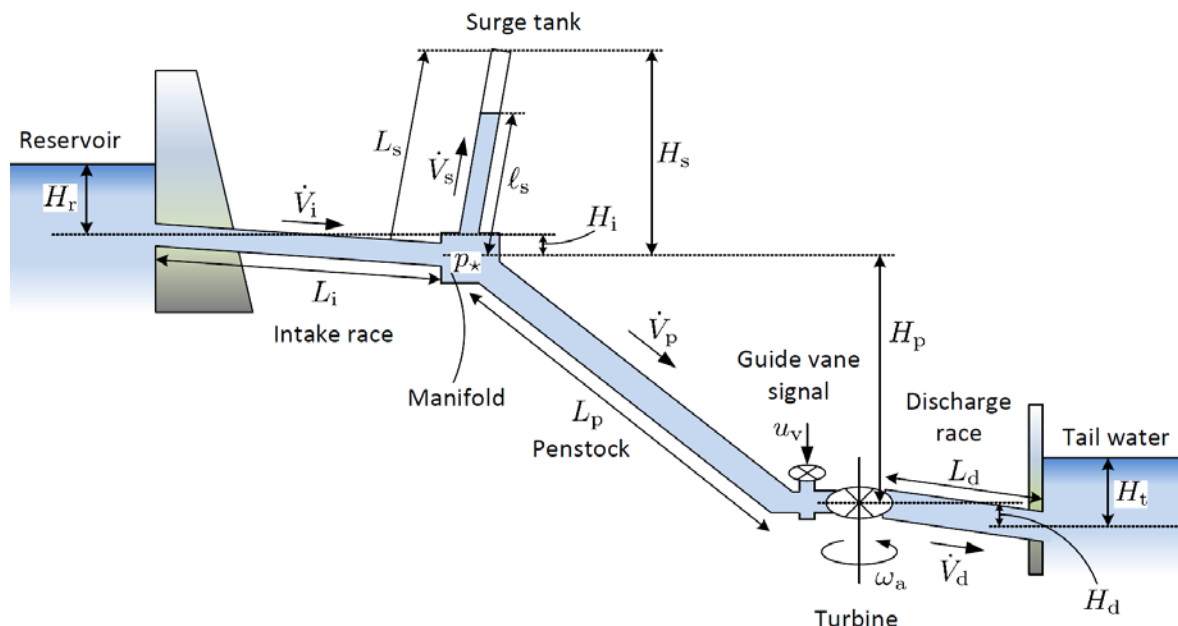


Figure 1. Structure of the high head hydropower plant.

⁶ <http://www.modelon.com/products/modelica-libraries/hydro-power-library>

⁷ Agu, C., E., Vytvytskyi, L., Lie, B. (2016) Project, FM1015 Modelling of Dynamic Systems. University College of Southeast Norway, Porsgrunn, Norway.

water can flow through a discharge race if the powerhouse is situated some distance from the tail water. Normally the turbine is installed below the level of the tail water in order to increase the pressure at the outlet of the turbine to reduce the possibility of cavitation.

Two types of turbines are common for high head hydropower systems. When the height difference is large (300 – 4000 m), a Pelton turbine is used with relatively small flow rate (<30 m³/s). Alternatively, with smaller height differences and large flow rates, Francis turbines are preferred. In our simulations, a Francis turbine is used, and the control of the flow rate through the turbine is done by manipulating the guide vane.

The turbine is rotating an axis which also holds the rotor of the generator producing electricity to the power grid. Normally, a synchronous generator is used.

2.1 Geometry

For simulations in this paper, the data from the Sundsbarm hydropower plant in Telemark, Norway is used with data provided in (Winkler, et al., 2011), see Table 1 and Table 2.

Table 1. The waterway geometry of Sundsbarm hydropower plant.

Waterway unit	Height difference, m	Length, m	Diameter, m
Reservoir	48	–	–
Conduit	23	6600	5.8
Penstock	428.5	600	3
Surge tank	120	140	3.4
Discharge race	0.5	600	5.8
Tail water	5	–	–

Table 2. The turbine geometry of Sundsbarm hydropower plant.

Turbine type	Nominal head, m	Nominal flow rate, m ³ /s	Nominal power, MW
Francis	460	24.3	104.4

3 Modeling and discretization

3.1 Model presentation

Models for all of the waterway units can be described with mass and momentum balances. For the mechanical part (turbine with aggregate), a simplified energy balance is used assuming that the turbine behaves as a simple valve. All of these models for different units of

⁸ Modelica® is a non-proprietary, object-oriented, equation based language to conveniently model complex physical systems. <https://www.modelica.org>

⁹ OpenModelica is an open-source Modelica-based modeling and simulation environment intended for

the hydropower system have been developed and collected for our own hydropower Modelica⁸ library that can be used in either OpenModelica⁹ or Dymola¹⁰.

In this paper, a more detailed description is presented for the models that will be compared, namely a simplified pipe (tunnel) model that can be used for the penstock and a more realistic model with compressible water and elastic walls of the penstock.

3.1.1 Waterway pipe (tunnel)

In some of the waterway units such as conduit, there are only small pressure variations due to the small slope angle (height difference between inlet and outlet of the component). That is why the model for these units can be simplified by considering incompressibility of the water and inelasticity of the walls. A sketch of the pipe with all needed terms for modeling is shown in Figure 2.

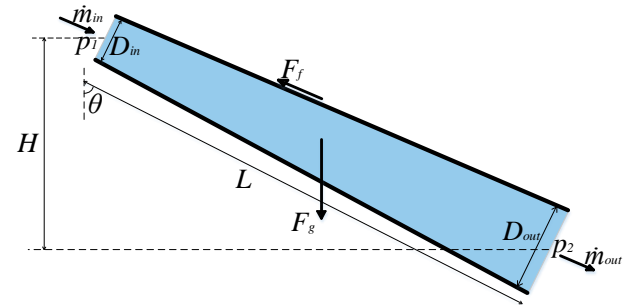


Figure 2. Model for flow through a pipe.

In the case of incompressible water, mass in the filled pipe is constant, and:

$$\frac{dm}{dt} = \dot{m}_{in} - \dot{m}_{out} = 0 \quad (1)$$

Here, the mass of the water in the pipe is $m = \rho V = \rho L \bar{A}$, where ρ is the water density, V – the volume of the water in the pipe, L – the length of the pipe and \bar{A} – the averaged cross section area of the pipe that defined from averaged pipe diameter \bar{D} . The inlet and outlet mass flow rates are equal with $\dot{m}_{in} = \rho \dot{V}_{in}$ and $\dot{m}_{out} = \rho \dot{V}_{out}$ respectively, where $\dot{V}_{in} = \dot{V}_{out}$ – the inlet and outlet volumetric flow rates in the pipe.

The momentum balance for this simplified model can be expressed as:

$$\frac{dM}{dt} = \dot{M}_{in} - \dot{M}_{out} + F_p + F_g + F_f \quad (2)$$

Here, the momentum of the water in the pipe is $M = mv$, where v is the average water velocity and can be define as $v = \dot{V} / \bar{A}$. The inlet and outlet momentum flow

industrial and academic usage.

<https://www.openmodelica.org>

¹⁰ Dymola is a commercial complete tool for modeling and simulating integrated and complex systems; is based on the Modelica open standard language.

<http://www.modelon.com/products/dymola>

rates are $\dot{M}_{in} = \dot{m}_{in}v_{in}$ and $\dot{M}_{out} = \dot{m}_{out}v_{out}$ respectively, where $v_{in} = \dot{V}_{in}/A_{in}$ and $v_{out} = \dot{V}_{out}/A_{out}$ are the velocities in the inlet and outlet of the pipe respectively and are equal in a case with constant diameter of the pipe ($A_{in} = A_{out}$). F_p – the pressure force, due to the difference between the inlet and outlet pressures p_1 and p_2 and can be calculated as follows: $F_p = A_{in}p_1 - A_{out}p_2$. There is also gravity force that is defined as $F_g = mg \cos \theta$, where g – the gravitational acceleration and θ – angle of the pipe slope that can be defined from ratio of height difference and length of the pipe. The last term in the momentum balance is friction force, which can be calculated as $F_f = -\frac{1}{8}L f_D \pi \rho \bar{D} |v|$ using Darcy friction factor f_D .

3.1.2 Penstock with elastic walls and compressible water

Unlike the conduit, the penstock has considerable pressure variation due to a considerable height drop. Thus, to make model for the penstock more realistic, compressible water and elastic walls of the penstock should be taken into account. To express the compressibility/elasticity, some compressibility coefficients which show the relationship between pressure, water density and pipe inner radius, are used.

According to (Sharefi, 2011), isothermal compressibility β_T is defined as follows:

$$\beta_T = \frac{1}{\rho} \frac{d\rho}{dp} \quad (3)$$

Here ρ and p denote density and pressure, respectively. Assuming that the isothermal compressibility is independent of the pressure, this equation can be rewritten in a way that is convenient to calculate fluid density at different pressures:

$$\rho = \rho^{atm} e^{\beta_T(p-p^{atm})} \quad (4)$$

Here p^{atm} is the atmospheric pressure and ρ^{atm} is the water density at atmospheric pressure. The relation between density and pressure from this equation can be seen in Figure 3.

Figure 3 shows fairly linear dependency of the density with respect to the pressure in the range that is normal in hydropower plants. That is why the previous equation (4) can be simplified as follows:

$$\rho \approx \rho^{atm} (1 + \beta_T(p - p^{atm})) \quad (5)$$

In the same way, the relation between pressure and pipe cross section area can be defined using equivalent compressibility coefficient β^{eq} due to the pipe shell elasticity (Sharefi, 2011); after simplification the relation looks as follows:

$$A \approx A^{atm} (1 + \beta^{eq}(p - p^{atm})) \quad (6)$$

Here A^{atm} is the pipe cross section area at atmospheric pressure.

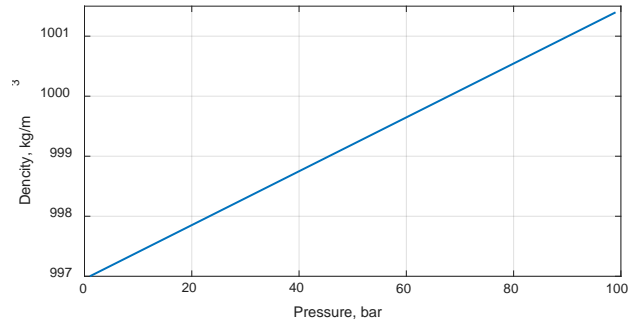


Figure 3. Variation of density with respect to pressure.

In reference to (Sharefi, 2011), it is also possible to define a linear relationship for the product of density and cross sectional area that change with pressure.

$$A \cdot \rho = A^{atm} \rho^{atm} (1 + \beta^{tot}(p - p^{atm})) \quad (7)$$

Here β^{tot} is the total compressibility due to water compressibility and pipe shell elasticity ($\beta^{tot} = \beta^{eq} + \beta_T$), and is related to the speed of sound in water inside the pipe.

Hence, using the previous equations for the relationship between density of the water, cross sectional area of the pipe, and pressure in the pipe, ODEs (1) and (2) for mass and momentum balances can be further developed into the PDEs:

$$\begin{aligned} A^{atm} \rho^{atm} \beta^{tot} \frac{\partial p}{\partial t} &= -\frac{\partial \dot{m}}{\partial x} \\ \frac{\partial \dot{m}}{\partial t} &= -\frac{\partial}{\partial x} (\dot{m}v + Ap) + \rho Ag \cos \theta \\ &\quad - \frac{1}{8} f_D \pi \rho D v |v| \end{aligned} \quad (8)$$

3.2 Model discretization

There are many discretization techniques for PDEs, but from previous work (Vytvytskyi, et al., 2015) it was observed that the well-balanced second order Kurganov-Petrova (KP) scheme shows reasonably good results for hyperbolic PDEs. The KP scheme is therefore also chosen for discretization of the model for the elastic penstock with compressible water. The detailed development of the KP scheme is shown in (Kurganov & Petrova, 2007) with some run-of-river case studies in (Sharma, 2015; Vytvytskyi, et al., 2015; Dissanayake, et al., 2016; Dissanayake, et al., 2017).

Firstly, PDEs (8) for the elastic penstock model should be presented in vector form as a standard formulation for KP scheme (Sharma, 2015):

$$\frac{\partial U}{\partial t} + \frac{\partial F}{\partial x} = S \quad (9)$$

with: $U = [p, \dot{m}]^T$ – vector of conserved variables,
 $F = \left[\frac{\dot{m}}{A^{atm} \rho^{atm} \beta^{tot}}, \dot{m}v + Ap \right]^T$ – vector of fluxes,

$S = \left[0, \rho Ag \cos \theta - \frac{1}{8} f_D \pi \rho D v |v| \right]^T$ – source terms vector.

The result of discretizing the elastic penstock model using the KP scheme is the semi-discrete (time dependent ODEs) central-upwind scheme and can be written in the following from:

$$\frac{d}{dt} \bar{U}_i(t) = -\frac{H_{i+\frac{1}{2}}(t) - H_{i-\frac{1}{2}}(t)}{\Delta x} + \bar{S}_i(t) \quad (10)$$

Here, \bar{U}_i is the cell center averaged values while $H_{i\pm\frac{1}{2}}$ – the central upwind numerical fluxes at the cell interfaces, are defined as:

$$H_{i+\frac{1}{2}}(t) = \frac{a_{i+\frac{1}{2}}^+ F(U_{i+\frac{1}{2}}^-) - a_{i+\frac{1}{2}}^- F(U_{i+\frac{1}{2}}^+)}{a_{i+\frac{1}{2}}^+ - a_{i+\frac{1}{2}}^-} + \frac{a_{i+\frac{1}{2}}^+ a_{i+\frac{1}{2}}^-}{a_{i+\frac{1}{2}}^+ - a_{i+\frac{1}{2}}^-} [U_{i+\frac{1}{2}}^+ - U_{i+\frac{1}{2}}^-] \quad (11)$$

$$H_{i-\frac{1}{2}}(t) = \frac{a_{i-\frac{1}{2}}^+ F(U_{i-\frac{1}{2}}^-) - a_{i-\frac{1}{2}}^- F(U_{i-\frac{1}{2}}^+)}{a_{i-\frac{1}{2}}^+ - a_{i-\frac{1}{2}}^-} + \frac{a_{i-\frac{1}{2}}^+ a_{i-\frac{1}{2}}^-}{a_{i-\frac{1}{2}}^+ - a_{i-\frac{1}{2}}^-} [U_{i-\frac{1}{2}}^+ - U_{i-\frac{1}{2}}^-]$$

Here $a_{i\pm\frac{1}{2}}^\pm$ are the one-side local speeds of propagation, and can be defined as the smallest and the largest eigenvalues of the Jacobian $\frac{\partial F}{\partial U}$ of the system. These eigenvalues become:

$$\lambda_{1,2} = \frac{v \pm \sqrt{v^2 + \frac{4A}{A^{\text{atm}} \rho^{\text{atm}} \beta^{\text{tot}}}}}{2} \quad (12)$$

From these eigenvalues, it can be deduced that the speed of sound is given as $c = \sqrt{\frac{A}{A^{\text{atm}} \rho^{\text{atm}} \beta^{\text{tot}}}}$, thus confirming that the total compressibility factor β^{tot} is related to the speed of sound.

3.3 Operational data and parameters

The complete set of models for different units of the hydropower system now consists of a number of ODEs that can be simulated in OpenModelica or Dymola with the *der* operator for d/dt using the *dasdls* solver algorithm with simulation interval time equal to 0.4 s and tolerance 1e-4. All operational parameters for simulation are given in Table 3.

4 Simulation

Firstly, basic simulations of the system with various penstock models (inelastic and elastic penstock) are done to validate the models from our own library with a commercial one. Then, a more detailed comparison of models with different penstock complexities is given for various simulation scenarios.

Table 3. Parameters for simulating the high head hydropower system.

Variable	Value	Unit	Comments
g	9.81	m/s ²	Acceleration due to gravity
ρ (ρ^{atm})	997	kg/m ³	Density of water
μ	0.89e-3	Pa·s	Dynamic viscosity of water
ϵ	1.5e-5	m	Pipe roughness height
β_T	4.5e-10	Pa ⁻¹	Water compressibility
β^{tot}	1.003e-9	Pa ⁻¹	Total compressibility
p^{atm}	1.013e5	Pa	Atmospheric pressure
Δx	60	m	Cell length for penstock discretization
C_V	3.7	m ³ /s	Turbine valve capacity
η_h	0.9	–	Turbine hydraulic efficiency
η_e	0.99	–	Electricity generator efficiency
J_a	2e5	kg·m ²	Moment of inertia of the aggregate
$k_{f,b}$	1e3	$\frac{\text{W}\cdot\text{s}^2}{\text{rad}^2}$	Friction factor in the aggregate bearing

4.1 Validation

It is of interest to validate the developed models with the commercial Hydro Power Library in order to check that our own library shows reasonable results; some basic simulation is done for this validation. The scenario for this simulation is a simple turbine guide vane (valve) opening after time 30 s from 10% over a period of 30 s to 100%. The block diagrams for the hydropower systems using the Hydro Power Library and our own developed models are shown in Figure 4.

In case of both libraries, the turbine is presented as a simple valve. That is why the turbine valve capacity together with the pipe roughness height should be set to similar or equivalent values. After some tuning of these variables for our in-house models, the results of the simulation fits the results from the Modelon Hydro Power Library reasonably well and are shown in Figure 5: the pressure drop variations through the turbine are presented for different cases.

From Figure 5, it is seen that the system with simple, inelastic penstock shows smother dynamics after the beginning of disturbance (at time after 30 sec.), while some small oscillation take part in the results for the in-house elastic penstock model and using the Modelon Hydro Power Library. It should also be noted that the simulation time for the system with inelastic penstock is around one third of the two other models.

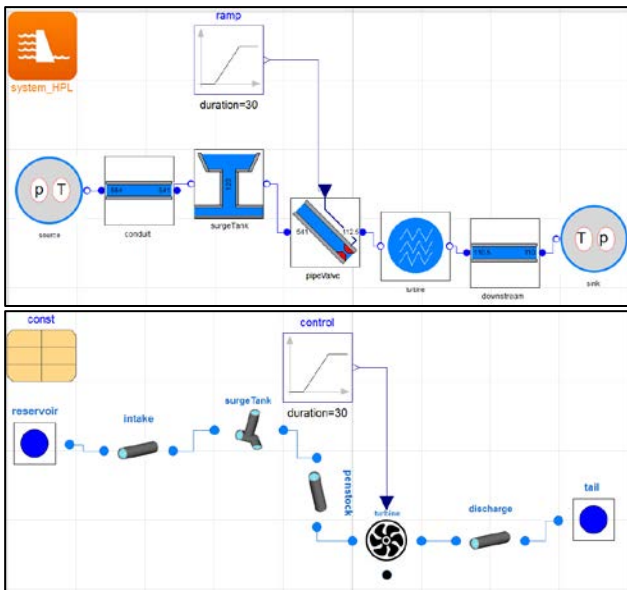


Figure 4. Block diagrams for hydropower system using Hydro Power Library (upper) and in-house library (lower).

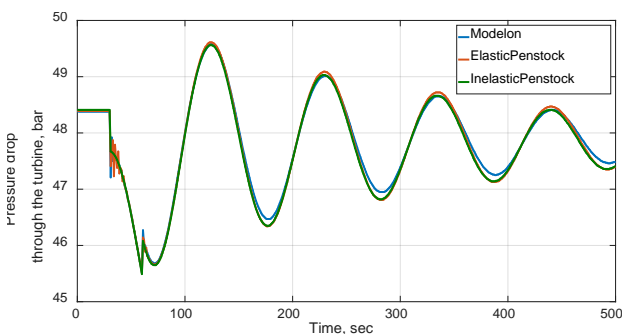


Figure 5. Validation of simulation results from own developed models (elastic and inelastic penstock) with Hydro Power Library.

4.2 Comparison

4.2.1 First simulation scenario

With the rudimentary validation in the previous section, a more detailed comparison of models with different penstock complexities can be studied. Firstly, the simulation scenario with sudden and small closing of the turbine guide vane (valve) is considered. Here, the systems are being simulated for 2000 s and the disturbance is applied at 600 s, when the valve is closed by 5% within 1 s. The results of simulation of the inelastic and the compressible/elastic models are presented in Figure 6, where plots are zoomed and shows just the time interval around disturbance (550 – 750 sec.)¹¹. In this figure the comparison of the pressure drop through the turbine (upper plot) and volumetric flow rate on the turbine (lower plot) are given for both

¹¹ The disturbance is not applied earlier in order to reach the steady state for the systems.

cases: systems with elastic and inelastic penstock models.

We observe smoother dynamics after disturbance for the inelastic penstock for both pressure drop and volumetric flow rate in Figure 6, which is similar to the validation case. From a power production perspective, this difference looks insignificant and may be neglected for control purposes if we take into account that the simulation time for a system with elastic penstock model is 3 times longer. On the other hand, it may be extremely important to observe these pressure oscillations to avoid cavitation and wear and tear of the turbine. That is why the outlet turbine pressure is also presented (see Figure 7) in order to compare models with elastic and inelastic penstock from the perspective of the cavitation problem.

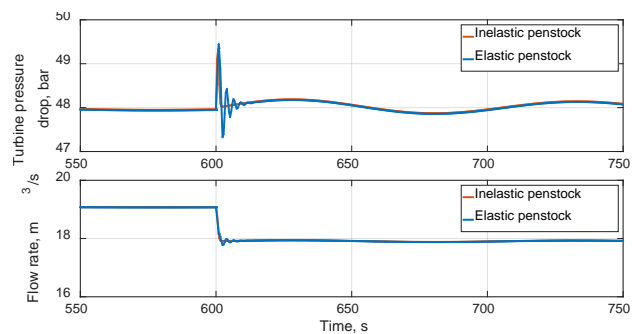


Figure 6. Comparison of simulation results for the systems with elastic vs. inelastic penstock models.

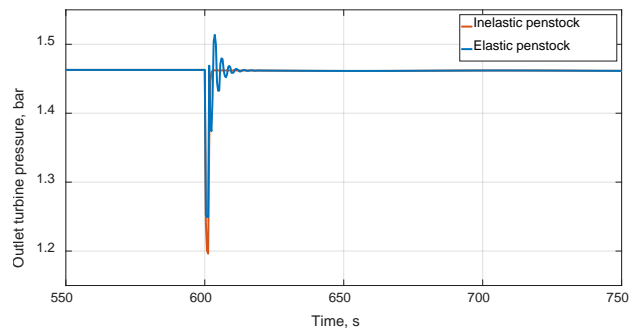


Figure 7. Comparison of the outlet turbine pressure for the systems with elastic vs. inelastic penstock models.

Figure 7 shows the same smoother dynamics with the simple inelastic penstock model, but the amplitude of the first oscillation is slightly higher for the model with elastic penstock.

4.2.2 Second simulation scenario

It is of interest to check another simulation scenario to see the effect of the penstock model complexity: a system without surge tank, but with the same disturbance as in the previous case (5% turbine valve closing at time 600 s). The results of simulating this scenario is shown in Figure 8, where only the

comparison of the pressure drop through the turbine is presented; the volumetric flow rate through the turbine shows similar results as in the previous simulation.

From Figure 8, it is seen that amplitudes of the first oscillation are different: in the system with inelastic penstock model the pressure drop rise higher after the disturbance than in the system with elastic penstock model. This difference can be related to the speed of increasing the pressure drop after disturbance: the pressure drop rises faster in the case with inelastic penstock model.

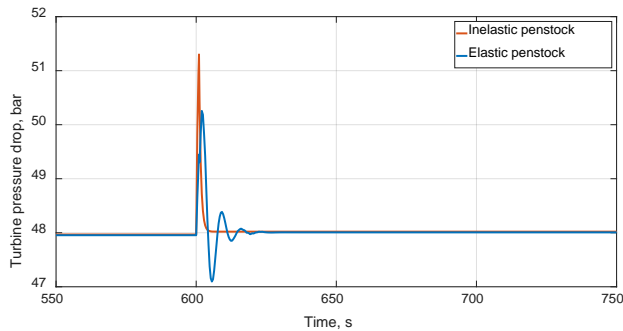


Figure 8. Comparison of the simulation results for the systems without surge tank.

It is also of interest, for these two penstock models, to see the difference at the outlet pressure from the turbine, which takes an important role in cavitation studies: due to the difference between the pressure drops through the turbine, here a point is to check from which side, inlet/outlet, of the turbine this difference was caused. Thus, this outlet turbine pressure is compared in Figure 9, where the simulation scenario is still the same (system without surge tank and 5% closing of the guide vane at time 600 s). Here, it is observed that the dynamics slightly differ between the system with elastic and inelastic penstock models, but the amplitude of the oscillation just after the disturbance is similar. This means that the inlet pressure to the turbine causes the difference in the turbine pressure drop.

The wave propagation is taken into account in the system with elastic penstock model and that is why models take some longer time for the turbine pressure drop to reach the maximum amplitude of the first oscillation after the disturbance, while in the system with inelastic penstock model all variables change simultaneously through the whole system. This can be observed in Figure 10, where the volumetric flow rate through the conduit is compared for cases with elastic vs. inelastic penstock models. Here, the flow rate through the conduit for the system with inelastic penstock starts to decrease at the time (600 s) when the disturbance occurs, while around half a second is needed for the wave in the system with elastic penstock model to reach the conduit.

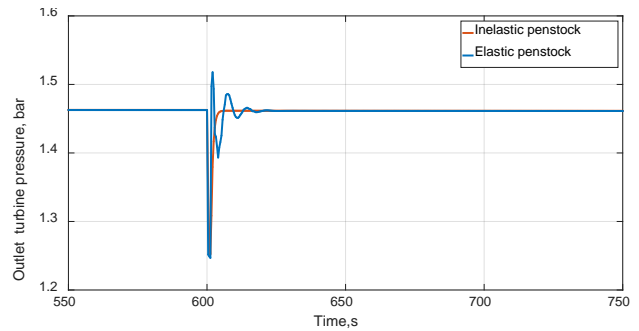


Figure 9. Comparison of the outlet turbine pressure for the systems without surge tank.

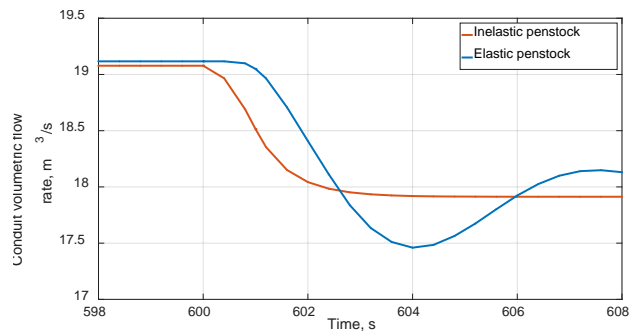


Figure 10. Comparison of the wave propagation in the systems with elastic vs. inelastic penstock models.

4.2.3 Third simulation scenario

In the last scenario, the effect of the wave propagation in the longest part of the hydropower system is studied. For this case, the elastic penstock model with compressible water is used for the conduit and the penstock units; the disturbance is the same as it was in the previous two scenarios. The simulations are done for both systems with (see Figure 11) and without (see Figure 12) surge tank and the turbine pressure drop is compared with the results for the previous two scenarios. It should be noted that the elastic model for the conduit is discretize with the same step length as for the penstock (60 m) and it leads to dramatic increasing of the simulation time, around 20-30 times.

From Figure 11, it is seen that the results for all three cases look almost the same. The system with the elastic conduit shows slightly more oscillatory results, but in general, there are no difference in overall dynamics. On the other hand, the dynamics differ substantially for the system without surge tank; the case with elastic conduit give a rather different behavior, which can be seen in Figure 12. Here, the oscillations after the disturbance need more time to reach a new steady state (compared to two other cases) and the amplitude of the first oscillation for the elastic conduit case is lower than for systems with elastic or inelastic penstock models.

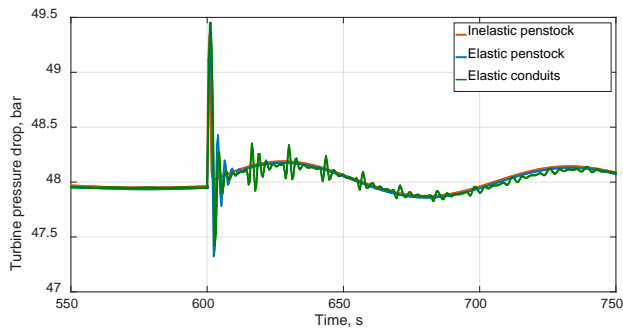


Figure 11. Comparison of the elastic conduit for the system with surge tank.

The longer oscillation time for the system with elastic penstock and conduit models is caused by the water wave moving back and forth (up and down) through the whole system. This is actually one of the reasons of using the surge tank: to keep mass oscillations within the limits: the oscillations in the system with surge tanks are much smoother and their amplitude variation is smaller.

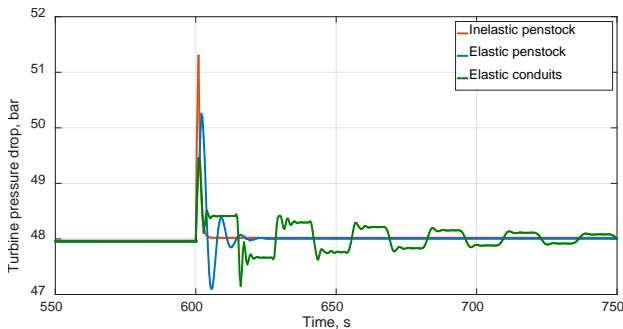


Figure 12. Comparison of the elastic conduit for the system without surge tank.

It is also of interest to compare the behavior of the outlet turbine pressure for the elastic model of the conduit. Thus, the comparisons have been done for both systems with and without the surge tank and results are shown in Figure 13 and Figure 14. Both figures show that the model with both the elastic conduit and penstock behaves more oscillatory, and at the same time, reaches the maximum amplitude values similar to the model with just the elastic penstock.

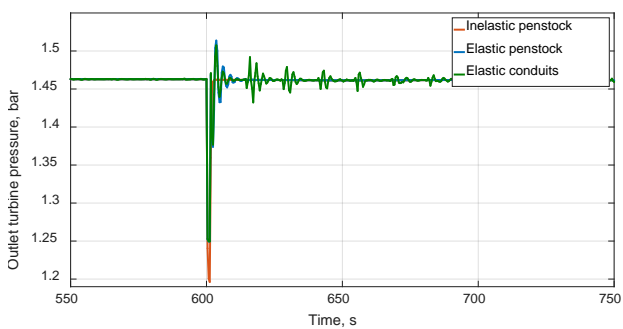


Figure 13. Comparison of the outlet turbine pressure for the systems with surge tank.

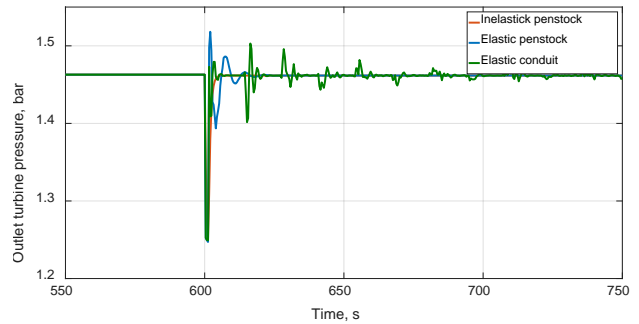


Figure 14. Comparison of the outlet turbine pressure for the systems without surge tank.

5 Discussion and conclusion

In this paper, the comparison of different penstock models for modeling and simulation of a high head hydropower system has been explored. The Kurganov-Petrova second order central upwind scheme has been implemented to discretize the more complicated penstock model with compressible water and elastic walls that is described by PDEs. This scheme has been implemented in Modelica and collected into an in-house library together with all other models for the hydropower elements. Then the models for simulating the hydropower system with different scenarios have been developed and simulated in OpenModelica. This in-house hydropower library has been validated with an already existing commercial Hydro Power Library.

Based on three simulation scenarios, it can be concluded that the system with inelastic penstock model exhibits a somewhat simpler dynamics, but on the other hand it has an advantage in the simulation time which is only one third of the same system but just with elastic penstock model (discretized by KP scheme). It is also observed that the wave propagation, which is taken into account in the elastic penstock model, affects the system, in particular the one without a surge tank. This effect leads to longer oscillations but also a smaller amplitude just after the disturbance (system without the surge tank). Despite all these difference, the inelastic penstock model can perhaps be used for control design problems due to the simplicity of this model, being less time consuming for simulation and reasonably good accuracy. Clearly, a model based controller based on a simple model should be tested on a more rigorous model, and, if necessary, re-tuned in order to ensure good performance. For a more detailed and accurate design, the elastic penstock model could be used in the controller, due to better representation of the system dynamics, which is caused by including the speed of the wave propagation to the model. Even better dynamic representation of the system can be reached by using the elastic model for the conduit. Then the delay caused by the speed of the wave propagation leads to more dramatic changes in the system dynamics (well observed in Figure 12).

Finally, our limited experience indicates that the simpler model appears to cover the worst case due to higher amplitude of the oscillation just after disturbance, even though it does not show proper dynamics. The systems with elastic and inelastic models do not behave in the same way for the outlet turbine pressure, the amplitude of the first oscillation after disturbance can differ, and this can be extremely important for a cavitation study.

References

- Dissanayake, S., Sharma, R. & Lie, B., 2016. *Semi Discrete Scheme for the Solution of Flow in River Tinnelva.* Oulu, Finland, EUROSIM 2016. IEEE, pp. 134-139.
- Dissanayake, S., Sharma, R. & Lie, B., 2017. Third Order Reconstruction of the KP Scheme for Model of River Tinnelva.. *Modeling, Identification and Control*, 38(1), p. 33–50.
- Kurganov, A. & Petrova, G., 2007. A second order well-balanced positivity preserving central-upwind scheme for the saint-venant system. *Communications in Mathematical Science*, Volume 5(1), p. 133–160..
- Saldamli, L., 2006. *PDEModelica A High-Level Language for Modeling with Partial Differential Equations*, Linköping, Sweden: Department of Computer and Information Science Linköping University.
- Sharefi, B. R., 2011. *Modeling for Control of Hydropower Systems*, Porsgrunn, Norway.: Master's Thesis. Telemark University College .
- Sharma, R., 2015. *Second order scheme for open channel flow.*, Porsgrunn, Norway: Technical report, Telemark Open Research Archive (TEORA), Telemark University College.
- Silar, J., Jezek, F. & Kofranek, J., 2017. *PDEModelica and Breathing in an Avalanche.* Prague, Czech Republic, Proceedings of the 12th International Modelica Conference.
- Vytvytskyi, L., Sharma, R. & Lie, B., 2015. Model based control for run-of-river system. Part 1: Model implementation and tuning. *Modeling, Identification and Control*, 36(4), p. 237–249.
- Winkler, D. et al., 2011. *Modelling and Optimisation of Deviation in Hydro Power Production.* Dresden, Germany, Modelica Conference.

Computational fluid dynamics study of flow depth in an open Venturi channel for Newtonian fluid

Prasanna Welahettige¹, Bernt Lie¹, Knut Vaagsaether¹

¹Department of Process, Energy and Environmental Technology
University College of Southeast Norway
Porsgrunn, Norway
knut.vagsaether@usn.no

Abstract

Open Venturi channel flow measurement could be a cheap method to be used in drill bit pressure control. The main objective of this study is to identify the factors related with the flow depth in an open Venturi channel. A commercial computational fluid dynamics tool was used for the simulations. The simulation results were validated with the previous related experimental results. The agreement between simulation and experimental data was satisfactory. The open Venturi channel at a horizontal angle gave a higher flow depth before the contraction region compared to its negative angles (downward). When the channel inclination angle was reduced, flow velocity increased and flow depth reduced. Likewise, flow became supercritical and created a hydraulic jump. The wall roughness played a significant role with the starting position of the hydraulic jump. This was due to the energy loss between wall and fluid. There is an energy loss in a hydraulic jump, when the supercritical flow transition into the subcritical flow. Large eddies were generated in a hydraulic jump. Flow depths difference between supercritical and subcritical is a factor to generate the large eddies. Fine meshes gave sharp interfaces, which was similar to what is seen in reality. The difference turbulence models: standard k- ϵ model, k- ω model, k- ϵ RNG model and k- ϵ realizable model gave almost the same flow depths.

Keywords: Flow depth, velocity, open Venturi channel, hydraulic jump, energy loss

1 Introduction

Hydraulic jumps generate due to transition of the supercritical flow into the subcritical flow in an open Venturi channel (Welahettige *et al.*, 2017). In a hydraulic jump, a strong shear layer is formed at the toe of the wave (Hornung *et al.*, 1995). The resistance phenomena in an open channel can be explained by using the inner and outer layer theory (Ben, 2002). A constant value for the roughness coefficient is not recommended for an open channel flow (Konwar & Sarma, 2015). The Colebrook White explicit equation is comparatively suitable for friction handling about the unsteady varied flow and the tidal computations in an open channel (Ahmed, 2015). The level jump in a

Venturi channel depends upon the fluid properties and the length of the flume (Berg *et al.*, 2015). There are few studies on flow depth parameters related to the open Venturi channel in literature. This study focused on the flow depth variation in an open Venturi channel for Newtonian fluid. Computational fluid dynamics (CFD) simulations were validated with experimental results (Welahettige *et al.*, 2017). ANSYS Fluent R16.2 commercial simulation tool was used for the simulations.

2 CFD models

The Volume of fluid (VOF) method was used for the simulations where phase interaction was based on the continuum surface force model and the phase localize compressive scheme (ANSYS, 2013). Equation. 1 gives the species mass balance. Here, α_2 is the water volume fraction, U is the three-dimensional velocity component, and U_r is the maximum velocity at the transition region. $\alpha_2 (1 - \alpha_2)$ is non zero only at the interface (Rusche, 2002), (Weller *et al.*, 1998) and (Ubbink, 1997).

$$\frac{\partial \alpha_2}{\partial t} + \text{div} (\alpha_2 U) = - \text{div} (\alpha_2 (1 - \alpha_2) U_r). \quad (1)$$

The normalized wall roughness (K_s^+) is given as, (ANSYS, 2013), (Akan, 2006) and (Versteeg & Malalasekera, 2007):

$$K_s^+ = \rho K_s u^* / \mu. \quad (2)$$

$$u^* = C_\mu^{1/4} \kappa^{1/2}$$

Here, K_s is the physical roughness. u^* is a constant equal to 0.346. Here $C_\mu = 0.09$ is a k- ϵ model constant and $\kappa = 0.4$ is the von Karman's constant. Density (ρ) and viscosity (μ) are considered as,

$$\rho = \alpha_2 \rho_2 + (1 - \alpha_2) \rho_1 \quad (3)$$

$$\mu = \alpha_2 \mu_2 + (1 - \alpha_2) \mu_1. \quad (4)$$

Here, ρ_1 and ρ_2 are the densities of air and water. μ_1 and μ_2 are the viscosities of air and water.

Time discretization was based on the implicit Euler method for transient simulations. The semi implicit method for pressure linked equations (SIMPLE) scheme was used to calculate the pressure-velocity coupling. The hyperbolic partial differential equations were solved by using the second order upwind scheme (Versteeg & Malalasekera, 2007) and (ANSYS, 2013).

3 Geometry

Figure 1 shows a 3-D geometry that was used for the simulations. Boundaries were inlet, outlet, wall, and atmosphere. X -direction was the main flow direction, from the inlet to the outlet. The channel width was in Y -direction. The flow depth was measured in Z -direction. The main mesh contained 0.74 million computational cells. The elements near to the wall boundaries were modified by adding inflation layers.

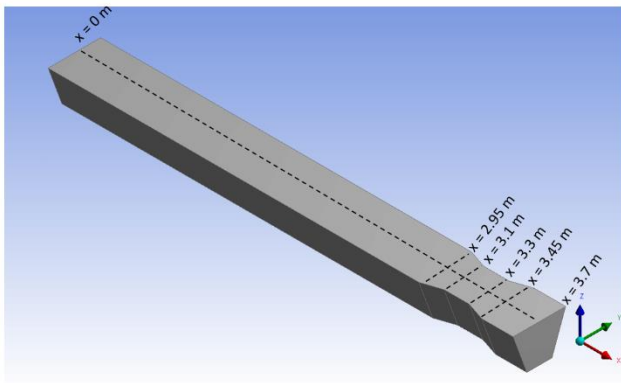


Figure 1. 3-D geometry of the trapezoidal channel; $x = 0$ m was defined as the inlet of the channel. The Venturi region was $x = 2.95$ m to $x = 3.45$ m. The bottom depth was 0.2 m for $0 \text{ m} < x < 2.95$ m and $3.45 \text{ m} < x < 3.7$ m. The bottom depth was 0.1 m for $3.1 \text{ m} < x < 3.3$ m. The trapezoidal angle was 70° .

4 Results and discussion

4.1 Flowrate and flow depth

Figure 2 shows flow depths along the channel central axis for different flow rates. The channel inclination angle was zero degrees (horizontal) for all the cases in Figure 2. Simulations were done for water the flow rates: 100 kg/min, 200 kg/min, 300 kg/min, 400 kg/min and 700 kg/min. The experimental water flow rate result, which was equal to 400 kg/min, was used for the validation (Welahettige *et al.*, 2017). The contraction region started at $x = 2.95$ m (see Figure 1). The flow depth increased with increased of the flow rate. The flow

depth increment with the flow rates was not a linear relationship due to the geometry of the channel. Flow depth near to the contraction walls slightly increased in high flow rates (e.g. 700 kg/min). Low flow rates showed almost horizontal flow depths until the Venturi contraction walls (e.g. 200 kg/min). The flow depth was reduced from the end of the Venturi contraction to the outlet of the channel for all the cases. There were no barriers at the end of the channel and the channel expanded after the contraction. Therefore, flow condition was changed from subcritical to supercritical, when flow depth reduced at the end of the channel (Welahettige *et al.*, 2017). In generally, the channel at horizontal angle gives subcritical flow before the contraction and supercritical flow after the contraction for all flow rates. The flow transition from subcritical to supercritical occurs at the Venturi region for all flow rates (when the channel at horizontal angle).

Figure 3 shows the average velocities along the x -axis for different flow rates. The average water velocity was calculated by considering the average of all cell's velocities in the considered cross section (except air velocities in the cross section). Velocities before the contraction region were averagely constant in each cases. This was due to the constant flow depths in this region (see Figure 2). Velocity gradually increased after the Venturi region due to the flow depth reduction. According to Bernoulli's law, the potential energy converts into the kinetic energy in this region. Mass flow rate (\dot{m}) is given as

$$\dot{m} = \rho h \left(b + \frac{h}{\tan \theta} \right) \bar{U}. \quad (5)$$

Here, b is the bottom width, θ is the trapezoidal angle, ρ is the density of water. Flow depth (h) and the average velocity perpendicular to the area (\bar{U}) are variables with the mass flow rate for a considered position. When the mass flow rate increases, both flow depth and flow velocity increase in the channel. Because of this, the high mass rates give higher flow depths and higher flow velocities compared to the low mass flow rates.

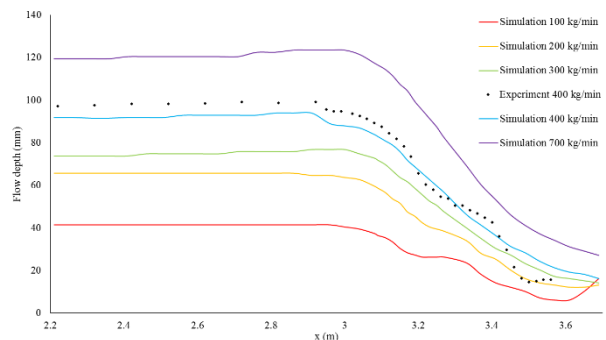


Figure 2. Flow depth changes along the channel centerline axis in the Venturi region for different flow rates. The channel inclination angle was zero degrees. The

experimental result was from (Welahettige et al., 2017) for 400 kg/min water flow rate.

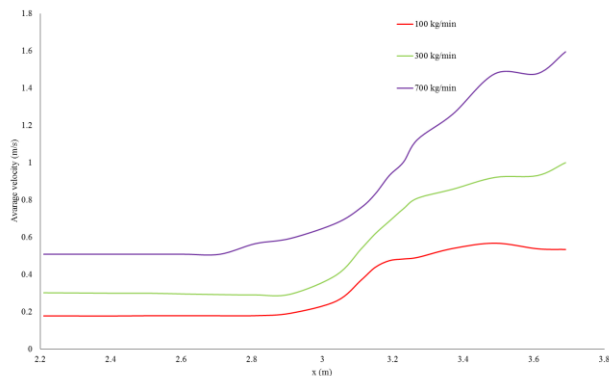


Figure 3. The average velocity along the x-axis for different water flow rates. The channel inclination angle was zero degrees for all cases. The average velocity was calculated as the average cross sectional velocity perpendicular to x-axis.

4.2 Different channel inclination angles and flow depths

Figure 4 shows the flow depth variation with the channel inclination angles. In this case, flow rate was 400 kg/min for all the cases. When the channel inclination angle was a negative value, a gravitational support added to the flow direction (x-direction). When the channel inclination angle was a positive value, a gravitational support added opposite to the flow direction. The highest flow depth was given before the Venturi contraction, when the channel inclination angle was +1.5 degree. In this region, flow became subcritical due to the barriers such that the contraction walls and the gravitation opposite force (only in the positive channel inclination cases). The channel at the horizontal angle, the flow depth was almost a flat surface. Because only the contraction walls hydraulic jumps were affected opposite to the flow direction, except the friction force. When the channel inclination angle was a negative value, the flow depth before the Venturi contraction reduced due to flow convert into the supercritical flow (Welahettige *et al.*, 2017). At -1.0 degree angle, the flow depth increased in the Venturi region due to the oblique jump propagation (Welahettige *et al.*, 2017). There was a level fluctuation in -0.7 degree angle case at $x = 2.2$ m. This was due to the hydraulic jump propagation. The flow depths after the Venturi showed almost equal values for all the angles because of all the cases reached to the supercritical flow condition at the end of the channel.

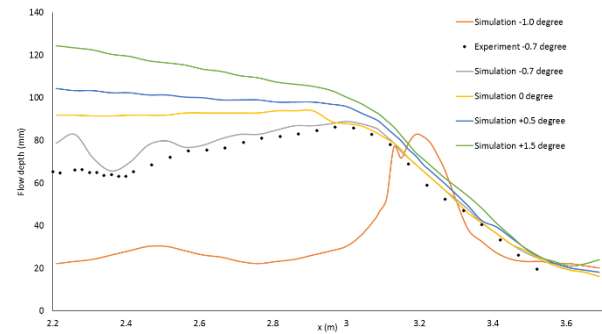


Figure 4. Flow depth change along the x-axis due to variation of channel inclination angles. The water flow rate was 400 kg/min. Flow depth was measured along the channel central axis. The experimental result was taken from (Welahettige *et al.*, 2017).

Figure 5 gives the average flow velocity for different inclination angles, the water flow rate at 400 kg/min. The high velocities for the negative inclination showed due to the supercritical flow behavior. There was a large difference of velocities between -1 degree case and horizontal case before the Venturi contraction. Even before the contraction walls; the flow reached to the supercritical condition in the negative inclination cases. However, there was no significant velocity difference after the contraction region in these cases. This was due to the fluid convert into the supercritical and the flow depths were averagely equal in all the cases.

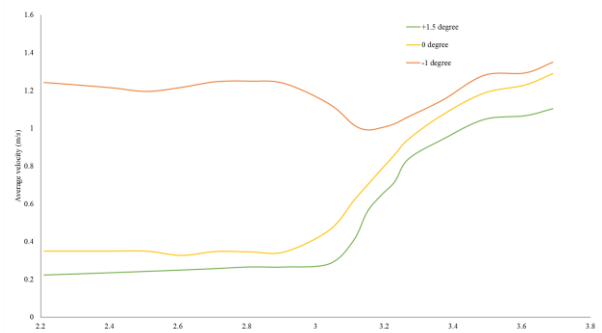


Figure 5. The average velocity along the x-axis for different channel inclination angles. The water flow rate was 400 kg/min.

4.3 Wall roughness height effect on flow depth

The wall roughness height related with wall friction and heat losses (ANSYS, 2013). Figure 6 shows the steady state water volume fraction for different the wall roughness values. The water flow rate was 400 kg/min and the channel at horizontal angle for all the cases. When the wall roughness height was increased, a hydraulic jump was generated before the Venturi region. In other words, toe of the hydraulic jump was moved to the upstream direction. This was due to increase of energy loss from the walls, when increased the wall roughness height. When energy loss increased, it could

not continue as a supercritical flow. Therefore, hydraulic jump moved to the upstream. Wall roughness height 0.000015 m was given a good matching with the experiment results.

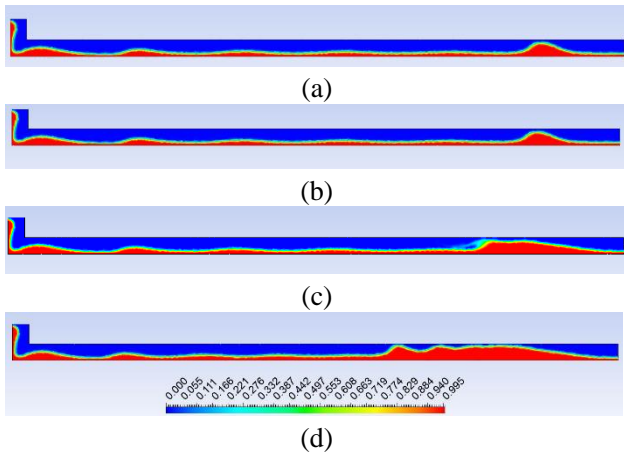


Figure 6. Steady state water volume fraction comparison for different wall roughness height. Water flow rate was 400 kg/min and the channel inclination angle was zero degrees; (a) Wall roughness height = 0 m, (b) Wall roughness height = 0.000015 m, (c) Wall roughness height = 0.0001 m, (d) Wall roughness height = 0.001 m.

4.4 Velocity distribution

The case with the flow rate 300 kg/min and the inclination angle zero degrees was used for the velocity distribution analysis. The average Reynolds number was approximately 46 000 and the flow was averagely turbulent. Air velocity was approximately zero above the water surface except at the interface. The VOF model solves a single momentum equation. Therefore, the interface has a same velocity for air and water. The water velocity at the wall was zero due to the no-slip boundary condition. Figure 7 shows water velocity magnitudes along the z-axis: before the Venturi contraction ($x = 2.51$ m), at the middle of Venturi ($x = 3.19$ m) and after the expansion of the Venturi ($x = 3.61$ m). The velocity distribution before the contraction walls were lower value compared to the other two locations because subcritical flow gave high flow depths and low velocities. The velocity increased from the bottom to the top in all the cases. This was due to the gradually reduction of friction from the bottom to the top.

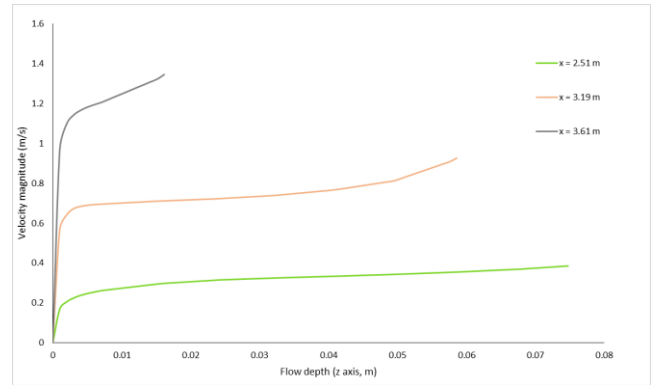


Figure 7. Water velocity magnitude along the vertical central lines in different location of the Venturi region; at $x = 2.51$ m (before the Venturi contraction), $x = 3.19$ m (at the middle of the Venturi), $x = 3.61$ m (after the Venturi expansion); The water flow rate was 300 kg/min and the channel inclination angle was zero degrees.

4.5 Mesh dependency evaluation

The mesh dependency evaluation was done with following meshes shown in Table 1. Total number of elements in a mesh was increased by reducing the maximum face size of cells.

Table 1. Mesh details for mesh dependency analysis: total number of elements and maximum face size

	Total number of elements	Maximum face size (mm)
01.	16 815	20
02.	23 217	15
03.	61 464	10
04.	104 910	8
05.	378 635	5
06.	159 8267	3

Figure 9 shows water volume fraction along the z-axis at $x = 3.19$ m for the different meshes. The coarse meshes (20 mm and 15 mm) gave wide range of interface variations. However, the fine meshes give sharp interfaces. In reality, there is very sharp interface between water and air. Therefore, the finer meshes gave more accurate results than the coarser meshes. This implies that mesh size is a critical factor for VOF simulations. It is recommended to have a fine mesh for small flow depths.

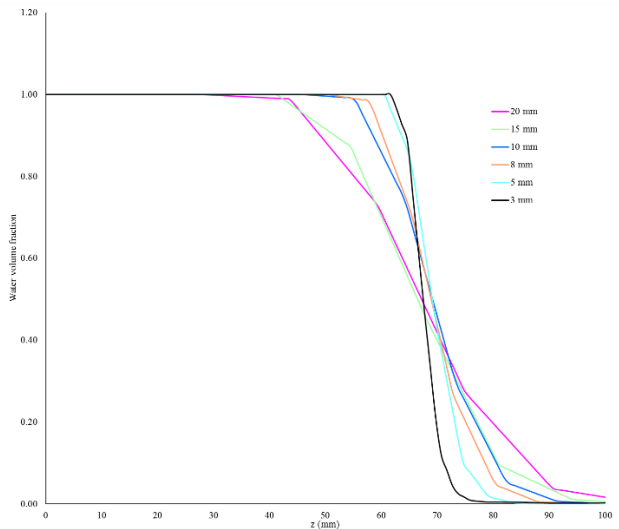


Figure 8. Mesh dependency analysis: The maximum cell face sizes in the meshes 20 mm, 15 mm, 10 mm, 8 mm, 5 mm and 3 mm: Water volume fraction along z-axis at $x = 3.19$ m.

4.6 Effect of turbulence models on flow depth

Figure 7 shows water volume fraction along the y-axis for different turbulence models at $x = 3.19$ m. There was no significant effect for the flow depth from different turbulence models: standard k- ϵ model, k- ω model, k- ϵ RNG model and k- ϵ realizable model. At the steady state, all the turbulence models gave similar results. However, the standard k- ϵ model took higher computational time compared to the other turbulence models.

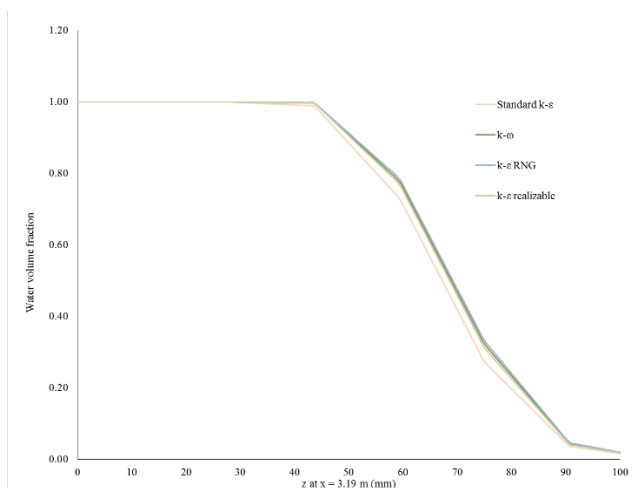
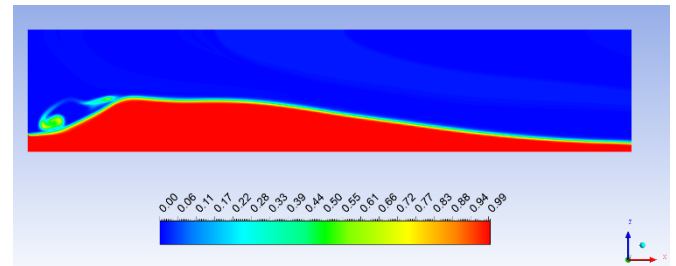


Figure 9. Water volume fraction along the z-axis at $x = 3.19$ m for different turbulence model: Standard k- ϵ model, k- ω model, k- ϵ RNG model and k- ϵ realizable model.

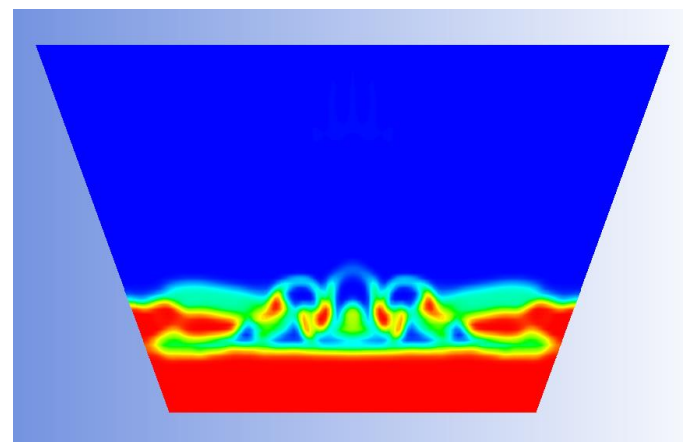
4.7 Energy loss in a hydraulic jump

Figure 10 shows a hydraulic jump. There were large eddies propagation in a hydraulic jump. Hydraulic jump

was very unstable due to the higher turbulence (Xiang *et al.*, 2014). A short and fine domain mesh (3 mm mesh in mesh dependency test) was used for the energy calculation. The flow rate was 400 kg/min and the channel inclination angle was -1.5 degree.



(a)



(b)

Figure 10. Water volume fraction of a hydraulic jump, (a) Central axis plane, (b) Channel cross sectional view at a hydraulic jump

The specific energy head (E_s) at a point can be given as the sum of the potential energy and the kinetic energy for 1-D system.

$$E_{s,1-D} = h + h_{hs} + \frac{\bar{U}^2}{2g} \quad (7)$$

Here, h is the flow depth, h_{hs} is the hydrostatic head, and \bar{U} is the average flow velocity. The potential energy head was a sum of the flow depth and the hydrostatic head. The gravity point of the flow depth was assumed at the half of the flow depth. The specific energy difference before and after the hydraulic jump was due to the energy loss. The hydraulic jump approximately was in $x = 2.7$ m to $x = 2.85$ m. Specific energy head, kinetic energy head and potential energy head is shown in Figure 11. When the flow depth increased, the kinetic energy reduced in the hydraulic jump. The kinetic energy was predominant before started the hydraulic jump. Then it was drastically reduced in the hydraulic jump. This was due to the main flow kinetic energy participated to increase the turbulence kinetic energy. There was a head loss in the hydraulic jump, which was approximately 0.47 m in this case. The head

loss was due to the turbulence eddies finally converted into the internal energy.

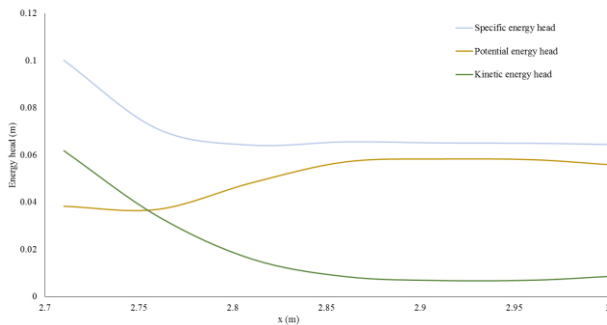


Figure 11. Energy loss in a hydraulic jump: specific energy head, potential energy head, and kinetic energy head.

This research study will be further extended into oil well drill mudflow analysis in an open Venturi channel.

5 Conclusions

The open Venturi channel at the horizontal angle gives a high flow depth before the contraction region. When the channel inclination angle is downward, the flow velocity increases and flow depth reduces. Because of this, flow becomes supercritical. The wall roughness height plays a significant role with the starting point of a hydraulic jump, due to the energy loss between wall and fluid. There is an energy loss in a hydraulic jump, when the supercritical flow transition into the subcritical flow. Fine mesh gives a sharp interface, which is similar with the reality. Turbulence models: Standard $k-\epsilon$ model, $k-\omega$ model, $k-\epsilon$ RNG model and $k-\epsilon$ realizable model give almost similar flow depths. However, standard $k-\epsilon$ model was taken higher computational time compared to the other models.

Acknowledgment

The economic support from The Research Council of Norway and Statoil ASA through project no. 255348/E30 “Sensors and models for improved kick/loss detection in drilling (Semi-kidd)” is gratefully acknowledged. As well as authors acknowledge to University College of Southeast Norway for giving resources for simulations.

References

- Ahmed Z. (2015). *Review of friction formulae in open channel flow* Paper presented at the Eighteenth International Water Technology Conference, IWTC18
- Akan O. (2006). *Open Channel Hydraulics*. Oxford: Butterworth-Heinemann.
- ANSYS I. (2013). ANSYS Fluent Theory Guide.
- Ben C. (2002). Open Channel Flow Resistance. *Journal of Hydraulic Engineering*, 128(1), 20-39. doi:doi:10.1061/(ASCE)0733-9429(2002)128:1(20)

- Berg C., Malagalage A., Agu C., Kaasa G., Vaagsaether K. and Lie B. (2015). Model-based drilling fluid flow rate estimation using Venturi flume. *IFAC Workshop on Automatic Control in Offshore Oil and Gas Production*, 2, 177-182.
- Hornung H., Willert C. and Turner S. (1995). The flow field downstream of a hydraulic jump. *Journal of Fluid Mechanics*, 287, 299-316. doi:10.1017/S0022112095000966
- Konwar L. and Sarma B. (2015). Analysis and Verification of Resistance Co-Efficient with Different Flow Parameters Having Different Bed Conditions to Open Channel Flow. *International Advanced Research Journal in Science, Engineering and Technology*, 2(8), 106-110.
- Rusche H. (2002). *Computational Fluid Dynamics of Dispersed Two-Phase Flows at High Phase Fractions*. (Doctor of Philosophy), University of London Exhibition Road, London.
- Ubbink O. (1997). *Numerical prediction of two fluid systems with sharp interfaces*. (Degree of Doctor of Philosophy), Imperial College of Science, Technology & Medicine.
- Versteeg H. and Malalasekera W. (2007). *An introduction to computational fluid dynamics: The finite volume method* (2 ed.). Harlow, England: Pearson Education.
- Welahettige P., Lie B. and Vaagsaether K. (2017). Flow regime changes at hydraulic jumps in an open Venturi channel for Newtonian fluid. *The journal of computational multiphase flow*, Accepted.
- Weller H., Tabor G., Jasak H. and Fureby C. (1998). A tensorial approach to computational continuum mechanics using object-oriented techniques. *Computers in Physics*, 12(6), 620-631. doi:http://dx.doi.org/10.1063/1.168744
- Xiang M., Cheung S. C. P., Tu J. Y. and Zhang W. H. (2014). A multi-fluid modelling approach for the air entrainment and internal bubbly flow region in hydraulic jumps. *Ocean Engineering*, 91, 51-63. doi:https://doi.org/10.1016/j.oceaneng.2014.08.016

Conceptual Models for Fracture Characterization at Reykjanes Geothermal Field

Lilja Magnúsdóttir¹ Magnus Thor Jonsson²

¹Ind. Eng. - Mech. Eng. and Computer Science, University of Iceland, Iceland, liljamag@hi.is

²Ind. Eng. - Mech. Eng. and Computer Science, University of Iceland, Iceland, magnusj@hi.is

Abstract

This paper describes conceptual models for an inverse analysis to investigate fracture topology at Reykjanes geothermal reservoir using electrical resistivity. The resistivity distribution of a field can be estimated by measuring potential differences between various points while injecting an electric current into the ground, and resistivity data can be used to infer fracture properties due to the large contrast in resistivity between water and rock. Furthermore, injecting water into the reservoir with higher resistivity than the conductive brine at Reykjanes would cause a time-dependent change in the resistivity of the fractures as the fluid flows through the fracture network. Thus, modeling the time history of the potential difference between two points (e.g. an injector and a producer) as water is injected into the reservoir and comparing simulated results to actual observation that depend on the fracture network in the field, could help estimate where fractures are located and the characterize their distribution.

Keywords: Fracture characterization, Reykjanes, IDDP, electrical resistivity, ERT

1 Introduction

Reykjanes geothermal field in Iceland is located about 50 km southwest of Reykjavík on the Reykjanes peninsula. At Reykjanes geothermal field, an existing well (RN-15) has been deepened down to a 4.7 km depth as a part of the Iceland Deep Drilling Project (IDDP) (Fridleifsson et al., 2017). Supercritical fluids can exist near heat sources in magmatic reservoirs and at Reykjanes the temperature is expected to reach up to 500°C in the deepened well (IDDP-2). At temperatures and pressures above the critical point (374°C and 22.064 MPa), the fluid has multiple power-producing potentials compared to fluid produced in conventional geothermal power plants. The enthalpy is significantly higher at such high temperatures and pressures, and the rates of mass transfer is greatly enhanced due to the increased ratios of buoyancy forces to viscous forces in the supercritical state. Thus, supercritical fluid is desired for optimized power productions since more energy could be produced from a single well extracting supercritical fluids compared to a conventional geothermal well.

For optimizing power production at Reykjanes, it is crucial to study the behavior of the fluid and heat transfer at the deep roots of the system. Connectivity of fractures is essential to ensure adequate supply of geothermal fluids and efficient thermal operation of the wells in the reservoir. The knowledge of the configuration of fractures and the fluid-flow patterns is extremely valuable for designing the recovery strategy appropriately, optimizing the placing of injection or production wells, and increasing the overall efficiency of the power production.

In this paper, a conceptual model of Reykjanes is described for estimating fracture connectivity by measuring time-lapse electric potential data while injecting a fluid into the reservoir with different conductivity than the geothermal fluid. If the injected fluid is less conductive than the geothermal fluid, the electric potential will increase as the injected fluid fills fractures from the injector towards the producers. Therefore, the time-lapse electric potential data are related to the connectivity of the fracture network.

A variety of approaches have been attempted to use time-dependent geophysical data that can indirectly measure time-varying hydrologic parameters (Day-Lewis et al., 2003; Lambot et al., 2004). Electrical resistivity has been shown to be sensitive to changes in fluid conductivity and water content in reservoirs (e.g., Binley et al., 2002; Yeh et al., 2002), and the concentration of a conductive tracer can be mapped from field measurements of resistance using cross-well Electrical Resistivity Tomography (ERT) (Singha and Gorelick, 2006). A number of studies have demonstrated the potential of ERT for monitoring tracer migration in soil, (Binley et al., 1996; Köstel et al., 2008; Olsen et al., 1999; Slater et al., 2000), and in shallow aquifers (Binley et al., 2002; Cassiani et al., 2006; Oldenborger et al., 2007; Singha and Gorelick, 2005; Singha et al., 2007). In these studies, usually many electrodes were used to obtain the resistivity distribution for the whole field under study at each time step and then this resistivity distribution was compared to the distribution without any tracer to observe resistivity changes in each block visually. Using this

approach for a whole reservoir would require a massive parameter space and likely not be solvable, except at very low resolution. However, in the method considered in this study, the potential difference between the wells which corresponds to the changes in resistivity is measured and plotted as a function of time while the injected water flows through the fracture network. Then, this time-lapse electric potential is used in an inverse analysis to estimate the connectivity between points (e.g. wells) in the reservoir.

The proposed plan includes first developing and verifying an iTOUGH2 model of Reykjanes geothermal reservoir. The model's depth has to be at least 5 km due to well RN-15 that has been deepened down to a 4.7 km depth. The plan involves using the supercritical module in iTOUGH2, EOS1SC, which allows for simulating the extreme temperature and pressure conditions at the roots of geothermal reservoirs (Magnusdottir and Finsterle, 2015). That way, the heat source can be included in the model. Then, the model is calibrated with an inverse analysis using production data from the field.

Next, an inverse analysis is proposed for estimating the fracture connectivity in the reservoir using time-lapse electric potential data as water with lower conductivity than the geothermal fluid is injected into the reservoir. The inverse analysis first requires a fracture model that can be created using a Discrete Fracture Network (DFN) based on the >5 km deep iTOUGH2 model of Reykjanes. Then, the flow through the reservoir of injected water needs to be simulated using iTOUGH2. In addition, the analogy between Ohm's law that describes electrical flow and Darcy's law describing fluid flow makes it possible to use iTOUGH2 to calculate the electric fields. Finally, the inverse analysis requires measuring the electric field in the reservoir for comparison to the simulated electric fields in order to estimate the fracture connectivity.

2 Numerical Model of Reykjanes

In geothermal modeling, the roots of the geothermal systems are normally avoided but in order to accurately predict the thermal behavior when wells are drilled close to magmatic intrusions, it is necessary to incorporate the heat sources into the modeling scheme. Thus, it is recommended to use the supercritical module in iTOUGH2, EOS1SC, for creating a >5 km deep numerical model of Reykjanes including the heat source at the bottom. Figure 1 shows an example of a grid in X and Y direction for a model of Reykjanes around well RN-15 with a finer grid where the wells are located. This grid can then be copied for the multiple layers in Z direction that represents the depth of the model. The model parameters are chosen to generally fit the measured data and other knowledge regarding the reservoir. Lower permeability is defined for the elements at the boundaries and the inverse analysis focuses on the permeability distribution of the smaller

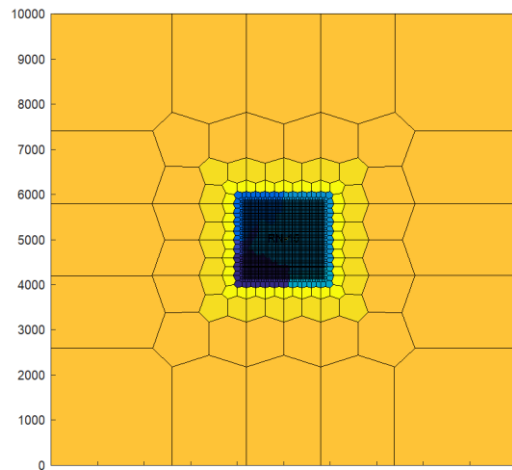


Figure 1. An example of a grid in X and Y direction for a model of Reykjanes. Color represents rock properties.

element net in the middle of the grid in Figure 1. The reservoir model is first simulated without any production until it reaches a steady-state. Then, production is simulated. The simulated pressure and temperature in the reservoir before and during the production is used to calibrate the model by comparing the simulated data to actual observations in the field. The input parameters for the inverse analysis are the permeability distribution in the field as well as the temperature of the heat source at the bottom and the output parameters are the production data and the measured pressure and temperature before production started. A possible solution for the permeability and temperature in the reservoir has been established once there is a good fit between the simulated output parameters and the observations in the field. Figure 2 shows an example of a fit between simulated and observed pressure and temperature for well RN-15 in Reykjanes at steady-state. The red data points are the measured data and the blue data points are the simulated data. For this example, the simulated data already fit relatively well to measured data. The next step would be to simulate the production and perform an inverse analysis to get a better fit.

3 Inverse Analysis for Fracture Characterization

In previous section, we discussed how in this study a numerical reservoir model would be first created based on an observation of the reservoir and measurements taken in the field. Then, in order to take full advantage of the data available for model construction, inverse analysis is used to calibrate the model. In inverse modeling, the results of actual observations such as measurements of pressure and temperature in the field or electrical resistivity measurements are used to infer the values of the parameters characterizing the system. In previous section we described how an inverse analysis can be used to estimate the permeability and the

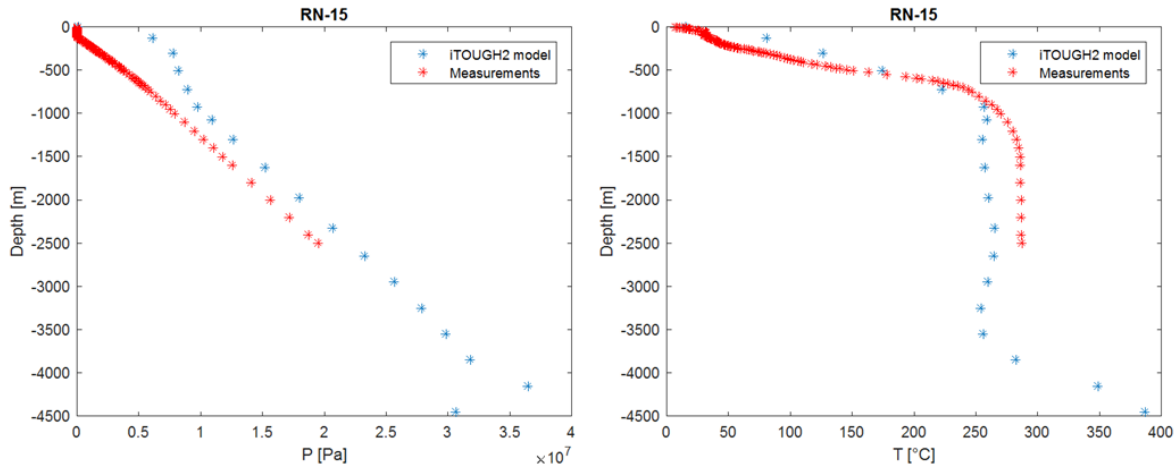


Figure 2. The measured pressure and temperature distribution at well RN-15 (now IDDP-2) before any production, compared to the steady-state pressure and temperature distribution in an iTOUGH2 model of Reykjanes.

temperature of a heat source in the reservoir for the model of Reykjanes using pressure and temperature measurements. Furthermore, this section will explain how inverse analysis can be used to characterize the fracture connectivity in the reservoir using electrical resistivity measurements. The output parameters are the potential differences between wells as a function of time and the input parameter is the character of the corresponding fracture network. The objective function measures the difference between the model calculation, which in this case is the calculated voltage difference between wells, and the corresponding observed data measured in the reservoir.

The inverse analysis is further illustrated in Figure 3. First, a fracture model is developed based on the existing iTOUGH2 model and observations in the field. The plan includes using a Discrete Fracture Network (DFN) model introduced by Karimi-Fard et al. (2003) so realistic fracture patterns can be modeled. DFN models represent fracture-dominated flow paths in geothermal reservoirs more accurately since the fractures are treated discretely instead of being defined by high permeability values in course-scale grid blocks, as done in the iTOUGH2 model previously described.

Once a conceptual fracture model of the reservoir has been constructed, a flow simulation is performed using iTOUGH2 to study how injected water flows through the fracture network of the reservoir. It is important that the conductivity of the water injected is lower than the conductivity of the fluid in the reservoir so that a change in the electric potential is produced between the injection well and the production well. Then, the electric potential field is solved for each time step as the injected water is flowing through the reservoir and the electric potential difference between the wells is recorded. iTOUGH2 can also be used to calculate the electric fields as explained in the next section. Then, this time-history of the simulated electric potential difference is compared to the true measured potential difference in the reservoir in the inverse

analysis. The fracture characteristics of the fracture model are changed until a good match has been established between the simulated potential difference and the potential difference observed in the reservoir during measurements. Inverse analysis is a powerful tool for validating the model and predicting the fracture connectivity in the reservoir as explained by Magnusdottir and Horne (2013).

4 Electric Field Simulated Using iTOUGH2

The potential distribution in steady-state porous flow is exactly the same as the potential distribution in an electric conducting medium due to the analogy between Darcy's law and Ohm's law, as formulated by Muskat (1932). Therefore, flow simulator iTOUGH2 can be used to calculate both the distribution of water injected to change the resistivity of the fractures in the reservoir and to calculate the electric field at each time step. The same grid can then be used for both electric and fluid flow models, making the simulation more efficient than if separate models were used.

Darcy's law is an empirical relationship similar to Ohm's law,

$$J = -\sigma \nabla \varphi \quad (1)$$

where J is current density [A/m^2], σ is the conductivity of the medium [Ωm] and φ is the electric potential [V], but instead of describing electrical flow Darcy's law describes fluid flow through a porous medium,

$$q = -\frac{k}{\mu} \nabla p \quad (2)$$

where q is the flow rate [m/s], k is permeability [m^2], μ is viscosity of the fluid [kg/ms] and p is pressure [Pa]. Table 1 presents the correspondence between the variables and relations of water flow (Darcy's law) and electric current flow (Ohm's law).

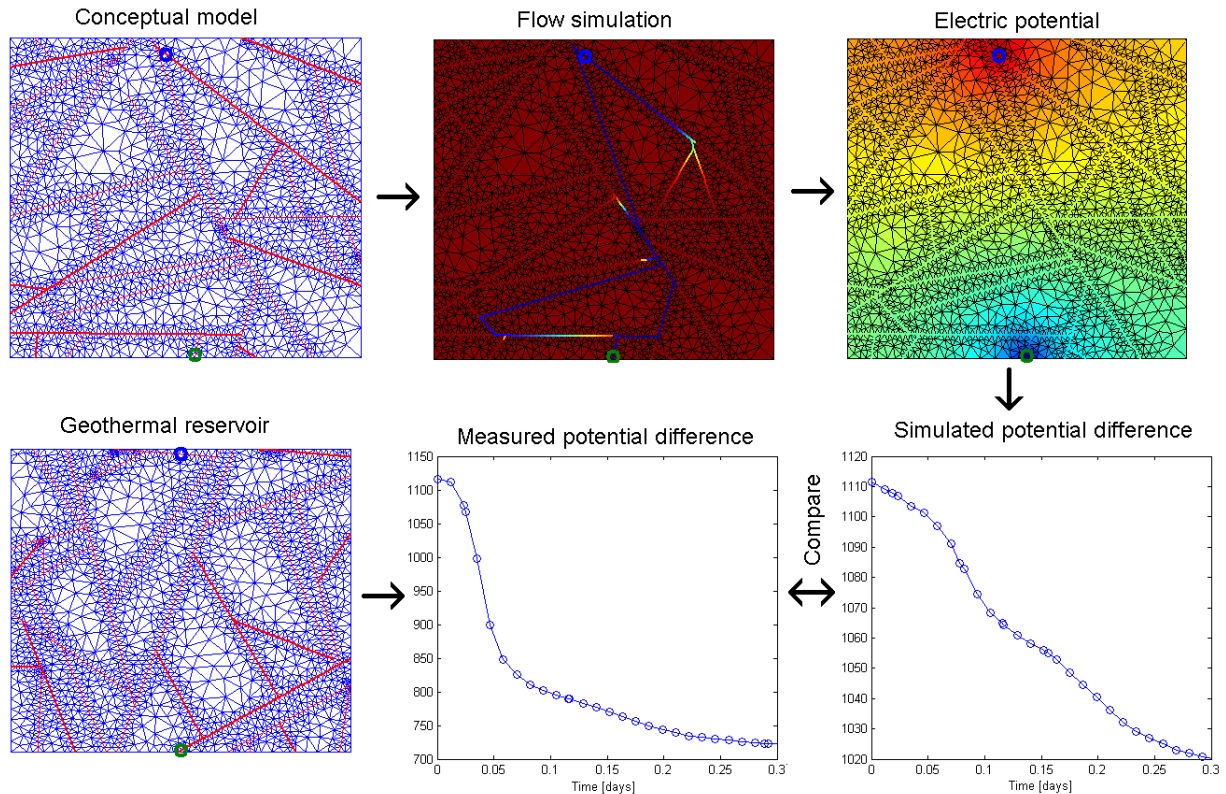


Figure 3. Schematic illustration of the inverse analysis proposed in this paper.

Table 1. Correspondence between electric current flow and water flow.

	<i>Darcy's law:</i>	<i>Ohm's law:</i>
<i>Flux of:</i>	Water q [m/s]	Charge J [A/m ³]
<i>Potential:</i>	Pressure p [Pa]	Voltage ϕ [V]
<i>Medium property:</i>	Hydraulic conductivity $\frac{k}{\mu}$ [m ² /Pa·s]	Electrical conductivity σ [1/Ωm]

The pressure results from iTOUGH2 correspond to the electric voltage, the current density to the flow of water and the electrical conductivity corresponds to the hydraulic conductivity, i.e.

$$\sigma = \frac{k}{\mu} \quad (3)$$

However, it must be taken into account that viscosity depends on pressure while conductivity of a reservoir does not depend on the electric voltage used. In order to take the pressure dependence into account, the EOS9 module in iTOUGH2 can be used. EOS9 considers flow of a single aqueous phase consisting of a single water component. The conditions are assumed to be isothermal so only a single water mass balance equation is solved for each grid block and the thermal properties

of water can be overwritten. Therefore, liquid viscosity, density and compressibility can be defined constant and reference pressure and temperature can be overwritten in iTOUGH2, making the imitation of electric flow possible.

5 Measurements

The final crucial part of the inverse analysis is observations in the field. Measurements of the electric current between the wells as the injected water flows through the reservoir gives information about the time-lapse resistivity in the field. The measurements are necessary for estimating the characteristics of the fracture model.

Well RN-15 in Reykjanes seems ideal for this experiment because once it was deepened during the Iceland Deep Drilling Project (IDDP), it was disconnected from the pipelines that go towards the powerplant and connect the other wells together. Thus, during experiments, the current will not travel from well RN-15 to other wells via these pipelines and will instead travel down the electrode (placed on the surface or inside the well, or the steel casings themselves are used as electrodes) into the ground. For measurements, it's important that significant current is going into the ground from one measurement point to another and not through the pipelines so the measured data will give information about the fracture connectivity in the ground.

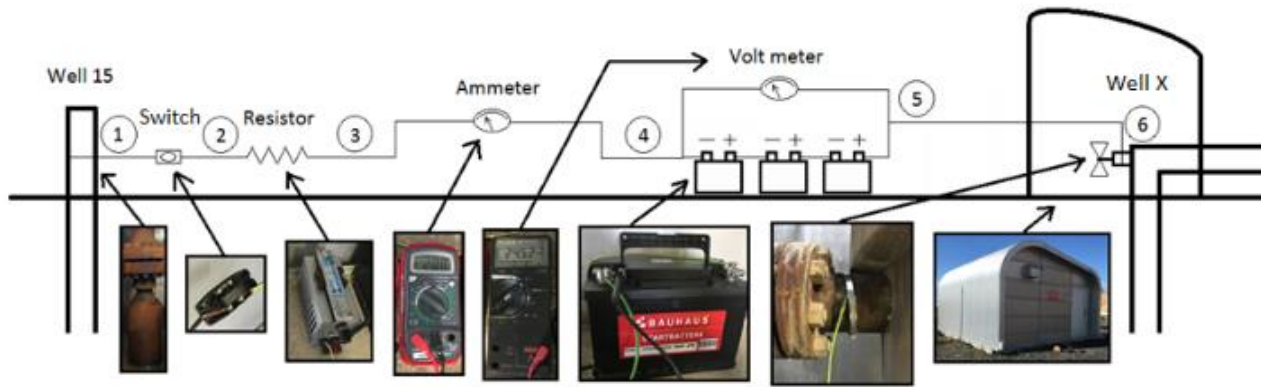


Figure 4. An example of a measurement setup at Reykjanes.

Figure 4 shows an example of a setup for measuring the resistivity between well RN-15 and another well as water is being injected into the reservoir. The setup can be constructed as follows. For using the steel casings as electrodes, an electric wire can be attached to the production casing of well RN-15 with a hose clamp. It is important to file down part of the casing to assure a good connection to the wire. Next, a switch is attached to the wire from well RN-15 to ease the process of connecting and disconnecting the electric circuit. Then, a resistor is attached to the circuit to control the amount of current flowing through the circuit. An ammeter is added to measure the current flowing through the circuit and a volt meter to measure the electric potential difference over one and up to three batteries. The batteries are 12 V 72 Ah batteries that should be connected in series when more than one battery is used. Then, the electric wire coming from well RN-15 connects to the negative terminal and the positive terminal connects to a casing (or a valve connected to the casing as shown in Figure 4) using a hose clamp on the other well being tested.

If the switch would be pressed so the circuit is closed, electric current flows from the positive terminal of the battery, down the production casing of well A in Figure 4, through the reservoir, up the production casing of well RN-15 and through the circuit to the negative terminal of the battery. Thus, the measured current and voltage will give information about the resistivity of the path the current travels through the reservoir. As fluid with higher resistivity than the fluid in the reservoir is injected, the measured resistivity between the wells will increase. This time-lapse resistivity can then be used in the inverse analysis as explained in previous section, to give information about the fracture connectivity in the reservoir.

6 Conclusions

This paper describes a conceptual model for estimating fracture connectivity in Reykjanes geothermal reservoir where a well has been drilled to a depth of 4.7 km. The

proposed method includes modeling changes in resistivity as injected water with lower conductivity than the fluid in the reservoir flows through the fracture network. Then, measurements of the time-lapse electric data are used in an inverse analysis to estimate the connectivity of the fracture data.

There are three conceptual models discussed in this paper; an over 5 km deep numerical model of Reykjanes where the permeability distribution and the temperature of the heat source are estimated using production data from the field, a fracture model where a discrete-fracture method is used to model realistic fracture networks, and a model for simulating the electric fields in the reservoir. All three models are created using iTOUGH2. Finally, the necessary measurements are discussed for using the models in an inverse analysis to estimate the fracture connectivity in the reservoir. The knowledge of the heat transfer and fluid-flow patterns in the reservoir is extremely valuable for efficient management of the system and optimal power production.

Acknowledgements

This research was supported by The Icelandic Research Fund, project number 163514-052.

References

- Binley A., Henry-Poulter S., Shaw B. (1996) Examination of Solute Transport in an Undisturbed Soil Column Using Electrical Resistance Tomography. *Water Resour. Res.* 32(4):763–769. Doi:10.1029/95WR02995.
- Binley A., Giorgio C., Middleton R., Winship P. (2002) Vadose zone flow model parameterisation using cross-borehole radar and resistivity imaging. *Journal of Hydrology* 267:147-159. Doi:10.1016/S0022-1694(02)00146-4.
- Cassiana G., Bruna V., Villaa A., Fusia N. Binley A. (2006) A saline trace test monitored via time-lapse surface electrical resistivity tomography. *Journal of Applied Geophysics* 59:244-259. doi:10.1016/j.jappgeo.2005.10.007.
- Day-Lewis F. D., Lane Jr. J. W., Harris J. M., Gorelick S. M. (2003) Time-lapse imaging of saline-tracer transport in

- fractured rock using difference-attenuation radar tomography. *Water Resour. Res.* 39:1290. Doi:10.1029/2002WR001722,10.
- G. O. Fridleifsson, W. Elders, R. Zierenberg, A. Stefansson, O. Sigurdsson, Th. Gislason, T. B. Weisenberger, B. S. Hardarson, K. G. Mesfin (2017) ICDP supported coring in IDDP-2 at Reykjanes – the DEEPEGS demonstrator in Iceland – Supercritical conditions reached below 4.6 km depth. 19th EGU General Assembly, *proceedings* from the conference held 23-28 April, 2017 in Vienna, Austria., p.14147.
- Karimi-Fard M., Durlofsky L. J., Aziz K. (2003) An Efficient Discrete Fracture Model Applicable for General Purpose Reservoir Simulators. SPE 79699, *SPE Reservoir Simulation Symposium*, Houston, TX.
- Koestel J., Kemna A., Javaux M., Binley A., Vereecken H. (2008) Quantitative imaging of solute transport in an unsaturated and undisturbed soil monolith with 3-D ERT and TDR. *Water Resour. Res.* 44. Doi:10.1029/2007WR006755.
- Lambota S., Antoineta M., Boschb I. van den, Slobc E. C., Vancloostera M. (2004) Electromagnetic Inversion of GPR Signals and Subsequent Hydrodynamic Inversion to Estimate Effective Vadose Zone Hydraulic Properties. *Vadose Zone Journal* 3:1072:1081. Doi:10.2113/3.4.1072.
- Magnusdottir, L., Finsterle, S. (2015) An iTOUGH2 equation-of-state module for modeling supercritical con in geothermal reservoirs, *Geothermics*, 57, 8–17. doi:10.1016/j.geothermics.2015.05.003.
- Magnusdottir, L., Horne, R. (2013) Inversion of time-lapse electrical resistivity data to estimate fracture connectivity. *Mathematical Geosciences*, 47, 85–104. Doi:10.1007/s11004-013-9515-9
- Muskat M. (1932) Potential Distributions in Large Cylindrical Disks with Partially Penetrating Electrodes. *Physics* 2:329-364. Doi:10.1063/1.1745061.
- Oldenborger G. A., Knoll M. D., Routh P. S., LaBrecque D. J. (2007) Time-lapse ERT monitoring of an injection/withdrawal experiment in a shallow unconfined aquifer. *Geophysics* 72:F177-F187. Doi:10.1190/1.2734365.
- Olsen P. A., Binley, A., Henry-Poulter, S. and Tych, W. (1999) Characterizing solute transport in undisturbed soil cores using electrical and X-ray tomographic methods. *Hydrol. Process.* 13:211–221. Doi:10.1002/(SICI)1099-1085(19990215)13:2<211::AID-HYP707>3.0.CO;2-P.
- Singha K., Day-Lewis F. D., Moysey S. (2007) Accounting for tomographic resolution in estimating hydrologic properties from geophysical data. *Geophysical Monograph Series* 171:227-241.
- Singha K., Gorelick S. M. (2005) Saline Tracer Visualized with Three-dimensional Electrical Resistivity Tomography: Field-scale Spatial Moment Analysis. *Water Resour. Res.* 41. Doi:10.1029/2004WR003460.
- Singha K., Gorelick S. M. (2006) Hydrogeophysical tracking of three-dimensional tracer migration: The concept and application of apparent petrophysical relations. *Water Resour. Res.* 42. Doi:10.1029/2005WR004568.
- Slater L., Binley A. M., Daily W, Johnson R. (2000) Cross-hole Electrical Imaging of a Controlled Saline Tracer Injection. *Journal of Applied Geophysics* 44:85-102. Doi:10.1016/S0926-9851(00)00002-1.
- Yeh T.-C. J., Liu S., Glass R. J., Baker K., Brainard J. R., Alumbaugh D. L., LaBrecque D. (2002) A geostatistically based inverse model for electrical resistivity surveys and its applications to vadose zone hydrology. *Water Resour. Res.* 38(12). Doi:10.1029/2001WR001204.

Modeling N/S ratio and temperature influences on simultaneous biological denitrification and sulfide oxidation

Michal Sposob¹ Rune Bakke¹ Carlos Dinamarca¹

¹Department of Process, Energy and Environmental Technology, University College of Southeast Norway, Norway
michal.sposob@usn.no

Abstract

A model describing the simultaneous removal of NO_3^- and HS^- by microorganisms is presented here. The oxidation of HS^- (electron donor) can be controlled by the appropriate dosage of NO_3^- . The developed model, which includes variable process stoichiometry, attempts to predict the distribution of sulfur oxidation products. Stoichiometric coefficients are based on a 150 days experimental study of temperature (25-10 °C) and N/S ratio (0.35-1.30) effects. The model can be used as a prediction tool for autotrophic denitrification with HS^- . Elemental sulfur production is included in the mathematical model, however, its accumulation and release (as SO_4^{2-}) with increasing feed N/S ratio (e.g. leading to higher effluent than feed total sulfur mass at N/S = 1.30) is not simulated. A conceptual model to account for biological accumulation and release of elemental sulfur is proposed here.

Keywords: autotrophic denitrification, elemental sulfur production, mathematical modeling, sulfate production

1 Introduction

The presence of sulfide (H_2S) in wastewaters is an important issue concerning wastewater networks and treatment plants maintenance due to its corrosive properties (Ma et al., 2000). Low concentrations of H_2S (lower than 10 mg/L) are present in domestic wastewaters (Pikaar et al., 2011). The exposure to H_2S in gaseous form is toxic to human even at low concentrations and can paralyze the olfactory nerves and lead to death (Reiffenstein et al., 1992).

Biological wastewater treatment plants used to remove carbon, nitrogen and phosphorus can be inhibited by extensive presence of H_2S (Chen et al., 2008; Jin et al., 2013; Joye and Hollibaugh, 1995). It has been reported that anaerobic digestion process can be inhibited at concentrations from 50 mg $\text{H}_2\text{S}/\text{L}$ (Chen et al., 2008). H_2S presence can vary due to the high complexity of the sulfur (S) cycle and its partial overlapping with cycles of other elements (i.e. C, Fe, Hg, N and Se). Knowledge of these cycles can be used for biochemical H_2S control and S removal.

Physicochemical H_2S removal is often used for H_2S removal (desulfurization) in industrial scale. The Claus

process, where elemental sulfur (S^0) is recovered from H_2S -containing gases under high temperature and oxygen (O_2) supply, is the most common method. Biological treatment, utilizing the unique properties of microorganisms, is gaining attention due to the environmental and economic advantages. Biological H_2S removal from wastewaters utilizes the ionic forms HS^- and/or S^{2-} (depending on pH) as the electron donor, while usually nitrate (NO_3^-), nitrite (NO_2^-) and O_2 are electron acceptor sources. The usage of these electron acceptors is not mutually exclusive, so they can be used together and separately. Addition of more than one electron acceptor can be applied to enhance the H_2S removal (Wang et al., 2015). Due to advantages such as a higher solubility of NO_3^- than O_2 , NO_3^- usage is studied here. It is argued that the continuous flow expanded granular sludge bed (EGSB) bioreactor is the most efficient design for biological desulfurization (Cai et al., 2010). Data from a previous EGSB study (Sposob et al., 2017a; 2017b) are used here.

The oxidation of HS^- can be controlled by the ratio between electron acceptor and electron donor to influence the relative amounts of the oxidation products: S^0 and sulfate (SO_4^{2-}). Extensive experimental and theoretical studies on the appropriate conditions for simultaneous N and S removal, i.e. C/N/S ratio, pH, load and temperature, have been conducted (Di Capua et al., 2017; Guo et al., 2016; Huang et al., 2016; Mahmood et al., 2007; Montalvo et al., 2016; Reyes-Avila et al., 2004; Sposob et al., 2017a). Modeling can facilitate further understanding and optimization of simultaneous biological NO_3^- and HS^- removal. So far, a few models based on artificial neural networks (Wang et al., 2009) and kinetic approach (Wang et al., 2010; Xu et al., 2016, 2014) have been developed. The kinetic models are based on batch experiments where only the initial phase of the process is accounted for. Fixed stoichiometry based on assumed chemical reactions or based on calculated and/or experimentally obtained yield values also limits published models, since the ratio between electron acceptor and electron donor can completely alter the output (Cai et al., 2008; Sposob et al., 2017b). The models describing simultaneous removal of NO_3^- and HS^- should take into account the fact that effluents from this kind of treatment can contain several products

especially at low N/S ratios. This is challenging since it has been observed in long-term experiment that SO_4^{2-} and S^0 were produced at the same time at feed N/S ratio that theoretically should lead to S^0 production only (Sposob et al., 2017a; Tan et al., 2016). It has also been observed that temperature has an impact on effluent sulfur components at constant N/S ratio (Sposob et al., 2017a). Thus, the need for the modeling including multicomponent effluent characteristic is required, especially in cases where lower N/S ratios are modeled.

The objective of this study is to develop a model for simultaneous removal of NO_3^- and HS^- at different N/S ratios and temperatures, which can be used to predict the distribution of produced sulfur components.

2 Methods and model development

2.1 Experimental design

The experimental trial was performed in a 0.5 L laboratory-scale EGSB reactor continuously fed by synthetic wastewater over 150 days. The feeding parameters are given in Table 1.

Table 1. Feeding parameters.

Time (d)	Temperature (°C)	N/S ratio	NO_3^- (mM/L)	HS^- (mM/L)		
1-25	25	0.35	1.08	3.12		
26-57	20					
58-90	15					
91-120	10					
121-134					0.40	1.25
135-142					0.60	1.87
143-150		1.30	4.05			

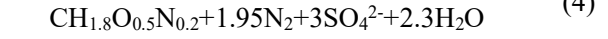
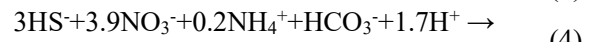
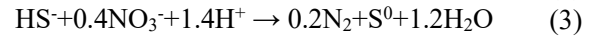
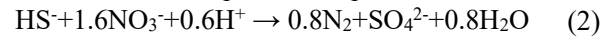
Synthetic wastewater was supplied from two feed tanks (separate for electron acceptor and donor) to avoid contamination and possible reactions in feeding tank. In addition to electron acceptor and donor sources, vitamins, buffer, macro- and microelements were supplied as described in Sposob et al. (2017a), where the more detailed description of experiment is given.

2.2 Stoichiometry

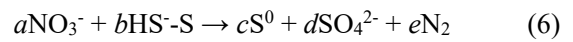
The model is developed and evaluated based on the stoichiometry derived by Kleerebezem and Mendez, (2002) and data from continuous flow expanded granular sludge bed (EGSB) experiments (Sposob et al., 2017a; 2017b). The collected data consists information about concentrations of accumulated elemental sulfur (S^0_{acc}), nitrate (NO_3^-), sulfate (SO_4^{2-}), sulfide (HS^-) and suspended elemental sulfur (S^0_{ss}) measured as thiosulfate ($\text{S}_2\text{O}_3^{2-}$). Accumulated sulfur (S^0_{acc}) was calculated based on the difference between influent HS^- concentration and effluent concentrations of HS^- , SO_4^{2-} and S^0_{ss} , according to Eq. 1 (Sposob et al., 2017a).

$$\text{S}^0_{\text{acc}} = \text{HS}^-_{\text{inf}} - \text{HS}^-_{\text{eff}} - \text{SO}_4^{2-}_{\text{eff}} - \text{S}^0_{\text{ss}} \quad (1)$$

The basic chemical reactions (Eqs. 2, 3) and reactions combining both anabolism (biomass production) and catabolism (energy release) (Eqs. 4, 5) according to Kleerebezem and Mendez (2002) serve as the core for the model. However, these equations assume production of only one sulfur component at specific N/S ratio and does not include temperature impact.



The new stoichiometry applied here includes simultaneous NO_3^- and HS^- removal and possibility to produce two sulfur components: S^0 (without distinguishing the S^0 fractions) and SO_4^{2-} according to Eq. 6.



Where c and d depend on feed molar ratio between a and b (N/S ratio) and temperature (T) (Eqs. 7, 8).

$$c = f(\text{N/S}; T) \quad (7)$$

$$d = f(\text{N/S}; T) \quad (8)$$

2.3 Kinetics

Process kinetics is modeled based on the Monod equation for reaction rates and assuming one general microbial community of sulfide oxidizing bacteria (SOB). The growth of microorganisms is thus described using the Bailey's equation that includes both required substrates (Eq. 9). The biomass concentration is assumed constant in the simulations due to the conditions with high biomass content in the EGSB reactor and low biomass yield of autotrophic denitrification bacteria (Tchobanoglous et al., 2003), implying that reactor biomass changes are insignificant during the experiments used in this study. The growth parameters maximum growth rate (μ_{max}) and half-saturation constants (K_{HS^-} , $K_{\text{NO}_3^-}$) applied are given in Table 2.

$$\mu = \mu_{\text{max}} \cdot X_{\text{SOB}} \left(\frac{S_{\text{HS}^-}}{K_{\text{HS}^-} + S_{\text{HS}^-}} \right) \left(\frac{S_{\text{NO}_3^-}}{K_{\text{NO}_3^-} + S_{\text{NO}_3^-}} \right) \quad (9)$$

Table 2. Growth parameters.

Parameter	Value	Source
μ_{max}	4.25 d ⁻¹	(Wang et al., 2010)
$K_{\text{NO}_3^-}$	7.84 mM NO_3^-/L	(Xu et al., 2016)
K_{HS^-}	1.8 mM S^2/L	

The mathematical model is implemented in the AQUASIM simulation software (Eawag, Switzerland). The established model is calibrated and used to simulate removal of NO_3^- and HS^- . Simulation results are

compared with the obtained experimental data published in Sposob et al. (2017a, 2017b).

2.4 Temperature

Temperature has an impact on bacterial kinetic coefficients like μ_{\max} and K_S leading to changes in the treatment efficiency. During the experimental trial the electron donor (HS^- -S) removal changed from 98 (25 °C) to 89 % at 10 °C. Temperature also influenced the effluent composition of sulfur components in the experiment modeled here (Figure 1). Electron acceptor (NO_3^-) removal was not significantly influenced by temperature as it was completely removed (effluent NO_3^- was detected only three times during 120 days temperature-trial).

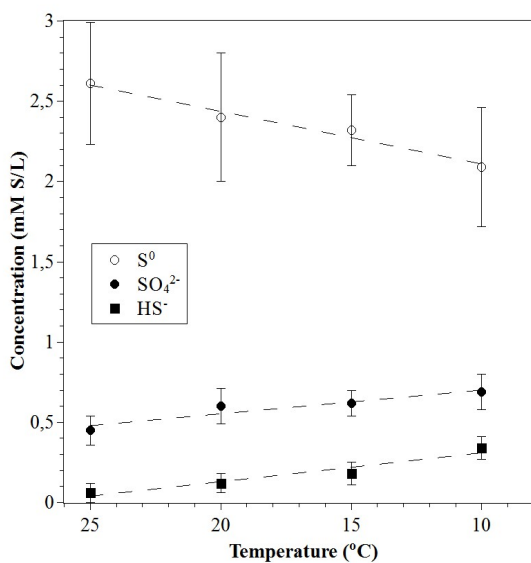


Figure 1. Average concentration of sulfur components at 25-10 °C and N/S = 0.35 (Sposob et al., 2017a).

With decreasing temperature and invariable feeding pattern, the share of S^0 decreased while SO_4^{2-} together with HS^- increased. Performed free Gibbs energy calculations (ΔG^0) revealed that the reaction energy at the different temperatures remained nearly constant due to this shift in products formation from S^0 to SO_4^{2-} (Sposob et al., 2017a). The reaction energy maintained at invariable feeding conditions is dependent on the relationships given in Eqs. 10 and 11. The culture evidently preferred to use more NO_3^- per mole of HS^- at lower temperatures. Whether this is due to a shift in microbial community or a metabolic shift within cells is currently under investigation. Until such information is available an empirical temperature effect is implemented in the model by temperature dependent stoichiometric coefficients (Table 3) based on the experimental results given in Figure 1.

$$\text{Reaction energy} = \text{oxidation to } \text{S}^0 + \text{oxidation to } \text{SO}_4^{2-} \quad (10)$$

$$\text{Reaction energy} \approx \text{constant} \quad (11)$$

Table 3. Temperature coefficient for stoichiometric parameters calculated based on the experimental trial.

Temperature	T_{sulfur}	T_{sulfate}
25	0.84	0.14
20	0.77	0.19
15	0.74	0.2
10	0.67	0.22

2.5 N/S ratio

Changes in N/S ratio have been reported as a way to control the level of HS^- oxidation (Cai et al., 2008). However, the results at different ratios at 10 °C show a significant offset from the theoretical values (Figure 2). The highest offset was obtained for S^0 . Experimental results equaled the theoretical values only at N/S = 1.30. A more detailed description of N/S ratio impact at psychrophilic conditions (10 °C) is given in Sposob et al. (2017b). Modeling effects of N/S ratios in Eq. 7 and 8 based on these observations is implemented through correction coefficients given in Table 4.

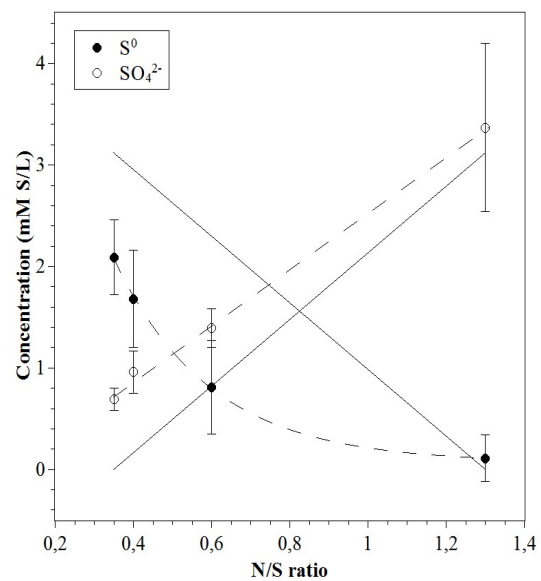


Figure 2. Average concentration of sulfur components at different N/S ratios at 10 °C. Whole lines are theoretical values based on Eqs. 4, 5 while dotted line connects the given experimental values.

Table 4. N/S ratio coefficient for stoichiometric parameters calculated based on the experimental trial.

N/S ratio	N/S_{sulfur}	N/S_{sulfate}
0.35	1	1
0.40	0.81	1.41
0.60	0.48	2.05
1.30	0.06	4.36

3 Results and Discussion

Simulations, with the calculated coefficients (Table 3) of products distribution (S^0 and SO_4^{2-}) with different temperatures and constant feed $N/S = 0.35$ behaves similar to the experimental results (Figure 3). The implemented model with the temperature coefficients (Table 3) simulates the pseudo-steady state relative amounts of effluent S^0 and SO_4^{2-} . This may seem obvious since the coefficients are calculated based on average values for each temperature case of the same data set. The model, however, also simulates the transitions in relative amounts of products occurring following each 5 °C temperature drop (the initial part of each of the three last panels in Figure 3) quite accurately. The model significantly improved predictions at $N/S = 0.35$ compared to the equations (Eqs. 3, 5) that predict S^0 production only and no temperature effect.

Increasing the model complexity, including diversification of microbes and/or the implementation of energy terms, can further improve the model for better prediction of HS^- removal and products

distribution for a wider range of conditions. However, further experimental investigations are required to implement such.

Experimental data and predictions based on Kleerebezem and Mendez (2002) equations (Eqs. 4, 5) are compared in Figure 2 regarding N/S ratio effects on products distribution. The observed offset between experimental and theoretical values could be partly due to the oxidation of earlier accumulated S^0 (reaction 3 in the schematic presentation of the studied process in Figure 4), but this is not explicitly included in the mathematical model. The reaction energy from HS^- oxidation is increasing with increased amount of NO_3^- supplied. Probably both of these energy related phenomena influence the products distribution but insufficient results are yet available to distinguish these. Thus, further model refinement to include both hypothesized energy reactions separately is not attempted and the cumulative effect observed experimentally are covered by the coefficients given in Tables 3 and 4 and simulated (Figure 5).

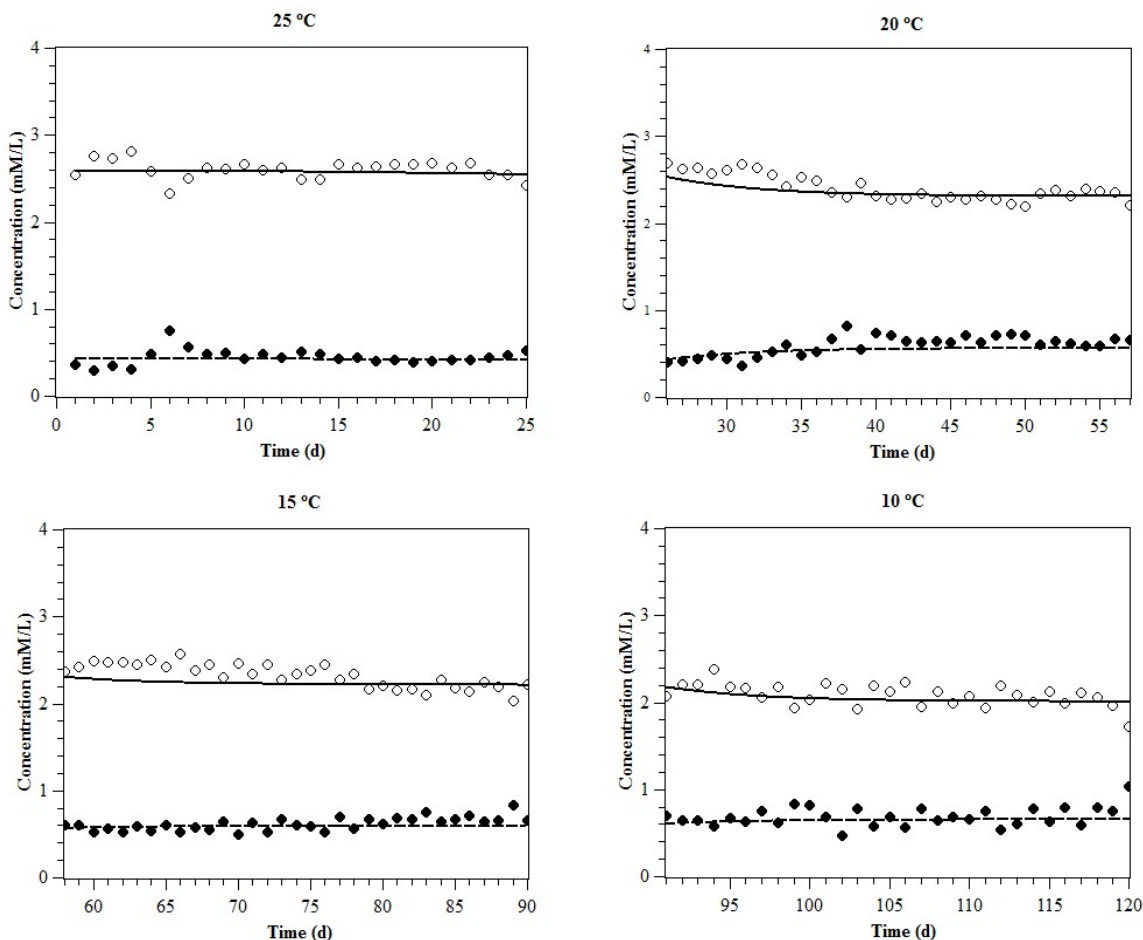


Figure 3. Model simulation results in comparison to experimental results at different temperatures. Solid and dash line represent simulated results for S^0 and SO_4^{2-} , respectively. Scatter points represent experimental results for S^0 (○) and SO_4^{2-} (●).

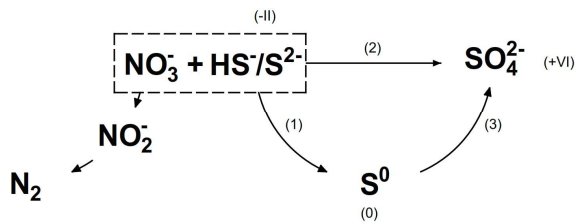


Figure 4. The scheme of autotrophic denitrification with HS^- as electron donor.

The simulations with the applied coefficients related to N/S ratio (Table 4) significantly improved predictions compared to those in Figure 2, except for N/S = 1.30, where simple stoichiometric calculations matched the experimental values best. The poor simulation of experimental results at N/S = 1.30 is assumed to be due to the fact that reaction 3 in Figure 4 is not explicitly accounted for in the model and that this reaction is especially important at this stage. This is due to the experimental scenario which at the beginning was focused on S^0 production leading to its accumulation, as

energy storage for the microorganisms. This S^0 energy reserve in the reactor was oxidized to SO_4^{2-} and is especially visible at N/S = 1.30. This implies that a more refined future model of simultaneous biological removal of HS^- and NO_3^- needs to consider the effect of S^0 accumulation and its possible oxidation (Figure 4) as occurred here under N/S ratio effects trial.

The energy related aspects discussed here are not included in the previously published models since these are based mainly on batch experiments and high N/S ratio situations. The observed phenomena probably occur only in cases when the N/S ratio is in or close to the range investigated here and are most observable when increasing from low (S^0 production related) to high N/S ratios (SO_4^{2-} production related). It can therefore be useful to develop the model further to better account for accumulation and consumption of S^0 . Some relevant information is available, such as: kinetics for S^0 leaching and usage as electron donor is available (Franzmann et al., 2005; Gourdon and Funtowicz, 1998; Koenig and Liu, 2001). Models including similar accumulation phenomena related to energy storage are developed, i.e. ASM2d where the accumulation and

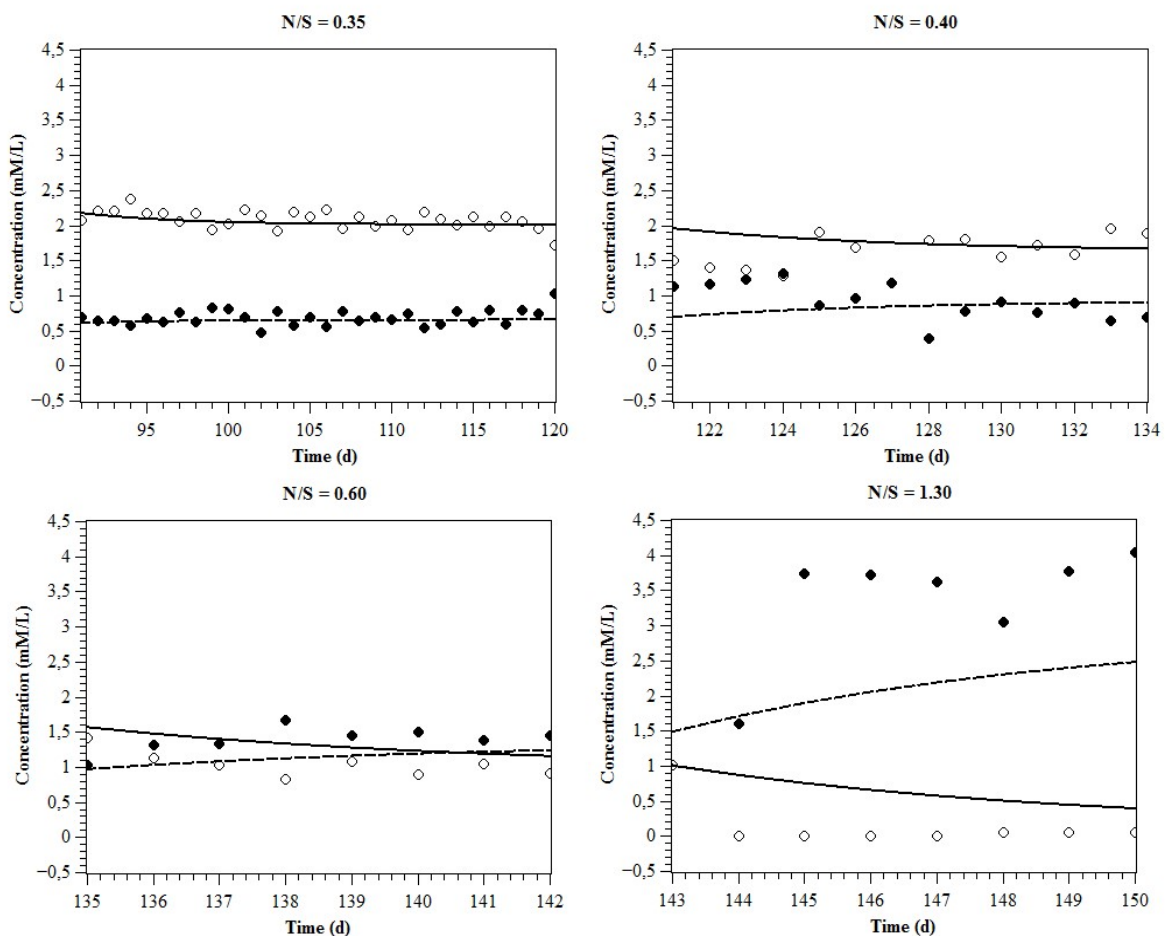


Figure 5. Model simulation results in comparison to experimental results at different N/S ratios at 10 °C. Solid and dash line represent simulated results for S^0 and SO_4^{2-} respectively. Scatter points represent experimental results for S^0 (○) and SO_4^{2-} (●).

consumption of polyhydroxybutyrate (PHB) and polyphosphate (PP) are taken into account (Henze et al., 1999). However, the factors triggering the oxidation of accumulated S^0 are not clear. It has been reported that the oxidation can only occur when the source of reduced sulfur compounds is depleted (Schedel and Trüper, 1980), but oxidation of accumulated S^0 can obviously occur (e.g. Figure 2) and be influenced by both temperature and N/S ratio changes when HS^- (sulfur reduced compound) is available (Sposob et al., 2017b, 2016). The observation that S^0 leaching increases with temperature (Franzmann et al., 2005) should also be accounted for in the further model development.

4 Conclusions

The presented model can serve as a prediction tool for autotrophic denitrification with HS^- as supplied electron donor, to account for effects of temperature and feed N/S ratio.

The model was able to simulate sulfur compound products distribution at different temperatures, more accurately at low than higher N/S ratios (N/S range 0.35 to 1.30).

The phenomena of S^0 production included in the mathematical model does not take into account its accumulation and release (as SO_4^{2-}). Thus, adequate prediction of products distribution caused by N/S ratio step increases (leading to higher concentration of sulfur components in the effluent than fed into the reactor) was not obtained. Therefore, a conceptual model is proposed to account for biological accumulation and release of S^0 . Further investigations on N/S ratio effects on S^0 accumulation and release can yield a more refined model of simultaneous biological removal of HS^- and NO_3^- .

Acknowledgements

The authors would like to thank YARA AS International and The Research Council of Norway for support of this research.

References

- Cai, J., Zheng, P., and Mahmood, Q. Effect of sulfide to nitrate ratios on the simultaneous anaerobic sulfide and nitrate removal. *Bioresource Technology*, 99(13):5520–5527, 2008.
- Cai, J., Zheng, P., and Mahmood, Q. Influence of transient pH and substrate shocks on simultaneous anaerobic sulfide and nitrate removal. *Journal of Hazardous Materials*, 174(1–3):162–166, 2010.
- Chen, Y., Cheng, J. J., and Creamer, K. S. Inhibition of anaerobic digestion process: A review. *Bioresource Technology*, 99(10):4044–4064, 2008.
- Di Capua, F., Milone, I., Lakaniemi, A. M., Lens, P. N. L., and Esposito, G. High-rate autotrophic denitrification in a fluidized-bed reactor at psychrophilic temperatures. *Chemical Engineering Journal*, 313:591–598, 2017.
- Franzmann, P. D., Haddad, C. M., Hawkes, R. B., Robertson, W. J., and Plumb, J. J. Effects of temperature on the rates of iron and sulfur oxidation by selected bioleaching Bacteria and Archaea: Application of the Ratkowsky equation. In *Minerals Engineering* 18:1304–1314, 2005.
- Gourdon, R., and Funtowicz, N. (1998). Kinetic model of elemental sulfur oxidation by Thiobacillus thiooxidans in batch slurry reactors: Effects of surface characteristics and suspended solid concentration. *Bioprocess Engineering*, 18(4):241–249, 1998.
- Guo, Q., Hu, H. Y., Shi, Z. J., Yang, C. C., Li, P., Huang, M., Ni, W. M., Shi, M. N., and Jin, R. C. Towards simultaneously removing nitrogen and sulfur by a novel process: Anammox and autotrophic desulfurization-denitrification (AADD). *Chemical Engineering Journal*, 297, 207–216, 2016.
- Henze, M., Gujer, W., Mino, T., Matsuo, T., Wentzel, M. C., Marais, G. V. R., and Van Loosdrecht, M. C. M. (1999). Activated Sludge Model No.2d, ASM2d. *Water Science and Technology* 39:165–182, 1999.
- Huang, C., Li, Z., Chen, F., Liu, Q., Zhao, Y., Gao, L., Chen, C., Zhou, J., and Wang, A. Efficient regulation of elemental sulfur recovery through optimizing working height of upflow anaerobic sludge blanket reactor during denitrifying sulfide removal process. *Bioresource Technology*, 200:1019–1023, 2016.
- Jin, R. C., Yang, G. F., Zhang, Q. Q., Ma, C., Yu, J. J., and Xing, B. S. The effect of sulfide inhibition on the ANAMMOX process. *Water Research*, 47(3):1459–1469, 2013.
- Joye, S. B., and Hollibaugh, J. T. Influence of sulfide inhibition of nitrification on nitrogen regeneration in sediments. *Science*, 270(5236):623–625, 1995.
- Kleerebezem, R., and Mendez, R. Autotrophic denitrification for combined hydrogen sulfide removal from biogas and post-denitrification. *Water Science and Technology*, 45(10):349–356, 2002.
- Koenig, A., and Liu, L. H. Kinetic model of autotrophic denitrification in sulphur packed-bed reactors. *Water Research*, 35(8):1969–1978, 2001.
- Ma, H., Cheng, X., Li, G., Chen, S., Quan, Z., Zhao, S., and Niu, L. The influence of hydrogen sulfide on corrosion of iron under different conditions. *Corrosion Science*, 42(10):1669–1683, 2000.
- Mahmood, Q., Zheng, P., Cai, J., Wu, D., Hu, B., and

- Li, J. Anoxic sulfide biooxidation using nitrite as electron acceptor. *Journal of Hazardous Materials*, 147(1–2):249–256, 2007.
- Montalvo, S., Huiliñir, C., Gálvez, D., Roca, N., and Guerrero, L. Autotrophic denitrification with sulfide as electron donor: Effect of zeolite, organic matter and temperature in batch and continuous UASB reactors. *International Biodeterioration and Biodegradation*, 108:158–165, 2016.
- Pikaar, I., Rozendal, R. A., Yuan, Z., Keller, J., and Rabaey, K. (2011). Electrochemical sulfide removal from synthetic and real domestic wastewater at high current densities. *Water Research*, 45(6):2281–2289, 2011.
- Reiffenstein, R. J., Hulbert, W. C., and Roth, S. H. Toxicology of hydrogen sulfide. *Annual Review of Pharmacology and Toxicology*, 32(1):109–134, 1992.
- Reyes-Avila, J., Razo-Flores, E., and Gomez, J. Simultaneous biological removal of nitrogen, carbon and sulfur by denitrification. *Water Research*, 38(14–15):3313–3321, 2004.
- Schedel, M., and Trüper, H. G. Anaerobic oxidation of thiosulfate and elemental sulfur in *Thiobacillus denitrificans*. *Archives of Microbiology*, 124(2–3):205–210, 1980.
- Sposob, M., Bakke, R., and Dinamarca, C. Effects of N/S molar ratio on products formation in psychrophilic autotrophic biological removal of sulfide. *Water*, 9(7):476, 2017a.
- Sposob, M., Bakke, R., and Dinamarca, C. Metabolic divergence in simultaneous biological removal of nitrate and sulfide for elemental sulfur production under temperature stress. *Bioresource Technology*, 233:209–215, 2017b.
- Sposob, M., Dinamarca, C., and Bakke, R. Short-term temperature impact on simultaneous biological nitrogen-sulphur treatment in EGSB reactor. *Water Science and Technology*, 74(7):1610–1618, 2016.
- Tan, W., Huang, C., Chen, C., Liang, B., and Wang, A. Bioaugmentation of activated sludge with elemental sulfur producing strain *Thiopseudomonas denitrificans* X2 against nitrate shock load. *Bioresource Technology*, 220:647–650, 2016.
- Tchobanoglous, G., Burton, F. L., and Stensel, H. D. (2003). *Wastewater Engineering: Treatment and Reuse (Fourth Edition)*. *Wastewater Engineering, Treatment, Disposal and Reuse*, 2003.
- Wang, A., Liu, C., Han, H., Ren, N., and Lee, D. J. Modeling denitrifying sulfide removal process using artificial neural networks. *Journal of Hazardous Materials*, 168(2–3):1274–1279, 2009.
- Wang, A., Liu, C., Ren, N., Han, H., and Lee, D. Simultaneous removal of sulfide, nitrate and acetate: Kinetic modeling. *Journal of Hazardous Materials*, 178(1–3):35–41, 2010.
- Wang, X., Zhang, Y., Zhou, J., Zhang, T., and Chen, M. Regeneration of elemental sulfur in a simultaneous sulfide and nitrate removal reactor under different dissolved oxygen conditions. *Bioresource Technology*, 182:75–81, 2015.
- Xu, G., Yin, F., Chen, S., Xu, Y., and Yu, H. Q. Mathematical modeling of autotrophic denitrification (AD) process with sulphide as electron donor. *Water Research*, 91:225–234, 2016.
- Xu, X., Chen, C., Wang, A., Guo, W., Zhou, X., Lee, D. J., Ren, N., and Chang, J. S. Simultaneous removal of sulfide, nitrate and acetate under denitrifying sulfide removal condition: Modeling and experimental validation. *Journal of Hazardous Materials*, 264:16–24, 2014.

Microalgae Activated Sludge: Process Modeling and Optimization

Jesús Zambrano Emma Nehrenheim

School of Business, Society and Engineering, Mälardalen University, Västerås, Sweden.

jesus.zambrano@mdh.se

Abstract

This work deals with steady-state simulation study of a process formed by a microalgae-bacteria photobioreactor (PBR) in an activated sludge configuration. In particular, the process behavior in terms of variations in the sludge retention time and carbon dioxide (CO₂) injected is presented. The optimization is done by considering the total PBR volume as two volumes in series, and aiming for the minimal substrate concentration in the effluent, for a given external light and CO₂ injected. Results suggest that it is possible to obtain an optimum volume distribution of the process that gives a lower effluent substrate concentration compared to the same process using a single volume.

Keywords: microalgae-bacteria, bioprocess design, effluent minimization, photobioreactor, volume distribution.

1 Background

In wastewater treatment applications, the bioreactors are disposed in a configuration known as activated sludge process (ASP), where the bioreactor effluent is connected to a settler. The settler increases the microorganism (biomass) concentration and part of the settled stream is recycle back to the bioreactor (Grady Jr. et al., 1999). The biomass separation given by the settler makes the residence time of particulate components greater than the residence time of soluble components. This residence time for particulate components, referred as the sludge retention time (SRT), is a key factor in the plant operation. SRT is defined as the ratio between the amount of biomass in the bioreactor and the amount of removed biomass per time unit, i.e. it represents the average time the biomass stays in a bioreactor. External aeration is another key factor in these processes, since it is needed for aerobic bacteria to consume nutrients (such as nitrogen and phosphorus).

Nowadays, the role of microalgae in wastewater treatment applications is becoming more relevant (de la Nouë et al., 1992; Dalrymple et al., 2013). Via photosynthesis, where a certain external illumination is applied to the bioreactor, microalgae require carbon dioxide to consume nitrogen and release oxygen, which is beneficial for the aerobic bacteria in the wastewater treatment processes. In this way, we refer to photobioreactors (PBRs) as bioreactors able to grow

microalgae.

In a PBR the biological dynamics is directly affected by the irradiance applied. Therefore, several models for the biology and the irradiance have been proposed in literature. Concerning the biological models, early works can be found in Droop (1968, 1973), where the growth rate of the microalgae is assumed to be associated to an internal substrate concentration. The basic form of this model includes three ordinary differential equations which describe the substrate (nutrient), the microalgae and the internal substrate cell quota in the microalgae. Jang and Baglama (2005) proposed a model which includes one main substrate and two microalgae species (zooplankton and phytoplankton). The study includes a global asymptotic analysis of the system considering different growth rates and changes in the input nutrient concentration. Decostere et al. (2013) proposed a model for microalgae growth on inorganic carbon which includes oxygen production. The model is based on the Activated Sludge Models (ASMs) and includes a calibration using data from respirometric-titrimetric experiments.

Regarding the models for the irradiance, several approaches have been proposed in the last decades. For example, Eilers and Peeters (1988) proposed a dynamic model for the irradiance, which links the light intensity and the rate of photosynthesis in phytoplankton microalgae. The model is based on physiological mechanisms, and includes the photoinhibition effect and the recovery from the photoinhibition. Geider et al. (1998) presented a simple model where the chlorophyll (a concentration that depends on the incident irradiance to the PBR) is included as a single variable. This models also includes the response of the photosynthesis to the nitrogen and light status in the microalgae. Other models linking the chlorophyll with the nutrient dynamics have been proposed, see for example Pahlow (2005). Results from this model replicate the nutrient:carbon ratio from experimental data.

The modeling of the microalgae-bacteria consortium has also been investigated in the last year. Dochain et al. (2003) reported a dynamic model with three microorganisms: microalgae, aerobic bacteria and sulphate-reducing anaerobic bacteria. The study includes a model calibration based on experimental data from different seasons. Zambrano et al. (2016) proposed a dynamic model for the microalgae-bacteria interaction, where the bacteria dynamics is inspired by the Activated

Sludge Model no. 1 (ASM1) (Henze et al., 1987) and the microalgae dynamics is inspired by the works from (Reichert et al., 2001) and (Solimeno et al., 2015). Experimental data from batch experiments presented by Krustok et al. (2016) was used for the model calibration.

When modeling bioreactors, a natural aim is to optimize the process in terms of volume and performance. The optimization of bioreactors has been investigated during decades (Aris, 1961; Herbert, 1964; Abu-Reesh, 1996), where mainly two typical approaches are done: (i) minimize the total bioreactor volume to achieve a given effluent substrate concentration, or (ii) from a given total volume of a set of bioreactors in series, optimize the volume distribution so to minimize the effluent substrate concentration.

The aim of the present study is, given a model for the microalgae-bacteria consortium, to study the behavior of a PBR-based activated sludge configuration (henceforth referred to as MAAS process) in terms of variations in key parameters such as the SRT and the CO_2 injected. The study includes the optimization of the total volume distribution when two PBRs in series are considered, so to minimize the effluent substrate concentration. A model based on Zambrano et al. (2016) is used for describing the microalgae-bacteria consortium. This model includes a modification in the effect that the irradiance has on the biological activity, which now depends on the amount of microalgae and bacteria concentration.

The paper is organized as follows. A description of the biological process and the model are given in Section 2. Section 3 gives a numerical illustration, and some conclusions are given in Section 4.

2 Methods

2.1 The MAAS process

The configuration of the MAAS process is shown in Figure 1, which consists of a PBR and a clarifier. In the PBR, the wastewater is treated by the biological activity of the microalgae-bacteria consortium. An external

illumination and CO_2 injection is applied to the PBR. In the clarifier (also called settler), the microorganisms are separated from the treated water. The PBR and clarifier are interconnected following the classical configuration of an ASP (Grady Jr. et al., 1999). To maintain the biomass population, part of the underflow from the clarifier goes as return sludge back to the PBR and the excess sludge is removed.

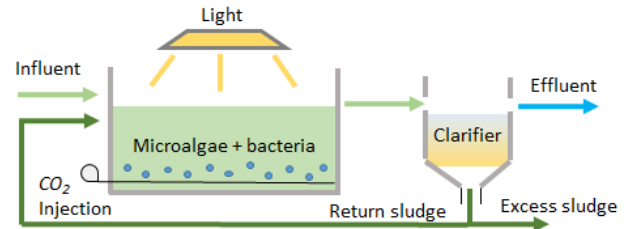


Figure 1. Layout of the MAAS process.

Since the main purpose of this study was to analyze the overall behavior of the MAAS process, an ideal clarifier was assumed, i.e, the amount of solids in the effluent is neglected, which means that all the sludge is thickened.

2.2 The model

A simple model for the microalgae-bacteria interaction (Zambrano et al., 2016) was used to describe the biological activity in the MAAS process. The model is formed by six components: two main biomass populations (microalgae (X_{alg}) and bacteria (X_{bac})), two dissolved substrate concentrations (ammonium (S_{nh4}) and nitrate (S_{no3})), and two dissolved gases concentrations (oxygen (S_{o2}) and carbon dioxide (S_{co2})), see Table 1.

The model is based on the following assumptions. There is only one class of microalgae and one class of bacteria. The microalgae growth on dissolved ammonium and nitrate and it is assumed that ammonium is preferred (Reichert et al., 2001). The autotrophic conversion of ammonium by the bacteria is considered as a single step process with the aid of oxygen (Henze et al., 1987).

Table 1. Model components and stoichiometric matrix.

Component (i) \rightarrow	(1)	(2)	(3)	(4)	(5)	(6)	Process rate
Process (j) \downarrow	X_{alg} $\left[\frac{gCOD}{m^3}\right]$	X_{bac} $\left[\frac{gCOD}{m^3}\right]$	S_{nh4} $\left[\frac{gN}{m^3}\right]$	S_{no3} $\left[\frac{gN}{m^3}\right]$	S_{o2} $\left[\frac{gO_2}{m^3}\right]$	S_{co2} $\left[\frac{gCO_2}{m^3}\right]$	ρ_j $\left[\frac{g}{m^3d}\right]$
(1) Algae growth on NH_4	1		$-\frac{1}{Y_{alg,nh4}^N}$		$Y_{alg,nh4}^O$	$-\frac{1}{Y_{alg,nh4}^C}$	ρ_1
(2) Algae growth on NO_3	1			$-\frac{1}{Y_{alg,no3}^N}$	$Y_{alg,no3}^O$	$-\frac{1}{Y_{alg,no3}^C}$	ρ_2
(3) Algae decay	-1		f_{alg}^N			f_{alg}^C	ρ_3
(4) Bacteria growth		1	$-iX_{bac} - \frac{1}{Y_{bac}}$	$\frac{1}{Y_{bac}}$	$-\left(\frac{4.57 - Y_{bac}}{Y_{bac}}\right)$	f_{bac}^C	ρ_4
(5) Bacteria decay		-1	iX_{bac}				ρ_5

The dependency of stoichiometric and biokinetics factors on temperature was not included. The inhibition of microalgae by excess of light or excess of CO₂ was not considered. The different processes and the stoichiometry involved in the biological model are shown in Table 1, whereas Table 2 shows the correspondent expressions for the process rates (ρ).

Table 2. Process rates.

ρ_j	Process rate
ρ_1	$\mu_{alg}\mu(I)\left(\frac{S_{co2}}{K_{co2}+S_{co2}}\right)\left(\frac{S_{nh4}}{K_{n,alg}+S_{nh4}}\right)X_{alg}$
ρ_2	$\mu_{alg}\mu(I)\left(\frac{S_{co2}}{K_{co2}+S_{co2}}\right)\left(\frac{S_{no3}}{K_{n,alg}+S_{no3}}\right)\left(\frac{K_{n,alg}}{K_{n,alg}+S_{nh4}}\right)X_{alg}$
ρ_3	$b_{alg}X_{alg}$
ρ_4	$\mu_{bac}\left(\frac{S_{nh4}}{K_{n,bac}+S_{nh4}}\right)\left(\frac{S_{o2}}{K_{o2}+S_{o2}}\right)X_{bac}$
ρ_5	$b_{bac}X_{bac}$

where $\mu(I) = I/(K_I + I)$.

In this work, a modification in the model for the irradiance was introduced. In Zambrano et al. (2016), the model for the irradiance considers that the illumination applied to the PBR does not change under any circumstances when it travels through the reactor, i.e. the irradiance I is constant in Table 2. Now, the model includes the effect of the biomass concentration on the light penetration. This was done in a similar way as the Beer-Lambert law (Huisman et al., 2002), giving the following irradiance factor:

$$\mu(\tilde{I}) = \frac{\tilde{I}(X_{alg}, X_{bac})}{K_I + \tilde{I}(X_{alg}, X_{bac})}, \quad (1)$$

$$\text{where } \tilde{I}(X_{alg}, X_{bac}) = I \times \exp[-\alpha(X_{alg} + X_{bac})], \quad (2)$$

where I [$\mu\text{mol}/\text{m}^2\text{s}$] is the total irradiance applied to the PBR, K_I [$\mu\text{mol}/\text{m}^2\text{s}$] is a half-saturation constant, and α [m^3/g] is the specific light attenuation coefficient. Expression (1) replaces $\mu(I)$ in the process rates for the algae growth on ammonium and nitrate (cf. Table 2). The rest of the model parameters are described in Table 3. See the reference of the parameters in Zambrano et al. (2016).

Since the PBR is assumed to be a completely mixed tank reactor, the expression (1) considers a homogeneous concentration of biomass in the liquid, therefore not dependency with depth was included. For simplicity, it is assumed that both microalgae and bacteria interrupt the light in the same way.

The combined effect of water-atmosphere gas exchange and gas injection were modeled as separated processes. Both processes follow the well known mass-transfer model:

$$G_{tr,gas} = K_L a_{gas}(S_{gas}^{sat} - S_{gas}), \quad (3)$$

Table 3. Model parameters.

Symbol	Definition [Unit]	Value
b_{alg}	Algae decay [1/d]	0.1
b_{bac}	Bacteria decay [1/d]	0.05
f_{bac}^C	CO ₂ produced per bacteria [gCO ₂ /gCOD]	1.375
f_{alg}^C	CO ₂ fraction in algae [gCO ₂ /gCOD]	0.383
f_{alg}^N	N fraction in algae [gN/gCOD]	0.065
I	Irradiance [$\mu\text{mol}/\text{m}^2\text{s}$]	100
$i_{X_{bac}}$	N used in bacteria growth [gN/gCOD]	0.08
$K_L a_{O_2}$	Mass transfer coeff. O ₂ [1/d]	4
$K_L a_{CO_2}$	Mass transfer coeff. CO ₂ [1/d]	3.538
$K_L a_{CO_2,inj}$	Mass transfer coeff. CO ₂ injected [1/d]	0-2.5
K_{CO_2}	Algae half-sat. coeff. for C [gC/m ³]	4×10^{-3}
K_I	Algae half-sat. coeff. for I [$\mu\text{mol}/\text{m}^2\text{s}$]	25
$K_{n,alg}$	Algae half-sat. coeff. for N [gN/m ³]	0.1
$K_{n,bac}$	Bacteria half-sat. coeff. for N [gN/m ³]	1
K_{O_2}	Bacteria half-sat. coeff. for O ₂ [gO ₂ /m ³]	0.4
$S_{O_2}^{sat}$	Sat. concentration for O ₂ in water [gO ₂ /m ³]	8.32
$S_{CO_2}^{sat}$	Sat. concentration for CO ₂ in water [gCO ₂ /m ³]	0.546
Y_{bac}	Bacteria growth yield [gCOD/gN]	0.24
$Y_{alg,nh4}^C$	Algae CO ₂ yield on NH ₄ [gCOD/gCO ₂]	0.842
$Y_{alg,nh4}^N$	Algae N yield on NH ₄ [gCOD/gN]	11.91
$Y_{alg,nh4}^O$	Algae O ₂ yield on NH ₄ [gO ₂ /gCOD]	0.996
$Y_{alg,no3}^C$	Algae CO ₂ yield on NO ₃ [gCOD/gCO ₂]	0.622
$Y_{alg,no3}^N$	Algae N yield on NO ₃ [gCOD/gN]	3.415
$Y_{alg,no3}^O$	Algae O ₂ yield on NO ₃ [gO ₂ /gCOD]	1.301
α	Light attenuation coefficient [m ³ /g]	5×10^{-4}
μ_{alg}	Algae specific growth rate [1/d]	1.6
μ_{bac}	Bacteria specific growth rate [1/d]	0.5

where $G_{tr,gas}$ is the amount of gas transferred from/to the atmosphere, $K_L a_{gas}$ is the mass transfer coefficient between the gas and the liquid phase, S_{gas}^{sat} is the saturation concentration of the gas, and S_{gas} is the dissolved gas concentration.

3 Results and Discussions

This section shows a numerical example of the MAAS process. Two main cases were evaluated: PBR as a single volume and as two volumes in series. The process was evaluated in steady-state conditions for different values of SRT and CO₂ injected. The SRT was adjusted by modifying the amount of excess sludge from the process.

The model programming and the simulation results

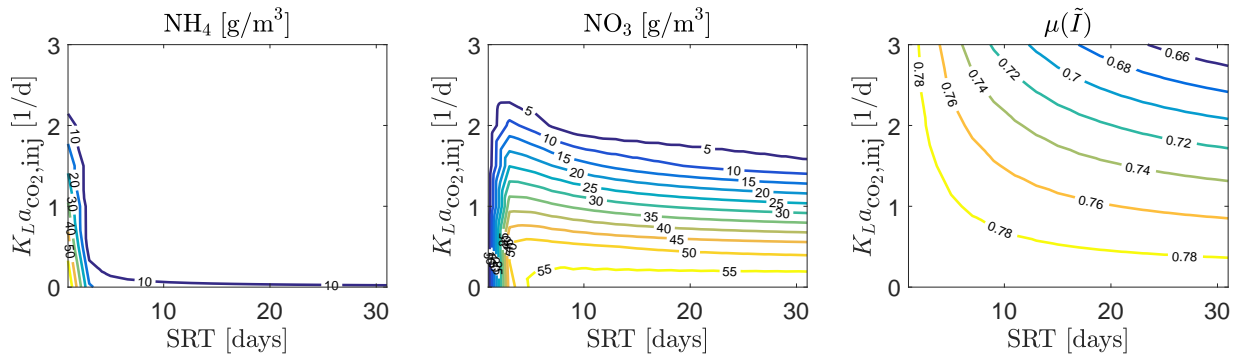


Figure 2. MAAS process with a single PBR. Contour plots showing steady-state values of NH_4 and NO_3 in the effluent, and $\mu(\tilde{I})$ as a function of SRT and $K_L a_{\text{CO}_2, \text{inj}}$. $K_L a_{\text{CO}_2, \text{inj}}$ refers to mass transfer coefficient of CO_2 injected. $\alpha = 5 \times 10^{-4} \text{ m}^3/\text{g}$.

were obtained using the MATLAB[®]/Simulink platform.

3.1 Influent characteristics and process parameters

We consider a PBR with total volume of $V = 0.07 \text{ m}^3$ and influent flow rate of 10.8 L/d . A constant influent flow rate was applied, with a composition of 70 g/m^3 of dissolved NH_4 , 2 g/m^3 of dissolved NO_3 , and no biomass concentration. The value of the model parameters used for the simulations are described in Table 3.

3.2 MAAS process with one PBR

The MAAS process was first simulated with a single PBR of volume V . The effluent ammonium concentration (NH_4), nitrate concentration (NO_3) and irradiance factor (cf. Expression (1)) were evaluated for different SRTs and CO_2 injected. Results are shown as contour plots in Figure 2, where a light attenuation coefficient $\alpha = 5 \times 10^{-4} \text{ m}^3/\text{g}$ was used.

See that the effluent NH_4 concentration is almost consumed in a wide range of SRT and that a low injection of CO_2 is needed. This is not the case for the effluent NO_3 , where high NO_3 concentration is obtained when low CO_2 is applied. See that this concentration decreases as the injected CO_2 increases, this is expected since the microalgae is the only microorganism that can consume this substrate (by injecting CO_2). Also note that the effluent NO_3 concentration does not show a significant change under variations in the SRT. As expected, for very low values in the SRT, the effluent NH_4 concentration starts to increase towards values of the influent concentration, i.e. the process is very close to wash-out condition.

Note also in Figure 2 that the irradiance factor decreases when SRT or the CO_2 injected increase. An increasing in the SRT promotes an accumulation of microalgae and bacteria concentration in the PBR, and more CO_2 injected promotes an increasing in the microalgae concentration. Therefore, this increment in

the microorganism concentration results in a decreasing of the irradiance factor (cf. Expressions (1)-(2)).

3.3 MAAS process with two PBRs

Next, the process was simulated considering the entire volume as two PBRs in series, subject to the restriction $V = V_1 + V_2$. It was decided that the irradiance applied to each PBR was proportional to its volume. Therefore, from the total irradiance I used in the case of a single PBR, now we have:

$$I_1 = \frac{V_1}{V} I, \quad I_2 = I - I_1, \quad (4)$$

where I_1 and I_2 are the irradiance in volumes V_1 and V_2 respectively.

From Figure 2, several points were taken as operational point to be optimized by distributing the total PBR volume V into two PBRs in series. As illustration, points with $\text{SRT} = 15 \text{ d}$ were selected. Different values for V_1 and CO_2 injected were evaluated. The CO_2 injected was assumed to be the same for each PBR, results are shown in Figure 3(left). See that each curve has a certain optimum value for the first PBR volume V_1 when a maximum reduction in the NO_3 is achieved. Also note that this optimum V_1 decreases as the CO_2 injected increases. Zambrano and Carlsson (2014) reported a similar behavior for the case of optimizing several bioreactors in series in an activated sludge process, where a simple bioreactor model (one main microorganism and one main dissolved substrate) and a Monod function for describing the growth kinetics were used. See also in Figure 3(left) that there is a wide range of optimum V_1 when a large amount of CO_2 is injected.

Figure 3(right) shows the value of the irradiance factor in each PBR for different values of V_1 and CO_2 injected. Note that a low value in V_1 means a low value in the irradiance of this PBR (cf. Expression (4)). Therefore, the irradiance factor $\mu(\tilde{I}_1)$ is close to zero and this value increases as V_1 increases. Since the total volume is fixed, the situation is the opposite for V_2 and $\mu(\tilde{I}_2)$, i.e. when V_1 increases V_2 decreases. See also that for a given V_1 ,

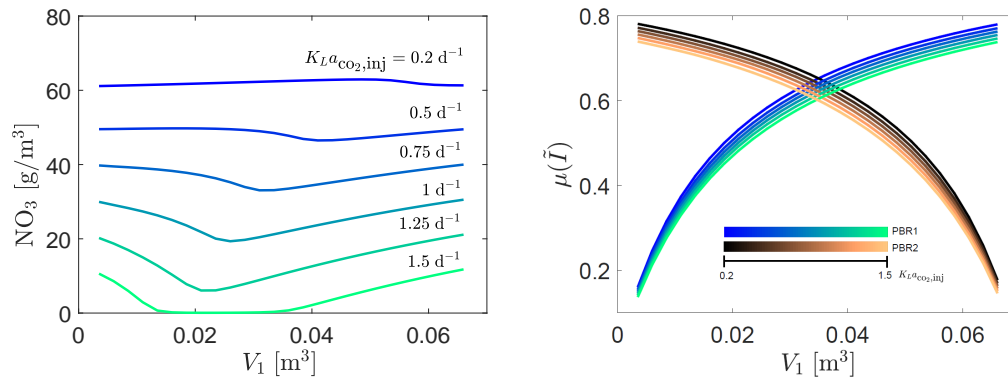


Figure 3. MAAS process with two PBRs in series. Left: Steady-state solution of effluent NO₃ as a function of V₁ and K_La_{CO₂,inj}. Right: Irradiance factor for the first (PBR1) and second (PBR2) PBR, as a function of V₁ and K_La_{CO₂,inj}. $\alpha = 5 \times 10^{-4} \text{ m}^3/\text{g}$.

the irradiance in each PBR decreases as the amount of CO₂ injected increases. As observed in Figure 2 for $\mu(\tilde{I})$ in a single PBR, this is because an increasing in the CO₂ promotes an increasing in the microalgae concentration, which reduces the amount of light penetration in the PBRs.

4 Conclusions

In this work, a steady-state simulation study of a PBR working in an ASP configuration was presented, referred as MAAS process. A simple model is used for the PBR, which includes one microalgae and bacteria species, two dissolved substrates and two dissolved gases. The model for the irradiation includes the effect of the microalgae and bacteria concentration in the PBR. This simple model gives relevant information about the behavior of the system for different SRTs and CO₂ injected.

Results show that, for a given SRT, it is possible to reduce the effluent substrate concentration by increasing the CO₂ injected, and this reduction is more sensitive to changes in the CO₂ injected than to changes in the SRT of the process. For the case of two PBRs in series, for a given SRT an optimum volume distribution can be achieved which depends on the CO₂ injected. This configuration gives a lower effluent substrate concentration than when a single PBR volume is assumed. Similar to the case of an ASP with bioreactors in series, one would expect that an increasing in the number of PBRs in series in the MAAS process would decrease the effluent substrate concentration.

Acknowledgments

The research leading to these results has received funding from the Knowledge Foundation (20140168) under the project More Sense, ABB, Mälarenergi, Flexiclean and Structor Miljöteknik.

References

- I. M. Abu-Reesh. Optimal design for CSTR's in series using reversible Michaelis-Menten reactions. *Bioprocess Engineering*, 15(5):257–264, 1996. doi:10.1007/bf02391587.
- Rutherford Aris. *The Optimal Design Of Chemical Reactors*. Academic Press, New York, 1st edition, 1961. ISBN 9781483221434.
- Omatoyo K Dalrymple, Trina Halfhide, Innocent Udom, Benjamin Gilles, John Wolan, Qiong Zhang, and Sarina Ergas. Wastewater use in algae production for generation of renewable resources: a review and preliminary results. *Aquatic Biosystems*, 9(1):2, 2013. doi:10.1186/2046-9063-9-2.
- Joël de la Noüe, Gilles Laliberté, and Daniel Proulx. Algae and waste water. *Journal of Applied Phycology*, 4(3):247–254, 1992. doi:10.1007/bf02161210.
- Bjorge Decostere, Natascha Janssens, Andres Alvarado, Thomas Maere, Peter Goethals, Stijn W.H. Van Hulle, and Ingmar Nopens. A combined respirometer–titrimeter for the determination of microalgae kinetics: Experimental data collection and modelling. *Chemical Engineering Journal*, 222:85–93, 2013. doi:10.1016/j.cej.2013.01.103.
- D. Dochain, S. Grégoire, A. Pauss, and M. Schaeffer. Dynamical modelling of a waste stabilisation pond. *Bioprocess and Biosystems Engineering*, 26(1):19–26, 2003. doi:10.1007/s00449-003-0320-6.
- M. Droop. Vitamin B12 and marine ecology. IV. The kinetics of uptake growth and inhibition in *Monochrysis lutheri*. *J. Mar. Biol. Ass. U.K.*, 48(3):689–733, 1968.
- M R. Droop. Some thoughts on nutrient limitation in algae. *J. Phycol.*, 9:264–272, 1973.
- P.H.C. Eilers and J.C.H. Peeters. A model for the relationship between light intensity and the rate of photosynthesis in phytoplankton. *Ecological Modelling*, 42(3-4):199–215, 1988. doi:10.1016/0304-3800(88)90057-9.

- Richard J. Geider, Hugh L. MacIntyre, and Todd M. Kana. A dynamic regulatory model of phytoplanktonic acclimation to light, nutrients, and temperature. *Limnol. Oceanography*, 43(4):679–694, 1998. doi:10.4319/lo.1998.43.4.0679.
- C.P.L. Grady Jr., Glen T. Daigger, and Henry C. Lim. *Biological Wastewater Treatment*. Marcel Dekker, Inc., New York, 1999. ISBN 0-8247-8919-9.
- M. Henze, C. Grady, W. Gujer, G. Marais, and T. Matsuo. Activated Sludge Model no. 1 - Scientific and Technical report no. 1. Technical report, IAWPRC, London, UK, 1987.
- D. Herbert. Multi-stage continuous culture. In *Continuous Cultivation of Microorganisms*, pages 23–44. Elsevier, 1964. doi:10.1016/b978-0-12-395496-1.50006-5.
- Jef Huisman, Hans C.P. Matthijs, Petra M. Visser, Hans Balke, Corrien A.M. Sigon, Jutta Passarge, Franz J. Weissing, and Luuc R. Mur. Principles of the light-limited chemostat: theory and ecological applications. *Antonie van Leeuwenhoek*, 81(1/4):117–133, 2002. doi:10.1023/a:1020537928216.
- S.R.-J. Jang and J. Baglama. Droop models of nutrient–plankton interaction with intratrophic predation. *Applied Mathematics and Computation*, 169(2):1106–1128, 2005. doi:10.1016/j.amc.2004.11.002.
- I. Krustok, M. Odlare, J. Truu, and E. Nehrenheim. Inhibition of nitrification in municipal wastewater-treating photobioreactors: Effect on algal growth and nutrient uptake. *Bioresource Technology*, 202:238–243, 2016. doi:10.1016/j.biortech.2015.12.020.
- M. Pahlow. Linking chlorophyll-nutrient dynamics to the redfield N:C ratio with a model of optimal phytoplankton growth. *Marine Ecology Progress Series*, 287:33–43, 2005. doi:10.3354/meps287033.
- P. Reichert, D. Borchardt, M. Henze., W. Rauch, P. Shanahan, L. Somlyódy, and P. Vanrolleghem. River water quality model no. 1 (RWQM1): II. Biochemical process equations. *Water Science and Technology*, 43(5):11–30, 2001.
- Alessandro Solimeno, Roger Samsó, Enrica Uggetti, Bruno Sialve, Jean-Philippe Steyer, Adrián Gabarró, and Joan García. New mechanistic model to simulate microalgae growth. *Algal Research*, 12:350–358, 2015. doi:10.1016/j.algal.2015.09.008.
- Jesús Zambrano and Bengt Carlsson. Optimizing zone volumes in bioreactors described by Monod and Contois growth kinetics. In *Proceeding of the IWA World Water Congress & Exhibition*, Lisbon, Portugal, 2014.
- Jesús Zambrano, Ivo Krustok, Emma Nehrenheim, and Bengt Carlsson. A simple model for algae-bacteria interaction in photo-bioreactors. *Algal Research*, 19:155–161, 2016. doi:10.1016/j.algal.2016.07.022.

Analysis of the Effect of Steam-to-Biomass Ratio in Fluidized Bed Gasification with Multiphase Particle-in-cell CFD Simulation

Janitha C. Bandara¹ Marianne S. Eikeland¹ Britt M. E. Moldestad¹

¹Faculty of Technology, Natural Sciences and Maritime Sciences, University College of Southeast Norway
{Janitha.bandara, Marianne.Eikeland, britt.moldestad}@usn.no

Abstract

Biomass has been identified as a key renewable energy source to cope with upcoming environmental challenges. Gasification of biomass is becoming interested in large scale operation, especially in synthesis of liquid fuels. Bubbling and circulating fluidized bed gasification technology has overrun the interest over fixed bed systems. CFD studies of such reactor systems have become realistic and reliable with the modern computer power. Gasifying agent, temperature and steam or air to biomass ratio are the key parameters, which are responsible for the synthesis gas composition. Therefore, multiphase particle-in-cell CFD modeling was used in this study to analyze the steam to biomass, S/B, ratio in fluidized bed gasification.

Due to the complexity of the full loop simulation of dual circulating fluidized bed reactor system, only the gasification reactor was considered in this study. Predicted boundary conditions were implemented for the particle flow from the combustion reactor. The fluidization model was validated against experimental data in beforehand where Wen-Yu-Ergun drag model was found to be the best. The effect of the S/B ratio was analyzed at a constant steam temperature of 1073K and a steam velocity of 0.47 m/s. Four different S/B of 0.45, 0.38, 0.28 and 0.20 were analyzed. The biomass was considered to be in complete dry condition where single step pyrolysis reaction kinetics was used. Each gasification simulation was carried out for 100 seconds. 8% reduction of hydrogen content from 57% to 49% and 17% increment of carbon monoxide from 13% to 30% were observed when the S/B was reduced from 0.45 to 0.20. Countable amounts of methane were observed at S/B of 0.28 and 0.20. The lower heating value of the product gas increased from 10.1 MJ/kg to 12.37 MJ/kg and the cold gas efficiency decreased from 73.2% to 64.6% when the S/B was changed from 0.45 to 0.20. The specific gas production rate varied between 1.64 and 1.04 Nm³/kg of biomass.

Keywords: Biomass gasification, fluidized beds, gasifying agent, multiphase particle-in-cell

1 Introduction

Biomass was one of the key energy sources until the invention of cheap refined petroleum fuels in the 1940s. Since then, biomass energy technologies were not impressively developed until the oil crisis in the 1970s. Since then, biomass-to-energy conversion technologies were subjected to enormous research and developments. Biomass is further outdoing among other renewable energy systems, as it demands to be the sole alternative to replace all use of fossil fuels (Demirbas 2008). Bioenergy is also a key component in setting up the EU energy target of 20-20-20¹ where 10% of the transport related energy is supposed to be achieved via renewables (Scarlat, Dallemand et al. 2011).

Approximately 125 billion liters of biofuels were produced in 2015 where 75% is bio-ethanol and 25% is bio-diesel (Century 2015). The main feedstocks for bio-ethanol have been sugarcane and corn. However, there has been a long term debate of utilizing food commodities for energy production (Naik, Goud et al. 2010). On the other hand, annual terrestrial biomass production by green plants is approximately 100 billion tons of dry organic matter where only a 1.25% is derived as food (Naik, Goud et al. 2010). In other words, 90% of the world accessible biomass stocks are lignocellulosic (Szczodrak and Fiedurek 1996). Therefore, liquid biofuels from lignocellulosic materials, referred as second-generation biofuels, will provide more aspects to the future transportation industry.

Combustion, pyrolysis and gasification are the three main thermo-chemical technologies for conversion of biomass to energy, which eliminate most of the drawbacks related to bio-chemical conversion. Gasification converts solid biomass into a gaseous mixture of carbon monoxide (CO), hydrogen (H₂), methane (CH₄), carbon dioxide (CO₂) and minor fractions of higher molecular hydrocarbons such as tars. The product gas, which is referred as synthesis gas, could be processed into biofuels either by biological fermentation or Fisher-Tropsch (Munasinghe and Khanal 2010). In contrast, the producer gas could be directly combusted in furnaces, boilers, turbines and IC engines or used in solid oxide fuel cells.

¹ 20% reduction of CO₂ emissions, 20% increase of energy efficiency and 20% renewable energy share by 2020

Carbon to Hydrogen (C:H) ratio is the most important parameter in downstream processing of synthesis gas into liquid fuels. It is therefore important to optimize both the syngas composition and flowrates. In this picture, steam is much more desired as the gasification agent compared to air. Steam is further useful in tar cracking via reforming reactions as well. Dual circulating fluidized bed (DCFB) gasification is the best technology, compared to fixed bed and single bubbling fluidized bed reactor, to achieve a high H₂ content in synthesis gas.

This particular DCFB system separates the gasification and combustion reactions into two reactors as illustrated in Figure 1. Drying, pyrolysis and gasification (gas reactions and part of the char reduction) reactions are carried out in the gasification reactor, which normally operates with steam in the bubbling fluidization regime. Temperature and steam-to-biomass ratio (S/B) are the most important parameters for the gas composition. The remaining char from the gasifier is oxidized in the combustion chamber, which provides the heat demand of the gasification via circulation of bed material. Computational fluid dynamic (CFD) simulations integrated with reactions are more convenient, cost effective and efficient in optimization compared to experimental investigations.

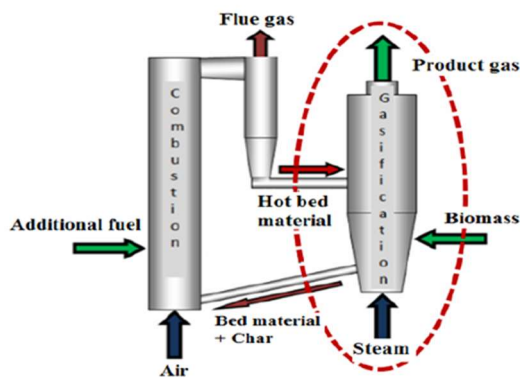


Figure 1. Dual circulating fluidized bed reactor

However, CFD modeling of particle systems are rather complex, and fluidized bed gasification is especially challenging due to the introduction of heterogeneous reactions together with heat and mass transfer. Eulerian-Eulerian (EE) and Eulerian-Lagrangian (EL) are the two basic approaches in modeling particle systems. The multiphase particle-in-cell (MP PIC) technique is an extended version of EL modeling which overcome certain limitations of conventional EL simulations such as modeling of dense particle systems with a large number of particles.

In the MP-PIC approach, the fluid phase is modeled in the Eulerian grid with Navier Stokes equations. Particles having similar characteristics such as size, density, etc. are parceled into units, which are referred as computational particles. Hence, billions of particles could be encapsulated into millions of computational

particles and modelled in the Lagrangian frame of reference (Andrews and O'Rourke 1996). Inter particle stresses are calculated in the Eulerian grid considering the particles as a continuum phase and those values are mapped back to the individual particles, using interpolation functions (Snider 2001). It has found that the required quantity of parcels to model the particle phase accurately is acceptable which realizes the simulation of large-scale particle systems.

The Barracuda VR commercial package is specially developed for multiphase CFD simulations, which uses the MP-PIC approach. This novel approach is referred to as computational particle fluid dynamics (CPFD). Solnordal, Kenche et al. 2015 and Liang, Zhang et al. 2014 have carried out MP PIC simulations for bubbling fluidized beds. Snider, Clark et al. 2011 has presented the integration of heat and reaction chemistry in MP PIC simulations whereas Loha, Chattopadhyay et al. 2014 and Xie et al Xie, Zhong et al. 2012 have carried out gasification simulations in a bubbling fluidized bed reactor. Liu, Cattolica et al. 2015, and Liu, Cattolica et al. 2016 have performed MP PIC simulations in a complete circulating dual fluidized bed system. The ability of defining multi-component particles is a distinctive feature of Barracuda, and facilitates the integration of volatization reactions involved in gasification and combustion.

A complete loop CFD simulation of the circulating fluidized bed gasification is complex in terms of generating the computational grid and expensive regarding simulation time. On the other hand, the underlying objective of this work is to analyze the effect of S/B in the gasification reactor. Hence, the CFD simulation was narrowed down to the gasification reactor as highlighted in Figure 1.

2 Barracuda CFD setup

The fluidization model was validated with cold bed fluidization experiments and the data has been published by the same author (Bandara, Thapa et al. 2016).

A simple cylindrical geometry of 2000 mm in height and 550 mm in diameter was used. The uniform grid option was applied with 4840 cells in total. The computational grid, boundary conditions and filling of the initial particle species in the bed are illustrated in Figure 2 where other operational and physical parameters are tabulated in Table 1. Uniform steam distribution was used while the steam velocity was maintained slightly above the minimum fluidization velocity. The hot bed material inlet was set as it guides the particle trajectory into the center of the reactor. Particle should driven into the system with a fluid flow where the fluid volume can be manipulated with “slip velocity” option. The bed material outflow was adjusted by changing the pressure at that particular cell where it was connected to the bed material inflow with “particle feed control” option.

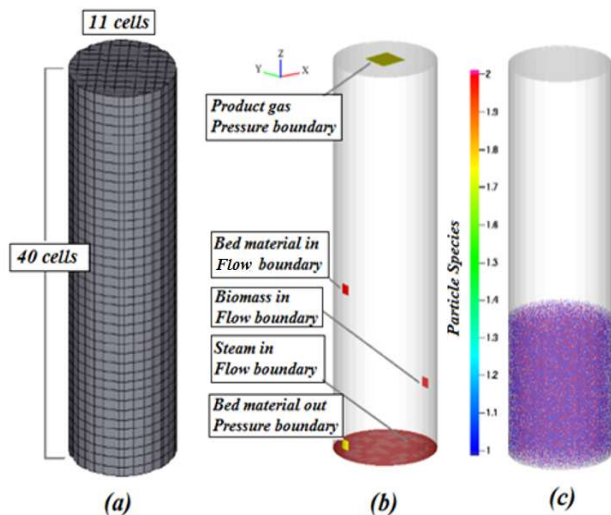


Figure 2. (a) Computational grid, (b) boundary conditions, (c) initial particle species

Table 1. Initial and boundary conditions

Flow boundary parameters			
Stream	Boundary	Parameters	Particle
Steam	Flow	1073 K, 101325 pa, 0.47 m/s	Nil
Gas out	Pressure	101325 pa	Nil
Biomass in	Flow	400 K, 101325 pa, 0.5 m/s,	0.05 kg/s
Bed Material in	Flow	1273 K, 101325 pa, 0.25 m/s	95% of bed material out
Bed Material out	pressure	101325 pa	Particle out flow
Initial conditions			
Fluid	1073 K, 101325 pa, steam, total volume		
Silica	1073 K, 101325 pa, 1000 μm , spherical, 0.48 volume fraction, density 2200 kg/m^3 , 600 mm height initial fill		
Char	1073 K, 101325 pa, 500 μm , spherical, 0.12 volume fraction, density 300 kg/m^3 , 600 mm height initial fill		

Steam pressure and the temperature of the incoming bed material were kept constant throughout all the simulations. It was intended to keep the fluidization behavior and residence time as similar as possible for all the simulations. Therefore, the steam flow boundary was maintained at 0.47 m/s. The S/B ratio was adjusted by changing the biomass flow. Four different S/B ratios of 0.45, 0.38, 0.28 and 0.2, were considered. As particle heating consumes high simulation time, initial particle temperature was set up same as that of the steam. It was further assumed that the initial bed composed with a fraction of char as well.

The Arrhenius reaction rates were used in the homogeneous and heterogeneous reactions. The constants in the reaction models were adapted from Thapa et al (R.K. Thapa, C. Pfeifer et al. 2014) and are tabulated in Table 2. The pyrolysis was modelled as a single step reaction, where the rate is given by,

$$264000 m_s \theta_f \exp \left[\frac{-1262}{T} \right] \quad (1)$$

Following the literature data, the composition of biomass was assumed to be 25% char and 75% volatiles

with no moisture and ash. Formation of tar and higher molecular hydrocarbons was neglected, and only H₂, CO, CO₂, CH₄ and H₂O were considered. Weight fractions of CH₄, CO, CO₂ and H₂ in the pyrolysis gas were taken as 0.1213, 0.6856, 0.1764 and 0.0167 respectively (R.K. Thapa, C. Pfeifer et al. 2014). Simulations were carried out for 100s and the gas composition, gas temperature and particle mass flow rates were analyzed.

Table 2. Reaction kinetics

Steam Reforming $C + H_2O \leftrightarrow H_2 + CO$	Forward	$1.272 m_s T \exp \left[\frac{-22645}{T} \right] [H_2O]$
	Reverse	$1.044 \times 10^{-4} m_s T^2 \exp \left[\frac{-6319}{T} - 17.29 \right] [H_2][CO]$
CO ₂ gasification $C + CO_2 \leftrightarrow 2CO$	Forward	$1.272 m_s T \exp \left[\frac{-22645}{T} \right] [CO_2]$
	Reverse	$1.044 \times 10^{-4} m_s T^2 \exp \left[\frac{-2363}{T} - 20.92 \right] [CO]^2$
Methanation $0.5C + H_2 \leftrightarrow 0.5CH_4$	Forward	$1.368 \times 10^{-3} m_s T \exp \left[\frac{-8078}{T} - 7.087 \right] [H_2]$
	Reverse	$0.151 m_s T^{0.5} \exp \left[\frac{-13578}{T} - 0.372 \right] [CH_4]^{0.5}$
Water-Gas shift $H_2O + CO \leftrightarrow H_2 + CO_2$	Forward	$7.68 \times 10^{10} m_s T \exp \left[\frac{-36640}{T} \right] [CO]^{0.5} [H_2O]$
	Reverse	$6.4 \times 10^9 m_s T \exp \left[\frac{-39260}{T} \right] [H_2]^{0.5} [CO_2]$
Methane reforming $CH_4 + H_2O \leftrightarrow CO + 3H_2$	Forward	$3.0 \times 10^5 T \exp \left[\frac{-15042}{T} \right] [CH_4][H_2O]$
	Reverse	$0.0265 T \exp \left[\frac{-32900}{T} \right] [CO][H_2]^2$

3 Results and discussion

A number of researchers have analyzed the effect of steam to biomass ratio and carried out CFD simulations related to biomass gasification. Wei, Xu et al. 2007 has carried out experiments in a free fall reactor and used S/B ratios from 0 to 1.00 in the same temperature ranges adopted in this work. Rapagnà, Jand et al. 2000 has looked into steam gasification in a bubbling fluidized bed reactor with olivine catalysts where S/B ratio between 0.4 to 1.00 had been analyzed. Campoy, Gómez-Barea et al. 2009 has used a mixture of oxygen and steam as the gasifying agent and carried out experiments in a fluidized bed reactor without external heating of the bed. The S/B ratio was between 0 and 0.58. The simulations in this work was initiated with S/B ratio of 0.45 and bed temperature of 1023 K.

3.1 Simulation with S/B ratio of 0.45

A reduction of bed mass from 178.3 kg to 177.1 kg and char fraction of the bed outflow from 3.25% to 0.6% were observed during the simulation time of 100s. However, bed particle outflow and bed particle inflow were connected with 95% mass efficiency (assuming 5% of char availability in the bed particle outflow). The incorrect match of mass flowrate of particle flows might

lead to reduction of the bed mass. On the other hand, there is a considerable reduction of char in the bed outflow. This might be due to insufficient biomass supply compared to char outflow.

Bed hydrodynamics, temperature distribution of particles in the bed and distribution of different particle species are illustrated respectively in (a), (b) and (c) of Figure 3. Referring to the same figure, the bubbling fluidization of the reactor is clearly depicted. However, the particle temperature shows uneven characteristics, especially along the cross section. Heated particles from the combustion reactor seem to be accumulated in the opposite half to the particle inlet of the reactor. Homogeneous distribution of three particle species is illustrated Figure 3 (c) where 1, 2 and 3 in the figure are referred to sand, char and biomass respectively.

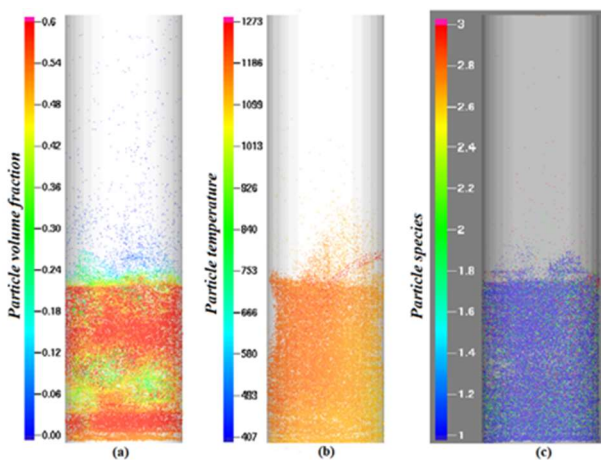


Figure 3. (a) Bubbling fluidization, (b) temperature of bed particles, (c) distribution of particle species

Product gas composition was observed in both axial and radial directions of the reactor, which are illustrated in Figure 4 and Figure 5. The final gas composition from the reactor was read from the center cell of the outflow pressure boundary, which actually acts as a sensor installed.

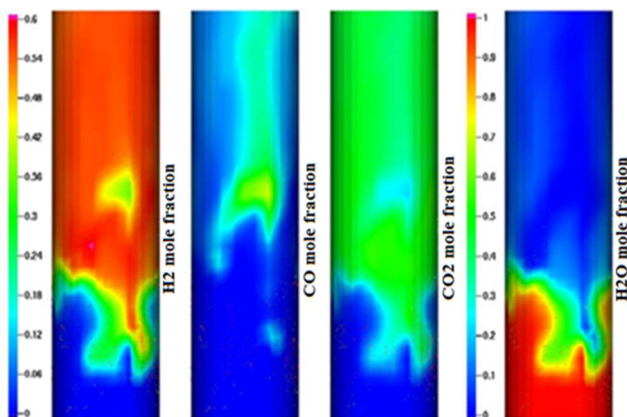


Figure 4. Product gas composition along the reactor height

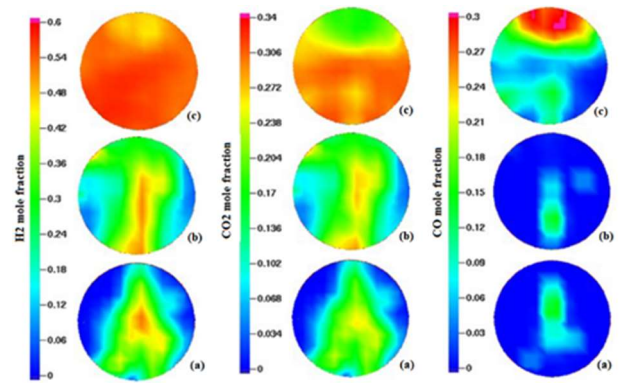


Figure 5. Gas composition at different cross sections along reactor height. (a), (b) and (c) refers to 0.3, 0.6 and 0.9m heights from the bottom of the reactor

No significant change in the gas composition is observed up to the biomass feeding point. This depicts the slow reaction kinetics of the char-steam heterogeneous reactions. The gas phase composition starts to change from the biomass feeding point, which is mainly due to pyrolysis reactions. Even though pyrolysis gas contains nearly 68% of CO, higher concentration cannot be observed even at the biomass feeding point. This is mainly due to high reaction rate of the water-gas shift reaction compared to the pyrolysis reaction, which consumes CO immediately to produce CO₂ and H₂. Therefore, H₂ and CO₂ increase along the reactor height with simultaneous decrease of CO and H₂O.

The gas production rate is also monitored, and the volumetric and mass gas production rates were approximately 0.33m³/s and 0.055kg/s respectively. The flow rates as function of time are plotted in Figure 6. Following the ideal gas law (high temperature and low pressure), the gas production rate was calculated as 1.64 Nm³/kg of biomass, which is well within the data published in literature. The area specific gas production rate, which is one of the useful parameters in reactor sizing, was observed as 0.34Nm³/s·m².

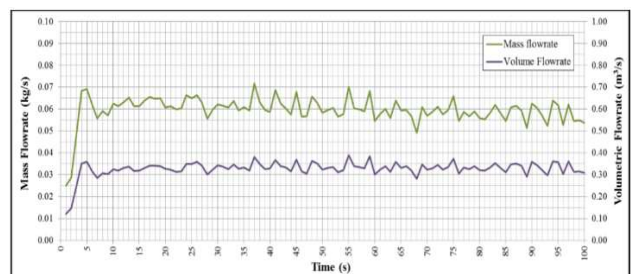


Figure 6. Time evolution product gas flowrates

The average molar gas composition during the final 25s was observed as 0.128-CO, 0.273-CO₂, 0.574-H₂ and 0.025-H₂O. The product gas heating value was calculated to be 10.1 MJ/kg where the lower heating values (LHV) of wood, CO and H₂ were taken as 16 MJ/kg (dry basis), 10 MJ/kg and 120 MJ/kg

respectively. The cold gas efficiency (CGE) was calculated as 73.3% using the equation:

$$CGE = \frac{mass_{gas}(kg)}{mass_{fuel}(kg)} \frac{LHV_{gas}(J/kg)}{LHV_{fuel}(J/kg)} \quad (2)$$

There is an uncertainty related to the calculation of cold gas efficiency because the actual operating conditions of the combustion reactor is not known. A guessed value of 200°C was taken for the temperature increment in the combustion reactor. However, there can be additional fuel supply into the combustion reactor to achieve the desired temperature rise, which indirectly affects for the cold gas efficiency.

3.2 Effect of Steam-to-Biomass ratio

The biomass flowrate was increased from 0.05kg/s to 0.06kg/s, 0.08kg/s and 0.11kg/s to adjust the S/B ratio from 0.45 to 0.38, 0.28 and 0.2 respectively. Temperatures and steam inlet flow velocity were kept unchanged. Similar characteristics of bed hydrodynamics, temperature and particle species distribution were observed as in the case with of S/B of 0.45. Figure 7 illustrates the final gas composition for the respective cases.

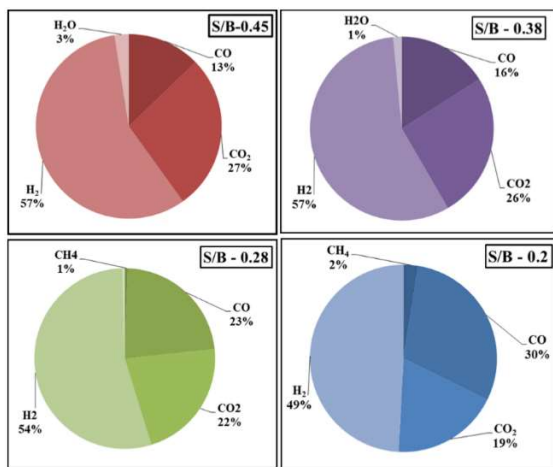


Figure 7. Molar composition of product gas

The molar concentration of H₂ is dramatically reduced from 57% at S/B of 0.45 to 49% at S/B of 0.2 showing a reduction of 8%. In contrast, the concentration of CO has increased by 17% within the respective range. According to the data presented in Figure 3-5, steam is almost totally consumed even for S/B of 0.45. However, the pyrolysis gas volumes in the successive cases of low S/B ratios is increased due to increasing biomass flowrates. As a result, low S/B operation experiences a deficiency of steam to perform the water-gas-shift reaction. Therefore, Product gas is consisted with a substantial share of raw pyrolysis gas. The unreacted fraction of the pyrolysis gas is the root cause for increasing CO concentrations in the product

gas at low S/B. This phenomenon is illustrated Figure 8. Steam reforming reaction adds mass to the pyrolysis gas, which is clear from the figure as product gas mass flowrate always runs above the pyrolysis gas curve. However, the gap between two curves gets narrowed at lower S/B. Further, two curves stand almost parallel to each other at lower S/B than approximately 0.3. The total consumption of steam at S/B of 0.3 is the reason for this behavior.

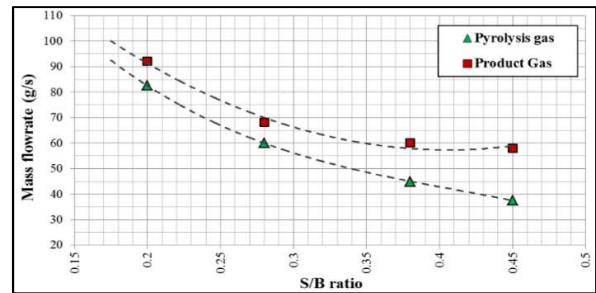


Figure 8. Pyrolysis and product gas mass flowrates

Further, noticeable amount of CH₄ is available in the product gas in both the case of 0.28 and 0.2 S/B. It is evident from the reaction kinetic data in Table 2 that the reaction rate of the water-gas-shift reaction is much higher than the methane reforming. Therefore, steam is initially consumed by CO and when it comes to the respective cases, no steam is left for methane reforming reactions.

As illustrated in Figure 9, the product gas temperature has dropped down by 50K at reduced S/B of 0.28 and 0.2. This happens as more energy is extracted for the pyrolysis reactions with increased biomass feed rate at lower S/B ratios.

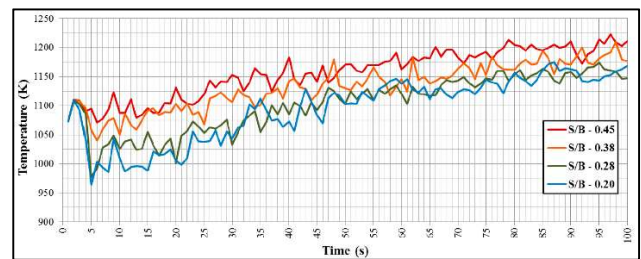


Figure 9. Time evolution product gas temperature at different S/B

The summary of other parameters at different S/B is given in Table 3. The volumetric gas production rate at S/B 0.2 has increased by 33% compared to S/B 0.45. Therefore, the gas production capacity can be increased in the same reactor, simply by changing the S/B ratio. The increase of the molar percentage of the total combustible gases (H₂+CO) in the product gas from 70% to 79% is the reason behind the increased calorific value by 22% from 10.1 MJ/kg to 12.37 MJ/kg in the respective cases. The reduction of the volumetric gas production per kg of biomass is because of the inadequate steam availability to react with the additional released pyrolysis gas at lower S/B.

Table 3. Simulation results for different S/B

	S/B-0.45	S/B-0.38	S/B-0.28	S/B-0.2
Steam flow (kg/s)	22.8	22.8	22.8	22.8
Biomass flow (g/s)	50	60	80	110
Product gas				
Mass flowrate (g/s)	58	60	68	92
Volume flowrate (m ³ /s)	0.331	0.34	0.36	0.44
Mole flowrate (mol/s)	3.36	3.5	3.9	5.1
LHV (MJ/kg)	10.1	10.54	11.5	12.37
Cold gas efficiency	73.2	65.8	61.1	64.6

4 Conclusion

Barracuda VR commercial package with the MP-PIC CFD principle, was used in this work. The product gas quality was observed at different steam-to-biomass ratios. The product gas composition, gas flowrates, heating value and cold gas efficiency showed a significant sensitivity regarding the S/B ratio and following conclusions could be made. As the steam-to-biomass ratio is reduced,

- H₂ content is decreased while CO is increased
- LHV is increased while cold gas efficiency is decreased
- Gas production rate per kg of biomass is reduced

Simulating complete dual fluidized bed reactor system together with a detailed characterization of biomass such as composition and pyrolysis kinetics, will overcome the uncertainties related to this work for a certain extent. Barracuda VR is a sophisticated tool for optimization of the effect of different parameters on the biomass gasification.

Acknowledgements

The authors would like to forward their gratitude to University College of Southeast Norway for providing of the Barracuda VR software package and computer facilities.

References

Andrews, M. J. and P. J. O'Rourke (1996). "The multiphase particle-in-cell (MP-PIC) method for dense particulate flows." *International Journal of Multiphase Flow* **22**(2): 379-402.

Bandara, J. C., R. K. Thapa, B. M. E. Moldestad and M. S. Eikeland (2016). "Simulation of Particle Segregation in Fluidized Beds." *9th EUROSIM Congress on Modelling and Simulation*, Oulu, Finland, IEEE.

Campoy, M., A. Gómez-Barea, F. B. Vidal and P. Ollero (2009). "Air-steam gasification of biomass in a fluidised bed: Process optimisation by enriched air." *Fuel Processing Technology* **90**(5): 677-685.

Century, R. E. P. N. f. t. s. (2015). "RENEWABLES 2015 - Global Status Report", Paris: REN21 Secretariat.

Demirbas, A. (2008). "Biofuels sources, biofuel policy, biofuel economy and global biofuel projections." *Energy Conversion and Management* **49**(8): 2106-2116.

Liang, Y., Y. Zhang, T. Li and C. Lu (2014). "A critical validation study on CPFD model in simulating gas-solid bubbling fluidized beds." *Powder Technology* **263**: 121-134.

Liu, H., R. J. Cattolica and R. Seiser (2016). "CFD studies on biomass gasification in a pilot-scale dual fluidized-bed system." *International Journal of Hydrogen Energy* **41**(28): 11974-11989.

Liu, H., R. J. Cattolica, R. Seiser and C.-h. Liao (2015). "Three-dimensional full-loop simulation of a dual fluidized-bed biomass gasifier." *Applied Energy* **160**: 489-501.

Loha, C., H. Chattopadhyay and P. K. Chatterjee (2014). "Three dimensional kinetic modeling of fluidized bed biomass gasification." *Chemical Engineering Science* **109**: 53-64.

Munasinghe, P. C. and S. K. Khanal (2010). "Biomass-derived syngas fermentation into biofuels: Opportunities and challenges." *Bioresource Technology* **101**(13): 5013-5022.

Naik, S. N., V. V. Goud, P. K. Rout and A. K. Dalai (2010). "Production of first and second generation biofuels: A comprehensive review." *Renewable and Sustainable Energy Reviews* **14**(2): 578-597.

R.K. Thapa, C. Pfeifer and B. M. Halvorsen (2014). "Modeling of reaction kinetics in bubbling fluidized bed biomass gasification reactor" *INTERNATIONAL JOURNAL OF ENERGY AND ENVIRONMENT* **5**(1): 10.

Rapagnà, S., N. Jand, A. Kiennemann and P. U. Foscolo (2000). "Steam-gasification of biomass in a fluidised-bed of olivine particles." *Biomass and Bioenergy* **19**(3): 187-197.

Scarlat, N., J.-F. Dallemand, O. J. Skjelhaugen, D. Asplund and L. Nesheim (2011). "An overview of the biomass resource potential of Norway for bioenergy use." *Renewable and Sustainable Energy Reviews* **15**(7): 3388-3398.

Snider, D. M. (2001). "An Incompressible Three-Dimensional Multiphase Particle-in-Cell Model for Dense Particle Flows." *Journal of Computational Physics* **170**(2): 523-549.

Snider, D. M., S. M. Clark and P. J. O'Rourke (2011). "Eulerian-Lagrangian method for three-dimensional thermal reacting flow with application to coal gasifiers." *Chemical Engineering Science* **66**(6): 1285-1295.

Solnordal, C. B., V. Kenche, T. D. Hadley, Y. Feng, P. J. Witt and K. S. Lim (2015). "Simulation of an internally circulating fluidized bed using a multiphase particle-in-cell method." *Powder Technology* **274**: 123-134.

Szczodrak, J. and J. Fiedurek (1996). "Technology for conversion of lignocellulosic biomass to ethanol." *Biomass and Bioenergy* **10**(5): 367-375.

Wei, L., S. Xu, L. Zhang, C. Liu, H. Zhu and S. Liu (2007). "Steam gasification of biomass for hydrogen-rich gas in a free-fall reactor." *International Journal of Hydrogen Energy* **32**(1): 24-31.

Xie, J., W. Zhong, B. Jin, Y. Shao and H. Liu (2012). "Simulation on gasification of forestry residues in fluidized beds by Eulerian-Lagrangian approach." *Bioresource Technology* **121**: 36-46.

Analyzing the Effects of Particle Density, Size and Size Distribution for Minimum Fluidization Velocity with Eulerian-Lagrangian CFD Simulation

Janitha C. Bandara¹ Marianne S. Eikeland¹ Britt M. E. Moldestad¹

¹Faculty of Technology, Natural Sciences and Maritime Sciences, University College of Southeast Norway
{Janitha.bandara, Marianne.Eikeland, britt.moldestad}@usn.no

Abstract

Fluidized bed reactor systems are widely used due to excellent heat and mass transfer characteristics followed by uniform temperature distribution throughout the reactor volume. The importance of fluidized beds is further demonstrated in high exothermic reactions such as combustion and gasification where fluidization avoids the hot spot and cold spot generation. A bed material, such as sand or catalyst, is normally involved in fluidized bed combustion and gasification of biomass. Therefore, it is vital to analyze the hydrodynamics of bed material, especially the minimum fluidization velocity, as it governs the fluid flowrate into the reactor system. There are limitations in experimental investigations of fluidized beds such as observing the bed interior hydrodynamics, where CFD simulations has become a meaningful way with the high computer power. However, due to the large differences in scales from the particle to the reactor geometry, complex interface momentum transfer and particle collisions, CFD modeling and simulation of particle systems are rather difficult. Multiphase particle-in-cell method is an efficient version of Eulerian-Lagrangian modeling and Barracuda VR commercial package was used in this work to analyze the minimum fluidization velocity of particles depending on size, density and size distribution.

Wen-YU-Ergun drag model was used to model the interface momentum transfer where default equations and constants were used for other models. The effect of the particle size was analyzed using monodispersed Silica particles with diameters from 400 to 800 microns. Minimum fluidization velocity was increased with particle diameter, where it was 0.225 m/s for the 600 microns particles. The density effect was analyzed for 600 microns particles with seven different density values and the minimum fluidization velocity again showed proportionality to the density. The effect of the particle size distribution was analyzed using Silica. Particles with different diameters were mixed together according to pre-determined proportions as the final mixture gives a mean diameter of 600 microns. The 600 microns monodispersed particle bed showed the highest minimum fluidization velocity. However, some particle mixtures were composed with larger particles up to 1000 micron, but with a fraction of smaller particles down to

200 microns at the same time. This shows the effect of strong drag from early fluidizing smaller particles. The only variability for pressure drop during packed bed is the particle size and it was clearly observed in all three cases.

Keywords: Fluidization, Bioenergy, Particle properties, Minimum fluidization velocity

1 Introduction

Fluidization occurs whenever a collection of particles is subjected to an upward fluid flow at a sufficient flowrate where the gravity and inter-particle forces are in counterbalance with the fluid drag force (Horio 2013). The fluidized bed technology was first introduced in the petroleum industry for catalytic cracking processes, which later penetrated into energy, environmental and processing industry (Horio 2013, Winter and Schratzer 2013, Vollmari, Jasevičius et al. 2016). The technology enhances the gas-solid contact and mixing, which leads to increased heat and mass transfer characteristics. Further, it guarantees the homogeneous temperature and concentrations throughout the reactor, which increases the possibility and reliability of scaled up operation. Good control over solid particles, large thermal inertia of solids (Esmaili and Mahinpey 2011), increased efficiency, reduced emissions and wide range of operating conditions are additional advantages of the fluidized bed systems (Winter and Schratzer 2013). The importance of the fluidized bed technology is highlighted specially in exothermic reactions such as biomass combustion as it avoids hot spot and cold spot generation due to intense mixing and particle collision. Hot spots lead to ash melting followed by agglomeration and clinkering (Behjat, Shahhosseini et al. 2008, Horio 2013) whereas cold spots reduces tar cracking and thus, reduced gas quality.

Bio-energy is the fourth largest energy source, which accounts for 10% to 14% of the world energy profile (REN21 2016). The lignocellulosic fraction of the biomass is the major contributor of bioenergy. In contrast to the simple, inefficient and small-scaled combustion practices, there is a tendency to use advanced technologies such as fluidized bed gasification followed by either heat & power generation or liquid fuel synthesis. However, due to low density, large particle size and extreme shapes of the particles,

biomass is difficult to fluidize alone (Cui and Grace 2007). Therefore, biomass fluidized bed combustors and gasifiers are operated with the assistance of fluidizing materials such as sand, alumina, catalysts etc., which is known as bed material (Fotovat, Ansart et al. 2015). Hence, it is meaningful to study the fluidization behavior of bed materials as it principally governs the bed hydrodynamics. Bubbling fluidization stands slightly above the minimum fluidization. Hence, it is important to manipulate the minimum fluidization velocity in bubbling fluidized bed gasification systems, because it governs the mass flowrate of gasifying agent into the reactor system.

The fluidization properties are governed by both particle properties such as particle size, particle density, particle shape etc. and fluid properties (Fotovat, Ansart et al. 2015). However, there can be additional effects from the bed diameter, geometry, aspect ratio and distributor design as well. The transition superficial gas velocity from fixed bed to fluidized bed is referred to as the minimum fluidization velocity, which is one of the most important parameters in the design of fluidized beds (Coltters and Rivas 2004). Depending on Geldart's powder classification and superficial gas velocity, particles tend to fluidize in homogeneous, bubbling, slugging or sprouting beds (Geldart 1973).

Computational Fluid Dynamics (CFD) simulations are beginning to appear in a meaningful way with the tremendous growth in computer power along with sophisticated mathematical models and efficient algorithms (Cooper and Coronella 2005, Kia and Aminian 2017). The faster and more accurate CFD simulations of fluidization systems, makes it easier to get detailed predictions compared to the expensive and time consuming experiments. On the other hand, CFD is a smart tool in optimizing the geometry, which is difficult or even impossible to achieve with experiments. Further, it provides an insight into the bed interior, which again is difficult to achieve with experiments unless more advanced technologies are used. Extreme operational conditions can also be analyzed in advanced to guarantee the safe operation of experimental setups.

However, modeling of gas-solid flow behavior is challenging due to the complexities arising from the coupling of turbulent gas flow and particle motions together with inter-particle collisions. The differences in scale from particles to geometry is another difficult parameter in the CFD simulations. Lagrangian-Eulerian and Eulerian-Eulerian are the basic modeling approaches in gas-solid multiphase systems. Lagrangian-Eulerian modeling solves the Newtonian equation of motion for each individual particle in the system while the gas phase is modeled as a continuum with Navier-Stokes equations. In contrast, the Eulerian-Eulerian modeling considers both phases as continuous and interpenetrating, which are modeled with the

Navier-Stokes equations (Xie, Zhong et al. 2013). Even though Eulerian-Eulerian modeling consumes less computer power, it is complex in modeling stage, as it needs more closure functions. In contrast, the Lagrangian-Eulerian simulations need high computer power, and it is unrealistic to use for industrial scale reactors. Multiphase particle-in-cell (MP-PIC) was developed as an extension to the Lagrangian-Eulerian simulations, where particles are modeled in both discrete and continuous phase (Snider 2001, Xie, Zhong et al. 2013). Instead of individual particles, it considers groups of particles sharing common characteristics. These groups are referred to as parcels or computational particles. Particle properties that are best calculated on the grid are calculated using continuous modeling in the advanced time step and interpolated back to individual particles. The successive development of the MP-PIC method is illustrated in the works of Snider, O'Rourke and Andrews (Andrews and O'Rourke 1996, Snider, O'Rourke et al. 1998, Snider 2001, Snider 2007, O'Rourke and Snider 2012). This particular method is embedded in Barracuda VR commercial software package, which is becoming popular in CFD modeling of gas-solid systems and has brought forward the concept of computational particle fluid dynamics (CPFDD). Hence, the objective of this work is to analyze the effect of particle properties of density, size and size distribution on the minimum fluidization velocity with CPFDD simulation.

2 Methods and Computational Setup

Barracuda VR 17.1.0 was used for the simulations where a simple cylindrical geometry of 1000 mm in height and 84mm in diameter was considered. A uniform grid was applied with 8000 cells in total, which is illustrated in Figure 1. Grid refinements at the wall was not performed as it was assumed that there was no boundary layer formation with the dense phase particle system. Default grid generator settings were used, which removes the cells having less fraction of volume than 0.04 and greater aspect ratio than 15:1.

Isothermal temperature of 300 K was used where sand (SiO_2) was used as the basic bed material. However, other materials as aluminum oxide (Al_2O_3), nickel oxide (NiO), calcium (Ca), ferric oxide (Fe_2O_3), titanium oxide (TiO_2) and zirconium (ZrO_2) were used to analyze the effect of density on the minimum fluidization velocity. Air at atmospheric pressure was used as fluidizing gas in all the cases. Particles were filled up to 350mm of height and the random packing option was used.

The close pack volume fraction, maximum momentum redirection from collisions, normal to wall momentum retention and tangent to wall momentum retention were set to 0.6, 40%, 0.3 and 0.99 respectively. Default values for the parameters in the particle stress model were kept unchanged. Blended acceleration model was activated

for the mixtures of different particle sizes. The column was operated at atmospheric pressure where the air outlet at the top plane was defined as a pressure boundary. Inlet boundary was defined as a flow/velocity boundary with varying air velocities over time. Each velocity was maintained for 4 seconds. Further, uniform air distribution at the inlet and no particle exit from the pressure boundary were assumed. The bed pressure was monitored in the center of the bed at five different heights. The boundary conditions and the pressure monitoring points are depicted in Figure 1.

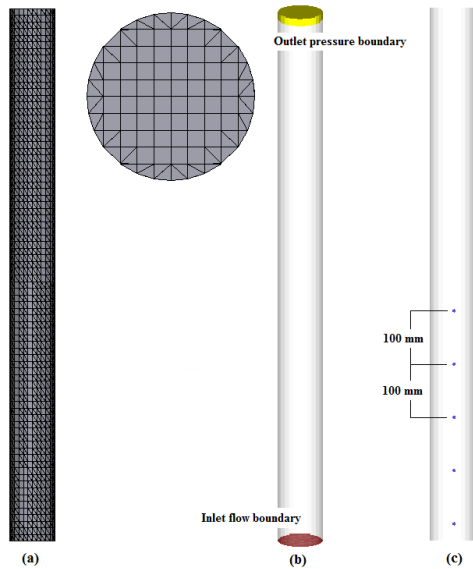


Figure 1. (a) Grid, (b) Boundary conditions, (c) Pressure data points

3 Results and Discussion

The bed materials used in fluidized bed gasification and combustion are usually polydispersed with a wide size distribution. However, monodispersed particle beds were used in this work to demonstrate the effect of particle size for minimum fluidization velocity. Attempts were made to analyze the effect of the particle size mixtures later in this work.

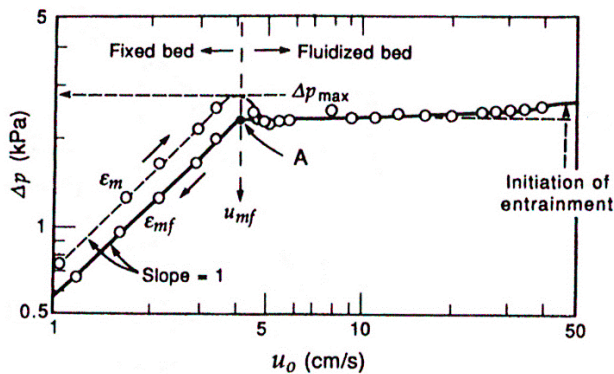


Figure 2. Gas velocity vs pressure drop diagram (Kunii and Levenspiel 1991)

The pressure drop (Δp) versus superficial gas velocity U_0 diagram is useful in determining the transition from fixed bed to fluidized bed. During the fixed bed operation, the bed pressure drop is proportional to the gas velocity. Once the bed reaches the minimum fluidization velocity, the bed pressure drop decreases a little, and stabilizes at the static bed pressure. The bed continues to stay around that pressure until the particle entrainment starts (Kunii and Levenspiel 1991). This behavior and figuring out of the minimum fluidization velocity U_{mf} , is illustrated in Figure 2.

Fluid drag force resulted from the upward fluid flow is one of the most important particle forces in any fluidized bed system. Due to this, many researchers have worked towards the optimization of drag models for particular cases. The author has experimentally validated the good performance of the Wen-Yu-Ergun drag model in a previous work (Bandara, Thapa et al. 2016). Gidaspow proposed a drag model where the interface momentum transfer coefficient, K_{sg} , is selected from either Wen-YU or Ergun correlation depending upon the gas volume fraction (Sobieski 2009). When the gas volume fraction is greater than 0.8, Wen-Yu correlation is applied which is given by:

$$K_{\frac{sg}{WenYu}} = \frac{3}{4} \frac{C_d \rho_g \varepsilon_g (1 - \varepsilon_g) (u_s - u_g)}{d_p} \varepsilon_g^{-2.65} \quad (1)$$

Where C_d is:

$$C_d = \begin{cases} \frac{24}{\varepsilon_g Re_s} \left[1 + 0.15 (\varepsilon_g Re_s)^{0.687} \right], & Re_s \leq 1000 \\ 0.44, & Re_s > 1000 \end{cases} \quad (2)$$

When the gas volume fraction is less than 0.8, Ergun correlation is used which is given by:

$$K_{\frac{sg}{Ergun}} = 150 \frac{\mu_g (1 - \varepsilon_g)^2}{\varphi^2 d_p^2 \varepsilon_g} + 1.75 \frac{\rho_g (u_g - u_s) (1 - \varepsilon_g)}{\varphi d_p} \quad (3)$$

Where, subscripts g , p and s refer to gas phase, particle and solid phase respectively. U is the velocity, ρ is the density ε is the volume fractions, φ is the sphericity, μ is the viscosity, Re is the Reynold's number and d is the particle diameter.

3.1 Effect of the Particle Size

Geldart has worked towards classifying the particles according to both size and density in the early 1970s (Geldart 1973). Same author has discussed the effect of the particle size distribution in fluidized beds in a separate publication. This work analyses these effects from computational fluid dynamic aspects. To demonstrate the effect of the particle size, sand particles from 400 to 800 microns were used. The particle density was 2200 kg/m³ and it was further assumed that the particles were spherical. As shown in Figure 3, the

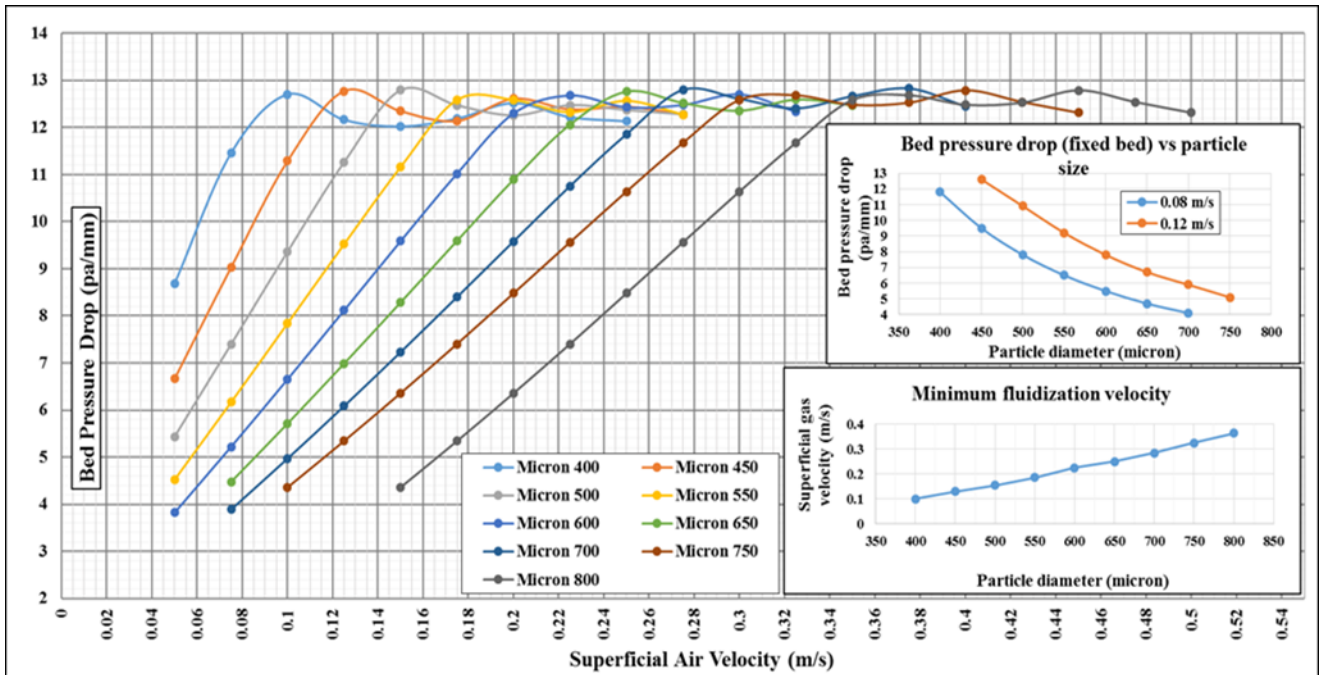


Figure 3. Minimum fluidization velocity plots for different size particles. Right upper corner sub-plot illustrates the pressure drop during fixed bed at two different gas velocities

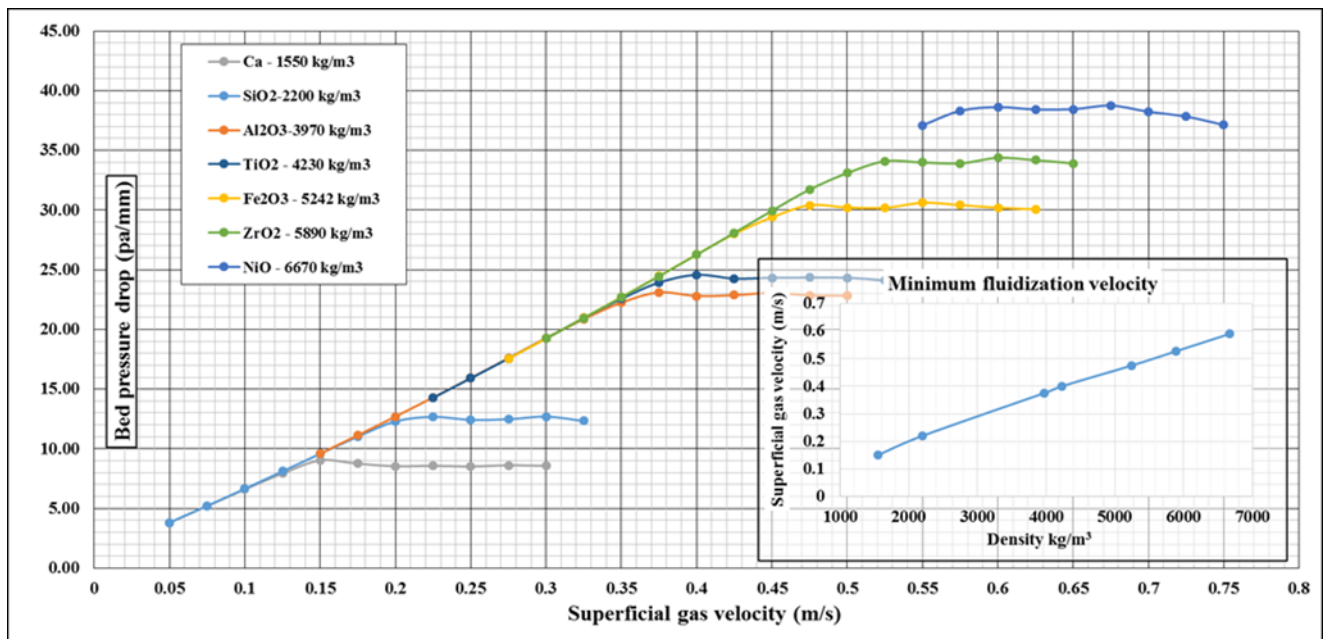


Figure 4: Effect of the particle density for minimum fluidization velocity

minimum fluidization velocity increases linearly with the particle diameter as expected. Bed pressure drop shows a linear relationship with the superficial gas velocity during the packed bed region. Further, it is clear from the figure that the bed pressure drop at the minimum fluidization is almost the same for all the particle sizes. It is also agreeable because, the bed weight is counter balanced by the pressure drop at the fluidization and the bed mass was approximately constant for all the sizes. The fluctuations of the pressure

drop in the fluidizing region is also realistic which can be observed in many experimental results as well.

3.2 Effect of the Particle Density

A 600-micron sand bed was considered as the reference and the effect of different densities were analyzed for 600-micron particles. According to the simulation results depicted in Figure 4, the minimum fluidization velocity is proportional to the particle density. As the particle diameter is similar, all the plots follow the same line during the packed bed operation.

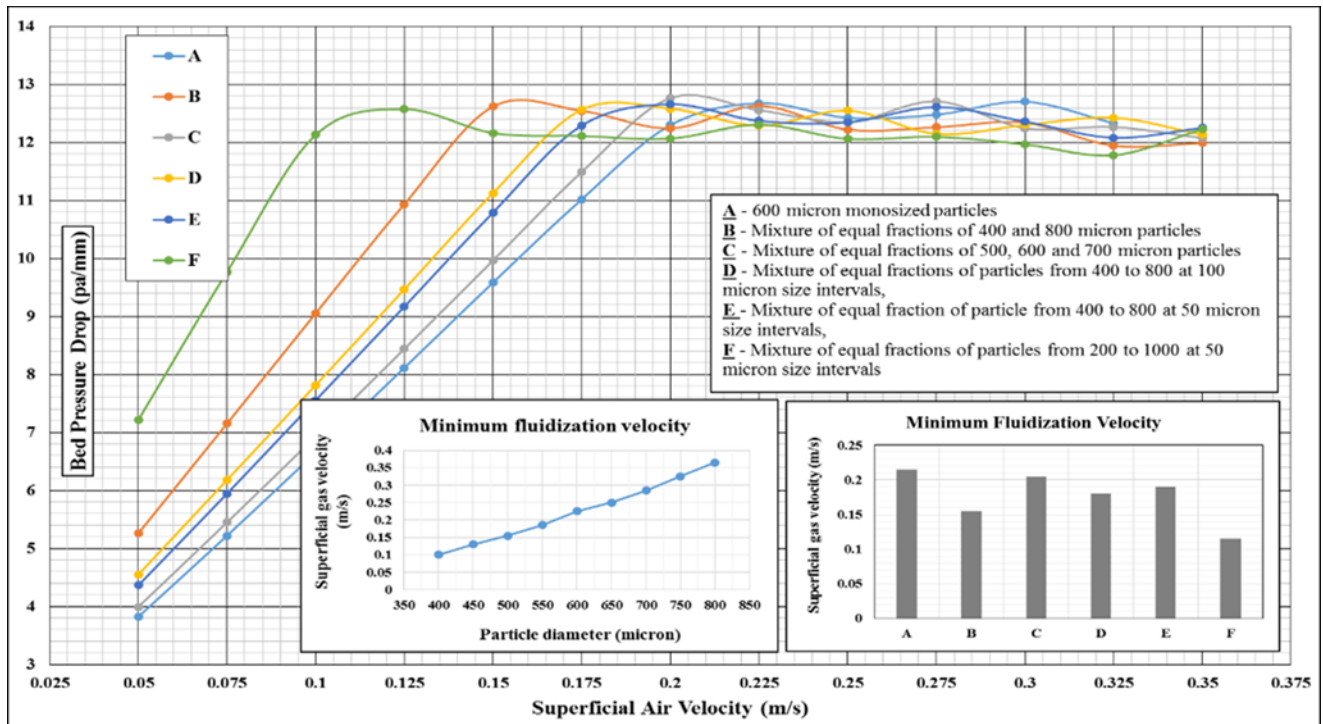


Figure 5. Effect of the particle size distribution on the minimum fluidization velocity

3.3 Effect of the Particle Size Distribution

The final and major task of this work is to see the functioning of CFD technique in predicting the minimum fluidization velocity behavior of particle mixtures of different sizes. Specially, empirical models for the drag force have been developed considering mono size particles. However, the particle drag force in a mixture of different size particles differs compared to that in a mono-size particle bed.

The effect of the particle size distribution was compared with the 600-micron monodispersed silica particles. Different particle mixtures of silica all with a mean particle diameter as 600-micron were simulated. The description of the particle mixtures are given in Figure 5. Particle mixtures were defined by introducing one particle species for each size and filling them randomly with pre-defined volume fractions, which collectively accounts for 0.6 solid/particle volume fraction.

According to the same Figure 5, 600-micron monodispersed particles has the highest minimum fluidization velocity, which is approximately 0.21 m/s. The minimum fluidization velocity of mixture C is close to the value of the 600-micron monodispersed sample. This might be due to the narrow size distribution of mixture C around 600 micron. The minimum fluidization velocity of mixtures D and E is closer to each other, but the values are less than A and C. The particle sizes of D and E mixtures are distributed between 400 and 800 micron in a similar way to a certain extent. The size distribution of pre-mentioned mixtures are in a broad range with oversized and undersized particles than 600 micron. The mixture B,

which is having equal fractions of 400 and 800 micron particles, shows a lower minimum fluidization velocity compared to A, C, D and E. This particular mixture contains half of the fraction with 400 microns, which is comparatively less compared to 600. Finally, the mixture F with the highest size distribution (between 200 to 1000 microns) shows the lowest minimum fluidization velocity among the six different mixtures considered.

It is important to note the possibility of reducing the minimum fluidization velocity by adding a certain fraction of smaller sized particles. As an example, even though the mixture F contains considerable amounts of particles larger than 600 micron, the minimum fluidization velocity still substantially drops below the value of monodispersed 600 microns sample. In this situation, the larger particles are affected both by the fluid drag force and by the momentum from smaller particles (particle drag). According to the simulations carried out for different diameters, smaller particles are prone to fluidized at lower gas velocities. Therefore, the drag force from the fine particles make the larger particles fluidize at lower gas velocities when those are in a mixture. However, the simulation time was increased considerably for particle mixtures than monodispersed particle beds.

4 Conclusion

The effects of particle size, density and size distribution on the minimum fluidization velocity were analyzed using the MP-PIC CFD simulation technique. Barracuda VR commercial software package was used in all the simulations. A previously validated model, which uses

the Wen-YU-Ergun model for the fluid drag, was used. However, the model had not been validated for particles with size distribution for several sizes. It is good to conduct experimental analysis further to guarantee the reproducibility of simulation data.

Minimum fluidization velocity was observed to be linearly proportional to the particle size. On the other hand, the minimum fluidization velocity increases approximately by a factor of two when the particle density is doubled. It is the pressure drop, which is more concerned during packed bed operation. Simulation results for different size and densities prove that it is the particle size, which governs the pressure drop. However, it is not easy to observe a clear relationship between minimum fluidization velocity and particle sizes when it comes to particle mixtures. The smaller particles in a mixture greatly affects and reduces the minimum fluidization velocity. Thus, this phenomenon is useful in operating a bubbling fluidized bed reactor at different gas velocities, simply by adding either larger or smaller particles depending on the requirement. Finally, the Barracuda CFPD simulations can provide precise and quick insight into the bed hydrodynamics.

Acknowledgement

The authors would like to forward their gratitude to University College of Southeast Norway for providing of the Barracuda VR software package and computer facilities.

References

- Andrews, M. J. and P. J. O'Rourke (1996). "The multiphase particle-in-cell (MP-PIC) method for dense particulate flows." *International Journal of Multiphase Flow* **22**(2): 379-402.
- Bandara, J. C., R. K. Thapa, B. M. E. Moldestad and M. S. Eikeland (2016). "Simulation of Particle Segregation in Fluidized Beds" *9th EUROSIM Congress on Modelling and Simulation*, Oulu, Finland, IEEE.
- Behjat, Y., S. Shahhosseini and S. H. Hashemabadi (2008). "CFD modeling of hydrodynamic and heat transfer in fluidized bed reactors." *International Communications in Heat and Mass Transfer* **35**(3): 357-368.
- Coltters, R. and A. L. Rivas (2004). "Minimum fluidation velocity correlations in particulate systems." *Powder Technology* **147**(1-3): 34-48.
- Cooper, S. and C. J. Coronella (2005). "CFD simulations of particle mixing in a binary fluidized bed." *Powder Technology* **151**(1-3): 27-36.
- Cui, H. and J. R. Grace (2007). "Fluidization of biomass particles: A review of experimental multiphase flow aspects." *Chemical Engineering Science* **62**(1-2): 45-55.
- Esmaili, E. and N. Mahinpey (2011). "Adjustment of drag coefficient correlations in three dimensional CFD simulation of gas-solid bubbling fluidized bed." *Advances in Engineering Software* **42**(6): 375-386.
- Fotovat, F., R. Ansart, M. Hemati, O. Simonin and J. Chaouki (2015). "Sand-assisted fluidization of large cylindrical and spherical biomass particles: Experiments and simulation." *Chemical Engineering Science* **126**: 543-559.
- Geldart, D. (1972). "The effect of particle size and size distribution on the behaviour of gas-fluidised beds." *Powder Technology* **6**(4): 201-215.
- Geldart, D. (1973). "Types of gas fluidization." *Powder Technology* **7**(5): 285-292.
- Horio, M. (2013). 1 - Overview of fluidization science and fluidized bed technologies A2 - Scala, Fabrizio. *Fluidized Bed Technologies for Near-Zero Emission Combustion and Gasification*, Woodhead Publishing: 3-41.
- Kia, S. A. and J. Aminian (2017). "Hydrodynamic modeling strategy for dense to dilute gas-solid fluidized beds." *Particuology* **31**: 105-116.
- Kunii, D. and O. Levenspiel (1991). *Fluidization Engineering*. Washington Street, Newton, MA, Butterworth-Heinemann.
- O'Rourke, P. J. and D. M. Snider (2012). "Inclusion of collisional return-to-isotropy in the MP-PIC method." *Chemical Engineering Science* **80**: 39-54.
- REN21 (2016). *Renewables 2016 Global Status Report*.
- Snider, D. M. (2001). "An Incompressible Three-Dimensional Multiphase Particle-in-Cell Model for Dense Particle Flows." *Journal of Computational Physics* **170**(2): 523-549.
- Snider, D. M. (2007). "Three fundamental granular flow experiments and CFPD predictions." *Powder Technology* **176**(1): 36-46.
- Snider, D. M., P. J. O'Rourke and M. J. Andrews (1998). "Sediment flow in inclined vessels calculated using a multiphase particle-in-cell model for dense particle flows." *International Journal of Multiphase Flow* **24**(8): 1359-1382.
- Sobieski, W. (2009). "Switch Function and Sphericity Coefficient in the Gidaspow Drag Model for Modeling Solid-Fluid Systems." *Drying Technology* **27**(2): 267-280.
- Vollmari, K., R. Jasevičius and H. Kruggel-Emden (2016). "Experimental and numerical study of fluidization and pressure drop of spherical and non-spherical particles in a model scale fluidized bed." *Powder Technology* **291**: 506-521.
- Winter, F. and B. Schratzer (2013). 23 - Applications of fluidized bed technology in processes other than combustion and gasification A2 - Scala, Fabrizio. *Fluidized Bed Technologies for Near-Zero Emission Combustion and Gasification*, Woodhead Publishing: 1005-1033.
- Xie, J., W. Zhong, B. Jin, Y. Shao and Y. Huang (2013). "Eulerian-Lagrangian method for three-dimensional simulation of fluidized bed coal gasification." *Advanced Powder Technology* **24**(1): 382-392.

Simulation of Starting and Stopping Vortices of an Airfoil

Roberto Agromayor Jairo Rúa Reidar Kristoffersen

Department of Energy and Process Engineering, Norwegian University of Science and Technology, Norway,
roberto.agromayor@ntnu.no

Abstract

When the flow around a streamlined body is accelerated or decelerated, starting and stopping vortices are shed from the trailing edge of the body, respectively. In this work, the transient flow around a NACA4612 airfoil profile was analyzed and simulated at $Re = 1000$ and $\alpha = 16^\circ$ paying especial attention to the starting and stopping vortices shed from the airfoil. A detailed review of the underlying physics of the generation of lift was presented with focus on the importance of viscosity as the essential factor for the generation of lift. The incompressible Navier-Stokes equations with constant density and viscosity in an inertial frame of reference were solved with OpenFOAM using a linear upwind finite volume method (FVM) for the space discretization and the implicit Euler method for the time integration. The results were verified using the Kelvin circulation theorem. Three flow animations were prepared with the simulation results and compared with the historical flow visualizations from Prandtl.

Keywords: Kelvin circulation theorem, Stokes theorem, CFD, PIMPLE algorithm, C-mesh, SnappyHexMesh, unsteady, non-inertial, NACA profile, aerofoil.

1 Introduction

When the flow around an airfoil starts from rest, either because a free stream velocity is imposed or because the body is set to motion, a *starting vortex* is formed at its trailing edge. Similarly, when the flow is decelerated or stopped, a *stopping vortex* of opposite sense is formed and shed from the trailing edge of the airfoil, see Figure 1.

These physical phenomena were recorded in the historical flow visualization by Prandtl. The original flow visualizations are shown in the more recent series of videos of the (National Committee for Fluid Mechanics Films, 1972). The reader is encouraged to watch these flow visualizations because they illustrate the physical phenomena brought to focus in this paper (Vorticity Part 2, 3:00-5:15).

The flow visualizations of Prandtl were analyzed by (Willert and Kompenhans, 2010) using particle image velocimetry (PIV) to compute and visualize the vorticity of the flow. In addition, (Vincent and Blackburn, 2014) performed a direct numerical simulation (DNS) of the transient flow over a symmetrical profile NACA0012 at $Re = 10000$ and $\alpha = 4^\circ$ using a spectral element method (SEM) that showed the formation of the starting and stopping vortices.

In this work the transient laminar flow over a NACA4612 airfoil profile at $Re = 1000$ and $\alpha = 16^\circ$ was simulated using a finite volume method (FVM) in OpenFOAM. The three flow visualizations by Prandtl: 1) starting flow over an airfoil, 2) impulsively started airfoil in a resting fluid, and 3) impulsively started and stopped airfoil in a resting fluid, were simulated. The lift and drag coefficients were computed as a function of time and the numerical results were verified (Section 3) and validated (Section 4) comparing them with the theoretical predictions (Section 2). The purpose of this paper is to study the physics of starting and stopping vortices from a computational point of view and to assess the performance of the OpenFOAM incompressible solvers.

2 Underlying Physics

2.1 The lift and drag forces

A body immersed in a flow will experience forces from the fluid. In the case of a plane flow, the force parallel to the direction of the free stream direction is known as *drag* and the force perpendicular to the flow direction is called *lift*. These forces are the result of the pressure and viscous stresses over the surface of the immersed body.

Lifting bodies, such as airfoils, are designed to provide large forces in the direction normal to the flow and low drag. The performance of a cylindrical airfoil section is characterized by the lift and drag coefficients, defined as:

$$C_L = \frac{D}{\frac{1}{2}\rho V_\infty^2 \cdot c} \quad (1) \quad C_D = \frac{L}{\frac{1}{2}\rho V_\infty^2 \cdot c} \quad (2)$$

where L and D are the lift and drag forces per unit of width, $\frac{1}{2}\rho V_\infty^2$ is the dynamic pressure, and c is the chord length of the airfoil profile.

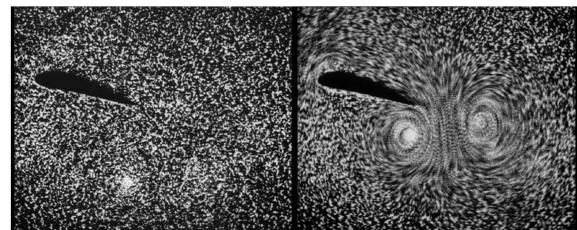


Figure 1. Prandtl's flow visualization. Left: fluid at rest. Right: Interaction of the starting and stopping vortices after the airfoil has been impulsively started and stopped.

2.2 Inviscid flow

One of the main tasks of aerodynamics and hydrodynamics is to determine lift and drag forces. The simplest approach is to analyze the forces caused by the motion of an ideal fluid without viscosity. This kind of flow is known as potential flow and it is based on the assumption that the flow is irrotational, that is, the vorticity of the field is zero everywhere. The vorticity is a kinematic flow variable defined as the curl of the velocity field:

$$\vec{\omega} = \vec{\nabla} \times \vec{v} \quad (3)$$

If the zero-vorticity condition is met, then the velocity field can be shown to be the gradient of a potential function that satisfies the Laplace equation. The details of this theory can be found in (White, 2011, Chapter 4 and 8). The solution of this problem is much simpler than the solution of the viscous Navier-Stokes equations and, in many cases, the flow can be solved analytically.

One of the drawbacks of the potential flow theory is that it fails to predict the drag felt by a body moving with constant velocity, relative to the fluid, caused by the viscous stresses (it accounts for drag due to pressure and acceleration though). This is known as the D'Alembert's paradox.

On the other hand, the potential flow theory can be used to predict the lift force on a body as a result of the pressure distribution. One of the most important results of the potential flow theory is the Kutta-Joukowski lift theorem. This theorem states that the lift force per unit of depth experienced by a cylinder with arbitrary shape immersed in a fluid with uniform free-stream velocity V_∞ and constant density ρ is given by:

$$L = -\rho V_\infty \Gamma \quad (4)$$

Where Γ is the circulation around the solid body, which is defined as:

$$\Gamma = \oint_C \vec{v} \cdot d\vec{l} \quad (5)$$

The Kutta-Joukowski theorem is based on the integration of the pressure distribution over the cylinder surface and its proof can be found in (Kundu and Cohen, 2002, Chapter 6).

The integral in Eq. 5 is performed in a counterclockwise sense and the minus sign of Eq. 4 indicates that a negative circulation leads to a positive lift force. Therefore, the main problem to determine the lift force acting on a body of arbitrary geometry is to determine the circulation Γ .

Despite the usefulness of the potential flow theory to predict lift forces, there is a *fundamental* inconsistency within it. The lift force in a potential flow is $L = \rho V_\infty \Gamma$ but, how does the flow develop the circulation Γ ?

Consider the example of an airfoil initially at rest that is moved in a inviscid fluid. At the beginning the velocity is zero everywhere and so is the circulation around the airfoil. When the airfoil starts to move, the fluid flows around

the airfoil, but the circulation will still be zero because the vorticity is zero everywhere. This can be explained using the Stokes' theorem to transform the line integral of velocity of Eq. 5 into the surface integral of vorticity. The meaning and the proof of the Stokes' theorem can be found in (Jeffrey, 2001, Chapter 12).

$$\Gamma = \oint_C \vec{v} \cdot d\vec{l} = \iint_S \vec{\nabla} \times \vec{v} \cdot d\vec{S} = \iint_S \vec{\omega} \cdot d\vec{S} \quad (6)$$

Since the vorticity is zero everywhere, there is no circulation and hence, the lift force is zero. The inconsistency of the potential flow theory is now apparent, it predicts that the lift force is proportional to the circulation, but at the same time the circulation must be zero because the flow is irrotational.

Kelvin's theorem is an important result related with circulation and vorticity. This theorem states that in an inviscid, constant density flow with conservative body forces, the circulation associated with a closed curve moving with the fluid does not change with time.

$$\frac{d\Gamma}{dt} = 0 \quad (7)$$

In other words, for the case of potential flow in the absence of non conservative forces, the circulation is *conserved*. The proof and an detailed discussion of the meaning of this theorem can be found in (Kundu and Cohen, 2002, Chapter 5). The main result is that for the case of a real fluid, the presence of viscous stresses in the integration path C leads to changes in the circulation, that in turn lead to lift forces. Therefore, the *origin of lift* is the presence of viscosity even if the contribution of viscous forces to the lift at steady motion is modest.

2.3 Viscous flow

Consider now an airfoil at rest within a stationary viscous fluid that is suddenly accelerated to V_∞ at $t = 0^+$. The arguments presented in this section are briefly considered in (White, 2011, Chapter 7 and 8) and (National Committee for Fluid Mechanics Films, 1972), and discussed in more detail in (Kundu and Cohen, 2002, Chapter 15) and (Batchelor, 2000, Chapter 6).

When the fluid is at rest the velocity and vorticity are zero everywhere and so is the circulation around any closed contour C that contains the airfoil. When the fluid motion starts the viscous boundary layers start to grow close to the surfaces of the airfoil, but at $t = 0^+$ the vorticity is still zero everywhere and the potential solution corresponding to $\Gamma = 0$, as shown in Figure 2, still holds. The flow pattern contains two stagnation points, one in the leading edge of the airfoil and the other on the upper side, close to the trailing edge. The trailing stagnation point is not exactly at the trailing edge and the flow turns abruptly at flow the lower side to the upper side at the trailing edge. In fact, the potential flow theory predicts an unphysical infinite velocity at the trailing edge.

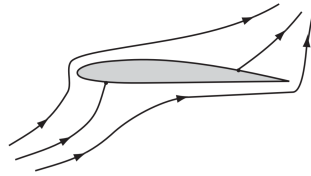


Figure 2. Potential flow solution at $t = 0^+$ for $\Gamma = 0$. Figure from (Darmofal, 2001).

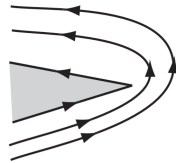


Figure 3. Sharp turn of the potential flow solution at the trailing edge. Figure from (Darmofal, 2001).

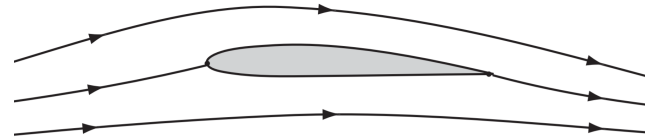


Figure 4. Viscous solution with the the second stagnation point at the trailing edge. Figure from (Darmofal, 2001).

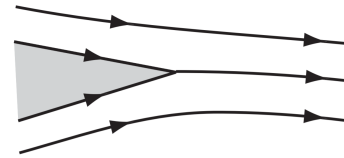


Figure 5. Detail of the *Kutta condition* with the stagnation point at the trailing edge. Figure from (Darmofal, 2001).

The potential flow solution is valid at $t = 0^+$, even if the fluid has viscosity, because the vorticity is generated at a finite rate close to the airfoil walls and it needs time to be convected and diffused to the main flow. The transport of vorticity in a 2D incompressible flow is described by:

$$\frac{D\vec{\omega}}{Dt} = \nu \nabla^2 \vec{\omega} \quad (8)$$

The left hand side of Eq. 8 is the material derivative of vorticity and the term in the right hand side is diffusion of vorticity due to the viscosity of the fluid. See (White, 2006, Chapter 2) or (Kundu and Cohen, 2002, Chapter 5) for the details of the derivation of this equation.

When $t > 0$ the boundary layers start to grow and the vorticity generated close to the walls is transported by the flow. Clockwise vorticity is generated on the upper side of the airfoil while counterclockwise vorticity is created on the lower side of the airfoil. The velocity of the fluid is large at the trailing edge as it flows from the lower to the upper side (see Figure 3) and the flow is decelerated as it approaches the stagnation point. This deceleration causes an adverse pressure gradient that in turn leads to the separation of the boundary layer and backflow. As a result of this backflow, a counterclockwise vortex is formed at the trailing edge of the airfoil. With the passing of time, the stagnation point is displaced closer the the trailing edge and the vortex is convected downstream by the flow. Eventually, the stagnation point occurs at the trailing edge, as pictured in Figure 4 and Figure 5. This situation is known as the *Kutta condition*.

The vortex shed from the trailing edge is known as the *starting vortex* and it is essential in the generation of lift. Once the *starting vortex* has been shed away from the airfoil we will consider three different integration paths for Eq. 5 as shown in Figure 6. The circulation of the *starting vortex* is given by the integration around $\langle e f g h \rangle$. This integral is clearly positive as the vorticity of the *starting vortex* is positive (counterclockwise) at all points. On the

other hand, the circulation around the airfoil (responsible for the lift) is given by the integration around $\langle a b c d \rangle$. The value of both circulations has to be equal in magnitude and opposite in sign, as it will be explained next. Therefore, there is a negative circulation around the airfoil that leads to a positive upwards lift force, see Eq. 4.

The reason why both integrals have to sum zero is explained with Kelvin's circulation theorem. If the circulation integral of Figure 6 is evaluated around an *inviscid* integration path far away from the airfoil, then the value of the circulation must have remained constant at all times and, since $\Gamma = 0$ at $t = 0$, the circulation around $\langle a e f g c d \rangle$ must be zero at all times. Finally, since:

$$\oint_{aefgcd} \vec{v} \cdot d\vec{l} = \oint_{abcd} \vec{v} \cdot d\vec{l} + \oint_{efgh} \vec{v} \cdot d\vec{l} \quad (9)$$

we can conclude that the the sum of the circulation around the airfoil and the *starting vortex* must be zero.

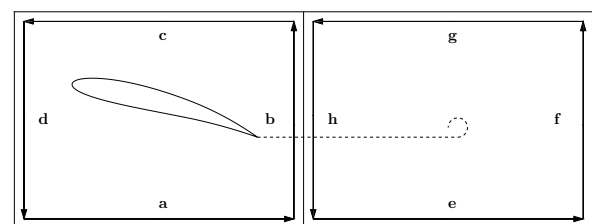


Figure 6. Scheme of the integration paths used to show that the lift is caused by the starting vortex.

2.4 Starting and stopping vortices

As it has been discussed, a *starting vortex* is formed when a flow is started over an airfoil. Likewise, if the free stream velocity is increased, the flow around the airfoil will be accelerated leading to a new *starting vortex*. In contrast, if the free stream velocity is reduced or stopped, a clockwise *stopping vortex* will be shed from the airfoil.

The situation when an airfoil starts its motion within a fluid at rest is very similar. In this case a *starting vortex* is also formed but instead of being convected downstream with the flow, it remains in the same location where it was generated while the airfoil moves away from the vortex. On the other hand, if the vortex is rapidly decelerated a clockwise *stopping vortex* will also be formed.

In this work, a numerical investigation of the starting and stopping vortices shed by a NACA4612 at an angle of attack $\alpha = 16^\circ$ was performed for the cases of a started flow, a started airfoil, and a started and stopped airfoil.

3 Computational Procedure

3.1 Mesh generation and verification

The transient two-dimensional flow over a NACA4612 airfoil with an angle of attack of 16° was simulated using a finite volume method (FVM) code. A laminar Reynolds number of 1000 was selected for the computations. The geometry of the NACA4612 profile, shown in Figure 7, was generated according to the procedure of the original NACA report presented in (Jacobs et al., 1933).

Two types of meshes were considered in this work. The former was a C-mesh type, which is a multiblock structured mesh that consists of a semicircle grid that follows the geometry of the airfoil on the leading edge, and a rectangular grid that captures the physics on the trailing edge and the wake region. This is one of the main advantages of the C-mesh, as the grid is finer in the regions where the flow requires higher resolution. The later type of mesh was an automatically-generated, unstructured, hexahedral mesh, which concentrates the vast majority of the cells near the surface of the airfoil.

The C-mesh was created in OpenFOAM importing the geometry of the airfoil from MATLAB. The division of the mesh in 6 blocks is shown in Figure 8, allowing it to have different cell density depending on the region. In addition, a grading on the cell size was applied in order to obtain as many cells as possible near the airfoil while having fewer at the borders of the computational domain.

The cell distribution is shown in Figure 9. The high density of cells close to the airfoil provides more accurate computations in the region where the gradients are more pronounced, which is fundamental to capture the vortex generation. The accuracy of the computations is not deteriorated by mesh skewness since the orthogonality of the first cell layers close to the surface is high. Furthermore, a C-mesh with grading on the cell size allows saving computational resources on regions where the physics are not

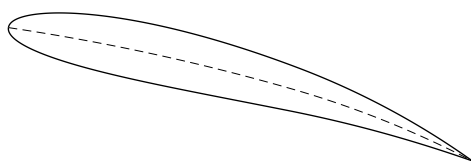


Figure 7. Geometry of the NACA4612 profile at $\alpha = 16^\circ$.

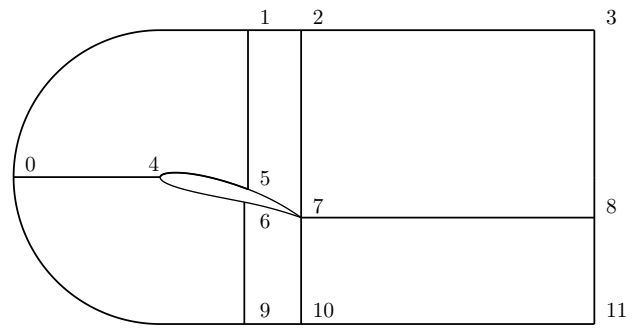


Figure 8. Scheme of the blocks used to generate the structured C-mesh.

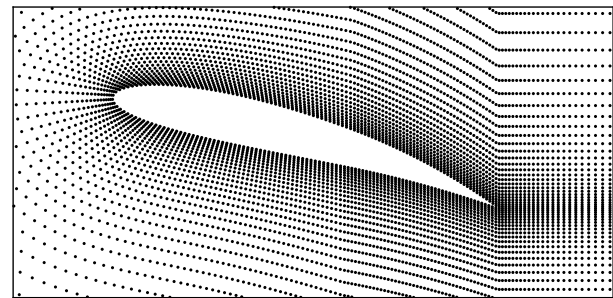


Figure 9. Details of the structured C-mesh close to the airfoil.

relevant, as the inlet, top and bottom of the control volume. Nevertheless, as the main drawback of the C-mesh configuration, some of these regions still have an excessive amount of cells that lengthen the simulation time.

C-meshes with three different dimensions (base case, double size and half size) and number of cells (as seen in Table 1) were tested in order to select the most appropriate one for the simulation and to verify the meshing procedure programmed in MATLAB. For this purpose, steady-simulations at $Re = 100$ were performed with a linear upwind FVM in OpenFOAM using the SIMPLE algorithm for the velocity-pressure coupling. The results for the torque (with respect to the leading edge), drag, and lift coefficients, as well as the computational time and number of iterations are shown in Table 1. The steady-state simulations were performed at $Re = 100$ instead of $Re = 1000$ because at high Reynolds numbers oscillatory vortex shedding occurs and it is not possible to reach a steady-state solution.

The results of the simulation tend to be grid independent, as they gradually converge to the same solution when the grid is refined. In addition, it can be observed that the size of the domain does not affect the results of the simulation and therefore, the solution is independent of the far field boundary conditions (see section 3.2). Thus, due to the similarity among the results, the small mesh with 20000 cells was selected to perform the transient simulations. The reason why the mesh with smallest dimensions was selected is because the shorter computational time it requires for a given level of accuracy. The transient simulations were performed with 20000 cells, even if the re-

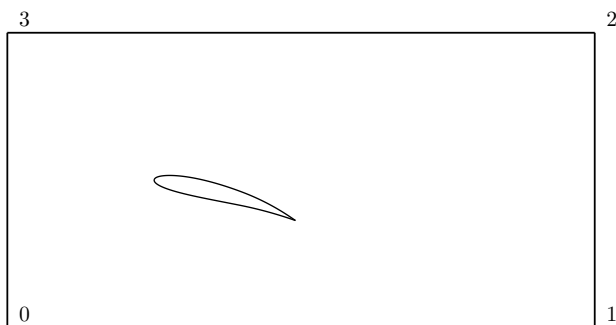
Table 1. C-mesh screening and validation.

Domain	Cells	C_T	C_D	C_L	Iterations	Time (s)
Large	5000	0.2698	0.5167	0.7530	458	10
	11400	0.2690	0.5155	0.7626	796	34
	20000	0.2692	0.5152	0.7675	1179	103
	45000	0.2707	0.5153	0.7749	2114	382
	80000	0.2723	0.5157	0.7801	3238	1115
Medium	5000	0.2739	0.5221	0.7787	464	10
	11400	0.2737	0.5210	0.7825	835	38
	20000	0.2740	0.5207	0.7844	1264	100
	45000	0.2753	0.5209	0.7892	2232	389
	80000	0.2767	0.5213	0.7930	3466	1115
Small	5000	0.2847	0.5351	0.8136	591	11
	11400	0.2845	0.5341	0.8143	1095	40
	20000	0.2846	0.5339	0.8147	1611	110
	45000	0.2846	0.5340	0.8150	2788	455
	80000	0.2851	0.5341	0.8163	4318	1256

sults with a lower number of cells seem accurate. because the authors wanted to ensure that the physics at the trailing edge were captured.

The unstructured mesh is shown in Figure 11. It was created using the *snappyHexMesh* tool in openFOAM together with the airfoil profile geometry generated in MATLAB. This mesh was validated following the same procedure described before but only for the small domain. The obtained results are summarized in Table 2. The torque, drag and lift coefficients are similar to the ones obtained for the structured mesh, whereas the time and number of iterations needed for convergence are smaller. Thus, it could seem that the unstructured grid is more suitable for the transient simulations since it requires less time to attain a similar solution. However, when the results were post-processed and the velocity and pressure fields were observed in detail, the solution was found to be unphysical as it followed the structure of the grid, even when *orthogonal correctors* were employed.

The structured C-mesh used in this work was able to capture the physics of the flow around the airfoil better than the unstructured grid. As a result, the C-mesh was chosen for the transient simulations.

**Figure 10.** Scheme of the block used to generate the unstructured mesh.**Table 2.** Unstructured mesh validation

Mesh	Cells	C_T	C_D	C_L	Iterations	Time (s)
Small	3480	0.2462	0.5115	0.7519	97	1
	13037	0.2574	0.5081	0.7507	193	8
	21988	0.2722	0.5127	0.7867	196	14
	32939	0.2672	0.5087	0.7745	275	97
	125490	0.2797	0.5126	0.8007	303	439

Table 3. Boundary conditions in OpenFOAM.

Boundary	U	P
Inlet	<i>tableFile</i>	<i>zeroGradient</i>
Outlet	<i>zeroGradient</i>	<i>fixedValue (0)</i>
Top	<i>slip</i>	<i>slip</i>
Bottom	<i>slip</i>	<i>slip</i>
Airfoil	<i>fixedValue (0 0 0)</i>	<i>zeroGradient</i>

3.2 Initial and Boundary Conditions

In order to simulate the motion of the fluid from rest, uniform zero velocity and pressure fields were used as initial conditions. The boundary conditions used in OpenFOAM for the simulations are described in the next subsections and an overview is given in Table 3.

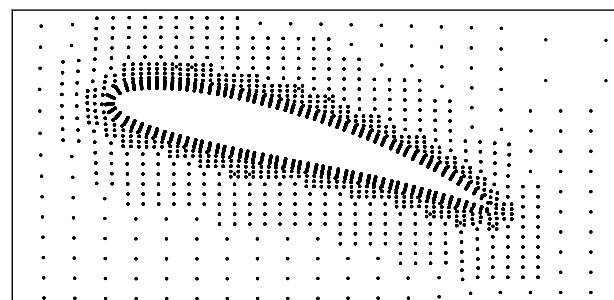
3.2.1 Inlet boundary conditions

The velocity field at the inlet boundary is prescribed as a function of time and read from a table. The pressure at the inlet is defined with a *zeroGradient* boundary condition to simulate the undisturbed far field flow.

The function for the inlet boundary velocity was the same for the simulation of the starting flow over the airfoil and for the simulation of the airfoil that moves within a fluid at rest. The only difference between both cases is a change in the frame of reference. The function chosen for the simulations is given by:

$$u = V_{\infty} \cdot (1 + e^{-\frac{t-t_1}{T}}) \quad (10)$$

This is a logistic function with an *S* shape and it was chosen to simulate a very steep jump in velocity with a smooth function in order to avoid numerical problems. The shape of this curve is given in Figure 13. The simula-

**Figure 11.** Details of the unstructured mesh close the the airfoil.

tion time step was set small enough to capture the velocity variation along the jump.

For the case of the airfoil that is suddenly started and then stopped the inlet boundary condition is given by the following function:

$$u = \begin{cases} V_{\infty} \cdot (1 + e^{-\frac{t-t_1}{T}}) & \text{for } t \leq \frac{t_1+t_2}{2} \\ V_{\infty} \cdot (1 + e^{\frac{t-t_2}{T}}) & \text{for } t \geq \frac{t_1+t_2}{2} \end{cases} \quad (11)$$

This piecewise smooth function is given by two logistic equations and its shape is shown in Figure 16. The values of the parameters used in all the simulations are $V_{\infty} = 1$ m/s $t_1 = 0.5$ s, $t_2 = 1.5$ s and $T = 0.01$ s.

3.2.2 Airfoil boundary conditions

A *noSlip* velocity boundary condition is used at the surface of the airfoil. The velocity of the airfoil is always set to zero during the simulations and its motion is accounted with the inlet boundary conditions. A *zeroGradient* boundary condition is used for the pressure, this is usually a good approximation for viscous flows.

3.2.3 Top and bottom boundary conditions

A *slip* boundary condition is used for the velocity and pressure fields at the top and the bottom boundaries. This implies zero velocity normal to the boundary and no condition for the tangential direction. The pressure condition was set as a *zeroGradient* boundary condition. This simulates that the far field behaves as an inviscid fluid.

3.2.4 Outlet boundary condition

The velocity at the outlet is defined with a *zeroGradient* boundary condition to simulate that the flow is fully developed downstream the airfoil. A value of zero is chosen for the pressure field at the outlet to set a reference level for pressure.

3.3 OpenFOAM solution

Once the mesh was generated and the boundary conditions were imposed, the incompressible (constant density and viscosity) Navier-Stokes equations were discretized using the linear upwind FVM in space and the implicit Euler method in time and then solved using the PIMPLE algorithm for the velocity-pressure coupling. Once the velocity and pressure fields were computed the results were post-processed to compute the vorticity field as well as the lift and drag coefficients. After that, the results were exported to MATLAB to prepare the flow visualizations.

The Navier-Stokes equations solved in the OpenFOAM PIMPLE algorithm are formulated without body forces in an inertial frame of reference. These equations can be expressed in differential form as:

$$\nabla \cdot \vec{V} = 0 \quad (13)$$

$$\frac{D\vec{V}}{Dt} = -\frac{\vec{\nabla}p}{\rho} + \nu \nabla^2 \vec{V} \quad (14)$$

For the cases when the airfoil was moving within a fluid at rest, the problem was solved imposing the time-varying boundary conditions on a stationary airfoil and then the results were post-processed to include the motion of the airfoil. The displacement of the airfoil was computed numerically as the integral of the airfoil velocity:

$$x = \int_0^t u \cdot dt \quad (15)$$

The displacement of the airfoil as a function of time is plot in Figure 12 for the case of the suddenly started airfoil and in Figure 15 for the case of the suddenly started and stopped airfoil. However, when the airfoil accelerates from rest, the frame of reference for the relative velocity field is non-inertial and Eq. 14 has to be modified to include the non-inertial effects (fictitious forces):

$$\frac{D\vec{V}}{Dt} = -\frac{\vec{\nabla}p}{\rho} + \nu \nabla^2 \vec{V} - \vec{a} \quad (16)$$

Where \vec{a} is the acceleration of the non-inertial frame of reference (in this case, the acceleration of the airfoil). A throughout derivation and discussion of the inclusion of non-inertial terms into the integral form of momentum equations is presented in (Fox et al., 2011, Chapter 4). As it can be seen from Eq. 16, the acceleration term behaves as a body force (similar to gravity) acting in the direction opposite to the acceleration of the airfoil.

This term was not included into the analysis as the solution algorithm was not prepared to include body forces. In order to asses the importance of this limitation the acceleration was computed numerically as the derivative of velocity and plotted in Figure 14 for the case of the suddenly started airfoil and in Figure 17 for the case of the suddenly started and stopped airfoil.

$$a = \frac{du}{dt} \quad (17)$$

For this velocity distribution the acceleration term peaked at $a \approx 25$ m/s² $\approx 2.5g$. The gravity term is usually negligible in most aerodynamic applications and, in this problem, the forces due to the acceleration term are of the same order of magnitude as gravity. In addition, the acceleration term is only acting for very short periods of time when the airfoil is impulsively started or stopped. For these reasons, it seems reasonable to neglect the effect of the acceleration in this problem.

3.4 Dimensionless considerations

The numerical simulations were performed at a $Re = 1000$, this Reynolds number was defined as:

$$Re = \frac{V_{\infty} \cdot c}{\nu} \quad (18)$$

where:

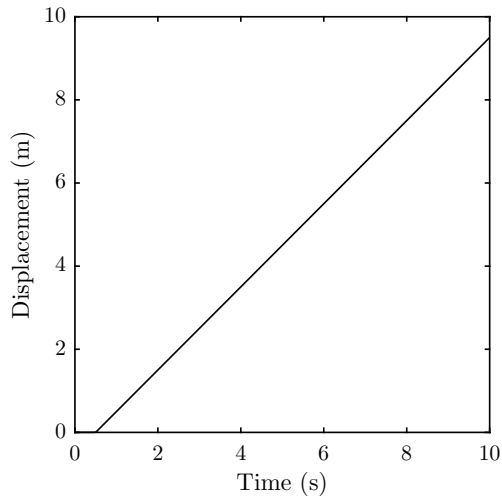


Figure 12. Airfoil displacement for the case when it is impulsively started.

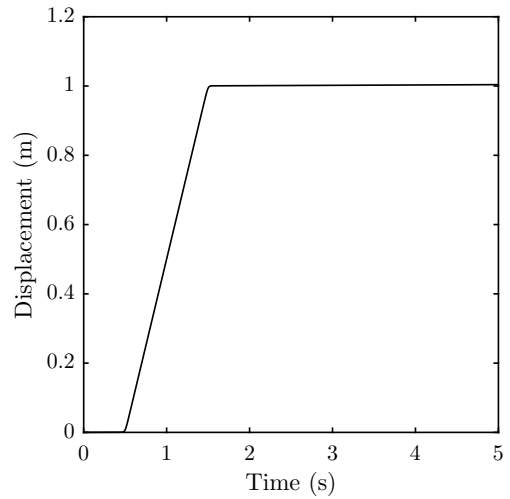


Figure 15. Airfoil displacement for the case when it is impulsively started and stopped.

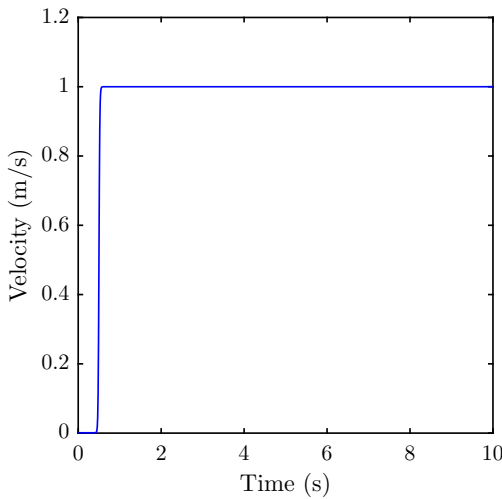


Figure 13. Airfoil velocity for the case when it is impulsively started or free stream velocity for the stationary airfoil.

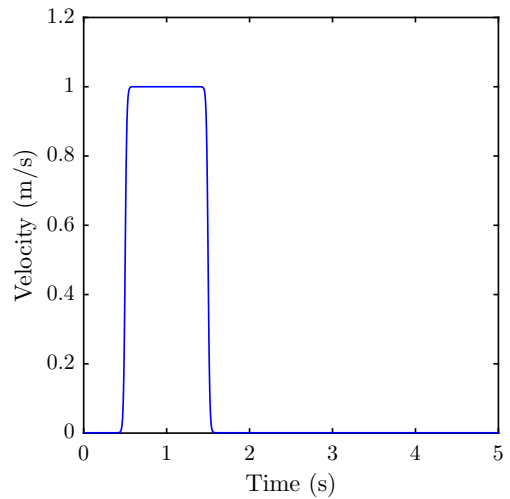


Figure 16. Airfoil velocity for the case when it is impulsively started and stopped.

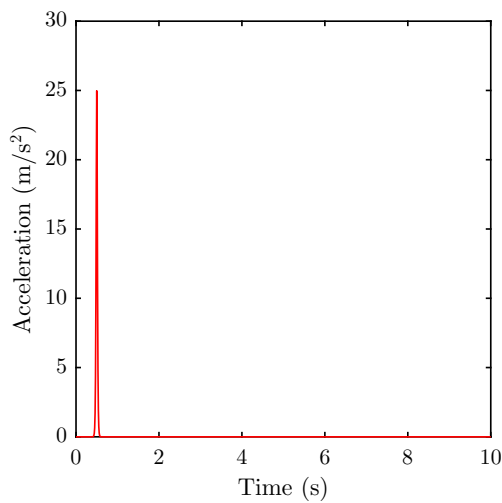


Figure 14. Airfoil acceleration for the case when it is impulsively started.

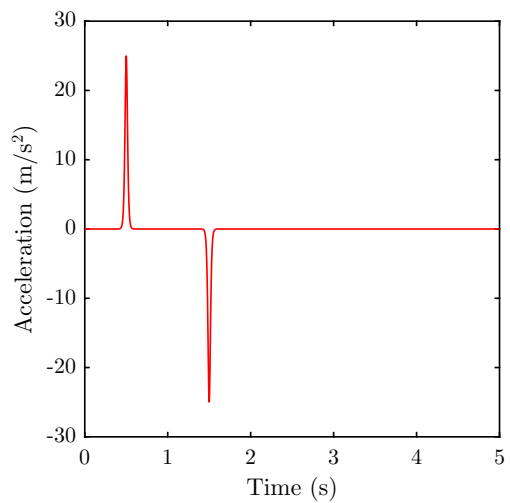


Figure 17. Airfoil acceleration for the case when it is impulsively started and stopped.

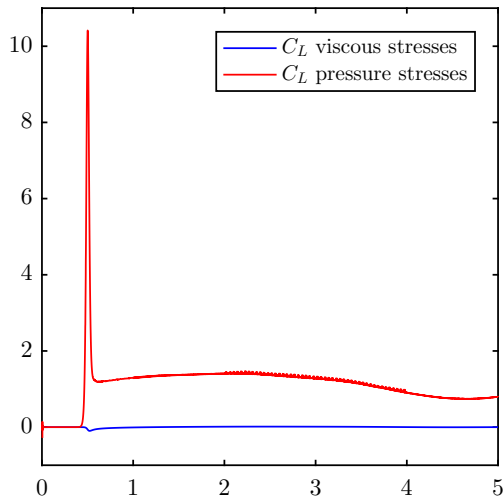


Figure 18. Components of the lift coefficient for the impulsively started airfoil or the stationary airfoil.

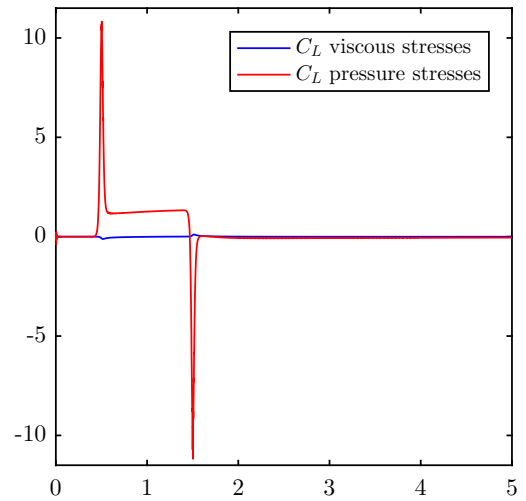


Figure 21. Components of the lift coefficient for the impulsively started and stopped airfoil.

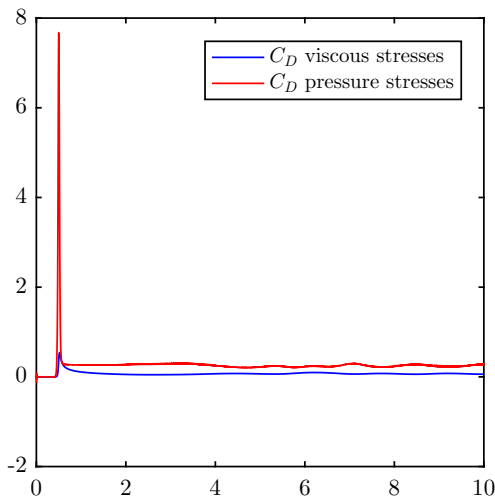


Figure 19. Components of the drag coefficient for the impulsively started airfoil or the stationary airfoil.

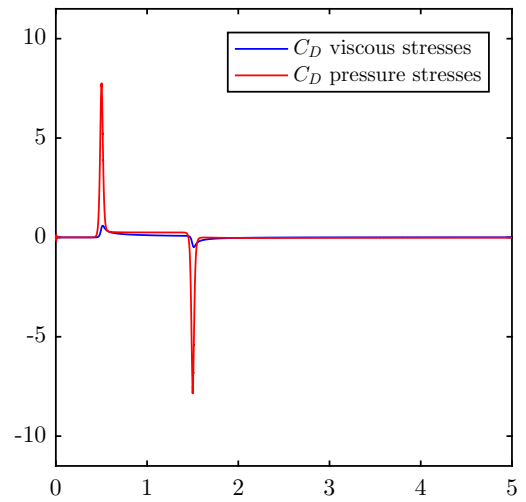


Figure 22. Components of the drag coefficient for the impulsively started and stopped airfoil.

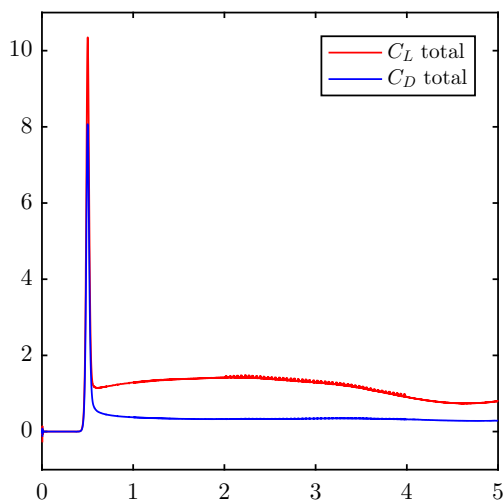


Figure 20. Drag and lift coefficients for the impulsively started airfoil or the stationary airfoil.

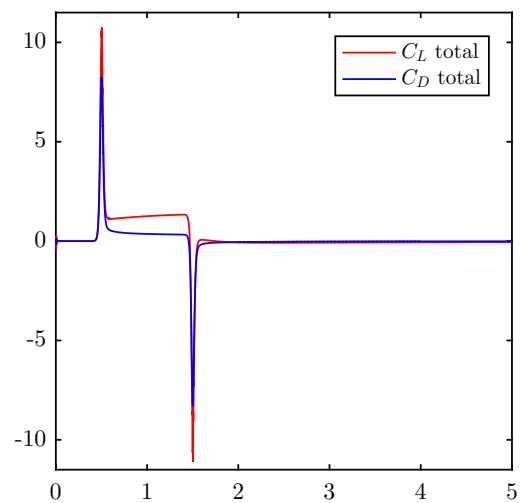


Figure 23. Drag and lift coefficients for the impulsively started and stopped airfoil.

- The reference velocity V_∞ was set to 1 m/s. This velocity is either the maximum free stream velocity or the maximum speed of the airfoil.
- The reference length c is the chord length of the airfoil and it was set to 1 m.
- The dynamic viscosity μ was set to 10^{-3} kg/(m · s) and the density was set to 1 m³/kg ($\nu = \frac{\mu}{\rho}$) to meet the Reynolds number requirement.

Using c as length scale, V_∞ as velocity scale, and $p_{ref} = \rho V_\infty^2$ as pressure scale the incompressible Navier-Stokes equations with constant viscosity can be written in dimensionless form, see (White, 2011, Chapter 5) for details:

$$\frac{D\vec{V}}{Dt} = -\vec{\nabla}p + \frac{1}{Re}\nabla^2\vec{V} \quad (19)$$

This equation shows that the only parameter present in the governing differential equations is the Reynolds number. As a consequence, the flow around the airfoil does only depend on the geometry of the airfoil (shape and angle of attack), the time variation of the inlet boundary conditions and the value of the Reynolds number (but not on the particular values of velocity, viscosity, and chord).

4 Results and Discussion.

4.1 Lift and drag coefficients

The lift and drag coefficients as a function of time are shown from Figure 18 to Figure 23. The results of the simulations when the airfoil is impulsively started and when it is stationary are shown in Figure 18 to Figure 20. The results when the airfoil motion is started and stopped are shown from Figure 21 to Figure 23. The graphs include a comparison of the viscous and pressure components of the lift and drag coefficients as well as a comparison of the overall lift and drag coefficients.

The most remarkable result is the sudden jump of the lift and drag when the acceleration occurs and the little impact that viscosity has on the value of the coefficients during this acceleration. The low influence of the viscous stresses is striking considering that, as discussed in Section 2.3, viscosity is responsible for the formation of the *starting vortex* and the development of the circulation that leads to the lift force in steady state.

The large drag during acceleration is not caused by the viscous stresses, instead it is an *added mass* effect resulting from the pressure distribution that arises when the airfoil accelerates the fluid around it (note the close relation between the acceleration peaks and the lift and drag peaks). Another interesting result is the negative peak of lift and drag when the airfoil is decelerated.

As a final remark, the variation of the lift coefficient contains higher order harmonics of small amplitude superimposed to the main variation with time.

4.2 Verification of Kelvin's and Stoke's theorems

As discussed at the end of Section 2.3, Kelvin's circulation theorem states that the circulation around an inviscid contour far away from the airfoil must be zero at all times. In addition, according to Stokes' theorem, the value of the the circulation must be given both by the line integral of velocity over the contour and the area integral of vorticity over the surface enclosed by the contour.

These two conditions were checked for the simulation of the started and stopped airfoil at $t = 5$ s using the contours shown in Figure 24. For these integration contours, the integration of Eq. 5 is given by Eq. 20 to Eq. 25, where the superscripts V or ω indicate that the circulation is computed as the line integral of velocity or as the area integral of vorticity, respectively, and the subscripts *net*, *left* or *right* indicate the the domain of integration

$$\Gamma_{net}^V = \oint_{aeabcd} (u, v) \cdot (dx, dy) \quad (20)$$

$$\Gamma_{left}^V = \oint_{abcd} (u, v) \cdot (dx, dy) \quad (21)$$

$$\Gamma_{right}^V = \oint_{efgh} (u, v) \cdot (dx, dy) \quad (22)$$

$$\Gamma_{net}^\omega = \iint_{D_1 \cup D_2} \omega(x, y) \cdot dx dy \quad (23)$$

$$\Gamma_{left}^\omega = \iint_{D_1} \omega(x, y) \cdot dx dy \quad (24)$$

$$\Gamma_{right}^\omega = \iint_{D_2} \omega(x, y) \cdot dx dy \quad (25)$$

The results of the integrals are shown in Table 4 and they show excellent agreement with the theoretical results. The integrals were performed with the MATLAB built-in functions *integral* and *quad2d* using an interpolation of the OpenFOAM simulation results as the integrand at point (x, y) . All line integrals converged successfully to the default tolerances, but only the area integral over D_2 satisfied the tolerance criteria. The reason why the other area integrals did not converge is that the airfoil is a discontinuity of vorticity in a non-linear region that the Cartesian integration algorithms of MATLAB can not handle effectively. Despite this the values of line and area integrals are virtually identical.

Table 4. Computation of circulation.

Type of integration	Γ_{net}	Γ_{left}	Γ_{right}
Γ^V	-0.0007	-0.5206	0.5199
Γ^ω	0.0009	-0.5205	0.5214

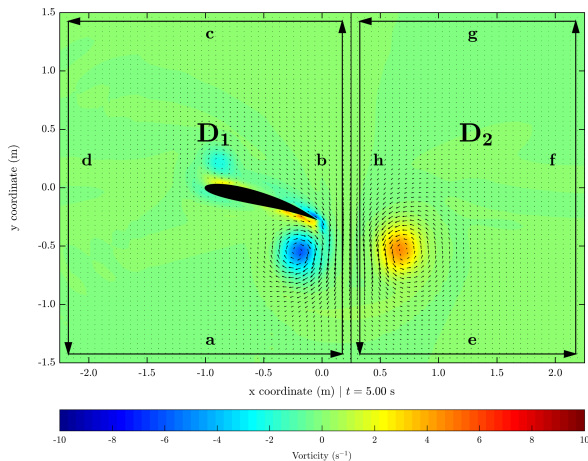


Figure 24. Integration paths for the computation of circulation.

4.3 Flow Animations

The results exported to MATLAB were used to prepare an animation of the three different flow configurations considered in this work. The video with the flow animations can be found in <https://www.youtube.com/watch?v=bvV7-9wAXc0>. The flow animations are qualitatively similar to the historical flow visualization from Prandtl, see (National Committee for Fluid Mechanics Films, 1972), including the formation of starting and stopping vortices as well as oscillatory vortex shedding for the case of the stationary airfoil.

4.4 Further works

The inclusion of the non inertial term in the Navier-Stokes equations could be considered in future works to show if its influence is indeed negligible or not. In addition, other transient effects such as the vortices shed when the angle of attack is abruptly changed could be analyzed.

5 Conclusions

The transient flow around a NACA4612 airfoil profile was analyzed and simulated at $Re = 1000$ and $\alpha = 16^\circ$. The main features of the flow were captured and the flow pattern agreed qualitatively with the flow visualizations from (National Committee for Fluid Mechanics Films, 1972).

The solution was confirmed to be grid independent and the C-mesh structured grid was found to be superior for this case as the flow was resolved with higher detail for the same number of cells.

Once the lift and drag coefficients were computed it was found that both peaked during the accelerations and decelerations due to added mass effects and that the effect of the viscous stresses on lift was modest even if viscosity is responsible for the development of lift. In addition, the solution was verified using the Kelvin's circulation theorem. Both the line integral of the velocity and the surface integral of vorticity matched with reasonable accuracy and were almost equal to zero for an inviscid contour and non-zero for viscous contours.

References

- G. K. Batchelor. *An Introduction to Fluid Dynamics*. Cambridge Mathematical Library, 1st edition, 2000.
- D. Darmofal. Aerodynamics, fall 2005, 2001. URL <https://ocw.mit.edu>.
- R. W. Fox, P. J. Pritchard, and A. T. McDonald. *Fox and McDonald's Introduction to Fluid Mechanics*. John Wiley & Sons, 9th edition, 2011.
- E. N. Jacobs, K. E. Ward, and R. M. Pinkerton. The characteristics of 78 related airfoil sections from tests in the variable-density wind tunnel. *National Advisory Committee for Aeronautics Report No. 460*, 1933.
- A. Jeffrey. *Advanced Engineering Mathematics*. Academic Press, 1st edition, 2001.
- P. K. Kundu and I. M. Cohen. *Fluid Mechanics*. Academic Press, 2nd edition, 2002.
- National Committee for Fluid Mechanics Films. Illustrated experiments in fluid mechanics: the NCFMF book of film notes, Vorticity, 1972. URL <http://web.mit.edu/hml/ncfmf.html>.
- M. Vincent and H. M. Blackburn. Simulation of starting/stopping vortices for a lifting aerofoil. *Proceedings of the 19th Australasian Fluid Mechanics Conference*, 2014.
- F. M. White. *Viscous Fluid Flow*. McGraw-Hill, 3rd edition, 2006.
- F. M. White. *Fluid Mechanics*. McGraw-Hill, 7th edition, 2011.
- C. Willert and J. Kompenhans. PIV Analysis of Ludwig Prandtl's Historic Flow Visualization Films. *arXiv preprint arXiv:1010.3149*, 2010.

Validation of results from Barracuda[®] CFD modelling to predict minimum fluidization velocity and pressure drop of Geldart A particles

Chameera K. Jayarathna^{1,2}, Britt E. Moldestad¹, Lars-Andre Tokheim¹

¹Department of Process, Energy and Environmental Technology, University College of South East Norway, {britt.moldestad, Lars.A.Tokheim}@usn.no

²Tel-Tek, Research institute, Porsgrunn, Norway, chameera.jayarathna@tel-tek.no

Abstract

Fluidization characteristics such as the minimum fluidization velocity and the bed pressure drop are important for the design of an efficient fluidized bed. These characteristics can be measured experimentally, but also modelled by CFD simulations. The aim of this study was to use experimental data to validate drag models applied in the CFD software Barracuda.

Most of the drag models available in the literature are validated against Geldart B or D particles and are not necessarily suitable for Geldart A particles, such as the zirconia particles used in the present study. However, by adjusting one of the constants in the Wen-Yu and Ergun drag models, it should be possible to apply these equations also for Geldart A particles.

Data from an in-house built lab-scale fluidized bed unit were used in the study. Reducing the k_f value in the drag model from 180 to 47 gave a reasonable representation of the minimum fluidization velocity and the pressure drop over the bed.

Keywords: CFD, CFPD, Barracuda, fluidization, pressure drop, minimum fluidization velocity, MP-PIC

1 Introduction

Gas-solids fluidized beds are used in the chemical, energy, and process industries as key equipment units due to their high contact area, homogeneity, heat and mass transfer rates, and solids handling capabilities (Kunii, 1991). Process examples are fluid catalytic cracking (FCC), gasification, combustion of solid fuels, Fischer-Tropsch synthesis, drying, granulation and coating (Cano-Pleite et al., 2017).

The current work is linked to a multistage cross-flow fluidized bed to be applied for high temperature solids classification (Jayarathna et al., 2017). A hot-flow pilot-scale system was downscaled to a cold-flow lab-scale unit by applying Glicksman scaling rules (Glicksman, 1984, 1988, Glicksman et al., 1993).

Computational Fluid Dynamics (CFD) simulations were used as a tool in the design process. Simulations were done for both cold-flow (ambient conditions) and

hot-flow systems. The cold-flow experiments were done with a scaled particle mixture, i.e. the particle size and density were not the same as in the hot-flow system (Jayarathna et al., 2017).

The particle mixture contained zirconia particles ($\rho_p = 3800 \text{ kgm}^{-3}$, $d_{mean} = 69 \mu\text{m}$) and steel particles ($\rho_p = 7800 \text{ kgm}^{-3}$, $d_{mean} = 290 \mu\text{m}$). The fluidization behavior of the particles were investigated by Chladek et al. (Chladek et al., 2017) and Amarasinghe et al. (Amarasinghe et al., 2017) applying an in-house built cold-flow cylindrical fluidized bed test unit. The particles were close to spherical (Chladek et al., 2017, Amarasinghe et al., 2017) and could be categorized as Geldart A and D particles, respectively, based on the particle size distribution (PSD), density and the particle fluidization behavior. CFD simulations were also run, using Barracuda[®] version 17.1, and the simulation results were compared with the experimental observations.

Chladek et al. (Chladek et al., 2017) found that the Barracuda predictions of minimum fluidization velocity was accurate enough for the steel particles, but there was a significant discrepancy for the zirconia particles. Several drag models were used for the simulations and the best results were obtained using the Ergun drag model for steel particles and the Wen-Yu model for zirconia particles.

Amarasinghe et al. (Amarasinghe et al., 2017) did similar CFD simulations and experiments with zirconia, steel and bronze particles, with the aim to evaluate the ability of Barracuda to predict the minimum fluidization velocity of Geldart A (zirconia), B (bronze) and D (steel) particles. The prediction of minimum fluidization velocity (with a combined Wen-Yu/Ergun drag model) was quite good for the Geldart B and D particles, but the simulated results for the Geldart A particles were not in line with the experimental results.

The above-mentioned studies were done with the default drag model settings in Barracuda. In the current study, the results from the minimum fluidization velocity experiments with zirconia particles done by Chladek et al. (Chladek et al., 2017) are used to validate an adjusted

drag model in Barracuda, with the aim to get a better prediction of the fluidization behavior of this Geldart A particle type.

2 CFD Simulations with the MP-PIC method

The CFD simulations applied the multiphase particle-in-cell (MP-PIC) method (Andrews and O'Rourke, 1996, D. M. Snider, 2001), which is also called the computational particle fluid dynamics (CPFDF) method (D. M. Snider, 2001). The method is developed based on a new Eulerian–Lagrangian multiphase flow scheme, and the commercially developed platform is known as Barracuda. In this study, version 17.1 was used.

In the MP-PIC method, the real particles in the system are replaced by a computational particle representing a large number of particles which are assumed to behave the same way in the real system. This makes the MP-PIC method more computationally efficient than the more commonly used discrete element method (DEM) (Tsuji et al., 1993, Goldschmidt et al., 2004, Gera et al., 2004), hence it can be applied to larger systems. The CPFDF method models the fluid as a continuum and the computational particles as discrete particles exposed to three-dimensional forces as fluid drag, gravity, static–dynamic friction, particle collision and possibly other forces (Dale M. Snider, 2007).

The calculation of particle-to-particle forces in the CPFDF method is different from the calculation in the DEM method. In DEM, the particle-to-particle forces are calculated using a spring–damper model and direct particle contact, whereas in the CPFDF method collision forces on each particle are modeled as a spatial gradient (Dale M. Snider, 2007). The CPFDF method takes into account the forces on a particle hit by other particles, but it does not pay attention to the impact created on the other particles by the first one (Dale M. Snider, 2007). It is common for all other particles as well.

2.1 Model description

The continuity and momentum equations (Gidaspow, 1993) for the gas phase without reactions and interface mass transfer in Barracuda (D. M. Snider, 2001, Gidaspow, 1993) are, given in Equation (1) and (2).

$$\frac{\partial \theta_g \rho_g}{\partial t} + \nabla \cdot (\theta_g \rho_g u_g) = 0 \quad (1)$$

$$\begin{aligned} \frac{\partial (\theta_g \rho_g u_g)}{\partial t} + \nabla \cdot (\theta_g \rho_g u_g u_g) \\ = -\nabla p + \nabla \cdot (\theta_g \tau_g) + \theta_g \rho_g g \\ - F \end{aligned} \quad (2)$$

Here $\theta_g, \rho_g, u_g, p, \tau_g$ are the volume fraction (initial), density, velocity, pressure and stress tensor of the gas in the system, respectively. F is the momentum exchange rate per volume between gas and particles, t

is the time interval and g is the gravitational acceleration.

The rate of momentum transfer between fluid and solid phases per unit volume (D. M. Snider, 2001, Dale M. Snider et al., 2011) is described in Equation (3).

$$F = \iiint f V_p \rho_p \left[D(u_g - u_p) - \frac{1}{\rho_p} \nabla p \right] dV_p \cdot d\rho_p \cdot du_p \quad (3)$$

The dynamics of the particle phase are described by the particle probability distribution function $f(x, u_p, \rho_p, V_p, t)$. Here x is the particle position, u_p is the particle velocity, ρ_p is the particle density, V_p is the particle volume, θ_p is the particle volume fraction and D is the drag function. The time evolution of f is obtained by solving a Liouville equation for the particle distribution function (D. M. Snider, 2001), as given in Equation (4).

$$\frac{\partial f}{\partial t} + \nabla \cdot (f u_p) + \nabla u_p \cdot (f A) = 0 \quad (4)$$

The particle acceleration balance A (D. M. Snider, 2001, Andrews and O'Rourke, 1996) is given as,

$$A = D(u_g - u_p) - \frac{1}{\rho_p} \nabla p + g - \frac{1}{\theta_p \rho_p} \nabla \tau \quad (5)$$

In Barracuda, particle interactions are modelled through the use of a computationally efficient particle stress function. The particle normal stress τ (D. M. Snider, 2001) is a function of particle volume fraction θ_p and is given in Equation (6). The continuum particle stress model used by Snider is an extension of the model from Harris and Crighton (Harris and Crighton, 1994).

$$\tau(\theta_p) = \frac{10 P_s \theta_p^\beta}{\max[\theta_{cp} - \theta_p, \varepsilon(1 - \theta_p)]} \quad (6)$$

Where P_s is a constant with units of pressure, θ_{cp} is the close pack particle volume fraction, β is a constant with a recommended value between 2 and 5, and ε is a very small number. The original expression by Harris and Crighton was modified by Snider to remove the singularity at close pack by adding the ε expression in the denominator. Values for the stress model constant and the close pack volume fraction must be specified by the user.

The default values 1[Pa], 3[-] and 10^{-8} [-] are used for P_s, β and ε respectively.

The fluid drag force on the particles is given in Equation (7). In many models, the drag function (Wen, 1966) is dependent on the fluid conditions, the drag coefficient (C_D), and the Reynolds number (Re). Re is shown in Equation (8).

In many models, the drag function D is related to the drag coefficient, as shown in Equation(9).

$$F_p = m_p D(u_g - u_p) \quad (7)$$

$$Re = \frac{2\rho_g r_p |u_g - u_p|}{\mu_g} \quad (8)$$

$$D = \frac{3}{8} C_d \frac{\rho_g |u_g - u_p|}{\rho_p r_p} \quad (9)$$

The Wen-Yu model given in Equation (10) is suitable for dilute systems, and the Ergun model (Ergun, 1952, Beetstra et al., 2007) given in Equation (12) is suitable at higher packing fractions (Gidaspow, 1993). The Wen-Yu/Ergun drag function (Wen, 1966, Patel et al., 1993) combines the Wen-Yu function and the Ergun function, hence can be used for dilute as well as dense systems. The Wen-Yu and Ergun drag function is calculated by Equation (13).

The Wen-Yu model is based on single particle drag models and a dependence on the fluid volume fraction θ_g to account for the particle packing. In the Wen-Yu model, the drag function is calculated by equation (9), and the drag coefficient is a function of the Reynolds number. The model constants are: $c_0 = 1.0$, $c_1 = 0.15$, $c_2 = 0.44$, $n_0 = -2.65$ and $n_1 = 0.687$.

$$C_d = \begin{cases} \frac{24}{Re} \theta_g^{n_0} & Re < 0.5 \\ (C_d)_1 & 0.5 \leq Re \leq 1000 \\ c_2 \theta_g^{n_0} & Re > 1000 \end{cases} \quad (10)$$

$$(C_d)_1 = \frac{24}{Re} \theta_g^{n_0} (c_0 + c_1 Re^{n_1}) \quad (11)$$

The Ergun drag model, developed from dense bed data, is given by Equation (12). The model constants are: $k_0 = 2$ and $k_1 = 180$.

$$D = 0.5 \left(\frac{k_1 \theta_p}{\theta_g Re} + k_0 \right) \frac{\rho_g |u_g - u_p|}{\rho_p r_p} \quad (12)$$

Pitault et al. (Pitault et al., 1994) recommended values of 1.75 and 150 for k_0 and k_1 , respectively, but in Barracuda the default values are set to 2 and 180.

$$D = \begin{cases} D_1 & \theta_p < 0.75\theta_{CP} \\ D_3 & 0.75\theta_{CP} \geq \theta_p \geq 0.85\theta_{CP} \\ D_2 & \theta_p > 0.85\theta_{CP} \end{cases} \quad (13)$$

$$D_3 = (D_2 - D_1) \left(\frac{\theta_p - 0.75\theta_{CP}}{0.85\theta_{CP} - 0.75\theta_{CP}} \right) \quad (14)$$

Here, D_1 is the Wen-Yu drag function defined in equation (9) and (10), and D_2 is the Ergun drag function defined in equation (12).

3 Computational mesh and input values for the simulation

The cold-flow lab rig-system used to collect data is shown in Figure 1. A three-dimensional cartesian coordinate system was used to describe the vertical cylindrical bed with a diameter of 84 mm and a height of 1.2 m which is 0.3 m shorter than the actual height in order to reduce the computation time. The computational grid is shown in Figure 2 (a). The mesh size was $6.4 \times 6.4 \times 6.4 \text{ mm}^3$ and the number of control volumes was around 25 000.

The initial bed height of zirconia solid particles was 17cm. Properties of the zirconia particles are summarized in Table 1.

In the present study, the close pack volume fraction is used as 0.6. Atmospheric air at room temperature was used as the fluidization medium.

The simulation was run for 30 seconds for each air flow rate and increased to the next level. This is also the operational procedure followed in the study of Chladek et al. (Chladek et al., 2017). The total pressure was monitored at positions 2.5 and 12.5 cm above the distributor plate, i.e. at the same positions as in the experiments, as shown in Figure 2 (b). Transient data were recorded for each 0.1 s.

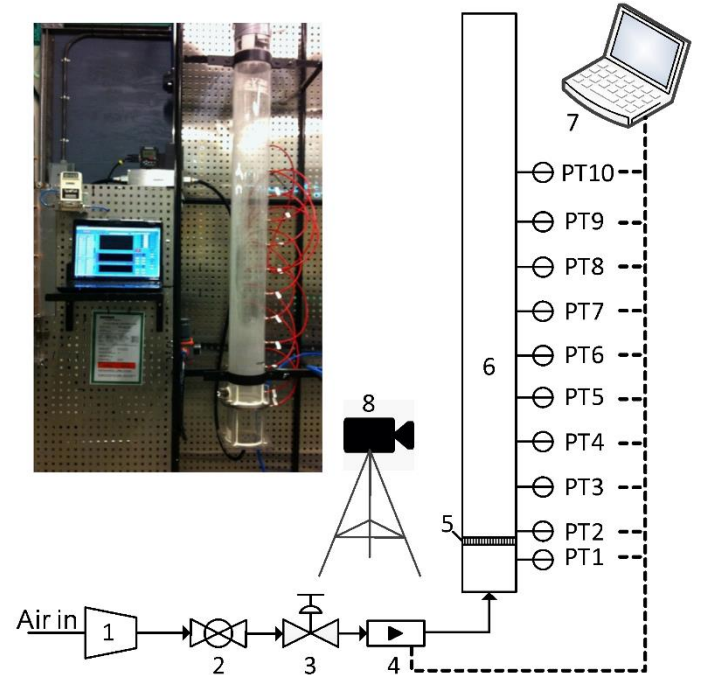


Figure 1: Fluidized bed experimental rig: 1 – compressor, 2 – ball valve, 3 – pressure regulator, 4 – mass flow controller, 5 – air distribution plate, 6 – fluidized bed column, 7 – DAQ and LabVIEW, 8 – video camera.

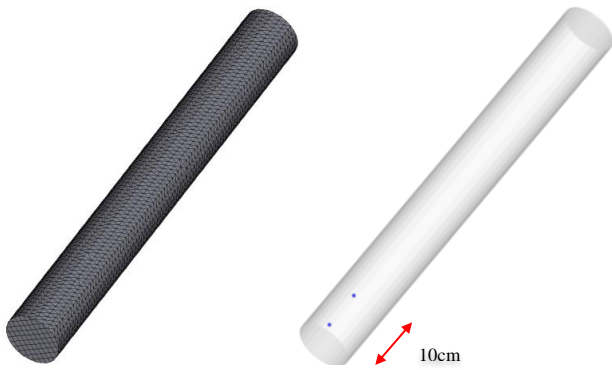


Figure 2: (a) Cylindrical mesh used in the simulations (b) Transient data points for monitoring the total pressure

The properties of the zirconia particles and the steel particles are summarized in Table 1.

Table 1: Properties of the zirconia particles

Property	Unit	Value
Skeletal density	kg/m ³	3830
Bulk density	kg/m ³	2270
Particle size range	μm	45-100
D50	μm	70
Porosity	-	0
Sphericity*	-	0.95

* The sphericity was estimated from optical micrographs of the particles.

The combined Wen-Yu/Ergun drag model was used in the present study. The coefficient k_1 was set to different values, and the simulation results were compared with experimental values. The following k_1 values were tried: 180 (default value), 70, 50, 47 and 35.

The average pressure-drop over the particle bed (see Figure 3) in the last 5 seconds of each constant air flow supply period was calculated, assuming that a pseudo steady state was reached after 15 to 25 seconds.

4 Results and discussion

4.1 Adjustment of Wen-Yu/Ergun drag model

As explained above, the combined Wen-Yu/Ergun drag model gives a wide range of accuracy by being able to capture the behavior of both dense and dilute particle systems. Predictions of pressure drop as a function of superficial air velocity at different k_1 values are presented in Figure 3.

According to the Figure 3, the predictions deviate strongly from the measured values when the default k_1 value (180) is used. The reason could be that this model was validated with Geldart B particles, and the original model value (150) is not far from the default value (180) used in Barracuda.

Lowering the coefficient value to 70 or 50 gives more accurate predictions but the predicted stabilized

pressure after minimum fluidization velocity are too high. This value is directly connected to the static pressure head of the particle bed or the weight of the particle bed, and it is important that the model can predict this value correctly. A further lowering of coefficient value to 35 gives a too low static pressure head. However, for an intermediate k_1 value of 47, both the pressure and minimum fluidization are predicted quite well. The experimental value and the CFD predictions of the minimum fluidization velocity are then 0.015 and 0.016 m/s, respectively. This shows that correct prediction of the fluidization behavior of Geldart A particles is possible by a drag model adjustment. The potential drawback is that the adjusted model may be valid only for the studied air flow rates. Further studies are needed to investigate a wider range of air flow as the further increased of the airflow will increase the pressure drop and bed will convert from dense to dilute phase.

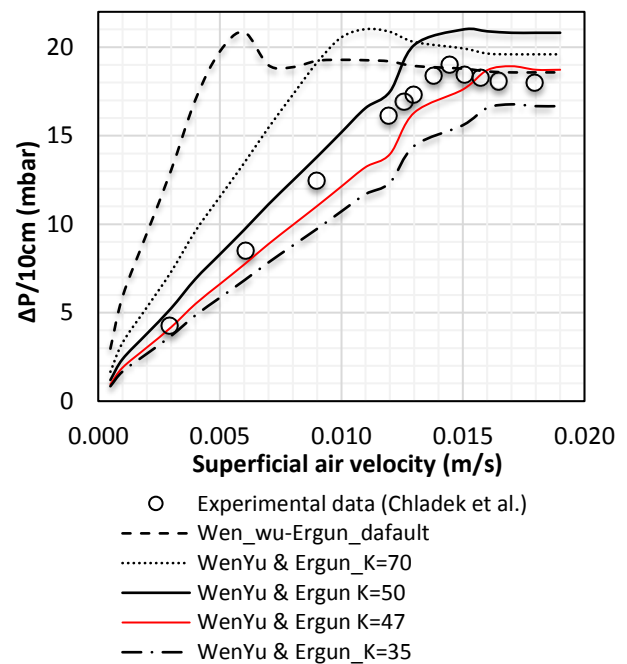


Figure 3: Change of the pressure drop in the bed with increased superficial air flow rate

Lowering the coefficient value to 70 or 50 gives more accurate predictions but the predicted stabilized pressure after minimum fluidization velocity are too high. This value is directly connected to the static pressure head of the particle bed or the weight of the particle bed, and it is important that the model can predict this value correctly. A further lowering of coefficient value to 35 gives a too low static pressure head. However, for an intermediate k_1 value of 47, both the pressure and minimum fluidization are predicted quite well. The experimental value and the CFD predictions of the minimum fluidization velocity are then 0.015 and 0.016 m/s, respectively.

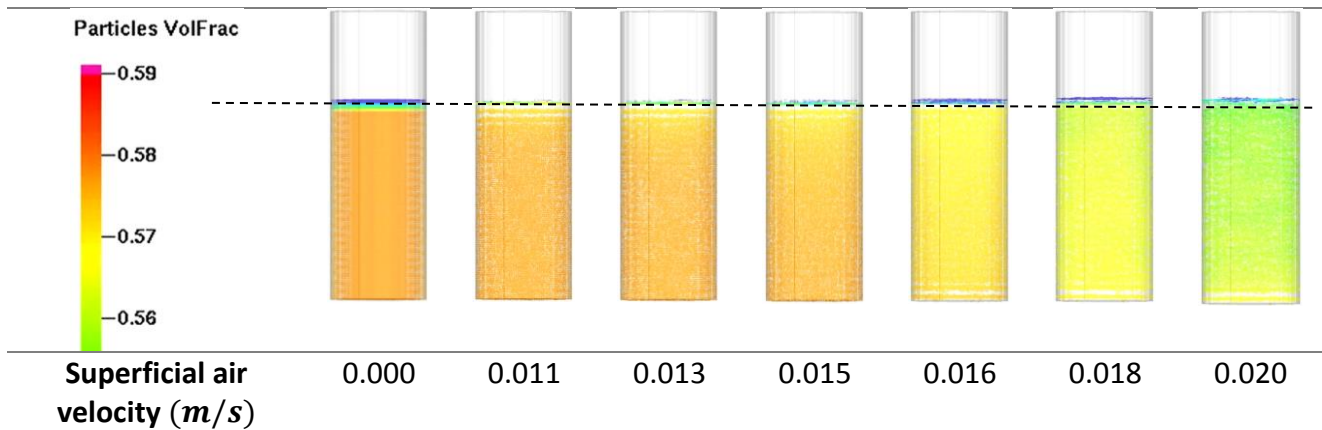


Figure 4: Simulation result snapshots of the lower part of the FB at different superficial air velocities

This shows that correct prediction of the fluidization behavior of Geldart A particles is possible by a drag model adjustment. The potential drawback is that the adjusted model may be valid only for the studied air flow rates. Further studies are needed to investigate a wider range of air flow as the further increased of the airflow will increase the pressure drop and bed will convert from dense to dilute phase.

Figure 4, illustrates the change of solids volume fraction in the bed with the increased air flow rates. At the minimum fluidization velocity (u_{mf}) the weight of the particle bed is balanced by the drag force on the particles and then the gas starts to fluidize the particles. This phenomenon is clearly illustrated in the simulation by the change in color and ~4% bed expansion with around ~4% void fraction increase.

Equation (15) (Rhodes, 2008) explains the connection of the fixed bed pressure drop with the liner coefficient (k_1) of the Ergun drag model. Here x_{sv} is the surface volume diameter (diameter of a sphere having the same volume as the particle).

$$\frac{(-\Delta p)}{H} = \left[k_1 \frac{\mu}{x_{sv}^2} \frac{(1 - \theta_g)^2}{\theta_g} \right] |u_g - u_p| + \left[k_0 \frac{\rho_g}{x_{sv}} \frac{(1 - \theta_g)}{\theta_g} \right] |u_g - u_p|^2 \quad (15)$$

Equation (15) is only valid for the fixed bed stage before the fluidization but it is clearly indicated liner effect of the coefficient k_1 on the pressure drop as represented in Figure 3 with different k_1 values. As explained by Rhodes (Rhodes, 2008), after the minimum fluidization stage the pressure drop is independent from the relative gas velocity ($u_g - u_p$). Assuming that in the fluidized bed the entire apparent weight of the particles is supported by the gas flow, then the pressure drop is given by Equation (16)

(Rhodes, 2008). According to the equation, the pressure drop is independent of the coefficient k_1 .

$$\frac{(-\Delta p)}{H} = (1 - \theta_g)(\rho_p - \rho_g)g \quad (16)$$

As explained in the introduction, the role of the drag model is one of the key factors when modelling the fluidization behavior of a dense gas-solids bed, but also other parameters may be important, for example particle-to-wall and particle-to-particle interactions. The model constants related to those phenomena were kept at their default values in this work.

4.2 CFD predictions with BAM

O'Rourke and Snider (O'Rourke and Snider, 2014) developed a new acceleration model called the blended acceleration model (BAM) and it is claimed to give improved predictions of the fluidization behavior of non-uniform (polydisperse) particle collections, i.e. particles of differing sizes or densities. BAM was implemented in Barracuda recently.

A separate simulation was done by using BAM with the Wen-Yu/Ergun drag model (with $k_1 = 47$). Figure 5 shows the results compared with those from applying the Wen-Yu/Ergun drag model (with $k_1 = 47$) without BAM (shown in Figure 4) as well as with the experimental results. The bed pressure-drop predictions at superficial air velocities below the minimum fluidization velocity match the experimental observations when BAM is enabled, but the predictions of the stabilized pressure are higher than the experimental values. However, the simulated minimum fluidization velocity is the same both with and without BAM.

With BAM included, the individual particle accelerations are a blend between the particle acceleration of the original MP-PIC method appropriate for rapid granular flows and an average particle acceleration that applies to closely packed granular flows. As a result, particles at or near close-pack tend to

move together with velocities close to the averaged velocity due to enduring particle-particle contacts. In dilute regions, particles tend to move independently of each other due to less contacts with the surrounding particles (O'Rourke and Snider, 2014). The solids volume fraction of a just fluidized bed is still close to that of the close-pack bed and the particles therefore tend to move together when BAM is enabled.

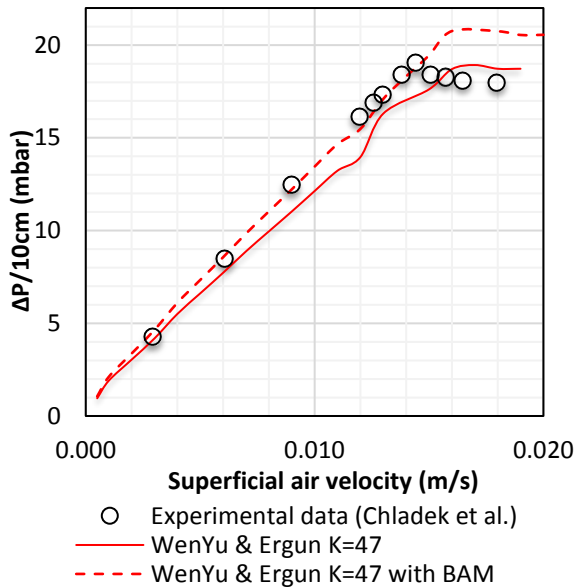


Figure 5: Change of the pressure drop in the bed with increased superficial air flow rate with and without BAM

One of the reasons could be that in the real system, air finds open passages to escape and this leads to a lower stabilized fixed bed pressure drop after the minimum fluidization conditions have been reached. Further investigations of BAM at minimum fluidization conditions of Geldart B and D particles will be useful to come to a better conclusion.

5 Conclusion

By reducing the coefficient k_1 in the Ergun drag model and the combined Wen-Yu/Ergun model from a value of 180 to 47, the CFD predictions of minimum fluidization velocity and pressure drop fit quite well with experimentally measured values for zirconia (Geldart A) particles. For minimum fluidization velocity, the values were 0.015 and 0.016 m/s, respectively. This means that it is possible to give a quite good prediction of the fluidization behavior of Geldart A particles by doing a drag model adjustment.

Barracuda simulations were done with the so-called blended acceleration model (BAM) at $k_1 = 47$. The predictions for the fixed bed pressure drop fit well with experimental observations, but the pressure drop after fluidization was somewhat over predicted. One of the reasons could be that in the real system, the air finds open escape passages, and this leads to a lower

stabilized fixed bed pressure drop after the minimum fluidization velocity has been reached.

Further investigations of BAM at minimum fluidization conditions for Geldart B and D particles may be useful to come to a better conclusion.

Acknowledgements

The financial support from Gassnova and GE is greatly acknowledged. The authors would also like to thank Sam Clark from CPFD Software, LLC for valuable technical support on Barracuda and Dr. Anette Mathisen from Tel-Tek for commenting on the manuscript.

References

- Amarasinghe, W. S., Jayarathna, C. K., Ahangama, B. S., Moldestad, B. M. E. & Tokheim, L.-A. (2017) Experimental study and CFD modelling of fluidization velocity for Geldart A, B and D particles. *International Journal of Modeling and Optimization*, 7, 3.
- Andrews, M. J. & O'Rourke, P. J. (1996) The multiphase particle-in-cell (MP-PIC) method for dense particulate flows. *International Journal of Multiphase Flow*, 22, 2, p. 379-402.
- Beetstra, R., Van Der Hoef, M. A. & Kuipers, J. A. M. (2007) Drag force of intermediate Reynolds number flow past mono- and bidisperse arrays of spheres. *AIChE Journal*, 53, 2, p. 489-501.
- Cano-Pleite, E., Hernández-Jiménez, F. & Acosta-Iborra, A. (2017) Bulk oscillation and velocity wave propagation in a vibrated fluidized bed at minimum fluidization conditions. *Powder Technology*, 308, p. 346-361.
- Chladek, J., Jayarathna, C. K., Tokheim, L. A. & Moldestad, B. M. E. (2017) Classification of Solid Particles with Size and Density Difference in a Gas Fluidized Bed. *Chemical Engineering Science*, in preparation.
- Ergun, S. (1952) Fluid flow through packed columns. *Chemical Engineering Progress*, 48, p. 89.
- Gera, D., Syamlal, M. & O'Brien, T. J. (2004) Hydrodynamics of particle segregation in fluidized beds. *International Journal of Multiphase Flow*, 30, 4, p. 419-428.
- Gidaspow, D. (1993) *Multiphase Flow and Fluidization: Continuum and kinetic theory description*. 24-28 Oval Road, London, Academic Press, Inc.
- Glicksman, L. R. (1984) Scaling relationships for fluidized beds. *Chemical Engineering Science*, 39, 9, p. 1373-1379.
- Glicksman, L. R. (1988) Scaling relationships for fluidized beds. *Chemical Engineering Science*, 43, 6, p. 1419-1421.
- Glicksman, L. R., Hyre, M. & Woloshun, K. (1993) Simplified scaling relationships for fluidized beds. *Powder Technology*, 77, 2, p. 177-199.
- Goldschmidt, M. J. V., Beetstra, R. & Kuipers, J. A. M. (2004) Hydrodynamic modelling of dense gas-fluidised beds: comparison and validation of 3D discrete particle and continuum models. *Powder Technology*, 142, 1, p. 23-47.
- Harris, S. E. & Crighton, D. G. (1994) Solitons, solitary waves, and voidage disturbances in gas-fluidized beds. *Journal of Fluid Mechanics*, 266, p. 243-276.
- Jayarathna, C. K., Chladek, J., Balfe, M., Moldestad, B. M. E. & Tokheim, L. A. (2017) Impact of solids loading and mixture composition on the classification efficiency of a novel cross-flow fluidized bed classifier. *Powder Technology*, In preparation.
- Kunii, D. L. O. (1991) *Fluidization engineering*. Boston, Mass., Butterworths.

- O'rouke, P. J. & Snider, D. M. (2014) A new blended acceleration model for the particle contact forces induced by an interstitial fluid in dense particle/fluid flows. *Powder Technology*, 256, p. 39-51.
- Patel, M. K., Pericleous, K. & Cross, M. (1993) Numerical Modelling of Circulating Fluidized Beds. *International Journal of Computational Fluid Dynamics*, 1, 2, p. 161-176.
- Pitault, I., Nevicato, D., Forissier, M. & Bernard, J.-R. (1994) Kinetic model based on a molecular description for catalytic cracking of vacuum gas oil. *Chemical Engineering Science*, 49, 24, p. 4249-4262.
- Rhodes, M. J. (2008) *Introduction to particle technology*. Second utg. Chichester ; New York, John Wiley.
- Snider, D. M. (2001) An Incompressible Three-Dimensional Multiphase Particle-in-Cell Model for Dense Particle Flows. *Journal of Computational Physics*, 170, 2, p. 523-549.
- Snider, D. M. (2007) Three fundamental granular flow experiments and CPFD predictions. *Powder Technology*, 176, 1, p. 36-46.
- Snider, D. M., Clark, S. M. & O'rouke, P. J. (2011) Eulerian–Lagrangian method for three-dimensional thermal reacting flow with application to coal gasifiers. *Chemical Engineering Science*, 66, 6, p. 1285-1295.
- Tsuji, Y., Kawaguchi, T. & Tanaka, T. (1993) Discrete particle simulation of two-dimensional fluidized bed. *Powder Technology*, 77, 1, p. 79-87.
- Wen, C. Y. Y., Y.U. (1966) Mechanics of fluidization. *Chemical Engineering Progress Symposium*, p. 100-111.

Numerical Modelling of the Calcination Process in a Cement Kiln System

Amila Chandra Kahawalage Morten C. Melaaen Lars-André Tokheim

Department of Process, Energy and Environmental Technology, Faculty of Technology, Natural Sciences and Maritime Sciences, University College of Southeast Norway, 3918, Porsgrunn, Norway
{amila.c.kahawalage, Morten.C.Melaaen, Lars.A.Tokheim}@usn.no

Abstract

The calcium carbonate decomposition into calcium oxide and carbon dioxide is a key process step in a cement kiln. The reaction requires thermal energy input, and pulverized coal is the fuel typically used for this purpose in the cement industry. Coal can in many cases be replaced by different types of alternative fuels, but this may impact process conditions, emissions or product quality. In this study, CFD simulations were carried out to investigate the possibility to replace 50 % of the coal by refuse derived fuel (RDF). The spatial distribution of gas and particle temperatures and concentrations were calculated, and the simulations indicated that replacement of coal by RDF resulted in a reduction of fuel burnout, lower gas temperatures and a lower degree of calcination.

Keywords: precalciner, calcination, refuse derived fuel, computational fluid dynamics

1 Introduction

Cement is a key building material in construction industries and its demand is continually going up due to population growth and development. The energy required in cement production is supplied by electricity and thermal energy. In the manufacturing process, thermal energy is used mainly during the burning process.

The typical manufacturing process, which is schematically represented in Figure 1, starts with mining of limestone (high in calcium carbonate, CaCO_3) and is followed by crushing, adding of additives such as clay, sand and iron to get the required chemical composition and grinding of this mixture. The intermediate product is called 'raw meal'. After homogenization, the raw meal becomes suitable for burning in the kiln system. The kiln feed is preheated, calcined, sintered and cooled in the kiln system, resulting in a dark grey nodular material called clinker. The clinker is mixed with some gypsum and other additives and ground to the final product cement.

A precalciner kiln system is the basis for this study. It normally consists of a preheater, a precalciner (also known as a calciner), a rotary kiln and a cooler. The kiln feed (i.e. the raw meal) is heated in the preheater and

then sent to the precalciner where typically 85-95% of the calcination takes place. Calcination is the process of calcium carbonate decomposition into calcium oxide (CaO) and carbon dioxide (CO_2), typically occurring at a temperature around 850-900°C. As the calcination is an endothermic reaction ($\sim 1.7 \text{ MJ/kgCaCO}_3$), fuel is combusted in the calciner. In the rotary kiln, the remaining calcination is completed and clinker is formed.

Numerical modelling is a widely used tool for analysis and optimization of industrial process because it reduces time consumption and costs of doing full-scale tests. Computational fluid dynamics (CFD) modelling can be used to make numerical 3D simulations of different processes, for example the decarbonation and combustion in the cement kiln precalciner.

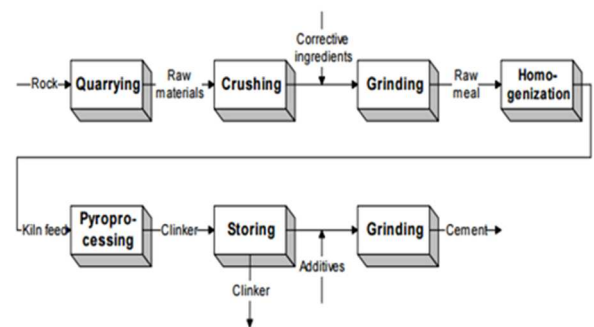


Figure 1. Principal drawing of the cement manufacturing process (Tokheim, 1999)

Results from modelling of cement kiln systems have been reported in some articles. When coal was co-combusted with meat and bone meal (MBM), the impact of fuel particle size and feeding positions in a rotary kiln was investigated (Ariyaratne et al., 2015) using a CFD simulation. This study revealed that although same thermal energy was supplied, when introducing MBM the kiln inlet temperature was reduced due to combined effect of moisture content, ash content and air demand. (Mikulčić et al., 2014) conducted a numerical study of co-firing pulverized coal and biomass inside a cement calciner and found that when coal was replaced with biomass, the fuel burnout and the CaCO_3 decomposition

was reduced. Another numerical modeling study reports a CFD simulation of a calciner with two different case studies of 100% coal and 100% pet coke (Fidaros et al., 2007). The use of CFD to predict the precalciner process behavior was proven by (Kurniawan, 2004).

Energy-wise and product efficiency-wise the precalciner plays CFD can be used to predict the precalciner process behavior was an important role in a cement kiln system as it completes around 85 % of the calcination. CFD is a well-proven method to investigate flow, heat transfer and mass transfer phenomena in process equipment units. The aim of this study was to get detailed information about temperatures, calcination degree and fuel burnout in the precalciner system of a Norwegian cement plant with an annual clinker production capacity of about 1 Mt. The commercial software ANSYS Fluent was used to conduct the study.

2 Theory

The gas phase was modelled using the Euler approach, and to model the flow of the solid particles, the Lagrange method was used. For the gas phase, the equations for conservation of mass, momentum and energy (equations 1-4) are used.

$$\frac{\partial \rho}{\partial t} + \nabla \cdot (\rho \vec{v}) = S_m \quad (1)$$

$$\frac{\partial(\rho \vec{v})}{\partial t} + \vec{v} \cdot \nabla(\rho \vec{v}) = -\nabla p + \nabla \cdot (\bar{\tau}) + \rho \vec{g} + \vec{F} \quad (2)$$

$$\bar{\tau} = \mu \left[(\nabla \vec{v} + \nabla \vec{v}^T) - \frac{2}{3} \nabla \cdot \vec{v} I \right] \quad (3)$$

$$\frac{\partial(\rho E)}{\partial t} + \nabla \cdot (\vec{v}(\rho E + p)) = \nabla \cdot [k_{eff} \nabla T - \sum_j h_j \vec{j}_j + (\bar{\tau}_{eff} \cdot \vec{v})] + S_h \quad (4)$$

Here, S_m is the mass added to the continuous phase from particles due to fuel devolatilisation, char combustion and raw meal calcination, and S_h is the added energy to the continuous phase due to chemical reactions. To model the turbulence, the two equation $k - \epsilon$ turbulence model was used. Particle trajectories were defined by equation 5.

$$\frac{d\vec{u}_p}{dt} = F_D(\vec{v} - \vec{u}_p) + \frac{\vec{g}(\rho_p - \rho)}{\rho_p} + \vec{F} \quad (5)$$

Here, F_D is the drag force on the particle, which for spherical particles can be calculated by equation 6.

$$F_D = \frac{18\mu}{\rho_p d_p^2} \frac{C_D Re}{24} \quad (6)$$

Figure 2 shows how a CFD modelling is sequenced for combustion of a solid fuel particle. First the fuel particle is heated whereby moisture evaporates. When the particle reaches the boiling point of water, all free moisture evaporates. After that the volatile part of the

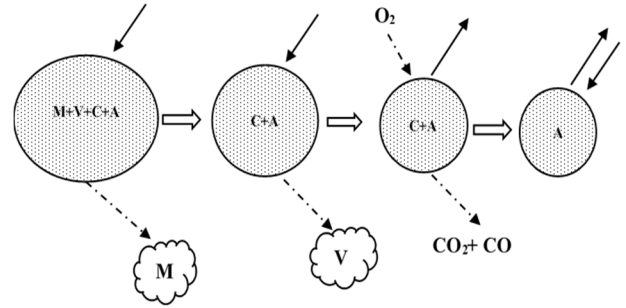


Figure 2. CFD Modelling steps of combustion of a solid fuel particle (M=moisture, C=char, V=volatile compounds, A= ash)

fuel particle is devolatilized, and finally the char fraction, which is very rich in carbon, reacts with O_2 and produces CO and CO_2 . (In the present study, it was assumed that only CO_2 is produced in this reaction.) When the fuel particle is 100% burnt, i.e. when all the carbon has been oxidized, only ash is left.

A single rate devolatilisation model was used for both coal and refuse derived fuel (RDF). Char combustion was modelled with the kinetic/diffusion limited method. Devolatilisation was modeled by the single rate devolatilisation model given in equation 7 and 8. The rate constants for coal and RDF were taken from (Badzioch and Hawksley, 1970) and (Wang et al., 2014), respectively.

$$-\frac{dm_p}{dt} = k[m_p - (1 - f_{v,o})(1 - f_{w,o})m_{p,o}] \quad (7)$$

$$k = A_1 e^{-(E/RT)} \quad (9)$$

Char combustion was modeled the by kinetic/diffusion surface rate model. The rate constant for coal was used as in (Baum and Street, 1971) and (Field, 1969). The rate constant for RDF was taken from (Wang et al., 2014).

$$D_o = C_1 \frac{[(T_p + T_\infty)/2]^{0.75}}{d_p} \quad (10)$$

$$R = C_2 e^{-(E/RT_p)} \quad (11)$$

$$\frac{dm_p}{dt} = -A_p p_{ox} \frac{D_o R}{D_o + R} \quad (12)$$

Particle heat transfer during the initial heating and after the devolatilization and char combustion is given by equation 13.

$$m_p c_p \frac{dT_p}{dt} = h A_p (T_\infty - T_p) + \epsilon_p A_p \sigma (\theta_R^4 - T_p^4) \quad (13)$$

The particle heat transfer during devolatilization is given by equation 14.

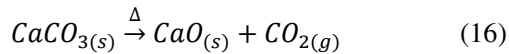
$$m_p c_p \frac{dT_p}{dt} = h A_p (T_\infty - T_p) - \frac{dm_p}{dt} h_{fg} + \epsilon_p A_p \sigma (\theta_R^4 - T_p^4) \quad (14)$$

The particle heat balance during the char combustion is given by equation 15.

$$m_p c_p \frac{dT_p}{dt} = h A_p (T_\infty - T_p) - f_h \frac{dm_p}{dt} H_{rec} + \epsilon_p A_p \sigma (\theta_R^4 - T_p^4) \quad (15)$$

The P-1 radiation model was used to implement the radiation heat transfer for the gas phase and the particle phase. The gas phase reaction was modelled using a finite-rate/eddy-dissipation model. In this study, it was considered that the volatile fraction of coal and RDF reacts with O₂ and produces CO and H₂O. Then CO reacts with O₂ and produce CO₂. The required kinetic and eddy-dissipation model data were obtained from (Kurniawan, 2004).

Char was assumed to be 100% carbon (C), which reacts with O₂ and produces CO₂. It was assumed that raw meal is pure CaCO₃. The CaCO₃ decomposition kinetics were according to (Borgwardt, 1985).



$$\frac{dm_{CaCO_3}}{dt} = -k_s A_{CaCO_3} \quad (17)$$

$$k_s = A e^{-(E_a/RT)} \quad (18)$$

3 Simulation setup

Figure 3 shows a 3-D model of the precalciner unit currently in operation at Norcem cement plant in Brevik. Figure 4 shows its front view.

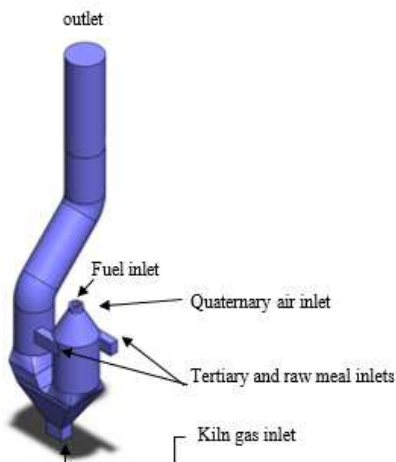


Figure 3. 3-D view of precalciner at Norcem cement plant

It has two tangential inlets to introduce raw meal and tertiary air. Quarternary air is introduced at the top of the calciner via a separate inlet, and there is also a separate inlet at the top for fuel (coal) supplied with conveying air. Moreover, there is a separate cooling air inlet.

The ANSYS Fluent CFD software was used to model the unit. The computational domain has 489,766 elements and is a combination of hexahedral, tetrahedral and prism elements.

Table 1. Approximate analysis of coal and RDF

Content	Coal (Ariyaratne, 2014)	RDF (Tokheim, 1999)
Moisture (%)	1	8.3
Volatiles (%)	23	71.1
Char (%)	62.4	10.3
Ash (%)	13.6	10.3

Table 2. Ultimate analysis of coal and RDF

Element (dry and ash-free basis)	Coal (Ariyaratne, 2009)	RDF (Tokheim, 1999)
C (%)	85.3	54.3
H (%)	4.6	8.1
O (%)	6.5	35.8
N (%)	2.0	1.2
S (%)	1.6	0.6

The approximate and ultimate analyses of coal and RDF are shown in Table 1 and Table 2, respectively, and these values were used as input values in Fluent. The Mean particle size values of 53, 2500 and 60 μm were used for coal, RDF and raw meal respectively.

Two cases were defined. In Case 1, which can be taken as the reference case for comparison purposes, coal was used as the only fuel. In Case 2, a mixture of 50 % coal and 50 % RDF was used. In both cases the same fuel energy was supplied. The boundary conditions and process conditions for the test cases are given in the Table 3. A slightly higher tertiary air flow rate was used in Case 2 in order to operate with the same excess air value in both cases.

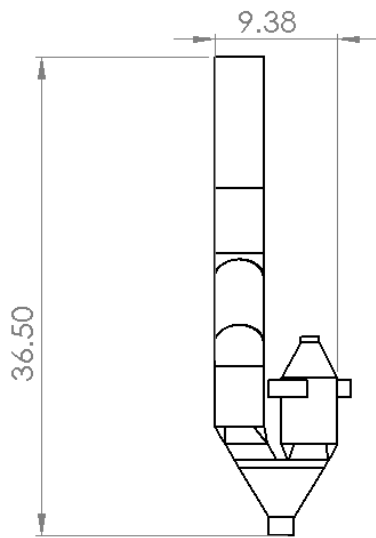


Figure 4. Front view of the precalciner (dimensions are in meters)

Table 3. Definition of cases

Parameter	Case 1	Case 2
Fuel Energy (MW)	79.5	79.5
Tertiary air (t/h)	94.5	93.0
Quarternary air (t/h)	17.1	17.1
Raw meal mass flow rate (t/h)	184.3	184.3
Coal mass flow rate (t/h)	10.1	5.1
RDF mass flow rate (t/h)	-	7.8

The composition of tertiary and quarternary air were taken as 21 % O₂ and 79 % N₂. The kiln gas composition was taken as 74.4 % N₂, 7.6 % O₂, 5.0 % H₂O and 13.0 % CO₂. The tertiary air, quarternary air and raw meal inlet temperatures were all set to 800 °C, which are quite typical values for the given kiln system. The kiln gas inlet temperature was taken as 1050 °C.

As the convergence criteria, all variables were kept below the residual value of 10⁻⁴. The SIMPLE algorithm was used to solve the Navier-Stokes equations. The PRESTO! scheme was used for pressure discretization, and first order discretization schemes were used for momentum, turbulent dissipation and turbulent kinetic energy. All other parameters were discretized with second order schemes.

During the simulation, the progress of the gas phase temperature and species mole fractions were monitored at the outlet. When they approached steady state, the simulation was considered as converged.

Results and discussion

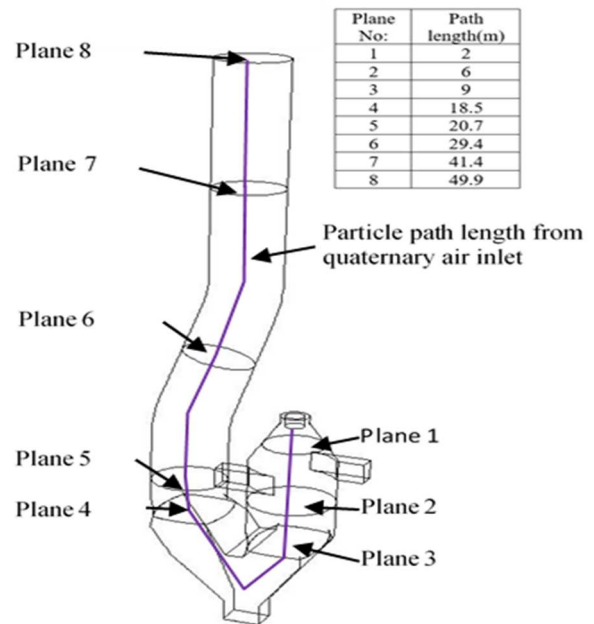
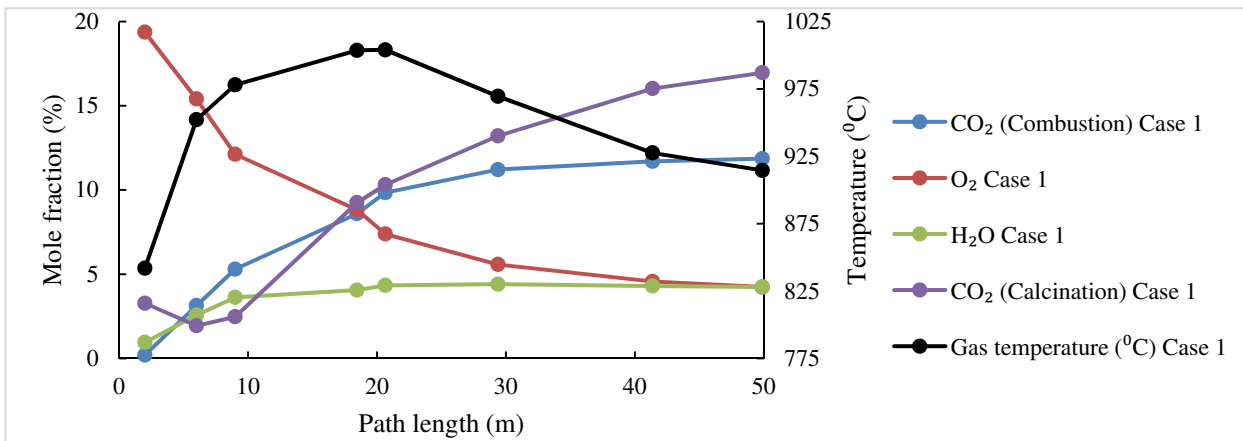


Figure 5. Particle path along the precalciner

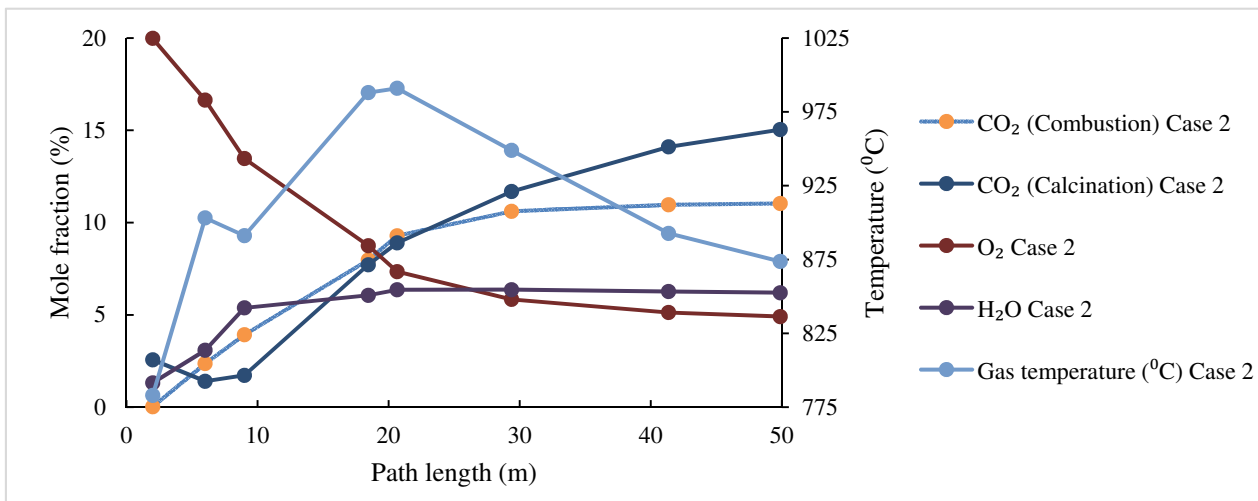
Eight planes were created along the precalciner, as shown in Figure 5, to extract data of the gas phase and the particle phase. Gas phase data were calculated as area-weighted averages for each plane.

Figure 6 (a) and (b) shows the variation of temperature and gas phase composition along the precalciner path length. The connection between path length and plane position is seen in Figure 5. In both cases, the oxygen mole fraction is reduced along the path length due to combustion. Carbon dioxide and water are generated proportionally due to combustion. In both cases, the CO₂ generated by the calcination reaction also increases, and the temperature resulting from fuel combustion is used to heat and calcine the raw meal. This can also be seen in Figure 7. At the end of the path length, the gas, fuel and meal temperatures are quite close, ranging from about 860 to 900 °C, which is typically what is experienced in the real process.

There is an increase in gas temperature over the the initial path length (the first 20 m). However, as the calcination process escalates, the temperature is gradually reduced due to heat transfer from the gas to the meal.



(a)



(b)

Figure 6. Variation of gas temperature and mole fraction of CO₂ (from calcination + combustion) O₂ and H₂O (a) for Case 1 (b) for Case 2

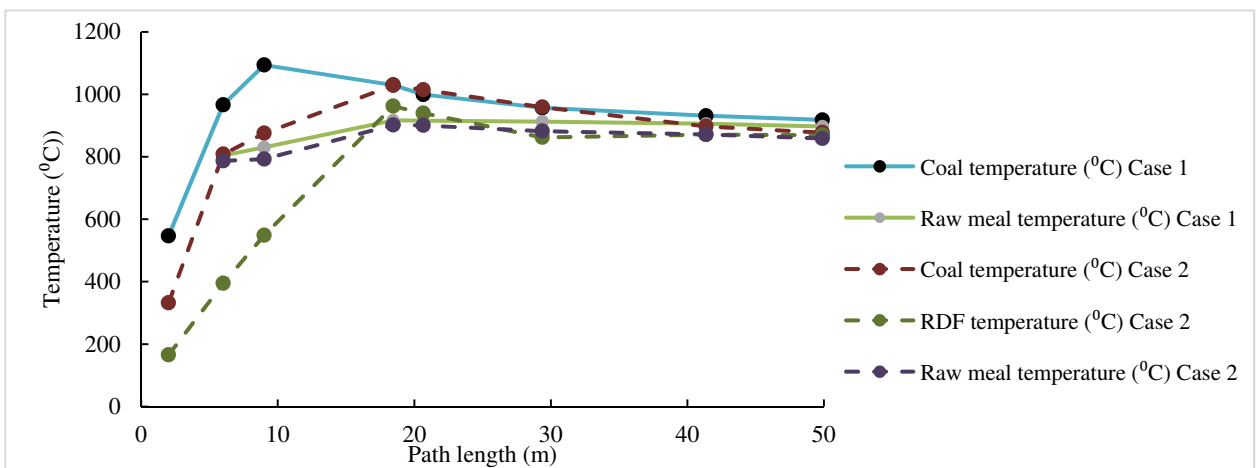


Figure 7. Temperature distribution of coal, raw meal and RDF for Case 1 and Case 2

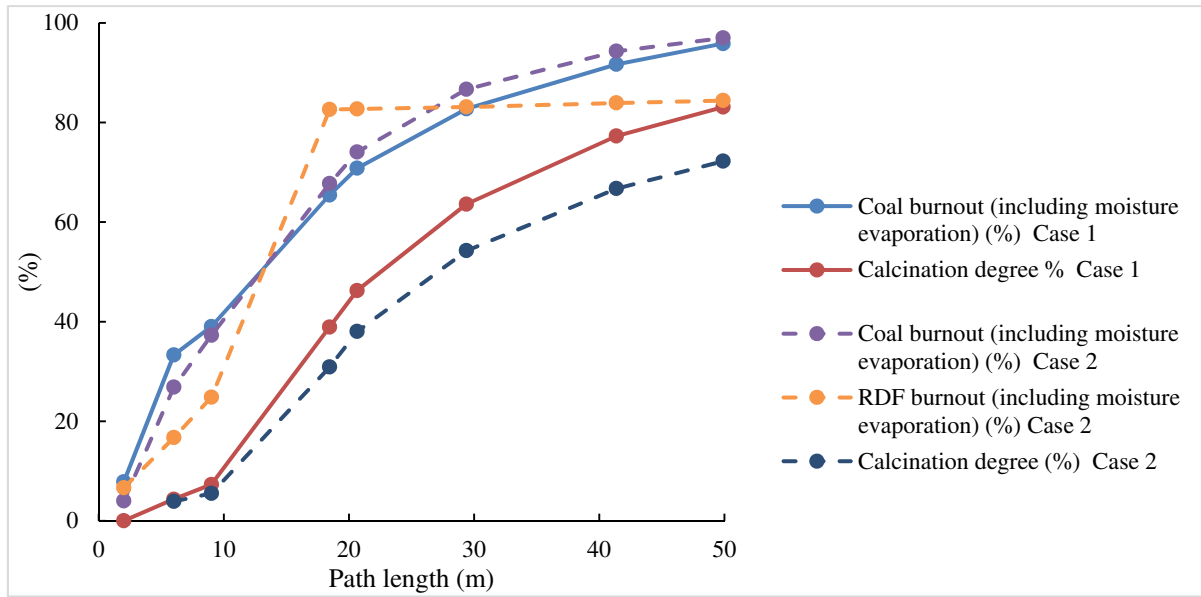


Figure 8. Calcination degree and fuel burnout for Case 1 and Case 2

Figure 8 shows the calcination degree and fuel burnout for both cases. Although the same energy was supplied in Case 1 and Case 2, the calcination degree is lower in the latter case. There are two reasons for this. The main reason is the high moisture content of RDF (see Figure 6), which reduces the particle temperature and gives a lower burnout of this fuel (see Figure 8).

Hence, less energy is released to support the decarbonation. This happens because in the initial stage, energy is spent on evaporating the moisture. A consequence of this is that RDF char burning takes place later, i.e. more downstream along the path length. In addition, since the RDF particles are bigger, it takes more time to reach complete combustion.

Conclusion

In this study CFD tool has been applied to get detailed information about temperatures, calcination degree and fuel burnout in a precalciner system. Even if the fuel energy supply is not changed, replacing part of the coal with RDF reduces the calcination degree in the process, which can be seen as quality reduction in precalcined meal. The reason for the reduced calcination degree is the poorer burnout of the RDF particles caused by higher moisture content and larger particles. The method applied in this study can be used to evaluate the calcination process under different process conditions and to optimize the process when coal is replaced by other alternative fuels with different characteristics.

Acknowledgement

Financial support from Telemark Fylkeskommune is greatly acknowledged, as is the support from the Norwegian Research Council through the project "Optimised and increased use of Refuse Derived Fuel as

substitute for coal at Norcem Brevik cement plant" (BIA project 245690).

Nomenclature

ρ	Gas density (kgm^{-3})
\vec{v}	Gas velocity vector (ms^{-1})
S_m	Mass source ($\text{kgm}^{-3}\text{s}^{-1}$)
p	Static pressure (Nm^{-2})
$\bar{\tau}$	Stress tensor (Nm^{-2})
\vec{g}	Acceleration of gravity (ms^{-2})
\vec{F}	External body force (N)
μ	Molecular viscosity ($\text{kgm}^{-1}\text{s}^{-1}$)
I	Unit tensor
E	Total energy (m^2s^{-2})
k_{eff}	Effective conductivity ($\text{Wm}^{-1}\text{K}^{-1}$)
T	Gas temperature (K)
h_j	The enthalpy formation of species j (Jkg^{-1})
\vec{j}_j	Diffusion flux of species j ($\text{kgm}^{-2}\text{s}^{-1}$)
$\overline{\tau_{eff}}$	Viscous dissipation term
S_h	Source of energy ($\text{kgm}^{-1}\text{s}^{-3}$)
\vec{u}_p	Particle velocity vector (ms^{-1})
F_D	Drag force on particle (s^{-1})
ρ_p	Particle density (kgm^{-3})
d_p	Particle diameter (m)
C_D	Drag coefficient
Re	Particle Reynold number
m_p	Particle mass (kg)
k	Devolatilisation reaction rates constant
$f_{v,0}$	Initial volatile fraction in fuel particle (%)
$f_{w,0}$	Initial moisture fraction in particle (%)
$m_{p,0}$	Particle initial weight (kg)

A_1	Pre exponential factor for k
E_1	Activation energy for k (Jkmol^{-1})
A_p	Surface area of particle (m^2)
T_∞	Local temperature of continuous phase (K)
p_{ox}	Partial pressure of oxidant (Nm^{-2})
D_o	Diffusion rate coefficient (m^{-1})
R	Universal gas constant ($\text{Jkmol}^{-1}\text{K}^{-1}$)
c_p	Heat capacity of particle ($\text{Jkg}^{-1}\text{K}^{-1}$)
h	Convection heat transfer coefficient ($\text{Wm}^{-2}\text{K}^{-1}$)
h_{fg}	Latent heat of devolatilisation (Jkg^{-1})
ϵ_p	Particle emissivity
σ	Stefan-Boltzmann constant ($5.67 \times 10^{-8} \text{Wm}^{-2}\text{K}^{-4}$)
θ_R	Radiation temperature (K)
f_h	Particle absorb energy fraction from char combustion
H_{rec}	Heat release by the char combustion (Jkg^{-1})

- Mikulčić, H., Berg, E. V., Vujanović, M. & Duić, N. Numerical study of co-firing pulverized coal and biomass inside a cement calciner. *Waste Management & Research*, 32, 661-669.2014.doi:10.1177/0734242X14538309
- Tokheim, L. A. *The impact of staged combustion on the operation of a precalciner cement kiln*. PhD thesis, Telemark College, Norway. 1999.
- Wang, G., Silva, R. B., Azevedo, J. L. T., Martins-Dias, S. & Costa, M. Evaluation of the combustion behaviour and ash characteristics of biomass waste derived fuels, pine and coal in a drop tube furnace. *Fuel*, 117, 809-824.2014.<http://dx.doi.org/10.1016/j.fuel.2013.09.080>

References

- Ariyaratne, W. K. H. *Alternative fuels in cement kilns – characterization and experiments* Master thesis, Telemark University College, Norway. 2009.
- Ariyaratne, W. K. H. *Utilization of Waste-derived Biofuels and Partly CO₂-neutral Fuels in Cement Kilns*. PhD thesis, Telemark University College. 2014.
- Ariyaratne, W. K. H., Malagalage, A., Melaaen, M. C. & Tokheim, L.-A. CFD modelling of meat and bone meal combustion in a cement rotary kiln – Investigation of fuel particle size and fuel feeding position impacts. *Chemical Engineering Science*, 123, 596-608.2015.<http://dx.doi.org/10.1016/j.ces.2014.10.048>
- Badzioch, S. & Hawksley, P. G. W. Kinetics of Thermal Decomposition of Pulverized Coal Particles. *Industrial & Engineering Chemistry Process Design and Development*, 9, 521-530.1970.10.1021/i260036a005
- Baum, M. M. & Street, P. J. Predicting the Combustion Behaviour of Coal Particles. *Combustion Science and Technology*, 3, 231-243.1971.10.1080/00102207108952290
- Borgwardt, R. H. Calcination kinetics and surface area of dispersed limestone particles. *AIChE Journal*, 31, 103-111.1985.10.1002/aic.690310112
- Fidaros, D. K., Baxevanou, C. A., Dritselis, C. D. & Vlachos, N. S. Numerical modelling of flow and transport processes in a calciner for cement production. *Powder Technology*, 171, 81-95.2007.<http://dx.doi.org/10.1016/j.powtec.2006.09.011>
- Field, M. A. Rate of combustion of size-graded fractions of char from a low-rank coal between 1 200°K and 2 000°K. *Combustion and Flame*, 13, 237-252.1969.[http://dx.doi.org/10.1016/0010-2180\(69\)90002-9](http://dx.doi.org/10.1016/0010-2180(69)90002-9)
- Kurniawan, K. P. *Studies of Fundamental Process Occurring in Pre-calciners and Cyclone Pre-heater Tower Using CFD*. PhD thesis, University of Wales. 2004.

Use of Orthogonal Collocation Method for a Dynamic Model of the Flow in a Prismatic Open Channel: For Estimation Purposes

Asanthi Jinasena¹ Glenn-Ole Kaasa² Roshan Sharma¹

¹Faculty of Technology, Natural Sciences and Maritime Sciences, University College of Southeast Norway, Norway

asanthi.jinasena@usn.no, roshan.sharma@usn.no

²Kelda Drilling Controls A/S, Porsgrunn, Norway, gok@kelda.no

Abstract

The modeling and simulation of free surface flows are complex and challenging. Especially, the open channel hydraulics are often modeled by the well-known and efficient Saint-Venant equations. The possibility of efficiently reducing these partial differential equations into ordinary differential equations with the use of orthogonal collocation method is studied with the goal of application in estimations. The collocation method showed the flexibility of choosing the boundary conditions with respect to the flow behavior. The results were comparable enough to the selected finite volume method. Further, a significant reduction in computational time in the collocation method is observed. Therefore, the collocation method shows a good possibility of using it for the real-time estimation of flow rate in an open channel.

Keywords: orthogonal collocation, open channel, prismatic, flow estimation, dynamic modeling

1 Introduction

The real-time estimation of flow rates in fluid flows with the use of mathematical models is a widely known practice in the industry, especially in oil drilling processes, hydro power industry and in agricultural industries. The simplicity and the robustness of the mathematical model are influential in estimation. However, the modeling and simulation of free surface flows are complex and challenging. Especially, the open channel hydraulics are often modeled by the well known and efficient shallow water equations, which are also known as the *Saint-Venant Equations* (SVEs). These are a set of nonlinear, hyperbolic *Partial Differential Equations* (PDEs). These equations are widely used throughout the history, yet the discretization remains tricky which makes it difficult to solve.

Although the classical methods such as *finite difference* and *finite volume* methods are of high precision, it needs numerous spatial discretization points to obtain a realistic solution and consumes a considerable amount of computational time. Hence, these numerical solvers could create complications in applications of online state and parameter estimation. On the contrary, the collocation method, which is a special case of the weighted residual method, could lead to simple solutions with less computational

time. This method is commonly used in computational physics for solving PDEs and in chemical engineering for model reduction.

Therefore, the main aim of this work is to study the possibility of reducing the PDEs into *Ordinary Differential Equations* (ODEs) efficiently, with a future goal of an application in estimations. This paper describes the numerical approach which is taken to solve the 1-D shallow water equations in the reduced ODE form. Further, it includes the verification of the used numerical approach in comparison to the other well-known and accurate numerical schemes for selected case studies.

In this paper, the orthogonal collocation method is used for converting the PDEs into ODEs, and then the ODEs are solved using the Runge-Kutta fourth order numerical scheme (for the discretization in the time domain). The Lagrange interpolating polynomials are used for the approximation of the shallow water equations and the shifted Legendre polynomials are used for the selection of collocation points. For the case study, a prismatic channel with a trapezoidal cross-section along the length is selected as the open channel. Different numbers of collocation points were tested and the results are compared with the numerical simulation results obtained from a classical finite volume method. The finite volume method used in this study is a semi-discrete, second order and a central upwind scheme developed by Kurganov and Petrova (Kurganov and Petrova, 2007) for the spatial discretization and the Runge-Kutta fourth order numerical scheme for the temporal discretization.

2 Mathematical Model

There are a large number of versions of the SVEs, based on the physical natures those are assumed upon (Chalfen and Niemiec, 1986; Chaudhry, 2008). The SVEs are a set of hyperbolic, non-linear PDEs, and the used version of the SVEs in this study are derived with the assumptions listed below (Chaudhry, 2008; Litrico and Fromion, 2009).

- The pressure distribution is hydrostatic.
- The velocity of the flow is uniform over the cross section of the channel.

- The channel is prismatic *i.e.* the cross sectional area perpendicular to the flow and the channel bed slope do not change with the direction of the flow.
- The channel bed slope is small *i.e.* the cosine of the angle it makes with the horizontal axis may be replaced by unity.
- The head losses in unsteady flow (due to the effect of boundary friction and turbulence) can be calculated through resistance laws analogous to those used for steady flow.
- No lateral inflow rates are considered.

The Equations for a 1D, unsteady, prismatic, open channel system, can be expressed as,

$$\frac{\partial A}{\partial t} + \frac{\partial Q}{\partial x} = 0, \quad (1)$$

$$\frac{\partial Q}{\partial t} + \frac{\partial(Q^2/A)}{\partial x} + Ag \left(\frac{\partial z}{\partial x} + S_f - S_b \right) = 0, \quad (2)$$

where $A(x, h, t)$ is the wetted cross sectional area normal to the flow, $h(x, t)$ is the depth of flow, $Q(x, t)$ is the volumetric flow rate, $S_f(Q, x, h)$ is the friction slope, z is the absolute fluid level, which changes with the geometry of the channel, g is the gravitational acceleration, t is the time and x is the distance along the flow direction (Chow, 1959; Chaudhry, 2008). The channel bed slope $S_b(x)$ is calculated by $-\frac{\partial z}{\partial x}$, which is considered positive when sloping downwards. The friction slope S_f is calculated from the Gauckler–Manning–Strickler formulae as shown in Equation 3 (Chow, 1959),

$$S_f = \frac{Q|Q|n_M^2}{A^2R^{\frac{4}{3}}}, \quad (3)$$

where n_M is the Manning friction coefficient $\left(\frac{1}{k_s}\right)$ and R is the hydraulic radius given by $\frac{A}{P}$. Here, k_s is the Strickler friction coefficient and P is the wetted perimeter. The analytical solution for these equations exists only for the simplified cases (Chalfen and Niemiec, 1986; Chung and Kang, 2004; Bulatov, 2014), therefore, these are generally solved by numerical methods. Two different numerical methods are considered in this study, the orthogonal collocation method and the Kurganov and Petrova (KP) Scheme, which are described in the following sections 2.1 and 2.2.

2.1 The Orthogonal Collocation Method

The states A and Q in the SVEs can be approximated by the general polynomial interpolation, using the Lagrange interpolating polynomial (Isaacson and Keller, 1966). The Lagrange interpolating polynomial of n^{th} order for a general function $f(x)$, at $n + 1$ data points, is given by (Szegő, 1939),

$$f_n(x) = \sum_{i=0}^n L_i(x)f(x_i), \quad (4)$$

where,

$$L_i(x) = \prod_{\substack{j=0 \\ j \neq i}}^n \frac{x - x_j}{x_i - x_j}. \quad (5)$$

Here, $L_i(x)$ is a weighting function, which is considered as the basis function for the Lagrange function. Now, the approximated states can be defined as A_a and Q_a , where,

$$A_a(x, t) = \sum_{i=0}^n L_i(x)A_i(t), \quad \text{and} \quad (6)$$

$$Q_a(x, t) = \sum_{i=0}^n L_i(x)Q_i(t). \quad (7)$$

Using these approximations in the SVEs, the Equations 1 and 2 can be re-written as follows,

$$\frac{\partial A_a}{\partial t} + \frac{\partial Q_a}{\partial x} = R_1, \quad (8)$$

$$\frac{\partial Q_a}{\partial t} + \frac{\partial(Q_a^2/A_a)}{\partial x} + A_a g \left(\frac{\partial z}{\partial x} + S_f - S_b \right) = R_2, \quad (9)$$

where $R_1(x, \bar{A}, \bar{Q})$ and $R_2(x, \bar{A}, \bar{Q})$ are the residuals and \bar{A} and \bar{Q} are the vectors of the coordinates of A_a and Q_a , respectively.

The spatial length x is divided into $n - 1$ inequidistant spaces for n nodes, which are named as the *collocation points*. Two of these collocation points will be placed at the boundaries. When the residuals are closer to zero, the unknowns (\bar{A} and \bar{Q}) can be computed for each collocation point x_i^c .

$$R_1(x_i^c, \bar{A}, \bar{Q}) \approx 0, \quad i = 1, 2, \dots, n \quad (10)$$

$$R_2(x_i^c, \bar{A}, \bar{Q}) \approx 0, \quad i = 1, 2, \dots, n \quad (11)$$

The corresponding collocation points x_i^c , can be found by choosing the points carefully. When the points are at the roots of any orthogonal polynomial such as the Legendre or Chebyshev polynomial, the approximation error can be minimized (Isaacson and Keller, 1966; Quarteroni and Valli, 2008). The Legendre polynomials are selected in this study. As the number of points are increased, these collocation points cluster towards the two endpoints of the selected total length. This prevents the formation of Runge's phenomenon, which occurs when the nodes are equispaced.

When the residuals are closer to zero, the Equations 8 and 9 can be re-written as follows,

$$\frac{\partial A_a}{\partial t} + \frac{\partial Q_a}{\partial x} \approx 0, \quad (12)$$

$$\frac{\partial Q_a}{\partial t} + \frac{\partial(Q_a^2/A_a)}{\partial x} + A_a g \left(\frac{\partial z}{\partial x} + S_f - S_b \right) \approx 0. \quad (13)$$

Further, the Equation 13 can be simplified as,

$$\begin{aligned} \frac{\partial Q_a}{\partial t} + \frac{2Q_a}{A_a} \frac{\partial Q_a}{\partial x} - \frac{Q_a^2}{A_a^2} \frac{\partial A_a}{\partial x} \\ + A_a g \left(\frac{\partial z}{\partial x} + S_f - S_b \right) \approx 0. \end{aligned} \quad (14)$$

From the Equations 6 and 7, the derivatives are expressed as,

$$\frac{\partial A_a}{\partial x} = \sum_{i=0}^n L'_{ij} A_i, \quad \text{and} \quad (15)$$

$$\frac{\partial Q_a}{\partial x} = \sum_{i=0}^n L'_{ij} Q_i, \quad (16)$$

where

$$L'_{ij}(x_i) = \frac{\partial L_i(x)}{\partial x}. \quad (17)$$

The substitution of this expression in the Equations 12 and 14 will give two ODEs.

$$\frac{dA_a}{dt} + \sum_{i=0}^n L'_{ij} Q_i \approx 0, \quad (18)$$

$$\frac{dQ_a}{dt} + \frac{2Q_a}{A_a} \sum_{i=0}^n L'_{ij} Q_i - \frac{Q_a^2}{A_a^2} \sum_{i=0}^n L'_{ij} A_i + A_a g \left(\frac{dz}{dx} + S_f - S_b \right) \approx 0. \quad (19)$$

At the selected collocation points, the approximated value is the same as the functional value,

$$A_a(x = x_i, t) = \sum_{i=0}^n L_i A_i(t) = A_i(x = x_i, t) \quad \text{and} \quad (20)$$

$$Q_a(x = x_i, t) = \sum_{j=0}^n L_j Q_j(t) = Q_i(x = x_i, t). \quad (21)$$

Therefore, the approximated Equations 18 and 19 become as follows,

$$\frac{dA_i}{dt} + \sum_{i=0}^n L'_{ij} Q_i = 0 \quad \text{and} \quad (22)$$

$$\frac{dQ_i}{dt} + \frac{2Q_i}{A_i} \sum_{i=0}^n L'_{ij} Q_i - \frac{Q_i^2}{A_i^2} \sum_{i=0}^n L'_{ij} A_i + A_i g \left(\frac{dz}{dx} + S_f - S_b \right) = 0. \quad (23)$$

which produces a set of ODEs as shown in Equations 24 and 25.

$$\dot{A}_i = - \sum_{i=0}^n L'_{ij} Q_i \quad (24)$$

$$\dot{Q}_i = - \frac{2Q_i}{A_i} \sum_{i=0}^n L'_{ij} Q_i + \frac{Q_i^2}{A_i^2} \sum_{i=0}^n L'_{ij} A_i - A_i g \left(\frac{dz}{dx} + S_f - S_b \right), \quad i = 0, 1, \dots, n \quad (25)$$

Two more equations can be build up using the boundary conditions, which we can choose according to the condition of the flow. For sub-critical flows, one boundary can be chosen from the upstream and the other from the downstream. For super-critical flows, both the boundaries have to be on the upstream (Georges et al., 2000).

To obtain a stable solution, the discretized time Δt , should satisfy the 'current number condition' Cr (Dulhoste et al., 2004),

$$Cr = \frac{\Delta t}{\Delta x} \leq \frac{1}{|v| + c}, \quad (26)$$

where v is the velocity and c is the celerity. The celerity for a trapezoidal channel is defined as $\sqrt{g \frac{A}{T}}$, where T is the top width of the free surface of the channel.

2.1.1 Selection of Collocation Points for Different Number of Points (n)

The points are selected using the Legendre polynomials. The Legendre functions of the first kind is selected over the Chebyshev polynomials of the first kind, due to the less numerical oscillations given by the Legendre functions.

The Legendre polynomials are a set of orthogonal polynomials, which are the solutions to the Legendre differential equations (Whittaker and Watson, 1920). The Legendre polynomials are in the range of $x \in [-1, 1]$ and the shifted Legendre polynomials are analogous to the Legendre polynomials, but are in the range of $x \in [0, 1]$. Therefore, the shifted Legendre polynomials are selected in this study, due to the easiness in converting the collocation points over the selected channel. The shifted Legendre polynomials of the first kind can be generated from the Rodrigues' formulae (Equation 27) (Whittaker and Watson, 1920; Isaacson and Keller, 1966; Quarteroni and Valli, 2008),

$$P_n(x) = \frac{1}{n!} \frac{d^n}{dx^n} \{ (x^2 - x)^n \}. \quad (27)$$

2.1.2 Development of the ODEs for a Sample Set of Collocation Points

The polynomials $P_n(x)$ for n from 3 to 5 can be derived from the Equation 27 as follows,

$$\begin{aligned} P_1(x) &= 2x - 1, & n &= 3, \\ P_2(x) &= 6x^2 - 6x + 1, & n &= 4, \\ P_3(x) &= 20x^3 - 30x^2 + 12x - 1, & n &= 5. \end{aligned} \quad (28)$$

Each collocation point x_i , lies at the roots of these polynomials along the normalized length of the channel. For a channel with a length of l , the positions of the collocation points can be expressed as follows,

$$\begin{aligned} x_i &\in [0, 0.5l, l], & i &= 1, 2, 3 \\ x_i &\in [0, 0.2113l, 0.7887l, l], & i &= 1, 2, 3, 4 \\ x_i &\in [0, 0.1127l, 0.5l, 0.8873l, l]. & i &= 1, 2, 3, 4, 5 \end{aligned} \quad (29)$$

For a case of three collocation points ($n = 3$), the corresponding Lagrange interpolating polynomial coefficients,

L' , can be calculated by differentiating $L(x)$ with respect to x from the Equation 5,

$$L'_1(x) = \frac{d}{dx} \left(\frac{x-x_2}{x_1-x_2} \times \frac{x-x_3}{x_1-x_3} \right) = \frac{(x-x_3) + (x-x_2)}{(x_1-x_2)(x_1-x_3)},$$

$$L'_2(x) = \frac{d}{dx} \left(\frac{x-x_1}{x_2-x_1} \times \frac{x-x_3}{x_2-x_3} \right) = \frac{(x-x_3) + (x-x_1)}{(x_2-x_1)(x_2-x_3)},$$

$$L'_3(x) = \frac{d}{dx} \left(\frac{x-x_1}{x_3-x_1} \times \frac{x-x_2}{x_3-x_2} \right) = \frac{(x-x_2) + (x-x_1)}{(x_3-x_1)(x_3-x_2)}.$$

The coefficient matrix L' at each collocation point x_i , can be calculated by solving L'_i at each point ($L'_i(x = x_i)$), using the position values from Equation 29. The coefficient matrix for the case of the three collocation points is as follows,

$$L' = \begin{bmatrix} L_1 \\ L_2 \\ L_3 \end{bmatrix}^T = \frac{1}{l} \begin{bmatrix} -3 & 4 & -1 \\ -1 & 0 & 1 \\ 1 & -4 & 3 \end{bmatrix}.$$

Similarly, for $n = 4$,

$$L' = \frac{1}{l} \begin{bmatrix} -7.0005 & 8.1964 & -2.1959 & 1 \\ -2.7326 & 1.7328 & 1.73190 & -0.7321 \\ 0.7321 & -1.7319 & -1.7328 & 2.7326 \\ -1 & 2.1959 & -8.1964 & 7.0005 \end{bmatrix},$$

and for $n = 5$,

$$L' = \frac{1}{l} \begin{bmatrix} -13.0001 & 14.7884 & -2.6666 & 1.8783 & -1 \\ -5.3239 & 3.8731 & 2.0656 & -1.2910 & -0.6762 \\ 1.5 & -3.2275 & 0 & 3.2275 & -1.5 \\ -0.6762 & 1.291 & -2.0656 & -3.8731 & 5.3239 \\ 1 & -1.8783 & 2.6666 & -14.7884 & 13.0001 \end{bmatrix}.$$

The substitution of the L' in Equations 24 and 25, will give the corresponding set of ODEs. The ODEs for the case of the three collocation points are as follows,

$$\dot{A}_1 = \frac{1}{l}(-3Q_1 + 4Q_2 - Q_3), \quad (30)$$

$$\dot{A}_2 = \frac{1}{l}(-Q_1 + Q_3), \quad (31)$$

$$\dot{A}_3 = \frac{1}{l}(Q_1 - 4Q_2 + 3Q_3), \quad (32)$$

$$\dot{Q}_1 = -\frac{2Q_1}{A_1 l}(-3Q_1 + 4Q_2 - Q_3) + \frac{Q_1^2}{A_1^2 l}(-3A_1 + 4A_2 - A_3) - A_1 g \left(\frac{dz}{dx} + S_{f_1} - S_b \right), \quad (33)$$

$$\dot{Q}_2 = -\frac{2Q_2}{A_2 l}(-Q_1 + Q_3) + \frac{Q_2^2}{A_2^2 l}(-A_1 + A_3) - A_2 g \left(\frac{dz}{dx} + S_{f_2} - S_b \right), \quad (34)$$

$$\dot{Q}_3 = -\frac{2Q_3}{A_3 l}(Q_1 - 4Q_2 + 3Q_3) + \frac{Q_3^2}{A_3^2 l}(A_1 - 4A_2 + 3A_3) - A_3 g \left(\frac{dz}{dx} + S_{f_3} - S_b \right). \quad (35)$$

One or two equations from the above set of equations, can be replaced by the chosen boundary conditions.

2.2 The Kurganov and Petrova (KP) Scheme

The KP scheme (Kurganov and Petrova, 2007) is a well balanced scheme which utilizes a central upwind scheme. Further, it does not have the Riemann problem. To illustrate this scheme, the SVEs stated in Equations 1 and 2 are re-written as follows,

$$\frac{\partial U}{\partial t} + \frac{\partial F}{\partial x} = S, \quad (36)$$

where,

$$U = \begin{bmatrix} A \\ Q \end{bmatrix}, \quad (37)$$

$$F = \begin{bmatrix} Q \\ \frac{Q^2}{A} \end{bmatrix}, \quad \text{and} \quad (38)$$

$$S = \begin{bmatrix} 0 \\ -Ag \left(\frac{\partial z}{\partial x} + S_f - S_b \right) \end{bmatrix}. \quad (39)$$

The space is discretized in to a grid for a finite volume cell of a cell size of Δx and $x_{j-\frac{1}{2}} \leq x_j \leq x_{j+\frac{1}{2}}$ in a uniform grid. The KP scheme for the given Equation 36, can be written as the following set of ODEs,

$$\frac{d\bar{U}_j(t)}{dt} = -\frac{H_{j+\frac{1}{2}}(t) - H_{j-\frac{1}{2}}(t)}{\Delta x} + \bar{S}_j(t), \quad (40)$$

where $H_{j\pm\frac{1}{2}}(t)$ are the central upwind numerical fluxes at the cell interfaces (Kurganov and Petrova, 2007; Sharma, 2015; Vytvytskyi et al., 2015). More details in this scheme is included in (Kurganov and Petrova, 2007). The time step Δt is restricted by the standard Courant–Friederich–Levy (CFL) condition as follows (Kurganov and Petrova, 2007; Bollermann et al., 2013),

$$\text{CFL} = \frac{\Delta t}{\Delta x} \max_j \left| a_{j+\frac{1}{2}}^\pm \right| \leq \frac{1}{2}, \quad (41)$$

where $a_{j\pm\frac{1}{2}}^\pm$ is a one sided local speed of propagation.

2.3 The Parameters of the Open Channel

The selected open channel is a prismatic channel with a trapezoidal cross section. The total length l of the channel is 2.95 m. The bottom width of the channel is 0.2 m, with a zero channel bed slope S_b . The Strickler friction coefficient, k_S is taken as $42 \frac{\text{m}^{1/3}}{\text{s}}$.

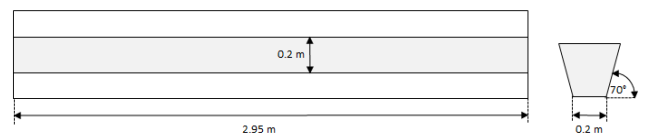


Figure 1. Plan View and the Side Elevation of the Prismatic Channel

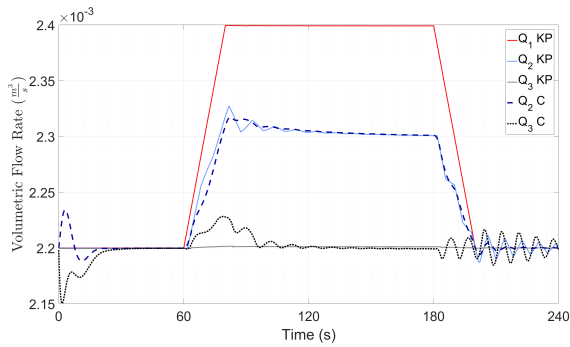


Figure 2. Comparison of the Flow Rates between the KP method and OC Method, at the Three Collocation Points. ‘KP’: Results from KP, ‘C’: Results from OC

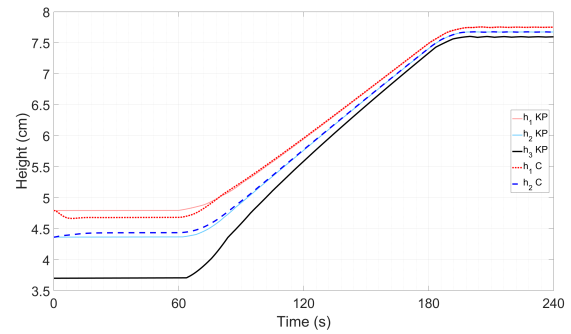


Figure 3. Comparison of the Fluid Levels between the KP method and the OC Method, at the Three Collocation Points. ‘KP’: Results from KP, ‘C’: Results from OC

3 Simulation, Results and Discussion

A prismatic channel is selected for the dynamic simulations in MATLAB(9.0.1), with three cases of different number of collocation points. For the collocation method, the selected boundary conditions are the flow rate into the channel and the wetted cross sectional area out of the channel. For the simulations with KP, the two boundaries are the flow rates into and out of the channel. For both the methods, the sets of ODEs are solved by the use of Runge Kutta fourth order numerical scheme with a fixed step length.

3.1 Simulation Setup

The simulations for the KP method were started from a steady state, and after 60 seconds, the volumetric flow rate at the inlet was changed from $0.0022 \frac{m^3}{s}$ to $0.0024 \frac{m^3}{s}$ within 20 seconds. This increased flow rate was maintained for about 120 seconds, and then it was reduced back to the previous value within 20 seconds. The flow rate at the end of the channel was kept at the same value of $0.0022 \frac{m^3}{s}$, throughout the simulations.

The inlet flow rate conditions of the KP method and the outlet wetted cross section area resulted from the simulations, were used as the boundary conditions for the simulations of the collocation method.

3.2 Results and Discussion

Three case studies were simulated using the orthogonal collocation (OC) method. Those results are compared with the results from the KP method and are described in the sections 3.2.1, 3.2.2 and 3.2.3.

3.2.1 Case 1: Three Collocation Points ($n=3$)

The results from the simulations of the KP scheme are compared with the results from the method with three collocation points. The volumetric flow rates and the heights of the fluid level at the three points are shown in Figures 2 and 3, respectively.

The flow rates obtained from the collocation method are similar to the results from the KP method, but with a few numerical oscillations. At the start of the simulation, the numerical oscillations can be observed due to the unsteady state conditions in the collocation method. These deviations can also be clearly seen in the deviations of the heights in Figure 3 at the beginning. During the transient conditions, the flow rate at the middle of the channel, which is obtained by the collocation method, *i.e.* $Q_2 C$ in Figure 3 after 60 seconds, has less numerical

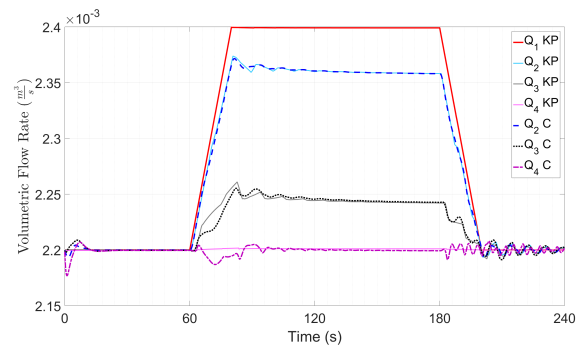


Figure 4. Comparison of the Flow Rates between the KP method and the OC Method, at the Four Collocation Points. ‘KP’: Results from KP, ‘C’: Results from OC

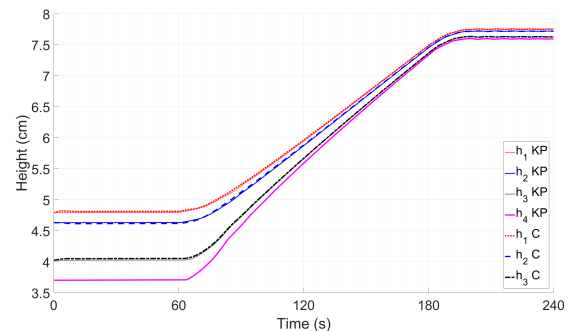


Figure 5. Comparison of the Fluid Levels between the KP method and the OC Method, at the Four Collocation Points. ‘KP’: Results from KP, ‘C’: Results from OC

oscillations than the same from the KP method, but the flow rate at the end of the channel *i.e.* $Q_3 C$ has more oscillations than from the KP method.

3.2.2 Case 2: Four Collocation Points ($n=4$)

The volumetric flow rates and the heights of the fluid level at the selected four points, are shown in Figures 4 and 5, respectively.

The results of the simulation from the OC method with four collocation points are more comparable with the results from the KP method, than the same with the three collocation points. Although the amplitude of the oscillations are reduced, the frequency of the oscillations are increased than in the previous case (in section 3.2.1). The reason could be the dual effect of the better approximation due to the increase of the number of collocation points, and the oscillatory behavior of the polynomial approximation due to the increase of the order of the polynomial. This could be observed further by increasing the number of collocation points to five.

3.2.3 Case 3: Five Collocation Points ($n=5$)

The results for the five collocation points are shown in Figures 6 and 7, respectively. The better approximation due to the increase of the number of collocation points has dominated over the oscillatory behavior caused by the increase of the order of the polynomial, as shown in Figure 6. The oscillations in OC method are the same as from KP, except for $Q_5 C$, which is at the end of the channel.

3.2.4 Selection of an Orthogonal Polynomial for the Collocation Points

A comparison between the Legendre and Chebyshev polynomials of the first kind was done to justify the selection of the Legendre polynomial. The simulations were done for the case of five collocation points. As shown in the zoomed areas of the Figure 8, it can be justified that the Legendre polynomials tend to produce less oscillations compared to the Chebyshev polynomials.

The OC method is accurate enough with four or more collocation points, as oppose to the numerous discretization points (100) in the KP method. Therefore, to satisfy the CFL condition, the time step Δt of the KP scheme has to be small due to the small Δx . On the contrary, to satisfy the different Current number condition, the OC method allows a larger time step due to the comparatively bigger Δx . Altogether, the computational time taken for the OC method was about 5-20 times less than the computational time taken by the KP method. Handling the ODEs that are

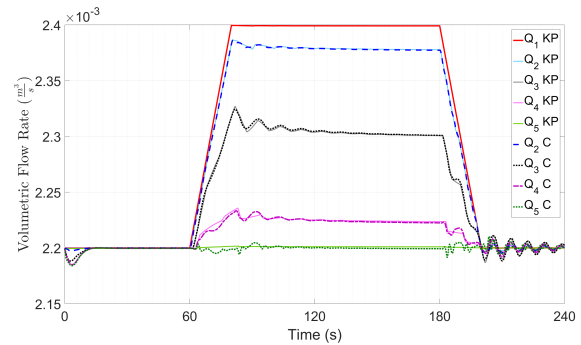


Figure 6. Comparison of the Flow Rates between the KP method and the OC Method, at the Five Collocation Points. ‘KP’: Results from KP, ‘C’: Results from OC

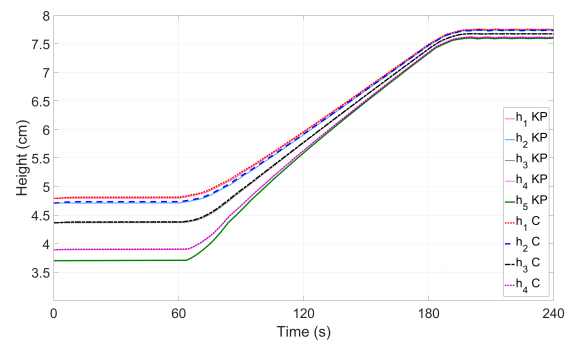


Figure 7. Comparison of the Fluid Levels between the KP method and the OC Method, at the Five Collocation Points. ‘KP’: Results from KP, ‘C’: Results from OC

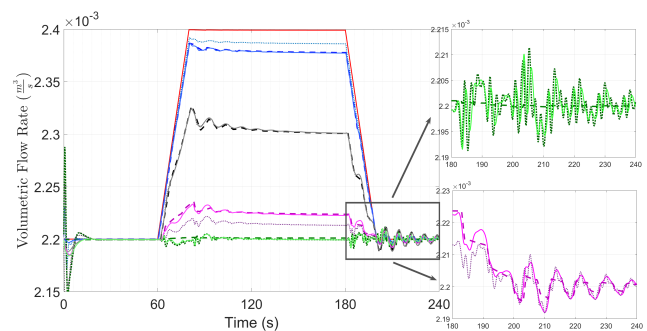


Figure 8. Comparison of the Legendre and Chebyshev polynomials of the first kind. (dashed lines: Results from KP at different collocation points, dotted lines: Results from the OC using Chebyshev polynomials, solid lines: Results from OC using Legendre polynomials.

generated by the OC method is computationally simpler than the KP method. Further, it has a considerably similar accuracy, specially takes much less computational time, which makes the use of OC method in the application of online state and parameter estimation, to be promising.

4 Conclusion

The possibility of efficiently reducing the PDEs into ordinary differential equations (ODEs) using orthogonal col-

location method, is studied with the goal of application in state and parameter estimations in real-time. The collocation method showed the flexibility of choosing the boundary conditions with respect to the flow behavior. The results were comparable enough to the selected finite volume method, which is a widely used, central-upwind scheme. Further, a significant reduction in the computational time in the collocation method is observed. Therefore, the collocation method shows a promising potential of using it in the estimation of state and parameters of open channel flows.

5 Acknowledgment

The economic support from The Research Council of Norway and Statoil ASA through project no. 255348/E30 ‘Sensors and models for improved kick/loss detection in drilling (Semi-kidd)’ is gratefully acknowledged.

References

- Andreas Bollermann, Guoxian Chen, Alexander Kurganov, and Sebastian Noelle. A Well-Balanced Reconstruction of Wet/Dry Fronts for the Shallow Water Equations. *Journal of Scientific Computing*, 56(2):267–290, 2013. doi:10.1007/s10915-012-9677-5.
- O. V. Bulatov. Analytical and Numerical Riemann Solutions of the Saint Venant Equations for Forward- and Backward-Facing Step Flows. *Computational Mathematics and Mathematical Physics*, 54(1):158–171, 2014. doi:10.1134/S0965542514010047.
- Mieczyslaw Chalfen and Andrzej Niemiec. Analytical and Numerical Solution of Saint-Venant Equations. *Journal of Hydrology*, 86:1–13, 1986.
- M. Hanif Chaudhry. *Open-Channel Flow*. Springer, New York, 2nd edition, 2008. ISBN 9780387301747.
- V. T. Chow. *Open-Channel Hydraulics*. McGraw-Hill, New York, 1959. ISBN 0070107769.
- W. H. Chung and Y. L. Kang. Analytical Solutions of Saint Venant Equations Decomposed in Frequency Domain. *Journal of Mechanics*, 20(03):187–197, 2004. doi:10.1017/S1727719100003403.
- Jean-François Dulhoste, Didier Georges, and Gildas Besançon. Nonlinear Control of Open-Channel Water Flow Based on Collocation Control Model. *Journal of Hydraulic Engineering*, 130(3):254–266, 2004. doi:10.1061/(ASCE)0733-9429(2004)130:3(254).
- Didier Georges, Jean-françois Dulhoste, and Gildas Besançon. Modelling and Control of Water Flow Dynamics via a Collocation Method. *Math. Theory of Networks and Systems*, 2000.
- Eugene Isaacson and Herbert Bishop Keller. *Analysis of Numerical Methods*. John Wiley & Sons, New York, 2nd edition, 1966. ISBN 9780486680293.
- Alexander Kurganov and Guergana Petrova. A Second-Order Well-Balanced Positivity Preserving Central-Upwind Scheme for the Saint-Venant System. *Communications in Mathematical Sciences*, 5(1):133–160, 2007. doi:10.4310/CMS.2007.v5.n1.a6.
- Xavier Litrico and Vincent Fromion. *Modeling and Control of Hydrosystems*. Springer, 2009. ISBN 9781848826236.
- Alfino Quarteroni and Alberto Valli. *Numerical Approximation of Partial Differential Equations*. Springer, Berlin, 1st edition, 2008. ISBN 9783540852674.
- Roshan Sharma. Second order scheme for open channel flow. Technical report, Telemark University College, 2015. URL <http://hdl.handle.net/11250/2438453>.
- Gabor Szegő. *Orthogonal Polynomials*, volume 23. American mathematical society, 4th edition, 1939. ISBN 9780821810231.
- Liubomyr Vytvytskyi, Roshan Sharma, and Bernt Lie. Model Based Control for Run-of-river System. Part 1: Model Implementation and Tuning. *Modeling, Identification and Control*, 36(4):237–249, 2015. doi:10.4173/mic.2015.4.4.
- E.T. Whittaker and G.N. Watson. Legendre Functions. In *A Course of Modern Analysis*, chapter XV, pages 302–336. Cambridge University Press, 3rd edition, 1920.

Evaluation of drag models for CFD simulation of fluidized bed biomass gasification

Kjell-Arne Solli, Cornelius Agu

Department of Process, Energy and Environmental Technology, University College of Southeast Norway, Norway
kjell-arne.solli@usn.no

Abstract

Gasification of biomass into suitable feedstock has become a feasible alternative technology for reducing the use of energy feedstock from fossil sources. Usually, fluidized bed technology is used in the biomass gasification reactor.

Optimization of a fluidized bed reactor needs to take into account the bed behavior in the presence of both biomass and bed material, as well as chemical conversion of particles and volatiles, among other process parameters. CFD simulation of the process is a valuable tool to go about the optimization. However, simulation result validation is limited by the accuracy of input parameters such as those characterizing several drag models given in the literature. This study is focusing on the drag model parameters.

The simulation is aimed at validating some of the commonly used models for drag forces against the bed material(s) used in the fluidized bed gasification reactor. Drag models included in this study are those given by Syamlal and O'Brien, Gidaspow, and BVK. The MFIX CFD-software (version 2016.1) from The National Energy Technology Laboratory (NETL) is used. The Two-Fluid Model (TFM) are applied for comparison of the results. The key factors for validation of the drag models are based on the superficial gas velocity at the minimum fluidization condition and the degree of bed expansion.

The simulation results show that the minimum fluidization velocity could be predicted using the Gidaspow and BVK drag models by adjusting the particle diameter used in the simulation. For the Syamlal & O'Brien drag model, two parameters are fitted to predict the minimum fluidization velocity. The bubbling bed behavior is not captured using the Syamlal & O'Brien drag model while Gidaspow and BVK drag models fairly captures this phenomenon. The bed expansion from the simulation is higher than that observed in the experiment, and the deviation is even higher with the Syamlal & O'Brien drag model.

Keywords: CFD, fluidized bed, drag model, TFM

1 Introduction

This study is part of ongoing research project at Porsgrunn campus of University College of Southeast

Norway, aiming at improving on the processes utilizing alternative fuels from biomaterials.

1.1 Background

Gasification of biomass into suitable feedstock for energy production has become a feasible alternative technology for reducing the use of energy feedstock from fossil sources. Usually, fluidized bed technology is used in the biomass gasification reactor

Optimization of a fluidized bed for a biomass gasification process needs to take into account the fluidization behavior of a mixture of biomass and bed material, as well as chemical conversion of particles and volatiles, among other process parameters. CFD simulation of the process is a valuable tool to go about the optimization. However, simulation result validation is limited by the accuracy of input parameters such as those characterizing several drag models given in the literature. Due to limited space, this study is focusing on the drag model parameters.

The simulation setup is based on the physical dimensions used in a cold flow experiments (1.5 m high, 8.4 cm diameter). This study supports simulation of a 20 kW fluidized bed gasification reactor located at University College of Southeast Norway.

1.2 Aims

The simulation is aimed at validating some of the commonly used models for drag forces against the bed material used in the fluidized bed gasification reactor. Drag models included in this study are those given by Syamlal and O'Brien (Syamlal & O'Brien, 1988), Gidaspow (Ding & Gidaspow, 1990), and Beetstra et al. (BVK model) (Beetstra *et al.*, 2007).

2 Methods

The bed material has been characterized, and tested in cold bed setup. The results are compared with CFD simulations using different drag models. The key factors for validation of the drag models are based on the superficial gas velocity at the minimum fluidization condition and the degree of bed expansion. Distribution of void fraction and bubbles within the bed are also considered.

2.1 Cold bed experimental setup

The experimental setup consists of a vertical cylindrical column of height 1.5 m and base diameter of 0.084 m as shown in Figure 1. The bottom of the column is fitted with a porous plate. The porous plate ensures even distribution of air within the bed. The rig is fitted with ten pressure sensors, measuring the fluid pressure in the column up to the height of about 1.0 m. The pressure measurement P2 is placed 0.038 m above porous plate. Compressed air at ambient temperature is used as the fluidizing medium. Characterization of bed material and the experimental conditions are given in Table 1 and Table 2.

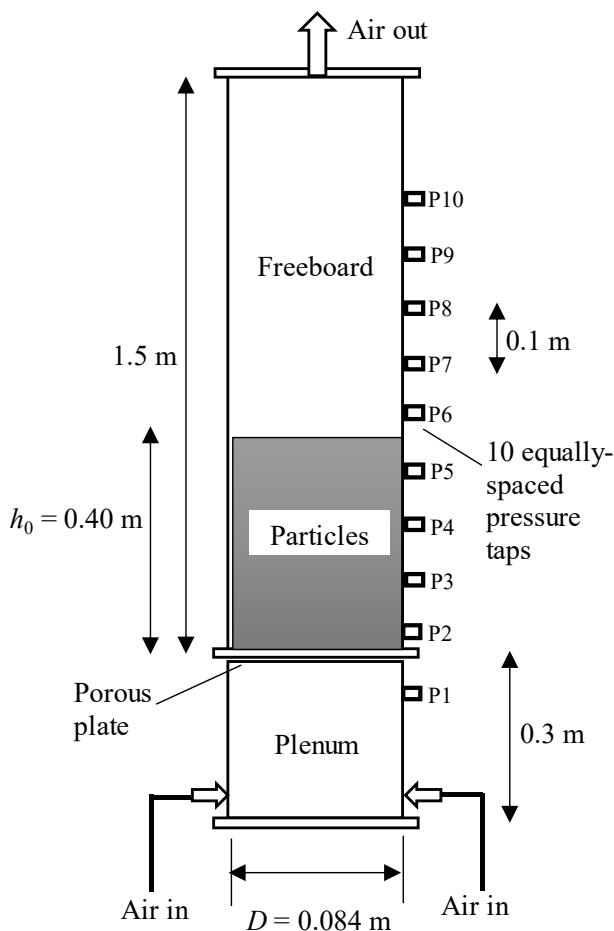


Figure 1. Physical dimensions of the fluidized bed column. Positions of pressure sensors P1 to P10 are indicated.

The experiments were conducted at increasing gas flow rate from 0.02 m/s to 0.40 m/s. For each volumetric airflow rate, the pressure data were acquired over 60 s. Two cases were demonstrated to compare the influence of gas distributor plate on the hydrodynamics of the bed. In one case, the porous plate is fitted while air is allowed into the bed across the plate. In the second case, the plate was removed for the same range of gas velocities. With

porous plate removed, the bed material falls down into plenum, and extra bed material was added to compensate the dead zone below air inlet. With the porous plate in place, the pressure drops across the bed at two different positions were computed from $\frac{\Delta P}{\Delta L} = (P2 - P4)/L$ and $\frac{\Delta P}{\Delta L} = (P4 - P6)/L$, where $L = 0.02$ m. With no porous plate, the pressure drops were obtained from $\frac{\Delta P}{\Delta L} = (P1 - P3)/L$ and $\frac{\Delta P}{\Delta L} = (P3 - P5)/L$.

Table 1. Characterization of bed material.

Sand particles	
Sauter particle diameter	484 μm
Sphericity	0.75
Particle density	2650 kg/m^3
Bulk density	1444 kg/m^3
Calculated solids void fraction	0.545

Table 2. Experimental conditions.

Fluid	Compressed air
Fluid temperature	Ambient
Fluidizing air velocity	0.02 to 0.40 m/s
Initial bed height h_0	0.40 m
Outlet pressure	Atmospheric

2.2 CFD Simulation software

The CFD simulations are performed using the MFIX CFD-software (version 2016.1) from The National Energy Technology Laboratory (NETL)¹. The theory used for simulations is outlined by Syamlal et al. (Syamlal *et al.*, 1993) and a brief overview of MFIX equations is given by Li et al. (Li *et al.*, 2010).

The interaction of solids and fluid has been simulated using the two-fluid-model (TFM), which is an Euler-Euler fluid-particle multiphase transport model. For fluidized beds, the Eulerian formulation of the solid phase conservation equations is favorable due to the high solids loading occurring in such systems. The solid phase is treated as a continuous fluid although it actually consists of many individual particles. Thus, the tangential and normal forces are represented by a solids viscosity and the so-called solid pressure. Furthermore, a model for the drag force between the phases is required. One disadvantage of the Eulerian approach is the necessity to use a separate set of conservation equations for each size and density class of particles.

¹ <https://mfix.netl.doe.gov/>

2.3 Particle diameter in fluid dynamics

Fluid-particles drag forces mostly characterize the fluidized beds. The drag forces act against the forces due to the weight of solid particles in the bed. At the minimum fluidization condition, these two opposite forces become equal. This indicates that the bed bulk density (product of material density and the solids volume fraction), is a key input parameter for the simulation. Since the fluid-particles drag forces depends on the particle size, particle size distribution and particle shape, these parameters play also key roles in the simulation inputs. Most models for calculating drag forces assume spherical and mono-sized particles, thus it is necessary to apply some corrections factors to account for differences in simulation model against the real situation when the non-spherical particles are used. In general, this can be achieved by replacing the nominal particle diameter with an equivalent diameter that results in the correct forces calculated.

The Sauter mean diameter, D_{sd} , is commonly used to characterize particles having the same volume/surface area ratio as a particle of interest. In its simplest form, it can be expressed as:

$$D_{sd} = 6 \frac{V_p}{A_p} \quad (1)$$

where V_p and A_p are the volume and the surface area of the particle, respectively. Several measurements are usually carried out to obtain the average value.

Another property characterizing particles is the sphericity, which measures the extent a single particle resembles a perfect spherical particle. As defined by Wadell (Wadell, 1935), it is the ratio of the surface area of a sphere (with the same volume as the given particle) to the surface area of the particle:

$$\phi = \frac{\pi^{1/3}(6V_p)^{2/3}}{A_p} \quad (2)$$

Another definition is given by Krumbein (Krumbein, 1941) as:

$$\phi = \sqrt[3]{\frac{V_p}{V_c}} \approx \frac{D_p}{D_c} \quad (3)$$

where V_c and D_c are the volume and the diameter of a circumscribed sphere around the particle, respectively, and D_p is the nominal diameter of the particle. Nominal diameter of particle can be considered as the average diameter of sieve used and the circumscribed sphere diameter can be obtained from optical measurements.

The effect of broad or narrow particle size distribution (PSD) on the decision made on which equivalent diameter results in the correct forces, is not well described in literature. Furthermore, the outcome of a measurement of PSD depends on the method used (optical measurements, sieving, laser diffraction etc). For this study, the equivalent diameter, D_{eq} used in the simulation is obtained by trials based on computation of

minimum fluidization velocity and comparing the results with the experimental data. The trial simulation is initiated with the effective particle diameter ϕD_p , which corresponds to the equivalent diameter where $a = 1$ as given in Equation (4).

$$D_{eq} = \phi^a \times D_p \quad (4)$$

2.4 Drag models

The drag models considered in this study are those given by Syamlal and O'Brien (Syamlal & O'Brien, 1988), Gidaspow (Ding & Gidaspow, 1990), and Beetstra et al. (BVK model) (Beetstra *et al.*, 2007). The implementation in MFiX software requires no further input for the Gidaspow and BVK models. The MFiX implementation of the Syamlal and O'Brien drag model requires two parameters to fit the experimental data or calculated value for minimum fluidization velocity. A calculation sheet for this parameter fitting is supplied at the NETL web site (Syamlal). The parameters used for this work are given in Table 3.

Table 3. Syamlal and O'Brien drag model parameters

Particle diameter	Parameter c1	Parameter d1
484 μm	0.299	8.70669
363 μm	0.428	6.50441

2.5 CFD Simulation Parameters

The simulation parameters are listed in Table 4.

Table 4. CFD simulation parameters.

<i>Materials:</i>	
Fluid: Air, density = 0.001178 g/cm ³	
Particles: See Table 1	
<i>TFM parameters:</i>	
Coefficient of Restitution	
Particle-Particle	0.95
Particle-Wall	1.0
Specularity	0.6
Friction Coefficient	0.5
Friction Angle	60.0
Minimum Solid Fraction	0.5
Packed Void Fraction	0.455
<i>Simulation Grid = 2D Cartesian:</i>	
X Length = 8.4 cm	10 X-Cells á 0.84 cm
Y Length = 150 cm	100 Y-Cells á 1.5 cm
<i>Boundary Conditions:</i>	
Mass Inflow bottom at 300K	
Gas velocities varied	
Pressure outflow top at 101325 Ba	

3 Results and discussion

The minimum gas velocity for fluidization is obtained from the variation of the calculated bed pressure drops with gas velocities. Typically, the pressure drop over the bed is linearly increasing with gas velocity for gas velocities below the minimum fluidization velocity, and invariant of gas velocities above the minimum fluidization velocity. Bubbles rising in the fluidized bed results in fluctuations of the pressure drops. The reported data for pressure drops are timed-average values taken over the last 1.5 min of the 4 min simulation time. The minimum fluidization velocity is obtained at the point of intersection between the lines fitting the data within the fixed and fluidized states.

The rate of bubble rise and eruption from the bed is visible through the increase in pressure fluctuations, and based on this the bubble frequency is calculated for different velocities. Similarly, the time profile of void fraction at a fixed height also gives information about bubble frequency and size.

In the simulation, the total bed height at a given gas velocity is deduced from the pressure profile along the vertical positions in the column. The center of the lowest computational cell where there is no further increase in pressure is used as the top of bed; see Figure 2 for an example. This method results in a small systematic error due to a limited cell resolution used for the calculation. The error is cancelled out when calculating the bed height increase.

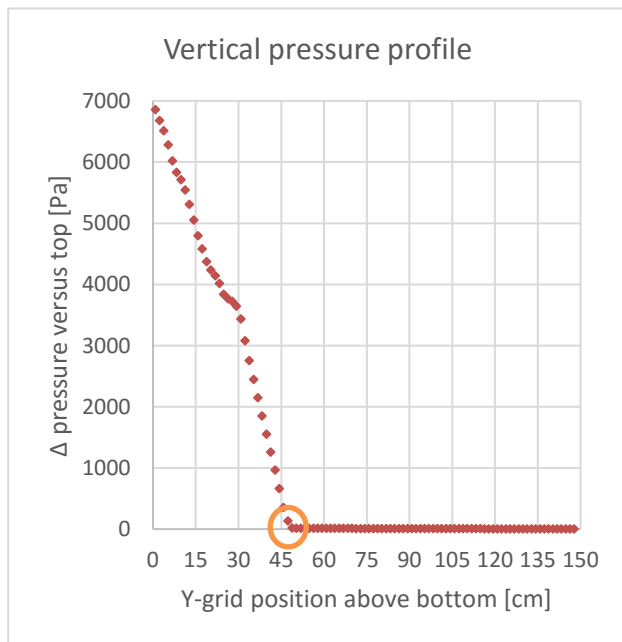


Figure 2 Vertical pressure profile taken for X-grid = 4.2 cm (middle). The top of bed is marked with the circle. This curve shows results from Gidaspow drag model simulation for 0.21 m/s superficial gas velocity (319 μm particles); see Figure 14. The pressure profile also shows an evidence of bubble flow at height = 28 cm.

3.1 Cold bed results

The experimental bed pressure drops at different gas velocities are shown in Figure 3. Results from similar runs with the porous distributor plate removed are also shown. From these results, the minimum fluidization velocity of the sand particles is determined as 0.156 m/s for the case with gas distributor. For the case where there is no gas distributor, the figure shows that a slightly higher minimum fluidization velocity could be obtained. The results also show that the bed pressure drop is lower without a gas distributor for the same superficial air velocity. There are also variations in the maximum pressure drops in both cases compared with the static pressure due to weight of the bed.

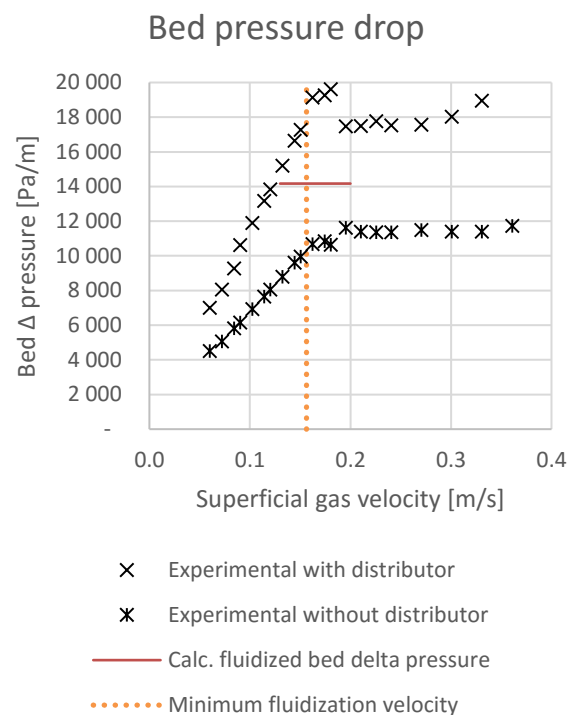


Figure 3. Experimental bed pressure drop. The red line shows static pressure calculated from weight of bed material.

3.2 CFD Simulation Results

Initial simulations were performed using the sphericity corrected nominal diameter, that is for $a = 1$ in Equation (4). Results from simulations are shown in Figure 4 through Figure 6 for the different drag models. The simulated minimum fluidization velocity based on Syamlal & O'Brien drag model agrees very well with the experimental result as expected since the model parameters have been fitted. Moreover, the agreement between the simulated result and the experimental data is better using the BVK drag model compared with the Gidaspow drag model. For the bed height increase, there is a significant variation in the results obtained from the different drag models.

It should be noted that for further comparison of the drag models, each drag model is modified by incorporating the effect of sphericity in the nominal particle diameter as described in Equation (4). The value of the parameter a for each drag model is obtained by trial based on the simulated minimum fluidization velocity compared with the experimental data. Linear interpolation is also employed to reduce the number of trial simulations. The results are summarized in Table 5 and Figure 7. When the optimum particle diameter are used, all the drag models give the same minimum fluidization velocity as the experiment.

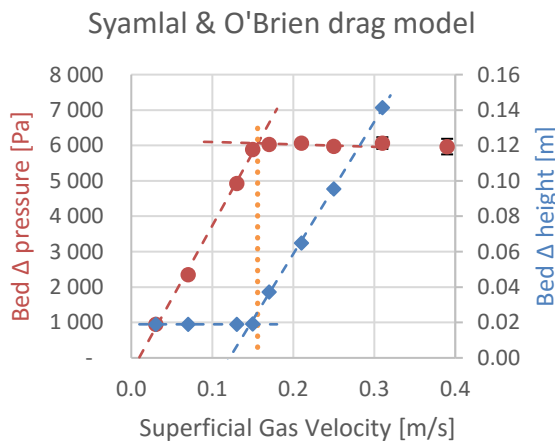


Figure 4. Bed pressure drop (red-left) and bed height increase (blue-right) from simulation using Syamlal & O'Brien drag model, particle diameter $363 \mu\text{m}$. Error bars indicate variation due to bubbles. Dotted line marks the experimental minimum fluidization velocity.

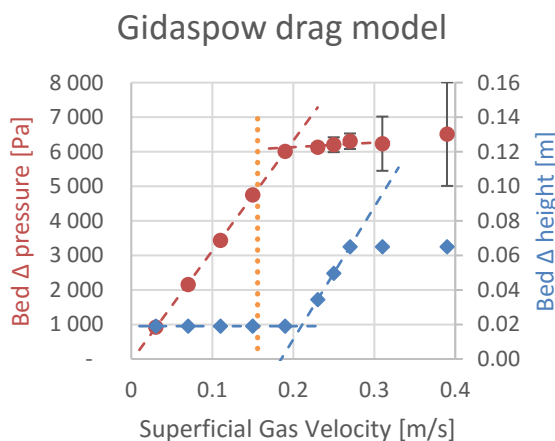


Figure 5. Bed pressure drop (red-left) and bed height increase (blue-right) from simulation using Gidaspow drag model, particle diameter $363 \mu\text{m}$. Error bars indicate variation due to bubbles. Dotted line marks the experimental minimum fluidization velocity.

BVK drag model

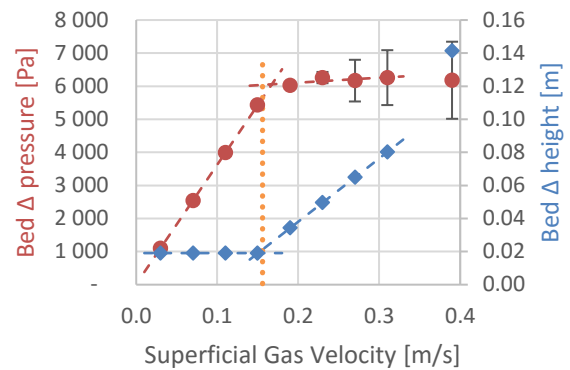


Figure 6. Bed pressure drop (red-left) and bed height increase (blue-right) from simulation using BVK drag model, particle diameter $363 \mu\text{m}$. Error bars indicate variation due to bubbles. Dotted line marks the experimental minimum fluidization velocity.

Table 5. Minimum fluidization velocity from simulations using various particle diameters and drag models. The experimentally determined minimum fluidization velocity is 0.156 m/s . The value a refers to Equation (4).

Particle diameter	Syamlal & O'Brien (fitted)	Gidaspow	BVK
$242 \mu\text{m}$		0.076 m/s	0.075 m/s
$363 \mu\text{m}$	0.156 m/s	0.200 m/s	0.167 m/s
$484 \mu\text{m}$	0.153 m/s	0.330 m/s	0.350 m/s
Optimum diameter from interpolation		$319 \mu\text{m}$ $a = 1.45$	$358 \mu\text{m}$ $a = 1.05$

3.3 Bed behavior

The simulated bed heights at different gas velocities are compared for different drag models as shown in Figure 8. The optimum equivalent diameters from Table 5 are used for these simulations. The two different particle diameters using Syamlal & O'Brien drag model show identical bed behavior: Steady increase in the bed height and particulate fluidization above minimum fluidization velocity. No evidence of bubble flow using this model.

Using the Gidaspow and BVK drag models, the bed shows a similar behavior. There is a strong evidence of a well-defined bubble formation and less defined bed height. The bed height obtained from these models are smaller than those from the Syamlal & O'Brien drag model for the same gas velocity above the minimum fluidization velocity. However, the results from the BVK model are slightly lower when compared with those from the Gidaspow model. The two sets of simulations using BVK drag model with two close

particle diameters do not overlap, indicating strong sensitivity of this model with particle diameter.

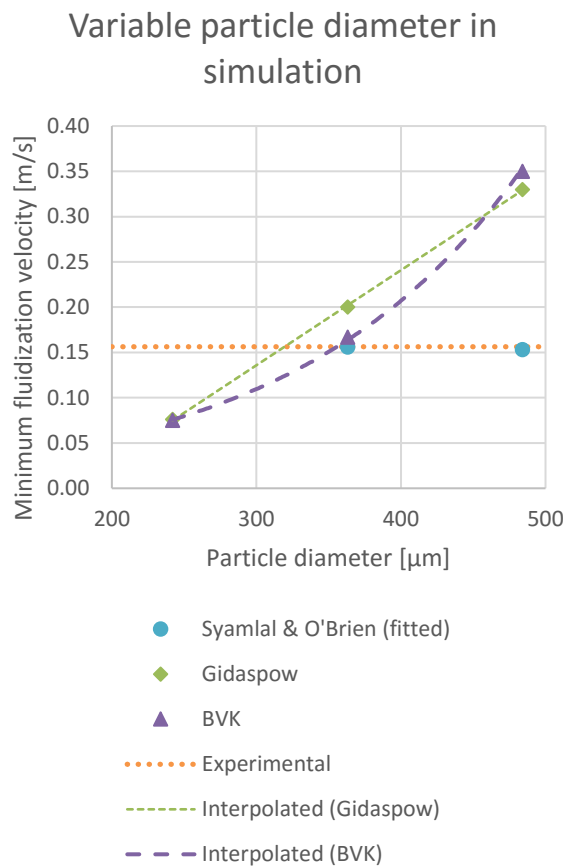


Figure 7. Minimum fluidization velocity from simulations using particle diameters 242, 363 and 484 μm .

Figure 9 shows the simulated pressure drops using different drag models as compared with the experimental data. As the superficial gas velocity is increased, the bed pressure drop per unit length increases up to the minimum fluidization velocity. As can be seen, the simulation results lie between the two sets of experimental data. The experimental data show a substantial effect of using a distributor plate. The lower pressure drop without distributor plate might be explained from the channeling effects where only a part of the bed is lifted upon fluidization. The red line in Figure 9 corresponds to the calculated static pressure from lifting the weight of the bed, which is independent on bed height though. Theoretically, this corresponds to the bed pressure drop at the point of minimum fluidization velocity.

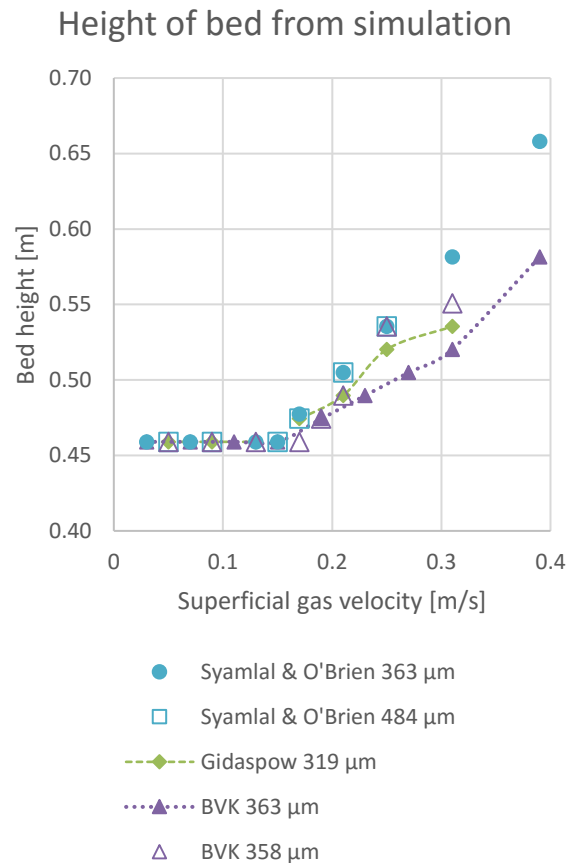


Figure 8. Height of bed from simulation.

Slightly above the point of minimum fluidization velocity, the bed pressure drop decreases and then remains constant. This effect is also accompanied with a slight bed expansion to allow passage of bubbles. As the bed remains in bubbling regime, the bed pressure drop remains constant. This behavior is also captured with the simulation results.

In (Agu *et al.*, 2017), the solids fraction distribution was measured at different gas velocities in a set up equipped with a dual-plane Electrical Capacitance Tomography (ECT) sensors with the 484 μm sand particles as the bed material. Figure 10 and Figure 11 show the ECT images of the solid fraction in the bed, which are stacked in time for 10 s of the airflow at 0.25 and 0.31 m/s, respectively. The number of bubbles passing through the bed per unit time can easily be seen. The bubbles coalesce into single larger bubbles as they rise up the bed.

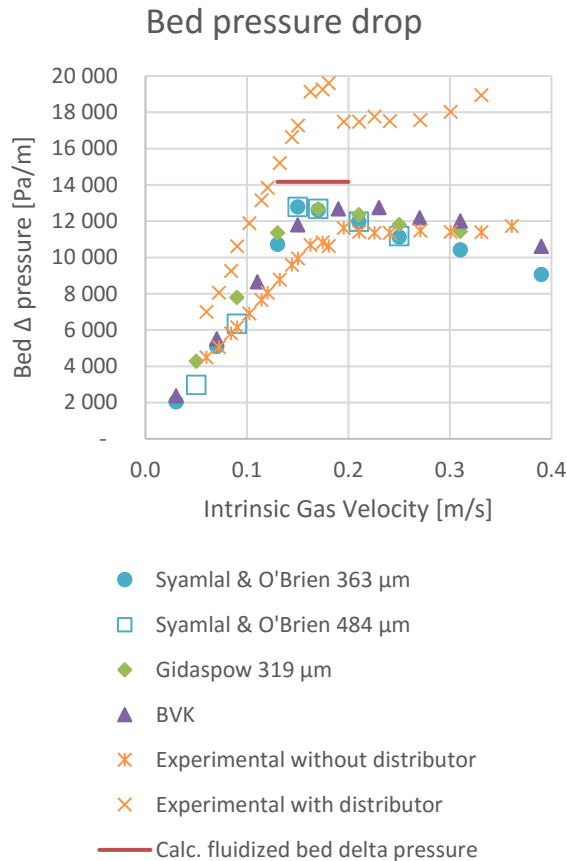


Figure 9. Bed pressure drop per unit bed length, experimental and simulated.

Variations of simulated pressure at the bottom of the bed against the time are shown in Figure 12 through Figure 17. The variations of void fraction at the same position in the bed are also shown for comparison.

Table 6 compares the computed bubble frequencies based on the simulation using the Gidaspow and BVK drag models and with those obtained from the experimental results shown in Figure 10 and Figure 11. For the Syamlal & O'Brien drag model, no bubble flow is predicted. As can be seen, the bubble frequencies from the Gidaspow and BVK are fairly in agreement with the experimental data.

Table 6. Frequency of bubbles escaping the bed.

Superficial gas velocity	Gidaspow drag model	BVK drag model	Experimental (28.7 cm from bottom)
0.19 m/s	5 – 6 s ⁻¹	5 – 6 s ⁻¹	
0.23 – 0.31 m/s	2.2 – 2.6 s ⁻¹	2.2 – 2.6 s ⁻¹	
0.25 m/s			1.5 s ⁻¹
0.31 m/s			1.1 s ⁻¹

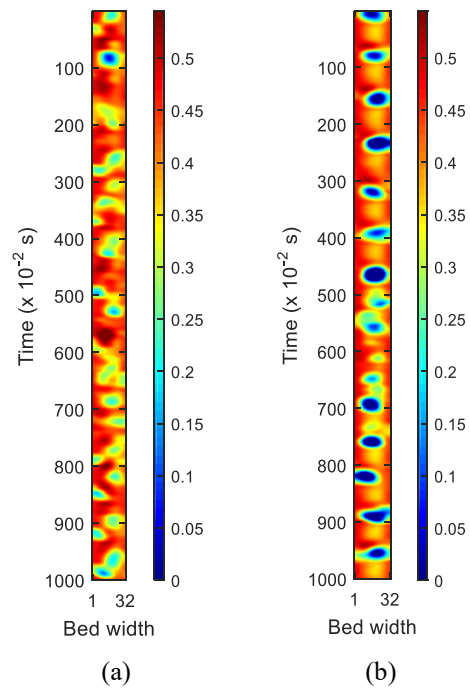


Figure 10. ECT images for 10 s of the flow in bed of 483 μm sand particles at 25 cm/s: (a) lower plane: 15.7 cm from the bottom (b) upper plane: 28.7 cm from bottom. Time axis increases from top to bottom.

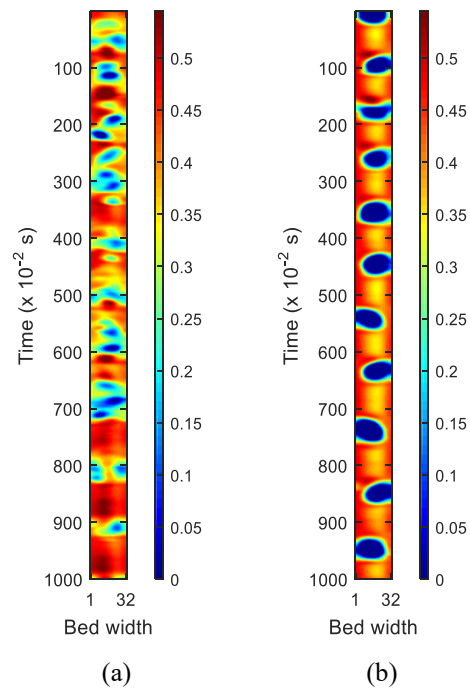


Figure 11. ECT images for 10 s of the flow in bed of 483 μm sand particles at 31 cm/s: (a) lower plane: 15.7 cm from the bottom (b) upper plane: 28.7 cm from bottom. Time axis increases from top to bottom.

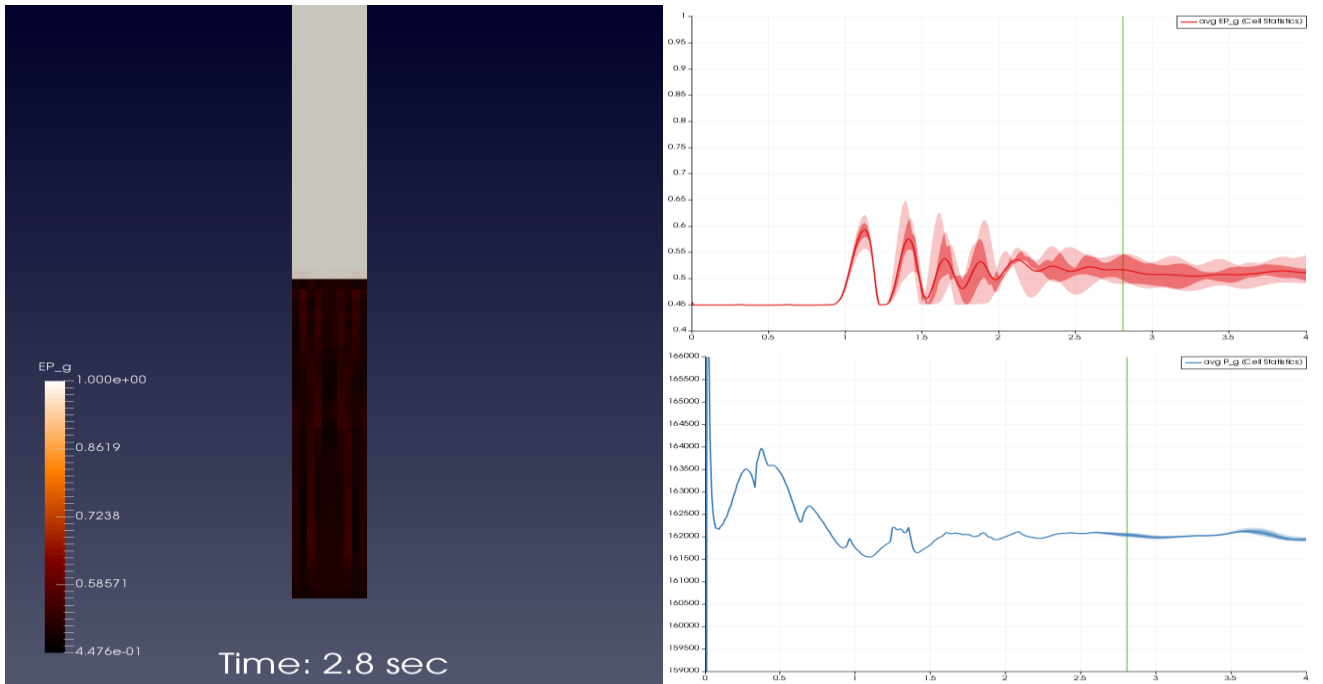


Figure 12. Syamlal & O'Brien drag model simulation for 0.21 m/s intrinsic gas velocity (363 μm particles). Top right shows time profile for void fraction at initial top of bed (scale 0.4 to 1.0). Bottom right shows time profile for pressure at bottom of bed (scale Δ pressure range 700 Pa).

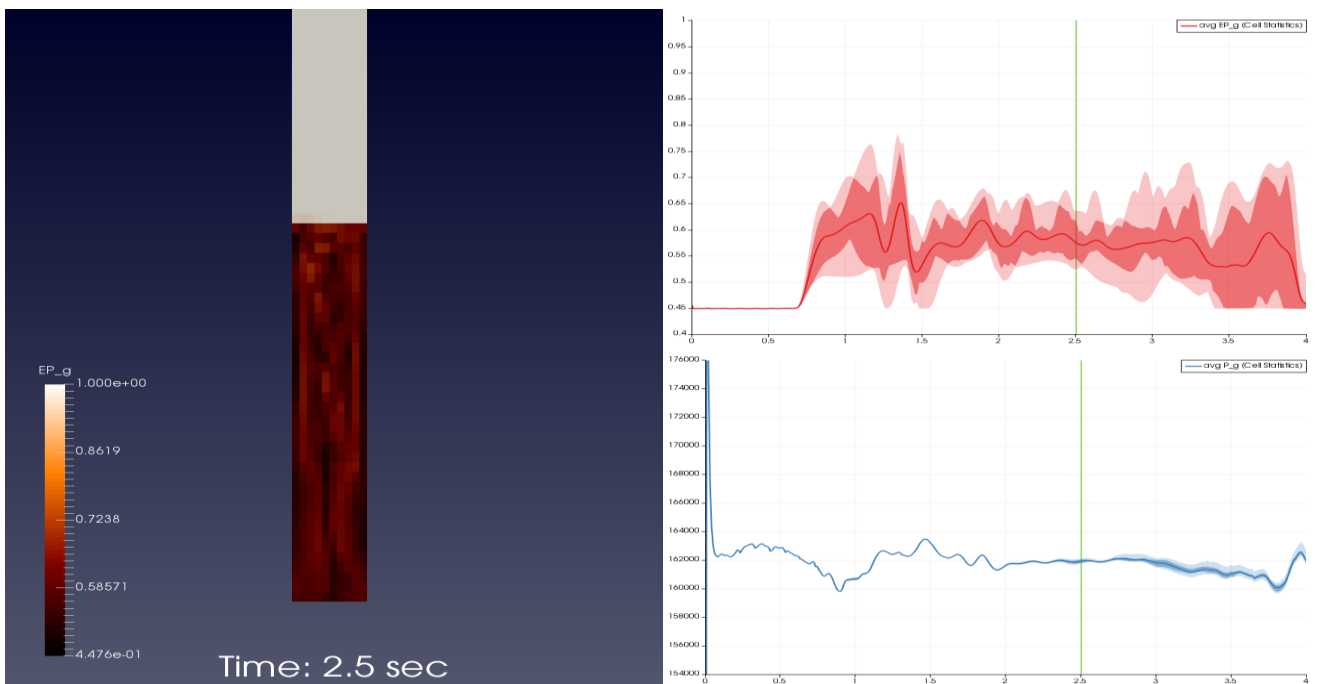


Figure 13. Syamlal & O'Brien drag model simulation for 0.31 m/s intrinsic gas velocity (363 μm particles). Top right shows time profile for void fraction at top of bed (scale 0.4 to 1.0). Bottom right shows time profile for pressure at bottom of bed (scale Δ pressure range 2200 Pa). More channeling evolved at later simulation times.

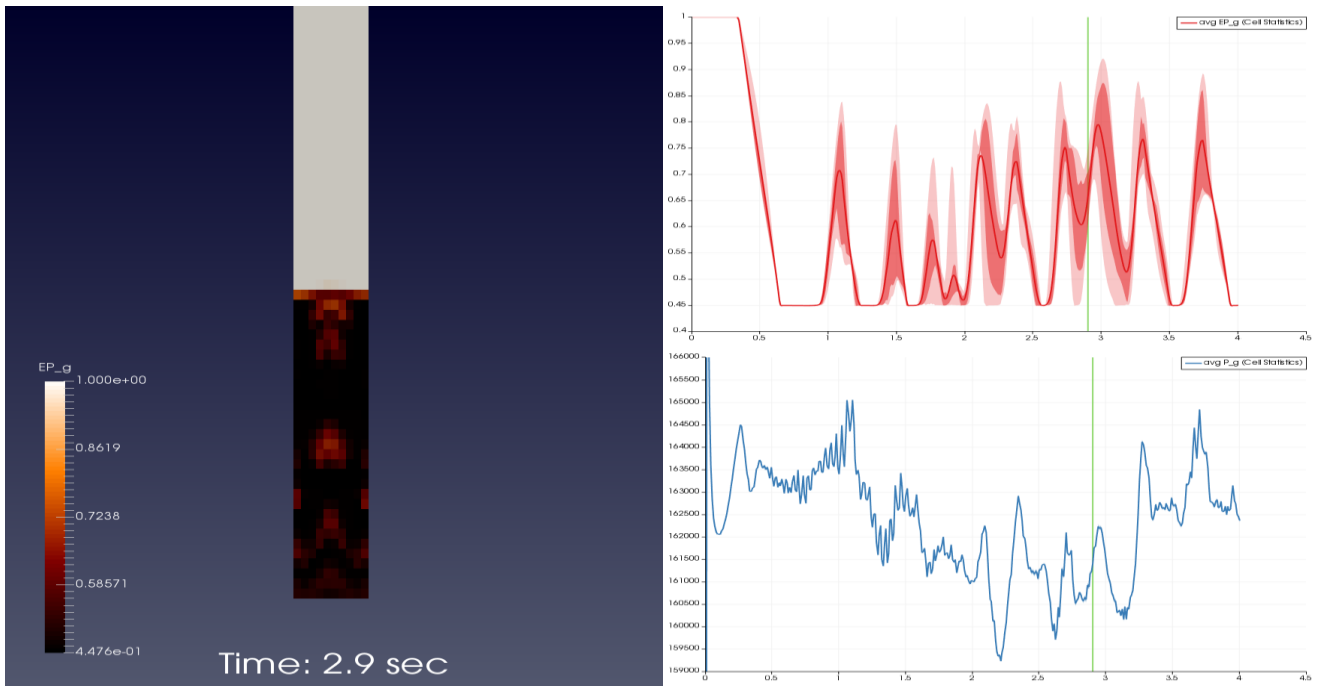


Figure 14. Gidaspow drag model simulation for 0.21 m/s intrinsic gas velocity (319 μm particles). Top right shows time profile for void fraction at top of bed. Bottom right shows time profile for pressure at bottom of bed (scale Δ pressure range 700 Pa).

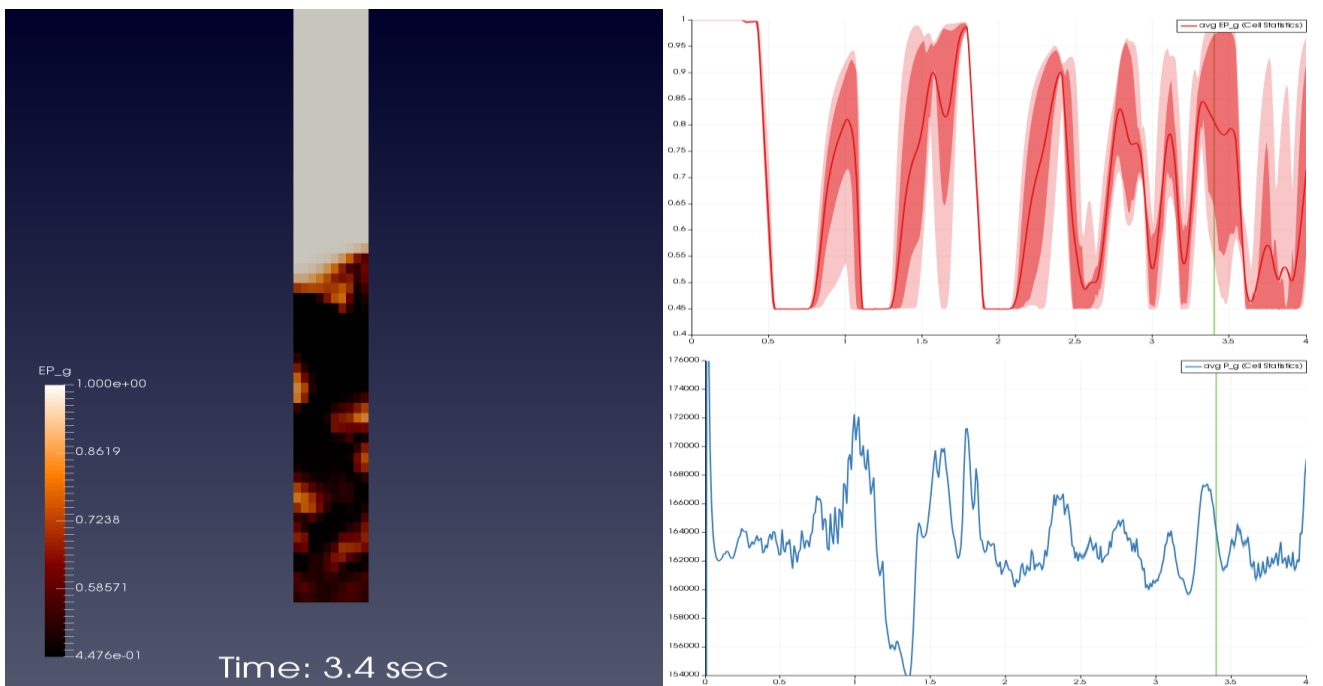


Figure 15. Gidaspow drag model simulation for 0.31 m/s intrinsic gas velocity (319 μm particles). Top right shows time profile for void fraction at top of bed (scale 0.4 to 1.0). Bottom right shows time profile for pressure at bottom of bed (scale Δ pressure range 2200 Pa).

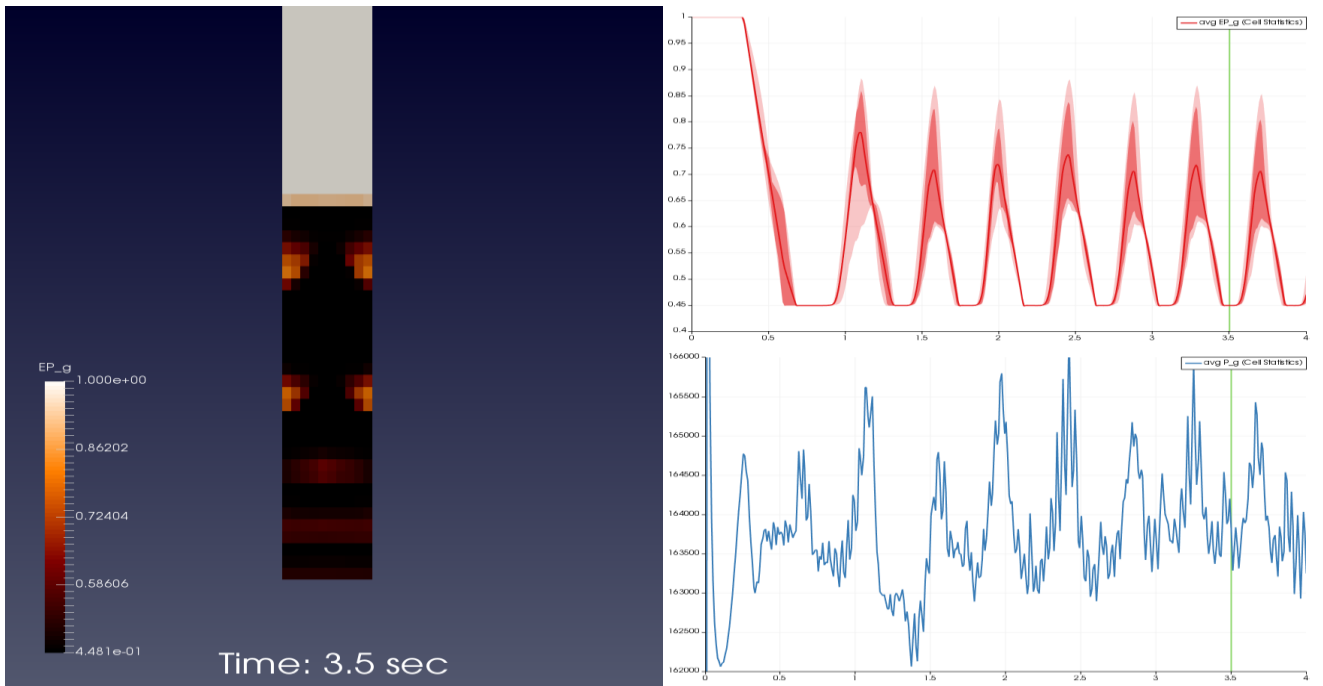


Figure 16. BVK drag model simulation for 0.23 m/s intrinsic gas velocity. Top right shows time profile for void fraction at top of bed (scale 0.4 to 1.0). Bottom right shows time profile for pressure at bottom of bed (scale Δ pressure range 400 Pa).

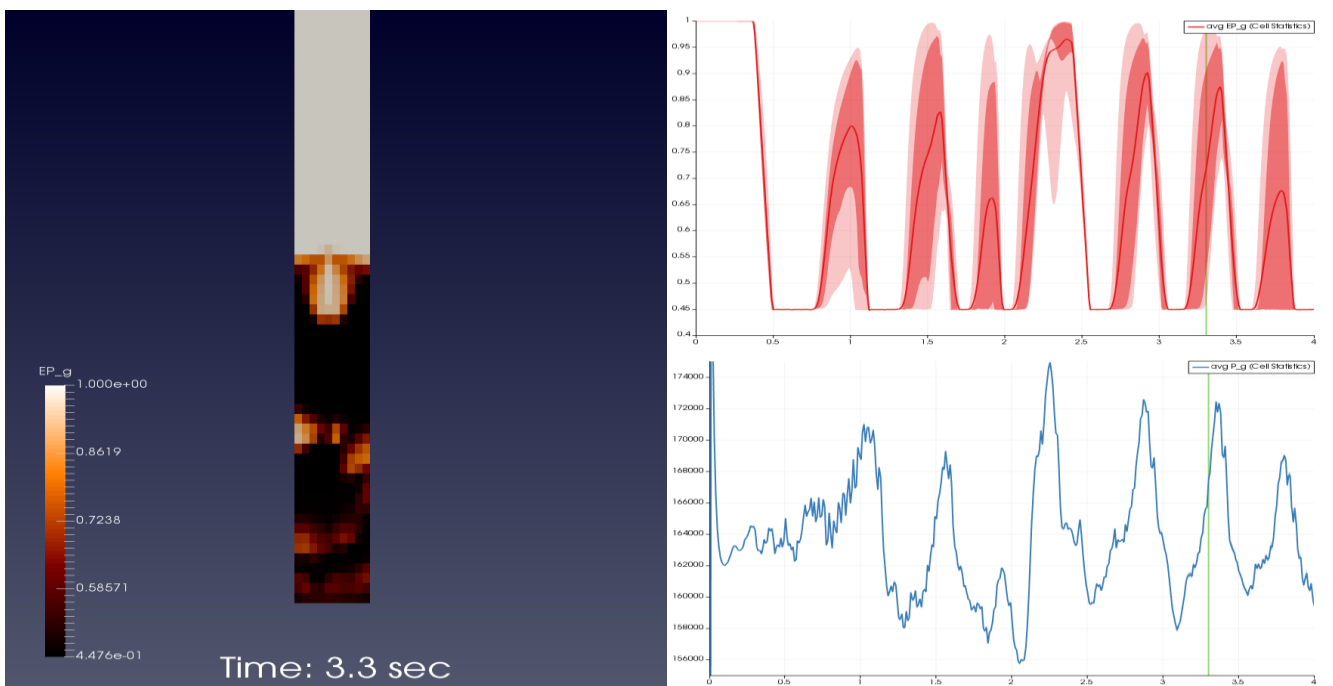


Figure 17. BVK drag model simulation for 0.31 m/s intrinsic gas velocity. Top right shows time profile for void fraction at top of bed (scale 0.4 to 1.0). Bottom right shows time profile for pressure at bottom of bed (scale Δ pressure range 2000 Pa).

4 Conclusions

The Syamlal & O'Brien drag model parameters are fitted versus the experimental minimum fluidization velocity and thereby reproduce this bed behavior independent from choice of particle diameter used in simulation. This allows for the number of particles in simulation being close to the actual number of particles used experimentally. The bubbling bed behavior was not captured.

The BVK drag model reproduced the experimental minimum fluidization velocity when sphericity corrected diameter of particles were used. On the other hand, simulations using alternative particle diameters showed rather high sensitivity to simulation particle diameter, and verification versus experimental data is recommended.

The Gidaspow drag model resulted in a rather large deviation from experimental results when the sphericity corrected diameter was used. On the other hand, optimizing the simulation particle diameter resulted in bed behavior close to using the BVK drag model. Both models resulted in similar bed height increase and bubble size and frequency. There was a significant deviation from experimental results on bed height increase (unit length pressure drop) and bubble frequency for both models.

References

- Agu C. E., Tokheim L.-A. and Halvorsen B. M. (2017, May). *Measurement Of Bubble Properties In A Fluidized Bed Using Electrical Capacitance Tomography*. Paper presented at the 12th International Conference on Circulating Fluidized Bed CFB-12, Krakow, Poland.
- Beetstra R., van der Hoef M. A. and Kuipers J. A. M. (2007). Numerical study of segregation using a new drag force correlation for polydisperse systems derived from lattice-Boltzmann simulations. *Chemical Engineering Science*, 62(1–2), 246-255. doi:<http://dx.doi.org/10.1016/j.ces.2006.08.054>
- Ding J. and Gidaspow D. (1990). A bubbling fluidization model using kinetic theory of granular flow. *AIChE Journal*, 36(4), 523-538. doi:10.1002/aic.690360404
- Krumbein W. C. (1941). Measurement and Geological Significance of Shape and Roundness of Sedimentary Particles. *Journal of Sedimentary Petrology*, 11(2), 64-72.
- Li T., Grace J. and Bi X. (2010). Study of wall boundary condition in numerical simulations of bubbling fluidized beds. *Powder Technology*, 203(3), 447-457. doi:<http://dx.doi.org/10.1016/j.powtec.2010.06.005>
- Syamlal M. Determining Drag Coefficients to Match Umf [Excel calculation sheet]: Fluent, Inc. Retrieved from <https://mfix.netl.doe.gov/mfix/mfix-documentation/>
- Syamlal M. and O'Brien T. J. (1988). Simulation of granular layer inversion in liquid fluidized beds. *International Journal of Multiphase Flow*, 14(4), 473-481. doi:[http://dx.doi.org/10.1016/0301-9322\(88\)90023-7](http://dx.doi.org/10.1016/0301-9322(88)90023-7)
- Syamlal M., Rogers W. and O'Brien T. J. (1993). *MFIX documentation theory guide*. Retrieved from <http://www.osti.gov/scitech/servlets/purl/10145548>
- Wadell H. (1935). Volume, Shape, and Roundness of Quartz Particles. *The Journal of Geology*, 43(3), 250-280. doi:10.1086/624298

Passivity-Based Analysis of Biochemical Networks Displaying Homeostasis

Daniel M. Tveit Kristian Thorsen

Department of Electrical Engineering and Computer Science, University of Stavanger, Norway,
{daniel.m.tveit,kristian.thorsen}@uis.no

Abstract

Homeostasis refers to the ability of organisms and cells to maintain a stable internal environment even in the presence of a changing external environment. On the cellular level many compounds such as ions, pH, proteins, and transcription factors have been shown to be tightly regulated, and mathematical models of biochemical networks play a major role in elucidating the mechanisms behind this behaviour. Of particular interest is the control theoretic properties of these models, e.g. stability and robustness. The simplest models consist of two components, a controlled compound and a controller compound. We have previously explored how signalling between these two compounds can be arranged in order for the network to display homeostasis, and have constructed a class of eight two-component reaction kinetic networks with negative feedback that shows set-point tracking and disturbance rejection properties. Here, we take a closer look at the stability and robust control inherent to this class of systems. We show how these systems can be described as negative feedback connections of two non-linear sub-systems, and show that both sub-systems are output strictly passive and zero-state detectable. Using a passivity-based approach, we show that all eight systems in this class of two-component networks are asymptotically stable.

Keywords: Passivity, homeostasis, adaptation, stability, robust control, integral control, negative feedback

1 Introduction

Control theoretic methods are useful when uncovering the mechanism behind cellular control processes. Especially properties such as stability and robust control are of interest. One structure with these properties is the negative feedback connection, which is employed in several biochemical processes, such as the regulation of enzyme synthesis and activity (Keener and Sneyd, 2009; Tyson and Othmer, 1978). Other more complicated control systems, such as the control of calcium in yeast cells, have also been analysed in this manner (Liu, 2012). We have previously investigated a class of simple two-component biochemical networks displaying homeostasis. These networks have been used in modelling ionic homeostasis in enterocytes (Thorsen et al., 2014), the development of biochemical

controllers with robust control to perturbations changing rapidly in time (Fjeld et al., 2017), and developing yeast cells with an increased tolerance to high copper concentrations (Thorsen et al., 2016a). The networks consist of a controlled compound x_1 and a controller compound x_2 , and through certain signalling reactions between these two compounds, the systems form negative feedback connections with integral action, giving robust control of x_1 . We have identified eight such two-component systems, termed controller motifs (Drengstig et al., 2012). Figure 1 shows the structure of these controller motifs. For the class of two-component systems considered here, x_1 acts on either the synthesis or the degradation of x_2 , and x_2 acts on either the synthesis or the degradation of x_1 . This gives eight controller motifs with two components, each acting on the other through a single signalling reaction.

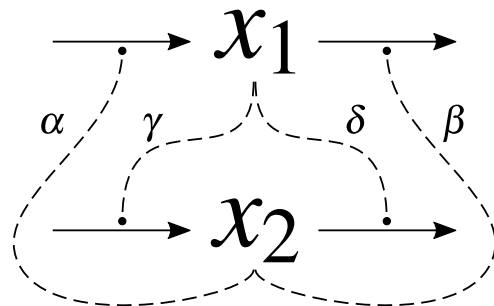


Figure 1. The controller motifs are formed by two compounds, x_1 and x_2 , with signalling reactions α , β , γ , δ between them. For each controller motif, there is one signalling reaction from x_1 acting on x_2 , and one signalling reaction from x_2 acting on x_1 . These signalling reactions form a negative feedback connection with the two compounds. There are in total eight such controller motifs.

In general, the controller motifs take the form

$$\dot{x}_1 = k_{s,1} \cdot \alpha(x_2) - f_{d,1}(x_1) \cdot \beta(x_2) \quad (1)$$

$$\dot{x}_2 = k_{s,2} \cdot \gamma(x_1) - f_{d,2}(x_2) \cdot \delta(x_1) \quad (2)$$

where $k_{s,i}$ are positive rate constants determining the basal synthesis of x_i , the functions $f_{d,i}$ determine the degradation rate of x_i following Michaelis–Menten kinetics (Cornish-Bowden, 2012), and α , β , γ , δ are signalling functions between the two chemical compounds. Only one of the signalling functions α and β , and one of γ and δ , will be non-constant for a given controller motif.

The Michaelis–Menten equation models the reaction rate of a compound x_i by an enzyme reaction

$$f_{d,i}(x_i) = \frac{k_{d,i} \cdot x_i}{K_{M,i} + x_i} \quad (3)$$

where $f_{d,i}$ is the reaction rate, $k_{d,i}$ is a positive constant determining the maximal reaction rate, and $K_{M,i}$ is a positive constant called the Michaelis constant (Cornish-Bowden, 2012).

The signalling functions α , β , γ , δ can either be activating or inhibiting. Activating signalling follow the expression for mixed activation (Cornish-Bowden, 2012)

$$f_{act}(x_i) = \frac{x_i}{K_{A,i} + x_i} \quad (4)$$

where the activation of some reaction is determined by the level of x_i , and $K_{A,i}$ is a positive constant for the activation reaction. Inhibiting signalling follow the expression for mixed inhibition (Cornish-Bowden, 2012)

$$f_{inh}(x_i) = \frac{K_{I,i}}{K_{I,i} + x_i} \quad (5)$$

where the amount of inhibition is determined by the level of x_i , and $K_{I,i}$ is a positive constant for the inhibition reaction.

2 Stability

To show asymptotic stability of the controller motifs, we first perform a change of variables, $z_1 = x_1 - x_1^*$ and $z_2 = x_2 - x_2^*$, where (x_1^*, x_2^*) is the equilibrium point of the system. The states x_1 and x_2 represent physical concentrations of compounds. Therefore, a global result corresponds to positive values of the states and the equilibrium point. The change of variables moves the equilibrium point to the origin. Using the fact that $k_{s,1} \cdot \alpha(x_2^*) = f_{d,1}(x_1^*) \cdot \beta(x_2^*)$ and $k_{s,2} \cdot \gamma(x_1^*) = f_{d,2}(x_2^*) \cdot \delta(x_1^*)$, the system is rewritten to the form

$$\dot{z}_1 = -f_1(z_1) + h_{2,\alpha}(z_2) - g_1(z_1) \cdot h_{2,\beta}(z_2) \quad (6)$$

$$\dot{z}_2 = -f_2(z_2) + h_{1,\gamma}(z_1) - g_2(z_2) \cdot h_{1,\delta}(z_1) \quad (7)$$

where these new functions are defined as follows

$$f_1(z_1) = f_{d,1}(z_1 + x_1^*) \cdot \beta(x_2^*) - f_{d,1}(x_1^*) \cdot \beta(x_2^*) \quad (8)$$

$$f_2(z_2) = f_{d,2}(z_2 + x_2^*) \cdot \delta(x_1^*) - f_{d,2}(x_2^*) \cdot \delta(x_1^*) \quad (9)$$

$$g_1(z_1) = f_{d,1}(z_1 + x_1^*) \quad (10)$$

$$g_2(z_2) = f_{d,2}(z_2 + x_2^*) \quad (11)$$

$$h_{1,\gamma}(z_1) = k_{s,2} \cdot \gamma(z_1 + x_1^*) - k_{s,2} \cdot \gamma(x_1^*) \quad (12)$$

$$h_{1,\delta}(z_1) = \delta(z_1 + x_1^*) - \delta(x_1^*) \quad (13)$$

$$h_{2,\alpha}(z_2) = k_{s,1} \cdot \alpha(z_2 + x_2^*) - k_{s,1} \cdot \alpha(x_2^*) \quad (14)$$

$$h_{2,\beta}(z_2) = \beta(z_2 + x_2^*) - \beta(x_2^*) \quad (15)$$

The functions f_i and h_i are strictly increasing and satisfy $f_i(0) = h_i(0) = 0$ for the interval $(-x_i^*, \infty)$. The functions

$g_i > 0$ for the same interval. As noted earlier, only one of the signalling functions α and β , and one of γ and δ will be non-constant for a given controller motif. This means that only one of the output functions $h_{2,\alpha}$ and $h_{2,\beta}$, and one of $h_{1,\gamma}$ and $h_{1,\delta}$ will be non-zero. In addition, if the signalling functions $\alpha, \beta, \gamma, \delta$ are inhibiting instead of activating, the corresponding output functions h_i are defined to be negative. For example, the controller motif shown in Figure 2 has non-constant signalling functions β and δ , while $\alpha = \gamma = 1$. Therefore, the corresponding output functions $h_{2,\beta}$ and $h_{1,\delta}$ are non-zero, while $h_{2,\alpha} = h_{1,\gamma} = 0$. In addition, the signalling function δ is inhibiting, and the corresponding output function $h_{1,\delta}$ is defined to be negative.

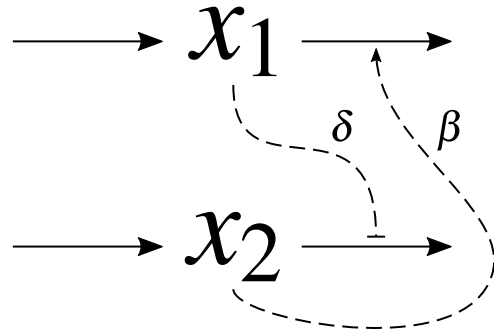


Figure 2. One of eight controller motifs that form a negative feedback connection. In this case, x_1 is acting on x_2 by inhibiting its degradation, and x_2 is acting on x_1 by activating its degradation.

The system equations for this controller motif are given by

$$\dot{x}_1 = k_{s,1} - f_{d,1}(x_1) \cdot \beta(x_2) = k_{s,1} - \frac{k_{d,1} \cdot x_1}{K_{M,1} + x_1} \cdot \frac{x_2}{K_{A,2} + x_2} \quad (16)$$

$$\dot{x}_2 = k_{s,2} - f_{d,2}(x_2) \cdot \delta(x_1) = k_{s,2} - \frac{k_{d,2} \cdot x_2}{K_{M,2} + x_2} \cdot \frac{K_{I,1}}{K_{I,1} + x_1} \quad (17)$$

and the transformed system equations are then

$$\dot{z}_1 = -f_1(z_1) - g_1(z_1) \cdot h_2(z_2) \quad (18)$$

$$\dot{z}_2 = -f_2(z_2) + g_2(z_2) \cdot h_1(z_1) \quad (19)$$

where $h_1 = h_{1,\delta}$ and $h_2 = h_{2,\beta}$.

To show that the controller motifs are asymptotically stable, we think of them as negative feedback connections of two sub-systems. In general, these sub-systems take the form

$$H_1 : \begin{cases} \dot{z}_1 = -f_1(z_1) + g_1(z_1) \cdot u_1 \\ y_1 = h_1(z_1) \end{cases} \quad (20)$$

$$H_2 : \begin{cases} \dot{z}_2 = -f_2(z_2) + g_2(z_2) \cdot u_2 \\ y_2 = h_2(z_2) \end{cases} \quad (21)$$

where the negative feedback connection can be formed either by having

$$u_1 = -y_2, \quad u_2 = y_1 \quad (22)$$

or by

$$u_1 = y_2, \quad u_2 = -y_1 \quad (23)$$

This corresponds to which of H_1 and H_2 is in the negative feedback.

2.1 Passivity

The next step is to determine if the two sub-systems are output strictly passive. This is done by using the storage function S_i for sub-system H_i

$$S_i = \int_0^{z_i} \frac{h_i(\sigma)}{g_i(\sigma)} d\sigma \quad (24)$$

where h_i and g_i are the functions in (20) and (21). The derivative of S along trajectories is then

$$\dot{S}_i = \frac{h_i(z_i)}{g_i(z_i)} \cdot \dot{z}_i = -f_i(z_i) \cdot \frac{h_i(z_i)}{g_i(z_i)} + u_i \cdot y_i \quad (25)$$

The sub-systems are output strictly passive if the following inequality is satisfied (Khalil, 2002; Sepulchre et al., 1997)

$$\dot{S}_i \leq -y_i \cdot \rho_i(y_i) + u_i \cdot y_i \quad (26)$$

where $y_i \cdot \rho_i(y_i) > 0 \forall y_i \neq 0$. Systems whose stored energy can only increase through the supply of an external source, are passive (Khalil, 2002). For inequality (26), the “energy” absorbed by the system, $u_i \cdot y_i$, is greater than the increase in stored “energy”, \dot{S}_i . In addition, the system has an “excess” of passivity from the term $y_i \cdot \rho(y_i)$. For the controller motifs, we choose $y_i \cdot \rho_i(y_i) = p_i \cdot y_i^2$, where p_i is a positive constant. Inequality (26) is then satisfied by choosing p_i such that

$$0 < p_i \leq \frac{f_i(z_i)}{h_i(z_i) \cdot g_i(z_i)} \quad (27)$$

for the interval $(-x_i^*, \infty)$. For the same interval, the right-hand side expression can be shown to be greater than zero, and either strictly increasing, or strictly decreasing. Inequality (27) is then satisfied by finding p_i as the lower bound of the right-hand side expression. The lower bound is given by the minimum value of the right-hand side expression at the limits $z_i \rightarrow -x_i^*$ and $z_i \rightarrow \infty$. Therefore, the value of p_i is determined by

$$p_i = \min \left\{ \lim_{z_i \rightarrow -x_i^*} \frac{f_i(z_i)}{h_i(z_i) \cdot g_i(z_i)}, \lim_{z_i \rightarrow \infty} \frac{f_i(z_i)}{h_i(z_i) \cdot g_i(z_i)} \right\} \quad (28)$$

Thus, the sub-systems (20) and (21) are output strictly passive.

It has been shown that the negative feedback connection of two output strictly passive systems is asymptotically stable if the sub-systems are zero-state detectable (Sepulchre et al., 1997). To show that H_1 and H_2 are zero-state detectable, we consider the system

$$H : \begin{cases} \dot{z} = f(z, u) \\ y = h(z, u) \end{cases} \quad (29)$$

with $u = 0$. H is said to be zero-state detectable if the origin is asymptotically stable conditionally to Z , where Z is the largest positively invariant set in $\{z \in \mathbb{R}^n \mid y = h(z, 0) = 0\}$. For the special case when $Z = \{0\}$, we say that H is zero-state observable (Khalil, 2002; Sepulchre et al., 1997). We now consider the sub-systems H_1 and H_2 , with inputs $u_1 = u_2 = 0$. From the the output functions (12)–(15), it can be seen that

$$y_1 = y_2 = 0 \implies z_1 = z_2 = 0 \quad (30)$$

Therefore, the sub-systems H_1 and H_2 are zero-state observable if the origin is locally asymptotically stable. We verify this by linearisation of the sub-systems at the origin. With $u_i = y_i = 0$, the system equations of (20) and (21) are reduced to $\dot{z}_i = -f_i(z_i)$, and linearisation gives

$$H_1 : \left. \frac{\partial(-f_1)}{\partial z_1} \right|_{z_1=0} = -\frac{k_{d,1} \cdot K_{M,1}}{(K_{M,1} + x_1^*)^2} \cdot \beta(x_2^*) < 0 \quad (31)$$

$$H_2 : \left. \frac{\partial(-f_2)}{\partial z_2} \right|_{z_2=0} = -\frac{k_{d,2} \cdot K_{M,2}}{(K_{M,2} + x_2^*)^2} \cdot \delta(x_1^*) < 0 \quad (32)$$

where f_i are the functions given by (8) and (9).

Finally, to show that the entire system is asymptotically stable, we use the combined storage function

$$S = S_1 + S_2 \quad (33)$$

Because S_1 and S_2 are positive definite, so is S . Since the two sub-systems form a negative feedback connection given by (22) or (23), the derivative of S along trajectories is reduced to

$$\dot{S} = \dot{S}_1 + \dot{S}_2 \leq -p_1 \cdot y_1^2 - p_2 \cdot y_2^2 \quad (34)$$

which is negative definite. This shows that all bounded solutions converge to the set $\{(z_1, z_2) \mid y_1 = y_2 = 0\}$. From (30), we know that this corresponds to the origin. Since the origin has been shown to be locally asymptotically stable by linearisation, we conclude that the controller motifs are asymptotically stable. If the storage functions S_1 and S_2 are radially unbounded, so is S , and the controller motifs are globally asymptotically stable.

3 Integral Control

The system given by equations (1) and (2) can be shown to include integral control. This is done by rewriting equation (2). For example, the controller motif given by equations (16) and (17), shown in Figure 2, can have equation

(17) rewritten to

$$\dot{x}_2 = -\frac{k_{s,2}}{K_{I,1} + x_1} \cdot \left(\frac{x_2}{K_{M,2} + x_2} \cdot \frac{k_{d,2} \cdot K_{I,1}}{k_{s,2}} - K_{I,1} - x_1 \right) \quad (35)$$

For $K_{M,2} = 0$, this is reduced to

$$\dot{x}_2 = -\frac{k_{s,2}}{K_{I,1} + x_1} \cdot \left(\frac{k_{d,2} \cdot K_{I,1}}{k_{s,2}} - K_{I,1} - x_1 \right) \quad (36)$$

$$= G_i \cdot (x_{1,set} - x_1) \quad (37)$$

which has the form of the integral control law. This means that for $K_{M,2} = 0$, or $K_{M,2} \ll x_2$, the system behaves as an integral controller for x_1 with a set-point given by

$$x_{1,set} = \frac{k_{d,2} \cdot K_{I,1}}{k_{s,2}} - K_{I,1} \quad (38)$$

For the case when $K_{M,2} > 0$, the set-point in (35) is defined as

$$x_{1,set} = \frac{x_2}{K_{M,2} + x_2} \cdot \frac{k_{d,2} \cdot K_{I,1}}{k_{s,2}} - K_{I,1} \quad (39)$$

Thus, there is still integral action, however, the set-point changes with perturbations. The effect of this is shown in Figure 3, where the case with $K_{M,2} = 0$ results in perfect adaptation to perturbations in the synthesis of x_1 , and the case with $K_{M,2} > 0$ results in only partial adaptation.

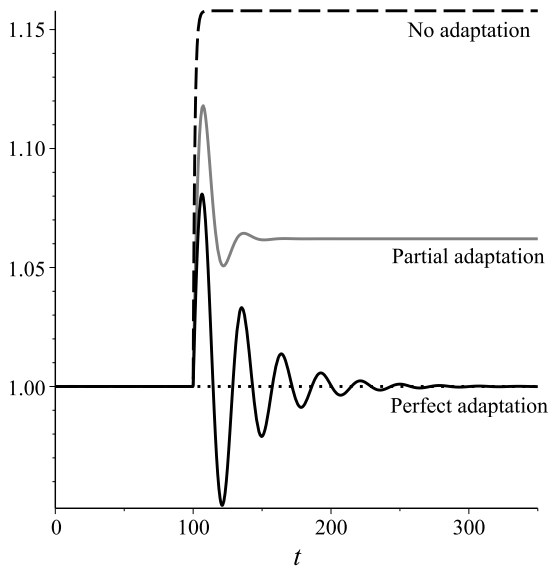


Figure 3. The response to a step-wise perturbation in the synthesis of x_1 . Dashed line shows no adaptation, grey line shows partial adaptation, and black line shows perfect adaptation. These three cases correspond to the controller motifs having no integral control (no signalling between x_1 and x_2), integral control with $K_{M,2} > 0$, and integral control with $K_{M,2} = 0$, respectively.

It has previously been shown that all the controller motifs include integral control (Drengstig et al., 2012;

Thorsen et al., 2016b). The system equation of the controller compound x_2 is written to the form of the integral control law

$$\dot{x}_2 = G_i \cdot (x_{1,set} - x_{1,meas}) \quad (40)$$

Where G_i is the controller gain, $x_{1,set}$ is the set point of the controlled compound x_1 , and $x_{1,meas}$ is a measurement function of x_1 . Just like the system in Figure 2, the other controller motifs show partial or perfect adaptation depending on the value of $K_{M,2}$ (Drengstig et al., 2012).

Because we are able to show that the controller motifs are asymptotically stable, as well as incorporating integral control, they must be robust to all parameter perturbations that do not destroy the stability of the closed-loop system (Khalil, 2002). An implication of asymptotic stability, is that the error $x_{1,set} - x_{1,meas}$ must be zero at the equilibrium point. With any parameter perturbation that does not destroy the stability of the closed-loop system, the equilibrium point may change, however, the error must return to zero. Thus, regulation will be achieved for as long as the perturbed equilibrium point remains asymptotically stable.

4 Example

We demonstrate our approach by considering the controller motif shown in Figure 2, given by the system equations (16) and (17). This system is transformed to the system equations given by (18) and (19). The transformed system can be represented as a negative feedback connection of two sub-systems H_1 and H_2 , given by (20) and (21), with

$$u_1 = -y_2 = -h_2(z_2), \quad u_2 = y_1 = h_1(z_1) \quad (41)$$

We use some arbitrary values for the constants $k_{s,1} = 1$, $k_{s,2} = 1$, $k_{d,1} = 3$, $k_{d,2} = 4$, $K_{M,1} = 1.5$, $K_{M,2} = 0.75$, $K_{I,1} = 1.5$, and $K_{A,2} = 2$, such that $x_1^*, x_2^* > 0$. Thereby, the storage function for H_1 is given by

$$S_1 = \int_0^{z_1} \left(0.114 - \frac{0.329}{\sigma + 2.893} \right) d\sigma \quad (42)$$

and the derivative of S_1 along trajectories satisfy the inequality

$$\dot{S}_1 \leq -p_1 \cdot y_1^2 + u_1 \cdot y_1 \quad (43)$$

with the constant p_1 determined by

$$0 < p_1 \leq \frac{f_1(z_1)}{h_1(z_1) \cdot g_1(z_1)} = 0.506 + \frac{0.759}{z_1 + 2.893} \quad (44)$$

For the interval $(-x_1^*, \infty)$, the right-hand side is always greater than or equal to 0.506, and so we choose this value for p_1 . This is illustrated in Figure 4. Similarly, for sub-system H_2 , the inequality

$$0 < p_2 \leq \frac{f_2(z_2)}{h_2(z_2) \cdot g_2(z_2)} = 0.185 + \frac{0.370}{z_2 + 2.050} \quad (45)$$

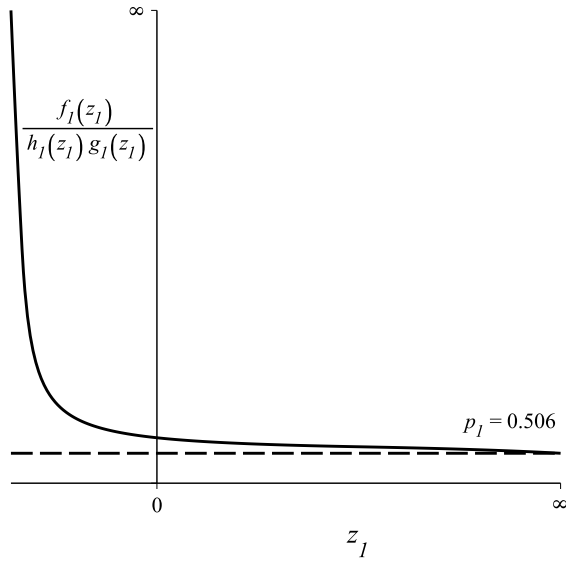


Figure 4. To determine the value of p_1 in inequality (44), we find the lower bound of the right-hand side expression. The figure shows that the lower bound is given by the limit of the right-hand side expression as $z_1 \rightarrow \infty$. In this case $p_1 = 0.506$.

is satisfied by choosing $p_2 = 0.185$, such that

$$\dot{S}_2 \leq -p_2 \cdot y_2^2 + u_2 \cdot y_2 \quad (46)$$

where the storage function S_2 is given by

$$S_2 = \int_0^{z_2} \left(0.123 - \frac{0.095}{\sigma + 2.050} - \frac{0.312}{\sigma + 4.050} \right) d\sigma \quad (47)$$

Thus, the combined storage function $S = S_1 + S_2$ is positive definite and radially unbounded, because S_1 and S_2 are both positive definite and radially unbounded. In addition, the derivative of S along trajectories satisfies

$$\dot{S} \leq -0.506 \cdot y_1^2 - 0.185 \cdot y_2^2 \quad (48)$$

which implies that \dot{S} is negative definite. S and \dot{S} are shown in Figure 5.

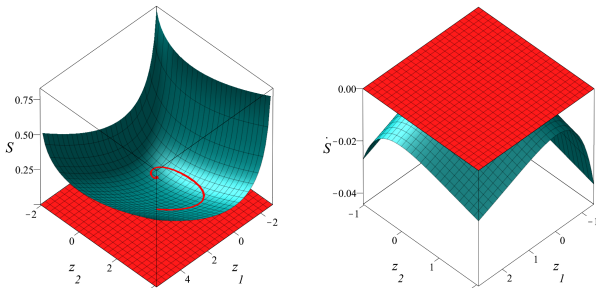


Figure 5. The storage function $S = S_1 + S_2$ is shown to the left, and its derivative along trajectories is shown to the right. The red surfaces are at zero. We see that S is positive definite, and \dot{S} is negative definite. Therefore, all bounded solutions must converge to the set where $y_1 = y_2 = 0$. A trajectory converging to the origin is shown as a red curve within the bowl formed by S in the left figure.

Similarly to Lyapunov functions, we use the combined storage function S , and its derivative along trajectories \dot{S} to draw conclusions about the stability of the system. The difference being that although the combined storage function is positive definite, and its derivative along trajectories negative definite, asymptotic stability is not implied. Instead it merely implies that all bounded solutions converge to the set where the outputs $y_1 = y_2 = 0$. In general, this set could correspond to a number of values (z_1, z_2) , however, because the output functions (12)–(15) are strictly increasing and satisfy $h_i(0) = 0$, this set corresponds to the origin. This implies that the sub-systems H_1 and H_2 are zero-state observable if the origin is locally asymptotically stable. This is shown by linearisation at the origin, using equations (31) and (32)

$$H_1 : \left. \frac{\partial(-f_1)}{\partial z_1} \right|_{z_1=0} = -0.118 < 0 \quad (49)$$

$$H_2 : \left. \frac{\partial(-f_2)}{\partial z_2} \right|_{z_2=0} = -0.131 < 0 \quad (50)$$

Thus, the sub-systems are zero-state observable, and the entire system must be asymptotically stable. In addition, as noted earlier, the combined storage function S is radially unbounded, and therefore the system is globally asymptotically stable.

5 Conclusion

In this paper we have shown that a class of eight two-component biochemical networks displaying homeostasis, called controller motifs, are asymptotically stable. We have shown that the general system equations for these networks can be represented as negative feedback connections of two individual sub-systems. Then, these sub-systems are shown to be output strictly passive, and the feedback connection in its entirety is shown to be asymptotically stable. In addition, it is shown that the controller motifs are robust to perturbations because they incorporate integral control.

When modelling cellular processes, it is beneficial to know that uncertainties in parameters do not fundamentally change the behaviour of the model. Because the controller motifs are asymptotically stable with integral action, processes which can be modelled within the framework of the controller motifs will have a qualitative behaviour which aligns well with experimental measurements, even with large uncertainties in parameter values. On the other hand, processes which do not conform well to the controller motifs can have wildly different qualitative responses in the face of parameter uncertainties, and the controller motifs can be excluded as models for such processes. Thus, it is not a matter of parameter tuning. This is a helpful property of the controller motifs, especially in system identification.

Here we have chosen to focus on controller motifs with zero-order synthesis, degradation by an enzyme reaction, and signalling following mixed activation/inhibition.

However, other functions could be used. For example, we could use Hill kinetics for the degradation of the two compounds, or we could use linear activation for the signalling functions. In that case we would have to make sure that the properties assumed still hold.

References

- Athel Cornish-Bowden. *Fundamentals of Enzyme Kinetics*. Wiley-Blackwell, fourth edition, 2012. ISBN 978-3-527-33074-4.
- T. Drengstig, I. W. Jolma, X. Y. Ni, K. Thorsen, X. M. Xu, and P. Ruoff. A basic set of homeostatic controller motifs. *Biophysical Journal*, 103(9):2000–2010, 2012. ISSN 00063495. doi:10.1016/j.bpj.2012.09.033.
- Gunhild Fjeld, Kristian Thorsen, Tormod Drengstig, and Peter Ruoff. The Performance of Homeostatic Controller Motifs Dealing with Perturbations of Rapid Growth and Depletion. *The Journal of Physical Chemistry B*, 2017. ISSN 1520-6106. doi:10.1021/acs.jpcc.7b01989. URL <http://pubs.acs.org/doi/abs/10.1021/acs.jpcc.7b01989>.
- James Keener and James Sneyd. *Mathematical Physiology I: Cellular Physiology*. Springer, second edition, 2009. ISBN 978-0-387-75846-6. doi:10.1007/978-0-387-75847-3.
- Hassan K. Khalil. *Nonlinear Systems*. Prentice Hall, third edition, 2002. ISBN 0-13-067389-7.
- Weijiu Liu. *Introduction to Modeling Biological Cellular Control Systems*. Springer, 2012. ISBN 978-88-470-2489-2. doi:10.1007/978-88-470-2490-8.
- Rodolphe Sepulchre, Mrdjan Jankovic, and Petar Kokotovic. *Constructive Nonlinear Control*. Springer, 1997. doi:10.1007/978-1-4471-0967-9.
- K. Thorsen, T. Drengstig, and P. Ruoff. Transepithelial glucose transport and Na⁺/K⁺ homeostasis in enterocytes: an integrative model. *AJP: Cell Physiology*, 307(4):C320–C337, 2014. ISSN 0363-6143. doi:10.1152/ajpcell.00068.2013. URL <http://ajpcell.physiology.org/content/307/4/C320>.
- K. Thorsen, G. Risvoll, M. Mazumder, and D. R. McMillen. A controller for regulation of intracellular copper in *S. cerevisiae*. In *Poster presented at ICSB2016*, 2016a. doi:10.3252/pso.eu.17ICSB.2016. URL <http://www.postersessiononline.eu/pr/congreso.asp?cod=392299830>.
- Kristian Thorsen, Geir B Risvoll, Daniel M Tveit, Peter Ruoff, and Tormod Drengstig. Tuning of Physiological Controller Motifs. In *2016 9th EUROSIM Congress on Modelling and Simulation*, pages 28–33, 2016b. ISBN 9781509041190. doi:10.1109/EUROSIM.2016.174.
- John J. Tyson and Hans G. Othmer. The Dynamics of Feedback Control Circuits in Biochemical Pathways. In *Progress in Theoretical Biology Volume 5*, pages 1–62. Academic Press, 1978. ISBN 0-12-543105-8.

Methane from Syngas by Anaerobic Digestion

Sanjay Shah Wenche Hennie Bergland Rune Bakke

Department of Process, Energy and Environmental Technology, University College of Southeast Norway, Norway
shahsanjaay@gmail.com, Wenche.Bergland@usn.no, Rune.Bakke@usn.no

Abstract

Anaerobic digestion (AD) is a prominent green technology used for methane production from organic waste. Previous studies have shown that the amount of CH₄ produced during anaerobic digestion can be increased by adding inorganic electron donors such as H₂ and CO, both which can be produced as syngas from wood. Syngas inflow is implemented in the ADM1 model and simulations are carried out with different syngas additions to a well-documented case of wastewater treatment plant sludge AD. Three different compositions; (1) pure hydrogen, (2) 86 vol.% H₂, 7 vol.% CO and 7 vol.% CO₂, and (3) 44.4 vol.% H₂, 33.3 vol.% CO and 22.2 vol.% CO₂ were used for a first set of simulations testing process limitations. The second set of simulations were used to find out how much methane production can be increased for the given case if syngas composition is optimized. The CH₄ production can be increased by 33 % by adding H₂ (1) and was limited by pH going too high. Biogas CH₄ content reached 92 % at this limit. The H₂-rich syngas addition (2) reached 47 % CH₄ production increase with 81 % CH₄ content. The low H₂ syngas case (3) produce more biogas but the CH₄ content is reduced to 42 %. There is a narrow syngas composition range for which methane production can be increased by a factor >~ 2.7, limited by available nitrogen in the treated sludge.

Keywords: Anaerobic digestion, ADM1, Syngas addition, CH₄ production, CO degradation

1 Introduction

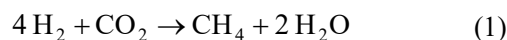
The concept of waste to energy from wet organic waste like manure for biogas generation by Anaerobic Digestion (AD) is a prominent green technology since it reduces greenhouse gases and odors (Deublein & Steinhauser, 2011).

Anaerobic digestion is a biochemical process, where microbial activity comes into play and reduce complex organic pollutant by extracellular (disintegration, hydrolysis) and intracellular (acidogenesis, acetogenesis, methanogenesis) (Fig. 1) to produce biogas (Batstone et al., 2002). The generated biogas consists of (55-75) % methane and (25-45) % carbon dioxide (De Mes et al., 2003).

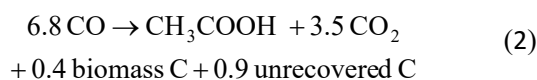
Several techniques are being used for biogas upgrading like water washing, polyglycolic adsorption, pressure swing adsorption and chemical treatment (Osorio & Torres, 2009). These methods are performed outside of the anaerobic reactor for biogas upgrading which requires extra investments. Previous studies have shown that CH₄ in AD can be increased by adding inorganic electron donors such as H₂ and CO (Luo & Angelidaki, 2013). These can, for example, be produced as syngas from wood through a gasification process. Gasification is a thermochemical process where biomass is converted into a mixture of gases that contains H₂, CO and CO₂ (Bridgwater, 2003). The produced syngas can be directly fed into the AD reactor for methane production, making AD a method to convert syngas into methane.

Adding syngas to AD can potentially have significant environmental impact on organic waste handling. It can for instance be a way to obtain more bio-fuel as methane from AD than what is obtainable from the wet organic wastes currently used as feed for biogas production. This study can help estimate how much production can increase and under which conditions. This approach may also serve as a way to mineralize all organic matter in sludge by combining AD and thermal gasification.

Hydrogen can be used to upgrade the methane production directly in the reactor by increasing the hydrogenotrophic methanogenesis (Luo & Angelidaki, 2013), which consumes hydrogen together with CO₂ in the biogas, with methane as product (Luo & Angelidaki, 2012):

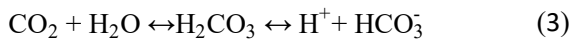


Many degradation paths for CO has been suggested, but experiments have shown acetogenesis to be dominating (Luo et al., 2012) under anaerobic condition at mesophilic temperatures. Acetogens utilize the CO and yields acetate, CO₂, cell material and unrecovered Carbon (Mörsdorf et al., 1992):



The reaction (Eq. 2) is added to the ADM1 model which is the standard platform of modelling and simulations of AD process developed by IWA in 2002. ADM1 model is a structured model that describes the

biochemical (Fig.1) and physiochemical reactions that are responsible for methane production (Batstone et al., 2002). The biochemical reactions are the core of this model which includes disintegration of complex organic material to carbohydrates, proteins, and lipids. These are then hydrolysed into sugars, amino acids and long-chain fatty acids (LCFAs) which are further fermented into molecular hydrogen and volatile organic acids (acidogenesis). The acids are broken down to acetate and hydrogen (acetogenesis). The last step is the split of acetate ions into methane and carbon dioxide (acetoclastic methanogenesis). The hydrogenotrophic methanogenesis step (Eq. 1) also produces methane when hydrogen reduces carbon dioxide (Batstone et al., 2002). The hydrogenotrophic methanogens are thus already present in an AD reactor and can grow to handle more hydrogen or syngas. If H₂ is added in excess, it can remove so much CO₂ (Eq. 3) that pH rise too high for efficient methanogenesis (Luo et al., 2012) ultimately causing failure of the reactor. The ratio of added H₂/feed load and effect of composition in the added syngas are therefore evaluated here to evaluate syngas addition limitations.



The physiochemical processes are liquid-liquid mass transfer process (i.e. ion dissociation) and liquid-gas exchange (i.e. liquid-gas mass transfer) (Batstone et al., 2002). Inefficient syngas mass transfer can limit its degradation in AD process due to the low solubility of CO and H₂ (Guiot, Cimpoia, & Carayon, 2011) which can result in syngas loss to headspace. In this work it is assumed that such loss is avoided by adding the gas through a membrane by diffusion.

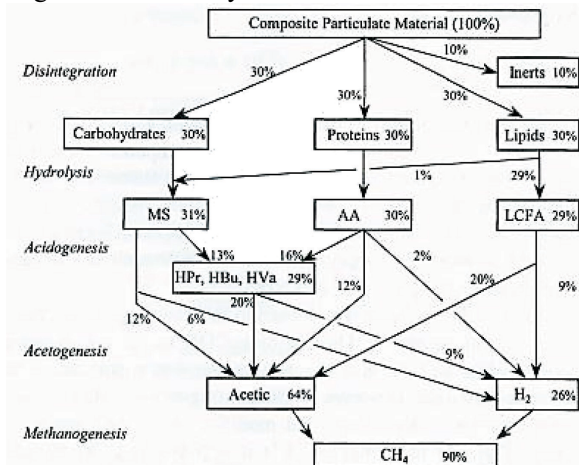


Figure 1. Systematic representation of anaerobic digestion process showing biochemical reactions described in ADM1 model (Batstone et al., 2002).

The purpose of this study is to evaluate effects of syngas composition and quantity on methane production and biogas composition, when added to an AD reactor running on sludge. The ADM1 model implemented in the AQUASIM software is applied and includes:

- (1) Implementation of CO degradation in ADM1.
- (2) Simulating hydrogen alone or syngas as AD feed supplements.
- (3) Evaluation of syngas component effects on the AD reactor performance by adding different ratios of H₂/CO/CO₂.

2 Materials and Methods

The ADM1 model was extended by adding CO degradation (Table 1 and 2). H₂ or syngas was supplied as input to the reactor compartment. The simulations were based on a reported sludge digestion experiment with ADM1 simulations (Siegrist et al., 2002), to which H₂ or syngas was added in various amounts. Applicable supply range is assumed to be between zero and the level at which methane production fails.

2.1 Syngas degradation in ADM1

Syngas addition requires two new biochemical reactions to be added into the model. One is the uptake of carbon monoxide to acetate and the second is decay of carbon monoxide degrading organism. The parameters used for uptake are in Table 1 and the rate equations and stoichiometry coefficients are given in Table 2.

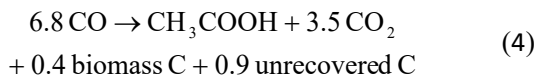
Table 1: Parameters used for uptake of CO.

Parameters	Description	units
km_CO_ac	Maximum uptake rate for CO degrading organisms.	kg COD S kg ⁻¹ COD X d ⁻¹
X_CO_ac	CO degrading organisms.	kg COD m ⁻³
Ks_CO_ac	Half-saturation constant for CO degradation (same as for H ₂ degradation).	kg COD m ⁻³
I_ph_CO_ac	pH inhibition of CO to acetate degrading organisms (same as for propionate degradation).	-
I_H2_CO_ac	Hydrogen inhibition for CO to acetate degrading organism.	-
kdec_x_CO_ac	Decay rate for CO degrading organisms	d ⁻¹
Y_CO_ac	Yield of biomass on the uptake of CO to acetate.	kg COD kg ⁻¹ COD
S_CO	Total carbon monoxide.	kg COD m ⁻³
KH_CO	Non-dimensional Henry's law constant for CO	M (liq) M ⁻¹ (gas)

Table 2: Uptake rate of CO and decay rate of CO degrading organism in the model.

Dynamic process	Rate equation
uptake_CO_ac	$\text{km_CO_ac} * \text{X_CO_ac} * \text{S_CO} / (\text{Ks_CO_ac} + \text{S_CO}) * \text{I_ph_CO_ac} * \text{I_H2_CO_ac} * \text{I_NH_limit}$
decay_CO_ac	$\text{X_CO_ac} * \text{kdec_x_CO_ac}$

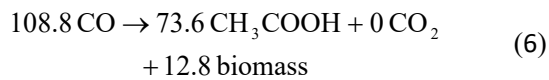
Estimations of k_m and Y for CO uptake are based on reported experimental results (Mörsdorf et al., 1992) and the observed stoichiometric reaction of CO utilization (Eq. 4).



The unrecovered carbon is here assumed to be divided between acetate and CO₂ in the same way as the recovered part observed by Mörsdorf et al. (1992), according to (Eq. 5).



Eq.5 is further converted into COD basis (Eq. 6) using 5 mole carbon per mole biomass and 160 g COD mole⁻¹ for biomass (Batstone et al., 2002).



From equation 6, it can be seen that biomass yield per g COD of CO is obtained by:

$$Y = \frac{12,8}{108,8} = 0,12 \text{ g COD biomass g}^{-1} \text{ COD CO}$$

The relation between maximum uptake rate of substrate (k_m) and maximum specific growth rate (μ^{\max}) per day is (Eq. 7):

$$k_m = \frac{\mu^{\max}}{Y} \quad (7)$$

Where Y is the yield of biomass and μ^{\max} of the organism can be calculated from doubling times under batch exponential growth condition (Eq. 8).

$$\mu^{\max} = \ln 2 / \text{doubling times} \quad (8)$$

The reported doubling times for acetogenesis bacteria which shows the fastest growth on CO is 0.125 day (Mörsdorf et al., 1992).

This gives

$$\mu^{\max} > \frac{\ln 2}{0,125} = 5.54 \text{ d}^{-1}$$

Now,

$$k_m = \frac{5.54}{0,12} = 46.20 \text{ kg COD S kg}^{-1} \text{ COD X d}^{-1}$$

The values $k_{m_CO_ac} = 46.20 \text{ kg COD S kg}^{-1} \text{ COD X d}^{-1}$ and $Y_{CO_ac} = 0.12 \text{ kg COD biomass kg}^{-1} \text{ COD CO}$ are used in all simulations.

2.2 Reactor operation

A 28 m³ reactor was fed wastewater treatment plant sludge continuously for 50 days (Fig. 2) with feed step increases at day 16 and 37 (Siegrist et al., 2002).

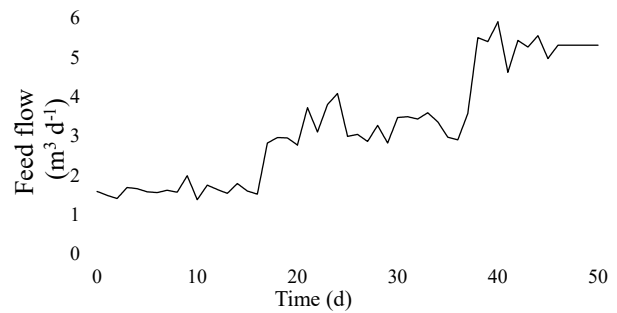


Figure 2: Sludge feed flow to the pilot reactor (Wang et al., 2013).

The feed composition of amino acid, fatty acid, sugar and composite organic material are in Table 3.

Table 3: Feed composition (Wang et al., 2013).

Components in reactor feed	Concentration (kg COD m ⁻³)
Amino acids	4.2
Fatty acids	6.3
Monosaccharides	2.8
Composite material	10
Total	23.3

The average feed flow the first 16 days is 1.61 m³ d⁻¹ or 37.5 kg COD d⁻¹. The average is 3.2 m³ d⁻¹ at days 17-36 and 5.24 m³ d⁻¹ during days 37-50.

2.3 H₂/syngas additions simulated

Three main cases with increasing gas supply complexity are simulated: 1) pure hydrogen, 2) two selected compositions of syngas and 3) a wider range of gas mixtures. Syngas composition depends on the gasification process and the two chosen here for case 2 are from steam based gasification processes (Pfeifer et al., 2009): 1) Gasification included capture of CO₂ produces synthesis gas with high hydrogen content, called H₂-rich syngas i.e. 86 vol.% H₂, 7 vol.% CO and 7 vol.% CO₂. 2). Gasification without CO₂ capture produces syngas that consists of 44.4 vol.% H₂, 33.3 vol.% CO and 22.2 vol.% CO₂ (Pfeifer et al., 2009). These compositions are used in the simulations here (Table 4). For these simulations (1, 2 and 3 in Table 4) the load of hydrogen and syngas are in Table 5.

Four different syngas compositions were used during the third simulation case (simulation 4-7), to search for the AD process syngas load limitation. Process capacity limits are found by increasing the load of hydrogen until failure of the AD process. The load of CO and CO₂ is according to the composition ratio in Table 4.

Table 4: Composition of gas feed during simulations.

Gas	Vol. %							
	Ref ¹	Sim 1	Sim 2	Sim 3	Sim 4	Sim 5	Sim 6	Sim 7
H ₂	0	100	86	44.4	80	74	70	60
CO	0	0	7	33.3	10	13	15	20
CO ₂	0	0	7	22.2	10	13	15	20

Table 5: Load of wastewater, pure H₂, and syngas.

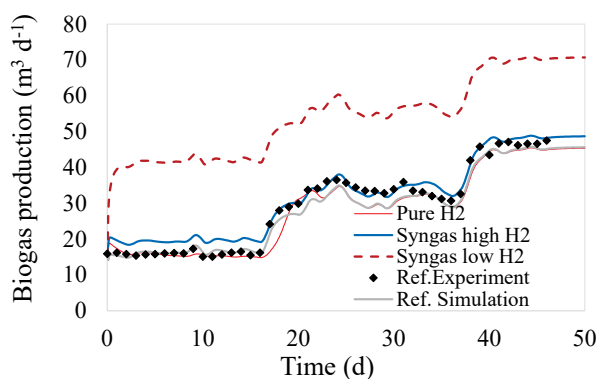
	Load H ₂ (kg COD d ⁻¹)	Load CO (kg COD d ⁻¹)	Load WW feed (kg COD d ⁻¹)
Ref	0	0	37.5
Sim 1	10.43	0	37.5
Sim 2	10.43	0.849	37.5
Sim 3	10.43	7.82	37.5

3 Results and discussion

The hydrogen and various syngas additions to the AD process simulated strongly influence the conditions in the reactor and thereby the produced biogas.

3.1 Biogas production

The biogas production rate for 50 days of reactor operation increases with increase in the organic loading rate (Fig. 3). The constant addition of pure hydrogen or H₂-rich syngas shows only a small variation in biogas production rate while syngas with low H₂ concentration almost doubled the biogas production.

**Figure 3:** Biogas production rate of AD reactor added pure H₂ or two compositions of syngas. Included reference (Siegrist et al., 2002) experimental and simulated result.

Pure hydrogen addition in AD process enhances the hydrogenotrophic methanogenesis process (Eq. 1) and increases production of methane while consuming carbon dioxide.

In the case of H₂-rich syngas (composition 86 % H₂, 7 % CO and 7 % CO₂), biogas production rate increases

¹Reference simulations were based on a reported sludge digestion experiment with ADM1 simulations (Siegrist et al., 2002).

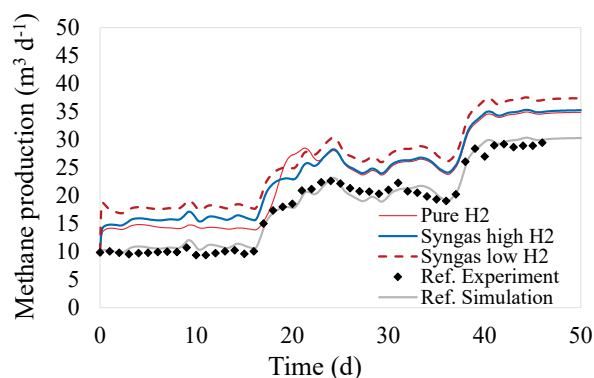
slightly more than pure H₂; since syngas also contains some CO and CO₂.

In the case of syngas composition of 44.4 %, 33.3 % CO and 22.2 % CO₂, the biogas production rate is higher than pure H₂ and H₂-rich syngas because of the higher CO and CO₂ addition to the reactor.

During both the syngas additions, the fast degradation of CO to acetic acid and CO₂ avoid loss of CO to headspace and result in almost zero CO concentrations in the produced gas.

3.2 Methane production

The methane production rate is 14.3 m³d⁻¹ for pure H₂, 15.7 m³d⁻¹ for high H₂ syngas and 17.9 m³d⁻¹ for low H₂ syngas at days 1-16 when adding gases, which is more than the pilot case without gas supply (10.7 m³ d⁻¹ in Fig. 4, the experimental values presented by black diamonds). The methane production rate increased by 33 % and 47 % by adding pure H₂ and H₂-rich syngas and by 67 % by adding syngas with low H₂ concentration.

**Figure 4:** Methane production rate of AD reactor added pure H₂ or two compositions of syngas. Included reference (Siegrist et al., 2002) experimental and simulated results.

3.3 pH and inhibition effects

NH₃ is increased because of pH increase in the reactor (Eq. 9), especially pronounced when pure H₂ is supplied. pH (Fig. 5) increase as supplied hydrogen leads to CO₂ consumption, which reduces the acid concentration in the reactor due to the equilibrium reaction between CO₂ and water (Eq. 3).

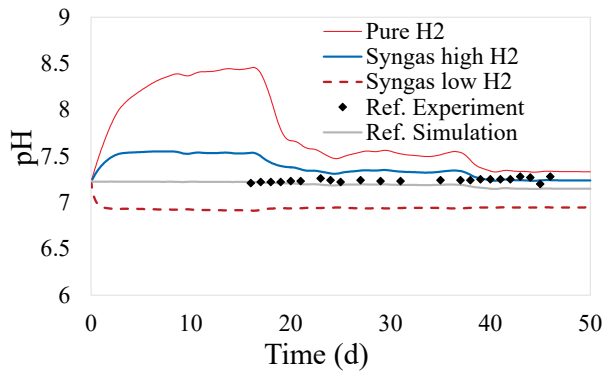
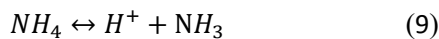


Figure 5: pH of bulk reactor volume for AD reactor added pure H₂ or two compositions of syngas. Included reference (Siegrist et al., 2002) experimental and simulated result.

Inhibition (Fig. 6) following pH increase (Fig. 5) is explained by more NH₃ (Eq. 9). The biomass responsible for methane production from acetate belongs to the archaeal group (aceticlastic methanogens) and is inhibited by NH₃ and slows down the conversion of acetate to methane (Bergland et al., 2011).



The inhibition is reduced after the step increase in organic feed supply on day 16 (Fig. 6). This can also be observed as acetate concentration reduction during the same time (Fig. 7). During the initial stage i.e. day (0-16), the acetate concentration rises due to inhibition (Fig. 7). During the initial stage, pH rises to 8.5. (Fig. 5) at pure H₂ addition. After day 16, the increase in wastewater addition increases the organic loading rate resulting in more CO₂ available through degradation of feed, the pH goes down and the reactor stabilize.

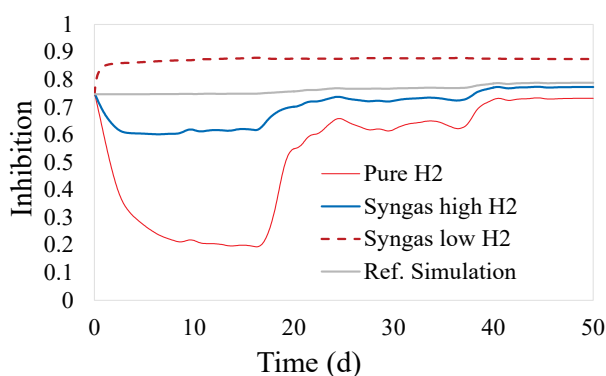


Figure 6: NH₃ inhibition for AD reactor added pure H₂ and two different syngas composition. Included reference (Siegrist et al., 2002) simulated result.

The two syngas additions follow a similar path for methane production as the experimental values. The acetate concentrations are low during both syngas additions because NH₃ is low and does not much inhibit the methanogens (Fig. 6). The extreme pH effect of

adding hydrogen alone is avoided when CO and CO₂ are also supplied.

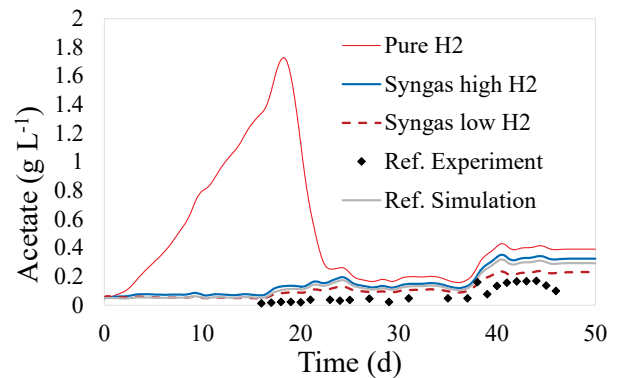


Figure 7: Acetate concentration of AD reactor added pure H₂ or two compositions of syngas. Included reference (Siegrist et al., 2002) experimental and simulated result.

The inorganic carbon simulations show decrease (Fig. 8) corresponding to acetate increase (Fig. 7) and inhibition (Fig. 6). The loads applied before and after 16 days of the pure hydrogen case indicates how much hydrogen to organic load ratio such AD can handle. The simulated pH (~8.5) is close to the pH 9 observed experimentally under similar conditions (Wang et al., 2013).

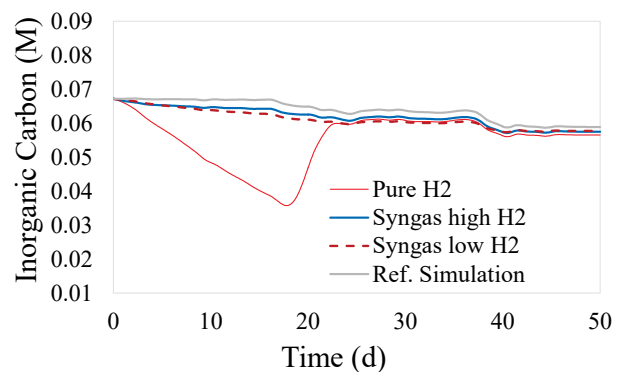
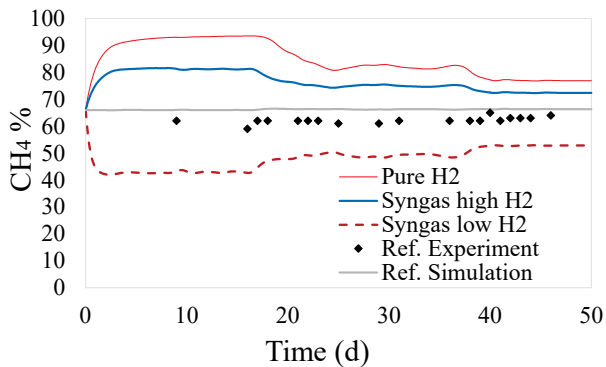


Figure 8: Inorganic carbon curve for AD reactor added pure H₂ and two different syngas composition. Included reference (Siegrist et al., 2002) simulated result.

The simulated percentage of methane (Fig. 9A) in produced biogas rises very high for the pure H₂ case and reaches up to 92 %. The carbon dioxide concentration follows a similar but opposite behavior (Fig. 9B). The addition of hydrogen enhances the produced biogas concentration of methane. Syngas composition with low H₂ concentration gives less methane percentage than no gas, pure H₂ and H₂-rich syngas supply since it contains more carbon dioxide (CO₂).

A



B

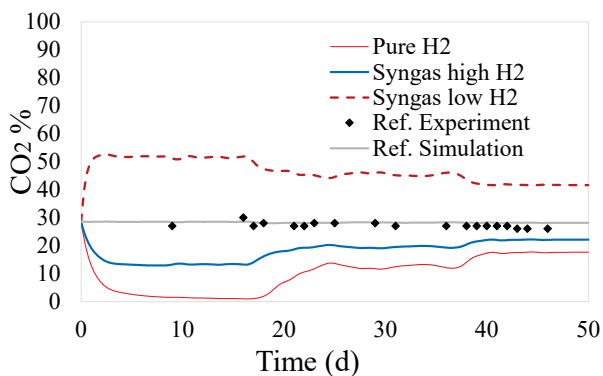


Figure 9: Percentage of biogas in the headspace (A) methane and (B) carbon dioxide of AD reactor added pure H₂ or two compositions of syngas. Included reference (Siegrist et al., 2002) experimental and simulated result.

The methane percentage is around 92 % (Fig. 9A) with pure H₂, around 81 % with H₂-rich syngas and at least 42 % with syngas with low hydrogen concentration due to the different H₂/CO₂ ratios in the added gas.

The yield of methane as kg COD methane kg⁻¹ COD feed (wastewater + gas addition) was for days 1-16 0.72, 0.75, 0.82, and 0.81 for reference (Siegrist et al., 2002), pure H₂, syngas with high H₂ and syngas with low H₂. This shows that the yield was almost similar for the syngas with high H₂ and syngas with low H₂ concentration. The high CO₂ content of produced biogas is however a drawback for further processing of the biogas when syngas with low H₂ is added. These simulations suggest that there is some optimal range of syngas supply, defined by gas composition and amount relative to organic feed.

3.4 Loading ratio and syngas supply limitation

Steady state simulations of four different syngas compositions (Table 4) operated close to failure of the AD process are summarized in Fig. 10. 70 – 80 % hydrogen in the supplied syngas evidently can sustain

much higher total methane production than lower and higher fractions. Methane production is approximately proportional to the gas to organic feed ratio (abscissa in Fig. 10), explained using loading with pure H₂ as example.

The production rate can be increased (by a factor of ~ 2.7) with 74 % hydrogen content in the added syngas. The reason for failure of the AD reactor for H₂ content higher than 74 % is lack of available CO₂ while pH drop limits the process when the H₂ content is lower than 74 %, due to high CO₂ concentration in the reactor. pH remains stable at 74 % hydrogen content in the added syngas and production is nutrient (N) limited.

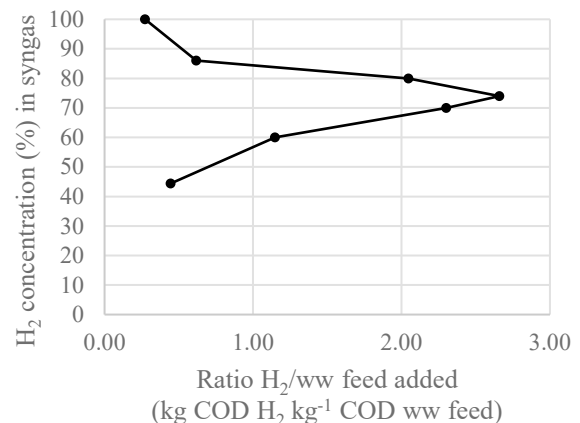


Figure 10: Threshold limit for ratio of hydrogen load and load of wastewater feed as a function of H₂ concentration (%) in added syngas.

4 Conclusion

Addition of pure H₂ and different compositions of syngas (down to 44.4 % H₂) to an AD treating sludge are simulated in an ADM1 model extended to include CO reactions. Comparisons of experimental and simulated results suggest realistic simulations.

Addition of syngas with high or low H₂ concentration to the sludge fed AD reactor showed a methane production increase of respectively 47 and 67 % while the methane content in the produced biogas was 81 and 42 % (66 % without gas addition).

Addition of pure H₂ gives the highest methane content (up to 92 % which is close to vehicle fuel quality) but overall biogas production is limited by available CO₂ in the AD reactor. Low CO₂ caused pH increase leading to NH₃ inhibition of methanogenesis and the methane production could only be increased by 33%.

The best syngas composition to feed AD processes for enhanced methane production has a hydrogen content of 70-80 %. It can more than triple methane production compared to organic feed only and is nitrogen (as nutrient for biomass growth) limited.

References

- Bastone, D.J., et al., The IWA anaerobic digestion model no 1 (ADM1). *Water Science and Technology*, 2002. 45(10): p. 65-73.
- Bridgwater, A. V., Renewable fuels and chemicals by thermal processing of biomass. *Chemical Engineering Journal*, 2003. 91(2): p. 87-102.
- De Mes, T., et al, Methane production by anaerobic digestion of wastewater and solid wastes. *Bio-methane & Bio-hydrogen*, 2003: p. 58-102.
- Deublein, D. and A. Steinhauser, *Biogas from waste and renewable resources: an introduction 2011*: John Wiley & Sons.
- Guiot, S. R., R. Cimpoaia, and G. Carayon, Potential of wastewater-treating anaerobic granules for biomethanation of synthesis gas. *Environmental science & technology*, 2011. 45(5): p. 2006-2012.
- Luo, G. & I. Angelidaki, Integrated biogas upgrading and hydrogen utilization in an anaerobic reactor containing enriched hydrogenotrophic methanogenic culture. *Biotechnology and bioengineering*, 2012. 109(11): p. 2729-2736.
- Luo, G. and I. Angelidaki, Co-digestion of manure and whey for in situ biogas upgrading by the addition of H₂: process performance and microbial insights. *Applied microbiology and biotechnology*, 2013. 97(3): p. 1373-1381.
- Luo, G., et al., Simultaneous hydrogen utilization and in situ biogas upgrading in an anaerobic reactor. *Biotechnology and bioengineering*, 2012. 109(4): p. 1088-1094.
- Mörsdorf, G., et al., Microbial growth on carbon monoxide. *Biodegradation*, 1992. 3(1): p. 61-82.
- Osorio, F. and J. Torres, Biogas purification from anaerobic digestion in a wastewater treatment plant for biofuel production. *Renewable energy*, 2009. 34(10): p. 2164-2171.
- Pfeifer, C., B. Puchner, and H. Hofbauer, Comparison of dual fluidized bed steam gasification of biomass with and without selective transport of CO₂. *Chemical Engineering Science*, 2009. 64(23): p. 5073-5083.
- Siegrist, H., et al., Mathematical model for meso-and thermophilic anaerobic sewage sludge digestion. *Environmental science & technology*, 2002. 36(5): p. 1113-1123.
- Wang, W., et al., Performance and microbial community analysis of the anaerobic reactor with coke oven gas biomethanation and in situ biogas upgrading. *Bioresource technology*, 2013. 146: p. 234-239.
- Bergland, W., Botheju, D., Dinamarca, C., Bakke, R., Considering Culture Adaptations to High Ammonia Concentration in ADM1. In *proceedings of the 52nd International Conference of Scandinavian Simulation Society: SIMS. 2011*.

Effect of natural convection and radiation inside of a hollow beam in a standard fire

Turo Välikangas¹ Sami Pajunen² Jolanta Baczkiewicz² Singh Shobhana³ Kim Sørensen³

¹Laboratory of Chemistry and Bioengineering, Technical University of Tampere, Finland, turo.valikangas@tut.fi

²Laboratory of Civil Engineering, Technical University of Tampere, Finland sami.pajunen@tut.fi

³Energy Technology, Aalborg University, Denmark ssi@et.aau.dk

Abstract

In the design of steel structures, special attention must be paid on structural fire design in order to ensure a specified safe time period that the structure can withstand the fire without collapse. In the European design rules, the standard practise assumes uniform temperature for steel beam cross sections while the surrounding area is subjected to the so called standard fire. When the ambient temperature field is not uniform (e.g. at beam joint areas) neither will be the beam cross section temperature field. This paper studies the contribution of natural convection and cavity radiation to the temperature field of a hollow beam cross section in the case of non-uniform ambient temperature by using transient CFD-simulations. *Hollow beam, natural convection, cavity radiation, structural fire design, Open-Foam*

1 Introduction and background

The current European standards for the structural fire design are given in Eurocode 1, Part 1-2 and in Eurocode 3, Part 1-2. In these design codes, the most common assumption is that the temperature field around the beam cross-section is uniform during the standard ISO-834 fire. Following that assumption, the structural design can be done in a straightforward manner, but it may result in a non-economic and too conservative solution. Particularly, steel beams are almost invariably assembled so that the fire does not affect equally on all the sides of the beam. Typically such situation arises in beam joint areas and in beam connections to surrounding structures. The Eurocode 3 includes some recommendations for open I-sections and steel slabs subjected to fire on three sides. However, no unified rules are available for the hollow sections in non-uniform surrounding temperature, and only some studies are available in the literature. One of the studies investigated steel pipes subjected to partial fire acting longitudinally along the pipe (Wong, 2017). In this study a parametrically coded generic element method was proposed to solve the heat transfer problem, which was more effective and accurate than Eurocode 3 calculations, but the paper did not consider the non-uniform temperature in the cross-section. The non-uniform heating of tubular sections was

experimentally tested in (Yang et al., 2013) numerically in (Heinisuo and Jokinen, 2014) but only for concrete-filled columns. All above mentioned tests came to the same conclusion that the number of sides subjected to fire, has a great influence on the heat distribution and on the fire resistance.

In general, there is a large number of experimental and numerical research results concerning tubular sections in the uniform fire conditions, see e.g. (Fung et al., 2015), (Shao et al., 2016), (He et al., 2013) for circular hollow sections, and e.g. (Yang et al., 2014), (Ozyurt et al., 2014) for square hollow sections. Nevertheless, the non-uniform fire condition is far less studied, and to the authors' best knowledge there exist no reliable experimental results for the square hollow sections. Numerical studies are also rather few, the analytic approach of (Mills, 1999) can be used for radiation calculations, but for the natural convection only simplified geometries and numerical boundary conditions are covered (Kays, 2012). The natural convection inside a cavity is affected by the ratio between the height and the width of the cavity as well as the inclination of the roof wall. Temperature differences and their influence on the Rayleigh number of the situation has a significant effect on the turbulence level in the flow. This is why a three dimensional computational fluid dynamics approach was chosen in this study. This way the difference between convective and radiation heat transfer can be simulated in the laminar, transition and in the turbulent regime.

In this paper, the effects of natural convection and surface-to-surface radiation inside the square hollow beam due to the non-uniform fire condition are studied and some recommendations about their importance are given. On the other hand, the paper presents modelling principles for taking these phenomena into account in the structural fire design.

2 Model development

2.1 Governing equations and boundary conditions

1. Continuity equation

$$\frac{\partial \rho}{\partial t} + \frac{\partial(\rho u_i)}{\partial x_i} = 0 \quad (1)$$

2. Momentum equation

$$\frac{\partial \rho u_i}{\partial t} + \frac{\partial(\rho u_i u_j)}{\partial x_j} = \frac{\partial}{\partial x_i} \left(\mu \frac{\partial u_j}{\partial x_i} \right) - \frac{\partial p}{\partial x_j} \quad (2)$$

where u is the velocity and x the coordinate location and where i, j and k are the summation identities according Newton's formula in all three Cartesian coordinate directions. The others t, μ and p are the time, dynamic viscosity and pressure.

3. Energy equation for fluid region

$$\frac{\partial \rho T}{\partial t} + \frac{\partial}{\partial x_i} (\rho u_i T) = \frac{\partial}{\partial x_i} \left(\frac{\lambda_f}{C_p^f} \frac{\partial u_i}{\partial x_i} \right) \quad (3)$$

where T is the temperature, C_p is the specific heat and λ_f is the thermal conductivity.

4. Energy equation for solid region

$$-\frac{\lambda_s}{C_p^s} \frac{\partial^2 u}{\partial x_i^2} = 0 \quad (4)$$

To validate how much heat is transferred through the boundary patch that is connecting the air and solid domain, conduction and radiation heat fluxes are calculated separately on the air. The conduction heat flux is calculated according to the equation 5.

$$\lambda_f \nabla T = 0 \quad (5)$$

In this study radiation is calculated with a view factor model that says that the sum of all view factors from a given surface, S_i , is unity as explained in equation 6

$$\sum_{n=1}^i F_{S_i \rightarrow S_j} = 1 \quad (6)$$

To save computational resources an agglomeration script is ran before the calculation of the view factors. This means that the surfaces that are in the same plane and next to each other are embedded together because their view factors can be assumed to be equal. Then matrix system in equation 7

$$Q_{rad} = C^{-1} b \quad (7)$$

where C calculates the ratio between reflection and absorption and b is the emissivity matrix as follows.

$$b = A e_b - H_o \quad (8)$$

Where A is the view factor matrix that takes into account the agglomeration calculation and e_b is the emissivity of a black surface. H_o combines all the external radiation heat fluxes.

3 Computational model

In this section the computational model, the meshing process, solvers used and the grid independence study are illustrated.

3.1 Computational geometry

The simulated domain is divided in to two different regions. The hollow solid beam and the air inside the cavity. The solver that was used to solve the time dependent temperature equation and the three dimensional laminar flow field inside the hollow beam is chtMultiRegionFoam. Second order accurate upwind schemes were used for the velocity and temperature field and only first order accurate upwind for all the others. The coupling between momentum and pressure equation in chtMultiRegionFoam is solved using PIMPLE algorithm which is a combination between PISO (Pressure Implicit with Splitting of Operator) and SIMPLE (Semi-Implicit Method for Pressure Linked Equations) algorithms. For schemes a second order accurate upwind schemes was used for velocity and temperature equation and a first order upwind scheme was used for all the others. In figure 1 the computational domain on the solid side is illustrated. The boundary patches are called **insulated**, **the cold wall**, **the warm wall** and the **solid to fluid patch** according to the color coding in the figure.

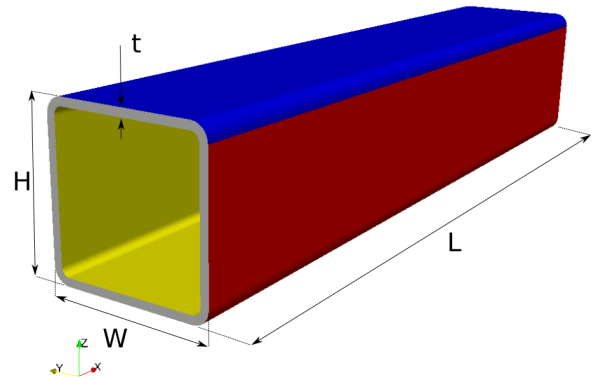


Figure 1. Illustration of the boundary patches on the solid region and the geometry variables

Table 1. Geometric dimensions of the hollow beam

Parameter	Symbol/unit	Value
Length of the beam	L /mm	500
Height of the beam	H /mm	100
Width of the beam	W /mm	100
Thickness of the beam wall	t /mm	5

Because the patches of the meshes that are connecting the two regions together are not conformal, an interpolative mapping needs to be used for fields that are communicating. For this a boundary condition called mappedWall in OpenFOAM is used. (Foundation, 2017) To define how the information is mapped between the regions a sample mode can be chosen and for this study the nearestPatch-FaceAMI(Arbitrary mesh interface) is used. This means that the information is exchanged between nearest faces and if the matching is not identical, weight functions are used. In figure 2 the computational domain for the air side is illustrated. The boundary patches are called **insulated** and **fluid to solid patch** as illustrated in the figure.

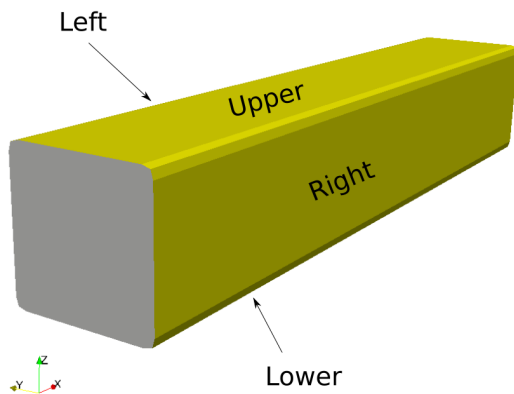


Figure 2. Illustration of the boundary patches on the fluid region

3.2 Boundary conditions

In the effort of analyzing what is the effect of natural convection and radiation inside the hollow beam during a fire, an artificial fire boundary condition is used outside the beam. In equation 9 the boundary condition ISO-834 curve for the warm wall is illustrated.

$$\theta_g = 293 + 345 \log\left(8\left(\frac{t}{60}\right) + 1\right) \quad (9)$$

in which t is time given in seconds and the illustration of the curve can be seen figure 3.

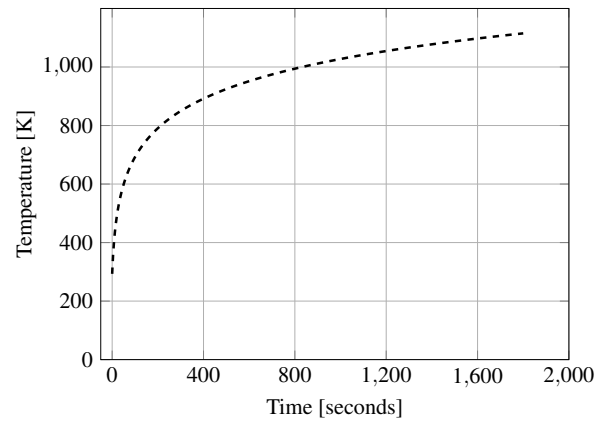


Figure 3. Illustration of the standard fire - - - in equation 9

In this paper the validity of this stand fire boundary conditions or its representation on the real fire is not studied more thoroughly. This is why an artificial temperature difference boundary condition between the warm side and cold side of the beam is used. For this study the cold side will be kept 50K lower than the warm side.

Table 2. Boundary conditions used for the computational model

Boundary name	Boundary condition
Solid region	
Warm wall	$u_i = 0, T = \text{standard fire}$
Cold wall	$u_i = 0, T = \text{standard fire} - 50K$
Insulated ends	$\frac{\partial u_i}{\partial x_n} = \frac{\partial T}{\partial x} = 0$
Solid-to-Fluid interface	$T_s = T_f, -\lambda_s \frac{\partial T_s}{\partial n} = -\lambda \frac{\partial T_f}{\partial n}$
Fluid region	
Insulated ends	$\frac{\partial u_i}{\partial x} = \frac{\partial T}{\partial x} = 0$
Fluid-to-Solid interface	$T_s = T_f, -\lambda_s \frac{\partial T_s}{\partial n} = -\lambda \frac{\partial T_f}{\partial n}$

The temperatures are measured in specific locations on the air side close to the solid and they are illustrated in figure 4.

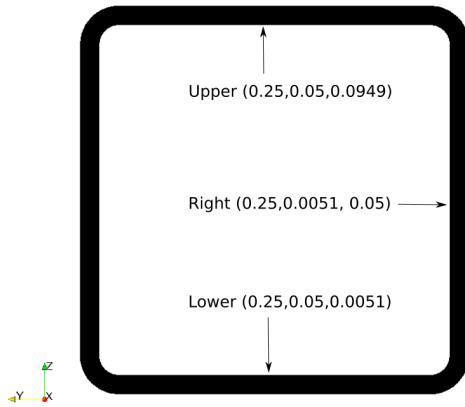


Figure 4. Illustration of the probe locations in meters

The thermal conductivity for the beam is calculated according to equation 10.

$$\lambda_s = 54 - 0.00333 * T \quad (10)$$

And the specific heat for the beam is calculated according to the equation 11.

$$C_p^s = 425 + 0.773 * T - 0.00169T^2 + 0.00000222 * T^3 \quad (11)$$

For the air side the specific heat capacity used was $C_p^f = 1000 \frac{J}{kgK}$, Prandtl number 0.7 and for viscosity the sutherland approximation formula is used with the reference temperature being 110.4K.

3.3 Mesh creation and independence study

Both the air and the solid mesh were created ny using open source meshing software called Swiftblock (Nogenmyr, 2016) meshing tool. It creates structured meshes by using Blender. Blender is a 3D modelling software that is created and developed by the Blender Online Community (Community, 2017). When the blocking strategy of the mesh is created in Blender, swiftblock transforms that into a blockMeshDict which is used by a primitive meshing software called blockMesh in OpenFOAM package to finally create the computational mesh used by OpenFOAM. (Foundation, 2017) Illustration of the meshing strategy and the boundary layers at the wall in figure 5

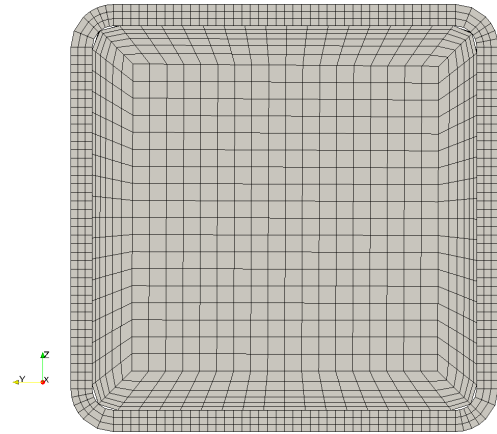


Figure 5. Illustration of the mesh structure in both fluid and solid regions

To validate that the computed results are independent on the mesh size a grid independence study was done for the mesh inside the hollow beam. Four different mesh sizes where studied and with all of them the ratio between the biggest cell size and the y-value at the wall was kept 3. The results can be seen in figure 6 where the convective heat transfer from the lower side of the beam is plotted against the time.

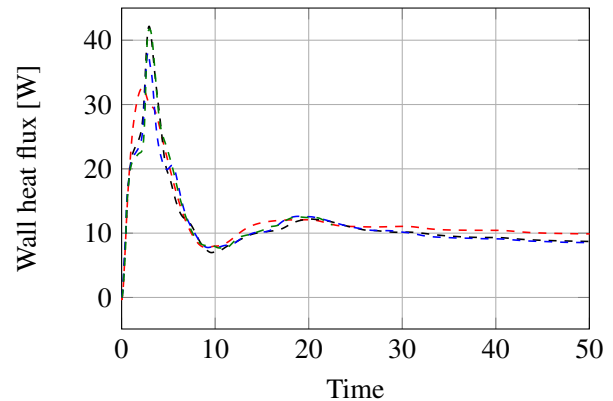


Figure 6. Convective heat flux at the lower side wall with: 5k ---, 27k ---, 64k --- and 192k --- meshes

From the results the conclusion was made that 64000 cells was sufficient amount of cells to capture the turbulent scales of natural convection inside the beam. No turbulence models was used in the simulations.

4 Results and Discussion

In this section the wall heat flux through the boundary **fluid to solid patch** is calculated and compared between the case where the momentum equation is calculated and the case where the velocity field is frozen and not calculated through the calculation. Two differen wall heat fluxes are calculated, the other one being the flux cause by conduction and convection and is calculated according to

the equation 5 and the other one being the radiation heat flux coming from other surfaces and is calculated according to the equation 7. In figure 7 these wall heat fluxes through the lower side of the air domain is shown.

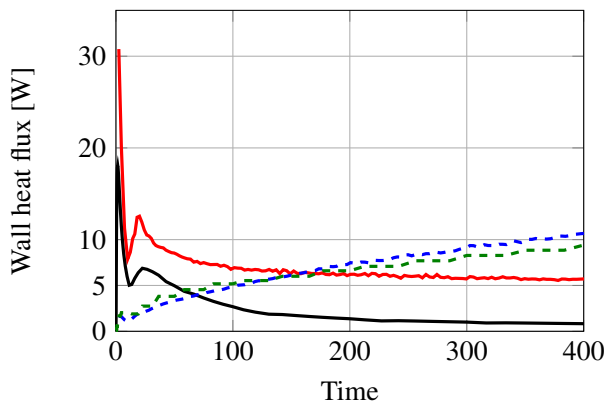


Figure 7. Wall heat flux through the lower side of the beam; conduction and convection —, conduction with frozen flow —, radiation - - - and radiation in the frozen flow - - -

The convection can be seen to dominate in the first 50 seconds of the computation but radiation will be increasing as the temperature level rise. The convection and conduction can be seen to converge after the 200 seconds, convection and conduction — being 5.5 watts and only the conduction in the frozen flow simulation — being around 0.55 watts.

The right side of the beam and the heat fluxes through that patch can be seen in figure 8.

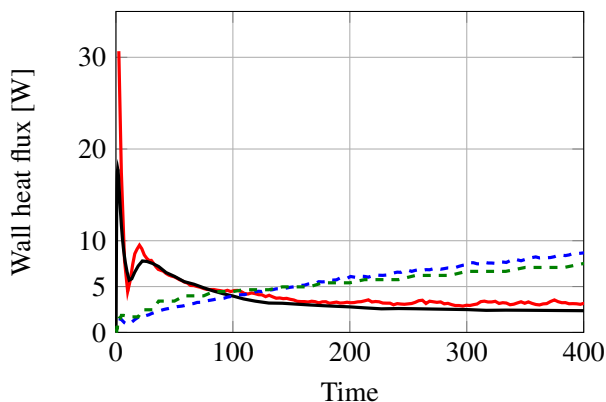


Figure 8. Wall heat flux through the right side of the beam; conduction and convection —, conduction with frozen flow —, radiation — and radiation in the frozen flow - - -

The combined convection and conduction — and only conduction in the frozen flow simulation — can be seen to be almost equal during the first 400 seconds. The value for conduction in the frozen flow simulation — being 2.22 watts. The radiation heat flux in both of these cases can be seen to increase as the temperature increases and the absolute value being slightly higher for the case with the convection included in the simulation.

The different heat fluxes through the upper side of the beam are of course negative because the heat is going out from the air domain and the values can be seen in figure 9.

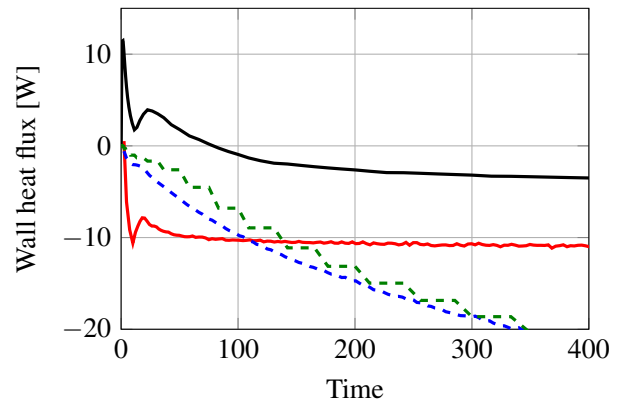


Figure 9. Wall heat flux through the right side of the beam; conduction and convection —, conduction with frozen flow —, conduction with frozen flow —, radiation - - - and radiation in the frozen flow - - -

Through the upper side of the cavity, inside the beam, the convection and conduction can be seen to converge after the first 200 seconds, convection and conduction — being -10.8 watts and only the conduction in the frozen flow simulation — being around -4.2 watts. The radiation in the convection case - - - and the radiation in the frozen flow case - - - are increasing as the temperature is increasing. The sign of course being opposite because of the opposite direction of the heat.

To show what is the difference in the temperature between the case with convection, and the one without, the results can be seen in figure 10.

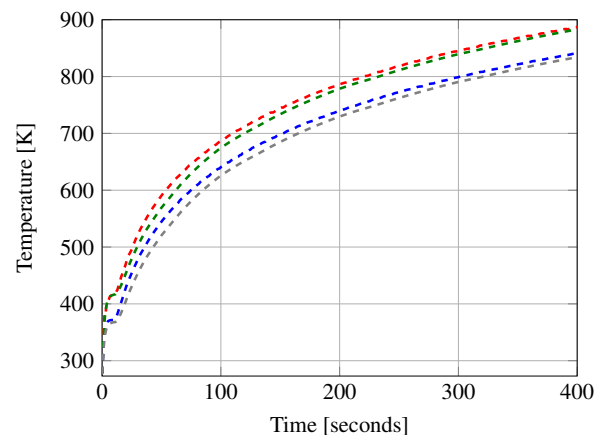


Figure 10. Temperatures in the air in the probe locations according to the figure 4: Lower side - - -, lower side frozen flow - - -, upper side - - - and upper side frozen flow - - -

The temperatures are pretty close to each other but the ones in the with convection are slightly higher than the ones without.

To illustrate that the temperature field and the wall heat flux fields inside the beam are not constant during the fire the figure 12, figure 11 and figure 13 are presented.

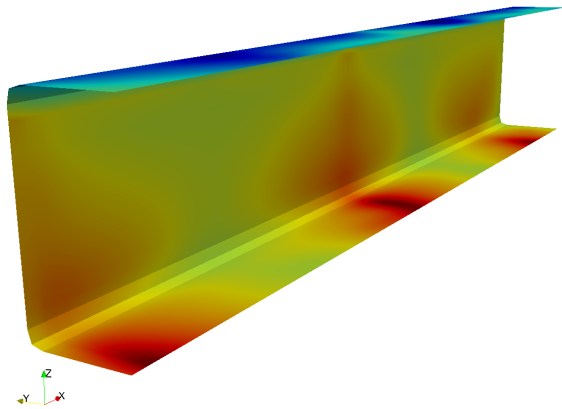


Figure 11. Illustration of the non-constant wall heat flux inside the beam when $t = 400s$

As can be seen from the figures, inside the beam a wandering recirculation zone is travelling as the simulations continues. The size of this travelling vortex is around the size of the hydraulic diameter of the insides of the hollow beam.

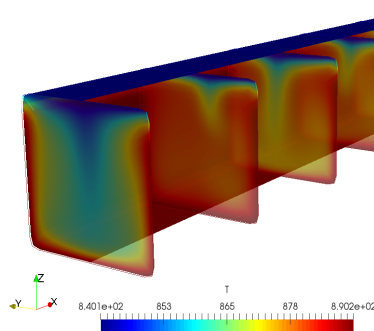


Figure 12. Illustration of the non-constant temperature field inside the beam when $t = 400s$

Final illustration of the non-constant temperature field we look at the velocity field in the middle of the beam where $x = 0.25m$ in figure 13.

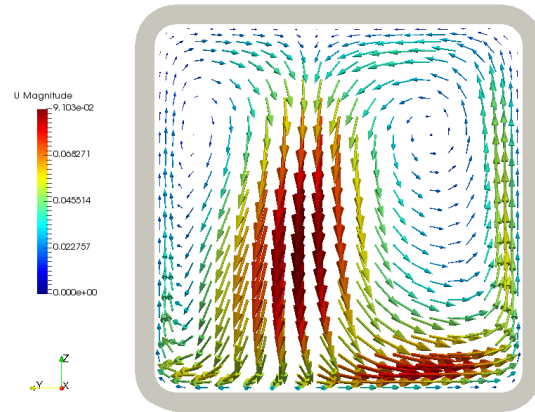


Figure 13. Illustration of the velocity field inside the beam when $t = 400s$ and $x = 0.25m$

5 Conclusions

In this study the effect of natural convection inside the hollow beam in a standard fire was studied. A conjugate heat transfer solver in OpenFOAM was used and all the meshes were created with open source software. To simulate what is the effect of solving the momentum and pressure equation inside the beam the case was solved with the equation and without as a frozen flow field simulation. The key findings were as follows.

1. In the beginning the convection and conduction are dominating the heat transfer.
2. After 100 seconds the radiation heat transfer is equal to the conduction and convection.
3. On the lower side of the beam the convection heat transfer is 5 times higher than conduction in the similar case with a frozen flow field simulation.
4. After 400 seconds of simulation, the radiation heat transfer is double to the amount of convection and will keep increasing as the temperature increases with the propagating fire.

As depicted in figures 11 and 12, the internal heat transfer due to non-constant ambient temperature field causes fluid temperature variations that are meaningful when compared to ambient temperature differences. In future studies, this phenomenon will be investigated in the context of practical steel joints.

References

- Blender Online Community. Blender – a 3d modelling and rendering package, 2017. URL <http://www.blender.org>.
- The OpenFOAM Foundation. The openfoam documentation, 2017. URL <https://openfoam.org/>.

- Tat Ching Fung, KH Tan, and Minh Phuong Nguyen. Structural behavior of chs t-joints subjected to static in-plane bending in fire conditions. *Journal of Structural Engineering*, 142(3): 04015155, 2015.
- Shu-Bin He, Yong-Bo Shao, Hong-Yan Zhang, Dong-Ping Yang, and Feng-Le Long. Experimental study on circular hollow section (chs) tubular k-joints at elevated temperature. *Engineering Failure Analysis*, 34:204–216, 2013.
- Markku Heinisuo and Timo Jokinen. Tubular composite columns in a non-symmetrical fire. *Inzenerno-Stroitel'nyj Zurnal*, (5):107, 2014.
- William Morrow Kays. *Convective heat and mass transfer*. Tata McGraw-Hill Education, 2012.
- Anthony F Mills. *Basic heat and mass transfer*. Pearson College Div, 1999.
- Folkersma M Nogenmyr, K.J., 2016. URL <https://openfoamwiki.net/index.php/Contrib/SwiftBlock>.
- E Ozyurt, YC Wang, and KH Tan. Elevated temperature resistance of welded tubular joints under axial load in the brace member. *Engineering Structures*, 59:574–586, 2014.
- Yongbo Shao, Yijie Zheng, Haicheng Zhao, and Dongping Yang. Performance of tubular t-joints at elevated temperature by considering effect of chord compressive stress. *Thin-Walled Structures*, 98:533–546, 2016.
- MB Wong. Temperature analysis of partially heated steel members in fire. *Journal of Constructional Steel Research*, 128: 1–6, 2017.
- Hua Yang, Faqi Liu, and Leroy Gardner. Performance of concrete-filled rhs columns exposed to fire on 3 sides. *Engineering Structures*, 56:1986–2004, 2013.
- J Yang, YB Shao, and C Chen. Experimental study on fire resistance of square hollow section (shs) tubular t-joint under axial compression. *Advanced Steel Construction*, 10(1):72–84, 2014.

Study of Fluidization Regimes using OpenFOAM Computational Fluid Dynamics

Prasanna Welahettige¹, Bernt Lie¹, Knut Vaagsaether¹, Britt M.E Moldestad¹

¹Department of Process, Energy and Environmental Technology
University College of Southeast Norway
Porsgrunn, Norway
knut.vagsaether@usn.no

Abstract

The objective of this study was using computational fluid dynamics simulation with OpenFOAM to study the fluidization properties for four types of particles classified as Geldart A, B, C and D. Fluidization regimes were studied for particles with the same density but different diameters. The particle diameters were selected based on Geldart's classification of particles. The simulation results were validated against experimental data. Pressure gradient, flow regime change, bubble rise, bubble splitting and bed expansion were studied for all four types of particles for different superficial velocities. Group-B and D particles easily produced bubbles. However, Group-C and A particles gave very high bed expansion, and no clear bubbles were observed. Bed with the Group-D particles, the bubbles was large and some of the bubbles reached the diameter of the bed. Group-B particles gave smaller and on average more stable bubbles than Group-D particles. There was no bubble formation from Group-C and Group-A until the inlet superficial velocity was 25 times and 5 times larger, respectively, than their minimum fluidization velocities.

Keywords: Fluidization, bubble, Geldart's classification, pressure gradient, flow regimes, OpenFOAM

1 Introduction

The gas-solid fluidization process can be divided into two basic steps: the packed bed and the fluidization regime. The packed bed pressure drop can be explained using the Ergun equation up to a minimum fluidization. The pressure drop across the fluidization flow regime can be explained using the mixture momentum balance equation. At the minimum fluidization condition, the buoyant force and the drag force are equal and balance each other in opposite directions (Gidaspow, 1994). According to Geldart's classifications of powder, uniformly sized powders can be classified into four basic types: aeratable (Group-A), bubbling (Group-B), cohesive (Group-C) and spoutable (Group-D), (Geldart, 1972). Group-A particles show considerable bed expansion before the bubbles appear. Group-B particles give bubbles as soon as the gas velocity exceeds the minimum fluidization condition (Kunii & Levenspiel,

1991). The agglomerate diameter of Group-A particles depends upon a force balance between cohesive, drag, gravity, and collision forces (Motlagh *et al.*, 2014). Group-C particles have difficulties in rising due to the inter particle forces that are stronger than the fluid forces exerted on particles (Gidaspow, 1994). Group-D particles give a slower bubble rise velocity than the gas velocity (Kunii & Levenspiel, 1991). (Wang X. *et al.*, 2007) showed that Nano-sized particles possess both Group-A and Group-B behavior. Group-B bubbles, which are at the interface between dense phase and freeboard, affect bed collapse time (Pei *et al.*, 2009). (Pandit *et al.*, 2005) found that high bed expansion happens at the particle size boundary between Group-A and B. (Alavi & Caussat, 2005) found that the fluidization behavior improved for the highest vibration strengths. (Zhang *et al.*, 2008) simulated Group-A and B particles using a commercial computational fluid dynamics (CFD) tool. There are a number of CFD studies on the gas-solid fluidization. However, few open source CFD studies about all four types of Geldart's groups of particles are published. In this work, all four types of particles were simulated using OpenFOAM 4.0, 2-D simulations. The standard "twoPhaseEulerFoam" model was used for the simulations. All the four particle types were studied with respect to of pressure gradients, flow regime changes, bed expansion, bubble formations and bubble rises.

2 Numerical models

The Euler-Euler model was used to simulate both phases. In this approach, the sum of phase volume fractions equals unity and the phase volume fraction is a continuous function of space and time (Rusche, 2002).

$$\alpha_g + \alpha_s = 1 \quad (1)$$

Here, α is the volume fraction and subscripts g and s indicate gas and solid phases. Continuous phase velocity varies significantly over the volume when the flow becomes turbulent. Therefore, average velocities are introduced in the continuity equation (Crowe *et al.*, 2011),

$$\frac{\partial \rho_g \alpha_g}{\partial t} + \nabla \cdot (\rho_g \bar{U}_g \alpha_g) = 0. \quad (2)$$

The x momentum equation for continuous phase can be given as (Rusche, 2002) and (Crowe *et al.*, 2011).

$$\begin{aligned} \frac{\partial \rho_g \alpha_g \bar{u}_g}{\partial t} + \nabla \cdot (\alpha_g \rho_g \bar{u}_g \bar{U}_g) \\ = -\alpha_g \frac{\partial \bar{p}}{\partial x} + \nabla \cdot \bar{\tau}_{g,x} \\ + \alpha_g \rho_g g_x + \bar{M}_{g,x} \end{aligned} \quad (3)$$

Here, \bar{u}_g is the x directional velocity of the continuous phase, ρ_g is the density of the continuous phase, \bar{U}_g is three dimensional velocity components of the continuous phase, \bar{p} is the pressure, $\bar{\tau}_{g,x}$ is the x component Reynold average stresses, g_x is the acceleration of gravity in the x direction, $\bar{M}_{g,x}$ is the average interface momentum transfer term per unit volume,

$$\bar{M}_{g,x} = F_d + F_l + F_{vm} + F_o \quad (4)$$

Here, F_d is the drag force, F_l is the lift force, F_{vm} is the virtual force and F_o is the other force. Lift force, virtual force and other forces were neglected. The drag force for unit volume is,

$$F_d = \beta' (v_s - v_g) \quad (5)$$

The friction coefficient between fluid and solid (β') (Gidaspow, 1994) depends on α_g :

if $\alpha_g < 0.8$, Ergun's formula applies,

$$\beta' = 150 \frac{\alpha_s^2 \mu_g}{\alpha_g (d_p \phi_s)^2} + 1.75 \frac{\rho_g |v_g - v_s| \alpha_s}{\phi_s d_p}, \quad (6)$$

while if $\alpha_g > 0.8$, Wen and Yu's formula applies,

$$\beta' = \frac{3}{4} C_D \frac{\alpha_g |v_g - v_s| \rho_g \alpha_s}{d_p} \alpha_g^{-2.65}. \quad (7)$$

Here, μ_g is the gas viscosity and the drag coefficient (C_D) depends on Reynold's number:

if $Re_s < 1000$,

$$C_D = \frac{24}{Re_s} (1 + 0.15(Re_s)^{0.687}), \quad (8)$$

if $Re_s \geq 1000$,

$$C_D = 0.44. \quad (9)$$

Here,

$$Re_s = \frac{\alpha_g \rho_g |v_g - v_s| d_p}{\mu_g}. \quad (10)$$

The restitution coefficient, which evaluates the particle-particle collision, was 0.8. The Johnson-Jackson model calculates friction stress between wall and particles. The minimum fluidization velocity ($u_{g,mf}$) is

$$u_{g,mf} = \frac{d_p^2 (\rho_p - \rho_g) g \alpha_{g,mf}^3 \phi_p^2}{150 \mu_g \alpha_{s,mf}}. \quad (11)$$

Here, d_p is the particle diameter, ρ_p is the density of the particle, ϕ_p is the sphericity of the particle. Maximum bubble size ($d_{b,max}$) according to Mori and Wen (Kunii & Levenspiel, 1991) is

$$d_{b,max} = 0.65 \left(\frac{\pi}{4} d_t^2 (u_0 - u_{mf}) \right)^{0.4}. \quad (12)$$

Here, d_t is the channel width. According to the Grace correlation (Gidaspow, 1994), a single bubble velocity (u_{br}),

$$u_{br} = 0.711 \sqrt{g d_b}. \quad (13)$$

The velocity of bubbles in a bubbling bed is

$$u_b = u_0 - u_{mf} + u_{br}. \quad (14)$$

Here, d_B is the average bubble diameter and u_0 is the inlet gas velocity.

2-D simulations were done using the open source CFD code OpenFOAM 4.0. The forward Euler method was used for the time discretization. Pressure-velocity coupling was solved by the pressure implicit with splitting of operators (PISO) algorithm with second order upwind correction.

Grid size (mesh resolution) is a critical factor for the gas-solid two fluid method (TFM). Grid size needs to have sufficient scale resolution to accurately predict the bed expansion (Wang J. *et al.*, 2011). When the grid size is smaller than 10 times the particle diameter, a homogenous drag model reached its asymptotic results (Lu *et al.*, 2009). The simulations failed to predict Geldart's A particle when using a fine mesh (Lu *et al.*, 2011) and (Wang J. *et al.*, 2009). Therefore, 7 mm minimum cell size mesh was used for 1.5 mm maximum size particle diameter.

3 Physical properties of gas-solid system

Table 1 shows physical properties of the particle groups. Particle density and fluid density were constants for the groups. Corresponding particle diameters were selected

based on Geldart's powder classification diagram (Geldart, 1972).

Table 1. Physical properties of gas-solid system

Parameters	Group-A	Group-B	Group-C	Group-D
Particle diameter, d_p , (μm)	60	350	15	1500
Particle density, ρ_s , (kg/m^3)	2500	2500	2500	2500
Fluid density, ρ_g , (kg/m^3)	1.225	1.225	1.225	1.225
Calculated minimum fluidization velocity, $u_{g,mf}$, (m/s)	0.0035	0.15	0.00024	2.4

4 Results and discussion

Results were categorized for each group as a comparison. Pressure gradient across a bed was calculated as an average pressure difference between two points in the bed, which were 30 mm and 235 mm vertical height from the bed bottom. The average pressure was calculated as an area average pressure. The channel width was 0.084 m and channel height was different depending on the expansion of the groups.

4.1 Group-A

4.1.1 Pressure gradient

The pressure gradient increased proportionally with the inlet superficial velocity until the minimum fluidization velocity was reached. At minimum fluidization, the packed bed gave a maximum pressure gradient as shown in Figure 1. The minimum fluidization velocity was 0.006 m/s. (Ye *et al.*, 2005) also observed a similar pressure drop pattern with the inlet superficial velocities for Group-A particles.

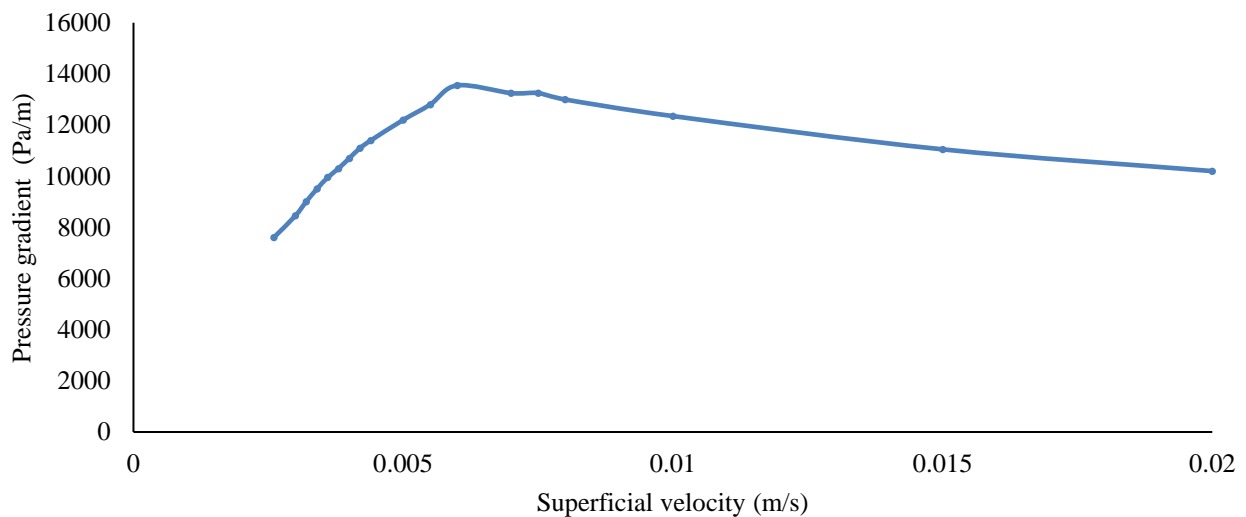


Figure 1. Group-A particles pressure-gradient variation with the inlet superficial velocity

4.1.2 Fluidization regimes

Figure 3 shows bed expansions with different inlet superficial velocities. There was no considerable bed expansion before the minimum fluidization velocity was reached. However, after the minimum fluidization, the bed expanded considerably. Here, the dense phase was gradually transitioned into the dilute phase. There was no bubble formation until the inlet superficial velocity was five times higher than the minimum fluidization velocity. This bubble less bed expansion behavior was also observed by (Wang X. *et al.*, 2007). However, when the inlet velocity was further increased, the airflow tried to create flow channels in the expanded bed. (Karimipour & Pugsley, 2010) also observed a similar behavior, when the bed expanded, it gradually compromised into a normal bubbling bed.

4.2 Group-B

4.2.1 Pressure gradient

Figure 4 shows pressure gradient variation with the inlet superficial velocity. The pressure gradient gradually increased until minimum fluidization occurred, and then it became (on average) constant. The minimum fluidization velocity was 0.16 m/s in the experiment and 0.18 m/s in the simulation. The average particle diameter was 350 μm in the experiment (Thapa & Halvorsen, 2013). However, in the simulation only 350 μm diameter particles was used. This could be the reason for having a little difference between the simulation result and the experimental result.

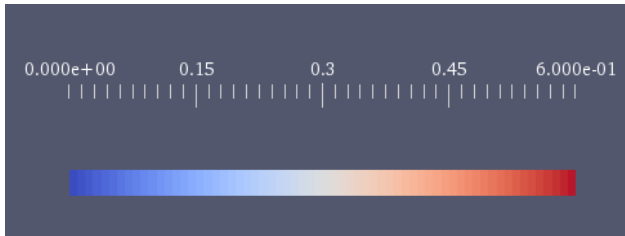


Figure 2. Color map for Figure 3, 5, 6, 7, 9, 11 and 12. Value zero (dark blue) represents the gas and value one (dark red) represents the solid.

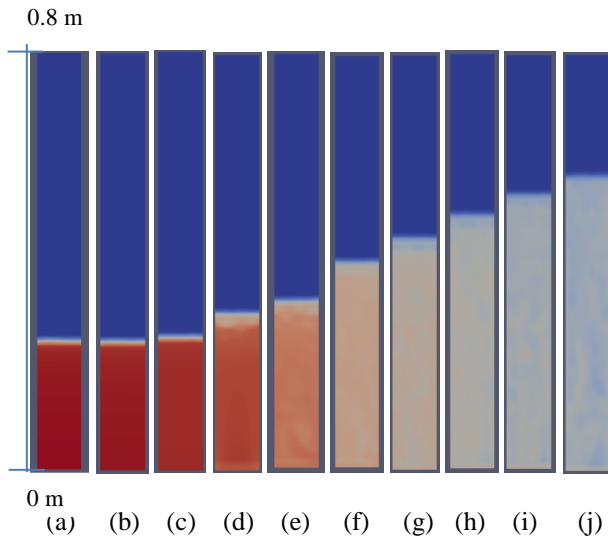


Figure 3. Solid volume fraction with different inlet superficial velocities, Geldart's classification Group-A, $\rho_s = 2500 \text{ kg/m}^3$, $d_p = 60 \text{ }\mu\text{m}$, the maximum column height is 0.8 m ; (a) 0.0026 m/s, (b) 0.0042 m/s, (c) 0.006 m/s, (d) 0.008 m/s, (e) 0.015 m/s, (f) 0.03 m/s, (g) 0.04 m/s, (h) 0.05 m/s, (i) 0.06 m/s, (j) 0.07 m/s

4.2.2 Fluidization regimes

Figure 5 shows a flow regime change with increase of the inlet superficial velocity. The packed bed can be considered as a normal packing (neither a dense packing nor a loose packing), because the minimum void fraction was 0.3564 and the sphericity was equal to one (Kunii & Levenspiel, 1991). There is no bubble formation in Figure 5.a. This was due to the gas velocity lower than the minimum fluidization velocity. Approximate minimum fluidization is shown in Figure 5.b. There was no bubble formation at this stage. The size of bubbles is expanded from Figure 5.c to Figure 5.f. The minimum bubbling occurred at the inlet superficial velocity in range 0.2 m/s to 0.25 m/s. Figure 5.f shows a slug formation. A spouted bed behavior is shown in Figure 5.g. The spouted bed behavior was occurred, when the inlet superficial velocity was five times larger than the minimum fluidization velocity.

4.2.3 Bubble formation and rise

Figure 6 shows a bubble formation from the bottom of the bed and travel until the top of the bed. The bubble size increased gradually with time. The circular shape of the bubble changed into an elliptical shape at the end. This was due to the lower hydrostatic pressure applied to the bubble at the top of the bed. The average bubble-rise velocity from the formation to the end was 0.426 m/s (for the inlet superficial velocity 0.35 m/s), which was higher than the gas inlet velocity and higher than the minimum fluidization velocity. The diameter of the bubble varied from 0 mm to 42 mm. Here, the average bubble size was 50% of the bed diameter. According to Equation-14, the calculated average bubble-rise velocity was 0.482 m/s, which was approximately equal to the simulation result. Most of the bubbles rise faster than the inlet superficial gas velocity (Geldart, 1972). The high bubble velocity is due to the low void fraction in the bed. These low voidages support to rise the bubbles faster than the inlet superficial velocity. Increase or decrease of bubble diameter depends on the balance of coalescence and splitting frequencies (Horio M & Nonaka A, 1987). Group-B particle showed higher mixing than Group-A particles due to the more bubbles in the bed.

4.2.4 Bubble splitting

Figure 7 shows the bubble-splitting behavior. Here, dense phase particles collapsed onto the bubble and because of this, the bubble splits into two. Other bubbles and wall effects were also reasons to the bubble splitting.

4.3 Group-C

4.3.1 Pressure gradient

There are very few simulations related to Group-C particle fluidization found in literature. There is a real practical difficulty of the simulations, which takes higher simulation time due to very small velocities at minimum fluidization. In this study, a time step of 10^{-4} s was used for the simulations. Figure 8 shows pressure gradient variation with the inlet superficial velocity for Group-C particles. The minimum fluidization velocity was 3.75×10^{-4} m/s.

4.3.2 Flow regimes

Group-C particles behaved as a fluid as shown in Figure 9 and it gave the higher flow behavior compared to the other groups. Even though the inlet superficial velocity was 25 times larger than the minimum fluidization velocity, there was no bubble formation. This was due to the high cohesive properties of Group-C particles. Due to strong extra inter-particle forces, bubble formation does not occur in beds with Group-C particles

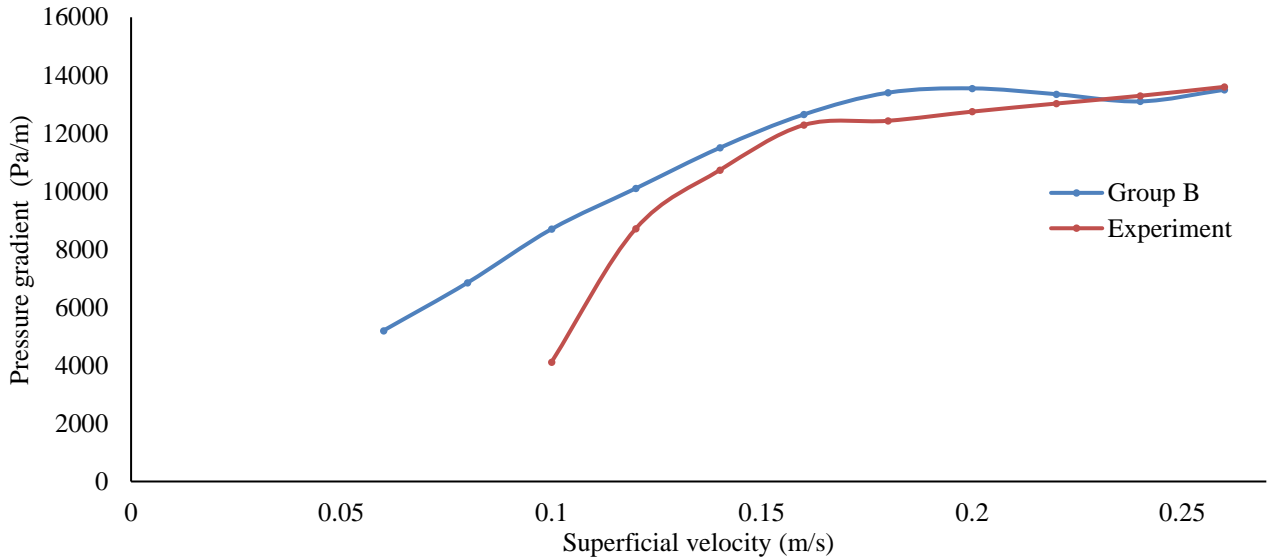


Figure 4. Group-B pressure-gradient variation with the inlet superficial velocity, the experimental result from (Thapa & Halvorsen, 2013).

(Yao *et al.*, 2002). However, the standard “twoPhaseEulerFoam” does not include the cohesive forces.

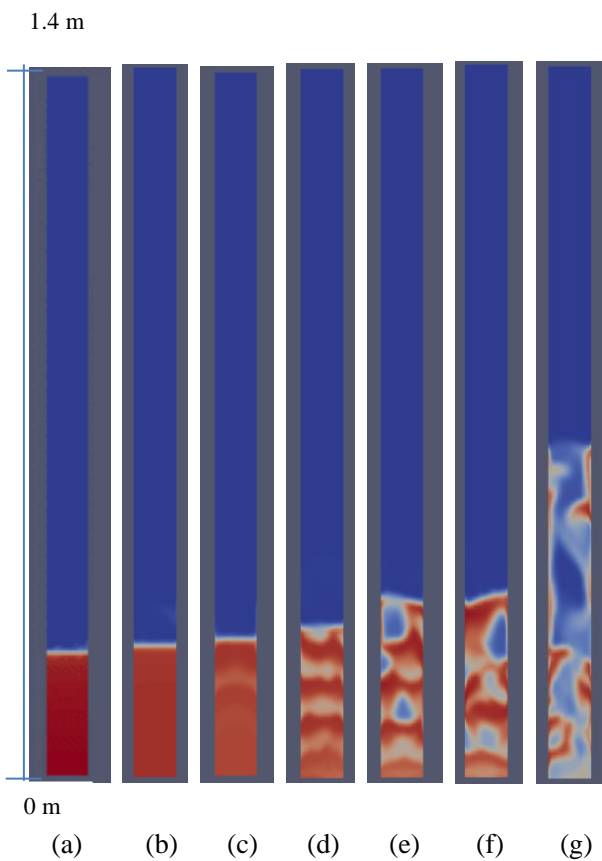


Figure 5. Solid volume fraction with different inlet superficial velocities, Geldart’s classification, Group-B, $\rho_s = 2500 \text{ kg/m}^3$, $d_p = 350 \text{ }\mu\text{m}$, the maximum column height is 1.4 m ; (a) 0.05 m/s, (b) 0.2 m/s, (c) 0.25 m/s, (d) 0.3 m/s, (e) 0.4 m/s, (f) 0.45 m/s, (g) 1.0 m/s

4.4 Group-D

4.4.1 Pressure gradient

Figure 10 shows the pressure gradient variation with the inlet superficial velocity. The minimum fluidization velocity was 1.15 m/s and the pressure gradient in the bed was 2600 Pa.

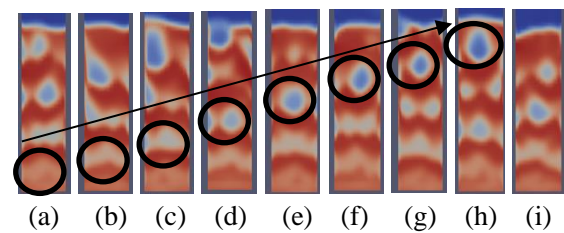


Figure 6. Bubble formation and rise vs. time, $d_p = 350 \text{ }\mu\text{m}$, $v = 0.35 \text{ m/s}$; (a) $t = 2.5 \text{ s}$, (b) $t = 3.0 \text{ s}$, (c) $t = 3.5 \text{ s}$, (d) $t = 4.0 \text{ s}$, (e) $t = 4.5 \text{ s}$, (f) $t = 5.0 \text{ s}$, (g) $t = 5.5 \text{ s}$, (h) $t = 6.0 \text{ s}$, (i) $t = 6.5 \text{ s}$

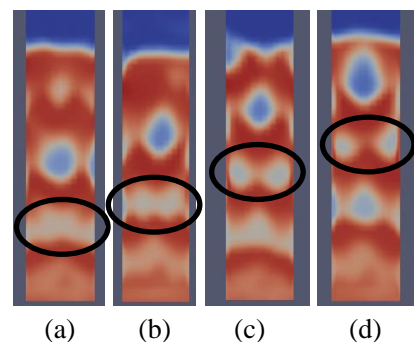


Figure 7. Bubble splitting, $d_p = 350 \text{ }\mu\text{m}$, $v = 0.35 \text{ m/s}$; (a) $t = 2.5 \text{ s}$, (b) $t = 3.0 \text{ s}$, (c) $t = 3.5 \text{ s}$, (d) $t = 4.0 \text{ s}$

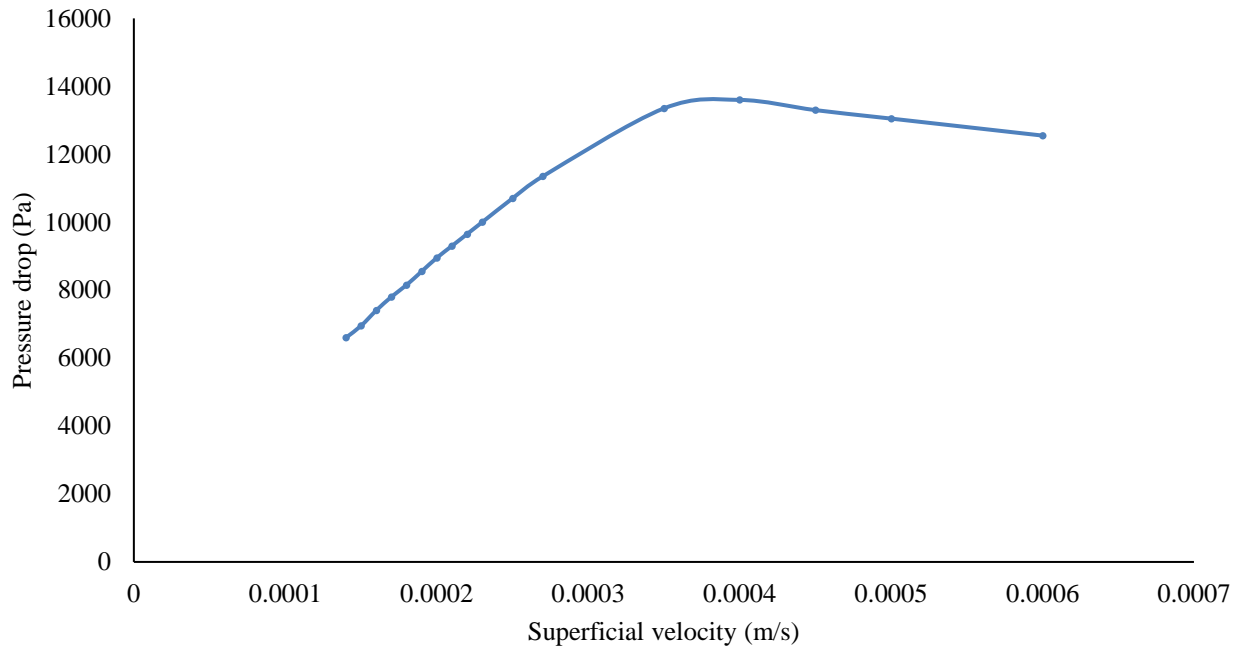


Figure 8. Group-C particles pressure-gradient variation with the inlet superficial velocity

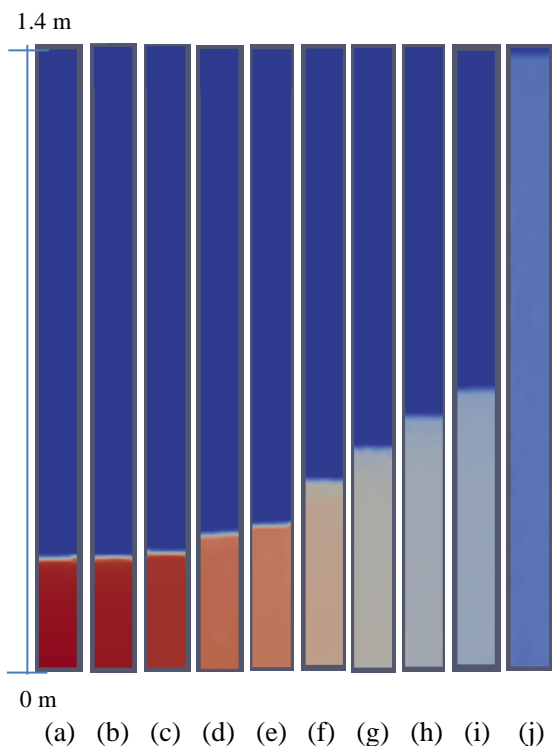


Figure 9. Solid volume fraction, Geldart's classification, Group-C, $\rho_s = 2500 \text{ kg/m}^3$, $d_p = 15 \mu\text{m}$, the maximum column height is 1.4 m; (a) 0.00014 m/s, (b) 0.00027 m/s, (c) 0.0004 m/s, (d) 0.0008 m/s, (e) 0.001 m/s, (f) 0.002 m/s, (g) 0.003 m/s, (h) 0.004 m/s, (i) 0.005 m/s, (j) 0.01 m/s after 380 s

4.4.2 Flow regimes

Figure 11 shows solid volume fraction change with increase of the inlet superficial velocity. Flow behavior was similar with Group-B particles. However, bubbles were not stable as for Group-B and they were splitting faster. Back mixing was slower compared to Group-B particles (Geldart, 1972).

4.4.3 Bubbles formation

The shapes of the bubbles changed rapidly. The average size of the bubbles is larger than the average size of Group-B bubbles. The bubbles were very unstable at the top of the bed. There were large openings of bubbles at the top of the bed as shown in Figure 12. The average bubble size was 0.07 m, which was approximately equal to the width of the column ($d_t = 0.082 \text{ m}$). The calculated average bubble-rise-velocity was 1.04 m/s from Equation-14. However, the simulated average bubble rise velocity was 0.4 m/s. Group-D bubbles rose at lower speed than the inlet superficial velocity. This is due to Group-D bubbles being comparatively larger and this creates higher voidages to rise the gas compared to the other groups.

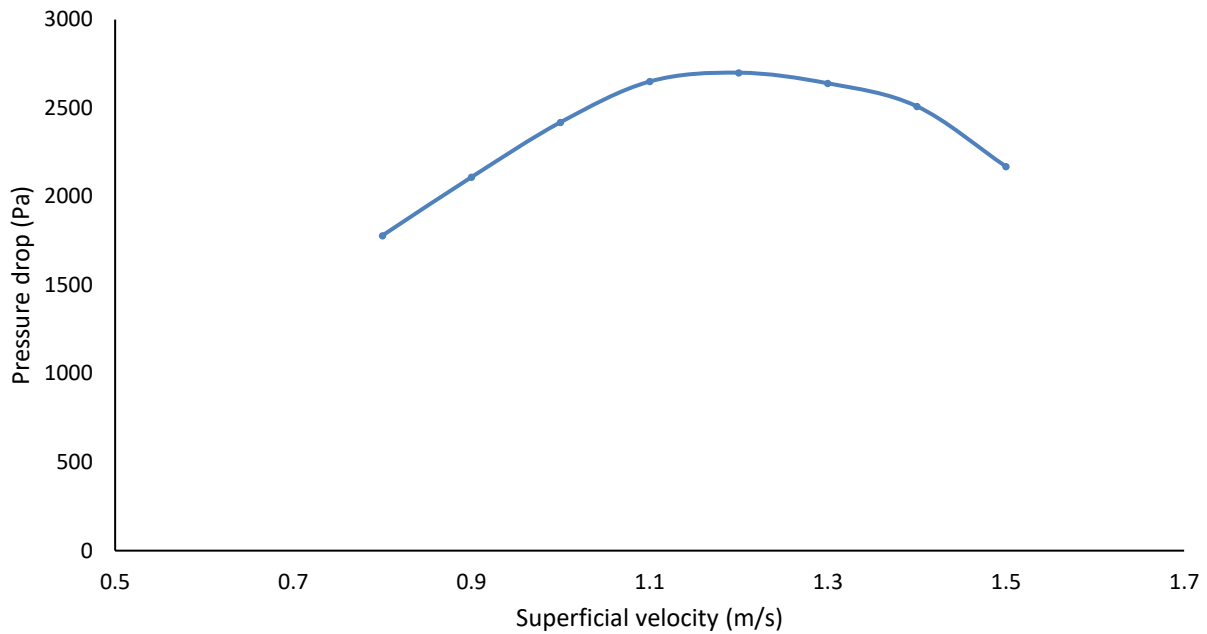


Figure 10. Group-D particle pressure-gradient variation with the inlet superficial velocity

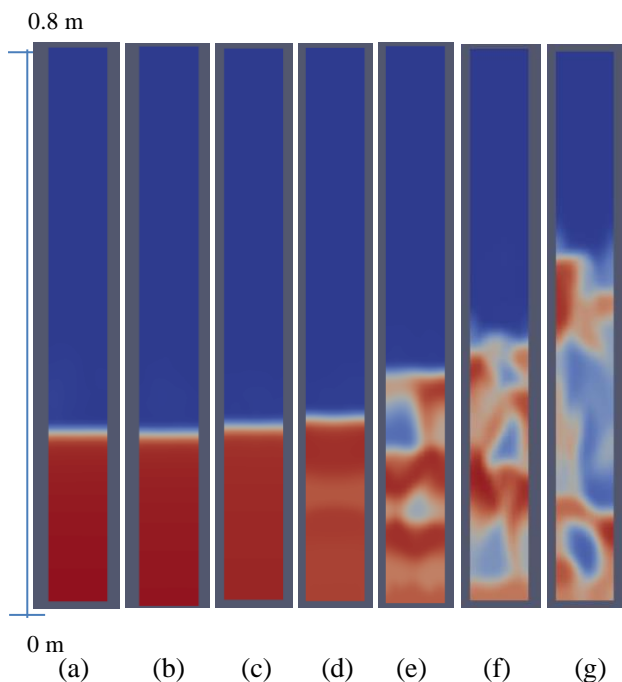


Figure 11. Solid volume fraction after 70 s, Geldart's classification, Group-D, $\rho_s = 2500 \text{ kg/m}^3$, $d_p = 1500\mu\text{m}$, the maximum column height is 0.8 m; (a) 0.8 m/s, (b) 0.9 m/s, (c) 1.1 m/s, (d) 1.3 m/s, (e) 1.5 m/s, (f) 2.0 m/s, (g) 2.5 m/s

5 Comparison of Group-A, B, C, and D

5.1 Bed expansion

Figure 13 shows bed expansion with the inlet superficial velocity for the all four particle groups. The bed

expansion factor was defined as $\frac{h}{h_{mf}}$. Here h was the bed height and h_{mf} was the bed height at the minimum fluidization. The expansions were considered until the bubble formation occurred. Group-C particles showed the highest bed expansion ratio, which was 1 to 2.5 times. Group-A particles showed a bed expansion 1 to 2.1 times. Group-B particles showed a bed expansion 1 to 1.2 times. Group-D particles gave lowest bed expansion that was 1 to 1.05 times. Group-C expanded with the smallest velocities and Group-D expanded with the largest velocities.

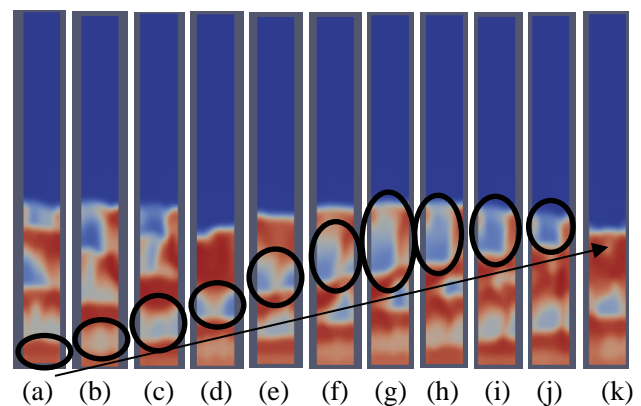


Figure 12. Bubble formation and rise of Group-D particles, $d_p = 1500\mu\text{m}$, $v = 1.6 \text{ m/s}$; (a) $t = 1.55 \text{ s}$, (b) $t = 1.72 \text{ s}$, (c) $t = 1.80 \text{ s}$, (d) $t = 1.91 \text{ s}$, (e) $t = 2.05 \text{ s}$, (f) $t = 2.13 \text{ s}$, (g) $t = 2.18 \text{ s}$, (h) $t = 2.23 \text{ s}$, (i) $t = 2.28 \text{ s}$, (j) $t = 2.32 \text{ s}$, (k) $t = 2.38 \text{ s}$

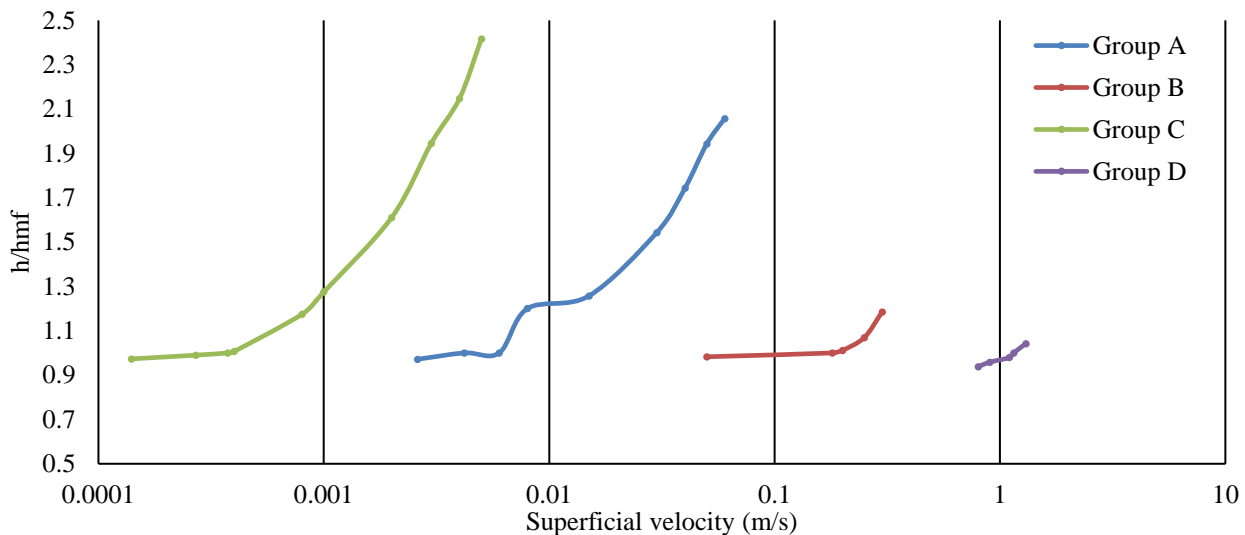


Figure 13. Bed expansion with the inlet superficial velocity for Group-A, B, C and D particles. x-axis is given in log

5.2 Void fraction at the minimum fluidization

The void fraction at the minimum fluidization is an important parameter for many calculations. Table 2 gives minimum fluidization velocity (u_{mf}), bed height at the minimum fluidization (h_{mf}) and void fraction at minimum fluidization (α_{mf}). The minimum allowable void fraction was defined as 0.3564 during the simulations. The void fraction at minimum fluidization was calculated as the average void fraction in a packed bed.

Table 2. Simulated results at minimum fluidization for all the four groups

	Group-A	Group-B	Group-C	Group-D
d_p (μm)	60	350	15	1500
u_{mf} (m/s)	0.006	0.19	0.000375	1.15
h_{mf} (mm)	255	263	256	259
α_{mf}	0.4427	0.4539	0.4467	0.4565

6 Conclusions

Group-A and -C particles show bubble-less bed expansion. Group-C particles show the highest bed expansion ratio and Group-D particles show the lowest bed expansion ratio, respectively 2.5 times and 1.05 times, before bubble formation. A higher average bubble size occurs in Group-D particles than Group-B particles. Group-A and Group-C particles are less prone to mixing than Group-B and Group-D particles due to less bubble formation. Group-C particles show higher flow properties than the others. The minimum fluidization

velocities become gradually smaller from Group-D, B, A to C.

Acknowledgement

Economic support from The Research Council of Norway and Statoil ASA through project no. 255348/E30 "Sensors and models for improved kick/loss detection in drilling (Semi-kidd)" is gratefully acknowledged. The authors also gratefully acknowledge the resources for experiments and simulations provided by the University College of Southeast Norway.

References

- Alavi S. and Caussat B. (2005). Experimental study on fluidization of micronic powders. *Powder Technology*, 157(1–3), 114-120. doi:http://dx.doi.org/10.1016/j.powtec.2005.05.017
- Crowe C. T., Schwarzkopf J. D., Sommerfeld M. and Tsuji Y. (2011). *Multiphase flows with droplets and particles*: CRC press.
- Geldart D. (1972). Types of Gas Fluidization *Powder Technology*, 7(1973), 285-292.
- Gidaspow D. (1994). *Multiphase flow and fluidization : continuum and kinetic theory descriptions*. Boston: Academic Press.
- Horio M and Nonaka A. (1987). A generalized bubble diameter correlation for gas-solid fluidized beds *AIChE Journal*, 33(11), 1865-1872.
- Karimipour S. and Pugsley T. (2010). Study of gas streaming in a deep fluidized bed containing Geldart's Group A particles. *Chemical Engineering Science*, 65(11), 3508-3517. doi:http://dx.doi.org/10.1016/j.ces.2010.02.045
- Kunii D. and Levenspiel O. (1991). *Fluidization engineering* (2. ed.). Boston, Mass.: Butterworth-Heinemann.
- Lu B., Wang W. and Li J. (2009). Searching for a mesh-independent sub-grid model for CFD simulation of gas-solid riser flows. *Chemical Engineering Science*,

- 64(15), 3437-3447.
doi:<http://dx.doi.org/10.1016/j.ces.2009.04.024>
- Lu B., Wang W. and Li J. (2011). Eulerian simulation of gas–solid flows with particles of Geldart groups A, B and D using EMMS-based meso-scale model. *Chemical Engineering Science*, 66(20), 4624-4635.
doi:<http://dx.doi.org/10.1016/j.ces.2011.06.026>
- Motlagh A. H. A., Grace J. R., Salcudean M. and Hrenya C. M. (2014). New structure-based model for Eulerian simulation of hydrodynamics in gas–solid fluidized beds of Geldart group “A” particles. *Chemical Engineering Science*, 120, 22-36.
doi:<http://dx.doi.org/10.1016/j.ces.2014.08.042>
- Pandit J. K., Wang X. S. and Rhodes M. J. (2005). Study of Geldart's Group A behaviour using the discrete element method simulation. *Powder Technology*, 160(1), 7-14.
doi:<http://dx.doi.org/10.1016/j.powtec.2005.04.044>
- Pei P., Zhang K., Lu E. and Wen D. (2009). CFD simulation of bubbling and collapsing characteristics in a gas-solid fluidized bed. *Petroleum Science*, 6(1), 69-75.
doi:10.1007/s12182-009-0013-0
- Rusche H. (2002). *Computational fluid dynamics of dispersed two-phase flows at high phase fractions*. (Doctor of Philosophy), Imperial College London (University of London).
- Thapa R. and Halvorsen B. (2013). *Study of Flow Behavior in Bubbling Fluidized Bed Biomass Gasification Reactor Using CFD Simulation*. Paper presented at the The 14th International Conference on Fluidization-From Fundamentals to Products.
http://dc.engconfintl.org/fluidization_xiv/69
- Wang J., van der Hoef M. A. and Kuipers J. A. M. (2009). Why the two-fluid model fails to predict the bed expansion characteristics of Geldart A particles in gas-fluidized beds: A tentative answer. *Chemical Engineering Science*, 64(3), 622-625.
doi:<http://dx.doi.org/10.1016/j.ces.2008.09.028>
- Wang J., van der Hoef M. A. and Kuipers J. A. M. (2011). The role of scale resolution versus inter-particle cohesive forces in two-fluid modeling of bubbling fluidization of Geldart A particles. *Chemical Engineering Science*, 66(18), 4229-4240.
doi:<http://dx.doi.org/10.1016/j.ces.2011.06.004>
- Wang X., Rahman F. and Rhodes M. (2007). Nanoparticle fluidization and Geldart's classification. *Chemical Engineering Science*, 62(13), 3455-3461.
doi:<http://dx.doi.org/10.1016/j.ces.2007.02.051>
- Yao W., Guangsheng G., Fei W. and Jun W. (2002). Fluidization and agglomerate structure of SiO₂ nanoparticles. *Powder Technology*, 124(1–2), 152-159.
doi:[http://dx.doi.org/10.1016/S0032-5910\(01\)00491-0](http://dx.doi.org/10.1016/S0032-5910(01)00491-0)
- Ye M., van der Hoef M. A. and Kuipers J. A. M. (2005). The effects of particle and gas properties on the fluidization of Geldart A particles. *Chemical Engineering Science*, 60(16), 4567-4580.
doi:<http://dx.doi.org/10.1016/j.ces.2005.03.017>
- Zhang K., Brandani S., Bi J. and Jiang J. (2008). CFD simulation of fluidization quality in the three-dimensional fluidized bed. *Progress in Natural Science*, 18(6), 729-733. doi:<http://dx.doi.org/10.1016/j.pnsc.2008.02.002>

CFD study of Particle Flow Patterns in a Rotating Cylinder Applying OpenFOAM and Fluent

Susantha Dissanayake¹ Sumudu S Karunaratne¹ Joachim Lundberg¹ Lars-Andre Tokheim¹

¹Department of Process, Energy, and Environmental Technology, University College of Southeast Norway, Norway.
susanthadmscd@gmail.com, {Sumudu.Karunaratne, Joachim.Lundberg,
Lars.A.Tokheim}@usn.no

Abstract

A rotating cylinder (RC) is a common type of reactor used in the industry, the most typical example being a cement kiln. The particle flow pattern inside such a unit is necessary for the mass and energy transfer, and this flow pattern depends on the operational Froude number and the degree of filling. The main aim of this study is to compare the simulation results from OpenFOAM and Fluent applying a Eulerian multiphase flow modeling concept to study the behavior of dense particle gas mixtures under different operational conditions. Six different flow patterns are simulated, varying the degree of filling from 10 to 45 % and the Froude number from 0.0001 to 5. OpenFOAM is capable of producing results very close to those generated with Fluent, and both software appears to be suitable for simulating the RC dense particle flow using the Eulerian approach.

Keywords: Particle flow, OpenFOAM, Fluent, Rotating cylinder, Froude number

1 Introduction

The behavior of particles inside a rotating cylinder (RC) has a significant influence on the mass and energy transfer, both in the solids phase and between the solids and the surrounding medium [1-4]. A cement kiln is a typical example of a RC which has mass and energy transfer between the phases [5, 6]. Six different flow patterns can be identified, depending on the degree of filling and the rotational speed; slipping, slumping, rolling, cascading, cataracting and centrifuging [2, 7].

Such flow patterns have previously been simulated by some of the authors using the CFD software Fluent, applying the Eulerian approach to model both the particle phase and the gas phase [8].

OpenFOAM is an open source CFD toolbox that can be downloaded and used free of charge¹. The OpenFOAM solver “twoPhaseEulerFoam” can be used to model incompressible fluid phases, such as one particle phases and one gas phase. This approach applies the Eulerian conservation equations for both the gas and the solids phases, meaning that the phases are modeled as interpenetrating continua [2, 9, 10].

¹ www.openfoam.com

The purpose of the current study is to investigate the ability of OpenFOAM to map the flow pattern mentioned above and to compare the simulation results with those from Fluent simulations.

2 Theoretical background

Heydenrych [7] studied the flow pattern inside a RC for particles in size range 0.1-10 μm . The flow pattern depends on the degree of filling and the Froude number (Fr). The degree of filling can be expressed as the ratio H/R , i.e. bed depth H (m) to cylinder radius R (m). The Froude number is a function of the rotational speed ω ($\frac{\text{rad}}{\text{s}}$), the cylinder radius and the gravitational constant, g ($9.81 \frac{\text{m}}{\text{s}^2}$):

$$Fr = \frac{\omega^2 R}{g} \quad (1)$$

Six different flow patterns can be mapped into the Fr - H/R space based on the particle behaviour: Slipping slumping, rolling, cascading, cataracting and centrifuging [7, 8], see Figure 1.

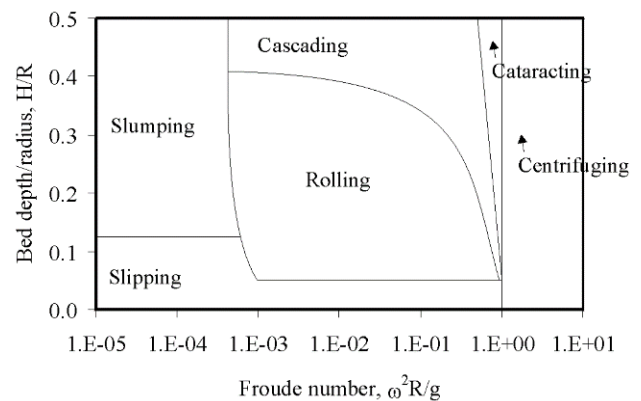


Figure 1. Flow regime as a function of operational conditions [7].

A particle bed in motion may have an active and a passive layer. When the cylinder rotates, the particles adjacent to the wall obtain some velocity. Other particles are located at a distance from the cylindrical wall and stay stagnant [2, 7, 11, 12]. The particle layer

that gains some velocity due to the cylindrical wall rotation is called the active layer, whereas the stagnant layer of particles is referred to as a passive layer. When the rotational speed increases, the active layer thickness increases. An illustration of active and passive layers is shown in Figure 2.

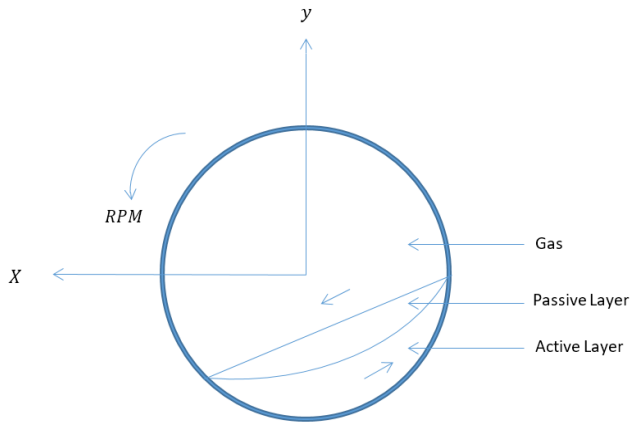


Figure 1. The active and passive layers development in an RC.

2.1 Basic Flow patterns

The six different basic flow patterns are described in this section.

2.1.1 Slipping

The slipping mode can be observed for $H/R < 0.15$ and $Fr < 0.001$. In the slipping mode, the active layer shows very little particle movement [7, 13], and the active layer is very thin compared to the passive layer, see Figure 3. In other words, the passive layer is predominant in this flow mode. As a result, the particle mixing, the mass transfers and the heat transfer between particles and between gas and particles is at a minimum.

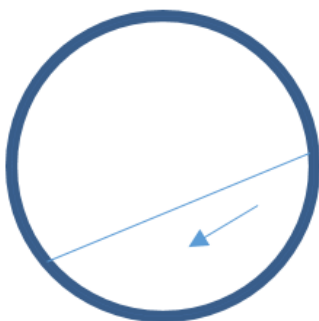


Figure 3. The slipping mode.

2.1.2 Slumping

If Fr is kept below 0.001, but H/R is increased above 0.15, the particle bed tends to move with the moving wall, but then at a some elevation the particles suddenly collapse and move back towards the initial position [13], see Figure 4. Due to the slumping behavior, the bed is

predominantly a passive layer, hence slumping is not very usable in industrial applications.

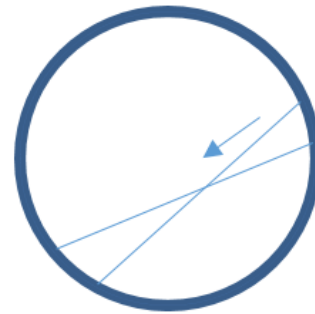


Figure 4. The slumping mode.

2.1.3 Rolling

When Fr increases to the range 0.001-1 and H/R is in the range 0.05-0.35, the rolling mode can be observed.

In the rolling mode, particles close to the cylindrical wall moves with the wall to a certain elevation and then roll back on the surface of the bed. As a result, a circular bed movement can be observed in the rolling mode, see Figure 5. Due to this circular particle motion, most of the particles touch the cylinder bottom and the upper surface during operation, meaning that the active layer is dominant. Subsequently, the transfer of heat and mass between particles and between gas and particles is increased.

For typical industrial operations like that of a cement kiln, the rolling mode is used [1, 5]. According to the Nielsen, et al. [5] a cement kiln is operated at 3-4 rpm.



Figure 5. Rolling mode.

2.1.4 Cascading

When the degree of filling increases to a certain level above that of the rolling mode, the cascading mode can be seen [11, 13]. In this mode, the active and passive layers are difficult to distinguish from each other.

In the cascading mode, the particles show a stronger accumulation on the elevated side, and the top layer of the particle bed moves more compared to the rolling mode, see Figure 6. The cascading mode actually gives maximum mixing and maximum mass and heat transfer. However, since this operation mode consumes extra energy, it is usually not considered the optimal solution.

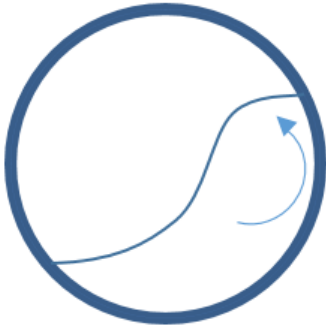


Figure 6. The cascading mode.

2.1.5 Cataracting

For $Fr > 1$ and high H/R values, the cataracting mode occurs [7, 11], see Figure 7. The cataracting mode can be seen in RCs operating at high rotational speeds. The cataracting mode has free falling particles at the elevated end of the cylinder, see Figure 7. Such a flow pattern gives improved mixing with gas phase inside the cylinder. However, the cataracting mode is not considered a viable option in the industrial applications as the operational range is very narrow and the rotational speed must be very high.

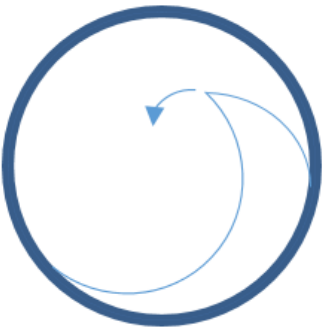


Figure 7. Cataracting mode.

2.1.6 Centrifuging

A further increase in Fr will give the centrifugal mode. In this mode, most of the particles are pressed towards the cylindrical wall due to the centrifugal force, see Figure 8. This mode requires extremely high rotational speeds. In the centrifugal mode the active layer is dominant.

For normal industrial operations, in which particle mixing and heat transfer are expected, the centrifugal mode is not used. However, it may be utilized in some applications, such as drying or separation of solids from a fluid [14].

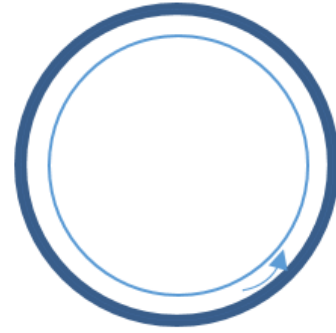


Figure 8. The centrifuging mode.

3 Simulation study

In this study, OpenFOAM (version 4.1) and ANSYS Fluent (release 16.2) were used, applying the Euler-Euler approach, in which a set of continuity and momentum equations was solved for each phase. This means that gas and solids phases are modeled as two interpenetrating continua [2]. The method is based on property averaging in the time domain, where the local instantaneous balance of each phase is obtained. Moreover, time averaging of the fluid flow motion is applied; the Reynolds-Average Navier-Stokes (RANS) method is used to solve the properties of the turbulent flow field [15].

The details of the Eulerian model and the particle drag model, as well as additional information, are given in a previous article by some of the present authors [8, 16] and are therefore not repeated here.

The six different flow patterns illustrated in Figure 1 were simulated using the operational conditions given in Table 1.

In the simulation, a lab-scale RC with a radius of 0.20 m was considered. The diameter of full-scale cement kilns are typically 10-20 times bigger than this, but lab-scale RC has been practical to use in verification of results simulated with the Fluent software [8]. To enable comparison of OpenFOAM and Fluent results, the same RC is the basis for the current study.

In the slipping and slumping modes, the rotational speed was low (0.67 rpm), so a relatively long operational time (90 s) had to be simulated to make sure there was enough time for the flow pattern to develop. In the rolling and cascading modes, the rotational speed was 10 times higher (6.67 rpm), so the time could be reduced by a factor of 10. Moreover, in the cataracting and centrifuging modes, the rotational speeds were higher by a factor of 10 and 22.5, respectively, so the time could be reduced accordingly.

Table 1. Simulation parameters ($R = 0.20$ m).

Detail	Slipping	Slumping	Rolling	Cascading	Catarecting	Centrifuging
Degree of filling, H/R	0.10	0.35	0.20	0.45	0.45	0.45
Rotational speed (RPM)	0.67	0.67	6.67	6.67	66.7	150
Froude number	0.0001	0.0001	0.01	0.01	1	5
Total time simulated (s)	90	90	9	9	0.9	0.4

4 Results and Discussion

Figure 9 and 10 show the results of OpenFOAM and Fluent simulations. The red color in Figure 9 designates pure solids, whereas the blue color means no solids (i.e. gas only). Colors in between blue and red indicate areas where both phases are present. Both the Fluent and OpenFOAM simulation results match fairly well the outlined slipping mode flow pattern shown in Figure 3.

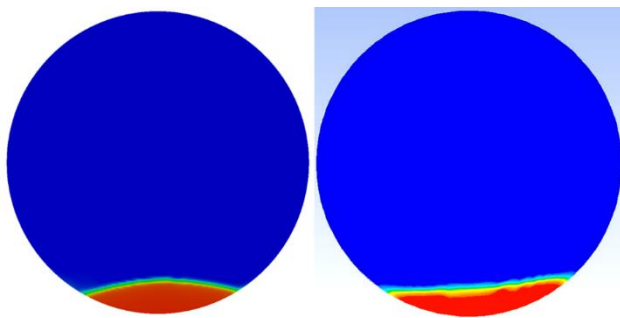


Figure 9. Slipping mode solids fraction (left: OpenFOAM, right: Fluent). Red = 100 % solids, Blue = 0 % solids.

The OpenFOAM velocity vectors (Figure 10, left) show both the gas phase and the particle phase, while the Fluent velocity vectors (Figure 10, right) only show the particle phase (this is due to different features of the graphics processing procedures in the two software packages). The velocity vectors are qualitatively in agreement with results from previous studies [6, 12].

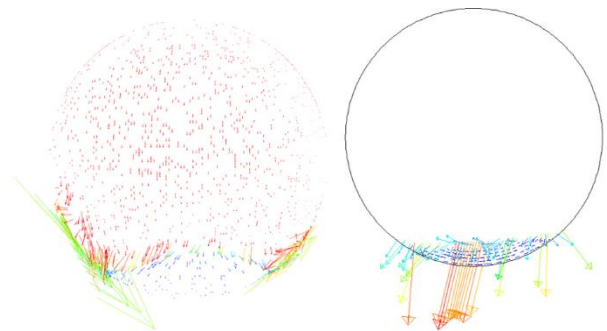


Figure 10. Slipping mode velocity vectors (left: OpenFOAM gas and particle velocities, right: Fluent particle velocities).

Figure 11 and 12 shows a comparison of the OpenFOAM and the Fluent flow patterns for the slumping mode (Figure 4), which appear after an increase in filling degree from 10 to 35 %. In Figure 11, the particle bed at an elevated point is shown. It is hard to capture the exact point at which the particle bed collapses.

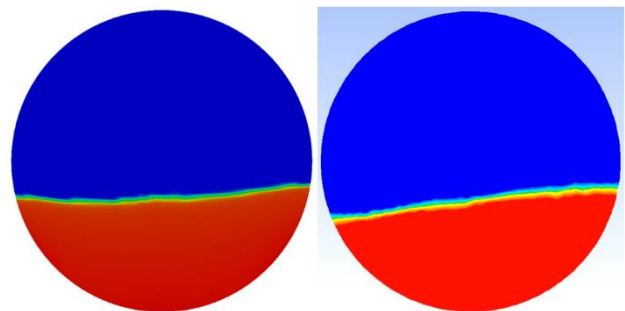


Figure 11. The slumping mode solids fraction (left: OpenFOAM, right: Fluent).

The velocity vectors are shown in Figure 12. According to the figure, the particles at the bottom move in parallel with the cylindrical wall, and the top of the bed has a backward-directed velocity. Moreover, the velocity at the top of the bed is higher than the bottom velocity. Both simulation software is capable of producing results in agreement with the theory.

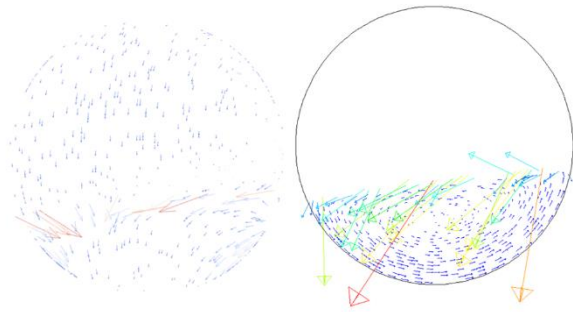


Figure 12. Slumping mode velocity vectors (left: OpenFOAM gas and particle velocities, right: Fluent particle velocities)

Figure 13 and 14 shows the rolling mode (Figure 5) results that appear after increasing the rotational speed by a factor of 10 (from 0.67 to 6.67 rpm) and reducing the filling degree slightly (from 35 to 20 %). The characteristics of this mode are observed both in OpenFOAM and Fluent.

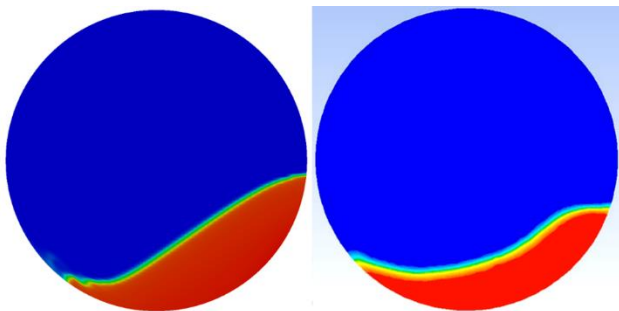


Figure 13. Rolling mode solids fraction (left: OpenFOAM right: Fluent).

The velocity vector plots in Figure 14 match each other quite well, even if the different graphics processing procedures makes the gas phase visible in OpenFOAM, but not in Fluent. The bottom particle movement and the surface particle movement are both visible from the plot, and the velocity vectors are also in line with previous studies [6, 17].

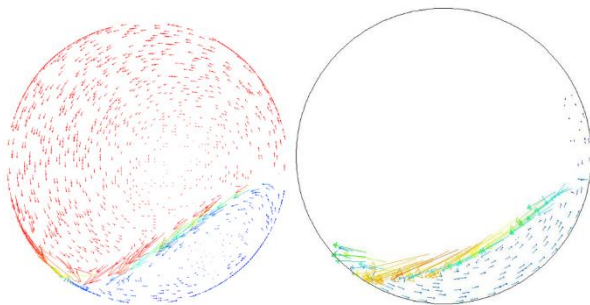


Figure 14. Rolling mode velocity vectors (left: OpenFOAM gas and particle velocities, right: Fluent particle velocities).

The cascading mode flow pattern is observed in Figure 15 and 16. This mode was reached by increasing the filling degree from 20 to 45 % (while maintaining

the rotational speed at 6.67 rpm) and is in line with the sketch of the pattern shown in Figure 6.

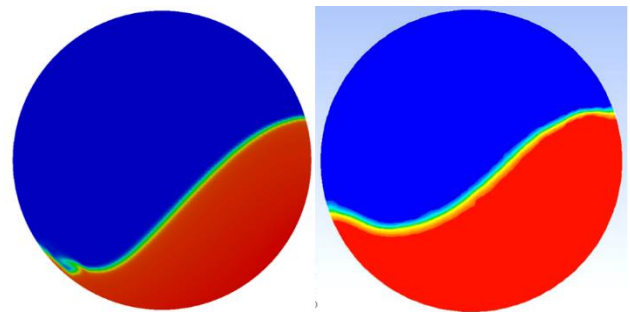


Figure 15. The cascading mode solids fraction (left: OpenFOAM, right: Fluent).

According to Figure 15, the particles accumulate more heavily on the elevated side. The particle elevation in this mode is higher than in the rolling mode.

Velocity vectors are plotted in Figure 16, and similarities can be observed. The particle velocity at the surface is higher in this mode, as the particle elevation is higher than the rolling mode.

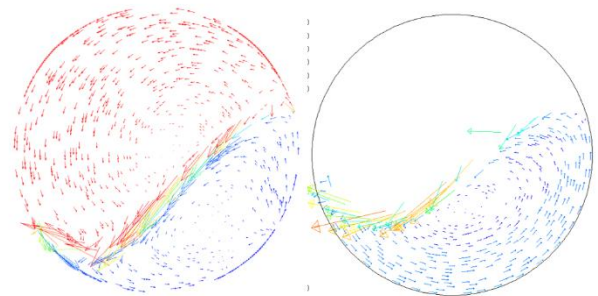


Figure 16. Cascading mode velocity vectors (left: OpenFOAM gas and particle velocities, right: Fluent particle velocities).

An increase in rotational speed by a factor of 10 (from 6.67 to 66.7) causes the cataracting mode (Figure 7) to appear when the filling degree is kept at 45 %, see Figure 17 and 18.

Figure 17 illustrates that both OpenFOAM and Fluent simulation results show particle showering down, creating a circular type of motion. The OpenFOAM contours appear to be particularly illustrative in this respect.

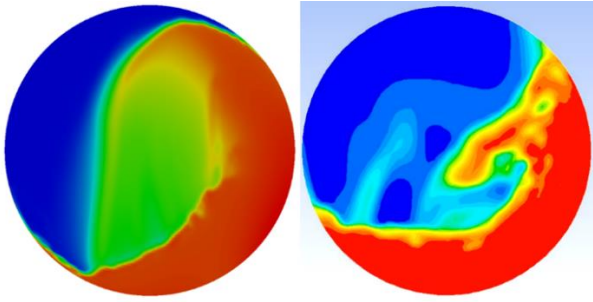


Figure 17. Cataracting mode solids fraction (left: OpenFOAM, right: Fluent).

The velocity vectors in Figure 18 match each other quite closely and also correspond well with results reported by Finnie, et al. [17].

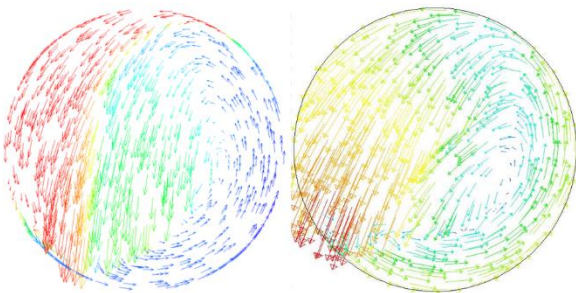


Figure 18. Cataracting mode velocity vectors (Left: OpenFOAM gas and particle velocities, right: Fluent particle velocities).

Finally, when the rotational speed is increased even more (from 66.7 to 150 rpm) while keeping the degree of filling unchanged (45 %), the particle bed reaches the centrifugal mode (Figure 8).

Both simulation software shows similar behavior for the solids fraction given in Figure 19.

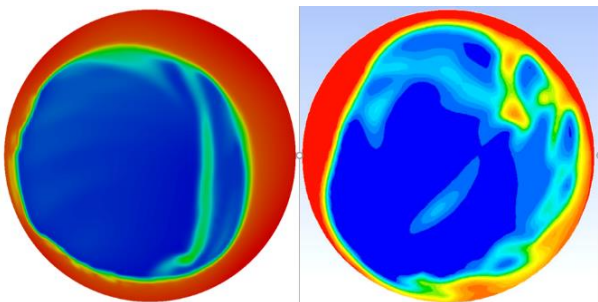


Figure 19. Centrifuging mode solids fraction (left: OpenFOAM right: Fluent).

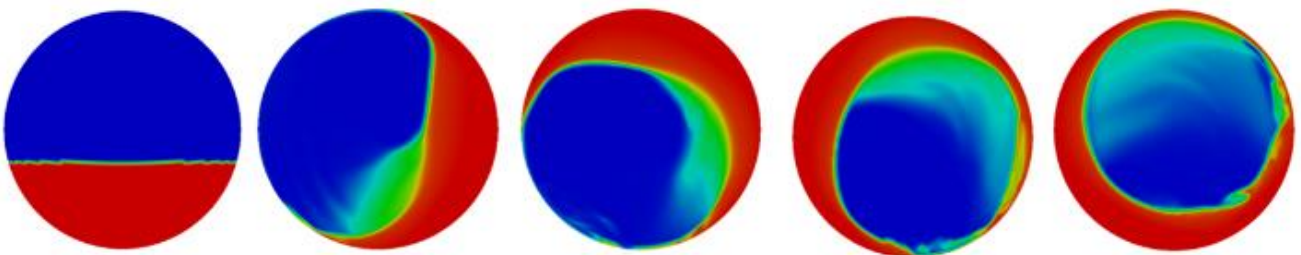


Figure 21. Flow pattern development over time (OpenFOAM); elapsed time from left to right: 0, 0.1, 0.2, 0.3 and 0.4 s.

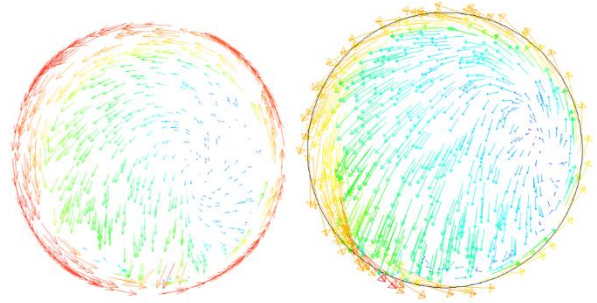


Figure 20. Centrifuging mode velocity vectors (left: OpenFOAM gas and particle velocities, right: Fluent particle velocities).

Also the velocity vector plots in Figure 20 show a close match with each other. The particle velocity at the wall has the highest velocity, and this is more or less equal to the cylindrical wall velocity.

The flow pattern development in both software for a particular case is shown in Figure 21 and Figure 22. The centrifugal mode was selected in this demonstration as it shows significant differences with time. Images were captured at 0, 0.1, 0.2, 0.3, 0.4 s.

The flow development over time is very comparable in OpenFOAM and Fluent. At the very beginning, particles are gathered at the bottom of the cylinder at the same filling degree. As time proceeds, the particles move with the cylindrical wall, and after 0.4 s, a more or less circular flow pattern is observed in both Fluent and OpenFOAM results.

It should be mentioned that the OpenFOAM simulations converged faster than the Fluent simulations, which can be a decisive factor when selecting what software to use. As an example, OpenFOAM converges to the solution within a day for the rolling mode, whereas the Fluent simulation takes about a week. Moreover, as the OpenFOAM is an open source software, the scripts are easily adjustable and easily manipulated by users. Contrary, the Fluent is a commercial software and the user has no access to the original scripts. The graphical interface in OpenFOAM is also very user-friendly.

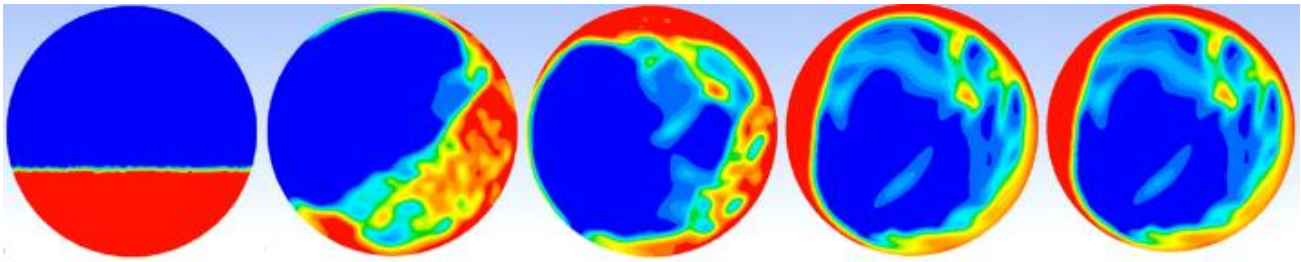


Figure 22. Flow pattern development over time (Fluent); elapsed time from left to right: 0, 0.1, 0.2, 0.3 and 0.4 s.

5 Conclusion

Based on simulations executed with OpenFOAM and Fluent, applying the same approach and the same drag models, it can be concluded that two software packages produce very similar results. The simulated results also agreed well with flow patterns described in the literature. Hence, for a particular particle diameter, different flow regimes in an RC can be mapped in a diagram of filling degree vs. Froude number (which in turn depends on the rotational speed and the cylinder diameter).

OpenFOAM appears to be faster in producing the same results, and the interface is user-friendly. However, the two simulation softwares have different graphics processing procedures, which makes it difficult to generate plots that are directly comparable.

Based on the study it can be concluded that the Euler-Euler approach can be successfully utilized in particle-gas phase simulations and that both software platforms can be used for this purpose.

References

- [1] A. A. Boateng, "4 - Granular Flows in Rotary Kilns," in *Rotary Kilns*, ed Burlington: Butterworth-Heinemann, 2008, pp. 59-100.
- [2] V. Romero, "Numerical Modelling of Granular Beds in Rotary Kilns," Master of Science in Computer Simulations for Science and Engineering Faculty of Electrical Engineering, Mathematics and Computer Science, Delft University of Technology, 2012.
- [3] Y. L. Ding, J. P. K. Seville, R. Forster, and D. J. Parker, "Solids motion in rolling mode rotating drums operated at low to medium rotational speeds," *Chemical Engineering Science*, vol. 56, pp. 1769-1780, 3// 2001.
- [4] K. S. Mujumdar and V. V. Ranade, "Simulation of Rotary Cement Kilns Using a One-Dimensional Model," *Chemical Engineering Research and Design*, vol. 84, pp. 165-177, 3// 2006.
- [5] A. R. Nielsen, R. W. Aniol, M. B. Larsen, P. Glarborg, and K. Dam-Johansen, "Mixing large and small particles in a pilot scale rotary kiln," *Powder Technology*, vol. 210, pp. 273-280, 7/10/ 2011.
- [6] Y. Demagh, H. Ben Moussa, M. Lachi, S. Noui, and L. Bordja, "Surface particle motions in rotating cylinders: Validation and similarity for an industrial scale kiln," *Powder Technology*, vol. 224, pp. 260-272, 7// 2012.
- [7] M. D. Heydenrych, "Modeling of Rotary Kilns," Doctor of philosophy University of Twente, 2011.
- [8] S. Karunarathna, "Investigation of Mixing and Segregation of Solids in a Rotary Kiln by CFD Simulations," Masters in Process Technology Department of Process, Energy and Environmental Technology University College of Southeast Norway
- [9] H. Arastoopour, "Numerical simulation and experimental analysis of gas/solid flow systems: 1999 Fluor-Daniel Plenary lecture," *Powder Technology*, vol. 119, pp. 59-67, 9/24/ 2001.
- [10] S. Benyahia, H. Arastoopour, T. M. Knowlton, and H. Massah, "Simulation of particles and gas flow behavior in the riser section of a circulating fluidized bed using the kinetic theory approach for the particulate phase," *Powder Technology*, vol. 112, pp. 24-33, 10/5/ 2000.
- [11] Q. J. Zheng and A. B. Yu, "Modelling the granular flow in a rotating drum by the Eulerian finite element method," *Powder Technology*, vol. 286, pp. 361-370, 12// 2015.
- [12] H. Yin, M. Zhang, and H. Liu, "Numerical simulation of three-dimensional unsteady granular flows in rotary kiln," *Powder Technology*, vol. 253, pp. 138-145, 2// 2014.
- [13] G. R. Woodle and J. M. Munro, "Particle motion and mixing in a rotary kiln," *Powder Technology*, vol. 76, pp. 241-245, 1993/09/01 1993.
- [14] N. Barman and L. S. Badwaik, "Effect of ultrasound and centrifugal force on carambola (*Averrhoa carambola* L.) slices during osmotic dehydration," *Ultrasonics Sonochemistry*, vol. 34, pp. 37-44, 1// 2017.
- [15] H. K. Versteeg and W. Malalasekera, *An Introduction to Computational Fluid Dynamics*, 2nd edition ed.: Pearson Education Limited, 2007.
- [16] S. Karunarathna, C. Jayarathna, and L. A. Tokheim, "Impact of Particle Diameter, Particle Density and Degree of Filling on the Flow Behavior of Solid Particle Mixtures in a Rotating Drum," in *The 9th Eurosim Congress on Modelling and Simulation*, Oulu, Finland, 2016, pp. 955-960.
- [17] G. J. Finnie, N. P. Kruyt, M. Ye, C. Zeilstra, and J. A. M. Kuipers, "Longitudinal and transverse mixing in rotary kilns: A discrete element method approach," *Chemical Engineering Science*, vol. 60, pp. 4083-4091, 8// 2005.

Model Uncertainty of Interfacial Area and Mass Transfer Coefficients in Absorption Column Packings

Sumudu S. Karunaratne¹ Dag A. Eimer² Lars Erik Øi¹

¹Department of Process, Energy and Environmental Technology, University College of Southeast Norway,

{Sumudu.Karunaratne,Lars.Oi}@usn.no

²Tel-Tek, Norway, dag.a.eimer@tel-tek.no

Abstract

Uncertainty in model input parameters propagates through the model to make model output imprecise. Here, mathematical models used to calculate interfacial area and mass transfer coefficient for both random and structured packing in a packed bed absorption column was studied to investigate the propagation of model input parameters of viscosity, density and surface tension through the models. Monte Carlo simulation was used to examine the uncertainty propagation, and expectation $E(Y)$ and standard deviation σ for the model output values were determined. This study reveals $\pm 5\%$ model output uncertainty for mass transfer coefficient and $\pm 3.7\%$ uncertainty for interfacial area for the Onda, Bravo and Fair models used in random packings. Further, the analysis predicts $\pm 1.3\%$ of uncertainty for interfacial area and $\pm 0.8\%$ of uncertainty for mass transfer coefficient for the Rocha's correlations used in structured packings.

Keywords: *uncertainty, absorption, mass transfer, interfacial area*

1 Introduction

A mathematical model is a simplified version of a complex phenomenon in which assumptions are made during the model derivation to formulate the relations between parameters through mathematical equations. When input data are not precise, this leads to imprecise output results from the model. It is vital to quantify the uncertainty in model output to acquire an understanding about how accurate the estimated values through models. Generally, uncertainties are described by a probability distribution (Loucks *et al*, 2005).

Uncertainty of a model output is a result of both uncertain model structure and parameter values (Loucks *et al*, 2005). In model structure uncertainty, the errors in the model structure compared to the real system, assumptions and numerical approximations in simulation caused to create uncertainty in model output. The uncertain estimates of model parameters also make the model output uncertain. It is difficult to estimate the model structure uncertainty compared to model uncertainty caused by the parameter value. Increase of precision in model parameters can reduce the parameter uncertainty but it does not mean that predictions are accurate.

The analysis of model uncertainty is useful in many scientific applications. Krewski *et al*, (1995) performed an uncertainty analysis on physiological models using Monte Carlo Simulation. In this study, most of the model parameters were assumed to have a nature of the doubly truncated normal distribution. Spek *et al*, (2016) discussed improving uncertainty evaluation of process models in CO₂ capture by using pedigree analysis. A study on investigating the effect of process uncertainty on the optimal design of a CO₂ capture plant was done by Bahakim and Ricardez-Sandoval, (2014). The intention was to find the most economically feasible design for process equipment and acquire optimal operating conditions under uncertain conditions. Mathias and Gilmartin, (2014) evaluated the effect of uncertainty in property models on the simulated performance of solvent-based CO₂ capture process.

Gas absorption is a frequently used unit operation in gas treating processes. Packed bed absorption columns are made of either random or structured packing materials. The mass transfer coefficient and the interfacial area are the most important parameters involved with efficiency of packing materials. There have been many attempts to make mathematical models to evaluate both mass transfer coefficient and interfacial area for the both packing materials. Physical properties of viscosity, density and surface tension have an influence on the mass transfer coefficient. Uncertainties of those physical properties propagate through the mass transfer and interfacial area models to make the uncertain model output.

In this study, model uncertainty $U(Y/X)$ analysis was performed to investigate the input uncertainty propagation of a selected amine through the mass transfer and interfacial area models of the packed bed. The mass transfer coefficient and interfacial area of random packings are calculated by Onda, Bravo and Fair's models (Onda *et al*, 1967, Bravo and Fair, 1982). Rocha's correlations are used to calculate the mass transfer coefficient of structured packings including sheet metal packing (Rocha *et al*, 1996). The uncertainties related to measurements and predictions of physical properties were considered as the input uncertainties in Gaussian probability distributions.

2 Theory

In the field of gas treating, various mathematical models are available to calculate desired physical properties in the absorption process. Calculation of gas and liquid side mass transfer coefficients and interfacial area of packed beds have been highly concerned in many research works. Several mathematical models were built to approximate those properties using physical properties of an absorbent such as density, viscosity and surface tension. Most of the available models are based on either two-film theory or penetration theory with some reasonable assumptions (Wang *et al*, 2005).

The model developed by Onda, Bravo and Fair (Onda *et al*, 1967, Wang *et al*, 2005) is widely used to determine the gas and liquid side mass transfer coefficients of random packings. The model is given as,

For the gas side mass transfer coefficient,

$$k_G = c \left(\frac{D_G}{a_p d_p^2} \right) \left(\frac{\rho_G u_G}{a_p \mu_G} \right)^{0.7} Sc_G^{1/3} \quad (1)$$

For the liquid side,

$$k_L = \frac{0.0051}{(a_p d_p)^{-0.4}} \left(\frac{\mu_L g}{\rho_L} \right)^{1/3} \left(\frac{\rho_L u_L}{a_e \mu_L} \right)^{2/3} Sc_L^{-0.5} \quad (2)$$

The interfacial area can be determined by,

$$\frac{a_e}{a_p} = 1 - \exp \left[-1.45 \left(\frac{\sigma_c}{\sigma_L} \right)^{0.75} Re_L^{0.1} Fr_L^{-0.05} We_L^{0.2} \right] \quad (3)$$

For this study, Rocha's correlations were considered for structured packing (Rocha *et al*, 1996).

$$k_G = 0.054 \frac{D_G}{s} \left[\frac{\rho_G s (u_{Le} + u_{Ge})}{\mu_G} \right]^{0.8} Sc_G^{0.33} \quad (4)$$

$$k_L = 2 \sqrt{\frac{0.9 D_L u_{Le}}{\pi s}} \quad (5)$$

$$\text{Where } u_{Ge} = \frac{u_G}{\varepsilon(1-h_L)\sin\alpha} \quad (6)$$

$$\text{And } u_{Le} = \frac{u_L}{\varepsilon h_L \sin\alpha} \quad (7)$$

The interfacial area is determined by

$$\frac{a_e}{a_p} = F_{SE} \frac{29.12 (We_L Fr_L)^{0.15} S^{0.359}}{Re_L^{0.2} \varepsilon^{0.6} (1 - 0.93 \cos(\theta)) (\sin(\alpha))^{0.3}} \quad (8)$$

For the models mentioned, physical properties of density, viscosity and surface tension in amines were considered as input parameters and the uncertainty associated with these parameters were taken into account for the examination of model uncertainty. This analysis mainly focuses on the evaluation of parameter uncertainty of the models and uncertainty due to models structure will not be discussed here.

Physical properties can be determined by laboratory experiments. In addition to that, it can be determined by models, created using experimental data. Both approaches deal with some level of uncertainty. Eventually, the physical properties are needed to be presented with an uncertainty to get an idea about the level of accuracy. Table 1 lists some measurement uncertainty of viscosity, density and surface tension of different amines.

Guide to the expression of uncertainty in measurement (GUM) (JCGM, 2011) discussed the way of distributions propagate in mutually independent inputs through a model. *Figure 1* illustrates the concept of propagation of distribution through a model. The assigned probability distribution function (PDF) for the inputs are represented as $g_{X_i}(\xi_i)$ and model output Y is characterized by joint PDF $g_Y(\eta)$.

During the model validation, the physical properties predictions are compared with the measured values to observe the model predictability. It gives information about deviation between model predictions and actual values. This also can be considered as a model uncertainty and it contains many uncertainty sources. Onda's correlations for liquid-phase mass transfer fulfill $\pm 20\%$ of agreement with the large amount of data on organic liquids and water (Potnis and Lenz, 1996).

Table 1. Measurement Uncertainty of physical properties

Property	Uncertainty
Viscosity	± 0.015 mPa·s (95% confident level, k=2) (Arachchige <i>et al</i> , 2013)
	± 0.12 mPa·s (95% confident level, k=2) (Sobrino <i>et al</i> , 2016)
Density	± 4.42 kg/m ³ (95% confident level, k=2)(CO ₂ loaded solution) (Jayarathna <i>et al</i> , 2013)
	± 0.05 kg/m ³ (Standard uncertainty) (CO ₂ loaded solution) (Amundsen <i>et al</i> , 2009)
Surface tension	± 0.02 mN/m (accuracy) (Vazquez <i>et al</i> , 1997)
	± 1.2 mN/m (95% confident level, k=2) (Jayarathna <i>et al</i> , 2013)

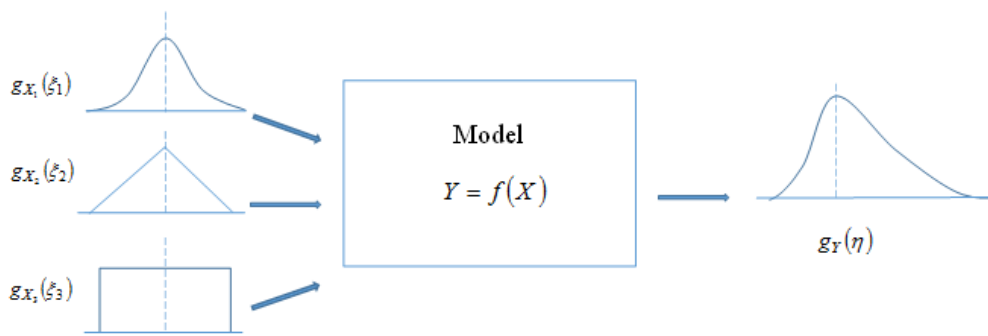


Figure 1. Illustration of the propagation of distribution (JCGM, 2011)

Nookuea *et al.*, (2016) summarized possible uncertainty ranges for different properties of gas and liquid CO₂ mixtures and a sensitivity analysis was done considering $\pm 20\%$ deviation of physical properties to investigate their impact on the design of an absorber.

The standard uncertainty in Y due to uncertainty in X

$$U(Y) = \sqrt{\text{Var}(Y)} \quad (9)$$

$$RU(Y) = \frac{\sqrt{\text{Var}(Y)}}{E(Y)} \times 100\% \quad (10)$$

The standard uncertainty in Y due to uncertainty in X_j is $U(Y \setminus X_j)$

Then the relative uncertainty is defined as

$$RU(Y \setminus X_j) = \frac{U(Y \setminus X_j)}{E(Y)} \times 100\% \quad (11)$$

3 Methodology

In this study, CO₂ absorption into 30% (by weight) monoethanol amine was considered as the physical process. It was assumed that the uncertainty of the physical properties has a Gaussian distribution. Experimentally measured values of viscosity, density and surface tension of monoethanol amine with standard uncertainty $\pm 5\%$ at 313.15 K were considered as model input parameters and Monte Carlo techniques were used to estimate uncertainty for the liquid side mass transfer coefficient and interfacial area of the packing materials. Simulations were performed in MATLAB environment and a built-in random number generator was used to generate values from Gaussian distribution for the input properties within the considered uncertainty levels. Table 2 shows the values for the considered inputs with uncertainties.

For the random packings, Ceramic Raschig Rings (25mm) and for the structured packings, Sulzer BX

(Gauze) packing were selected for this study. The diffusion coefficients of CO₂ (m²/s) in gas and liquid are 1.70×10^{-5} and 2.82×10^{-9} respectively (Eimer, 2014). The gas and liquid flow rates were assumed as 1.7 kg/m²·s and 1.85 kg/m²·s.

Table 2. Input parameter values and uncertainties

Parameter	Value	Uncertainty
Viscosity	1.628 mPa·s	± 0.0814 mPa·s
Density	1003.3 kg/m ³	± 50.165 kg/m ³
Surface tension	0.0624 N/m	± 0.00312 N/m

4 Results

Initially, all the input parameters were considered together to evaluate uncertainty propagation through the model. The model of interfacial area (Eq (3)) for random packing was considered first and the model output was described using a histogram. Subsequently, the uncertainty predicted for interfacial area was used for the uncertainty evaluation of liquid side mass transfer coefficient from Eq (2). *Figure 2* illustrates a histogram of values obtained for the interfacial area of random packing.

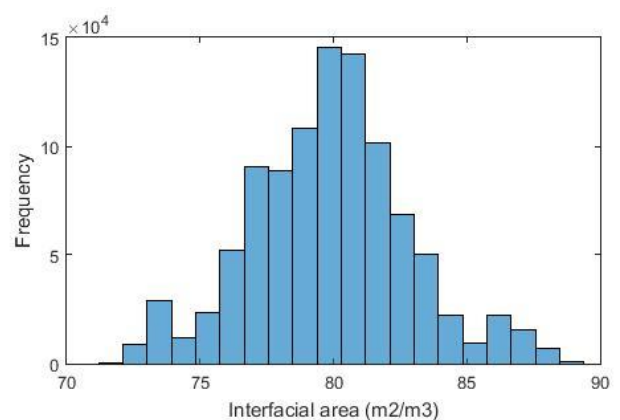


Figure 2. Histogram of interfacial area of random packing

Figure 3 shows the variation occurred for the liquid side mass transfer coefficient under considered input

uncertainty. Table 3 summarized the calculated expectation and standard deviation for both interfacial area and mass transfer coefficient of Onda, Bravo and Fair's correlations.

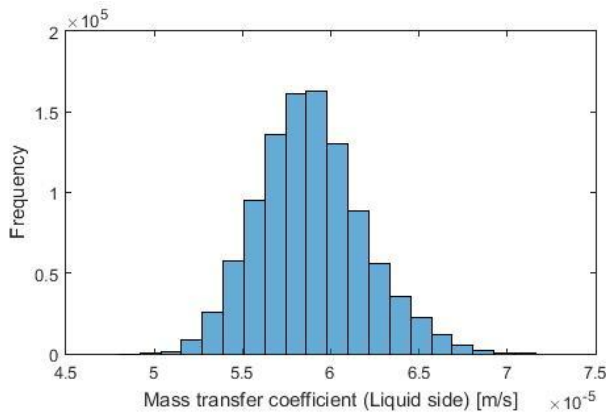


Figure 3. Histogram of mass transfer coefficient (liquid side) of random packing

Table 3. Estimated expectation and standard deviation for the random packings

Model	Expectation $E(x)$	Standard deviation (σ)
Interfacial area	$79.88 \text{ m}^2/\text{m}^3$	$2.97 \text{ m}^2/\text{m}^3$
Mass transfer coefficient	$5.9 \times 10^{-5} \text{ m/s}$	$2.97 \times 10^{-06} \text{ m/s}$

Similarly, for the structured packing, Figure 4 shows a histogram created from the values obtained for the interfacial area of structured packing.

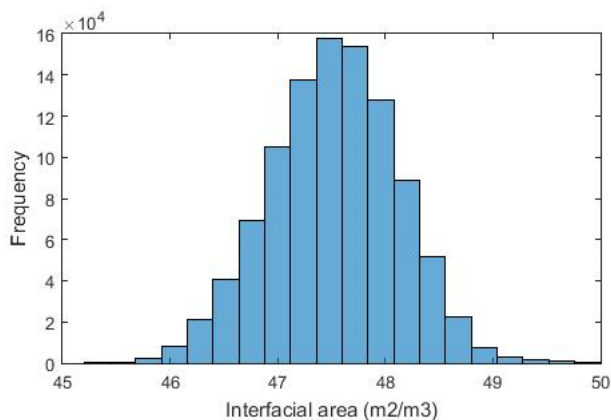


Figure 4. Histogram of interfacial area of structured packing

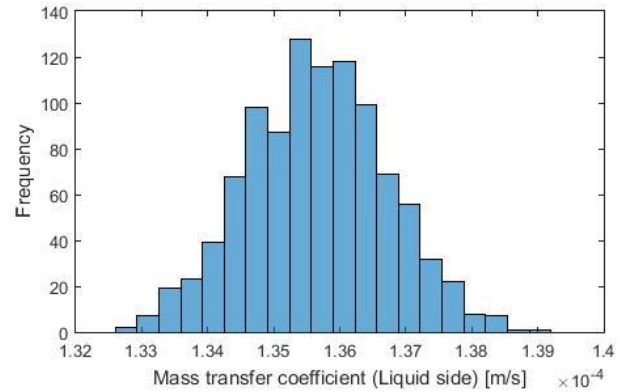


Figure 5. Histogram of mass transfer coefficient (liquid side) of structured packing

Simulation results on mass transfer coefficient (liquid side) of structured packing are shown in Figure 5. Calculated expectation and standard deviation for the interfacial area and mass transfer coefficient of Rocha's correlations under Sulzer BX (Gauze) packing is listed in Table 4.

Table 4. Estimated expectation and standard deviation for the structured packings

Model	Expectation $E(x)$	Standard deviation (σ)
Interfacial area	$47.5 \text{ m}^2/\text{m}^3$	$0.6 \text{ m}^2/\text{m}^3$
Mass transfer coefficient	$1.36 \times 10^{-04} \text{ m/s}$	$1.04 \times 10^{-06} \text{ m/s}$

Results reveal the propagation of uncertainty in model parameters through the mathematical model. This method only addresses the parameter uncertainty and uncertainty due to the model structure is not discussed here.

The relative uncertainty of the parameters uncertainty was evaluated according to the Eq (10). It shows $\pm 3.7\%$ of uncertainty for interfacial area and $\pm 5\%$ of uncertainty for mass transfer coefficient for the random packing. Similarly for the structured packings, $\pm 1.3\%$ of uncertainty for interfacial area and $\pm 0.8\%$ of uncertainty for mass transfer coefficient.

One advantage of performing this analysis is being able to estimate the relative impacts of input parameter uncertainties. This relative effect of uncertain parameters (viscosity, density and surface tension) were considered individually in uncertainty analysis. Estimated expectations and standard deviations due to the relative parameters in Onda, Bravo and Fair's correlation for random packings are shown in Table 5.

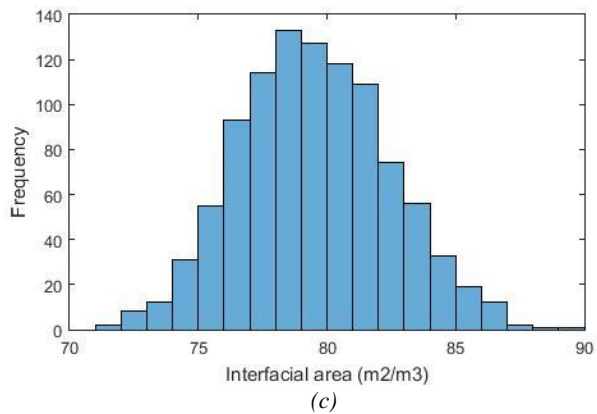
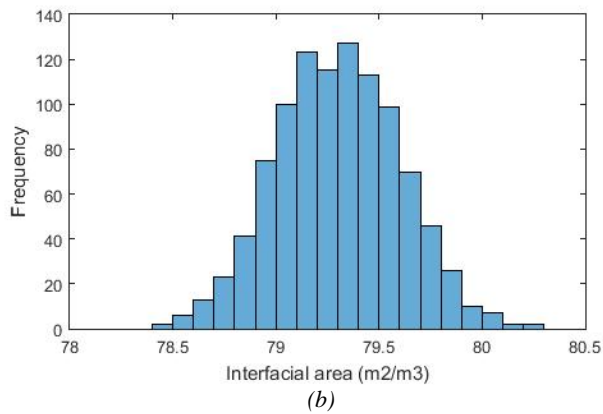
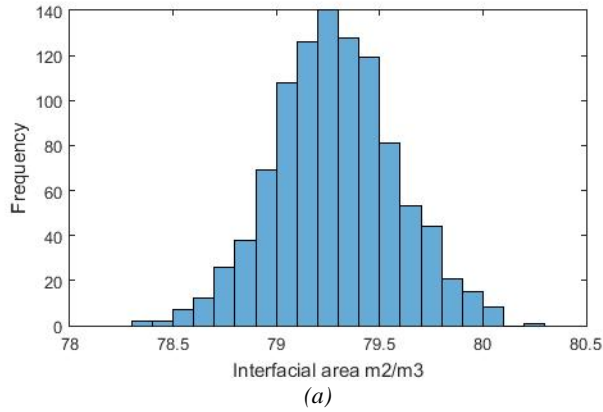


Figure 6. Histogram of the interfacial area under relative parameter uncertainty. (a,b,c for interfacial area due to viscosity, density and surface tension respectively)

Table 5. Estimated expectations and standard deviations due to the relative parameters. a_e (m²/m³), k_L (m/s)

		Viscosity	Density	Surface tension
a_e	E(Y/X _j)	79.3	79.3	79.5
	σ (Y/X _j)	0.3	0.3	2.9
k_L	E(Y/X _j)	5.9×10^{-5}	5.9×10^{-5}	5.9×10^{-5}
	σ (Y/X _j)	2.42×10^{-6}	0.5×10^{-6}	1.36×10^{-6}

The relative uncertainty $RU(Y|X_j)$ of the effect created by individual model parameters are shown in Table 6. Uncertainties were estimated for random packings under same input parameter uncertainties as shown in Table 2. The histogram created from model outputs

within the study of the effect of individual parameter uncertainty are shown in figure 6 and 7.

Table 6. The relative uncertainty $RU(Y|X_j)$ of the effect created by individual model parameters

Parameter	Model	
	Mass transfer coefficient k_L	Interfacial area a_e
Viscosity	$\pm 4.1\%$	$\pm 0.38\%$
Density	$\pm 0.85\%$	$\pm 0.38\%$
Surface tension	$\pm 2.3\%$	$\pm 3.65\%$

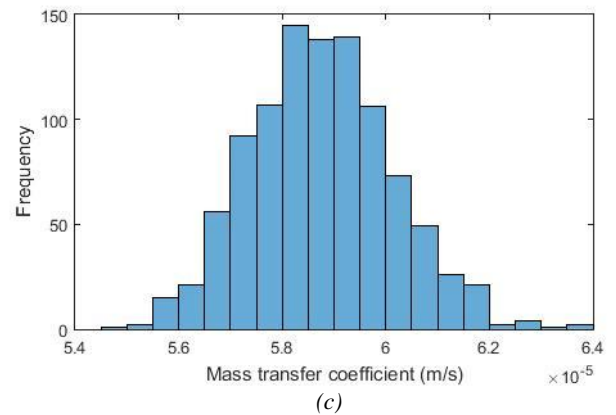
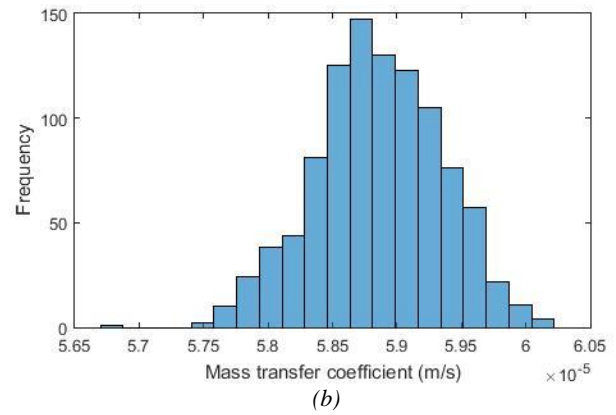
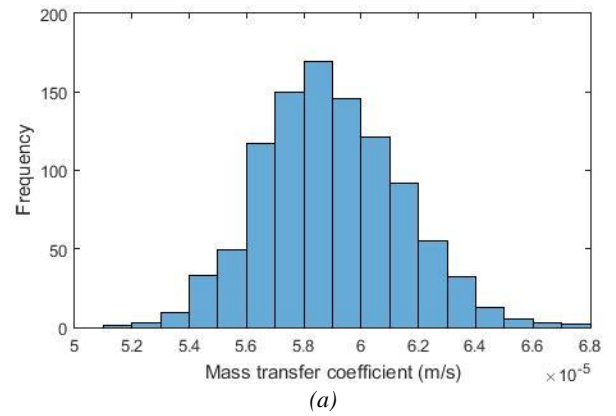


Figure 7. Histogram of the mass transfer coefficient under relative parameter uncertainty. (a,b,c for mass transfer coefficient due to viscosity, density and surface tension respectively)

The effect of individual parameters on parameter uncertainty of the model was compared. Uncertainty of surface tension has a major impact on interfacial area as shown in the results. Viscosity and density have a minor effect in interfacial area. For the mass transfer coefficient, viscosity shows a significant influence in model uncertainty. There, density and surface tension has minor effects.

5 Conclusion

Monte Carlo simulation was used to examine uncertainty propagation of model input parameters of viscosity, density and surface tension on the interfacial area and mass transfer coefficients in random and structured packings.

Overall uncertainty of model output gives information about how the model behaves under random behavior of all the input parameters. This study reveals $\pm 5\%$ model output uncertainty for mass transfer coefficient and $\pm 3.7\%$ uncertainty for interfacial area for the Onda, Bravo and Fair models used in random packings. Further, the analysis predicts $\pm 1.3\%$ of uncertainty for interfacial area and $\pm 0.8\%$ of uncertainty for mass transfer coefficient for the Rocha's correlations used in structured packings.

The relative impact of individual parameters predicts the model sensitivity and individual uncertainty contribution. Uncertainty in surface tension has a significant effect on the uncertainty of interfacial area in random packings that is $\pm 3.65\%$. According to the considered correlations on random packing, the uncertainty of interfacial area can be reduced by reducing the imprecision of surface tension. Mass transfer coefficient gets a greater influence from viscosity with $\pm 4.1\%$. Precise input parameter values on viscosity enhance the precision of the mass transfer coefficient.

Nomenclature

a_e	Effective specific interfacial area, (m^2/m^3)
a_p	Packing specific surface area, (m^2/m^3)
c	Packing-specific constant
D	Diffusion constant, m^2/s
d_p	Particle diameter, m
F_{SE}	Packing surface enhancement factor
Fr	Froude number
g	Gravitational acceleration, m/s^2
h_L	Liquid holdup m^3/m^3
k	Mass transfer coefficient, m/s
s	Corrugation side length, m
Sc	Schmidt number
u	Superficial velocity, m/s
We	Weber number

Greek letters

α	Corrugation inclination angle, deg
ε	Void fraction of packing
θ	Contact angle between liquid and surface
μ	Viscosity, $\text{Pa}\cdot\text{s}$
ρ	Density, kg/m^3
σ	Surface tension, N/m

Subscripts

G	Gas
L	Liquid
e	Effective
c	Critical

References

- D. Krewski, Y. Wang, S. Bartlett and K. Krishnan. Uncertainty, variability, and sensitivity analysis in physiological pharmacokinetic models. *Journal of Biopharmaceutical Statistics*, 5: 245-271, 1995.
- D. P. Loucks, E. V. Beek, J. R. Stedinger, J. P. M. Dijkman and M. T. Villars. Water resources systems planning and management: An introduction to methods, models and applications. *UNESCO*, 2005.
- D. Eimer. *Gas Treating* John Wiley & Sons, Ltd, 2014.
- G. Vazquez, E. Alvarez, J. Navaza, R. Rendo and E. Romero. Surface tension of binary mixtures of water + monoethanolamine and water + 2-amino-2-methyl-1-propanol and tertiary mixtures of these amines with water from 25 °c to 50 °c. *Journal of Chemical & Engineering Data*, 42: 57-59, 1997.
- G. Wang, X. Yuan and K. Yu. Review of mass-transfer correlation for packed column. *Ind.Eng.Chem.Res.*, 44: 8715-8729, 2005.
- J. A. Rocha, J. Bravo and J. Fair. Distillation Columns Containing Structured Packings: A comprehensive model for their performance. 2. mass-transfer model. *American Chemical Society*, 1660-1667, 1996.
- JCGM. Evaluation of measurement data – supplement 2 to the “guide to the expression of uncertainty in measurement” – extension to any number of output quantities. *JCGM 102:2011*.
- J. L. Bravo and J. R. Fair. Generalized correlation for mass transfer in packed distillation columns. *Ind. Eng. Chem. Process Des. Dev.*, 21: 162-170, 1982.
- K. Onda, E. Sada and H. Takeuchi. Gas absorption with chemical reaction in packed columns. *Journal of Chemical Engineering of Japan*, 62-66, 1967.
- M. Spek, A. Ramirez and A. Faaij. Improving uncertainty evaluation of process models by using pedigree analysis. a

- case study on CO₂ capture with monoethanolamine. *Computers and Chemical Engineering*, 85: 1-15, 2016.
- M. Sobrino, E. Concepcion, A. Hernandez and M. Martin. Viscosity and density measurements of aqueous amines at high pressures: mdea-water and mea-water mixtures for CO₂ capture. *J.Chem.Thermodynamics*, 98, 231-241, 2016.
- P. Mathias and J. Gilmartin. Quantitative evaluation of the effect of uncertainty in property models on the simulated performance of solvent-based CO₂ capture. *Energy Procedia : GHGT-12*, 63: 1171-1185, 2014.
- S. Bahakim and L. Ricardez-Sandoval. Optimum steady-state design of a post-combustion CO₂ capture plant under uncertainty. *Energy Procedia*, 63: 1608-1616, 2014.
- S. Jayarathna, A. Weerasooriya, S. Dayarathna, D. Eimer and M. Melaaen. Densities and surface tensions of CO₂ loaded aqueous monoethanolamine solutions with $r = (0.2 \text{ to } 0.7)$ at $t = (303.15 \text{ to } 333.15) \text{ K}$. *Journal of Chemical & Engineering Data*, 58: 986-992, 2013.
- S. Potnis and T. Lenz. Dimensionless mass-transfer correlations for packed-bed liquid desiccant contactors. *American Chemical Society*, 4185-4193, 1996.
- T. Amundsen, L. Øi and D. Eimer. Density and viscosity of monoethanolamine+water+carbon dioxide from (25 to 80) °C. *Journal of Chemical & Engineering Data*, 54: 3096-3100, 2009.
- U. Arachchige, N. Aryal, D. Eimer and M. Melaaen. Viscosities of pure and aqueous solutions of monoethanolamine (mea), diethanolamine (dea) and n-methyldiethanolamine (mdea). *Annual Transaction of the Nordic Rheology Society*, 21: 299-306, 2013.
- W. Nookuea, Y. Tan, H. Li, E. Thorin and J. Yan. Impact of thermo-physical properties of gas and liquid phases on design of absorber for CO₂ capture using monoethanolamine. *International Journal of Greenhouse Gas Control*, 52: 190-200, 2016.

Comparison of the Influence of Drag Models in CFD Simulation of Particle Mixing and Segregation in a Rotating Cylinder

Sumudu S. Karunaratne Lars-Andre Tokheim

Department of Process, Energy and Environmental Technology, University College of Southeast Norway,
{sumudu.karunaratne, lars.a.tokheim}@usn.no

Abstract

CFD modelling was used to simulate particle segregation in a transverse plane of a rotating cylinder under different particle-particle drag models. The Eulerian method was used to model the dense particulate phases in the system. Two types of particles, with different density and size, were used in the study. The simulations were performed under the rolling mode since this mode is believed to give good particle-particle mixing. The drag models of Schiller-Naumann, Morsi-Alexander and Syamlal-O'Brien Symmetric were applied in the modelling of particle-particle drag and results were compared with experiments. All the drag models were able to model the particle segregation. The Schiller-Naumann model and the Morsi-Alexander model showed good agreement with the experimental results while the Syamlal-O'Brien-Symmetric model had some deviations.

Keywords: particle segregation, rotating cylinder drag models, CFD

1 Introduction

Particulate materials are used in various types of industrial processes. Mixing is a physical process in which several granular phases are mixed together with the aim to make a homogeneous particle mixture. Rotating cylinders are widely used process units in many industrial applications, such as in cement, mineral and pharmaceutical industries. However, unlike in liquids, mixing time does not always improve the degree of particle mixing. The particle motion in the bed may give mixing of the different particle phases, but it may also give segregation (Karunaratne *et al.*, 2016), as indicated in *Figure 1*. Consequently, it is vital to have a better understanding of factors that may cause particle segregation in such units.

When simulating mixing of particulate phases, it is quite common to apply the Euler-Lagrange method. The Discrete Element Method (DEM) is a Lagrangian approach (Yamada *et al.*, 2011) that uses laws of motion (Newton's second law) in simulation to provide dynamic information about particles in motion (Yang *et al.*, 2003). It allows studying micro-dynamics of powder flows that is difficult measure through experiments. DEM has been used in simulations of ball mills, rotary

vessel mixtures, bin-hopper systems and several other applications, as DEM simulations can generate accurate results on granular behavior (Yamada *et al.*, 2011). The disadvantage of DEM is that it is computationally intensive when the particle size becomes small (Soni *et al.*, 2016). In such cases, the Euler-Euler method may be useful. In this method, both fluid and solid phases are treated as interpenetrating continua and show the flow dynamics by using averaged equations of motion. Compared to the Euler-Lagrange approach, the Euler-Euler approach is often preferred due to the less computational demand (Mazzei, 2008).

In the current study, the Euler-Euler method was applied to model the particulate phases, which are quite dense. In this method, the particle bed is considered as a continuum, and granular kinetic theory is used to evaluate the viscosity terms in the transport equation. The drag force describes the momentum exchange between phases in the system. This interaction can be described through a set of mathematical formulations that apply to different conditions.

In a rotating cylinder, two types of drag forces are present and must be considered in CFD modelling of a binary solid mixture. In Fluent, several drag models can be selected to calculate the fluid-fluid drag, the particle-fluid drag and the particle-particle drag.

This study was performed to better understand the behavior of particle mixing and segregation in a binary mixture in a rotating drum. The calculation problem was simplified to a two-dimensional transverse plane, and the CFD simulations were done with the commercial software Fluent, version 16.2. Three different models the drag between particles in two phases were compared. The Schiller-Naumann (Fluent, 2013) model is a general model for fluids; the Morsi-Alexander model covers a large range of Reynolds numbers (Morsi and Alexander, 1972); the Syamlal-O'Brien-Symmetric model is specifically derived for a pair of solid phases (Syamlal, 1987). The simulation results were compared with lab experiments to identify which model that gives the best fit with experimental results.

2 Theory

There are two approaches that can be applied in CFD simulations of particles in a rotating cylinder: In the Lagrange method, Newton's second law is used to

calculate the particle velocities and their trajectories (Fluent, 2013). This is a good approach for dilute particle phases. If the particle phase is dense, it can be modelled as a continuum using the Eulerian method. The flow properties of a granular phase can be evaluated using granular kinetic theory in that the term called granular temperature is considered to be proportional to the square of the velocity fluctuations in the solid phase. This is an analogy to the thermodynamic temperature of gases (Benzarti *et al*, 2012).

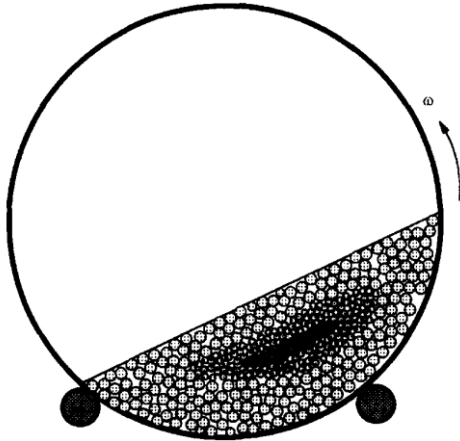


Figure 1. Schematic of radial segregation of particles of different size in a rotary kiln (Boateng and Barr, 1996)

A drag model gives valuable information about the momentum exchange between the phases in a multiphase flow situation. Several articles have focused on finding the optimum drag model for various engineering applications. Benzarti *et al*, (2012) performed a numerical parametric study to model the fluid behavior in the riser of a bubbling fluidized bed (BFB). The gas-solids drag was modelled and compared using three drag models: Gidaspow, Syamlal and O'Brien and EMMS. A similar type of work has been done by Lundberg and Halvorsen, (2008), who also implemented the Richardson-Zaki drag model, the RUC drag model and the Hill-Koch-Ladd drag model in the Fluent environment. Silva *et al*, (2015) studied the particle distribution in a highly concentrated particle-liquid stream in a pipe using a mixture model. The drag models of Schiller-Naumann and Gidaspow-Schiller-Naumann were used to model the drag force between the particles and the fluid. For a solids-liquid suspension with a high particle concentration at intermediate velocities, the Schiller-Naumann drag correlation showed the best agreement.

A detailed description of the Eulerian method is given in a previous paper by Karunarathne *et al*, (2016) and is not repeated here. Instead, the focus is put on discussing the drag models used in this study.

2.1 Drag models for fluid flows

The exchange coefficient for bubbly liquid-liquid mixtures or bubbly gas-liquid mixtures can be written as (Fluent, 2013):

$$k_{pq} = \frac{\alpha_p \alpha_q \rho_p f}{\tau_p} \quad (1)$$

$$\tau_p = \frac{\rho_p d_p^2}{18\mu_q} \quad (2)$$

Different drag models apply different equations to represent the drag function f . Some drag models even use another representation of the exchange coefficient k_{pg} .

2.1.1 Schiller-Naumann

This model is used for modelling of drag between fluid phases in multiphase flow. The drag function f is given as:

$$f = \frac{C_D \text{Re}}{24} \quad (3)$$

The drag coefficient C_D is given as:

$$C_D = \begin{cases} 24(1 + 0.15 \text{Re}^{0.687}) / \text{Re} & \text{Re} \leq 1000 \\ 0.44 & \text{Re} \geq 1000 \end{cases} \quad (4)$$

The relative Reynolds number Re for the primary phase q and secondary phase p is given as:

$$\text{Re}_{pq} = \frac{\rho_q |\vec{v}_p - \vec{v}_q| d_p}{\mu_q} \quad (5)$$

Then the relative Reynolds number for the secondary phases p and r is:

$$\text{Re}_{rp} = \frac{\rho_{rp} |\vec{v}_r - \vec{v}_q| d_{rp}}{\mu_{rp}} \quad (6)$$

The mixture viscosity of phase p and r is:

$$\mu_{rp} = \alpha_r \mu_r + \alpha_p \mu_p \quad (7)$$

2.1.2 Morsi-Alexander

The drag function f in the Morsi-alexander model is:

$$f = \frac{C_D \text{Re}}{24} \quad (8)$$

The drag coefficient is:

$$C_D = a_1 + \frac{a_2}{\text{Re}} + \frac{a_3}{\text{Re}^2} \quad (9)$$

a is defined as:

$$a_1, a_2, a_3 = \begin{cases} 0, 24, 0 & 0 < \text{Re} < 0.1 \\ 3.690, 22.73, 0.0903 & 0.1 < \text{Re} < 1 \\ 1.222, 29.1667, -3.8889 & 1 < \text{Re} < 10 \\ 0.6167, 46.50, -116.67 & 10 < \text{Re} < 100 \\ 0.3644, 98.33, -2778 & 100 < \text{Re} < 1000 \\ 0.357, 148.62, -47500 & 1000 < \text{Re} < 5000 \\ 0.46, -490.546, 578700 & 5000 < \text{Re} < 10000 \\ 0.5191, -1662.5, 5416700 & \text{Re} > 10000 \end{cases} \quad (10)$$

2.1.3 Syamlal-O'Brien Symmetric

This model is applied for drag between particulate phases. The solid-solid exchange coefficient k_{ls} is given as:

$$k_{ls} = \frac{3(1 - e_{ls}) \left(\frac{\pi}{2} + C_{fr,ls} \frac{\pi^2}{8} \right) \alpha_s \rho_s \alpha_l \rho_l (d_l + d_s)^2 g_{0,ls}}{2\pi(\rho_l d_l^3 + \rho_s d_s^3)} \left| \vec{v}_l - \vec{v}_s \right| \quad (11)$$

3 Method

3.1 Simulation setup

The geometry was represented by a two-dimensional transverse plane with a diameter of 0.19 m, which was also the size of the experimental setup, and a mesh with 3500 elements was created.

The transverse plane was set to rotate around its axis, and a no-slip condition was applied between the granular material and the wall, i.e. the relative velocity between the particles and the wall is considered to be zero.

The fluids in the system were considered as incompressible and model equations for the Eulerian approach were solved using a pressure-based solver with the finite volume method. The pressure-velocity coupling was done by the SIMPLE algorithm (Patankar and Spalding, 1972). The transport equations were discretized according to the second order upwind scheme, and the QUICK scheme was used to discretize volume fraction of the phases (Versteeg and Malalasekera, 2007). The time step of the simulation was set to 10^{-3} s, and the residual values for convergence were set to 10^{-3} .

The simulations were performed with three different drag models to investigate the effect of particle-particle drag forces on mixing and segregation. These simulations were carried out with four different cylinder filling degrees: 10, 15, 20 and 25 %. The rotational velocity of the transverse plane was set to 3 rpm in all

simulations to maintain the motion of the particle bed under rolling mode.

3.2 Experimental setup

Mixing of two particular phases was tested in lab experiments using a rotating drum made of Lexan, 19 cm in diameter and with a length of 29 cm. Two types of spherical particles with different densities and diameters were used in the experiments, see Table 1. The particles were coloured yellow (A) and blue (B) to make the mixing and segregation pattern more visible.

Microscopy and sieving analysis were used to determine the particle diameters, and the true density of the particles was measured using an autopycnometer of model 1320 from Micromeritics. Figure 2 illustrates particle filling through a transverse plane; initially the particles were arranged as separate layers stacked on top of each other. As in the simulations, the rotational velocity of the drum was set to 3 rpm in all experiments. In order to compare results with the simulations, all experiments were done at particle filling degrees of 15 and 25 % in order to observe its influence on mixing and segregation.

Table 1. Particle properties

Description	Symbol	Value
Particle A density	ρ_A	2537 kg/m ³
Particle B density	ρ_B	2417 kg/m ³
Particle A size	d_A	1500 μm
Particle B size	d_B	3000 μm
Particle A colour	-	Yellow
Particle B colour	-	Blue

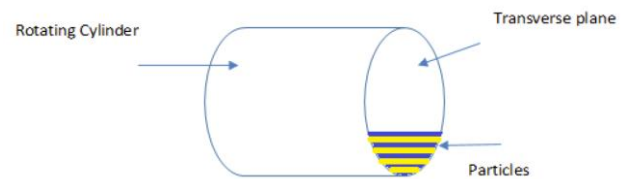


Figure 2. View of the particle filling through a transverse plane in the rotating cylinder

4 Results

The experimental results show that the particles segregate when the cylinder rotates around its main axis. This segregation, which is seen in Figures 3-6, is mainly due to the variation of particle diameter in the two different particle phases. Particle dynamics in the active layer of the rolling mode allow finer particles to concentrate at the mid-chord section (Boateng and Barr, 1996). Subsequently, fine particles move through the voids between bigger particles under the action of gravity and this is called percolation. As a result, fine particles accumulate at the middle of the particle bed.

The Euler-Euler method was able to simulate the particle mixing in the transverse plane of a rotating cylinder under different drag models. The simulations showed that particles with a small diameter tend to concentrate at the middle of the particle bed in the transverse plane. At the same time, particles with a larger diameter tend to move to the bottom of the particle bed.

Figures 3-6 show compare the simulated results from the three drag models and the results obtained from experiments. The volume fractions of both particulate phases were calculated in all simulation cases. Considering the particle segregation, the simulations indicate that the Schiller-Naumann and Morsi-Alexander drag models are in better agreement with the experimental results. Both these models were able to simulate the segregation behavior observed in the experiments. The results obtained through the use of the Syamlal-O'Brien Symmetric model deviate from the results of the other two drag models. Although the model was able to simulate some segregation, it did not

show the complete separation of the two particulate phases which was found by applying the other two models and in the experiments.

In rolling mode, particles in the passive layer do not experience much particle collision when they move. The Syamlal-O'Brien Symmetric model is often used in CFD simulations of fluidized beds, and it gives good results as those systems involve a high rate of collision among the particles. The Schiller-Naumann and Morsi-Alexander models are, however, more appropriate to model the drag between continua (as opposed to particles), and in the current simulation, the particulate phases are modelled as continua.

In order to examine the effect of degree of particle filling on mixing and segregation, the experiments were done at two different degrees of filling under rolling mode. There was, however, no significant improvement in particle mixing after increasing the particle bed height from 15 to 25 %. The simulations confirmed this observation, see Figures 3-6.

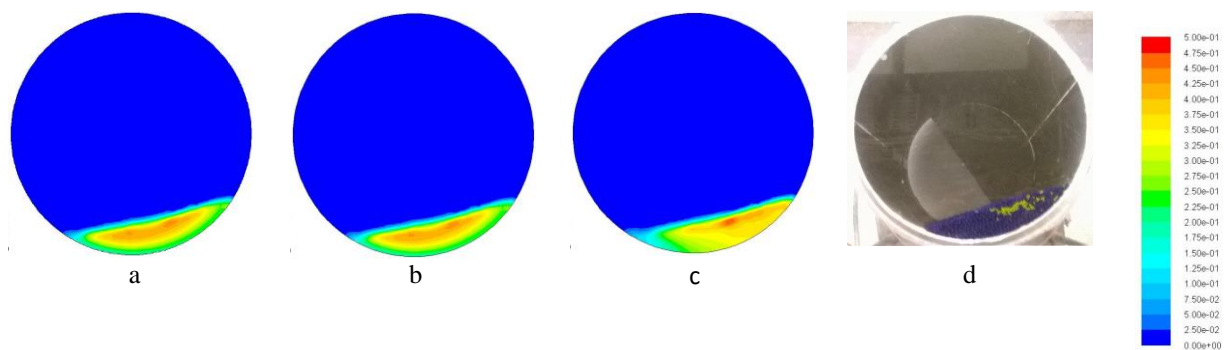


Figure 3. Volume fraction of “A” particles at 15% of degrees of particle filling (a: Schiller-Naumann, b: Morsi-Alexander, c: Syamlal-O'Brien-Symmetric, d: Experiment). Yellow (A) and Blue (B) particles

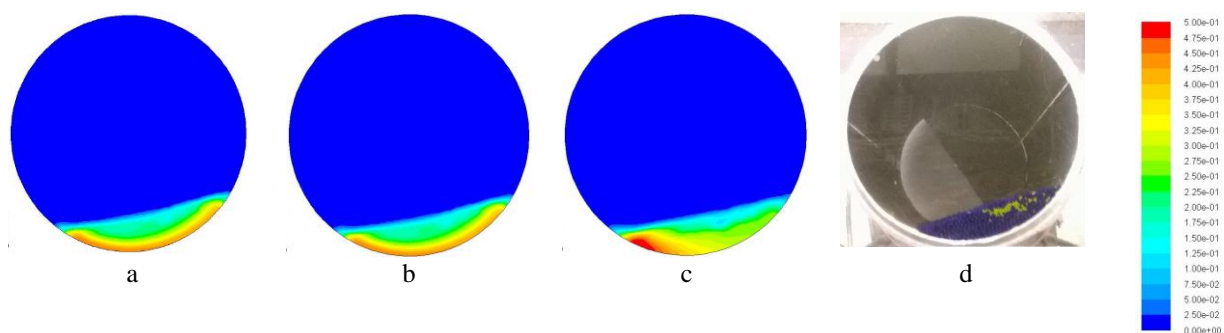


Figure 4. Volume fraction of “B” particles at 15% of degrees of particle filling (a: Schiller-Naumann, b: Morsi-Alexander, c: Syamlal-O'Brien-Symmetric, d: Experiment). Yellow (A) and Blue (B) particles

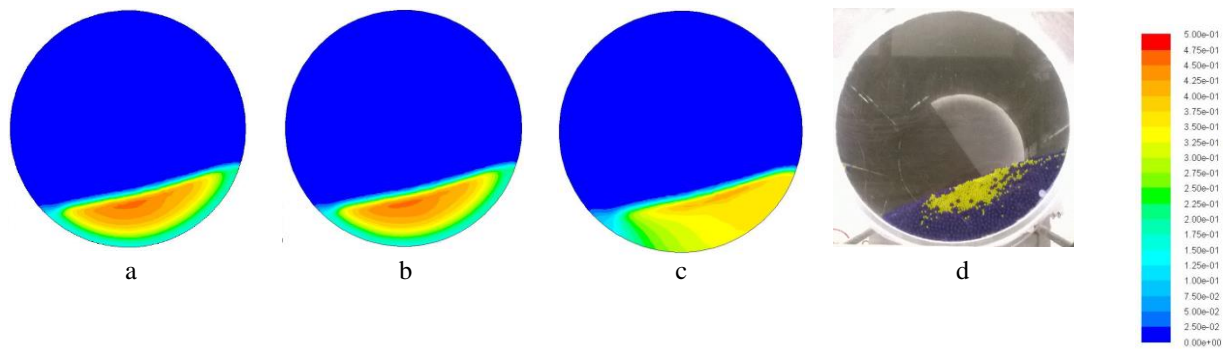


Figure 5. Volume fraction of “A” particles at 25% of degrees of particle filling (a: Schiller-Naumann, b: Morsi-Alexander, c: Syamlal-O’Brien-Symmetric, d: Experiment). Yellow (A) and Blue (B) particles

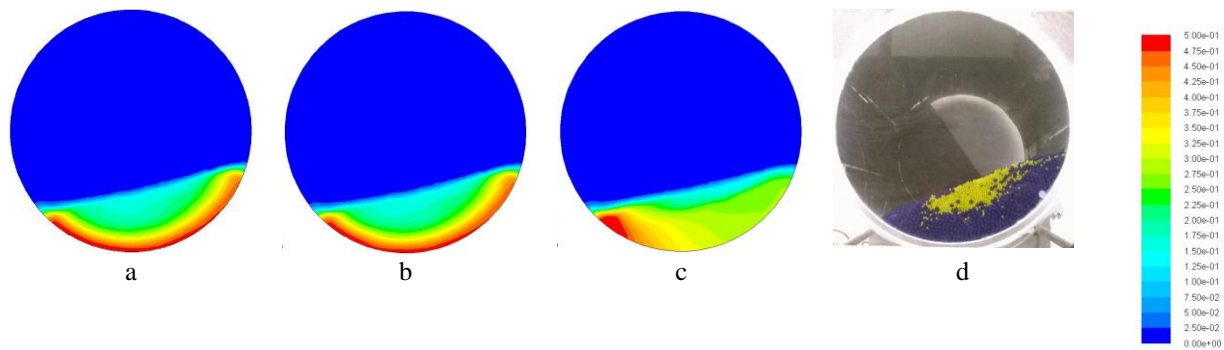


Figure 6. Volume fraction of “A” particles at 25% of degrees of particle filling (a: Schiller-Naumann, b: Morsi-Alexander, c: Syamlal-O’Brien-Symmetric, d: Experiment). Yellow (A) and Blue (B) particles

5 Conclusion

The Euler-Euler approach was able to simulate the particle dynamics in a transverse plane of a rotating cylinder applying different drag models. The particle-particle drag model has a significant influence on the mixing and segregation of particles in a transverse rotating plane.

The predicted particle distribution patterns from applying the Schiller-Naumann and Morsi-Alexander drag models under rolling mode were in better agreement with the experimental results than those obtained by using the Syamlal-O’Brien Symmetric drag model.

The increase of degree of particle filling did not show any significant effect on the mixing behavior. This was seen in simulations as well as in experiments.

Nomenclature

C_D	Drag coefficient [-]
C_{fr}	Coefficient of friction [-]
d	Diameter [m]
e	Coefficient of restitution [-]
f	Drag function [-]
g_0	Radial distribution [-]

k	Exchange-coefficient [$\text{kg}/(\text{m}^3 \cdot \text{s})$]
v	Velocity [m/s]
Re	Reynolds number [-]
α	Volume fraction [-]
μ	Viscosity [$\text{Pa} \cdot \text{s}$]
ρ	Density [kg/m^3]
τ	Particulate relaxation time [s]

References

- A. A. Boateng and P.V. Barr. Modelling of particle mixing and segregation in the transverse plane of a rotary kiln. *Chemical Engineering Science*, 51: 4167-4181, 1996.
- Fluent . ANSYS Fluent Theory Guide. *Ansys Fluent*, 2013.
- H. K. Versteeg and W. Malalasekera. *An introduction to computational fluid dynamics*, England, Pearson Education Limited, 2007.
- J. Lundberg and B. M. Halvorsen. A review of some existing drag models describing the interaction between phases in a bubbling fluidized bed. Proceedings of the 49th Conference on Simulation and Modelling, SIMS 49, October 7th-8th 2008 Oslo, Norway.
- L. Mazzei. Eulerian modelling and computational fluid dynamics simulation of mono and polydisperse fluidized suspensions. Department of Chemical Engineering, University College London, 2008.

- M. Syamlal. *The particle-particle drag term in a multiparticle model of fluidization*, 1987.
- R. Silva, C. Cotas, P. Garcia, M. Faia and G. Rasteiro. Particle distribution studies in highly concentrated solid-liquid flows in pipe using the mixture model. The 7th world congress on particle technology (WCPT7). *Procedia Engineering*, 1016-1025, 2015.
- R. K. Soni, R. Mohanty, S. Mohanty and B.K. Mishra. Numerical analysis of mixing of particles in drum mixers using DEM. *Advanced Powder Technology*, 27: 531-540, 2016.
- R.Y. Yang, R.P. Zou and A.B. Yu. Microdynamic analysis of particle flow in a horizontal rotating drum. *Powder Technology*, 130: 138-146, 2003.
- S. A. Morsi and A. J. Alexander. An investigation of particle trajectories in two-phase flow systems. *Journal of Fluid Mechanics*, 55: 193-208, 1972.
- S. Benzarti, H. Mhiri and H. Bournot. Drag models for simulation gas-solid flow in the bubbling fluidized bed of fcc particles. *International Journal of Chemical, Molecular, Nuclear, Materials and Metallurgical Engineering*, 6 :111-116, 2012.
- S. Karunarathne, C. Jayarathna and L.A. Tokheim. 2016. Impact of particle diameter, particle density and degree of filling on the flow behavior of solid particle mixtures in a rotating drum. *9th EUROSIM Congress on Modelling and Simulation*, 2016.
- S. Patankar and D. Spalding. A calculation procedure for heat, mass and momentum transfer in three-dimensional parabolic flows. *International Journal of Heat and Mass Transfer*, 15, 1972.
- Y. Yamada, M. Sakai, T. Nonoue and K. Takahashi. Development of a Lagrangian-Lagrangian coupling method for solid-liquid flows. Chemeca 2011, Engineering a better world, September 18th-21st, NSW, Australia, 2831-2840, 2011.

Simulation of burning velocities in gases vented from thermal run-a-way lithium ion batteries

Jonathan Johnsplass, Mathias Henriksen, Knut Vågsæther, Joachim Lundberg and
Dag Bjerketvedt

University College of Southeast Norway, Porsgrunn, Norway, knutv@usn.no

Abstract

This paper describes the results from simulations of laminar burning velocities in the premixed air and flammable gases vented from abused Li-ion batteries. The released mixture from such batteries contain mixtures of hydrogen, methane, ethylene, carbon monoxide and carbon dioxide. The study also includes the combustion properties of an electrolyte, dimethyl carbonate. The simulation results show the laminar burning velocities as a function of concentration, pressure and temperature for the gas mixtures and electrolyte. The goal of the present project is to use the simulated burning velocities in curve fitted functions for use in computational fluid dynamics (CFD) codes.

Keywords: Li-ion battery, Safety, Laminar burning velocity

1 Introduction

In the recent years, we have seen a strong increase in the use of Li ion batteries as an energy carrier in the transport sector. This growth is expected to continue in future transport applications on road, rail, and sea. The advantage of Li ion batteries is the relatively high energy density. However the high energy density also represents a hazard. If the battery experiences a thermal run-a-way or overheating it might vent combustible gases, mists and particles which can cause fires or explosions. Such an explosion occurred in Sweden in 2016 during a Li-ion battery test.

Harris et al. (2009) studied the impact from the carbonate solvents used in Li-ion batteries where they reported that flames of carbonate solvents are less energetic than hydrocarbons as propane.

Most lithium-ion studies are primarily focused on the gases vented from the batteries, the other phases are neglected. The study by Ponchaut et al. (2014) studied two combustion properties, the deflagration index and the overpressure at constant volume combustion of the vented gases from two lithium-ion pouch batteries. The study concludes that the gases vented from the li-ion pouch battery are comparable to the hydrocarbons methane, and propane, but that vented gas have a broader

combustion range, due to the presence of hydrogen, and carbon monoxide.

In order to make a risk assessment and consequence analysis we need to know the combustion properties of the gases involved. Such information is lacking in the open literature today. There are two ways of finding that type of information; one way is to carry out experimental investigations the other is to perform simulations. In this paper we describe the simulation approach using the open-source chemical kinetics software Cantera.

The overall objective of this activity is to develop a CFD (Computational Fluid Dynamics) tool for simulation of dispersion and combustion of gas, mist and particles emitted from abused Li-ion batteries. The present paper presents the first part of this activity, which is to simulate the laminar burning velocity of the different mixtures. In order to find these coefficients we use the Cantera program (Goodwin et al, 2017) to simulate the laminar burning velocities and the thermodynamic properties of the combustion products for different stoichiometry, initial pressure and temperature. The planned path from these simulated velocities is to use a Python LMFIT non-linear optimization program to find the fitted functions to be used in the CFD software. The route from Cantera simulations to the CFD simulation is illustrated in figure 1. The aim of presented paper is to show the method and the results of the simulation of the burning velocity as a function of stoichiometry (equivalent ratio), pressure and temperature.

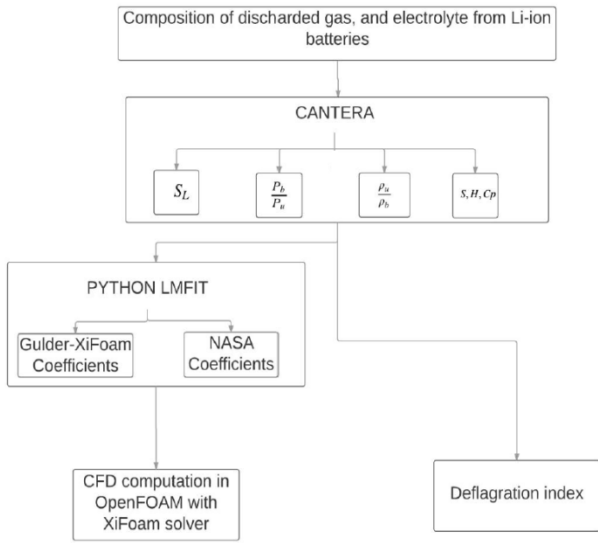


Figure 1. The planned activity path from simulated burning velocities to CFD simulations.

2 Materials and Methods

In this section we describe the Cantera program and the reaction mechanisms that we used to simulate the laminar flames for the different pre-mixed gas mixtures. The following subsections describe the flammable substances we have studied; i) gas composition emitted from 18650 Li-ion batteries, ii) dimethyl carbonate electrolyte and iii) methane, propane and hydrogen.

2.1 Cantera Software

Cantera 2.3.0 is an open-source software (Goodwin *et al*, 2017) for simulations of thermodynamic states, homogeneous and heterogeneous chemistry, chemical equilibrium, reactor networks, steady 1-D flames, reaction path diagrams, non-ideal equations of state and electrochemistry. It can easily be used as plugin or toolbox in Python and Matlab.

2.2 reaction mechanisms

We used the laminar flame model in Cantera 2.3.0 which takes into account the multi-component heat and mass transfer, convective transport and elementary chemical reactions. The K+2 conservation equations below have to be solved to find the laminar burning velocity, S_L . Where K is the number of species. Equation (1) is the continuity equation, equation (2) is the mass conservation of each specie and equation (3) is the conservation equation for energy.

$$\dot{m} = \rho u A = \rho_0 S_L A \quad (1)$$

$$\dot{m} \frac{dY_k}{dx} + \frac{d}{dx} \rho Y_k V_k + A \dot{\omega} W_k = 0 \quad (2)$$

$$\dot{m} \frac{dT}{dx} - \frac{1}{c_p} \frac{d}{dx} \left(\lambda A \frac{dT}{dx} \right) + \frac{A}{c_p} \sum_{k=1}^K \left(\rho Y_k V_k c_{p,k} \frac{dT}{dx} + \dot{\omega}_k h_k W_k \right) = 0 \quad (3)$$

Where, \dot{m} is the mass flow, ρ is the density, u is the flow velocity, Y_k is the mass fraction of specie k, V_k is the diffusion velocity of specie k, $\dot{\omega}_k$ is the reaction rate of specie k, W_k is the molecular weight of specie k, T is the temperature, c_p is the specific heat capacity, λ is the heat conductivity, A is the cross sectional area, h_k is the specific enthalpy of specie k.

The reaction rate of specie k is calculated from the elementary reaction mechanism, which is solved as shown in equation 4. Equation 5 is the Arrhenius rate constant.

$$\dot{\omega}_k = \sum_{j=1}^J k_j \prod_{i=1}^I c_i^{\nu_i} \quad (4)$$

$$k_j = A_j T^{\beta_j} \exp\left(\frac{-E_{a,j}}{RT}\right) \quad (5)$$

Where: J is the the elementary reactions containing specie k, k_j is the rate konstant for reaction j, I is the number of reactants in reaction j, c is the molar concentration of the reactants, ν is the stoichiometric index of component i, A_j is the pre-exponential factor, β is the temperature index, E_a is the activation energy. The three constants in the Arrhenius rate constant are found in the reaction mechanism.

2.3 Reaction Mechanisms

To calculate the reaction rates we use Cantera 2.3.0 with the GRI-Mech 3.0 mechanism (Gregory *et al*). The mechanism has 325 reactions and 53 species. It is optimized for natural gas combustion, i.e. CH₄, but includes several other species, e.g. H₂, CO, C₂H₄ and C₂H₆. GRI-Mech3.0 is the only default reaction mechanism in Cantera which includes all the relevant species from the Li-ion vented gas. We have therefore chosen GRI-Mech 3.0 for all simulation except for the dimethyl carbonate (i.e. DCM) simulations.

For the dimethyl carbonate electrolyte, we used the reaction mechanism of Glaude *et al* 2004 with 805 reactions and 102 species



Figure 2. Picture of an 18650 Li-ion battery after a rupture test.

2.4 Gas Composition emitted from Li ion batteries

Golubkov et al, (2014) analyzed the gas composition of the vented gas emitted from three different 18650 batteries, i.e. an LCO (Lithium Cobalt Oxide: LiCoO_2), NMC (Lithium Nickel Manganese Cobalt Oxide: $\text{LiNi}_{0.5}\text{Mn}_{0.25}\text{Co}_{0.25}\text{O}_2$) and LFP (Lithium Iron Phosphate: LiFePO_4) lithium-batteries. Table 1 gives the specifications for the three Li-ion batteries. We should notice that these batteries contain flammable materials in form of Li, electrolytes and graphite. When an 18650 battery is overheated or experiences a thermal run-a-way the pressure inside the battery will increase. If the battery reaches around 150°C a rupture disc will open and relief the pressure and combustible gases, mists and possible particles will then be vented into the surrounding atmosphere. Figure 2 shows a picture of an 18650 battery.

Table 1. Specifications of three different types of Li-ion batteries.

Property	Variable	LCO	LNMC	LFP
Cell mass	g	44.3	43.0	38.8
Capacity	Ah	2.6	1.5	1.1
Minimum voltage	V	3.0	3.0	2.5
Maximum voltage	V	4.2	4.1	3.5
Electrolyte solvents		DMC:EMC:EC (6:2:1) ³	DMC:EMC:EC:PC (7:1:1: 1)	DMC:EMC:EC:PC (4:2:3:1)
Cathode material		LiCoO_2 $\text{Li}(\text{Ni}_{0.5}\text{Mn}_{0.25}\text{Co}_{0.25})\text{O}_2$ (2:1)	$\text{Li}(\text{Ni}_{0.5}\text{Mn}_{0.25}\text{Co}_{0.10})\text{O}_2$	LiFePO_4
Anode material		Graphite	Graphite	Graphite

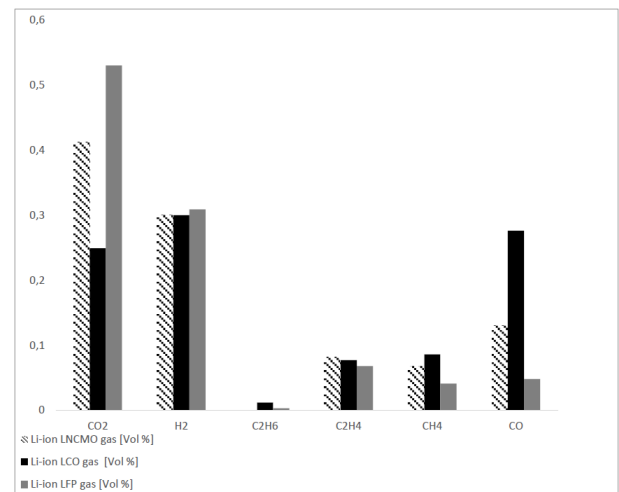


Figure 3. The composition of the emitted gas from three different Li-ion batteries.

Golubkov et al. used a GC to quantify composition of the vented gas. The result from the measurements is shown in Figure 3. For all the three batteries the H_2 content was around 30%. The emitted gas contains also significant amounts of combustible hydrocarbons in form of ethylene, C_2H_4 , and methane, CH_4 . The sum of CO_2 and CO was more or less constant, but the CO_2 and CO concentration vary for the three cases. The LCO battery gave nearly 30% CO while LFP gave less than 5%.

3 Results and Discussions

The present simulations are for air mixtures with DMC, hydrogen, methane and ethylene. The hydrogen, methane and ethylene included as reference fuels.

3.1 Burning Velocity vs. Equivalence Ratio

Figures 4 and 5 show the laminar burning velocity as a function of equivalence ratio for initial condition 1 atm and 298.15 K. The equivalence ratio, ϕ , is the fuel-to-air ratio to the stoichiometric fuel-to-air ratio. For an equivalence ratio less than one (i.e. $\phi < 1$), the fuel-air mixture is fuel lean and we have an excess of air (or oxidizer). For $\phi > 1$, the mixture is fuel rich. It is evident from that the maximum burning velocity is slightly on the rich side for all components, i.e. when $\phi > 1$.

Except for pure H_2 the maximum laminar burning velocities are in the range of 0.35-0.65 m/s. Hydrogen however, has a maximum laminar burning velocity of 3 m/s. This value reflects the high reactivity and the high thermal diffusivity of H_2 . The two other reference fuels gave maximum laminar burning velocities of 0.45 m/s for propane and 0.38 m/s for methane, which is typical values for gaseous hydrocarbons. We found that the electrolyte component; dimethyl carbonate (DMC) had maximum laminar burning velocity in the same range as methane but with higher burning velocities on the rich side. The Li-ion LFP gas and methane are also similar with respect to laminar burning velocity.

The Li-ion LCO gas shows a higher laminar burning velocity than the other gasses at a maximum of 0.65 m/s at equivalence ratio at 1.28. The simulation of S_L for LCO gas gave the highest S_L when we exclude H_2 . This high S_L for the Li-ion LCO gas is likely due to the low CO_2 content and high CO content in the gas mixture.

Li-ion LNCMO gas propagates at the same burning velocity as propane.

We also observe that the CO content in the emitted gas has a significant influence on the laminar burning velocity.

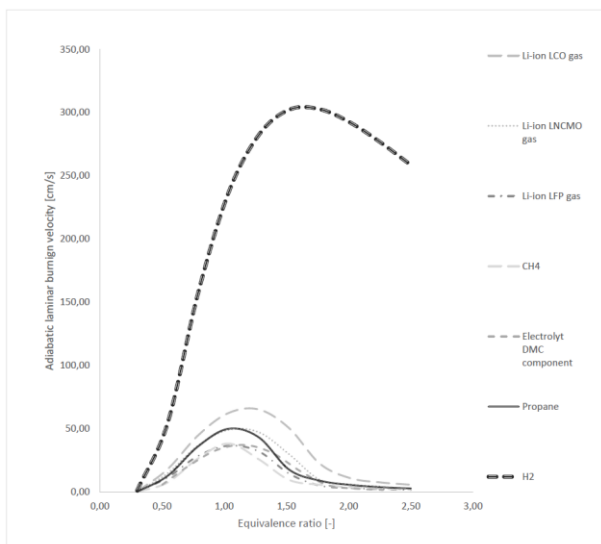


Figure 4. Comparison of the laminar burning velocity of the discharged gas emitted from an LCO, LNCM, and an LFP battery premixed with air, dimethyl carbonate-air and methane-air at initial conditions of 1 atm, and 298.15 K, were the burning velocity is a function of equivalence ratio.

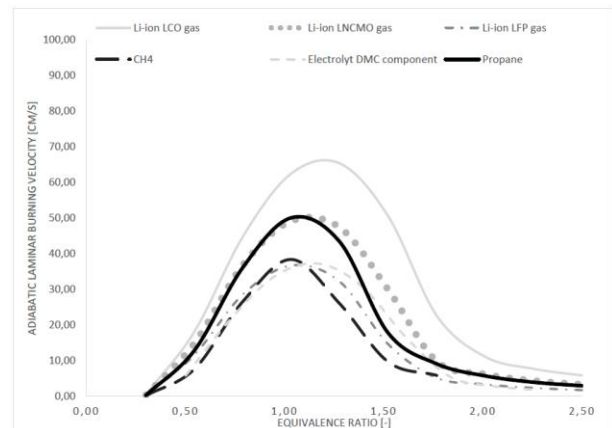


Figure 5. Comparison of the laminar burning velocity of the discharged gas emitted from an LCO, LNCM, and an LFP battery premixed with air, electrolyte component dimethyl carbonate-air and methane-air at initial conditions of 1 atm, and 298.15 K, were the burning velocity is a function of equivalence ratio.

3.2 Burning Velocity vs. Initial Pressure

Figure 6 shows the laminar burning velocity, S_L , for stoichiometric mixtures at 298 K and initial pressure from 0.5 to 10 bar. The burning velocity, in general, decreases with the pressure rise for all the Li-ion battery mixtures. However, the burning velocity for hydrogen has a peak at 2.25 bar. Even though the gas from the Li-ion LCO, LNCMO and LFP batteries constitute approximately of 30 % hydrogen this does not seem to cause the pressure dependency for the burning velocity of the gaseous mixtures to behave as a pure hydrogen-air mixture. The pressure dependency for the burning velocity is equal to the Li-ion battery gases, and the electrolyte component; dimethyl carbonate.

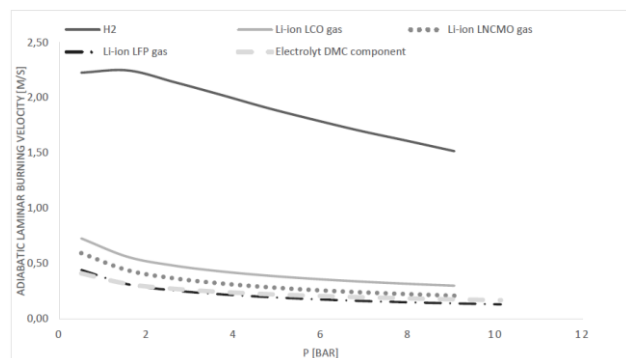


Figure 6. Comparison of the laminar burning velocity of the discharged gas emitted from an LCO, LNCM, and an LFP battery premixed with air, dimethyl carbonate-air and methane-air at initial conditions of 298.15 K, were the burning velocity is a function of the initial pressure in bar.

3.3 Burning Velocity vs. Initial Temperature

Figure 7 shows the laminar burning velocity, S_L , for stoichiometric mixtures at 1 bar and initial temperature from

250 to 950 K. The laminar burning velocity is a strong function of the initial temperature of the reactants. The gases from the Li-ion batteries are behaving uniformly; the velocity is steadily increasing from $250 \leq T \leq 950$ with a very rapid increase at $T = 950$ K. For the purpose of this study, temperatures below 650 K is the most interesting. The sudden increase in burning velocity at 950 K is probably because the mixture is close to the auto ignition temperature.

The electrolyte component; dimethyl carbonate, is less sensitive to temperature compared to the vented gases from the Li-ion batteries.

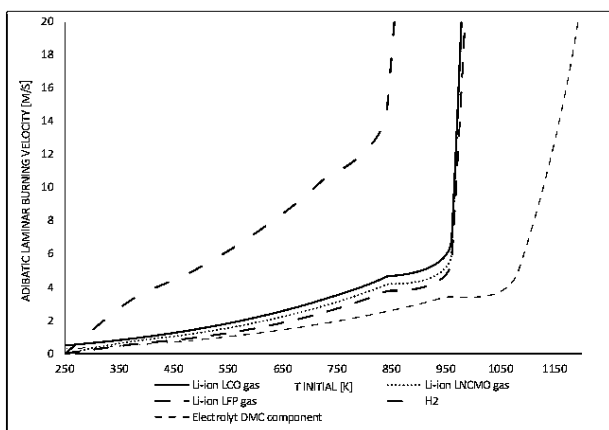


Figure 7. Comparison of the laminar burning velocity of the discharged gas emitted from an LCO, LNCM, and an LFP battery premixed with air, and methane-air at initial conditions of 1 atm, where the burning velocity is a function of the initial temperature in Kelvin.

4 Conclusion

We have simulated the laminar burning velocity for three gas mixtures vented from thermal runaway lithium batteries, one electrolyte and three reference fuels. The laminar burning velocities for these gases are similar to methane or even higher. This finding is important knowledge and will be used as input to computational fluid dynamics (CFD) codes for simulating gas explosions. To our knowledge these data is unique. The Cantera software has proven to be a useful tool for estimation of the laminar burning velocities for gas vented from Li-ion batteries and dimethyl carbonate electrolyte, DCM.

The emitted gas from Li-ion batteries and the DMC electrolyte, when mixed with air, burns at flame speeds similar to hydrocarbons such as methane and propane.

The burning velocity for all mixtures is decreasing for elevated initial pressure and increases for elevated temperature.

It is clear from our simulations that the gas vented from a thermal runaway in a Li ion battery burns comparable

to methane and propane. These gases will therefore under certain conditions, such as confinement and obstructed areas, represent a serious hazard with regard to explosions and fires.

Acknowledgements

This work is part of an activity on safety in the MoZEES project (www.mozees.no), a Norwegian national center for environment friendly energy research (NFR-FME) with a focus on battery and hydrogen technology for transport applications. This paper is based on a M.Sc. thesis at USN.

References

- Glaude, P. A., W. J. Pitz, and M. J. Thomson, "Chemical Kinetic Modeling of Dimethyl Carbonate in an Opposed-Flow Diffusion Flame," *Proceedings of the Combustion Institute* 30, pp. 1095-1102 (2004); Lawrence Livermore National Laboratory, Livermore, CA, UCRL-JC-201358.
- Golubkov, A. W., Fuchs, D., Wagner, J., Wiltse, H., Stangl, C., Fauler, G. & Hacker, V. (2014). Thermal-runaway experiments on consumer Li-ion batteries with metal-oxide and olivin-type cathodes. *RSC Advances*, 4(7), 3633-3642.
- Goodwin, D. G., Moffat, H. K., and Speth, R. L.. Cantera: An object-oriented software toolkit for chemical kinetics, thermodynamics, and transport processes. <http://www.cantera.org>, 2017. Version 2.3.0. doi:10.5281/zenodo.170284
- Gregory P. Smith, David M. Golden, Michael Frenklach, Nigel W. Moriarty, Boris Eiteneer, Mikhail Goldenberg, C. Thomas Bowman, Ronald K. Hanson, Soonho Song, William C. Gardiner, Jr., Vitali V. Lissianski, and Zhiwei Qin http://www.me.berkeley.edu/gri_mech
- Harris, S. J., Timmons, A., & Pitz, W. J. (2009). A combustion chemistry analysis of carbonate solvents used in Li-ion batteries. *Journal of Power Sources*, 193(2), 855-858.
- Ponchaut NF, Colella F, Spray R, Horn Q. Thermal management modeling for avoidance of thermal runaway conditions in lithium-ion batteries. SAE Technical Paper, 2014.

Detonation Propagation in Stratified Reactant Layers

Gaathaug A.V. Vaagsaether K. Lundberg J. Bjerketvedt D.

Department of Process, Energy and Environmental Technology, University College of Southeast Norway, Norway,
andre.v.gaathaug@usn.no

Abstract

A numerical investigation of detonation propagation in stratified reactant layers is presented in this paper. It is based on the reactive Euler equations using a two step chemical kinetics approach. The numerical simulations are based on the reactive Euler equations. Turbulence is solved with a one equation model, and the chemical kinetics is modeled as a two steps. The first step is an induction time step, and the second step is an exothermic step. The numerical setup is scaled to keep the numerical resolution of the induction zone constant to 10 cells. Initial simulations were conducted to generate detonation structures in homogeneous reactants and with cyclic boundary conditions. The developed structures were mapped into a domain with a stratified reactant layer on top of a inert layer. The results show that the detonations fail to propagate as the triple points of the propagating detonation is "lost" into the inert layer.

Keywords: CFD, Detonation, Simplified kinetics

1 Introduction

Detonations are supersonic combustion waves relative to the reactants in front of the wave. Its subsonic counterpart is known as deflagrations. The two modes of combustion differ fundamentally as the deflagration is driven by mass diffusion into the reaction zone and heat conduction from the reaction zone into the reactants. The downstream boundary conditions are also important, as the combustion product density is lower than the reactants. The detonation propagates as a leading shock wave in front of the reaction zone and compresses the reactants and increasing the temperature. This increased temperature and pressure lead to an onset of exothermic chemical reactions.

The 1D CJ (Chapman-Jouget) theory gives the detonation velocity S_{CJ} as a function of the reactant initial conditions and the energy released in the reaction zone, hence it is a property of the reactant mixture, (Lee, 2008). In the CJ theory, the detonation is evaluated at the upstream and equilibrium downstream conditions.

The extension of the Chapman-Jouget theory is known as the ZND (Zel'dovich (Zel'dovich, 1940), Neumann (von Neumann, 1963) and Döring (Döring, 1943)) theory, which is a 1D consideration of detonations. In the ZND theory, a leading shock (no reactions) is followed by a induction zone, where firstly radicals are produced and later follows the exothermic reaction zone where heat is pro-



Figure 1. Results from detonation experiments. Sooted plate triple point trajectories of structured cellular pattern. From (Austin and Shepherd, 2003)



Figure 2. Results from detonation experiments. Sooted plate triple point trajectories of unstructured cellular pattern. From (Austin and Shepherd, 2003)

duced. An illustration of the pressure across a detonation wave is given in figure 3. The state behind the leading shock wave is referred to as the von Neumann state (example velocity: u_{vN}). It is given by the normal shock relations, and the state in front of the wave.

Real detonations are three dimensional and highly unsteady. They are driven by shock-shock interactions, and a dominant feature of real detonations are the trajectories of the shock triple point. Depending on the reactant mixture, the trajectories could be regular or irregular when recorded on sooted plates inside experimental equipment. Two examples are given in figures 1 and 2, from (Austin and Shepherd, 2003).

Fluid dynamic simulations of detonations must cap-

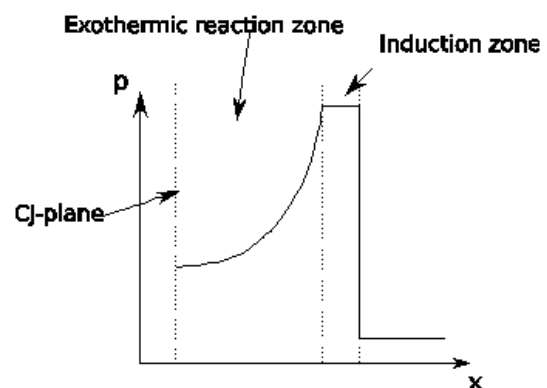


Figure 3. Pressure profile across a detonation front as described by the ZND theory.

ture the important physics of the phenomenon as well as the chemistry. As real gaseous detonations involve real gaseous reactions. The most simple reactant system is the H₂-O₂, which can include 8 species and up to 21 elementary reactions. It is manageable to include them in simulations, but more complex fuel-air mixtures can reach many hundred species and thousands of reactions.

Detonation propagation in stratified fuel layers, also known as semi confined detonations, has gained a recent interest in the safety research community as well as the jet propulsion research community. One aspect is related to the emerging world wide hydrogen infrastructure where the safety aspect must be clarified. An other classical aspect of hydrogen safety is the nuclear industry, where hydrogen leakage has been a valid concern since the first reactors were built. An accidental leak of hydrogen will likely form a fuel layer at the ceiling, where it is bound by a solid ceiling above and an compressible boundary of inert air below. The same issue apply to dense gas leakage which could make a combustible layer of reactants along the floor.

In jet propulsion research there is an effort to make a rotating detonation engine. This engine will inject reactants axially and have a tangentially propagating detonation propagating through the reactants. In the system the detonation will be bound by a solid inlet wall on one side and combustion products on the other side.

A sketch of the problem is given in figure 4. The shock plane is the leading shock wave, as no transverse waves are included. The CJ plane represent the end of the exothermic reactions. The shock is an oblique wave into the inert, while the dotted line is the contact surface. The expansion into the inert is drawn as a fan at the CJ plane. This is of course a simplified illustration of the problem.

This work aim to understand detonation propagation in reactant layers, especially the limits to where the detonation will fail. Recent studies by the KIT group and the Warsaw University of Technology (Grune et al., 2011; Rudy et al., 2013) have found a criteria for successful detonation propagation in a layer to be three cell size thick. An other study show that the critical layer thickness varies with the mixtures (Grune et al., 2016). The Warsaw University of Technology group showed that addition of methane to a hydrogen-air mixture increased the critical layer thickness, as shown by Rudy et al. (Rudy et al., 2016). A study by Houim and Fievisohn (Houim and Fievisohn, 2017) investigated the influence of the ratio of acoustic impedence between the reactant and inert layer on the detonation propagation. Their work focused concluded that a much denser inert or a much lighter inert gas is required to have a successful detonation propagation. They showed numerically how new triple points originate from the interface between inert and reactants. The earlier work by Sommers (Sommers, 1961) also showed the influence on inert gas density on the propagation of detonations. It was discussed how the diffraction gave a lower pressure and temperature, and also how a higher adiabatic

index gave a higher post shock pressure and thus a lower velocity deficit. The influence of adiabatic index is not discussed in this work.

The current study aims to address the detonation propagation problem based on a simplified analysis, described later. The overall procedure includes initial simulations to establish several credible detonation structures. The credibility criteria are explained later. And the detonation structures are later mapped onto a domain with reactants on top of an inert gas layer. This paper will mostly focus on the simulation method, as the actual results are believed to be more interesting for a specialized audience.

2 Numerical method

The numerical method is based on the 2D Euler equations, where mass momentum and energy is solved using a flux limited centered scheme. It is developed in MATLAB and details on the TeleCoDet code is given by Vaagsaether (Vaagsaether, 2010).

$$\frac{\partial \rho}{\partial t} + \frac{\partial}{\partial x_i} (\rho u_i) = 0 \quad (1)$$

$$\frac{\partial \rho u_i}{\partial t} + \frac{\partial}{\partial x_j} (\rho u_j u_i) = - \frac{\partial p}{\partial x_i} \quad (2)$$

$$\frac{\partial E}{\partial t} + \frac{\partial}{\partial x_i} (u_i E) = - \frac{\partial}{\partial x_i} (p u_i) \quad (3)$$

The energy E is given by the internal energy (given by the pressure and heat capacity ratio $\gamma = \frac{C_p}{C_v}$, kinetic energy and change of enthalpy energy due to chemical reactions:

$$E = \frac{p}{\gamma - 1} + \frac{1}{2} \rho u_i u_i + E_{ch} \quad (4)$$

The turbulence is modeled as transport of turbulent kinetic energy with source and sink terms. More details of the numerical method is given by Vaagsaether (Vaagsaether, 2010).

The exothermic chemical reactions of a detonation is given as a source in the energy equation. It is modeled in two steps as a simplification of a real combustion wave. Both steps are modeled as transported progress variables. The α variable is the normalized induction time progress variable. α varies between 0 and 1, where $\alpha = 0$ represent a gas mixture too cold to start exothermic chemical reactions. A $\alpha = 1$ represent a gas where the exothermic reactions can start. The β is the normalized exothermic reaction progress variable, where $\beta = 0$ is reactants and $\beta = 1$ is products.

$$\frac{\partial \rho \beta}{\partial t} + \frac{\partial}{\partial x_i} (\rho u_i \beta) = \dot{\omega} \quad (5)$$

$$\frac{\partial \rho \alpha}{\partial t} + \frac{\partial}{\partial x_i} (\rho u_i \alpha) = \dot{\vartheta} \quad (6)$$

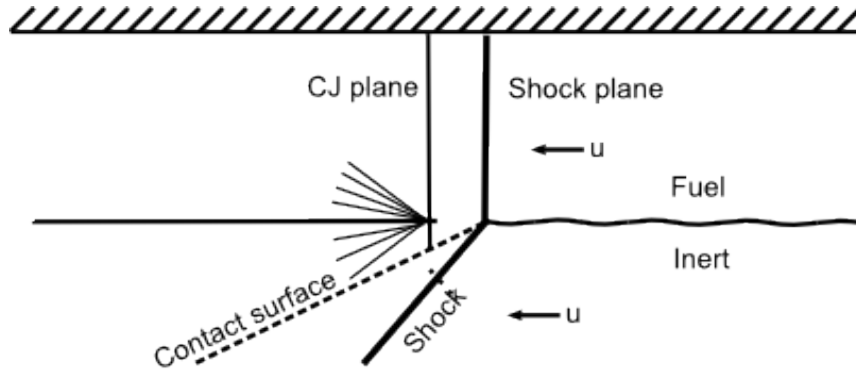


Figure 4. A sketch of a simplified wave structure where a detonation propagate in a stratified reactant (fuel) layer.

The idea behind this method is to constrain the β source term, i.e. the heat produced by exothermic reactions, until after an induction period (modeled by the α variable). The total β source term is given by:

$$\dot{\omega} = \max[\dot{\omega}_t, \dot{\omega}_k] \quad (7)$$

Where the $\dot{\omega}_t$ is the reaction rate given by the gradient of β . It is also given by the unburned gas density and the turbulent burning velocity S_T . The gradient of β term is used to model the combustion propagation of deflagrations. The turbulent burning velocity is modeled as given by Flohr and Pitsch (Flohr and Pitsch, 2000).

$$\dot{\omega}_t = \rho_u S_T \sqrt{\sum_i \left(\frac{\partial \beta}{\partial x_i} \right)^2} \quad (8)$$

The kinetic term of the β source is given by an Arrhenius type kinetics.

$$\dot{\omega}_k = \begin{cases} 0 & \alpha < 1 \\ B(1 - \beta) \exp\left(-\frac{E_\beta}{RT}\right) & \alpha = 1 \end{cases} \quad (9)$$

The E_{ch} of the energy equation is given by the progress variable and the change of enthalpy per unit mass of reactants (q) as

$$E_{ch} = \rho q (1 - \beta) \quad (10)$$

The induction time progress variable (α) source term is model with an Arrhenius kinetics term as

$$\dot{\varphi} = \rho A \exp\left(-\frac{E_\alpha}{RT}\right) \quad (11)$$

Numerical simulations are sensitive to the numerical resolution, especially reacting flow with a high temperature dependence. A key concept in this study is to limit

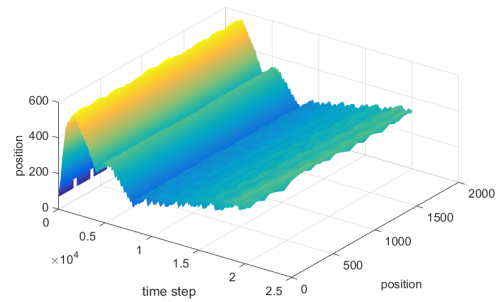


Figure 5. The detonation front for all time steps. Variables are: $q = 30$ and $E_\alpha = 30$. This is expected to give regular cellular structure of the front.

the variables of investigation to the energy (q) and the induction time activation energy (E_α). All other variables should be constant. To keep the numerical resolution constant, the pre-exponential coefficient A , was adjusted to give 10 cells in the induction zone. This was calculated for a stable 1D detonation as, the simulation cell size $\Delta x = 0.1$:

$$(u_{vN} - S_{CJ}) \tau = (S_{CJ} - u_{vN}) A \exp\left(\frac{E_\alpha}{RT}\right) = 1 \quad (12)$$

which gives the pre-exponential factor to be

$$A = \frac{1}{(S_{CJ} - u_{vN}) \exp\left(\frac{E_\alpha}{RT}\right)} \quad (13)$$

For the numerical setup, the initial pressure and density were both set to 1, as well as the gas constant. The heat capacity ratio γ was set to 1.4 and the input to the β progress variable source term was: $B = 4.9738$ and $E_\beta = 15$.

3 Initial calculations

3.1 Setup

The detonations were simulated two dimensionally, as a simplification of the real three dimensional structure of

detonation front. The first step of calculation was to develop a realistic 2D detonation structure. It was initiated as a slightly perturbed front with a 10 cells induction zone, and a 50 cells reaction zone. The top and bottom boundary condition (BC) were cyclic to account for an infinitely large domain. The right hand side inlet BC was zero-gradient with a semi-constant velocity (velocity was adjusted during the simulation). The left hand side outlet was a zero-gradient BC.

3.2 Results

This setup had to run until it developed wave structure with transverse waves propagating up and down the leading shock of the detonation. This is also the structure of real detonations. In real detonations the transverse waves propagate in two perpendicular directions to the leading shock. The point of collision of these three waves is known as the triple point, and will leave a cellular pattern (see figure 1 and 2) on sooted surfaces in experimental investigations of detonations. In the 2D simulations a pattern will be made of the leading shock and the up-down transverse shock. To investigate this, the pressure was used to find the position of the leading shock in the domain. This leading shock position was averaged for every time step to give a representation of the curvature (i.e. semi-triple-point recording). An illustration of the detonation front is shown in figure 5.

To investigate if the detonation simulations was developed, two parameters were used. One was the overall induction zone length, which was supposed to be close to 10 cells. This varied in the beginning of the simulation, but converged to 10. The second parameter was the development of cellular structure of the detonation front. For this, an analysis was developed to find the cellular pattern in the detonation front history. It was based on gradient evaluation and thresholding, as well as artificial diffusion. At last it was converted to a binary variable and analyzed with a tool used for image analysis. The result is shown in figure 6. It is shown that the cells appear some time after initiation, and that the development of cell sizes take some time before they converge.

When the numerical variables were changed, the cellular pattern also changed. It is expected from the theory by Lee and Stewart (Lee and Stewart, 1990), that a more irregular cellular pattern would be the result of increased activation energy of the α variable. This can be seen in figure 7. It is also shown that the variance of cell sizes is increased. The cyclic boundaries of the simulation was assumed to not influence the cell size, as long as there were more than three cells in the total height of the domain.

4 Simulations of detonations in stratified reactant layers

A 2D approach was used to investigate the detonation propagation in stratified reactant layers bound by one solid wall and an inert.

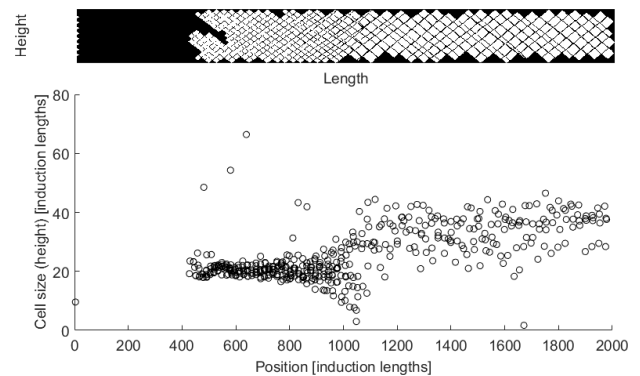


Figure 6. Top: Cellular pattern from the detonation front history. Bottom: The size of the cells vs the position. Variables are: $q = 30$ and $E_\alpha = 30$. This is expected to give regular cellular structure of the front.

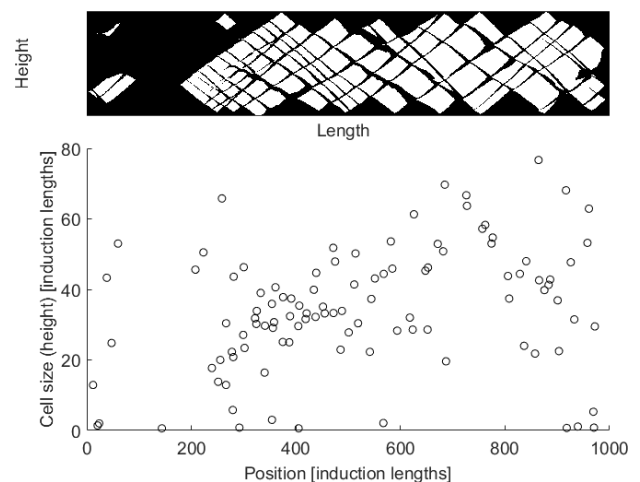


Figure 7. Top: Cellular pattern from the detonation front history. Bottom: The size of the cells vs the position. Variables are: $q = 30$ and $E_\alpha = 50$. This is expected to give an irregular cellular structure of the front.

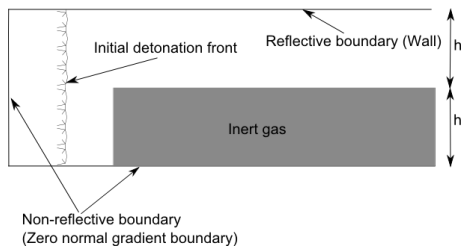


Figure 8. A sketch showing how the computational domain is set up with the mapped detonation structure to the left, the solid wall at the top and the inert layer along the lower boundary.

4.1 Setup

The initial simulations were mapped onto a larger domain where the inert was mapped as well. A sketch of the computational domain is given in figure 8.

The right, left and bottom BC was a zero gradient, while the top wall was a reflecting BC. The domain was moving to enable an investigation of the cellular structure by integrating (over time) the pressure in the induction zone. This makes up a more correct cellular structure as the thickness of the integrated variable represent the thickness of the induction zone. As this zone thickens, it is also expected that the detonation will fail and change to a deflagration following a leading shock wave.

4.2 Results and discussion

The detonation propagation is illustrated in figure 9 ($E_\alpha = 30$) where the triple point trajectories are shown and also how they are "lost" into the inert below the reactants. This is assumed to be the main reason for the failure of the detonation, as it will lead to an expansion loss into the inert. This gives a velocity deficit of the detonation, which result in a reduced strength of the leading shock wave, hence a lower von Neumann temperature and a longer induction zone. This eventually cause the detonation to fail after 1800 induction lengths.

The simulation results in figure 9 show that despite fulfilling the three detonation cells in the layer thickness this detonation still fails to propagate in the layer. A comparable real mixture to the case shown in figure 9 is stoichiometric hydrogen-air mixtures. As a comparison, that mixture have expected cell sizes of 8mm. The failure length would then be about 80mm to 100mm. The regularity of the detonation cellular pattern is also connected to the propensity to generate new triple points. The main reason for this is the increased activation energy. With a higher activation energy the reaction becomes more sensitive to small perturbations, and could make new triple point on its own. By keeping the layer thickness fixed to 150 induction lengths, an irregular cellular pattern case was investigated, see figure 10. This was expected to be able to propagate longer into the reactant layer compared to the $E_\alpha = 30$ case. It is clearly not the case, as one possible cause to the issue is the reduced number of detonation cells in the layer thickness. Much of a problem is also the definition of a cell

Table 1. List of all simulations in the project.

Layer thickness [ind length]	q	E_α
100	25	30
100	30	30
100	30	40
100	30	50
100	30	60
150	25	30
150	30	30
150	30	40
150	30	50

size, as it is very much an expected size with a rather large variance.

The project has so far investigated 9 cases, each take about 1 to 2 weeks to simulate on a standard workstation, using about 30 GB memory. It typically has a $9e6$ numerical cells, solve 24 equations in each cell up to 15000 times. The simulation has to be adjusted by stepwise skipping the domain to the right as the simulation progresses. The list of completed cases is given in table 1. The results so far show that all detonations fail at a short distance after entering the stratified reactant layer.

A further work on this project is first to simulate cases with a higher enthalpy per unit mass of reactants to investigate if it is within the limit of successful detonation propagation. The other case will be to further thicken the reactant layer, and lastly include a denser gas as the inert to allow for wave reflections at the boundary.

5 Summary

This paper have reported some of the work done on simulating detonations in stratified reactant layers. The simulations are based on the reactive Euler equations with a two step model for the chemical kinetics. The first step is a waiting time (induction time) progress variable which represent the induction time seen in simulations of detailed chemical kinetics. the second step is the exothermic reaction progress variable, which is linked to the energy equation. The numerical setup varied the change of enthalpy due to chemical reactions q and the induction time activation energy E_α . The numerical resolution was set to 10 cells in the induction zone (calculated on 1D steady state). The initial simulations had to run for a long time to ensure a developed detonation front. Due to the unsteady nature of detonations, a 10 cells criteria was used as well as a steady cellular detonation front. The initial detonation structure was mapped onto a stratified domain with proper boundary conditions and the failure on detonation was observed. The triple points were lost into the inert layer, and the expansion into the inert lead to a velocity deficit. This was assumed to be the reason for the detonation failure. The expected criteria from the literature of three detonation cells in the height of the reactant layer,

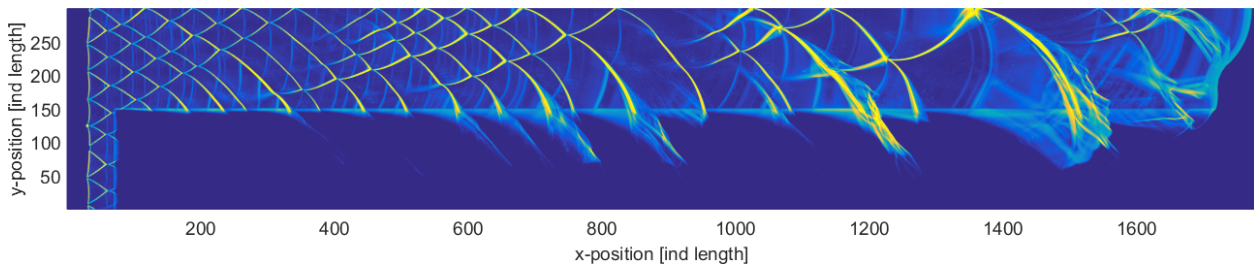


Figure 9. The triple point trajectory of a detonation in a stratified reactant layer. Variables are: $q = 30$ and $E_\alpha = 30$.

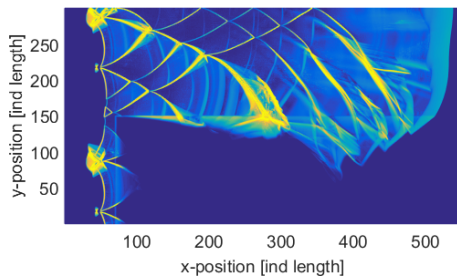


Figure 10. The triple point trajectory of a detonation in a stratified reactant layer. Variables are: $q = 30$ and $E_\alpha = 50$.

did not seem to be a general criteria for successful detonation propagation. The detonations with more irregular detonation cellular patterns also had a large variance in cell sizes, thus it might not be valid to base the thickness on the expected cell size. All simulated cases showed that the detonation failed as it propagated in the stratified reactant layer.

References

- J.M. Austin and J.E. Shepherd. Detonations in hydrocarbon fuel blends. *Combustion and Flame*, 132(1-2):73–90, 2003. ISSN 00102180. doi:10.1016/S0010-2180(02)00422-4. URL <http://linkinghub.elsevier.com/retrieve/pii/S0010218002004224>.
- W. Döring. Über Detonationsvorgang in Gasen [On detonation processes in gases]. *Annals of Physics*, 1943.
- P. Flohr and H. Pitsch. A turbulent flame speed closure model for LES of industrial burner flows. *Proceedings of the Summer Program*, pages 169–179, 2000.
- J. Grune, K. Sempert, H. Haberstroh, M. Kuznetsov, and T. Jordan. Experimental investigation of hydrogen–air deflagrations and detonations in semi-confined flat layers. *Journal of Loss Prevention in the Process Industries*, 26(2):317–323, oct 2011. ISSN 09504230. doi:10.1016/j.jlp.2011.09.008. URL <http://linkinghub.elsevier.com/retrieve/pii/S0950423011001677><http://dx.doi.org/10.1016/j.jlp.2011.09.008>.
- J. Grune, K. Sempert, A. Friedrich, M. Kuznetsov, and T. Jordan. ScienceDirect Detonation wave propagation in semi-confined layers of hydrogen e air and hydrogen e oxygen mixtures. *International Journal of Hydrogen Energy*, 42(11):7589–7599, 2016. ISSN 0360-3199.
- doi:10.1016/j.ijhydene.2016.06.055. URL <http://dx.doi.org/10.1016/j.ijhydene.2016.06.055>.
- Ryan W Houim and Robert T Fievisohn. The influence of acoustic impedance on gaseous layered detonations bounded by an inert gas. *Combustion and Flame*, 179:185–198, 2017. ISSN 0010-2180. doi:10.1016/j.combustflame.2017.02.001. URL <http://dx.doi.org/10.1016/j.combustflame.2017.02.001>.
- H.I. Lee and D.S. Stewart. Calculation of linear detonation instability : one-dimensional instability of plane detonation. *Journal of fluid mechanics*, 216:103–132, 1990. ISSN 0022-1120. doi:10.1017/S0022112090000362.
- J.H.S. Lee. *The Detonation Phenomenon*. Cambridge University Press, 2008. ISBN 0521897238. URL <http://www.amazon.co.uk/Detonation-Phenomenon-John-H-Lee/dp/0521897238><http://www.amazon.fr/The-Detonation-Phenomenon-ebook/dp/B001EHE7RA>.
- W. Rudy, M. Kuznetsov, R. Porowski, a. Teodorczyk, J. Grune, and K. Sempert. Critical conditions of hydrogen-air detonation in partially confined geometry. *Proceedings of the Combustion Institute*, 34(2):1965–1972, jan 2013. ISSN 15407489. doi:10.1016/j.proci.2012.07.019. URL <http://linkinghub.elsevier.com/retrieve/pii/S1540748912003112>.
- Wojciech Rudy, Mateusz Zbikowski, and Andrzej Teodorczyk. Detonations in hydrogen-methane-air mixtures in semi confined flat channels. 116:1479–1483, 2016. doi:10.1016/j.energy.2016.06.001.
- W.P. Sommers. *The Interaction of a Detonation Wave with an Inert Boundary*. PhD thesis, 1961.
- K. Vaagsaether. *Modelling of Gas Explosions*. PhD thesis, Telemark University College – NTNU, Norway, 2010.
- J. von Neumann. *Theory of Detonation waves, John von Neumann: Collected Works*. Pergamon Press, Oxford, 1963.
- Ya.B. Zel'dovich. On the theory of the propagation of detonations on gaseous system. *Journal of Experimental and Theoretical Physics*, 10:542–568, 1940.

Using Image Processing for Flame Diagnostics

Joachim Lundberg¹ Mathias Henriksen¹ André Gaathaug¹

¹ Department of process, energy and environmental technology, University College of Southeast Norway, Norway,
Joachim.lundberg@usn.no

Abstract

An image processing routine was developed to determine the flame height of a hydrogen jet flame. Two different techniques were tested, where one was based on Wien's distribution of a black body and one based on intensity of the flame. The method based on intensity gave the best results.

Keywords: Image Processing, Hydrogen jet, Wien's distribution, Experimental, high-speed imaging.

1 Introduction

Due to both practical and economic reasons, image processing can be a valuable technique for determining flame diagnostics. This study uses image processing to determine the height of a hydrogen jet flame.

A hydrogen jet flame is a diffusion flame as shown in Figure 1. The fuel, and in this case hydrogen, flows from a nozzle or an orifice. On the surface of the jet, the fuel will meet the oxidizer (air/oxygen) and make up the reaction zone or flame. This thin layer will position itself where the mixture of fuel and oxidizer is stoichiometric and the temperature will be about 2000°C. Since the jet flame is a spatial phenomenon, the flame will be visible all around the jet flame.

Direct measurements of physical properties of fires can be demanding to conduct. Often the high temperature of the fire can harm the measurement equipment or the measurement equipment itself can affect the measurements to give faulty results.

Image based techniques have an advantage in non-intrusiveness and take the measurement equipment away from the fire. This assures the results to be representative for the fire.

In the literature, several flame/fire diagnostic methods are provided using laser based techniques such as PLIF (planar laser induced fluorescence). This technique can provide information of the shape/thickness/position of the flame and reaction zone. The disadvantage with this technique is however the price of the equipment and the robustness of the measurements. Often, soot and particles of a fire can interfere with the measurement equipment to make the usage of PLIF demanding.

In a study by (Trindade et al, 2014) a normal color CCD camera was used to find the air/fuel ratio of a methane and propane flame. The color RGB images were experimentally observed to provide information of the flame.

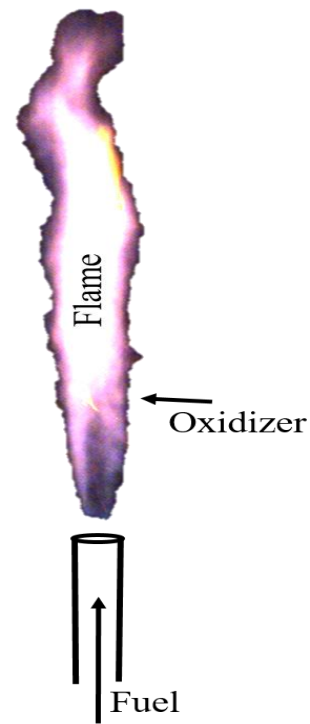


Figure 1. Example of a jet flame

In studies by (Li et al, 2011 and Yan et al., 2017) an image processing routine was developed to estimate temperatures in coal-fired boilers.

These studies base their image processing codes on Wien's distribution law. It assumes black body radiation from the coal or soot particles to be dominating the radiation in the flame.

Alternatively, a model based on intensity and visual considerations of the flame could be used. The model relates the intensity of the flame to the position of the flame.

In a study by Mogi et al. (2005) the flame length and diameter of a hydrogen jet was measured. To visualize the flame, a salt-solution was added to the flame as atomized droplets.

In this work, a hydrogen flame was investigated. It radiated much less than a comparable hydrocarbon or coal flame, but by visual considerations the flame radiated yellow/orange. This might be due to impurities in the hydrogen, but the radiation of the flame was enhanced. The aim of this study was to compare the two methods and find a method to determine the flame height of a hydrogen flame using image processing.



Figure 2. The experimental setup: 1) Hydrogen gas cylinder, 2) mass flow meter, 3) pressure sensor, 4) nozzle unit with changeable nozzle configurations, 5) radiation sensors (currently not in use).

An experimental setup was used with flow and pressure sensors. The images of the hydrogen flame was captured with a color CMOS high-speed camera. The property extracted from the images by an image processing techniques was flame height. The flames investigated, was a hydrogen flame in the range 24 to 1027 kW (based on lower heating value).

MATLAB was used as a platform for image processing. The purpose of the code was to find the flame height and diameter automatically from the images. The code had the possibility to find the frame height and diameter in every image of the movie, not just the average height.

2 Experimental Setup

The experimental setup is shown in Figure 2. The experimental setup was supplied with compressed hydrogen at 20 MPa from a cylinder and pressure controlled by a pressure regulator with a range from 1.0 to 12 MPa. A Coriolis mass flow meter from Micro-Motion was used to accurately measure the mass flow of hydrogen. A pressure sensor close to the nozzle was mounted to get the pressure before the nozzle. The nozzle unit with interchangeable nozzles was mounted on an aluminum table. A row of radiation sensors was mounted for future use.

The flame was captured using a color high-speed camera with frame rate of 250 frames per second (fps). The data from the logging instruments, such as mass flow meter, pressure sensors etc, was synchronized with the camera and recorded at 2000 Hz. Each experiment

had a duration of 5 seconds after the system had stabilized, which took approximately 2-4 seconds after ignition. For each experiment, 1250 images and 9999 data points for each of the other sensors was stored. Afterwards the image was analyzed with an in-house developed image-processing tool to determine the flame height. The flame height was determined to be from the nozzle exit (top of the nozzle) to the tip of the flame.

3 Choice of Method

The key feature of the image processing code was to determine the flame in high speed images to find the flame height of a hydrogen flame. Two methods was considered for this task: One based on Wiens distribution and one on image intensity.

The method that used Wiens distribution by (Huang et al., 2000) was an image based method to monitor the temperature of a 500-kW model furnace with both coal and gas as a fuel. The temperature of the flame was found by relating the intensity of two separate wavelengths from the flame using the expression:

$$T = \frac{C_2 \left(\frac{1}{\lambda_2} - \frac{1}{\lambda_1} \right)}{\left[\ln \frac{G(\lambda_1, T)}{G(\lambda_2, t)} + \ln \frac{S_{\lambda_2}}{S_{\lambda_1}} + \ln \left(\frac{\lambda_1}{\lambda_2} \right)^6 \right]} \quad (1)$$

where T is the temperature, C_2 is a constant, λ_1 and λ_2 is the first and second wavelength, $G(\lambda_i, T)$ is the measured grayscale value of each wavelength and $S(\lambda_i)$ is the spectral sensitivity of the sensor for the respectively wavelength. The measured grayscale

values was found by using two spectral filters. One monochrome camera was used to capture the two wavelengths using quick temporal shifting of the filters. In a hydrogen diffusion flame the temperature can reach more than 2000°C. This made the gasses radiate. If the flame was a sooting flame, most of the soot will radiate as a solid, and be combusted in the flame. When observing a diffusion flame with a digital camera the radiation can be observed as an intensity. The digital image will have an elevated intensity where the flame occurs.

(Zhang & Hui, 2011) has performed a study on 200-MW boiler. They capture digital images of a flame and remove the background of the image, then threshold the image by intensity to find the outline of the flame.

In this study, a hydrogen diffusion jet flame was investigated. A hydrogen jet is radiating considerably less than a coal or hydrocarbon flame. Figure 3a shows the intensity scaled image of the hydrogen jet. The actual image of the flame is in Figure 3b. The radiation from the flame is very low, which was expected from a hydrogen flame.

To identify the flame in the image of the hydrogen flame, the temperature could be used; The temperature in the diffusion flame will be at the highest where the stoichiometry equals unity. In an image, the flame will be a “shell” on the hydrogen jet hence a constant high temperature from one side of the flame to the other. This is demonstrated in Figure 3a.

Equation 1 can be used to find the temperature in a flame based on images. In this study it was not important to determine the temperature, just the position of the flame. Since the value of the temperature was irrelevant, the equation can be simplified. The wavelengths λ_1 and λ_2 is the green and red part of the original RGB image. Both of these parts will capture a range of wavelengths, but was assumed to have just one. The spectral sensitivity of the sensor was assumed to be equal for the two wavelengths. By inserting this into the Equation 1, the correlation in Equation 2 is found.

$$T \propto C_1 / \left[\ln \frac{G(\lambda_1, t)}{G(\lambda_2, t)} + C_2 \right] \quad (2)$$

The constants C1 and C2 was arbitrarily.

In Figure 4 the values of the different RGB colors from a line through the flame was plotted without amplification. It shows the different channels to be fairly equally shaped. This made the assumption of a Wiens distribution false.

The light sensitivity of the high speed camera can be fairly high, but due to the high repetition rate the light level of each image will be low. In the experiments on the hydrogen jet the maximum light intensity was about 3 % of the maximum obtainable on the sensor. This will make the images highly sensitive to noise.

Figure 5 shows a histogram of all the values of the pixels in the image.



Figure 3. a) Scaled image of hydrogen jet. b) Original image of hydrogen jet

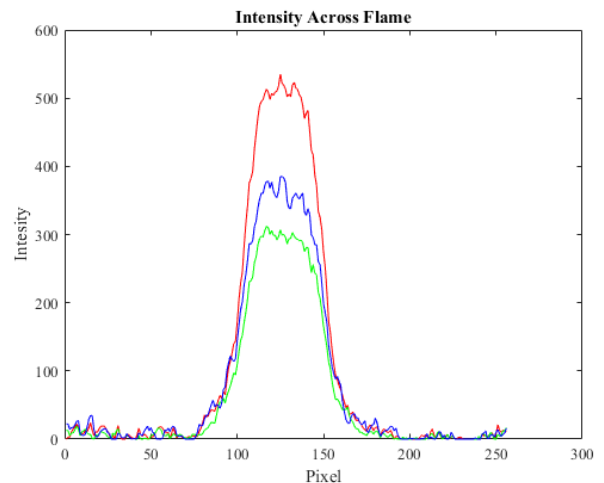


Figure 4. Intensity of a line profile of a horizontal line through the flame.

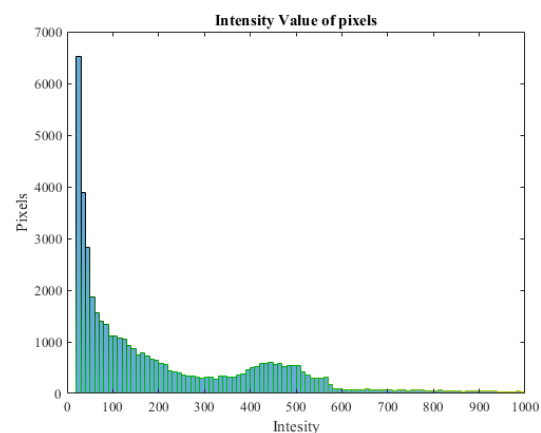


Figure 5. Histogram of pixel values in an image of a hydrogen jet.

As a comparison, the same technique was used on an image of a hydrocarbon fire shown in Figure 6. The

same image was processed with an expression like Equation 2 shown in Figure 7. Mogi et al. (2005) calculated the emissivity coefficient of a hydrogen flame to be $\epsilon = 0.03$ which is fairly low.

During the experiments on the hydrogen jet, an infrared camera was tested to see the temperature distribution in the flame. Figure 8 shows the infrared image from one of the experiments with the hydrogen jet flame. It shows a clear temperature distribution in the flame. Unfortunately, the infrared imaging has limited temporal resolution that will smoothen the shape of the flame.

Instead of using some expression based on Wiens distribution, flame intensity in the image was used. Where the image intensity was high, the flame was present.

Since the image was a color image, the image was separated in three monochrome images, one for each color channel (red, green, blue). This is shown in Figure 9. The three color channels to shows be almost identical in shape and value. Due to this, the red channel was chosen to represent the intensity of the image. The framework to isolate the flame and measure the flame height was developed in a MATLAB script.

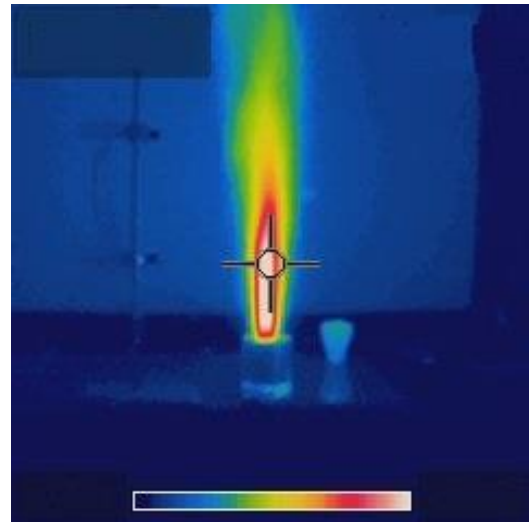


Figure 8. Infra red image of hydrogen jet flame

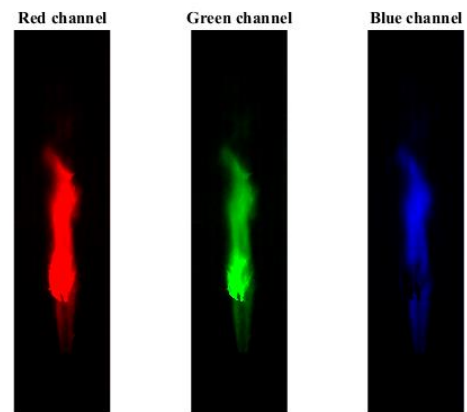


Figure 9. RGB-Color channels of an image of a hydrogen jet flame



Figure 6. Original image of a hydrocarbon flame.

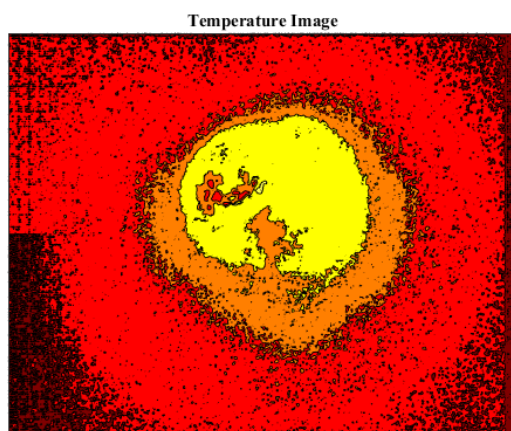


Figure 7. Calculate image of a hydrocarbon flame based on Wiens distribution.

4 Image Processing

To transfer each image from the movie of the hydrogen flame to a numerical value, an image-processing tool was developed in MATLAB.

Thresholding the image was the most crucial part of the image processing. The threshold value was the set point which distinguished background noise from signal. Background noise in the image could be mistaken for a flame if the procedure for thresholding was too crude. Thru several tests with manual/visual verification, the procedure for thresholding showed good correlation between manually finding the flame height in the images.

To reduce the computation time only the red image was analyzed for the whole data set, but it was thoroughly investigated that each color gave close to identical flame heights. The red color was chosen above the other colors since it had a higher intensity.

The noise in the background of the images was assumed to be normal distributed.

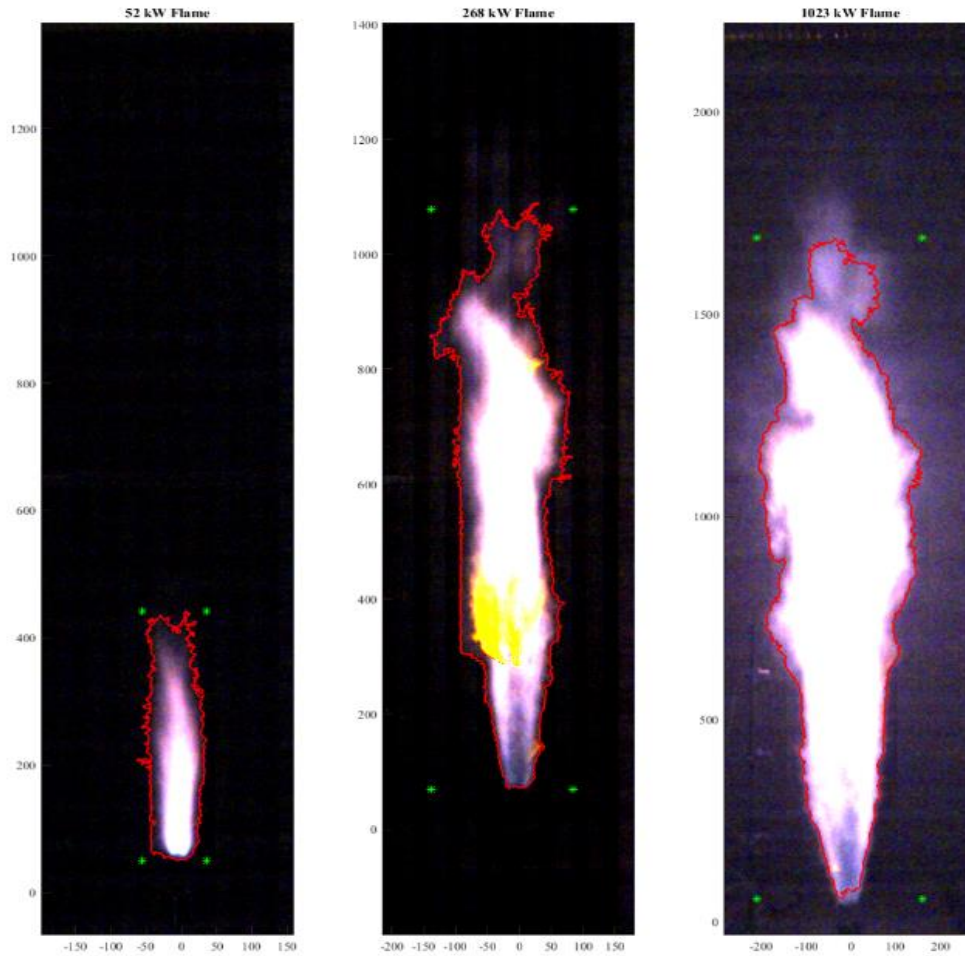


Figure 10. Three different sized hydrogen jet flames with contours of the calculated flame (red contours). The units are mm from exit nozzle.

The image-processing tool is explained in subsequent steps. The method used was iterative and the intermediate values are marked with an asterisk (*).

Step 1.

Read RAWW image from image sequence (movie). From the camera, the movies are built up by 16 bits images. The images are built up by a string of 16 bits values for every color and pixel. For every movie, a header file tells how to read the string.

Step 2

The color image was converted into three monochrome images or channels,

$$I_{RGB} = (I_R, I_G, I_B). \quad (3)$$

The monochrome 16 bits images was converted into numerical values (double). Since the different color channels showed no significant difference, the image was represented using

$$I = I_R \quad (4)$$

Step 3

The image was divided into flame and background using

$$I = \begin{cases} F & : I_{i,j} \geq t \\ B & : I_{i,j} < t \end{cases} \quad (5)$$

Where F is the flame and B is the background. t is the threshold intensity value that separate the flame from the background. The value t was not known and could be found iteratively.

Step 4

An initial value for t was found by using

$$t^* = \overline{S_B} + 2 \cdot std(S_B) \quad (6)$$

where S_B is a small area selection of the background of the image I . This was not a critical step, just an initial guess.

Step 5

The objects was isolated by finding the objects with an intensity above the threshold value t^* using Equation 5. The largest object was assumed to be the flame F^* . The rest was background, B^* .

Step 6

The new background B^* was used to find a new threshold value using

$$t^* = \overline{B^*} + 3 \cdot std(B^*). \quad (7)$$

Then the routine was repeated from Step 5 until the change in t^* was small. The final value of t^* was the threshold value t , separating the flame and background.

Step 7

The properties for the flame was collected and stored as a numerical value. The same thing was done to all the imaged of the movies providing the variation by time.

Figure 10 show the average flame height of three experiments with all three colors used to determine the flame height.

5 Discussion

In this work, the main target was to find a method to determine the height of a hydrogen jet flame using imaging techniques. The height of the jet flame was considered to represent the size of the hydrogen flame.

Two separate image processing techniques was considered, one based on Wiens distribution and one on intensity.

The technique based on Wiens distribution did not give any representable result due to low radiation from the flame and the high level of noise in the background.

The technique based an intensity was used and was compared to visual considerations of the flame.

6 Conclusion

An image processing technique was developed to determine the flame height of a hydrogen jet flame. The technique was based on the flame intensity and gave good results compared to visual considerations.

References

- W. Li, C. Lou, Y. Sun, H. Zhou. Estimation of radiative properties and temperature distributions in coal-fired boiler furnaces by a portable image processing system, *Exp. Therm. Fluid Sci.* 35(2), 416–421, 2011.
- T. Mogi, H. Nishida, S. Horiguchi, Flame Characteristics of High-pressure Hydrogen Gas Jet, *Proceedings of the HySafe International Conference on Hydrogen Safety*, Pisa, Italy, 8-10 Sept 2005.
- T. Trindade, A. Ferreira, E. Fernandes. Characterization of Combustion Chemiluminescence: An Image Processing Approach, *Proc. Tec.*, 17, 194-201, 2014.
- W. Yan, S. Zheng, H. Zhou, Experiments investigation on 2D distribution of soot temperature and volume fraction by image processing of visible radiation, *Applied Thermal Engineering*, Volume 124, Pages 1014-1022, 2017.
- Y. Zhang, S. Hui, Y. Zhang. The Research of Flame Combustion Diagnosis System Based on Digital Image Processing, *CSEE* 2011, pp. 225 – 230, 2011.

OPEN ACTIVE CONTOUR MODEL FOR FRONT TRACKING OF DETONATION WAVES

Samee Maharjan¹ Andre Vagner Gaathaug¹ Ola Marius Lysaker¹

¹Department of process, energy and environmental technology, University College of Southeast Norway, Norway.

samee.maharjan@usn.no

Abstract

This paper presents an image processing framework for tracking the front of the detonation wave from a sequence of images. The images are captured by high speed camera during a laboratory gas explosion experiment. By tracking the fronts in two or three consecutive frames, it is possible to calculate the thermodynamic properties like velocity and pressure along the entire wave front. Alternatively, these calculations are limited to measurements recorded by sensors at some fixed, locations. An active contour model having Gradient Vector Flow (GVF) as an external force field is used to track the wave front in each image. The structure and the properties of detonations in combustion physics has been the point of interest since early 80's. In the present paper, detonation is studied in the stratified layer of combustible gas above a non-reacting layer of air. The recorded images are digitally processed, and the local velocities are calculated based on the tracked fronts. The calculated velocities are then used to estimate the pressure ahead of the wave front with the help of the normal shock relations. The estimated pressure is compared with the measured values from pressure transducers mounted on the top and bottom of the experiment tube.

Keywords: Open contour, Front Tracking, Detonation

1 Introduction

Active contours, popularly known as snakes, have been an essential part in image processing and computer vision applications. Snakes are mainly used for edge detection and boundary contouring in the field of image segmentation. A snake is a moving curve within an image, which eventually lie itself around the surface/edge of the desired object. The snake moves under the influence of internal forces within the curve itself and the external force calculated from the image data. It was first developed by Kass et al. in 1988 (Kass et al., 1988). Many developments and improvements have been purposed thereafter, for example the Chan-Vese (CV) model (Chan and L.Vese, 2001) that detects the boundary of an object using the Mumford-Shah functional (Mumford and Shah, 1989), the level set method (Osher and Sethian, 1988) to name a few. The application of active contours are seen mainly in the field of medical research see, (Phama and Tranc., 2015; Yan

et al., 2014) and the references therein. For the last decade, active contour models have been an active research field. However most applications are based on closed contours. But for some application like front tracking, where the edge/boundary expands from top to bottom of the image an open snake is more efficient. This study will show the development of an open contour model and its application in the field of physical science of detonations.

Detonations are among the worst consequences of accidents related to gas handling and explosion in which a generated wave can exert pressure around 40 bar and velocity of more than 2000 *m/s*. It is relevant for many combustible gases, while mostly considered for the more reactive gases such as propane, ethylene, hydrogen and acetylene (Law, 2010). The detonation study of this work regards the detonations in a stratified layer of hydrogen gas above a non-reacting layer of air. The formation of a high-pressure Mach stem at the lower wall (see Figure 4) is of particular interest in the field of Combustion.

The paper is organized as follows: In Section 2, there is a short description of the experimental setup that was used for the experiment and image recording. In Section 3, a general snake model is described which is followed by Section 4, where the numerical implementation of an open snake is shown. The front tracking and velocity calculation is put together in Section 5. Finally, the results and the conclusions of the study is presented in Section 6.

2 Experimental Setup

Figure 1 illustrates the experimental setup for conducting the gas explosion experiments. The setup is made of a 3 *m* long channel with transparent polycarbonate walls. One end is closed and the other is open to the atmosphere, and an adjustable baffle type obstacle is located at 1 *m* from the closed end. The channel was filled with hydrogen and air and then ignited from the closed end such that the wave propagated towards the open end. Kistler 603b type pressure transducers were used to record the pressure at various locations along the top and the bottom wall of the tube. A high speed camera recorded the wave propagation behind the obstacle at 500 *KHz*. A schlieren imaging method was used to record the propagation at 23 *cm* diameter window expanding from a 1.2 *m* to 1.4 *m* behind the obstacle. The schlieren system is a double mirror system which is based on the fact that light rays

bends whenever there is a change in the refractive index of the medium in which the light passed (Settles, 2001). All experiments are done with premixed hydrogen and air at ambient temperature and pressure. Detail description of the setup can be found in (Gaathaug et al., 2010).

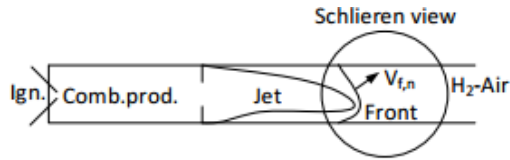


Figure 1. Experimental setup for premixed hydrogen and air combustion in a long tube.

Figure 2(a) shows the portion of captured high speed frame sequence during an experiment and Figure 2(b) shows the schlieren images captured at the highlighted rectangle portion in Figure 2(a). An overview of the over-

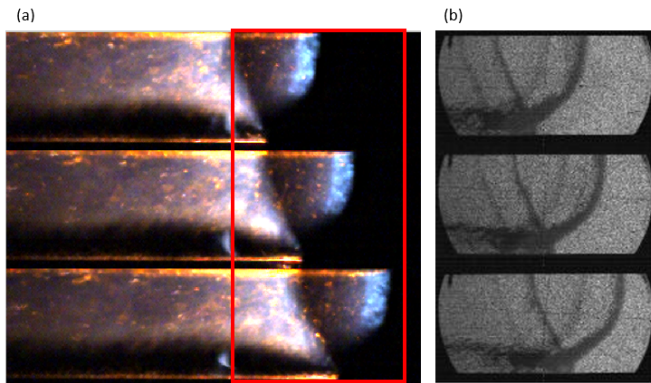


Figure 2. (a) High speed images showing a detonation wave in an experiment tube. (b) The schlieren images captured within the red rectangle in (a).

all designed framework for tracking the fronts from the image is depicted in the flowchart shown in Figure 3.

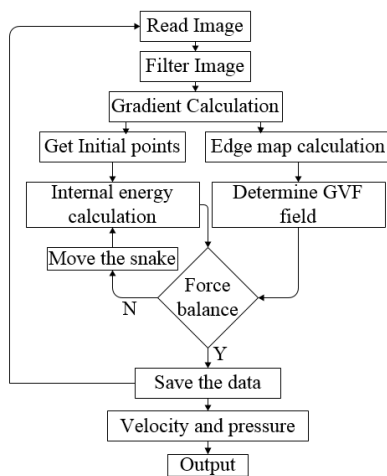


Figure 3. Flow chart showing the designed framework.

3 Active Contour Model

A basic snake defined in (Kass et al., 1988) is a parametric curve formed within an image. The snake is initialized manually by a set of x - y points around the object of interest and simultaneously interpolates between the points. By representing the position s of the snake parametrically as $V(s) = (x(s), y(s))$ in x - y coordinate system, its energy function is defined as in (1). The energy is calculated for each point along the snake and the snake will move in the direction where there is minimum energy compare to the previous position. The snake will be stationary once the energy is balanced in all directions.

$$E_{snake} = \int_s E_{int}(V(s)) + E_{ext}(V(s)) ds. \quad (1)$$

The first term in (1), E_{int} is an internal energy which can be defined as

$$E_{int} = 1/2[\alpha(s)|V'(s)|^2 + \beta(s)|V''(s)|^2]. \quad (2)$$

Here $\alpha(s)$ and $\beta(s)$ are positive weighting parameters for controlling the snake's tension and rigidity respectively. $V'(s)$ and $V''(s)$ are the first and the second derivative of $V(s)$ with respect to s . The second term in (1), E_{ext} is the external energy function which is calculated from the image such that it takes minimum values at the point of interest like edges and boundaries. For example, for a gray scale image $Im(x, y)$, the external energy can be calculated as

$$E_{ext} = -|\nabla Im(x, y)|^2, \quad (3)$$

where ∇ is the gradient operator. A snake that minimizes E_{snake} must also satisfy the Euler equation

$$\alpha V''(s) - \beta V''''(s) - \nabla E_{ext} = 0, \quad (4)$$

which can be viewed as force balance between the internal and the external forces. Both $\alpha(s)$ and $\beta(s)$ are taken as constant for the entire framework. Mathematically,

$$F_{int} + F_{ext} = 0. \quad (5)$$

The internal force term $F_{int} = \alpha V''(s) - \beta V''''(s)$ prevents the snake from stretching and bending whereas the external force term $F_{ext} = -\nabla E_{ext}$ attracts the snake towards the desired location (Xu and Prince, 1997). To solve (4), $V(s)$ is taken also as a function of time t such that $V(s)$ moves with time step t i.e. $V(s, t)$. The external energy E_{ext} for the image does not change with time.

$$\frac{\partial V(s, t)}{\partial t} = \alpha V''(s, t) - \beta V''''(s, t) - \nabla E_{ext}. \quad (6)$$

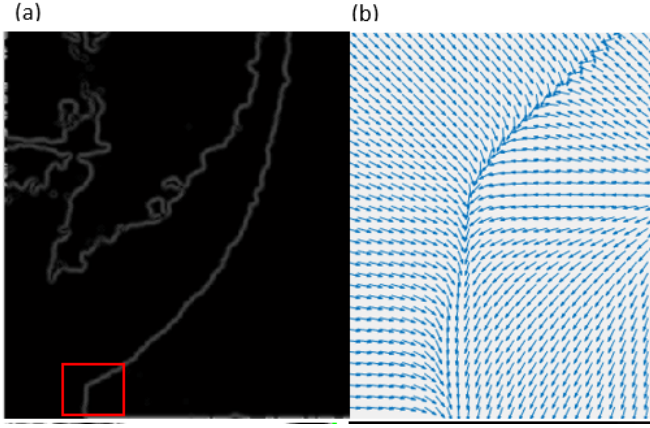


Figure 4. (a) Edge map of the image, Mach stem area is highlighted with red square. (b) External force field around the Mach stem.

4 Numerical Implementation

The numerical solution of (6) can be found when $\frac{\partial V(s,t)}{\partial t}$ tends to zero and (6) becomes,

$$\alpha V''(s,t) - \beta V''''(s,t) - \nabla E_{ext} = 0. \quad (7)$$

The solution for (7) can be obtained by discretizing the continuous snake $V(s,t)$ as in (8). The details can be found in (Kass et al., 1988).

$$\begin{aligned} \alpha[V_i - V_{(i-1)}] - \alpha[V_{(i+1)} - V_i] + \beta[V_{(i-2)} - 2V_{(i-1)} + V_i] \\ - 2\beta[V_{(i-1)} - 2V_i + V_{(i+1)}] + \beta[V_i - 2V_{(i+1)} + V_{(i+2)}] \\ + (f_x(i), f_y(i)) = 0. \end{aligned} \quad (8)$$

Here $V_i = (x_i, y_i)$ is the i^{th} point of the contour/snake s and $(f_x(i), f_y(i))$ which are equal to $(-\partial E_{ext}/\partial x_i, -\partial E_{ext}/\partial y_i)$ are the external force at point i .

4.1 Internal energy

The overall internal energy at each point can now be described in a matrix form as

$$AV + (f_x(i), f_y(i)) = 0. \quad (9)$$

Here A is pentadiagonal matrix ,

$$A = \begin{bmatrix} \beta & 0 & 0 & 0 & 0 \\ 0 & \alpha - 3\beta & 0 & 0 & 0 \\ 0 & 0 & 2\alpha + 6\beta & 0 & 0 \\ 0 & 0 & 0 & -\alpha - 4\beta & 0 \\ 0 & 0 & 0 & 0 & \beta \end{bmatrix}$$

and V is a vector of the 5 consecutive points, $V = [V_{i-2} \ V_{i-1} \ V_i \ V_{i+1} \ V_{i+2}]^T$.

If n is the total number of points in each contour, then for closed contour $V_1 = V_n$, the internal energy can be estimated using (8) for all points along the contour. However, for open contours the end points should remain at the top and bottom boundary, hence $V_{(i-1)}$ and $V_{(i-2)}$ will not exist for the first two points whereas $V_{(i+1)}$ and $V_{(i+2)}$ for the last two points. The matlab program is designed in such a way that these points stays at the boundary and therefore only move in x -direction with respect to its own external energy and its own previous position. Using Euler method with time step t for (8), the contour point V_i^t at time t can be related to its previous point V_i^{t-1} as,

$$AV_i^t + (f_x(i), f_y(i))V_i^{t-1} = -\gamma(V_i^t - V_i^{t-1}) \quad (10)$$

where γ is a step size. Solving (10) by matrix inversion and separating V_i into x_i and y_i ,

$$x_i^t = (A + \gamma I)^{-1}[\gamma x_i^{(t-1)} - f_x(x_i^{(t-1)}, y_i^{(t-1)})] \quad (11)$$

$$y_i^t = (A + \gamma I)^{-1}[\gamma y_i^{(t-1)} - f_y(x_i^{(t-1)}, y_i^{(t-1)})], \quad (12)$$

where I is an identity matrix.

4.2 External energy

One of the main drawback of the snake models is that the calculated external energy were not sufficient for attracting the snake from long distance. The simple external energy calculated by using (3) works nicely when the initial snake is near to the object but fails to attract the snake when it is placed far away. To overcome this drawback, the gradient vector flow (GVF) proposed in (Xu and Prince, 1997) is used for the external force field. For estimating GVF, first the edge map $E_{edge}(x, y)$ is formed in such a way that it has a larger value at the edges and at the boundaries, compared to homogeneous region. Later, the estimated edge map is used to estimate the over all external force field. For this study, the edge map is taken as the gradient magnitude of the image,

$$E_{edge}(x, y) = \sqrt{(g_x^2 + g_y^2)}, \quad [g_x, g_y] = \nabla Im(x, y).$$

and the result is shown in Figure 4(a). The Mach stem is marked by a red rectangle in this figure. Following the steps described (Xu and Prince, 1997), the final external external force $(f_x(i), f_y(i))$ for an image is calculated by iterating the equations (13) and (14) until it converges.

$$f_x(i) = \mu \nabla^2 f_x(i) - |\nabla E_{edge}(x)|^2 (f_x(i) - \nabla E_{edge}(x)) \quad (13)$$

$$f_y(i) = \mu \nabla^2 f_y(i) - |\nabla E_{edge}(y)|^2 (f_y(i) - \nabla E_{edge}(y)) \quad (14)$$

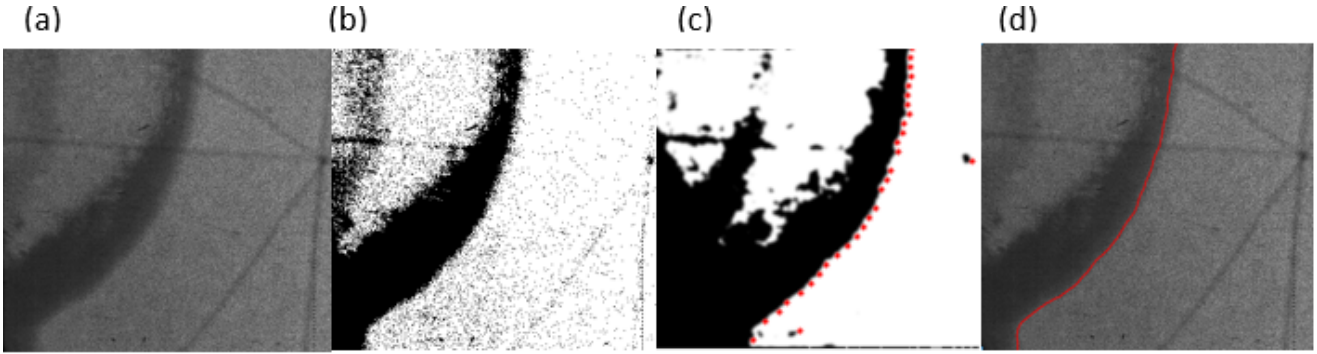


Figure 5. (a) Original raw image (b) Binary image (c) Filtered binary image with initial points for the snake. (d) Final contour along the wave front.

Here ∇^2 is the laplacian operator and μ is a regularization parameter governing the trade off between the first term and second term. Generally, μ is taken as a constant which is set according to the noise present in the image. For a sequence of images where the noise varies with time, μ along with $|\nabla E_{edge}(x,y)|^2$ can be taken as spatially varying weighting factor as presented in (Xu and Prince, 1998). The initial value for $(f_x(i), f_y(i))$ is taken as $\nabla E_{edge}(x,y)$. The computed GVF field points towards the edges and varies smoothly over homogeneous regions, see Figure 4(b).

5 Front tracking and velocity calculation

It is necessary to reduce the background noise presents in the images before actual tracking of the front. For this purpose, the pre-processing of the image is done by first changing each image into binary form using Otsu method (Otsu, 1976), followed by filtering using median filter. Figure 5(a) shows the raw image from the experiment and in Figure 5(b) the binary version of the same image is visualized. Though the GVF force field has advantages compared to the external forces used in (Kass et al., 1988), the formation of the initial points for the snake highly influence the overall performance of the framework. One possible way to initialize the snake automatically to a location close to the object, is to use the information of the gradient values in the image. For this task, a priori information of the direction of the wave propagation is used. By starting a search from the opposite direction of the wave propagation for predefined set of rows (every 20^{th}), an initial point is chosen to be the first point where the gradient value exceeds a given threshold value, see Figure 5(c). The snake is then initialized by interpolating these initial points such that there exist the snake point $V(s)$ for each unique row value of the image. For example, if size of an image Im is $[300 \times 800]$ then the size of the snake is $[300 \times 1]$. By implementing, the method defined in Section 4, the final contour is obtained as shown in Figure 5(d).

Suppose $V^K(s)$ is the final snake (tracked front) in K^{th} image of the sequence. For calculation of a normal ve-

locity at point $V_i = (x_i, y_i)$ of the front $V^K(s)$, a local normal vector \vec{n} is calculated by forming a local polynomial function around the point V_i (5 points above and 5 points below are used). The normal vector \vec{n} will forms a triangle between the fronts with an angle θ at point V_i . The normal displacement is now estimated by using the final snake of the $V^{K+1}(s)$ of $(K+1)^{th}$ image of the sequence as shown in Figure 6. By using the value of $V^{K+1}(s)$ for the same row y_i the displacement d_m can be calculated and an angle θ can be estimated by calculating the slope of the normal vector \vec{n} .

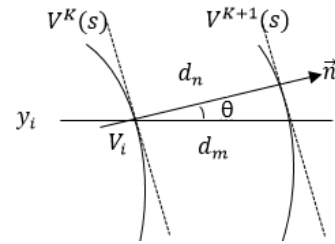


Figure 6. Method for estimating normal front velocity.

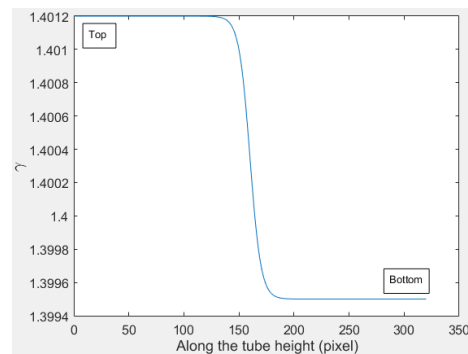


Figure 7. Spatially varying γ for top and bottom of the tube.

By assuming the normal vector \vec{n} is locally normal to both fronts at K and $K+1$, a normal displacement d_n is estimated as $d_n = d_m * \cos\theta$.

The normal displacement d_n is then changed to standard unit of meter with system configuration of $(1px = 0.0002778 m)$ and the normal velocity V_f is calculated at

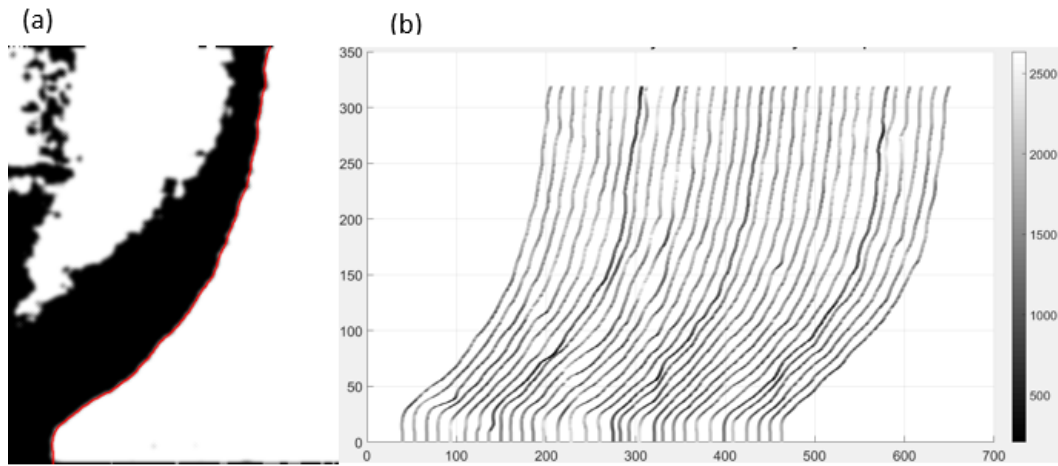


Figure 8. (a) A final contour in filtered binary image. (b) The front contours with local velocity (m/s) given by the color according to the colormap.

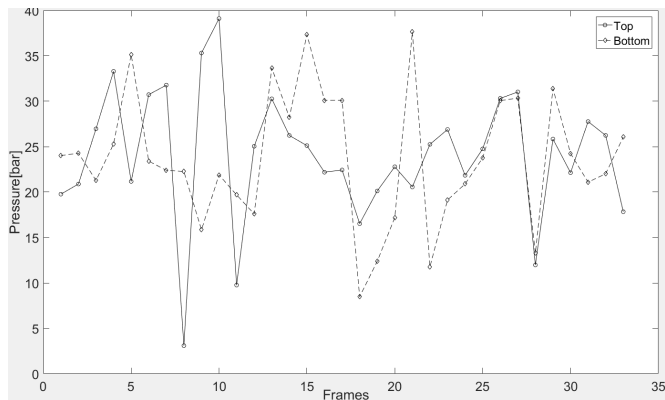


Figure 9. Pressure estimated for top and bottom of each front.

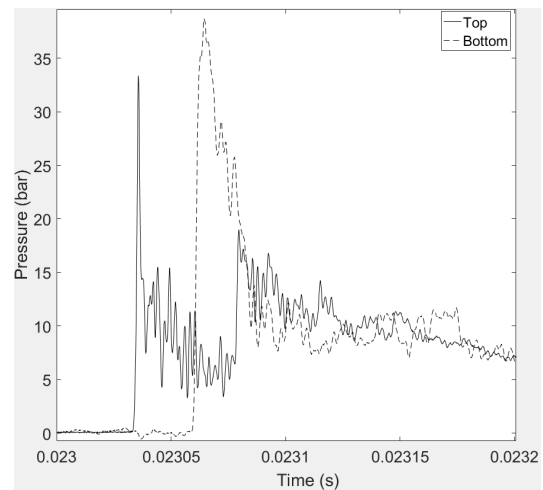


Figure 10. Pressure records from the experiment by the pressure transducers.

frequency of 500 kHz. By using the calculated velocity to estimate the Mach number M , the pressure behind the front is estimated by normal shock relation shown in (15) (Law, 2010).

$$\frac{P_1}{P_0} = \frac{2\gamma M^2 - (\gamma - 1)}{\gamma + 1}. \quad (15)$$

Here, P_1 is the pressure behind of the wave front and P_0 is the pressure ahead the wave front. The pressure ahead of the wave front is assumed to be 1 bar in this case. The Mach number M is defined as,

$$M = \frac{V_f}{c}, \quad (16)$$

$c = \sqrt{\gamma RT/M}$ is the speed of sound in medium (H_2) at temperature T . R , M and γ are respectively gas constant, Molecular mass and specific heat ratio of H_2 . As the gas is different in top and bottom of the tube, γ is taken as spatially varying along the tube from 1.3995 to 1.4012 as shown in Figure 7 (γ for H_2 is 1.4). The speed of sound for hydrogen is calculated and considering temperature T ahead the wave front is uniform at 25° C. The estimated M is then used for finding pressure P_1 from (15).

6 Results and Conclusion

For clarity, the final contour along the detonation wave front is plotted in filtered image shown in Figure 8(a). The calculated velocities along all the tracked wave fronts from a sequence is plotted in Figure 8(b). As expected the velocity in the upper layer that is filled with combustible gas is relatively higher than the velocity in the bottom layer. Due to the generation of Mach stem along the lower boundary of the tube, velocity of the front around the lower boundary is noticeably high. The average pressure estimated at top and bottom of each front is plotted in Figure 9 (top and bottom 10 points are used). The reading from pressure transducers mounted on the top and the bottom of the tube at fixed location is shown in Figure 10. Due to the difference between the location of pressure transducers and the moving wave front, direct comparison cannot be justified. Nevertheless, it can be seen that maximum and minimum pressure on both the figure are almost in same range.

The designed image processing framework was also used to calculate the velocity for a benchmark experiment. The results of the experiment shows an average detonation velocity of 1967 m/s which is 9 m/s lower than the theoretical value (Gaathaug et al., 2016). Thus, it can be assumed that the framework gained detailed information of the detonation front within expected precision. Further work need to be done considering assumptions made during pressure estimation using a normal shock relation.

Zhou Yan, Ren Shia Wei, Wei Chenc, Yong lin Chenc, Ying Lid, Li-Wen Tand, and Dai-Qiang Chenb. Active contours driven by localizing region and edge-based intensity fitting energy with application to segmentation of the left ventricle in cardiac ct images. *Neurocomputing*, 156:199–210, 2014.

References

- Tony F. Chan and L.Vese. Active contours without edges. *Image Processing, IEEE Transactions.*, 10:266–277, 2001.
- Andre Vagner Gaathaug, Dag Bjerketvedt, and Knut Vaagsaether. Experiments with flame propagation in a channel with a single obstacle and premixed stoichiometric h₂-air. *Combustion Science and Technology.*, 182:1693–1706, 2010.
- Andre Vagner Gaathaug, Samee Maharjan, Ola Marius Lysaker, Knut Vaagsaether, and Dag Bjerketvedt. Velocity and pressure along detonation fronts - image processing of experimental results. *Proc. of the Eighth International Seminar on Fire and Explosion Hazards (ISFEH8)*, 2016.
- Michael Kass, Andrew Witkin, and Demetri Terzopoulos. Snakes: Active contour models. *International Journal of Computer Vision*, 1:321–331, 1988.
- Chung K. Law. *Combustion Physics*. Cambridge University Press, New York, USA, 2010.
- David Mumford and Jayant Shah. Optimal approximations by piecewise smooth functions and associated variational problems. *Communications on Pure and Applied Mathematics.*, 42:577–685, 1989.
- Stanley Osher and James A. Sethian. Fronts propagating with curvature dependent speed: Algorithms based on hamilton-jacobi formulations. *Journal of Computational Physics.*, 79:12–49, 1988.
- Nobuyuki Otsu. A threshold selection method from gray-level histograms. *IEEE Transactions on Systems, Man, and Cybernetics.*, 9:62–66, 1976.
- Van-Truong Phama and Thi-Thao Tranc. Active contour model and nonlinear shape priors with application to left ventricle segmentation in cardiac mr images. *Optik - International Journal for Light and Electron Optics*, 127:991–1002, 2015.
- Gary S. Settles. *Schlieren and Shadowgraph Techniques: Visualizing Phenomena in Transparent Media*. Springer-Verlag Berlin Heidelberg New York, 2001. ISBN 0.
- Chenyang Xu and Jerry L. Prince. Gradient vector flow: A new external force for snakes. *IEEE Proc. Conf. on Computer vision and Pattern Recognition*, pages 66–71, 1997.
- Chenyang Xu and Jerry L. Prince. Generalized gradient vector flow external forces for active contours. *Signal Processing.*, 71:131–139, 1998.

Modeling and Simulation of Light Oil Production using Inflow Control Devices

Ramesh Timsina¹ Nora C. I Furuvik² Britt M. E. Moldestad³

¹Faculty of Technology, University college of Southeast Norway, Norway, timsinarames@gmail.com

²Faculty of Technology, University college of Southeast Norway, Norway, nora.c.i.furuvik@usn.com

³Faculty of Technology, University college of Southeast Norway, Norway, britt.moldestad@usn.com

Abstract

Light crude oil production is the most economical and is currently serving as benchmark together with medium crude oil. The most of the conventional oil fields in the worlds are either light or medium crude oil. Conventional inflow control devices (ICDs) are designed to delay water breakthrough but do not have the capability to control the water inflow after breakthrough. Autonomous inflow control devices (AICDs) are developed to choke the inflow of water after breakthrough has occurred.

Simulations is done by developing integrated transient wellbore-reservoir model in OLGA-Rocx. The specifications of the reservoir are specified in Rocx and the wellbore model is developed from the different modules available in OLGA. Simulations include fractured reservoir, heterogeneous reservoir and the homogeneous reservoir. The results show that autonomous inflow controllers have a higher potential to limit the water influx compared to the conventional ICDs.

The benefit of using AICDs was less significant in the homogenous reservoir than heterogeneous reservoir because of low frictional pressure drop along the well.

The functionality of the different inflow controllers for light oil reservoir is studied and results are compared.

Keywords: light oil production, inflow control devices, Oil and gas, water breakthrough, OLGA, Rocx, near well simulation

1 Introduction

One of the major challenges that the oil industry faces today is early water breakthrough and high production of water from mature oil fields. Early water breakthrough can occur due to high frictional pressure drop in the well or due to high permeability zones or fractures in the reservoirs. This causes reduction of the oil production. In fact, some of the wells are shut down because of excessive water production.

There are different types of inflow control devices (ICDs) developed for delaying breakthrough of water and gas. They are designed to improve completion

performance, the overall efficiency and the lifetime of the wells.

Conventional ICDs are designed to delay water or gas breakthrough but do not have the capability to control the water inflow after breakthrough. So, there is no solution other than to choke the entire flow from the system after a certain time. Hence, there has been various development in this inflow control technologies with the autonomous operation. Autonomous inflow control device (AICD) chokes the fluid flow into the wellbore from the high permeable zone after the water breakthrough, allowing normal oil production from the other zones. This will enhance the well performance and increases the recovery of oil from existing reservoirs.

The oil reservoirs will show different behaviors at different conditions and this will affect the well performance. The objective of this work is to perform near well simulations of oil production from light oil reservoir using different types of ICDs with water drive. The studied ICDs include conventional ICDs and autonomous inflow controllers.

2 Background

Presently, the conventional oil, which is referred to as light or medium oil is the benchmark of the crude oil. The crude like West Texas Intermediate (WTI) (API = 39.6), Brent crude (API = 38.06) and Dubai crude (API = 31) serves as the benchmark crude across the globe. The light crude oil has low viscosity and flows freely at room temperature. It has low specific gravity because of low density. Light crude oils also have low wax content.

Heavy oils have low mobility due to its high viscosity. This makes transportation of heavy oils difficult. Extra costs will be added to make the heavy oil viable (Alomair et al, 2013). It is also important to optimize the oil production and recovery from light oil reservoirs.

3 Inflow control technologies

An ICD is a well completion device used to choke the fluid flow entering the base pipe from the annulus. It is a passive inflow control device, i.e. it does not have any

active parts, which can be controlled or modified to regulate the flow through it. ICD adds up an additional pressure drop across the completion and restricts the inflow along the well. Generally, all the ICDs are self-regulating in nature, as the settings cannot be changed after installation (Torbergsen, 2010).

The higher flow rates from the high permeability zones cause early water breakthrough. The early water breakthrough can be delayed by having a higher flow restriction in high permeable zones. Further, ICD can produce at high rates from zones that have poorer production rate. This will increase the production and recovery (Fernandes et. al, 2009).

The common types of ICDs present in the industry use either friction or restriction to create a pressure drop across it. The most commonly used ICDs are presented in this section.

3.1 Channel type ICD

Figure 1 shows the schematics of the channel type ICD that uses surface friction to develop the desired pressure drop. The fluid passes through a multi-layered screen into the annulus and enters the wellbore through the channels. The fluid is forced to change its flow direction several times, causing a pressure drop across it. The chances of erosion and plugging are low because of low fluid velocity. Channel ICDs are dependent on fluid viscosity. So, a large difference in oil and water viscosity after water breakthrough can cause non-uniform inflow to the wellbore (Fernandes et. al, 2009).

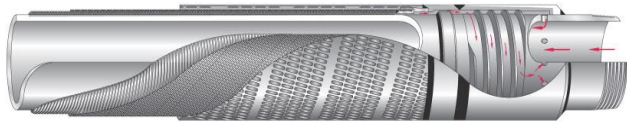


Figure 1. Channel ICD schematics (Birchenko et al, 2010)

3.2 Orifice/nozzle type ICD

Figure 2 shows the schematics of the orifice type of ICD that uses restriction of fluid flow to develop the desired pressure drop. Orifice ICDs are simple in design where the fluid passes through small diameter nozzles or orifices that create resistance. The pressure drop across the orifice ICD is instantaneous and is highly dependent on the density and velocity of the fluid. An orifice ICD is likely to have high sand erosion rate.

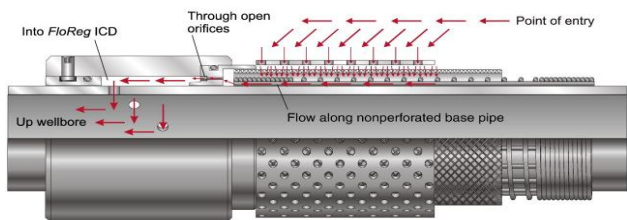


Figure 2. Orifice ICD schematics (Birchenko et al, 2010)

The pressure drop across an orifice can be expressed by:

$$\nabla P = C \cdot \frac{1}{2} \cdot \rho \cdot v^2 \quad (1)$$

Where, C is the geometrical constant, ρ is the fluid density and v is the fluid velocity. This type of ICD is not dependent on fluid viscosity, thus ideal for applications where the viscosity sensitivity is low (Fernandes et. al, 2009).

According to Fernandes et al., an ICD can work effectively when the frictional pressure drop across the wellbore is relatively high compared to the drawdown pressure. Fractured reservoir with long wells also favors the ICDs installations (Fernandes et. al, 2009).

ICD is a passive device and cannot choke for water or gas breakthrough occurs. The oil industry has therefore focused on developing new technology for choking of such unwanted fluids. Inflow control valves (ICVs) are the example of this development. ICVs are active sliding sleeve valves, operated remotely by means of a controlling system. The electrical connection to the control room favors only for short wells. But the unpredicted reservoir behavior favors ICVs for higher recovery compared to ICDs. ICVs have flexible operation with the change in the operating conditions. ICVs are more expensive than ICDs as they have moving parts. ICDs are simple and have low installation risks as they do not have any moving parts, (Al-Khelaiwi et al, 2010).

There has been new development on these ICVs to adjust the inflow autonomously. Autonomous technology can adjust their performance based on the wellbore dynamics. Autonomous inflow control device (AICD) are being developed by companies like Halliburton, Statoil and others. The autonomous inflow control device developed by Statoil is called Rate Controlled Production (RCP) devices. RCP is capable of that choking for low viscous fluids, and is allowing high viscous fluid to flow through it without any restriction (Halvorsen et al, 2012). The AICD developed by Inflow control AS is called Autonomous inflow control valve (AICV). AICV is capable to restrict the influx of unwanted fluids. AICV can shut off unwanted fluids autonomously when there is viscosity change in the fluids.

4 Development of OLGA Rocx model

A simulation model was developed using OLGA-Rocx. The methodology adopted to build this dynamic reservoir-wellbore model is described along with a selection of different input parameters for the model.

4.1 Reservoir (Rocx) model

The reservoir dimensions are listed in Table 1. The length is divided into 10 sections (99.2 m) with one AICD in each section. This is the equivalent AICD, representing 8 normal AICDs (12.4×8=99.2m). Generally, the normal AICDs are installed at a length of 12.4m of well.

Table 1. Dimension of the reservoir

Reservoir	Span (m)
Length (x)	992
Width (y)	80
Height (z)	20

The horizontal well is located along the x-direction. The well location in y-z plane is shown in Figure 3.

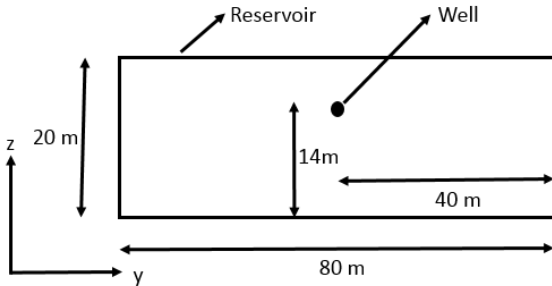


Figure 3. Location of the well in yz plane

The computational simulation should be accurate and time efficient. Finer grids and small-time steps give more accurate results but require a significant amount of time as well as computational resources. Finer mesh towards the well in y-direction was chosen with 29 elements. The simulation was done for 10 equivalents AICDs, hence the length was divided into 10 elements of constant size and the height was divided into 10 elements of constant size. The developed grid in three-dimension is shown in Figure 4.

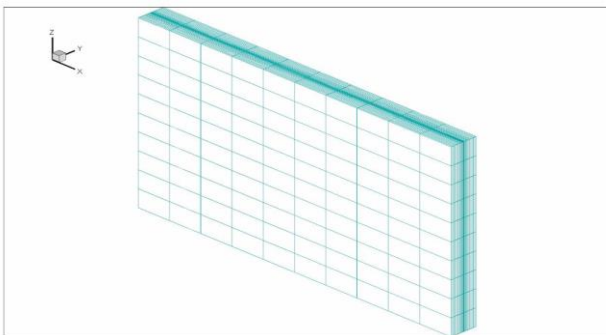


Figure 4. 3-D view of the grid

4.2 Fluid Properties

It is essential to know the Pressure Volume Temperature (PVT) relation of the fluids that is being used in simulations. The crude oils have a wide range of physical and chemical properties. One of the models used to estimate the PVT relations is the black oil fluid model. The black oil fluid model is a model that assumes that the oil components will always be in the liquid phase and does not evaporate at any conditions. The reservoir temperature is significantly lower than critical temperature and reservoir pressure is more than cricondenbar.

The black oil model was selected over the PVT table model in Rocx. The basic properties of light oil used for the simulation are presented in Table 2. These values were considered at measured reservoir temperature of 100°C and pressure of 130 bar.

Table 2. Oil properties used for simulations

Oil viscosity (cP)	3
Oil specific gravity	0.85
Gas specific gravity	0.64
GOR (Sm ³ /Sm ³)	150

This simulation was done with the bottom water drive. So, for simulation with water drive, two feed streams were defined for oil and water. These feed streams are presented in Table 3.

Table 3. Feed streams

Stream	Fraction type	Fraction	Watercut
Oil	GOR	150	0.0001
Water	GLR	0.0001	0.99

4.3 Reservoir properties

The porosity of the reservoir was taken as 0.3 and is constant throughout the reservoir. The permeability in each direction was defined by giving a value for each block in the reservoir in the respective direction. The simulated reservoir model based on the permeability profile were as follows:

- Fractured reservoir with a very high permeable zone
- Heterogenous reservoir with one relatively high permeable zone and with one relatively low permeable zone
- Homogenous reservoir

The horizontal permeability was taken as 10 times higher than the vertical permeability in each block of the reservoir. The vertical permeability profiles of these reservoirs are shown in Figure 5.

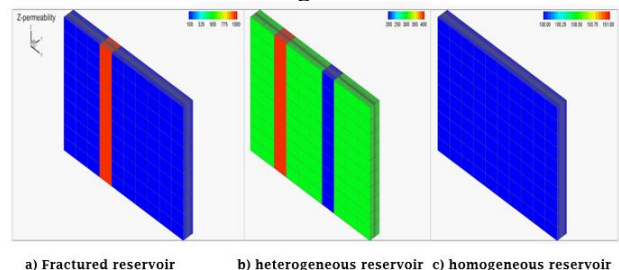


Figure 5. Vertical permeability profile

4.4 Simulation

Initially, the black oil feed was defined as 100% oil and the reservoir were fully saturated with oil. The reservoir

temperature is 100°C and the reservoir pressure is 130 bar.

The boundary conditions are defined according to the well location in the reservoir. The feed is defined as the oil feed flowing in x-direction. The bottom water drive is defined accordingly and the main direction of flow is set in z-direction. The water drive temperature and pressure were also set to 100°C and 130 bar and the main direction of flow in the reservoir is set along z-direction.

The simulation was performed using a linear iterative solver named ‘Linsolver’. The minimum time step was set to 100s and the maximum time step to 3600s, with an initial time step of 0.01s.

4.5 Development of wellbore model

Two pipes are taken to represent the well (Flowpath) and the annulus (Pipeline) of the flow system. The length of the well is 992m and diameter is 0.1m. The surface roughness was set to 5×10^{-5} m and is divided into ten zones. Each zone is further divided into two sections. The details of two sections are presented in Figure 6.

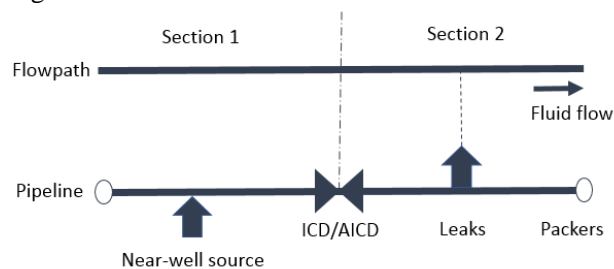


Figure 6. Representation of single zone of well

The inflow from the reservoir source (Near-well source) enters the pipeline from section 1. Then this fluid passes through the inflow controllers into section 2. Now, this fluid enters the Flowpath at section 2 from the pipeline via leaks. The different zones of annulus were separated by means of a closed valve (opening = 0) which represents a packer. This packer ensures that there is no flow between the zones in the annulus section. Finally, the fluid from each zone is collected in the well and moves towards the heel section of the wellbore. The OLGAs modules that were used to develop this model are presented in Table 4.

Table 4. Components used in OLGAs

Components	OLGA module	Description
Inflow source	Nearwell source	Coupled with reservoir model (Rocx file)
Leak	Leak	• Diameter – 35 mm, CD ¹ – 1

¹ Coefficient of Discharge

		<ul style="list-style-type: none"> • No mass transfer between the phase • Connects to the Flowpath
ICD	Valve	<ul style="list-style-type: none"> • Diameter – 20 mm, CD – 0.84 • The diameter of the valve was used to decide the required pressure drop.
AICD	Valve/PID controller	<ul style="list-style-type: none"> • Diameter – 20 mm, CD – 0.84, • The valve opening was controlled by a PID controller
Packers	Valve	<ul style="list-style-type: none"> • Diameter – 0.1 m, opening – 0 (fully closed)

The boundary conditions at the end of Flowpath (heel) is set to 120 bar and 100C.

The AICD is a valve module controlled by a PID controller module. The control variable for this PID controller was in situ water cut percentage (75%) which was transmitted to the PID controller by the transmitter module in OLGAs. The parameters of the PID controller are defined in Table 5.

Table 5. PID controller parameters

Parameter	Value
Amplification	-0.01
Bias (Initial signal)	1
Integral constant [s]	50
Maximum signal	1
Minimum opening	0.01

4.6 Simulated cases

The three-main type of reservoir mentioned in Figure 5 are simulated with different inflow control technologies. The simulated types of inflow control technologies are presented in Table 6.

Table 6. Types of simulated inflow control technologies

ICD	Wells with ICDs (Diameter – 20 mm, CD – 0.84)
AICD	Wells with AICDs (Diameter – 20 mm, CD – 0.84)
ICD _{res}	ICD with relatively high flow restriction at the high permeable zone (Diameter – 0.2mm) and normal ICDs (Diameter – 20 mm) in the rest of the zones

5 Simulation results

This chapter contains the simulation results for the different cases.

5.1 AICD and ICD performance in fractured reservoir

The accumulated oil and water are presented in Figure 7 for the cases mention in Table 6.

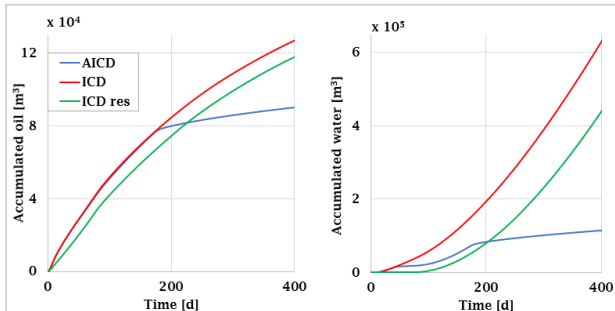


Figure 7. Accumulated liquid for fractured reservoir

The case with AICD has the highest potential to reduce the water accumulation among the considered inflow control technologies. The ICD case with restriction gives less accumulation of water compared to normal ICDs. The accumulated oil and water volume with different inflow control technologies are presented in Table 7. The results are obtained after 400 days of production.

Table 7. Accumulated liquids

Case	Accumulated oil [m³]	Accumulated water [m³]
ICD	127145	634733
AICD	89943	113654
ICDres	118123	441054

These data show that the well with non-uniform ICDs can be a good choice to reduce the accumulated water. The restriction imposed on the high permeability zones, reduces the water accumulation by 30% compared to normal ICDs. However, the autonomous device gives remarkably higher potential of reducing the water influx. The AICDs produces 82% less water compared to the normal ICDs.

The use of both AICD and the non-uniform ICD have decreased the water production as well as oil production. As both AICD and non-uniform ICD have reasonable potential to control water inflow causing a slight change in oil production, they have to be studied further depending on the types of applications.

The liquid flow rates with different inflow control technologies for the fractured reservoir are presented in Figure 8. There are significant changes in the oil and water flow rates throughout the production time. This illustrates the features of the different inflow controllers.

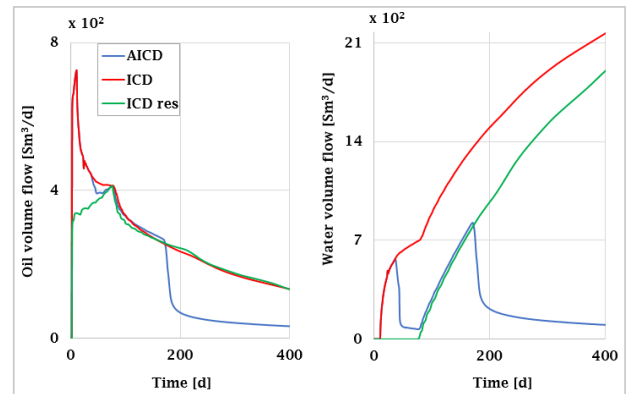


Figure 8. Liquid flow rates for fractured reservoir

According to Figure 8, initial water breakthrough occurs on day 9 of production for the cases with AICD and normal ICD. Once the water is produced, the oil volume flow rate decreased significantly.

By installing a higher restrictive ICD with higher pressure drop, in the high permeable zone, the first water breakthrough has been delayed to 76 days of operation which is the same as the second water breakthrough for the two other cases. The oil production has also been reduced due to the introduction non-uniform ICDs. Table 8 shows the accumulated oil after the first and second water breakthrough.

Table 8. Oil production at breakthroughs

Case	Accumulated oil after 1 st breakthrough [m³]	Accumulated oil after 2 nd breakthrough [m³]
ICD	6889 [9 days]	42116 [76 days]
ICDres	32979 [76 days]	-
AICD	6889 [9 days]	41005 [76 days]

The accumulated oil with AICD is slightly less than that of normal ICD at the time of the second breakthrough because of the closure of the autonomous device in the fractured zone. It can be seen that the non-uniform ICD model has the capability to delay water breakthrough by 67 days in this reservoir. This is the most positive features of this model, while its inability to restrict water influx after breakthrough is the drawback. It is challenging to find the precise location of the high permeable zone, and therefore there would be a high risk installing restrictive ICDs.

Figure 8 shows that the restrictive ICD model has been able to delay the water breakthrough significantly. However, the accumulated water goes on increasing after breakthrough occurred. This indicates that the autonomous model has large benefits compared to other models.

5.2 AICD and ICD performance in homogeneous reservoir

The liquid flow rates for the homogeneous reservoir with vertical permeability of 1000 mD are presented in Figure 9.

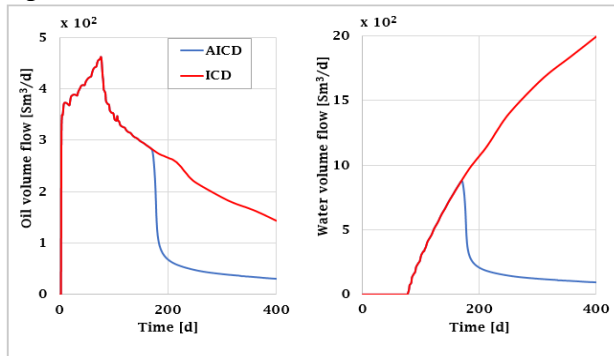


Figure 9. Liquid flow rates for homogeneous reservoir

The oil volume flow increases continuously and reaches 456 Sm³/d just before the water breakthrough. After the water breakthrough at 75 days, the oil volume flow decreases and the water volume flow increases. There has been a continuous decrease of the oil flow rate and increase of the water flow rate after breakthrough for the ICD case. The flow rates for the AICD case are heavily reduced after closing of the valves.

The frictional pressure drop along the wellbore was observed to be around 0.2 bar just before the water breakthrough. The rather low frictional pressure drop causes water breakthrough at about same time in all the zones. The use of the autonomous device is not so significant because of closure of all the AICDs within a short time interval.

Figure 10 shows the accumulated liquids for the homogeneous reservoir.

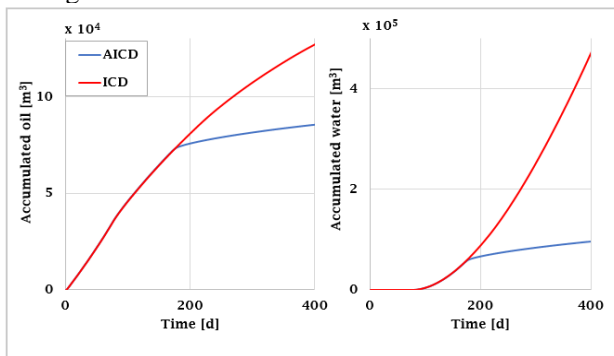


Figure 10. Accumulated liquid for homogeneous reservoir

There has been a continuous increment of the accumulated oil with ICD while it drops for the case with AICD after closing the valves. Once the water breakthrough has started, accumulated water is also increasing continuously for the ICD. The autonomous inflow controllers are able to reduce the water significantly. Although there has been a reduction in accumulated oil, the accumulated water reduces by 80% with the use of autonomous devices.

5.3 AICD and ICD performance in heterogeneous reservoir

An intermediate reservoir between the homogeneous and fractured reservoir was also simulated. It has one zone with relatively high permeability and one zone with relatively low permeability compared to the rest of the zones. The liquid flow rates at standard conditions are presented in Figure 11.

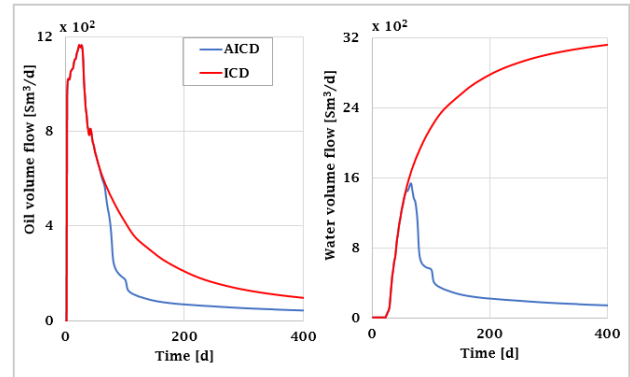


Figure 11. Liquid flow rates for heterogeneous reservoir

The plots show that the oil volume flow reaches a maximum value of 1156 Sm³/d and decreases considerably once the water breakthrough has occurred. The water breakthrough occurred on day 25 from the start of the operation. The closing of the first valve is in the high permeability zone.

There is a reduction of liquid flow rates after the autonomous devices have been shut off. The water volume flow increases continuously and reaches around 3200 Sm³/d with the use of ICD. This, in turn, gives high accumulation of water as presented in Figure 12.

Figure 12 shows the accumulation of oil and water for the heterogeneous reservoir. The accumulation of oil is reduced with the use of autonomous devices compared to that of ICDs. However, the accumulation of water decreases significantly by around 88% after 400 days of operation.

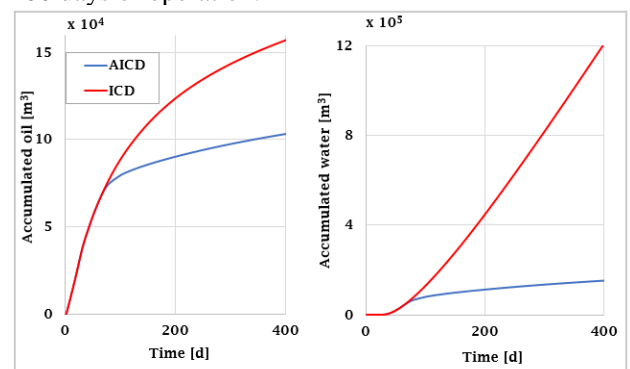


Figure 12. Accumulated liquid for heterogeneous reservoir

5.4 Effects of different model parameters

5.4.1 Oil viscosity

This simulation was performed to see the effect of changing the oil viscosity in the model. Light oils with oil viscosity of 3 cP, 1.5cP, and 0.8 cP were studied. The simulations were done with AICD for light oil in the fractured reservoir. The oil and water flow rates at standard condition are presented in Figure 13.

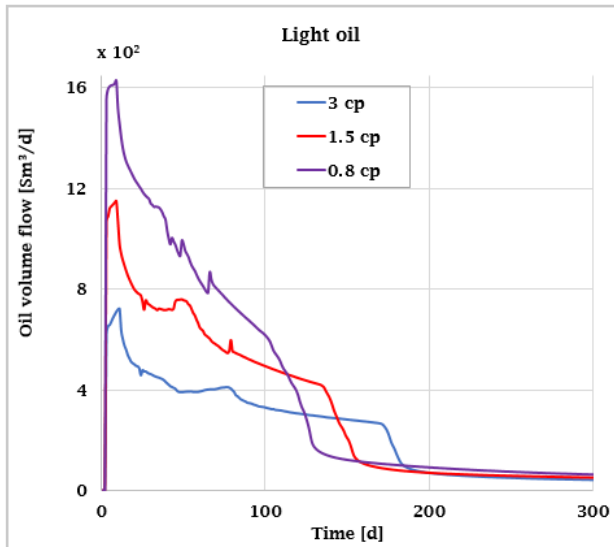


Figure 13. Oil volume flow with different oil viscosity

The graphs show that the oil volume flow increases with the decrease of oil viscosity. The water breakthrough was observed earlier for the lesser light oil. The oil volume flow for the less light oil decreases more compared to others after water breakthrough.

The mobility ratio of oil with respect to water is given by:

$$M = \frac{k_{rw}}{\mu_w} \cdot \frac{\mu_o}{k_{ro}} \quad (2)$$

This shows that, for a constant relative permeability of oil, water, and constant viscosity of water inside a reservoir, the mobility ratio is directly proportional to oil viscosity. As the oil viscosity decreases, the mobility ratio will decrease. And the expression for the definition of mobility ratio is given by:

$$M = \frac{\text{mobility of water}}{\text{mobility of oil}} \quad (3)$$

Hence, the mobility of oil increases with the reduction of the mobility ratio. This is illustrated in Figure 13 The oil volume flow after the closing of the autonomous valves is almost the same for all the cases as they all have the same minimum opening when the valve is in closed positions.

5.4.2 Mesh size

This study was done to see the effects of changing the mesh size of the simulated reservoir. It can be argued that the finer grid gives more accurate results than the coarse grid. The grid along the y-direction was already finer close to the wellbore. It is interesting to see the results with finer grids in the x-direction also. Therefore, the mesh size in the x-direction is reduced to half the original size. This simulation was done with AICD for light oil in the fractured reservoir. Figure 14 shows the liquid flow rates at standard conditions with two different mesh sizes along the flow direction.

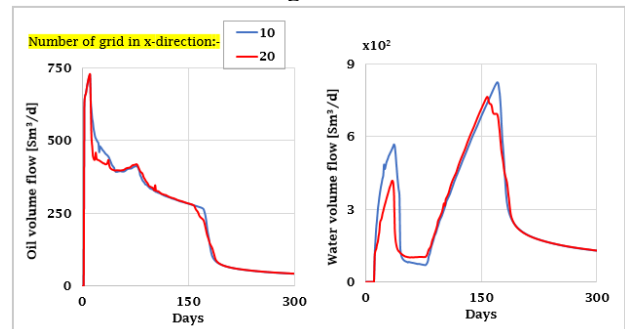


Figure 14. Oil and water flow rates for different mesh sizes

The flow rates with the increased number of grids deviate slightly from that of the normal grid. The oil volume flow is slightly different particularly during the closure of autonomous devices. The flow rates with 20 grids show closer overview of actual flow rates during this period. The water volume flow rate before the closure of the valves drop slightly from each other. However, the flow rates after the closure of AICD is the same for both the cases. It can be argued that the overall flow rate is insignificantly sensitive to the mesh sizes which is the good features of this model.

6 Conclusion

Near-well simulations using the OLGA-Rocx simulation software are performed during this study. Early water breakthrough occurred due to the fractures or the heterogeneity in the reservoirs. The water breakthrough from the fractured, heterogeneous and homogenous light oil reservoirs is observed after 9, 25 and 75 days of production respectively.

The non-uniform ICDs has the ability to delay the early water breakthrough. The restriction introduced on an ICD at the high permeable zone of the light oil reservoir is able to delay the initial water breakthrough from day 9 to day 76. The main drawback of this case is the high installation risks as it is difficult to pre-locate the fractured zones inside a reservoir. The restrictive ICD will reduce the oil production if installed in zones other than the high permeable zones.

The frictional pressure drop along the well is around 0.1 bar for homogeneous reservoir causing almost same production in all zones of the well. The water

breakthrough occurred at about same time along the whole well and all the AICDs closed during a short time interval. Therefore, the effects of AICDs are less significant in the homogeneous reservoir.

From the above simulations results, water accumulation can be reduced by the use of AICDs or the non-uniform ICDs. After a specified amount of water associated with the flow, AICD choked the total flow entering the wellbore. AICDs are better to limit the water accumulation and the water production was reduced with 88% compared to the normal ICDs in the heterogeneous reservoir. The water accumulation in the fractured reservoir reduced significantly by around 82% and oil accumulation by 29% by the use of AICD compared to normal ICDs. The production from the high permeability zones is choked locally by using AICDs, allowing normal oil production from the other zones. Therefore, AICDs are better suited for heterogeneous and fractured reservoirs.

The oil volume flow increased with the decrease of oil viscosity. This is due to the higher mobility of oil. For the same relative permeability, there is around 47% increase in oil flow rate with the decrease of oil viscosity from 3 cP to 1.5 cP and 120 % increase in oil flow rate with the decrease of oil viscosity from 3 cP to 0.8 cP after 10 days. The oil volume flow and water volume flow are almost the same with doubling the number of the grid along the well. Thus, confirming that the developed model is insignificantly sensitive to the mesh sizes in the well direction.

This study shows that the oil reservoirs behaves different at different reservoir conditions. The functionalities of different inflow controllers are different and show their unique characteristics.

Acknowledgements

This study was done as a part of the master's program in Process Technology in University college of Southeast Norway during spring 2017. The University college provided all the necessary software arrangement during the study.

Abbreviations

AICD	Autonomous Inflow Control Device
API	American Petroleum Institute
ICD	Inflow Control Device
ICV	Inflow Control Valve
GLR	Gas Liquid Ratio
GOR	Gas Oil Ratio
WTI	West Texas Intermediate

References

Al-Khelaiwi F. T., Birchenko V. M., Konopczynski M. R. and Davies D. R. Advanced wells: a comprehensive approach to the selection between passive and active inflow-control

completions. *SPE Production & Operations*, vol. 25 no. 03, pp 305-326, 2010. doi: 10.2118/132976-PA

Alomair A. Osamah and Almusallam S. Abdulwahab. Heavy crude oil viscosity reduction and the impact of asphaltene precipitation. *Energy & Fuels*, vol. 27, no. 12, pp. 7267-7276, 2013.

Birchenko V. M., Muradov K. M. and Davies D. R. Reduction of the horizontal well's heel-toe effect with inflow control devices. *Journal of Petroleum Science and Engineering*, vol. 75 no. 1, pp. 244-250, 2010. doi: 10.1016/j.petrol.2010.11.013

Fernandes X. Preston, Li Zhuoyi and Zhu Ding. Understanding the roles of inflow-control devices in optimizing horizontal-well performance. *SPE Annual Technical Conference and Exhibition*, 2009, Society of Petroleum Engineers. doi: 10.2118/124677-MS

Halvorsen Martin, Elseth Geir, and Naevdal M. Olav. Increased oil production at Troll by autonomous inflow control with RCP valves. *SPE Annual Technical Conference and Exhibition*, 2012, Society of Petroleum Engineers. doi: 10.2118/159634-MS

Torbergsen H.-E. Bensnes. Application and design of passive inflow control devices on the Eni Goliat oil producer wells. University of Stavanger, Norway, 2010.

Simulation of Oil Production from Homogenous North Sea Reservoirs with Inflow Control using OLGA/Rocx

Sveinung M. Sund, Thomas Berg Iversen, Magnus S. Hansen, Jørgen Bohlin, Ole K. Vøllestad, Nora C.I. Furuvik, Britt M. E. Moldestad

¹Department of Technology, University College of South-East Norway, Norway,
{94.thomas.berg.iversen@gmail.n; msh_89@hotmail.com; okvl@hotmail.com;
sveinungsund@gmail.com; britt.moldestad@usn.no; nora.c.i.furuvik@usn.no}

Abstract

Advances in drilling technology have made long, horizontal wells the preferred method to extract oil from reservoirs in the Norwegian Sector. Horizontal wells give increased oil contact, enabling production from reservoirs with shallow, high viscosity oil columns. Under these conditions, early water or gas breakthrough is a major challenge. To postpone breakthrough, passive inflow control devices (ICD) are installed to even out the drawdown. However, a new technology called Autonomous Inflow Control Valve (AICV[®]) has the ability to autonomously close each individual inflow zone in the event of gas or water breakthrough. The objective of this paper was to study and compare these inflow control technologies. This was accomplished by conducting simulations in OLGA/Rocx. For this study, a high-permeability homogenous sandstone heavy oil reservoir was modelled based on data from the Grane oil field in the North Sea. Comparison of the oil production from the simulations with ICD and AICV completion was performed. The results, based on a time interval of 600 days, show that the oil production is 8% less and the water production is 43% less if AICV is used compared to ICD. This indicates that AICV has the potential to reduce the water production significantly in a homogeneous reservoir.

Keywords: Inflow control, ICD, AICV, oil reservoir, oil production, breakthrough, multiphase flow, OLGA, Rocx.

1 Introduction

A major challenge in oil production is to increase the ability to recover the oil that is present in the reservoir. Estimates show that although the oil is localized and mobile, about half of the oil remains in the reservoir after shutdown. Therefore, there are strong incentives for using technologies that can increase the oil production and recovery. Two factors are of particular importance in order to increase oil production and recovery; obtaining maximum reservoir contact and preventing the negative effects of early gas or water breakthrough. (Mathiesen *et al.*, 2014) Long horizontal wells are used to obtain maximum reservoir contact. In the North Sea, the oil columns are very thin, and it is therefore a challenge to avoid early water and gas breakthrough to the well. Inflow controllers are implemented to limit early gas and water breakthrough. (Terry and Rogers, 2014; Geoscience News and

Information, 2017) Inflow control devices adjust the inflow volume to the well to avoid high volume flow in zones with high permeability or high drawdown. This paper focuses on studying the effect of inflow controllers in a homogeneous oil reservoir with an underlying water aquifer in the North Sea. Two types of technologies were studied; a passive inflow control device (ICD) and an autonomous inflow control valve (AICV). Passive ICD is capable of equalizing the production along the well. AICV can close for unwanted fluids when breakthrough occurs. Several studies have been carried out to investigate the effect of inflow controllers in different types of reservoirs. (Furuvik and Moldestad, 2017; Ugwu and Moldestad, 2016; Abbasi and Moldestad, 2016; Jonskås *et al.*, 2016) Near-well simulation have been performed by using simulation tools like Eclipse, OLGA/Rocx, Aspen/Hysys and NETool. The conclusion has been that there is a high potential of increasing the oil recovery by using inflow controllers. This study includes OLGA/Rocx simulations of the oil production from the Grane field in the North Sea. The Grane field is often presented as a homogeneous reservoir, but still fractures and heterogeneities are observed in parts of the field (Skotner, 1999). This paper focuses on oil production from homogeneous parts of the Grane field.

1.1 Driving forces for oil production

During oil production from a reservoir, the driving force is the pressure difference between the reservoir and the well. It is important to maintain a sufficient reservoir pressure to sustain an acceptable oil production rate. During oil production, the reservoir pressure decreases, and if it drops too low, the oil production stops. (Nasjonal Digital Læringsarena, 2016) The pressure in the reservoir can be maintained by gas or water drive. Some reservoirs have a large gas cap above the oil layer that acts as a buffer for the reservoir pressure. During oil production, the gas expands and pushes the oil towards the well. This is described as gas cap drive. (Nasjonal Digital Læringsarena, 2015) Some reservoirs have a large aquifer below the oil layer. In these types of reservoirs, the water is replacing the oil during the oil production, and since the aquifer is significantly larger than the oil reservoir, the reservoir pressure will decrease slowly over time. Water does not expand in the

reservoir, but due to the size of the aquifer, water flows into the reservoir and oil will be pushed towards the well. (Nasjonal Digital Læringsarena, 2015; Petrowiki, 2015) However, after years of production, the reservoir pressure will decrease. At that point injection of water into the reservoir can be used to maintain the reservoir pressure. Injection wells are installed in the reservoir for this purpose. The reservoir conditions are essential when determining whether water injection, gas injection or a combination of these are most effective. (Oljedirektoratet, 2009) Treated sea water, or formation water, can be used for the water injection. Natural gas from the reservoir or other reservoirs are often used in gas injection systems, but other gases such as nitrogen and carbon dioxide can also be used as pressure support in mature oil fields (Nasjonal Digital Læringsarena, 2017). In the present study, heavy oil production from a homogeneous reservoir with an underlying aquifer is considered.

1.2 Horizontal wells

The oil reservoirs at Grane have thin oil columns. Long horizontal wells are used to increase the reservoir contact and thereby obtain higher oil recovery (Terry and Rogers, 2014; Geoscience News and Information, 2017). The frictional pressure drop in the well is proportional to the length of the well as given by:

$$\Delta P = f \cdot \frac{L}{D} \cdot \frac{\rho \cdot v^2}{2} \quad (1)$$

where f is the friction factor, L is the length of the well, D is the diameter of the well, v is the average fluid velocity and ρ is the fluid density.

Due to frictional pressure drop along the well, the driving forces for oil production are different from one location to another in the well. This is called the heel (low pressure) – toe (high pressure) effect. In a homogeneous reservoir, the oil production rate will be significantly higher in the heel than in the toe, and this may lead to early water or gas breakthrough in the heel section. Figure 1 illustrates a long horizontal well with water and gas breakthrough in the heel section.

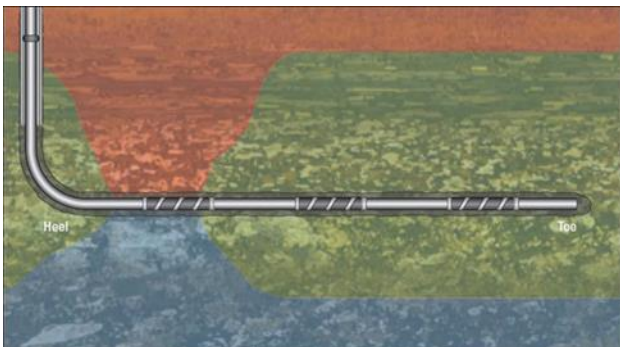


Figure 1. Horizontal well with gas and water breakthrough in the heel section. (Ellis *et al.*, 2010)

Breakthrough of unwanted fluids to the production well is a big challenge for the oil industry. Different types of

inflow controllers are developed to avoid early breakthrough and even choke or close off zones when breakthrough occurs. In the present study, two types of inflow controllers have been considered; a passive inflow controller (ICD) and an autonomous inflow control valve (AICV).

1.2.1 Inflow controllers

In this study, a standard nozzle ICD was used. ICDs are designed to give a more uniform oil production along the well, and the technology has opened up for production from reservoirs with thin oil columns. The capacity of an ICD is often given as the ICD strength, which is defined as the pressure drop over the ICD when 1m^3 of fluid passes through per hour. The pressure drop highly depends on the nozzle diameter and the density of the fluid, and less on the viscosity. ICDs are capable of delaying the gas/water breakthrough significantly. (Al-Khelaiwi and Davis, 2007). Well completion with ICDs includes a large number of ICDs equally distributed along the well. ICDs neither choke nor close for the undesired fluids after breakthrough. In order to avoid overloading the downstream separation facilities, the whole well has to be choked. Reservoir simulations have been used for different types of ICD completion and the results have been useful for ICD design. (Al-Khelaiwi and Davis, 2007) Krinis & al. used the reservoir model NETool to determine the optimal number and location of ICDs, and they stated that the simulations were the key factor in the successful optimization of the horizontal well performance (Krinis *et al.*, 2009). Figure 2 shows a nozzle ICD installed in a pipeline. The arrows show the direction of the fluid flow through the sand screen via the nozzle ICD and into the well.

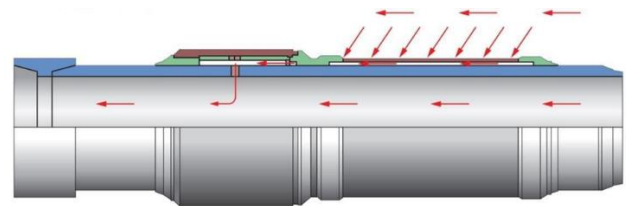


Figure 2. Nozzle ICD installed in a pipe section. (Ellis *et al.*, 2010)

This paper also includes the use of AICV in oil production. AICV is completely self-regulating and does not require any electronics or connection to the surface. AICV is capable of both delaying water/gas breakthrough and to close almost completely for the unwanted fluids when breakthrough occurs. The valves will locally close in the zones with water or gas breakthrough, and simultaneously produce oil from the other zones along the well. The AICV technology enables drilling of longer wells. The technology eliminates the gas and water breakthrough problems, and removes the risk, cost and requirement for separation, transportation and handling of unwanted

fluids. (Aakre *et al.*, 2013) Near-well simulations with Rocx have shown the potential of increased oil recovery with AICV completion. (Aakre *et al.*, 2013) Figure 3 shows a drawing of the AICV in open and closed position. The thick blue arrow indicates the fluid flow into the AICV, and the two horizontal arrows represents the outlet from the AICV to the well. The yellow area is a piston, and this piston is moving from open to closed position depending on the viscosity of the fluid surrounding the AICV. The principle of the AICV technology is described in detail by Mathiesen *et al.*, Aakre *et al.* and Ransis *et al.* (Mathiesen *et al.*, 2014; Aakre *et al.*; 2013; Ransis *et al.*, 2016)

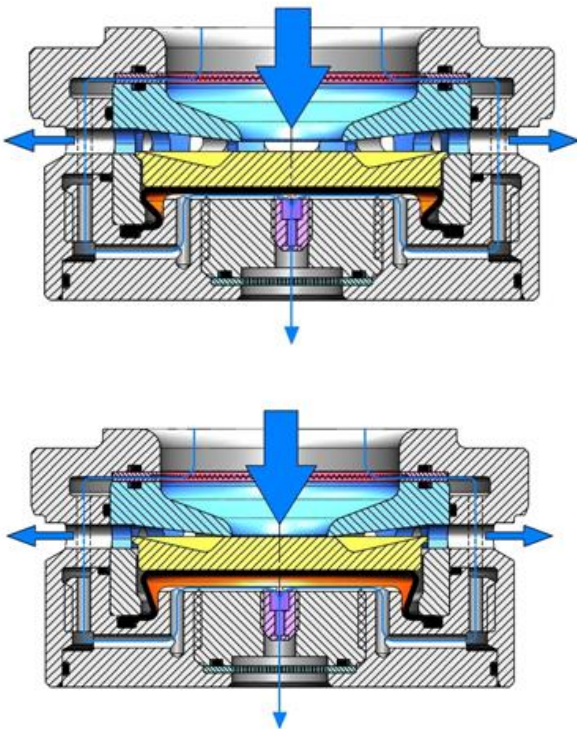


Figure 3. Drawing of AICV in open and closed position. (Aakre, *et al.*, 2014)

2 Simulation set-up

Simulations of oil production are carried out by using the near well simulation tool Rocx in combination with OLGA.

2.1 Rocx

Rocx is a three-dimensional transient near well simulation tool and is used to simulate three-phase flow in permeable rocks. Rocx gives information about changes in pressure, temperature and fluid saturation in the reservoir with time. The information from the near well simulations is transferred to OLGA.

2.1.1 Grid

The dimensions of the reservoir and the position of the well are defined in Rocx. The reservoir is divided into 3900 control volumes; 10 in x-direction, 39 in y-direction and 10 in z-direction. The simulated reservoir is 1219 m in x-direction, 308 m in y-direction and 31 m in z-direction. The grid sizes are 121.9 m in the x-direction. A normal well in the North Sea consists of pipe sections of 12.19 m. Each pipe section is equipped with sand screen and one or more inflow controllers. In the present study, pipe sections of 121.9 m are used to reduce the simulation time. The simulations are performed for the Grane field, where the height of the oil column is typically 31 m (Skotner, 1999). The width of the reservoir is chosen as 308 m to secure sufficient initial volume of oil. The grid sizes in the x- and z-directions are constant, whereas in the y-direction the grid sizes are decreasing towards the wellbore. This is done to get a better prediction of the distribution of the fluids in the reservoir, the water breakthrough time, and the coning effect. The well is located about 9 m above the lower boundary of the reservoir. The water-oil boundary is in the bottom of the reservoir. Figure 4 shows the final grid including the position of the well.

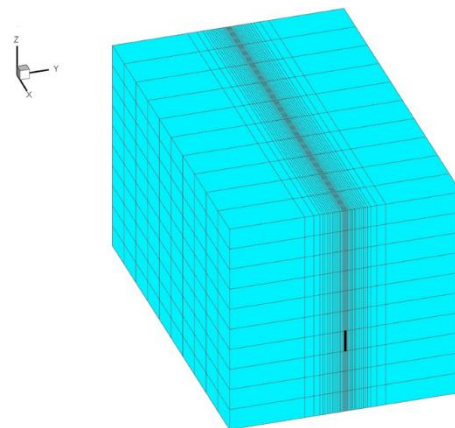


Figure 4. Pipe section with nozzle ICD.

2.1.2 Permeability

This paper presents the simulations of a homogeneous reservoir. The horizontal (x-y) permeability is 8000 mD and the vertical (z) permeability is 800 mD, corresponding to 1/10 of the horizontal permeability. The relative permeability is the ratio of the effective permeability to the absolute permeability, and is highly dependent on the type of reservoir. Grane is modelled as a water-wet sandstone reservoir. In water-wet conditions, a thin film of water coats the surface of the rock, which is desirable for efficient oil transport in the reservoir. The relative permeability for oil and water at Grane is calculated based on the Corey correlation. The Corey model is derived from capillary pressure data and is accepted as a good approximation for relative permeability curves in a two-phase flow. The required input data is limited to the irreducible water saturation

(Swc) and the residual oil saturation (Sor), and their corresponding relative permeability. (Furuviik and Moldestad, 2017; Tangen, 2017) Swc defines the maximum water saturation that a reservoir can retain without producing water, and Sor refers to the minimum oil saturation at which oil can be recovered by primary and secondary oil recovery. The relative permeability curves implemented in the simulations are presented in Figure 5. The blue line represents the relative permeability for water (Krw) and the red line represents the relative permeability for oil (Kro).

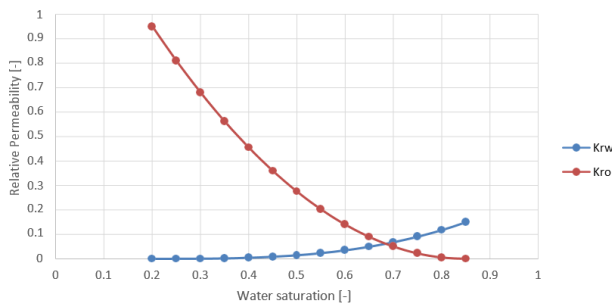


Figure 5. Relative permeability curves for water and oil.

The calculation and implementation of the relative permeability curves in Rocx, is described in detail by Furuviik and Moldestad (Furuviik and Moldestad, 2017).

The reservoir and fluid properties used as input to Rocx are summarized in Table 1.

Table 1. Input data to Rocx.

<i>Fluid properties</i>	
Oil viscosity	12 cP
Oil density	895 kg/m ³
Oil PVT model	Black oil
<i>Reservoir properties</i>	
Porosity	0.33
Permeability (x-y-z- direction)	8000 – 8000- 800 mD
Pressure	176 bar
<i>Initial conditions</i>	
Pressure	176 bar
Temperature	76°C
Oil saturation	0.8
<i>Boundary conditions</i>	
Water drive from the bottom	176 bar

2.2 OLGA

OLGA is a one-dimensional transient dynamic multi-phase simulator used to simulate flow in pipelines and connected equipment. OLGA consists of several modules depicting transient flow in a multiphase

pipeline, pipeline networks and processing equipment. The OLGA simulator is governed by conservation of mass equations for gas, liquid and liquid droplets, conservation of momentum equations for the liquid phase and the liquid droplets at the walls, and conservation of energy mixture equation with phases having the same temperature (Thu, 2013; Schlumberger 2007)

2.2.1 Setup in OLGA

The set-up in OLGA includes annulus, pipeline, packers and inflow controllers. Annulus is the space between the rock and the pipeline. Figure 6 shows a drawing of the location of the annulus and the well in the reservoir.

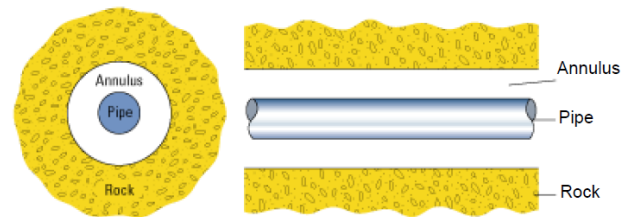


Figure 6. A drawing of the pipe and the annulus. (Schlumberger, 2007)

The OLGA version used in this project does not have any available routine for annulus simulations. The production well and the annulus are therefore implemented as two separate pipelines, as presented in Figure 7. The lower and the upper pipelines illustrate the annulus and the production well respectively.

In OLGA, the inflow controllers are defined as valves. ICDs are passive inflow controllers and are modelled as fully open valves. The AICVs are operating in open or closed position depending on the properties of the surrounding fluid.

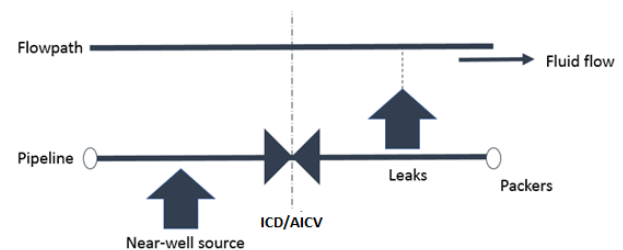


Figure 7. Representation of single zone of well. (Timsina, 2017)

Figure 8 illustrates one pipe section including the flow from the reservoir (NWSOUR-2) to annulus, one inflow controller (VALVE2), two packers (PACKER and PACKER-2) and the flow through the inflow controller to the production well (LEAK).

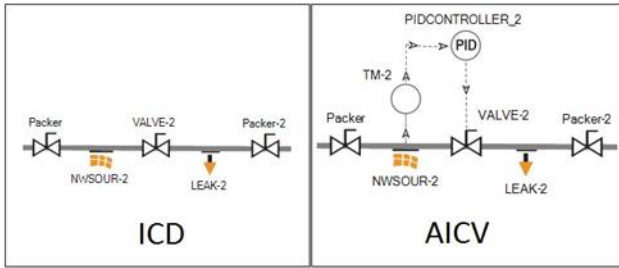


Figure 8. Set-up of ICD and AICV in OLGA.

The ICD and AICV both have an inlet diameter of 19.5 mm. There are no options to choose autonomous inflow controllers in OLGA, and transmitters and PIDs are used to model the functionality of the AICVs. The transmitters register the water cut (WC), and if the WC is higher than the set point given for the PID, the AICV starts to close. When the AICVs are in closed position, the flow area of the valves is reduced to 0.8% of the fully open valve area. The diameters of the pipeline and the annulus are set to 0.1397 m (5.5") and 0.2159 m (8.5") respectively. The roughness of the well is assumed to be $1.5 \cdot 10^{-4}$ m. The production well has a length of 1279.5 m and is divided into 10 sections of m each, and one outlet part (60.95 m) including a PID controller to adjust the total flow rate to the downstream facilities. Figure 9 illustrates the outlet section of the well including the choke and the PID controller.

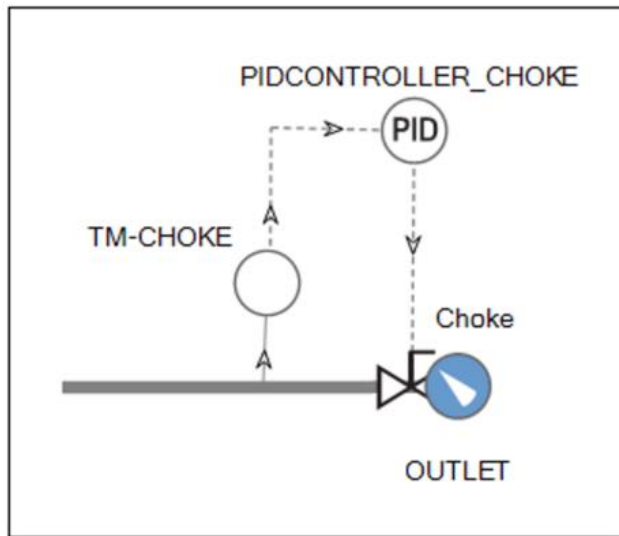


Figure 9. Flow control at the outlet of the well.

The PID is controlling the total flow rate, and the set point is $1200 \text{ m}^3/\text{day}$. The set point value is calculated based on production data from Grane. The PID controller parameters are presented in Table 2.

Table 2. PID controller parameters.

Parameter	Value
Set point	$1200 \text{ m}^3/\text{day}$
Initial opening	0.10 %
Maximum opening	100 %
Minimum opening	0.10 %
Amplification	-0.18
Sample time	60.0 s
Integral time	540 s
Derivative time	0.00 s

3 Results

Based on the input data in Rocx and OLGA, simulations were performed for 600 days of production. The results presented are volume rates of oil, and accumulated oil and water volume, for ICD and AICV. The closure characteristics for the AICVs is also presented. In addition, the results from a time step sensitivity analysis are included. Malagalage and Halvorsen did grid resolution tests for the same system (Malagalage and Halvorsen, 2015). The recommended grid resolution is utilized in this study.

3.1 Time step sensitivity analysis

Preliminary simulations were performed to study the influence of the minimum time step size on the oil and water production rates. Minimum and maximum time steps are input values in OLGA. During the simulations, OLGA will use the most convenient time step between the minimum and the maximum. When small minimum time steps are used, the simulations are more time-consuming. Large time steps result in less total simulation time, but it will also result in lower accuracy. A time sensitivity analysis was performed to study the consequences of increasing the minimum time step (MinDT) for the ICD and AICV simulations. The values for MinDT were chosen as 0.001s and 50s. Other values for MinDT, like 70s, 80s, 90s and 100s, were also tested, but were too high and the simulations stopped. The consequence of using a MinDT of 50s compared to 0.001s was investigated by comparing the number of days before key events occur. The events were defined as first water breakthrough (O1), 65% water cut in the first zone (O2), 65% water cut in all zones (O3) and 70% water cut in the total production (O4). The results are shown in Table 3.

Table 3. Results from the time sensitivity tests.

MinDT	Type	O1	O2	O3	O4
50 s	ICD	36 d	122 d	-	452 d
0.001 s	ICD	37 d	118 d	-	455 d
50 s	AICV	36 d	122 d	319 d	-
0.001 s	AICV	37 d	109 d	264 d	-

O1, O2 and O4 show that ICD is very little affected by the increase in time step. However, the results indicate that AICV is more sensitive to the size of MinDT. This is probably due to large variations in volume flow through the valves during the period of closing. It can be concluded that the closing time for the AICVs increases with decreasing MinDT.

Table 4 presents the effect of MinDT on the accumulated oil and water volumes during 600 days of production. The results show that the accumulated oil and water production with ICD are almost insensitive to the variation in MinDT. This is also the case for oil when AICV is used, although the water production decreases with about 5% when MinDT is increased from 0.001s to 50s. Based on these results, it was found that 50s would be an adequate MinDT.

Table 4. Accumulated production for different MinDT.

MinDT [s]	Type	Acc. Oil [$10^5 m^3$]	Acc. water [$10^5 m^3$]
0.001	ICD	2.63	4.58
50	ICD	2.60	4.60
0.001	AICV	2.45	2.76
50	AICV	2.39	2.61

3.2 Oil and water production with ICD and AICV

The simulations using OLGA/Rocx were performed with ICD and AICV completed horizontal wells. The simulations were performed for 600 days, and the set point for the water cut through AICVs was used as 65%. The set point for the total flow was specified as 1200 m³/day. The minimum time step was set to 50s and the maximum time step was 3600 s. Figure 10 shows the oil production rates with time for ICD and AICV. The plot is divided into three time intervals, T1, T2 and T3. T1 presents the period when AICV are fully open, and AICVs and ICDs are operating at the same production rates. During T2, the AICVs are producing more oil than the ICDs and in T3, when all the AICVs are closing, ICDs are producing more oil than AICVs.

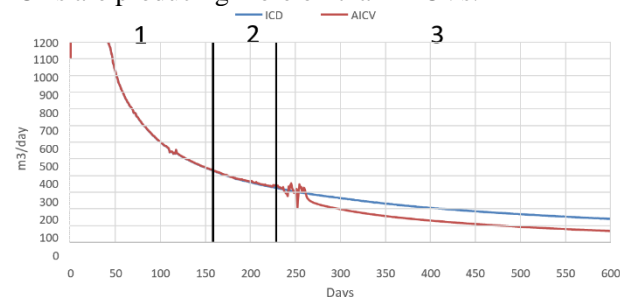


Figure 10. Volume flow rate of oil through ICD and AICV.

The production rates are equal for the two types of inflow controllers until the water cut through the first AICV exceeds 65%. This occurs after 163 days of production. When the first AICV starts closing, more oil

is produced through the other zones in the well due to increased capacity. In the same period, the ICDs are producing less oil and more water than the AICVs. After 232 days, when all the AICVs are closing and the total capacity is limited by the AICVs, the ICDs produce more oil than the AICVs.

Figure 11 shows the closing characteristics for AICV. All the AICVs start to close during a period of about 50 days, and it takes about 70 days from the first AICV starts closing until all the valves are 70% closed. All the valves start to close within a short period due to a rather low frictional pressure drop in the well. The frictional pressure drop creates the heel-toe effect, and the time intervals between the closing of the different AICVs along the well are increasing with increasing pressure drop. Because the heel-toe effect influences the water-cut of each section, the AICVs in the heel section start closing first.

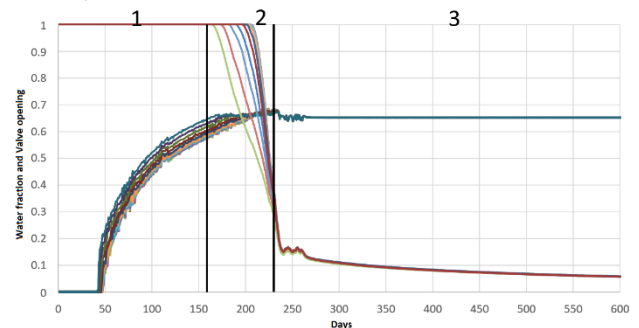


Figure 11. Closure characteristic for the AICVs.

The instability in the oil production after about 250 days is due to the high activity in the well when all the AICVs are closing. The instabilities are probably due to numerical diffusion.

Figure 12 shows the accumulated oil production for AICV and ICD versus time. The oil production is slightly higher for AICV than ICD in T2 and lower in T3.

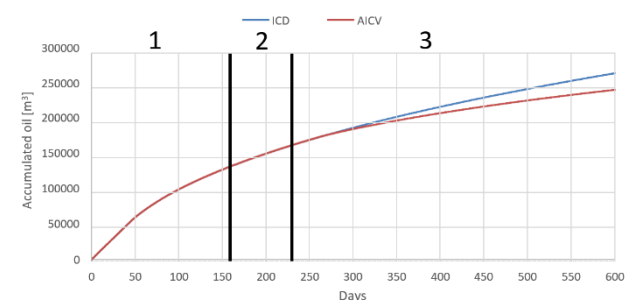


Figure 12. Accumulated oil production for ICD and AICV.

Figure 13 presents the water production data for ICD and AICV. During time period T3, ICD is producing significantly more water than AICV.

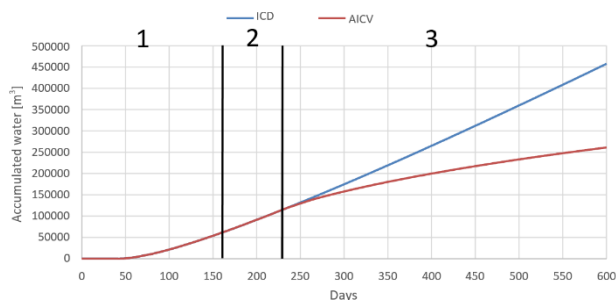


Figure 13. Accumulated water production for ICD and AICV.

Table 5 and Table 6 show a comparison of the accumulated water and oil production for ICD and AICV. The accumulated production is given for the different time intervals and the total simulation period. The total oil production is 9% less and the water production is 43% less if AICV is used compared to ICD.

Table 5. Accumulated oil and water production through AICVs and ICDs.

Time interval	Accumulated water ICD[m ³]	Accumulated water AICV[m ³]
T1	63 095	63 095
T2	53 901	53702
T3	340 809	143 997
Total	457 805	260 794

Table 6. Accumulated oil and water production through AICVs and ICDs.

Time interval	Accumulated oil [m ³] ICD	Accumulated oil [m ³] AICV
T1	132 591	132 591
T2	28 899	29 058
T3	100 693	77 081
Total	262 183	238 730

The heel-toe effect increases with high flow rates, small pipe diameter and high roughness. In the case simulated, the frictional pressure drop was relatively low, and all the AICVs closed during a short period. In addition, the WC set-point was set low; 65%, and all the AICVs started to close after a short time of production. The oil production rate for the AICV case was therefore relatively low. The AICV technology is reversible, which means that the valve will open again when the WC is reduced to below 65%. However, in the simulations there is no boundary oil source, and no new oil will come from the surrounding parts of the reservoir and increase the oil fraction around the well. The reversible function of AICV can be taken into consideration in further studies by changing the boundary conditions.

4 Conclusion

Oil production from the Grane field in the North Sea was simulated with the near-well simulation tool Rocx in combination with OLGA. A long horizontal well was modelled, and it was assumed that the reservoir was homogeneous with a horizontal permeability of 8000mD. Two cases were simulated, one with passive inflow control devices (ICDs) and one with autonomous inflow control valves (AICVs) installed along the well. A time step sensitivity test was carried out to find the largest minimum time step that can be used while maintaining sufficient accuracy. It was concluded that a minimum time step of 50s was acceptable for simulations with both AICV and ICD. PID controllers were used to adjust flow through each AICV, with a desired value of 65% WC. A PID controller was also used to control the total volumetric flow rate for the two cases, with a desired value of 1200 m³/day. The simulations were run for 600 days. WC of 65% in the heel section was registered after 163 days, and the AICV started to close. In time interval 163-232 days, AICV produces slightly more oil than ICD. After 232 days, the ICD well produces more oil than the AICV well, but also considerably more water, due to a higher total production. The total oil production was 9% less and the water production was 43% less for the AICV well compared to the ICD well. This indicates that for oil production from homogenous reservoirs with small differences in pressure and water cut along the well, the benefits of AICV technology are small compared to ICD completion. For real AICV installations, the AICVs should be designed for the reservoir conditions and should not limit the total production at an economically acceptable water cut.

References

- Haavard Aakre, Britt Margrethe Halvorsen, Bjørnar Werswick and Vidar Mathiesen. Smart Well With Autonomous Inflow Control Valve Technology. I: *18th Middle East Oil & Gas Show and Conference (MEOS)*, March 10 - 13, 2013.
- Aakre, Haavard; Halvorsen, Britt Margrethe; Werswick, Bjørnar; Mathiesen, Vidar. Autonomous inflow control valve for heavy and extra-heavy oil. I: *2014 SPE Heavy and Extra Heavy Oil Conference: Latin America*. Society of Petroleum Engineers 2014 ISBN 978-1-61399-345-3.
- Arash Abbasi, Britt M. E. Moldestad, Simulation of light oil production from heterogeneous reservoirs: Well completion with inflow control devices. I: *2016 9th EUROSIM Congress on Modelling and Simulation Oulu, Finland 12-16 September 2016*. IEEE 2016 ISBN 978-1-5090-4119-0. pp. 836-841.
- T. Ellis, A. Erkal, G. Goh, T. Jokela, S. Kvernstuen, E. Leung, et al. Inflow Control Devices- Raising Profiles, *Oilfield Review*, pp. 30-31, 2010.

Nora C. I Furuviik and Britt M. E. Moldestad. Distribution of CO₂ in Fractured Carbonate Reservoirs. *International Journal of Energy Production and Management*, Volume 2 (1) pp. 28-38, 2017.

Geoscience News and Information. Directional and Horizontal Drilling in Oil and Gas Wells, *Geology.com*, date: 23.04.2017. Available from: <http://geology.com/articles/horizontal-drilling/>

M. H. Jonskås, V. Mathiesen and B. M.E. Moldestad. Heavy oil production with energy effective Steam Assisted Gravity Drainage. *Energy Quest 2016, 2nd International Conference on Energy Production and Management in the 21st Century*, September 6th-8th, Ancona, Italy, 2016.

Ransis Kais, Vidar Mathiesen, Haavard Aakre and Glenn Woiceshyn. First autonomous Inflow Control Valve (AICV) Well Completion Deployed in a Field under an EOR (Water & CO₂ Injection) Scheme, *SPE-181552-MS*, 2016.

F.T. Al-Khelaiwi and D.R. Davies. Inflow Control Devices: Application and Value Quantification of a Developing Technology, *International Oil Conference and Exhibition in Mexico, 27-30 June 2007*, Veracruz, Mexico. 2007

Dimitrios Krinis, Drew Hembling, Naseem Al-Dawood and Sadiq Al-Qatari, Sam Simonian and Giovanni Salerno. Optimizing Horizontal Well Performance in Non-Uniform Pressure Environments Using Passive Inflow Control. *OTC 20129 Texas*, May, 2009.

Anjana Malagalage and Britt M. Halvorsen. Near Well Simulation and Modelling of Oil Production From Heavy Oil Reservoirs. *Linköping Electronic Conference Proceedings 2015* (119) s. 289-298. , 2015.

Vidar Mathiesen, Haavard Aakre and Bjørnar Werswick. The Next Generation Inflow Control-the Next Step to Increase Oil Recovery on the Norwegian Continental Shelf, *SPE 169233*, 2014.

Nasjonal Digital Læringsarena. Fagstoff/Leting og Boring/ Produksjonsoppstart. *ndla.no*, date 10.05.2017. Anna Aabø, 2016. Available from: <http://ndla.no/nb/node/156340?fag=137414>

Nasjonal Digital Læringsarena. Fagstoff/Leting og Boring/ Drivmekanismer i reservoaret. *ndla.no*, date: 01.05.2017. Anna Aabø, 2015. Available from: <http://ndla.no/nb/node/153039?fag=137414>

Nasjonal Digital Læringsarena. Fagstoff/Leting og Boring/ Gassinjeksjon i reservoaret. *ndla.no*, date: 28.04.2017. Anna Aabø, 2015. Available from: <http://ndla.no/nb/node/153041?fag=137414>

Oljedirektoratet. Verktøy for økt utvinning. *npd.no*, date: 28.04.2017. 2009. Available from: <http://www.npd.no/no/Tema/Okt-utvinning/Temaartikler/Verktoy-for-okt-utvinning/>

Petrowiki. Waterdrive reservoirs. *Petrowiki.org*, date: 21.04.2017. 2015. Available from: http://petrowiki.org/Waterdrive_reservoirs

Schlumberger. Rocx Reservoir Simulator. *1.2.5.0 edit*, 2007.

Schlumberger. Fundamentals of Wettability. *Oilfield Review*, number 2, Volume 19, page 66-71. Summer 2007.

P.Skotner. Evaluation of CO₂ flooding on the Grane Field, *Norsk Hydro pp.4*, 1999.

Mathias Tangen. Wettability Variations within the North Sea Oil Field Frøy. *Master Thesis, Norwegian University of Science and Technology*, Department of Petroleum Engineering and Applied Geophysics, 2012.

R.E. Terry and J.B. Rogers. Introduction to Petroleum Reservoirs and Reservoir Engineering. *Applied Petroleum Reservoir Engineering*, third edition, 2014.

E. S. Thu. Modeling of transient CO₂ flow in pipeline and well. *Master Thesis, Norwegian University of Science and Technology*, Trondheim, 2013.

Ramesh Timsina. Near-well simulations and modelling of oil production from reservoir. *Master Thesis, University College of South-East Norway*, Faculty of Technology, Natural sciences and Maritime sciences, 2017.

Ambrose A. Ugwu and Britt M. E. Moldestad, Simulation of Horizontal and Vertical Water Flooding in a Homogeneous Reservoir using ECLIPSE, *9th EUROSIM Congress on Modelling and Simulation*, EUROSIM 2016, September 12th -16th, Oulu, Finland, 2016.

Simulation of Oil Production from Heterogeneous North Sea Reservoirs with Inflow Control using OLGA/Rocx

Thomas Berg Iversen, Magnus S. Hansen, Sveinung M. Sund, Ole K. Vøllestad, Jørgen Bohlin, Nora C.I. Furuvik, Britt M. E. Moldestad

¹Department of Technology, University College of South-East Norway, Norway,
{94.thomas.berg.iversen@gmail.com; msh_89@hotmail.com; okvl@hotmail.com;
sveinungsund@gmail.com; britt.moldestad@usn.no; nora.c.i.furuvik@usn.no}

Abstract

Advances in drilling technology have made long, horizontal wells the preferred method to extract oil from reservoirs in the Norwegian Sector. Horizontal wells give increased oil contact, enabling production from reservoirs with shallow, high viscosity oil columns. Under these conditions, early water or gas breakthrough is a major challenge. To postpone breakthrough, inflow control devices (ICD) are installed to even out the drawdown. A new technology, Autonomous Inflow Control Valve (AICV[®]) also has the ability to autonomously close each individual inflow zone in the event of gas or water breakthrough. The objective of this paper was to study and compare these inflow control technologies by conducting simulations in OLGA/Rocx. A heterogeneous fractured sandstone heavy oil reservoir was modelled. The results show that during 2000 days of production, the AICV well produces 2950 m³ more oil and 158300 m³ less water than the ICD well. This indicates that AICV has the potential to reduce the water production significantly, and thereby increase the oil recovery.

Keywords: Inflow control, ICD, AICV, heterogeneous oil reservoir, oil production, breakthrough, multiphase flow, OLGA, Rocx

1 Introduction

Long horizontal wells are drilled to increase the contact area between the reservoir and the production well, and thereby increase the oil production and oil recovery. In the North Sea, the oil columns are very thin, and it is therefore a challenge to avoid early breakthrough of gas and water. To limit the early gas and water breakthrough inflow controllers are implemented in the inflow zones along the well. (Terry and Rogers, 2014; Geoscience News and Information, 2017) Inflow control devices adjust the inflow volume to the well, avoiding high volume flow in zones with high permeability or high drawdown. This paper focuses on the effect of inflow controllers in a heterogeneous oil reservoir with an underlying water aquifer in the North Sea. Two types of technologies are studied; a passive inflow control device (ICD) and an autonomous inflow control valve (AICV). Passive ICD is capable of equalizing the production along the well. AICV can close for unwanted fluids when

breakthrough occurs. The effect of inflow controllers in different types of reservoirs has been studied by several researchers (Furuvik and Moldestad, 2017; Ugwu and Moldestad, 2016; Abbasi and Moldestad, 2016; Jonškås *et al*, 2016; Wijerathne and Halvorsen, 2015; Aakre *et al*, 2013) by using simulation tools like OLGA/Rocx, Eclipse, NETool and Aspen/Hysys. The conclusion has been that there is a high potential of increasing the oil recovery by using inflow controllers. This study includes OLGA/Rocx simulations of the oil production from the Grane field in the North Sea.

1.1 Horizontal wells

A horizontal well consists of several elements. After the wellbore is drilled in vertical direction down to the planned depth and horizontally to the design length, the production well is installed into the wellbore. The production well is composed of several sections where each of the sections include 1-2 joints of 12.19 m (40 feet) (Schlumberger, 2017). In each zone, inflow controllers can be installed to reduce or regulate the volume flow into the production well. The wellbore has a larger diameter than the production well, and the open space in between is called the annulus. Packers are used to isolate the different sections along the well to avoid water or gas flow from one section to another. In addition, sand screens are installed in each section to avoid production of sand into the well. (Halliburton, 2017) Figure 1 shows the structure of a horizontal well.

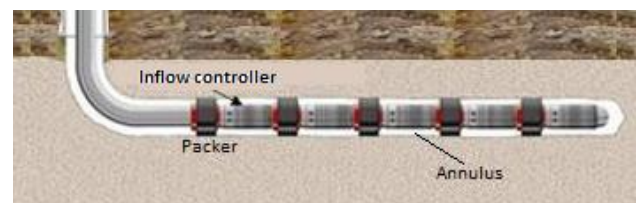


Figure 1. Structure of a horizontal well including production pipe, annulus, packers, sand screens and inflow control devices. (Halliburton, 2017)

1.2 Inflow controllers

Several inflow controllers are installed along a horizontal well; typically one controller per 12.19 m. In this study nozzle ICDs and AICVs are used in the simulations. Figure 2 shows a section of a pipeline

including a nozzle ICD. The fluid flows from the annulus, via the sand screen and through the ICD into the well. The red arrows in Figure 2 illustrates the flow path. The additional pressure drop over the nozzle ICD regulates the flow rates into the well and contributes to equalize the production along the well. The nozzle ICD is passive, and is not capable of choking or closing for unwanted fluids after breakthrough. (Ellis *et al*, 2010)

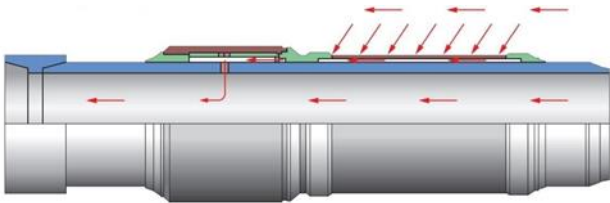


Figure 2. Pipe section with nozzle ICD. (Ellis *et al*, 2010)

Figure 3 shows an autonomous inflow controller, AICV, in open and closed position. AICV is a completely self-regulating inflow controller and does not require any electronics or connection to the surface. The AICV is in open position when oil is produced, and closes locally in zones where breakthrough of unwanted fluids occurs. The principle of AICV is described in detail in different publications (Mathiesen *et al*, 2014; Aakre *et al*, 2013; Aakre *et al*, 2014; Kahawalage and Halvorsen, 2015; Badalge and Halvorsen, 2015).

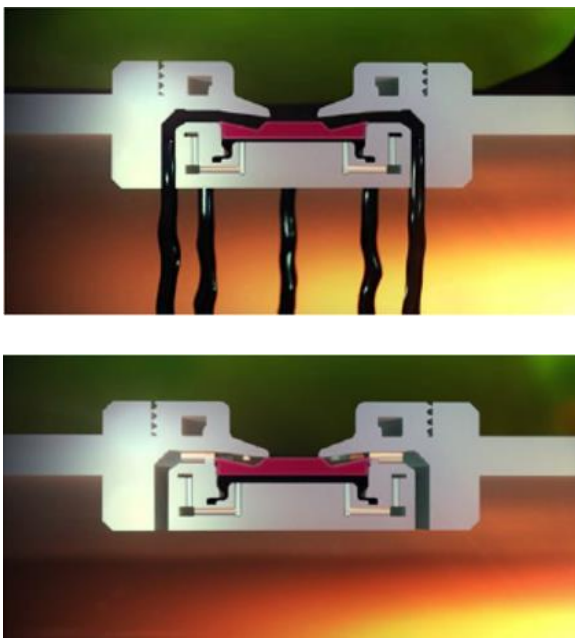


Figure 3. AICV in open (upper picture) and closed (lower picture) position. (Guadong and Halvorsen, 2015)

2 Simulation set-up

Simulations are performed using the near-well simulation tool Rocx in combination with OLGA. Rocx simulations can be run without the coupling to the

OLGA software, but the combination gives more accurate predictions of well start-up and shut-down, flow instabilities, cross flow between different layers, water coning and gas dynamics. (Schlumberger, 2017) The input to Rocx and OLGA is described in Chapter 2.1 and 2.2.

2.1 Rocx

Rocx is a three-dimensional transient near-well simulation tool and is used to simulate three phase fluid flow in permeable rocks. Rocx gives information about changes in pressure, temperature and fluid saturation in the reservoir as a function of time, and the information is transferred to OLGA.

2.1.1 Grid

The dimensions of the reservoir and the position of the well are defined in Rocx. The reservoir is divided into a number of control volumes as shown in Figure 4. The simulated reservoir is 1219 m in x-direction, 308 m in y-direction and 31 m in z-direction. The total number of control volumes are 3900 (10x39x10). The grid sizes are 121.9 m in the x-direction, which is corresponding to ten pipe sections of 12.19 m each. The simulations are performed for the Grane field, where the height of the oil column is typically 31 m. The width of the reservoir is chosen to be 308 m to ensure sufficient initial volume of oil. The grid sizes in the x- and z- directions are constant, whereas in the y-direction the grid sizes is reduced towards the wellbore. This is done to be able to simulate the coning effect, and to get better prediction of the water breakthrough time. The well is located about 9 m above the lower boundary of the well. The water-oil boundary is in the bottom of the reservoir. Figure 4 shows the final grid including the position of the well.

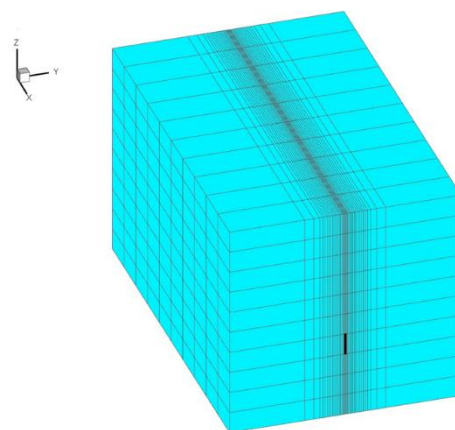


Figure 4. Final grid including the position of the well

2.1.2 Permeability

This paper presents the simulations of a homogeneous reservoir with one high permeable zone, also considered as a fracture. Figure 5 shows the permeability in the reservoir. The x-z permeability is 5000mD in the

homogeneous part of the reservoir (blue colour), and 35000mD in the high permeable zone (orange colour). The vertical (z) permeability is 1/10 of the horizontal (x-y) permeability.

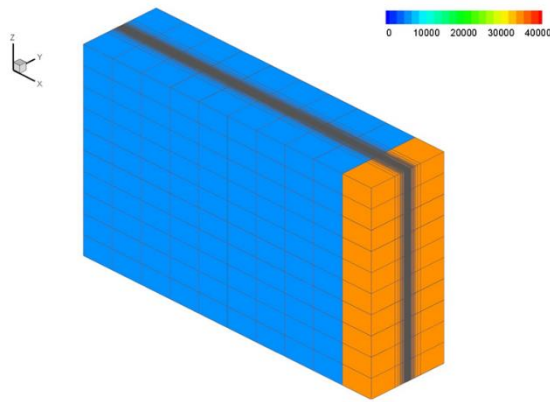


Figure 5. Permeability in the reservoir.

The relative permeability is defined as the ratio of the effective permeability to the absolute permeability, and is highly dependent on the type of reservoir. The relative permeability curves for oil and water, for water-wet sandstone at Grane, is calculated based on the Corey correlation. The Corey model is derived from capillary pressure data and is accepted as a good approximation for relative permeability curves in a two-phase flow. The required input data is limited to the irreducible water saturation (S_{wc}) and the residual oil saturation (S_{or}), and their corresponding relative permeabilities. (Furuvik and Moldestad, 2017; Tangen, 2017) S_{wc} defines the maximum water saturation that a reservoir can retain without producing water, and S_{or} refers to the minimum oil saturation at which oil can be recovered by primary and secondary oil recovery.

The relative permeability curves implemented in the simulations are presented in Figure 6. The blue line represents the relative permeability for water (K_{rw}) and the red line represent the relative permeability for oil (K_{ro}).

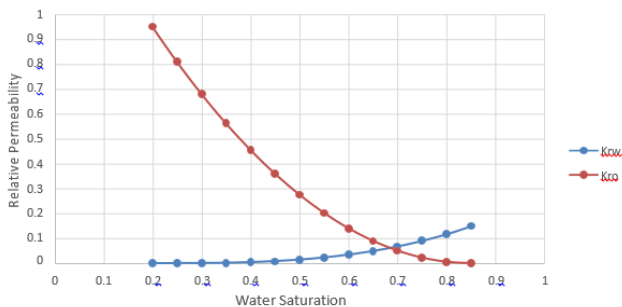


Figure 6. Relative permeability curves for water and oil.

2.2 OLGA

OLGA is a one-dimensional transient dynamic multiphase simulator used to simulate flow in pipelines and connected equipment. OLGA consists of several modules depicting transient flow in a multiphase pipeline, pipeline networks and processing equipment. The OLGA simulator is governed by conservation of mass equations for gas, liquid and liquid droplets, conservation of momentum equations for the liquid phase and the liquid droplets at the walls, and conservation of energy mixture equation with phases having the same temperature. (Schlumberger, 2017)

2.2.1 Set-up in OLGA

The set-up in OLGA includes the annulus, the pipeline, packers and inflow controllers. The annulus is the space between the rock and the pipeline. Figure 7 shows a schematic of the location of the annulus and well in the reservoir.

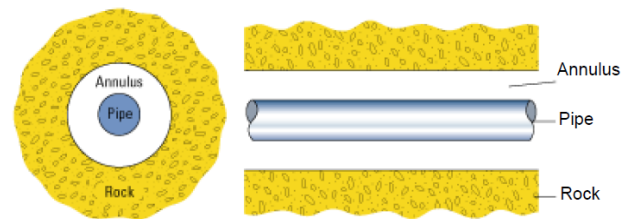


Figure 7. A schematic of the pipe and the annulus. (Schlumberger, 2007)

The OLGA version used in this project has no available routines for annulus simulations. The production well and annulus are therefore defined as two separate pipelines, as presented in Figure 8. The lower pipeline illustrates the annulus, and the upper pipeline illustrates the production well.

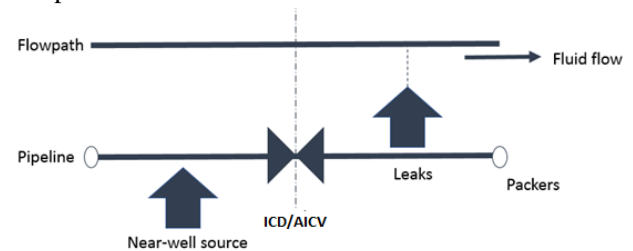


Figure 8. Representation of single zone of well. (Timsina, 2017)

In OLGA, the inflow controllers are defined as valves. ICDs are passive inflow controllers and are therefore modelled as fully open valves. The AICVs are operating in open or closed position depending on the properties of the surrounding fluids. There are no options to choose autonomous inflow controllers in OLGA, and the function of the AICV was modelled as a valve where the valve opening was adjusted based on the water cut (WC). Figure 9 illustrates one pipe section including the flow from the reservoir (NWSOUR-2) to annulus, one inflow controller (VALVE2), two packers (PACKER

and PACKER-2) and the flow through the inflow controller to the production well (LEAK).

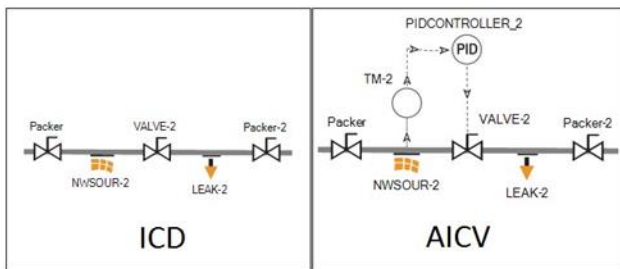


Figure 9. Set-up of ICD and AICV in OLGA.

The ICD and the AICV both have an inlet diameter of 19.5 mm. Transmitters and PIDs are used to model the function of the AICVs. The transmitters register the WC. If the WC is higher than the set point given for the PID, the AICV will begin to close. When the AICVs are in closed position, the flow area of the valves is reduced to 0.8% of the flow area in fully open position. The diameters of the pipeline and the annulus are set to 0.1397 m (5.5”) and 0.2159 m (8.5”) respectively. The roughness of the well is assumed $1.5 \cdot 10^{-4}$ m. The production well has a length of 1279.5m and are divided into 20 sections of 121.9 m and one outlet part (60.95 m), including a PID controller to adjust the total flow rate to the downstream facilities. Figure 10 shows the outlet part of the well including the choke and the PID controller.

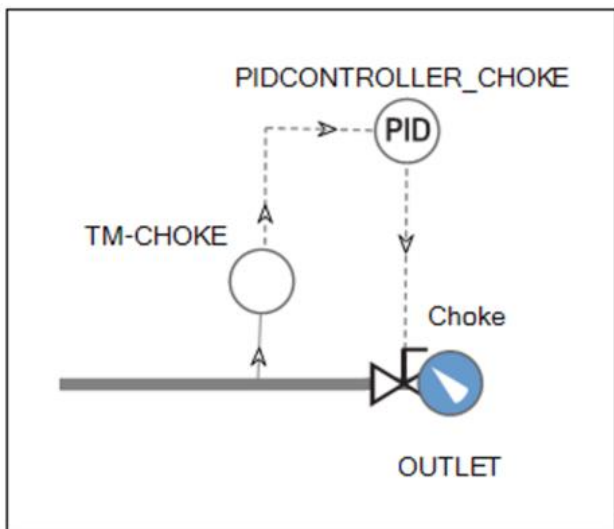


Figure 10. Flow control at the outlet of the well.

The PID is controlling the total flow rate of oil and water from the well. The set point is $1200 \text{ m}^3/\text{day}$, and is calculated based on production data from the Grane field. The PID controller parameters are summarized in Table 1.

Table 1. PID controller parameters

Parameter	Value
Set point	$1200 \text{ m}^3/\text{day}$
Initial opening	0.10 %
Maximum opening	100 %
Minimum opening	0.10 %
Amplification	-0.18
Sample time	60.0 s
Integral time	540 s
Derivate time	0.00 s

3 Results

Simulations using ICDs and AICVs were performed for 2000 days. The set point for the water cut through the AICVs was set to 90%. This means that the AICVs start closing when the fluid from the reservoir contains 90% water.

The oil and water flow rates through AICVs and ICDs as a function of time are shown in Figure 11 and 12 respectively. The plots are divided into three time intervals. Time interval 1 (T1) represents the period when all the valves are open (0-500 days), Time interval 2 (T2) represents the period when the AICVs produce more oil than the ICDs (500-1600 days), and Time interval 3 (T3) is the period from the end of T2 to the end of the simulation (1600-2000 days). AICVs and ICDs have the same inflow area in fully open position, and are therefore producing equal quantities of oil and water during T1.

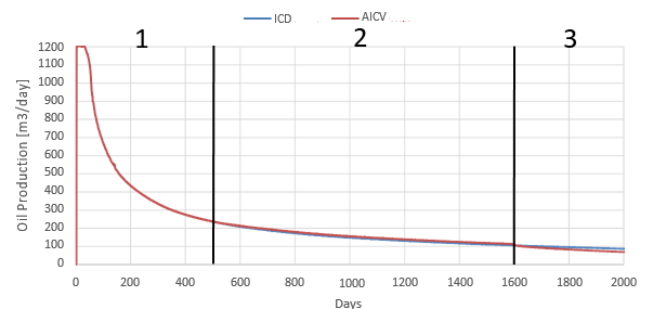


Figure 11. Oil production through ICD and AICV.

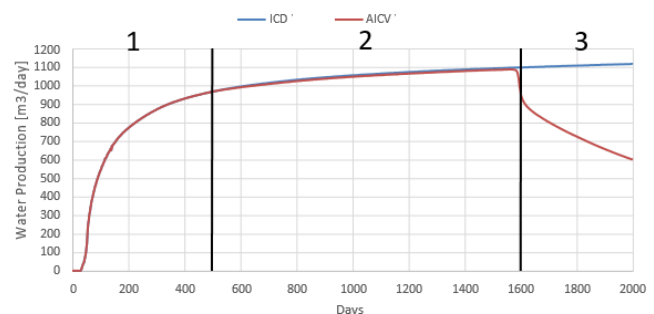


Figure 12. Water production through ICD and AICV.

The deviation in oil and water flow rates through the two inflow controllers is not clearly observed until the end of T2. In T3, the ICDs are producing significantly more water than the AICVs.

Figure 13 illustrates the closure characteristics of the AICVs. The water fraction (0-1) and the valve opening (0-1) are given at the y-axis, and the x-axis represents the time in days.

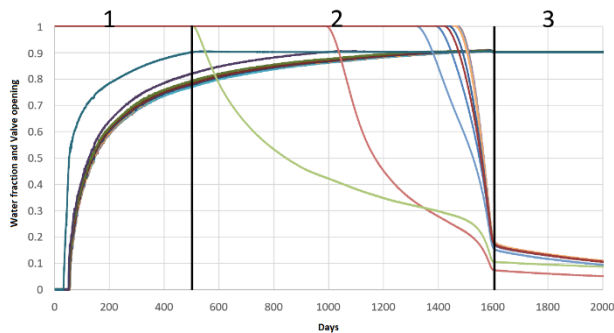


Figure 13. Closure characteristic for the AICV.

The AICV located in the high permeability zone (35000 mD) starts closing after 500 days of production. The next well, located near the heel section of the well, starts closing after about 1000 days. After about 1600 days, all the AICVs are nearly closed.

The accumulated volume of oil and water as a function of time are presented in Figure 14 and 15 respectively. Figure 14 shows that the AICVs are producing slightly more oil than the ICDs during T2, whereas the ICDs are producing more oil during T3. Figure 15 shows that ICD produce significantly more water than AICV during T3.

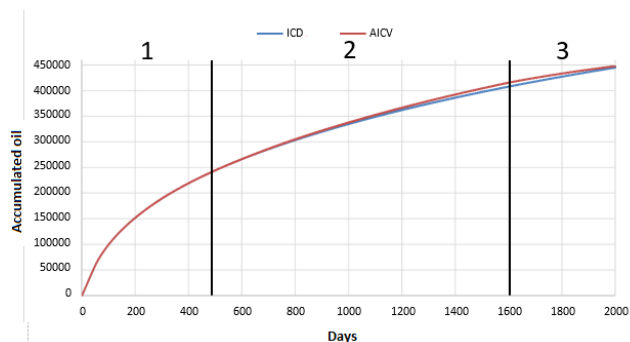


Figure 14. Accumulated oil as a function of time through ICD and AICV.

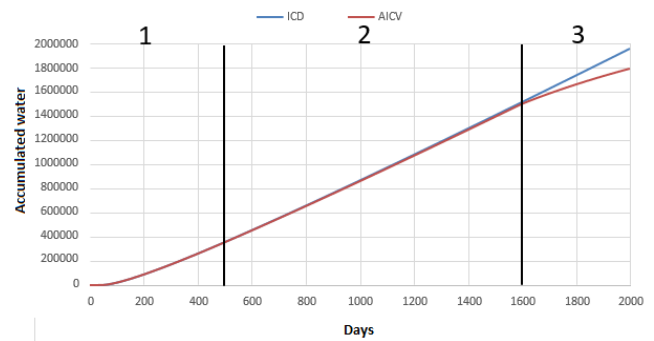


Figure 15. Accumulated water as a function of time through ICD and AICV

The results, given as the difference between the accumulated oil and water volume for the two cases, are summarized in Table 2. Positive values indicate higher production with AICV than ICD.

Table 2. Difference between accumulated oil and water production through AICVs and ICDs.

Time interval	Δ Accumulated oil [m ³]	Δ Accumulated water [m ³]
T1	0	0
T2	7000	-9300
T3	-4050	-149000
Total	2950	-158300

The AICV well is producing 7000 m³ more oil than the ICD well in T2, whereas the ICD well is producing 4050 m³ more oil than the AICV well during T3. Regarding the water production, AICVs are producing less water than ICD during T2 and T3. Totally, during the time period of 2000 days, the AICV well is producing 2950m³ more oil and 158300m³ less water than the ICD well.

In the simulations, the ICDs and AICVs were designed with the same ICD strength. The ICD strength is defined as the pressure drop over the inflow controller when 1 m³ of fluid is passing through. A high ICD strength is used to delay the water breakthrough. However, the AICVs are activated to close when the water reaches the well, and the AICVs can therefore be designed with a lower ICD strength. In that case, the AICVs would be able to produce oil at higher flow rates, and the production time could be reduced. The choke on the total flow was restricting the production to 1200 m³/day. The choke could also be adjusted based on the total water cut. In that case, the initial oil production would be higher, water breakthrough would occur earlier, and the advantage of using AICVs might be more significant. This can be taken into consideration in further studies.

In a horizontal well at Grane, the length of each section is 12.19 m, and each section includes one inflow controller. In the simulations, sections of 121.9 m was used and one large inflow controller was replacing 10 normal inflow controllers. This was done to reduce the

simulation time, and may have an effect on the production rates. However, both the technologies, AICV and ICD, were effected in the same way. Further simulations are needed to study the effect of using long compared to short sections.

4 Conclusion

The objective of this work was to study the effect of inflow controllers in a heterogeneous oil reservoir with an underlying water aquifer in the North Sea. The study included near-well simulations of oil production, using the reservoir software Rocx in combination with OLGA. Two types of technologies were studied; a passive inflow control device (ICD) and an autonomous inflow control valve (AICV). The results show that during 2000 days of production, the well with AICV completion produces 2950 m³ more oil and 158300 m³ less water than the well with ICD completion. This indicates that AICV technology can increase oil production and simultaneously decrease water production in reservoirs with fractures or other heterogeneities.

References

H. Aakre, B. M. Halvorsen, B. Werswick, V. Mathiesen. Autonomous Inflow Control Valve for Heavy and Extra-Heavy Oil, *SPE171141, SPE Heavy and Extra Heavy Oil Conference*, Latin America, Medellin, Colombia, 24-26 September, 2014

H. Aakre, B.M. Halvorsen, B. Werswick, V. Mathiesen. Smart well with autonomous inflow control valve technology, *SPE 164348-MS, SPE Middel East Oil and Gas Show and Exhibition*, Barhain, March, 2013

Arash Abbasi and Britt M. E. Moldestad. Simulation of light oil production from heterogeneous reservoirs. Well completion with inflow control devices. *9th EUROSIM Congress on Modelling and Simulation Oulu, Finland 12-16 September 2016*. IEEE 2016 ISBN 978-1-5090-4119-0. pp. 836-841/2016, 2016.

Jayalanka L. Badalge, Britt M. Halvorsen, Near well simulation of CO₂ injection for Enhanced Oil Recovery (EOR), *Linköping Electronic Conference Proceedings* (119) pp. 309-318, 2015

T. Ellis, A. Erkal, G. Goh, T. Jokela, S. Kvernstuen and E. Leung. Inflow Control Devices- Raising Profiles, *Oilfield Review*, pp. 30-31, 2010.

Nora C. I Furuvik and Britt M. E. Moldestad. Distribution of CO₂ in Fractured Carbonate Reservoirs. *International Journal of Energy Production and Management*, Volume 2 (1) pp. 28-38, 2017.

Geoscience News and Information. *Directional and Horizontal Drilling in Oil and Gas Wells*, *Geology.com*, date: 23.04.2017. Available from: <http://geology.com/articles/horizontal-drilling/>

Kou Guandong, Britt M. Halvorsen, (2015) Near Well Simulation of Extra Heavy Oil Production Using SAGD. *Linköping Electronic Conference Proceedings 2015* (119) pp. 157-168.

Halliburton. *Inflow Control Devices: Extending the Life of Mature Field Wells*, *Halliburtonblog.com*, date: 13.05.2017. Available from: <http://halliburtonblog.com/inflow-control-devices-extending-the-life-of-mature-field-wells/>

M. H. Jonskås, V. Mathiesen, B. M.E. Moldestad. Heavy oil production with energy effective Steam Assisted Gravity Drainage. *International Journal of Energy Production and Management*; Volum 1. (4) pp. 349-358, 2016.

Amila C. Kahawalage, Britt M. Halvorsen. Near well CFD simulation for extra heavy oil production using SAGD. *Linköping Electronic Conference Proceedings* (119) pp. 247-254, 2015.

Kais, R., Mathiesen, V., Aakre, H., Woiceshym, G., Elarabi, A., Hernandez, R., First Autonomous Inflow Control Valve (AICV) Well Completion Deployed in a Field under an EOR (Water & CO₂ Injection) Scheme, *SPE-181552-MS*, Dubai, UAE, 26-28 September 2016

V. Mathiesen, H. Aakre, B. Werswick The Next Generation Inflow Control-the Next Step to Increase Oil Recovery on the Norwegian Continental Shelf, *SPE 169233*, 2014.

Emmanuel Okoye and Britt M. E. Moldestad. Simulation of heavy oil production using Inflow Control Devices, A comparison between the Nozzle Inflow control Device and Autonomous Inflow Control Device. *9th EUROSIM Congress on Modelling and Simulation Oulu, Finland 12-16 September 2016*. IEEE 2016 ISBN 978-1-5090-4119-0. pp. 808-813, 2016.

Schlumberger. *Oilfield Glossary/Joint*, *slb.com*, date: 11.05.2017. Available from: <http://www.glossary.oilfield.slb.com/Terms/j/joint.aspx>, 2017.

Schlumberger. Fundamentals of Wettability. *Oilfield Review*, number 2, Volume 19, page 66-71. Summer 2007.

Mathias Tangen. Wettability Variations within the North Sea Oil Field Frøy. *Master Thesis, Norwegian University of Science and Technology*, Department of Petroleum Engineering and Applied Geophysics, 2012.

R.E. Terry and J.B. Rogers. Introduction to Petroleum Reservoirs and Reservoir Engineering. *Applied Petroleum Reservoir Engineering*, third edition, 2014.

Ramesh Timsina. Near-well simulations and modelling of oil production from reservoir. *Master Thesis, University College*

of South-East Norway, Faculty of Technology, Natural sciences and Maritime sciences, 2017.

D.I. Erandi N. Wijerathne and Britt M. Halvorsen, Computational study of fingering phenomenon in heavy oil reservoir with water drive, *Fuel Vol. 158*, pp. 306-314, 2015.

Ambrose Ugwu and Britt M. E. Moldestad. The Application of Inflow Control Device for an Improved Oil Recovery Using ECLIPSE. I: 2016 9th EUROSIM Congress on Modelling and Simulation Oulu, Finland 12-16 September 2016. *IEEE 2016 ISBN 978-1-5090-4119-0*. pp. 689-694, 2016.

Towards Effective Automatic Feedback for Simulator Training

Laura Marcano¹ Anis Yazidi² Mexhid Ferati² Tiina Komulainen¹

¹ Department of Electronic Engineering, Oslo and Akershus University College of Applied Sciences (HiOA), Norway

² Department of Computer Science, Oslo and Akershus University College of Applied Sciences (HiOA), Norway,
{Laura.Marcano, Anis.Yazidi, Mexhid.Ferati, Tiina.Komulainen}@hioa.no

Abstract

The presence of an expert instructor during simulator training is of great importance for the trainees, if not indispensable. The instructor's role is to give feedback and guide the trainees to help them make the right decisions on time as effectively as possible. The instructor starts or pauses the training scenarios when needed and facilitates reflection during and after the scenarios. However, the fact that simulator-training sessions are very dependent on the participation of a guiding instructor can be a drawback, since there are not always sufficient expert instructors to fulfil the training demands. In this work, an intelligent tutoring system (ITS) is proposed as an automatic feedback solution for simulator training. It is based on effective assessment of the system conditions using a clustering based anomaly detection technique as a core component. Furthermore, we provide insights into the design of a proper interface for our ITS. The article presents the methodology for developing such a system which consists of three stages: data collection, data analysis and delivering feedback.

Keywords: simulator training, anomaly detection, automatic feedback, intelligent tutoring system

1 Introduction

Operators training is a matter of great importance in different industries, as effective training leads to highly competent operators, which are able to maintain safe operations and handle abnormal plant situations when needed (Nazir et al., 2015). The most common training practice necessitates the physical presence of operators in a simulator training center, where they can be in a room that is designed and furnished in such a way that it closely represents an actual control room. In there the operators interact with an Operator Training Simulator (OTS) (Kluge et al., 2009, Patle et al., 2014). During the simulator training sessions, the operators are guided by an expert instructor, and the presence of the instructor is essential since s/he takes care of starting or pausing the simulation scenarios, gives feedback to the operators and guides them to find the best possible solution to the encountered incidents. Although the guidance of the instructors is of great advantage thanks to their experience and the knowledge they can share with the

trainees, the traditional operator training practices also have several drawbacks as the operators need to be physically collocated with the instructor in the simulator training center. This scenario is illustrated in Figure 1. The mobilization of the operators can represent a high economical cost for the company investors in addition to a loss of personal time for the participants of the training session. Further, the availability of instructors is limited, which also limits the amount of operators that can be trained at the same time. Therefore, there is a need for more independent operator training practices that could overcome the current disadvantages.

In the search for more independent training practices, several simulator training sessions have been carried out with students at Oslo and Akershus University College of Applied Sciences (HiOA), in order to observe and evaluate the needs of the trainees during simulator training sessions (Marcano and Komulainen, 2016, Marcano et al., 2017b). In our latest research (Marcano et al., 2017a) an automatic assessment tool was tested, and even though the trainees found it helpful, they still considered that the feedback and direction given by the instructor was necessary. Hitherto, this indicated that the relevance of the instructor lies in the feedback and

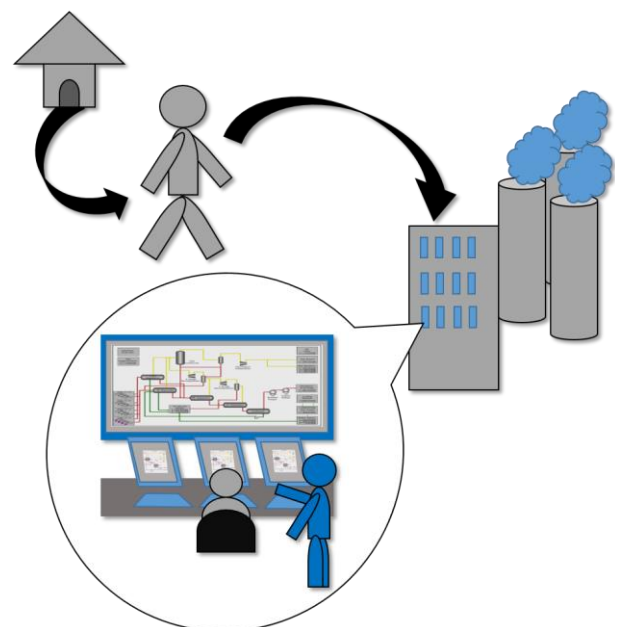


Figure 1. Traditional operator training

guidance s/he gives to the trainees. Consequently, for an independent simulator training session to be successful, an effective automatic feedback is required. In this way, the dependence on the instructor can be decreased for certain aspects of the training scenarios. Moreover, there already exists extensive research on systems that represent an alternative to expert human instructors and provide automatic guidance and feedback to trainees. These systems are known as intelligent tutoring systems (ITS) (Gonzalez-Sanchez et al., 2014). ITS are better known for being implemented in academic purposes, especially in higher education. Nevertheless, the concept of ITS is widely applied in different fields as it consists of offering independent computerized learning, which in the current era could be applicable to almost everything. A relevant example of ITS implementation is found in game-based training (Goldberg and Cannon-Bowers, 2015, Hooshyar et al., 2016), which can be compared to simulator training, and is a motivation for considering the implementation of ITS as a possible option towards more independent simulator training practices.

Combining an ITS with simulator training implies that the ITS must know the state of the process in order to be able to give any feedback to the user. It must be able to recognize the abnormal situations when they occur and inform the trainee about it in an effective way, so that s/he can handle the emergencies in time and prevent them from escalating.

There are different key parameters that characterize industrial processes, such as temperature, pressure, flow rates, energy consumption, mass and energy balances, environmental factors, equipment key performance indicators (KPI) and optimal value ranges for some key measurements of the process. Prompt feedback from the ITS can be based on the analysis of these key parameters, which can represent an extensive amount of data. Therefore, the ITS integrated to simulator training must be based on a proper data analysis technique. A well-known technique for monitoring the well-functioning of a system based on data flow is anomaly detection. In simple terms, anomaly detection aims to identify patterns in data that move away from the expected behavior. Anomaly detection is applied within an extensive range of different domains such as fraud detection for credit cards, health care, intrusion detection for cyber-security, and fault detection in safety critical systems (Chandola et al., 2009). The industrial processes simulated for operator training are safety critical systems that produce a large amount of data. Due to this reason, anomaly detection is considered as a suitable technique for the ITS to determine the process status. This work proposes a suitable architecture design for an ITS based on anomaly detection, integrated into an operator training simulator. The aim of this proposal is to settle a basis towards autonomous simulator training.

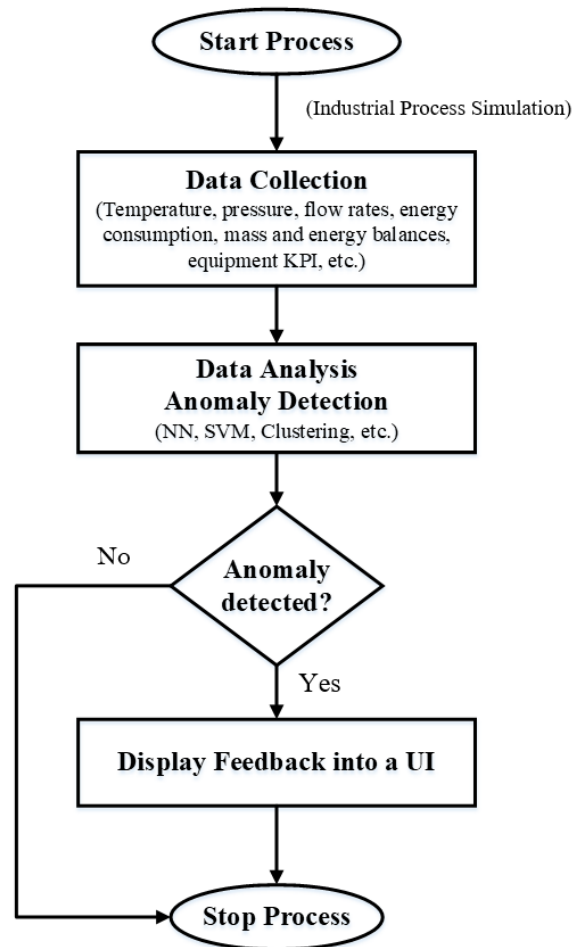


Figure 2. Technical Implementation

2 Methodology

The functioning of the proposed ITS integrated to a dynamic simulator consists of three stages online. First, data from the simulation process is collected. Next, the data must be analyzed in order to determine the status of the process and identify changes or abnormalities. Finally, the results from the data analysis are shown to the trainee through a smart user interface (UI), so that they can easily understand the status of the process. Further, the presentation of the process status should be accompanied with relevant feedback and suggestions when necessary to improve the system conditions. Figure 2 shows an overview of the technical implementation of the proposed ITS for simulator training.

2.1 Data collection

Relevant information that describe the system must be collected. Industrial processes are monitored by distributed control systems, which are characterized by producing a large amount of data that correspond to

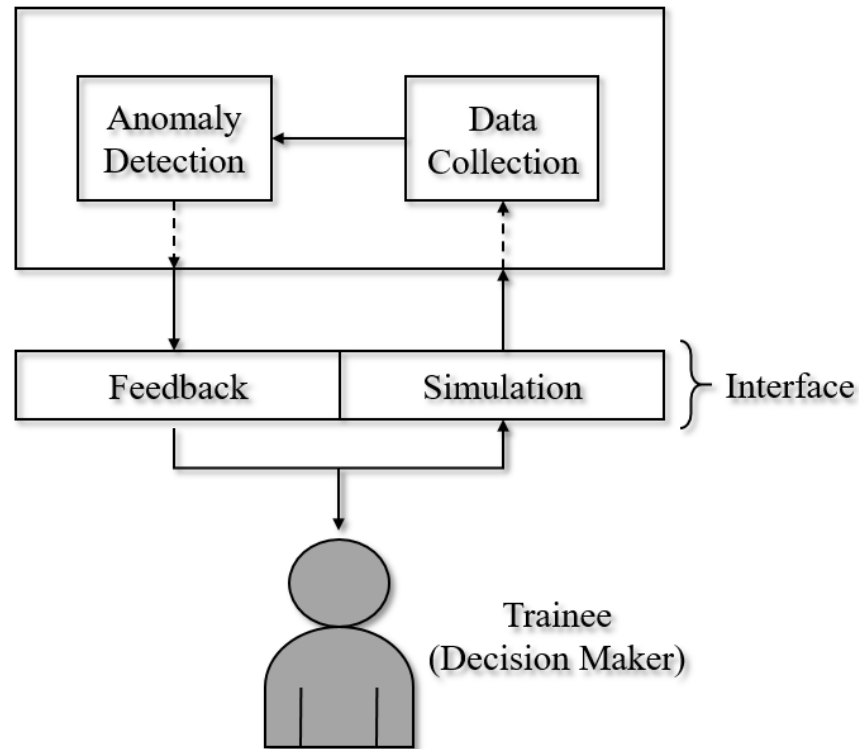


Figure 3. Interaction design

many different sensor signals with information about the process. Therefore, the data should be chosen strategically, it must be determined which parameters are significant enough to represent the status of the system. Further, since industrial processes consist of a combination of different smaller subsystems, in order to be able to monitor the process to all its extension, relevant data must be gathered from each of the subsystems involved in the process. Some examples of pertinent parameters that describe an industrial process are temperature, pressure, flow rates, energy consumption, mass and energy balances, environmental factors, and KPI of the equipment. Further, there exist optimal value ranges for certain key measurements of the process.

In order to handle data properly, a well-structured database is needed. As long as the user is training with the simulator, the representative parameters of the process should be sent to the database, so that the status of the process is analyzed continuously. This is illustrated in Figure 3, which was inspired by Figure 1.1 shown in Chapter 1 of Polson and Richardson (2013).

2.2 Data Analysis

Data handling is an important aspect considering that numerous processes generate large amount of data, and it is imperative that this data is properly studied and analyzed so these processes can be kept with a good functioning. Anomaly detection consists of finding patterns in data that do not follow the expected behavior

(Chandola et al., 2009). Any deviation from the normal profile of the model is considered as an anomaly (Zaher and McArthur, 2007); its most common applications are related to cyber security. However, the concept of anomaly detection is applied in different fields, among which is the industrial damage detection, which refers to detection of different faults and failures in complex industrial systems (Chandola et al., 2009). This highlights the reason why this technique is considered suitable for monitoring the status of the simulation processes during simulator training.

On the other hand, simulator training is commonly implemented to train operators working with industrial processes; these processes are organized as distributed systems. A distributed anomaly detection technique is needed, so that a proper monitoring of an entire industrial process can be done, considering that relevant changes or abnormalities in the process can come from many different sources. Centralized methods are not suitable for distributed systems since they may not scale easily for real-time management (Thottan and Chuanyi, 1998). In order to detect anomalies for a complex system on a global level, the integration of information about the anomalies identified in single locations is required (Banerjee et al., n.d.). This means that an entity capable of integrating multiple data sources and interpretation techniques is needed.

There exists different anomaly detection techniques. In a survey conducted by Chandola et al. (2009) these techniques are organized into four main categories:

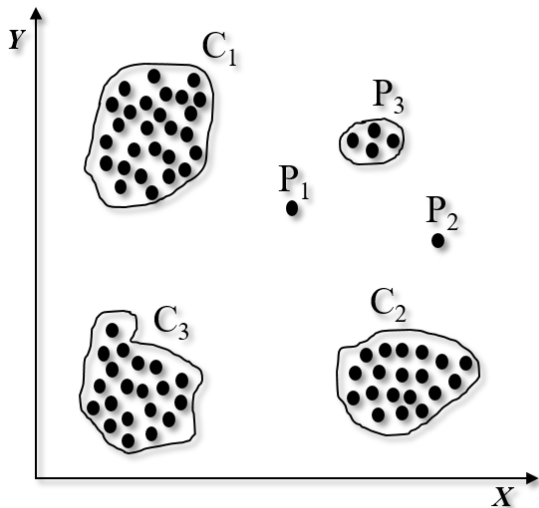


Figure 4. Example of clustering based outlier detection

- classification based, among which are included neural networks (NN), Bayesian network, support vector machine (SVM) and rule based;
- nearest neighbor based, which includes density and distance based techniques;
- clustering based;
- and statistical, which can be parametric or non-parametric.

For the case of the system proposed in this work, the chosen anomaly detection technique is clustering based, due to its simplicity and practicality for evaluating changes in data and sequences.

Clustering is used to group similar data instances into clusters (Chandola et al., 2009). Based on this concept, “normal” data instances belong to a specific cluster, while anomalies do not belong to any cluster.

For the proposed ITS, the first step is to observe the key parameters received from the simulated industrial process over a time window. The average of these parameters characterizes the “normal” system behavior. After gathering enough data to describe the system’s normal behavior, the clusters can be created. Consequently, abnormal operating modes can be identified if data falls out of the defined clusters. Figure 4 shows a simple example of this, where C_1 , C_2 and C_3 are regions of normal behavior, while P_1 , P_2 and P_3 are outliers that fall out of the defined clusters.

Moreover, the dynamicity of the system can be learned by studying the transitions that occur among clusters, the system can move from a normal behavior to an abnormal behavior. Nevertheless, the transitions can also indicate that the system is moving from a normal behavior to another type of normal behavior. Hence the importance of studying the dynamicity, so normal and abnormal changes are identified and classified correctly. The evaluation of the transitions among clusters is known as sequential pattern mining

(Rahman et al., 2016). Based on the definition given in Rahman et al. (2016), a sequence of cluster transitions can be defined as follows:

Let $C = \{c_1, c_2, \dots, c_l\}$ be a set of all clusters. A cluster set $C_x = \{c_1, c_2, \dots, c_m\} \subseteq C$ is a nonempty and unordered set of distinct clusters. A sequence S is an ordered list of clusters expressed as $\langle C_1, C_2, C_3, \dots, C_n \rangle$ such that $C_k \subseteq C$ ($1 \leq k \leq n$). An example of a sequence can be $S_1 = \langle \{3\}, \{1\}, \{2\}, \{1,3\} \rangle$, which is shown in Figure 5. Based on the normal sequence patterns of the system, abnormal changes can be identified to inform the operator.

2.3 Delivering Feedback

Once the data is analyzed, the results of the analysis must be presented to the user. This is a crucial stage, because successful training is related to effective feedback. Consequently, it is necessary to design a suitable user interface, which shows effectively what is relevant for the user to know, in a clear and understandable way. Figure 3 shows the design of the interaction between the user and the interface of the proposed ITS. The trainee should be able to see the simulation and the feedback about the process status at the same time. As long as the simulation is active, data should be gathered and analyzed in order to identify if there is any abnormal change in the process. Any abnormality must be indicated to the trainee together with some guidance on what could have caused the situation or how it could be solved. However, the trainee has the final decision on how to proceed after getting feedback from the system.

The design of the user interface is a very important matter because it must guarantee that the user will be comfortable with it, it should be easy to use and understand, and it should enable the users to attain the

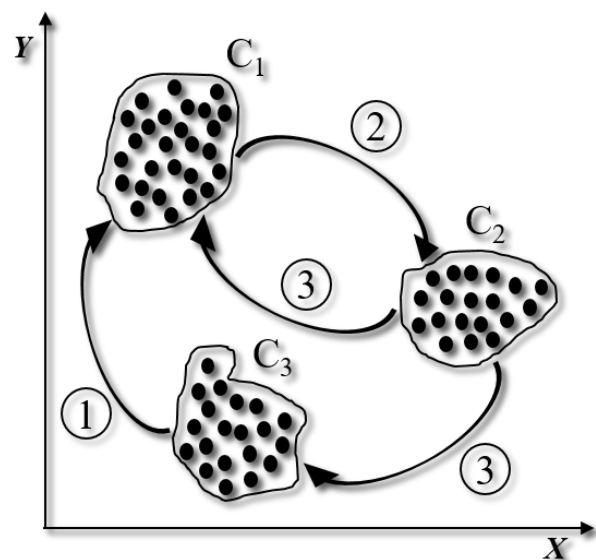


Figure 5. Example of a sequence of clusters transition

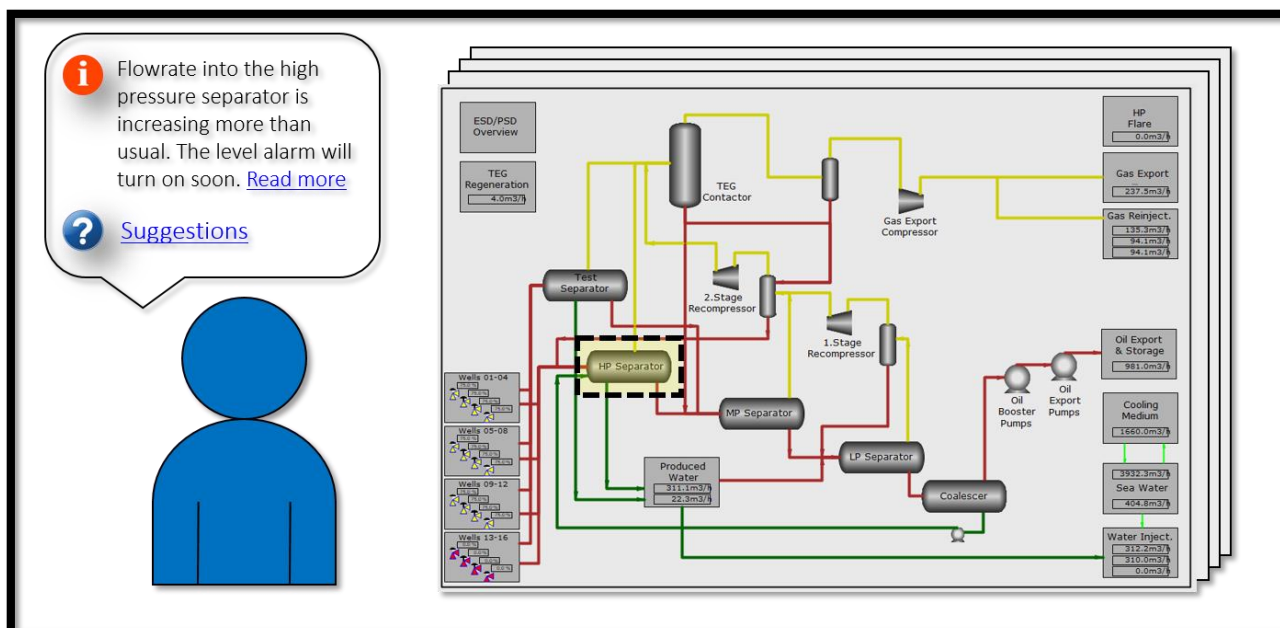


Figure 6. Example of a user interface for the proposed ITS (K-Spice®)

goal of handling successfully any abnormality or emergency that may occur in the system. Stone et al. (2005) indicate that a good user interface design promotes easy, natural, and engaging interaction between the user and the system, making the user forget that s/he is using a computer. These characteristics must (Chandola et al., 2009) be targeted in order to ensure a proper feedback delivery to the user about the simulation process.

There exists different guidelines to create a proper interface, and according to Johnson (2010) the two best-known are Shneiderman and Plaisant (2009) and Nielsen and Molich (1990). There are several matching points between these two guidelines, and both agree that a user interface must (Nielsen, 1995):

- be consistent: the user should not be wondering about the meaning of what is shown on the interface i.e., it should follow platform conventions.
- prevent errors: the design should be made in such a way that it avoids the user from making mistakes.
- make the users feel they are in control: one way to give freedom to the user is by supporting undo and redo options.
- minimize the user's memory load: the user should not have to remember information from one dialogue to another, it should be easy to access any information needed.

Based on these guidelines, Figure 6 illustrates how the final user interface of the proposed ITS should look like. The figure shows an example where the tutoring system informs the trainee that the flowrate into the high-pressure separator is increasing more than usual and that the alarm will activate soon. It also offers more

information in case the trainee wants to know more details about what is happening in the system. Further, the tutoring system generates suggestions to help the user handle the abnormal situation, enabling her/him to decide freely if s/he wants to read the suggestions or not.

3 Discussion

It is expected that the implementation of automatic feedback for simulator training will lead to more independent operators and will enable the possibility of training a higher number of operators at the same time, currently an instructor may work with two to six operators in one simulation session. With an intelligent tutoring system, this number can increase. Moreover, given the independence offered by an ITS, operators will be able to train and practice with the simulator in any place, at any time, which will allow them to be more prepared for the training at the simulator training center. Hence, the training time at the center can be decreased, which in turn represents economic savings for the company investors and time saving for the operators and the instructors.

With the ITS, the operators will be able to receive feedback shortly after they make changes in the process or while they are following certain procedures, which will give them the opportunity to solve in time any mistake they could possibly make. Further, the ITS, compared to control alarms, is more susceptible to process changes, which will also help the operators to practice identifying and solving problems before they escalate. It is expected that all the proposed advantages of the ITS will give as a result more prepared and competent operators.

4 Conclusion and Future Work

In this article, the integration of an intelligent tutoring system (ITS) into simulator training was proposed. This, with the aim to offer training independence to industrial operators through an effective automatic feedback tool. There exist important challenges with this proposal since in order to produce effective feedback for the operator, the status of the process must be evaluated constantly. Because of that, a clustering based anomaly detection technique is suggested. Further, the way feedback is delivered to the operator is an important challenge, because if relevant information fails to be delivered effectively, the operator will not be able to understand the message given by the ITS. Therefore, guidelines for user interface design especially for simulation and training contexts should be studied.

Future work includes the development and actual implementation of the proposed ITS. The ITS must be tested by users during simulator training sessions. A careful study of user's experience about the tool must be done in order to evaluate the performance of the ITS and its usability, so that it can be improved and developed further.

Acknowledgements

The authors would like to thank Marielviz Canelones and the PhD Candidate Ashish Rauniyar for their valuable input in designing Figures 1 and 2, respectively.

References

- Banerjee, A., Chandola, V., Kumar, V., Srivastava, J. & Lazarevic, A. n.d. *Anomaly Detection: A Tutorial* [Online]. University of Minnesota and United Technology Research Center. Available: <https://www.siam.org/meetings/sdm08/TS2.ppt> [Accessed 21 April 2017].
- Chandola, V., Banerjee, A. & Kumar, V. 2009. Anomaly detection: A survey. *ACM Computing Surveys (CSUR)*, 41, 1-58. DOI 10.1145/1541880.1541882
- Goldberg, B. & Cannon-Bowers, J. 2015. Feedback source modality effects on training outcomes in a serious game: Pedagogical agents make a difference. *Computers in Human Behavior*, 52, 1-11. <http://doi.org/10.1016/j.chb.2015.05.008>
- Gonzalez-Sanchez, J., Chavez-Echeagaray, M. E., Vanlehn, K., Burleson, W., Girard, S., Hidalgo-Pontet, Y. & Zhang, L. 2014. A system architecture for affective meta intelligent tutoring systems. DOI 10.1007/978-3-319-07221-0_67
- Hooshyar, D., Ahmad, R. B., Yousefi, M., Fathi, M., Horng, S.-J. & Lim, H. 2016. Applying an online game-based formative assessment in a flowchart-based intelligent tutoring system for improving problem-solving skills. *Computers & Education*, 94, 18-36. <https://doi.org/10.1016/j.compedu.2015.10.013>
- Johnson, J. 2010. Introduction. *Designing with the Mind in Mind*. Boston: Morgan Kaufmann. <https://doi.org/10.1016/B978-0-12-375030-3.00020-X>
- Kluge, A., Sauer, J., Schüler, K. & Burkolter, D. 2009. Designing training for process control simulators: a review of empirical findings and current practices. *Theoretical Issues in Ergonomics Science*, 10, 489-509. DOI 10.1080/14639220902982192
- Marcano, L. & Komulainen, T. 2016. Constructive Assessment Method for Simulator Training. *9th EUROSIM Congress on Modelling and Simulation*. Oulu, Finland: IEEE. DOI 10.1109/EUROSIM.2016.190
- Marcano, L., Komulainen, T. & Haugen, F. A. 2017a. Implementation of performance indicators for automatic assessment. *27th European Symposium on Computer Aided Process Engineering – ESCAPE 27*. Barcelona, Spain: (Accepted on May 2017).
- Marcano, L. A., Komulainen, T. M. & Sannerud, R. 2017b. An Interactive Teaching Module for Combined Simulation and Laboratory Work. *MNT-konferansen 2017*. Oslo, Norway.
- Nazir, S., Sorensen, L. J., Øvergård, K. I. & Manca, D. 2015. Impact of training methods on Distributed Situation Awareness of industrial operators. *Safety Science*, 73, 136–145. <http://dx.doi.org/10.1016/j.ssci.2014.11.015>
- Nielsen, J. 1995. *10 Usability Heuristics for User Interface Design* [Online]. Available: <https://www.nngroup.com/articles/ten-usability-heuristics/> [Accessed 22 May 2017].
- Patle, D. S., Ahmad, Z. & Rangaiah, G. P. 2014. Operator training simulators in the chemical industry: review, issues, and future directions. *Reviews in Chemical Engineering*, 30, 199–216. DOI 10.1515/revce-2013-0027
- Polson, M. C. & Richardson, J. J. 2013. *Foundations of Intelligent Tutoring Systems*, Routledge. doi:10.4324/9780203761557. 978-1-138-16101-6
- Rahman, A., Xu, Y., Radke, K. & Foo, E. 2016. Finding anomalies in SCADA logs using rare sequential pattern mining. DOI 10.1007/978-3-319-46298-1_32
- Stone, D., Jarrett, C., Woodroffe, M. & Minocha, S. 2005. *User interface design and evaluation*, Amsterdam, Elsevier. ISBN: 978-0-12-088436-0
- Thottan, M. & Chuanyi, J. 1998. Proactive anomaly detection using distributed intelligent agents. *IEEE Network*, 12, 21-27. DOI 10.1109/65.730748
- Zaher, A. S. a. E. & McArthur, S. D. J. 2007. A multi-agent fault detection system for wind turbine defect recognition and diagnosis. *2007 IEEE Lausanne Powertech Proceedings*. IEEE. DOI 10.1109/PCT.2007.4538286

Augmented and Virtual Reality for Engineering Education

Jaroslav Cibulka¹ George Anthony Giannoumis²

¹Department of Electronics Engineering, ²Department of Computer Science, Oslo and Akershus University College of Applied Sciences, Norway, {jaroslav.cibulka, gagian}@hioa.no

Abstract

Research on the application of augmented and virtual reality (AVR) in education shows that students self-motivation and performance increases as well as their attractiveness to new ICT-enhanced classes. The aim of this article is to explore the use of AVR as an engaging learning tool for engineering education and to present a framework for an AVR-lab for engineering education. The AVR-lab will encourage teachers to adapt classroom practices for state-of-the-art lectures that integrate AVR educational technology. The graduates of AVR-enhanced curriculum will attain new competencies in AVR, which industry analysts anticipate are vital for the 21st century labour market.

Keywords: Augmented Reality (AR), Virtual Reality (VR), Mixed Reality (MR), Engineering Education Pedagogy, Science, Technology, Engineering and Mathematics (STEM), Research-based Learning, Meta-learning, Technology-Enabled Active Learning (TEAL)

1 Introduction

To encourage interest of students and increase the attractiveness of engineering as a field of study remains a long-term challenge in the Norwegian education system. This article argues that this challenge may be remediated through the use of research-based learning methods, (NationalResearchCouncil, 2012, Singer and Smith, 2013, Nehm, 2014).

The augmented and virtual reality (AVR)-lab project at Oslo and Akershus University College of Applied Sciences originates from the idea of constructivist-oriented pedagogy established in a technology-enabled learning environment (TEAL) (Shieh, 2012). Scholars have shown that technology-enhanced constructivist pedagogy improves students' non-test learning outcomes - e.g., interest in classes, labs and extracurricular science activities (Shieh, 2012). Consequently, student achievement (performance, higher learning outcomes) can provide motivation for teachers to change traditional teaching practices (structured lectures, note-taking) and teaching beliefs, allowing for the integration of new technology - i.e., state-of-the-art lectures with integrated educational technology.

The AVR-lab project aims to encourage teachers to use new information and communication technology (ICT) pedagogical tools in teaching and learning. This

article argues that several mechanisms including communication and awareness, peer collaboration, evidence of improved student performance, and support from experts may help teachers to transform traditional instruction methods (structured lectures, note-taking) and adopt state-of-the-art lectures that integrate ICT.

This paper also relates to research on active learning methods such as the Flipped Classroom (FC), including methods to evaluate the study progress. Scholars have reported significant performance increase for students from the use of FC methods (Moravec et al., 2010, Day and Foley, 2006).

In comparison with typical definitions of FC methods (Bishop and Verleger, 2013), this article focuses on interactive and augmented learning resources (eBooks, exercises, games) instead of passive sources, such as instructional videos (asynchronous video lectures).

The AVR-lab aims to promote the practical application of active ICT-based pedagogy in teaching. Hence this article is dedicated to promoting ICT-enhanced cooperative learning using the FC, problem-based learning and meta-learning. Models of problem-based learning suggest that students gain topic-specific knowledge and skills related to meta-learning by engaging in activities that simulate "real-world" contexts and challenges. Research refers to meta-learning as an experiential process where students internalize norms, values and practices related to knowledge and skills acquisition (Rose et al., 2005).

In traditional approaches to learning, educational institutions treat the student as an object in the teaching process - i.e., the student is only a recipient of knowledge and information without any active role (Rose et al., 2005). Some scholars have argued that meta-learning provides a basis for students' to change their identity from recipients to creators of knowledge and understanding (Rose et al., 2005). As such, meta-learning may promote "employability" by enhancing self-efficacy and resilience among students. In the context of the FC, the roles, identities and implicit norms, values and expectations of students and teachers may act to subvert the implementation of the FC approach (Hagerup, 2017).

However, research has also shown that students experience barriers to education in curriculum design, teaching methods and learning resources (Coppola et al., 2015, Nicholas et al., 2014, Boles and Whelan, 2016, Litzinger et al., 2011).

According to (Rose et al., 2005) the Universal Design for Learning (UDL) is a reference model that guides educational practices, and aims to identify and remove barriers in educational methods, curricula and teaching materials. Taking a cue from research carried out on brain activity and the adoption of education technology, the UDL model provides the following guidelines:

- Representing the information in multiple formats and on different media.
- Providing students with multiple paths.
- Promoting many possibilities for expression and providing diversified ways to motivate students and arouse their interest.

UDL also frames learning as a process that can be designed to be accessible and inclusive for all students. The three principles stated above are supported by ICT to improve the learning process as follows:

- allow the manipulation and control of the learning environment.
- offer multi-sensory alternatives for learning materials.
- allow greater personal autonomy, especially for students with disabilities, such as attention and learning disabilities or sensory disabilities
- provide meaningful access to learning for all students by enabling students to grasp abstract concepts more fully.

This article argues that the combination of UDL and new ICT technologies in education can enable and empower students across the diversity of the human experience.

2 Need for research

Research shows that there is a need for continuous improvement in teaching, focusing on development of feedback culture and the use of new educational methods and tools (Deslauriers et al., 2011, Froyd et al., 2012, Singer et al., 2012, Nicol, 2010).

Currently, the textbooks and digital textbooks constitute the main source of learning materials (Vasileva et al., 2016, Hilton, 2016, Fan et al., 2013, Beetham and Sharpe, 2013). Nonetheless, research shows that students provided with only textbooks are less prepared for class than students provided with optional video lectures (de Grazia et al., 2012). Furthermore, students do not generally complete reading assignments (Sappington et al., 2002).

Textbooks are a passive source of information, in particular abstract terms, relationships, concepts, principles and processes, that lack multimedia interactivity - i.e., animations, visualizations and active simulations. Furthermore, feedback mechanisms, which are essential for improving learning outcomes, are also missing.

This article suggests updating pedagogical and curriculum approaches by transforming learning materials using state-of-the-art multimedia - e.g., using AVR, and Mixed Reality (MR). Student's attention and motivation are key factors for academic performance (Savage et al., 2011, Panisoara et al., 2015, Harandi, 2015, Law et al., 2010, Mendez and Gonzalez, 2011). Hence the aim is to encourage active learning by delivering interactivity into traditionally passive learning approaches and materials - e.g., lectures and textbooks.

Gamification in engineering education has not been fully adopted in schools, although the benefits of gamification have been shown in other fields (Pedreira et al., 2015, Dubois and Tamburrelli, 2013, Vasilescu, 2014, Hamari et al., 2014). Learning is best achieved through experiences - i.e., by using gamification to make tasks challenging and more engaging (Hamari et al., 2016, Ibáñez et al., 2014, Li et al., 2012, Barata et al., 2013b). Gamification supports peer-to-peer collaboration, social interaction and transcultural communication (Ducheneaut and Moore, 2004, Thorne, 2008, Thorne et al., 2009). Scholars have presented an AR crossover gamified design for engineering education in high school (Salman and Riley, 2016). Research has also posed a framework for using MR in gamification to assist teaching and learning in ICT (Muñoz et al., 2016). Active engagement and game challenges lead to improved learning processes and student outcomes (Guillén-Nieto and Aleson-Carbonell, 2012, Nicholson, 2015, Barata et al., 2013a, Domínguez et al., 2013, Clark et al., 2011).

MR provides immersive and engaging experiences through creative problem solving (Gardner and Elliott, 2014, Lindgren et al., 2016, Janßen et al., 2016, Thornhill-Miller and Dupont, 2016). MR has the potential to be a transformative technology in education - i.e., the ability to evoke empathy and the ability to trick the brain into experiencing another environment as real.

Social media are not implemented in curriculum although they can play important role as a beneficial infrastructure in learning processes (Krokan, 2012). Sharing allows students to collaborate and compete on assignments. Furthermore, social media often supports intercultural adaptation (Sawyer, 2011, Kosinski et al., 2015).

MR allows users to perceive the real world while virtual elements are superimposed upon or composited with the real world in real-time. Therefore, this article proposes to implement MR technologies to enhance learning, which may be applicable as an educational technology in various engineering courses.

The AVR-lab promotes the inclusion of new technology, teachers and all students - i.e., the target audience comprises students who experience barriers using traditional learning materials, students not engaged in engineering as a field of study, and students

with disabilities. Research has yet to examine the usability and accessibility of MR educational technologies for students with physical, sensory or cognitive disabilities.

Demands for MR-competences are increasing in the labour market and industry in Norway (Urke, 2016, Armstrong, 2017). However, MR as a pedagogical tool has yet to fulfill these demands and has yet to be fully adopted in the Norwegian education system. One exception is the one year programme in AVR at Høgskolen i Innlandet (INN, 2017). Nevertheless, governmental and institutional support for using AVR in education has yet to fully emerge. The Norwegian technology sector and entrepreneurs have yet to fully embrace MR as an educational technology and a viable business venture.

Regarding engineering education in higher education, a survey has been carried out at HiOA based on data from internal, external and student reports (Cibulka, 2017). The survey reveals the following common problems: fixed learning style; non-inclusive education; lack of motivation and engagement; less graduates; infrastructure issues; high drop-out rate; lonely students; low competence prerequisites from high school; lack of teacher's feedback; high students-to-faculty ratio; staff shortage; overworked staff; lack of research and development (R&D) activities; lack of student R&D extracurricular activities; lack of supervision; low attendance in lectures; labs and group classes; low levels of encouragement; equipment issues; lack of adoption of recent educational technology; lack of clarification of concepts and theories; poor results in exams (high failure-rate); lack of applicants, low recruitment, lack of attractiveness, lack of uniqueness; students have personal obligations; teachers missing tools (technology gap, training gap); teacher's knowledge gap; decision-makers missing knowledge; equipment cost; environmental load.

Engineering in higher education also experiences a high drop-out rate in mathematics (58% at HiOA). Research shows the economic benefit for the Norwegian economy if fewer students drop-out – i.e., approximately 1 million NOK per student (Falch et al., 2009, E24, 2013, Tunstad, 2013, Holstad, 2016). Furthermore, higher education institutions lose income for each student who fails a course and who drops out of a degree program.

3 State-of-the-Art

MR has been proven as efficient educational tool in many recent academic and magazine articles. A search in both popular and scientific literature has been conducted. Positive experiences with AVR in engineering education have shown that students self-motivation and performance increases as well as an attractiveness of the new ICT-enhanced classes.

Pearson, the leader in educational courseware, collaborate with Microsoft on MR learning content for colleges, universities and secondary schools (Overland, 2016). (Kosowatz, 2017) summarized current engineering applications (civil eng., manufacturing, mining, maintenance, medical) of MR and its further potential. (Park, 2016) presented MR platform Peer (internet-enabled sensors and headset) for middle school students allowing interaction with visualized abstract concepts and complex forces.

(Wu et al., 2013) presented current AR technologies used in education as a productive concept for educators, researchers, and designers. Three categories of instructional AR approaches to help students in learning are presented: roles, tasks and locations. The solutions for AR-related challenges for educators and students are also proposed, i.e. technological (multiple devices), pedagogical and learning issues (cognitive overloading, complex tasks).

(Kirner et al., 2012) presented a concept of AR multiple-point 3D artifacts allowing precise action point interactions and thus reduce the amount of markers. The empowered artifact with smart AR reactions is an authoring tool with use in education and cognitive rehabilitation. Tests shown its low cost, availability, user-friendly interfaces, multi-sensory, tangible interaction and non-demanding dexterity.

(Gutiérrez Martín and Meneses Fernández, 2014) presented a state-of-the-art review of AR in higher education in engineering, training and multimedia. This paper practically demonstrated its benefits in comparison with traditional instructional learning. AR effects enhances, motivates and stimulates the learning process by interacting on the augmented environments.

This paper presents a state-of-the-art review of AVR in education of Science, Technology, Engineering and Mathematics (STEM). The use of MR-pedagogy in engineering education was explored, particularly in chemistry, physics, automation, electrical, civil and mechanical engineering.

Ad electrical eng., (Martín-Gutiérrez et al., 2015) presented empirical study of 3 AR-Apps, incl. interactive learning scenarios. Tests were carried out with students of electrical engineering, specifically electrical machines course. Both autonomous studying and collaborative lab practices were evaluated positively (in usability and feedback surveys). The need for a teacher's assistance was reduced.

a) *ElectARmanual*

Authors tested AR-manual as a solution for overcrowded lab for electric machines, incl. 3D models and animations, wiring diagrams and sounds (Martin-Gutierrez et al., 2012). The App assists with sequential instructions to fulfill different tasks, e.g. installations and configurations of electrical machines.

b) *ELECT3D*

This Android AR-App enhances reading and comprehension of circuit diagrams, drawings, electrical symbols (both complex and realistic) and images. The App is universal since it uses extended library of normalized standard symbols and objects. AR is performed “marker-less”, i.e. by means of cloud of points (normalized symbol).

c) *ElectAR_notes*

In order to explain abstract (invisible) and difficult topics, principles and concepts in electrical engineering (vectors, electromagnetism, ferromagnetism, electrical machines), the notes book (Basic Electrical Machines) were enhanced with AR content, e.g. images, 3D objects, 3D animations; audio, video and text explanations. Such upgraded and interactive notes led to better interlink between theoretical (abstract) and practical teaching. The AR-notes have double AR-mark, i.e. both marker-less image and fiducial 4x4 AR-mark.

(Desai et al., 2013) included interactive features between multiple virtual electrical 3D components to complete and simulate simple circuits. Users appreciated understanding the causal relationship based on the changes made to the parameter of the 3D electrical components. (Souza and Kirner, 2012) presented AR-tool to practice simple circuits tasks related to electromagnetism.

Ad automation, (Frank and Kapila, 2017) integrated MMR (tablet) to interact with motor test-bed in lab activities. Students demonstrated improvement in their knowledge of dynamic systems and control concept.

Ad Physics, (Chi-Poot and Martin-Gonzalez, 2014) presented using AR in learning of Euclidean vectors properties. The system aids the user to understand physical concepts, such as magnitude and direction, along with operations like addition, subtraction and cross product of vectors. Kinect sensor was used to visualize virtual components merged in a user-interaction (body interactive) environment. Users were able to virtually create vectors with different magnitudes and directions, and visualize their properties and operations.

Ad Chemical engineering, (Andrade et al., 2014, Maier and Klinker, 2013b, Maier and Klinker, 2013a, Maier and Klinker, 2013c) demonstrated a haptic wireless hand held device, i.e. an AR cubic-marker tool, and the tracking software “Augmented Chemical Reactions”. This tool enables 3D molecules visualization, visualizing chemical properties, spatial relations and free direct manipulation with 3D interaction methods. The user immersion in chemistry learning had been improved, in comparison with a 2D representation in textbooks and molecular formula. The included chemical dynamics simulation helps to grasp the

abstract internals of chemical reactions (dynamics of the atoms in and between molecules). This AR tool also helps researchers in prototyping, developing and understanding new chemical molecules. Gesture control (a self-tuning gesture recognition algorithm) allows prototyping with creating multiple bonds between two virtual molecules.

(Cai et al., 2014) presented an empirical case study with interactive 3D AR-models to control and visualize abstract chemical structures, microstructures, composition of substances and concepts. Study also included set of inquiry-based AR learning tools. Data analysis has shown the AR tool improved cognitive performance and is effective for low-achieving students.

Ad mechanical eng., Autodesk and Microsoft integrates CAD software Fusion 360 into collaborative MR-app “FreeForm” for HoloLens, (Gardiner, 2015).

EON Reality, the worldwide leader in the field of interactive training (Cheben, 2017), and educational software (Singletary, 2017), presented AR Diesel Engine Training (Hio, 2016).

(Martín-Gutiérrez, 2011, Gutiérrez Martín and Meneses Fernández, 2014) introduced an augmented book for mechanical engineering course “L-Elira”. The virtual machine elements are represented by matching technical card containing information, e.g. use, rule number, standard element designation, graphic information, photorealistic images and an AR marker. AR fiducial marker allows visualization and animation of the 3D model. The authors reported in (Gutierrez and Fernandez, 2014) a better academic results and motivation of the first year mechanical engineering students. The exam results showed a significant statistical difference between academic performances of two groups (AR and classical notes), proving to be higher in the experimental group (AR); this group also showed a higher level of motivation than the control group (classical notes).

(Martín-Gutiérrez et al., 2010, Gutiérrez Martín and Meneses Fernández, 2014) introduced an augmented book AR-Dehaes for improving spatial abilities of mechanical engineering students by providing 3D virtual models and visualization tasks. A validation study of the remedial course confirmed positive impact on students’ spatial ability.

(Rizov and Rizova, 2015) presented the benefits of using AR in higher education, by measuring outcomes (improved results) of the students which used AR as a teaching tool in the mechanical engineering course.

Ad Civil eng., Microsoft, Trimble and University of Cambridge collaborate towards MR-apps for MS HoloLens (Scialom, 2017), e.g. SketchUp Viewer (Vardhan, 2016).

(Vassigh et al., 2016) presented AR-app AR-SKOPE for civil engineering education with integrated Building Information Modelling, showing the building's mechanical system information overlaid on the real building.

(Shirazi and Behzadan, 2015) presented a building structure model assembly using wooden blocks, equipped with AR-markers in order to teach abstract construction and civil engineering topics in a practical manner. This AR-based pedagogical tool led to a better performance, collaboration, communication and autonomous learning experience. Students in the test session worked in groups and received instructions from the virtual avatar, and scanned the tracking image attached to each building element to access information.

(Kirner et al., 2012) presented AR Spatial Tutor, a tool for interaction with panels and mockups (Styrofoam) using AR, to expose AR-layer (dynamic content), 3D objects, annotations, sounds and animations. Interactive points have multiple information elements that allow the expansion of contents or the fulfilling of different types of users.

As conclusion, the State-of-the-Art review revealed current trends in AR-Apps for engineering education. Good results from the exams and feedback surveys indicate beneficial use in engineering degrees. AR-approach can be applied in different engineering courses due to similar didactics and software. However, complex dynamic simulations are still missing in current AR-apps. Simulations should be implemented since it is important to see and understand any system response. For example, to study electrical circuits it is vital to understand the effects of value adjustment or component configuration. The training framework including instant learning feedback of learning outcome is also missing.

Current learning approaches does not reflect each individual student's skills and learning style. The AR-App should include feedback learning system with interactive examples and tasks. Such feedback is beneficial for student/teacher, allowing them to track the learning effectiveness and focus on difficult parts. Utilization of advances in Biofeedback and Artificial Intelligence (AI) is missing.

4 Concept of AVR-lab “Mi-ity”

We will utilize novel mobile MR solutions. We will focus on an engineer from the life-span perspective, i.e. all age scholar groups from kindergarten towards adult vocational training. We will establish hub “Mi-ity”, the mobile MR innovation hub for lifelong engineering education, at HiOA, together with our key industrial partners. The hub concept is illustrated in Figure 1.

We will test both engineering and non-engineering students to reveal if MR has positive learning effect (high learning outcomes) regardless background and interest. Mi-ity targets 3 user groups in lifelong spectra: students, teachers and decision makers. Testing and validation of MR-apps will be conducted in the selected pilot courses. We will conduct experiments in cooperation with our research and user partners.

4.1 Development of MR-education

The learning modules with MR will be designed based on the didactic model presented by (Bjørndal and Lieberg, 1978). Didactic model is used to design all the learning modules in a course.

Universal Design for Learning (Rose et al., 2005) is a reference model that will guide the development of educational MR-contents and practices, i.e. enables the learning process to be more accessible, universally

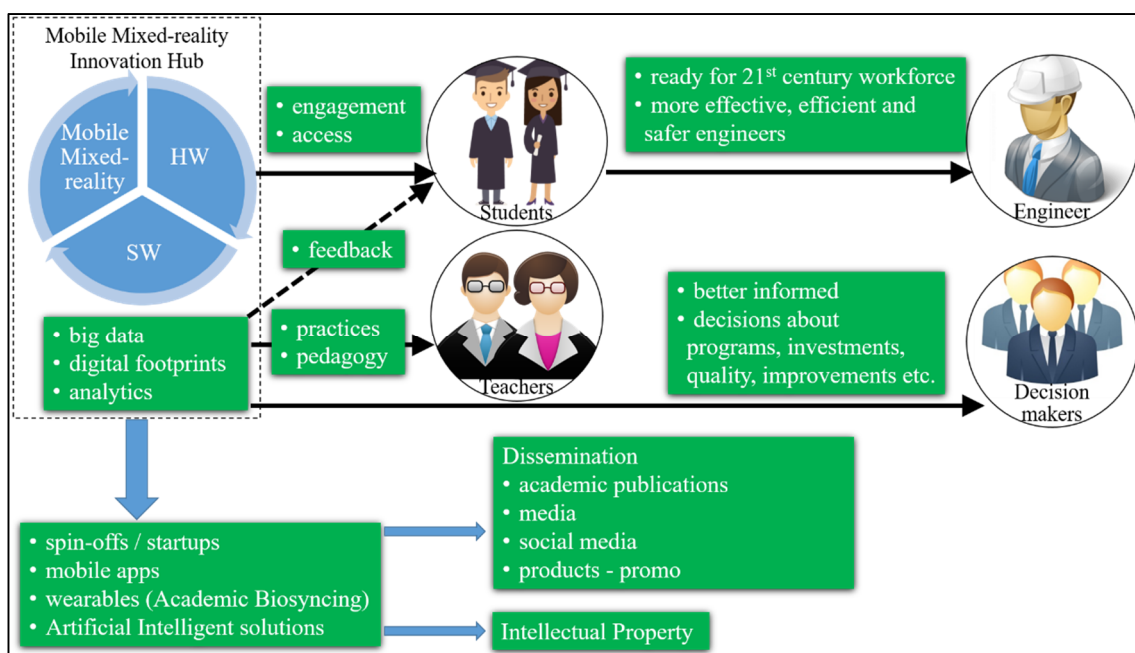


Figure 1. Concept of Mi-ity: the mobile mixed-reality innovation hub for lifelong engineering education

designed and inclusive for all students, incl. with learning or sensory disabilities.

MR platform comprises challenging tasks with gamification features. It covers engineering-related topics: mathematics, mechanical, electrical, control, biochemistry etc.

4.2 MR tool “MixRALF”

The new MR tool will cover virtual teaching contents, a multi-platform and interactive MR-Apps, learning feedback system, dynamic simulations, biofeedback and integration to social media.

We will develop “MixRALF”, the mobile mixed-reality system with the real-time autonomous learning feedback. MixRALF comprises MR, academic biosyncing (biometric wearables) and AI, see Figure 2. This unique combination has not been reported yet.

MR educational and engineering-related content will be developed in multiplatform tools, e.g. EON Studio, Unity 3D and Unreal. The MR content is scalable in both platform compatibility (smartphone ↔ headset) and contents (kindergarten ↔ university).

Microsoft HoloLens, a self-contained wearable holographic computer, will be used as mobile MR headset. We will also test wireless HTC Vive and smartphones.

We will further enhance the immersive MR-experience with an academic biosyncing. Academic biosyncing is a new concept of bio-mechanical symbiosis where scholar and machine are in a reactive, performance-augmenting loop, by means of biofeedback (biometric data, wearables) and AI, see Figure 2. Similarly to athletic biosyncing, it is expected that scholar change learning routines, i.e. enters into an automatic reactive state.

We will use biometric wearables to measure focus level, engagement, excitement or stress. Selected

biometric wearables: Insight by Emotiv (EEG headset for brain activity); wristband E4 by Empatica (galvanic skin response - electrodermal activity sensor, cardiovascular features - blood volume pulse, heart beat, heart rate variability, blood pressure etc.), see Figure 3.



Figure 3: Emotiv Insight (EEG headset) and wristband Empatica E4 (electrodermal and cardiovascular activity)

Voice (tone), gesture (controlled commands) and facial reaction recognition is already possible with HoloLens. Eye movement tracking is possible with HTC Vive (Durbin, 2017), and will be integrated in the next version of HoloLens as well (Walker, 2017).

MixRALF system comprises “Big Data” problem to be solved by AI. Integrative AI, i.e. generative AI and MR, will provide awareness about cognitive state, focus level and mental preparedness, and thus improve educational experiences in combination with MR. AI can be in the form of virtual teacher, capable to recognize skills, learning style and mental state. He (AI) will customize the learning approach and contents accordingly, to fit each individual student, i.e. he will track and train focus, and track and improve educational experiences.

For this mission we have selected IBM Watson (Bluemix developer platform) as the best AI technology. It is an advance AI cognitive system, already successfully proven in educational experiments (Goel et al., 2015, Goel, 2016). HiOA is the first “Watson-University” in Norway.

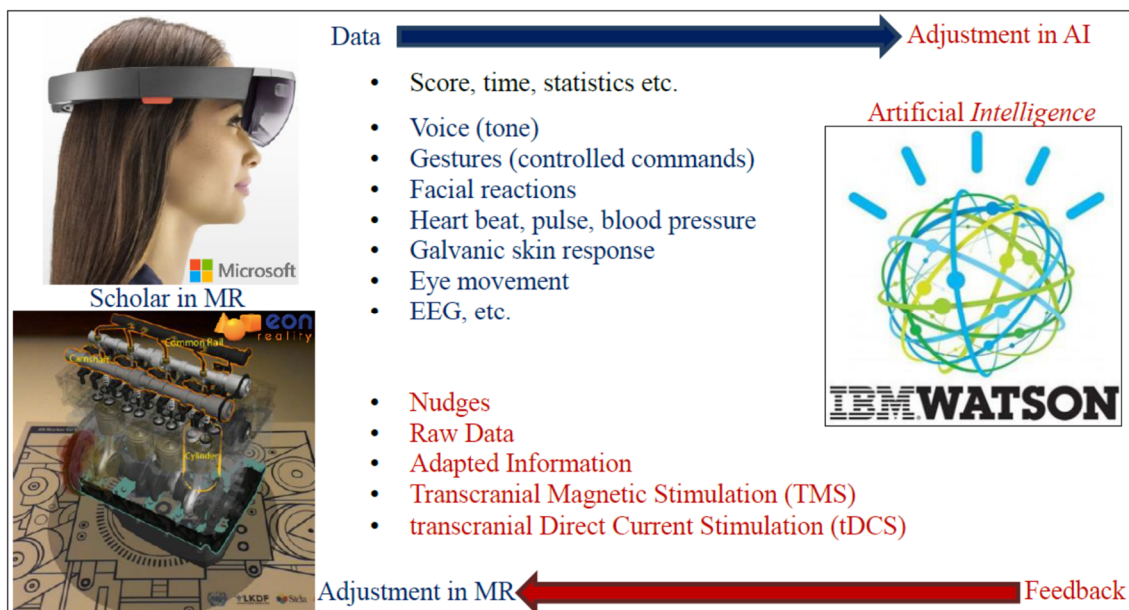


Figure 2. MixRALF - the mobile mixed-reality system with the real-time autonomous learning feedback

AI will also utilize digital footprints to recognize student's personally traits and mental state by digital means, e.g. intelligence, basic emotions etc. (Lambiotte and Kosinski, 2014). Introverts tend to belong to fewer but larger and denser communities, while extroverts tend to act as bridges between more frequent, smaller, and overlapping communities.

(Kosinski et al., 2016) presented methods to extract patterns and build predictive models using large data sets of digital footprints (mining big data). (Youyou et al., 2015) demonstrated that AI can predict personality, based on digital footprints, automatically and more accurately than human (friend), i.e. without involving human social-cognitive skills. AI and digital footprints will further help to state the learning ability and thus help to select the optimal MR tool for the best learning outcome.

With the help of AI and biometrics the scholar will be able to respond to its learning environments and more fully realize its learning potential. Student become aware of its cognitive state, mental preparedness and focus level, and thus improve educational experiences. The whole-body wellness and overall activity will be tracked and better understood. AI will identify personal traits and mental states of a student.

MixRALF will track and evaluate student's performance with combination of qualitative (observation by AI) and quantitative data (score, time, task statistics, biometrics), and adjust the individual learning approach accordingly. For example, the system identifies if student is bored and thus offer him a more challenging tasks and engagement in his studies. It will also feature the dynamic difficulty, i.e. AI will adjust the difficulty of task instantaneously, based on the real-time feedback. Thus AI decrease the difficulty level for

failing student in order to keep him engaged, motivated and prevent frustration, and vice versa, AI increases difficulty for prospering student.

MixRALF will output self-contained results about student's learning outcome and recommendation for improvement, i.e. includes feedback about scoring, time, interpretation of results and task statistics, e.g. design-related parameters such as cost, reliability, lifetime, stress strength etc. The feedback on learning progress will be available for students, teachers and decision makers, incl. comprehensive methodology to evaluate the study progress. The key performance indicators are learning outcomes, e.g. speed of learning.

4.3 Expected benefits

The potential for value creation is illustrated in Figure 4. Mi-ity will train next-gen students and teachers in the use of MR in educational settings and real pedagogical practice, i.e. reduce gap between education and new ICT.

Lab will provide rich, interactive, responsive and accessible learning experience. Real-time feedback and adjustment of learning scenario allows individual approach, i.e. for both students with disabilities and students with an over average mental capacity.

Mi-ity will promote active participation in lifelong learning process. Mi-ity enable faster adoption of Problem-based Learning and Flipped Classrooms by using MR-tools in interactive learning activities and teaching practice. MixRALF will increase the learning outcomes, i.e. students recognize, identify and grasp the knowledge, especially abstract concepts, faster and more meaningfully.

With AI training guidance the student will study independently and thus saves the teacher's time.

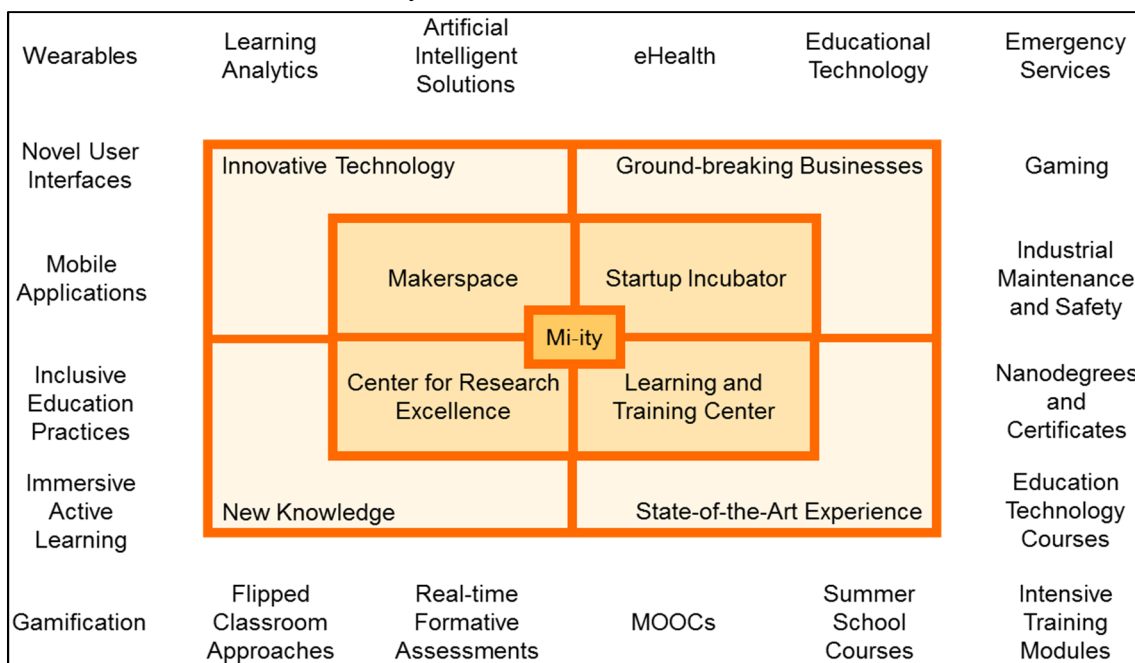


Figure 4. Mi-ity - Value Creation Potential

Teacher will have more time for creative work such as content development, class preparation, R&D, publishing etc. Teacher will be able to provide closer individual feedback to the student and encourage his critical thinking, reflection and creativity.

Decision makers will get more and accurate information/knowledge to perform better decisions about programs, investments, quality and improvements.

Mi-ity will reduce drop-out rate and thus reduce high expenses related to the failure-rate. The new educational system will increase the attractiveness of engineering curriculum and thus improve the recruitment of applicants.

Students will become better engineers and meet the increasing demands for MR-competences in labour market and industry in Norway. MR-enhanced curriculum will result in faster and effective development of engineering competences, i.e. instrumental competences (analysis and synthesis skills, planning and organization skills, solving problems, managing information as well as taking decisions), personal competences (teamwork, workplace interpersonal relations skills, critical reasoning), systemic skills (autonomous learning, leadership, initiative, entrepreneur, motivation for quality) and spatial skills. Students become self-motivated, independent and competent professional, reducing the ad-hoc occupational training cost.

Project promotes entrepreneurship in education technologies (release new MR apps) by collaboration of partners, HW- and SW-related students.

MR replaces physical equipment and thus eliminate the safety risk, expenses and power. Training with virtual equipment decreases a fear for further real practice with e.g. electric circuits, soldering, welding etc. MR decrease demands and cost for physical infrastructure e.g. study rooms, labs, auditoriums. MR shifts physical learning space into a virtual learning environment, which also allows student's remote participation.

MR, gamification and social media will diminish the intercultural differences and support better cooperation and communication between peers with different cultural background.

5 Conclusion

The State-of-the-Art review revealed positive experiences with application of MR in engineering education. However, the recent solutions does not reflect advances in biofeedback wearables and AI, towards further improvement of learning feedback and outcome. Therefore we proposed a project concept of AVR-lab, where we will test the mobile MR in closed-loop combination with biometrics and AI. We focus on improving student's learning performance and teacher's

knowledge transfer in the lifelong perspective. The real-time learning feedback will tailor the educational approach to fit each student individually. The new autonomous learning system will allow independent study and thus save the teacher's time. Gamification of task challenges will create an attractive and motivational tool for the student. The new MR-enhanced curriculum will reflect the rapidly increasing competence demands for MR technology in the engineering industry and labor market in Norway.

Acknowledgments

The authors would like to thank assoc. prof. Tiina M. Komulainen for her valuable inputs.

References

- Andrade, T. F., Maier, P., Quintas, M. R., Klinker, G. & Restivo, M. T. Adding sensorial capabilities to the augmented chemical reactions application. 2014 11th International Conference on Remote Engineering and Virtual Instrumentation (REV), 26-28 Feb. 2014. 217-218. <http://dx.doi.org/10.1109/REV.2014.6784259>
- Armstrong, V. 2017. Teknologi som kan forandre verden. *E24*.
- Barata, G., Gama, S., Jorge, J., Gon, D., #231 & Alves 2013a. Improving participation and learning with gamification. *Proceedings of the First International Conference on Gameful Design, Research, and Applications*. Toronto, Ontario, Canada: ACM. <https://doi.org/10.1145/2583008.2583010>
- Barata, G., Gama, S., Jorge, J. & Goncalves, D. Engaging Engineering Students with Gamification. 2013 5th International Conference on Games and Virtual Worlds for Serious Applications (VS-GAMES), 11-13 Sept. 2013 2013b. 1-8. <https://doi.org/10.1109/VS-GAMES.2013.6624228>
- Beetham, H. & Sharpe, R. 2013. *Rethinking Pedagogy for a Digital Age: Designing for 21st Century Learning*, Taylor & Francis.
- Bishop, J. L. & Verleger, M. A. The Flipped Classroom: A Survey of the Research. 2013 ASEE Annual Conference, 2013 Atlanta. American Society for Engineering Education.
- Bjørndal, B. & Lieberg, S. 1978. *Nye veier i didaktikken?: en innføring i didaktiske emner og begreper*, Oslo, Aschehoug.
- Boles, W. & Whelan, K. 2016. Barriers to student success in engineering education. *European Journal of Engineering Education*, 1-14. <https://doi.org/10.1080/03043797.2016.1189879>
- Cai, S., Wang, X. & Chiang, F.-K. 2014. A case study of Augmented Reality simulation system application in a chemistry course. *Computers in Human Behavior*, 37, 31-40. <http://dx.doi.org/10.1016/j.chb.2014.04.018>
- Cheben, M. 2017. EON Reality Releases EON Enterprise Virtual Trainer (EVT) To Address Today's Growing Knowledge Gap In The Global Industrial Workforce. *Marketwired*.
- Chi-Poot, A. & Martin-Gonzalez, A. 2014. Euclidean Vectors in Physics Education Using Augmented Reality. In: DE PAOLIS, L. T. & MONGELLI, A. (eds.) *Augmented and Virtual Reality: First International Conference, AVR 2014, Lecce, Italy, September 17-20, 2014, Revised Selected Papers*. Cham: Springer International Publishing. http://dx.doi.org/10.1007/978-3-319-13969-2_30
- Cibulka, J. 2017. Problems in quality of engineering education at HiOA: Faculty of Technology, Art and Design (TKD), survey report. HiOA.

- Clark, D. B., Nelson, B. C., Chang, H.-Y., Martinez-Garza, M., Slack, K. & D'angelo, C. M. 2011. Exploring Newtonian mechanics in a conceptually-integrated digital game: Comparison of learning and affective outcomes for students in Taiwan and the United States. *Computers & Education*, 57, 2178-2195. <http://dx.doi.org/10.1016/j.compedu.2011.05.007>
- Coppola, S. M., Madariaga, L. A. & Schnedeker, M. H. 2015. Assessing Teachers' Experiences with STEM and Perceived Barriers to Teaching Engineering. *2015 ASEE Annual Conference & Exposition*. Seattle, WA: American Society for Engineering Education.
- Day, J. A. & Foley, J. D. 2006. Evaluating a Web Lecture Intervention in a Human-Computer Interaction Course. *IEEE Transactions on Education*, 49, 420-431. <http://dx.doi.org/10.1109/TE.2006.879792>
- De Grazia, J. L., Falconer, J. L., Nicodemus, G. & Medlin, W. Incorporating ScreenCasts into Chemical Engineering Courses 2012 ASEE Annual Conference, 2012.
- Desai, R., Dave, R., Mehta, R., Joshi, A. & Benjamin, S. 2013. Interactive Circuits Using Augmented Reality. *International Journal Of Scientific and Engineering Research*, 4, 778-781.
- Deslauriers, L., Schelew, E. & Wieman, C. 2011. Improved Learning in a Large-Enrollment Physics Class. *Science*, 332, 862-864. <https://doi.org/10.1126/science.1201783>
- Domínguez, A., Saenz-De-Navarrete, J., De-Marcos, L., Fernández-Sanz, L., Pagés, C. & Martínez-Herráiz, J.-J. 2013. Gamifying learning experiences: Practical implications and outcomes. *Computers & Education*, 63, 380-392. <http://dx.doi.org/10.1016/j.compedu.2012.12.020>
- Dubois, D. J. & Tamburrelli, G. 2013. Understanding gamification mechanisms for software development. *Proceedings of the 2013 9th Joint Meeting on Foundations of Software Engineering*. Saint Petersburg, Russia: ACM. <https://doi.org/10.1145/2491411.2494589>
- Ducheneaut, N. & Moore, R. J. 2004. The social side of gaming: a study of interaction patterns in a massively multiplayer online game. *Proceedings of the 2004 ACM conference on Computer supported cooperative work*. Chicago, Illinois, USA: ACM. <http://dx.doi.org/10.1145/1031607.1031667>
- Durbin, J. 2017. HTC Vive Is Getting A \$220 Plug-And-Play Eye Tracking Peripheral Next Month. *UploadVR*.
- E24 2013. Professor: Elever forstår tall dårligere enn før. *E24*.
- Falch, T., Johannesen, A. B. & Strøm, B. 2009. Kostnader av frafall i videregående opplæring. TRONDHEIM: SENTER FOR ØKONOMISK FORSKNING AS.
- Fan, L., Zhu, Y. & Miao, Z. 2013. Textbook research in mathematics education: development status and directions. *ZDM*, 45, 633-646. <https://doi.org/10.1007/s11858-013-0539-x>
- Frank, J. A. & Kapila, V. 2017. Mixed-reality learning environments: Integrating mobile interfaces with laboratory test-beds. *Computers & Education*, 110, 88-104. <https://doi.org/10.1016/j.compedu.2017.02.009>
- Froyd, J. E., Wankat, P. C. & Smith, K. A. 2012. Five Major Shifts in 100 Years of Engineering Education. *Proceedings of the IEEE*, 100, 1344-1360. <https://doi.org/10.1109/JPROC.2012.2190167>
- Gardiner, G. 2015. Microsoft HoloLens + Autodesk Fusion 360 = Mixed Reality for Product Design and Engineering. *In the Fold, Autodesk*.
- Gardner, M. R. & Elliott, J. B. 2014. The Immersive Education Laboratory: understanding affordances, structuring experiences, and creating constructivist, collaborative processes, in mixed-reality smart environments. *EAI Endorsed Transactions on Future Intelligent Educational Environments* 1. <https://doi.org/10.4108/fiee.1.1.e6>
- Goel, A. 2016. Using Watson for Constructing Cognitive Assistants. *Advances in Cognitive Systems*, 4.
- Goel, A., Creeden, B., Kumble, M., Salunke, S., Shetty, A. & Wiltgen, B. 2015. *Using Watson for Enhancing Human-Computer Co-Creativity*.
- Guillén-Nieto, V. & Aleson-Carbonell, M. 2012. Serious games and learning effectiveness: The case of It's a Deal! *Computers & Education*, 58, 435-448. <http://dx.doi.org/10.1016/j.compedu.2011.07.015>
- Gutiérrez Martín, J. & Meneses Fernández, M. D. 2014. Augmented Reality Environments in Learning, Communication and Professional Contexts in Higher Education. *Digital Education Review*, 26, 22-34.
- Gutierrez, J. M. & Fernandez, M. D. M. 2014. Applying Augmented Reality in Engineering Education to Improve Academic Performance & Student Motivation. *International Journal of Engineering Education*, 30, 625-635.
- Hagerup, N. 2017. Challenging the Auditorium: How to Flip a Classroom in a Room that cannot be Flipped? *19th International Conference on Engineering and product Design Education*. Oslo.
- Hamari, J., Koivisto, J. & Sarsa, H. Does Gamification Work? -- A Literature Review of Empirical Studies on Gamification. 2014 47th Hawaii International Conference on System Sciences, 6-9 Jan. 2014. 3025-3034. <https://doi.org/10.1109/HICSS.2014.377>
- Hamari, J., Shernoff, D. J., Rowe, E., Coller, B., Asbell-Clarke, J. & Edwards, T. 2016. Challenging games help students learn: An empirical study on engagement, flow and immersion in game-based learning. *Computers in Human Behavior*, 54, 170-179. <https://doi.org/10.1016/j.chb.2015.07.045>
- Harandi, S. R. 2015. Effects of e-learning on Students' Motivation. *Procedia - Social and Behavioral Sciences*, 181, 423-430. <http://dx.doi.org/10.1016/j.sbspro.2015.04.905>
- Hilton, J. 2016. Open educational resources and college textbook choices: a review of research on efficacy and perceptions. *Educational Technology Research and Development*, 64, 573-590. <https://doi.org/10.1007/s11423-016-9434-9>
- Hio, L. 2016. Augmented and virtual reality firm Eon Reality sets up R&D centre in Singapore. *The Straits Times*.
- Holstad, G. 2016. Forsker på drop outs. *Adresseavisen*.
- Ibáñez, M. B., Á, D.-S. & Delgado-Kloos, C. 2014. Gamification for Engaging Computer Science Students in Learning Activities: A Case Study. *IEEE Transactions on Learning Technologies*, 7, 291-301. <https://doi.org/10.1109/TLT.2014.2329293>
- Inn. 2017. Add-On programme in Augmented and Virtual Reality at Høgskolen i Innlandet
- Janßen, D., Tummel, C., Richert, A. & Isenhardt, I. 2016. Towards Measuring User Experience, Activation and Task Performance in Immersive Virtual Learning Environments for Students. In: ALLISON, C., MORGADO, L., PIRKER, J., BECK, D., RICHTER, J. & GÜTL, C. (eds.) *Immersive Learning Research Network: Second International Conference, iLRN 2016 Santa Barbara, CA, USA, June 27 – July 1, 2016 Proceedings*. Cham: Springer International Publishing. https://doi.org/10.1007/978-3-319-41769-1_4
- Kirner, C., Kirner, T. G. & Cerqueira, C. S. 2012. *Using Augmented Reality Artifacts in Education and Cognitive Rehabilitation*. 39046
- Kosinski, M., Matz, S. C., Gosling, S. D., Popov, V. & Stillwell, D. 2015. Facebook as a research tool for the social sciences: Opportunities, challenges, ethical considerations, and practical guidelines. *American Psychologist*, 70, 543-556. <http://dx.doi.org/10.1037/a0039210>
- Kosinski, M., Wang, Y., Lakkaraju, H. & Leskovec, J. 2016. Mining big data to extract patterns and predict real-life

- outcomes. *Psychological Methods*, 21, 493-506. <http://dx.doi.org/10.1037/met0000105>
- Kosowatz, J. 2017. Mixed Reality Changes How Engineers Work. *The American Society of Mechanical Engineers*.
- Krokan, A. 2012. *Smart læring – hvordan ikt og sosiale medier endrer læring*, Fagbokforlaget.
- Lambiotte, R. & Kosinski, M. 2014. Tracking the Digital Footprints of Personality. *Proceedings of the IEEE*, 102, 1934-1939. <http://dx.doi.org/10.1109/JPROC.2014.2359054>
- Law, K. M. Y., Lee, V. C. S. & Yu, Y. T. 2010. Learning motivation in e-learning facilitated computer programming courses. *Computers & Education*, 55, 218-228. <http://dx.doi.org/10.1016/j.compedu.2010.01.007>
- Li, W., Grossman, T. & Fitzmaurice, G. 2012. GamiCAD: a gamified tutorial system for first time autocad users. *Proceedings of the 25th annual ACM symposium on User interface software and technology*. Cambridge, Massachusetts, USA: ACM. <https://doi.org/10.1145/2380116.2380131>
- Lindgren, R., Tscholl, M., Wang, S. & Johnson, E. 2016. Enhancing learning and engagement through embodied interaction within a mixed reality simulation. *Computers & Education*, 95, 174-187. <http://dx.doi.org/10.1016/j.compedu.2016.01.001>
- Litzinger, T., Lattuca, L. R., Hadgraft, R. & Newstetter, W. 2011. Engineering Education and the Development of Expertise. *Journal of Engineering Education*, 100, 123-150. <https://doi.org/10.1002/j.2168-9830.2011.tb00006.x>
- Maier, P. & Klinker, G. 2013a. Augmented Chemical Reactions: 3D Interaction Methods for Chemistry. *International Journal of Online Engineering (iJOE)*, 9, 80-82. <http://dx.doi.org/10.3991/ijoe.v9iS8.3411>
- Maier, P. & Klinker, G. Augmented chemical reactions: An augmented reality tool to support chemistry teaching. 2013 2nd Experiment@ International Conference (exp.at'13), 18-20 Sept. 2013 2013b. 164-165. <http://dx.doi.org/10.1109/ExpAt.2013.6703055>
- Maier, P. & Klinker, G. 2013c. Evaluation of an Augmented-Reality-based 3D User Interface to Enhance the 3D-Understanding of Molecular Chemistry. *Proceedings of the 5th International Conference on Computer Supported Education (CSEDU-2013)*. SCITEPRESS (Science and Technology Publications, Lda.). <http://dx.doi.org/10.5220/0004349502940302>
- Martín-Gutiérrez, J. Proposal of methodology for learning of standard mechanical elements using augmented reality. 2011 Frontiers in Education Conference (FIE), 12-15 Oct. 2011 2011. T1J-1-T1J-6. <http://dx.doi.org/10.1109/FIE.2011.6142708>
- Martín-Gutiérrez, J., Fabiani, P., Benesova, W., Meneses, M. D. & Mora, C. E. 2015. Augmented reality to promote collaborative and autonomous learning in higher education. *Computers in Human Behavior*, 51, Part B, 752-761. <http://dx.doi.org/10.1016/j.chb.2014.11.093>
- Martin-Gutierrez, J., Guinters, E. & Perez-Lopez, D. 2012. Improving Strategy of Self-Learning in Engineering: Laboratories with Augmented Reality. *Procedia - Social and Behavioral Sciences*, 51, 832-839. <http://dx.doi.org/10.1016/j.sbspro.2012.08.249>
- Martín-Gutiérrez, J., Luís Saorín, J., Contero, M., Alcañiz, M., Pérez-López, D. C. & Ortega, M. 2010. Design and validation of an augmented book for spatial abilities development in engineering students. *Computers & Graphics*, 34, 77-91. <http://dx.doi.org/10.1016/j.cag.2009.11.003>
- Mendez, J. A. & Gonzalez, E. J. 2011. Implementing Motivational Features in Reactive Blended Learning: Application to an Introductory Control Engineering Course. *IEEE Transactions on Education*, 54, 619-627. <https://doi.org/10.1109/TE.2010.2102028>
- Moravec, M., Williams, A., Aguilar-Roca, N. & O'dowd, D. K. 2010. Learn before Lecture: A Strategy That Improves Learning Outcomes in a Large Introductory Biology Class. *CBE-Life Sciences Education*, 9, 473-481. <http://dx.doi.org/10.1187/cbe.10-04-0063>
- Muñoz, J. C., Cowling, M. A. & Birt, J. Using gamification and mixed reality visualization to improve conceptual understanding in ICT system analysis and design. 33rd International Conference on Innovation, Practice and Research in the Use of Educational Tehnologies in Tertiary Education, 2016 University of South Australia, Adelaide. 455-460.
- Nationalresearchcouncil 2012. *Discipline-Based Education Research: Understanding and Improving Learning in Undergraduate Science and Engineering*, Washington, DC, The National Academies Press. <https://doi:10.17226/13362>
- Nehm, R. H. 2014. Discipline-Based Education Research: Understanding and Improving Learning in Undergraduate Science and Engineering, by Susan R.Singer, Natalie R.Nielsen, and Heidi A.Schweiggruber (Eds.). PB - National Academies Press , Washington, DC, USA, 2012. xi + 264 pp. ISBN 978-0-309-25411-3. *Science Education*, 98, 543-546. <https://doi:10.1002/sce.21091>
- Nicholas, D. F., Senay, P. & Paul, D. M. 2014. I'm Not the Creative Type: Barriers to Student Creativity within Engineering Innovation Projects. Indianapolis, Indiana: ASEE Conferences.
- Nicholson, S. 2015. A RECIPE for Meaningful Gamification. In: REINERS, T. & WOOD, L. C. (eds.) *Gamification in Education and Business*. Cham: Springer International Publishing. https://doi.org/10.1007/978-3-319-10208-5_1
- Nicol, D. 2010. From monologue to dialogue: improving written feedback processes in mass higher education. *Assessment & Evaluation in Higher Education*, 35, 501-517. <https://doi.org/10.1080/02602931003786559>
- Overland, S. 2016. Pearson Announces Mixed Reality Pilots Designed to Solve Real World Learning Challenges at Colleges and Universities. *Pearson Education*.
- Panisoara, G., Duta, N. & Panisoara, I.-O. 2015. The Influence of Reasons Approving on Student Motivation for Learning. *Procedia - Social and Behavioral Sciences*, 197, 1215-1222. <http://dx.doi.org/10.1016/j.sbspro.2015.07.382>
- Park, D. 2016. Introducing Peer—A Mixed Reality Educational Experience. *Design Intelligence*.
- Pedreira, O., García, F., Brisaboa, N. & Piattini, M. 2015. Gamification in software engineering – A systematic mapping. *Information and Software Technology*, 57, 157-168. <http://dx.doi.org/10.1016/j.infsof.2014.08.007>
- Rizov, T. & Rizova, E. D. 2015. AUGMENTED REALITY AS A TEACHING TOOL IN HIGHER EDUCATION.
- Rose, D. H., Meyer, A. & Hitchcock, C. 2005. *The Universally Designed Classroom: Accessible Curriculum and Digital Technologies*, Harvard Education Press, Cambridge.
- Salman, F. H. & Riley, D. R. Augmented reality crossover gamified design for sustainable engineering education. 2016 Future Technologies Conference (FTC), 6-7 Dec. 2016 2016. 1353-1356. <http://dx.doi.org/10.1109/FTC.2016.7821781>
- Sappington, J., Kinsey, K. & Munsayac, K. 2002. Two Studies of Reading Compliance among College Students. *Teaching of Psychology*, 29, 272-274. http://dx.doi.org/10.1207/s15328023top2904_02
- Savage, N., Birch, R. & Noussi, E. 2011. Motivation of engineering students in higher education. *Engineering Education*, 6, 39-46. <https://doi.org/10.11120/ened.2011.06020039>

- Sawyer, R. 2011. The Impact of New Social Media on Intercultural Adaptation. *Senior Honors Projects*. University of Rhode Island.
- Scialom, M. 2017. How engineers and architects can benefit from HoloLens. *Cambridge news*.
- Shieh, R. S. 2012. The impact of Technology-Enabled Active Learning (TEAL) implementation on student learning and teachers' teaching in a high school context. *Computers & Education*, 59, 206-214. <http://dx.doi.org/10.1016/j.compedu.2012.01.016>
- Shirazi, A. & Behzadan, A. H. 2015. Content Delivery Using Augmented Reality to Enhance Students' Performance in a Building Design and Assembly Project. *Advances in Engineering Education: A Journal of Engineering Education Applications* 4, 24.
- Singer, S. & Smith, K. A. 2013. Discipline-Based Education Research: Understanding and Improving Learning in Undergraduate Science and Engineering. *Journal of Engineering Education*, 102, 468-471. <https://doi.org/10.1002/jee.20030>
- Singer, S. R., Nielsen, N. R., Schweingruber, H. A., Committee on the Status, C. F. D. D. B. E. R., Education, B. S., Education, D. B. S. S. & Council, N. R. 2012. *Discipline-Based Education Research: Understanding and Improving Learning in Undergraduate Science and Engineering*, National Academies Press.
- Singletary, C. 2017. EON Reality and ORU Open Dedicated AR/VR Learning Facility. *UploadVR*.
- Souza, R. C. & Kirner, C. 2012. *MiniLabElectroMag-AR* [Online]. Available: <http://ckirner.com/apoio/eletromag/> [Accessed 8.12.2016].
- Thorne, S. L. 2008. Transcultural communication in open internet environments and massively multiplayer online games. In: PIERCE, S. M. (ed.) *Mediating Discourse Online*. John Benjamins Publishing Company. <http://dx.doi.org/10.1075/aals.3.17tho>
- Thorne, S. L., Black, R. W. & Sykes, J. M. 2009. Second Language Use, Socialization, and Learning in Internet Interest Communities and Online Gaming. *The Modern Language Journal*, 93, 802-821. <http://dx.doi.org/10.1111/j.1540-4781.2009.00974.x>
- Thornhill-Miller, B. & Dupont, J.-M. 2016. Virtual Reality and the Enhancement of Creativity and Innovation: Under Recognized Potential Among Converging Technologies? *Journal of Cognitive Education and Psychology*, 15, 102-121. <https://doi.org/10.1891/1945-8959.15.1.102>
- Tunstad, H. 2013. Matte bestemmer frafall i skolen. *Forskning.no*.
- Urke, E. H. 2016. Virtual reality-utdanning skal gi 100 arbeidsplasser. *Teknisk Ukeblad*.
- Vardhan, H. 2016. SketchUp Viewer for Microsoft HoloLens is here. *Geospatial World*.
- Vasilescu, B. 2014. Human aspects, gamification, and social media in collaborative software engineering. *Companion Proceedings of the 36th International Conference on Software Engineering*. Hyderabad, India: ACM. <https://doi.org/10.1145/2591062.2591091>
- Vasileva, S., Vasilev, D. & Culciar, A. Some opportunities for integrating activities in the creation of electronic textbook. 2016 SAI Computing Conference (SAI), 13-15 July 2016 2016. 881-885. <https://doi.org/10.1109/SAI.2016.7556083>
- Vassigh, S., Elias, A., Ortega, F. R., Davis, D., Gallardo, G., Alhaffar, H., Borges, L., Bernal, J. & Rishe, N. D. Integrating Building Information Modeling with Augmented Reality for Interdisciplinary Learning. 2016 IEEE International Symposium on Mixed and Augmented Reality (ISMAR-Adjunct), 19-23 Sept. 2016 2016. 260-261. <http://dx.doi.org/10.1109/ISMAR-Adjunct.2016.0089>
- Walker, D. 2017. Microsoft HoloLens release date, rumours, specs & pricing: HoloLens will beam maintenance data to the International Space Station. *IT Pro*.
- Wu, H.-K., Lee, S. W.-Y., Chang, H.-Y. & Liang, J.-C. 2013. Current status, opportunities and challenges of augmented reality in education. *Computers & Education*, 62, 41-49. <http://dx.doi.org/10.1016/j.compedu.2012.10.024>
- Youyou, W., Kosinski, M. & Stillwell, D. 2015. Computer-based personality judgments are more accurate than those made by humans. *Proceedings of the National Academy of Sciences*, 112, 1036-1040. <http://dx.doi.org/10.1073/pnas.1418680112>

Smart Integration of Energy Production

Esko K. Juuso

Control Engineering, Faculty of Technology, University of Oulu, Finland, esko.juuso@oulu.fi

Abstract

Heat is primarily important in the world's total energy consumption and especially, peak loads and seasonal variations result in problems which are difficult to efficiently come up with electricity networks. Renewable energy sources bring important new possibilities, especially for the heat energy. This paper focuses on heat energy: compact parametric models are essential in the smart integration of production in the district heating and efficient collection of the solar thermal energy. Thermal masses of the buildings are used in the peak load cutting as energy storages. The physical parameters calculated from the building information facilitate the use of different types of buildings simultaneously in the calculations. Smart adaptive control solutions extend feasible operating periods in collecting solar thermal energy. A combination of multiple control actions is essential in keeping the system in control during strong fluctuations in cloudiness and energy demand. Heat storages increase the collecting power and extend the utilisation of the solar energy utilisation over daily and seasonal periods.

Keywords: energy production, sustainable energy, district heating, solar thermal power, smart adaptive systems

1 Introduction

Heat represents more than half of the world's total energy consumption and three-quarters of the fuels used to meet this heat demand consist of fossil fuels (Eisentraut and Brown, 2014). Peak load cutting is highly important in reducing both production costs and environmental impacts (Hietaharju and Ruusunen, 2016). Prediction of the future energy demand and modelling the thermal behaviour of the building, i.e. the indoor temperature, have been used in (Hietaharju and Ruusunen, 2016) to cut peak loads and optimise the heat consumption.

Future trends in global energy consumption and associated environmental issues are pushing for an increased use of renewable energy sources, smaller-size power plants and distributed generation. Consumers are increasingly willing to take an active role. Storage capacities are essential in optimisation, especially solar energy which has daily and seasonal variation. Solar collector fields are combined with storage tanks []. In district heating, building thermal mass can be utilised as short term heat storage (Hietaharju and Ruusunen, 2015).

Building thermal mass and its use in peak load cutting has also been discussed in (Braun, 2003; Henze et al.,

2007; Sun et al., 2013; Kensby et al., 2015; Hagentoft and Kalagidis, 2015; Ståhl, 2009). High peak load reductions and energy savings can be achieved (Sun et al., 2013) and relatively large variations in district heating energy are tolerated in maintaining desired indoor temperature. However, the results depend highly on the thermal characteristics of the buildings. (Hagentoft and Kalagidis, 2015) The storage capacity of a building can be estimated by using thermal effusivity, which is a function of thermal conductivity and heat capacity and represents the materials ability to exchange thermal energy with its surroundings. Heavy buildings have higher thermal effusivity and offer higher energy storage capacity and more stable indoor temperatures compared with light buildings. Models are typically based either on physical principles or they are data driven or a combination of both. (Zhao and Magoulès, 2012; Kramer et al., 2012; Fouquier et al., 2013). A new parametric physical modelling approach to predict and control the indoor temperature was proposed in (Hietaharju et al., 2017).

Integration of smart grid ideas has mostly focused on electricity where the integration requires fast adaption since the storage problem is not solved for real practice. The wind power is increasing fast but the production hours are limited. The solar electricity has the same problems and as whole this leads to very volatile production situations: there are periods of over production and periods when the demand is high but hardly any electricity can be produced with wind or solar power stations. This has experienced in Finland on a winter day when it was very calm. In Germany, there have been periods of negative electricity prices when the wind and solar power production has been on a very high level. This has made the production windows of the condensing power plants difficult. Hydropower together with gas and multi-fuel power plants help in balancing.

Solar power plants should be efficient in collecting any available thermal energy in a usable form at the desired temperature range. Seasonal and daily cyclic variations as well as atmospheric conditions, such as cloud cover, humidity, and air transparency, need to be taken into account to get a fast start-up and efficient operation in varying cloudy conditions. A solar collector field is a good test platform for control methodologies (Camacho et al., 1997; Juuso, 1999; Johansen and Storaas, 2002; Cirre et al., 2007; Limon et al., 2008; Roca et al., 2011; Ayala et al., 2011). The control strategies include basic feedforward and PID schemes, adaptive control, model-based predic-

tive control, frequency domain and robust optimal control and fuzzy logic control.

Feedforward approaches based on the energy balance use the measurements of solar irradiation and inlet temperature (Camacho et al., 1992). Lumped parameter models taking into account the sun position, the field geometry, the mirror reflectivity, the solar irradiation and the inlet oil temperature have been developed for a solar collector field (Camacho et al., 1997). A feedforward controller has been combined with different feedback controllers, even PID controllers operate for this purpose (Valenzuela and Balsa, 1998). The classical internal model control (IMC) can operate efficiently in varying time delay conditions (Farkas and Vajk, 2002). Genetic algorithms have also been used for multiobjective tuning (Bonilla et al., 2012).

Linguistic equations (LE) have been used in various industrial applications (Juuso, 1999, 2004). Modelling and control activities with the LE methodology started by the first controllers implemented in 1996 (Juuso et al., 1997) and the first dynamic models developed in 1999 (Juuso et al., 2000). The LE based dynamic simulator is an essential tool in fine-tuning of these controllers (Juuso, 2005). The LE controllers use model-based adaptation and feedforward features, which are aimed for preventing overheating, and the controller presented in (Juuso and Valenzuela, 2003) already took care of the actual setpoints of the temperature. The manual adjustment of the working point limit has improved the operation considerably. Linguistic equation (LE) control includes solutions also for cloudy conditions and varying load situations (Juuso and Yebra, 2013b). Model-based predictive control (MPC) has been used for tuning the control of large setpoint changes (Juuso, 2006). The main challenge is to handle harmful situations efficiently to reach an unattended operation as a part of a smart grid.

Heat should be strongly taken into account since it is the primary way of using energy. This paper focuses on integrating heat demands and varying operating conditions. Approaches are compared at two levels: predictive model-based approaches for optimization in the district heating and fast intelligent control solutions in solar thermal energy collection.

2 Smart energy network

Smart adaptive systems provide solutions to this need: a smart energy network indicates energy production, transmission and distribution network based on a two-way communication between suppliers and consumers. A real time monitoring of the network condition, i.e. energy production, consumption and distribution, is expected to allow for a more prominent position on the market of those renewable energy resources characterised by a discontinuous and irregular generation.

The expected benefit of a decentralised energy system can be described in terms of redistribution of peak loads and the flattening of the overall power demand curve.

The negative aspects of the integrated decentralised energy production can be formulated in terms of control: the decentralised energy production can be characterised by a strong seasonal variation; each plant depends on the needs and preferences of single users; some of the production units can be subjected to weather and climate conditions. Low carbon requirements have an effect on the trend of the thermal power production. Industry requires a basic high power source which is covered by the nuclear power production.

In this paper, the energy system includes district heating, solar thermal collectors and storages (Figure 1).

2.1 District heating

Combined heat and power (CHP) production together with district heating is a balancing solution. Peak loads and variations in heat demand are caused by the fluctuation of outdoor temperature. Cutting peak loads in district heating network is one of such measures.

In district heating systems, the heating demand may exceed the capacity of power plants, which means that reserve power plants needs to be started. This raises production costs (and also environmental impact) for the energy producer as more expensive oil is used for fuel instead of wood, peat or coal. The peak loads are come up by scheduling energy use. At the same time, more accurate and stable indoor temperature control could be achieved by implementing the optimization routines for energy consumption.

2.2 Solar thermal energy

The usage of renewable energy sources is growing as a consequence of global climate effect and enacted legislation (EED). Solar thermal energy offers considerable opportunities in this connection. The aim of solar thermal power plants is to provide thermal energy for use in an industrial process electricity generation. With fast and well damped controllers, unnecessary shutdowns and start-ups can be avoided and the plant can be operated close to the design limits (Juuso et al., 1998).

2.3 Storage

Heat storage is needed to cut peak loads and even the heat demand out. The storage capacity of buildings together with adaptive automation solutions offer practical solution for this. Model-based optimization solutions developed for district heating can also be applied to electric heating. This reduces the need for electricity storage.

Geothermal energy is more flexible and can be used together with solar thermal energy to utilise solar energy more efficiently.

3 Methods

Model-based control and optimization solutions with demand predictions are efficient in the district heating. In solar thermal applications, seasonal and daily variations could be handled with theoretical models based on energy

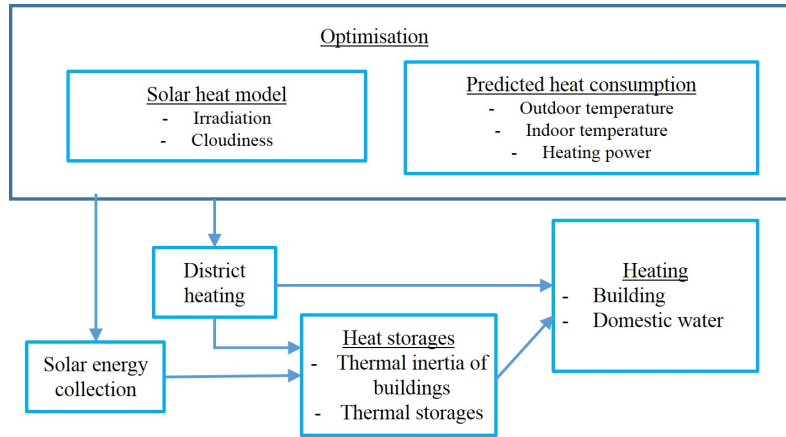


Figure 1. Optimisation of a energy system including district heating, solar thermal collectors and storages.

balances but these approaches do not provide sufficient number of operating hours. Fast variations of the operating conditions require smart adaptive control.

3.1 Modelling

District heating Predicting the indoor temperature evolution over time in the buildings is the key to optimizing the use of district heating. The model structure is based on Newton's cooling law: the rate of heat loss of an object is proportional to the temperature difference between the object and its surroundings. The peak load concept was introduced in (Hietaharju and Ruusunen, 2015), tested in (Hietaharju and Ruusunen, 2016) and further developed in (Hietaharju et al., 2017) to improve the efficiency of the calculations:

$$\Delta T_{in}(t) = \frac{\Delta t}{C} [P(t-k) - U[T_{in}(t-1) - T_{out}(t-1)]] \quad (1)$$

$$T_{in}(t) = T_{in}(t-1) + \Delta T_{in} \quad (2)$$

where the physical parameters are obtained for buildings: C (JK^{-1}) is the heat capacity and U the heat loss coefficient (WK^{-1}): $U = hA$, where h is the heat transfer coefficient ($Wm^{-2}K^{-1}$) and A is the surface area through which the heat is being transferred (m^2). Inputs for the model are the indoor temperature (T_{in}), outdoor temperature (T_{out}) and heating power P (W) which can include a lag of k hours. Time step Δt for the model is one hour. Model output is the hourly indoor temperature along the defined prediction horizon.

The physical parameters C and U are calculated by using ground plans and elevation drawings. Some assumptions were made about the construction materials due to insufficient information. This model was tested for two building in (Hietaharju and Ruusunen, 2016) and for a large number of buildings in (Hietaharju et al., 2017). The characteristics of these buildings are presented in (Hietaharju et al., 2017). The modelling approach can be efficiently generalised: the measured data acquired from five different types of buildings has been utilised in the model performance analysis. Use of easily available mea-

surements and rough estimates for physical parameters are other important features of the model.

Solar collector field The energy balance of the collector field can be represented by expression (Valenzuela and Balsa, 1998):

$$I_{eff}A_{eff} = (1 - \eta_p)F\rho cT_{diff}, \quad (3)$$

where I_{eff} is effective irradiation (Wm^{-2}), A_{eff} effective collector area (m^2), η_p a general loss factor, F flow rate of the oil (m^3s^{-1}), ρ oil density kgm^{-3} , c specific heat of oil ($Jkg^{-1}K^{-1}$) and T_{diff} temperature difference between the inlet and the outlet ($^{\circ}C$). The effective irradiation is the direct irradiation modified by taking into account the solar time, declination and azimuth. The density decreases and the specific heat increases resulting a nonlinear increase of the term ρc (Figure 2). In the start-up, the flow is limited by the high viscosity. The volumetric heat capacity increases very fast in the start-up stage but later remains almost constant because the normal operating temperature range is fairly narrow.

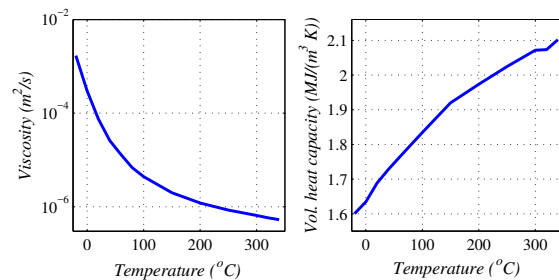


Figure 2. Oil properties (Santotherm 55) (Juuso et al., 1998).

Conventional mechanistic models do not work since there are problems with oscillations and irradiation disturbances. In dynamic LE models, the new temperature difference $\tilde{T}_{diff}(t + \Delta t)$ between the inlet and outlet depends on the irradiation, oil flow and previous temperature difference:

$$\tilde{T}_{diff}(t + \Delta t) = a_1\tilde{T}_{diff}(t) + a_2\tilde{I}_{eff}(t) + a_3\tilde{F}(t), \quad (4)$$

where coefficients a_1 , a_2 and a_3 depend on operating conditions, i.e. each submodel has different coefficients. The membership definition of the outlet temperature does not depend on time. Model coefficients and the scaling functions for T_{diff} , I_{eff} and F are all model specific.

A fuzzy LE system with four operating areas is clearly the best overall model (Juuso, 2003, 2009): the simulator moves smoothly from the start-up mode via low mode to normal mode and later visits shortly in the high mode and low mode before returning to the low mode in the afternoon. Even oscillatory conditions, including irradiation disturbances, are handled correctly. The dynamic LE simulator predicts the average behaviour well but requires improvements for predicting the maximum temperature since the process changes considerably during the first hour. For handling special situations, additional fuzzy models have been developed on the basis of the Fuzzy–ROSA method (Juuso et al., 2000).

3.2 Smart adaptive control

The smart control system consists of a nonlinear LE controller with predefined adaptation models, some smart features for avoiding difficult operating conditions and a cascade controller for obtaining smooth operation (Figure 3).

Data analysis The data analysis is based on the generalised norms

$$\|\tau M_j^p\|_p = (\tau M_j^p)^{1/p} = \left[\frac{1}{N} \sum_{i=1}^N (x_j^p)_i^p \right]^{1/p}, \quad (5)$$

where $p \neq 0$, is calculated from N values of a sample. Several samples with length τ are used at each control step.

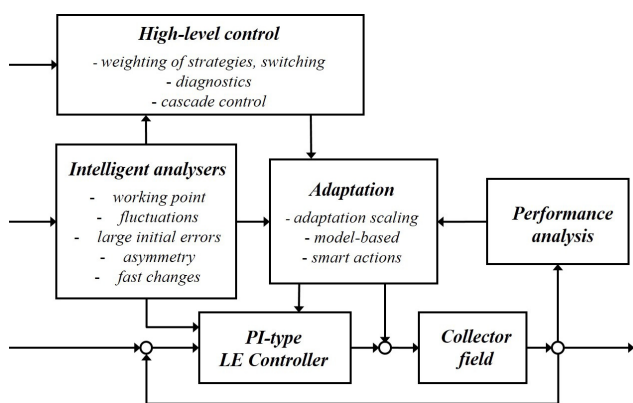


Figure 3. Smart adaptive LE control system.

Nonlinear LE control Feedback PI type controllers use errors $e_j(k)$ and derivatives of the errors $\Delta e_j(k)$ calculated for the controlled variables j at each time step k . These real values are mapped to the linguistic range $[-2, 2]$ by nonlinear scaling with variable specific membership definitions (f_e and $f_{\Delta e}$), respectively. All these functions consist of two second order polynomials and the corresponding inverse functions consist of square root functions. The scaled inputs, $\widetilde{e}_j(k)$ and $\widetilde{\Delta e}_j(k)$, are limited to

the range $[-2, 2]$ by using the functions only in the operating range: outside the scaled values are -2 and 2 for low and high values, respectively. The operation is enhanced with braking and asymmetry corrections.

Intelligent analysers Intelligent analyzers are used for detecting changes in operating conditions to activate adaptation and model-based control and to provide indirect measurements for the high-level control. Nonlinearities between different operating points are handled with working point models which use scaled values.

Fluctuations are detected by calculating the difference of the high and the low values of the variables as a difference of two moving generalised norms:

$$\Delta x_j^F(k) = \|\|^{K_s \tau} M_j^{p_h} \|_{p_h} - \|\|^{K_s \tau} M_j^{p_l} \|_{p_l}, \quad (6)$$

where the orders $p_h \in \mathfrak{R}$ and $p_l \in \mathfrak{R}$ are large positive and negative, respectively. The moments are calculated from the latest $K_s + 1$ values, and an average of several latest values of $\Delta x_j^F(k)$ is used as an indicator of fluctuations. (Juuso, 2012)

Additional indicators have been developed for high levels and fast changes to detect anomalies and avoid overshoot (Juuso and Yebra, 2014).

Adaptive control Adaptive LE control uses correction factors which are obtained from the working point value. In the solar collector field, the working point model is

$$wp = \widetilde{I}_{eff} - \widetilde{T}_{diff}, \quad (7)$$

where \widetilde{I}_{eff} and \widetilde{T}_{diff} are obtained by the nonlinear scaling of variables: efficient irradiation I_{eff} and temperature difference between the inlet and outlet, $T_{diff} = T_{out} - T_{in}$. The outlet temperature T_{out} is the maximum outlet temperature of the loops. This model handles the nonlinear effects: the volumetric heat capacity increases very fast in the start-up stage and remains almost constant in the normal operating temperatures. The predictive braking and asymmetrical actions are activated when needed. Intelligent indicators introduce additional changes of control if needed in special situations.

Model-based control Model-based control provide limits for the acceptable range of the temperature setpoint by setting a lower limit of the working point (7). The fluctuation indicators are now used for modifying the lower working point limit to react better to cloudiness and other disturbances. This overrides the manual limits if the operation conditions require that (Juuso and Yebra, 2013a, 2014). The model-based extension is an essential part in moving towards reliable operation in cloudy conditions: the control system should operate without manual interventions. The high-level control moves towards control strategies for modifying intelligent analyzers and adaptation procedures (Figure 3).

4 Applications

Applications are active at two levels: predictive model-based approaches for optimization in the district heating and fast intelligent control solutions in solar thermal energy collection.

4.1 District heating network

A concept for peak load cutting has been presented in (Hietaharju and Ruusunen, 2015) and tested with simulation: first for two buildings in (Hietaharju and Ruusunen, 2016) and later (Hietaharju et al., 2017) for a large number of buildings categorised in five types.

The indoor temperature models (1) and (2) have been utilised to optimise heating power in pilot buildings. First tests considered different peak load cutting scenarios based on 30%, 50%, and 70% reduction in the heating power in the morning hours between 7 and 10 am. Load cuts were calculated from the actual measured district heating power. During the simulations, maximum allowed power was restricted accordingly during the peak load hours. Cost function for peak load cutting minimised the power consumption while keeping the indoor temperature between the control limits. This was achieved by penalizing the cost function value when the indoor temperature exceeded the limits according to the model prediction. Also the increase and decrease in the amount of heating power was restricted to prevent too large hourly power changes.

Recently, the parametric physical model has been used together with a residual model to forecast heat demand of individual buildings and the city-wide demand, aiming to provide predictive information on the heat consumption. District heating data from over 4000 different buildings at a city level has been utilised in the validation of the modelling procedure. (Hietaharju and Ruusunen, 2017)

4.2 Solar thermal energy

The LE control system has been tested in the solar power plant where the error variable is the deviation of the outlet temperature from the set point. The control is achieved by means of varying the flow pumped through the pipes to avoid hazardous situations, e.g. oil temperatures greater than 300 °C. The goal is to reach the nominal operating temperature 180 – 295 °C and keep it in changing operating conditions. The temperature increase in the field may rise up to 110 °C. (Juuso, 2011, 2012).

The intelligent indicators of the levels and fast changes of the temperatures (inlet, outlet and difference) based on intelligent indices which detect anomalies: the fast change of the inlet temperature provides feedforward information.

Fast start-up, smooth operation and efficient energy collection is achieved even in variable operating condition. The state indicators react well to the changing operating conditions and can be used in smart working point control to further improve the operation. The working point can be chosen in a way which improves the efficiency of the

energy collection. A trade-off of the temperature and the flow is needed to achieve a good level for the collected power. (Juuso, 2016)

5 Discussion

The peak load cutting in district heating can be done efficiently with the model-based optimisation. The collection of the solar thermal energy requires smart controllers with nonlinear scaling, intelligent indicators together with adaptive and model-based extensions. Parametric systems are needed for the models and control: parameters modify the systems to different buildings and operating conditions, respectively. The models used in the district heating could be used in the solar power plant to optimise the collection demand. The smart control used in the solar application could control the heating of the buildings in varying operating conditions.

Geothermal energy is an additional energy source for district heating and individual houses. It can also enhance the use of solar thermal energy by providing efficient storages for excess solar energy. New business models based on decentralised energy production systems are arising where the end-users can simultaneously be also energy producers. This has various effects on the operation of the energy systems.

In the future, smart-grid entities formed by energy production and consumption are controlled by smart energy systems. Energy storages and coordination between electricity and heat sources are essential. A feasible production level depends on seasonal and weather condition and the dynamics of different systems need to be taken into account.

6 Conclusions

Parametric models are essential in the smart integration of energy production. Large networks including various types of buildings can be controlled and optimised by using same compact model structures where the physical parameters are calculated from the building information. This is highly beneficial in the peak load cutting which can efficiently utilise the thermal masses of the buildings as energy storages.

Varying operating conditions are unavoidable in collecting solar thermal energy. Smart adaptive control solutions extend feasible operating periods by nonlinear scaling, intelligent analysers, predefined adaptation and model-based cascade control. The combination of multiple control actions is essential in keeping the system in control during strong fluctuations in cloudiness and energy demand. Heat storages are needed to increase the collecting power and extending the utilisation of the solar energy utilisation over daily and seasonal periods.

The efficient control and optimisation of the heat production and consumption can improve considerably the overall energy systems by reducing the peak loads and storage requirements of electricity.

Acknowledgment

This work was supported by the Finnish Funding Agency for Innovation (TEKES) through the project KLEI (40267/13) and project ICOSLE as a part of the EU SFERA Grant Agreement 228296.

References

- C. O. Ayala, L. Roca, J. L. Guzman, J. E. Normey-Rico, M. Berenguel, and L. Yebra. Local model predictive controller in a solar desalination plant collector field. *Renewable Energy*, 36:3001–3012, 2011. doi: 10.1016/j.renene.2011.03.037.
- J. Bonilla, L. J. Yebra, S. Dormido, and E. Zarza. Parabolic-trough solar thermal power plant simulation scheme, multi-objective genetic algorithm calibration and validation. *Solar Energy*, 86:531–540, 2012. doi: 10.1016/j.solener.2011.10.025.
- J. E. Braun. Load control using building thermal mass. *J. Sol. Energ.-T. Asme.*, 125:292–301, 2003. doi:10.1115/1.1592184.
- E. Camacho, M. Berenguel, and F. R. Rubio. *Adaptive Control of Solar Plants*. Springer, London, 1997.
- E.F Camacho, F.R. Rubio, and F.M. Hughes. Self-tuning control of a solar power plant with a distributed collector field. *IEEE System Control Magazine*, 12(2):72–78, 1992.
- C. M. Cirre, M. Berenguel, L. Valenzuela, and E. Camacho. Feedback linearization control for a distributed solar collector field. *Control engineering Practice*, 15:1533–1544, 2007. doi: 10.1016/j.conengprac.2007.03.002.
- A. Eisentraut and A. Brown. *Heating without global warming - Market developments and policy considerations for renewable heat*. IEA, Paris, 2014.
- I. Farkas and I. Vajk. Internal model-based controller for a solar plant. In L. Basanez and J. A. de la Puente, editors, *Proceedings of the 15th Triennial World Congress, Barcelona, Spain, July 21-26, 2011*, pages 49–54. IFAC, 2002. <http://www.ifac-papersonline.net/>.
- A. Fouquier, S. Robert, F. Suard, L. StÄlphan, and A. Jay. State of the art in building modelling and energy performances prediction: A review. *Renew. Sustain. Energy Rev.*, 23:272–288, 2013. doi:10.1016/j.rser.2013.03.004.
- C.-E. Hagentoft and A. S. Kalagidis. Effect smart solutions for district heating networks based on energy storage in buildings. impact on indoor temperatures. *Energy Procedia*, 78: 2244–2249, 2015. doi:10.1016/j.egypro.2015.11.346.
- G. P. Henze, T. H. Le, A. R. Florita, and C. Felsmann. Sensitivity analysis of optimal building thermal mass control. *J. Sol. Energ.-T. Asme.*, 129:473–485, 2007. doi:10.1115/1.2770755.
- P. Hietaharju and M. Ruusunen. A concept for cutting peak loads in district heating. In *Automaatio XXI seminar, March 17-18, 2015, Helsinki, Finland*, 2015.
- P. Hietaharju and M. Ruusunen. Peak load cutting in district heating network. In *9th EUROSIM Congr. Model. Simul., Oulu*, pages 140–144, 2016.
- P. Hietaharju and M. Ruusunen. Heat demand forecasting by combining a parametric physical and a non-parametric model. Unpublished, 2017.
- P. Hietaharju, M. Ruusunen, and K. Leiviskä. A parametric physical model for indoor temperature prediction in buildings. Submitted, 2017.
- T. A. Johansen and C. Storaas. Energy-based control of a distributed solar collector field. *Automatica*, 38:1191–1199, 2002.
- E. K. Juuso. Fuzzy control in process industry: The linguistic equation approach. In H. B. Verbruggen, H.-J. Zimmermann, and R. Babuška, editors, *Fuzzy Algorithms for Control, International Series in Intelligent Technologies*, volume 14 of *International Series in Intelligent Technologies*, pages 243–300. Kluwer, Boston, 1999. doi: 10.1007/978-94-011-4405-6_10.
- E. K. Juuso. Intelligent dynamic simulation of a solar collector field. In A. Verbraeck and V. Hlupic, editors, *Simulation in Industry, 15th European Simulation Symposium ESS 2003*, pages 443–449. SCS, Gruner Druck, Erlangen, Germany, 2003.
- E. K. Juuso. Integration of intelligent systems in development of smart adaptive systems. *International Journal of Approximate Reasoning*, 35(3):307–337, 2004. doi: 10.1016/j.ijar.2003.08.008.
- E. K. Juuso. Modelling and control of a solar thermal power plant. In P. Horacek, M. Simandl, and P. Zitek, editors, *Proceedings of 16th Triennial World Congress, Prague, July 3-8, 2005*, pages 368–373. IFAC, 2005. doi: 10.3182/20050703-6-CZ-1902.01790.
- E. K. Juuso. Modelling and simulation in development and tuning of intelligent controllers. In I. Troch and F. Breitenacker, editors, *Proceedings of 5th Vienna Symposium on Mathematical Modelling, February 8-10, 2006, Vienna, Austria, Argesim Report 30*, pages 6–1 – 10. Argesim Verlag, Vienna, 2006. ISBN 3-901608-30-3.
- E. K. Juuso. Dynamic simulation of solar collector fields in changing operating conditions. In B. Elmegaard, Christian Veje, Mads Pagh Nielsen, and Tommy Mølbak, editors, *Proceedings of SIMS 50 - the 50th International Conference of Scandinavian Simulation Society, October 7-8, Fredericia, Denmark*, pages 341–348. DTU, Lungby, Denmark, 2009.
- E. K. Juuso. Recursive tuning of intelligent controllers of solar collector fields in changing operating conditions. In S. Bittani, A. Cenedese, and S. Zampieri, editors, *Proceedings of the 18th World Congress The International Federation of Automatic Control, Milano (Italy) August 28 - September 2, 2011*, pages 12282–12288. IFAC, 2011. doi: 10.3182/20110828-6-IT-1002.03621.
- E. K. Juuso. Model-based adaptation of intelligent controllers of solar collector fields. In I. Troch and F. Breitenacker, editors,

- Proceedings of 7th Vienna Symposium on Mathematical Modelling, February 14-17, 2012, Vienna, Austria, Part 1*, volume 7, pages 979–984. IFAC, 2012. doi: 10.3182/20120215-3-AT-3016.00173.
- E. K. Juuso. Intelligent control of a solar thermal power plant - adaption in varying conditions. In *2016 5th International Conference on Power Science and Engineering, Venice, Italy, 14-17 December 2016*, 2016.
- E. K. Juuso and L. Valenzuela. Adaptive intelligent control of a solar collector field. In *Proceedings of Eunit 2003 - European Symposium on Intelligent Technologies, Hybrid Systems and their implementation on Smart Adaptive Systems, July 10-11, 2003, Oulu, Finland*, pages 26–35. Wissenschaftsverlag Mainz, Aachen, 2003.
- E. K. Juuso and L. J. Yebra. Model-based intelligent control of a solar energy collector field. In *Proceedings - 8th EUROSIM Congress on Modelling and Simulation, EUROSIM 2013, 10-13 September, 2013, Cardiff, UK*, pages 513–518, 2013a. URL www.scopus.com. doi: 10.1109/EUROSIM.2013.92.
- E. K. Juuso and L. J. Yebra. Optimisation of solar energy collection with smart adaptive control. In *IECON Proceedings (Industrial Electronics Conference), 10-14 November, 2013, Vienna, Austria*, pages 7938–7943, 2013b. URL www.scopus.com. doi: 10.1109/IECON.2013.6700459.
- E. K. Juuso and L. J. Yebra. Smart adaptive control of a solar collector field. In *IFAC Proceedings Volumes (IFAC PapersOnline)*, volume 19, pages 2564–2569, 2014. URL www.scopus.com.
- E. K. Juuso, P. Balsa, and K. Leiviskä. Linguistic Equation Controller Applied to a Solar Collectors Field. In *Proceedings of the European Control Conference -ECC'97, Brussels, July 1 - 4, 1997*, volume Volume 5, TH-E I4, paper 267 (CD-ROM), page 6 pp., 1997.
- E. K. Juuso, P. Balsa, and L. Valenzuela. Multilevel linguistic equation controller applied to a 1 MW solar power plant. In *Proceedings of the ACC'98, Philadelphia, PA, June 24-26, 1998*, volume 6, pages 3891–3895. ACC, 1998.
- E. K. Juuso, D. Schauten, T. Slawinski, and H. Kiendl. Combination of linguistic equations and the fuzzy-ROSA method in dynamic simulation of a solar collector field. In L. Yliniemi and E. Juuso, editors, *Proceedings of TOOLMET 2000 Symposium - Tool Environments and Development Methods for Intelligent Systems, Oulu, April 13-14, 2000*, pages 63–77, Oulu, 2000. Oulun yliopistopaino.
- J. Kensby, A. Tr?schel, and J.-O. Dalenb?ck. Potential of residential buildings as thermal energy storage in district heating systems - results from a pilot test. *Appl. Energ.*, 137:773–781, 2015. doi:10.1016/j.apenergy.2014.07.026.
- R. Kramer, J. van Schijndel, and H. Schellen. Simplified thermal and hygric building models: A literature review. *Front. Archit. Res.*, 1:318–325, 2012. doi:10.1016/j.foar.2012.09.001.
- D. Limon, I. Alvarado, T. Alamo, M. Ruiz, and E. F. Camacho. Robust control of the distributed solar collector field ACUREX using MPC for tracking. In *Proceedings of 17th IFAC World Congress, Seoul, Korea, July 6-11, 2008*, volume 17, pages 958–963. IFAC, 2008. <http://www.ifac-papersonline.net/>.
- L. Roca, J. L. Guzman, J. E. Normey-Rico, M. Berenguel, and L. Yebra. Filtered smith predictor with feedback linearization and constraints handling applied to a solar collector field. *Solar Energy*, 85:1056–1067, 2011. doi: 10.1016/j.solener.2011.02.026.
- F. Ståhl. *Influence of thermal mass on the heating and cooling demands of a building unit*. PhD thesis, Chalmers University of Technology, Sweden, 2009.
- Y. Sun, S. Wang, F. Xiao, and D. Gao. Peak load shifting control using different cold thermal energy storage facilities in commercial buildings: A review. *Energ. Convers. Manage*, 71: 101–114, 2013. doi:10.1016/j.enconman.2013.03.026.
- L. Valenzuela and P. Balsa. Series and parallel feedforward control schemes to regulate the operation of a solar collector field. In *Proceedings of the 2nd User Workshop Training and Mobility of Researchers Programme at Plataforma Solar de Almeria, November 10-11, 1998*, pages 19–24. Ciemat, 1998.
- H. Zhao and F. Magoulès. A review on the prediction of building energy consumption. *Renew. Sustain. Energy Rev.*, 16:3586–3592, 2012. doi:10.1016/j.rser.2012.02.049.

Euler-Granular Approach for Modelling of Dilute Phase Pneumatic Conveying in a Vertical Pipe

Prasanna Welahettige¹ W.K. Hiromi Ariyaratne¹ Morten C. Melaaen¹

¹ Faculty of Technology, Natural Sciences and Maritime Sciences, University College of Southeast Norway, Post box 235, N-3603 Kongsberg, Norway, {prasanna.welahettige, hiromi.ariyaratne, morten.c.melaaen}@usn.no

Abstract

In the present study, vertically upward dilute phase pneumatic conveying flow was predicted using Euler-Granular method. Three dimensional computational fluid dynamics simulations were carried out for an 8 m long and 30.5 mm diameter circular pipe. The density of conveyed materials was 1020 kg/m³. Simulations for different particle diameters; 200 μm and 500 μm were performed. The air velocities ranged from 9 to 17 m/s and solid to air mass flow ratios ranged from 0.0 to 3.8. Pressure drop, air and particle velocity profiles and solid distribution profiles were studied and some of the results were compared with experimental data from existing literature. Predicted pressure drop and air velocity profiles are in good agreement with experimental results.

Keywords: Computational Fluid Dynamics, pneumatic conveying, pressure drop, velocity, solid distribution, experimental data

1 Introduction

Pneumatic conveying method is widely used for granular particles transport in cement, mining, petroleum and other industries. The materials are conveyed along horizontal and vertical distances; therefore the vertical upward flows can be expected in any industrial pneumatic conveying line. Vertical pneumatic flow is generally used in dilute phase pneumatic conveying systems (Haim *et al*, 2003). Particulate material transportation in suspension mode by employing gas which are at high velocities, is usually termed as dilute phase conveying (Ratnayake, 2005). In addition to the experimental studies, Computational Fluid Dynamics (CFD) modelling has been identified as a powerful and versatile tool for understanding the complex gas-solid interactions in a pneumatic conveying system (Ouyang *et al*, 2005). In general, there are two basic modelling approaches in use; Eulerian-Eulerian and Eulerian-Lagrangian. Euler-Granular model is such an Eulerian-Eulerian model approach in where both gas and solid phases are treated as inter-penetrating continua (Ariyaratne *et al*, 2016a).

Several modelling studies have been performed previously for vertical pneumatic conveyors (Manjula *et al*, 2017). Azizi *et al* (2012) studied dense to dilute gas-solid flow behavior in a vertical pneumatic conveyor. The turbulence interaction between gas and solid particles were investigated by using Simonin's and Ahmadi's models. Ahmadi's model predicted lower granular temperature and pressure drop compared to Simonin's model. According to their predictions, the minimum voidage and the maximum particle velocity in dilute phase were found along the centerline of the vertical pipe. It was showed that the solid phase turbulence plays a significant role in numerical predictions of pneumatic conveying of 1.91 mm particles and the capability of those models depends on tuning of the parameters of slip-wall boundary condition. The combined "Computational Fluid Dynamics – Discrete Element Method (CFD-DEM)" developed by Kuang *et al* (2009) gives satisfactory predictions for vertical pneumatic conveying characteristics. The mechanisms underlying the relation between pressure drop and gas velocity were analysed for dilute and dense phases. The forces that govern the flow of particles were investigated and a new phase diagram was established for the particular conveying system. Bilirgen *et al* (1998) used FLOW3D to determine vertical pipe flow characteristics and the pressure drop and velocity profiles were compared with available experimental data. Haim *et al* (2003) carried out a parametric study for dilute gas-particle flow in a vertical pipe using Eulerian-Lagrangian approach. It was concluded that the increase of Reynolds number, solid loading ratio, particle density and particle diameter increases the slip velocity and the acceleration length. Moreover, the pipe diameter has no significant effect on acceleration length and slip velocity as long as the particle mass flow rate and solid loading ratio are constant. The effects of different turbulent modulation models in vertical pipe pneumatic conveying were investigated by El-Behery *et al* (2011) using Eulerian-Lagrangian approach. The effects of solid loading ratio and particle size on boundary layer thickness and pressure drop results were analysed. It was also

identified that the concentration distribution is dependent on particle-particle collision, turbulence dispersion and lift force. Li *et al* (2013) carried out CFD-DEM simulations for a vertical pipe flow in order to investigate the effects of friction coefficient on pressure drop, solid concentration, the transition velocity from slug flow regime to dispersed flow regime and any reverse flow in the slug flow regime. In a previous study that was carried out by current authors, the sensitivity of a model parameter (specularity coefficient) on the predictions of pneumatic conveying characteristics in a vertical pipe was investigated (Ariyaratne *et al*, 2017).

In the current work, the characteristics of dilute upward vertical pneumatic conveying flow are investigated. The pressure drop, mean air and solid velocity profiles, solid distribution over the pipe cross section are studied for conveying of 200 μm and 500 μm diameter particles. Some of the simulation results are validated by experimental data from existing literature (Tsuji *et al*, 1984). The commercial CFD software ANSYS Fluent, version 16.2, was used for modelling and simulation. Steady state three-dimensional simulations were carried out using Euler-Euler approach for granular flows (Euler-Granular model).

2 Numerical Model

Both gas and solid phases are considered as continuous phases in Euler-Granular approach. Since the volume of a phase cannot be occupied by the other phases, the sum of volume fractions is equal to one. The steady state mass and momentum equations are solved for both gas and solid phases. To model the turbulent viscosity in the gas phase, the standard k-epsilon model is used. The Gidaspow model is used for the calculation of gas-solid exchange coefficient. The aerodynamic lift and vorticity induced lift force are calculated using Saffman-Mei model. The solid-phase stresses are derived by making an analogy between the random particle motion arising from particle-particle collisions and the thermal motion of molecules in a gas (kinetic theory of granular flow). Constitutive model from Lun *et al.* is used to calculate the solids pressure. The collisional and kinetic contributions are taken into account when modelling the solids shear viscosity. The bulk viscosity of solids is modeled through Lun *et al.* The equations of the models are not presented here and more details can be found elsewhere (Ariyaratne *et al*, 2016b).

3 Computational Domain, Boundary Conditions and Material Properties

ANSYS DesignModeler 16.2 and ANSYS Meshing 16.2 were used for the geometry drawing and mesh generation, respectively. The diameter of the vertical pipe is 30.5 mm which was selected based on the experimental setup used by Tsuji *et al* (1984). The

simulated pipe length is 8 m which is a good enough length to achieve a fully developed flow situation. The gas-solid mixture enters from bottom of the pipe and leaves from top of the pipe. Figure 1 shows the mesh. The total number of elements in the mesh is 46080 and the maximum skewness is less than 0.39. The computational time is around 4 hrs for a run when 2.4 GHz Intel $\text{\textcircled{R}}$ Xeon $\text{\textcircled{R}}$ processor and 32 GB installed memory are used.

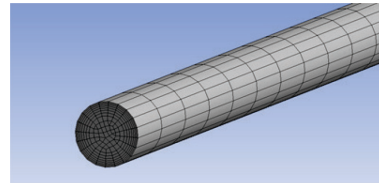


Figure 1. The mesh.

There are two types of boundary conditions, particularly for the gas phase and for the solid phase. Air and the solid particles enter to the pipe with similar and uniform velocities. The real velocities of air and particles and the solid volume fraction at the inlet defined for each case are shown in Table 1. The turbulence intensity of the air at the inlet is assumed as 10%. Solid phase granular temperature at the inlet is calculated according to the formula mentioned by Patro and Dash (2014) and it is in the range of values between 0.44-0.49 for all the cases. The outlet is treated as a pressure outlet. The pipe wall is considered as hydrodynamically smooth and no-slip for the gas phase. Johnson and Jackson (1987) wall boundary condition is used for the solid phase. According to the recommendation from a previous study, the specularity coefficients 0.0001 and 0.0004 were selected for 200 μm and 500 μm diameter particles, respectively (Ariyaratne *et al*, 2017). Coefficient of restitution for particle-wall collisions used in the simulations is 0.95 for all particle sizes.

The conveying medium is air which is having 1.225 kg/m^3 density and 1.7894×10^{-5} $\text{kg/m}\cdot\text{s}$ viscosity. The particles are polystyrene particles which are having spherical shape and 200 μm and 500 μm diameters. The particle density is 1020 kg/m^3 .

4 Case Definition

Table 1 shows the cases simulated in the present study. The cases are in accordance with experimental cases carried out by Tsuji *et al* (1984). The real air and particle velocities at the inlet ranged from 9 to 17 m/s and the corresponding Reynolds numbers are $1.8 \times 10^4 - 3.6 \times 10^4$. The solid loading ratios are in the range of 0.0-3.8 and the corresponding solid volume fractions at the inlet vary in between 0.0000 and 0.0045. Coefficient of restitution for particle collisions used in all simulation cases is 0.9.

Table 1. Details of Simulated Cases.

Case	Particle diameter (mm)	Real air velocity at the inlet (m/s)	Real particle velocity at the inlet (m/s)	Solid loading ratio (kg solids/kg air)	Solid volume fraction at the inlet (-)	Reynolds number of the flow (-)
Case -1.1	0.5	10.5795	10.5795	3.4	0.00407	2.2×10^4
Case -1.2	0.5	10.5731	10.5731	2.9	0.00347	2.2×10^4
Case -1.3	0.5	10.5630	10.5630	1.3	0.00156	2.2×10^4
Case -1.4	0.5	10.5529	10.5529	0.0	0.00000	2.2×10^4
Case -2.1	0.5	8.9200 - 17.1800	8.9200 - 17.1800	2.0 - 3.8	0.00230 - 0.00450	1.8×10^4 - 3.6×10^4
Case -3.1	0.2	11.0577	11.0577	3.2	0.00383	2.3×10^4
Case -3.2	0.2	11.0405	11.0405	1.9	0.00228	2.3×10^4
Case -3.3	0.2	11.0220	11.0220	0.5	0.00060	2.3×10^4
Case -3.4	0.2	11.0154	11.0154	0.0	0.00000	2.3×10^4

5 Results and Discussion

The predicted pressure drop profiles, particle and air velocity profiles and solid distribution profiles for two different particle sizes and for different solid loading ratios are presented for the vertical upward pneumatic conveying system. The pressure drop profiles do not include the hydrostatic pressure. The mean air and particle velocity profiles and the solid volume fraction profiles (Figure 4, Figure 5, Figure 6 (a) and Figure 7) are taken along a diameter of pipe cross section at 7.5 m height from the bottom of the pipe which ensures the fully developed profiles. Some of the profiles are compared with experimental results from Tsuji *et al* (1984).

Figure 2 shows the simulated pressure profiles along the pipe axis for 500 μm diameter particles for a certain superficial air velocity but for different solid loading ratios. The pressure drop has been increased from 457 Pa to 786 Pa in the entire pipe when the solid loading ratio is increased from 0.0 to 3.4. The total pressure drop can be considered as the summation of gas phase pressure drop and solid phase pressure drop (Ratnayake *et al*, 2007). When the solid loading ratio is increased by increasing the solid mass flow rate, the work that should be done by unit mass of air on particles is increased. In the same time, the higher solid mass flow rate increases the particle number density in the system which in turn increases the collisions between particle-particle and particle-wall hence the pressure drop.

Figure 3 shows the pressure drop dependence of 500 μm diameter particles on inlet air velocity for the solid mass flow rate of 0.03 kg/s. In contrast to the Figure 2, the pressure drop increases when solid loading ratio is

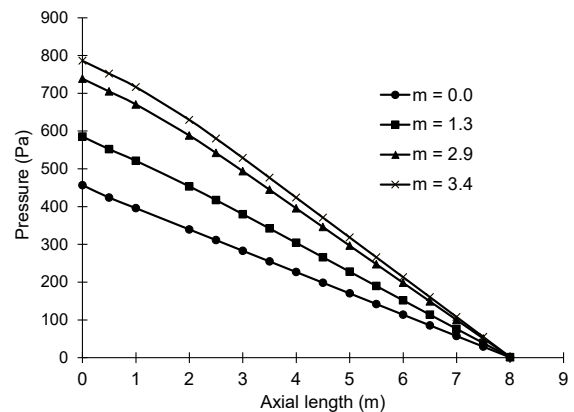


Figure 2. Axial static pressure variation for particle diameter 500 μm and $\text{Re} = 2.2 \times 10^4$ (from Case-1.1 to Case-1.4).

decreased (the solid loading ratio is decreased when increasing air velocity by keeping the solid mass flow rate constant). Similar to the explanation for Figure 2, the work that should be done by unit mass of air in order to move the particles ahead is decreased when the air velocity is increased; hence the pressure drop is decreased. Nevertheless, the pressure drop increases with increased air velocity due to increase of gas phase shear similar to a single phase flow (Azizi *et al*, 2012). The latter is dominant compared to former; hence the result is increase of pressure drop with increase of air velocity.

The predicted results are compared with experimental data from Tsuji *et al* (1984) and it shows a good agreement. The difference between experimental and predicted results is in the range of 9-19%. It should be noted that the simulations are carried out with

specularity coefficient 0.0004 and the pressure drop prediction is significantly sensitive to this parameter (Ariyaratne *et al*, 2017).

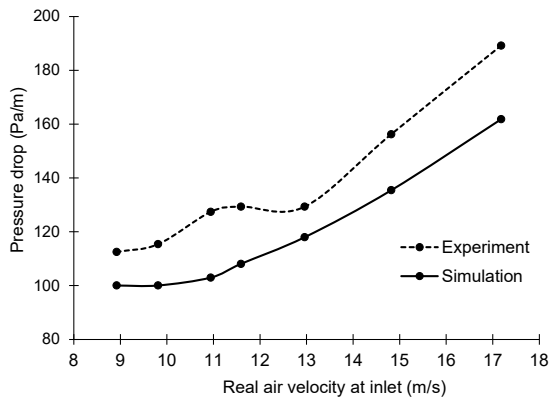


Figure 3. Comparison of simulated pressure drops with experimental data for particle diameter 500 μm and solid mass flow rate 0.03 kg/s (Case-2.1).

In general, Patro and Dash (2014) who used Euler-Granular method to predict vertical pipe pneumatic conveying have shown that the pressure drop depends on gas phase Reynolds number, solid loading ratio, particle diameter and density and on model collision coefficients such as specularity coefficient.

The predicted real mean air velocity profiles along a diameter in a pipe cross section at fully developed

region are shown in Figure 4 and Figure 5 for 200 μm and 500 μm diameter particles and for different solid loading ratios. The profiles are also compared with the experimental data (Tsuji *et al*, 1984).

Since the Reynolds number of the flow is around 22000, the single phase velocity profiles should show a turbulence behavior ((a) in both figures). Inclusion of solids into the system changes the air velocity profile remarkably for both particle sizes. In general, the air velocity gets reduced with increase of solid loading ratio because of the increased drag. Moreover, the air velocity profiles become more flattened with increased solid loading ratios (e.g. $m=1.9$ and $m=3.2$) for 200 μm diameter particles (Figure 4). Tsuji *et al* (1984) also have observed increase of turbulence intensity in core region of the pipe when the loading is increased from 1.3 to 3.2 for 200 μm diameter particles. The effect of particles on air velocity profiles is more significant for larger particles (500 μm diameter), in where the profile becomes concave when increasing the solid loading ratio (Figure 5). This is reasonable as the larger particles restrict the air flow more than that of the smaller particles.

The agreement between experiments and predictions are significantly good for single phase flows. The deviation between experiments and predictions becomes larger when increasing the solid loading ratio for 200

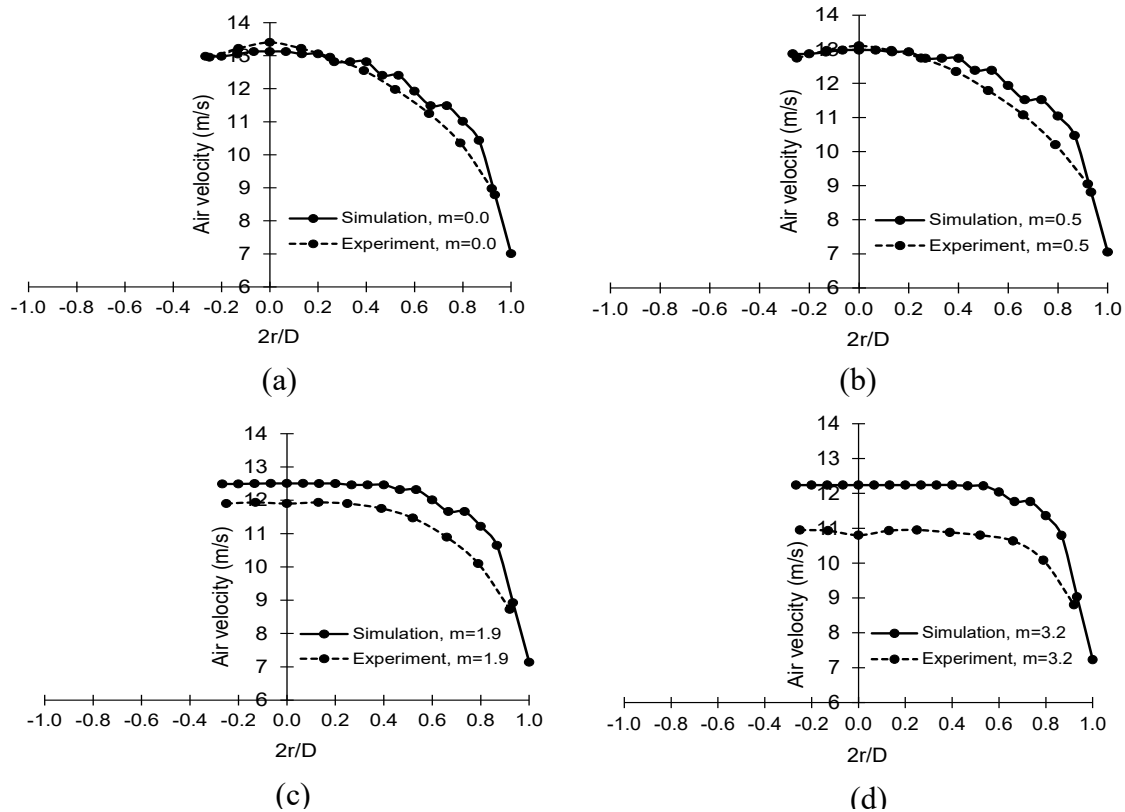


Figure 4. Comparison of predicted and experimental mean real air velocity profiles along a diameter in a pipe cross section at fully developed region for particle diameter 200 μm and $\text{Re} = 2.3 \times 10^4$ (from Case-3.1 to Case-3.4).

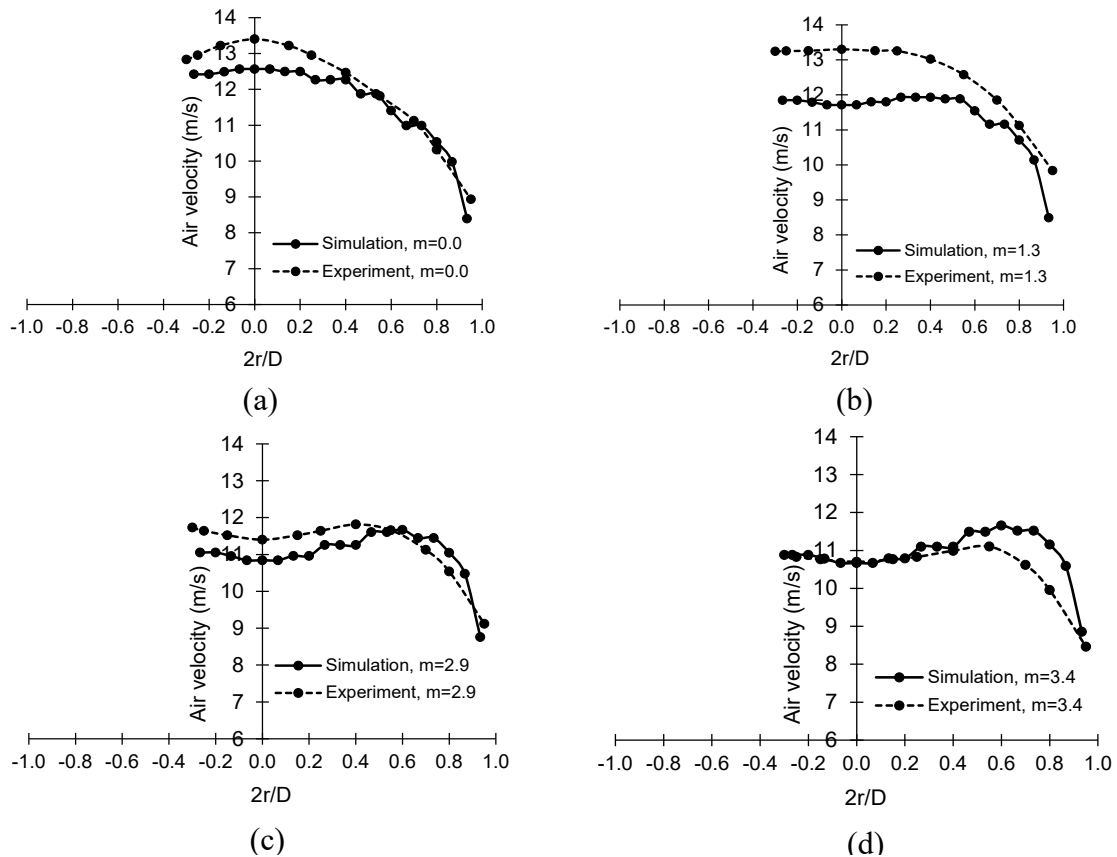


Figure 5. Comparison of predicted and experimental mean real air velocity profiles along a diameter in a pipe cross section at fully developed region for particle diameter $500 \mu\text{m}$ and $\text{Re} = 2.2 \times 10^4$ (from Case-1.1 to Case-1.4).

μm diameter particles (Figure 4). However, the agreement between experimental and predicted results is good for $500 \mu\text{m}$ diameter particles for the range of solid loading ratios studied (Figure 5). For the highest solid loading ratio (3.4), the maximum velocity predicted by the model is higher than that of the experiments and the experimental maximum is located at around $2r/D = 0.5$ while the predicted maximum is located at around $2r/D = 0.6$. In general, having lower velocities in core region compared to annulus region is better explained by solid distribution profiles (Figure 6 (a)).

The predicted solid volume fractions along a diameter in a pipe cross section at fully developed region for $500 \mu\text{m}$ diameter particles and for different solid loading ratios are shown in Figure 6 (a). It shows that the highest concentration of the solid particles is located in the central part of the pipe cross section. Due to roughness of the wall, the rebound angle of particles increases resulting in particle movement into core region of the pipe. The solid concentration in central region is further increased when increasing the solid mass flow rate (i.e. the solid loading ratio). This is the reason for having lower air velocities in the core region of the pipe (Figure 5). Nevertheless, the extremely low solid concentration nearby walls is peculiar.

Figure 6 (b) shows the solid volume fraction variation along the central axis of the vertical pipe. At steady state, from inlet ($z = 0 \text{ m}$) to the outlet ($z = 8 \text{ m}$), the solid volume fractions have been increased for all solid loading ratios tested. The particles might tend to move to the core region of the pipe cross section when the particles move along the pipe. However, the reasons for the observation should be further investigated.

Figure 7 shows the predicted particle velocity profiles corresponding to Case 1-1, Case 1-2 and Case 1-3. The air velocities corresponding to these cases are shown in Figure 5. The particle velocities are lower than the air velocities providing drag force to move the particles ahead. When solid loading ratio is increased by increasing solid mass flow rate, the particle velocity is reduced because the work that is done by unit volume of gas on unit mass of particles gets reduced. Moreover, the profiles become concave with increased solid input. The maximum velocities are located in the range of $2r/D = 0.5-0.6$ for the solid loading ratios, 2.9 and 3.4. The higher particle concentration in the core region of the pipe might restrict the flow of the particles resulting in lower particle velocity in the core region of the pipe cross section.

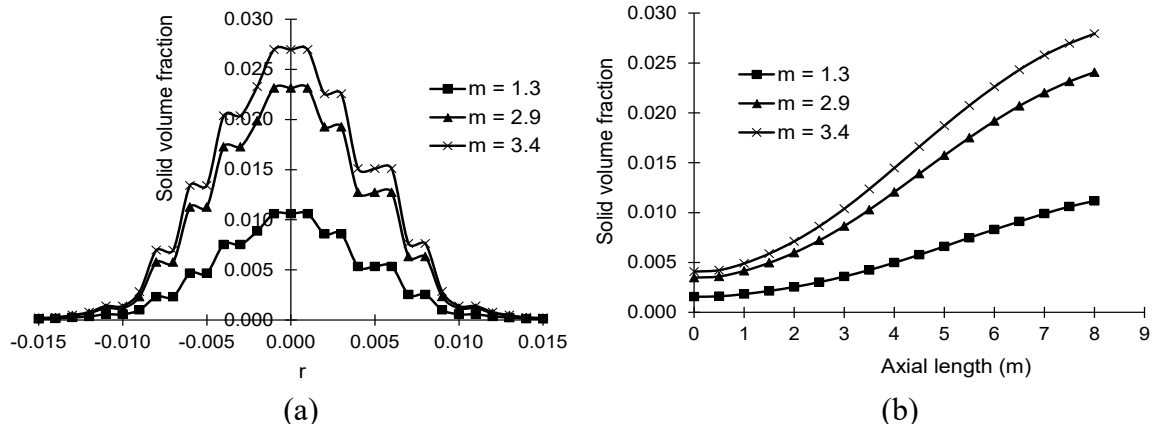


Figure 6. Solid volume fraction along a diameter in a pipe cross section at fully developed region (a) and solid volume fraction along the pipe axis (b) for particle diameter $500 \mu\text{m}$ and $\text{Re} = 2.2 \times 10^4$ (Case-1.1 to Case-1.3).

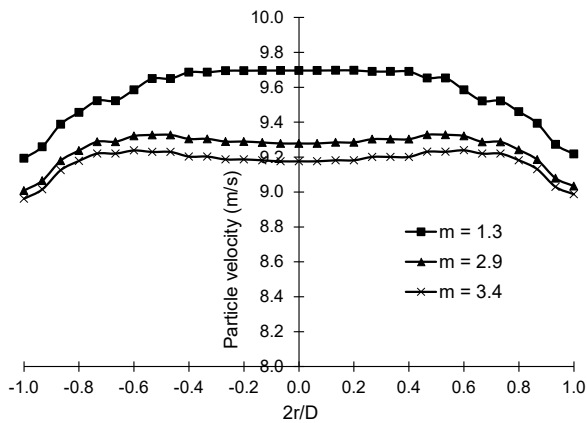


Figure 7. Mean real particle velocity profiles along a diameter in a pipe cross section at fully developed region for particle diameter $500 \mu\text{m}$ and $\text{Re} = 2.2 \times 10^4$ (Case-1.1 to Case-1.3).

6 Conclusion

Euler-Granular approach is used to study the pneumatic conveying characteristics of dilute phase vertical upward flow. Cases with different operating conditions and particle diameters are simulated and some of the results are compared with experimental data from the existing literature. The pressure drop profiles, air and particle velocity profiles and solid distribution profiles are analysed.

The pressure drop results show good agreement with experimental data for $500 \mu\text{m}$ diameter particles and the deviation between experimental and predicted pressure drops is in the range of 9-19%. The prediction of air velocity profiles is also good; however the deviation is increased when the solid loading ratio is increased for $200 \mu\text{m}$ particles. At the higher solid loading ratios tested, the air velocity profiles become concave for $500 \mu\text{m}$ diameter particles. A higher solid concentration could be observed in the core region of the pipe cross section. However no experimental data is available to

validate solid distribution. Finally, it should be noted that the specular coefficient used in Johnson and Jackson particle-wall boundary conditions in the present model has significant effects on the predictions and the predictions made here is by using certain specular coefficient values.

Nomenclature

- D Pipe diameter, (m)
- m Solid loading ratio (solid mass flow rate/air mass flow rate), (-)
- Re Reynolds number of the flow, (-)
- r Horizontal distance from pipe vertical axis, (m)
- z Vertical distance from the pipe inlet, (m)

Acknowledgements

The authors would like to acknowledge the financial support provided by the Research Council of Norway under PETROMAKS II program and Aker BP ASA for the scientific investigation.

References

- W. K. H. Ariyaratne, E. V. P. J. Manjula, C. Ratnayake and M. C. Melaaen. CFD Approaches for Modeling Gas-Solids Multiphase Flows – A Review, in: Proceedings of EUROSIM 2016, September 13-16 2016 Oulu, Finland. Published by IEEE, ISBN 978-1-5090-4119-0, pp. 629-634; <http://eurosims2016.info>, 2016a.
- W. K. H. Ariyaratne, C. Ratnayake and M. C. Melaaen. Eulerian-Eulerian Approach for Modeling Dilute Phase Pneumatic Conveying in a Horizontal Pipe. Proceedings of ICBMH 2016 July 11-14 2016, Darwin, Australia, pp. 409-416, 2016b.
- W. K. H. Ariyaratne, P. Welahettige and M. C. Melaaen. A parametric study for Euler-Granular model in dilute phase vertical pneumatic conveying. International Journal of Computational Methods and Experimental Measurements, 2017, accepted.
- S. Azizi, D. Mowla and G. Ahmadi. Numerical evaluation of turbulence models for dense to dilute gas–solid flows in

- vertical conveyor. *Particuology*, 10 (5): 553-561, 2012. doi: 10.1016/j.partic.2011.12.006.
- H. Bilirgen, E. Levy and A. Yilmaz. Prediction of pneumatic conveying flow phenomena using commercial CFD software. *Powder Technology*, 95 (1): 37-41, 1998. doi: 10.1016/S0032-5910(97)03313-5.
- S. M. El-Behery, W. A. El-Askary, M. H. Hamed and K. A. Ibrahim. 2011. Hydrodynamic and thermal fields analysis in gas–solid two-phase flow. *International Journal of Heat and Fluid Flow*, 32 (3): 740-754, 2011. doi: 10.1016/j.ijheatfluidflow.2011.02.003.
- Fluent. ANSYS Fluent theory guide. ANSYS, Inc.2013.
- D. Gidaspow, R. Bezburuah and J. Ding. Hydrodynamics of circulating fluidized beds: Kinetic theory approach. Proceedings of 7th international conference on fluidization, Gold Coast (Australia), 3-8 May 1992.
- M. Haim, Y. Weiss and H. Kalman. Turbulent Gas-Particles Flow in Dilute State: A Parametric Study. *Particulate Science and Technology*, 21 (1): 1-24, 2003. doi: 10.1080/02726350307498.
- P. C. Johnson and R. Jackson. Frictional–collisional constitutive relations for granular materials, with application to plane shearing. *Journal of Fluid Mechanics*, 176: 67-93, 1987. doi:10.1017/S0022112087000570.
- S. B. Kuang, A. B. Yu and Z. S. Zou. Computational Study of Flow Regimes in Vertical Pneumatic Conveying. *Industrial & Engineering Chemistry Research*, 48 (14): 6846-6858, 2009. doi:10.1021/ie900230s.
- K. Li, S. B. Kuang, R. P. Zou, R. H. Pan and A. B. Yu. Numerical study of vertical pneumatic conveying: Effect of friction coefficient. *AIP Conference Proceedings*, 1542 (1): 1154-1157, 2013. doi:10.1063/1.4812141.
- C. K. K. Lun, S. B. Savage, D. J. Jeffrey and N. Chepurmiy. Kinetic theories for granular flow: inelastic particles in Couette flow and slightly inelastic particles in a general flow field. *Journal of Fluid Mechanics*, 140: 223-256, 1984. doi:10.1017/S0022112084000586.
- E. V. P. J. Manjula, W. K. H. Ariyaratne, C. Ratnayake and M. C. Melaaen. A review of CFD modelling studies on pneumatic conveying and challenges in modelling offshore drill cuttings transport. *Powder Technology*, 305: 782-793, 2017. doi:10.1016/j.powtec.2016.10.026.
- S. Ogawa, A. Umemura and N. Oshima. On the equations of fully fluidized granular materials. *Zeitschrift für angewandte Mathematik und Physik, ZAMP* 31 (4): 483-493, 1980. doi:10.1007/BF01590859.
- J. Ouyang, A. B. Yu and R. H. Pan. Simulation of gas-solid flow in vertical pipe by hard-sphere model. *Particulate Science and Technology*, 23: 47-61, 2005. doi:10.1080/02726350590902479.
- P. Patro and S. K. Dash. Two-fluid modeling of turbulent particle–gas suspensions in vertical pipes. *Powder Technology*, 264: 320-331, 2014. doi:10.1016/j.powtec.2014.05.048.
- C. Ratnayake. A comprehensive scaling up technique for pneumatic transport systems. PhD thesis, Telemark University College, Norway, 2005.
- C. Ratnayake, B. K. Datta and M. C. Melaaen. A Unified Scaling-Up Technique for Pneumatic Conveying Systems. *Particulate Science and Technology*, 25 (3): 289-302, 2007. doi:10.1080/02726350701375949.
- M. Syamlal, W. Rogers and T. J. O'brien. MFIx Documentation; Theory Guide. National Technical Information Service, Springfield, 1993.
- Y. Tsuji, Y. Morikawa and H. Shiomi. LDV measurements of an air-solid two-phase flow in a vertical pipe. *Journal of Fluid Mechanics*, 139: 417-434, 1984. doi:10.1017/S0022112084000422.

Concrete based thermal energy storage for steam generation: A numerical investigation

Shobhana Singh Kim Sørensen

Department of Energy Technology, Aalborg University, Pontoppidanstræde 111, 9022, Aalborg, Denmark,
{ssi,kso}@et.aau.dk

Abstract

Establishing enhancement methods to develop cost-effective thermal energy storage technology requires a detailed analysis. In this paper, a numerical investigation of the concrete based thermal energy storage system is carried out. The storage system consists of a heat transfer fluid flowing inside the heat exchanger tubes embedded in a cylindrical shape concrete configuration. Three-dimensional multiphysics model of the storage system is developed to investigate transient conjugate heat transfer between the two mediums, the heat transfer fluid, and the concrete. The model comprehends the dynamics of storing thermal energy in the storage at the temperature range of 350 – 390 °C. To evaluate the performance of the storage system using finned heat exchanger tubes, thermal characteristics such as charging/discharging time, energy, and exergy efficiency are predicted. The developed model satisfactorily demonstrates the dynamic behavior of the concrete based thermal storage system and its sub-processes, and thus offers a suitable framework for future investigations leading to an easier and more economical solution.

Keywords: Dynamic model, thermal energy storage system, heat transfer enhancement, energy and exergy efficiency

1 Introduction

Thermal energy storage (TES) technologies have been of great merit in eliminating inconsistencies in the demand and supply of energy. TES stores thermal energy typically from renewable sources, waste heat or surplus energy production by heating or cooling a storage medium for later use in industrial processes mainly for power generation, heating, and cooling in buildings, etc. Moreover, TES minimizes fossil fuel consumption, reduce CO₂ emissions and lower the need for costly peak power and heat production capacity. TES systems are extensively categorized into three kinds, namely: sensible heat storage, latent heat storage, and thermo-chemical storage. Concrete thermal energy storage (CTES) is one of the preferable sensible heat storage systems due to low exergy loss, low cost and easy management of the material.

Many research and development projects to demonstrate high temperature TES for concentrated solar power (CSP) have been reported. Solid media thermal storage systems, each with a storage capacity of 350 kWh and a maximum temperature of 390 °C, have been developed by the German Aerospace Center (DLR) for parabolic trough power plants (Tamme et al., 2004; Laing et al., 2006, 2009; Feldhoff et al., 2012). Researchers have also studied the application of TES systems for a direct steam generation (DSG) (Laing et al., 2011; Seitz et al., 2014). A detailed review of case studies on high-temperature thermal energy storage for power generation is reported by Gil et al. (2010) and Medrano et al. (2010). From the reported research, it has become clear that using the sensible heat of solid material to store thermal energy is a promising technology for concentrated solar power plants, however, for DSG, feasible storage designs and heat transfer enhancement techniques are needed to be studied.

Performance improvements are associated mainly with thermo-physical properties of the storage material and design parameters of tubular heat exchanger integrated within that storage material. For a cost-effective TES, it is necessary to select a viable mechanical design with a higher thermodynamic efficiency of the processes involved. Augmentation in heat transfer is one of the enhancement techniques that are used to improve the performance of energy storage systems. Heat transfer augmentation can be achieved by increasing the thermal conductivity of the storage material, by using finned tubes and by dispersing highly conductive particles in the heat transfer fluid (HTF), etc. An experimental study to compare the heat transfer enhancement in a storage system with phase change material (PCM) using circularly and longitudinal finned concentric heat exchanger is reported by Agyenim et al. (2009). They analyzed the heat transfer characteristics using isotherm plots and temperature curves and found that longitudinal finned system performs the best during charging with an insignificant sub-cooling during discharging.

Depending on the application type, CTES requires proper designing to charge and discharge thermal energy which is difficult to anticipate without any prior knowledge of its physical behavior under certain operating conditions. Numerical Heat transfer and fluid

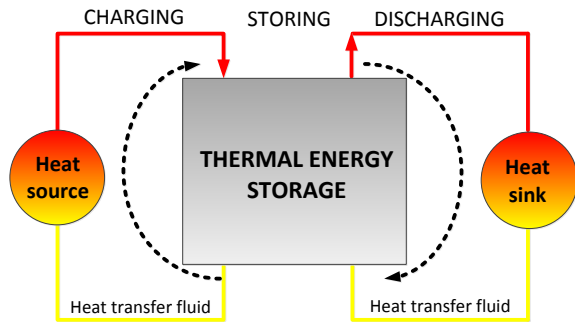


Figure 1. Thermal energy storage system and its sub-process

flow models, in most of the cases, help to understand the critical factors that influence the performance such as variations in spatial and temporal temperature and energy flow, thereby, predict improvements in the system design. Despite this advantage, limited work mainly focused on charging process is available in the literature. Therefore, the aim of this study is to analyze both charging and discharging by developing a three-dimensional (3D) numerical model of CTES to implement a heat transfer enhancement technique for a cost-effective operation. The model is utilized to analyze the influence of finned tubes on storage characteristics during the charging and discharging processes. Determination of the objective variables can help develop a useful framework for future multi-objective optimization of the storage system.

2 Concrete thermal energy storage system: Design description

CTES is a sensible heat storage system which stores the thermal energy in concrete as a storage medium. The HTF flows through the tubes and transfers the thermal energy to concrete where it is stored as sensible heat. Figure 1 shows a schematic of a simple storage process where three main sub-processes namely charging, storing and discharging can be seen. The amount of the energy stored in the storage is equal to the temperature rise and the specific heat capacity of the concrete and is governed by Eq.1 as:

$$Q_s = m \cdot C_p \cdot \Delta T = \rho \cdot V \cdot C_p \cdot \Delta T \quad (1)$$

where Q_s is the amount of thermal energy stored, m is the mass of the storage media, ρ is the density of the storage material, C_p is the specific heat of the storage material, V is the volume of storage media and ΔT is the temperature difference.

The CTES system design investigated in this paper typically consists of a cylindrical concrete unit with a fixed number of embedded heat exchanger tubes. Thermal oil is used as the HTF and the properties are adopted from (Tamme et al., 2004). Figure 2 represents the computational geometry of the CTES unit simulated in the present study. The design can be employed for

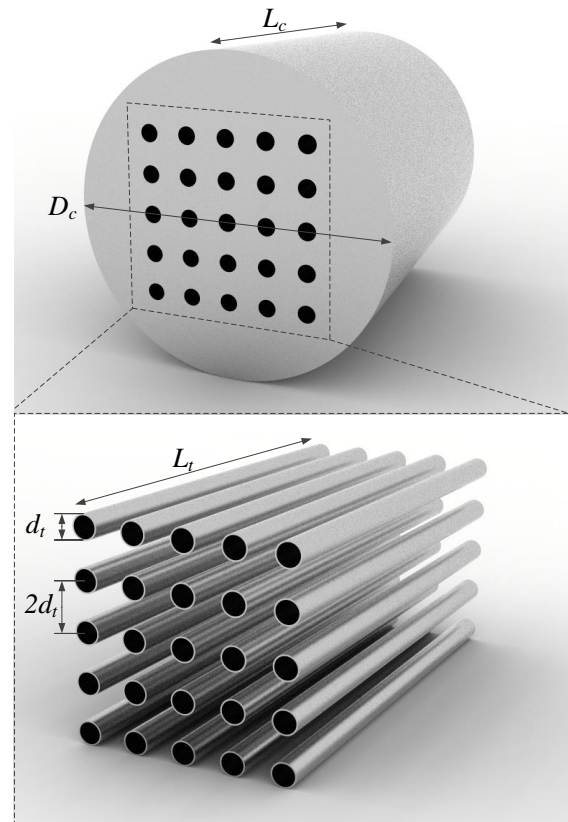


Figure 2. Computational model of the CTES system unit

higher storage capacities when the unit is connected in series to compose a complete module. Longitudinal fins have found to perform better than circular fins in thermal response during charging and discharging (Agyenim et al., 2009); therefore, longitudinal fins are chosen to investigate the impact of finned tubes as shown in Fig.3. The tubes with four longitudinal fins are arranged parallel to the flow direction of HTF. Since the technical feasibility depends upon the system design and excellent thermo-mechanical material properties, high temperature concrete with higher thermal conductivity is used. Table 1 shows the list of system design parameters and thermo-physical properties of the materials used to simulate the system are described in Table 2. The physical processes such as conjugate heat transfer (heat transfer by conduction and convection) and fluid flow in the system are simulated with following assumptions:

- The inlet velocity profile of HTF is fully developed.
- The pressure loss through the tubes is neglected.
- Losses from the system are negligible.
- Concrete properties are isotropic.
- Non-adiabatic storage boundaries.

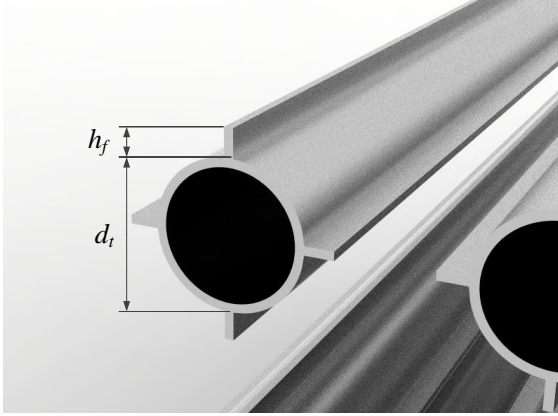


Figure 3. Longitudinal finned tube

3 Model development

3.1 Governing equation and boundary conditions

The dynamic behavior of the HTF flowing inside the heat exchanger tubes is simulated using the continuity equation and the Navier-Stokes equations as:

$$\frac{\partial \rho_f}{\partial t} + \nabla \cdot (\rho_f \mathbf{v}) = 0 \quad (2)$$

where ρ_f is the density of the HTF and \mathbf{v} is the velocity vector.

$$\rho_f \frac{\partial \rho_f}{\partial t} = -\nabla P + \mu \nabla^2 \mathbf{v} \quad (3)$$

where P is the pressure and μ is the dynamic viscosity of the HTF.

During operation of CTES, convective heat transfer takes place from the flowing HTF to the wall of the tube which is governed by the energy equation as:

$$\rho_f C_{p,f} \frac{\partial T}{\partial t} + \rho_f C_{p,f} \mathbf{v} \cdot \nabla T = \nabla \cdot (k_f \nabla T) + Q \quad (4)$$

where $C_{p,f}$ is the specific heat of HTF, k_f is the thermal conductivity of HTF, T is the temperature field in fluid and Q is a source or sink term.

Governing equation for the Simultaneous conductive heat transfer from the heat exchanger tubes to the

Table 1. Design parameters of the CTES system unit

Property	Value
Length of the concrete unit, L_t	0.5 m
Diameter of the concrete unit, D_t	0.3 m
Diameter of the tube, d_t	0.02 m
Length of the tube, L_t	0.5 m
Height of the fin, h_f	0.01 m
Thickness of the fin, δ_f	0.001 m

Table 2. Thermo-physical properties of materials

Property	Concrete	Heat transfer fluid	Heat exchanger tube
Density (kg/m ³)	2200	761	7850
Thermal Conductivity (W/mK)	2.0	0.121	44.5
Heat capacity at constant pressure (J/kgK)	1000	2800	475
Dynamic viscosity (Pas)	–	0.02	–

Table 3. Boundary conditions used to solve the numerical model for the charging mode

Property	Value
Initial temperature during charging, $T_{c,0}$	350°C
Inlet temperature of the HTF during charging, $T_{c,in}$	390°C
Initial temperature during discharging, $T_{d,0}$	390°C
Inlet temperature of the HTF during discharging, $T_{d,in}$	350°C
Flow velocity of the HTF, v	0.25 m/s

concrete is expressed as:

$$\rho_c C_{p,c} \frac{\partial T}{\partial t} = \nabla \cdot (k_c \nabla T) + Q' \quad (5)$$

where $C_{p,c}$ is the specific heat of concrete, k_c is the thermal conductivity of concrete, T is the temperature field in concrete and Q' is a source or sink term.

3.2 Boundary conditions

At $t = 0$ s, $T = T_{c,0}$ for the entire domain during the charging process, while $T = T_{d,0}$ is set for discharging process. In order to simulate the charging and discharging, the flow direction of the heat transfer fluid is reversed so as the initial condition. CTES system is analyzed for only 3600 s for each case. The temperature of HTF at the inlet of the tube is set $T = T_{c,in}$ during charging, and during discharging $T = T_{d,in}$. No slip boundary condition, $\mathbf{v} = 0$ is applied to the tube wall. External insulation of the storage module is usually sufficiently thick to avoid the heat losses. All outer walls of the cylindrical concrete module are simulated as insulated walls by setting the boundary condition $\mathbf{n} \cdot k \nabla T = 0$. Initial and boundary conditions used to solve the model for both sub-processes of the storage unit are given in Table 3.

3.3 Solution procedure

The governing equations (Eqs.2-5) are valid for both charging and discharging process and are solved numerically with the appropriate initial and boundary conditions using a commercially available finite element method (FEM) software COMSOL v. 5.2a (Multiphysics, 2017). Sufficiently fine grid with 993 785 and 1 074 263 elements is used to obtain the grid independent solution. Present model results are validated by the results achieved by Tamme et al. (2004). Figure 4 shows a

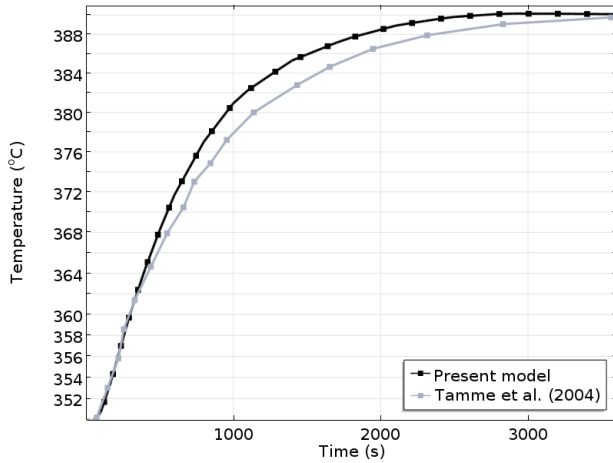


Figure 4. Comparison of storage temperature at distance 0.04 m from tube during charging

comparison between the average temperature at a distance 0.04m in the storage predicted by the present model and that of Tamme et al. (2004). Reasonably good agreement between the results can be seen from the figure which confirms the reliability of the developed model.

4 Results and discussion

4.1 Average temperature profile

Figures 5a and b show a change in average temperature of the concrete storage unit with time during charging and discharging process. During charging, the thermal energy is stored as sensible heat which increases the average storage temperature with time. It can be seen that the system with finned tubes charges relatively faster than the system without finned tubes. At $t = 3600s$, the average temperature with bare tubes reaches $377^{\circ}C$ while the temperature with finned tubes is observed $378^{\circ}C$. Discharging of the storage systems can be seen in Fig.5b where the average temperature of the storage units decrease with time. Like charging process, the storage system with finned tubes tends to discharge relatively faster than the system with bare tubes. Note that in the present study, the system discharges from a fully charged state, i.e. from $T = 390^{\circ}C$. For better visualization, temperature distribution on a axial cross-sectional plane of the storage, with and without finned tubes, at different spans of time during the charging process is shown in Fig. 6. The dark blue contour lines around the tubes indicate the high temperature regions which spreads as the charging time progresses. The cooler region can be seen as green contour lines that exists close to the outer walls of the storage.

4.2 Charging and discharging time

During charging, heat is transferred from a higher temperature HTF to a lower temperature concrete storage while the reverse takes place in discharging. Implementation of fins on tubes increases the heat

transfer rate and thus decreases charging and discharging period. Comparing time periods of the sub-processes provide a rational way to test the effectiveness of an enhancement method. It can be observed from Fig. 5a that finned tubes can considerably reduce the charging time. For instance, the storage system with finned tubes takes approximately 200 s less charging time to attain the average temperature of $366^{\circ}C$ than the system without finned tubes. In other words, the charging time with finned tubes is reduced by approximately 50%. The reduction, however, decreases with the charging time. For instance, to attain the average storage temperature of $377^{\circ}C$, the charging time with finned tubes is reduced by approximately 11%. Similar impact is observed in the case of discharging (Fig. 5b). It is worth to note that for a system to be cost-effective, the reduction in the charging time has to be balanced by additional cost appended by the fin material on the tubes that are used in the enhancement. The TES system is considered cost-effective if the cost of implementing finned tubes instead of bare tubes increase the production capacity for the application they are installed.

4.3 Energy and exergy analysis

Energy and exergy analysis is necessary to understand the thermodynamic behavior and the performance of thermal energy system. Energy based performance measures are often misleading, and do not reflect the useful energy correctly. Exergy analysis, on the other hand, helps to overcome such shortcomings of the energy analysis (Dincer and Rosen, 2002). In the present study, energy and exergy input during charging, and energy and exergy recovered during discharging are evaluated.

The amount of thermal energy stored or recovered in CTES system can be calculated using Eq.(1) as:

$$E(t) = mC_p(T(t) - T_0) \quad (6)$$

where $T(t)$ and T_0 are the volume-averaged temperatures of the concrete module at any instance of time, t and at $t = 0s$, respectively. Note that losses from the system are considered negligible, and therefore, are not taken into account in the present study.

The exergy content at each time step of the simulation can be calculated by monitoring the volume-averaged temperature in the storage as (Dincer and Rosen, 2002):

$$\xi(t) = mC_p \left[(T(t) - T_0) - T_0 \ln \left(\frac{T(t)}{T_0} \right) \right] \quad (7)$$

The impact of using finned tubes can be seen from the rate of charging and discharging the thermal energy in Figs.7a and b. The change energy input during charging as a function of time can be seen in Fig. 7a. Within the charging time of 3600s, 1.85MJ of thermal energy is stored by the system with bare tubes, whilst, the amount of energy stored by a system with finned tubes is 1.95MJ. During the discharging, fully charged storage has 2.8MJ

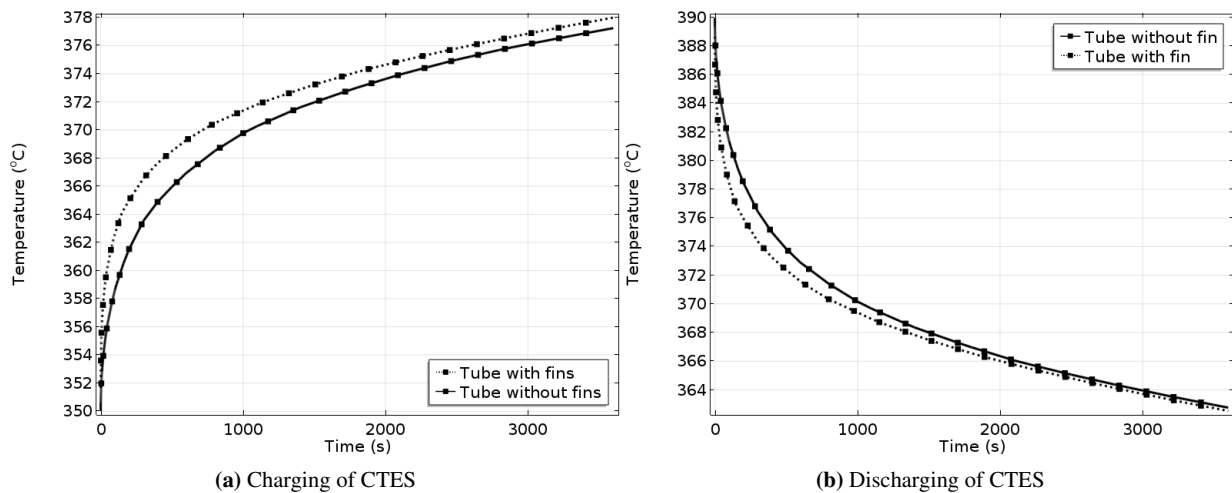


Figure 5. Variation of axial temperature of the concrete thermal energy storage system during sub-processes

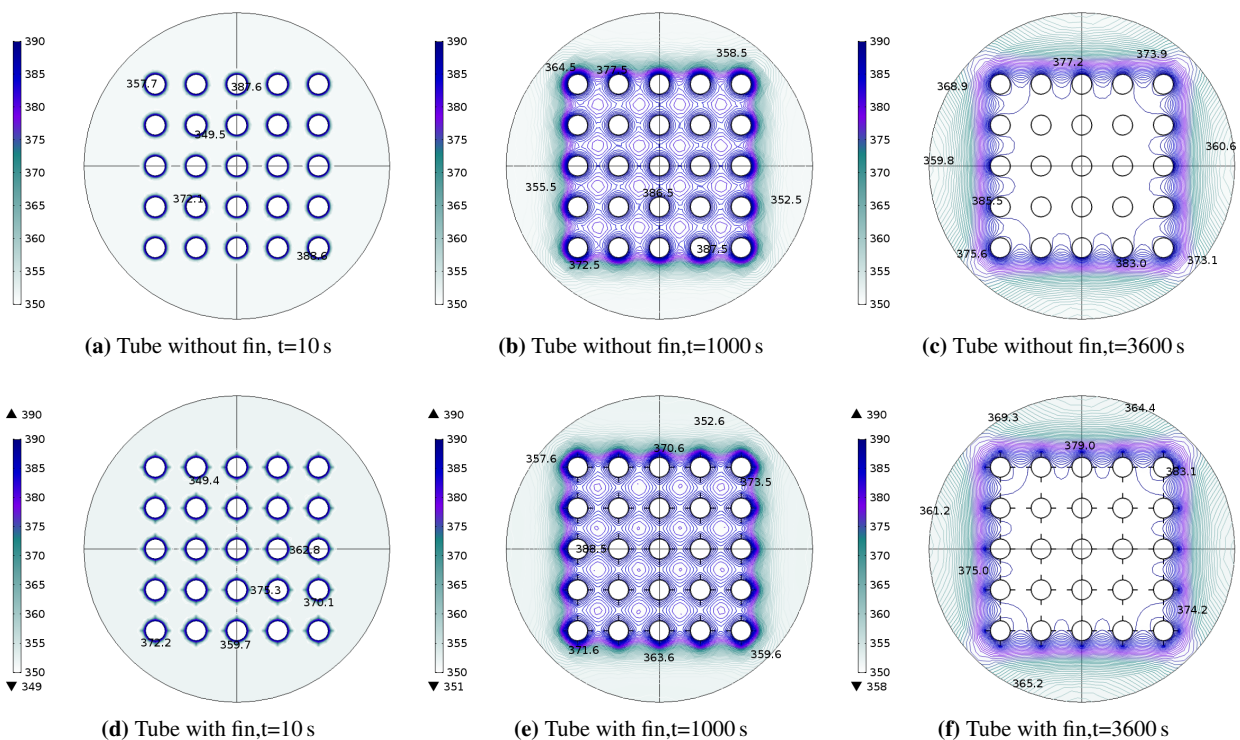


Figure 6. Average temperature of the concrete thermal energy storage system with and without fins during charging

stored thermal energy which decreases with the discharging time as the HTF recovers it. Furthermore, the change in CTES exergy content during charging and discharging can be seen in Fig.8a and b, respectively.

4.4 Energy and exergy efficiency

Charging period energy efficiency can be defined as the ratio of energy accumulated in the CTES system to the input thermal energy during the charging process which can be mathematically expressed as (Dincer and Rosen,

2002):

$$\eta_c = \frac{E(t)}{E_0} \quad (8)$$

Exergy efficiency for charging period is defined as the ratio of exergy accumulation in CTES to the exergy input to CTES during the charging process and can be expressed as:

$$\psi_c = \frac{\xi(t)}{\xi_0} \quad (9)$$

Furthermore, energy and exergy efficiencies for discharging period is determined as the ratio of thermal

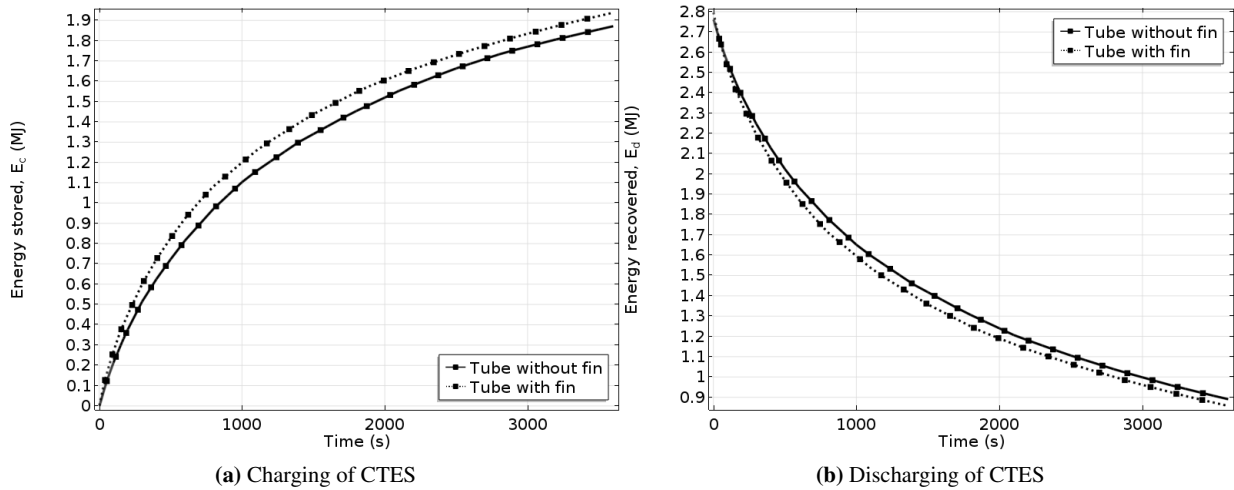


Figure 7. Change in thermal energy of concrete thermal energy storage system during sub-processes

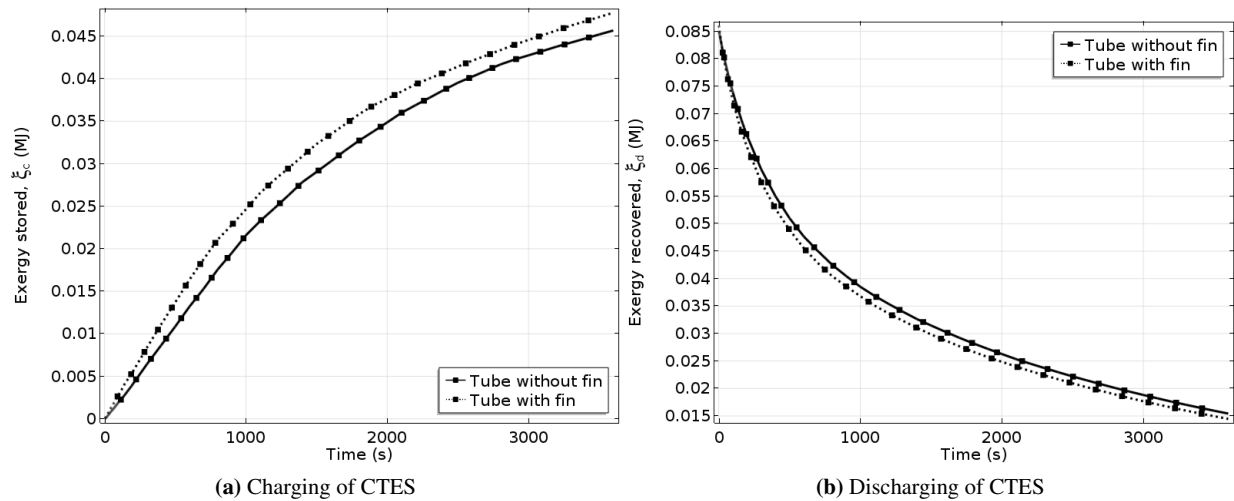


Figure 8. Change in exergy of the concrete thermal energy storage system during sub-processes

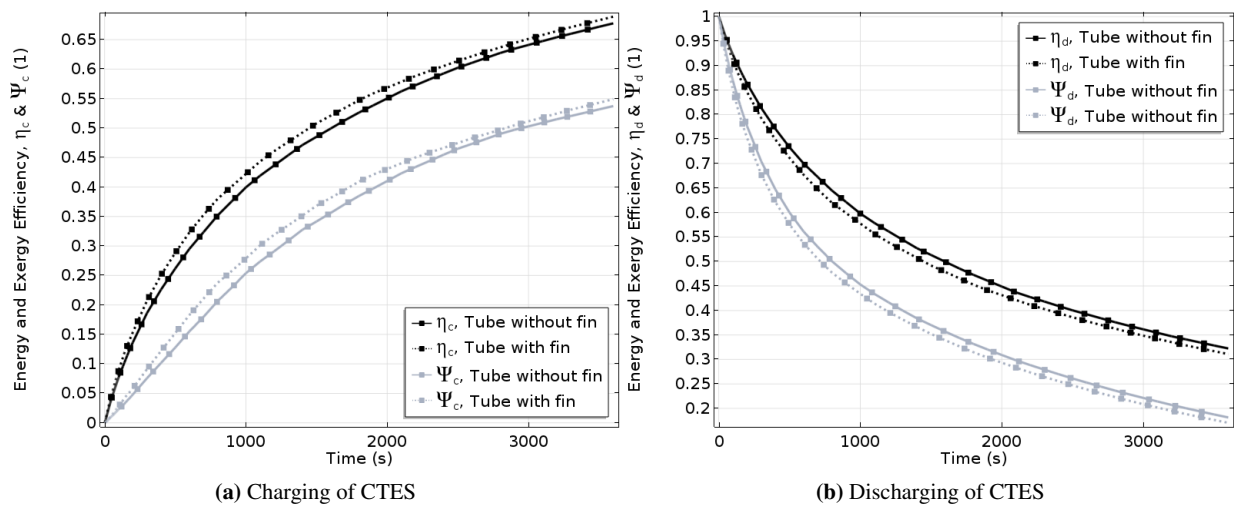


Figure 9. Energy and exergy efficiencies of the concrete thermal energy storage system during sub-processes

energy or exergy recovered from CTES to the energy or exergy input to CTES. Efficiencies for both sub-processes are evaluated by monitoring the volume-averaged temperature within the storage system at each time step.

Figures 9a and b show the variation of energy and exergy efficiencies during charging and discharging of the CTES unit with and without finned tubes. The charging efficiency is zero at $t = 0$ s which increases with time due to the accumulation of thermal energy in the concrete. At charging time $t = 3600$ s, the energy efficiency of the system without fins is observed 67.77%. For the system with finned tubes, the charging energy efficiency is 68.90%, which is slightly higher than the system without finned tubes. The efficiency can, however, be improved with optimized design and operating parameters. Due to negligible heat losses, the system would eventually attain charging efficiency of 100% where the storage is said to be fully charged. The exergy efficiency of the system is found lower than energy efficiency which shows a more meaningful value of the storage system performance that could be further improved by enhancement methods. It is apparent from Fig.9b that the thermal energy and exergy are being recovered from the fully charged mode during discharging period, therefore, both efficiencies decrease with time. From the results, it can be concluded that system with finned tubes has a relatively higher efficiency than the storage system without finned tubes.

5 Conclusion

The numerical investigation on concrete based thermal energy storage is carried out. Multiphysics model is developed to couple the heat transfer with the fluid flow in the storage system of heat exchanger tubes with and without fins. From the simulation results, the potential of finned tubes to enhance the heat transfer is determined in terms of storage temperature distribution, energy, and exergy efficiencies. For a given design of the storage system, selection of finned tubes can decrease the charging time by approximately 50 – 11%. In addition, energy and exergy analysis concludes a considerable impact of finned heat exchanger tubes on energy and exergy efficiencies. The developed model can be employed as a framework to investigate the time-dependent performance of the CTES system integrated with a thermal power plant for steam generation. Efficient and cost-effective energy storage technology plays a key role in the grid integration of the renewables. Based on the present model, optimization of the design parameters such as number fins and tubes, heat exchanger tubes diameter that could significantly lower the investment cost for large scale storage capacity will be the focus of future studies.

References

F. Agyenim, P. Eames, and M. Smyth. A Comparison of Heat Transfer Enhancement in Medium Temperature Thermal

Energy Storage Heat Exchanger Using Fins and Multitubes. *Solar Energy*, 83(9):1509–1520, 2009. ISSN 0038092X. doi:10.1016/j.solener.2009.04.007.

- I. Dincer and M. Rosen. *Thermal energy storage: systems and applications*. John Wiley & Sons, 2002.
- J. F. Feldhoff, K. Schmitz, M. Eck, L. Schnatbaum-Laumann, D. Laing, F. Ortiz-Vives, and J. Schulte-Fischedick. Comparative system analysis of direct steam generation and synthetic oil parabolic trough power plants with integrated thermal storage. *Solar Energy*, 86(1):520–530, 2012. ISSN 0038092X. doi:10.1016/j.solener.2011.10.026.
- A. Gil, M. Medrano, I. Martorell, Ana Lázaro, P. Dolado, B. Zalba, and L. F. Cabeza. State of the art on high temperature thermal energy storage for power generation. Part 1-Concepts, materials and modellization. *Renewable and Sustainable Energy Reviews*, 14(1):31–55, 2010. ISSN 13640321. doi:10.1016/j.rser.2009.07.035.
- D. Laing, W. D. Steinmann, R. Tamme, and C. Richter. Solid media thermal storage for parabolic trough power plants. *Solar Energy*, 80(10):1283–1289, 2006. ISSN 0038092X. doi:10.1016/j.solener.2006.06.003.
- D. Laing, D. Lehmann, M. Fi, and C. Bahl. Test results of concrete thermal energy storage for parabolic trough power plants. *Journal of Solar Energy Engineering, Transactions of the ASME*, 131(4):410071–410076, 2009. ISSN 01996231. doi:10.1115/1.3197844.
- D. Laing, C. Bahl, T. Bauer, and W. D. Lehmann, D. and Steinmann. Thermal energy storage for direct steam generation. *Solar Energy*, 85(4):627–633, 2011. ISSN 0038092X. doi:10.1016/j.solener.2010.08.015.
- M. Medrano, A. Gil, I. Martorell, X. Potau, and L. F. Cabeza. State of the art on high-temperature thermal energy storage for power generation. Part 2-Case studies. *Renewable and Sustainable Energy Reviews*, 14(1):56–72, 2010. ISSN 13640321. doi:10.1016/j.rser.2009.07.036.
- COMSOL Multiphysics. COMSOL Multiphysics®. Technical report, <https://www.comsol.com/>, 2017.
- M. Seitz, P. Cetin, and M. Eck. Thermal storage concept for solar thermal power plants with direct steam generation. *Energy Procedia*, 49:993 – 1002, 2014. ISSN 1876-6102. doi:http://dx.doi.org/10.1016/j.egypro.2014.03.107.
- R. Tamme, D. Laing, and W. D. Steinmann. Advanced Thermal Energy Storage Technology for Parabolic Trough. 126(2): 794–800, 2004. doi:10.1115/1.1687404.

Dynamic Modeling and Simulation of an Offshore Combined Heat and Power (CHP) Plant

Jairo Rúa Rubén M. Montañés Luca Riboldi Lars O. Nord

Department of Energy and Process Engineering, NTNU - Norwegian University of Science and Technology,
Trondheim - Norway, jairo.r.pazos@ntnu.no

Abstract

The design and analysis of a flexible combined heat and power (CHP) system where the exhaust of two gas turbines is utilized as the heat source for a steam Rankine cycle is proposed in this paper. The case of study is the Johan Castberg off-shore facility, located in the Barents Sea, Norway. The steady-state design of the CHP system is developed with a specialized software based on the peak demand conditions of the platform, which account for 58 MW of electric and shaft power, and 52 MW of heat. A multi-objective optimization approach is followed in order to attain optimal designs where high efficiency is achieved while keeping reasonable weight to power ratios. Once the power cycle design is selected, the detailed dynamic modeling of the different components integrating the cycle is presented and implemented in Modelica language. Steady-state design and off-design validation of the thermal power plant model is carried out, and preliminary results are presented to show the ability of the dynamic model to provide reasonable information of the steam bottoming cycle transient operation.

Keywords: dynamic process simulation, steam Rankine cycle, waste heat recovery, multi-objective optimization, offshore flexible operation, Modelica, genetic algorithm.

1 Introduction

The implementation of mitigation policies, like CO_2 emission taxation (Ministry of Environment, 2012) and the participation of Norway in the European Union emission trading system (ETS), has motivated the improvement of heat and power generation systems employed in offshore oil and gas facilities. The petroleum sector is responsible of 30% of the total CO_2 emissions of Norway, with the simple gas turbine cycles currently employed in the Norwegian continental shelf being the source of more than 80% of the CO_2 emissions generated by this sector (Norwegian Ministry of Petroleum and Energy, 2017).

New power generation systems with better performance and lower emissions are needed in order to mitigate the effects of the oil and gas facilities on the environment, and make this industry more competitive from an economic point of view. Combined cycles are regarded as a promising and feasible alternative to the traditional gas turbines due to their higher efficiency and to their technology matu-

riety (Kloster, 1999). Low weight and operation flexibility are also fundamental criteria in the design of combined cycles. The cost of offshore facilities increases rapidly with the weight while the operation as a stand-alone systems requires that the fluctuations in power and heat demand must be entirely matched by the power system. A trade-off among compactness, flexibility and high efficiency may be achieved, even during off-design conditions, if the traditional heat recovery steam generator with several pressures levels and steam drums is replaced by a once-through steam generator (OTSG) for offshore applications (Nord and Bolland, 2012, 2013). The low weight and flexibility of this basic configuration allows the installation of different tailor-made alternatives, which enhances the utilization of combined cycles for waste heat recovery applications as different objectives may be achieved with different bottoming cycles (Pierobon et al., 2014a).

In addition to the design and off-design performance, the analysis of unsteady operation is specially useful for offshore combined cycles since they work in transient mode due to the variations in heat and power demand and fuel composition. Dynamic modeling and simulation of these systems may predict possible imbalances between power generation and consumption, and may identify unstable scenarios where a reliable and optimum performance cannot be guaranteed. Moreover, critical scenarios as the trip of a gas turbine may be analyzed, ensuring the operation robustness and safety of the power plant (Benato et al., 2014).

The utilization of dynamic models can also improve the design of control systems and strategies (Montañés et al., 2017). Traditional steady design procedures aim to achieve the highest possible efficiency or the correct balance between efficiency and weight to power ratio. Unsteady performance is not considered at this stage but it is studied when the control strategy is being designed, leading to excessively aggressive control configurations where the off-design operation is worsen as a result of the limitations established by the dynamic operation. Evaluating the unsteady performance of a certain power plant design by means of a dynamic model may discard its implementation due to the violation of specific performance constraints, albeit its possible high efficiency or low weight during nominal operation (Pierobon et al., 2014b). Therefore, the integration of dynamic models in the selection

criteria of a power cycle design can improve the overall performance of the system. Dynamic response and effectiveness of the control strategy of a thermodynamic cycle for waste heat recovery applications may be tested under certain off-design conditions if a dynamic model is developed for such purpose (Mazzi et al., 2015). A dynamic model of a small-scale ORC was also employed to propose and compare three different control strategies, showing that with the correct control strategy the efficiency remains in reasonable levels even if the heat source conditions are modified (Quoilin et al., 2011).

Dynamic models can also be utilized to analyze critical scenarios where extreme conditions for the equipment may be expected and steady-state models do not provide enough information. As a result, new start-up conditions with higher thermal gradients but similar maximum temperatures that allow to halve the time required to generate the maximum power may be achieved (Alobaid et al., 2008). A reduction in the start-up time without increasing the stress limits was also found by (Casella and Pretolani, 2006), who also proposed another strategy that reduces the stress peak extending the lifetime without increasing the start-up time.

This paper aims at developing dynamic models for power plant components and testing their performance during transient operation of a combined heat and power plant. In addition, preliminary results of the operation flexibility of the selected CHP design, i.e. the adaptability to fast operation changes, are shown. The description of the case study and the methodology followed to assess the dynamic performance of the CHP plant are presented in Section 2. The modeling approach utilized for the development of the steady and dynamic model is covered in Section 3. Results of the dynamic simulations are reported and discussed in Section 4. Concluding remarks are given in Section 5.

2 Case study and methodology

The case study is the power system needed in the Johan Castberg field, located in the Barents sea. The heat and power requirements have been assessed for its lifetime, expecting heat demands between 32 MW and 52 MW, and power demands ranging from 42 MW to 58 MW (Statoil ASA, 2016).

A combined heat and power plant is proposed as an alternative power generation system where heat from the exhaust gases of two gas turbines is utilized as a heat source for a steam bottoming cycle. Figure 1 shows a simplified layout of the CHP plant. Two GE LM2500+G4 gas turbines produce the majority of the required power while the energy contained in their exhaust gases is recovered in a OTSG to produce the steam utilized in the bottoming cycle. The design point specifications of this gas turbine model are specified in Table 1. The high ratios between the heat and power demand entail a challenge for the steam Rankine cycle and a back-pressure steam turbine has to

Table 1. Design point specifications of the GE LM2500+G4 gas turbine.

Variable	Design point value
Net power output [MW]	32.50
Net efficiency [%]	36.50
Exhaust gas flow rate [kg/s]	89.90
Exhaust temperature [°C]	552
Net heat rate [kJ/kWh]	9867
Gas turbine inlet Δp [mbar]	10
Gas turbine exhaust Δp [mbar]	10
Ambient temperature [°C]	10
Ambient pressure [bar]	1.0 13
Air humidity [%]	60.00
Gas turbine fuel	Production gas

be utilized. Thus, the superheated steam produced in the OTSG is not totally expanded in order to have enough energy to produce the required process heat. A fraction of this steam is sent to one of the condensers of the selected parallel configuration where pressurized water at 150°C is produced to meet the heat demand. The remaining superheated steam is condensed in the second branch condenser using sea water as cooling fluid.

The large variations in heat and power demand that may be experienced in the offshore facility and the fact that the power generation system operates as a stand-alone system require that the CHP plant operates in a flexible manner. Therefore, the dynamic operation of the proposed design must be assessed in order to ensure the correct functioning of the power plant under varying conditions. In addition, as previously mentioned, low weight and compactness are fundamental conditions in this kind of thermal power systems. Thus, a dynamic analysis of a preliminary design of the CHP plant obtained from a multi-objective optimization was carried out in order to verify that the combined cycle performs correctly during unsteady operation.

2.1 Steady state design and multi-objective optimization

The life-time assessment of the energy requirements expected for the offshore oil field shows that maximum demands of heat and power may occur simultaneously (Statoil ASA, 2016). Hence, the nominal operation point was selected to correspond to peak demands of heat and power, 52 MW and 58 MW respectively, in order to ensure that these conditions are met by the power generation system.

Once the design conditions of the CHP plant were defined, the steady state modeling and design was carried out utilizing the specialized software Thermoflex (Thermoflow Inc, 2016). The selection of this tool was based on its reliability, as it has been extensively tested and validated with industrial data. The thermodynamic states were determined by means of mass and energy conservation laws, and the boundary conditions imposed to the

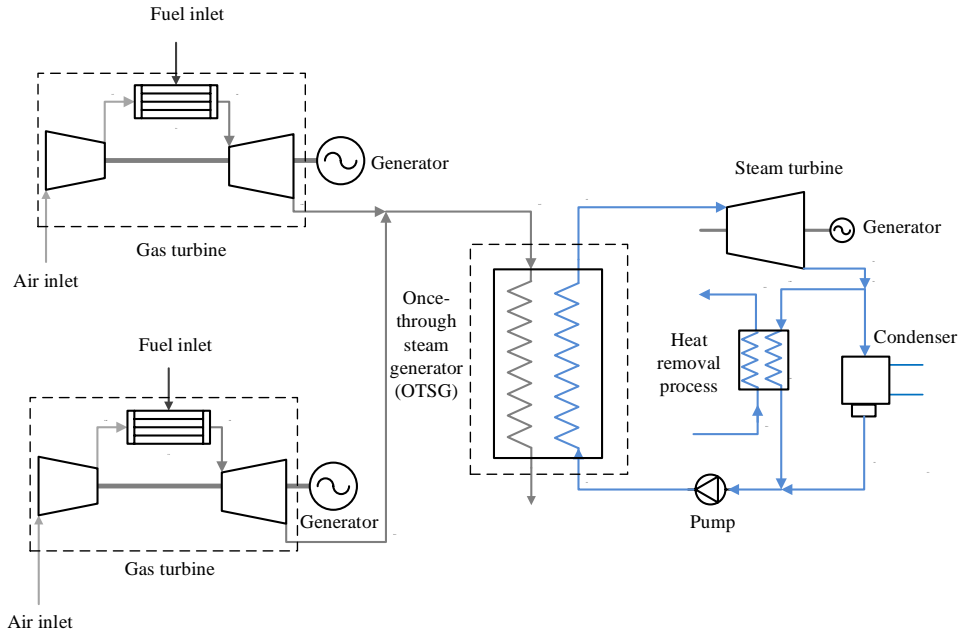


Figure 1. Simplified layout of the proposed power generation system for the offshore facility in Johan Castberg field.

model. From this data, the sizing of the components of the steam Rankine cycle was carried out. Subsequently, a constrained multi-objective optimization based on a genetic algorithm included in the global optimization MATLAB toolbox (MathWorks, 2017) was performed, where the heat rate and the weight to power ratio were the objective functions to be minimized (Riboldi and Nord, 2017). The selected decision variables during the optimization procedure were the steam turbine inlet pressure, p_{steam} , and temperature, T_{steam} , the pinch point difference in the evaporating section of the OTSG, ΔT_{pinch} , and the gas turbine load of one turbine, $GT_{2,load}$, utilizing the other unit to match the power demand. The bounds of the decision variables are reported in Table 2. A population size of 150 was selected while a maximum of 15 generations were allowed. Crossover and tolerance were set equal to 0,8 and 10^{-3} respectively. The stopping criterion utilized in this optimization procedure was either the exceedance in the maximum number of generations or having an average change in the spread of the Pareto front lower than the tolerance selected. A two-dimensional Pareto front was obtained as a result of this procedure. The solution that provides the best balance for the requirements of the offshore facility was selected.

2.2 Dynamic model development and unsteady performance assessment

A dynamic model of the preliminary CHP plant design must be built in order to evaluate its operation under varying scenarios, e.g. load changes or unit trips. The dynamic modeling language Modelica was utilized for the development of such model, as its object-oriented nature and the existence of specialized libraries ease the implementation

Table 2. Lower and upper bounds of the selected decision variables.

Decision variables	Lower bound	Upper bound
p_{steam} [bar]	10	40
T_{steam} [$^{\circ}$ C]	400	515
ΔT_{pinch} [$^{\circ}$ C]	10	30
$GT_{2,load}$ [%]	75	94

of transient conservation laws, correlations and the component dimensions calculated in the previous step. In this work, the open-source library specialized in power plants ThermoPower (Casella and Leva, 2003) was employed.

Open-loop simulations, i.e. without control, may be carried out from this model in order to achieve a deeper understanding of the intrinsic unsteady behavior of the cycle. However, a suitable control strategy with appropriate tuning parameters was implemented in the dynamic model in order to simulate real plant operation. The steam turbine was operated in sliding pressure mode, while the mass flow rate of steam through the primary condenser was utilized to regulate the temperature of the pressurized water employed as a process heat means. The water level of this condenser was controlled in order to ensure a stable operation of the system, whereas the water level of the secondary condenser was allowed to vary, absorbing the fluctuations of the process heat section and acting as a water buffer under off-design loads. In addition, the live steam temperature was controlled by means of the mass flow rate circulating in the Rankine cycle. PI controllers were utilized in order to ensure a stable operation.

3 Modeling Approach

3.1 Gas turbine model

Gas turbines' dynamics were not considered as their transient operation is much faster than that of the steam Rankine cycle. Instead, the gas turbines were modeled with validated quasi-static models, and the exhaust gas stream was utilized as boundary conditions to the dynamic process model (Montañés et al., 2017). Off-design conditions were obtained from the compressor and turbine maps of the gas turbine validated by Thermoflex, and a variable characteristic that simulates the fluctuating exhaust gas conditions was implemented in the dynamic model.

3.2 OTSG model

The different sections of the OTSG were modeled as three individual heat exchangers: an economizer, a once-through boiler (OTB), and a superheater. The preheating of the liquid fluid takes place in the economizer, where sufficient difference between the boiling point and the outlet temperature, i.e. an approach point, was left in order to ensure that no evaporation occurred in this component during off-design operation. The OTB mainly modeled the vaporization of the working fluid, but it also included the preheating of the water leaving the economizer until saturation conditions and some superheating of the steam during design operation. The final degree of superheating of the steam produced in the OTB is achieved in the superheater.

Each of the heat exchangers was spatially discretized in (N-1) cells, where mass and energy conservation laws, and heat transfer correlations were applied (see Figure 2). Momentum conservation law was not included as the inertia of the fluid was neglected and the pressure drops were modeled as lumped parameters at the outlet of each component.

The mass and energy conservation laws were equally modeled in the three heat exchangers and for both gas and water/steam sides. The discretized mass conservation expression for a one-dimensional flow is:

$$\sum_{j=1}^{N-1} \frac{dM_j}{dt} = \dot{m}_{in} - \dot{m}_{out} \quad (1)$$

where \dot{m}_{in} and \dot{m}_{out} are, respectively, the mass flow rates at the inlet and outlet of each heat exchanger; and M_j is the mass of fluid in each cell, given by:

$$\frac{dM_j}{dt} = V_j \cdot \left(\frac{\partial \bar{\rho}}{\partial h} \Big|_j \cdot \frac{dh'_j}{dt} + \frac{\partial \bar{\rho}}{\partial p} \Big|_j \cdot \frac{dp}{dt} \right) \quad (2)$$

being V_j the volume of each cell, and with the average partial derivatives of density respect to enthalpy and pressure, $\frac{\partial \bar{\rho}}{\partial h} \Big|_j$ and $\frac{\partial \bar{\rho}}{\partial p} \Big|_j$, in the center of the cell calculated from their nodes values.

$$\frac{\partial \bar{\rho}}{\partial h} \Big|_j = \frac{1}{2} \left(\frac{\partial \rho}{\partial h} \Big|_{j+1} + \frac{\partial \rho}{\partial h} \Big|_j \right) \quad (3)$$

$$\frac{\partial \bar{\rho}}{\partial p} \Big|_j = \frac{1}{2} \left(\frac{\partial \rho}{\partial p} \Big|_{j+1} + \frac{\partial \rho}{\partial p} \Big|_j \right) \quad (4)$$

The one-dimensional spatially discretized energy conservation law is:

$$V_j \cdot \bar{\rho}_j \cdot \frac{dh'_j}{dt} - \bar{m}_j \cdot (h_{j+1} - h_j) = \dot{Q}_j + V_j \cdot \frac{dp}{dt} \quad (5)$$

where $\bar{\rho}_j$ is the average density of each discretization, h'_j is the enthalpy state variable at the center of the cell, h_j the fluid specific enthalpy evaluated at the nodes, \dot{Q}_j the heat flow from or to the wall, p is the pressure, and \bar{m}_j the mass flow rate in each cell, defined as:

$$\bar{m}_j = \dot{m}_{in} - \sum_{j=1}^{j-1} \frac{dM_j}{dt} - \frac{1}{2} \frac{dM_j}{dt} \quad (6)$$

The heat flows between the hot and cold fluids, sub-index h and c respectively, and the metal tube were calculated in the center of each cell as:

$$\dot{Q}_{j,h} = \gamma_h \cdot A_{j,h} \cdot \left(\frac{T_{j+1,h} + T_{j,h}}{2} - T_{wall,j,h} \right) \quad (7)$$

$$\dot{Q}_{j,c} = \gamma_c \cdot A_{j,c} \cdot \left(\frac{T_{j+1,c} + T_{j,c}}{2} - T_{wall,j,c} \right) \quad (8)$$

being T_{j+1} and T_j the temperatures at the nodes, $T_{wall,j}$ the temperature of the wall in the outer or inner tube surfaces evaluated at the center of the cell, A_j the heat transfer surface for each fluid, and γ the convection heat transfer coefficient. In the gas side this coefficient can be calculated with the relation (Incropera et al., 2007):

$$\gamma = \gamma_{nom} \left(\frac{\dot{m}}{\dot{m}_{nom}} \right)^{0.6} \quad (9)$$

where γ_{nom} is the convection heat transfer coefficient during steady-state nominal operation utilized in Thermoflex.

In the water side of the economizer and superheater constant heat transfer coefficients were employed since they were calculated in the design stage and the main thermal resistance was the heat transfer in the gas side. However, the value of this coefficient in the water side of the OTB varies substantially due to the phase changes that occur, and an overall coefficient could not be utilized. Thus, the Dittus-Boelter correlation with constant heat transfer value consisting on the saturated boiling region heat transfer coefficient was employed:

$$\gamma = 0.023 \frac{k}{D_{hyd}} Re^{0.8} Pr^{0.4} \quad (10)$$

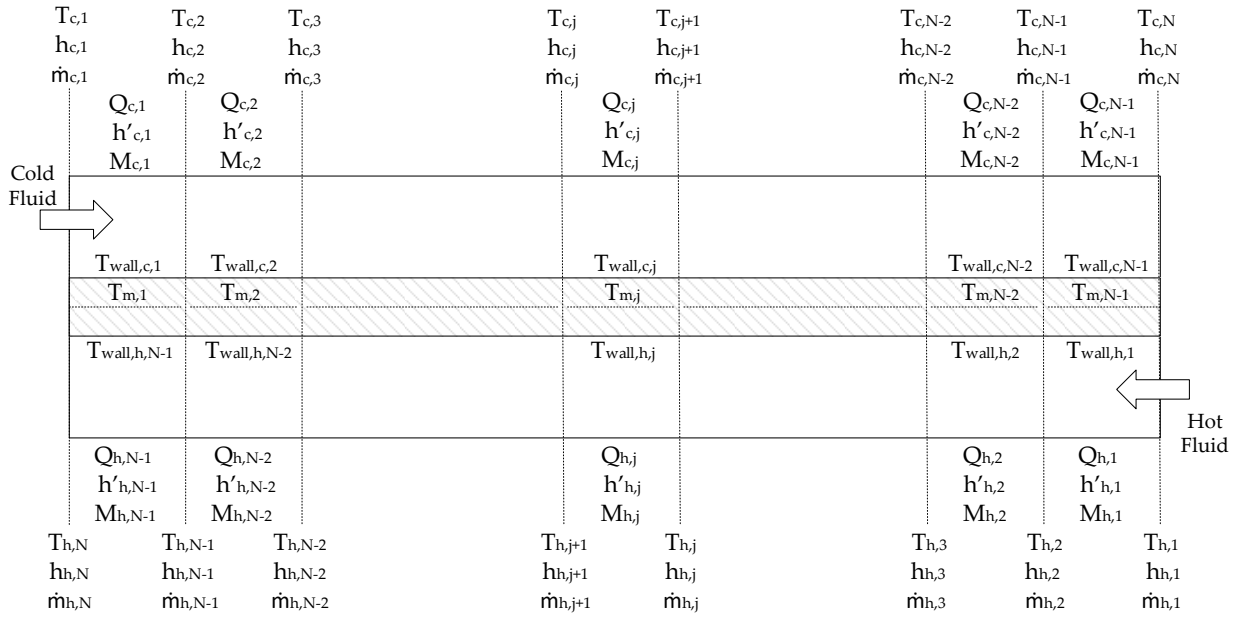


Figure 2. Modeling paradigm of the once-through steam generator.

where k is the thermal conductivity of the fluid, D_{hyd} is the hydraulic diameter, Re is the Reynolds number, and Pr is the Prandtl number.

The heat capacity of the metal tubes that accounts for the thermal inertia of the heat exchangers during dynamic operation is included in the model as:

$$V_m \cdot \rho_m \cdot C_{p_m} \cdot \frac{dT_m}{dt} = \dot{Q}_h + \dot{Q}_c \quad (11)$$

Here, V_m is the volume of metal, ρ_m is the metal density, and C_{p_m} is the metal heat capacity. T_m is the temperature in between both sides of the metal tube, and \dot{Q}_h and \dot{Q}_c are the heat flows coming from the hot and cold sides, respectively.

The heat conduction through the metal tubes is defined as:

$$\dot{Q}_h = Nt \cdot \frac{\lambda \frac{2\pi L}{N-1} \cdot (T_{wall,h} - T_m)}{\log\left(\frac{2 \cdot r_{ext}}{r_{ext} + r_{int}}\right)} \quad (12)$$

$$\dot{Q}_c = Nt \cdot \frac{\lambda \frac{2\pi L}{N-1} \cdot (T_{wall,c} - T_m)}{\log\left(\frac{r_{ext} + r_{int}}{2 \cdot r_{int}}\right)} \quad (13)$$

where N_t is the number of tubes, L is the length of the tubes, r_{ext} and r_{int} are the external and internal radius, and λ is the conduction coefficient of the tubes.

3.3 Steam turbine model

A quasy-static model of the steam turbine was utilized in this work. The dynamics of this unit are faster than those of the OTSG, and since frequency fluctuations were not analyzed, the dynamic behavior of the steam turbine was

neglected. Therefore, the differential conservation equations are reduced to algebraic equations.

The steam turbine performance during off-design operation was predicted by means of Stodola's cone law (Stodola, 1927):

$$\dot{m}_{in} = K_t \sqrt{\rho_{in} p_{in} \sqrt{1 - \left(\frac{1}{PR}\right)^2}} \quad (14)$$

with K_t being the Stodola's coefficient, ρ_{in} and p_{in} the density and pressure at the inlet of the steam turbine, and PR the pressure ratio, defined as:

$$PR = \frac{p_{in}}{p_{out}} \quad (15)$$

where p_{out} is the pressure after the expansion.

The mechanical power, P_m , extracted by the steam turbine from the steam is obtained by:

$$P_m = \eta_{mech} \cdot \dot{w} \cdot (h_{in} - h_{out}) \quad (16)$$

where η_{mech} is the mechanical efficiency, w is the mass flow rate along the turbine, and h_{out} is obtained, assuming constant isentropic efficiency η_{iso} , from:

$$\eta_{iso} = \frac{h_{in} - h_{out}}{h_{in} - h_{iso}} \quad (17)$$

3.4 Condenser model

The modeled condenser is a shell and tube heat exchanger where the cooling fluid circulates within the tubes while the condensing fluid flows through the tube bundle on the shell side. The utilization of a back-pressure steam turbine implies that the steam entering the condensers is superheated. Thus, this feature must be taken into account in the model of the component.

The modeling of the cooling flow on the tube side is done similarly as in Section 3.2. Mass conservation is given by Eq. (1), whereas Eq. (5) is utilized to describe the energy balance. Heat transfer to the cooling fluid is modeled by Eq. (8) where the heat transfer coefficient is calculated by means of the Dittus-Boelter correlation (see Eq. (10)). The thermal dynamics of the metal tubes of the condenser are accounted by the utilization of Eqs. (11) and (13).

Since the working fluid enters the condenser as superheated steam, the shell side is discretized in order to account for the change in temperature and fluid properties. Saturated conditions at the outlet of the shell side and constant volume of the shell, V_{shell} , are set as constraints of the model. The division of this volume into sub-units, $V_{shell,j}$, is done gradually in order to obtain more accuracy at the outlet of the shell, where the density changes of the two-phase mixture are abrupt and a lot of detail is required. Hence, the volume of each discretization is defined as:

$$V_{shell,j} = \frac{V_{shell}}{2^j} \quad (18)$$

The mass of working fluid in each volume, $M_{shell,j}$, and the energy it contains, $E_{shell,j}$, are calculated using the average of the density, ρ_j , and the specific enthalpy, h_j , at both nodes of the cell:

$$M_{shell,j} = V_{shell,j} \cdot \frac{\rho_{j+1} + \rho_j}{2} \quad (19)$$

$$E_{shell,j} = M_{shell,j} \cdot \frac{h_{j+1} + h_j}{2} - p \cdot V_{shell,j} \quad (20)$$

Dynamic mass and energy conservation are employed to model the flow in the shell side:

$$\frac{dM_{shell,j}}{dt} = \dot{m}_j - \dot{m}_{j+1} \quad (21)$$

$$\frac{dE_{shell,j}}{dt} = \dot{m}_j \cdot h_j - \dot{m}_{j+1} \cdot h_{j+1} - \dot{Q}_j \quad (22)$$

where $dM_{shell,j}/dt$ and $dE_{shell,j}/dt$ are the time rate of mass and energy change in the center of the cell, \dot{m}_j and \dot{m}_{j+1} the mass flow rates evaluated at the nodes of the cell, and \dot{Q}_j is the heat flow from the discretized volume, which is calculated from Eq. (7).

The modeling of the hotwell was done in order to account for the increase in the outlet pressure, p_{out} , due to

the static pressure of the water column and the time rate of mass change, $\frac{dM_{hotwell}}{dt}$. Hence:

$$p_{out} = p_{in} - h_{hotwell} \cdot g \cdot \bar{\rho}_{hotwell} \quad (23)$$

$$\frac{dM_{hotwell}}{dt} = \dot{m}_{in} - \dot{m}_{out} \quad (24)$$

being $h_{hotwell}$ the level of water, p_{in} the inlet pressure, and $\bar{\rho}_{hotwell}$ the average density of the water contained in the hotwell.

In addition, the change in the outlet mass flow rate due to the accumulation of water and the increase in static pressure was modeled based on:

$$\dot{m}_{out} = \sqrt{2gh_{hotwell}} \cdot A_{duct} \cdot \bar{\rho}_{hotwell} \quad (25)$$

with A_{duct} being the area of the duct leaving the hotwell.

3.5 Pump model

A variable speed pump model was employed in this work, i.e. the mass flow rate is adapted by modifying the rotation speed. A third-order polynomial equation was utilized to describe the curves relating the mass flow to the head since the map of performance of the pump was not available. This equation was generated as a regression curve from the set of data generated by Thermofex in order to smooth the transient behavior of the pump model. The enthalpy increase through the unit was given by an energy balance. Constant efficiency during off-design conditions was assumed.

4 Results and discussion

4.1 CHP plant static design

The Pareto front of solutions of the preliminary design of the CHP plant obtained from the multi-objective optimization are shown in Figure 3. From this set of results, the most suitable alternative for the off-shore facility was chosen. Table 3 displays the main design characteristics of the selected solution.

Table 3. Nominal characteristics of the preliminary plant design.

Variable	Nominal value
Gas turbine 1 load [%]	72.38
Gas turbine 2 load [%]	85.19
Steam turbine inlet pressure [bar]	33.79
Steam turbine inlet temperature [°C]	444.20
Steam turbine outlet pressure [bar]	4.76
OTB temperature difference [°C]	20.30
Efficiency [%]	40.81
Weight [kg]	207068

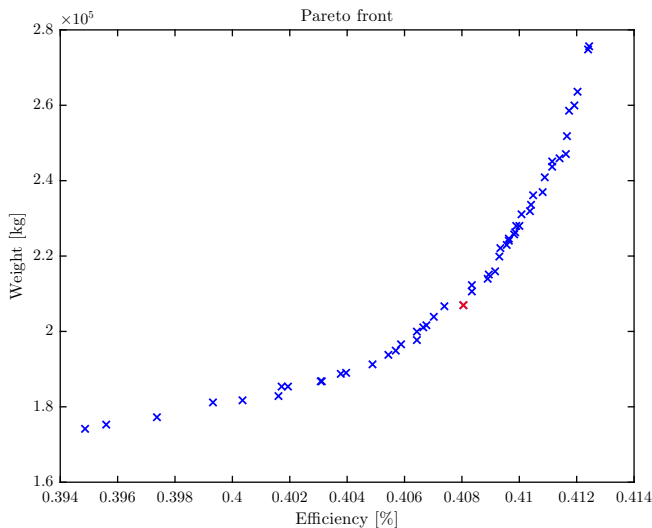


Figure 3. Pareto front of optimum solutions for the preliminary design of the CHP plant. The selected design configuration is marked in red.

4.2 Dynamic model validation

A thorough validation of the dynamic model was performed in order to ensure that results generated by the dynamic simulations are reliable. Dynamic data was not available, neither experimental nor generated by Thermoflex, and hence only a validation of the dynamic process model under steady-state operating conditions was carried out.

Several operation points including both design and off-design gas turbine loads were simulated, being the results produced by the dynamic model in satisfactory agreement with the validation data. For brevity, only design validation results for the heat transferred in the OTSG sections and the primary condenser, the shaft power produced in the steam turbine, and the steam live pressure and temperature are shown (see Table 4). Extensive validation data during both design and off-design steady-state operation may be found in the literature (Rúa, 2017). Absolute errors between results generated by Dymola and Thermoflex were calculated as:

$$Error \Big|_u = \frac{|u_{Dymola} - u_{Thermoflex}|}{u_{Thermoflex}} \quad (26)$$

where u may be any variable included in Table 4.

4.3 Dynamic simulation

The ability of the developed combined heat and power plant model to simulate operation under transient conditions was assessed by a dynamic simulation where the load of both gas turbines was decreased from nominal operation point, i.e. 72.38% and 85.19%, to 60%. This was equivalent to a reduction of 20% in the power demand of the entire thermal power plant. In addition, the modification of the gas turbines load means an *increase* of the

Table 4. Validation results during nominal operation.

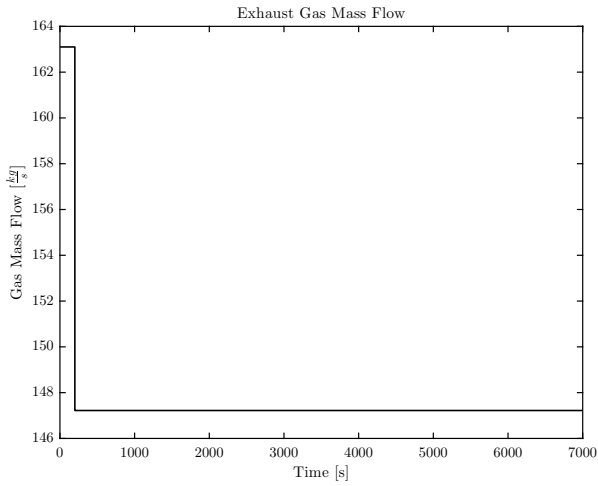
	Dymola	Thermoflex	Error
$\dot{Q}_{economizer}$ [MW]	10.403	10.343	0.580%
$\dot{Q}_{evaporator}$ [MW]	40.497	40.582	0.209%
$\dot{Q}_{superheater}$ [MW]	9.729	9.652	0.798%
P_m [MW]	8.348	8.601	2.942%
$\dot{Q}_{condenser,1}$ [MW]	52.015	52.050	0.067%
T_{steam} [°C]	442.220	442.600	0.086%
p_{steam} [bar]	33.809	33.730	0.234%

exhaust gas temperature of more than 20 °C. Therefore, two step changes, one decreasing the exhaust gas mass flow rate and the other increasing its temperature (see Figure 4), were implemented simultaneously in order to test ability of the steam cycle to handle a disturbance in the gas turbine load.

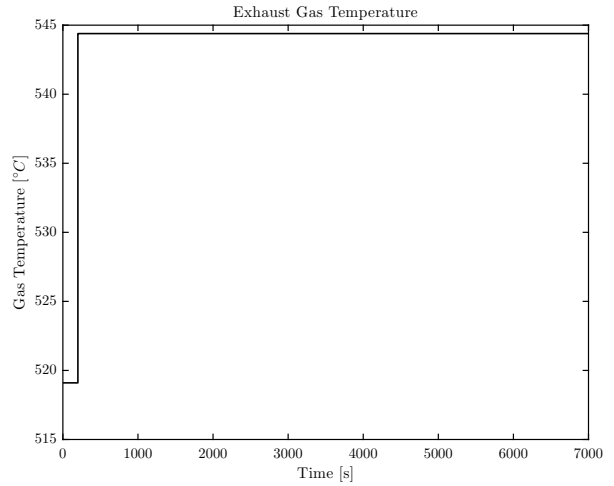
The variation of the relevant temperature variables, i.e. the steam live temperature and the process heat stream temperature, was analyzed under both open-loop conditions and with a control strategy implemented. The behavior of these two variables is represented in Figure 5. The former covers the live steam temperature while the latter shows the temperature of the process heat produced in the primary condenser. As it may be observed, both variables return to their set-point when the control strategy is applied, albeit the large change in operation conditions. However, the requirements of the offshore facility are unfulfilled when the plant is operated in open-loop conditions. A more restrictive control, i.e. with a larger controller gain, was designed for the process heat temperature in order to ensure that big fluctuations from the set point did not occur, as the pressurized high-temperature water stream is employed in the treatment of the products produced in the offshore facility and large deviations from the defined operating temperature may damage such products.

The dynamics of the controlled temperatures are slower than their open-loop counterparts. This phenomena may also be observed in Figure 6a, where the live steam pressure reaches faster a new steady-state operation point when no control is applied. This behavior is because of variation of the working fluid mass flow rate, which is the variable manipulated to control the steam live temperature, is also slow (see Figure 6b).

The water level fluctuation of both condensers is shown in Figure 7. The level of the primary condenser was controlled in order to ensure a stable operation. The control strategy applied to the primary water level responded properly to the changes experienced in the mass flow. The step changes in both exhaust gas mass flow and temperature produced, after an initial increase, a deep decrease in the steam live temperature that originated a decrease in the mass flow circulating in the bottoming cycle (see Figure 5a and Figure 6b). Thus, the water levels in the

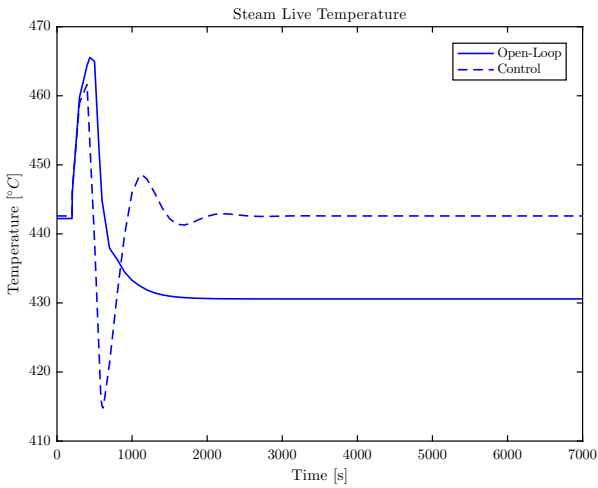


(a) Exhaust gas mass flow rate.

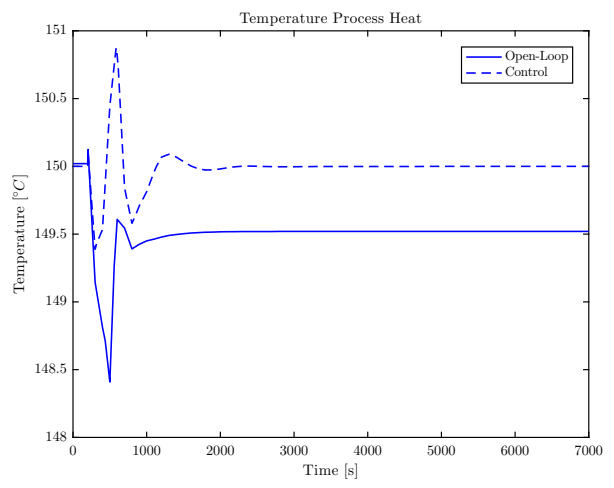


(b) Exhaust gas temperature.

Figure 4. Dynamic model boundary conditions.

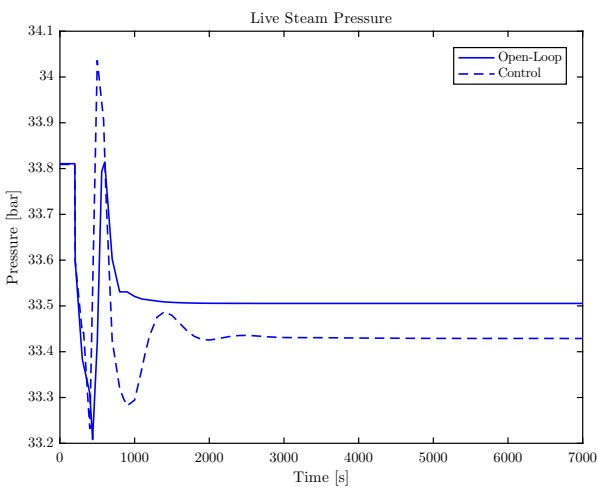


(a) Steam live temperature variation.

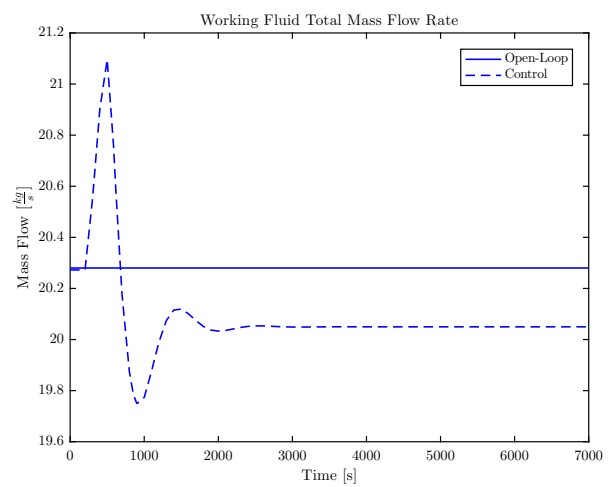


(b) Process heat temperature variation.

Figure 5. Variation of the controlled temperatures.

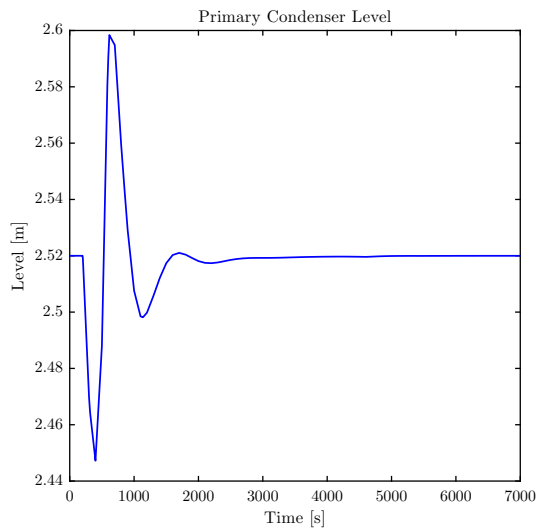


(a) Steam live pressure variation.

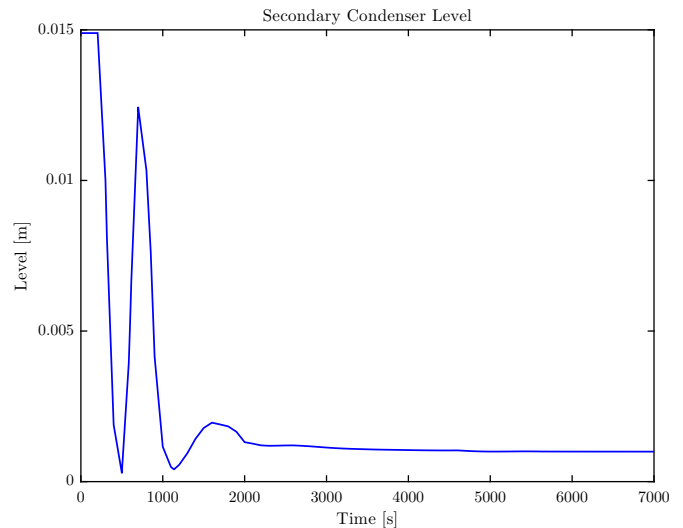


(b) Working fluid mass flow variation.

Figure 6. Variation of the working fluid mass flow and the steam live pressure.

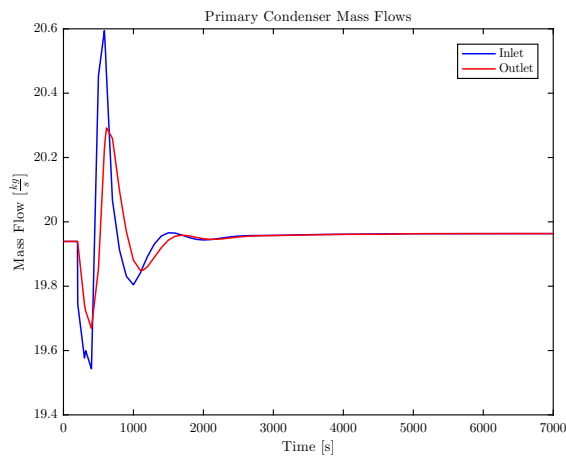


(a) Water level in the primary condenser.

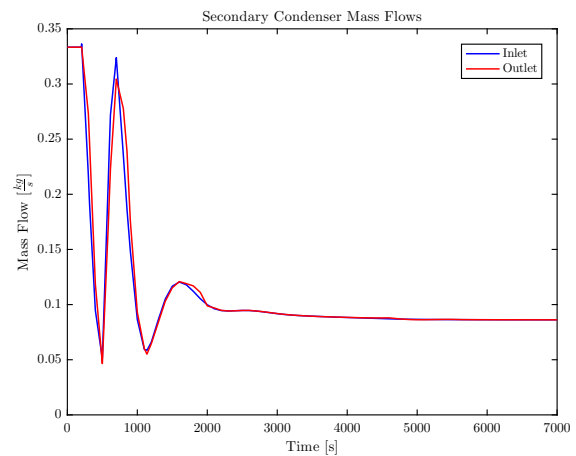


(b) Water level in the secondary condenser.

Figure 7. Water level in both condenser hotwells.



(a) Working fluid mass flow in the primary condenser.



(b) Working fluid mass flow in the secondary condenser.

Figure 8. Working fluid mass flow in both condensers.

hotwells were firstly reduced and then increased as a consequence of the variations in the mass flows entering and leaving both condensers. Steady-state values of the water levels showed that the secondary condenser absorbed the fluctuations in the operating conditions originated by the reduction of the working fluid’s mass flow rate.

The mass flow rate of the steam entering and the water leaving these components is represented in Figure 8. Similar trends among the water levels and mass flows in the condenser may be observed between Figure 7a and Figure 8a, and Figure 7b and Figure 8b, where both variables present the same pattern but the water level response is slightly shifted in time.

It is worth noting the buffering effect that the hotwell of the condensers has in the cycle, as it smears out the fluctuations (see Figure 8). This effect is specially observable in the primary condenser as the water level is larger and hence the static pressure changes are smoothed, reducing

the variation in the mass flow rate of water leaving the hotwell.

5 Conclusions

The dynamic modeling of the components integrating an offshore combined heat and power plant was presented in this work. Preliminary results on disturbance rejection show that the developed models produce reasonable results on the transient behaviour of the studied system.

The offshore platform in Johan Castberg field was selected as case study to test the validity of the models developed. A steady-state design procedure accounting for the need of high efficiency while keeping a reduced weight was briefly presented, pointing out the demanding restrictions in offshore facilities. A dynamic model of the selected design was developed under the Modelica environment, utilizing the ThermoPower library to develop the models of the components integrating the steam Rankine

cycle. A discretized condenser was programmed in order to accurately calculate the superheating conditions that were expected at the outlet of the back-pressure turbine.

The dynamic model of the combined heat and power plant was validated for steady-state design and off-design conditions obtained by the software Thermoflex. A preliminary evaluation of the developed models' capability to produce reasonable results under transient conditions was carried out by means of a reduction in the power demand of the combined heat and power plant, which was implemented by simultaneous step changes in the exhaust gas mass flow rate and temperature. The dynamic performance of relevant variables during the dynamic operation was shown and analyzed, showing that these models could be utilized for assessing that, with a suitable control strategy, the CHP plant would be able to produce the demanded heat at the required temperature even if changes to the nominal operation conditions of the power plant occurred. In addition, it was verified that limiting conditions, e.g. maximum temperature in the steam turbine, are not reached during unsteady performance, which is a valuable information for the operator of the plant.

The proposed assessment methodology has been applied for an offshore facility where restrictions are harder than in on-shore power plants. However, it is readily applicable to any waste heat recovery application where performance under transient conditions needs to be analyzed.

References

- F. Alobaid, R. Postler, J. Ströhle, B. Epple, and K. Hyun-Gee. Modeling and investigation start-up procedures of a combined cycle power plant. *Applied Energy*, 85(1):1173–1189, 2008.
- A. Benato, L. Pierobon, F. Haglind, and A. Stoppato. Dynamic performance of a combined gas turbine and air bottoming cycle plant for off-shore applications. In: *Proceedings of the ASME 2014 12th Biennial Conference on Engineering Systems Design and Analysis*, 2014.
- F. Casella and A. Leva. Modelica open library for power plant simulation: design and experimental validation. In: *Proceedings of the 3rd International Modelica Conference*, pages 41–50, 2003.
- F. Casella and F. Pretolani. Fast start-up of a combined-cycle power plant : A simulation study with modelica. In: *6th Modelica Conference*, pages 3–10, 2006.
- F. P. Incropera, D. P. DeWitt, T. L. Bergman, and A. S. Lavine. *Fundamentals of heat and mass transfer*. 6 ed. Jefferson City, United States of America: John Wiley & Sons, Inc, 2007. ISBN 9780470501979.
- P. Kloster. Energy optimization on offshore installations with emphasis on offshore combined cycle plants. In: *Offshore Europe Conference*, 1999.
- MathWorks. Global Optimization Toolbox, 2017.
- N. Mazzi, S. Rech, and A. Lazzaretto. Off-design dynamic model of a real organic rankine cycle system fuelled by exhaust gases from industrial processes. *Energy*, 90(1):537–551, 2015.
- Ministry of Environment. White Paper on Climate Efforts. Technical report, Norwegian Government, 2012.
- R. M. Montañés, S. Ó. GarDarsdóttir, F. Normann, F. Johnsson, and L. O. Nord. Demonstrating load-change transient performance of a commercial-scale natural gas combined cycle power plant with post-combustion co2 capture. *International Journal of Greenhouse Gas Control*, 63:158–174, 2017.
- L. O. Nord and O. Bolland. Steam bottoming cycles offshore - challenges and possibilities. *Journal of Power Technologies*, 92(3):201–207, 2012.
- L. O. Nord and O. Bolland. Design and off-design simulations of combined cycles for offshore oil and gas installations. *Applied Thermal Engineering*, 54(1):85–91, 2013.
- Norwegian Ministry of Petroleum and Energy. Emissions to Air. <http://www.norskpetroleum.no/en/environment-and-technology/emissions-to-air/>, 2017. [Accessed: 2017-05-15].
- L. Pierobon, A. Benato, E. Scolari, F. Haglind, and A. Stoppato. Waste heat recovery technologies for offshore platforms. *Applied Energy*, 136(1):228–241, 2014a.
- L. Pierobon, E. Casati, F. Casella, F. Haglind, and P. Colonna. Design methodology for flexible energy conversion systems accounting for dynamic performance. *Energy*, 68(1):667–679, 2014b.
- S. Quoilin, R. Aumannb, A. Grill, A. Schuster, V. Lemort, and H. Spliethoff. Dynamic modeling and optimal control strategy of waste heat recovery organic rankine cycles. *Applied Energy*, 88(1):2183–2190, 2011.
- L. Riboldi and L. O. Nord. Lifetime Assessment of Combined Cycles for Cogeneration of Power and Heat in Offshore Oil and Gas Installations. *Energies*, 10(6):744, 2017.
- Jairo Rúa. Master thesis: Dynamic modeling and process simulation of steam bottoming cycle. 2017.
- Statoil ASA. A Structural Approach to Operational Semantics. Technical report, 2016.
- A. Stodola. *Steam and Gas Turbines*. McGraw-Hill Book Company, Inc., 1927.
- Thermoflow Inc. Thermoflex, Version 26.0, 2016.

Thermodynamic Optimization of an Organic Rankine Cycle for Power Generation from a Low Temperature Geothermal Heat Source

Inés Encabo Cáceres Roberto Agromayor Lars O. Nord

Department of Energy and Process Engineering
Norwegian University of Science and Technology (NTNU)
Kolbjørn Hejes v.1B, NO-7491
Trondheim, Norway
inese@stud.ntnu.no

Abstract

The increasing concern on environment problems has led to the development of renewable energy sources, being the geothermal energy one of the most promising ones in terms of power generation. Due to the low heat source temperatures this energy provides, the use of Organic Rankine Cycles is necessary to guarantee a good performance of the system. In this paper, the optimization of an Organic Rankine Cycle has been carried out to determine the most suitable working fluid. Different cycle layouts and configurations for 39 different working fluids were simulated by means of a Gradient Based Optimization Algorithm implemented in MATLAB and linked to REFPROP property library. The heat source was hot water from a geothermal reservoir with an inlet temperature of 120°C and an outlet temperature limit of 75°C. For each working fluid, an optimal configuration was obtained, based on the optimization of the second law efficiency. In addition, a sensitivity analysis for the polytropic efficiencies of the pump and turbine was carried out. Results show that those working fluids with a critical temperature close to the maximum temperature of the cycle give the highest plant efficiencies (being propylene and R1234yf the best ones). Using a recuperator increases the plant efficiency in all cases with exception of wet working fluids. The cycles experiencing the highest sensitivity on the pump performance are those using working fluids with low critical temperatures. Increasing the number of stages of the turbine increases the overall plant efficiency for all working fluids, but some fluids are more sensitive to the turbine efficiency than others.

Keywords: Process modelling, process simulation, working fluid selection, parametric optimization, second law efficiency.

1 Introduction

Historically, the preferred methods for power generation have been related to Brayton or Rankine power cycles,

fueled by natural gas or other fossil fuels (Macchi and Astolfi, 2017). However, during the last years, the increasing concern of the greenhouse effect and climate change has led to an increase of renewable energy, such as wind and solar power. In addition to these listed renewable energies, there is an energy source that shows a promising future due to the advantages it provides when compared to other renewable energies. This developing energy is geothermal energy, and its advantages are related to its availability (Macchi and Astolfi, 2017): it does not depend on the ambient conditions, it is stable, and it offers the possibility of renewable energy base load operation. One of the challenges of geothermal energy is that it does not provide very high temperatures, and this fact has made researches and engineers to focus their studies on how to obtain high thermodynamic efficiencies at low- and medium-temperature heat sources. One of the solutions for this problem are Organic Rankine Cycles (ORCs), which present a simple structure with a high reliability, an easy maintenance and, most importantly, a high potential to produce power from low source temperatures when compared to other power generation cycles (Saleh *et al*, 2007).

The design of the ORC requires a thorough analysis, since there are many parameters affecting its performance, and any change of these parameters will have a major impact on the efficiency of the cycle. With this aim, many different studies have been carried out. (Saleh *et al*, 2007) analyze the performance of 31 different working fluids, finding that those working fluids with the highest boiling temperatures are giving the highest efficiencies, being cyclopentane the best one for the given conditions and assumptions. (Roy *et al*, 2011), by means of a parametric ORC optimization, found that R123 is the best working fluid due to its high efficiency and high power production. (Hung *et al*, 2010) studied the efficiency of an ORC where benzene, ammonia, R11, R12, R1234a and R113, are used as the working fluids, differencing between wet, dry and isentropic working fluids and concluding that isentropic

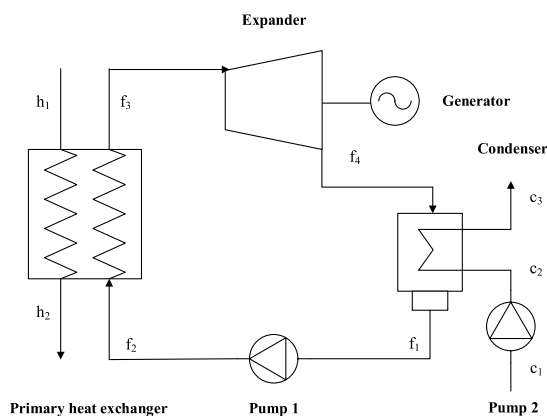
fluids are preferred for ORC systems, since they are giving the best efficiencies. (Shu *et al*, 2014) studied the thermal efficiency and exergy losses in an ORC, using pure hydrocarbons and mixtures; zeotropic mixtures seem to present a better thermodynamic performance than pure working fluids. These conclusions were also found by (Haberle *et al*, 2012), who use a mixture of i-butane and i-pentane for studying the second law efficiency.

Even though many studies have been carried out, none of them shows the same results regarding which is the best working fluid for an ORC with low heat source temperature, and all of them agree on the fact that the thermodynamic boundaries of the cycle, the working fluid selection, the constraints, and choice of the degrees of freedom are key parameters for analyzing and designing the cycle. In this work, a thermodynamic analysis has been carried out, focused on the optimization of the cycle (being the second law efficiency the objective function), analyzing more than 35 different pure working fluids from different classes, and investigating the pump and expander efficiencies impact on the cycle performance.

2 Organic Rankine Cycle

2.1 Cycle design

The ORC is the main technology used to transform low temperature thermal energy into electrical power. The heat is transferred to the working fluid in an evaporator (or primary heat exchanger), which evaporates and may superheat. Then, the working fluid reaches the expander, normally a turbine, in which it is expanded and experiences an enthalpy drop between the inlet and outlet, transforming the energy from the fluid into mechanical work. This mechanical work is transformed into electrical energy in a generator. After the expander, the working fluid reaches the condenser, where it rejects the surplus heat and changes its phase again. Once all the vapour has been condensed, the remaining liquid is pumped back to the evaporator. This is the simplest



ORC, which can be seen in Figure 1, together with a typical T-s diagram for the same cycle layout.

This simple configuration can be modified to obtain higher efficiencies (by adding more pressure levels, different types of regeneration, reheating, etc). Multiple pressure levels are normally used when the available heat to be absorbed from the heat source is high; otherwise, the expensive and complex cycle layout would not be justified. The reheating unit is installed in the cycle when the amount of liquid that is formed during the expansion process is so high that it could damage the turbine (Macchi and Astolfi, 2017; Agromayor, 2017). For the case study of this work, the heat source does not provide a high temperature; therefore, multiple pressure levels and reheating configuration were not considered.

Regeneration is a common practice in ORC layouts. It is beneficial from a thermodynamic point of view when the fluid at the outlet of the expander is superheated vapour and there exists a limitation for the lower temperature of the heat source (Agromayor, 2017). Figure 2 shows the regenerative cycle layout. The regeneration allows to preheat the liquid that enters the primary heat exchanger, and, at the same time, to cool the superheated vapour coming out of the turbine. This results into lower cooling loads and smaller condensers. Both cycle layouts (the simple and the regenerated one) allow to work in different cycle configurations: saturated, superheated and transcritical. For this project, all the configurations were considered for each working fluid, to determine which one gives the best results in terms of efficiency.

2.2 Working fluid selection

The fluid selection for an ORC is the key parameter to design the cycle, meaning that it is the most important degree of freedom during its analysis. The complexity of the process is not just a consequence of the large amount of working fluids that can be found in the market, but also of the infinite number of mixtures that

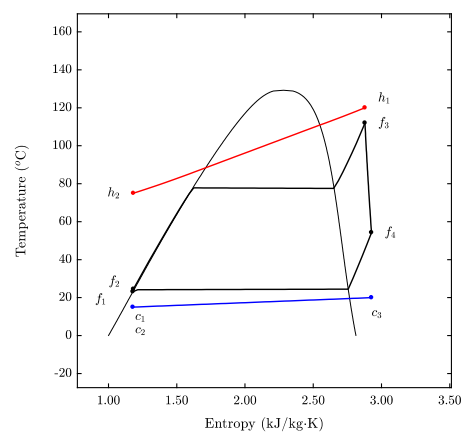


Figure 1. Simple ORC layout and typical T-s diagram for a random pure working fluid

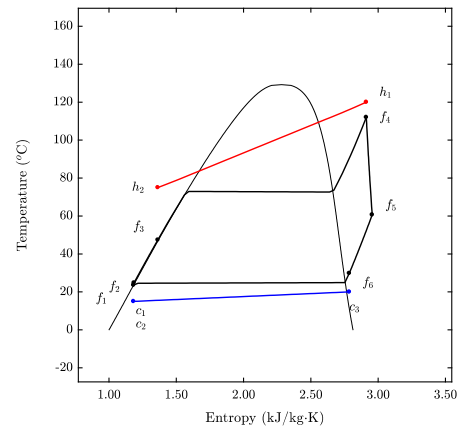
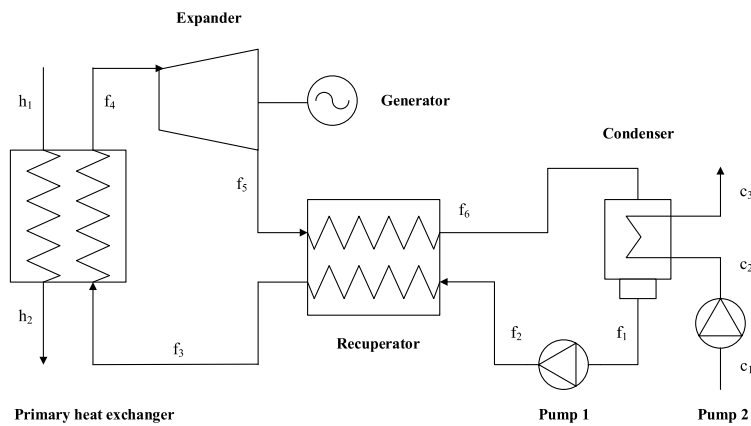


Figure 2. Recuperated ORC layout and typical T-s diagram for a random pure working fluid

can be obtained from these pure substances. Taking a decision when choosing the working fluid for the ORC has a major impact on the cost, the components and cycle performance and on the safety requirements (Macchi and Astolfi, 2017).

(Feng *et al.*, 2015) propose the use of mixtures in the ORC, due to the non-isothermal change of phase in the evaporator, which allows to obtain better gliding temperature matches between the heat source and the working fluid. However, the analysis reflects that mixtures are not always giving better cycle performances than pure working fluids. Due to the high complexity that this problem has, the study of different mixtures was not included in this work.

The uncertainty fluid properties can influence the reliability of the optimized cycles, and, for this reason J. Frutiger *et al.* propose in (Frutiger *et al.*, 2016) an analysis of the impact of uncertainty of the fluid properties in the behavior of the ORC, including the Molecular Weight (MW), critical temperature, critical pressure and acentric factor. This gives an idea of how important the working fluid properties are when choosing the working fluid. There are different factors or properties to consider when taking this decision, and we can find, among others (Macchi and Astolfi, 2017):

- The molecular complexity. It influences the T-s diagram shape (differencing between dry, isentropic and wet fluids) which is essential for the performance of the turbine, since it determines the amount of liquid that may be formed during the expansion. (Zhai *et al.*, 2014) demonstrate that complex molecules that include double bonds or cycle bonds are much more efficient than molecules with only single bonds, with a lower molecular complexity
- The molecular mass. This parameter has a major influence on the design of the turbine. When the molecular weight increases, the enthalpy drop in the turbine is lower, and this is translated into a need of less stages for the expansion, lower peripheral

velocities and mechanical stresses, although the heat transfer coefficient diminishes and heat exchangers with larger heat transfer areas are needed (higher costs).

- The critical temperature. It is recommended to use working fluids with critical temperatures as closest as possible to the highest temperature of the cycle, since they guarantee an efficient heat exchange process.

The impact of the working fluid on the environment is important. Fluids with a high Ozone Depletion Potential (ODP) are undesirable, while organic fluorinated fluids (HFCs) are to be avoided because of their high Global Warming Potential (GWP). From (Zhai *et al.*, 2014) it was found that the GWP is not only important for the environment concern, but also for the efficiency of the cycle (results show that those working fluids with a GWP lower than 1500 can absorb more energy from the heat source, improving the cycle efficiency).

The most common working fluid for conventional Rankine cycles is H₂O. However, when the heat source temperature is low, H₂O shows poor performances. As H₂O is a wet working fluid, it condensates during the expansion, and this may damage the turbine. To solve this problem, H₂O requires a too high degree of superheating and a low enthalpy drop across the expander, meaning that the power produced is low (low plant efficiencies). It was found to be of interest to investigate how H₂O behaves in our case of study even if the performance was expected to be poor.

3 Methodology

The Rankine cycle model was implemented in MATLAB and optimized with a Gradient Based Algorithm (Sequential Quadratic Programming, SQP). The advantage of Gradient Based Algorithms against the popular direct search algorithms, such as the Genetic Algorithm, is that the former has a faster convergence rate. The code can simulate and optimize both the simple

and the recuperated Rankine cycles and it computes all the thermodynamic states of the cycle, using the REFPROP library.

3.1 Fluid screening selection

Most of the manufacturers opt to work with organic fluids that have already been tried, to reduce the uncertainty and simplify the fluid selection process. However, this does not necessarily mean that they are the best choice. In fact, (Colonna *et al*, 2015) insist on the need of carrying out research on new substances. In this work, some of the most used working fluids were analyzed, although others fluids that are not so well known were also included. After a literature search, we found that the most commonly used organic working fluids for ORC applications are: R134a, R245fa, n-pentane, octamethyltrisiloxane, toluene (Maraver *et al*, 2014), and, among the hydrocarbons (HCs), butane (R600), iso-butane (R600a), pentane (R601), iso-pentane (R601a) and hexane (Liu *et al*, 2013).

To select the working fluid, we took as a starting point a list of more than 130 different pure substances. Since not all of these pure substances were suitable for the given conditions, a first screening selection based on the need of meeting four main requirements was carried out to discard unsuitable working fluids. The requirements were:

1. The ODP had to be zero or close to zero
2. The GWP must be lower than 2000
3. The fluid critical temperature needed to be higher than the ambient temperature to make condensation possible
4. The saturation pressure at ambient temperature had to be higher than 1 kPa to limit vacuum in the condenser

From these requirements, a revised list of 44 working fluids was obtained. 39 working fluids were simulated and optimized by means of the Gradient Based Algorithm in MATLAB.

3.2 Assumptions and boundary conditions

The main assumptions and boundary conditions can be found in Table 1. Some data such as the pump and turbine efficiencies were assumed based on the information found during the literature review process, although the impact of these parameters was studied by means of a sensitivity analysis.

Values for the pump polytropic efficiency between 10% and 100% were simulated for the most optimal working fluids under subcritical and transcritical conditions. For the expander, the correlation from (Astolfi and Macchi, 2015) for axial turbines of one, two, and three stages to compute the polytropic efficiency as a function of the volume ratio and the size parameter was also analyzed for some of the best working fluids. This correlation states:

$$\eta_{turb} = f(V_r, SP) \quad (1)$$

$$V_r = \frac{\rho_{in}}{\rho_{out}} \quad (2)$$

$$SP = \frac{(\dot{m}_{out}/\rho_{out,s})^{1/2}}{(\Delta h_s)^{1/4}} \quad (3)$$

Table 1. Assumptions and boundary conditions.

<u>Hot source</u>		
$T_{h,in}$	[°C]	120
$T_{hmin,out}$	[°C]	75
$T_{hmax,out}$	[°C]	85
\dot{m}	[kg/s]	13.23
P_{out}	[bar]	3
Working fluid	[-]	H ₂ O
<u>Cold source</u>		
T_{in}	[°C]	10
Working fluid	[-]	H ₂ O
$\Delta T_{c,max}$	[°C]	10
$\Delta T_{c,min}$	[°C]	5
<u>Ambient conditions</u>		
P_{amb}	[bar]	1.013
T_{amb}	[°C]	15
<u>Pinch points</u>		
ΔT_{max}	[°C]	8
ΔT_{min}	[°C]	5
<u>Pressure drops</u>		
ΔP (evap,cond,rec)	[bar]	$0.01 \cdot P_{in}$
<u>Pump</u>		
Polytropic efficiency	[%]	70
<u>Turbine</u>		
Polytropic efficiency	[%]	80

Regarding the minimum outlet temperature of the hot source, the limitation was given to allow for use of the remaining heat in a low-temperature district heating system (this system is not considered in this work).

3.3 Objective function

Defining the objective function is crucial when it comes to optimizing the cycle. For this work, the variable to be optimized was the second law efficiency of the plant. A natural choice would have been optimizing the net power output or the first law efficiency (these three objective functions would give the same thermodynamic optimum), but optimizing the second law efficiency gives insight about how much potential for improvement is left.

The parameter to be optimized was the second law efficiency of the whole power plant, considering the recovery efficiency in the main heat exchanger. This is because not all the heat which was available from the heat source could be used (due to the limitation of the

hot source outlet temperature). The plant second law efficiency, cycle second law efficiency and recovery second law efficiency are related according to Equations. 4-5-6.

$$\eta_{II.cycle} = \frac{\dot{W}_{net}}{\dot{E}_{in}} \quad (4)$$

$$\eta_{II.rec} = \frac{\dot{E}_{in}}{\dot{E}_{max}} \quad (5)$$

$$\eta_{II.plant} = \frac{\dot{W}_{net}}{\dot{E}_{max}} = \eta_{II.cycle} \cdot \eta_{II.rec} \quad (6)$$

Where \dot{E}_{max} is the maximum exergy flow rate that can be extracted from the hot source (if the hot source stream is cooled down to ambient conditions, $T_0=15\text{ }^\circ\text{C}$ and $p_0=1.013\text{ bar}$). All these equations were applied to the list of working fluids which have been studied (see Table 2).

The first law efficiency can be defined as:

$$\eta_{I.plant} = \frac{\dot{W}_{net}}{\dot{Q}_{in,max}} \quad (7)$$

Where $\dot{Q}_{in,max}$ is the maximum heat flow rate that can be extracted from the hot source

Table 2. List of studied and simulated working fluids

	Chemical name	Alternative name	Class	$T_{crit}/T_{hot,in}$
1	Methyl alcohol	Methanol	Alcohol	1.3038
2	Ethyl alcohol	Ethanol	Alcohol	1.3092
3	Ethane	R170	Alkane	0.7766
4	Propane	R290	Alkane	0.9408
5	2-Methylpropane	Isobutane – R600a	Alkane	1.0373
6	Butane	R600	Alkane	1.0813
7	2,2-Dimethylpropane	Neopentane	Alkane	1.1032
8	2-Methylbutane	Isopentane – R601a	Alkane	1.1709
9	Pentane	R601	Alkane	1.1947
10	2-Methylpentane	Isohexane	Alkane	1.2659
11	Hexane	-	Alkane	1.2917
12	Heptane	-	Alkane	1.3739
13	Propene	Propylene – R1270	Alkene	0.9283
14	2-Methyl-1-propene	Isobutene	Alkene	1.0634
15	Ethylethylene	1-Butene	Alkene	1.0665
16	Cis-2-butene	Cis-butene	Alkene	1.1084
17	Propyne	-	Alkyne	1.0235
18	Benzene	Benzol	Aromatic	1.4295
19	Methylbenzene	Toluene	Aromatic	1.5052
20	Dimethyl carbonate	DMC	Carbonate ester	1.4168
21	Cyclopropane	-	Cycloalkane	1.0131
22	Cyclopentane	-	Cycloalkane	1.3016
23	Cyclohexane	-	Cycloalkane	1.4081
24	Dimethylether	DME	Ether	1.0184
25	Fluoromethane	R41	HFC	0.8070
26	Difluoromethane	R32	HFC	0.8934
27	1,1,1,2-Tetrafluoroethane	R134a	HFC	0.9518
28	Fluoroethane	R161	HFC	0.9545
29	1,1-Difluoroethane	R152a	HFC	0.9829
30	1,1,1,3,3-Pentafluoropropane	R245fa	HFC	1.0865
31	1,1,2,2,3-Pentafluoropropane	R245ca	HFC	1.1384
32	1,1,1,3,3-Pentafluorobutane	R365mfc	HFC	1.1700
33	2,3,3,3-Tetrafluoroprop-1-ene	R1234yf	HFO	0.9356
34	Trans-1,3,3,3-tetrafluoropropene	R1234ze	HFO	0.9729
35	Propanone	Acetone	Ketone	1.2924
36	Hexamethyldisiloxane	MM	Linear Siloxane	1.3193
37	Carbon Dioxide	CO ₂ – R744	Inorganic	0.7736
38	Ammonia	R717	Inorganic	1.0312
39	H ₂ O	R718	Inorganic	1.6459

3.4 Degrees of freedom and constraints

When it comes to optimize an ORC, choosing the constraints and defining the degrees of freedom is of special importance. For this work, the simple cycle had 6 degrees of freedom, while the recuperated one had 7. These degrees of freedom were defined as dimensionless parameters related to the cycle variables which have maximum and minimum values, and take values between 0 and 1.

- x_1 Heat source outlet temperature
- x_2 Condenser temperature jump
- x_3 Pressure at the inlet of the turbine
- x_4 Pressure at the outlet of the turbine
- x_5 Enthalpy at the inlet of the turbine
- x_6 Enthalpy at the inlet of the primary heat exchanger
- x_7 Enthalpy at the outlet of the condenser (only for the recuperated cycle)

Regarding the constraints, they are the same for the simple and the recuperated cycles. These are:

- c_1 The working fluid has to be subcooled at the inlet of the pump to avoid cavitation
- c_2 If the pressure is subcritical, the working fluid has to be subcooled at the inlet of the evaporator to avoid the phase change in the recuperator
- c_3 If the pressure is subcritical, the working fluid has to be saturated or superheated at the outlet of the evaporator (avoid trilateral and partial evaporation cycles)
- c_4 The working fluid has to be saturated or superheated at the outlet of the expander (avoid vapour qualities lower than 1)
- c_5 The pinch point in the evaporator has to be higher than the minimum temperature difference specified to avoid temperature crossing
- c_6 The pinch point in the condenser has to be higher than the minimum temperature difference specified to avoid temperature crossing
- c_7 The pinch point in the recuperator has to be higher than the minimum temperature difference specified to avoid temperature crossing

4 Results and discussion

4.1 Thermodynamic analysis

Some of the obtained results can be found in Table 3, which includes the working fluid mass flow, turbine and pump powers, net power output and first and second law efficiencies for the plant. The best obtained results for each different working fluid family have been included.

Figure 3 shows the results of the thermodynamic optimization as a function of the ratio of the critical temperature to the highest temperature of the cycle (hot source inlet temperature). Results show that those cycles with $T_{crit}/T_{hot,in}$ between 0.93 and 1.02 are giving the best plant second law efficiencies (between 31.33% and

33.46%). For values of $T_{crit}/T_{hot,in}$ lower than 0.9, the second law efficiency considerably drops, reaching values down to 21%, which correspond to fluids such as R41, CO₂ or ethane, whose best cycle configuration is the transcritical one. The reason for this is that, when the $T_{hot,in}$ is above the critical temperature, the best match between the hot source and the working fluid in the primary heat exchanger is found when the working fluid operates above its critical pressure. This is consistent with the conclusions from (Hærvig, 2016; Xu and Liu, 2013). The rest of the working fluids show their best performance at subcritical conditions, except for propylene and R1234yf. For $T_{crit}/T_{hot,in}$ values higher than 1.02, the performance of the cycle is slightly worse than the one found for the most optimal working fluids, although the difference found for the second law efficiency is not large. The working fluids showing the worst performance for the analyzed range were ammonia (recuperated) and methanol. The reason for this is that they are wet fluids and, in case of the ammonia, it has no potential for heat recovery (what is more, the recuperator would decrease the temperature at the inlet of the evaporator and the cycle efficiency). For the rest of the working fluids, the efficiencies are all above 31%, showing a better performance when the recuperator unit is installed.

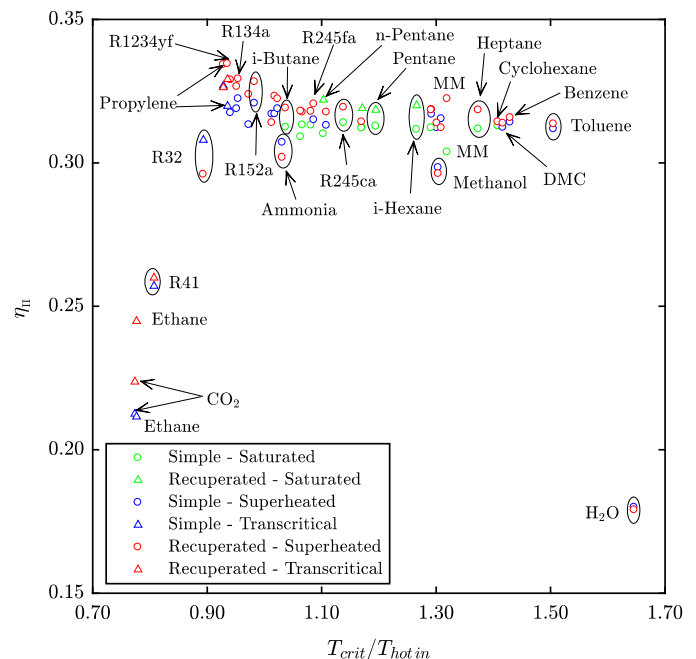


Figure 3. Influence of the relationship between the working fluid critical temperature and the highest cycle temperature on the plant second law efficiency

As it happens when the H₂O is used as the working fluid, some wet fluids require superheating to prevent condensation during the expansion (Bao and Zhao, 2013). For example, ammonia, H₂O, and ethanol (wet

fluids) require a high degree of superheating, while some isentropic fluids such as the R245fa or R365mfc require a low one. Most of the dry working fluids such as the butane heptane or n-pentane are operating at saturated conditions due to the positive slope of their diagram, which avoids the need of superheating the working fluid before its expansion.

As Figure 3 and Table 3 show, the working fluids giving the highest potential of improvement are alkanes, followed by the HFOs and HFCs, while the cycloalkanes do not show an appreciable efficiency increase when installing a recuperator unit. Even though ethane is the working fluid showing the highest potential of improvement when installing a recuperator unit, its performance is still one of the worst among all the analyzed working fluids. The highest efficiency gains are observed for the dry working fluids, because they have higher recuperation potentials than wet working fluids (ethanol and methanol experience an efficiency drop of 0.22% and 0.32% respectively when a regenerator unit is used). For the simple cycle layout, propylene shows the best results, operating at transcritical conditions and reaching an efficiency of 32.69%. For the recuperated cycle, R1234yf becomes the best working fluid, reaching a second law plant efficiency of 33.46%. It can also be seen that, while for the simple cycle layout many fluids are working at saturated conditions, for the recuperated configuration they show a better performance operating at superheated conditions. The reason is that a higher power production can be achieved when superheating, but this makes the cooling load to be higher (Bao and Zhao, 2013) unless a recuperator is used to decrease the cooling load and avoid wasted heat.

Regarding inorganic working fluids, the results for ammonia deviate from the tendency of Figure 3, while the H₂O is giving the worst performance. For both H₂O and ammonia, the recuperator is cooling down the working fluid at the inlet of the evaporator. Also, H₂O is giving the lowest power output. This is a consequence of the too low enthalpy drop taking place across the turbine for avoiding wet expansion. Regarding CO₂, it is also giving a low second law efficiency that improves with the use of a recuperator but it is still lower than the one for the rest of organic fluids. The results of this work indicate that the studied inorganic working fluids are not recommended for power generation in Rankine Cycles with low-heat source temperatures and low power capacities.

The Backwork Ratio (BWR) was plotted as a function of T_{crit} in Figure 4. It can be seen that those working fluids with the lowest critical temperatures (from 0°C to 92°C) are giving the highest BWRs. For subcritical cycles with a critical temperature between 100°C and 160°C, the simple cycles have higher BWRs than the recuperated cycles, due to the lower power production and higher power consumption they have.

For those working fluids with critical temperatures higher than 160°C, the BWRs of the recuperated and simple cycles are very similar, since they can operate at lower pressures, guaranteeing a low pump power that does not appreciably change when moving from one cycle layout to another.

Finally, for toluene, the working fluid with the highest critical temperature, the maximum pressure to guarantee an efficient heat transfer process is the lowest one (0.33 bar), and this results into the lowest power consumption among all the results (only 0.39 kW), giving the lowest BWR.

The choice of the working fluid depends on the application at hand. If the target is power generation, the working fluids giving the highest second law efficiencies (those ones with a critical temperature close to the highest temperature of the cycle) should be chosen. Among these fluids, an economic analysis should be carried out to determine whether the use of a recuperator is justified or not. For those working fluids with a low second law efficiency, the power production is lower when comparing to the rest, and, since the amount of heat into the cycle is fixed, the heat rejected in the condenser is higher. This means that those working fluids with a low second law efficiency may have a promising potential for co-generation if the rejected heat in the condenser is used. For example, the ethane, with a second law efficiency of 21.15% rejects 2326.23 kW in the condenser at an inlet temperature of almost 56 °C, while the recuperated propylene rejects 2225.36 kW with a plant efficiency of 33.42% and an inlet condenser temperature lower than 32 °C.

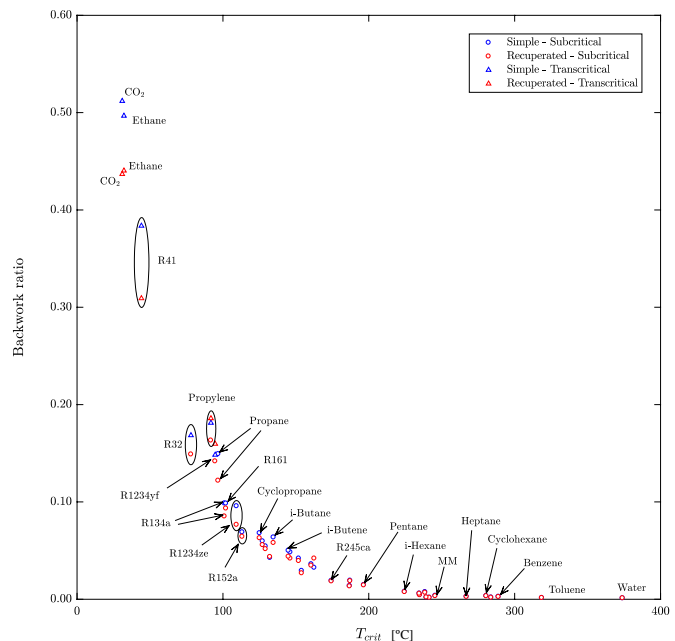


Figure 4. Influence of the critical temperature on the BWR for all the simulated working fluids

Table 3. Main obtained results

<i>Fluid</i>	<i>Cycle layout</i>	<i>Cycle configuration</i>	$\dot{m}_{w.f}$	\dot{W}_{turb}	\dot{W}_{pump}	\dot{W}_{net}	$\eta_{I.plant}$	$\eta_{II.plant}$
<i>[-]</i>	<i>[-]</i>	<i>[-]</i>	<i>[kg/s]</i>	<i>[kW]</i>	<i>[kW]</i>	<i>[kW]</i>	<i>[%]</i>	<i>[%]</i>
Acetone	Simple	Subcritical	3.83	274.76	1.23	273.53	4.69	31.69
Ammonia	Simple	Subcritical	1.91	276.88	11.80	265.08	4.55	30.71
Benzene	Simple	Subcritical	4.64	271.89	0.71	271.17	4.66	31.41
Butane	Simple	Subcritical	5.64	282.08	11.84	270.24	4.64	31.31
Cis-butene	Simple	Subcritical	5.36	279.29	9.06	270.23	4.64	31.30
CO ₂	Simple	Transcritical	12.00	375.77	192.37	183.40	3.15	21.25
Cyclopropane	Simple	Subcritical	4.87	293.58	19.95	273.62	4.70	31.70
DMC	Simple	Subcritical	4.73	270.10	0.50	269.60	4.63	31.23
DME	Simple	Subcritical	4.87	291.00	17.36	273.65	4.70	31.70
Ethanol	Simple	Subcritical	2.38	272.65	0.47	272.18	4.67	31.54
i-Hexane	Simple	Subcritical	5.64	271.14	2.14	269.00	4.62	31.16
MM	Simple	Subcritical	7.75	263.19	0.97	262.22	4.50	30.38
Propane	Simple	Subcritical	5.91	322.06	48.05	274.00	4.70	31.74
Propylene	Simple	Transcritical	6.15	344.63	62.44	282.19	4.84	32.69
Propyne	Simple	Subcritical	4.27	291.07	15.85	275.22	4.72	31.88
R134a	Simple	Subcritical	10.75	305.29	30.1	275.19	4.72	31.88
R152a	Simple	Subcritical	7.05	297.40	20.50	276.91	4.75	32.08
R161	Simple	Subcritical	5.91	308.65	30.38	278.27	4.78	32.24
R1234yf	Simple	Transcritical	13	324.11	48.09	276.02	4.74	31.98
R1234ze	Simple	Subcritical	12.16	299.04	28.62	270.42	4.64	31.33
Toluene	Simple	Subcritical	0.96	269.53	0.40	269.13	4.62	31.18
Water	Simple	Subcritical	0.96	155.44	0.18	155.26	2.67	17.99
Acetone	Recuperated	Subcritical	4.13	276.81	1.19	275.63	4.72	31.86
Ammonia	Recuperated	Subcritical	1.89	273.08	11.91	261.18	4.47	30.19
Benzene	Recuperated	Subcritical	5.09	273.85	0.68	273.17	4.68	31.57
Butane	Recuperated	Subcritical	6.01	286.31	11.27	275.03	4.71	31.79
CO ₂	Recuperated	Transcritical	12.59	343.64	150.12	193.53	3.32	22.37
Cyclohexane	Recuperated	Subcritical	5.75	272.76	0.90	271.86	4.66	31.43
DMC	Recuperated	Subcritical	5.26	271.96	0.47	271.49	4.65	31.38
DME	Recuperated	Subcritical	5.43	296.11	16.51	279.61	4.79	32.32
Heptane	Recuperated	Subcritical	5.98	276.23	0.72	275.51	4.72	31.85
i-Hexane	Recuperated	Subcritical	6.48	278.96	2.08	276.88	4.74	32.01
i-butane	Recuperated	Subcritical	6.58	293.03	16.97	276.06	4.73	31.91
Methanol	Recuperated	Subcritical	1.91	256.80	0.52	256.27	4.39	29.62
MM	Recuperated	Subcritical	9.40	279.85	0.94	278.91	4.78	32.24
n-Pentane	Recuperated	Subcritical	7.40	288.55	10.00	278.55	4.77	32.20
Propane	Recuperated	Subcritical	6.34	324.08	39.52	284.56	4.87	32.89
Propylene	Recuperated	Subcritical	6.31	345.57	56.41	289.17	4.95	33.42
Propylene	Recuperated	Transcritical	6.31	346.72	64.43	282.29	4.84	32.63
Propyne	Recuperated	Subcritical	4.68	294.02	15.17	278.85	4.78	32.23
R134a	Recuperated	Subcritical	13.16	308.82	26.31	282.50	4.84	32.66
R152a	Recuperated	Subcritical	7.74	303.48	19.53	283.96	4.86	32.82
R161	Recuperated	Subcritical	6.34	314.20	29.34	284.86	4.88	32.93
R245fa	Recuperated	Subcritical	11.42	284.94	7.63	277.31	4.75	32.05
R1234yf	Recuperated	Transcritical	14.41	337.61	53.89	283.73	4.88	32.92
R1234yf	Recuperated	Subcritical	14.48	337.26	47.84	289.42	4.96	33.46
R1234ze	Recuperated	Subcritical	13.90	303.39	23.24	280.16	4.80	32.38
Toluene	Recuperated	Subcritical	5.35	271.63	0.38	271.25	4.65	31.36
H ₂ O	Recuperated	Subcritical	0.96	154.92	0.18	154.74	2.65	17.90

4.2 Pump sensitivity analysis

Geothermal energy allows to work at part-load conditions when desired. (Landelle *et al*, 2017) stated efficiency losses of more than a 50% when operating below the nominal power plant conditions, and this, joint to the fact that each working fluid has a single and limited operating range in which it is optimal (Hærvig, 2016) has led to the conclusion that a pump sensitivity analysis should be carried out in this work. In this sensitivity analysis, one of the goals is to determine which working fluid is the optimal and for which range of pump polytropic efficiency, setting the nominal pump efficiency as 70% based on the literature review (Brosukiewicz-Gozdur, 2013). The analysis was then performed for 5 different working fluids. These were:

- Toluene: Working fluid operating under subcritical conditions with the lowest power consumption
- R161: Working fluid operating under subcritical conditions with the highest power consumption
- R1234yf: Working fluid operating under transcritical conditions with the lowest power consumption
- CO₂: Working fluid operating under transcritical conditions with the highest power consumption
- Propylene: Best working fluid for the non-recuperated layout.

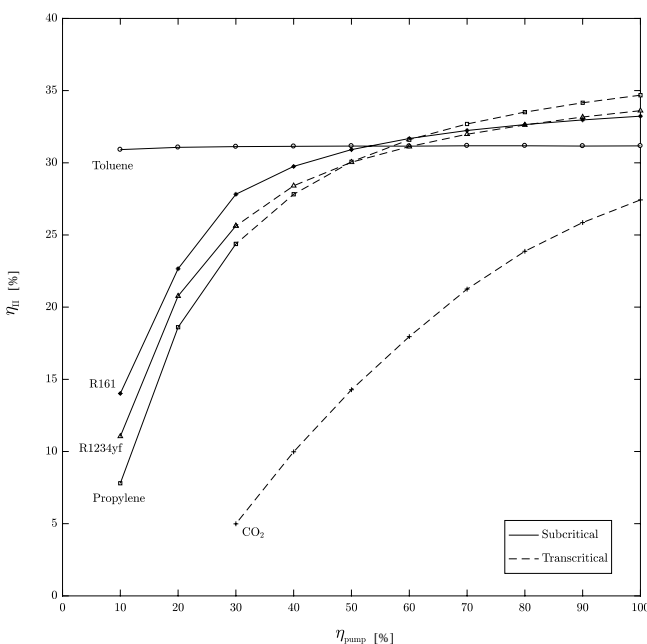


Figure 5. Effect of the pump polytropic efficiency on the overall plant second law efficiency for different working fluids

Efficiencies from 10% to 100% were analyzed for all these fluids. Results for the second law plant efficiency can be found in Figure 5. It can be seen that the second

law efficiency suffers a great variation for all the fluids except for toluene. CO₂ shows the greatest variation, because it is the working fluid that requires the highest power consumption in the pump (high operating pressures), and any small change in the pump polytropic efficiency leads to important changes on the net power output and plant efficiency. For pump efficiencies reduced below 30%, the efficiency of the plant turns out to be negative (the power consumption is higher than the power produced in the expander). Even at a 100% pump efficiency, the CO₂ would still be the worst working fluid because of other irreversibilities in the cycle. The pump efficiency determines which working fluid is the best one at each operating point. Toluene is found to be the working fluid giving the second worst efficiency for efficiencies higher than a 70%, but, for pump efficiencies lower than 50%, it becomes the best choice. The reason for this is that the BWR for this fluid is low, and this means that any change of the pump polytropic efficiency has a minor impact on the efficiency. Propylene, which was the working fluid giving the best efficiency for the base case is still giving the best results for efficiencies higher than 70%. However, when the pump efficiency drops below this value, it is the second worst working fluid. This gives insight about how important the pump efficiency is for the performance of the cycle. Despite transcritical cycles might appear as the most sensible to pump efficiency changes, some subcritical cycles can be more sensitive. The BWR can be used as a good indicator of the sensitivity of the cycle to the pump efficiency. At the same time, the BWR is a strong function of the critical temperature of the working fluid. Figure 5 also shows that R1234yf and propylene need to move from transcritical to subcritical conditions to reach the optimal performance when the pump efficiency is below 30%, due to the high power consumption that operating at transcritical conditions with a low pump efficiency implies.

When comparing the obtained results with the literature, it was found that similar results were obtained in (Brosukiewicz-Gozdur, 2013). Even though this work includes the simulation of working fluids that were not considered by (Brosukiewicz-Gozdur, 2013), the same tendencies were obtained for the same studied working fluids, meaning that propylene is the working fluid with the highest specific power consumption, followed by the propane, while toluene presents the lowest one.

4.3 Turbine stages analysis

Since the specific work produced in the turbine is lower in the ORC than for gas and steam turbines, the expansion process can be handled in few stages. Assuming a fixed efficiency for the turbine (independent of factors such as the working fluid) leads to unrealistic results (Astolfi and Macchi, 2015). In this work, 1, 2 and 3 stage axial turbines have been studied in order to determine how this may affect the

performance of the whole plant when different working fluids are used. To do so, the turbine efficiency was studied as a function of the Volume Ratio (which accounts for compressibility effects (Macchi, 2013)) and the Size Parameter (which accounts for the dimensions of the expander). Each pair of SP and V_R gives a specific turbine efficiency, which increases with lower V_R and higher SP (Astolfi and Macchi, 2015). For the low density at the outlet of the turbine results into a high SP, which benefits the turbine efficiency. shows how the expander efficiency influences the overall power plant second law efficiency. Three different efficiencies were obtained for each studied working fluid, corresponding to a 1-, 2- or 3-stage expansion.

Results from Figure 6 show that increasing the number of stages leads to an increase of the expander efficiency for all the simulated working fluids, although some of them are more sensitive to this change than others. The best and worst working fluids are still the same (propylene and CO₂ respectively) when moving from 1 to 3 expansion stages. Regarding the rest of the working fluids, some as acetone, butane, and MM are experiencing the greater improvements when increasing the turbine number of stages, while the R32 and the propyne are experiencing the lowest ones.

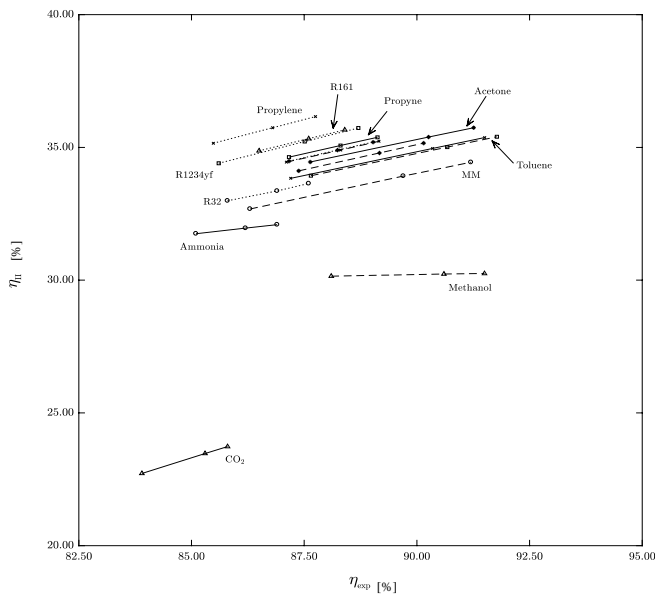


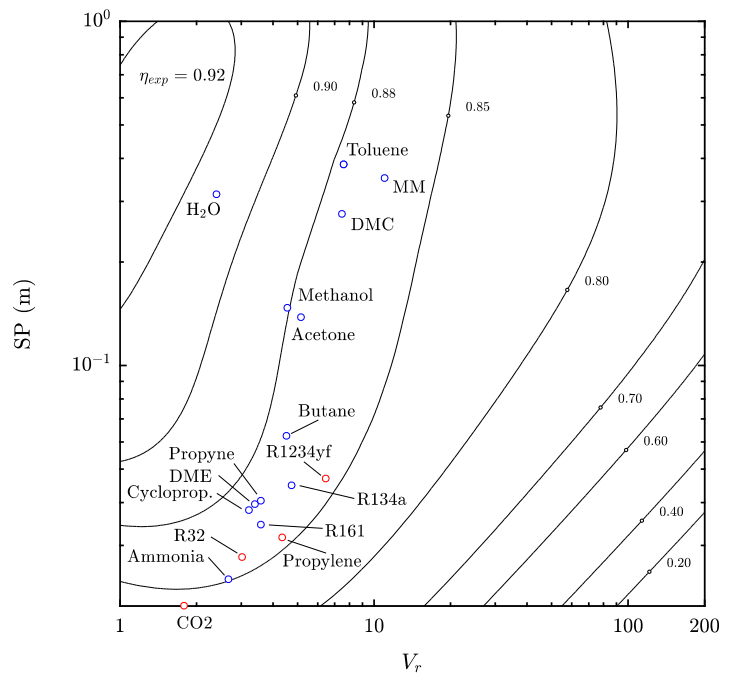
Figure 6. Influence of the expander efficiency on the second law efficiency of the whole power plant for different working fluids

Increasing the number of expansion stages for MM results into an increase of the turbine efficiency close to a 5%, which implies a second law efficiency improvement of 1.76%. Acetone also shows a great turbine efficiency improvement when increasing the

number of stages, a 3.63%, which results into a second law efficiency rise of 1.29%.

Fluids such as R32 experience only an improvement of 1.83% on the turbine efficiency when moving from 1 to 3 stages of expansion, and this means a plant efficiency increase of only 0.65%. On the other side, for CO₂, even though the turbine efficiency experiences one of the highest improvements (3.72%), the second law efficiency does not experience a great change (only 1%).

Figure 7 shows how the SP and V_R influence the efficiency of the turbine with only one stage for the different simulated working fluids. Working fluids with the highest efficiencies are the H₂O, methanol, acetone and toluene, while those ones with the lowest turbine efficiencies are CO₂, ammonia and propylene. For the low density at the outlet of the turbine results into a high



SP, which benefits the turbine efficiency.

Figure 7. Volume ratio and Size Parameter influence on the expander efficiency with one stage of expansion and for the different simulated working fluids.

5 Conclusions

After having carried out an analysis of the ORC for 39 different working fluids and under different cycle layouts and configurations, some conclusions have been reached:

1. Those working fluids with a critical temperature and maximum temperature of the cycle relationship between 0.93 and 1.02 (such as propylene and R1234yf) are showing the best results. Fluids with too low critical temperatures are giving the lowest efficiencies.

- Regarding the use of a recuperator, the dry and isentropic fluids are experiencing the highest efficiency improvements, while some wet fluids do not have potential to operate under this cycle layout (the second law efficiency for the whole power plant drops).
- Fluids with a low critical temperature are much more dependent on the pump performance than those ones with a high critical temperature, due to the high Backwork Ratios of the former.
- Increasing the number of stages for the turbine results into an efficiency improvement for all the studied cases. The degree of improvement is a function of the variation of the V_R and SP.
- It was demonstrated that H_2O and CO_2 are not suitable working fluids for an ORC with a low-temperature heat source for low-capacity power plants. In case of co-generation for the cycle or higher power productions, their potential may increase, but this should be studied.

Nomenclature

Acronyms and symbols

BWR	Backwork Ratio	[kW/kW]
ρ	Density	[kg/m ³]
η	Efficiency	[%]
h	Enthalpy	[J/kg]
\dot{E}	Exergy flow	[kW]
\dot{Q}	Heat flow	[kW]
\dot{m}	Mass flow	[kg/s]
MW	Molecular Weight	[kg/mole]
\dot{W}	Power	[kW]
p	Pressure	[bar]
SP	Size Parameter	[m]
T	Temperature	[K]
V_r	Volume ratio	[-]

GWP	Global Warming Potential
HC	Hydrocarbon
HFC	Hydrofluorocarbon
HFO	Hydrofluoroolefin
ODP	Ozone Depletion Potential
ORC	Organic Rankine Cycle

Subscripts

amb	ambient
c	condenser
crit	critical
hot	hot-source
in	turbine inlet
s	isentropic
out	turbine outlet
rec	recuperator
turb	turbine
w.f	working fluid

Acknowledgements

This research was supported by the NTNU Department of Energy and Process Engineering, which provided the funding. We would like to thank them for having made this research and study possible.

References

- Agromayor, R., Nord, L.O. (2017). Fluid selection and thermodynamic optimization of organic Rankine cycles for waste heat recovery applications. *Energy Procedia* (in press).
- Astolfi, M., Macchi, E. (2015). Efficiency correlations for axial flow turbines working with non-conventional fluids. *Asme Orc 2015* (83), 1-12.
- Bao, J., Zhao, L. (August, 2013). A review of working fluid and expander selections for organic Rankine cycle. *Renewable and Sustainable Energy Reviews* (24), 325-342. doi: 10.1016/j.rser.2013.03.040
- Borsukiewicz-Gozdur, A. (2013). Pumping work in the organic Rankine cycle. *Applied Thermal Engineering* (51), 781-786. doi: 10.1016/j.applthermaleng.2012.10.033
- Colonna, P., Casati, E., Trapp, C., Mathijssen, T., Larjola, J., Turunen-Saaresti, T., Uusitalo, A. (2015). Organic Rankine Cycle Power Systems: From the Concept to Current Technology Applications, and an Outlook to the Future. *Journal of Engineering for Gas Turbines and Power*, 137, 100801-19. doi: 10.1115/1.4029884
- Feng, Y., Hung, T., Greg, K., Zhang, Y., Li, B., Yang, J. (2015). Thermodynamic comparison between pure and mixture working fluids of organic Rankine cycles (ORCs) for low temperature waste heat recovery. *Energy Conversion and Management*. doi: 10.1016/j.enconman.2015.09.042
- Frutiger, J., Andreasen, J., Liu, W., Spliethoff, H., Haglind, F., Abildskov, J., Sin, G. (2016). Working fluid selection for organic Rankine cycles - Impact of uncertainty of fluid properties. *Energy* (109), 987-997. doi: 10.1016/j.energy.2016.05.010
- Haberle, F., Preisinger, M., & Brüggemann, D. (2012). Zeotropic mixtures as working fluids in Organic Rankine Cycles for low-enthalpy geothermal resources. *Renew Energy* (37), 364-370. doi: 10.1016/j.renene.2011.06.044
- Hærvig, J. S. (2016). Guidelines for optimal selection of working fluid for an organic Rankine cycle in relation to waste heat recovery. *Energy* (96), 592-602. doi: 10.1016/j.energy.2015.12.098
- Hung, T.C., Wang, S.K., Kuo, C.H., Pei, B.S, Tsai, K.F. (2010). A study of organic working fluids on system efficiency of an ORC using low-grade energy sources. *Energy* (35), 1403-1411. doi: 10.1016/j.energy.2009.11.025
- Landelle, A., Tauveron, N., Revellin, R., Haberschill, P., Colasson, S., Roussel, V. (2017). Performance investigation of reciprocating pump running with organic fluid for organic Rankine cycle. *Applied Thermal Engineering* (113), 962-969. doi: 10.1016/j.applthermaleng.2016.11.096
- Liu, Q., Duan, Y., Yang, Z. (2013). Performance analyses of geothermal organic Rankine cycle with selected

- hydrocarbon working fluids. *Energy* (63), 123-132. doi: 10.1016/j.energy.2013.10.035
- Macchi, E. (2013). *The choice of working fluid: The most important step for a successful organic Rankine cycle (and an efficient turbine)*. Politecnico di Milano, Department of Energy, Milano.
- Macchi, E., Astolfi, M. (2017). *Organic Rankine Cycle (ORC) Power Systems. Technologies and Applications*. (W. P. Energy, Ed.) Elsevier.
- Maraver, D., Royo, J., Lemort, V., Quoilin, S. (2014). Systematic optimization of subcritical and transcritical organic Rankine cycles (ORCs) constrained by technical parameters in multiple applications. *Applied Energy* (117), 11-29. doi: 10.1016/j.apenergy.2013.11.076
- Roy, J., Mishra, M., Ashok, M. (2011). Performance analysis of an Organic Rankine Cycle with superheating under different heat source temperature conditions. *Applied Energy* (88), 2995-3004. doi: 10.1016/j.apenergy.2011.02.042
- Saleh, B., Koglbauer, G., Wendland, M., Fischer, J. (2007). Working fluids for low temperature organic Rankine cycles. *Energy* (32), 1210-1221. doi: 10.1016/j.energy.2006.07.001
- Shu, G., Gao, Y., Tian, H., Wei, H., Liang, X. (2014). Study of mixtures based on hydrocarbons used in ORC (Organic Rankine Cycle) for engine waste heat recovery. *Energy* (74), 428-438. doi: 10.1016/j.energy.2014.07.007
- Xu, J., Liu, C. (2013). Effect of the critical temperature of organic fluids on supercritical pressure Organic Rankine Cycles. *Energy* (63), 109-122. doi: 10.1016/j.energy.2013.09.068
- Zhai, H., Shi, L., An, Q. (2014). Influence of working fluid properties on system performance and screen evaluation indicators for geothermal ORC (organic Rankine cycle) systems". *Energy* (74), 2-11. doi: 10.1016/j.energy.2013.12.030

Electrical Power System Modelling in Modelica – Comparing Open-source Library Options

Dietmar Winkler

University College of Southeast Norway, dietmar.winkler@usn.no

Abstract

The past modelling of electrical power systems used to be a the domain of a few major power system modelling tools.

Commercial tools¹ like DIGSILENT PowerFactory [3], POWERSYS EMTP-RV [17], PSCADTM [14], Siemens PSS/E[®] [20] are just some examples. All of them very powerful but with their own proprietary format for the models created makes it hard to exchange validated models of power systems.

In order to disconnect the dependency of the power system *model* from the power system *tool* a project funded by the European Commission was started called “iTesla – Innovative Tools for Electrical System Security within Large Areas” [7]. One of the results of the project was the creation of an open-source modelling library called iPSL [24].

The library was created using the open-source Modelica modelling language which in turn allows to be used with several different Modelica modelling tools. The strong focus during the project was the validation of the models contained in the library. Most components stem from other tools (e.g., PSAT [15], PSS/E[®] [20]).

But the iPSL is by far not the first open-source power system library written in Modelica. Other libraries

which have been around before are: SPOT [1], ObjectStab [11] and PowerSystems [6] (an updated subset of SPOT). In addition the iPSL library has been “forked” as OpenIPSL [21] by SmartTS Lab which is one partner of the original “iTesla” project.

This paper is going to investigate the differences of the different available power system libraries. Point out their specific strength and weaknesses with respect to user-friendliness, robustness, physical representation and validation.

Keywords: electrical power systems, modelling, simulation, modelica, open-source, libraries

1 The Libraries

1.1 SPOT

The “Modelica Power Systems Library SPOT” [25] is one of the first Modelica libraries to model power systems both in transient and steady-state mode. As a note, the capitalised spelling was changed to `spot` in the Modelica package in order to follow Modelica naming conventions.

1.1.1 History

The theory behind the library was first presented at the *Modelica Workshop 2000* in “Advanced Modeling of Electromagnetic Transients in Power Systems” [1].

1.1.2 Concept

The SPOT library can be described as a general purpose library suitable to model and simulate power systems in DC and AC. Due to the special role of 3-phase AC systems it received a special role in the library. AC systems are periodically driven systems. An inherent limitation for efficient integration of such systems is the necessary small step size

Traditionally, power systems have always been treated differently depending on the size. Whilst smaller systems can be investigated using general transient methods, larger systems are normally restricted to the “power-flow” approximation. Normally different simulation tools are used in order to serve the different methods.

The SPOT library treats both cases within one common framework and brings the power-flow approximation closer to the general case. This is achieved by use of a transformed representation of the electrical equations. The transformed equations contain a steady-state or power-flow limit, obtained by choosing a synchronously rotating reference system and omitting the time-derivative. That implementation leads to a considerable increase of simulation speed for linear or linearised symmetric systems, compared to the direct representation. The increase in simulation speed is only available for linear systems or as long as when sources do not contain harmonics. As the electric equations are valid in reference systems with arbitrary angular orientation, the standard cases ‘inertial’ (non-rotating) and ‘synchronous’ (rotating with electrical frequency) system can simply be obtained by an appropriate parameter choice. The same goes for the choice of frequency, where 50Hz and 60Hz is an option.

¹Listed in alphabetical order.

1.1.3 Library Structure

The structure of the SPOT library is a bit special since it is shipped as two packages. One containing the library and its components itself, see Figure 1, and an additional examples package.

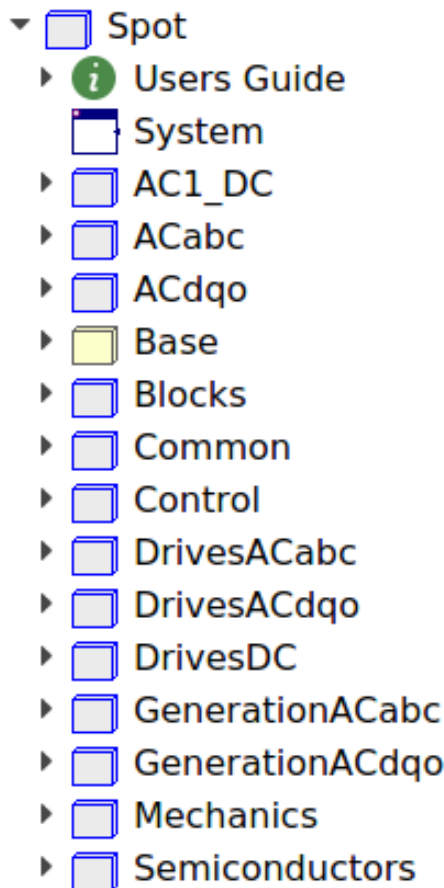


Figure 1. Structure of the SPOT library

The library tries to sort the main application areas into:

- 1-phase and DC applications
- 3-phase periodic signals, i.e., “abc”
- 3-phase transformed, i.e., “dq0”

Components that are common to all the main application areas only appear once. For others one has to decide which system sub-package to choose from in order to create the appropriate simulation model. This split into several sub-packages of identical components but with different equation systems is one of the short-comings from the usability point of view. Something that has been improved in derivatives of the SPOT library.

1.1.4 Licence

The SPOT library has been released under the “Modelica License 1.1” [22], a licence similar to the BSD license.

1.1.5 State of Development

The last official feature release “v0.706” dates back to the 11th September 2007 and was compatible with the Modelica 2 language specification. Some years later the library was cleaned up and upgraded to Modelica 3 language specification and using the Modelica Standard Library 3.2.1. This version was called “v0.706.1” and did not contain any additional functional changes.

The original Author, Hans Jürg Wiesmann, died in 2015 and the SPOT library is no longer officially developed. However some successors using parts of or all of the SPOT library are available and are described later on.

1.2 ObjectStab

The ObjectStab library [12] is a Modelica Library for Power Systems Voltage and Transient stability simulations.

1.2.1 History

This library was just like the theory behind SPOT presented at the *Modelica Workshop 2000* in “ObjectStab Library – A Modelica Library for Power System Stability Studies” [11].

1.2.2 Concept

Where the SPOT library was more a general purpose power systems library, the ObjectStab library concentrates mainly on electrical transmission and generation systems. Standard assumptions for multi-machine transient stability simulations are made. For example generator stator and network time constants are neglected and voltages and currents are assumed to be sinusoidal and symmetrical. Most components are modelled according to the guidelines from the book given in “Power System Dynamics and Stability” [13].

1.2.3 Library Structure

The structure of the ObjectStab library is shown in Figure 2.

It contains:

- Generators with constant frequency and voltage as slack or PV nodes, or using 3rd or 6th order dq-models with excitation and prime mover control systems.
- Transmission lines in π -link or series impedance representation.
- Reactive power compensation devices; shunt reactors, shunt capacitances and series capacitances according to [13].
- Fixed ratio transformers.
- On-load tap changing transformers (OLTC) modelled as detailed discrete models or using their corresponding continuous approximations according to [19].

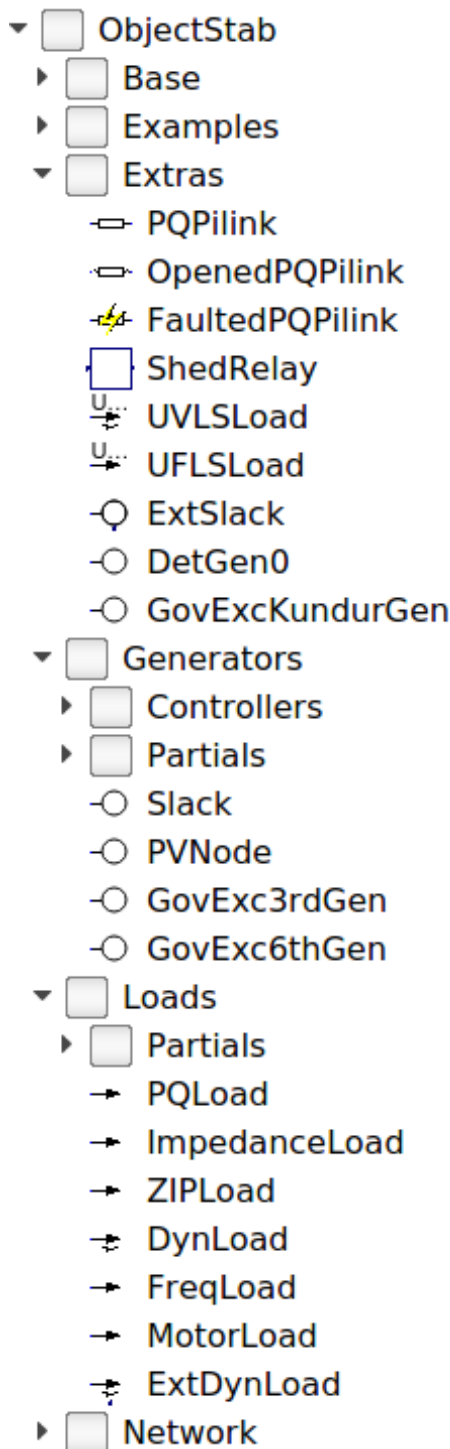


Figure 2. Structure of the ObjectStab library

- Static and dynamic loads, including induction motor according to [13] and generic exponential recovery loads according to [9].
- Busses.
- Faulted lines and busses including fault impedance.

1.2.4 Licence

The ObjectStab library has been released under the “Modelica License 1.1” [22], a licence similar to the BSD license.

1.2.5 State of Development

The last official feature release “v1.0c” dates back to the 25th September 2002 and was compatible with the Modelica 1 language specification. That release is still using the Modelica Standard Library 1.6 and ModelicaAdditions 1.5, something that makes it hard to use with current Modelica tools.

In 2014 and 2015 some effort was made to upgrade the ObjectStab library to current Modelica, i.e., make it work with Modelica Standard Library 3.2.1. This work was executed by Dietmar Winkler and with some help of the late Hans Jürg Wiesmann. However due to the dependencies of Petrinet models that are no longer available in the current Modelica Standard Library and the lack of any correct and Modelica standard conform state machine successor, some models will not work fully in standard Modelica tools.

There have been some non-official updated versions of the ObjectStab library distributed to individuals to by the original Author but those have never been published officially and contained changes were not documented.

The current state of the development version can be obtained from [12].

1.3 PowerSystems

The PowerSystems library [26] is intended for the modelling of electrical power systems at different levels of detail both in transient and steady-state mode.

1.3.1 History

Given that latest version of ObjectStab was published in 2002 and the the SPOT library has not been further developed since 2007 a new attempt to revive power system modelling using Modelica was presented at the 10th International Modelica Conference in the paper “Flexible modeling of electrical power systems – the Modelica PowerSystems library” [6]. That paper presented the PowerSystems library which could be called a slimlined successor to the SPOT library. Interesting is that the original developer of SPOT was helping developing this new PowerSystems library.

1.3.2 Concept

The SPOT library was offering nice features like use of per-unit systems or SI-unit system depending on choice. At the same time the multiplication of components for the different phase-systems was creating a lot of code-duplications.

The PowerSystems library introduces a nice replaceable phase-system which allows to have one instance of a component but with different equation systems activated. This makes the library more compact and user-friendly. It

can be used to calculate simple power balances but also allows for usage of quasi-static models up to the treatment of detailed transient effects. The main focus are electric power network applications, something that lead to only using only part of the SPOT library

1.3.3 Library Structure

The structure is shown in Figure 3 and if compared with Figure 1 the heritage is quite obvious.

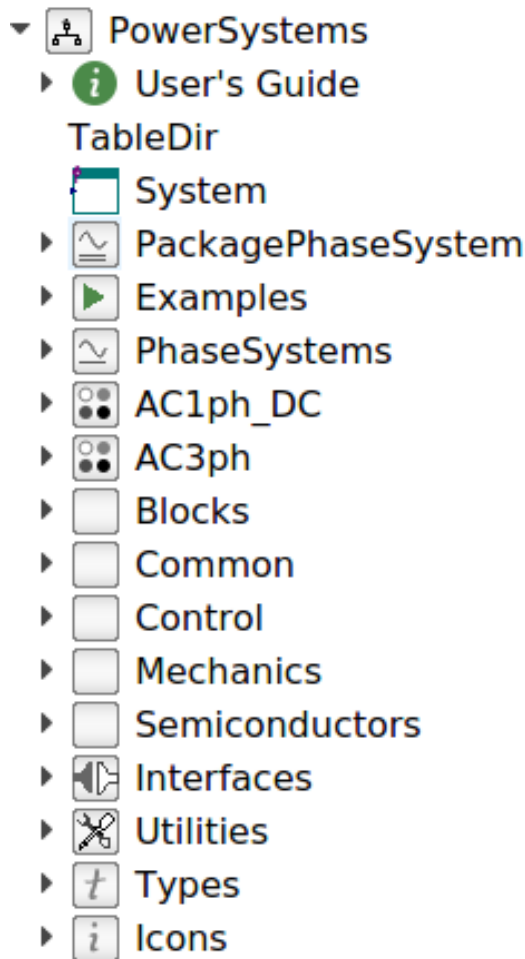


Figure 3. Structure of the PowerSystems library

One can see that the PowerSystems library got rid of unnecessary duplications of sub-packages (by use of the phase-systems feature). Also the Examples sub-package is now part of the library as is much more common in Modelica library, rather than having them as external package.

1.3.4 Licence

The PowerSystems library has been released under the “Modelica License 2” [23].

1.3.5 State of Development

The last official feature release “v0.6.0” is from the 18th January 2017 and is under active development on

GitHub [26] by Rüdiger Franke and contributors. The progress and issues can be followed publicly.

1.4 iPSL

The iPSL stands for “iTesla Power System Library” [8] and is a Modelica library developed as part of the iTesla project [7].

1.4.1 History

Developed as part of the “iTesla – Innovative Tools for Electrical System Security within Large Areas” - project (supported by the European Commission under the 7th Framework Programme). The original project ran from 2012 to 2016.

1.4.2 Concept

The library contains a set of power system component models for phasor time domain simulations especially. The goal was to build a model library that allows to use different tools to compare results in order to validate power system models. Hence instead of building up models using generic electrical equations to describe the physical behaviour, reference models that are used other existing power system tools are implemented (e.g., EUROSTAG [4], PSAT [15], PSS/E[®] [20]). That way the results can first be compared to the different tools they originate from and then also with each other.

1.4.3 Library Structure

The structure of the iPSL is shown in Figure 4.

The structure demonstrates that instead of having one model for a specific machine, e.g., generator, there are several models based on the originating implementation reference.

This is quite a special way to build up a modelling library and brings some caveats which will be discussed later.

1.4.4 Licence

The iPSL has been released under the “Mozilla Public License Version 2.0” [5].

1.4.5 State of Development

The last official feature release “v1.1.1” is from the 9th June 2017 and is under active development on GitHub [8]. The development progress and issues can be followed publicly.

1.5 OpenIPSL

The OpenIPSL stands for Open-Instance Power System Library and is a fork of of the iTesla Power System Library - iPSL, currently developed and maintained by the SmarTS Lab research group, collaborators and friends.

1.5.1 History

When the original iTesla project was completed on 31st March 2016, part of iTesla consortium continued the development of the iTesla Power System Tool [18] which

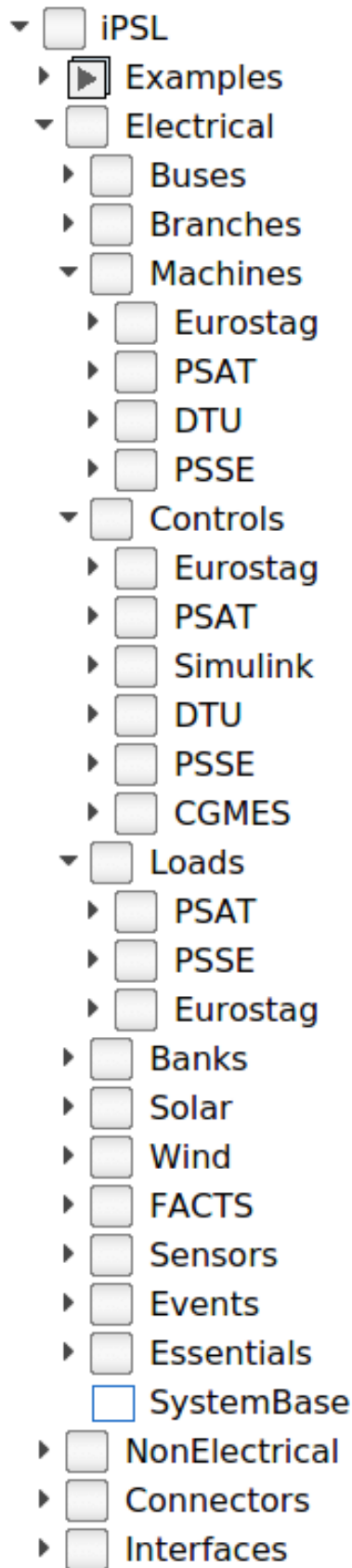


Figure 4. Structure of the iPSL

utilises the iPSL. Hence the iPSL continued to be developed in such a way to fulfil the needs of the iTesla Power System Tool which not necessarily fits the needs of general power system researcher and teachers.

The developers attached to the SmartTS Lab decided therefor to fork the iPSL under the new name OpenIPSL. Approximately 75% of the original iPSL developers continue the development of OpenIPSL.

1.5.2 Concept

In principle, the concept of OpenIPSL is of course the same as the iPSL. But in contrast its to be used as a research library with maximum compatibility with OpenModelica [2] (to provide a free/libre and cost-free alternative for power system dynamic simulation) and to provide as many as possible typical "test networks" for use in research and teaching. Not having to serve a certain tool interface, it is now also free to adapt the models to a more object-oriented coding style.

1.5.3 Library Structure

The structure of the OpenIPSL is shown in Figure 5.

Due to the recent split from the iPSL the general structure is still very similar. The difference is mainly some better usage of Modelica language features and cleaner diagram representation. In addition the SMART Lab group removed all sub-packages that are based on models from tools where they do not have access to and/or are lacking any documentation on the implementation background.

1.5.4 Licence

The OpenIPSL has been released under the "Mozilla Public License Version 2.0" [5].

1.5.5 State of Development

The last official feature release "v1.0.0" is from the 16th December 2016 and is under active development on GitHub [oipsl-lib]. The development progress and issues can be followed publicly.

2 Example Application

In order to demonstrate how the libraries appear visually when modelling an example power system was chosen. The following figures show the "Example 13.2" from [10] which is used to analyse the transient stability of a power system which experiences a three-phase to ground fault at one of the busses.

Figure 6 shows the OpenIPSL version, Figure 7 shows the PowerSystems version and Figure 8 shows the ObjectStab version.

The representation from the iPSL would be very much alike the OpenIPSL though lately also dynamic displays of the dynamic power-flow values were added to the OpenIPSL on the diagram. Similarly the model from SPOT would have looked identically to that of the PowerSystems library, since the graphic properties have not been changed much.

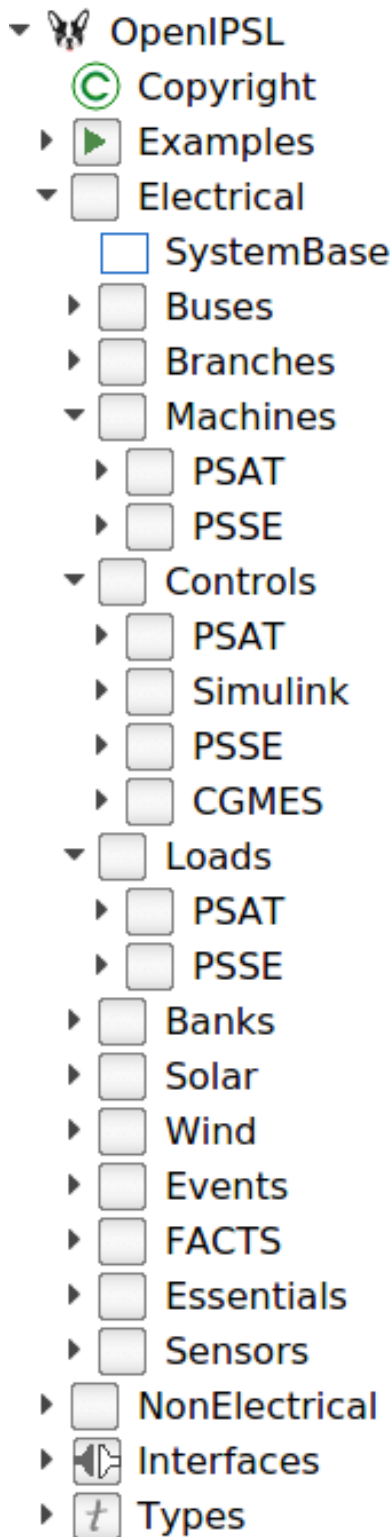


Figure 5. Structure of the OpenIPSL

3 Usability

3.1 User-friendliness

One thing that becomes very apparent when working with the different power system libraries is the different focus

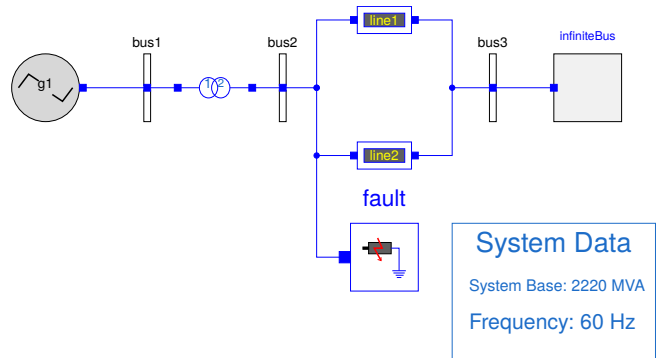


Figure 6. Kundur, example 13.2 with OpenIPSL

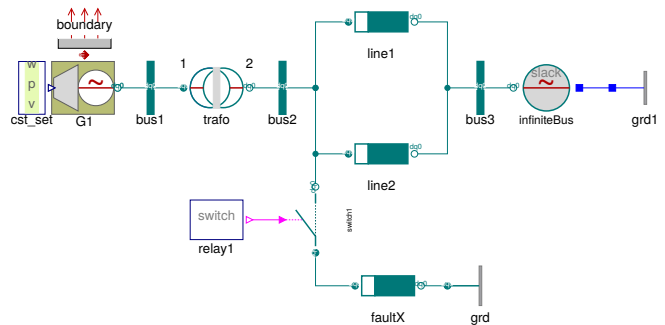


Figure 7. Kundur, example 13.2 with PowerSystems library

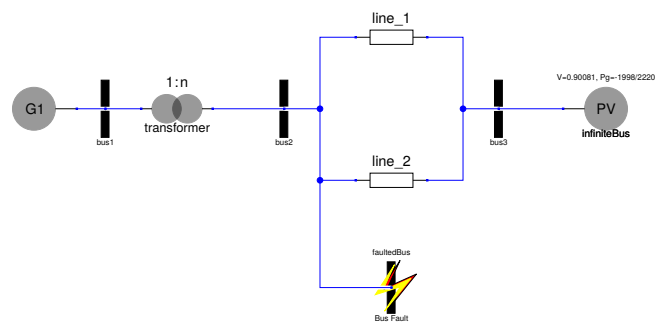


Figure 8. Kundur, example 13.2 with ObjectStab library

on usability vs. compliance with other tools. Both the SPOT and PowerSystems library on the one end of the scale providing models of lines and machines with standard parameter sets as seen in real live. For the PowerSystems library even providing ready to use parameter for different standard line types. One can enter the length in *Km* and the material and will get the reactance and resistance values accordingly.

The three other candidates (ObjectStab, iPSL, OpenIPSL) are on the other end of the scale. Here needs to provides parameters like reactance and resistance directly. Also one needs to take care of possible per-unit conversion due to different system or machine base one-self.

Both methods have their benefits and drawbacks.

E.g., implementing a text book example with given per-unit values would be easier more straight forward in `ObjectStab`, `iPSL`, `OpenIPSL`. The same goes for models taken from other power system simulation tools like `PSS/E`, where the parameter set is normally given in per-unit values and not physical dimensions.

Implementing a practical problem on the other hand would be easier using the `PowerSystems` library (and `SPOT` for that matter).

3.2 Use of Modelica features

When looking at the level usage of Modelica features then basically the `SPOT` and `PowerSystems` library are the winner. Here the full power of switched models (e.g., phase-system) and inheritance and library structure are fully put into use.

The `ObjectStab` library is simply too old to make use of features that have been implemented in later versions of the Modelica language. `iPSL` and `OpenIPSL` had the challenge to stay as close to the original reference models, which often meant system-flow oriented modelling and not making use of the power of equations.

3.3 Documentation

Unfortunately only the `PowerSystems` and `SPOT` library contain extensive and usable documentation of the models and a user's guide as part of the library.

The other library basically point either to the original presentation paper (`ObjectStab`) or to the reference tools where the models were taken from.

3.4 Robustness

The `SPOT` and `PowerSystems` library were developed as generic multi-purpose libraries (the latter less so). Unfortunately this leads to a certain amount of complexity which in turn again leads to a series of parameters that can/must be set. Not knowing the correct fitting parameters can easily lead to a non-solvable equation system and can be frustrating to the user.

The `ObjectStab`, `iPSL` and `OpenIPSL` have a restricted set of parameters available (when compared with the other two) and therefore tend to lead to more robust simulation models with less numerical issues.

All of the libraries on the other hand depend on initial conditions that are in the proximity of a stable power system. Basically that meant one needs steady-state power flow calculations before hand to parameterise the systems. One can get lucky to be able to get the model running and converging towards a stable power flow but often this is not the case.

4 Validations

The `PowerSystems` and `SPOT` library do not name specific validation cases. The only reference for them are basically some real-life applications that were published.

The `ObjectStab` library notes that the component library has been validated using comparative simulations

with `EUROSTAG`.

The `iPSL` and `OpenIPSL` basically only contain validated modes using software-to-software comparison. This was the original reason to build the `iPSL` in the first place. They contain models validated against `CGMES`², `Simulink`, `EUROSTAG` (`iPSL` only), `PSAT` and `PSS/E`.

5 Other options

Despite the open-source libraries presented here so far, the Modelica Standard Library itself contains the quasi-static library package "`Modelica.Electrical.Quasistationary`" that could potentially also be used for power systems modelling.

Another library that needs to be mentioned in this context is another successor of the `SPOT` library, the "`ElectricPower` library" [16]. It is a commercial product of Modelon and therefore not part of the comparison.

6 Outlook

When looking at the future of the presented library options, from my perspective both, the `iPSL` and the `OpenIPSL`, will continue to be actively developed. It will be interesting to see to what degree the `iPSL`'s dependency of the `iTesla` Power Tool will restrict the "clean up" of the structure. This is something that the `OpenIPSL` might be able to use to its advantage of a more flexible development future.

As for the `PowerSystems` library, it is actively developed, has better documentation and is more user-friendly. Something that might push its application further especially for new-comers.

The `ObjectStab` library is most likely deprecated by `iPSL` and `OpenIPSL` alike.

The `SPOT` library has already two active projects carrying on. In a reduced form as `PowerSystems` library and in the commercial `ElectricPower` library,

References

- [1] Bernhard Bachmann and Hansjürg Wiesmann. "Advanced Modeling of Electromagnetic Transients in Power Systems". In: *Modelica Workshop 2000 Proceedings*. Oct. 23, 2000, pp. 93–97.
- [2] Open Source Modelica Consortium. *OpenModelica*. 2017. URL: <https://openmodelica.org/>.
- [3] DiGSILENT. *PowerFactory*. URL: <http://www.digsilent.de/index.php/products-powerfactory.html>.
- [4] Tractebel Engineering. *EUROSTAG*. URL: <http://www.eurostag.be/en/products/eurostag/the-reference-power-system-dynamic-simulation/>.
- [5] Mozilla Foundation. *Mozilla Public License Version 2.0*. Jan. 3, 2012. URL: <https://www.mozilla.org/en-US/MPL/2.0/>.

²Common Grid Model Exchange Standard

- [6] Rüdiger Franke and Hans Jürg Wiesmann. “Flexible modeling of electrical power systems—the Modelica Power-Systems library”. In: *Proceedings of the 10 th International Modelica Conference; March 10-12; 2014; Lund; Sweden*. 096. Linköping University Electronic Press. Linköping University Electronic Press, Mar. 11, 2014, pp. 515–522. DOI: 10.3384/ecp14096515.
- [7] *iTesla - Innovative Tools for Electrical System Security within Large Areas*. URL: <http://www.itesla-project.eu/>.
- [8] ITesla project. *iPSL on GitHub*. 2017. URL: <https://github.com/itesla/ipsl>.
- [9] Daniel Karlsson and David J Hill. “Modelling and identification of nonlinear dynamic loads in power systems”. In: *IEEE Transactions on Power Systems* 9.1 (1994), pp. 157–166.
- [10] Prabha Kundur and Neal J. Balu. *Power system stability and control*. The EPRI power system engineering series. New York, NY: McGraw-Hill, 1994. 1176 pp. ISBN: 978-0-07-035958-1.
- [11] Mats Larsson. *ObjectStab Library – A Modelica Library for Power System Stability Studies*. 2000.
- [12] Mats Larsson. *ObjectStab on GitHub*. Sept. 25, 2002. URL: <https://github.com/modelica-3rdparty/ObjectStab>.
- [13] Jan Machowski, Janusz Bialek, and Dr Jim Bumby. *Power System Dynamics and Stability*. Wiley, 1997. ISBN: 978-0-471-97174-0.
- [14] Manitoba Hydro International Ltd. *PSCAD™*. URL: <https://hvdc.ca>.
- [15] Federico Milano. *PSAT*. URL: <http://faraday1.ucd.ie/psat.html>.
- [16] Modelon AB. *Electric Power Library*. Modelon. URL: <http://www.modelon.com/products/modelica-libraries/electric-power-library/> (visited on 05/28/2016).
- [17] POWERSYS. *EMTP-RV*. URL: <http://www.emtp-software.com>.
- [18] iTesla PST group. *iTesla Power System Tools*. 2017. URL: <http://www.itesla-pst.org/>.
- [19] P.W. Sauer and M.A. Pai. “A comparison of discrete vs. continuous dynamic models of tap-changing-under-load transformers”. In: *Proceedings of NSF/ECC Workshop on Bulk power System Voltage Phenomena - III : Voltage Stability, Security and Control*. Davos, Switzerland, 1994.
- [20] Siemens. *PSS/E[®]*. URL: <http://siemens.com/power-technologies/software>.
- [21] SmarTS Lab. *OpenIPSL on GitHub*. 2017. URL: <https://github.com/SmarTS-Lab/OpenIPSL>.
- [22] The Modelica Association. *The Modelica License 1.1*. June 30, 2000. URL: <https://modelica.org/licenses/ModelicaLicense1.1>.
- [23] The Modelica Association. *The Modelica License 2*. Nov. 19, 2008. URL: <https://modelica.org/licenses/ModelicaLicense2>.
- [24] L. Vanfretti et al. “iTesla Power Systems Library (iPSL): A Modelica library for phasor time-domain simulations”. In: *SoftwareX* 5 (2016), pp. 84–88. DOI: 10.1016/j.softx.2016.05.001.
- [25] Hans Jürg Wiesmann. *SPOT library on GitHub*. Sept. 11, 2007. URL: <https://github.com/modelica-3rdparty/Spot>.
- [26] Hans Jürg Wiesmann and Rüdiger Franke. *Power Systems library on GitHub*. Jan. 18, 2017. URL: <https://github.com/modelica/powersystems>.

Comparison of control strategies for a 2-DOF helicopter

Roshan Sharma Carlos Pfeiffer

Department of Electrical Engineering, IT, and Cybernetics, University College of Southeast Norway, Norway,
{roshan.sharma, carlos.pfeiffer}@usn.no

Abstract

The two degrees of freedom (2-DOF) helicopter is an openloop unstable multi-variable process. Various control strategies can be applied to stabilize the system for tracking and regulation problems but not all control methods show equal capabilities for stabilizing the system. This paper compares the implementation of a classical PID controller, a linear quadratic regulator with integral action (LQR+I) and a model predictive controller (MPC) for stabilizing the system. It has been hypothesized that for such an unstable MIMO (multi input multi output) process showing cross coupling behavior, the model based controllers produces smoother control inputs than the classical controller. The paper also discusses the necessity of including the derivative part of the PID controller for stabilization and its influence to the measurement noises. A Kalman filter used for estimating unmeasured states may produce bias due to model mismatch. The implementation and comparison is based on a 2-DOF experimental helicopter prototype.

Keywords: 2-DOF helicopter, MPC, LQR, PID, Kalman filter, qpOASES

1 Introduction

In many publications where various control strategies are implemented and compared, there is a lack of verification of the implementation and experimentation with a real process. Most of the studies are simply based on simulation results and there are no experimental data to back-up their results. In this paper, we have tried to bridge the gap between simulation results and the real world implementation.

This paper is based on a 2-DOF helicopter unit. Various studies about this process can be found in literature with respect to tracking and regulation problem, see (Su et al., 2002; Lopez-Martinez et al., 2004; Yu, 2007; M. et al., 2010; Barbosa et al., 2016; Neto et al., 2016). The results of these studies look very promising, however, many of these studies are solely based on simulation results. At the university college of Southeast Norway (USN), a prototype of a two degrees of freedom helicopter model has been built from the scratch. All the control and estimation strategies discussed in this paper are actually implemented to the real unit.

Figure 1 shows the schematic of a 2 DOF helicopter unit at USN with the side view and the top view. It consists of

two propellers (pitch and yaw) driven by motors.

The unit has two inputs: (a) voltage to the front or pitch motor/propeller system, and (b) voltage to the back or yaw motor/propeller system. When voltage is applied to the pitch motor, the pitch propeller rotates and it generates thrust, and the helicopter lifts up. Thus voltage to the pitch motor/propeller control the elevation (or pitch) of the helicopter nose about the pitch axis. When voltage is applied to the yaw motor, the yaw propeller rotates and it generates torque in anti-clockwise direction, and the helicopter rotates about the yaw axis. The angle between the pitch axis and the helicopter body axis is called the pitch angle. The angle between the yaw axis and the helicopter body axis is called the yaw angle. The pitch and the yaw angles are measured by using the angle sensors as shown in Figure 1. Thus, these are the two outputs of the system which are measurable.

When designing a controller for this process, the goal is to stabilize the system and keep track of the pitch angle and the yaw angle. Initially this task seems straight forward and simple. In reality, it is not so due to the presence of the cross coupling nature and the dead band feature in the process making the control task very challenging.

In this paper, three different control strategies are implemented for stabilizing the system. The response shown by the real unit for these control strategies are compared and discussed in detail. The paper is organized as follows: In section 2, a brief description of the mathematical model of the process is given. Section 3 describes the implementation of the three control strategies. Experimental results are presented in section 4. A detailed discussion on the experimental results and their comparison is provided in section 5. Finally, conclusion are drawn in section 6.

2 Model of the 2-DOF helicopter unit

Let us define that $V_{mp} :=$ voltage applied to the pitch motor, $V_{my} :=$ voltage applied to the yaw motor, $\theta :=$ pitch angle and $\psi :=$ yaw angle.

The process is a cross-coupled MIMO system. When sufficient voltage is applied to the front motor, the helicopter not only pitches up but it also starts to rotate at the same time i.e. the input V_{mp} affects both outputs θ and ψ . Similarly, when sufficient voltage is applied to the back motor, the helicopter rotates in the anti-clockwise direction and at the same time, it also changes its pitch a little i.e. the input V_{my} affects both outputs θ and ψ . The effect of V_{mp} on ψ is very strong denoted by strong cross-

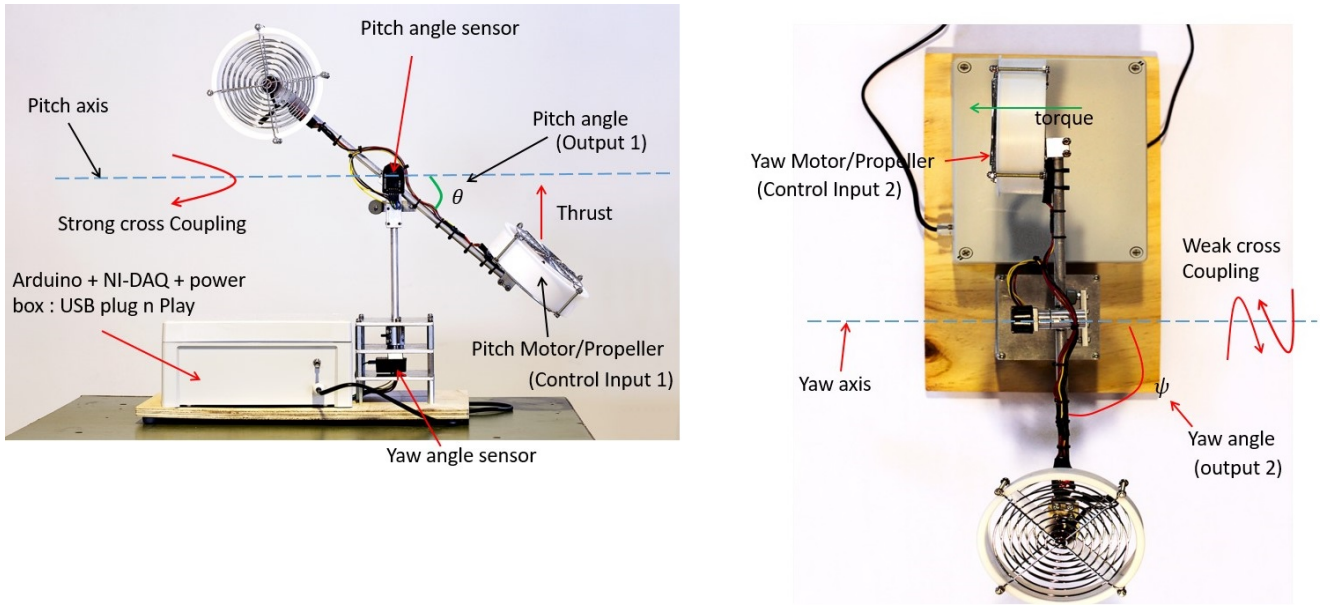


Figure 1. 2-DOF helicopter unit at USN (side view and top view)

coupling in Figure 1, while the effect of V_{my} on θ is weak denoted by weak cross-coupling.

The system can be described with four states: θ , ψ , pitch angular velocity (ω_θ) and yaw angular velocity (ω_ψ). The dynamics of the 2-DOF helicopter unit is modelled using Newton's laws of motion and Euler-Lagrange equations of energy. The model is described by a set of four ordinary differential equations (ODEs) developed by Quansar Inc. (Quansar Inc., 2011).

$$\frac{d\theta}{dt} = \omega_\theta, \quad (1)$$

$$\frac{d\psi}{dt} = \omega_\psi, \quad (2)$$

$$\frac{d\omega_\theta}{dt} = \frac{K_{pp}V_{mp}}{J_{eq,p} + m_{heli}l_{cm}^2} - \frac{K_{py}V_{my}}{J_{eq,p} + m_{heli}l_{cm}^2} - \frac{m_{heli}\omega_\psi^2 \sin(\theta)l_{cm}^2 \cos(\theta) + m_{heli}g \cos(\theta)l_{cm}}{J_{eq,p} + m_{heli}l_{cm}^2} - \frac{B_p \omega_\theta}{J_{eq,p} + m_{heli}l_{cm}^2}, \quad (3)$$

$$\frac{d\omega_\psi}{dt} = \frac{K_{yp}V_{mp}}{J_{eq,y} + m_{heli}\cos^2(\theta)l_{cm}^2} - \frac{K_{yy}V_{my}}{J_{eq,y} + m_{heli}\cos^2(\theta)l_{cm}^2} - \frac{2m_{heli}\omega_\psi \sin(\theta)l_{cm}^2 \cos(\theta)\omega_\theta}{J_{eq,y} + m_{heli}\cos^2(\theta)l_{cm}^2} - \frac{B_y \omega_\psi}{J_{eq,y} + m_{heli}\cos^2(\theta)l_{cm}^2}. \quad (4)$$

The parameters of the system with the description is listed in Table 1.

2.1 Dead band

The real process features dead band dynamics. There exists a minimum positive voltage on the pitch motor that is required to just lift up the helicopter, here defined as V_{mp}^{dead} . Application of pitch voltage lower than V_{mp}^{dead} produces no effect on the unit. Similarly, there exists a range of positive voltages to the yaw motor for which the system does not react at all (including the case when $V_{mp} > V_{mp}^{dead}$). This voltage range, here defined as V_{my}^{dead} is the minimum voltage on the yaw motor required to just rotate the helicopter. In the helicopter units at USN, V_{my}^{dead} is not a constant parameter but varies slightly with how much V_{mp} is being applied to the system. However, V_{my}^{dead} which is found experimentally is assumed to be constant in this paper.

To incorporate the effect of dead band, the process model should be adjusted. If the yaw voltage is less than V_{my}^{dead} , then $V_{my} = 0$ in Equations 3 and 4, i.e. for $0 \leq V_{my} \leq V_{my}^{dead}$, $V_{my} = 0$. Further more, if the pitch voltage is less than V_{mp}^{dead} , then it has no effect on the yaw angle ψ . Thus, the first term of Equation 4 is set to zero, i.e. for $0 \leq V_{mp} \leq V_{mp}^{dead}$,

$$\frac{d\omega_\psi}{dt} = - \frac{K_{yy}V_{my}}{J_{eq,y} + m_{heli}\cos^2(\theta)l_{cm}^2} - \frac{2m_{heli}\omega_\psi \sin(\theta)l_{cm}^2 \cos(\theta)\omega_\theta}{J_{eq,y} + m_{heli}\cos^2(\theta)l_{cm}^2} - \frac{B_y \omega_\psi}{J_{eq,y} + m_{heli}\cos^2(\theta)l_{cm}^2}. \quad (5)$$

2.2 Linear Model

To implement a linear MPC and LQR, a linearized version of the nonlinear model was developed. Linearization was carried out as the truncated Taylor series expansion

Table 1. Parameters of the system.

Parameter	Description	Value
l_{cm}	Distance between the pivot point and the center of mass of helicopter	0.015 [m]
m_{heli}	Total moving mass of the helicopter	0.479 [kg]
$J_{eq,p}$	Moment of inertia about the pitch axis	0.0172 [kg - m ²]
$J_{eq,y}$	Moment of inertia about the yaw axis	0.0210 [kg - m ²]
g	Acceleration due to gravity on planet earth	9.81 [m - s ²]
K_{pp}	Torque constant on pitch axis from pitch motor/propeller	0.0556 [Nm/V]
K_{yy}	Torque constant on yaw axis from yaw motor/propeller	0.21084 [Nm/V]
K_{py}	Torque constant on pitch axis from yaw motor/propeller	0.005 [Nm/V]
K_{yp}	Torque constant on yaw axis from pitch motor/propeller	0.15 [Nm/V]
B_p	Damping friction factor about pitch axis	0.01 [N/V]
B_y	Damping friction factor about yaw axis	0.08 [N/V]

sion and the details have not been shown in this paper. Let $x = [\theta, \psi, \omega_\theta, \omega_\psi]^T$ represent the states of the system, $u = [V_{mp}, V_{my}]^T$ are the control inputs to the system and $y = [\theta, \psi]^T$ are the measured outputs from the system. If x_{op}, u_{op} and y_{op} denotes the operating points for the states, control inputs and outputs, and $dt = 0.1$ is the sampling time, then the linearized model in the deviation form in discrete time domain is written as,

$$\delta x_{k+1} = A\delta x_k + B\delta u_k \quad (6)$$

$$\delta y_k = C\delta x_k \quad (7)$$

Here, A, B, C and D are the system matrices such that $A \in \mathbb{R}^{n_x \times n_x}$, $B \in \mathbb{R}^{n_x \times n_u}$ and $C \in \mathbb{R}^{n_y \times n_x}$ with $n_x = 4$ is the number of states, $n_u = 2$ is the number of control inputs and $n_y = 2$ is the number of outputs. $\delta x_k = x_k - x_{op}$ is the deviation of the states from the operating point. Similarly, $\delta u_k = u_k - u_{op}$ and $\delta y_k = y_k - y_{op}$.

3 Control of the process

The primary use of controllers for this process is to stabilize the helicopter such that the pitch angle (θ) and the yaw angle (ψ) are kept at their given setpoints. The voltages to the pitch and yaw motors are the control inputs. Although in real life, a helicopter remains horizontal during normal flight i.e with a setpoint of $\theta_{SP} = 0^\circ$, for this helicopter unit at USN, the performance of the controller will be studied for different setpoint changes for both angles. Three control structures are utilized to control the process. Each of them will be discussed briefly in this section.

3.1 PID controller

The classical PID control algorithm is described by,

$$u(t) = K_p \left(e(t) + \frac{1}{T_i} \int_0^t e(\tau) d\tau + T_d \frac{de(t)}{dt} \right) \quad (8)$$

where e is the control error given by $e = y_{ref} - y$ with y_{ref} being the reference variable or the setpoint. K_p is the pro-

portional gain, T_i is the integral time and T_d is the derivative time; the three parameters of the control algorithm. The PID controller was implemented in Simulink along with the anti-windup feature.

Two independent PID controllers were used: one to control the pitch angle by manipulating the pitch voltage, and the other to control the yaw angle by manipulating the yaw voltage. The parameters of the PID controllers were obtained by using the auto tuning feature (which utilizes the model of the process) available in the simulink PID block. The values of the PID parameters obtained from the auto tuning was manually refined slightly. For this particular process, it is worth mentioning that manual tuning of the PID parameters is not trivial and can be difficult even with an expert knowledge on both the process and the controller.

3.2 LQR with integral action

The linear quadratic regulator is a well established model based control algorithm. The theory behind LQR is not the aim of the paper and hence is not included here. Interested readers can refer to Bertsekas (2017) for theoretical details. Due to the presence of dead band and large uncertainty in the model parameters, it is necessary to add integrators to the two controlled outputs (the pitch angle and the yaw angle) for obtaining the integral action for zero steady state offset. The four states of the system denoted by x are,

$$x = [\theta, \psi, \omega_\theta, \omega_\psi]^T \quad (9)$$

For the unmeasured states (ω_θ and ω_ψ), a standard Kalman filter is used to estimate them. Let \tilde{x} denote the estimated states. With an infinite horizon cost function defined as

$$\min J = \int_0^\infty (\tilde{x}^T Q \tilde{x} + u^T R u) dt, \quad (10)$$

the feedback control law is given by,

$$u = -K(\tilde{x} - \tilde{x}_{SP}) + u_{op} \quad (11)$$

Here, K is the state feedback gain and is calculated using MATLAB function *lqr*. Q and R are the weighting matrices for the outputs and the inputs respectively. The control

signal produced by the output integrators are added to u to generate the control signal applied to the actual process,

$$u_{app} = u + K_i \int (y - y_{SP}) dt \quad (12)$$

Here, y are the controlled outputs (pitch and yaw angles) with their setpoints y_{SP} and K_i are the output integrators gain vector. The estimates of the states are obtained as,

$$\delta \tilde{x}_{k+1} = A \delta \tilde{x}_k + B \delta u_k + L(\delta y_k - \delta \tilde{y}_k) \quad (13)$$

$$\tilde{x}_k = \delta \tilde{x}_k + x_{op} \quad (14)$$

Here, L is the Kalman filter gain and is calculated using the MATLAB function *kalman* for appropriately chosen covariance matrices for states and measurements.

3.3 MPC with integral action

MPC is an advanced model based control where process constraints can be systematically included in the optimal control problem formulation. Details about the theory of MPC is discarded in this paper as it is not the main aim. Interested readers can refer to Rawlings and Mayne (2009) for theoretical details. To achieve offset-free performance and disturbance rejection, the system state is augmented with integrating constant nonzero disturbance model as,

$$\underbrace{\begin{bmatrix} \delta x_{k+1} \\ d_{k+1} \end{bmatrix}}_{\delta \tilde{x}_{k+1}} = \underbrace{\begin{bmatrix} A & B_d \\ 0 & I \end{bmatrix}}_{\tilde{A}} \underbrace{\begin{bmatrix} \delta x_k \\ d_k \end{bmatrix}}_{\delta \tilde{x}_k} + \underbrace{\begin{bmatrix} B \\ 0 \end{bmatrix}}_{\tilde{B}} \delta u_k \quad (15)$$

$$\delta y_k = \underbrace{\begin{bmatrix} C & C_d \end{bmatrix}}_{\tilde{C}} \underbrace{\begin{bmatrix} \delta x_k \\ d_k \end{bmatrix}}_{\tilde{x}_k} \quad (16)$$

where, $d_k \in \mathbb{R}^{n_d}$ with $n_d = n_y$ being the number of unmeasured disturbance variables and equal to the number of measurements. The matrices $B_d \in \mathbb{R}^{n_x \times n_d}$ and $C_d \in \mathbb{R}^{n_y \times n_d}$ are chosen appropriately such that the following condition holds true for detectability (Pannocchia and Rawlings, 2003).

$$\text{rank} \begin{bmatrix} I - A & -B_d \\ C & C_d \end{bmatrix} = n_x + n_y \quad (17)$$

With a prediction horizon of N , the MPC problem is formulated as a tracking problem with the disturbance augmented model as,

$$\min J = \frac{1}{2} \sum_{k=1}^N \delta e_k^T Q \delta e_k + \delta u_{k-1}^T P \delta u_{k-1}$$

subject to,

$$\delta \tilde{x}_{k+1} = \tilde{A} \delta \tilde{x}_k + \tilde{B} \delta u_k, \text{ with } \delta \tilde{x}_0 \text{ known} \quad (18)$$

$$\delta y_k = \tilde{C} \delta \tilde{x}_k$$

$$\delta e_k = \delta r_k - \delta y_k$$

$$u_L \leq u_k \leq u_H$$

Here, δr_k is the reference, $Q \in \mathbb{R}^{n_y \times n_y}$ and $P \in \mathbb{R}^{n_u \times n_u}$ are the weighting matrices, $u_L = 0[V]$ and $u_H = 3[V]$ are the lower and the upper values of the voltage applied to the motors and $\delta \tilde{x}_0$ is the known initial values of the augmented state. Let the choice of the vector of unknowns be $z^T = [\delta u^T, \delta x^T, \delta e^T, \delta y^T]$ with n_z number of variables. The MPC problem of Equation 18 is formulated as a standard quadratic programming (QP) problem as,

$$\min_z \frac{1}{2} z^T H z + c^T z$$

subject to,

$$b_{\epsilon,L} \leq A_{\epsilon} z = b_{\epsilon,H}$$

$$z_L \leq z \leq z_H$$

Without going into details of the problem formulation, only the final matrices and vectors are listed here.

$$H = \begin{bmatrix} I_N \otimes P & 0 & 0 & 0 \\ 0 & I_N \otimes 0_{n_x} & 0 & 0 \\ 0 & 0 & I_N \otimes Q & 0 \\ 0 & 0 & 0 & I_N \otimes 0_{n_y} \end{bmatrix} \quad (20)$$

$$c = 0_{n_z \times 1} \quad (21)$$

$$A_{\epsilon} = \begin{bmatrix} -I_N \otimes \tilde{B} & I_{Nn_x} - (I_{N,-1} \otimes \tilde{A}) & 0_{Nn_x \times Nn_y} & 0_{Nn_x \times Nn_y} \\ 0_{Nn_y \times Nn_u} & -I_N \otimes \tilde{C} & 0_{Nn_y \times Nn_y} & I_{Nn_y} \\ 0_{Nn_y \times Nn_u} & 0_{Nn_y \times Nn_x} & I_{Nn_y} & I_{Nn_y} \end{bmatrix} \quad (22)$$

Here, \otimes denotes the Kronecker product. For this particular problem there are no inequality constraints other than the bounds on the decision variables. So we have,

$$b_{\epsilon,L} = b_{\epsilon,H} = \begin{bmatrix} \tilde{A} \delta \tilde{x}_0 \\ 0_{(N-1)n_x \times 1} \\ 0_{Nn_y \times 1} \\ \delta r_1 \\ \vdots \\ \delta r_N \end{bmatrix} \quad (23)$$

The optimal control problem given by Equation 19 is implemented in Simulink and an opensource solver *qpOASES* (Ferreau et al., 2014; Potschka and Kirches, 2007–2017) is used to solved the QP problems. Out of Nn_u number of optimal values of the control inputs, only the first n_u control signals are applied to the process and the process is repeated at each sampling time (receding horizon strategy).

The unmeasured states ω_{θ} and ω_{ψ} and the unknown disturbances d_k are estimated using a standard Kalman filter algorithm. The details about Kalman filter algorithm can be found at Simon (2006).

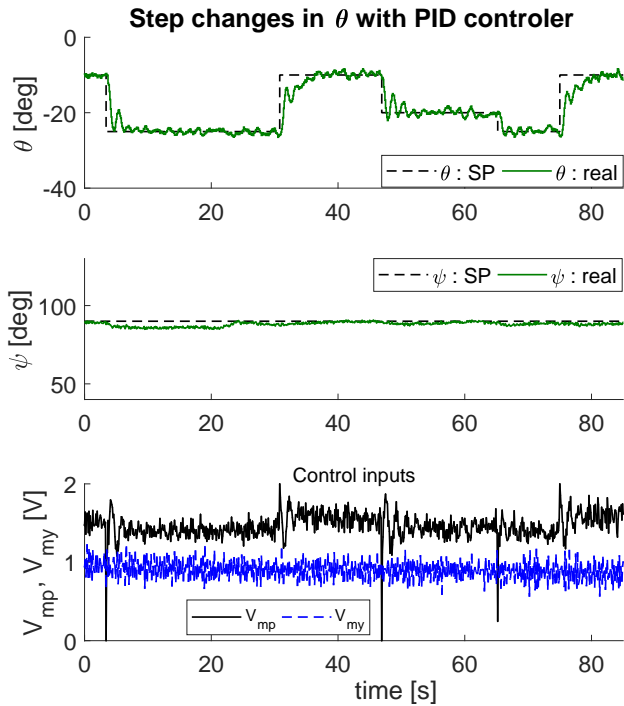


Figure 2. Step changes in θ with PID

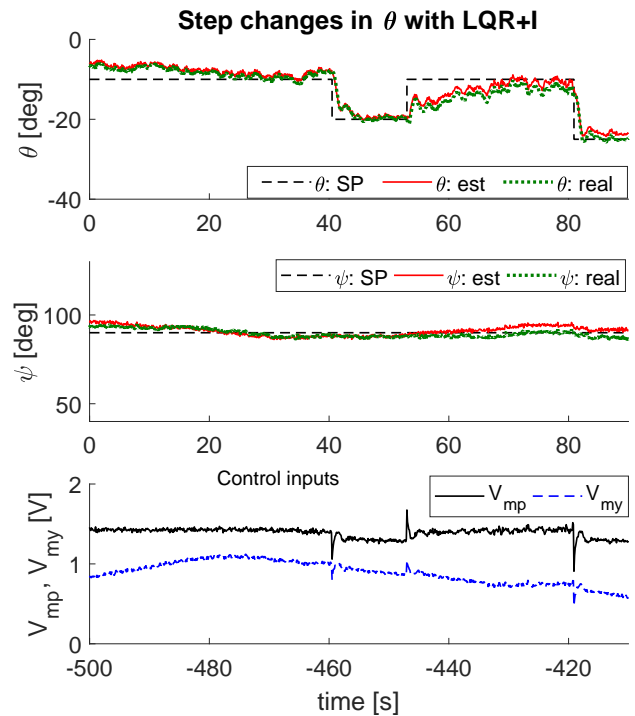


Figure 3. Step changes in θ with LQR

4 Experimental results

4.1 Tracking: step changes

In this section, the performance of the three control strategies for tracking the setpoint is compared. For easy comparison, the setpoints for the pitch angles and the yaw angles are changed separately for all three controllers. Figures 2, 3 and 4 show the results from the PID, LQR+I and MPC controllers respectively for tracking the pitch angle of the 2-DOF experimental helicopter unit with step changes.

Similarly, Figures 5, 6 and 7 show the results from the PID, LQR+I and MPC controllers respectively for tracking the yaw angle of the experimental helicopter unit with step changes.

4.2 Tracking: Ramping setpoint

In reality, the helicopters do not change angles (both pitch and yaw angles) in sharp steps. To turn the helicopter, the yaw angle setpoints should be instead ramped up and/or down. Similarly, to change the altitude of flight, the pitch angle setpoints should be ramped up and/or down. To illustrate the capability of controlling the helicopter unit when the setpoints are ramped up and down, the model predictive controller is used with ramped setpoint changes. For the sake of brevity and to save space, the other two controllers are not discussed. Figure 8 shows the results of ramping both the pitch angle and the yaw angle with MPC.

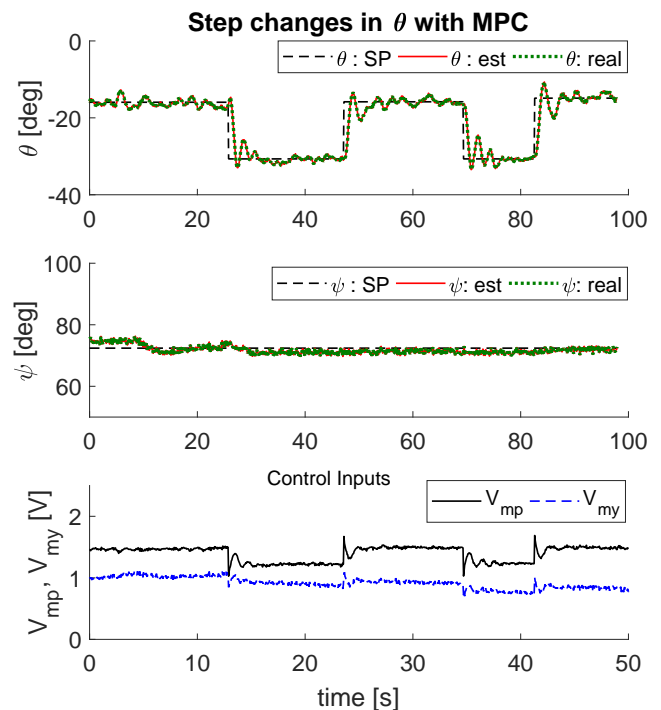


Figure 4. Step changes in θ with MPC

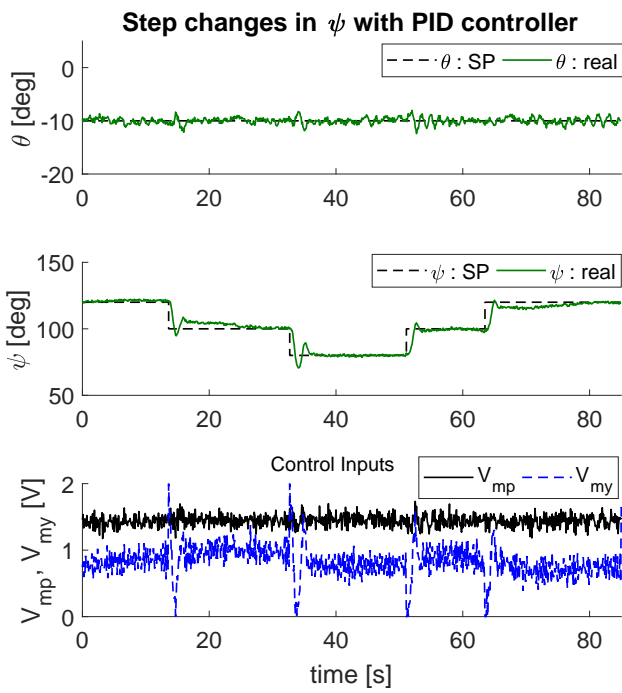


Figure 5. Step changes in ψ with PID

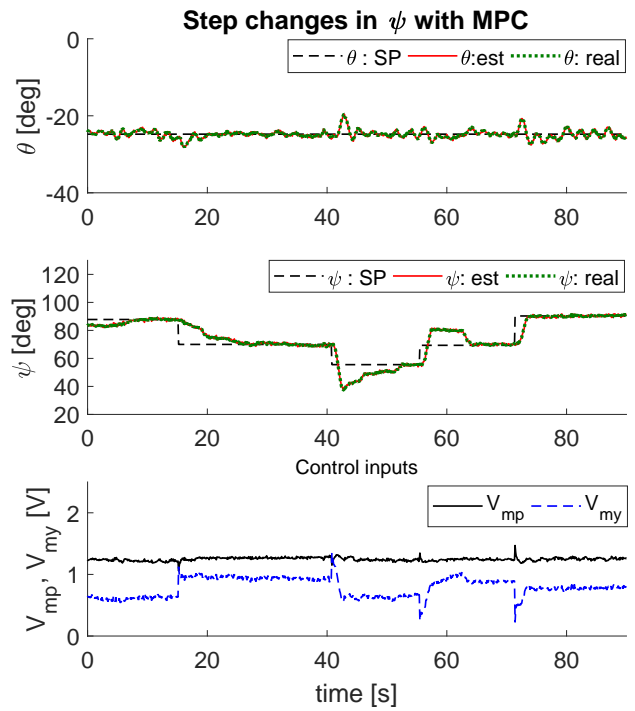


Figure 7. Step changes in ψ with MPC

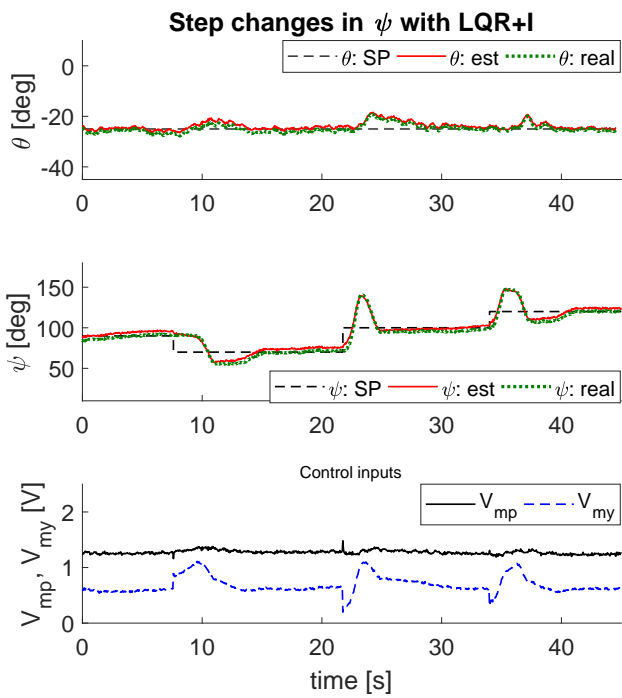


Figure 6. Step changes in ψ with LQR

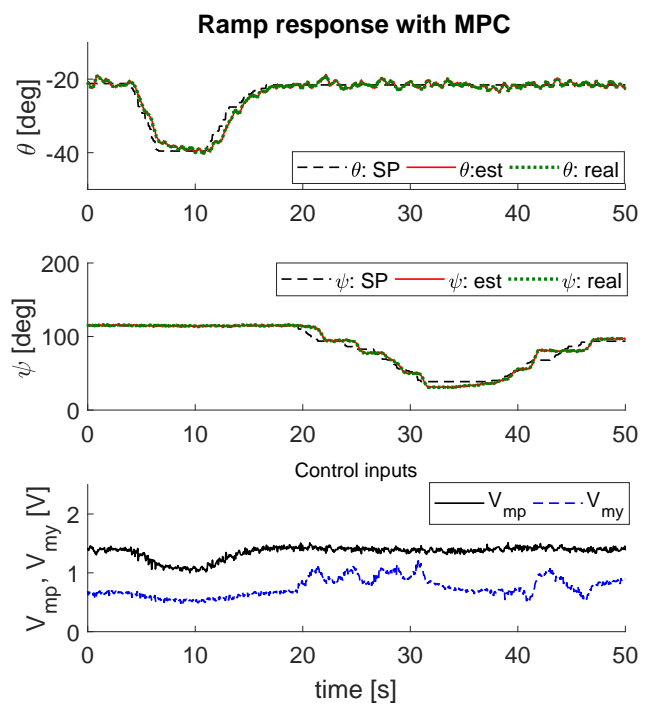


Figure 8. Ramp response with MPC

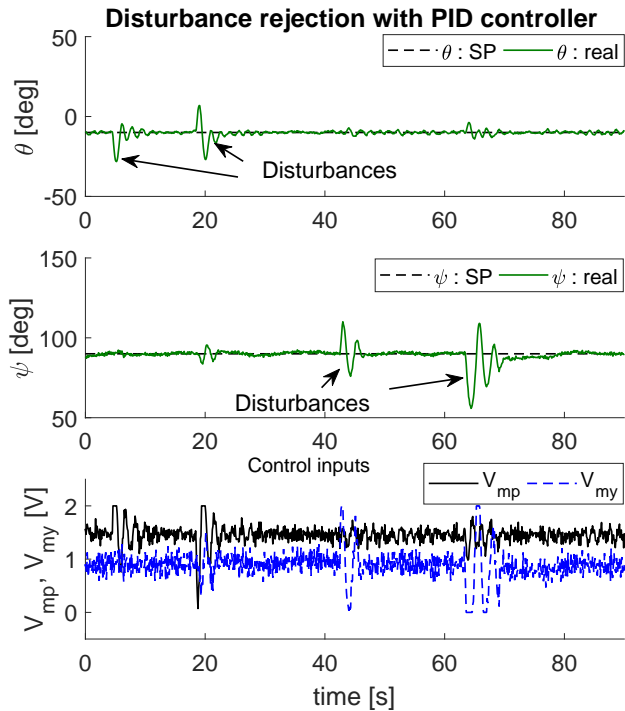


Figure 9. Disturbance rejection with PID

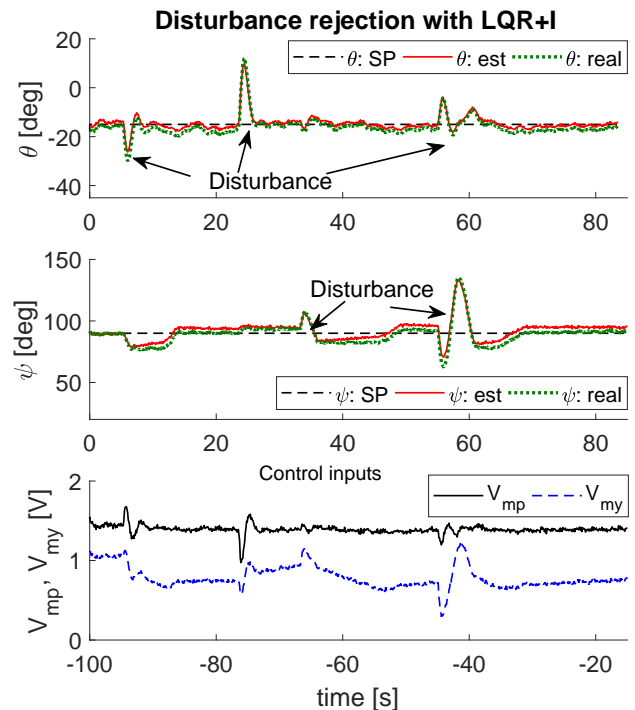


Figure 10. Disturbance rejection with LQR

4.3 Disturbance rejection

In real case scenarios, several disturbances can influence the flight path of a helicopter. A strong gust of wind, sudden drop in air pressure and density can all affect the pitch and the yaw angle of the helicopter. Such disturbances should be compensated by the controllers in order to stabilize the system. For the helicopter prototype at USN, to supply an external disturbance, the body of the helicopter was moved by applying force manually by hand. In other words, to mimic the presence of disturbance, external perturbation on the pitch and yaw angles were provided manually by the user. Figures 9, 10 and 11 show the performance of PID, LQR+I and MPC controller respectively under the presence of disturbances.

5 Discussion

5.1 Tracking performance

All the three control strategies could satisfactorily stabilize the system for different setpoint changes of both the pitch and the yaw angles. With the PID controller, the derivative term (D) is utmost important and should be used for stabilizing the system. A pure proportional and integral (PI) controller was not able to stabilize the system. However, the inclusion of D term was strongly influenced by the measurement noises and the resulting control inputs became noisy. There was chattering of the voltages applied to the motors. In the experimental helicopter unit, the chattering of the voltages resulted in unpleasant vibrational sounds from the propellers and mechanical vibra-

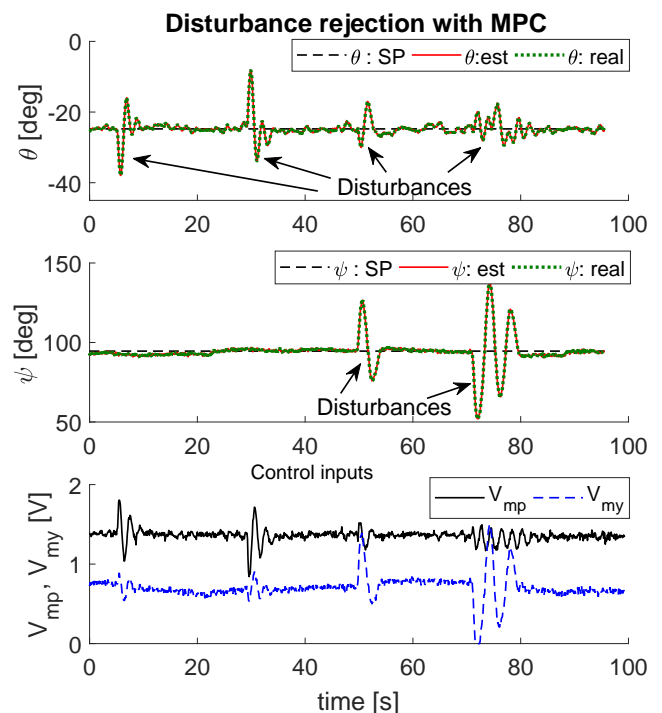


Figure 11. Disturbance rejection with MPC

tions of the whole rotor propeller system. On the other hand, the model based controllers (LQR+I and MPC) produced relatively cleaner control inputs without any chattering. In addition, proper tuning of the PID controllers was not straight forward owing to the cross coupling nature of the process. It is highly recommended that the model of the process should be used for tuning of the PID controllers. In contrast, it was relatively easier to tune the model based controllers.

When the setpoints on the pitch angles (yaw angles) were changed, all the three controllers could achieve the new setpoints while at the same time keeping hold or without losing control of the yaw angles (pitch angles), despite the presence of a strong cross coupling effect between the inputs and the outputs.

As has also been described before, in real life the pitch angle and the yaw angles are not changed in steps but are instead ramped. The model predictive controller showed a good response to the ramped setpoints. One benefit of ramping the helicopter angles is that the control inputs (voltages to the motors) are not suddenly changed by a large amount but instead they are changed gradually. This in practice may/will generate smoother response.

5.2 Disturbance rejection performance

Disturbances were applied manually by the user. Big disturbances (more than $\pm 50^\circ$ deviations) were applied to both the pitch and the yaw angles. All three controllers showed relatively equal and satisfactory performance in compensating the disturbances.

5.3 Comments on state estimation

The presence of dead band and the mismatch between the mathematical model and the real process makes it interesting for state estimation. A standard Kalman filter was applied to estimate the unmeasured states and the disturbances for the model based controllers (LQR+I) and MPC. In Figures 3, 6 and 10 (for the LQR+I controller), it can be seen that there is a small offset between the estimated angles ($\theta : est$ and $\psi : est$) and the angles measured by the sensors ($\theta : real$ and $\psi : real$). However, in Figures 4, 7 and 11 (for the MPC controller), it can be seen that there is no offset between the estimated angles ($\theta : est$ and $\psi : est$) and the angles measured by the sensors ($\theta : real$ and $\psi : real$).

With the MPC, the system states are augmented by a disturbance model (see Equation 15) and the disturbances are estimated using a Kalman filter. The estimated disturbances accounts for the dead band and the model mismatch and hence compensates for any offsets, thus producing zero offset between the estimated and the measured values. On the other hand, with the LQR+I controller, the system states are not augmented with any kind of disturbance model. The presence of dead band and model mismatch are hence not compensated, thus producing small offset between the estimated and the measured values. This clearly indicates the fact that due to model

mismatch, such offset can be expected as an output from a Kalman filter algorithm. The important thing is to judge whether such offsets are important for the control/estimation purpose at hand. If they are not important, and the closed loop response is stable and correct, such offsets may simply be discarded.

6 Conclusion

This paper has shown experimental results obtained from applying different control structures to a real process. The control structures used in this paper are standard algorithms. They are relatively easier to understand and to implement. To solve the QP optimal control problems, open source solver which supports code generation is chosen. This allows us to implement the model based control structures to a real process using Simulink. The built-in QP solvers in MATLAB/Simulink does not support code generation and hence cannot be used for real time control of processes with fast dynamics such as the helicopter unit.

For this particular process at USN, the classical PID controllers show relatively as good performance as the advanced model based control structures. However, the control inputs generated by PIDs are noisy. Chattered input signals applied to the motor cause vibrations and can induce mechanical damage to the unit with time. In addition, model based control such as the MPC has the added advantage of including process constraints directly into the optimization problem. With the PID and LQR+I, constraints on the inputs were implemented as ad-hoc if-else conditions. Finally, the paper also justifies that such experimental units can be built from the scratch and can be used for pedagogic purpose with both the classical and the advanced control algorithms.

References

- Fernando S. Barbosa, Gabriel P. das Neves, and Bruno A. Angélico. Discrete lqg/ltr control augmented by integrators applied to a 2-dof helicopter. In *2016 IEEE Conference on Control Applications (CCA)*, Sept 2016. doi:10.1109/CCA.2016.7587976.
- Dimitri P. Bertsekas. *Dynamic Programming and Optimal Control*, volume 1. Athena Scientific, fourth edition, 2017. ISBN 1-886529-26-4.
- Hans Joachim Ferreau, Christian Kirches, Andreas Potschka, Hans Georg Bock, and Moritz Diehl. qpOASES: A parametric active-set algorithm for quadratic programming. *Mathematical Programming Computation*, 6(4):327–363, 2014.
- M. Lopez-Martinez, J.M. Diaz, M.G. Ortega, and F.R. Rubio. Control of a laboratory helicopter using switched 2-step feedback linearization. In *Proceedings of the 2004 American Control Conference*, volume 5, pages 4330–4335, June 2004.
- Jose Guillermo Guarnizo M., Cesar Leonardo Trujillo, and Javier Antonio Guacaneme M. Modeling and control of a two dof helicopter using a robust control design based on dk

- iteration. In *IECON 2010 - 36th Annual Conference on IEEE Industrial Electronics Society*, pages 162–167, Nov 2010. doi:10.1109/IECON.2010.5675183.
- Giovanni Gallon Neto, Fernando dos Santos Barbosa, and Bruno Augusto Angélico. 2-dof helicopter controlling by pole-placements. In *2016 12th IEEE International Conference on Industry Applications (INDUSCON)*, pages 1–5, Nov 2016. doi:10.1109/INDUSCON.2016.7874535.
- Gabriele Pannocchia and James B. Rawlings. Disturbance models for offset-free model-predictive control. *AIChE Journal*, 49(2):426–437, 2003.
- Hans Joachim Ferreau and Andreas Potschka and Christian Kirches. qpOASES webpage. <http://www.qpOASES.org/>, 2007–2017.
- Qunasar Inc. *2-DOF helicopter: Reference Manual*, 2011.
- James B. Rawlings and David Q. Mayne. *Model Predictive Control Theory and Design*. Nob Hill Publishing, LLC, 2009. ISBN 978-0-9759377-0-9.
- Dan Simon. *Optimal state estimation*. John Wiley & Sons, Inc., Hoboken, New Jersey, 2006. ISBN 10 0-471-70858-5.
- Juhng-Perng Su, Chi-Ying Liang, and Hung-Ming Chen. Robust control of a class of nonlinear systems and its application to a twin rotor mimo system. In *Industrial Technology, 2002. IEEE ICIT '02. 2002 IEEE International Conference*, volume 2, pages 1272–1277, Dec 2002. doi:10.1109/ICIT.2002.1189359.
- Gwo-Ruey Yu. Robust-optimal control of a nonlinear two degree-of-freedom helicopter. In *6th IEEE/ACIS International Conference on Computer and Information Science (ICIS 2007)*, pages 744–749, July 2007. doi:10.1109/ICIS.2007.160.

Covering the Gap between Advanced Control Theory Design and Real Time Implementation Using Simulink

Carlos F. Pfeiffer Roshan Sharma

Department of Electrical Engineering, IT and Cybernetics, University College of Southeast Norway, Norway,
{carlos.pfeiffer, roshan.sharma}@usn.no

Abstract

New developments in sensor technology and control actuators make it viable to monitor and regulate more process variables, providing an opportunity to apply advanced multivariable control techniques. Although modern control techniques allows the implementation of true multiple inputs – multiple output controllers, there has been a big gap between theoretical developments and real life applications. At the University of Southeast Norway, we proposed a bachelor level course aimed to students who have had a previous introductory course to classic control, to teach them the fundamentals of modern multivariable control techniques, including state feedback, LQR and linear MPC. The use of Simulink is integrated with the course, to analyze and design modern controllers for two real multivariable experimental processes. We advocate the use of advanced simulation and data acquisition tools to help to cover the existing gap between the development of modern control algorithms, and their implementation with real processes. The experimental testing and final tuning of the controllers are an important part of the course.

Keywords: Control Education, Control Design, Control Simulation, Multivariable control, Simulink.

1 Introduction

Several authors have pointed to the big gap existing between theory and application of advanced multivariable control techniques. One popular claim is that most industrial regulatory control needs can be satisfied by using several single PID control loops, combined in different configurations (cascade, feedforward, ratio control, etc.), so modern techniques for advances multivariable control are not required.

A fundamental advantage of using PID control is that it does not require an explicit, accurate model of the process. Simple models can be fitted by using “bump” tests, or the controllers can be tuned by using closed loop “in situ” techniques like the classic ultimate gain method or several of its variations. In addition, several PID systems offer now the possibility of auto-tuning options, by automatically running a short test on the system to find appropriate controller parameters. It can

also be argued that processes are designed having in mind traditional PID systems, and that more efficient processes could be designed if modern control techniques were considered from the design stage (Bernstein, 1999).

On the other hand, academia focus on the formal teaching of classic control techniques using Laplace transform, poles and zeros location, and frequency domain analysis, and modern control techniques using state space representations. All of these methods require an explicit model, which can be obtained from first principles modelling, or from carefully designed experiments and using system identification techniques (or a combination of both). These models can be nonlinear and require linearization, and the analysis and modern control design techniques are laborious and more suitable to handle using appropriate control software tools. Implementation on the real process requires the use of data acquisition hardware, and it is communally done using software tools different than the ones used for the system analysis and controller design.

The final tuning of the controllers requires a trail and error testing procedure. The common approach in academia is to demonstrate the controllers using simulation tools, and seldom actually testing them on real multivariable processes. While the theory is sound and mature, the design process is laborious, and most industrial control systems do not facilitate the direct application of the resulting algorithms. This situation explains why there are very few reported applications of multivariable control in real experimental or industrial processes.

2 Experimental systems in academia

For many years instructors in academia have used experimental single input – single output control systems, like level control of a single tank, temperature control for air or water heaters, and different kinds of flow control systems. While these systems are extremely valuable to teach the fundamentals of classic control and practice different methods for tuning PID, they are not multivariable, nor challenging enough to justify the use of modern control techniques.

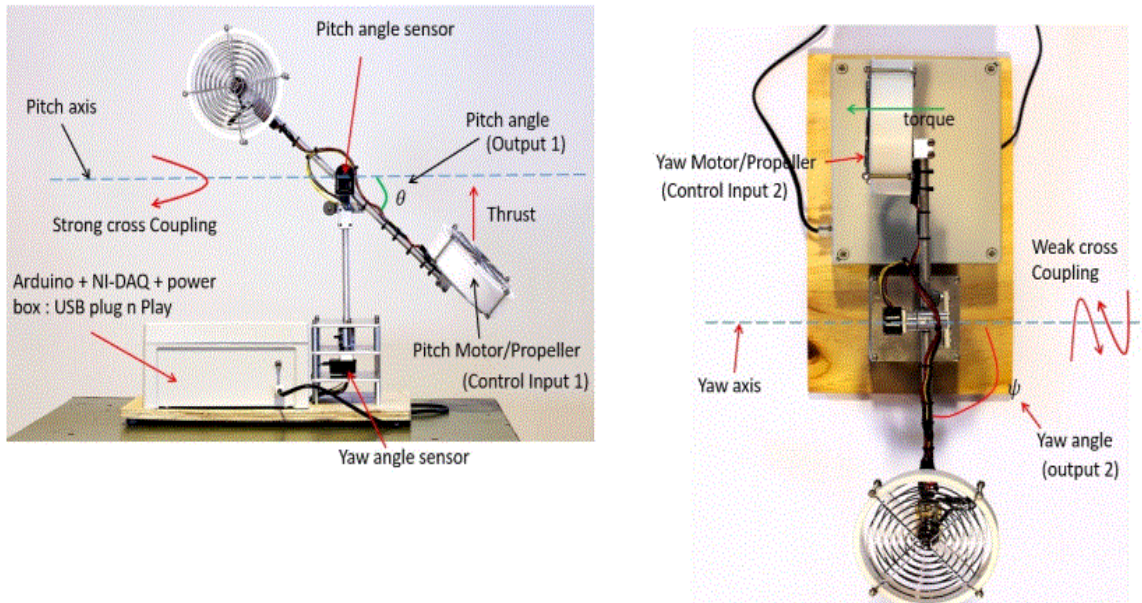


Figure 1: Two degrees of freedom helicopter prototype.



Figure 2: Pilot scale four tanks system.

In recent years, two true multivariable systems have become popular to use for teaching and research in academia: a helicopter prototype with two degrees of freedom (Neto, 2016), and a quadruple tank system for level control (Johansson, 2000; Pfeiffer, 2011). Both systems present different challenges: the helicopter is an open loop unstable system, highly nonlinear with strongly coupled input-output variables, and it requires very fast sampling times. The four tanks system is moderately nonlinear, but can be operated in different configurations to show challenging behaviors like inverse control and different degree of coupling among the input and output variables. Both of these

systems are good candidates to demonstrate the use of modern control multivariable techniques. At the University College of Southeast Norway (USN), we have developed a prototype for the two degrees of freedom helicopter system (Figure 1), and pilot size prototype for a four tank model is under construction (Figure 2), to be used with the course.

2.1 Experimental system models

Helicopter system: the goal for the helicopter system prototype is to control both the pitch θ and yaw Ψ angles, by modifying the input voltage to the front and rear motors, V_{mp} and V_{my} .

The model for the two degrees of freedom prototype is shown in Figure 3 (Qunasar Inc, 2011), with the corresponding parameters description in Table 1.

$$\begin{aligned} \frac{d\theta}{dt} &= \omega_\theta \\ \frac{d\Psi}{dt} &= \omega_\Psi \\ \frac{d\omega_\theta}{dt} &= \frac{K_{pp}V_{mp} - K_{py}V_{my} - B_p\omega_\theta}{J_{eq,p} + m_h l_{cm}^2} - \frac{m_h \omega_\psi^2 \sin(\theta) l_{cm}^2 \cos(\theta) + m_h g \cos(\theta) l_{cm}}{J_{eq,p} + m_h l_{cm}^2} \\ \frac{d\omega_\psi}{dt} &= \frac{K_{yp}V_{mp} - K_{yy}V_{my} - B_y\omega_\psi}{J_{eq,y} + m_h l_{cm}^2} - \frac{2 m_h \omega_\psi \sin(\theta) l_{cm}^2 \cos(\theta) \omega_\theta}{J_{eq,y} + m_h l_{cm}^2} \end{aligned}$$

Figure 3. Two degrees of freedom helicopter's model.

Table 1. Parameters for the helicopter model.

Parameter	Description	Units
l_{cm}	Distance between the pivot point and the center of mass of the helicopter	m
m_h	Total moving mass of the helicopter	kg
$J_{eq,p}$	Moment of inertia about the pitch axis	kg m ²
$J_{eq,y}$	Moment of inertia about the yaw axis	kg m ²
g	Earth gravity constant	m/s ²
K_{pp}	Torque constant on pitch axis from pitch motor/propeller	Nm/V
K_{yy}	Torque constant on yaw axis from yaw motor/propeller	Nm/V
K_{py}	Torque constant on pitch axis from yaw motor/propeller	Nm/V
K_{yp}	Torque constant on yaw axis from pitch motor/propeller	Nm/V
B_p	Damping friction factor about pitch axis	N/V
B_y	Damping friction factor about yaw axis	N/V

Four tanks system: the systems has two control inputs, V_1 and V_2 , representing control voltage inputs to two variable speeds pumps controlling the input flows. The flow from each pump is split using a three-way valve, with the splitting fraction defined by γ_1 and γ_2 for the flows from pump 1 and pump 2 respectively. The system outputs are the tanks levels given by h_1, h_2, h_3 and h_4 . The system diagram is given in Figure 4.

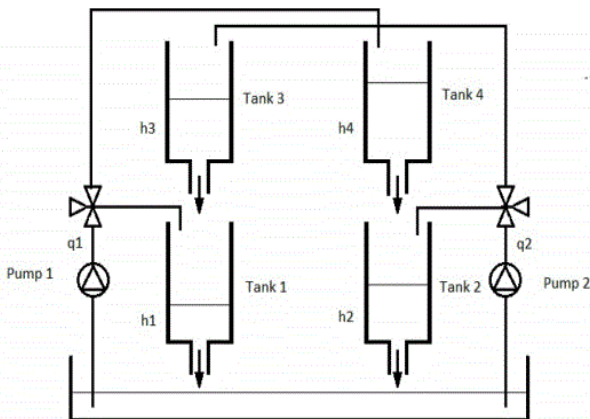


Figure 4. Four tanks control system.

The model for the four tanks system, assuming the pumps dynamics is much faster than the tanks dynamics, is included in Figure 5 (Pfeiffer, 2011), with the corresponding parameters description provided in Table 2.

$$\frac{dh_1}{dt} = \frac{c_3\sqrt{2gh_3} - c_1\sqrt{2gh_1} + \gamma_1 k_1 V_1}{A_1}$$

$$\frac{dh_2}{dt} = \frac{c_4\sqrt{2gh_4} - c_2\sqrt{2gh_2} + \gamma_2 k_2 V_2}{A_2}$$

$$\frac{dh_3}{dt} = \frac{-c_3\sqrt{2gh_3} + (1-\gamma_2)k_1 V_1}{A_1}$$

$$\frac{dh_4}{dt} = \frac{-c_4\sqrt{2gh_4} + (1-\gamma_1)k_1 V_1}{A_1}$$

Figure 5. Four tanks system model

Table 2. Parameters for four tanks model.

Parameter	Description	Units
c_1, c_2, c_3, c_4	Constants depending on the areas of the exit orifices.	m ²
γ_1, γ_2	Flows split fractions.	----
k_1, k_2	Pumps gains.	m ³ /V
g	Earth gravity constant	m/s ²
A_1, A_2, A_3, A_4	Torque constant on pitch axis from pitch motor/propeller	m ²

3 Course Description

3.1 Course requirements

The course “Simulation and Control of Dynamic Systems” has been designed for bachelor students who have had a previous introductory course in process control.

Additionally, the course requires calculus and fundamentals of programming. Most of the programming is done in MATLAB/Simulink, which uses a graphical and highly intuitive programming style.

3.2 Topics

The course topics are presented sequentially from modelling, simulation, analysis, design of multivariable controllers, testing in simulation, and testing with the real systems. Both the helicopter prototype and the four tanks system are used from the beginning of the course to demonstrate the different control concepts and techniques. The modelling requires using ordinary differential equations, linearization using Taylor series and model parameter fitting using least squares techniques. These operations are handled using MATLAB. The course follows with the representation of MIMO systems using transfer functions matrices and state space realizations. The concepts of controllability, observability and stability analysis using state space realizations are explored and analyzed using MATLAB. The effect of dead-time on closed loop stability is discussed and simulated using Simulink. Common non-linear characteristics in real processes are also discussed and simulated, including saturation, hysteresis, dead-band and backlash.

The analysis and simulation of systems with inverse response is discussed using the four tanks systems as an example. The course follows with an introduction to state space representation, controllability, observability

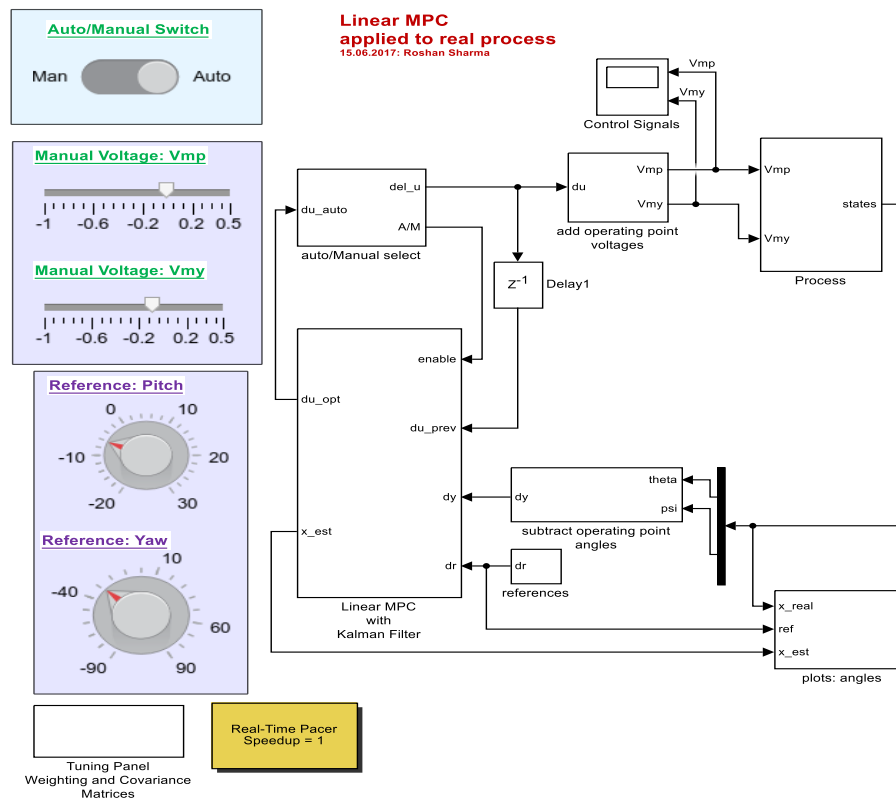


Figure 6: Simulink real time helicopter control system.

and stability analysis using state space realizations, observers, state feedback and the Kalman filter.

The course finishes with a hands on presentation of Linear Quadratic Regulator control and Model Predictive Control techniques, with the students simulating the controllers in Simulink and testing them on the real processes by using data acquisition modules with Simulink to connect to the processes interfaces.

An example diagram of the final implementation of MPC in Simulink to control the helicopter prototype is shown in Figure 6. Experimental results comparing different control methods for the 2-dof helicopter systems are provided in (Sharma and Pfeiffer, 2017).

4 Conclusions

An advanced bachelor level control course has been proposed to teach students at USN modern control techniques for multivariable processes. The course covers modeling, simulation, analysis, control design and implementation using MATLAB/Simulink with the control and data acquisition toolboxes as an integrated platform. All the topics are demonstrated using two real multivariable process: a two degrees helicopter system, and a four tanks level control system. The use of MATLAB/Simulink as an integrated platform facilitates the steps from the system analysis to the controller

implementation and final tuning refinement, helping to reduce the gap between the advanced modern control theory and real world applications.

References

- D.S. Bernstein. On bridging the theory/practice gap. *IEEE Control Systems*. 19(6):64–70, 1999.
- Giovanni Gallon Neto, Fernando dos Santos Barbosa, and Bruno Augusto Angélico. 2-dof helicopter controlling by pole-placements. The 12th IEEE International Conference on Industry Applications (INDUSCON), pages 1–5, Nov 2016. doi:10.1109/INDUSCON.2016.7874535.
- K.H. Johansson. The Quadruple-Tank Process: a multivariable laboratory process with an adjustable zero. *IEEE Transactions on Control*. 8(3):456–465, 2000. DOI: 10.1109/87.845876.
- C.F. Pfeiffer. Modeling, Simulation and Control for an Experimental Four Tanks System Using ScicosLab. *The 52nd International Conference of Scandinavian Simulation Society Conference (SIMS) 2011*. ISBN: 978-91-977493-7-4.
- Qunasar Inc. 2-DOF helicopter: Reference Manual, 2011.
- R. Sharma and C.F. Pfeiffer. Comparison of Control Strategies for a 2-DOF helicopter. *The 58th SIMS Conference on Simulation and Modelling. (SIMS 2017)*. To be held September 25-27 2017 in Reykjavik, Iceland.

Physiological based Modeling and Control of an Industrial Tank Process

Svein H. Stokka Kim A. Jakobsen Kristian Thorsen Tormod Drengstig

Department of Electrical Engineering and Computer Science, University of Stavanger, Norway,
{sh.stokka, ka.jakobsen}@stud.uis.no, {kristian.thorsen, tormod.drengstig}@uis.no

Abstract

In this paper we make a physiological based dynamic model of a laboratory scale industrial tank process configured with an inlet pump and an outlet valve. Thus, the pump and valve characteristics, and also the functional expression for the hydrostatic pressure, are fitted to enzymatic mechanisms and saturable signaling kinetics. The model is verified against process data and shows good compliance. Based on the model, we tune and apply a physiological inspired control structure to control the water level in the presence of disturbances in the inlet pump speed. This control structure is further compared to an I-controller, and we show that one of the main properties of physiological control is that the steady state level of the controlled variable may deviate from the setpoint value. We continue by showing how to lump this deviation and the setpoint into a *variable* setpoint controller. The main benefit of such a controller is reduced variation in the control signal (calculated as total variation, TV). Based on these results, we finally suggest an industrial control structure where the control signal participates in the continuous calculation of a variable setpoint.

Keywords: physiological control, integral control, tank process, variable setpoint

1 Introduction

1.1 Physiological and Industrial Control

Systems biology includes the study of how biochemical species in cells and organisms interact to create control structures. These control structures are often functionally compared to well known man-made industrial control systems such as PID-controller (Watson et al., 2011; Ang et al., 2010), feedforward structures (Savageau and Jacknow, 1979; Sontag, 2010; LeDuc et al., 2011), fuzzy control (Ding, 2000), positive feedback (Cloutier and Wang, 2011), robust control (Goulian, 2004), and adaptive control (Javaherian et al., 2009). Thus, some of the biochemical species are considered controlled variables, while other function as manipulated variables. The interaction between the species is termed *signalling* or *signal transduction* (Han et al., 2007), and compared to industrial processes these signalling events represents the measurement function and the connection between

the controller output and the actuator. Along this path of research, we have in a series of publications investigated biochemical mechanisms and kinetic properties behind *integral feedback* in physiology (Ni et al., 2009; Drengstig et al., 2012).

In this paper we take an opposite approach and apply physiological inspired control to a laboratory scale industrial tank process, illustrated in Figure 1a. The work is an extension of the bachelor's thesis of the first two authors (Stokka and Jakobsen, 2017). Our aim is here to explore the differences between physiological and industrial control, and to identify properties and functions of physiological control that might be useful in an industrial context.

In the literature, there are not many reports showing physiologically inspired control structures applied to industrial processes. One example, however, is found in (Pérez-Correa et al., 2015) where a repressor Hill function representing the proportional part, together with standard integrative part, are applied to control the level of a conic tank.

1.2 Controller Motifs

A biochemical network with regulatory properties must in its simplest form include at least two components or state variables, i.e. one controlled component and one controller component. The controller component acts on the controlled component in a way that it compensates for external disturbances, and thereby represents a negative feedback. We have earlier presented a collection of simple two-component regulatory networks (Drengstig et al., 2012), and we have used the name *controller motifs* to describe them. These motifs consist of two chemical species, *A* and *E*, both of them being formed and turned over. *A* may represent an intracellular compound which is subject to disturbances in the form of e.g. uncontrolled diffusive transport of *A* in and out of the cell, and *E* may represent a membrane bound compound such as a transporter protein. This is illustrated in Figures 1b and 1c.

So far, we have identified the eight different controller motifs shown in Figure 2. Based on the controller action, i.e. whether the *E* mediated compensatory flow is located upstream or downstream of *A*, these controller motifs are further classified as either *inflow* or *outflow* controllers with *activating* or *inhibiting* control actions (Figure 2).

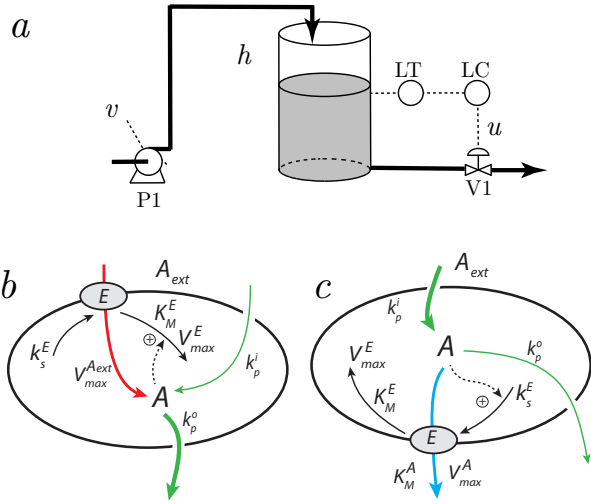


Figure 1. Panel *a*: Illustration of the laboratory scale industrial tank process used in this work. The level in the tank is maintained by the level controller manipulating the outlet valve in the presence of disturbances v (pump speed). Panels *b* and *c*: Illustration of a cell with a compound A being under homeostatic control by an inflow controller (panel *b*) or an outflow controller (panel *c*). Panel *b*: An inflow controller compensate for outflow perturbations, k_p^o (thick green line), in A by adding more A through an E -mediated inflow (red line). Panel *c*: An outflow controller compensate for inflow perturbations, k_p^i (thick green line), in A by removing excess of A through an E -mediated outflow (blue line).

2 Modeling

Applying the mass balance to the tank process in Figure 1a give the following differential equation describing the dynamics of the water level h :

$$\dot{h} = \frac{1}{A_{\text{tank}}} \left(f_{P1}(v) - \beta \cdot f_{V1}(u) \cdot \sqrt{h} \right) \quad (1)$$

where A_{tank} is the area of the tank, $f_{P1}(v)$ and $f_{V1}(u)$ are the pump and valve characteristics, \sqrt{h} is the influence of the hydrostatic pressure on the outlet flow, and β is a constant comprising density ρ , gravity g , valve flow coefficient K_v , and unit conversion factors. In order to represent the tank model in Eq. (1) as one of the motifs in Figure 2, we note first that the tank process is configured as an outflow controller. Thus, there are four possible candidates, i.e. outflow controller 5 to 8. Since the valve V1 is normally closed, there is a direct relationship between the control signal and the valve opening, which corresponds to activating kinetics¹. The pump P1 is at rest when the disturbance signal v is zero, and hence, this also represents activating kinetics. The tank process can therefore be described as an outflow controller 5 motif.

Based on the non-linearity of the functions $f_{P1}(v)$, $f_{V1}(u)$, and \sqrt{h} , all shown as solid lines in Figure 3, we express them as general Hill kinetic expressions in the physiological model. Thus, the physiological model

¹Thus, a normally open valve correspond to inhibiting kinetics.

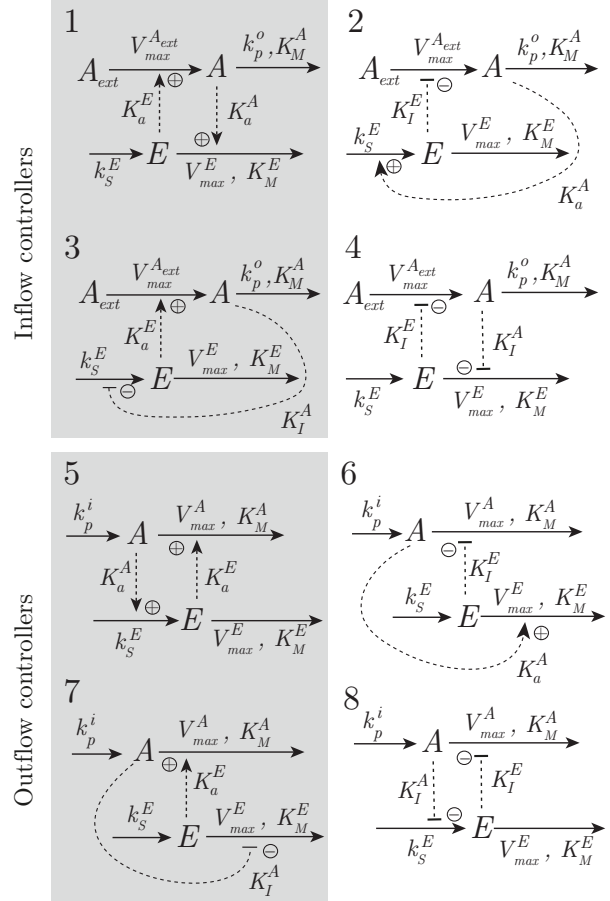


Figure 2. Inflow and outflow controller motifs with saturable activating action (gray background) or inhibiting action (white background). The controlled species A is subject to outflow or inflow perturbations (k_p^o or k_p^i). The controller species E compensates for this perturbation through an E -mediated inflow or outflow of A , respectively. The synthesis of E is modeled with a rate constant k_s^E , whereas the degradation E is assumed to be a first order Hill kinetics with a saturation constant K_M^E . Similar saturable enzymatic reactions are also assumed in the degradation of controlled species A .

written in terms of A , E and A_{ext} (corresponding to h , u and v) is shown in Eq. (2). Note that we use Hill coefficients $\{n, m, p\} \in \mathbb{N}^+$ in order to resemble enzymatic binding sites.

$$\dot{A} = \frac{k_p^i \cdot A_{\text{ext}}^n}{(K_M^{\text{Aext}})^n + A_{\text{ext}}^n} - \frac{V_{\text{max}}^A \cdot A^p}{(K_M^A)^p + A^p} \cdot \frac{E^m}{(K_a^E)^m + E^m} \quad (2)$$

From comparing Eq. (1) and Eq. (2), we identify the following three relationships:

$$\frac{1}{A_{\text{tank}}} \cdot f_{P1}(v) = \frac{k_p^i \cdot A_{\text{ext}}^n}{(K_M^{\text{Aext}})^n + A_{\text{ext}}^n} \quad (3)$$

$$\frac{1}{A_{\text{tank}}} \cdot \beta \cdot f_{V1}(u) = \frac{V_{\text{max}}^A \cdot E^m}{(K_a^E)^m + E^m} \quad (4)$$

$$\sqrt{h} = \frac{A^p}{(K_M^A)^p + A^p} \quad (5)$$

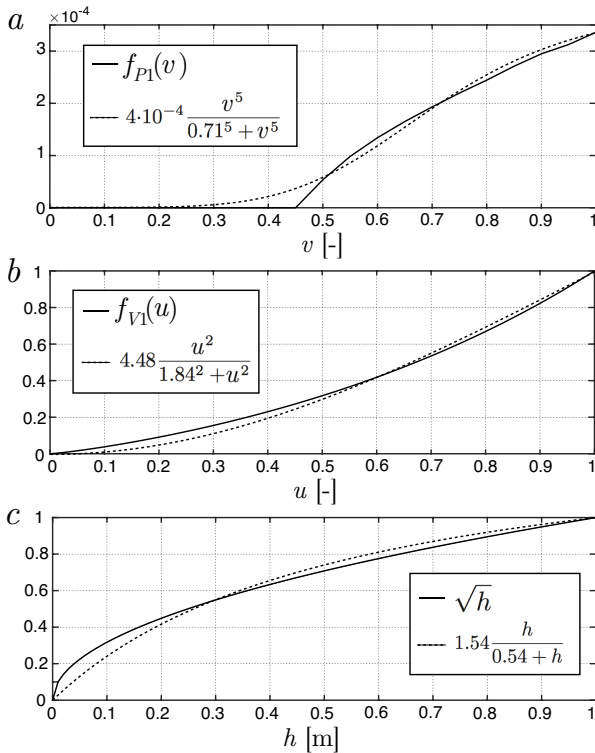


Figure 3. Least squares parameter fitting of model characteristics. Panel *a*: Pump characteristic $f_{P1}(v)$ fitted to a Hill kinetic expression with cooperativity of $n=5$. Note that we use a centrifugal pump placed approximately 3 meters below the tank inlet, which implies that there is no water delivery until the pump signal is $v > 0.45$. Panel *b*: Valve characteristic $f_{V1}(u)$ fitted to a Hill kinetic expression with cooperativity of $m=2$. Panel *c*: Fitting of \sqrt{h} to Hill kinetic expression with cooperativity of $p=1$. The height of the tank is 1m.

The least squares estimation of $f_{P1}(v)$, $f_{V1}(u)$ and \sqrt{h} are shown as dashed lines in Figure 3. The bottom area of the laboratory tank is $A_{\text{tank}}=0.01 \text{ m}^2$ (10x10 cm) and the valve flow coefficient is $K_v=11.25 \text{ m}^3/(\text{h}\sqrt{\text{bar}})$. Using $\rho=1000 \text{ kg/m}^3$ and $g=9.8 \text{ m/s}^2$, we find $\beta=9.78 \cdot 10^{-4} \text{ m}^3/(\text{s}\sqrt{\text{m}})$. Thus, the first principles based model in Eq. (1) can be written as the physiological based model in Eq. (6):

$$\dot{h} = \frac{0.04 \cdot v^5}{0.71^5 + v^5} - \frac{0.71 \cdot u^2}{1.84^2 + u^2} \cdot \frac{h}{0.54 + h} \quad (6)$$

The models in Eqs. (1) and (6) are in Figure 4 verified against real data from the tank process, and we see that both models displays good compliance with real data. Thus, it should be possible to tune a physiological controller for the tank process.

3 Tuning of an Integral Controller

We have previously shown that the motifs in Figure 2 share similarities with an integral controller (Drengstig et al., 2012). In order to have a base for comparison when applying physiological inspired

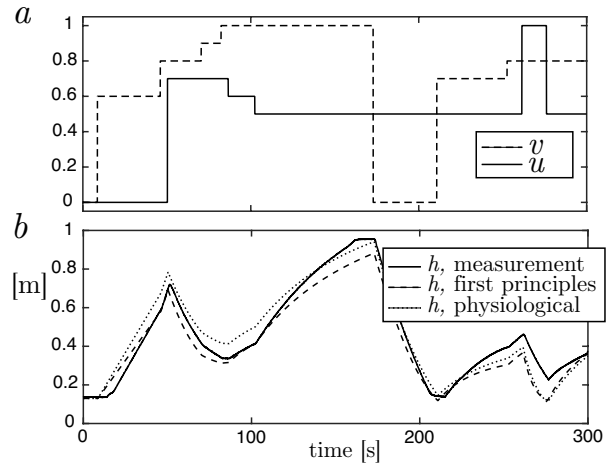


Figure 4. Model verification. Panel *a*: Valve control signal u (solid line) and pump signal v (dashed line) as a function of time. Panel *b*: Measured water level in tank (solid line), first principles model in Eq. 1 (dashed line) and physiological model in Eq. 6 (dotted line).

control, we will in this section tune the standard integral controller

$$u = -G_i \int_0^t (h_{\text{set}} - h) d\tau \quad (7)$$

using the pole-placement method. Note that the gain is negative since the controller is reverse-acting. We use the following experimentally found working point *WP*

$$WP : v_0=0.62, u_0=0.32, h_0=0.50 \quad (8)$$

and estimate from the model in Eq. (1) the following transfer function for the tank process

$$H_p(s) = \frac{-4.5}{86s + 1} \quad (9)$$

The closed loop transfer function is then readily found as

$$M(s) = \frac{G_i \cdot 4.5}{86s^2 + s + G_i \cdot 4.5} \quad (10)$$

Since we have only a single controller parameter, we cannot specify both the natural undamped frequency ω_n and the damping ratio ζ of $M(s)$. We consider overshoot to be the most important aspect of the step response, and thus, specify an underdamped response with 50% overshoot, corresponding to $\zeta=0.2$. Consequently, we find $\omega_n=0.029$ and an integral gain of $G_i=0.016$.

4 Tuning of Physiological Controllers

For a physiological regulatory system to be functional from a control theoretic point of view, it needs a setpoint. In contrast to an industrial control system where the setpoint represents an external input signal, setpoints in physiology are an inherent part of the regulatory mechanism. Even though the biochemical mechanisms behind setpoints in physiology is still not well understood, the notion

of a *fixed* setpoint has so far been dominating (Ma et al., 2009; Drengstig et al., 2012; Ang and McMillen, 2013). This implies, however, that there is often a need for a deviation measure to count for the fact that in many cases the steady state value of the controlled variable deviates from, what is believed to be, the setpoint value. An alternative way of interpreting this deviation is to consider a *variable* setpoint, and we will in the next two subsections investigate both approaches.

4.1 Fixed Setpoint Approach

The controller part of motif 5 is from Figure 2 generally given as

$$\dot{E} = k_s^E \cdot \frac{A}{K_a^A + A} - \frac{V_{max}^E \cdot E}{K_M^E + E} \quad (11)$$

where K_a^A is the activation constant. The basis for the fixed setpoint approach is the assumption that the enzyme which degrades the controller species E is operating under saturated conditions, i.e. $K_M^E \ll E$. An example of where such an approximation is valid is the degradation of alcohol by the enzyme alcohol dehydrogenase, where the degradation rate is independent of the alcohol content in blood.

In Eq. (11), the information about the level of A , i.e. the signaling between A and E , is based on mixed activation kinetics. However, the water level measurement in the tank process is a linear function of water level h , i.e. $K_a^A = 0$. Thus, using variable names from the tank process ($E = u$, $A = h$), we write Eq. (11) as

$$\dot{u} = k_s^u \cdot h - \frac{V_{max}^u \cdot u}{K_M^u + u} \quad (12)$$

which can be restructured as the integral control law in Eq. (13)

$$\dot{u} = \underbrace{-k_s^u \cdot \frac{u}{K_M^u + u}}_{G_i} \cdot \left(\underbrace{\frac{V_{max}^u}{k_s^u}}_{h_{set}} - \underbrace{\frac{K_M^u + u}{u}}_{h_{meas}} \cdot h \right) \quad (13)$$

Here G_i is still the controller gain and h_{set} is the fixed setpoint consisting of parameter values only. We note that the controller gain G_i is affected by the control signal u , and we observe also the premise for the necessary condition behind the fixed setpoint approach, i.e. $K_M^u \ll u$. If this condition is satisfied, the fraction $\frac{K_M^u + u}{u}$ acting on the measurement function becomes close to unity, and can hence be discarded. A visualization of Eq. (13) is shown in Figure 5a, which illustrates that the control signal u will have a (small) influence on the measurement h_{meas} and the controller gain.

From Eq. (13) we note that k_s^u is a part in both the controller gain G_i and the setpoint h_{set} . Thus, tuning the controller around a fixed setpoint implies that both parameters k_s^u and V_{max}^u must be adjusted in order to maintain the setpoint. Taking advantage of the controller tuning in the

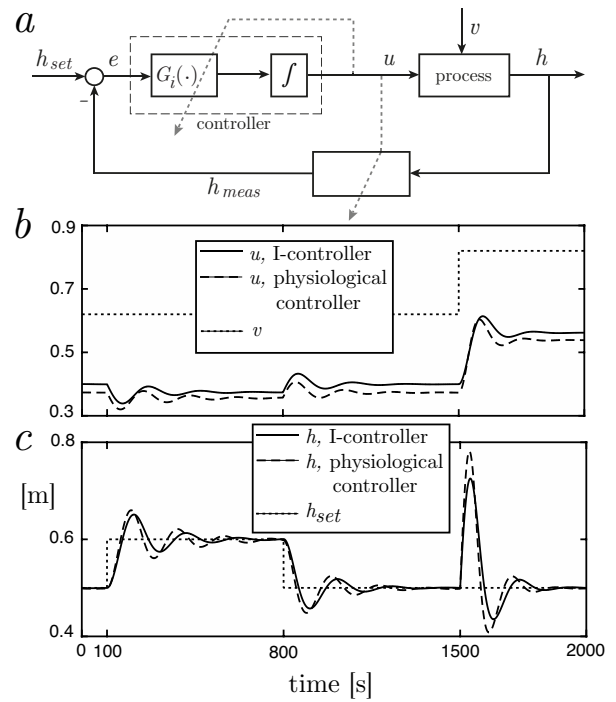


Figure 5. Panel *a*: Negative feedback loop for the fixed setpoint approach, where the setpoint depends only on parameter values. Panels *b* and *c*: Comparing the setpoint tracking and disturbance rejection properties of *i*) the first principles based model in Eq. (1) together with the I-controller in Eq. (7) (solid lines), and *ii*) the physiological model in Eq. (6) together with the controller in Eq. (12) (dashed lines). Panel *b*: Stepwise increase in disturbance v from 0.62 to 0.82 at $t=1500$ s (dotted line) and corresponding manipulated variables u (solid and dashed lines). Panel *c*: Response in water level h for a setpoint change from 0.5 to 0.6m at $t=100$ s and back again at $t=800$ s. The response also shows the disturbance rejection properties for the step in v at $t=1500$ s. The setpoint change for the physiological controller is caused by a 20% increase in V_{max}^u . Parameter values for the physiological controller are $V_{max}^u=0.008$, $k_s^u=0.016$, and $K_M^u=0.001$. Controller gain for the integral controller is $G_i=0.016$.

previous section, we specify $k_s^u = G_i = 0.016$, and hence, in order to have a setpoint of $h_{set} = 0.5$ m, we get $V_{max}^u = 0.008$.

We have in Figure 5, panels *b* and *c*, simulated the setpoint tracking and disturbance rejection properties of

- i) the first principles based model in Eq. (1) together with the I-controller in Eq. (7) (solid lines), and
- ii) the physiological model in Eq. (6) together with the physiological controller in Eq. (12) (dashed lines).

We note that both control systems display similar responses to both setpoint changes and stepwise disturbances in v . The difference between the control systems is due to the use of different process models and to the value of K_M^u (even though it is small).

4.2 Limitations of the Fixed Setpoint Approach

If the assumption of saturated removal of the controller species does not hold, i.e. $K_M^u \ll u$, there will be a deviation between the fixed setpoint and the actual water level. Thus, the fraction $\frac{K_M^u + u}{u}$ is *not* close to unity, and con-

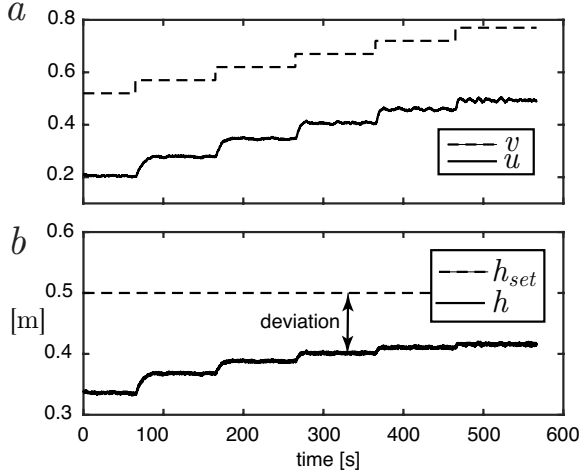


Figure 6. Physiological control of the tank process demonstrating the deviation between the fixed setpoint and the actual water level when $K_M^u \ll u$. The tank is controlled by the controller in Eq. (12) with $K_M^u=0.1$. In order to avoid oscillatory behaviour the controller gain is increased to $k_s^u=10$, giving $V_{max}^u=5$ for a fixed setpoint of $h_{set}=0.5\text{m}$. Panel *a*: The pump speed v is increased in a stepwise manner from $v=0.52$ to $v=0.77$ (dashed line), together with the corresponding control signal u (solid line). Panel *b*: Measured water level and the fixed setpoint. Note that the deviation decreases as v (and u) increases.

sequently the water level h will deviate from the setpoint h_{set} (even though the control error $e=0$). This behaviour is shown in Figure 6, which shows the results from an experiment applied to the tank process where we use $K_M^u=0.1$ instead of $K_M^u=0.005$ as in Figure 5. We observe that the deviation decreases as the control signal u increases, which motivates for a variable setpoint description.

4.3 Variable Setpoint Approach

Many physiological systems display variability in regulated species. Examples include blood glucose level as a function of constant glucose infusion (Elrick et al., 1964), and sodium content as a function of salt intake (Bonventre and Leaf, 1982). Such a behavior fits a variable setpoint regulatory system, which can mathematically be found by reorganizing Eq. (12) as follows:

$$\dot{u} = - \underbrace{k_s^u}_{G_i} \cdot \left(\underbrace{\frac{V_{max}^u}{k_s^u} \cdot \frac{u}{K_M^u + u}}_{h_{set}} - h \right) \quad (14)$$

A visualization of this feedback structure is given in Figure 7a, and we note that u now affects the setpoint, rather

than the measurement function and controller gain as in Figure 5a. In effect, this structure lumps the fixed setpoint and the deviation into a variable setpoint, and consequently adds the variation in the controlled variable h as an addition feature in the controller tuning.

We observe from Figure 6 that as the disturbance v increases, both the control input u and water level h increases. Thus, in order to obtain a control system with a *specified* variability in the water level h , we introduce the notion of a *low* and a *high* level of each variable, defined by the working points WP_1 and WP_2 as follows:

$$WP_1 : v_{low}, u_{low}, h_{low}, \quad WP_2 : v_{high}, u_{high}, h_{high} \quad (15)$$

In an industrial application the levels h_{low} and h_{high} would then correspond to the variation we consider as acceptable at the correlated levels of disturbances, i.e. v_{low} and v_{high} . Thus, the tuning of the physiological controller, i.e. determining the three parameters k_s^u , V_{max}^u and K_M^u , is based on the following two steady state versions of Eq. (14)

$$0 = -k_s^u \cdot \left(\frac{V_{max}^u}{k_s^u} \cdot \frac{u_{low}}{K_M^u + u_{low}} - h_{low} \right) \quad (16)$$

$$0 = -k_s^u \cdot \left(\frac{V_{max}^u}{k_s^u} \cdot \frac{u_{high}}{K_M^u + u_{high}} - h_{high} \right) \quad (17)$$

As this in an underspecified system, one of the parameters must be specified. This could typically be the controller gain, i.e. the synthesis rate k_s^u in Eq. (14).

We will illustrate the concept by tuning two different variable setpoint controllers and compare them for a stepwise increase in the disturbance from v_{low} to v_{high} , while the water level varies between the pre-specified values h_{low} and h_{high} . Both control systems are initially in the working point WP_1 corresponding to Eq. (8), i.e.

$$WP_1 : v_{low}=0.62, u_{low}=0.32, h_{low}=0.50 \quad (18)$$

We then specify the high level disturbance as $v_{high}=0.82$ together with the two different high water levels indicated with gray background in Table 1. Based on these specifications, we find from experiments on the tank process the corresponding two high level control signals u_{high} , also shown in Table 1.

Table 1. Controller parameters calculated for the given WP_1 in Eq. (18) and two different WP_2 .

Controller no.	$WP_2, v_{high}=0.82$		Parameters		
	h_{high}	u_{high}	k_s^u	V_{max}^u	K_M^u
i)	0.55	0.49	0.01	0.0071	0.137
ii)	0.66	0.47	0.01	0.0177	0.797

As we have one degree of freedom in selecting controller parameters, we apply an identical controller gain $k_s^u=0.01$ for both controllers, and solve Eqs. (16) and (17) to determine V_{max}^u and K_M^u as shown in Table 1.

In the simulation in previous subsection (Figure 5), we applied both a setpoint change and a step in the disturbance. In this subsection, however, the setpoint enters the control system as user specified high and low water levels during normal operation, and it is therefore counter-intuitive to apply a setpoint change as in Figure 5. Thus, the main task of a variable setpoint regulatory system is therefore to compensate for the disturbances. As this is also the case for many industrial control systems, we compare only the disturbance rejection properties of the two control systems. For this task, we calculate the *total variation* (TV) as a quantitative measure of controller performance, i.e.

$$TV = \sum |u(k) - u(k-1)| \quad (19)$$

Both physiological controllers are applied to the tank process in Figure 1a, and the results are shown in Figure 7, panels b-d. The disturbance is given as a step from $v_{low}=0.62$ to $v_{high}=0.82$ at $t=200$ seconds (not shown).

Even though the controller gain for both controllers are the same ($k_s^u=0.01$), we observe that the responses in h is less oscillatory for the controller with the highest acceptable water level h_{high} (controller ii). This observation is verified by the lowest total variation (TV) measure in panel d. From a physiological point of view, such a reduced control signal usage will save energy in that the

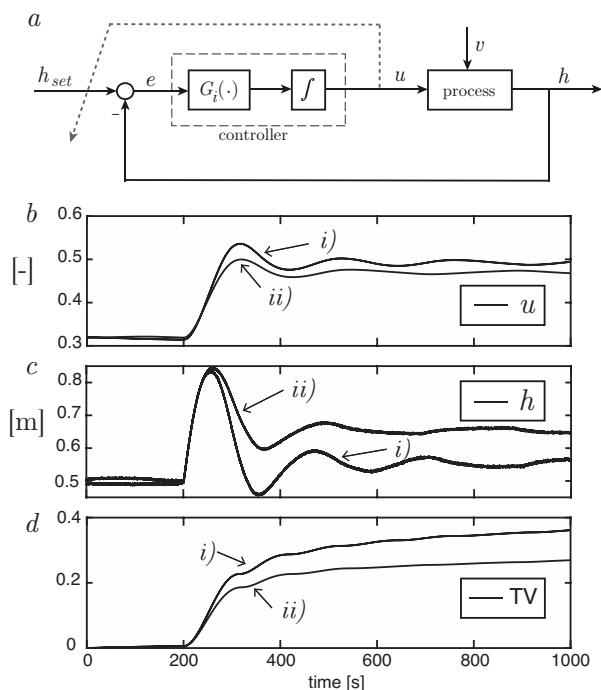


Figure 7. Panel a: Illustration of the negative feedback loop for a variable setpoint controller, where the control signal u have an impact on the setpoint. Panels b-d: Disturbance rejection properties of the two controllers in Table 1 applied to tank process in Figure 1a. The responses are numbered according to Table 1. A step in the disturbance from $v_{low}=0.62$ to $v_{high}=0.82$ (data now shown) is applied at $t=200$. Panel b: Control input u . Panel c: Water level h . Panel d: The performance measure *total variation* (TV) calculated as Eq. (19).

variation in synthesis and degradation of the manipulated species E is minimized.

The rationale behind the reduced TV-measure on the tank process is that an increased acceptable high water level h_{high} leads to increased hydrostatic pressure. This again reduces the necessary compensating valve motion in the outlet flow (compared to a fixed setpoint situation). If such a control system should be applicable in the process industry, it is of vital importance that product quality and safety issues is not affected by the variable setpoint.

5 An Industrial Control Structure Inspired by Physiology

Based on the underlying structure behind the variable setpoint controller and the results from the previous subsection, we propose in this section a novel industrial control structure applicable for the process industry. It is based on the feedback loop in Figure 7a, and is shown in Figure 8a.

The block termed *SP-calculation* in Figure 8a is where the variable setpoint is continuously calculated. Using two different working points as defined in Eq. (15), the variable setpoint can be calculated as follows

$$h_{set} = \frac{\Delta h}{\Delta u} \cdot u + \beta \quad (20)$$

where $\Delta h = h_{high} - h_{low}$, $\Delta u = u_{high} - u_{low}$, and $\beta = h_{low} - \frac{\Delta h}{\Delta u} \cdot u_{low}$. The expression in Eq. (20) is just the line going through (u_{low}, h_{low}) to (u_{high}, h_{high}) in a 2-dimensional space. In order to ensure that the water level is kept between some absolute minimum and maximum limits, the *SP-calculation*-block could also include the necessary logic for this.

In order to quantify the effect of this variable setpoint control structure, we have in a simulation study used i) a standard PI-controller and ii) a PI-controller with a variable setpoint, both applied to the model in Eq. (1). Both controllers use identical control parameters, i.e. $K_p=-1.5$ and $T_i=15$. Using the model in Eq. (1), we have specified/calculated the following working points:

- WP₁ : $v_{low}=0.55, u_{low}=0.33, h_{low}=0.44$
- WP₂ : $v_{high}=0.80, u_{high}=0.52, h_{high}=0.58$

The responses in the controls signal u , water level h , and calculated TV are shown in Figures 8c-e. As expected, the control signal usage is reduced for the variable setpoint controller. Note that the disturbance shown in Figure 8b has a wider range compared to the working points.

6 Conclusions

In this paper we have modelled a tank process, configured with a pompe and an outlet valve, from a physiological perspective. Both the pompe and valve characteristics are fitted to Hill kinetic expressions, and the model is verified against real process data.

We have developed a physiological inspired control system (with a fixed setpoint) and shown that it behaves similar to an integral controller (I-controller). Motivated by

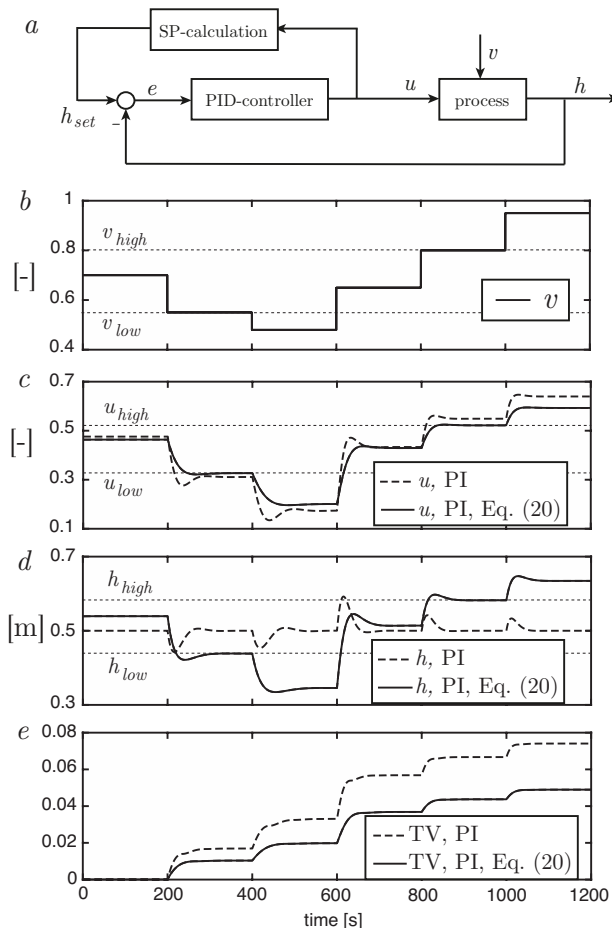


Figure 8. Panel *a*: Illustration of the negative feedback loop for an industrial control system using a variable setpoint. Panels *b-e*: Disturbance rejection properties of a standard PI-controller (dashed lines) and a PI-controller with variable setpoint (solid lines). The working points WP_1 and WP_2 are shown as dotted lines. Panel *b*: Disturbance v . Panel *c*: Control input u . Panel *d*: Water level h . The setpoint for the standard PI-controller is $h_{set}=0.5\text{m}$. Panel *e*: The performance measure *total variation* (TV) calculated as Eq. (19).

the fact that such a fixed setpoint controller is characterized by some deviation measure, we have further shown how this correspond to a control system with a variable setpoint. The benefit of such a structure is that the control signal usage is reduced when the user-specified acceptable variation in the controlled variable increases.

Inspired by this physiologically motivated variable setpoint structure, we finally propose an industrial control structure using a PI(D)-controller with a variable setpoint calculated as a function of the control signal u . Simulations indicate that this structure has advantages with respect to control signal usage, compared to a standard PI(D)-controller with an externally given fixed setpoint.

References

Jordan Ang and David R. McMillen. Physical Constraints on Biological Integral Control Design for Homeostasis and Sen-

sory Adaptation. *Biophysical Journal*, 104(2):505–515, January 2013.

Jordan Ang, Sangram Bagh, Brian P. Ingalls, and David R. McMillen. Considerations for using integral feedback control to construct a perfectly adapting synthetic gene network. *Journal of Theoretical Biology*, 266(4):723–738, October 2010.

J. V. Bonventre and A. Leaf. Sodium homeostasis: steady states without a set point. *Kidney International*, 21(6):880–883, 1982.

Mathieu Cloutier and Edwin Wang. Dynamic modeling and analysis of cancer cellular network motifs. *Integrative Biology*, 3(7):724, 2011.

Yongsheng Ding. A nonlinear PID controller based on fuzzy-tuned immune feedback law. In *Conf Proc Intelligent Control and Automation*, pages 1576–1580, 2000.

T. Drengstig, I. W. Jolma, X. Y. Ni, K. Thorsen, X. M. Xu, and P. Ruoff. A Basic Set of Homeostatic Controller Motifs. *Biophysical Journal*, 103:2000–2010, October 2012.

H. Elrick, L. Stimmler, C. J. Hlad, and Y. Arai. Plasma Insulin Response to Oral and Intravenous Glucose Administration. *Journal of Clinical Endocrinology & Metabolism*, 24:1076–1082, September 1964.

M. Goulian. Robust control in bacterial regulatory circuits. *Current Opinion in Microbiology*, 7:198–202, April 2004.

Zhangang Han, Thomas M. Vondriska, Ling Yang, W. Robb MacLellan, James N. Weiss, and Zhilin Qu. Signal transduction network motifs and biological memory. *Journal of Theoretical Biology*, 246(4):7–7, June 2007.

H. Javaherian, Ting Huang, and Derong Liu. A biologically inspired adaptive nonlinear control strategy for applications to powertrain control. In *Proc. IEEE Systems, Man and Cybernetics*, pages 2076–2082, 2009.

Philip R. LeDuc, William C. Messner, and John P. Wikswo. How do control-based approaches enter into biology? *Annu Rev Biomed Eng*, 13:369–396, August 2011.

Wenzhe Ma, Ala Trusina, Hana El-Samad, Wendell A. Lim, and Chao Tang. Defining Network Topologies that Can Achieve Biochemical Adaptation. *Cell*, 138:760–773, August 2009.

Xiao Yu Ni, Tormod Drengstig, and Peter Ruoff. The Control of the Controller: Molecular Mechanisms for Robust Perfect Adaptation and Temperature Compensation. *Biophysical Journal*, 97:1–11, August 2009.

José Ricardo Pérez-Correa, Gastón Lefranc, and Mario Fernández-Fernández. A New Application of the Hill Repressor Function: Automatic Control of a Conic Tank Level and Local Stability Analysis. *Mathematical Problems in Engineering*, 2015:1–6, 2015.

M.A. Savageau and G. Jacknow. Feedforward inhibition in biosynthetic pathways: Inhibition of the aminoacyl-tRNA synthetase by intermediates of the pathway. *Journal of Theoretical Biology*, 77:405–425, 1979.

- E.D. Sontag. Remarks on feedforward circuits, adaptation, and pulse memory. *IET Syst Biol*, 4(1):39–51, January 2010.
- S. H. Stokka and K. A. Jakobsen. Fysiologiske reguleringsmekanismer anvendt på tankprosess. B.Sc. thesis, University of Stavanger, 2017. In Norwegian.
- E.M Watson, M.J. Chappell, F. Ducrozet, S.M. Poucher, and J.W. T. Yates. A new general glucose homeostatic model using a proportional-integral-derivative controller. *Computer Methods and Programs in Biomedicine*, 102:119–129, May 2011.

Optimization of Gas Velocity and Pressure Drop in CO₂ Absorption Column

Kwangsu Park Lars Erik Øi

Department of and Process Technology, University College of Southeast Norway, Norway
lars.oi@usn.no

Abstract

For a traditional amine-based CO₂ capture system, the absorber column accounts for a significant part of the overall capital- and operating cost. One important design factor of absorber columns is the gas velocity through the absorber packing. Higher gas velocity leads to higher energy cost due to increased pressure drop, but at the same time lower packing cost due to increased effective interfacial area. By utilizing available correlations in the new version 9.0 of the simulation program Aspen HYSYS, the cost optimum gas velocity can be determined. This work evaluated six types of structured packings: Mellapak 250X, 250Y, 2X, 2Y, Mellapak Plus 252Y and Flexipac 2Y. The simulation results show that for all the packings, the cost-optimum gas velocity is in the range of 2.0 to 2.5 m/s giving a pressure drop through the absorber in the range of 10 to 15 mbar.

Keywords: CO₂ absorption, Aspen HYSYS, structured packing, pressure drop

1.1 Introduction

With growing interest in mitigating the level of global CO₂ emissions, carbon capture and storage technology is essential to abate the global warming. The most studied post-combustion method for capturing CO₂ from exhaust gases is to absorb CO₂ into an amine-based liquid solvent. Structured packings are often preferred as vapour-liquid contacting devices, especially because of their high mass transfer area and low pressure drop.

The absorber column internals, especially packing sections, contribute significantly to the overall capital cost of a CO₂ capture plant. The operating cost of the absorber column is dominated by the energy cost to overcome pressure drops across the column. Different structured packing types have different physical and hydraulic properties that will represent advantages and disadvantages depending on the application. The commercial process simulation program Aspen HYSYS V9.0 has built-in correlations to estimate such hydraulic properties, especially pressure drop and effective interfacial area.

Due to high interfacial area and low pressure drop, structured packing is probably the most optimum packing for large scale CO₂ absorption (Øi, 2012). Sulzer Chemtech, Montz and Koch-Glitsch are three well-known suppliers of structured packing. Structured packing types like Mellapak (from Sulzer Chemtech), Flexipac (from Koch-Glitsch) and Montz-Pak (from

Montz) have been recommended for large scale CO₂ absorption. Data for Montz-Pak are not available in Aspen HYSYS.

There are few references to calculations or evaluations of optimum gas velocity in the open literature. Sulzer Chemtech has published two papers (Sulzer, 2009; Menon and Duss, 2011) discussing structured packing for CO₂ capture and presenting a new packing type (Mellapak CC-2 and CC-3) especially suited for CO₂ capture. Some conclusions were that structured packing is more cost optimum than random packing, and that high packing efficiency combined with low pressure drop is the key factor for an optimum packing. An assumed gas velocity of 2.1 m/s was suggested (Menon and Duss, 2011). Data for Mellapak CC-2 or Mellapak CC-3 are not available in Aspen HYSYS.

At Telemark University College (now University College of Southeast Norway), Øi (2012) has cost optimized most of the process parameters in a CO₂ capture process in his PhD work. A (superficial) gas velocity in the absorption column of 3.0 m/s was assumed, and this value is probably too high because the cost due to the pressure drop becomes excessively high. Typical values for pressure drop in CO₂ capture absorbers from literature are 10-20 kPa (Øi, 2012).

In his Master Thesis work Amaratunga (2013) performed optimization calculations in order to find the most economical packing type and optimum design parameters. Traditional packing types such as 1 and 2 inch Pall rings (random packing) and Mellapak 250Y (structured packing) were considered. A trade-off between packing cost and cost of pressure drop was performed. A conclusion was that optimum gas velocity was probably between 1.5 to 2.0 m/s.

Paneru (2014) continued this work in his Master Thesis. The work of Paneru was based on measured pressure drops from literature (Zakeri et al., 2012). He concluded that the optimum gas velocity was approximately 2.0 m/s for most packings, and that the optimum pressure drop was about 10 mbar.

For such optimization calculations, estimation methods for pressure drop and effective interfacial area are important. References for estimation of pressure drop and interfacial area in structured packings are de Brito et al. (1994), Billet and Schultes (1999) and Bravo et al. (1985). Effective interfacial area (a_{EFF}) is a traditional way to specify the ratio of the effective gas/liquid mass transfer area to the nominal area.

In capital cost estimation, different data and methods have been used in literature. Equipment cost data from Peters and Timmerhaus have been used in the net

calculator (2002) and the program Aspen Icarus have been used. Installation factors have been used to estimate total investment (Paneru, 2014). To calculate operating cost, energy consumption to compensate for the pressure drop has been calculated (Amaratunga, 2013; Paneru, 2014).

This work utilizes Aspen HYSYS simulations including available correlations in “Internal Column Analysis” and cost data to calculate the optimum gas velocity and the optimum pressure drop. The general purpose of the work is to contribute to the cost optimum design of absorption columns for CO₂ capture. A more specific purpose is to show that a combination of process simulation, use of pressure drop correlations and cost estimation is an efficient way to determine the optimum design conditions.

2 Process simulation

2.1 Mass transfer and equilibrium model

The Acid Gas Property Package in Aspen HYSYS® V9.0 was used to simulate the absorption column to absorb CO₂ from a typical exhaust gas from a 400 MW natural gas based combined-cycle power plant.

Figure 1 shows the representation of the absorption column in the simulation program Aspen HYSYS. The inlet amine (lean amine) has a low CO₂ concentration and the outlet amine has a high CO₂ concentration (rich amine).

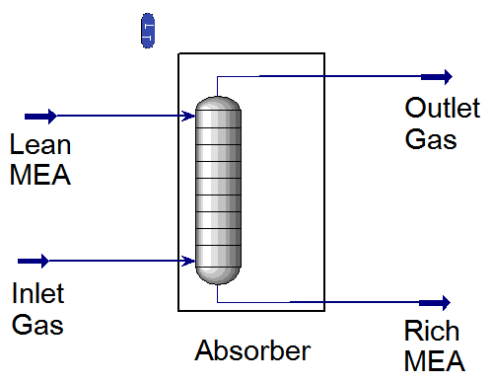


Figure 1. Absorption column in Aspen HYSYS

The rate-based model in Aspen HYSYS considers an individual phase on each stage, and calculates Murphree efficiencies and mass- and energy balances for different packing options. The Electrolyte NRTL thermodynamic model (Austgen et al., 1989) and rate-based simulation was used to model the absorption column. The six types of structured packing evaluated were Mellapak 250X, Mellapak 250Y Mellapak 2X, Mellapak 2Y, Mellapak Plus 252Y and Flexipac HC 2H (2Y). To predict the effective interfacial area and mass transfer coefficient for the different packings, the BRF-

85 correlation (Rocha et al., 1985) was used. To estimate column pressure drops, the in-built vendor correlations were used for Mellapak packings. For Flexipac HC 2H, the Aspen-Wallis method was used for pressure drop estimations.

2.2 Specifications and simulation of standard process for CO₂ capture

The specifications used are presented in Table 1. The specification are similar to the specifications in a simulation from Øi (2007).

Table 1. Process simulation input specifications

Parameter	Value
CO ₂ removal grade	85.0 %
Inlet gas pressure	40 °C
Inlet gas pressure	1.1 bar
Inlet gas molar flow rate	85000 kmol/h
CO ₂ in inlet gas	3.73%
Water in inlet gas	6.71%
Nitrogen in inlet gas	89.56%
Lean MEA temperature	40°C
Lean MEA pressure	1.1 bar
Lean MEA molar flow rate	Varied
MEA content in Lean MEA	29.0 mass-%
CO ₂ in Lean MEA	5.5 mass-%
Number of stages in absorber	10

2.3 Simulation procedures

The base case was specified for each type of packing with the gas velocity of 2.5 m/s and the total packed bed height of 10 meter. Based on the inlet gas volume flow and the gas velocity (2.5 m/s), the required absorber column diameter was calculated. The lean amine rate was then adjusted so that the absorption efficiency became 85 %. By exporting pressure drops from the absorber column top, a pressure drop across each stage was estimated. The sum of these pressure drops is the absorber column pressure drop. The top stage pressure was specified to be equal to the atmospheric pressure (101.3 kPa). The required inlet gas pressure to overcome pressure drop was determined by adding the estimated pressure drop to the atmospheric pressure. The inlet gas pressure obtained in this step is normally not exactly the same as the initially specified inlet gas pressure. Therefore, the inlet gas pressure was updated by a calculated value. This, in turn, causes a slight change in the column diameter (due to change in actual gas volume flow), absorption efficiency as well as the absorber pressure drop. It is therefore necessary to

adjust the lean amine rate, export pressure drops (from the top) and update the inlet gas pressure again. The procedures stated so far have been iterated until there is no notable change in the required inlet gas pressure, absorber column diameter and the absorption efficiency.

For other gas velocities than 2.5 m/s (1.5 m/s, 2.0 m/s and 3.0 m/s), the absorption efficiency of 85% was achieved by adjusting the packed height. The lean amine rate was kept at the same value as in the base case.

For simulation simplification, no static vapour head was considered for pressure drop calculations and pressure drop across the sump was not included.

3 Cost estimation

A total project cost was calculated by considering the equipment installation cost and operating cost. The flue gas fan, absorber column shell, packing and other column internals (liquid distributor, packing support, liquid catcher) were included in estimating the equipment cost. For fans and absorber columns, cost data from Smith (2005) were used. The equipment base size was converted to actual dimensions by using a power law with corresponding cost exponents. The unit cost of structured packings was assumed as 7600 €/m³ (2010 basis) based on cost data from Dimian et al. (2014). For Mellapak 252Y Plus only, a 50 % higher unit cost was assumed. For column internals, the unit cost was assumed as 4000 \$/m² for liquid distributor, 800 \$/m² for packing support and 2000\$/m² for liquid catcher based on data from Dejanovic (2011). Two separate packed sections were assumed in the absorber column, five stages in the upper and lower part respectively. The purchased cost values were converted to 2016 currency using the CPI index (McMahon, 2017) and then converted to Euro.

An installation factor for each equipment unit was determined based on the purchased equipment cost in carbon steel. To calculate installation costs in stainless steel, an installation factor of 2.87 was used for packings, liquid distributors, packing supports and liquid catchers. These installation factors were based on a table from Nils Eldrup as used by e.g. Øi (2012) with the assumptions that the direct cost factor contains equipment and erection factor only, that the engineering cost factor contains engineering, process and mechanical factor only and that no administration cost is considered.

The material factor of stainless steel was assumed to be 1.75 for all column internals (including packings). The ratio of the installation cost to the purchasing cost is therefore 1.64 (=2.87/1.75). For the flue gas fan in stainless steel, a material factor of 1.3 was used. For absorber column shell (in carbon steel), an installation factor of 4.44 was used.

To allow for the column internals, the absorber column was assumed to have an additional height of 15

meter besides the packing sections. The flue gas fan was specified to have an adiabatic efficiency of 0.75 which is the default efficiency in Aspen HYSYS. This is a reasonable efficiency for a high gas flow. For the full-flow alternative, the gas flow is 85000 kmol/h, and it is assumed that the flue gas fan is designed for a gas flow close to optimum conditions.

To estimate operating costs, a unit electricity cost of 0.05 €/kWh was assumed. The yearly interest rate was specified to be 7.0 %. It was also assumed that the calculation period is 20 years, including one year of construction. The operating time was 8000 hours/year.

4 Results

4.1 Results for optimum gas velocities

The total cost for different gas velocities is distributed on absorber packing, absorber shell, flue gas fan and operating cost (OPEX) in Figure 2, Figure 3, Figure 4, Figure 5, Figure 6 and Figure 7.

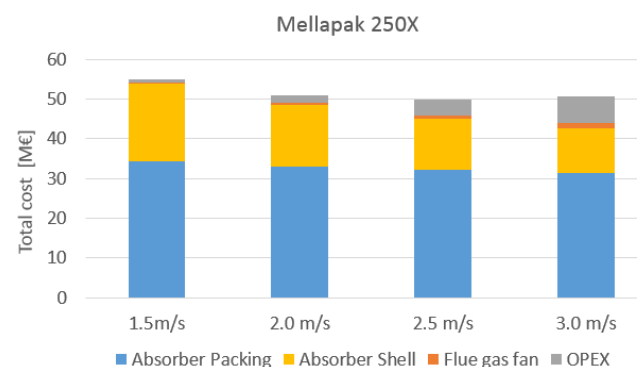


Figure 2. Cost distribution for packing 250X

For Mellapak 250X the optimum is at 2.5 m/s. The gas velocity at 3.0 m/s is close to be optimum. The investment in packing and shell decreases with increasing velocity, while the OPEX is increasing.

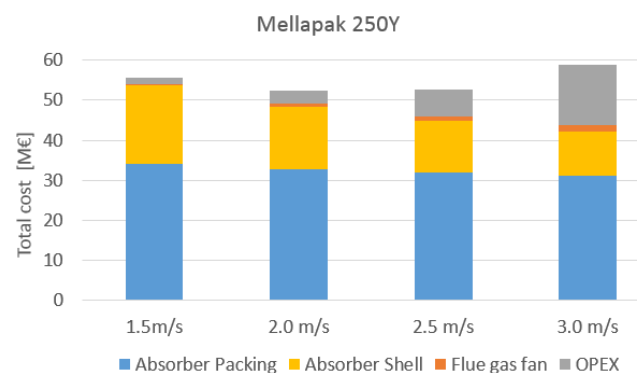


Figure 3. Cost distribution for packing 250Y

For Mellapak 250Y the minimum is at 2.0 m/s, but the gas velocity at 2.5 m/s is close to be optimum. It is seen that with increasing gas velocity, the energy cost increases much more noticeably than with 250 X.

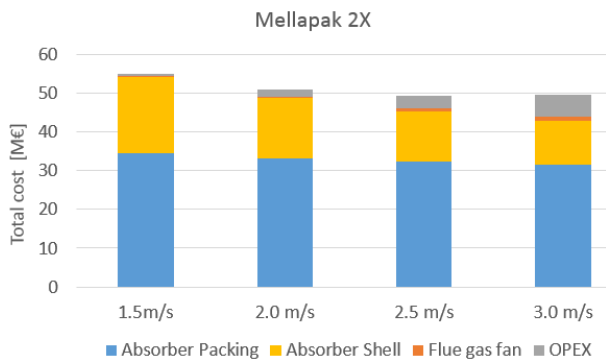


Figure 4. Cost distribution for packing 2X

The results for Mellapak 2X are highly similar to the results for 250X. The optimum is at 2.5 m/s but 3.0 m/s is close to be optimum.

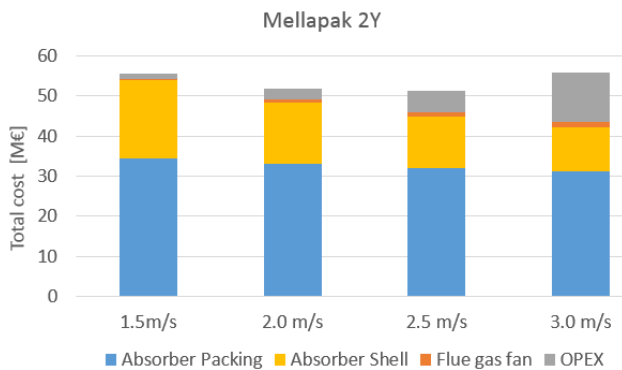


Figure 5. Cost distribution for packing 2Y

The results for Mellapak 2Y are very similar to the results for 250Y. However, for 2Y, the minimum total cost is achieved for 2.5 m/s, and 2.0 m/s is quite close to be optimum.

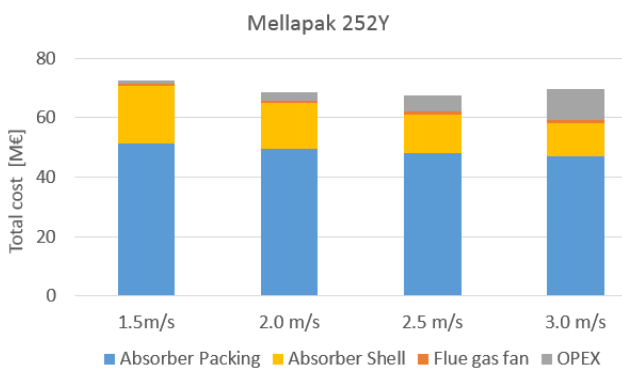


Figure 6. Cost distribution for packing 252Y

For Mellapak 252Y the energy cost is increasing only slightly with gas velocity. The optimum gas velocity is 2.5 m/s.

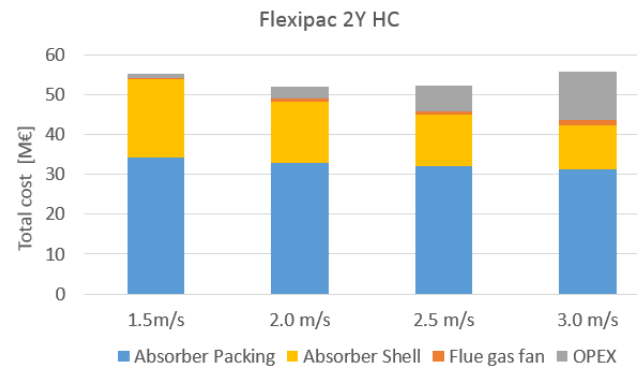


Figure 7. Cost distribution for packing Flexipac 2Y HC

For Flexipac 2Y HC, the optimum appears at 2.0 m/s. The results for Mellapak 250Y and Flexipac 2Y HC are very similar. For all packing types, the lowest total cost and then the optimum gas velocity was achieved at 2.0 or 2.5 m/s.

4.2 The results for optimum pressure drop

Figure 8 shows the pressure drop (per meter of packed bed) according to the type of packing and the gas velocity at the conditions in Figures 2 to 7. The packing with the lowest pressure drop is Mellapak 2X, followed by 250X. The Y type packings have higher pressure drop, and this becomes more clear at higher gas velocities. The special packing Mellapak 252Y has less increased pressure drop at higher gas velocities.

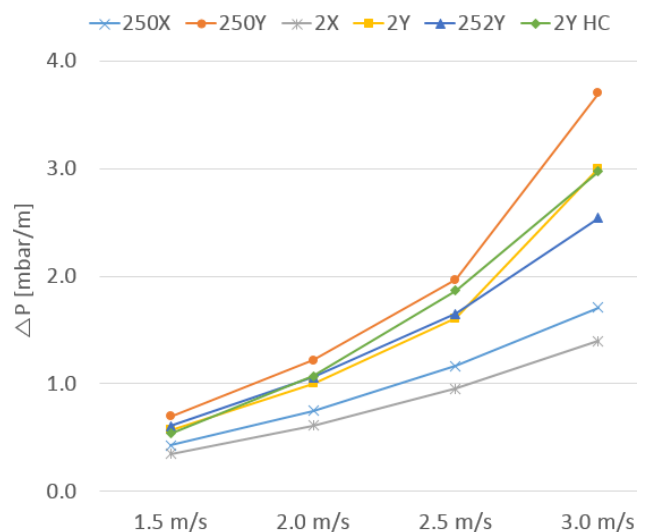


Figure 8. Pressure drop as a function of gas velocity for the different packings

Table 2 shows the optimum absorber pressure drop at the optimum velocity for each type of packing. The optimum pressure drop was calculated by combining the number of absorber stages, unit packing pressure drop [mbar/m] and the unit packing height [m/packing].

Table 2. Optimum gas velocity and pressure drop for different packings

	Optimum v [m/s]	Optimum ΔP [mbar]
Mellapak 250X	2.5	11.7
Mellapak 250Y	2.0	10.0
Mellapak 2X	2.5	9.5
Mellapak 2Y	2.5	16.1
Mellapak 252Y	2.5	16.5
Flexipac 2Y HC	2.0	8.7

4.3 Optimization including maintenance cost

An alternative calculation was performed including maintenance as a part of the operating cost. The yearly maintenance cost was specified to 3 % of the total investment and is a value in the lower range of recommended values (Smith, 2005). A low value is assumed because the investment of the absorption process is assumed to be high compared to the complexity. Including maintenance cost into the total cost does not affect the pressure drop data which were obtained from the Aspen HYSYS simulation.

The calculated optimum velocity was in most cases not changed. But for Mellapak 250Y the optimum velocity increased to 2.5 m/s and for Mellapak 2X the optimum gas velocity increased to 3.0 m/s. This is because including maintenance cost slightly increases the influence of the investment while there is no change in the operating cost. Overall, the maintenance cost does not have significant influence on determining the optimum velocity.

5 Discussion

The cost estimates are of course highly sensitive to changes in packing cost, change in calculation time (years of operation) and change in power cost. All these specifications have a large uncertainty. When optimizing the gas velocity and pressure drop, the optimum gas velocity (and then the optimum pressure drop) are however quite stable for a large range of the cost parameter values. This was also the experience in the work of Amaratunga (2013) and Paneru (2014). The calculation including maintenance as a part of the

operating cost also shows that the optimum conditions are not influenced much by changing the cost parameters.

The uncertainty in cost data for structured packing including installation cost is high. The uncertainty in the cost of liquid distribution and gas distribution equipment is also high. This is because these cost data are based on information from suppliers, and there is not much open information from the suppliers available.

The performance data of structured packings officially published by suppliers (Sulzer, Koch-Glitsch or Montz) may be overestimated or underestimated. The discrepancy between the supplier's correlations and experimental data becomes clearer when the pressure drop is measured at wet conditions compared to dry conditions (Zakeri et al., 2012). This might have caused the deviations between the results in Paneru (2014) compared to the results in this study.

The deviations in estimated effective interfacial area are assumed to be of less importance compared to the deviations in estimated pressure drop (Øi, 2012).

The optimum pressure drops in this work are in the same range as in the earlier works. The values of optimum gas velocities in this work are between the values reported in Øi (2012) which are higher (3.0 m/s), and Amaratunga (2013) and Paneru (2014) which are lower (from below 2.0 m/s to 2.5 m/s).

A low-pressure type of packing is the type with curved ends like in Mellapak Plus 252Y from Sulzer Chemtech. Other suppliers like Koch-Glitsch and Montz also have such types of packing. The curved-end packings are however not much different in pressure drop at normal gas velocities. Lower pressure drop for curved packings is achieved at high gas velocities that are not cost optimum conditions for any of the packings. Assuming a cost for the Mellapak Plus 252Y packing 50 % higher than other packings, Mellapak Plus 252Y was found not to be cost optimum.

Sulzer Chemtech also has the packing types Mellapak CC-2 and CC-3 especially developed for CO₂ capture. The suggested gas velocity of 2.1 m/s by Sulzer (Menon and Duss, 2012) is within the range of optimum gas velocities in this work. The cost of a commercial specialized packing has high uncertainty because of the possibility for the supplier to adjust the price according to the market conditions. Because of this, it is very difficult to evaluate generally whether a specialized packing is cost optimum.

6 Conclusion

Optimum gas velocity and pressure drop have been determined for different structured packings utilizing Aspen HYSYS simulation and cost estimation.

The calculated results show that the optimum gas velocity lies in the range of 2.0 to 2.5 m/s for all the six structured packings. The corresponding pressure drops through the absorber packing were in the range of 10 to 15 mbar. There is a large uncertainty in cost data, especially in the cost of purchase and installation of structured packing and other column internals. Alternative calculations show that this uncertainty in cost data has only a limited influence on determining the optimum gas velocity and pressure drop.

- Øi, L. E. (2007). *Aspen HYSYS simulation of CO₂ removal by amine absorption a gas based power plant*. The 48th Scandinavian Conference on Simulation and Modelling (SIMS2007) Göteborg, Sweden.
- Øi, L. E. (2012). *Removal of CO₂ from exhaust gas*. PhD Thesis, Telemark University College, Porsgrunn. (TUC 3: 2012)

References

- Amaratunga, P. D. M. M. (2013) *Optimization of gas velocity, pressure drop and column diameter in CO₂ capture*. Master Thesis, Telemark University College, Porsgrunn, Norway.
- Austgen, D. M., Rochelle, G. T., Peng, X., Chen, C. (1989). Model of Vapor-Liquid Equilibria for Aqueous Acid Gas-Alkanolamine Systems Using the Electrolyte-NRTL Equation, *Industrial and Engineering Chemistry Research*, 28, 1060-1073.
- Billet R., Schultes M. (1999). Prediction of mass transfer columns with dumped and structured packings. *Trans IChemE*, 77, 498-504.
- De Brito M. H., von Stockar U., Bangerter A. M., Bomio P., Laso M. (1994). Effective Mass-Transfer Area in a Pilot Plant Column Equipped with Structured Packings and with Ceramic rings. *Industrial and Engineering Chemistry Research*, 33, 647-56.
- Dejanovic I., Matijasevic L. J., Halvorsen, I., Skogestad, S., Jansen, H., Olujić Z. (2011). Conceptual design and comparison of four-products dividing wall columns for separation of a multicomponent aromatics mixture. *Chemical Engineering Research and Design*, 89, 1155-1167.
- Dimian, A., Bildea, C., Kiss, A. *Integrated design and simulation of chemical processes, 2nd ed.*, Elsevier. 2014.
- McMahon, T. (2017). *Historical Consumer Price Index (CPI)*. *Inflationdata.com*. Retrieved 9 June 2017, from https://inflationdata.com/Inflation/Consumer_Price_Index/HistoricalCPI.aspx?reloaded=true
- Menon A., Duss M. (2011). *Pushing the boundaries in process intensification*. Sulzer Technical Review, Sulzer Chemtech Ltd., Winterthur, Switzerland.
- Paneru C. P. (2014). *Optimum gas velocity and pressure drop in CO₂ absorption column*. Master Thesis, Telemark University College, Porsgrunn, Norway.
- Peters, M. S., Timmerhaus, K.D. *Internet cost estimation program* (2002). Available from (01.02.2016): <http://www.mhhe.com/engcs/chemical/peters/data/>
- Rocha, J. A., Bravo J. L., Fair J. R. (1985). Mass Transfer in Gauze Packings, *Hydrocarbon Processing*, 64(1), 91.
- Rocha, J. A., Bravo J. L., Fair J. R. (1993). Distillation Columns Containing Structured Packings: A Comprehensive Model for Their Performance. 1. Hydraulic Models. *Industrial and Engineering Chemistry Research*, 32, 641-651.
- Smith, R. *Chemical process design and integration*. Wiley, Chichester, West Sussex, 2005.
- Sulzer (2009). *Mellapak Plus – A new Generation of Structured Packing*, Sulzer Chemtech Ltd., Winterthur, Switzerland.
- Zakeri A., Einbu A., Svendsen H.F. (2012). Experimental investigation of pressure drop in structured packings. *Chemical Engineering Science*, 73, 285-98.

Simulation and Economic Optimization of Vapor Recompression Configuration for Partial CO₂ capture

Lars Erik Øi¹ Erik Sundbø¹ Hassan Ali¹

¹Department of and Process, Energy and Environmental Technology, University College of Southeast Norway, Norway
lars.oi@usn.no

Abstract

A standard method for CO₂ capture is by absorption in an amine based solvent followed by desorption. Such plants are traditionally designed for removal of 85-90 % CO₂ from the exhaust gas as a reasonable trade-off between high removal efficiency and low investment. The major challenge is the high energy demand for CO₂ desorption. In many industrial cases, a limited amount of cheap waste heat is available and this makes partial CO₂ capture an interesting option. It is not obvious whether a high removal efficiency from a part of the exhaust or a low removal efficiency from the total exhaust is the optimum solution. In this work, simulations of traditional and vapor recompression processes are performed, and it is found that vapour recompression treating the total exhaust is energy optimum. A traditional process with a low absorption column treating the total exhaust gives the lowest cost per ton CO₂ captured.

Keywords: CO₂ absorption, Aspen HYSYS, partial capture, vapor recompression

1 Introduction

The aim of this work is to perform simulations of various process configurations including vapour recompression to find the energy optimum and the most cost effective solution. Especially the focus is to perform a cost-benefit analysis of various configurations to evaluate whether it is cost optimum to treat all the exhaust gas or only a part of it.

1.1 Literature

There have been many research activities to identify the techno-economic feasibility of different CO₂ capture concepts. Several studies have investigated utilization of waste heat with a standard MEA (monoethanol amine) absorption and desorption process (IEAGHG, 2009), but there are few studies which have focused on different process configurations powered by waste heat. Several studies (Fernandez, 2012; Øi et al. 2014; Aromada and Øi, 2015) have concluded that vapour recompression is an attractive configuration.

(Dong et al., 2012) performed a study of the possibility to utilize waste heat from a cement plant to capture CO₂ effluent from the plant. Up to 78 % capture could be achieved using only waste heat by integrating heat recovery with CO₂ capture.

A project called CO₂stCap (a part of the Climit programme), is now run in Norway and Sweden to evaluate different possibilities for partial CO₂ capture from industrial sources.

At University College of Southeast Norway there have been performed simulations of possible CO₂ capture from Norcem's cement plant in Brevik (Svolsbru, 2013). (Park, 2016) simulated partial CO₂ capture and concluded that in case of partial CO₂ capture of approximately 40 % of the CO₂ in the flue gas from a cement plant, treating all the flue gas would probably be more cost optimum compared to treat only a part of the flue gas. (Sundbø, 2017) included an evaluation of vapor recompression for partial CO₂ capture. This work is based on the Master Thesis work of Erik Sundbø.

1.2 Process description

A sketch of a general post-combustion CO₂ capture process is presented in Figure 1. The whole or a part of a flue gas is sent to an absorber where CO₂ is absorbed in a solvent. The solvent is regenerated by releasing the CO₂ in a desorber and the regenerated solvent is sent back to the absorber.

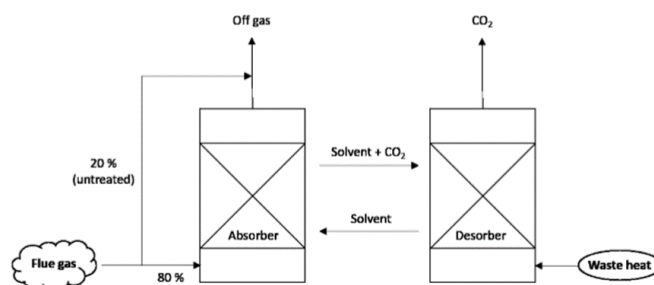


Figure 1. Principle of partial CO₂ capture (Park, 2016)

Figure 2 shows a standard process for CO₂ absorption into an amine based solvent. It comprises an absorption column, a stripping column including a reboiler and condenser, circulating pumps and heat exchangers.

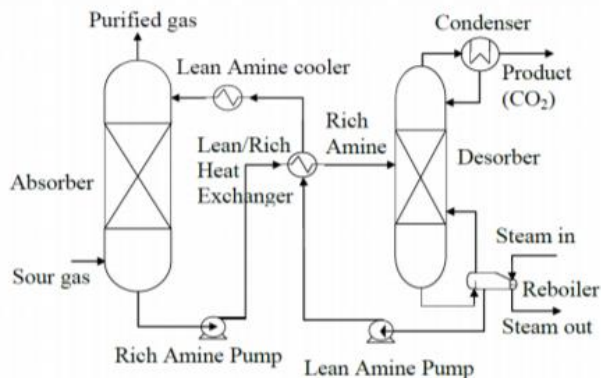


Figure 2. Principle of standard process (Aromada and Øi, 2015)

A process configuration which has been shown to be very energy efficient is vapor recompression where the regenerated amine from the desorption column is depressurized to a pressure below the desorption pressure, and then the liquid is recycled back to the top of the absorber while the gas is compressed and recycled back to the bottom of the desorption column. The principle is shown in Figure 3.

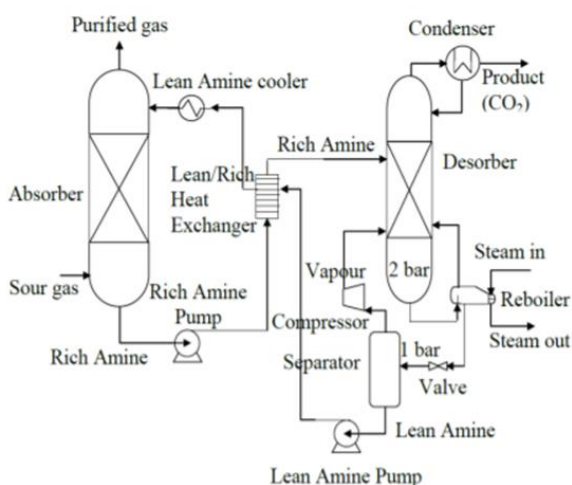


Figure 3. Principle of vapor recompression process (Aromada and Øi, 2015)

2 Process simulation program and specifications

2.1 Process simulation program

Aspen HYSYS is a commercial general purpose process simulation program from AspenTech. It contains several equilibrium models, process unit operation models and flow-sheeting calculation alternatives.

Different alternatives were simulated using Aspen HYSYS version 8.6 using the Kent-Eisenberg vapour/liquid equilibrium model.

The absorption and desorption columns can be simulated with equilibrium stages including a stage efficiency. Murphree efficiencies for CO₂ can be specified in the absorption column and the desorption column. The Murphree efficiency for a stage is defined by the change in mole fraction CO₂ from a stage to another divided by the change on the assumption of equilibrium. Pumps and compressors were simulated with an adiabatic efficiency of 0.75.

2.2 Specifications and simulation of standard process for CO₂ capture

A standard process as in Figure 2 has been simulated in Aspen HYSYS. The specifications for a base case calculation are presented in Table 1. The conditions are from a cement plant, and the (waste) heat is assumed to be constant 25 MW. Most of the specifications are the same as in (Øi, 2007) and (Svolsbru, 2013).

Table 1. Standard process simulation input specifications for 85% CO₂ removal

Parameter	Value
Inlet gas pressure	80 °C
Inlet gas pressure	1.1 bar
Inlet gas molar flow rate	8974 kmol/h
CO ₂ in inlet gas	17.8 %
Water in inlet gas	20.63 %
Nitrogen in inlet gas	89.56%
Lean MEA temperature	40 °C
Lean MEA pressure	1.01 bar
Lean MEA molar flow rate*	545000 kg/h
MEA content in Lean MEA	29.0 mass-%
CO ₂ in Lean MEA	5.5 mass-%
Number of stages in absorber	10
Murphree efficiency in absorber stages	0.15
Number of stages in desorber	8
Murphree efficiency in desorber stages	1.0
Reflux ratio in desorber	0.3
Reboiler temperature	120 °C
Temperature in amine before desorber	101.2 °C
Desorber pressure	2.0 bar
Pump efficiency	0.75

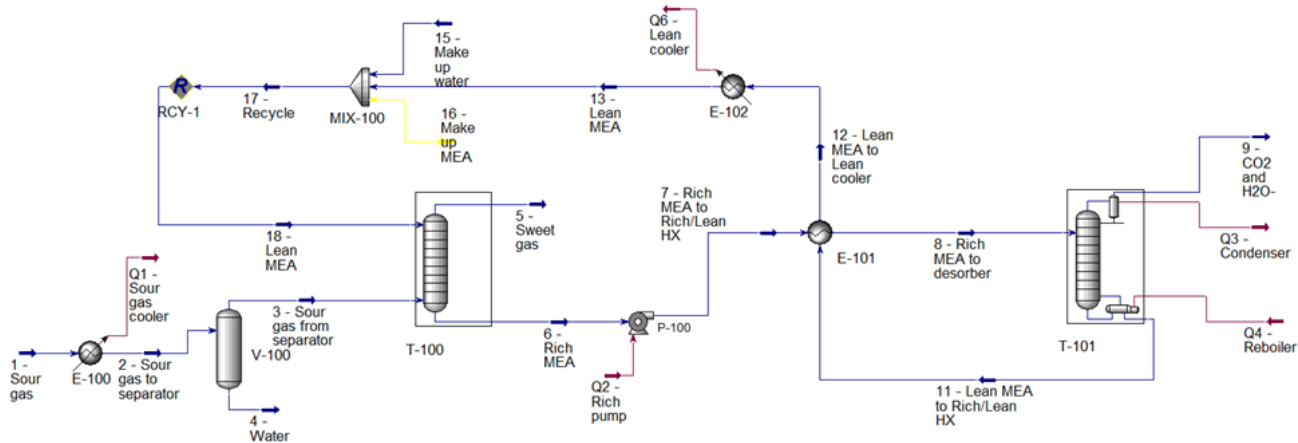


Figure 4. Aspen HYSYS flow-sheet of standard process

Figure 4 shows the representation of the standard process in the simulation program Aspen HYSYS. The calculation sequence is similar to earlier works (Øi, 2007; Aromada and Øi, 2015). First the absorption column T-100 is calculated from the inlet gas and the lean amine (which is first guessed). The rich amine from the bottom of the absorption column passes through the pump P-100 and the main rich/lean heat exchanger E-101 and gains heat from the lean amine from the desorption column. The heated rich amine is entering the desorption column T-101 which calculates the hot lean amine leaving the desorption column. The lean amine from the lean/rich heat exchanger passes through the lean cooler E-102 and is checked in a recycle block RCY-1. It is checked whether the

recycled lean amine is sufficiently close to the earlier guessed lean amine stream, which may be changed by iteration. To simulate a process with vapor recompression, a few specifications in addition to the specifications in Table 1 are necessary. The pressure after depressurization is 1.2 bar and the compressor efficiency is 0.75.

Figure 5 shows the representation of the vapor recompression process in the simulation program Aspen HYSYS. The calculation is slightly more complex than in the standard case. In the calculation sequence, the recompressed gas has to be guessed prior to the calculation of the desorber. After recompression, the recompressed gas has to be iterated by utilizing a recycle block until convergence.

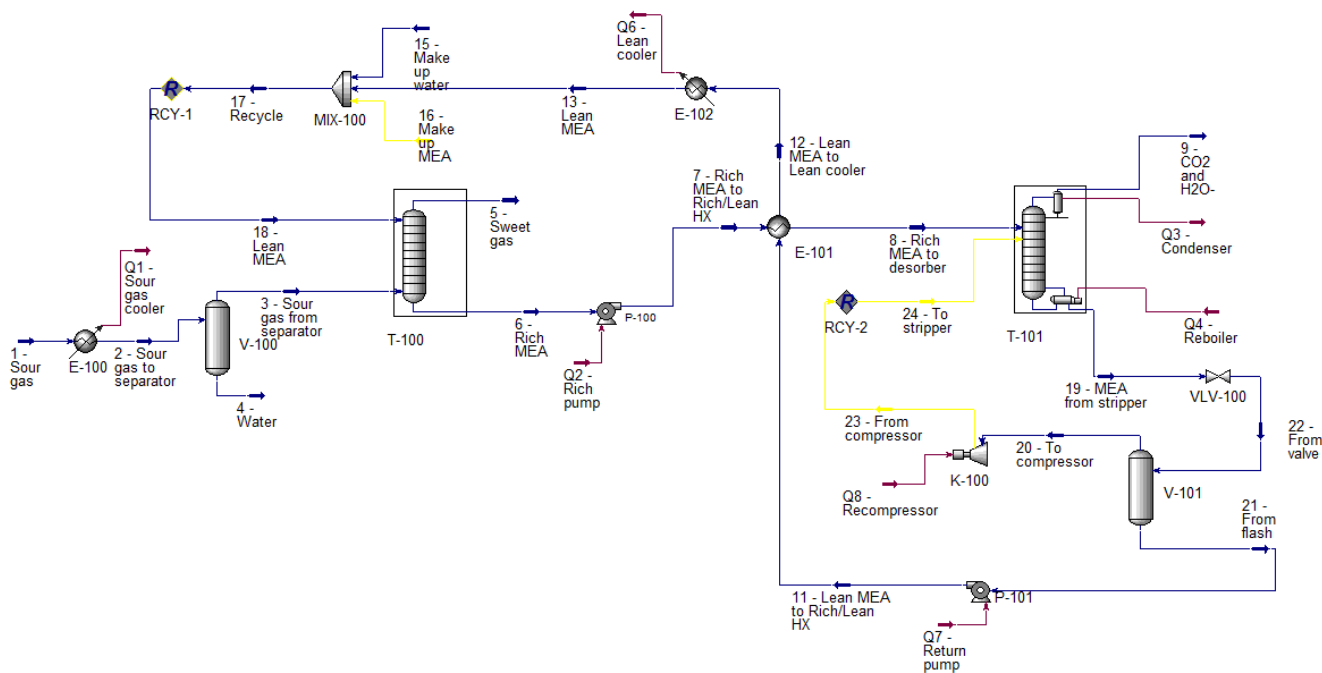


Figure 5. Aspen HYSYS flow-sheet of vapor recompression process

3 Specification of dimensioning and cost estimation calculations

3.1 Scope analysis

The process and cost analysis is limited to the equipment in the flow-sheets in Figure 4 and 5. No pre-treatment like inlet gas purification or cooling is considered. And no treatment after stripping like compression, transport or storage of CO₂ is considered.

The cost estimate is limited to installed cost of listed equipment. It does not include e.g. land procurement, preparation, service buildings or owners cost.

3.2 Assumptions

The dimensions of the process equipment are estimated based on typical dimension factors. The absorption column diameter is based on a gas velocity of 2.0 m/s and the desorption column is based on a gas velocity of 1 m/s. The packing height of the absorption and desorption column is 1 meter per stage with a specified stage efficiency. The total height of the absorption column is the packing height plus 23 meter and the total height of the desorption column is the packing height plus 17 meter.

The heat transfer area of the heat exchangers are calculated based on heat transfer numbers. The main amine/amine heat exchanger has 1500 W/(m²K), the reboiler has 2500 W/(m²K) and the condenser has 2000 W/(m²K). The compressor effect is calculated with an adiabatic efficiency of 0.75.

The electricity cost is set to 0.05 Euro/kWh. The cooling cost is neglected, and the waste heat is specified to be free (zero cost) except for a sensitivity calculation. The maintenance cost was set to 4 % of the total investment per year. The yearly operating time was 8000 hours, the calculation time was set to 25 years and the interest was set to 7.5 %. The construction time was not included.

3.3 Methods used

The equipment cost is calculated in 2013-\$ by the program Aspen In-Plant v8.4. The cost is escalated to 2016 using the CEPCI index and converted to EURO with an exchange rate of 0.904. Stainless steel (SS316) with a material factor of 1.75 was assumed for all equipment units. To calculate the installed cost, all equipment cost (in carbon steel) was multiplied with a detailed installation factor based on data from Eldrup as in earlier works (Øi, 2012; Park, 2016). The installation factors was decreasing with equipment cost. Details can be found in the Master Thesis (Sundbø, 2017).

4 Results and discussion

4.1 Results from removal rate and energy consumption

The CO₂ removal efficiency and energy consumption was calculated for all the alternatives. The process was simulated with a part of the total exhaust gas (part-flow) from 40 up to 100 % (which is full-flow) of the gas through the absorber column. Both the standard case as in Figure 4 and the vapor recompression case as in Figure 5 were simulated. The results are presented in Figure 6 and Figure 7 for the standard case.

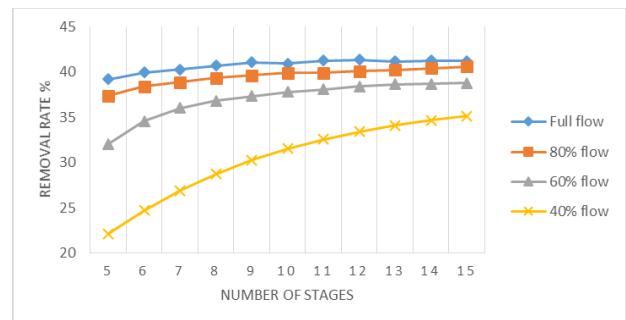


Figure 6. Removal rate as a function of percent full flow and number of stages for the standard case

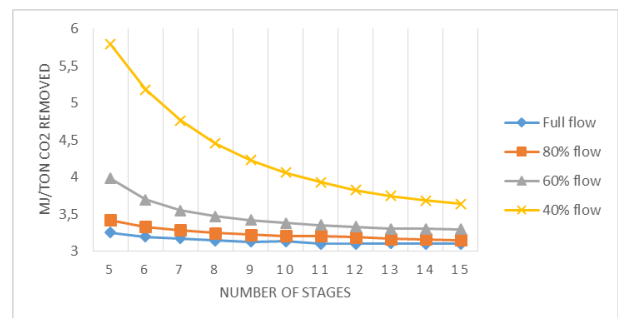


Figure 7. Energy consumption as a function of percent full flow and number of stages for the standard case

Figure 6 clearly shows that the full flow alternative gives a higher removal rate at all column heights and Figure 7 shows that the energy use (per kg CO₂ captured) is lower with full flow. The figures also show that the removal rate increases and the energy use decreases with the number of stages up to about 10 stages. Above 10 stages, there is only small changes.

The results are presented in Figure 8 and Figure 9 for the vapour recompression case.

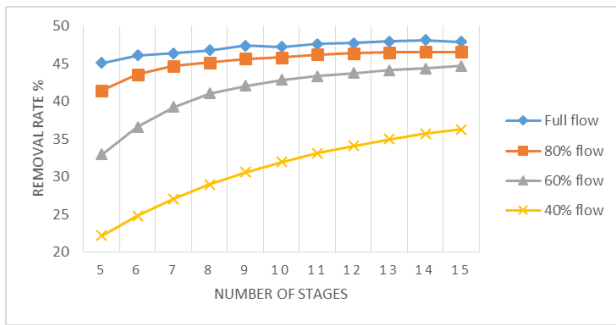


Figure 8. Removal rate as a function of percent full flow and number of stages for the vapor recompression case

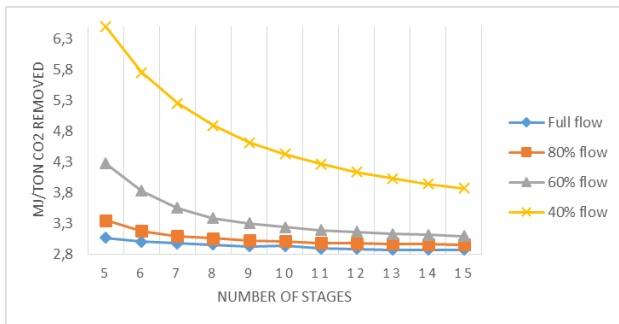


Figure 9. Energy consumption as a function of percent full flow and number of stages for the vapor recompression case

The results show that the full-flow alternative achieved the highest removal efficiency and lowest energy consumption for both the traditional and for the vapour recompression configuration. Without vapour recompression, the removal efficiency varied between 39 and 41 % where the highest removal efficiency was achieved with 15 absorption stages. With vapour recompression, 45 to 48 % was achieved with 5 and 15 absorption stages, respectively. The vapor recompression solution with the highest removal efficiency and the lowest energy consumption at 15 stages, was regarded as the energy optimum process.

4.2 Cost optimization results

The cost estimate was performed after process simulation in Aspen HYSYS and dimensioning of the process equipment. Figure 10 shows the cost estimate distributed on each equipment type for the full-flow standard case and the vapor recompression case.

The cost for 80 % flow was also estimated, and had a higher capital cost. This indicates that a full-flow process is more cost optimum.

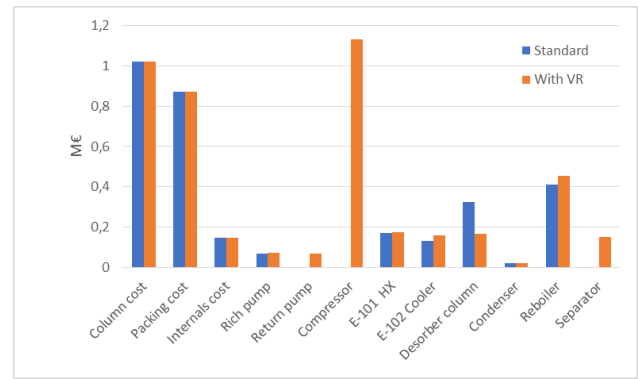


Figure 10. Cost comparison of standard and vapor recompression full-flow process as a function of number of stages

The cost including operating cost was used to calculate the total cost per ton CO₂ captured. Calculated cost for a standard and vapour recompression as a function of number of stages is shown in Figure 11.

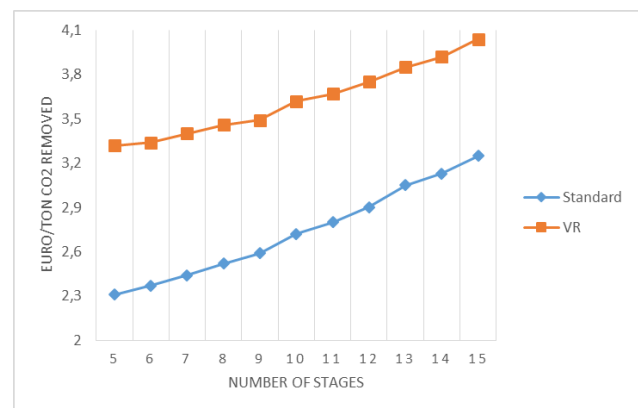


Figure 11. Cost comparison of standard and vapor recompression full-flow process as a function of number of stages

The figure shows that a standard process with a low number of stages gives the lowest cost per ton CO₂ capture. 2.3 Euro/ton CO₂ captured is a very low cost. However, a vapour recompression process will capture considerably more CO₂ as shown in Figure 6 and 8. 3.3 EURO/ton CO₂ captured is also an attractively low cost for CO₂ capture. Another way to compare the two alternatives using the optimum 5 stages, is to calculate the additional cost to capture the additional amount of CO₂. In this case this cost is 10.3 EURO/ton.

In Figure 12, the total project cost for the two alternatives as a function of captured amount CO₂ is shown. The figure shows the cost for the standard process removing 5.5 Mton CO₂ compared to the higher cost for the vapour recompression process removing 6.4 Mton CO₂. The figure illustrates that the capture cost per ton CO₂ captured (which is the slope) increases when the amount of CO₂ captured increases.



Figure 12. Total project cost for the standard and vapour recompression full-flow alternatives as a function of amount CO₂ captured

4.3 Comparisons with earlier work

(Dong et al., 2012) calculated that it was possible to capture 78 % CO₂ in a cement case under other conditions. The amount captured was dependent on the degree of integration. (Park, 2016) concluded as in this work that the lowest total cost per ton CO₂ captured was calculated for the standard full-flow process with 5 absorption stages. This conclusion was however based on the assumption that transport and treating of the gas before or after CO₂ capture was not considered.

4.4 Sensitivity analysis

The capture cost was calculated for varied specifications. The packing equipment cost was doubled in one case, and the recompression compressor cost was doubled in another case. These changes increased the capture cost, but it did not change the conclusions of the optimum solution.

The price of heat was increased from 0 and up to 0.02 EURO/kWh. At a price of 0.02 EURO/kWh, the total cost for both the standard process and the vapor recompression process was 10.6 Euro/ton CO₂ captured. At a higher heat cost, the vapor recompression process would give the lowest cost per ton CO₂ captured.

5 Conclusion

Different process alternatives for partial CO₂ capture were simulated and cost estimated using the process simulation tool Aspen HYSYS.

The number of absorption stages was varied between 5 to 15. The process was simulated with a part of the total exhaust gas (part-flow) from 40 up to 100 % (which is full-flow) of the gas through the absorber column.

The total CO₂ removal efficiency and energy consumption was calculated for all the alternatives. The results showed clearly that the full-flow alternative achieved the highest removal efficiency for both the traditional and for the vapor recompression configuration. The solution with the highest removal efficiency with a heat consumption of 25 MW, was regarded as the energy optimum process.

For some of the process alternatives, the process was cost estimated to find the cost optimum alternative. The lowest total cost per ton CO₂ captured was calculated for the standard full-flow process with a low number of absorption stages. However, the full-flow process with a vapor recompression configuration and a low number of absorption stages had a considerably higher CO₂ removal rate and only a slightly higher total cost per ton CO₂ captured.

References

- Aromada, S. A., Øi, L. E. (2015). Simulation of Improved Absorption Configurations for CO₂ Capture. *Linköping Electronic Conference Proceedings*, 21-30.
- Dong, R., Zhang, Z., Lu, H., Yu, Y. (2012). Recovery of waste heat in cement plants for the capture of CO₂. *Frontiers of Chemical Science and Engineering*, 6(1):104-111.
- Fernandez, E. S., Bergsma, E.J., de Miguel Mercader, F., Goetheer, E.L.V., Vlugt, T.J.H. (2012). Optimisation of lean vapour compression LVC as an OPTION for post-combustion CO₂ capture: Net present value maximisation. *International Journal of Greenhouse Gas Control*, 11:114-121. [doi: http://dx.doi.org/10.1016/j.ijggc.2012.09.007](http://dx.doi.org/10.1016/j.ijggc.2012.09.007)
- IEAGHG (2009). *Partial Capture of CO₂*, IEA Greenhouse Gas R&D Programme, 2009/TR2, Cheltenham, UK.
- Kent, R. L., Eisenberg, B. (1976). Better data for amine treating. *Hydrocarbon processing*, 55(2), 87-90.
- Park, K. (2016). *Optimization of partial CO₂ capture*. Master Thesis, Telemark University College, Porsgrunn, Norway.
- Sundbø, E. (2017). *Partial CO₂ capture simulation and cost estimation*. Master Thesis, University College of Southeast Norway.
- Svolsbru, C. B. (2013). *CO₂ capture alternatives in cement plant*. Master Thesis, Telemark University College, Porsgrunn, Norway.
- Øi, L. E. (2007). *Aspen HYSYS simulation of CO₂ removal by amine absorption a gas based power plant*. The 48th Scandinavian Conference on Simulation and Modelling (SIMS2007) Göteborg, Sweden.
- Øi, L. E. (2012). *Removal of CO₂ from exhaust gas*. PhD Thesis, Telemark University College, Porsgrunn. (TUC 3: 2012)
- Øi, L. E., Bråthen, T., Berg, C., Brekne, S. K., Flatin, M., Johnsen, R., Moen, I. G., Thomassen, E. (2014). Optimization of configurations for amine based CO₂ absorption using Aspen HYSYS. *Energy Procedia*, 51: 224-233.

Modelling and Validation of Hybrid Heavy Duty Vehicles with Exhaust Aftertreatment Systems

Olov Holmer Lars Eriksson

Vehicular Systems, Dept. Electrical Engineering, Linköping University, Sweden, {olov.holmer, lars.eriksson}@liu.se

Abstract

A model of a hybrid electric vehicle including an aftertreatment system is developed and validated. The model describes a vehicle with the same parallel hybrid architecture that is commonly used in commercial heavy duty vehicles and is validated using data gathered from vehicles during real world driving. The goal with the model is to describe the main dynamics of the system and give accurate estimations of fuel consumption and emissions while at the same time keeping simulation times short. The model consists of several sub components, out of which the most important ones are: combustion engine, electric motor, aftertreatment system, driveline, and vehicle chassis. The different components are interchangeable making it possible for the user to change specific components to make the model fit their needs.

Keywords: hybrid heavy duty vehicle, aftertreatment system, vehicle model

1 Introduction

When designing controls systems, models of the system often makes the work significantly easier. This is because the development can be done using simulations which often is faster, and cheaper than using the real system. To facilitate model based development there is a need to have simulation models for the system, and development of models is therefore important. Well documented models for conventional and hybrid heavy duty vehicles exist. Some models of hybrid vehicles with aftertreatment systems also exist, like (Willems and Foster, 2009), however, to the authors knowledge no work where the interplay between exhaust system and hybrid vehicle, where the engine can be shut of, is studied and modeled can be found. Therefore we here aim to fill this gap.

1.1 Contributions

The main contribution is a complete vehicle model with powertrain, vehicle chassis, and after treatment system. In addition, some new component models have been created and a study where the interplay between the aftertreatment system and the hybrid vehicle has been done, to make sure the model can handle all conditions that arise in a hybrid vehicle where the engine can be shut of.

2 Modeling

The hybrid architecture used in the model is a parallel configuration where the engine and motor is connected before the gearbox using a torque coupler. The gearbox is then used to connect the torque coupler with the wheels. In Figure 1 the vehicle configuration and the different components in the model are shown.

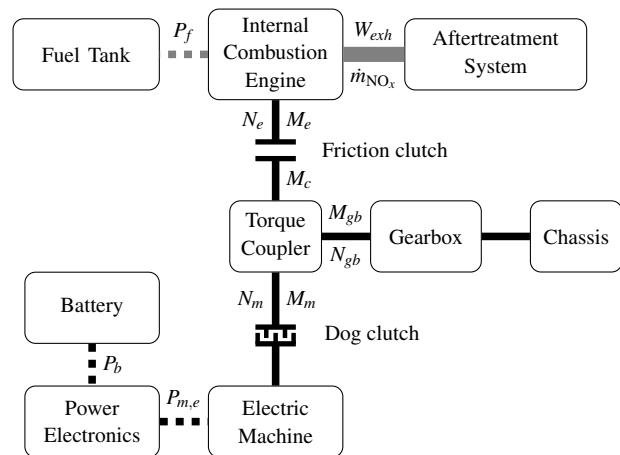


Figure 1. Configuration of the hybrid vehicle.

The sub-models are taken from previous work. However, some work have been done to make the models work in a hybrid vehicle application where the engine is sometimes turned of and the mass flow through the engine and aftertreatment system is zero. Also, a few new models have been developed that describe effects that are negligible in conventional vehicles but become clear in hybrid vehicles. These effects mainly come from that a hybrid vehicle can shut of the engine resulting in zero mass flow through the engine and aftertreatment system. In this section the sub-models are presented.

2.1 Engine

The engine model is taken from (Wahlström and Eriksson, 2011). Some modifications have been done to the model so that it is able to simulate zero exhaust mass flow when the engine is turned of and the model has also been extended with models for a compression release brake, an exhaust brake (or back pressure valve), and models for the composition of the exhaust gas. The model is complex

and well explained in (Wahlström and Eriksson, 2011), therefore only the essential equations and the modifications made to the model are presented here.

The remainder of this section is organized as follows: first the states in the model is described, then the model of the compression release brake is presented followed by an explanation of how the model has been modified to allow zero mas flow, and finally some of the most important equations in the model are presented.

2.1.1 States

The model has 9 states, out of these, four describe the main dynamics of the system and they are pressure in the intake manifold, p_{im} , pressure in the exhaust manifold, p_{em} , pressure before the back pressure valve, p_{bpv} , and turbo speed, ω_t . Two states describe oxygen mass fraction, one in the intake manifold, $X_{O_{im}}$, and one in the exhaust manifold, $X_{O_{em}}$. The last three describe dynamics in the actuators, $\tilde{u}_{egr,1}$ and $\tilde{u}_{egr,2}$ describes the dynamics of the EGR valve and \tilde{u}_{vgt} describes the dynamics of the VGT.

The differential equations for the manifold pressures are based on isothermal models (Eriksson and Nielsen, 2014), which gives

$$\dot{p}_{im} = \frac{RaT_{im}}{V_{im}}(W_c + W_{egr} - W_{ei}) \quad (1)$$

$$\dot{p}_{em} = \frac{RaT_{em}}{V_{em}}(W_{eo} - W_t - W_{egr}) \quad (2)$$

$$\dot{p}_{bpv} = \frac{RaT_{aft.trub}}{V_{bpv}}(W_t - W_{bpv}) \quad (3)$$

where W_i , $i \in \{c, egr, ei, eo, bpv\}$ is the mass flows in and out of the volumes. W_c is the compressor mass flow which mainly depends on ω_t and p_{im} . W_{egr} is the exhaust gas recirculation mass flow which mainly depends on the ratio p_{im}/p_{em} and the control signal u_{egr} . w_{ei} is the cylinder-in mass flow which mainly depends on p_{im} and n_e , W_{eo} is the engine out mass flow which is the sum of W_{ei} and the injected amount of fuel. W_{bpv} is the mass flow past the back pressure valve which is explained below.

The dynamics of the turbo speed follows Newton's second law

$$\dot{\omega}_t = \frac{P_t \eta_m - P_c}{J_t \omega_t} \quad (4)$$

where P_t is the power delivered by the turbine, P_c is the power required by the compressor, J_m is the turbo inertia, and η_m is the mechanical efficiency of the turbocharger. P_t mainly depends on the ratio p_{em}/p_{bpv} , T_{em} , and the control signal u_{vgt} . P_c mainly depends on the ratio p_{im}/p_{amb} .

The differential equations for the oxygen mass fractions

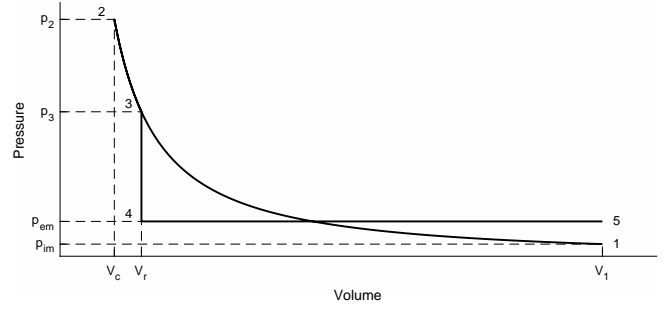


Figure 2. p-V diagram for the compression release brake.

are

$$\dot{X}_{O_{im}} = \frac{RaT_{im}}{p_{im}V_{im}}((X_{O_{em}} - X_{O_{im}})W_{egr} + (X_{O_c} - X_{O_{im}})W_{eo}) \quad (5)$$

$$\dot{X}_{O_{em}} = \frac{ReT_{em}}{p_{em}V_{em}}(X_{O_e} - X_{O_{em}})W_{eo} \quad (6)$$

where $X_{O_c} = 23.14\%$ is the oxygen concentration of air passing through the compressor and X_{O_e} is the oxygen concentration of the exhaust gases coming from the engine.

The states $\tilde{u}_{egr,1}$ and $\tilde{u}_{egr,2}$ are both first order systems with u_{egr} as input and together they make up the dynamics of the EGR valve. The state \tilde{u}_{vgt} is a first order system with u_{vgt} as input and describe the dynamics of the VGT.

2.1.2 Compression release brake

To model the compression release brake we study an ideal cycle shown in Figure 2. The cycle is without combustion and a compression release is done after top dead center at a volume $v_r \geq v_c$.

Exhaust Temperature

To get the exhaust temperature, when using the compression release brake, we start by calculating temperature at the different steps in the cycle.

Compression (1-2)

$$T_2 = T_1 \left(\frac{v_1}{v_2} \right)^{\gamma-1} = r_c^{\gamma-1} \quad (7)$$

Expansion (2-3)

$$T_3 = T_1 \left(\frac{v_2}{v_3} \right)^{\gamma-1} = p_1 \left(\frac{v_1}{v_2} \right)^{\gamma-1} \left(\frac{v_2}{v_3} \right)^{\gamma-1} = T_1 \left(\frac{v_1}{v_3} \right)^{\gamma-1} \quad (8)$$

Compression release (3-4)

$$T_4 = T_3 = T_{exh} \quad (9)$$

The exhaust temperature is thus

$$T_{exh} = T_1 \left(\frac{v_1}{v_3} \right)^{\gamma-1} \quad (10)$$

as can be seen it depends on the ration between v_1 and v_3 , we therefore introduce

$$r_r = \frac{v_1}{v_3} \in [1, r_c] \quad (11)$$

as a tuning parameter.

Brake Torque

To calculate the brake torque we first calculate the work done during this part of the cycle

$$\begin{aligned} W_{crb} &= \int_{1-5} (p - p_{amb}) dv = \int_{v_1}^{v_2} p dv + \int_{v_2}^{v_3} p dv \\ &+ \int_{v_3}^{v_4} p dv + \int_{v_4}^{v_5} p dv - \int_{1-5} p_{amb} dv \\ &= \int_{v_1}^{v_3} p_1 \left(\frac{v_1}{v} \right)^{\gamma} dv + \int_{v_4}^{v_5} p_{em} dv \\ &= \left[p_1 \frac{v_1^{\gamma}}{(1-\gamma)v^{\gamma-1}} \right]_{v_1}^{v_3} + (v_5 - v_4) p_{em} \\ &= \frac{p_1 v_1}{1-\gamma} \left(\left(\frac{v_1}{v_3} \right)^{\gamma-1} - 1 \right) + (v_5 - v_4) p_{em} \\ &= \frac{p_1 v_1}{1-\gamma} (r_r^{\gamma-1} - 1) + (v_5 - v_4) p_{em} \quad (12) \end{aligned}$$

this term can then be added to the torque model.

2.1.3 Engine Shutdown and Zero Mass Flow

Since the engine model contains some singularities at zero mass flow the original model has a saturation on the engine speed that ensures that the mass flow does not get to low. This saturation has been set at 400 RPM, which is well below the normal working range of the engine, however, in a hybrid, where the engine can be shut down, this causes problems since the engine then continues to blow cold air through the aftertreatment system.

To remedy this a switching function is used to calculate the exhaust mass flow, W_{exh} . The switching function chooses between the turbine mass flow, W_t , from the original model and a mass flow calculated based on the volumetric efficiency, $\eta_{vol}(p_{im}, N_e)$, of the engine in the following way

$$W_{exh} = \begin{cases} W_t, & N_e \geq 400 \\ \frac{\eta_{vol}(p_{im}, N_e) p_{im} N_e V_d}{120 R_a T_{im}}, & N_e < 400 \end{cases} \quad (13)$$

The result of the switching function can be seen in Figure 3. In the figure the engine is first idling at around 500 RPM and after one second the engine is turned off. As can be seen the exhaust mass flow in the original model first decreases but when the engine speed reaches 400 RPM the exhaust mass stops falling and remains constant, for the extended model however the exhaust mass

flow continues to drop all the way to zero. It should also be noted that the switching between the two models is smooth.

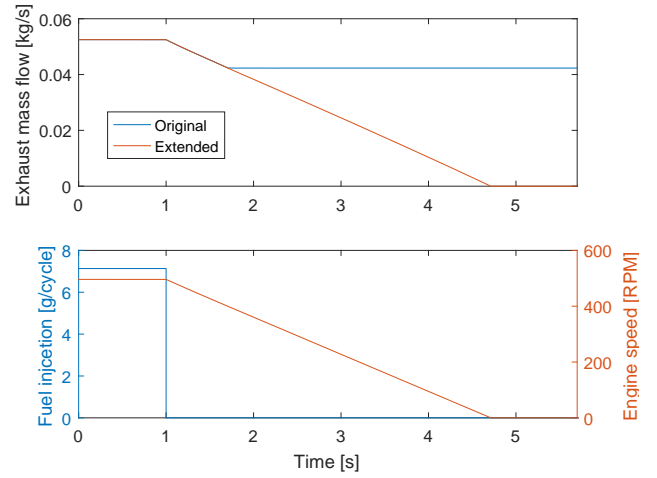


Figure 3. Figure showing mass flow and engine speed during an engine shutdown from both the original, saturated, model and the extended model.

2.1.4 Equations

Here the equations for the engine torque, turbine mass flow, back pressure valve, exhaust temperature, and exhaust gas conditions are presented.

Engine torque

The engine torque, M_e , is modeled using four components: gross indicated torque, M_{ig} , pumping torque, M_p , friction torque M_{fric} , and brake torque from the compression release brake, M_{crb} , in the following way

$$M_e = M_{ig} - M_p - M_{fric} + M_{crb}. \quad (14)$$

The pumping work is calculated as

$$M_p = \frac{V_d}{4\pi} (p_{em} - p_{im}), \quad (15)$$

the gross indicated torque is calculated according to

$$M_{ig} = \frac{u_{\delta} n_{cyl} Q_{HV} \eta_{igch} \left(1 - \frac{1}{r_c^{\gamma_{cyl}-1}} \right)}{4\pi}, \quad (16)$$

the friction torque is calculated using

$$M_{fric} = \frac{V_d}{4\pi} \left(c_{fric,1} \left(\frac{n_e}{100} \right)^2 + c_{fric,2} \frac{n_e}{100} + c_{fric,3} \right), \quad (17)$$

and the brake torque from the compression release brake is calculated as described in Section 2.1.2.

Turbine mass flow

The turbine mass flow is modeled as

$$W_t = \frac{A_{vgt,max} P_{em} f_{\pi_t}(\pi_t) f_{vgt}(\tilde{u}_{vgt})}{\sqrt{T_{em} R_e}} \quad (18)$$

where f_{π_t} and f_{vgt} are functions defined in (Wahlström and Eriksson, 2011). However, due to singularities in the model the engine and turbine speed have lower limit which implicitly induces a lower limit on W_t . Therefore, at engine speeds lower than this limit the turbine mass flow is instead taken as the mass flow given by the speed and volumetric efficiency of the engine:

$$W_t = \frac{\eta_{vol} P_{im} n_e V_d}{120 R_a T_{im}} \quad (19)$$

where the volumetric efficiency, η_{vol} , is modeled as

$$\eta_{vol} = c_{vol,1} \sqrt{P_{im}} + c_{vol,2} \sqrt{n_e} + c_{vol,3}. \quad (20)$$

Back pressure valve To model the back pressure valve a control volume with volume, $V_{b_{pv}}$, and pressure, $p_{b_{pv}}$, is first added after the turbine. The inflow to this control volume is the turbine mass flow and the out flow is the flow past the back pressure valve. The flow past the back pressure valve is modeled using a throttle mass flow model (Eriksson and Nielsen, 2014)

$$W_{b_{pv}} = \frac{P_{us}}{\sqrt{RT_{us}}} A_{b_{pv}} \Psi_{li}(\Pi) \quad (21)$$

where

$$\Pi = \max\left(\frac{p_{b_{pv}}}{p_{eats}}, \left(\frac{2}{\gamma+1}\right)^{\frac{\gamma}{\gamma-1}}\right) \quad (22)$$

and

$$\Psi_{li}(\Pi) = \begin{cases} \sqrt{\frac{2\gamma}{\gamma-1} \left(\Pi^{\frac{2}{\gamma}} - \Pi^{\frac{\gamma+1}{\gamma}}\right)}, & \Pi \leq \Pi_{li} \\ \sqrt{\frac{2\gamma}{\gamma-1} \left(\Pi_{li}^{\frac{2}{\gamma}} - \Pi_{li}^{\frac{\gamma+1}{\gamma}}\right)} \frac{1-\Pi}{1-\Pi_{li}}, & \Pi > \Pi_{li} \end{cases} \quad (23)$$

The linear region, $\Pi > \Pi_{li}$, is used to overcome problems when simulating the system that comes from that the Ψ does not fulfill the Lipschitz condition when the pressure ratio is equal to one (Eriksson and Nielsen, 2014).

Exhaust temperature

The cylinder-out temperature, T_e , is modeled using calculations for an ideal Seliger cycle and is explained in (Wahlström and Eriksson, 2011) when the compression release brake is not used. When the compression release brake is used T_e is modeled as described in Section 2.1.2. Between the turbine and cylinder heat losses are modeled so that the temperature before the turbine, T_{em} , is colder than the cylinder-out temperature.

The temperature after the turbine is calculated using the turbine efficiency, η_t , defined in (Heywood, 1988), giving

$$T_{aft.turb.} = T_{em} \left(1 - \eta_t \left(1 - \Pi_t^{1-1/\gamma_e}\right)\right) \quad (24)$$

The temperature of the pipe between the engine and the EATS is governed by the following dynamic model (Eriksson, 2002)

$$\dot{T}_w = \dot{Q}_i(T_w, T_{aft.turb.}) - \dot{Q}_e(T_w, T_{amb}) \quad (25)$$

where

$$\dot{Q}_i = h_{g,i} A (T_{aft.turb.} - T_w), \quad (26)$$

$$h_{g,i} = \frac{1 - e^{-\frac{h_{cv,i} A}{W c_p}}}{\frac{h_{cv,i} A}{W c_p}} h_{cv,i} \quad (27)$$

and

$$\dot{Q}_e = A (h_{cv,e} (T_w - T_{amb}) + F_v \epsilon \sigma (T_w^4 - T_{amb}^4)). \quad (28)$$

The temperature of the gas entering the EATS can now be calculated as

$$T_{EATS} = T_w + (T_{aft.turb.} - T_w) e^{-\frac{h_{cv,i} A}{W c_p}} \quad (29)$$

Exhaust gas conditions

The NO_x , NO_x , and O_2 concentrations are calculated based on maps depending on the engine torque and speed. The rest of the values are taken direct as the values given by the dynamic engine model.

2.2 Electrical Components

Here the models of the electrical components in the powertrain are described.

2.2.1 Battery

The battery model is based on a Thévenin equivalence circuit with an open circuit voltage, U_{oc} , that depends on the state of charge, SOC , and internal resistance R_i .

The battery current, I_b , is calculated as

$$I_b = \frac{U_{oc}(SOC)}{2R_i} - \sqrt{\frac{U_{oc}(SOC)^2}{4R_i^2} - \frac{P_b}{R_i}} \quad (30)$$

where P_b is the terminal power of the battery, R_i is the internal resistance of the battery, and U_{oc} is the open circuit voltage. The dynamics of the SOC is

$$\dot{SOC} = -\frac{I_b}{Q_0} \quad (31)$$

and U_{oc} is calculated using maps based on the SOC .

2.2.2 Power Electronics

The model of the power electronics takes a desired motor power, $P_{m,d}$, and the required power from the auxiliary units, P_{aux} , and calculates the necessary battery power, P_b , and actual electrical power to the motor $P_{m,e}$. Since the losses in the power electronics are included in the motor model, the power electronics is modeled as ideal. This means that the model of the power electronics only have to ensure that the battery and electric machine work within there limits. The battery power is calculated as

$$P_b = \begin{cases} P_{b,max}, & P_{m,d} + P_{aux} \geq P_{b,max} \\ P_{m,d} + P_{aux}, & P_{b,min} \leq P_{m,d} + P_{aux} \leq P_{b,max} \\ P_{b,min}, & P_{m,d} + P_{aux} \leq P_{b,min} \end{cases} \quad (32)$$

and the motor power is calculated as

$$P_{m,e} = \begin{cases} P_{b,max} - \bar{P}_{aux}, & P_{m,d} \geq P_{b,max} - \bar{P}_{aux} \\ P_{m,d}, & P_{b,min} - \bar{P}_{aux} \leq P_{m,d} \leq P_{b,max} - \bar{P}_{aux} \\ P_{b,min} - \bar{P}_{aux}, & P_{m,d} \leq P_{b,min} - \bar{P}_{aux} \end{cases} \quad (33)$$

where

$$\bar{P}_{aux} = \begin{cases} P_{b,max}, & P_{aux} \geq P_{b,max} \\ P_{aux}, & P_{b,min} \leq P_{aux} \leq P_{b,max} \\ P_{b,min}, & P_{aux} \leq P_{b,min} \end{cases} \quad (34)$$

2.2.3 Electric Motor

The motor model is a static model of a permanent magnet synchronous machine taken from (Sundström et al., 2015). When the model is parameterized the losses in the power electronics are included and in that way the model also include these losses. The current in the stator, I_m , is calculated as

$$I_m = \frac{1}{R_m}(U_m - k_i \omega_m) \quad (35)$$

where, U_m , is the voltage over the motor, calculated as

$$U_m = \frac{k_i \omega_m}{2} + \sqrt{\frac{k_i^2 \omega_m^2}{4} + P_{m,e} R_m}. \quad (36)$$

The output torque is calculated as

$$M_m = k_a I_m - c_f \omega_m \quad (37)$$

where k_a is defined as

$$k_a = \begin{cases} k_i \eta_m, & I_m \geq 0 \\ \frac{k_i}{\eta_m}, & I_m < 0 \end{cases}. \quad (38)$$

The limits $P_{m,max}$ and $P_{m,min}$ are calculated using maps depending on n_m .

2.3 Aftertreatment system

The aftertreatment system consists of three active components: a diesel oxidation catalyst, DOC, a diesel particulate filter, DPF, and a selective catalytic reduction, SCR, catalyst. The components are also enclosed inside a silencer.

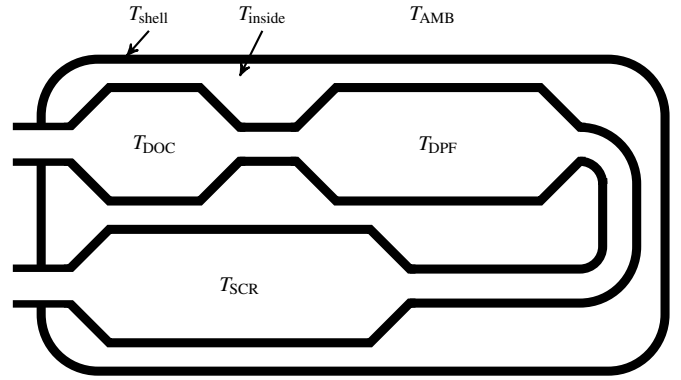


Figure 4. Temperatures of the different components inside the silencer.

2.3.1 Silencer

The silencer model has one state for the temperature inside the silencer, T_{inside} , governed by the following differential equation

$$\dot{T}_{inside} = \frac{h_{solid \leftrightarrow air}}{c_{p,air} m_{air}} (A_{doc} (T_{doc} - T_{inside}) + A_{dpf} (T_{dpf} - T_{inside}) + A_{scr} (T_{scr} - T_{inside}) + A_{shell} (T_{shell} - T_{inside})) \quad (39)$$

and one state for the temperature of the shell of the silencer, T_{shell} , governed by the following differential equation

$$\dot{T}_{shell} = \frac{A_{shell}}{c_{p,air} m_{air}} (h_{solid \leftrightarrow air} (T_{inside} - T_{shell}) + h_{solid \leftrightarrow amb} (T_{amb} - T_{shell})) \quad (40)$$

2.3.2 Energy Balance Modeling

To model the temperature inside the substrates the models in (Winkler et al., 2003; Van Helden et al., 2004) is used as a starting point. The following energy balance is used in the gas phase

$$\varepsilon \rho_g C_{p,g} \frac{dT_g}{dt} = -v \varepsilon \rho_g C_{p,g} \frac{\partial T_g}{\partial x} - h_{g \leftrightarrow s} a_{g \leftrightarrow s} (T_g - T_s) \quad (41)$$

and in the solid phase

$$(1 - \varepsilon) \rho_s C_{p,s} \frac{dT_s}{dt} = (1 - \varepsilon) \lambda_s \frac{\partial^2 T_s}{\partial x^2} + h_{g \leftrightarrow s} a_{g \leftrightarrow s} (T_g - T_s) - h_{s \leftrightarrow a} a_{s \leftrightarrow a} (T_s - T_a) + \sum_{reactions} r_j \Delta H_j \quad (42)$$

To simplify the model the following assumptions are then made

1. Instantaneous equilibrium between brick material and exhaust gas, resulting in $dT_g/dt = 0$ and $T_g = T_s$
2. Conductive heat transport \ll convective heat transport, and the term $(1 - \varepsilon) \lambda_s \frac{\partial^2 T_s}{\partial x^2}$ in (42) can therefore be omitted

3. No significant endothermic or exothermic reactions, i.e. we assume

$$\sum_{\text{reactions}} r_j \Delta H_j = 0$$

Using the assumption $dT_g/dt = 0$ and (41), we get

$$v \varepsilon \rho_g C_{p,g} \frac{\partial T_g}{\partial x} = -h_{g \leftrightarrow s} a_{g \leftrightarrow s} (T_g - T_s) \quad (43)$$

Using assumptions 1 and 2, (42) becomes

$$(1 - \varepsilon) \rho_s C_{p,s} \frac{dT_s}{dt} = h_{g \leftrightarrow s} a_{g \leftrightarrow s} (T_g - T_s) - h_{s \leftrightarrow a} a_{s \leftrightarrow a} (T_s - T_a) \quad (44)$$

By combining (43), (44) and the assumption that $T_g = T_s$ we get

$$(1 - \varepsilon) \rho_s C_{p,s} \frac{dT_g}{dt} = -v \varepsilon \rho_g C_{p,g} \frac{\partial T_g}{\partial x} - h_{s \leftrightarrow a} a_{s \leftrightarrow a} (T_g - T_a) \quad (45)$$

On a catalyst segment of length L we can use the following approximation

$$\frac{\partial T_g}{\partial x} = \frac{T_{g,out} - T_{g,in}}{L} \quad (46)$$

where $T_{g,in}$ and $T_{g,out}$ is the temperature of the gas entering and leaving the segment, respectively. Finally, by combining (45) and (46) we get

$$\frac{dT_{g,out}}{dt} = -\frac{1}{(1 - \varepsilon) \rho_s C_{p,s}} \left(v \varepsilon \rho_g C_{p,g} \frac{T_{g,out} - T_{g,in}}{L} + h_{s \leftrightarrow a} a_{s \leftrightarrow a} (T_{g,out} - T_a) \right) \quad (47)$$

2.3.3 Temperature Sensors

Since the dynamics of the temperature sensors can be quite significant models for these are needed. The model includes conduction from the gas surrounding the sensor and radiation from the surroundings and is described below.

The density of the gas can, using the ideal gas law, be calculated as

$$\rho = \frac{p}{RT_g} \quad (48)$$

using this the velocity of the gas can be calculated using

$$V = \frac{W_{exh}}{A_{pipe} \rho} \quad (49)$$

The Reynolds number is calculated as

$$Re = \frac{VD_{sens}}{\gamma} \quad (50)$$

where

$$\gamma = \frac{\mu}{\rho} \quad (51)$$

The Nusselt number is calculated according to (Holman, 1986) as

$$Nu = \begin{cases} 0.3 + \frac{0.62 Re^{1/2} Pr^{1/3}}{\left(1 + \left(\frac{0.4}{Pr}\right)^{2/3}\right)^{1/4}} \left(1 + \left(\frac{Re}{282000}\right)^{5/8}\right)^{4/5} & RePr \geq 0.2 \\ \frac{1}{0.8237 - 0.5 \ln(RePr)} & RePr < 0.2 \end{cases} \quad (52)$$

however this gives very low values for low mass flows and therefore a lower saturation, Nu_{min} , is used.

The heat transfer coefficient can now be calculated as

$$h = \frac{k_{exh} Nu}{D_{sens}} \quad (53)$$

By assuming that the length of the sensor is twice the diameter of the sensor, the area of the sensor is

$$A_{sens} = \pi D_{sens}^2 \quad (54)$$

and the mass of the sensor is

$$m_{sens} = \rho_{sens} \frac{\pi D_{sens}^3}{2} \quad (55)$$

The dynamics of the sensor can now be written

$$\dot{T}_s = \frac{h A_{sens} (T_g - T_s) - \varepsilon \sigma A_{sens} (T_s^4 - T_w^4)}{m_{sens} c_p} \quad (56)$$

2.3.4 Diesel Oxidation Catalyst

The temperature of the DOC calculated as described Section 2.3.2. The oxidation of NO is calculated using a map depending on the temperature of the DOC and exhaust mass flow.

2.3.5 Diesel Particulate Filter

The DPF is split lengthwise into five segments and each segment has a state describing its temperature. The temperature in each segment is calculated as described in Section 2.3.2, and the surface temperature is taken as the mean of the temperatures of all segments. No reactions or filtering is modeled in the DPF.

2.3.6 Selective Catalytic Reduction Catalyst

Like the DPF, the SCR is split lengthwise into five segments and each segment has a state describing its temperature and ammonia surface coverage. The temperature in each segment is calculated as described in Section 2.3.2. The reactions and mass balances in the catalyst is modeled similarly to (Winkler et al., 2003; Van Helden et al., 2004) and is described below.

In each segment NH_3 adsorption and desorption



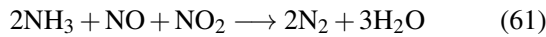
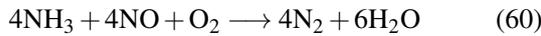
are modeled using the reaction rate expressions

$$r_a = k_a^0 \exp\left(\frac{-E_a^0}{R} \left(\frac{1}{T_s} - \frac{1}{T_{ref}}\right)\right) C_{\text{NH}_3} (1 - \Theta_{\text{NH}_3}) \quad (58)$$

$$r_d = k_d^0 \exp\left(\frac{-E_d^0 (1 - \alpha \Theta_{\text{NH}_3})}{R} \left(\frac{1}{T_s} - \frac{1}{T_{ref}}\right)\right) \Theta_{\text{NH}_3} \quad (59)$$

where k_i and E_i^0 is the pre-exponential factor and activation energy for reaction i , respectively, C_i is the concentration of specie i , T_s is the substrate temperature, and Θ_{NH_3} is the ammonia surface coverage.

In the SCR catalyst the following NO_x reducing reactions modeled are:



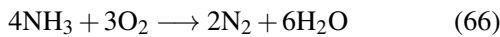
and they are modeled using the following reaction rate expressions

$$r_{std} = k_{std}^0 \exp\left(\frac{-E_{std}}{R} \left(\frac{1}{T_s} - \frac{1}{T_{ref}}\right)\right) C_{\text{NO}} \Theta_{\text{NH}_3}^* \times \left(1 - \exp\left(\frac{-\Theta_{\text{NH}_3}}{\Theta_{\text{NH}_3}^*}\right)\right) \quad (63)$$

$$r_{fst} = k_{fst}^0 \exp\left(\frac{-E_{fst}}{R} \left(\frac{1}{T_s} - \frac{1}{T_{ref}}\right)\right) C_{\text{NO}} C_{\text{NO}_2} \Theta_{\text{NH}_3} \quad (64)$$

$$r_{slw} = k_{slw}^0 \exp\left(\frac{-E_{slw}}{R} \left(\frac{1}{T_s} - \frac{1}{T_{ref}}\right)\right) C_{\text{NO}_2} \Theta_{\text{NH}_3} \quad (65)$$

NH_3 oxidation



is modeled by

$$r_{ox\text{NH}_3} = k_{ox\text{NH}_3}^0 \exp\left(\frac{-E_{ox\text{NH}_3}}{R} \left(\frac{1}{T_s} - \frac{1}{T_{ref}}\right)\right) \Theta_{\text{NH}_3} \quad (67)$$

Finally, hydrolysis of HNCO



is modeled by

$$r_{\text{HNCO}} = k_{\text{HNCO}}^0 \exp\left(\frac{-E_{\text{HNCO}}}{R} \left(\frac{1}{T_s} - \frac{1}{T_{ref}}\right)\right) C_{\text{HNCO}} \quad (69)$$

Using these reaction rates, the surface coverage mass balance is modeled as

$$\frac{d\Theta_{\text{NH}_3}}{dt} = r_a - r_d - 4r_{std} - 2r_{fst} - 8r_{slw} - 4r_{ox\text{NH}_3} \quad (70)$$

and species mass balances in the gas phase are modeled by

$$\frac{dC_{\text{HNCO}}}{dt} = -v \frac{\partial C_{\text{HNCO}}}{\partial x} - r_{\text{HNCO}} \quad (71)$$

$$\frac{dC_{\text{NH}_3}}{dt} = -v \frac{\partial C_{\text{NH}_3}}{\partial x} - \Omega(r_a - r_d) + r_{\text{HNCO}} \quad (72)$$

$$\frac{dC_{\text{NO}}}{dt} = -v \frac{\partial C_{\text{NO}}}{\partial x} - \Omega(4r_{std} + r_{fst} + r_{slw}) \quad (73)$$

$$\frac{dC_{\text{NO}_2}}{dt} = -v \frac{\partial C_{\text{NO}_2}}{\partial x} - \Omega(r_{fst} + 6r_{slw}) \quad (74)$$

where v is the velocity of the gas in the segment. All of these concentrations can be written on the form

$$\frac{dC_i}{dt} = -v \frac{\partial C_i}{\partial x} + \sum_j k_j r_j \quad (75)$$

with appropriate choices of k_j . By assuming the catalyst is working as a plug flow reactor, meaning there is no local accumulation of gas phase species, we get

$$\frac{dC_i}{dt} = 0 \implies \frac{\partial C_i}{\partial x} = \frac{1}{v} \sum_j k_j r_j \quad (76)$$

and for a segment of length L , given the concentration at the inlet, $C_{i,in}$, we can calculate the concentration at the outlet, $C_{i,out}$, using the approximation

$$C_{i,out} = C_{i,in} + \frac{L}{v} \sum_j k_j r_j \quad (77)$$

When using this approximation we get a singularity at $v = 0$. However, this can easily be handled by limiting v and not let it become smaller than a given value. By choosing a small enough limit on v the model can still produce accurate results since for small v the mass flow out of the aftertreatment system is small and does not influence the results very much.

2.3.7 Pressure Drop

The back pressure from the EATS, p_{eats} , is modeled by a control volume between the turbine and the EATS using following differential equation

$$\dot{p}_{eats} = \frac{R_a T_{eats}}{V_{eats}} (W_t - W_{eats}) \quad (78)$$

where the, W_{eats} is the mass flow thorough the EATS. To get W_{eats} the EATS is modeled as a incompressible turbulent restriction (Eriksson and Nielsen, 2014), giving us

$$W_{eats} = \begin{cases} C_{tu} \sqrt{\frac{p_{eats}}{RT_{eats}}} \sqrt{\Delta p}, & \Delta p \geq \Delta p_{lin} \\ C_{tu} \sqrt{\frac{p_{eats}}{RT_{eats}}} \frac{\Delta p}{\sqrt{\Delta p_{lin}}}, & \Delta p < \Delta p_{lin} \end{cases} \quad (79)$$

where $\Delta p = p_{eats} - p_{amb}$, and Δp_{lin} is the size of the linear region and is used to make the model Lipschitz continuous.

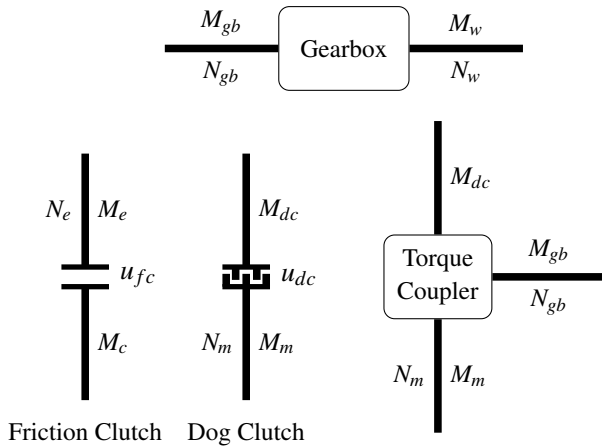


Figure 5. Components in the driveline.

2.4 Driveline

The driveline model consists of four components: a friction clutch, a dog clutch, a torque coupler, and a transmission. Here the equations of the components are described using the notation shown in Figure 5.

Torque coupler

The torque coupler connects the engine and the motor. To match the speed of the components a gear ratio, i_{tc} , is used. The equations for the torque coupler becomes

$$M_{tc} = \bar{M}_e + i_{tc}\bar{M}_m \quad (80)$$

$$J_{tc} = \bar{J}_e + i_{tc}^2\bar{J}_m \quad (81)$$

$$n_e = n_{tc} = i_{tc}n_m \quad (82)$$

Gearbox

The gearbox has a gear ratio $i_g = i_g(u_g)$ that connects the speed of the torque coupler with the speed of the wheels

$$\omega_{tc} = i_g\omega_w. \quad (83)$$

The efficiency of the gearbox is also modeled using $\eta_{gb} = \eta_{gb}(u_g)$ in the following way

$$M_w = \eta_{gb}^{\text{sgn}(M_{tc})} i_g M_{tc}. \quad (84)$$

Note that η_{gb} depends on which gear that is engaged (typically the highest gear is more efficient than the rest of the gears).

Dog clutch

The dog clutch is used to decouple the motor from the rest of the driveline. The dog clutch can either be locked ($u_{dc} = 1$) or completely open ($u_{dc} = 0$). Mathematically this is expressed as

$$\bar{M}_m = \begin{cases} M_m, & u_{dc} = 1 \\ 0, & u_{dc} = 0 \end{cases} \quad (85)$$

$$\bar{J}_m = \begin{cases} J_m, & u_{dc} = 1 \\ 0, & u_{dc} = 0 \end{cases} \quad (86)$$

Friction Clutch

The clutch model is taken from (Eriksson, 2001). The clutch position $u_{fc} \in [0, 1]$ controls the friction clutch (0 means fully separated clutch and 1 means full force on the clutch discs). The clutch can either be slipping $\omega_e \neq \omega_c$ or locked $\omega_e = \omega_c$. When the clutch is slipping the two masses move independently governed by the following differential equations

$$J_e \dot{\omega}_e = M_e - M_c \quad (87)$$

$$J_{tot} \dot{\omega}_c = M_c - M_{tot} \quad (88)$$

where J_{tot} and M_{tot} is the total inertia and torque, respectively, on the wheel side. The total inertia is the sum of the equivalent inertia of the vehicle and motor, which is

$$J_{tot} = \frac{J_w}{i_g^2} + u_{dc} i_{tc}^2 J_m \quad (89)$$

and the total torque is

$$M_{tot} = u_{dc} i_g M_m - \frac{M_w}{i_g}. \quad (90)$$

In this case the torque transferred through the clutch is

$$M_c = M_{max,k} u_{cl} \text{sgn}(\omega_e - \omega_c) \quad (91)$$

When the clutch is locked the two systems should rotate with identical speed. The governing differential equation now becomes

$$(J_e + J_{tot}) \dot{\omega}_e = M_e - M_{tot}. \quad (92)$$

For this to hold the transferred torque through the clutch must be

$$M_c = \frac{M_e J_{tot} + M_{tot} J_e}{J_e + J_{tot}}. \quad (93)$$

This torque is also compared with the maximum static torque possible to transfer through the clutch, in order to determine if the clutch should start slipping. More information about the clutch model can be found in (Eriksson, 2001).

2.5 Chassis

The chassis model describes the vehicles interaction with the environment by calculating the resistive forces acting on the vehicle. The total resistive force acting on the vehicle is a sum of four components

$$F = F_a + F_r + F_g + F_b \quad (94)$$

where

$$F_a = \frac{1}{2} \rho C_d A v^2 \quad (95)$$

is the aerodynamic resistance,

$$F_r = \cos \alpha mg (C_{r,0} + C_{r,1} v^2) \quad (96)$$

is the rolling resistance,

$$F_g = \sin \alpha mg \quad (97)$$

is the gravitational force, and

$$F_b = \min(u_b K_b, mg) \quad (98)$$

is the force generated by the brakes. The vehicle torque is calculated as

$$M_{vehicle} = r_w F. \quad (99)$$

and the equivalent vehicle inertia is

$$J_{vehicle} = mr_w^2. \quad (100)$$

3 Parameterization and Validation

The parameterization and validation have been done using data from two vehicles, some specifications of these vehicles are shown in Table 1. The data that was used consist of measurements from a set of sensors during real world driving. All models are based on physical properties of the system and as a starting point physically reasonable values on all parameters are chosen, but to get a better agreement with measurements tuning of some parameters have been done. The rest of this section contains the parameterization and validation of the different components in the model.

Table 1. Vehicle specifications

	Vehicle 1	Vehicle 2
Type	Bus	Truck
Engine	5 Liter	10.6 Liter
Motor	100 kW / 900 Nm	136 kW / 1050 Nm
Weight	14.5 Tonnes	14.5 Tonnes

3.1 Engine

In the engine model the parameters in Table 2 was tuned. V_d was taken as the actual engine size of the vehicle. The rest of the parameters were tuned using the fact that the change in mass flow is proportional to the change in engine size, i.e.

$$W = \gamma W_{org} \quad (101)$$

where

$$\gamma = \frac{V_d}{V_{d,org}} \quad (102)$$

where the index *org* refers to the mass flow and size of the original engine. From the model equations we also get that

$$R_c \propto W^{1/3} \quad (103)$$

$$R_t \propto W^{1/3} \quad (104)$$

$$A_{vgt,max} \propto W \quad (105)$$

and therefore the new values are taken as

$$R_c = \gamma^{1/3} R_{c,org} \quad (106)$$

$$R_t = \gamma^{1/3} R_{t,org} \quad (107)$$

$$A_{vgt,max} = \gamma A_{vgt,max,org} \quad (108)$$

When validating the engine, the measured engine speed and torque was used as inputs to the model. The rest of the control signals were held constant, VGT at 60%, EGR fully closed, and no engine brakes were used. From the measured engine torque the appropriate amount of fuel was calculated using the inverse of the torque model. The result from vehicle 2 is shown in Figure 6, where it can be seen that the exhaust flow from the model agree well with the measured. However, the temperature does not agree quite as well. One possible explanation for this is that relatively small errors in mass flow induce large errors in the temperature, and therefore the model can be better than what this figure gives the impression of.

Table 2. Tuned parameters in the engine model.

V_d	Engine displacement
R_c	Compressor radius
R_t	Compressor radius
$A_{vgt,max}$	Maximal VGT area

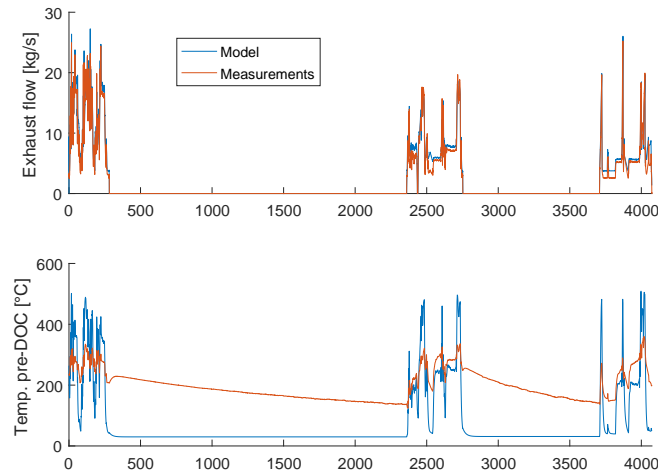


Figure 6. Measured and simulated exhaust mass flow and exhaust temperature for vehicle 2.

3.2 EATS

In the EATS model the parameters in Table 3 was tuned. The lengths L_i and diameters D_i was scaled, compared to the original model, so that the volumes of the components scaled proportional to the change in maximal mass flow. The rest of the parameters was tuned by simulating the system using the measured mass flow and temperature before the DOC as inputs.

Since the measured temperature before the DOC was measured with a temperature sensor, the measurements

also include the dynamics of the sensor. Therefore the measurements was first inverse filtered. By using the following model for the sensor

$$\dot{T}_s = C_s h(W_{exh})(T_g - T_s) \quad (109)$$

where T_s is the temperature measured by the sensor, T_g is the temperature of the exhaust gas, C_s is a tuning constant, and h is defined in (53). Using this we can calculate T_g as

$$T_g = T_s + \frac{1}{C_s h(W_{exh})} \dot{T}_s. \quad (110)$$

\dot{T}_s was calculated numerical from the measurements and C_s was chosen so that the time constant of the sensor was around 7 seconds at a mass flow of an idling engine. The filtered measurements and time constants for the sensor can be seen in Figure 7.

Table 3. Tuned parameters in the EATS model.

L_i	Length of component $i \in \{doc, dpf, scr\}$
D_i	Diameter of component $i \in \{doc, dpf, scr\}$
$\rho_{solid,i}$	Density of component $i \in \{doc, dpf, scr\}$
$h_{solid \leftrightarrow amb}$	Heat transfer coefficient, solid to ambient
$h_{solid \leftrightarrow air}$	Heat transfer coefficient, solid to air

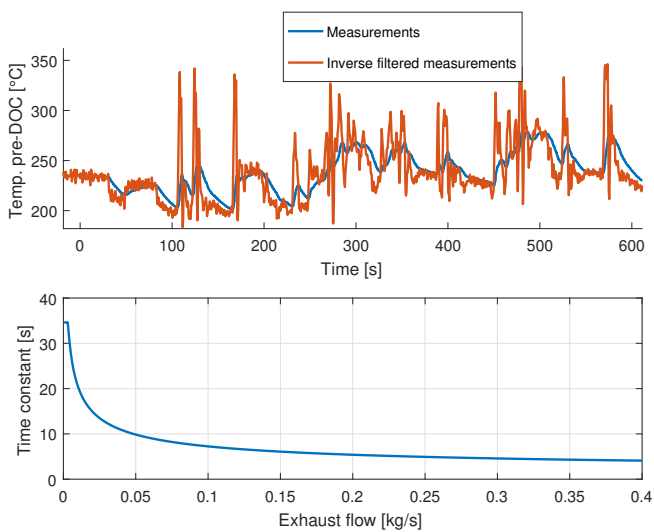


Figure 7. Inverse filtered temperature measurements and time constant for the temperature sensor.

The validation for vehicle 1 and 2 can be seen in Figure 8 and Figure 9, respectively. As can be seen the model and measurements agree well at higher mass flows. When the mass flow is zero, however, they do not agree well, but when the mass flow increases they quickly converge again. No validation data for the temperature after the SCR was available, but in Figure 10 measured temperature after the DPF and modeled temperature after the SCR, for vehicle 2, is shown. As expected the temperature after the SCR is a slightly smoothed version of the temperature after the DPF, however, fast transient due to changes in mass flow are not smoothed.

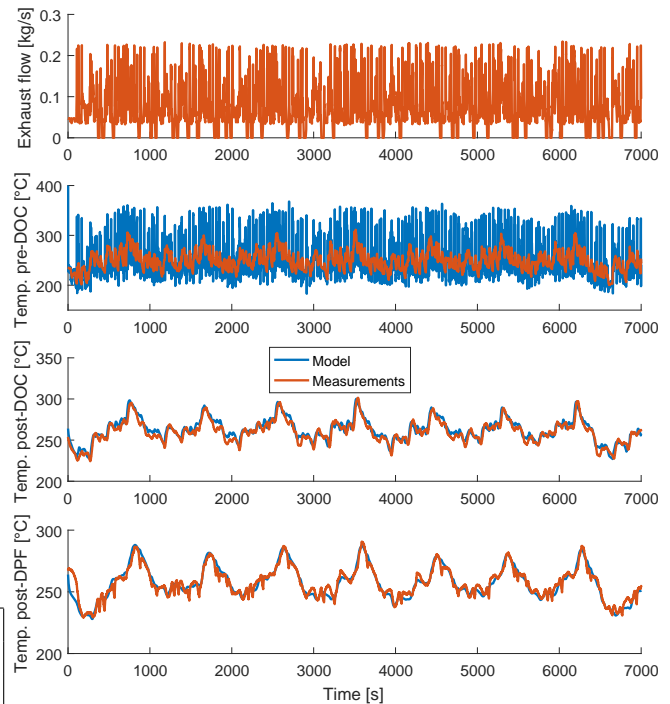


Figure 8. Exhaust flow and modeled and measured temperatures in the following places: before the DOC (here model is inverse filtered measurements), after the DOC, and after the DPF. All data is from vehicle 1.

3.3 Electrics

The parameters for the motor model was estimated, using least squares, from a map of the power losses of a motor that was produced by a motor design tool developed in (Le Berr et al., 2012). The parameters for the battery was taken from (Energy, 2016).

To validate the model the required current from the motor model, when producing the same torque and at the same speed as the measured, was compared to the measured current. The measured current also include the current required from auxiliary components and therefore a current equivalent to a power of 10 kW was subtracted from the measured current. The result for vehicle 1 is shown in Figure 11, where it can be seen that the modeled and measured current mostly agree well, especially considering that the power required by the auxiliary components most likely varies a little with the time.

3.4 Chassis

The parameters for the chassis model are taken from (Eriksson et al., 2016). The validation of the chassis model was done by using the measured road slope, motor torque, engine torque, and gear as input signals to the model. The torque from the engine and motor was transformed to appropriate input signals to the engine and motor model by using the inverse of their torque models. Since no information of how the friction brakes were used was available a brake controller was also included. The brake controller

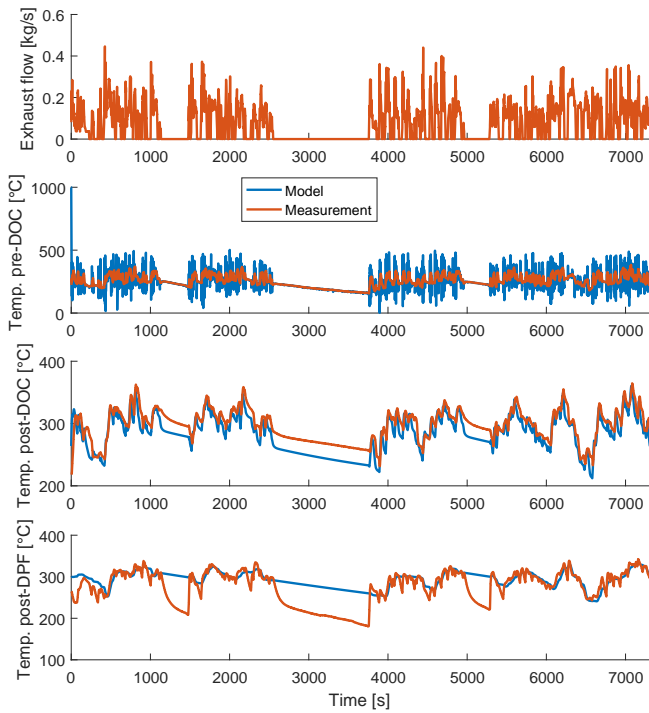


Figure 9. Exhaust flow and modeled and measured temperatures in the following places: before the DOC (here model is inverse filtered measurements), after the DOC, and after the DPF. All data is from vehicle 2.

is a proportional controller with a dead band. The dead band is 5 km/h and is included to avoid unnecessary braking. Also, when the measured speed was zero the brakes were applied to make sure the vehicle is standing still even if it is in a down or uphill. The result for vehicle 1 is shown in Figure 12. As can be seen the modeled and measured velocity agree well large parts of the simulation and the simulated speed is about as often higher than the measured as it is lower.

4 Conclusions

A model of a complete hybrid vehicle with an aftertreatment system has been developed and documented. The model contains several subcomponents and is based on the physical properties of the system. Parameterization and validation of the model have been done using measurements gathered from two vehicles during real world driving, and the model has shown to agree well with the measurements.

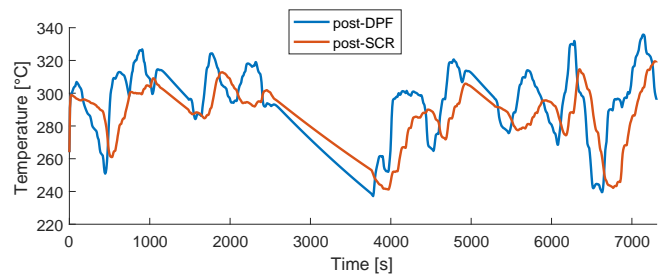


Figure 10. Measured temperature after the DPF and modeled temperature after the SCR for vehicle 2.

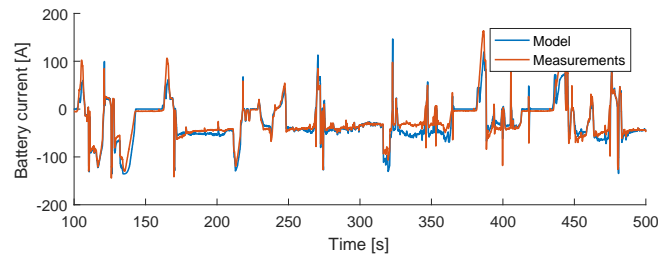


Figure 11. Measured and modeled current required by the motor for vehicle 1.

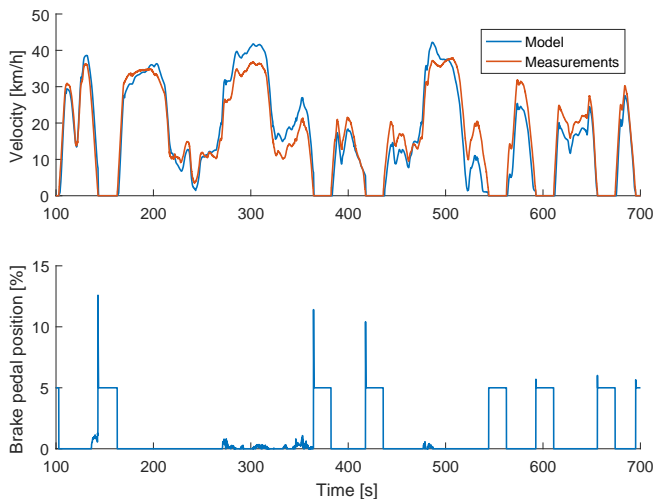


Figure 12. Measured and simulated vehicle speed or vehicle 1.

References

- XALT Energy. Xalt 31 ah high power (hp) superior lithium ion cell. Available from: <http://www.xaltenergy.com>, [28 October 2016], 2016.
- Lars Eriksson. Simulation of a vehicle in longitudinal motion with clutch lock and clutch release. *Vehicular Systems, ISY Linköping Institute of Technology, Linköping*, 2001.
- Lars Eriksson. Mean value models for exhaust system temperatures. Technical report, SAE Technical Paper, 2002.
- Lars Eriksson and Lars Nielsen. *Modeling and control of engines and drivelines*. John Wiley & Sons, 2014.
- Lars Eriksson, Anders Larsson, and Andreas Thomasson. The aac2016 benchmark-look-ahead control of heavy duty trucks on open roads. *IFAC-PapersOnLine*, 49(11), 2016.
- John Heywood. *Internal combustion engine fundamentals*. McGraw-Hill Education, 1988.
- JP Holman. Heat transfer, 1986. *Mc Gran-Hill Book Company, Southern Methodist University*, 1986.
- Fabrice Le Berr, Abdenour Abdelli, D-M Postariu, and R Benlamine. Design and optimization of future hybrid and electric propulsion systems: An advanced tool integrated in a complete workflow to study electric devices. *Oil & Gas Science and Technology—Revue de l'IFP Energies nouvelles*, 67(4): 547–562, 2012.
- Christofer Sundström, Erik Frisk, and Lars Nielsen. A new electric machine model and its relevance for vehicle level diagnosis. *International Journal of Modeling, Identification and Control (IJMIC)*, 24(1):1–9, 2015.
- Rinie Van Helden, Ruud Verbeek, Frank Willems, and Reinier van der Welle. Optimization of urea scr denox systems for hd diesel engines. Technical report, SAE Technical Paper, 2004.

Johan Wahlström and Lars Eriksson. Modelling diesel engines with a variable-geometry turbocharger and exhaust gas recirculation by optimization of model parameters for capturing non-linear system dynamics. *Proceedings of the Institution of Mechanical Engineers, Part D: Journal of Automobile Engineering*, 225(7):960–986, 2011.

Frank Willems and Darren Foster. Integrated powertrain control to meet future co 2 and euro-6 emissions targets for a diesel hybrid with scr-deno x system. In *2009 American Control Conference*, pages 3944–3949. IEEE, 2009.

Christian Winkler, Peter Flörchinger, MD Patil, Jürgen Gieshoff, Paul Spurk, and Marcus Pfeifer. Modeling of scr denox catalyst-looking at the impact of substrate attributes. Technical report, SAE Technical Paper, 2003.

A Notation and Subscripts

Notation

γ	Specific heat capacity ratio (-)
ε	Emissivity (-)
η	Efficiency (-)
Θ	Surface coverage (-)
ρ	Density (kg/m^3)
σ	Stefan-Boltzmann constant ($\text{W}/\text{m}^2\text{K}^4$)
ω	Rotational speed (rad/s)
A	Area (m^2)
c_p	Const. pressure specific heat capacity (J/kgK)
D	Diameter (m)
E^0	Activation energy (J)
F_v	Gray body view factor (-)
g	Acceleration due to gravity (m/s^2)
h	Heat transfer coefficient ($\text{W}/\text{m}^2\text{K}$)
I	Current (A)
i	Gear ratio (-)
J	Inertia (kgm^2)
k^0	Pre-exponential factor (-)
M	Torque (Nm)
m	Mass (kg)
N	Rotational speed (r/min)
Nu	Nusselt number (-)
P	Power (W)
p	Pressure (Pa)
Q	Heat (J)
q_{HV}	Heating value of fuel (J/kg)
R	Gas constant (J/kgK)
R	Resistance (Ω)
Re	Reynolds number (-)
T	Temperature (K)
U	Voltage (V)
u	Control signal
V	Volume (m^3)
v	Velocity (m/s)
W	Mass flow (kg/s)
X	Mass fraction (-)

Subscripts

a	Air
aft.turb	After turbo
amb	Ambient
b	Battery
bpv	Back pressure valve
c	Compressor
crb	Compressing release brake
cv	Convection
cyl	Cylinder
d	Displacement
dc	Dog clutch
e	Internal combustion engine
eats	Engine after treatment system
egr	Exhaust gas recirculation
ei	Engine in
em	Exhaust manifold
eo	Engine out
exh	Exhaust
f	Fuel
fc	Friction clutch
fric	Friction
gb	Gearbox
g	Gas
i	Internal
ig	Indicated gross
igch	Ignition chamber
im	Intake manifold
m	Electric machine
O	Oxygen
oc	Open circuit
p	Pump
t	Turbine
us	Upstream
vgt	Variable geometry turbine
vol	Volume
w	Wall

Optimal Control of Wastegate Throttle and Fuel Injection for a Heavy-Duty Turbocharged Diesel Engine During Tip-In

Kristoffer Ekberg¹ Viktor Leek¹ Lars Eriksson¹

¹Vehicular Systems, Dept. of Electrical Engineering, Linköping University, Sweden, {kristoffer.ekberg, viktor.leek, lars.eriksson}@liu.se

Abstract

The diesel engine remains one of the key components in the global economy, transporting most of the world's goods. To cope with stricter regulations and the continuous demand for lower fuel consumption, optimization is a key method. To enable mathematical optimization of the diesel engine, appropriate models need to be developed. These are preferably continuously differentiable, in order to be used with a gradient-based optimization solver. Demonstration of the optimization-based methodology is also necessary in order for the industry to adapt it. The paper presents a complete mean value engine model structure, tailored for optimization and simulation purposes. The model is validated using measurements on a heavy-duty diesel engine. The validated model is used to study the transient performance during a time-optimal tip-in, the results validate that the model is suitable for simulation and optimization studies.

Keywords: Diesel Engine Modeling, Diesel Engine Control, Mean Value Models, Optimal Control, Optimization, Tip-in.

1 Introduction

The diesel engine is one of the prime movers of the global economy (Smil, 2010). It propels everything from cargo ships to passenger cars, and helps sustain modern life as we know it. Over the years, diesel emission regulations have become more and more strict, but it seems as the pace is not fast enough. Urban air pollution possibly caused by vehicle emissions, has led to major cities now saying they will ban diesel engines completely (Harvey, 2016). Zero-emission vehicles, benefiting from electrification, is one potential way of solving the emissions problem. However, the solution to the problem still lies in the future while diesel engines continues to be used today. It is therefore important that the diesel engine continues to be improved in order to reduce the environmental impact, local emissions, and fuel consumption. However, making improvements on a diesel powertrain is not a trivial task. Firstly, the diesel engine itself is very complex, and combining it with modern aftertreatment systems makes it considerably more complex because of the symbiotic dependence

between the two systems. The engine needs the aftertreatment system to meet the regulations and the aftertreatment system needs heat from the engine to reduce the emissions. Secondly, more than 120 years of continuous development has led to the fact that the low-hanging fruits have already been picked. To overcome this, and continue to develop the diesel engine, there is a demand for new and different methodologies. Such a methodology that is starting to gain acceptance within the automotive industry is *optimization*. Together with modeling and simulation, it can help balance conflicting interests, such as keeping the aftertreatment warm while maintaining a low fuel consumption. For the transition to optimization-based methodologies to work, models suitable for optimization are needed, which is the focus of this paper. In it, a continuously differentiable heavy-duty diesel engine model, suitable for use with gradient-based optimization software is developed, and a simple use-case, showing how it can be used in an optimization framework, is demonstrated.

The developed model is a so-called mean value engine model, which is a control-based model for the study of the air and fueling system. The model is developed from stationary measurements on a heavy duty diesel engine and has four states, intake manifold pressure, exhaust manifold pressure, pressure after the compressor, turbocharger speed. The system also has three actuator inputs, fuel injection per cycle, throttle position, and wastegate position. Also, since there is no load connected to the engine model, the engine speed is treated as an exogenous input into the system, meaning that it is set from outside the model, which enables studying the engine under load conditions.

For a comprehensive treatment of modeling diesel engines for optimal control, the reader is referred to Asprión (2013), and for the modeling of hybrid electric powertrains for optimal control the reader is referred to Sivertsson (2015). Numerical optimal control is extensively treated in Betts (2010); Biegler (2010). For the solution of the optimal control problems in this paper, a toolbox called YOP[†] is used. It is based on CasADi (Andersson, 2013), which is a general symbolic framework for dynamic optimization. The resulting nonlinear program (NLP) from the optimal control algorithm is solved using the general NLP-solver IPOPT (Wächter, Andreas and Biegler, Lorenz T., 2006). Similar optimal control prob-

*This work was supported by the Vinnova Industry Excellence Center LINK-SIC Linköping Center for Sensor Informatics and Control.

[†]Contact the authors for more information about YOP.

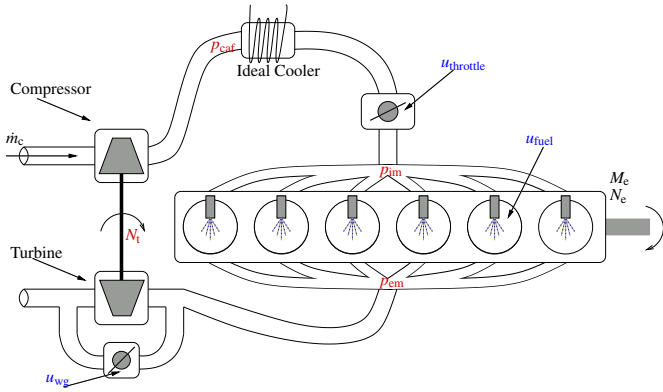


Figure 1. Sketch of a diesel engine equipped with turbocharger, charge air cooler, throttle and wastegate. The model states are pressure after compressor p_{caf} , pressure in the intake manifold p_{im} , pressure in the exhaust manifold p_{em} and turbocharger rotational speed N_t . The charge air cooler is assumed to be ideal, therefore there is no pressure drop from the compressor to the throttle.

lems, as studied in this paper, have previously been solved in for example Nezhadali and Eriksson (2016), Sivertsson and Eriksson (2014), and Leek et al. (2017).

The paper is outlined as follows. In Section 3 the model is presented and validated sub-model by sub-model. In Section 4 an optimal control problem for optimizing the transient response, for a tip-in, is formulated. In Section 5 the problem is solved numerically and the results presented. In Section 6 the conclusions are presented.

The contributions are, a complete model structure for a heavy-duty diesel engine equipped with a fixed geometry turbocharger and inlet throttle, and optimal control trajectories for a parametrization of the model during a tip-in.

2 Model

The model is intended to be used for controller design and evaluation of, both controller structures and control strategies. To reduce computational time when simulating the model, the number of states is kept low. The model is a mean value engine model, a model structure suitable for study of the air and fueling system of the engine. The sub-models are parametrized using sum of least squares method, the results from the parametrization's are shown as R^2 of the model fit, displayed in the figure title of each model that is adapted to measurement data.

Symbol	Description	Unit
\dot{m}	Massflow	kg/s
n_r	Revolutions per stroke	-
p	Pressure	Pa
q_{hv}	Fuel Lower heating value	J/kg
q_{in}	In-cylinder specific heat	J/kg
r_c	Compression ratio	-
t	Time	s
u_{fuel}	Injected fuel	mg/cycle
u_{wg}	Wastegate position	-, [0, 1]
u_{thr}	throttle position	-, [0, 1]
A	Area	m ²
BSR	Blade speed ratio	-
C_d	Drag coefficient	-
J	Rotational inertia	kg m ²
M	Torque	Nm
N	Rotational speed	rpm
\bar{N}	Normalized rotational speed	rpm
P	Power	W
R	Gas constant	J/(kg K)
T	Temperature	K
V	Volume	m ³
W	Work	J
γ	ratio of specific heats	-
η	Efficiency	-, [0, 1]
λ	Air-fuel equivalence ratio	-
ϕ	Fuel-air equivalence ratio	-
$(A/F)_s$	Air-Fuel stoichiometry relation	-
ψ	Flow condition function	-
ω	Angular velocity	rad/s
Π	Pressure ratio	-

Table 1. List of Symbols

2.1 States

The model states is described by four dynamic equations

$$\frac{dp_{caf}}{dt} = \frac{R_a T_{amb}}{V_{cac}} (\dot{m}_c - \dot{m}_{thr}) \quad (1a)$$

$$\frac{dp_{im}}{dt} = \frac{R_a T_{amb}}{V_{im}} (\dot{m}_{thr} - \dot{m}_{air}) \quad (1b)$$

$$\frac{dp_{em}}{dt} = \frac{R_e T_{em}}{V_{em}} (\dot{m}_{air} + \dot{m}_{fuel} - \dot{m}_t - \dot{m}_{wg}) \quad (1c)$$

$$\frac{d\omega_t}{dt} = \frac{1}{J_{tc} \omega_t} (P_t \eta_t - P_c), \quad (1d)$$

and consequently has four states $x = [p_{caf} p_{im} p_{em} \omega_t]^T$. It also has three actuator inputs $u = [u_{fuel} u_{thr} u_{wg}]$, and one exogenous input, the engine speed N_e .

2.2 Control Signals

The control signals in the model are the amount of fuel injected in the cylinders u_{fuel} in [mg/cycle], the wastegate control signal u_{wg} in a range from 0 to 1 [-], the throttle

Index	Description
<i>a</i>	Air
<i>amb</i>	Ambient
<i>cac</i>	Charge air cooler
<i>caf</i>	Compressor after
<i>ch</i>	Choke line
<i>c</i>	Compressor
<i>corr</i>	Corrected
<i>crit</i>	Critical
<i>cyl</i>	Cylinder
<i>d</i>	Displacement (cylinder)
<i>D</i>	Displacement (engine)
<i>des</i>	Desired
<i>e</i>	Engine
<i>em</i>	Exhaust manifold
<i>f</i>	Final
<i>fric</i>	Friction
<i>ig</i>	Indicated gross
<i>ign</i>	Ignition
<i>im</i>	Intake manifold
<i>lin</i>	Linear
<i>ref</i>	Reference
<i>sc</i>	Seiliger cycle
<i>thr</i>	Throttle
<i>t</i>	Turbine
<i>vol</i>	Volumetric
<i>zsl</i>	Zero-slope line

Table 2. List of subscripts

control signal u_{thr} in a range from 0 to 1 [-], and the engine speed N_e in [rpm]. The engine speed is treated as an exogenous input to be able to investigate the engine behavior in different load and speed conditions without having a driveline model.

2.3 Engine

The engine model is divided into four sub models; one for engine torque, one for cylinder air charge, one for engine stoichiometry, and one for exhaust temperature.

2.3.1 Engine Torque

The torque delivered by the combustion engine (Eriksson and Nielsen, 2014) is described by

$$\dot{m}_{fuel} = \frac{u_{fuel} N_e n_{cyl} 10^{-6}}{n_r} \quad (2a)$$

$$W_{pump} = V_d n_{cyl} (p_{em} - p_{im}) \quad (2b)$$

$$W_{ig} = \frac{\eta_{ign} \dot{m}_{fuel} Q_{HV} n_r}{N_e} \left(1 - r_c^{1-\gamma_{cyl}}\right) \quad (2c)$$

$$W_{fric} = V_d n_{cyl} \left(c_{fr1} + c_{fr2} \frac{N_e}{1000} + c_{fr3} \left(\frac{N_e}{1000} \right)^2 \right) \quad (2d)$$

$$M_e = \frac{W_{ig} - W_{pump} - W_{fric}}{2\pi n_r} \quad (2e)$$

where the parameters η_{ig} , c_{fr1} , c_{fr2} and c_{fr3} are model parameters. The control signal is the fuel flow u_{fuel} and the engine rotational speed N_e , expressed in *rps*.

2.3.2 Engine Air Massflow

The amount of fresh air entering the cylinders is dependent of the pressure in the intake manifold p_{im} and the engine rotational speed N_e (Eriksson and Nielsen, 2014).

$$\dot{m}_{cyl} = \frac{\eta_{vol} p_{im} N_e V_D}{n_r 60 R_a T_{im}} \quad (3a)$$

$$\eta_{vol} = c_{vol1} \sqrt{p_{im}} + c_{vol2} \sqrt{N_e} + c_{vol3} \quad (3b)$$

Where c_{vol1} , c_{vol2} , and c_{vol3} are model parameters.

2.3.3 Air-to-Fuel Equivalence Ratio

The air-to-fuel equivalence ratio λ is described by

$$\lambda = \frac{\dot{m}_{air}}{\dot{m}_{fuel} (A/F)_s} \quad (4)$$

where $(A/F)_s$ is the stoichiometric air to fuel ratio.

2.3.4 Exhaust Gas Temperature

The exhaust gas temperature from the engine cylinders is needed to get the correct power to the turbine. The gas temperature leaving the cylinders and entering the exhaust manifold is described in a similar way as Skogtj rn (2002), but by an ideal diesel cycle (constant pressure during combustion), with a correction parameter η_{sc} which is a compensation factor for non ideal cycles.

$$q_{in} = \frac{\dot{m}_{fuel} Q_{HV}}{\dot{m}_{fuel} + \dot{m}_{air}} \quad (5a)$$

$$T_{em} = \eta_{sc} \left(\frac{p_{em}}{p_{im}} \right)^{\frac{\gamma_{air}-1}{\gamma_{air}}} r_c^{1-\gamma_{cyl}} \left(\frac{q_{in}}{c_{p,air}} + T_{im} r_c^{\gamma_{air}-1} \right) \quad (5b)$$

The model validation for models (2)-(5) is displayed in Figure 2. Since the charge air cooler after the compressor is assumed to be ideal, the inlet manifold temperature $T_{im} = T_{amb}$.

2.4 Turbocharger

The compressor model consists of two parts, the first models the compressor air massflow, and the second the compressor efficiency.

2.4.1 Compressor Massflow

The compressor massflow model is developed in Leufv n and Eriksson (2013) and further described in Eriksson and Nielsen (2014). The model used in this paper is the representation from Eriksson and Nielsen (2014), described as

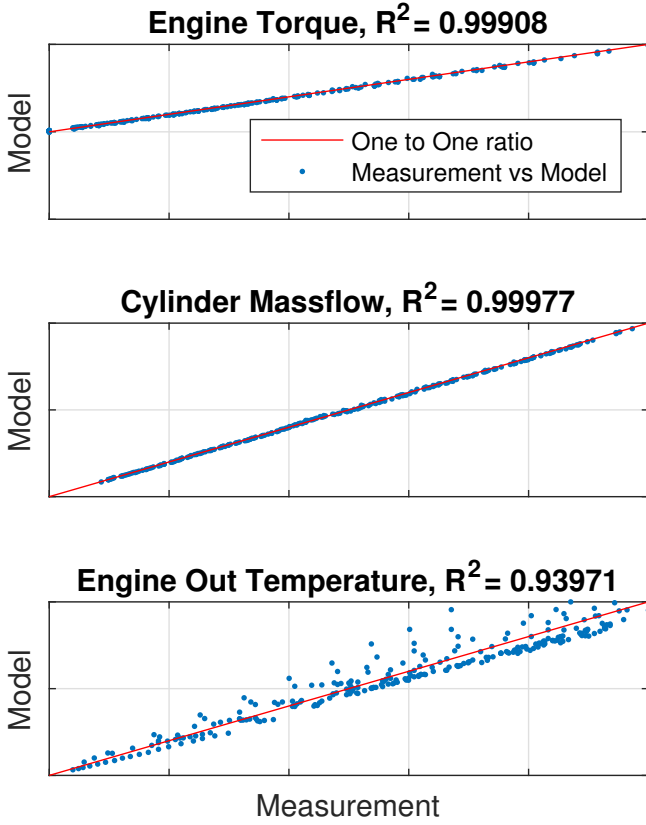


Figure 2. Model validation, blue dots represent measurement plotted against model, and the red line represents the line indicating an exact fit.

$$\bar{N} = N_t / 10^5 \quad (6a)$$

$$\Pi_{zsl} = 1 + c_{11}\bar{N}^{c_{12}} \quad (6b)$$

$$\dot{m}_{zsl} = c_{20} + c_{21}\bar{N} + c_{22}\bar{N}^2 \quad (6c)$$

$$\Pi_{ch} = c_{30} + c_{31}\bar{N}^{c_{32}} \quad (6d)$$

$$\dot{m}_{ch} = c_{40} + c_{41}\bar{N}^{c_{42}} \quad (6e)$$

$$C = c_{50} + c_{51}\bar{N} + c_{52}\bar{N}^2 \quad (6f)$$

$$\dot{m}_{c,corr} = \dot{m}_{zsl} + (\dot{m}_{ch} - \dot{m}_{zsl}) \left(1 - \left(\frac{\Pi_c - \Pi_{ch}}{\Pi_{zsl} - \Pi_{ch}} \right)^C \right)^{\frac{1}{c}} \quad (6g)$$

There are 14 model parameters to estimate, the complete model fit is displayed in Figure 3. Equation (7) is used to translate the corrected massflow to massflow in [kg/s].

$$\dot{m}_c = \dot{m}_{c,corr} \frac{p_{amb}}{p_{ref}} \sqrt{\frac{T_{ref}}{T_{amb}}} \quad (7)$$

where p_{amb} and T_{amb} are the pressure and temperature in the compressor inlet, p_{ref} and T_{ref} are the reference pressure and temperature for which the compressor is tested.

2.4.2 Compressor Efficiency

The compressor efficiency model (Eriksson and Nielsen, 2014) has two inputs, the corrected compressor massflow

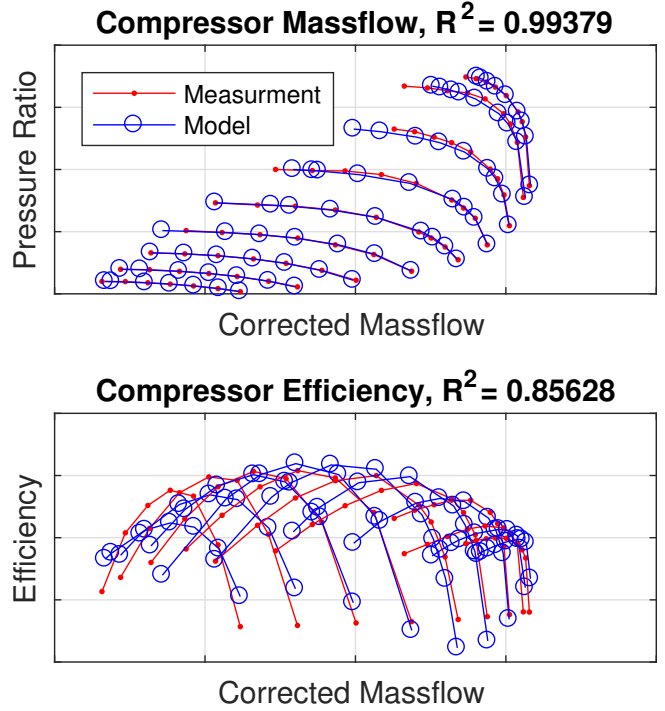


Figure 3. Compressor model validation, the measurement data (red) is compared with the massflow model (plot above) and the efficiency model (plot below), the models output data is shown in blue.

$\dot{m}_{c,corr}$ and the pressure ratio over the compressor Π_c . The model is described as

$$\chi = \left(\frac{\sqrt{\Pi_c - 1} - \sqrt{\Pi_c^{max} - 1}}{\dot{m}_{c,corr} - \dot{m}_{c,corr}^{max}} \right) \quad (8a)$$

$$\eta_c = \eta_c^{max} - \chi^T Q \chi \quad (8b)$$

where Q is a symmetric positive definite matrix. In Figure 3, the model output is compared to the measured data.

2.4.3 Turbine Massflow

The turbine model (9) is found in Eriksson and Nielsen (2014), but (9b) has been extended to get a better model fit. The model output is compared to measured data in Figure 4, where it is seen, that the estimation of the turbine massflow is better at higher expansion ratios. When the turbocharger speed is higher, the estimation at lower expansion ratios gets less accurate.

$$\Pi_t = \frac{p_{amb}}{p_{em}} \quad (9a)$$

$$k_0 = c_{20} + c_{21}N_t + c_{22}N_t^2 \quad (9b)$$

$$\Pi_0 = c_{10} + c_{11}N_t^{c_{12}} \quad (9c)$$

$$\dot{m}_t = k_0 \sqrt{1 - (\Pi_t - \Pi_0)^{k_1}} \quad (9d)$$

2.4.4 Compressor Out Temperature

The compressor outlet temperature is calculated by using the inlet air temperature, the assumption of an isentropic

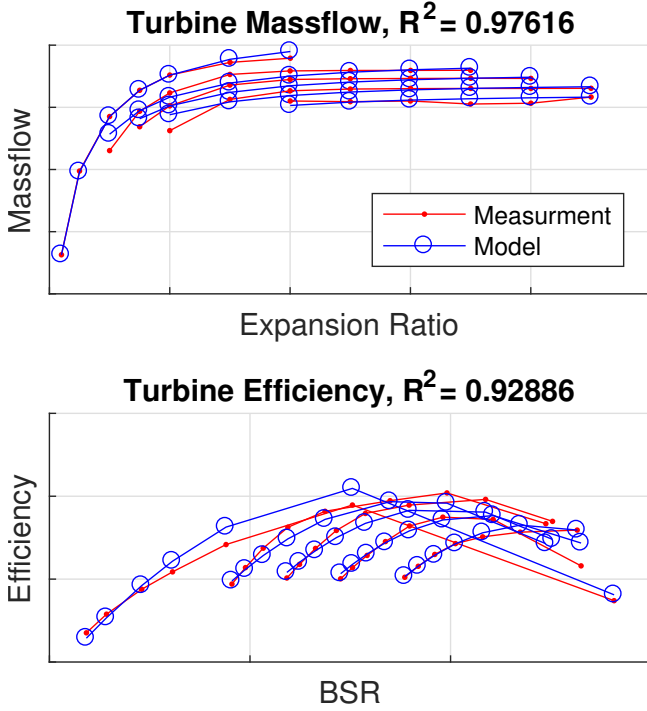


Figure 4. Turbine model validation, the measurement data (red) is compared with the turbine massflow model (plot above) and the turbine efficiency model (plot below), the output data from the models is shown in blue.

compression, and the compressor efficiency. (Eriksson and Nielsen, 2014)

$$T_c = T_{amb} + \frac{T_{amb}}{\eta_c} \left(\Pi_c^{\frac{\gamma_{air}-1}{\gamma_{air}}} - 1 \right) \quad (10)$$

2.4.5 Turbine Efficiency and BSR

Figure 4 shows a spreading of the speed lines that relate efficiency to BSR, to be able to capture this, a turbocharger rotational speed dependent model has been adapted (11). The efficiency model consists of three sub-models, the first describing the relation between the maximum turbine efficiency and the turbine rotational speed (11b), the second describing the relation between the mechanical losses parameter c_m and rotational speed (11c), and the third describing the relation between BSR_{opt} and the rotational speed (11e). The models are found in Wahlström and Eriksson (2011), but the equations are slightly modified to take the spreading of the speed lines into account, also a max-selector used in Wahlström and Eriksson (2011) has been removed (in Equation 11c) to ensure continuous properties. To handle the loss of the switch, a boundary constraint is added to the optimization procedure, to make sure that the turbocharger speed never drops below the value of c_{22} .

$$N_{t,corr} = \frac{N_t}{\sqrt{T_{em}}} \quad (11a)$$

$$\eta_{tm}^{max} = c_{11} + c_{12} \left(\frac{N_{t,corr}}{10^5} \right)^2 \quad (11b)$$

$$c_m = c_{21} (N_{t,corr} - c_{22})^{c_{23}} \quad (11c)$$

$$BSR = \frac{r_t \omega_t}{\sqrt{2c_{p,exh} T_{em} (1 - \Pi_t^{1-1/\gamma_{exh}})}} \quad (11d)$$

$$BSR_{opt} = c_{31} + c_{32} \left(\frac{N_{t,corr}}{10^5} \right)^{c_{33}} \quad (11e)$$

$$\eta_t = \eta_{tm}^{max} - c_m (BSR - BSR_{opt})^2 \quad (11f)$$

2.4.6 Compressor and Turbine Power

The turbine and compressor powers are described as in Eriksson and Nielsen (2014)

$$P_t \eta_t = \eta_t \dot{m}_t c_{p,exh} T_{em} \left(1 - \Pi_t^{1-1/\gamma_{exh}} \right) \quad (12a)$$

$$P_c = \frac{\dot{m}_c c_{p,air} T_{amb}}{\eta_c} \left(\Pi_c^{1-1/\gamma_{air}} - 1 \right) \quad (12b)$$

2.5 Controllable Flow Restrictors

2.5.1 Throttle Massflow

The throttle is described as an isentropic compressible restriction, the massflow through the throttle is dependent on the temperature T_{caf} and pressure p_{caf} before the throttle, and the pressure p_{im} after the throttle. Eriksson and Nielsen (2014) describes the model Equations (13). The model is linearized when the pressure ratio exceeds $\Pi_{lin} = 0.98$. At low pressure ratios the massflow increases, and eventually the flow reaches sonic velocity, which is reached at the critical pressure ratio Π_{thr}^{crit} .

$$\Pi_{thr}^{crit} = \left(\frac{2}{\gamma_{air} + 1} \right)^{\frac{\gamma_{air}}{\gamma_{air}-1}} \quad (13a)$$

$$\Pi_{thr} = \max \left(\frac{p_{im}}{p_{caf}}, \Pi_{thr}^{crit} \right) \quad (13b)$$

$$\Psi = \sqrt{\frac{2\gamma_{air}}{\gamma_{air}-1} \left(\Pi_{thr}^{\frac{2}{\gamma_{air}}} - \Pi_{thr}^{\frac{\gamma_{air}+1}{\gamma_{air}}} \right)} \quad (13c)$$

$$\Psi_{lin} = \sqrt{\frac{2\gamma_{air}}{\gamma_{air}-1} \left(\Pi_{lin}^{\frac{2}{\gamma_{air}}} - \Pi_{lin}^{\frac{\gamma_{air}+1}{\gamma_{air}}} \right)} \frac{1 - \Pi_{thr}}{1 - \Pi_{lin}} \quad (13d)$$

To handle the change in characteristics, happening at Π_{lin} and Π_{thr}^{crit} , two tanhshyperbolicus-based functions (tanhyp) are adapted to switch from 0 to 1 when the pressure ratios exceed Π_{lin} and Π_{thr}^{crit} . The main benefit of the tanh hyp switch, compared to a conditional function, is that it holds the property of being continuously differentiable, which is a property desired by the optimal control software. Equations (13) and the tanh hyp function forms the

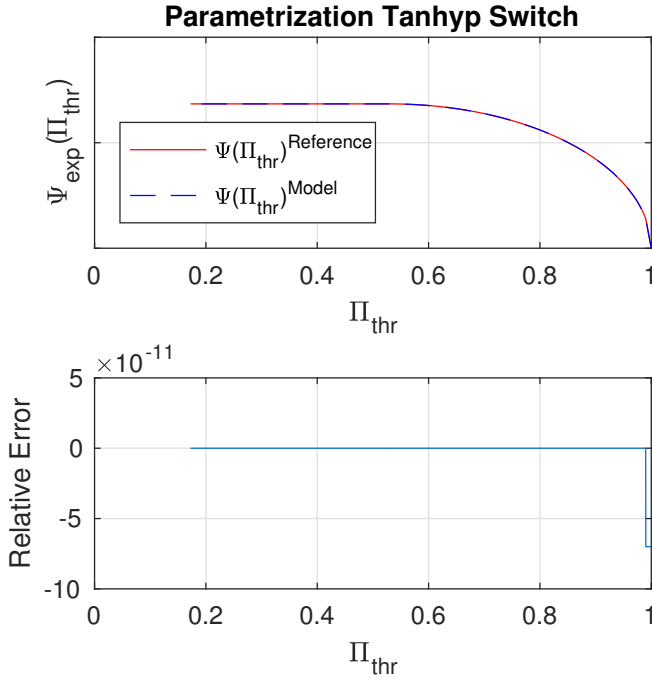


Figure 5. Model validation, the reference value of $\Psi_{exp}(\Pi_{thr})$ data (red) is compared with the tanh switch model output data (blue). The relative error when introducing the tanh switches are shown in the lower plot.

following expressions for the flow condition Ψ_{exp} through the throttle

$$\Psi_{exp} = \Psi(\Pi_{thr}^{crit}) + f_{tanhyp,1}(-\Psi(\Pi_{thr}^{crit}) + \Psi(\Pi_{thr}) + f_{tanhyp,2}(\Psi_{lin}(\Pi_{thr}) - \Psi(\Pi_{thr}))) \quad (14a)$$

$$f_{tanhyp,x}(\Pi_{thr}) = \frac{1 + \tanhyp(c_{x1}(\Pi_{thr} - c_{x2}))}{2} \quad (14b)$$

The error introduced when using the tanh functions, compared to using a conditional function switching between the pressure ratio and the critical pressure ratio (13b), and the linearized and non-linearized flow equations (13c) and (13d), is shown in Figure 5.

The resulting massflow through the throttle is described as (Eriksson and Nielsen, 2014)

$$\dot{m}_{thr} = \frac{P_{caf}}{\sqrt{R_a T_{caf}}} C_d A_{thr}(u_{thr}) \Psi_{exp}(\Pi_{thr}). \quad (15)$$

No measurement data for different throttle positions was available (other than fully open), but the throttle area A_{thr} for different control signals u_{thr} was known and has been used to build the throttle model. The relation between the throttle area and the control signal is described by a fourth order equation (16), the result is displayed in Figure 6.

$$A_{thr} = c_1 u_{thr} + c_2 u_{thr}^4 \quad (16)$$

2.5.2 Wastegate Massflow

The model describing the wastegate massflow is developed in the same way as the throttle model (Equations

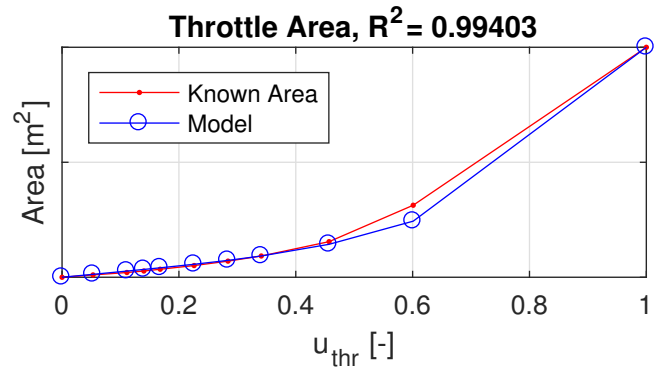


Figure 6. Model validation, the known throttle area (red) is compared with the model output data (blue).

(13)-(16)) but with another area A_{wg} , and flow coefficient $C_{d,wg}$. The wastegate model is developed without the first tanh function in Equation (14a). There was no measurement of the wastegate massflow, the wastegate model is therefore used without any validation, other than making sure that the wastegate control signal is able to bypass massflow from the turbine. $C_{d,wg}$ is a scaling constant to ensure that the wastegate is working properly.

$$\dot{m}_{wg} = \frac{P_{em}}{\sqrt{R_a T_{em}}} C_{d,wg} A_{wg}(u_{wg}) \Psi_{exp}(\Pi_{wg}) \quad (17)$$

3 Optimal Control

To demonstrate the model's optimization and simulation capabilities an optimal control problem is solved. The optimization scenario is a so-called *tip-in*, this means transitioning the engine from a low load operating point to a high load operating point, essentially this corresponds to pushing the accelerator. Since no vehicle model is added, the tip-in is performed at constant engine speed, simply making a load increase. The problem is solved using a toolbox called YOP, using the direct collocation algorithm and NLP-solver IPOPT.

3.1 Objective

The optimization objective is to transition between the low load operation point to the high load operating point as fast as possible. This type of problem is interesting for investigating the performance boundaries of the engine. This can for instance be used for analyzing the engine design, controller benchmarking, or comparing engine performance. In mathematical terms the objective function is formulated as

$$\min_{x(t), u(t)} t_f, \quad (18)$$

where t_f is the duration of the tip-in.

3.2 Model Constraints

To restrict the optimization to meaningful solutions, constraints need to be introduced. The most basic of these are the model constraints:

$$\begin{aligned} \dot{x}(t) &= f(x(t), u(t)) & (19a) \\ x_{min} &\leq x(t) \leq x_{max} & (19b) \\ u_{min} &\leq u(t) \leq u_{max} & (19c) \\ 0 &\leq \phi(t) \leq 1/\lambda_{min} & (19d) \\ BSR_{min} &\leq BSR(t) \leq BSR_{max} & (19e) \\ \dot{m}_c(t) &\geq \dot{m}_{zsl}(N_t) & (19f) \\ \dot{m}_c(t) &\leq \dot{m}_{ch}(N_t) & (19g) \\ N_t(t) &\geq c_{22} \text{ (from Equation (11c))} & (19h) \\ N_e(t) &= N_{e, fixed} & (19i) \end{aligned}$$

The first constraint (19a) says that the state must follow the system dynamics, the second (19b) and third (19c) that the state and control must be operated within their limits, the fourth (19d) that the air-to-fuel equivalence ratio (expressed as the fuel-to-air equivalence ratio in $\phi(t)$ to avoid the singularity when no fuel is injected) must be above the smoke limit, the fifth (19e) that the turbine blade-speed-ratio must be within its bounds, the sixth (19f) and seventh (19g) that the compressor must stay below surge and above choke massflow, and the eight (19h) that the turbocharger speed should be above the value of the c_{22} parameter (from Equation (11c)), and the ninth (19i) that the engine speed is fixed at $N_{e, fixed}$. The sixth (19f) and seventh (19g) constraints are illustrated in Figure 7, where the red line represents the surge line and the green the choke line.

3.3 Boundary Constraints

To setup the tip-in scenario, boundary constraints defining the initial and terminal operating conditions of the optimization are introduced

$$x(0) = x_0 \quad (20a)$$

$$u(0) = u_0 \quad (20b)$$

$$M_e(t_f) = M_{e, des}, \quad (20c)$$

where x_0 and u_0 define the initial operating point, and $M_{e, des}$ the desired engine torque. When the desired torque is reached, the tip-in is completed.

3.4 Numerical Solution

The numerical solution to the optimal control problem was found using an open-source software called YOP. For the solution presented in the paper the direct collocation algorithm was used, using 9 Legendre points in each collocation interval. The control signal was discretized into 90 equidistant segments on which the control was parameterized as constant, making it piecewise constant over the entire time horizon. The resulting NLP from the direct collocation algorithm was solved using IPOPT.

4 Results

The optimal control problem was parameterized in such a way that the engine was running at 1300 RPM, starting

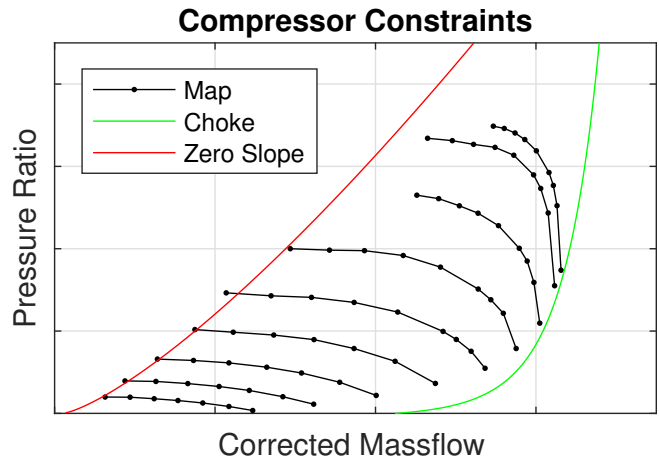


Figure 7. Compressor constraints. The minimum massflow bound is drawn in red and called the zero slope line. The maximum massflow bound is drawn in green and called the choke line. The black lines are speed lines from the compressor map.

at 15 Nm and required to reach 1800 Nm. The minimum time of doing this is 2.95 s, which is seen in the top plot of Figure 8. In Figures 9 and 10 the state and control trajectories are shown, in Figure 8 interesting internal system variables are shown, and in Figure 11 the turbocharger behavior can be studied from a turbo map perspective. Trivially, it takes oxygen to combust fuel, this is however what limits the tip-in performance. Looking at the bottom plot of Figure 8, it is seen that the minimum value of the fuel-to-air equivalence ratio λ_{min} is an active constraint as soon as the engine begins to increase the load. λ_{min} is set close to, but above 1 (below $\lambda = 1$ there is too little oxygen to burn all the fuel), which prevents smoke formation. However, even without this constraint there is still not enough air to be able to combust the necessary amount of fuel to produce the requested torque. To increase the air massflow, the compressor rotational speed needs to be increased in order to change the operating point. What restricts the transition time is the turbocharger inertia. Since it restricts how fast the compressor can change operating point, it consequently also restricts the entire engine's response time, limiting the tip-in performance.

Looking at the optimal control trajectories in Figure 10, the trajectories are predictable and intuitive. The fuel injection follows the smoke limit, the throttle stays open, and the wastegate is kept closed right until the end where it opens fully. The reason for the wastegate to open at the end, is that it decreases the pumping loss, this can be seen in the middle plot of Figure 8. For the presented parametrization of the problem, the engine is not required to be in a steady-state condition at the terminal boundary, which is why it opens the wastegate fully and not just partly.

The results shows that the model behaves in an intuitive way, which indicates that the model is physically sound and that it is suitable for simulation and optimization studies.

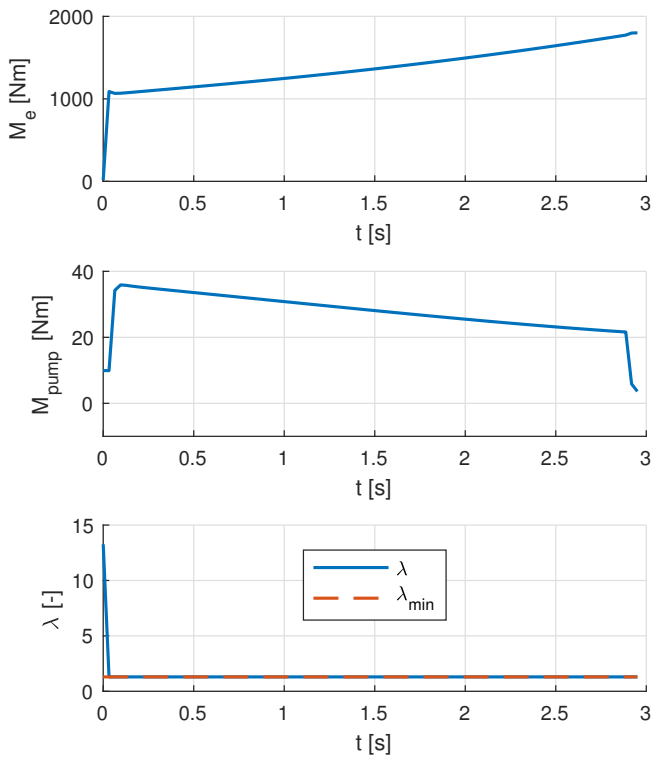


Figure 8. Internal system variables during tip-in. At the top, the engine torque is shown, in the middle the pumping torque, and at the bottom the air-to-fuel equivalence ratio.

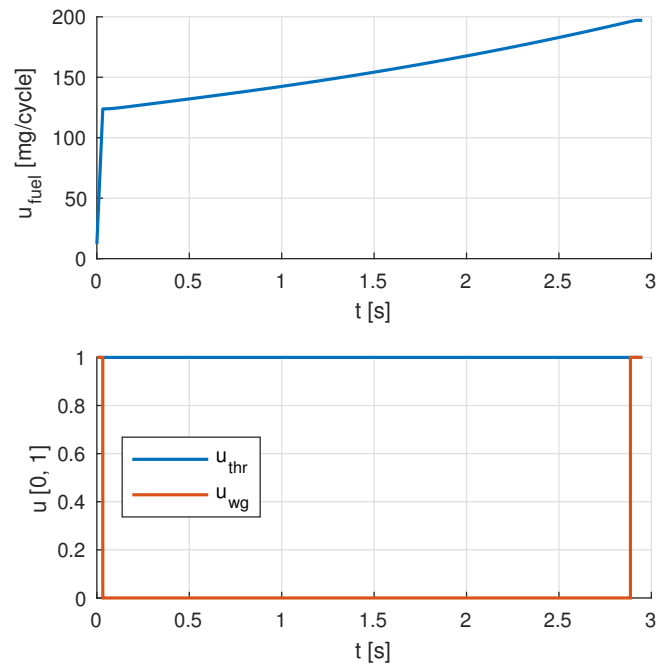


Figure 10. Tip-in control trajectories. At the top, fuel injection is seen, and at the bottom throttle and wastegate control are seen.

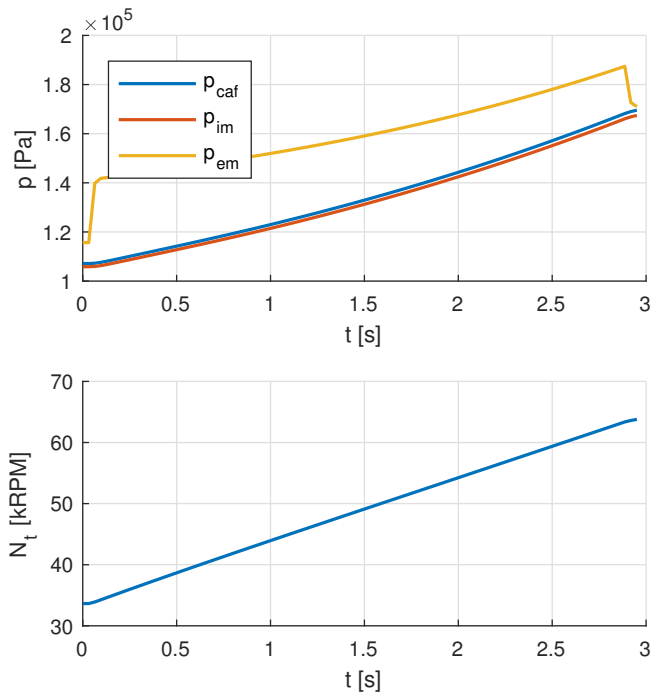


Figure 9. Tip-in state trajectories. Top plot showing the pressure states, and the bottom plot showing the turbocharger speed.

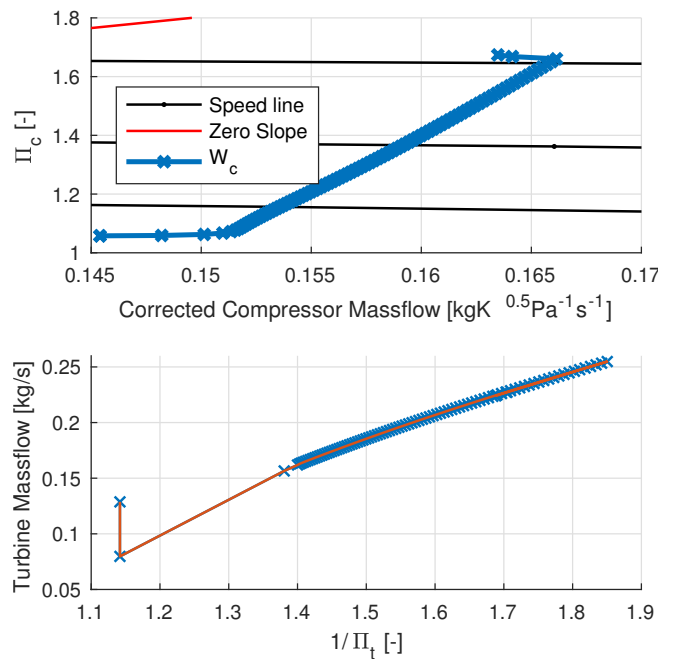


Figure 11. Tip-in turbocharger behaviour. Top plot showing the compressor behavior in the compressor map, and bottom plot showing the turbine behavior in the turbine map.

5 Conclusions

This paper has:

- Developed and validated a model of a turbocharged heavy-duty diesel engine equipped with throttle and wastegate.
- Developed a component based model, to make it easily adjustable for future use and further development.
- Shown, using optimization, that the model behaves in a sound and intuitive way, strongly indicating that it is suitable for optimization and simulation studies.

References

- Joel Andersson. *A General-Purpose Software Framework for Dynamic Optimization*. PhD thesis, Arenberg Doctoral School, KU Leuven, Department of Electrical Engineering (ESAT/SCD) and Optimization in Engineering Center, Kasteelpark Arenberg 10, 3001-Heverlee, Belgium, October 2013.
- Jonas Asprion. *Optimal Control of Diesel Engines: Modeling, Numerical Methods and Applications*. PhD thesis, ETH Zürich, Sonneggstrasse 3, CH-8092 Zurich, Switzerland, 2013.
- John T. Betts. *Practical Methods for Optimal Control and Estimation Using Nonlinear Programming*. SIAM, second edition, 2010.
- Lorenz T. Biegler. *Nonlinear Programming: Concepts, Algorithms, and Applications to Chemical Processes*. MOS-SIAM Series on Optimization, 2010.
- Lars Eriksson and Lars Nielsen. *Modeling and Control of Engines and Drivelines*. John Wiley and Sons Ltd, 2014.
- Fiona Harvey. Four of world's biggest cities to ban diesel cars from their centres. *The Guardian*, 2 December 2016. <https://www.theguardian.com/environment/2016/dec/02/four-of-worlds-biggest-cities-to-ban-diesel-cars-from-their-centres>.
- Viktor Leek, Kristoffer Ekberg, and Lars Eriksson. Development and Usage of a Continuously Differentiable Heavy Duty Diesel Engine Model Equipped with VGT and EGR. *SAE Technical Paper*, 2017.
- Oskar Leufvén and Lars Eriksson. A surge and choke capable compressor flow model—validation and extrapolation capability. *Control Engineering Practice*, 21(12):1871 – 1883, 2013. ISSN 0967-0661. doi:<http://dx.doi.org/10.1016/j.conengprac.2013.07.005>. URL <http://www.sciencedirect.com/science/article/pii/S0967066113001354>.
- Vaheed Nezhadali and Lars Eriksson. Optimal control of a diesel-electric powertrain during an up-shift. In *SAE 2016 World Congress, paper number 2016-01-1237*, 2016.
- Martin Sivertsson. *Optimal Control of Electrified Powertrains*. PhD thesis, Linköping University, Sweden, 2015.
- Martin Sivertsson and Lars Eriksson. An optimal control benchmark: Transient optimization of a diesel-electric powertrain. In *SIMS 2014 - 55th International Conference on Simulation and Modelling*, Aalborg, Denmark, 2014.
- Pål Skogtjärn. Modelling of the exhaust gas temperature for diesel engines. Master's thesis, Linköpings Universitet, SE-581 83 Linköping, 2002.
- Vaclav Smil. *Prime Movers of Globalization*. MIT Press, July 2010.
- J Wahlström and L Eriksson. Modelling diesel engines with a variable-geometry turbocharger and exhaust gas recirculation by optimization of model parameters for capturing non-linear system dynamics. *Proceedings of the Institution of Mechanical Engineers, Part D: Journal of Automobile Engineering*, 225(7):960–986, 2011. doi:10.1177/0954407011398177. URL <http://dx.doi.org/10.1177/0954407011398177>.
- Wächter, Andreas and Biegler, Lorenz T. On the implementation of a primal-dual interior point filter line search algorithm for large-scale nonlinear programming, 2006.

Wave Front Tracking using Template Matching and Segmented Regression

Eirik Siljan Samee Maharjan Marius Lysaker

Department of process, energy and environmental technology, University College of Southeast Norway, Norway,
120541@student.hit.no, samee.maharjan@usn.no, marius.lysaker@usn.no

Abstract

An experimental study was designed to measure shock waves (supersonic gas flow) in a shock tube. A high-speed camera captured images of the shock waves, at a framerate up to 500,000 frames per second. With respect to the huge number of images to be analyzed, an image-processing algorithm was developed for automatic tracking of the shock waves. However, each shock wave might be divided into two parts; a normal shock (the shock wave is perpendicular to the flow direction), and an oblique shock (the shock is at an oblique angle relative to the flow direction).

The proposed framework calculates the characteristics of the wave front, i.e. the angle and velocity of normal and oblique shocks. A technique based on Template Matching and an extended version of Segmented Regression is developed to track the wave front in the high-speed videos.

To our understanding, the proposed framework is novel, and our findings are in accordance with results derived from pressure sensors within the test tube

Keywords: front tracking, image processing template matching.

1 Introduction

This paper introduces a framework for automatic tracking of shock wave fronts in high-speed video films. One major challenge is that high-speed video films are often blurred and corrupted with noise, and accurate physical measurements of key elements within the wave front are difficult to obtain. Figure 1 illustrates wave front propagation throughout a high-speed video.

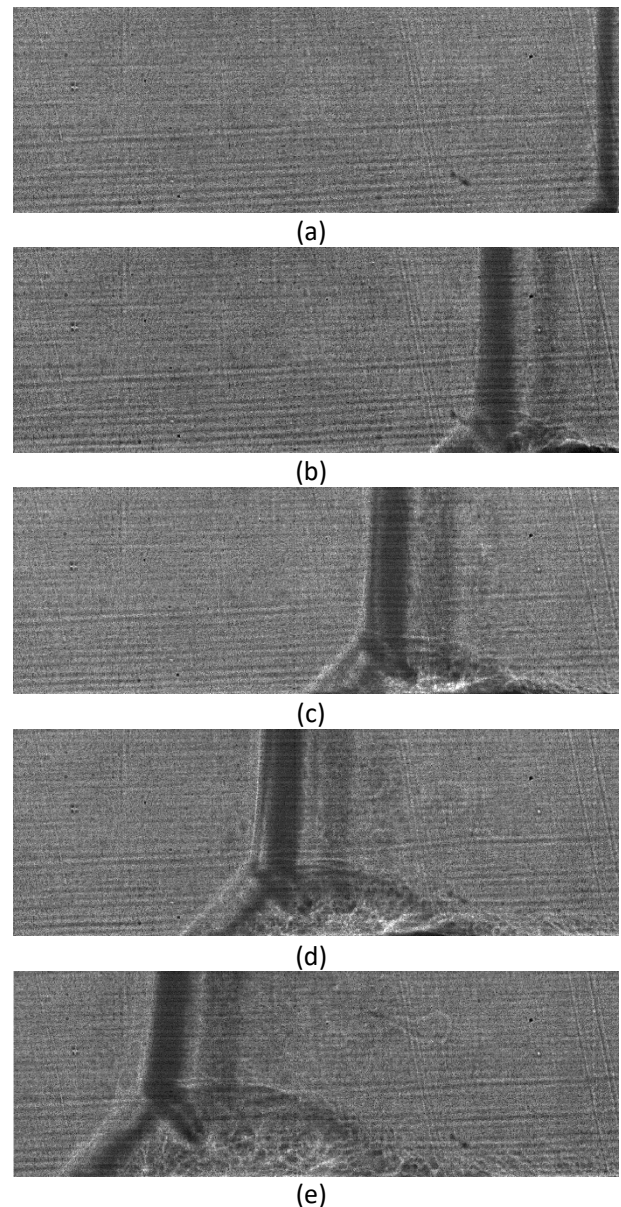


Figure 1. Illustration of wave front propagation through the test section of the test rig. Images (a) through (e) show frames from 62 through 142 with a 20-frame interval between each frame.

Figure 2 illustrates elements of interest within a wave front which are normal and oblique shock angles and velocities.

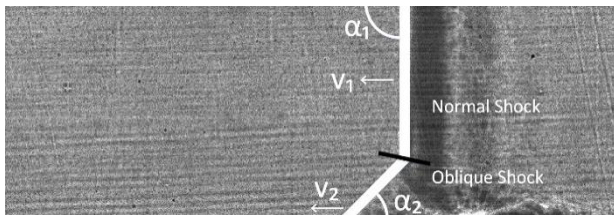


Figure 2. Illustration of key elements within a wave front where α_1 and α_2 are normal and oblique shock angles, and v_1 and v_2 are normal and oblique shock velocities, respectively.

It is observed in Figure 2 that the normal and oblique shock appears in approximately 90- and 45-degree orientations, relative to the horizontal plane. This orientation of the normal and oblique shocks is also the case throughout multiple videos which are studied.

2 Methods

This chapter describes the test rig and methods that first generates two datasets which are later combined using Segmented Regression.

2.1 Test Rig

The wave front is generated by a test rig where a flammable gas mixture is pumped into the shock tube, then ignited. The rest of the tube is filled with a specific gas to examine wave front velocities through the selected gases. Among the gases in which the wave front velocity is studied are Ar, N₂ and CO₂. Figure 3 shows a drawing of the test rig used in production of the high-speed videos. The test section of the test rig has a window in which the high-speed camera can film the wave front at up 500 000 frames per second.

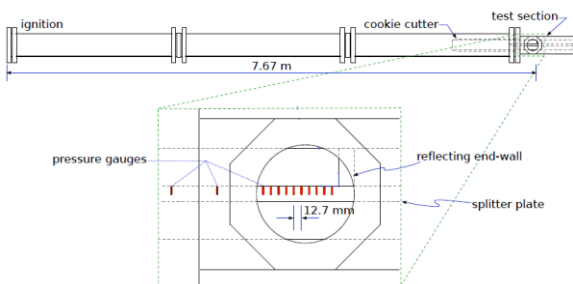


Figure 3. Drawing of the test rig used to produce shock wave experiments. Red lines in the splitter plate represents pressure sensors.

During the test procedure, the wave front hits the end-wall in the test section and reflects causing the desired shock phenomena to occur. The splitter plate is equipped with pressure sensors, and measurements from these sensors can be used to calculate both the normal and the oblique shock velocity.

The splitter plate contains pressure sensors which are placed in the holes in the splitter plate. The accuracy of which the holes have been drilled has an impact when calculating wave front velocities, as the wave front velocities are sometimes upwards of 400 [m/s], depending on the gas being studied. Unfortunately, the technique based on pressure sensors is limited to sparse measurements (1D+time). Even though, having velocities calculated through pressure sensors in addition to image processing creates a way to compare results. More importantly, with the framework based on image processing, the entire front is revealed (2D+time).

The outline of this paper is as follows: in Section 2, an edge detection algorithm based on Template Matching is introduced. Thereafter, a modified version of Segmented Regression is utilized to merge information generated by the Template Matching. In Section 3 the results are present, and the paper is closed with Conclusions in Section 4.

2.2 Removal of Outlier Frames

It was found that every 10th image (i.e. no.: 1, 11, 21, 31 etc.) in the high-speed video films were severely corrupted by noise and blur compared to the rest of the film, due to hardware failure. These frames were therefore removed and are not expected to have significant influence on the final results. The removed frames must, however, be considered when estimating velocities, as the number of frames dictates the elapsed time of a wave front over a given distance.

2.3 Template Matching

Template Matching is used to generate two wave front tracking datasets. One template is designed to track the oblique shock segment, and one template is designed to track the normal shock segment. Both these datasets are later (see Subsection 2.3) processed by a modified Segmented Regression technique, leading to an accurate location of the entire front.

2.3.1 Normal Shock Template

Figure 4 illustrates the process of normal shock Template Matching using two 5-by-5 pixel matrices. Each of the templates (a 5-by-5 matrix) is assigned a pre-allocated value representative for the shock wave.

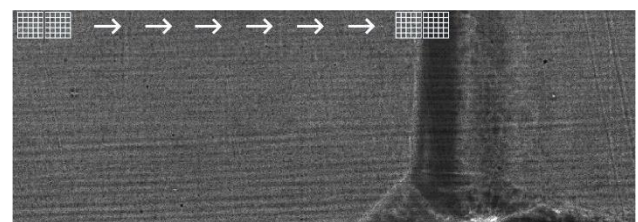


Figure 4. Normal shock Template Matching matrices on brightened raw image. Matrices are not to scale.

The left-hand template matrix is pre-allocated to best fit the brighter front portion of the wave front, while the

right-hand template matrix is pre-allocated to best fit the darker portion within the wave front. The template is moved pixel by pixel, through the entire image. At each location, the deviation between the pre-allocated template value and all pixels covered by the template, is calculated. This error is then assigned to an error matrix, i.e. if the template is centered at row i , column j , the deviation between the template and the pixels covered by the template, is assigned an error matrix at row i , column j . Results from the normal shock template matching is visualized in Figure 5.

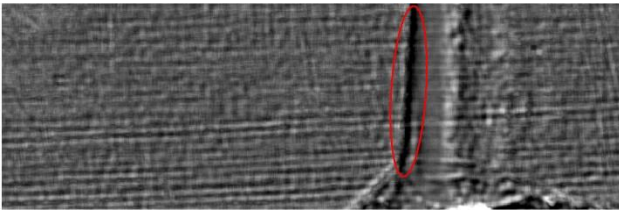


Figure 5. Error matrix produced by the normal shock Template Matching. A dark “ridge” is prominent where the normal shock is expected, indicated by the red ellipse.

The dataset for the normal shock is then generated from the error matrix by a simple approach; for each row, mark the position of the minimum value in the error matrix. The produced dataset is visualized as blue points in Figure 7. (a).

2.3.2 Oblique Shock Template

Figure 6 illustrates the process of oblique shock Template Matching using two 5-by-5 pixel matrices, both with the same pre-allocated average value, in a 45-degree skewed orientation.

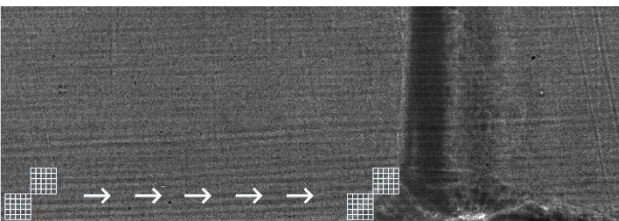


Figure 6. Oblique shock Template Matching matrices on brightened raw image. Matrices are not to scale.

The average value matches the brighter lower portion of the wave front, which is where the oblique shock occurs. At each location, the deviation between the pre-allocated template value and all pixels covered by the template, is calculated. This error is then assigned to an error matrix. The dataset for the oblique shock is then generated by the same approach as for the normal shock dataset, i.e. for each row, mark the position of the minimum value in the corresponding error matrix. The produced dataset is visualized as blue points in Figure 7. (b).

2.4 Modified Segmented Regression

A modified Segmented Regression technique is implemented to fit two line segments using two separate datasets. The modified approach is founded on the following observation; each of the templates is designed to track a specific feature in the shock wave. The normal shock template is designed to identify the vertical part of the shock wave, whereas the oblique shock template is designed to track the tilted part. However, the template designed to track normal shocks is, not expected to perform well in regions where oblique shocks occur, and vice versa. The datasets obtained through the Template Matching are illustrated in Figure 7. Please note that the normal shock template tracks the vertical part of the shock wave rather accurately, but fails to track the oblique part of the shock, see the lower part of Figure 7.(a). For the exact same input image, the oblique shock template tracks the tilted part of the shock wave rather accurately, but to some extent fails to track the vertical part of the shock, see the upper part of Figure 7.(b). Based on this, these two datasets should “merge” in such a way that coordinates describing the normal and the oblique shock, within these two datasets, are selected optimally.

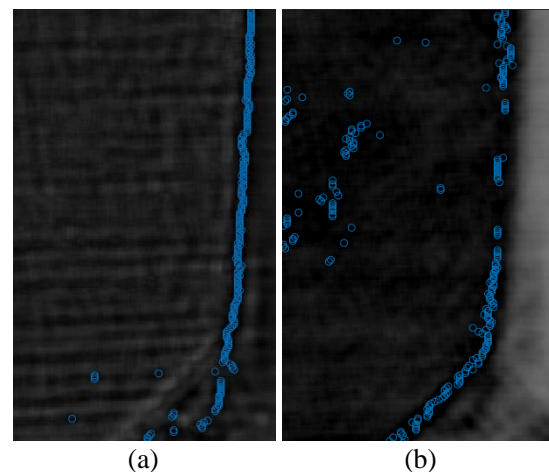


Figure 7. (a) and (b) are the resulting datasets of normal and oblique shock Template Matching.

To fit two line segments with the datasets illustrated in Figure 7, an optimization problem was formulated, and solved by a brute force approach:

$$S_i = \sum_{j=1}^i (\hat{y}_j - (a\hat{x}_j + b))^2 + \sum_{j=i+1}^n (\bar{y}_j - (c\bar{x}_j + d))^2, \quad (1)$$

for $i = 2:n - 2$

where S_i is a vector containing the combined error of both line segment estimates in each iteration, and n is the number of rows in the image. Moreover, \hat{y}_j, \hat{x}_j and

\bar{y}_j, \bar{x}_j represent the data points given by the normal and the oblique shock template, respectively. The constants a, b and c, d are the line segment coefficients representing the normal and oblique shock.

By minimizing S_i , the optimal combination of the two datasets is given. The index i which corresponds to the lowest error S_i becomes the breaking point. Meaning that coordinates situated at, and above, row number i should be collected from the normal shock dataset, and coordinates situated below row number i should be chosen from the oblique shock dataset. The result from the modified Segmented Regression technique is shown in Figure 8.

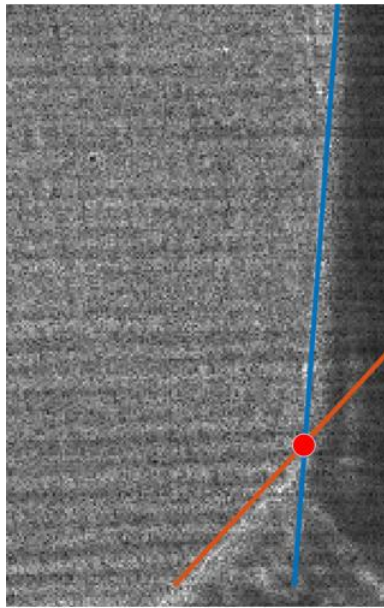


Figure 8. Resulting line segments obtained with a modified Segmented Regression approach. The red dot represents the breaking point, while the blue and orange line represents normal and oblique shock estimates, respectively.

2.5 Normal and Oblique Shock Angle Estimation

As first order polynomials are used to estimate both the normal and oblique shock, i.e. polynomials on the form $y = ax + b$, the slope of each shock is given by coefficient a , and thereby the angle is calculated by

$$\alpha = \frac{\pi}{2} - \tan^{-1}(a) \quad (2)$$

Where α is the calculated angle and a is the slope of the line segment representing the normal or the oblique shock. Formula (2) is applied to all wave front estimations throughout the videos, and the median of all normal angles is defined as α_1 and the median of all oblique angles is defined as α_2 .

2.6 Normal and Oblique Shock Velocity Estimation

The velocity is estimated by comparing the position of the wave front in the first and the last image, relative to the time interval between the frames, i. e.

$$v = \frac{\left(\Delta x \cdot \frac{P_{mm}}{px} \right)}{T_{cam} \cdot N_{frames}} \quad (3)$$

where v is the velocity of the shock wave in $\left[\frac{mm}{s} \right]$, Δx is the number of pixels the shock wave has moved, $\frac{P_{mm}}{px}$ is a pixel to millimeter conversion factor, T_{cam} is the elapsed time per frame capture and N_{frames} is the number of frames the wave front is tracked.

The reason for calculating wave front velocities globally (first to last frame) instead of locally (two subsequent frames), is due to variations in the wave front estimate. Through visual inspection it comes clear that each wave front estimation might vary around ± 7 pixels while still being considered a satisfactory wave front estimate. In Figure 9, the span of an accepted wave front estimate is shown.

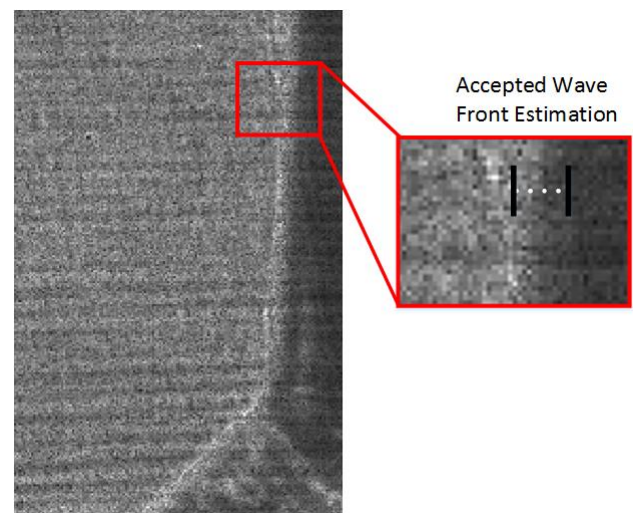


Figure 9. Illustration of expected wave front estimate. The black lines in the right-hand image displays the variation to be expected by a wave front estimate. The variation is around ± 7 pixels.

If the velocity is to be calculated from one frame to the next, ± 7 pixels could make a significant impact on the velocity estimate as a wave front moves approximately 5 pixels per frame. However, calculating the velocity over 100 frames, using the first and last frame, reduces the impact of wave front estimate variance.

A different solution to estimating the velocity could be calculating the velocity from one frame to the next for all frames, then find the median velocity of all the estimated velocities.

3 Results

The presented framework is tested on different high-speed videos to study the robustness of the framework. The results obtained through applying the framework to different high-speed videos are shown in Table 1 and Table 2.

Table 1. Velocity estimations of the shocks using the proposed framework.

Experiment no.	Caption freq.	Normal shock velocity	Oblique shock velocity
2516	500	230	262
2533	200	471	473
2543	200	236	268
2573	500	220	261
2592	500	450	486

Table 2. Angle estimations of the shocks in the high-speed videos using proposed framework

Experiment no.	Normal shock angle [deg]	Oblique shock angle [deg]
2516	87	50
2533	89	89
2543	87	54
2573	87	50
2592	89	62

Table 3 shows the confidence interval of the estimated normal and oblique shock angles.

Table 3. Confidence interval of normal and oblique shock angle estimations.

Experiment no.	Normal shock 95% confidence interval [deg]	Oblique shock 95% confidence interval [deg]
2516	[86 ... 87]	[47 ... 53]
2533	[88 ... 91]	[88 ... 91]
2543	[86 ... 88]	[50 ... 58]
2573	[85 ... 87]	[45 ... 52]
2592	[85 ... 93]	[57 ... 63]

A plot of all wave fronts tracked in experiment 2516 and 2573 can be seen in Figure 10 and Figure 11, respectively.

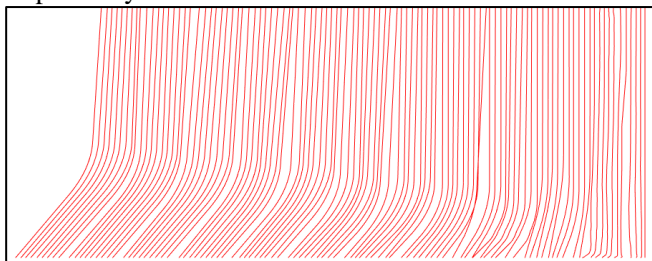


Figure 10. Result of all wave front estimations for experiment 2516 is displayed as red lines. The wave front in the first frame is the rightmost red line, while the wave front in the last frame is the leftmost red line.

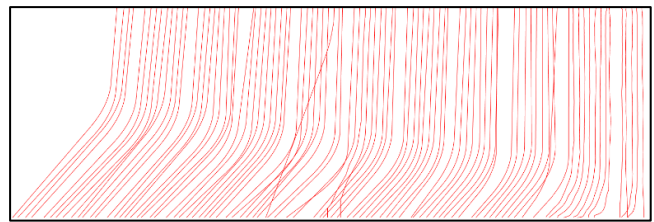


Figure 11. Result of all wave front estimations for experiment 2573 is displayed as the red lines. The wave front in the first frame is the rightmost red line, while the wave front in the last frame is the leftmost red line.

4 Conclusions

The task of developing a wave front tracking framework given by the Combustion, Process Safety and Explosions research group (CPSE) at University College of South-East Norway (USN) was approached with focus on finding a viable solution. As the high-speed videos provided is blurred and corrupted with noise, developing a solution which shows promise was prioritized. The result is a framework that estimates normal and oblique shock angle and velocity, as well as triple point estimation in each frame and triple point velocity in the given video. The framework is limited by the quality of the video provided, as the video is the only source of information the framework receives. Certain inputs from the user is required in order to ensure optimal performance of the framework.

The framework developed was first implemented on a single high-quality frame as a way to do a feasibility test during development. Secondly, the framework was expanded to automatically run for an entire video. Lastly, the framework was tested on different high-speed videos to test diversity of the framework.

An extended Segmented Regression method was developed in order to handle two separate data sets in parallel.

The proposed framework delivers results in accordance with theoretically calculated values and measured data presented by the CPSE research group at USN in cooperation with Caltech.

5 References

- Adaptive-Vision (2017). "Template Matching". (Accessed 13.02.2017) URL: http://docs.adaptive-vision.com/4.7/studio/machine_vision_guide/TemplateMatching.html
- R. Akbar (1997), "Mach Reflection of Gaseous Detonations". (Accessed 15.06.2017) URL: http://shepherd.caltech.edu/EDL/publications/reprints/akbar_thesis.pdf
- S. Bhardwaj, A. Mittal (2012). "A Survey on Various Edge Detector Techniques". (Accessed 10.03.2017) URL: [http://ac.els-cdn.com/S221201731200312X/1-s2.0-S221201731200312X-main.pdf?_tid=2e66faee-311c-11e7-9ff2-](http://ac.els-cdn.com/S221201731200312X/1-s2.0-S221201731200312X-main.pdf?_tid=2e66faee-311c-11e7-9ff2-11e7-9ff2-)

[0000aab0f01&acdnat=1493938456_f3c2fa0b010f920c87f9a17a81b5252e](https://doi.org/10.3384/ecp17138326)

- A. Coste (2012). "Filtering, Edge detection and Template matching ". (Accessed 15.02.2017) URL:
http://www.sci.utah.edu/~acoste/uou/Image/project2/ArthurCOSTE_Project2.pdf
- N. Otsu, "A Threshold Selection Method from Gray-Level Histograms", IEEE Transactions on Systems, Man, and Cybernetics, Vol. 9, No. 1, 1979, pp. 62-66.
- B. Schmidt (2013), "GALCIT 6-Inch Shock Tube". (Accessed 05.03.2017)
URL: http://shepherd.caltech.edu/T5/Ae104/Ae104b_handout2013.pdf
- B. E. Schmidt, B. Bobbitt, N. J. Parziale, and J. E. Shepherd (2013). "Experiments in a Combustion-Driven Shock Tube with an Area Change". (Accessed 19.05.2017) URL:
<http://shepherd.caltech.edu/EDL/publications/reprints/0246-000044.pdf>
- Wikipedia (January 2017), "Segmented Regression". (Accessed 12.04.2017) URL:
https://en.wikipedia.org/wiki/Segmented_regression

A multi-period optimization model for the design of new LNG supply chains

Alice Bittante Henrik Saxén Frank Pettersson

Åbo Akademi University, Turku, Finland, {alice.bittante, henrik.saxen, frank.pettersson}@abo.fi

Abstract

This paper presents a mathematical model developed to aid decision making in the design of a supply chain for liquefied natural gas (LNG). The supply problem considers the delivery of LNG from a number of supply ports to a set of consumers by maritime transportation to satellite terminals and by land-based truck transports from the terminals to consumers on or off the coast. The model addresses both tactical and strategic aspects in the design of a new supply chain, optimizing maritime routing of a heterogeneous fleet, truck connections and the strategic locations of the satellite terminals. The objective is to minimize the overall cost for the selected time horizon, considering both operation and investment costs. By contrast to an earlier effort by the authors, the present work also addresses storage sizes and inventory at the satellite terminals by applying a multi-period formulation. The performance of the model is illustrated by a case study, where the optimal LNG supply chain for a coastal region at a gulf was designed. The model was found to be a flexible tool for an initial design and feasibility analysis of small-scale LNG supply chains.

Keywords: Energy Systems; MILP; Optimization; Small Scale LNG; Supply Chain

1 Introduction

Liquefied natural gas (LNG) is produced by cooling natural gas (NG) below $-162\text{ }^{\circ}\text{C}$ (at atmospheric pressure), which reduces the volume to approximately one six-hundredth of the original. It is the cleanest form of fossil fuels since it has undergone purification during the liquefaction process, and it has a high H/C ratio as it is primarily composed of methane. The lower carbon intensity is the key of its recent growth of popularity: LNG is a perfect bridge fuel on the way to a world using 100 % renewable energy, providing grid stability and reliability during fluctuations in the electricity generation of intermittent renewable sources. Furthermore, the recent regulations against pollution in the maritime transportation within identified emission control areas imposed by the International Maritime Organization (IMO) have also increased the popularity of LNG, making it the most suitable fuel for maritime vessels propulsion.

The rising interest in LNG and the lack of infrastructures have served to activate several LNG-related projects worldwide. Among these, a new market segment of small-scale LNG supply chains has become increasingly important, promoting LNG utilization for middle- to small-scale applications and in sparsely distributed areas. Traditionally, the LNG supply chains have been designed for large volumes transported over long distances with LNG cargo capacities between $125,000\text{ m}^3$ and $140,000\text{ m}^3$ (but with tanker sizes up to $265,000\text{ m}^3$ currently available), in what is called liner shipping networks. Small-scale supply chains present specific characteristics and features, which differ substantially from larger chains. Vessels capacities vary from some thousand cubic meters to $30,000\text{--}40,000\text{ m}^3$ and the ship loads can be split on consecutive receiving ports. Demands are small and distributed over short distances, from hundred to a few thousand kilometers. Satellite terminals are equipped with small storage tanks ($<50,000\text{ m}^3$) to be refilled once or a few times a month. Given the high investment cost involved in both infrastructure and operation of such supply networks, the optimization of the supply chain design can have a very significant effect on the overall economics of an LNG project.

The model presented in this paper is partially based on previous work by the authors (Bittante et al. 2016), where a single-period model was introduced to aid decision making on crucial aspects in the design of small-scale LNG supply chains. The work focused on both strategic and tactic decisions, simultaneously optimizing location of the satellite terminals, size of the fleet and vehicle routing to solve the overall logistic problem. The contribution of the current paper lies in the consideration of storage size and inventory level optimization, achieved through the adoption of a multi-period formulation.

In general, the problem studied can be considered part of the broad research area of vehicle routing problems (VRP), for which the literature is rich and many variants and classes have been established (Braekers et al. 2015). However, classical VRP problems do not consider all aspects tackled by the proposed model. The subproblem defining the number and size of vessels needed to solve the maritime

transportation represents a fleet-size and mix-vehicle routing problem (FSMVRP), while the strategic subproblem of locating the satellite terminals and the linked routing belongs to the class of location-routing problems (LRP). Finally, the sizing of storage tanks and the associated inventory include aspects attributable to the class of inventory routing problems (IRP). For more detailed information on these classes of problems we refer to Hoff et al. (2010) for a review paper on FSMVRP with both maritime and land transport, Drexl and Schneider (2015) for a recent survey and classification on LRP, and Andersson et al. (2010) for a comprehensive review on IRP.

Most of the approaches proposed in the literature focus on heuristics solutions and very few papers present exact methods. Baldacci et al. (2009) designed a mixed integer linear programming (MILP) model to solve a FSMVRP problem similar to the one considered in this paper, but where each customer is associated with a single route as in the classic VRP. By contrast, in our approach we allow for multiple visits at the customers by multiple vehicles. This feature also occurs in the formulation of the LRP subproblem. While most of the variables used for describing the activation of satellite terminal and their associated routes and delivery are the same as those used in the literature (Gonzalez-Feliu 2009), the set of binary variables to activate the routes associated with an activated satellite terminal has been changed into integer variables to allow for multiple voyages to the same port. According to the classification given in the review paper by Andersson et al. (2010), our approach falls into the finite time class, featuring deterministic demand, many-to-many topology, multiple routing, fixed inventory, and heterogeneous fleet composition. A contribution listed in the reviewed literature presenting similar features and where a deterministic approach is used is the work by Al-Khayyal and Hwang (2007) for an IRP for a multi-commodity liquid bulk. Their problem is a classic IRP problem, where storage sizes are given as well as the fleet of ships. The model focuses on the key aspects of a multi-product pickup-delivery problem and the authors solve a small illustrative example for detecting the central parameters to be used in developing a strategy for solving larger instances. A recent paper by Koza et al. (2017) presents many characteristics similar to our problem, including the focus on LNG market and infrastructure. Our contribution differs by the market-segment it is directed to (i.e., small-scale logistics versus liner networks), the feature of locating the satellite terminals and the multi-period formulation for optimized storage sizing and inventory. Furthermore, our approach is based on an arc-flow formulation while the above-mentioned reference applies a path-based model.

The literature on routing problems often favors path-flow formulation over arc-based ones: with the feasible

routes being predefined, the path-flow formulations do not include constraints related to routing feasibility, but focus on the set of ports or customers to serve. This is usually beneficial when the size of the problem increases. Often, the solution time is anyhow unacceptably long and pure heuristics or early terminations in exact methods are preferred. This is mainly due to the intrinsic complexity of VRP in general. Usually only very small problems, not relevant for real-life studies, can be solved in reasonable computation time with a deterministic approach. To overcome this limitation — still applying an exact method — we neglected some operational aspects that were not considered essential at the first level of planning: We do not consider scheduling, supply availability according to production rate or inventory, boil-off loss, time windows at the ports, or load dependent fuel consumption for the ships. With these simplifications, a mixed integer linear programming (MILP) model was formulated that can solve realistic problems within a few hours of computation time. Both strategic infrastructure decisions and tactical planning are simultaneously optimized. The multi-period formulation allows for a more detailed evaluation of the storage tank sizes and inventory, offering the possibility for a more efficient routing. The multi-period formulation is illustrated by comparison to the single-period solution of a case study based on the emerging LNG market in the Gulf of Bothnia.

2 Problem description

In this paper we present a multi-period formulation as an extension of the model presented in Bittante et al. (2016). The problem tackled is a regional supply of LNG from a set of potential supply ports to inland end customers through a set of potential satellite terminals. At the supply ports LNG is loaded to specially designed vessels and transported to the satellite terminals. LNG can also be transported by truck from the ports to inland customers. Satellite terminals have potential locations and can be activated or not according to the overall objective. Potential satellite terminals and inland customers have given fixed demands for the time horizon considered, which must be satisfied either by transported LNG or by an alternative fuel. This generic fuel is merely used to allow the model to partly or fully exclude customers from the LNG supply chain; therefore we do not consider the transportation costs of the alternative fuel. It should be noted that the demand sites represent cluster of consumers, which justifies the use of multiple fuels. The fleet of vessels can be freely chosen from a set of heterogeneous ship types, each of which has a given cruising speed, capacity, fuel consumption and loading/unloading rate. The ships can perform split delivery and no limitations on routes or ship-port connections are imposed. Restrictions regarding the maximum amount of LNG available at the

supply ports is included in the formulation and can be parametrically activated. LNG tank trucks for the land-based transportation are chosen from a homogeneous fleet of given capacity and fuel consumption and cannot perform split delivery. Each truck is associated to a single supply or satellite terminal, cannot be swapped among ports and is limited to a maximum travelling distance. The number of trucks is constrained by the number of filling stations at the ports and the weekly working hours at the facilities. Inland customers are assumed to have enough storage capacity to stock the full LNG demand for the time horizon and no investment costs are considered at these sites. However, size dependent investment costs for the storage tanks are considered at the activated satellite terminals. There are three key decisions in the optimization: to locate the satellite terminals, to determine the fleet and routing for both maritime and land transport, and to size the storage tanks at the satellite terminals and to determine their inventory levels.

3 Mathematical model

3.1 Sets and variables

Let T denote the set of time periods indexed by t . Let J and S denote the sets of satellite terminals and supply ports, respectively. The set of all ports is denoted by $P = J \cup S$. Let D denote the set of inland customers and $L = J \cup D$ denote the set of all customers of given demand $D_{i,t}$. The indexed set of LNG ship types is K . The arc set A is defined as $\{(p,m): p \in P, m \in P, p \neq m\}$ and represents all the sailing legs between pairs of ports. Let $B = \{(p,l): p \in P, l \in L, d_{p,l} \leq d^{\max}\}$ denote the land-based port-consumer connection, the distance of which is below an upper limit d^{\max} . Maritime routing is described by the use of three sets of variables: Integer variables $y_{p,m,k,t}$ indicate how many times ship type k travels the sailing leg $(p,m) \in A$ in time period t . Continuous variables $x_{p,i,k,t}$ specify the number of LNG loads transported by ship type k on the route $(p,i) \in A$ in time period t . The ship types composing the fleet are given by binary variables z_k . Three sets of variables are also used to model the land-based transport. Continuous variables $q_{p,l}$ express the amount of LNG transported on the route $(p,l) \in B$. The number of allocated trucks per port and the number of trips per route are given by integer variables z_p and $z_{p,l}$, respectively. The activation of satellite terminals is controlled by the binary decision variables w_i . Continuous variables s_i and $q_{i,t}^S$ denote the storage size at the activated satellite terminals and the inventory at the beginning of each time period, respectively. Finally, the supply of alternative fuel to the consumers is represented by decision variables q_i^A .

3.2 Mathematical formulation

The objective of the problem is to minimize the combined fuel, operation and investment costs. The first term in Eq. (2), the fuel cost, is given as the quantity of LNG and/or alternative fuel used multiplied by the specific fuel price. The second term, representing the operation cost, is the sum of port calls fees, costs of ship propulsion, chartering of the ships, and truck fuel consumption. Finally, the investment cost includes the truck purchase and the construction of the satellite terminal infrastructure and storages. The parameter

$$\gamma = \frac{1}{365 d} \cdot \frac{e}{1 - (1 + e)^{-n}} \quad (1)$$

in the last term of Eq. (2) rescales the total investment cost to the contribution for the time horizon H considered in the optimization, where e is the interest rate and n is the life length of the investment.

The model is formulated as

$$\begin{aligned} \min C^{tot} &= \sum_{s \in S} \sum_{i \in J} \sum_{k \in K} \sum_{t \in T} C_s^G Q_k x_{s,i,k,t} \\ &+ N \left(\sum_{s \in S} \sum_{l \in L} C_s^G q_{s,l} + \sum_{l \in L} C^A q_l^A \right) \\ &+ \sum_{(p,m) \in P} \sum_{k \in K} \sum_{t \in T} C_p y_{p,m,k,t} \\ &+ NH \sum_{k \in K} C_k^R z_k \\ &+ \sum_{(p,m) \in P} \sum_{k \in K} \sum_{t \in T} C_k^F d_{p,m} y_{p,m,k,t} \\ &+ 2N \sum_{p \in P} \sum_{l \in L} C^F d_{p,l}^L z_{p,l} \\ &+ \gamma NH \left[I^T \sum_{p \in P} z_p + \sum_{i \in J} (I^W w_i + I^S s_i) \right] \end{aligned} \quad (2)$$

$$\begin{aligned} \sum_{p \in P} \sum_{k \in K} Q_k x_{p,i,k,t} - \sum_{j \in J} \sum_{k \in K} Q_k x_{i,j,k,t} \\ + \sum_{p \in P} q_{p,i} - \sum_{l \in L} q_{i,l} + q_i^A \\ + q_{i,t}^S \geq D_{i,t} H \quad \forall i \in J, t \in T. \end{aligned} \quad (3)$$

$$\sum_{p \in P} q_{p,d} + q_d^A \geq D_{d,t} H \quad \forall d \in D, t \in T \quad (4)$$

$$\begin{aligned} (1 - f^S) s_i \geq q_{i,t}^S + \sum_{p \in P} \sum_{k \in K} Q_k x_{p,i,k,t} \\ - \sum_{j \in J} \sum_{k \in K} Q_k x_{i,j,k,t} \quad \forall i \\ \in J, t \in T \end{aligned} \quad (5)$$

$$q_{i,t}^S \geq f^S s_i \quad \forall i \in J, t \in T \quad (6)$$

$$q_{i,t}^S = q_{i,t-1}^S + \sum_{p \in P} \sum_{k \in K} Q_k x_{p,i,k,t-1} - \sum_{j \in J} \sum_{k \in K} Q_k x_{i,j,k,t-1} - \sum_{l \in L} q_{i,l} - D_{i,t-1} H w_i \quad \forall i \in J, t \in T \text{ and } t > 1 \quad (7)$$

$$q_{i,t_{first}}^S = q_{i,t_{last}}^S + \sum_{p \in P} \sum_{k \in K} Q_k x_{p,i,k,t_{last}} - \sum_{j \in J} \sum_{k \in K} Q_k x_{i,j,k,t_{last}} - \sum_{l \in L} q_{i,l} - D_{i,t_{last}} H w_i \quad \forall i \in J \quad (8)$$

$$\sum_{p \in P} \sum_{k \in K} \sum_{t \in T} (y_{p,i,k,t} + y_{i,p,k,t}) \leq M w_i \quad \forall i \in J \quad (9)$$

$$s_i / \text{MWh} \leq M w_i \quad \forall i \in J \quad (10)$$

$$y_{p,i,k,t} \geq x_{p,i,k,t} \quad \forall p \in P, i \in J, k \in K, t \in T \quad (11)$$

$$\sum_{m \in P} y_{m,p,k,t} = \sum_{m \in P} y_{p,m,k,t} \quad \forall p \in P, k \in K, t \in T \quad (12)$$

$$\sum_{p \in P} x_{p,i,k,t} \geq \sum_{p \in P} x_{i,p,k,t} \quad \forall i \in J, k \in K, t \in T \quad (13)$$

$$M x_{p,i,k,t} \geq y_{p,i,k,t} \quad \forall p \in P, i \in J, k \in K, t \in T \quad (14)$$

$$a_k H z_k \geq \frac{1}{v_k} \sum_{(p,m) \in P} d_{p,m} y_{p,m,k,t} + \sum_{p \in P} \left(t_p^B \sum_{m \in P} y_{p,m,k,t} \right) + \frac{2}{r_k} \sum_{s \in S} \sum_{p \in P} Q_k x_{s,p,k,t} \quad \forall k \in K, t \in T \quad (15)$$

$$\sum_{i \in J} \sum_{k \in K} Q_k x_{s,i,k,t} + \sum_{l \in L} q_{s,l} \leq Q_s^U H \forall s \in S, t \in T \quad (16)$$

$$\sum_{l \in L} q_{i,l} \leq M w_i \text{ MWh} \quad \forall i \in J \quad (17)$$

$$z_{p,l} \geq \frac{q_{p,l}}{Q} \quad \forall p \in P, l \in L \quad (18)$$

$$z_p \leq Z_p^U \quad \forall p \in P \quad (19)$$

$$\sum_{l \in L} z_{p,l} \leq \frac{5}{7} H Z_p^U \quad \forall p \in P \quad (20)$$

$$a H z_p \geq \sum_{l \in L} \left(\frac{2}{v} d_{p,l}^L + t^0 \right) z_{p,l} \quad \forall p \in P \quad (21)$$

3.3 Constraints

Most of the constraints are identical or similar to the ones for the single period model, with the addition of the time period index. New sets of constraints are required to control the tank storage mass balance and sizing. Constraints (3) and (4) guarantee that the demand is fulfilled at the satellite terminals and at the inland consumers, respectively. Constraints (5) and (6) define the tank storage size, ensuring sufficient capacity for all the LNG delivered in the time period and for an additional fraction (heel). The storage mass balance is controlled by constraints (7), taking into account the storage levels between time periods. Rolling horizon constraints (eq. (8)) make the storage level at the beginning of the first time-period the same as that in the end of the last period. The activation of the satellite terminals is defined by constraints (9). If a terminal is activated, constraints (10) permit the existence of a storage tank by allowing variables s_i to be positive. As in the single-period formulation, four sets of constraints (eq. (11)-(14)) control the maritime routing. Constraints (15) determine the fleet composition (in terms of ship types) based on the ship time usage. Constraints (16) limit the amount of LNG available at the supply ports. Land-based transportation is controlled by five sets of constraints. Constraints (17) ban transportation of LNG from a non-activated satellite terminal. The number of required truck voyages from port to customer is obtained from constraints (18). The total number of trucks and truck voyages from each port are limited based on the maximum number of truck loads per day, by constraints (19) and (20). Finally, constraints (21) guarantee a sufficient number of trucks per port to carry out the total land-based LNG delivery.

4 Case study

The presented model has been applied to a study of LNG delivery in the Gulf of Bothnia (i.e., the northern part of the Baltic Sea). This fictitious was created inspired by

several LNG-related projects approved or under discussion in this region.

Two supply terminals (Tornio, Stockholm), one fixed satellite terminal (Pori, 30,000 m³) and three potential ones (Turku, Vaasa, Umeå) on the coasts of Finland and Sweden have been preselected. A total of twenty clusters distributed in Finland and Sweden were identified as inland customers. Demands were assigned as gross estimates based on population, extent of industrial activity and time horizon considered. Five ship types, with capacities Q_k of 3,000 m³, 5,000 m³, 6,500 m³, 7,500 m³ and 10,000 m³ were selected, with parameters inspired by small-scale LNG carrier designs by Wärtsilä (Wärtsilä 2015). Maritime distances were obtained from an online tool for calculation of distances between sea ports (Sea-Distances.org 2015), while road distances were collected from a web mapping service (Google Maps). A maximum distance $d^{\max} = 350$ km was used to identify the feasible port-customer road connections. The availability of vessels and trucks is a portion of the total time horizon, allowing for some extra time. An availability of 95 % was used for the ships ($a_k = 0.95$) while the corresponding number for trucks was $a = 0.298$; the latter factor also considers a rescaling of the total time to ten-hour working days in a five-day working week. The optimization was first performed for a 10-day single-period time horizon (H) and then successively for three identical time periods ($N = 3$) of 10 days each to study the impact of the multi-period formulation on the overall optimization. Tables with the numerical values of all the parameters used in the model are presented in the Appendix.

The MILP model was implemented in AIMMS 4.8 using the IBM ILOG CPLEX Optimizer (AIMMS-CPLEX). The problem of the case study results in 609 integer and 444 continuous variables. The solution time of this size of problem varied between 30 s and 40 min depending on parameter values, on a computer with a 3.5 GHz Intel Core i7 processor and 32 GB of RAM.

4.1 Single-period results

We first present results for the single-period case, where the price of LNG at the two supply ports is identical, $C_S^G = 30$ €/MWh, and the price of alternative fuel at the consumers is $C^A = 40$ €/MWh. Figure 1 illustrates the optimal maritime routing (curved arrowed arcs) and port-to-customer truck connections (straight arrowed lines). Detailed numerical results of the optimization are reported in Tables 1 and 2.

The results show that all the customers are served partially or entirely with LNG. Only two customers are partially supplied with alternative fuel (Sollefteå and Kokkola, both with 0.038 GWh). One ship of Type 3 (6,500 m³) is needed for the LNG maritime distribution to the satellite terminals, which in addition to the one in Pori have been activated in Umeå and Vaasa. The storage sizes of the latter ones are about 7500 m³ and

2500 m³, respectively, while Pori has a fixed capacity of 30,000 m³. The maritime routing is reported in Table 1. One split delivery is performed between Umeå, Pori and Vaasa. Totally, 113.4 GWh of LNG is shipped to the three satellite terminals; one third from Stockholm and the remaining from Tornio. The total amount of LNG transported by truck is 113 GWh, in 364 trips. The number of trucks per port is indicated in Table 2, ranging from 1 in Vaasa to 17 in Tornio. Supply ports have the highest number as they serve the majority of the land customers reached. Among the satellite terminals, Pori has the largest amount of LNG for truck transport, and therefore a high number of allocated trucks. For this case, the overall optimal cost is 32.406 €/MWh.

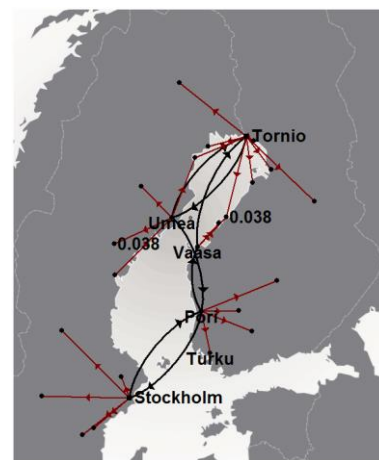


Figure 1. Optimal satellite terminal locations and LNG distribution from ports for the single-period case. Straight arrows indicate land transport by truck and arrowed arcs maritime routing. Alternative fuel is reported in GWh.

Table 1. Optimal results for the maritime routing for the single-period case, where y denotes the number of trips and x the ship loads.

Route	$y_{p,m,k}$	$x_{p,i,k}$
Stockholm-Pori	1	0.99
Pori-Stockholm	1	-
Tornio-Umeå	2	2.00
Umeå-Tornio	1	-
Umeå-Pori	1	0.97
Pori-Vaasa	1	0.35
Vaasa-Tornio	1	-

Table 2. Number of trucks per port and amount of LNG delivered to customers by truck.

Port	z_p	LNG trucked, GWh
Tornio	17	42.5
Stockholm	15	37
Pori	8	21
Umeå	4	9.1
Vaasa	1	3.4

4.2 Multi-period results

For the multi-period case, we consider three identical periods with a rolling time horizon. As it is interesting to optimize the storage tank sizes in combination with the maritime routing, the land-based transport solution was taken to be independent of the time period, so the amount of LNG delivered by truck, the number of trucks and the related port-customers connections are identical in the three periods. However, they need not be identical to the solution of the single-period case, as the land-based transport will still be optimized together with the time-period-dependent maritime routing and storage.

Results are presented in Figure 2 and Tables 3-4. The same satellite terminals as in the single-period case are seen to be activated, but the storage tank sizes are about 4,000 m³ larger: Umeå and Vaasa now have tanks of about 11,500 m³ and 6,500 m³, respectively. This increase in investment cost is outweighed by a shift to a smaller ship of Type 2, which is sufficient for carrying out the maritime LNG deliveries. Figure 2 a-c presents the routing, which is seen to be different for the time periods. The total amount of LNG transported by ship in all three time periods is 341.8 GWh, supplied roughly equally from Stockholm and Tornio. The amount of LNG transported by trucks is about 337.5 GWh. Comparing these numbers with the results for the single-period problem, on average and per period, LNG deliveries by sea have increased by 0.5 GWh while deliveries by road have decrease by 0.5 GWh. In more detail, the LNG transported by truck from Tornio and Pori has decreased by 1 GWh and 3.2 GWh, respectively, while the land transport from Vaasa has increased by 3.7 GWh. This explains how the increase in maritime delivery has been used to partially outweigh the decrease in Tornio by redistributing the land-based deliveries between Pori and Vaasa (see Table 4). The

remaining reduction in LNG use found in the optimal solution of the multi-period case has been fulfilled by a larger quantities of alternative fuel (see Figure 2, where alternative fuel amounts reported in GWh).

Table 3. Optimal maritime routing for multi-period case

Route	Time period	$y_{p,m,k,t}$	$x_{p,i,k,t}$
Stockholm-Pori	1	1	1
Pori-Stockholm	1	1	-
Tornio-Umeå	1	2	2.00
Umeå-Tornio	1	3	-
Tornio-Vaasa	1	1	0.84
Vaasa-Umeå	1	1	0.09
Stockholm-Pori	2	3	2.95
Pori-Stockholm	2	3	-
Tornio-Umeå	2	1	0.93
Umeå-Tornio	2	1	-
Stockholm-Pori	3	2	2.00
Pori-Stockholm	3	2	-
Tornio-Umeå	3	1	1.00
Umeå-Tornio	3	1	-
Tornio-Vaasa	3	1	1.00
Vaasa-Tornio	3	1	-

Table 4. Number of trucks per port and amount of LNG delivered to customers by truck.

Port	z_p	LNG trucked, GWh
Tornio	16	41.5
Stockholm	15	37
Pori	6	17.8
Umeå	4	9.1
Vaasa	3	7.1

Figure 3 and 4 show the use of the storage tank capacity by reporting the data of the stored and unloaded LNG at each port per time period. The stored LNG refer

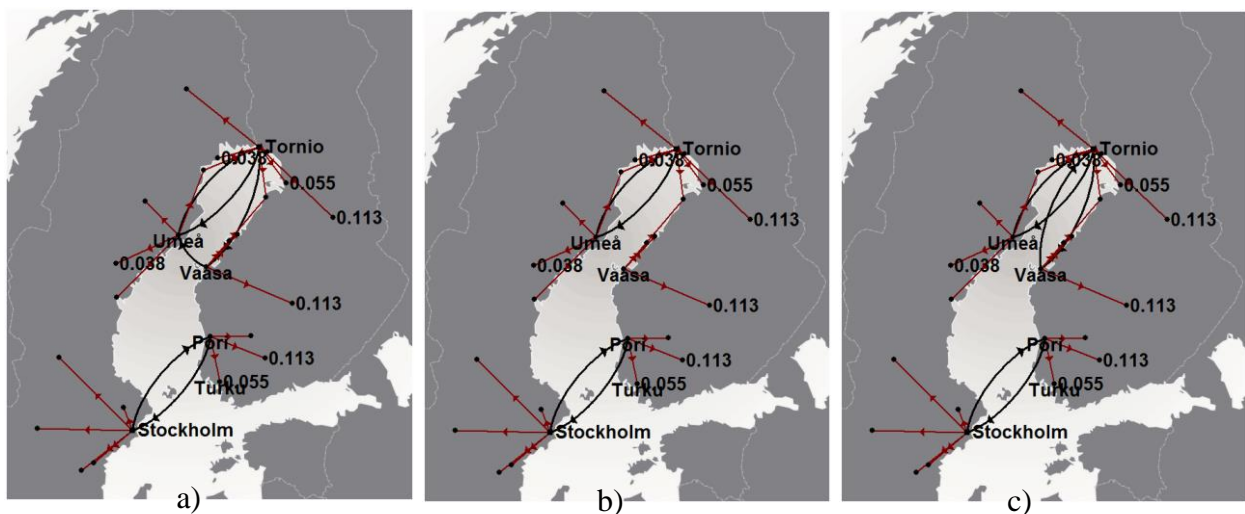


Figure 2. Optimal satellite terminal locations and LNG distribution from supply to satellite ports for the multi-period case. a) Time period 1, b) Time period 2, and c) Time period 3.

to the state at the beginning of the time periods, while the unloaded quantities refer to the ship deliveries for the time period. It can be seen that a bigger inventory is used for periods when the unloaded LNG is insufficient to cover the demand. This is particular the case for Vaasa, which does not have any ship visits during period 2 (Figure 4 vs. Figure 2 b) and instead uses the storage to satisfy the local demand and the demands of its inland customers (Figure 3). The overall cost for the multi-period solution is 32.333 €/MWh, which is more than 7 cents lower than the costs of the single-period solution, yielding a yearly saving of about half a million euro.

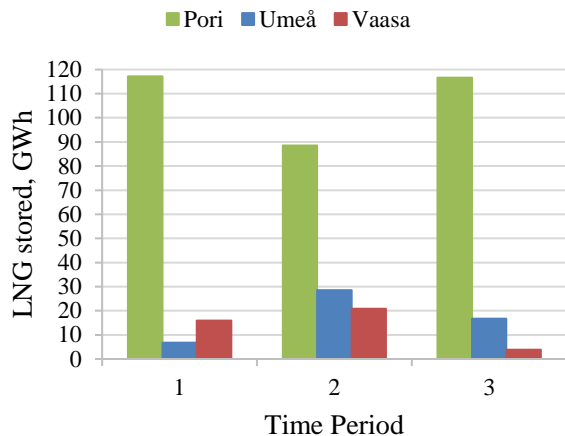


Figure 3. Amount of LNG stored at the satellite terminals in the beginning of every time period.

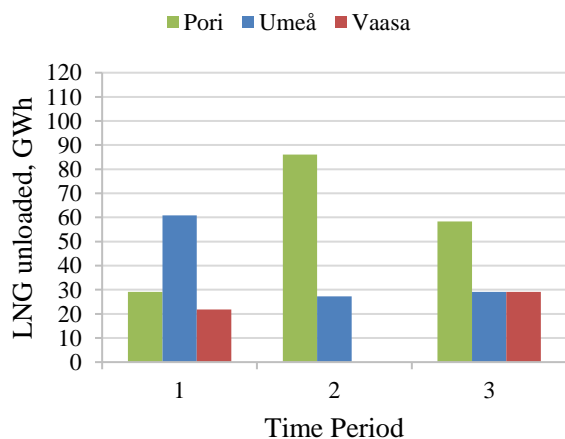


Figure 4. Amount of LNG unloaded at the satellite terminals per time period.

5 Conclusions and future work

An MILP model for the optimal design of a small-scale LNG supply chain has been presented. The model addresses both strategic and tactical aspects, often treated separately in logistics studies. This is realized by a simultaneous minimization of investment and operation costs in the objective function. The extension to a multi-period formulation makes it possible to

optimize storage tank sizing and inventory. The optimal solution gives the location of the satellite terminals (to be built), the fleet configuration in terms of number and type of ships and number of tank trucks per port, the associated distribution network (maritime routing and road connections), the size of the storage tanks at the satellite terminals, and their inventory levels. The results from a case study demonstrate the advantages of a multi-period formulation on the overall optimal supply chain design. In small-scale designs where demands and distances are relatively small, it is not clear at the outset whether, in terms of costs, operations should drive investments decisions or vice versa. This can be clarified by using the proposed model, which has proven to be a valuable tool for early evaluation of new LNG projects, but also for initial planning and design. The simplicity and flexibility of the formulation make it an ideal basis for studies of other supply chains, e.g., in the evaluation and upgrading of existing networks.

In the future work, attention will be directed to consider uncertainties since transportation conditions, equipment availability and market circumstances may vary. A stochastic model could be developed to consider parameters variation and different scenarios to find solutions that are robust, i.e., insensitive to parametric changes.

Acknowledgements

This work was carried out in the Efficient Energy Use (EFEU) research program coordinated by CLIC Innovation Ltd. with funding from the Finnish Funding Agency for Technology and Innovation (Tekes) and participating companies. The financial support is gratefully acknowledged.

Appendix

In this appendix we report all the numerical values of the parameters of the mathematical model. Table A.1 reports the sea distances expressed in kilometers. Parameters regarding port specifications are given in Table A.2. The parameter Z_p^U limiting the truck trips has been estimated considering the number of loading stations available at the ports (5 for supply ports, 3 for satellite terminals), an average two-hour time for loading operations and a ten-hour service at the port for twenty working days a month. Table A.3 reports parameters of the different ship types. Other miscellaneous model parameters are listed in Table A.4. Finally, Table A.5 reports the road distances between ports and customers, as well as the customers' demands.

Table A. 1. Sea distances between ports (Sea-Distances.org 2015).

$d_{p,m}$, km	<i>Tornio</i>	<i>Stockholm</i>	<i>Turku</i>	<i>Pori</i>	<i>Vaasa</i>	<i>Umeå</i>
<i>Tornio</i>	0	809	885	559	373	338
<i>Stockholm</i>	809	0	324	422	580	632
<i>Turku</i>	885	324	0	315	485	452
<i>Pori</i>	559	422	315	0	253	288
<i>Vaasa</i>	373	580	485	253	0	115
<i>Umeå</i>	338	632	452	288	115	0

Table A. 2. Port specific parameters

<i>Ports</i>	C_p , €	C_s^G , €/MWh	Q_s^U , GWh/d	t_p^B , h	Z_p^U , -
Tornio	5,000	30	40	5	25
Stockholm	5,000	30	40	5	25
Turku				5	15
Pori				5	15
Vaasa				5	15
Umeå				5	15

Table A. 3. Ship-related parameters

<i>Ship Type</i>	a_k , -	C_k^F , €/km	C_k^R , €/d	Q_k , MWh (m^3)	r_k , MW (m^3/h)	v_k , km/h
Type 1	0.95	4	11,000	17,499 (3,000)	4666.4 (800)	21
Type 2	0.95	5	14,000	29,165 (5,000)	4666.4 (800)	23
Type 3	0.95	5	17,000	37,914.5 (6,500)	4666.4 (800)	24
Type 4	0.95	6	19,000	43,747.5 (7,500)	4666.4 (800)	25
Type 5	0.95	6	23,000	58,333.0 (10,000)	4666.4 (800)	26

Table A. 4. Other model parameters

<i>Parameter</i>	
a , -	0.298
C^A , €/MWh	40
C^F , €/km	1
e , -	0,01
f^S , -	0.1
H , d	10
I^T , €	2,000,000
I^S , €/MWh	200
I^W , €	20,000,000
n , a	30
N , -	3
Q , MWh (m^3)	320.8 (55)
t^0 , h	2
v , km/h	50
γ , 1/d	0.0001

Table A. 5. Road distances between ports and customers (Google Maps) and customer daily demands.

$d_{p,l}^L, km$																								
	<i>Turku</i>	<i>Pori</i>	<i>Vaasa</i>	<i>Umeå</i>	<i>Kemi</i>	<i>Kokkola</i>	<i>Malmberget</i>	<i>Oulu</i>	<i>Pietarsaari</i>	<i>Piteå</i>	<i>Jyväskylä</i>	<i>Hämeenlinna</i>	<i>Kajaani</i>	<i>Tampere</i>	<i>Uppsala</i>	<i>Linköping</i>	<i>Norrköping</i>	<i>Karlstad</i>	<i>Mora</i>	<i>Lyckeå</i>	<i>Sollefteå</i>	<i>Raahe</i>	<i>Luleå</i>	<i>Sundsvall</i>
<i>Tornio</i>	778	639	450	386	28	330	260	131	368	175	470	658	313	618	957	1,219	1,182	1,198	945	388	589	206	130	649
<i>Stockholm</i>	1,000	455	747	638	1050	868	1,138	1,153	845	850	622	456	1,335	476	70	197	160	305	307	717	493	1228	906	375
<i>Turku</i>	0	142	334	1,163	752	436	1,036	647	413	951	308	143	622	162	1,000	511	474	599	590	581	647	563	907	1,425
<i>Pori</i>	142	0	191	1,024	612	309	897	508	286	813	263	186	577	111	459	654	617	742	864	438	508	434	767	1,285
<i>Vaasa</i>	334	191	0	835	424	121	709	320	98	624	267	321	367	240	686	948	911	927	674	1,000	1,000	246	579	1,097
<i>Umeå</i>	1,163	1,024	835	0	413	1,000	501	516	752	213	1,000	441	698	360	572	833	797	812	560	128	203	591	265	264
$D_{i,t}, GWh/d$																								
	1	4	1	3	0.7	0.1	0.6	1	0.3	0.3	0.3	0.3	0.3	0.5	1	1	1	0.5	0.2	0.5	0.1	1.2	0.1	0.3

Nomenclature

Sets

J	Set of satellite terminals
D	Set of inland customers
K	Set of ship types
L	Set of customers
P	Set of ports
S	Set of supply ports
T	Set of time periods

Indices

j	Satellite terminals $j \in I$
d	Inland customers $d \in D$
k	Ship types $k \in K$
l	Customers $l \in L$
p, m	Ports $(p, m) \in P$
s	Supply ports $s \in S$

Variables

q_l^A	Continuous variable indicating the amount of energy from alternative fuel, MWh
$q_{p,l}$	Continuous variable indicating the amount of energy from LNG trucked, MWh
s_i	Continuous variable indicating the size of the tank storage, MWh
z_p	Integer variable indicating number of trucks per port, -
$z_{p,l}$	Integer variable indicating number of truck trips between p and l , -
w_i	Binary variable, $w_i = 1$ if satellite terminal i is activated, -
$x_{p,i,k,t}$	Continuous variable indicating ship load transported, -
$y_{p,m,k,t}$	Integer variable indicating number of time the route between p and m is travelled, -
z_k	Binary variable indicating the ship types, -
$q_{i,t}^S$	Continuous variable indicating amount of LNG stored at the beginning of the time period, MWh

Parameters

a	Truck availability, -
a_k	Ship availability, -
C^A	Price of the alternative fuel, €/MWh
C_s^G	Price of LNG in supply port s , €/MWh
C_p	Port call cost, €
C^F	Truck fuel consumption cost, €/km
C_k^F	Ship propulsion cost, €/km
C_k^R	Ship renting cost, €/d
$d_{p,m}$	Maritime distance, km
$d_{p,l}^L$	Road distance, km

$D_{l,t}$	Energy demand, MWh/d
e	Interest rate, -
f^S	Fraction of storage capacity for LNG heel, -
H	Time horizon, d
I^T	Truck investment cost, €
I^S	Tank storage investment cost, €/MWh
I^W	Fixed investment cost of satellite terminal, €
M	Big-M parameter, -
n	Payback time, year
N	Number of time periods, -
Q	Truck capacity, MWh
Q_s^U	Maximum amount of LNG available at the supply port, MWh/d
Q_k	Ship capacity, MWh
r_k	Loading/unloading rate, MW
t_p^B	Berthing time, h
t^O	Operation time loading trucks, h
Z_p^U	Maximum number of truck's loads per day in port p , 1/d
v	Truck average speed, km/h
v_k	Ship average cruising speed, km/h
γ	Investment instalment factor, 1/d

References

- AIMMS-CPLEX, AIMMS-CPLEX. Available at: <https://aimms.com/english/developers/resources/solvers/cplex> [Accessed June 2, 2017].
- Al-Khayyal, F. & Hwang, S.-J., 2007. Inventory constrained maritime routing and scheduling for multi-commodity liquid bulk, Part I: Applications and model. *European Journal of Operational Research*, 176(1), pp.106–130. Available at: <http://dx.doi.org/10.1016/j.ejor.2005.06.047>.
- Andersson, H. et al., 2010. Computers & Operations Research Industrial aspects and literature survey: Combined inventory management and routing. *Computers and Operation Research*, 37(9), pp.1515–1536. Available at: <http://dx.doi.org/10.1016/j.cor.2009.11.009>.
- Baldacci, R., Battarra, M. & Vigo, D., 2009. Valid inequalities for the fleet size and mix vehicle routing problem with fixed costs. *Networks*, 54(4), pp.178–189. Available at: <http://doi.wiley.com/10.1002/net.20331>.
- Bittante, A. et al., 2016. Mixed integer optimization of an LNG supply chain in the Baltic Sea region. In *The 29th International Conference on Efficiency, Cost, Optimization, Simulation and Environmental Impact of Energy Systems*. p. P624.
- Braekers, K., Ramaekers, K. & Nieuwenhuyse, I. Van, 2015. The Vehicle Routing Problem: State of the Art Classification and Review. *Computers &*

- Industrial Engineering*. Available at:
<http://www.sciencedirect.com/science/article/pii/S0360835215004775> [Accessed June 2, 2017].
- Drexl, M. & Schneider, M., 2015. A survey of variants and extensions of the location-routing problem. *European Journal of Operational Research*, 241(2), pp.283–308. Available at:
<http://www.sciencedirect.com/science/article/pii/S0377221714006651> [Accessed June 2, 2017].
- Gonzalez-Feliu, J., 2009. *The N-echelon Location routing problem: concepts and methods for tactical and operational planning*. Available at:
https://halshs.archives-ouvertes.fr/halshs-00422492/file/Multi-echelon_LRP.pdf [Accessed June 2, 2017].
- Google Maps, Google Maps. Available at:
<https://www.google.fi/maps?source=tldsi&hl=en> [Accessed June 2, 2017].
- Hoff, A. et al., 2010. Industrial aspects and literature survey: Fleet composition and routing. *Computers and Operations Research*, 37(12), pp.2041–2061. Available at:
<http://dx.doi.org/10.1016/j.cor.2010.03.015>.
- Koza, D.F., Ropke, S. & Molas, A.B., 2017. The liquefied natural gas infrastructure and tanker fleet sizing problem. *Transportation Research Part E*, 99, pp.96–114. Available at:
<http://dx.doi.org/10.1016/j.tre.2017.01.003>.
- Sea-Distances.org, 2015. SEA-DISTANCES.ORG - Distances. Available at: <http://www.sea-distances.org/> [Accessed June 2, 2017].
- Wärtsilä, 2015. Gas Carriers. Available at:
<http://www.wartsila.com/products/marine-oil-gas/ship-design/merchant/gas-carriers> [Accessed June 2, 2017].

The Impact of Signalling Kinetics on Controller Motif Performance

Geir B. Risvoll Tormod Drengstig

Dept. of Electrical Engineering and Computer Science, University of Stavanger, Norway,
{geir.risvoll,tormod.drengstig}@uis.no

Abstract

In this paper we investigate how the disturbance rejection properties of physiological regulatory systems depend on the signalling kinetics between the biochemical species being considered as controlled and manipulated variables. Based on the mathematical model of a physiological regulatory system, we analyse the impact of three different signalling models, i.e. linear signalling, first order and second order Hill kinetics. We separate the analysis in two parts. First we identify to what extent the signalling from the manipulated variable to the controlled variable affect the range and ratio of manageable disturbances. In the second part we investigate whether and how the signalling from the controlled variable to the manipulated variable will affect the parameters of the controller part of the regulatory system. In this context, saturable Hill kinetics display advantages compared to linear signalling.

Keywords: Systems Biology, Control Engineering, Homeostasis, Signalling Kinetics

1 Introduction

In order for organisms to function properly it is imperative that their internal environment is maintained within certain thresholds independent on external conditions. This ability of living systems to adjust their own environment was first described by Claude Bernard with his definition of *milieu intérieur* (Cooper, 2008; Langley, 1973). Cannon later refined this concept and coined the term *homeostasis* (Cannon, 1929, 1939). The term homeostasis has since become the most commonly used concept when talking about an organism's ability to regulate its own internal environment in an ever changing external environment. This concept is closely related to that of control engineering, where the objective is to maintain a given setpoint, regardless of external perturbations (Skogestad and Postlethwaite, 2005).

An example of a physiological regulatory system is the regulation of cellular glucose concentration in the presence of varying blood glucose concentration. Related to the intracellular stability is also the cell's ability to counteract for e.g. large variations in intracellular consumption. For the blood glucose example, an intensive exercise session will dramatically increase the intracellular glucose consumption, leading to an increased glucose uptake from the blood stream. The physiological mechanisms behind this regulation include hormones acting as

signalling species, cellular membrane receptors transferring the signalling information within the cell, and cellular membrane proteins acting as pumps. For glucose to enter a cell, the insulin hormone secreted by the pancreas is sensed by the insulin receptor located in the cell membrane. This again leads to a cascade of signalling events inside the cell, which finally activates the glucose transporter facilitating glucose uptake. In order to utilize the glucose as cellular fuel, the glucose enters the glycolysis which is a chain of enzyme catalysed reactions converting glucose into pyrovalate which again is transported into the mitochondria and the TCA cycle (Jeoung and Harris, 2010; Lam et al., 2005).

The modelling of such systems involves enzymes and transporter proteins, and the models can be made at different levels of complexity, all depending on the aim of the modelling effort. If the goal is to make a detailed model of one part of the glycolysis, it can be very different compared to a model of the overall cellular homeostatic function (Ackerman et al., 1965; Swierkosz, 2015). In the latter case, the underlying model *structure* which would include signalling events from other cellular species is perhaps more important than *details* about certain enzymatic steps. In this respect, we are interested in the properties of different signalling models and how the underlying signalling kinetics will affect the performance of regulatory systems. Performance is, in this context, defined as the disturbance rejection properties of the regulatory systems, i.e. to what extent is different signalling kinetic implementations able to cope with increasing level of disturbances/perturbations. In order to compare the different signalling models we have defined a regulatory system where the involved species varies between some predefined levels. Thus, we maintain as much as possible of the surrounding cellular conditions enabling us to compare the results.

2 Controller Motifs

We have previously published the eight controller motifs shown in Figure 1, all being candidates for physiological regulatory systems (Drengstig et al., 2012). The function of these controller motifs show similarities with standard integral control (Drengstig et al., 2012), and their control theoretic properties have been investigated (Thorsen et al., 2013). From a synthetic biology approach, we have also shown how such controller structures can be tuned similar to an industrial control system (Thorsen et al., 2016), and

the motifs are also shown to be closed loop asymptotically stable (Tveit and Thorsen, 2017).

The analysis in this paper is based on controller motif 5, given in Eqs. (1) and (2).

$$\dot{A} = k_p^i - V_{max}^A \cdot \frac{A}{K_M^A + A} \cdot f(E) \quad (1)$$

$$\dot{E} = k_s^E \cdot g(A) - V_{max}^E \cdot \frac{E}{K_M^E + E} \quad (2)$$

The concentrations of A and E represent the controlled variable and the manipulated variable, respectively. Furthermore, k_p^i is the inflow perturbation and V_{max}^A is the maximum turnover number for A . The parameter K_M^A is the Michaelis-Menten constant for the degradation of A . The synthesis rate of E is given by k_s^E , and V_{max}^E is the maximum turnover number for E . The parameter K_M^E is the Michaelis-Menten constant for the degradation of E . All concentrations and rate constants are given in arbitrary units (a.u.) unless stated otherwise.

The function of the motif can be described as follows. When the inflow perturbation k_p^i increases, the level of A increases, which again will increase the synthesis rate of E through the signalling from A to E . As the level of E increases, the E -mediated compensatory outflow of A will also increase, bringing A back towards its pre-perturbed value. A necessary condition for this behaviour is that the enzyme degrading the controller species E is saturated, i.e. $K_M^E \ll E$ (Drengstig et al., 2012). If this condition is not satisfied, there will be a deviation between the level of A prior to and after the perturbation. Such deviation measures are found in many *in silico* studies of physiological regulatory systems, see e.g. (Ma et al., 2009).

The structure in Eqs. (1) and (2) is schematically illustrated in Figure 2, where the signalling from A to E is represented by the function $g(A)$. From a control theoretical point of view, this corresponds to the measurement in a negative feedback loop (see Figure 2.). Furthermore, the signalling from E to A is represented by the function $f(E)$, which is how the manipulated variable E enters the process.

In our analysis we have looked further into the following three types of signalling events for both $f(E)$ and $g(A)$, commonly used to model enzyme kinetics in physiology (Cornish-Bowden, 2012) :

1. Linear signalling, i.e. $f(E) = E$ and $g(A) = A$.
2. First order Hill kinetics, i.e. $f(E) = \frac{E}{K_a^E + E}$ and $g(A) = \frac{A}{K_a^A + A}$, where K_a^E and K_a^A are the activation constants. The enzymatic activation is assumed to be mixed activation.
3. Second order Hill kinetics, i.e. $f(E) = \frac{E^2}{(K_a^E)^2 + E^2}$ and $g(A) = \frac{A^2}{(K_a^A)^2 + A^2}$

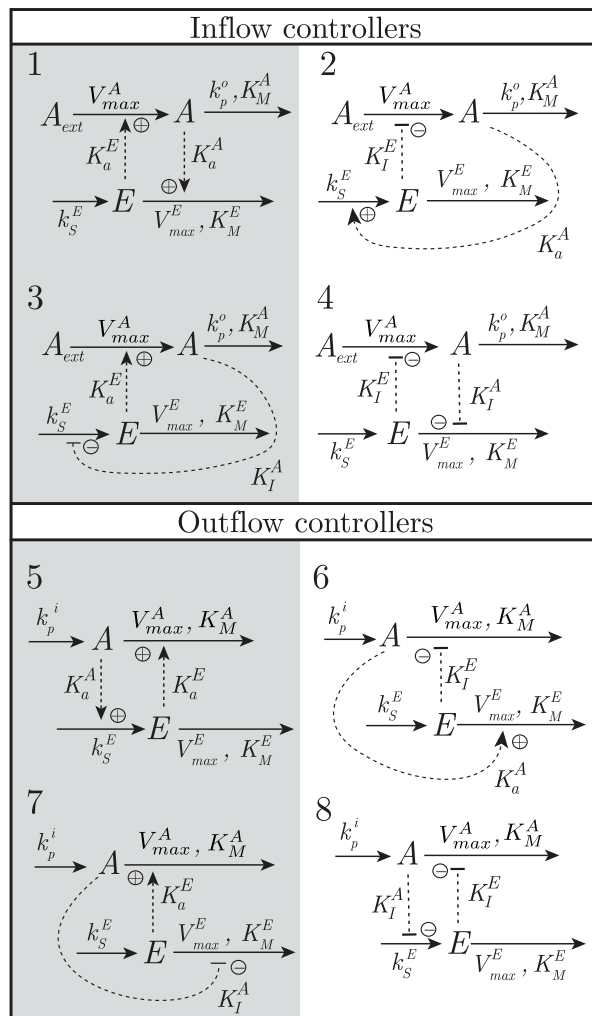


Figure 1. Eight different controller motifs, all representing negative feedback loops (Drengstig et al., 2012). Based on the location of the E -mediated compensatory flow, the controllers are either classified as inflow or outflow controllers. The species A represent the controlled variable, and the species E the manipulated variable. The perturbations are represented by the variables k_p^o and k_p^i . The signalling between A and E (dashed lines) are either based on activation (plus sign) or inhibition (minus sign).

To compare these different signalling events, we have, as mentioned above, defined levels of A and E , here represented as *low* and *high* levels, i.e.

$$A \in [A_{low}, A_{high}] = [1, 3] \quad (3)$$

$$E \in [E_{low}, E_{high}] = [2, 8] \quad (4)$$

These levels represent combinations of steady state values of the process. The numerical values in Eqs. (3) and (4) are arbitrary chosen, and are only used to illustrate the principle.

3 Signalling from E to A , $f(E)$

In the presence of inflow perturbation k_p^i , the signalling from E to A affect the compensatory outflow of A as shown in Eq. (1). Thus, the high and low levels in Eqs. (3) and (4)

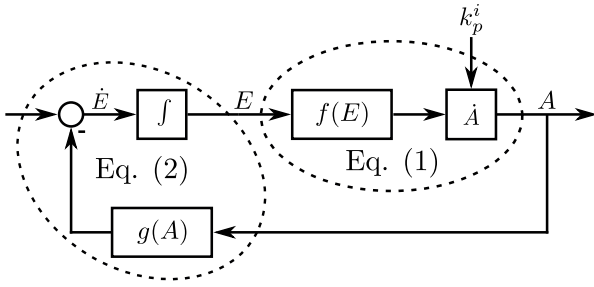


Figure 2. Representation of Eqs. (1) and (2) as a negative feedback loop. Eq. (1) represents the dynamics of the process, while Eq. (2) represents the controller dynamics.

are therefore related to corresponding high and low levels of k_p^i . In order to organize these 6 low/high levels into two working points, we note that a low inflow perturbation, $k_{p,low}^i$, will lead to a low level of A . A low level of A will again lead to a low level of E , as A activates the synthesis of E . Similarly, a high perturbation level $k_{p,high}^i$, will lead to high levels of both E and A . This behaviour is shown in the qualitative simulation shown in Figure 3, where the inflow perturbation is increased in a stepwise manner, and the corresponding levels of A and E are increased. Hence,

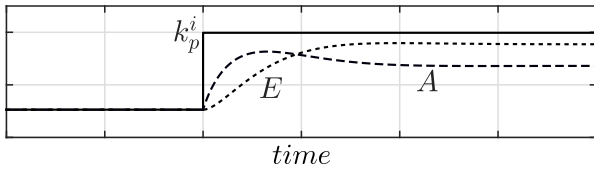


Figure 3. Qualitative simulation of motif 5. A low perturbation level k_p^i results in low levels of both E and A . Similarly, a high perturbation level k_p^i results in high levels of both E and A .

the following steady state combinations exist for motif 5¹:

$$[k_{p,low}^i, A_{low}, E_{low}] \quad (5)$$

$$[k_{p,high}^i, A_{high}, E_{high}] \quad (6)$$

In order to have a quantitative measure of the motif's disturbance rejection properties, we define both the *range* between the high and low perturbations (Δk_p^i), and the *ratio* of the high to low perturbations (λk_p^i) as:

$$\Delta k_p^i = k_{p,high}^i - k_{p,low}^i \quad (7)$$

$$\lambda k_p^i = \frac{k_{p,high}^i}{k_{p,low}^i} \quad (8)$$

Thus, our aim is to investigate how these two measures are affected by the choice of signalling event $f(E)$. The expressions for the range and ratio are found by inserting each of the steady state combinations in Eqs. (5) and (6)

¹The other motifs in Figure 1 will have other combinations, determined by the kind of signalling in $f(E)$ and $g(A)$, together with the kind of controller (inflow or outflow).

into Eq. (1). Thus, solving for $k_{p,low}^i$ and $k_{p,high}^i$, respectively, we find

$$\Delta k_p^i = V_{max}^A \frac{A_{high}}{K_M^A + A_{high}} \cdot f(E_{high}) - V_{max}^A \frac{A_{low}}{K_M^A + A_{low}} \cdot f(E_{low}) \quad (9)$$

$$\lambda k_p^i = \frac{\frac{A_{high}}{K_M^A + A_{high}} \cdot f(E_{high})}{\frac{A_{low}}{K_M^A + A_{low}} \cdot f(E_{low})} \quad (10)$$

There is, in general, an important distinction between linear and Hill based signalling. While Hill kinetics are saturable, i.e. $f(E) \in \{0, 1\}$, the linear signalling varies between $f(E) \in \{E_{low}, E_{high}\}$. Thus, using the same value of V_{max}^A would favour linear signalling with respect to range Δk_p^i . In order to make a fair comparison between linear and Hill signalling, we therefore choose V_{max}^A in the linear signalling case as

$$V_{max}^{A,lin} = \frac{V_{max}^A}{E_{high} - E_{low}} \quad (11)$$

3.1 Linear Signalling

In many cases, the use of linear signalling kinetics is motivated by the fact that the influence of an activator or inhibitor is not saturated, i.e. the influence is approximated to be in the linear domain of the saturation curve. As such, the $V_{max}^{A,lin}$ is therefore far from the actual maximum level V_{max}^A , and Eq. (11) is therefore a reasonable assumption. In the following, we use $V_{max}^A = 1$, and hence, $V_{max}^{A,lin} = \frac{1}{6}$.

Linear signalling for activating kinetics is often used when modelling physiological systems (Sedaghat et al., 2002). One of the benefits is that the models are easier to analyse analytically compared to more complex signalling kinetics (Thorsen et al., 2013, 2016).

Using $f(E) = E$ in Eqs. (9) and (10), leaves us with one unknown parameter, i.e. K_M^A . Thus, we present the disturbance rejection properties as a function of this parameter, see Figure 4.

We see from Figure 4a) that the range Δk_p^i is maximized when $K_M^A = 0$, and it is minimized when $K_M^A \rightarrow \infty$. At the same time, the ratio λk_p^i is maximized when $K_M^A \rightarrow \infty$ and minimized when $K_M^A = 0$. Thus, there exists a trade-off between range and ratio in the regulatory system. Figure 4b) shows the corresponding values of $k_{p,low}^i$ and $k_{p,high}^i$.

3.2 First Order Hill Signalling

The simplest saturable signalling event is the first order Hill expression:

$$f(E) = \frac{E}{K_a^E + E} \quad (12)$$

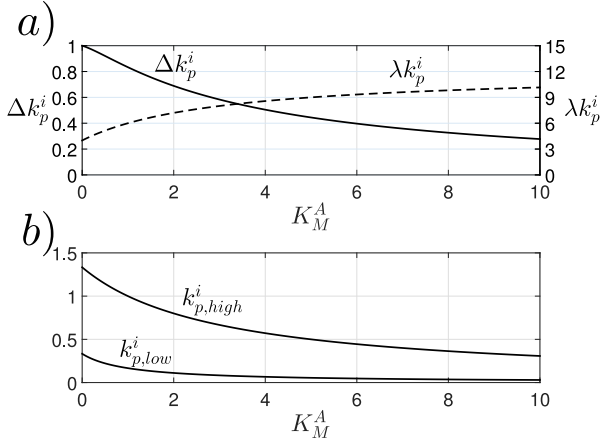


Figure 4. Panel a) The range Δk_p^i and ratio λk_p^i for controller motif 5 (using $f(E)=E$) as a function of K_M^A ($V_{max}^A=\frac{1}{6}$). Panel b) The corresponding low and high values of k_p^i .

Applying Eq. (12) in Eqs. (9) and (10), gives two unknown parameters, i.e. K_M^A and K_a^E , and thus, the range and ratio could have been presented as 3-dimensional surfaces. However, in order to focus on the effect of the *signalling*, we use $K_M^A=0$, and the results shown in Figure 5 are therefore comparable to the left part of Figure 4 were $K_M^A=0$.

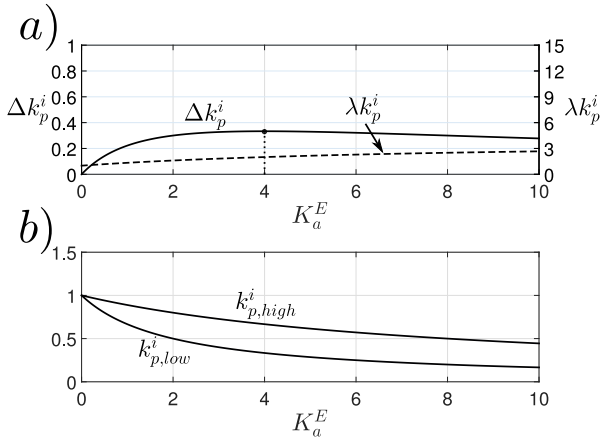


Figure 5. Panel a) The range Δk_p^i and ratio λk_p^i for controller motif 5 (using $f(E) = \frac{E}{K_a^E + E}$) as a function of the activation constant K_a^E ($V_{max}^A=1$ and $K_M^A=0$). The maximum range is found at $K_a^E = 4$ (indicated with a black dot). Panel b) The corresponding low and high values of k_p^i .

Unlike the results for the linear signalling in Figure 4a), there is a maximum value for the perturbation range. By differentiating the expression for the range Δk_p^i (Eq. (9)) with respect to K_a^E , we find the maximum value as

$$\frac{\partial \Delta k_p^i}{\partial K_a^E} = 0 \Rightarrow K_a^E = 4 \quad (13)$$

At $K_a^E=4$, the range is $\Delta k_p^i=0.33$ while the ratio is $\lambda k_p^i=2$.

The results indicate that the perturbation range and ratio, using first order Hill signalling from E to A , is re-

duced compared to linear signalling ($\Delta k_p^i=1$ and $\lambda k_p^i=4$ at $K_M^A=0$ in Figure 4). It is important to note that V_{max}^A at the same time is increased from $V_{max}^A=\frac{1}{6}$ to $V_{max}^A=1$ in the Hill signalling. The decline in both perturbation range and ratio was expected when considering the Hill-based signalling. In the next section we increase the enzymatic cooperativity by increasing the order of the Hill kinetic expression.

3.3 Second Order Hill Signalling

The second order Hill kinetic expression is given in Eq. (14).

$$f(E) = \frac{E^2}{(K_a^E)^2 + E^2} \quad (14)$$

As in the previous subsection, we assume $K_M^A=0$ and focus entirely on the effect of $f(E)$ through K_a^E , and the results are shown in Figure 6.

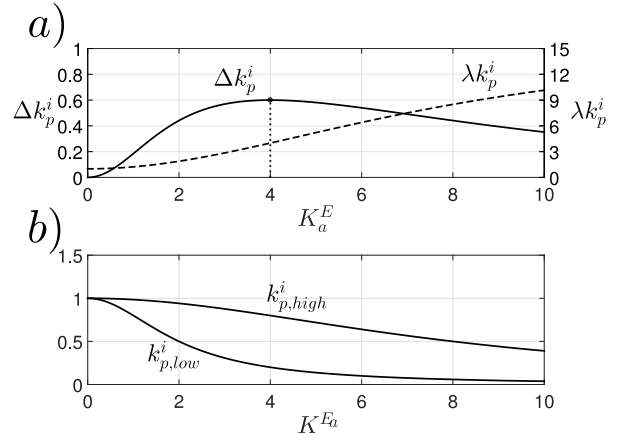


Figure 6. Panel a) The range Δk_p^i and ratio λk_p^i for controller motif 5 (using $f(E) = \frac{E^2}{(K_a^E)^2 + E^2}$) as a function of the activation constant K_a^E ($V_{max}^A=1$ and $K_M^A=0$). The maximum range is also here found at $K_a^E = 4$ (indicated with a black dot). Panel b) The corresponding low and high values of k_p^i .

As in Figure 5a), we find in Figure 6a) a similar peak for the perturbation range at $K_a^E=4$. The noteworthy difference is that the peak is substantially higher compared to first order Hill signalling ($\Delta k_p^i=0.6$ compared to $\Delta k_p^i=0.33$ in Figure 5a)). Moreover, the ratio λk_p^i is also significantly increased from 2 to 4. Thus, both values for perturbation range and ratio for the second order Hill signalling is comparable to those from linear signalling.

3.4 Higher Order Hill Signalling

The general expression for higher order Hill signalling is given in Eq. (15)

$$f(E) = \frac{E^n}{(K_a^E)^n + E^n} \quad (15)$$

and the effect on perturbation range and ratio of increasing n is shown in Figure 7. As n increases, so does the per-

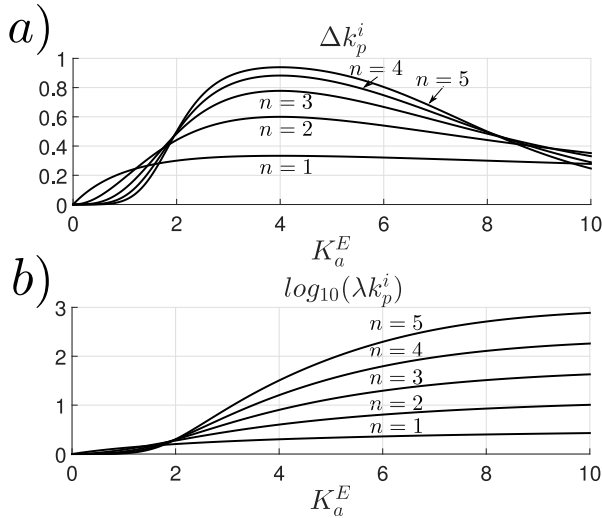


Figure 7. The range Δk_p^i and ratio λk_p^i for controller motif 5 (using $f(E) = \frac{E^n}{(K_a^E)^n + E^n}$ for $n \in \{1 \dots 5\}$) as a function of the activation constant K_a^E ($V_{max}^A = 1$ and $K_M^A = 0$). Panel a) The ranges Δk_p^i . Panel b) The ratios λk_p^i (note the logarithmic ordinate).

turbation range Δk_p^i and ratio λk_p^i . As $n \rightarrow \infty$, the range $\Delta k_p^i \rightarrow 1$ as obtained for the linear signalling.

To summarize, we have investigated the effect on the *range* and *ratio* of disturbances as function of the signalling from E to A given the low and high levels of A and E in Eqs. (3) and (4), respectively. The combination of low and high values represent therefore different possible steady state combinations (or working points) of the process.

In the next section, we investigate how the signalling $g(A)$ will affect the controller's ability to bring the process through these working points.

4 Signalling from A to E , $g(A)$

The signalling from A to E represented by the function $g(A)$ is a part of the dynamic model of the controller species E given in Eq. (2). Hence, the complexity of the signalling $g(A)$ will therefore, to a large degree, determine whether the steady state combinations from the previous subsection are obtainable when closing the feedback loop. As Figure 8 illustrates, the task of the controller is to match the low and high limits of A and E , and is therefore not directly affected by perturbation levels.

The procedure in this subsection is similar to what we did in the previous subsection, i.e. we apply the signalling $g(A)$ and insert each of the two steady state combinations in Eqs. (3) and (4) into Eq. (2). Thus, we have two equations and three unknowns i.e. k_s^E , V_{max}^E , and K_M^E . For the cases where we apply Hill based signalling, we have an additional unknown parameter in the activation constant K_a^E .

In general, the level of the synthesis rate k_s^E and degradation rate V_{max}^E of E is a measure of the swiftness of the controller (Thorsen et al., 2016). These two parameters are therefore *individually* not a part of the steady

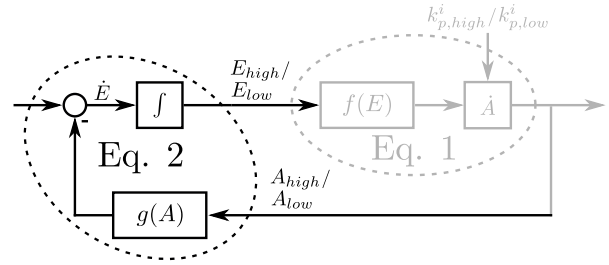


Figure 8. An illustration showing that the controller part is only dependent on the low and high levels of E and A , and indirectly dependent on the perturbation levels.

state properties of the controller. However, their ratio participate in the definition of the physiological setpoint (Thorsen et al., 2016), which represents the steady state levels of E . In this subsection, we therefore specify *one* of the parameters, i.e. $V_{max}^E = 1$, and calculate the other.

4.1 Linear Signalling

In case of linear signalling, we have $g(A) = A$. The two unknown parameters K_M^E and k_s^E are calculated by solving the two versions of Eq. (2). Interestingly, in order to find positive solutions to these parameter, the following condition on the steady state levels must be satisfied

$$\frac{E_{high}}{E_{low}} > \frac{A_{high}}{A_{low}} \quad (16)$$

Thus, if the variation in the controlled variable A is too large compared to the variation in the manipulated variable E , the controller is not able to bring the process through the identified working points using linear activation.

4.2 First Order Hill Signalling

If we apply first order Hill signalling from A to E , we have

$$g(A) = \frac{A}{K_a^A + A} \quad (17)$$

One could expect that this saturable expression would complicate the process of finding a suitable controller even further, i.e. introducing stricter conditions compared to Eq. (16). However, to our surprise, the signalling in Eq. (17) enables us to identify controllers where Eq. (16) is not fulfilled. Thus, if the low and high steady state levels of E and A do not satisfy Eq. (16), the following additional condition on K_a^A

$$K_a^A < \frac{A_{high} \cdot A_{low} \cdot (E_{high} - E_{low})}{A_{high} \cdot E_{low} - A_{low} \cdot E_{high}} \quad (18)$$

will make the control system feasible. The expression in Eq. (18) is found in the symbolic expression for the solution to K_M^E and k_s^E when solving the two versions of Eq. (2).

In order to illustrate this phenomena, we show in Figure 9 three different simulations where

$$A \in [A_{low}, A_{high}] = [1, 3] \quad (19)$$

$$E \in [E_{low}, E_{high}] = [2, 5] \quad (20)$$

Note that we have reduced $E_{high}=5$, and hence, the condition in Eq. (16) is therefore not satisfied. The signalling $f(E)$ from E to A is in all three simulations based on the first order Hill kinetics in Eq. (12). Thus, using the new low and high levels in Eqs. (19) and (20), the optimum K_a^E is found to be $K_a^E=3.16$.

For the linear signalling $g(A)=A$, we get the dashed lines in Figure 9. We note that, as expected, the controller is not able to bring the process through the working points. The solid line in Figure 9 represents the first order Hill signalling in $g(A)$ where the constraint on K_a^A in Eq. (18) is met, i.e. $K_a^A=5 < 9$. In order to show the effect of not satisfying either Eq. (16) nor Eq. (18), we have included this simulation as dotted lines as well. Both parameters K_M^E and k_s^E are kept constant for all three simulations. In order to avoid negative values of A , we have used $K_M^A = 0.001$.

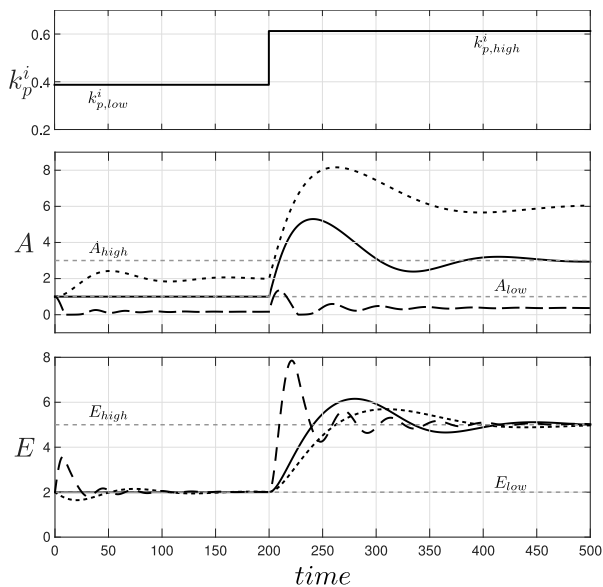


Figure 9. Simulations of controller motif 5 using three different signalling events between A and E , constrained by the steady state levels in Eqs. (19) and (20). Solid lines: First order Hill signalling using $K_a^A=5$, satisfying the condition in Eq. (18). Dotted lines: First order Hill signalling using $K_a^A=10$, violating the condition in Eq. (18). Dashed lines: Linear signalling. Other parameter values used in these simulations are: $K_M^A=0.001$, $K_a^E=3.16$, $V_{max}^E=1$, $k_s^E=0.44$ and $K_M^E=25$.

4.3 Second Order Hill Signalling

Extending the Hill signalling to second order, we have

$$g(A) = \frac{A^2}{(K_a^A)^2 + A^2} \quad (21)$$

Similar to the above results, we find conditions on both *i*) the values of steady state levels (similar to Eq. (16))

and *ii*) the parameter K_a^A (similar to Eq. (18)). These new conditions are shown in Eqs. (22) and (23).

$$\frac{E_{high}}{E_{low}} > \frac{A_{high}^2}{A_{low}^2} \quad (22)$$

$$K_a^A < \frac{\sqrt{(E_{high} - E_{low}) (E_{low} A_{high}^2 - E_{high} A_{low}^2)}}{E_{low} A_{high} A_{low}^{-1} - E_{high} A_{low} A_{high}^{-1}} \quad (23)$$

We observe that the condition in Eq. (22) is stricter compared to Eq. (16). Moreover, inserting the steady state levels in Eqs. (19) and (20) into Eq. (23) reveals that also this condition is strengthened compared to first order Hill signalling.

5 Conclusions

We have in this paper investigated the effects of different signalling kinetics between the controlled and manipulated variables in physiological regulatory systems. The results indicate that the level of complexity in the signalling certainly has an influence on the disturbance rejection properties.

By introducing first order Hill signalling from E to A via the function $f(E)$, we initially experience a drop in performance in both range (Δk_p^i) and ratio (λk_p^i). However if we allow second order Hill signalling the performance becomes comparable to the linear case, and by allowing higher order Hill signalling we find that the ratio Δk_p^i is significantly improved over linear signalling.

In the signalling from A to E , represented by the function $g(A)$, we find that the introduction of Hill signalling allows us to model data which would not be possible when using linear signalling.

References

- E. Ackerman, L. C. Gatewood, J. W. Rosevear, and G. D. Molnar. Model studies of blood-glucose regulation. *The Bulletin of Mathematical Biophysics*, 27:21–37, 1965. doi:10.1007/BF02477259.
- W. B. Cannon. Organization for physiological homeostasis. *Physiological Reviews*, 9(3):399–431, 1929.
- W. B. Cannon. *The Wisdom of the Body. Revised and Enlarged Edition*. Norton, New York, 1939. ISBN 978-0393002058.
- S. J. Cooper. From Claude Bernard to Walter Cannon. Emergence of the concept of homeostasis. *Appetite*, 51(3):419–427, 2008. doi:10.1016/j.appet.2008.06.005.
- A. Cornish-Bowden. *Fundamentals of Enzyme Kinetics, 4th Edition*. Wiley-Blackwell, 2012. ISBN 978-3-527-33074-4.
- T. Drengstig, I. W. Jolma, X. Y. Ni, K. Thorsen, X. M. Xu, and P. Ruoff. A basic set of homeostatic controller motifs. *Biophysical Journal*, 103(9):2000–2010, 2012. doi:10.1016/j.bpj.2012.09.033.

- N. H. Jeoung and R. A. Harris. Role of pyruvate dehydrogenase kinase 4 in regulation of blood glucose levels. *Korean Diabetes Journal*, 34(5):274–283, 2010. doi:10.4093/kdj.2010.34.5.274.
- T. K. T. Lam, R. Gutierrez-Juarez, A. Pocai, and L. Rossetti. Regulation of blood glucose by hypothalamic pyruvate metabolism. *Science*, 309(5736):943–947, 2005. doi:10.1126/science.1112085.
- L. L. Langley. *Homeostasis: Origins of the Concept*. Dowden, Hutchinson & Ross, 1973. ISBN 9780879330071.
- W. Ma, A. Trusina, H. El-Samad, W. A. Lim, and C. Tang. Defining network topologies that can achieve biochemical adaptation. *Cell*, 138(4):760–773, 2009. doi:10.1016/j.cell.2009.06.013.
- A. R. Sedaghat, A. Sherman, and M. J. Quon. A mathematical model of metabolic insulin signaling pathways. *American Journal of Physiology - Endocrinology And Metabolism*, 283(5):E1084–E1101, nov 2002. doi:10.1152/ajpendo.00571.2001.
- S. Skogestad and I. Postlethwaite. *Multivariable Feedback Control*. Wiley, 2005. ISBN 978-0470011683.
- A. Swierkosz. Modeling of metabolic diseases - a review of selected methods. *Bio-Algorithms and Med-Systems*, 11(4): 205–209, jan 2015. doi:10.1515/bams-2015-0016.
- K. Thorsen, P. Ruoff, and T. Drengstig. Control theoretic properties of physiological controller motifs. In *2013 International Conference on System Science and Engineering (ICSSE)*, pages 165–170. IEEE, jul 2013. doi:10.1109/ICSSE.2013.6614653.
- K. Thorsen, G. B. Risvoll, D. M. Tveit, P. Ruoff, and T. Drengstig. Tuning of physiological controller motifs. In *9th EUROSIM Congress on Modelling and Simulation*, pages 28–33, Oulu, 2016. ISBN 978-1-5090-4119-0.
- D. M. Tveit and K. Thorsen. Passivity-based analysis of biochemical networks displaying homeostasis. *To be presented at SIMS 2017*, 2017.

Data-driven Modeling of Ship Motion Prediction Based on Support Vector Regression

Bikram Kawan¹ Hao Wang¹ Guoyuan Li² Khim Chhantyal³

¹Faculty of Engineering and Natural Sciences, Norwegian University of Science and Technology, Norway,

bikramkawan@gmail.com, hawa@ntnu.no

²Faculty of Maritime Technology and Operations, Norwegian University of Science and Technology, Norway,

guoyuan.li@ntnu.no

³Faculty of Technology, Natural Sciences, and Maritime Sciences, University College of Southeast Norway, Norway,

khim.chhantyal@usn.no

Abstract

This paper presents a flexible system structure to analyze and model for the potential use of huge ship sensor data to generate efficient ship motion prediction model. The noisy raw data is cleaned using noise reduction, resampling and data continuity techniques. For modeling, a flexible Support Vector Regression (SVR) is proposed to solve regression problem. In the data set, sensitivity analysis is performed to find the strength of input attributes for prediction target. The highly significant attributes are considered for input feature which are mapped into higher dimensional feature using non-linear function, thus SVR model for ship motion prediction is achieved. The prediction results for trajectory and pitch show that the proposed system structure is efficient for the prediction of different ship motion attributes.

Keywords: Ship Motion time series Prediction, Support Vector Regression

1 Introduction

The maritime industry is one of the key business backbones in Norway and has experienced significant increase in recent years. Ships are - driving force for maritime business and - important in aspect of companies and safety, (Baldauf et al., 2013). The dynamics of ships is complex due to control system forces and external forces, (Fossen, 2002; Sørensen, 2011). Hydrodynamic perturbations are also induced from ship motions. The external forces are a combination of wind, waves and sea currents. The control system perturbation is defined by propulsion and steering system of the ship, (Fossen, 2002). The ship motion is non-linear due to resultant forces obtained from the combination of external forces and control system. The priority of health, safety, environment and economic loss are in high priority for ship maneuvering. Therefore, a prediction model will be useful to take consideration of different factors in ship motion planning which is important for human safety, loss of economy and eventually to increase the efficiency of the ship.

There are different types of sensors installed in the ship. The information collected from sensors are used directly or indirectly. The real-time purpose is to maneuver the ship and for control signals. The indirect use can be very useful for diagnose purpose in future to measure performance of different components of ships such as propeller blade, motor etc. The information produced from sensors are normally huge size which is in the form of big data, (Kaisler et al., 2013) for the several years' tenure. Big data are the huge source of information if we can dig into effectively. The information hidden are valuable for ship owners and companies for the prediction, identifying the patterns.

The accurate prediction of ship motion can be challenging due to high non-linearity of ship dynamics, the variable operational parameters of the vessel and the stochastic external excitations exerted by waves of the wind, (Pena et al., 2011). Many works are carried out for ship motion prediction. The use of traditional potential theory such as Kalman filter used in the frequency domain is not suitable due to the nonlinearity of ship dynamics and ocean for the estimation of actual ship behavior, (Blischke et al., 2011). Even though traditional algorithm may provide reasonable solutions, it gets complicated and requires more time to solve the problem mathematically, (Min-Seok, 2013). Classical model based approach lacks the generalization capabilities. Even though Extended Kalman filter can work in non-linearity to some extent but if failed when the non-linearity and complexity increases. SVR is one type of non-linear models which is good for solving a complex problem. Due to approximation ability, it solves models which are hard to solve using ordinary mathematical expression. Due to non-linearity behavior, there occurs some degree of uncertainty. Therefore, some intelligent techniques are required with the ability of generalization to solve the uncertainty in ship motion.

The successful manoeuvring operation of the ship is essential. Most important and key technique, such as information fusion, danger prediction technology traffic flow estimation, etc., cannot work without it. Therefore, the prediction of future time step for manoeuvring

of the ship is useful to implement the control forces accurately. The research based on the application of artificial intelligence such as neural network, genetic algorithm, and Fuzzy Logic have shown the great potential for the prediction of ship behavior. A lot of interesting work has been carried out such as ship roll motion time series forecasting (Pena et al., 2011), online ship roll motion prediction (Yin et al., 2014), ship motion prediction (Zhao et al., 2004), ship trajectory based on backpropagation neural network (Xu et al., 2011) and ship path following (Xia et al., 2013). From (Luo and Cai, 2014; Ristic et al., 2008; Ma et al., 2003; Yin et al., 2013) it shows great potential to implement the SVR for the ship motion prediction.

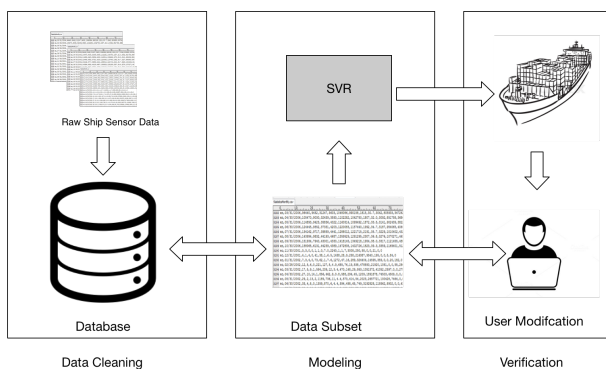


Figure 1. System structure of ship motion prediction. (Li et al., 2016)

2 Methods

The system structure for the prediction of ship motion will be based on the framework proposed as shown in Fig 1. The proposed framework consists three blocks. The first block of system structure is data cleaning. It is important to clean sensory noises and resampling the data if required to improve the model results. The second block i.e. Data analysis and modeling. Data analysis is carried out with the help of correlation analysis, which helps to identify the relation between different sensors attributes. The result obtained from correlation statistics is a guideline for the modeling of SVR. The third block is verification. The unique data which is not involved during learning is used for verification of our model. The user can import data from any ship model and make modification in the model to make the prediction better making our framework flexible.

2.1 Data Collection

The data is collected for three years from different sensors by our partner. The data module is divided into two category high frequency and low frequency. Each category has two subsets of data with frequencies from 1Hz to 4000Hz. The high frequencies information is useful for the analysis of propulsion system using information obtained from vibration and torque sensors.

The information related ship environment is provided by low frequencies as shown in Table I. The intrinsic control parameters like rotational speed, thruster forces (from M2) induces the ship's extrinsic representation (M1). Our prediction model is based on low frequencies data (i.e. M1 and M2) only.

Table 1. Specification of Low Sampling Frequency Data.

Module	Frequency [Hz]	Parameter	Unit
M1	1	Speed	[m/s]
		Position	[m, m]
		Heading	[deg]
		Roll	[deg]
		Pitch	[deg]
		Yaw Rate	[deg/s]
		Roll Rate	[deg/s]
M2	1.65	Rotational Speed	[RPM]
		Drive of motor	[W]
		Propeller pitch	[deg]

2.2 Data Cleaning

The raw data may contain noise, incomplete information and redundant information. So, it is necessary to perform data cleaning. In our case noise sources are internal or external. The internal noises can be corrected from statistical estimation. The external noises coming from sensor is unavoidable in most case. In our case, the major external noises are generated from cables and the coupling of electric and magnetic fields, the measured temperature is full of spikes. The natural way of eliminating the noise is to apply low pass filter and apply median filtering, (Liu, 2013). The raw data is not continuous due to several reasons such sensors are not actively running all the time, sensor is broken for some time. Due to this there are some gaps in recording data. In addition, there might be jumping of data for some parameter such as heading. The standard value is always within $[0^\circ, 360^\circ]$. The heading degree changes from 360 to 0 after making one complete cycle. To remove this kind of discontinuity an algorithm is used to correct the such parameter in order to make the data consistent, (Li et al., 2016).

2.3 Sensitivity Analysis

Sensitivity analysis is carried to find out the importance of input attribute for the contribution of output. It is not necessary that all the attributes have significant contribution for the prediction. To measure the strength of the attribute how much it is important for the contribution of output is calculated using correlation between the input attribute and the target attribute. (Hamby, 1994)

2.4 SVR Modeling

Support Vector Machine (SVM) was developed by Vapnik (Vapnik, 2013) and is used in many applications due to significant results. SVM are a set of related supervised learning methods applied in different machine learning applications like classification and regressions (Scholkopf and Smola, 2005). The basic process is to map the original data input space into the higher dimensional feature through non-linear mapping functions (Scholkopf and Smola, 2005). We have implemented SVM to solve regression problem as Support Vector Regression in our work (Chhantyal et al., 2016).

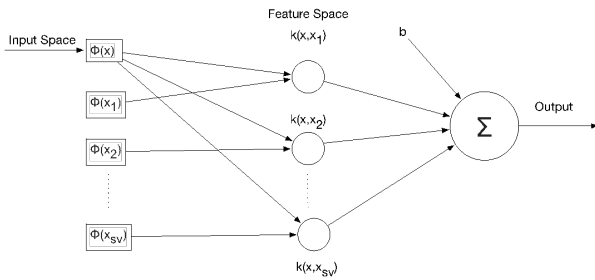


Figure 2. General architecture of SVR model. Input/output spaces consist of the variables shown in Table 1. (Chhantyal et al., 2016)

The linear regression model in feature space for SVR is represented as,

$$y = \sum_{i=1}^{N_{sv}} w_i \Phi_i(x) + b \quad (1)$$

where, $\Phi_i(x)$ is mapping function from input space to feature space and N_{sv} is number of support vectors.

The performance of SVR model is measured by ϵ -insensitive loss function and defined as,

$$L(d, y) = \begin{cases} |d - y| - \epsilon & \text{for } |d - y| \geq \epsilon \\ 0 & \text{otherwise} \end{cases} \quad (2)$$

The SVR approach is defined in (3) based on minimization of ϵ -insensitive loss and minimization of the norm of linear parameters $\|w\|^2$.

$$J = \frac{1}{2} \|w\|^2 + C \sum_{i=1}^N |y_i - d_i| \epsilon \quad (3)$$

$$\text{subjected to } \begin{cases} d_i - y_i \leq \epsilon + \xi_i \\ y_i - d_i \leq \epsilon + \xi_i^* \\ \xi_i \geq 0 \\ \xi_i^* \geq 0 \end{cases}$$

where, C- regularization parameter, ξ and ξ^* are non-negative slack variables, which describe the loss function J.

This primal optimization problem is then transformed into a dual problem (Chhantyal et al., 2016). The solution

is defined in (4)

$$y = \sum_{i=1}^{N_{sv}} (\alpha_i - \alpha_i^*) k(x_i, x) + b \quad (4)$$

where, α and α^* are Lagrange multipliers and $k(x_i, x)$ is the kernel function used in mapping the input space to a higher dimensional feature space.

Radial Basis Function (RBF) kernel used in our work is defined as (5)

$$k(x_i, x) = \exp\left(-\frac{\|x_i - x\|^2}{2\sigma^2}\right) \quad (5)$$

where, σ is the width parameter of RBF kernel.

Support Vectors are those data within the training set, which are very close to the ϵ -insensitive tube. The number of support vectors is equal to the number of non-zero $(\alpha_i - \alpha_i^*)$, which will determine the number of mapping vectors, determining the complexity of the model (Chhantyal et al., 2016). Therefore, the architecture of SVR depends on the number of support vectors as described in Fig. 2.

In this paper, the selection method for the parameters for the RBF and SVM is based on selecting C given by,

$$C = \max(|\bar{y} + 3\sigma_y|, |\bar{y} - 3\sigma_y|) \quad (6)$$

and the parameter ϵ dependent on the level of noise in the training data is computed as,

$$\epsilon = \tau \sigma_n \sqrt{\frac{\ln(n)}{n}} \quad (7)$$

$$\sigma_n = \left(\frac{k}{k-1} \frac{1}{n} \sum_{i=1}^n (y_i - \hat{y}_i)^2 \right)^{1/2} \quad (8)$$

For higher P-dimensional problems, RBF width parameter σ can be set in the range $\sigma \approx (0.2 \text{ to } 0.5)^{1/P}$, which can be optimized further using train and error (Haykin, 2009).

3 Experiment and Results

The experiment is performed based on the raw data stored for three years to verify the system structure proposed in Section II. The case study aims to extract information from raw data and verify the SVR model for prediction of ship motions. This section describes the steps to develop our system to predict ship motion.

First, we import raw data in our database storage. For our case study, we are going to use a small subset for simplicity. Data cleaning is carried as the second step. We performed three data cleaning methods i) removing noise using low pass filter ii) resampling is performed to make both module (M1 and M2 shown in Table I) in same frequency iii) phase correction is performed to make the continuity of raw data. The detail process is discussed in our previous article (Li et al., 2016). The third step is

to perform sensitivity analysis to find out the contribution of each attribute for the outputs as discussed in (Li et al., 2016). For our case study, we found that surge velocity, sway velocity, yaw velocity, roll velocity, yaw velocity, position x, position y, heading, and roll has a significant relation for the prediction of the pitch.

The next step is to model SVR. Fig 2 shows how SVR model is constructed for our case. The selected variables are considered in the input feature space that are further transformed into high-dimensional space using radial basis function. Finally, the output is computed based on the local induced outputs from each hidden unit also.

The models are evaluated using Root Mean Square Error (RMSE) and Square Correlation Coefficient (R^2). RMSE is a tool to measure a difference between the actual value and the value predicted by model defined in (9). The prediction results of the model are efficient, when RMSE value is near to 1 and the prediction results is treated bad when near to 0.

$$RMSE(\hat{\theta}) = \sqrt{E((\hat{\theta} - \theta)^2)} \quad (9)$$

where, $\hat{\theta}$ is estimated value and θ is the actual value.

R^2 is used to measure the goodness of fit of a model and defined in (10). The estimate of the model is better if the value is closer to 1.

$$R^2 = 1 - \frac{\sum_{i=1}^n (T_i - p_i)^2}{\sum_{i=1}^n (T_i - \bar{T})^2} \quad (10)$$

In this paper, we have only presented a case study for trajectory and pitch velocity. For both of our case studies, the size of the small subset of 2000 samples data was taken. The training size was 1750 and testing was 250 samples. The result obtained for trajectory is shown in Fig 3. The red line the actual trajectory while the blue one is trajectory predicted by SVR model.

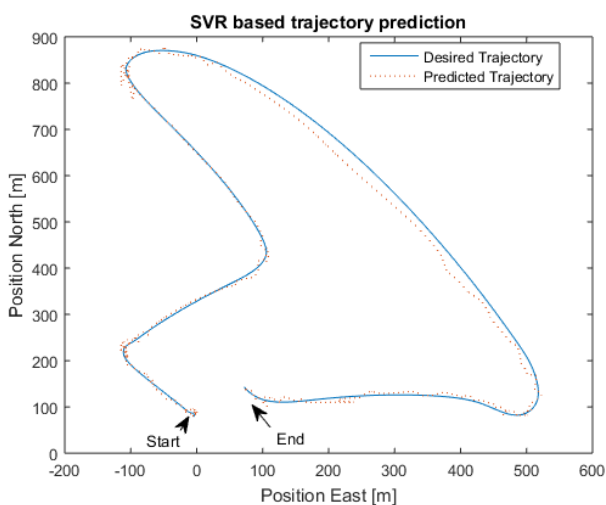


Figure 3. Prediction results of ship trajectory.

Fig 4 shows the prediction of the pitch. The red line is the desired pitch, and the blue line is the prediction obtained from SVR model.

In both of the case, it is clear from the Fig (3) and Fig (4) that the prediction from our model is good enough to predict trajectory and pitch. In addition, in both cases, R^2 is near to 1 and RMSE is around 0.1. This verifies that our model is good enough for the implementation.

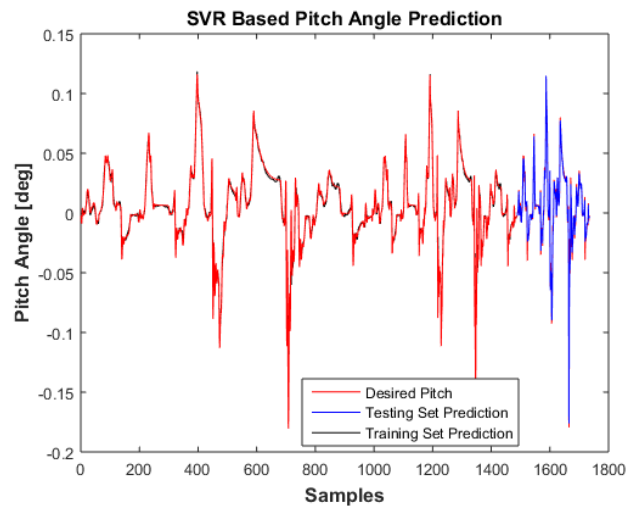


Figure 4. Prediction results of ship pitch.

4 Conclusion

In this paper, system structure for the prediction of ship motion is proposed from importing raw data to the verification of SVR model. First, the raw sensor data is cleaned before modeling. Then sensitivity analysis is performed to find the better relation between inputs to targets. Then flexible SVR model is constructed from which user can define the desired data set and user define model parameters. By applying training data set, SVR prediction model is obtained. As a final step, testing data is used for model verification. Two case studies for trajectory and pitch are carried out, and the results indicate that the proposed system outperformed for the ship motion prediction. In both case studies, RMSE is very small, and R^2 is close to 1.

Future work will focus on the online prediction of ship motion which will be helpful for real-time prediction. In addition, the multi-step prediction will be studied for the longer time steps prediction that is essential for real world ship motion.

Acknowledgement

The authors would like to thank Mechatronics Lab, Faculty of Maritime Technology and Operations, NTNU i Ålesund for providing the data set for the research.

References

- M Baldauf, R Baumler, A Olcer, T Nakazawa, K Benedict, and M Fischer, Sand Schaub. Energy-efficient ship operation training requirements and challenges. *TransNav: International Journal on Marine Navigation and Safety of Sea Transportation*, 7(2), 2013.
- W R Blischke, M R Karim, and D P Murthy. Reliability. Technical report, Warranty Data Collection and Analysis, 2011.
- K Chhantyal, H Viumdal, S Mylvaganam, and G Elseth. Ultrasonic level sensors for flowmetering of non-newtonian fluids in open venturi channels: Using data fusion based on artificial neural network and support vector machines. In *Sensors Applications Symposium (SAS), 2016 IEEE*, 2016.
- T I Fossen. Marine control systems: guidance, navigation and control of ships, rigs and underwater vehicles. Technical report, Marine Cybernetics, 2002.
- D M Hamby. A review of techniques for parameter sensitivity analysis of environmental models. *Environmental monitoring and assessment*, 32(2):135–154, 1994.
- S Haykin. *Neural networks and learning machines*. Pearson, Upper Saddle River, NJ, USA, 2009.
- S Kaisler, F Armour, J A Espinosa, and W Money. Big data: Issues and challenges moving forward. In *System Sciences (HICSS), 2013 46th Hawaii International Conference*, 2013.
- G Li, H Zhang, B Kawan, H Wang, O L Osen, and A Styve. Analysis and modeling of sensor data for ship motion prediction. In *OCEANS 2016-Shanghai, IEEE*, 2016.
- Y Liu. Noise reduction by vector median filtering. *Geophysics*, 78(3):V79–V87, 2013.
- W Luo and W Cai. Modeling of ship manoeuvring motion using optimized support vector machines. In *Intelligent Control and Information Processing (ICICIP), 2014 Fifth International Conference*, 2014.
- J Ma, J Theiler, and S Perkins. Accurate on-line support vector regression. *Neural computation*, 15(11):2683–2703, 2003.
- Kang Min-Seok. Ship motion prediction system development based on neural network. Technical report, 2013.
- F L Pena, M Gonzalez, V D Casas, and R J Duro. Ship roll motion time series forecasting using neural networks. In *Computational Intelligence for Measurement Systems and Applications (CIMSA), 2011 IEEE International Conference*, 2011.
- B Ristic, B La Scala, M Morelande, and N Gordon. Statistical analysis of motion patterns in ais data: Anomaly detection and motion prediction. In *Information fusion, 2008 11th international conference*, 2008.
- B Scholkopf and A Smola. Support vector machines. Technical report, Encyclopedia of Biostatistics, 2005.
- A J Sørensen. A survey of dynamic positioning control systems. *Annual reviews in control*, 35(1):123–136, 2011.
- V Vapnik. The nature of statistical learning theory. Technical report, Springer science & business media, 2013.
- G Xia, J Liu, and H Wu. Neural network based nonlinear model predictive control for ship path following. In *Natural Computation (ICNC), 2013 Ninth International Conference*, 2013.
- T Xu, X Liu, and X Yang. Ship trajectory online prediction based on bp neural network algorithm. In *Information Technology, Computer Engineering and Management Sciences (ICM), 2011 International Conference*, 2011.
- J C Yin, Z J Zou, and F Xu. On-line prediction of ship roll motion during maneuvering using sequential learning rbf neuralnetworks. *Ocean engineering*, 61:139–147, 2013.
- J C Yin, Z J Zou, F Xu, and N N Wang. Online ship roll motion prediction based on grey sequential extreme learning machine. *Neurocomputing*, 129:168–174, 2014.
- X Zhao, R Xu, and C Kwan. Ship-motion prediction: algorithms and simulation results. In *Acoustics, Speech, and Signal Processing, Proceedings (ICASSP'04) IEEE International Conference*, 2004.

Transient Stability of Fault Ride Through Capability of a Transmission System of a Distributed Hydropower System

J. Manjula Edirisinghe V.P.¹ Thomas Øyvang¹ Gunne John Hegglid¹

¹ Faculty of Technology, Natural Sciences and Maritime Sciences, University College of Southeast Norway, Post box 235, N-3603 Kongsberg, Norway, {jagathe.m.edirisinghe, Thomas.Oyvang, gunne.j.heggliid}@usn.no

Abstract

This paper describes the Fault Ride Through (FRT) capability of generators of a part of the 132 kV high voltage power network in Telemark region, Norway using a simplified power system simulator model. The organization, “European network of transmission system operators for electricity” (ENTSO-e) is introducing a network code for the Transmission System Operators (TSO) in Europe where the upper limit of the FRT requirement for 132 kV system is 0.25 s. However, according to the Norwegian network code, this limit is 0.40 s. The generators in the Norwegian power system are located in a distributed network and most of these are hydropower generators. The simulation results show that the structure of the Nordic power system enhances the system stability. The dynamic model of the power network is developed by using DIgSILENT PowerFactory simulation tool.

Keywords: power system, transient stability, Fault Ride Through capability, hydropower, simulations, DIgSILENT

1 Introduction

The electric power system is one of the complex man made networks, which is subjected to frequent improvements and changes. Power market today is more international and transmission system operators (TSO) in Europe operate in a connected power network (Statnett, 2017; ENTSO-e, 2017). Large introduction of renewable energy generations to systems such as wind power, has made the power network more complex (Delfanti et al, 2014; Gebremedhin et al, 2012; Bekele et al, 2012). TSOs have their own regulations and procedures. Therefore, the “ENTSO-e” is introducing a network code in order to harmonize the operating procedures among different TSOs and it is going to be a common network code in Europe. FRT capability of generators is one of the major consideration in harmonized power transmission systems (Diez-Maroto et al, 2016). For a generator, FRT capability is define as the ability of the generator to remain connected to the grid in the event of an external fault as long as the voltage at the connection point remains above a defined voltage level (Diez-Maroto et al, 2016).

ENTSO-e states that the synchronous generators need to stay connected if voltage at their connection point is above the voltage level defined by the FRT voltage profile. Advantage of this new code would prevent generation tripping in circuits when the fault is cleared in reasonable time. Lower time limit of the FRT requirement is set to 0.15 s, considering the clearing time of protection relays of the first zone, on the other hand, the upper time limit is set to 0.25 s considering the clearing time of protection relays of the first zone and the circuit breaker failure (ENTSO-e, 2017; Diez-Maroto et al, 2016).

The Norwegian transmission system operator, Statnett has published a network code called “FIKS”, which describes the functionality of the Norwegian power transmission system (FIKS, 2012). This local network code defines the FRT limit based on 220 kV voltage limit. FRT maximum requirement time for the network above 220 kV is 0.15 s, while it is 0.40 s for the network below 220 kV. The voltage level of regional transmission networks in Norway, which is studied in this article, is below 132 kV.

At present, the FRT requirement of the European network code is an interesting topic for the European electrical power producers and Diez-Maroto et al (2016) have investigated whether a typical round rotor turbogenerator fulfills the FRT requirement for this network code. Moreover, Delfanti et al (2014) have investigated the distributed renewable energy integration into the electrical grid. In addition to that, a preliminary study of the FRT requirements of the 132 kV simplified Telemark regional power network has been done by Adb (2016). There were 69 buses included in the study. In the present study, the Telemark model (Adb, 2016) is more simplified to 47 bus network and static stability of the simulator is improved.

The structure of the Norwegian power system is somewhat different from the many other countries in Europe where they use more centralized power sources (Delfanti et al, 2014). There are large numbers of hydroelectric generating units which supply electricity to the Norwegian power network (Gebremedhin et al, 2012). These generators are located throughout the country in a distributed network.

In the present study, the FRT performance of hydropower generators for a part of the 132 kV

transmission network in Telemark region of Norway is investigated. It also compares the simulation results with FIKS's FRT time limits. Finally, the transient stability impact on a distributed power system is discussed.

When the FRT requirements of some TSOs go far beyond than which are required by International Electrotechnical Commission (IEC) and Institute of Electrical and Electronic Engineering (IEEE) standards, the generator manufactures are facing more difficulties to fulfill the requirements (Diez-Maroto et al, 2016).

Therefore, it is an advantage to analyze FRT capability of Norwegian power system over the new code, because the future generating stations are supposed to follow the ENTSO-e regulations.

The paper is organized as follows. Section 2 provides a brief overview of a transient stability of a power system. The simulator is described in section 3. Selection criteria of cases for the simulations are provided in section 4. Results and discussion are provided in section 5. Finally in section 6, the conclusion is presented.

2 Transient stability of an electric power system

Transient stability of a power system describes the dynamic security of the system. It is a fast phenomenon where the power system operators do not have sufficient time to correct it manually (Vaahedi, 2014). Figure 1 shows the classification of power system stability.

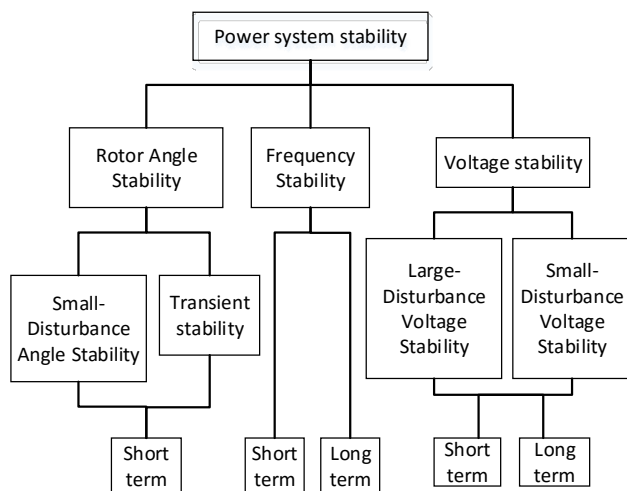


Figure 1. Classification of power system stability (Kundur et al, 2004).

According to the Figure 1, transient stability comes under the rotor angle stability. Equation (1) describes the swing equation for a generating station.

$$\frac{d\omega}{dt} = \frac{d^2\delta}{dt^2} = \frac{\omega_0}{2H} (P_m - P_e) \quad (1)$$

Where, ω is the angular speed of the machine, δ is the rotor angle of the machine, P_m is the mechanical input power to the machine, P_e is the electrical power output of the machine, H is the inertia constant of the machine in MWs / MVA, ω_0 is the synchronous speed which is related to synchronous frequency (Vaahedi, 2014).

The various components of the acceleration torque associated with the generator rotor are described in equation (2). Here, it is assumed that the damping is represented by damping torque which is proportional to the speed deviation of the machine.

$$T_a = T_{in} - T_e - D_g \Delta\omega \quad (2)$$

Where, T_a is the generator accelerating torque, T_{in} is the input torque, T_e is the output torque, D_g is the damping coefficient of the generator and $\Delta\omega$ is the speed deviation (Kundur, 1993).

The electric power output of a machine considering the single-machine infinite bus system is described in equation (3).

$$P_e = \frac{E \cdot V_{inf}}{X' + X_1} \sin(\delta) \quad (3)$$

Where, P_e is the electric power output of the machine, E is the internal voltage of the machine, δ is the phase angle induced by field voltage, V_{inf} is the infinite bus voltage, X' is the internal reactance of the machine and X_1 is the reactance of the transmission line (Vaahedi, 2014).

3 Simulator

A simplified model of a part of the 132 kV network in Telemark region, Norway (Adb, 2016) is simulated using a power analysis programme “Digisilent Powerfactory 2016”. The overview of the simplified local power network is shown in Figure 2.

The model consists of 49 buses. The voltage levels 11 kV, 22 kV, 66 kV, 132 kV, 300 kV and 420 kV can be found in the model. There are 18 power generators in this model. All generators are implemented with salient pole rotors. Each and every station is equipped with an “IEEET1” automatic voltage regulator and a “HYGOV” speed governor. These two models which can be found in the software are used with standard coefficients. Buses are connected in the network using 23 transmission lines and there are 24 power transformers included in this model. T-1_2 is an auto-transformer. External grid is acting as the local power reference point (slack bus).

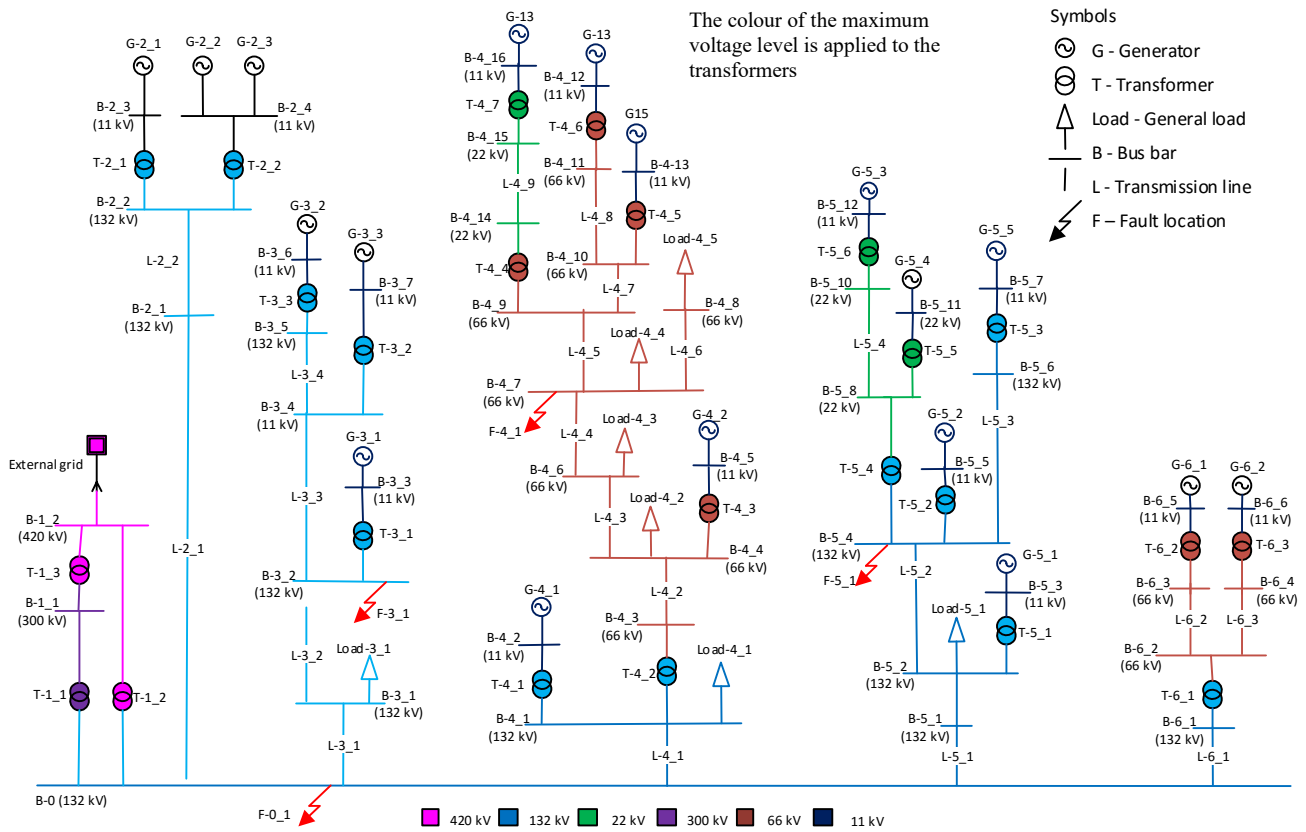


Figure 2. Simplified power system simulator for a part of 132 kV Telemark regional power network, Norway.

First, a balanced, positive sequence AC load flow is executed using Newton-Raphson method allowing automatic adaption of step size. All the generating stations are set to their maximum power. Voltages at all the buses remain between 1 and 0.97 per unit (p.u.).

A balanced 3 phase short circuit is created using an additional transmission line. Therefore, there is no any structure change in pre-fault and post-fault network structures. Then the stability of the generators were checked by changing the fault location as shown in Figure 2. The simulations were performed for six different fault-executing times as described in Table 1.

4 Case definition

The considered faults are three-phase symmetrical faults. Each fault scenario was selected for different radial circuits in the Figure 2 and the main 132 kV bus (B-0) was also selected. The manner of the voltage reduction in a fault location impacts on generating units, which are distributed with considerable impedance, was considered when the cases were selected. The selected cases are tabulated in Table 1. Each case is simulated for six different fault clearance times of 0.1, 0.2, 0.3, 0.4, 0.5 and 0.6 seconds.

Table 1. Simulated Cases; Refer to Figure 2.

Case	Fault No	Bus No	Bus Voltage /[kV]
1	F-0_1	B-0	132
2	F-3_1	B-3_2	132
3	F-4_1	B-4_7	132
4	F-5_1	B-5_4	66

5 Simulation Results and Discussion

FRT performance for four different cases as described in Table 1 is provided in Figure 3.

According to the results given in Figure 3, the available generation after a fault decreases with the increase in fault duration time for the cases 1, 2 and 4. This observation shows that the short circuit impacts to the generators increase when the fault duration time is increased. Case 1 out of four cases is selected at the main 132 kV bus (B-0) of the Figure 2, where the impact to the system stability is high. For the Case1, the voltage at the bus B-0 is reduced to a very low value (not 0, because of external fault to the bus) and according to the equation (3), power delivering ability decreases. Simultaneously, the electrical torque is reduced and acceleration torque is increased according to the equation (2). When the electrical power output suddenly get reduced, the delta angle of the machine is increased considerably as explained in equation (1). Case 1 condition is the worst case condition for the system

stability. Further, the cases 2, 3 and 4 show that more than 89 percent of the generating capacity stays in synchronism when the fault duration time is less than 0.20 seconds.

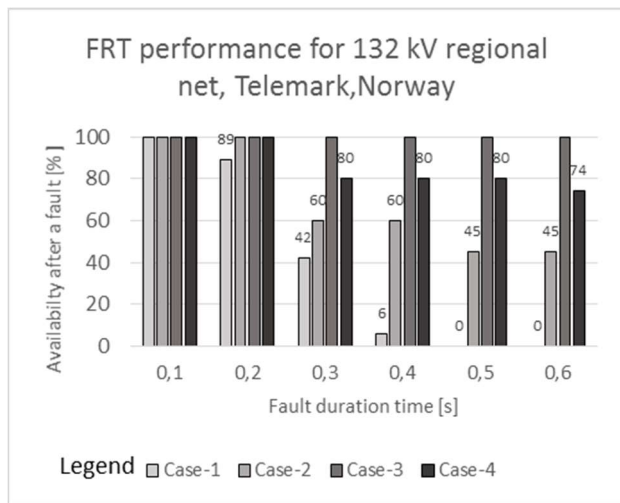


Figure 3. FRT performance of the generators for four different cases referred to Table 1, when a three-phase symmetric fault is executed. Generation capacity of the region is 418 MW.

Figure 4 shows the generator speed response of five generators, which are located in Figure 2 for the cases 1 and 3. For both cases, speed of the generators get stabilized. Figure 5 shows that the voltage of the same generators get stabilized for cases 1 and 3.

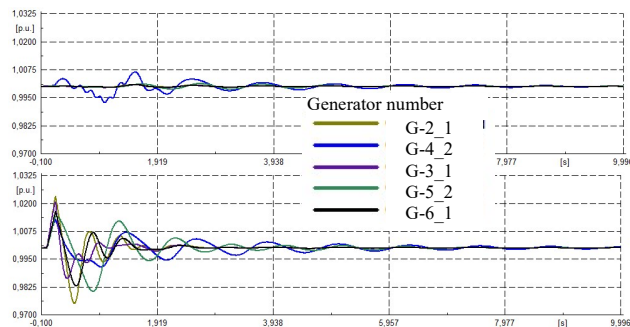


Figure 4. Generator speed response in p.u. in the event of 0.15 s three-phase fault: upper plot for the Case 3 and lower plot for the Case 1.

With respect to frequency stability of the Norwegian power system, the total system should withstand any single fault included loss of the biggest operating unit, which is a nuclear unit connected to Nordic network producing 1400 MW. The maximum stationary frequency deviation should be kept within 0.5 Hz (Statnett, 2017).

In a regional transmission system, the installed capacity is far less than 1400 MW and if the system remains interconnected during a fault as described above, the prospected system frequency deviation is negligible.

Frequency stability of the separated system (Islanded mode) is not discussed here.

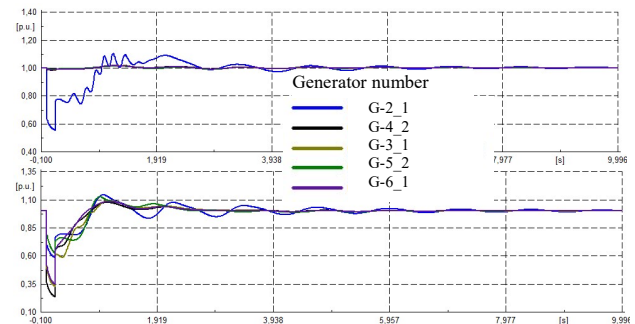


Figure 5. Generator voltage response in p.u. in the event of 0.15 s three-phase fault: upper plot for the Case 3 and lower plot for the Case 1.

6 Conclusion

The simulation results show that the structure of the Nordic power system has positive effects to the system stability. About 80 percent of the 132 kV generating capacity of the model stayed in synchronism for the fault clearance time between 0.25 - 0.3 s. If the upper time limit is reduced to 0.25 s, it positively affects to the construction of generating stations mainly by reducing the inertia of generating stations. The results encourage to analyze the topic further.

According to the simulation results, a fault generally gives significant impacts to the nearby generating stations. As many of the hydropower stations in Norway are located in a distributed network, the improvements in relay systems would be a better solution for the upper limit of the FRT requirement which is required by the Norwegian network code.

References

- Adb AH. Transient stability and Fault Ride Through (FRT) Capability of Hydropower units in Norwegian regional power networks: *University College of Southeast Norway*; 2016.
- Bekele G, Abdela A. Investigation of Wind Farm Interaction with Ethiopian Electric Power Corporation's Grid. *Energy Procedia*. 2012; 14:8. doi: 10.1016/j.egypro.2011.12.1165
- Delfanti M, Falabretti d, Merlo M, Monfredini G. Distributed Generation Integration in the Electric Grid: Energy Storage System for Frequency Control. *Journal of Applied Mathematics*. 2014; 2014:13. doi: 10.1155/2014/198427
- Diez-Maroto L, Rouco L, Fernandez-Bernal F. Fault ride through capability of round rotor synchronous generators: Review, analysis and discussion of European grid code requirements. *Electric Power Systems Research*. 2016;140:10. doi: 10.1016/j.epsr.2016.06.046
- ENTSO-e. European network of transmission system operators for electricity, available at www.entsoe.eu, 2017

- FIKS. Funksjonskrav i Kraftsystemet / Functional requirements in the Norwegian power system. *Tech. rep. available at www.statnett.no*, 2012
- Gebremedhin A., Granheim J.D.O. Is there a space for additional renewable energy in the Norwegian power system? Potential for reduced global emission? *Renewable and Sustainable Energy Reviews*, 2012. doi: 10.1016/j.rser.2011.11.032
- Kundur P. Power System Stability and Control: *McGraw-Hill*; 1993.
- Kundur P, Paserba J, Ajarapu V, Andersson G, Bose A, Canizares C, et al. Definition and Classification of Power System Stability. *IEEE TRANSACTIONS ON POWER SYSTEMS*. 2004;19(2):15.
- Statnett, the system operator in the Norwegian energy System. *Available at www.statnett.no*, 2017
- Vaahedi E. Practical Power System Operation: *John Wiley & Sons*; 2014.
- Weedy BM, Cory BJ, Jenkins N, Ekanayake JB, Strbac G. Electric Power Systems. 5 ed: *John Wiley & Sons Ltd*; 2012.

Flood Control Lake Toke: Model Development and Model Fitting

*Kvam K., Furenes B. *, Hasaas Å. *, Gjerset A., Skeie N.-O., Lie B.*

University College of Southeast Norway, Porsgrunn, Norway

*Skagerak Kraft, Porsgrunn, Norway

bernt.lie@usn.no

Abstract

In 2013, Skagerak Kraft AS started a project to automate control of the floodgates in cooperation with the University College of Southeast Norway, Porsgrunn (USN). A prototype of a system was installed in June 2014 using an MPC control algorithm due to the hard and soft concession constraints. However, the model of the system was found to give a poor description of severe floods during a major flood in September 2015.

This article details some adjustments done to the original model of the system. The paper also describes the introduction of a database to handle information for the system, and some uses of such a database.

The updated model shows improvement in flood-handling but other parts of the system model need to be reviewed. The database was successfully integrated in testing, it is to be added to the live server at a later stage.

Keywords: flood management, hydropower plant, MATLAB, MPC, SQL database, simulation.

1 Introduction

1.1 Background

The Dalsfos hydro power plant is located at the outlet of Lake Toke in Telemark, Norway. The waterways leading to Lake Toke, the rivers and lakes downstream of it and down to the ocean are known as the Kragerø waterway. Dalsfos is the first of five hydro power plants downstream of Lake Toke. Dalsfos consists of a dam with intakes to three turbines, two floodgates, and the power station itself just below the dam. The dam at Lake Toke creates a magazine for Dalsfos and the other four hydro power plants downstream, making the four downstream plants in effect run-of-river plants that are dependent on flow from Dalsfos. The turbines are Francis turbines with a combined production capacity of just under 6 MW at a flow rate of 36m³/s through the turbines. The two floodgates are controlled individually from a control room on the dam. The gates have a capacity of 450m³/s each.

Operating hydro power plants come with concession requirements from the Norwegian Water Resources and Energy Directorate (NVE). These concessions dictate the maximum and minimum water levels of Lake Toke, the minimum water flow downstream and the maximum change of water flow.

1.2 Problem description

The floodgates at Dalsfos are used to regulate the water level in Lake Toke during a flood. If the regulation is done successfully, it is possible to avoid property damage and risk of injury for people near Lake Toke and the Kragerø waterways. During a flood, water levels rise rapidly and if the floodgates are suddenly opened, the water will do extensive damage to the village downstream of the dam and the roads along the river. Any people close to, or on, the river at the time might also be in danger. During the flood in September 2015, the water inflow peaked at 700m³/s at hourly measurements. During this period, the roads downstream had to be closed and the operators had emptied the magazine for two weeks in advance to manage the inflow of water.

This project is a part of automating the floodgates at Dalsfos. The long-term goal for Skagerak Kraft is to ensure that the TUC flood server is functioning in a satisfactory manner under operating conditions so that the output from the system can be relied upon. This requires storage of input- and output values, receiving correct outputs and being able to check how previous outputs compare to actual results.

1.3 Previous work

The development work for the prototype implemented in 2014, was done by faculty members with help from master students at USN, resulting in the Telemark University College (TUC) flood server. The system was implemented as an advisory system to the operators at the power plant, as a first step in an automation project.

The TUC flood server is currently running at Skagerak Energi office in Porsgrunn. This system calculates the optimal floodgate opening for the Dalsfos hydro power plant based on inflow forecast and Model Predictive Control (MPC). How well an MPC controller performs is based on how accurate the model of the system is. The original model for Lake Toke was developed in Thoresen (2011). The model has been described and validated in Master theses at the University college of Southeast Norway (USN). During the flood in September 2015, it was discovered that the model for Lake Toke was insufficient for modeling such extreme conditions.

The MPC controller for TUC flood server was developed by faculty at current USN (Lie, 2014; Skeie, 2014). The MPC algorithm was implemented in MATLAB (Shampine *et al*, 2003). , while the TUC Flood Control Converter (TFCC) is the part of the TUC flood server that handles communication between the MPC controller and Skagerak’s internal systems, including when to start the MPC controller.

The original TUC flood server stored data in MATLAB matrices as *.mat files, making it difficult to access the data when trying to identify errors for troubleshooting the software. During the summer of 2016, a Data Handler and a Flood management database was developed to replace the storage of data in *.mat files¹.

2 System overview

Figure 1 shows the area around Lake Toke. The part marked in yellow is the catchment for Lake Toke, an area 1156 km² wide. This is the area where rain- and snowfall (or lack thereof) will affect the water level in Lake Toke.

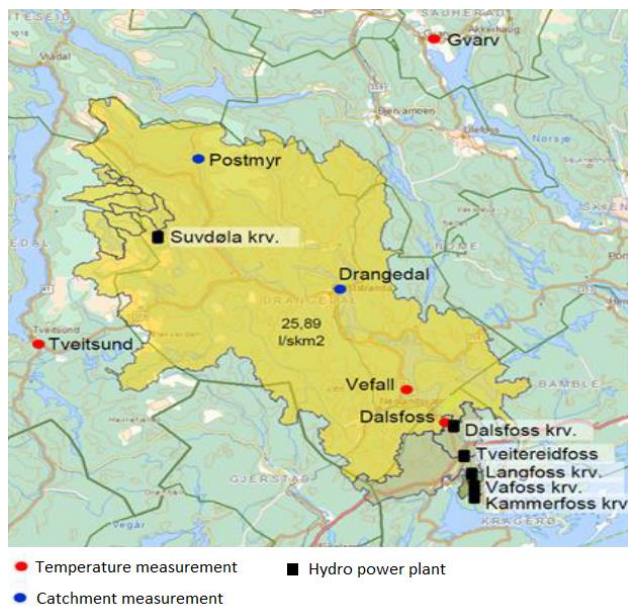


Figure 1. Catchment for Lake Toke. From (Furenes, 2016), legend modified.

Skagerak subscribes to a weather forecast service provided by Storm.no. The hydrologists at Skagerak analyze the catchment data to find a forecast for the water inflow to Lake Toke.

The hydrological data is stored in an internal database called TRADE. A representation of how the TUC flood server interacts with the system at Skagerak is shown in Figure 2. From the TRADE database, the hydrological data is sent along with measurement data from the Dalsfos dam to the TUC flood server. In the TUC flood

server, the input data is used to calculate a suggestion for the gate opening, and both the input and output data are stored in an internal database. The output data is sent to a measurement value comparison system, HIDACS. HIDACS will notify the dam operator via text message if any changes should be made to the floodgate opening. HIDACS is connected to sensors at the hydro power plant and sends these values to TRADE (Furenes, 2016).

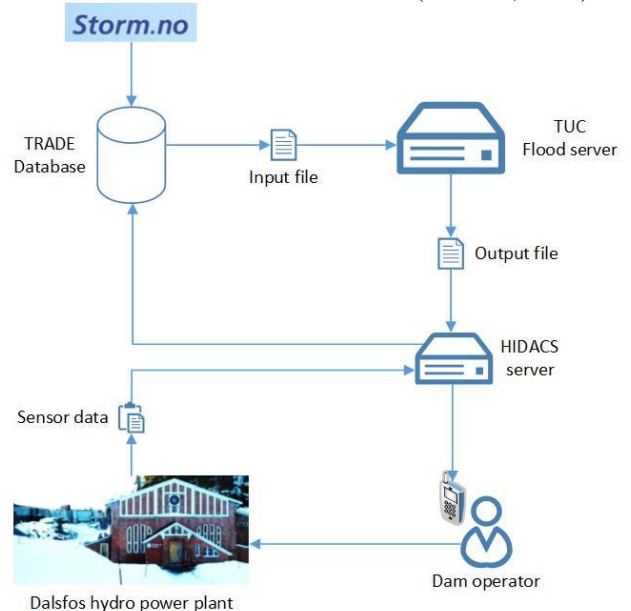


Figure 2. Network representation. From (Furenes, 2016), simplified.

3 Model tuning

3.1 System description

Experience with the model of Lake Toke and the Dalsfos hydro power plant have shown there is a need for modifying/tuning the model. This section presents the work done on the model. First, a summary of the updated model is presented, followed by a description of which parts were updated and how. Finally, a comparison of the old and the new model are presented.

In Figure 3, a description of the Lake Toke model and its parameters are presented. The model is divided into two parts. The larger part on the left represents the main part of the lake upstream of Merkebekk, and going all the way to Drangedal, etc. The smaller part on the right side of the sketch represents the Dalsfos magazine between Merkebekk and Dalsfos. The parameters presented in the sketch are as follows (beginning from the top of the sketch, left to right):

- x is the height of the water level relative to sea level [m.a.s.l.] (x_M - Merkebekk, x_D - Dalsfos).

¹ The Data Handler and the Flood management database were developed by A. Gjersest for Skagerak Kraft AS.

- h is the height [m] of the water level above the minimum height x_{LRV}^{\min} (h_1 - Merkebekk, h_2 - Dalsfos).
- \dot{V}_i is the inflow of water from the catchment to the lake/magazine [m^3/s].
- The β parameter determines the distribution of the catchment water inflow amongst the two parts.
- x_{HRV}^{\max} is the maximum allowed water level [m.a.s.l.].
- \dot{V}_{12} is the flow of water [m^3/s] from Merkebekk to Dalsfos magazine. This value is assumed to depend on the height difference between Merkebekk and Dalsfos.
- \dot{V}_g is the water flow through the floodgates at Dalsfos [m^3/s]. This value is derived from measuring the floodgate opening [m] and the level at Dalsfos.
- \dot{V}_t is the water flow through the turbines at Dalsfos [m^3/s]. This value is derived from measuring the power production of the turbines, \dot{W}_e [MWh].
- The α parameter determines the distribution of the surface area of each part, and thus the mass of water in each part.

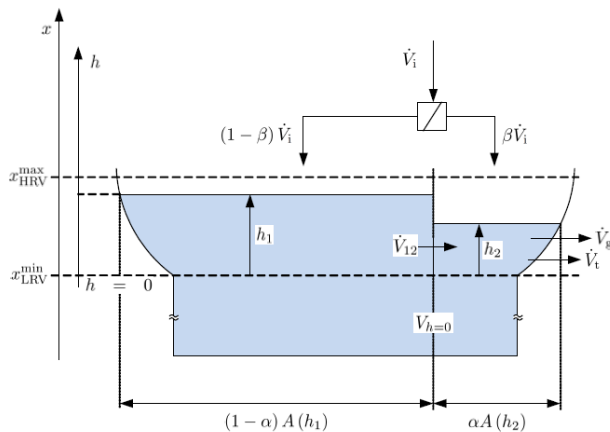


Figure 3. Sketch of Lake Toke (Lie, 2014).

3.2 New model summary

The updated model is presented below in Equations 1-9. The parameters, and their values, are given in Table 1.

- h_1 and h_2 are the states of the model
- h_g is the control input (which can be varied at will)
- \dot{V}_i is the predicted inflow of water given by the hydrology model (disturbance)
- \dot{W}_e is the planned power production (disturbance)
- The outputs are: x_M , x_D , \dot{V}_t and \dot{V}_g

$$\frac{dh_1}{dt} = \frac{1}{(1-\alpha)A(h_1)} [(1-\beta)\dot{V}_i - \dot{V}_{12}] \quad (1)$$

$$\frac{dh_2}{dt} = \frac{1}{\alpha A(h_2)} (\beta\dot{V}_i + \dot{V}_{12} - \dot{V}_t - \dot{V}_g) \quad (2)$$

Filling curve of Lake Toke:

$$A(h) = 28 \times 10^6 \cdot 1.1 \cdot h^{\frac{1}{10}} \quad (3)$$

Inter-compartmental flow (volumetric flow within Lake Toke, from Merkebekk to Dalsfos):

$$\dot{V}_{12} = k_1 \cdot \sqrt[4]{h_1 - h_2} + k_2 \cdot \sqrt{h_1 - h_2} \quad (4)$$

Volumetric water flow through the floodgate:

$$\dot{V}_g = C_d \cdot w \cdot \min(h_g, h_2) \sqrt{2g \cdot \max(h_2, 0)} \quad (5)$$

The volumetric flow through the turbines is found by choosing the correct root of Equation 6 and inserting the answer into Equation 7:

$$0 = c_1 x_q^3 + (c_2 - c_1 x_D) x_q^2 + (c_3 - c_2 x_D + c_4 \dot{V}_g) x_q + \dot{W}_e - c_3 x_D - c_4 \dot{V}_g x_D - c_5 \quad (6)$$

$$\dot{V}_t = a \frac{\dot{W}_e}{x_D - x_q} + b \quad (7)$$

Water levels above sea level are given for Dalsfos:

$$x_D = h_2 + x_{LRV}^{\min} \quad (8)$$

and for Merkebekk as:

$$x_M = h_1 + x_{LRV}^{\min} \quad (9)$$

Table 1. Lake Toke new model parameters.

Parameter	Value	Unit	Comment
α	0.01	-	Fraction of surface area in compartment
β	0.01	-	Fraction of inflow to compartment
C_d	0.7	-	Discharge coefficient, Dalsfos flood gates
w_1	11.6	m	Width of Dalsfos gate 1
w_2	11.0	m	Width of Dalsfos gate 2
x_{LRV}^{\min}	55.75	m	Minimal low regulated water level
x_{HRV}^{\max}	60.35	m	Maximum high regulated water level
g	9.81	m/s^2	Acceleration of gravity
k_1	100	-	Coefficient, Equation 4
k_2	1	-	Coefficient, Equation 4
c_1	0.1315	-	Coefficient, Equation 6
c_2	-9.524	-	Coefficient, Equation 6
c_3	172.34	-	Coefficient, Equation 6
c_4	-7.7e-3	-	Coefficient, Equation 6
c_5	-87.35	-	Coefficient, Equation 6
a	124.69	-	Coefficient, Equation 7
b	3.161	-	Coefficient, Equation 7

3.3 Historical data

The data used for model fitting was provided by Skagerak Kraft AS. The data contains hourly measurements and their derived values, from the period 01/01-2015 to 10/01-2017, totaling 17768 measurement points. The measurements for the water level in Lake Toke and the water inflow to the Dalsfos dam can be seen in Figure 4. The water inflow in the second part of Figure 4 is a derived value supplied by Skagerak Kraft AS, based on internal computations of measurement data. These measured values for water inflow are assumed to be more accurate than the water inflow prediction \dot{V}_i and used in evaluating the accuracy of the inflow predictions.

When evaluating the data, one can see that the first 4700 values seem to have some measurement errors. It does not make sense that the water level would be almost one meter higher at the point furthest downstream (points 1800-3300), thus creating a negative driving force from Merkebekk to Dalsfos. Then the sensor at Dalsfos seems to fail for an extended period, stuck at the same value. These assumptions can be further verified by looking at the water inflow in the lower half of the Figure 4. There is nothing to indicate the odd behavior that we see in the first 4700 data points. Based on these observations, the first 4800 measurement points of data were excluded from further work.

3.4 Gate flow parameter updating

The original floodgate model (Equation 5) is the same as the updated one, but the discharge coefficient C_d was 1.0 and is now updated to 0.7. This is simply an update based on information from Norwegian Water Resources

and Energy Directorate (NVE) supplied by Skagerak Kraft AS (NVE, 2017).

3.5 Inter-compartmental flow model reworking

The inter-compartmental flow for this model is the amount of water flowing from measuring point Merkebekk to Dalsfos based on the water height difference between these two points. The original equation (shown in Equation 10) needed to be reworked based on historical data.

$$\dot{V}_{12} = K_{12}(h_1 - h_2)\sqrt{h_1 - h_2} \quad (10)$$

Similar as to in the old model, it was assumed that the inter-compartmental volumetric flow rate is driven by the level difference between Merkebekk and Dalsfos. The available data was plotted as seen in Figure 5. In this description, it was assumed that the lower compartment (Dalsfos magazine) was at steady state so that the inter-compartmental flow rate equals the sum of the flow through the turbines and the floodgates. The height difference in water level values are from measurements made at the same time as the water flow.

Amongst many possible model structures, the structure proposed in Eq. 4 was used and fitted to the experimental data.

The “measured output” (in this case, the inter-compartmental water flow) is described as seen in Equation 4. The polynomial coefficients k_1 and k_2 were found by using the *Least Squares method* (Van Loan, 2000; Christensen and Christensen 2004).

Equation 4 was restructured as seen in Equation 11 where the right hand matrix is referred to as matrix Φ while the right hand parameter vector is referred to as

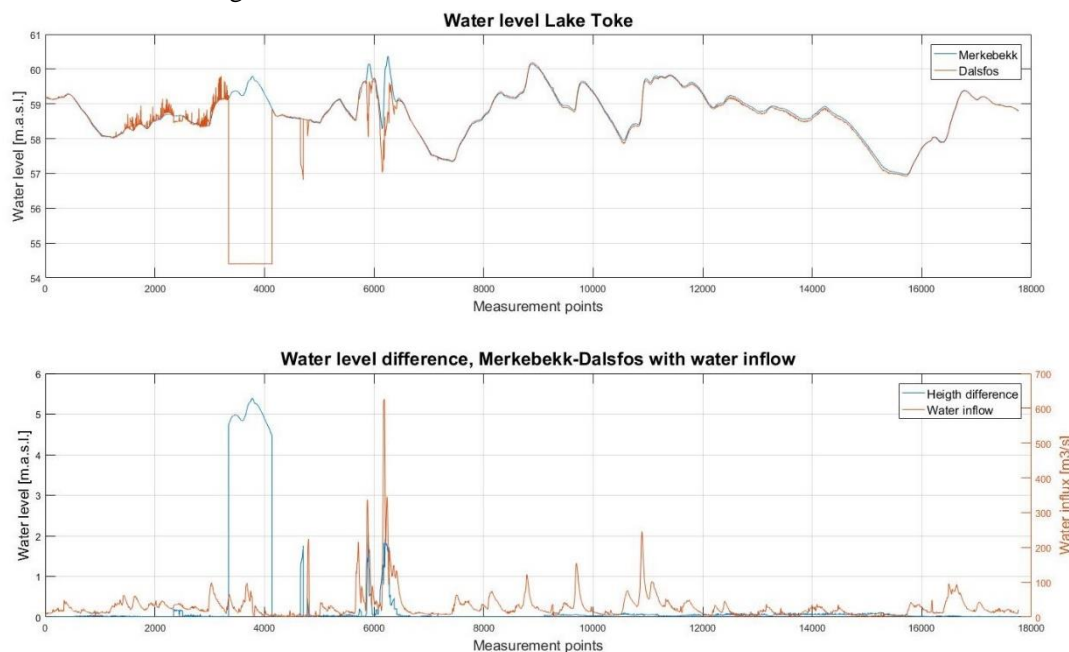


Figure 4. Water level in Lake Toke, 2 measuring points and the difference between them and the measured water inflow to Lake Toke.

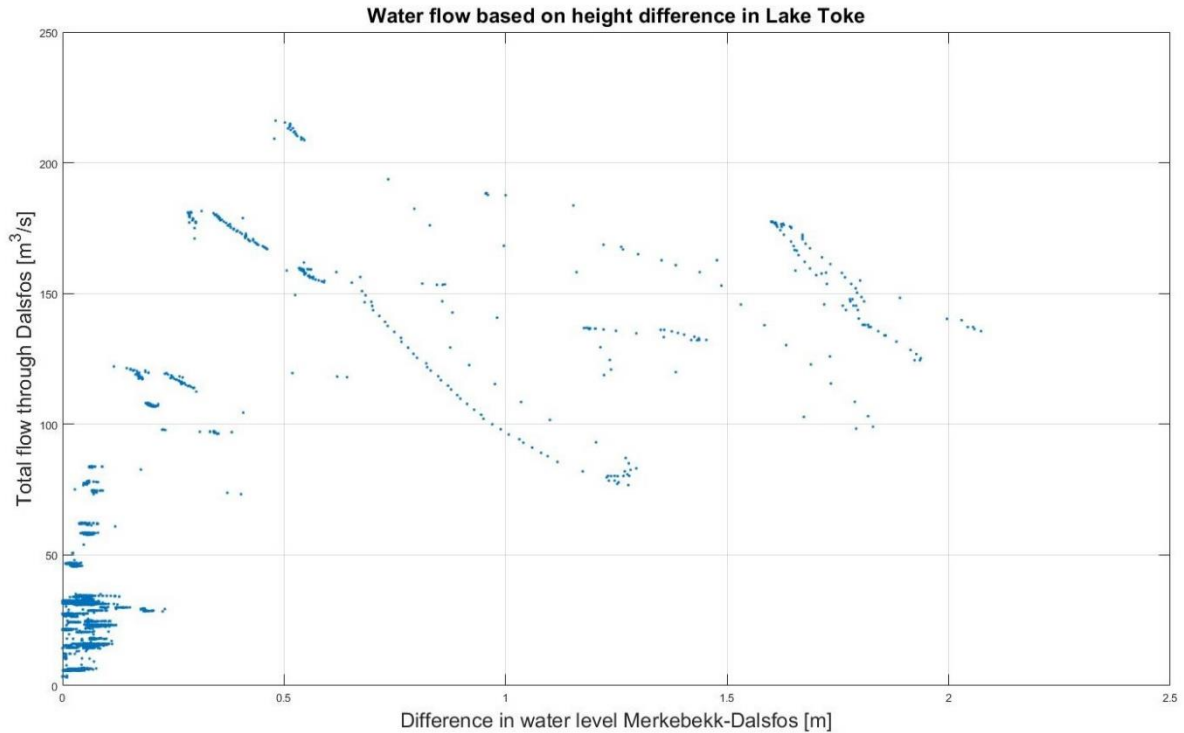


Figure 5. Total water flow through Dalsfos Dam vs. level difference Merkebekk-Dalsfos.

vector θ resulting in Equation 12. Here, y and Φ are known, θ is the unknown.

$$\begin{bmatrix} y_1 \\ y_2 \\ \vdots \\ y_N \end{bmatrix} = \begin{bmatrix} \sqrt[4]{x_1} & \sqrt{x_1} \\ \sqrt[4]{x_2} & \sqrt{x_2} \\ \vdots & \vdots \\ \sqrt[4]{x_N} & \sqrt{x_N} \end{bmatrix} \cdot \begin{bmatrix} k_1 \\ k_2 \end{bmatrix} \quad (11)$$

$$y = \Phi \cdot \theta \quad (12)$$

There is available a function in MATLAB called polyfit what will solve Equation 4, but there is no option to edit or weigh the factors. So this function cannot be used since we want the function to go through (0,0) in the plane. This is to ensure that when there is no level difference between the levels at Merkebekk and at Dalsfos, there is no flow of water between those locations either. To achieve this, we have to ensure that any constant term is equal to zero. Below is MATLAB code (Higham and Higham, 2005) used for finding the polynomial coefficients.

```
x = levelMerkebekk - levelDalsfos;
y = waterFlowTurbines + waterFlowGates;
Phi = [x.^1/4 x.^1/2];
theta = Phi\y;
```

This method of determining the polynomial coefficients was repeated with different orders of the polynomials in $\sqrt[4]{x}$ within matrix Φ to have polynomials from first to fourth order, all the time with constant term forced to zero to ensure the models goes through the origin. Equation 13 shows the fourth order equation, a simplification of the fractions is shown in equation 14.

To get the other orders of the polynomial:

- Third order, $k_4 = 0$
- Second order, k_3 and $k_4 = 0$ (Eq. 4)
- First order, k_2 , k_3 and $k_4 = 0$

For compactness, the water level difference is defined as $d_h = h_1 - h_2$ here.

$$\dot{V}_{12} = k_1 \cdot \sqrt[4]{d_h} + k_2 \cdot \sqrt[4]{d_h^2} + k_3 \cdot \sqrt[4]{d_h^3} + k_4 \cdot \sqrt[4]{d_h^4} \quad (13)$$

$$\dot{V}_{12} = k_1 \cdot \sqrt[4]{d_h} + k_2 \cdot \sqrt{d_h} + k_3 \cdot \sqrt[4]{d_h^3} + k_4 \cdot d_h \quad (14)$$

The resulting models were plotted in Figure 6 against the measurement data to determine how well they fit the target data. In this figure, we see that the first order polynomial (green) falls outside of the data. The fourth order polynomial (orange) results in a parabola which is counter intuitive; the flow of water should be strictly increasing with the level difference. Finally, we see that the second and third order polynomials are nearly identical and give a decent fit to the data. Since the third order polynomial offers no extra information, the second order polynomial was chosen.

3.6 ODE parameter tuning

The α and β parameters in Equations 1 and 2 were originally set to 0.05 and 0.02. This was an experience-based estimate done when the model was first

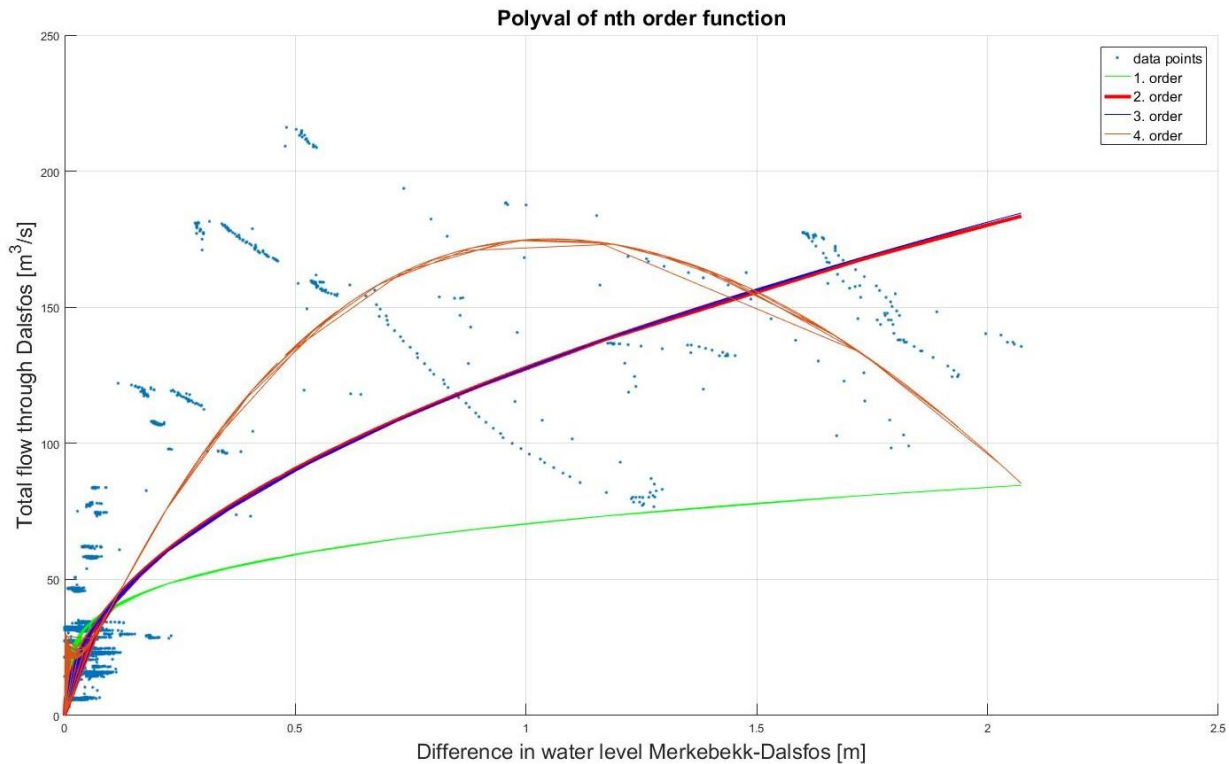


Figure 6. Polynomial evaluation, different order of fitted function.

developed. To estimate new values, the built-in MATLAB function `lsqnonlin` was used. "lsqnonlin" is a nonlinear least-squares solver that solves nonlinear least-squares curve fitting problems (Mathworks, 2017).

A MATLAB script was developed to tune the α - and β parameters. The historical measurement data provided by Skagerak was used as the target data. `lsqnonlin` was supplied with the updated model of Lake Toke and the option to vary the parameters. `lsqnonlin` tries out different values for the parameters, constantly trying to minimize the difference between the output of the model and the target data.

Once suitable values for the α and β parameters were obtained, the tuning of parameters k_1 and k_2 (as described in section 3.5, Equations 11-13) was redone with the updated α and β parameters. The values for k_1 and k_2 presented in Table 1 are those obtained from this second tuning.

3.7 Model verification

To test the model updates, a simulation (described in section 4.2) was run to compare new and the old model as seen in Figure 7. The data chosen was from early August 2015 and thirty days ahead into the beginning of

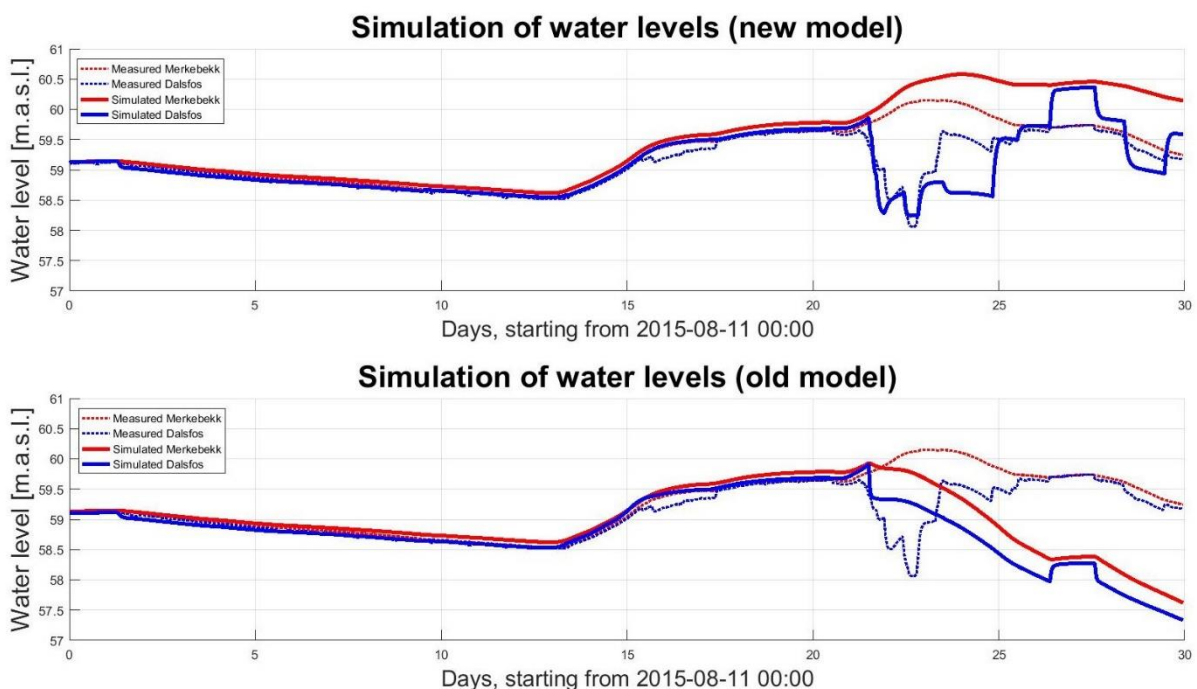


Figure 7. Model verification simulation.

the large flood in September 2015. The blue lines show the water level in Dalsfos and the red lines show the water level in Merkebekk. The dotted lines are measured data while the solid lines are the simulated values. How the plot in Figure 7 was created is described in section 4.2. The results of the plot are discussed in section 5.2.

4 TUC Flood Server

4.1 Server structure

The TUC flood server consists of three subsystems:

- Data Handler, a C# application
- Flood management, an SQL database
- MPC controller, a MATLAB application

The Data Handler runs continuously, monitoring the input folder for new files and starts the MPC controller at chosen intervals. When the Data handler detects a new file, it reads the input values in the file and stores all the input values in the Flood management database.

When the MPC controller is started, it queries the database for the newest input values and imports these. This data is used by the controller for simulating the system and calculating future gate openings. The output values are stored in both an output file and in the Flood management database. How the subsystems interact is shown in Figure 8.

4.2 Simulating the model by fetching data from the database

By using the model functions developed for the MPC controller and gathering data from the Flood management database, a simulator was developed. The main use of the simulator is for comparing the possible performance of the MPC algorithm compared to historical data.

The user chooses a start date and for how many days the simulation should run. Assuming that the needed data is available, the Simulator will use the values to

initiate the model. The model is supplied with the initial values of the levels at Merkebekk and Dalsfos, the current and future position of the floodgates and the current and future power production from the turbines. Under normal operations, the model would be supplied with predictions for the water inflow and a production plan for the turbines. Since historical data is available, the model is supplied with measurement data of the water inflow and of the turbine power production for the simulation period.

The data stored in the database is structured around which (input- or output) file it belongs too and the data type. So when querying the database, it is possible retrieve one or several values from a given file or data type. MATLAB has a built-in toolbox named ODBC which has been used to handle communication between the MPC controller and the database. The MATLAB functions developed to integrate the MPC controller with the database were designed to be as general as possible. This was done to ensure that the functions could be re-used for simulations and for specific queries by the user.

5 Discussion

5.1 Inter-compartmental flow model assumptions and available data

The model for the inter-compartmental flow (section 3.5) is based on the assumption that the flow of water from Merkebekk to Dalsfos is the same as the computed flow through the floodgates and turbines at Dalsfos. There are some issues with this assumption that needs to be considered.

First, it was observed in Figure 4 that some of the oldest measurement data was unreliable. It is possible that some of the more recent data also could be an error source.

The data plotted in Figure 5 is quite scattered, making it difficult to find a function to fit the data. One possible

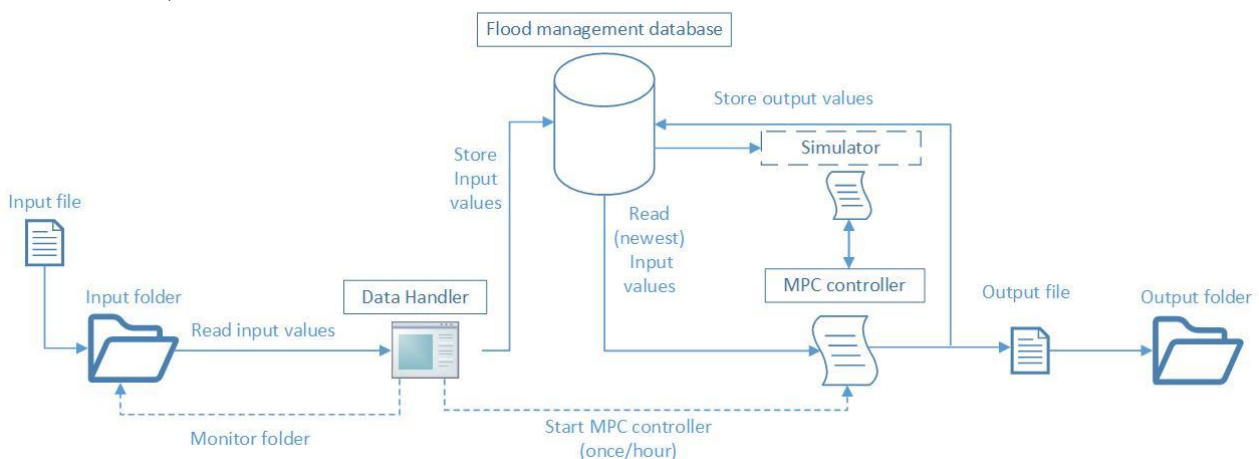


Figure 8. TUC Flood server subsystems and interactions.

source of error is that there may be accumulation of water in the lower volume, i.e., in the dam in front of the flood gates – we have neglected this dynamics by assuming that the flow into this dam equals the flow out of the dam. Another source of error is that the models for computing flow through the turbines and flow through the floodgates may be inaccurate.

Lastly, it is possible that during a flood, water “leaks” into the ground – at least if the flood comes after a dry period, and until the flooded area becomes saturated with water.

To further improve on the inter-compartmental flow model, some advanced analysis methods and strategies would have to be explored.

5.2 Model verification simulation

In Figure 7, we can observe how the new and the old models perform in simulation when compared to historical data.

The figure reflects some of the changes made to the model:

- Both models handle the simulation for the first 21 days well. This is as expected, as the old model functioned well under regular condition and there have not been made major changes in that regard.
- The new model shows improvement over the old one once the flood starts to build up. There is still deviation from the measured data, but the general trend is followed.

Some of the deviations in Figure 7 show up when the floodgates are opened, and it is thus reasonable to attribute them to inaccuracies of the floodgate model. On day 26-27, both models show a sudden jump of almost one meter of the level in Dalsfos in a very short period of time and then again an equally abrupt drop about one day later. These sudden jumps coincide with the sudden closing and opening of the flood gates.

6 Conclusions

The new model shows improvement compared to the old one; this improvement is particularly seen during floods, which is when the optimization of the floodgates actually is important. With the new database for handling information, the foundation is laid for further improving the model when more data becomes available.

The model still has room for improvement, in particular the models for the inter-compartment flow and the floodgate flow should be examined further.

Data storage and use has been made simpler now with the implementation of a database to store input- and output values. This inclusion has made troubleshooting and further work simpler.

There remains some work in regards to the user interface of the Data Handler and error handling for the MPC controller.

Future work:

- Further tuning of model, with particular emphasis of floodgate models.
- Improve efficiency of model.
- Data Handler: Include UI to display status messages directly to the user.
- MPC controller: Error- handling and reporting to the database should be implemented.

References

- B. Furenes. MPC PÅ FLOMLUKEHÅNDBTERING I KRAGERØVASSDRAGET. Presentation. Porsgrunn, Norway, 2016.
- O. Christensen and K.L. Christensen (2004). Approximation Theory. From Taylor Polynomials to Wavelets. Birkhäuser, Boston.
- A.Z. Gjerseth. Systembeskrivelse. Tech. rep. Telemark University College, Porsgrunn, Norway, Aug. 2016.
- D.J. Higham and N.J. Higham (2005). MATLAB Guide, third edition. SIAM, Philadelphia, USA. 978-1-61197-465-2.
- B. Lie. Final report: KONTRAKT NR INAN-140122 Optimal Control of Dalsfos Flood Gates - control algorithm. Tech. rep. Telemark University College, Porsgrunn, Norway, July 2014.
- Mathworks. Isqnonlin. Article on the Internet. 20 Mar 2017. [url:https://se.mathworks.com/help/optim/ug/Isqnonlin.htm](https://se.mathworks.com/help/optim/ug/Isqnonlin.htm).
- C. Van Loan (2000). Introduction to Scientific Computing. A Matrix-Vector Approach Using MATLAB, Second Edition. Prentice-Hall, Upper Saddle River, New Jersey. ISBN-13: 978-0139491573.
- L.F. Shampine, I. Gladwell, S. Thompson (2003). Solving ODEs with MATLAB. Cambridge University Press, Cambridge, UK.
- N-O. Skeie. KONTRAKT NR INAN-140122 Optimal styring av Dalsfos Flomporter - Grensesnitt mellom GS2 Filformat og Flomprognosesystem med MPC fra Høgskolen i Telemark (HiT). Tech. rep. Telemark University College, Porsgrunn, Norway, June 2014.
- H. M. Thoresen, "Control and optimization of Kragerøvassdraget," Telemark University College, Porsgrunn, 2011.
- NVE (Norges vassdrags- og energidirektorat). Retningslinjer for flomløp. Publication on the Internet. 17 Jan 2017. [url:http://publikasjoner.nve.no/retningslinjer/2005/retningslinjer2005_02.pdf](http://publikasjoner.nve.no/retningslinjer/2005/retningslinjer2005_02.pdf).

Hydropower Systems: Comparison of Mechanistic and Table Look-up Turbine Models

Valentyna Splavska Liubomyr Vytvytskyi Bernt Lie

University College of Southeast Norway, Porsgrunn, bernt.lie@usn.no, valentyna.splavska@gmail.com

Abstract

In this paper, a detailed overview of hydropower system components is given. Components of the system include intake race, upstream and downstream surge tanks, penstock, turbine and draft tube. A case study which includes a Francis turbine, taken from the literature, was used. The paper presents a case study hydropower system, with models implemented in Modelica. For simplicity, compressibility of water and elasticity of pipe walls were neglected. The main aims are to compare a turbine model based on the Euler equations vs. a table look-up model, and illustrate how the surge tanks influence the transients of the system.

Keywords: hydropower system, Modelica, mechanistic model, table look-up model, Francis turbine

1 Introduction

A hydropower plant, including the waterway, energy transformation block, and the distribution grid, constitutes a complex dynamic system that we must control to operate within constraints. A hydropower plant can be divided into subsystems where several of these belong to the same class, hence an object-oriented modeling language will greatly simplify the process of setting up a model.

Mechanistic models based on physical principles are useful in that they enable simulation of hypothetical systems. Empirical models, on the other hand, require fitting to experimental data. Accurate mechanistic CFD models are too computationally intensive for transient analysis and control design. Mechanistic models of turbines based on the Euler equations are suitable for simulation of hypothetical systems, but may have too constrained model structure to allow for perfect representation. Dimensionless models and hill chart models can be fitted to experimental data, hence are considered empirical models. On the other hand, it is possible to fit empirical models to accurate CFD simulations instead of experimental data. These empirical models typically consist of look-up tables for how turbine power efficiency varies with flow rate, control input, etc.

In Section 2, the models of the various parts of the system are presented. In Section 3, some simulation results are given. Finally, some conclusions are drawn in Section 4.

2 Model development

Hydropower systems are diverse in terms of plant size, generating unit, the water head and plant purposes (IEA, 2012). The common primary classification of hydropower plants includes four functional classes: run-of-river plants, reservoir (or storage), diversion system and pumped storage plants. In this paper, the model of a hydropower system is developed by neglecting compressibility of water and elasticity of pipe walls. A reservoir hydropower system, consisting of intake race, upstream and downstream surge tanks, penstock, turbine and draft tube, is considered.

2.1 Reservoir

The reservoir is assumed as an open pond (Figure 1). The water level difference from reservoir to tail water is a determining factor for hydraulic effect of the entire system. For model simplification the water level in the reservoir is assumed as constant.

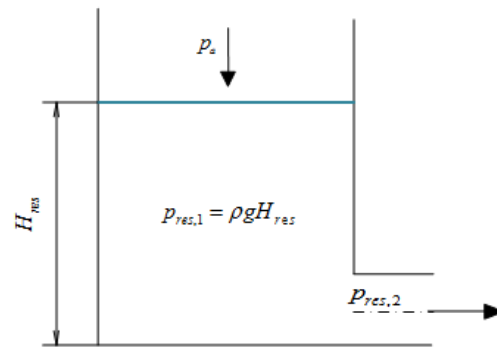


Figure 1. Schematic representation of the model for reservoir.

The mass and momentum balances for reservoir lead to:

$$\frac{dm_{res}}{dt} = \dot{m}_{i,res} - \dot{m}_{e,res} \quad (1)$$

$$p_{res,2} = p_a + \rho g H_{res} \quad (2)$$

2.2 Intake race

The intake race is a part of the waterway between the water intake and a surge tank, and ends with a sand trap (Figure 2). For model simplification, intake race, penstock and discharge tube are assumed as filled pipes, which leads to $\dot{m} = const.$ Since the momentum flow is $\mathcal{M} = \frac{\rho}{A} \dot{V}^2$,

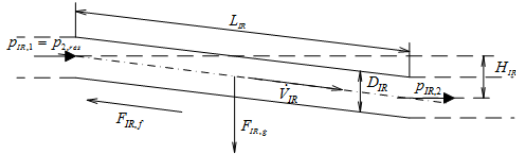


Figure 2. Schematic representation of the model for intake race.

an assumption of the water density constancy leads to $\dot{M}_{IR,i} = \dot{M}_{IR,e}$ (Lie et al., 2016). Thus, the mass and momentum balances can be expressed as:

$$\frac{dm_{IR}}{dt} = 0 \quad (3)$$

$$\frac{d\mathcal{M}_{IR}}{dt} = F_{IR} \quad (4)$$

The forces acting on the inlet race are given as:

$$F_{IR} = F_{IR,p} + F_{IR,g} - F_{IR,f} \quad (5)$$

$$F_{IR,p} = p_{IR,1}A_{IR} - p_{IR,2}A_{IR} \quad (6)$$

$$F_{IR,g} = m_{IR}g \frac{H_{IR}}{L_{IR}} \quad (7)$$

$$(8)$$

For friction forces component the Darcy description of friction is assumed:

$$F_{IR,f} = \frac{K'''_{IR} A_{IR,w} f_{IR,D}}{4} A_{IR,w} = \pi D_{IR} L_{IR} \quad (9)$$

$$K'''_{IR} = \frac{\rho}{2A_{IR}^2} \dot{V}_{IR} |\dot{V}_{IR}| \quad (10)$$

Darcy's friction coefficient $f_{IR,D}$ can be given by the following explicit approximation of the implicit Colebrook model (Lie et al., 2016):

$$\frac{1}{\sqrt{f_{IR,D}}} = -2 \lg \left(\frac{\epsilon_{IR}}{3,70D_{IR}} + \frac{5,74}{N_{IR,Re}^{0,9}} \right) \quad (11)$$

$$N_{Re,IR} = \frac{\rho \dot{V}_{IR} D_{IR}}{\mu A_{IR}} \quad (12)$$

2.3 Manifold

The manifold connects the inlet race, the surge tank, and the penstock. by assuming that there is negligible mass (inertia) inside the manifold, steady state for both mass and momentum balances can be assumed (Lie et al., 2016). Since no mass is accumulated, the mass and momentum balances can be represented as:

$$\frac{dm_*}{dt} = 0 \quad (13)$$

$$\frac{d\mathcal{M}_*}{dt} = 0 \quad (14)$$

leading to:

$$\dot{V}_i = \dot{V}_P + \dot{V}_{ST} \quad (15)$$

$$p_{IR,2} = p_{P,2} = p_{ST,1} = p_* \quad (16)$$

2.4 Penstock

A penstock is a steep pipe which connects the inlet part of a hydropower system (via the manifold) and a wicket gate inlet to a turbine (Figure 3). The mass and momentum balances for the penstock:

$$\frac{dm_P}{dt} = 0 \quad (17)$$

$$\frac{d\mathcal{M}_P}{dt} = F_P \quad (18)$$

The forces acting on the penstock are:

$$F_P = F_{P,p} + F_{P,g} - F_{P,f} \quad (19)$$

$$F_{P,p} = p_{P,1}A_P - p_{P,2}A_P \quad (20)$$

$$F_{P,g} = m_P g \frac{H_P}{L_P} \quad (21)$$

$$F_{P,f} = \frac{K'''_P A_{P,w} f_{P,D}}{4} \quad (22)$$

$$A_{P,w} = \pi D_P L_P \quad (23)$$

$$K'''_P = \frac{\rho}{2A_P^2} \dot{V}_P |\dot{V}_P| \quad (24)$$

$$\frac{1}{\sqrt{f_{P,D}}} = -2 \lg \left(\frac{\epsilon_P}{3,70D_P} + \frac{5,74}{N_{P,Re}^{0,9}} \right) \quad (25)$$

$$N_{Re,P} = \frac{\rho \dot{V}_P D_P}{\mu A_P} \quad (26)$$

2.5 Surge tank

While water flow is proceeding trough the waterway, it can accelerate or decelerate causing pressure variations with magnitude exceeding the nominal pressure in the waterway, which, in its turn, leads to the load changes causing the mass oscillations called "water hammer" effect (Kjoelle, 2001; Winkler et al., 2011). The surge tank serves to reduce harmful effect of these oscillations (Figure 4). The surge tank design is an iterative process, where the stability criterions (Thoma or Svee) are the determining factors (Brekke, 2001). Since the surge tank has varying mass, the mass and momentum balances can be repre-

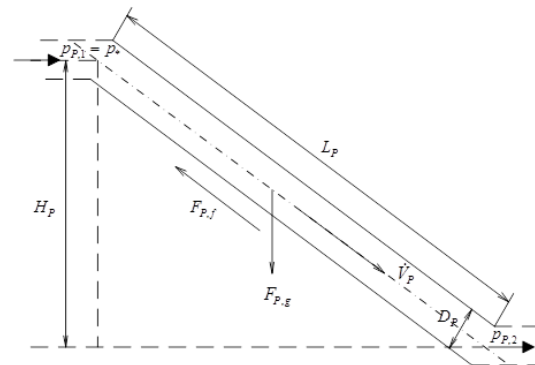


Figure 3. Schematic representation of the model for penstock.

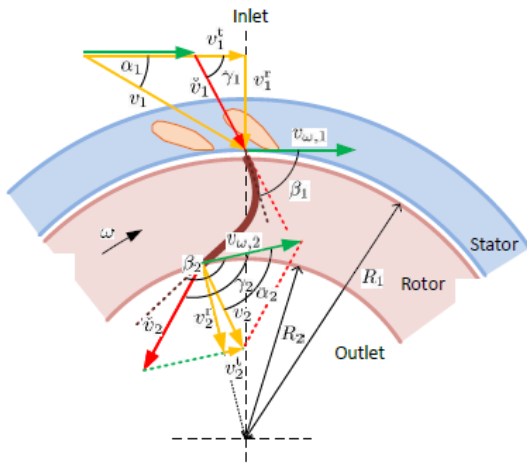


Figure 6. Key quantities in the Francis turbine model (the water effluent comes out from the paper plan; blade angles β_1, β_2) (Lie and Vytvytskyi, 2016).

Hence, the total pressure loss across the turbine can be found as:

$$\dot{W}_t = \Delta p_t \dot{V} \quad (54)$$

Thus, the efficiency of the turbine can be defined as:

$$\eta = \dot{W}_s / \dot{W}_t \quad (55)$$

3 Simulation results

The equation based modeling language Modelica supports differential algebraic equations, and is a good choice for modeling hydropower systems. OpenModelica is one of several free simulation tools based on Modelica; Dymola is an example of a commercial tool. Commercial hydropower libraries are available for Dymola, but a simple, free library is also under development at University College of Southeast Norway.

A case study from (Valaamo, 2016), including a Francis turbine, was used for illustration. This paper presents a case study hydropower system without surge tank, with upstream surge tank (UST) and both upstream and downstream surge tank (DST), with models implemented in Modelica (Vytvytskyi and Lie, 2016). The obtained results of turbine efficiency (Figure 7) were compared with a table look-up model (Figure 10). To make this comparison turbine efficiency was plotted with respect to volumetric flow rate (Figure 8). Pressure drop over the turbine for mentioned study cases are shown on (Figure 9).

From (Figures 7, 10), we see that a turbine model based on the Euler equations gives quite similar results to a table look-up model.

To investigate the influence of the surge tanks on the transients of the system, a ramp-up test (height=7%, duration=1s) was performed. Since the developed model is not suitable for analysis of cavitation, the water hammer effect is in focus.

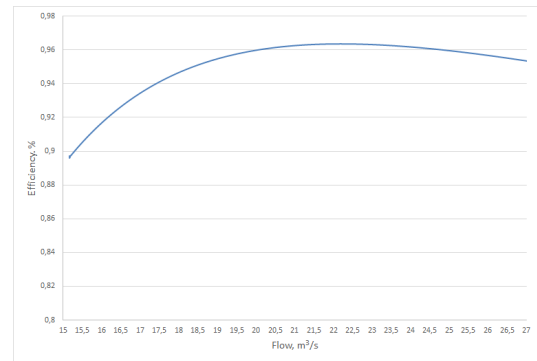


Figure 7. Turbine efficiency.

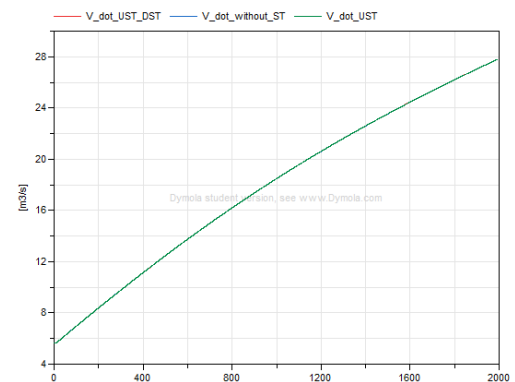


Figure 8. Volumetric flow rate.

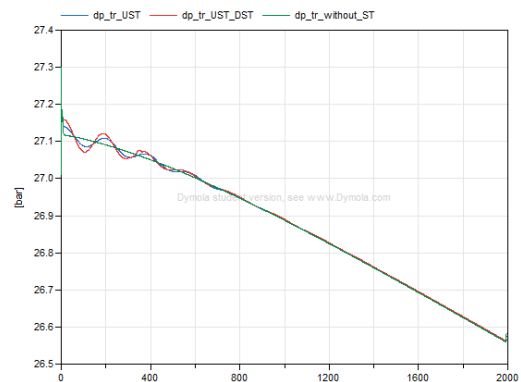


Figure 9. Pressure drop over the turbine.

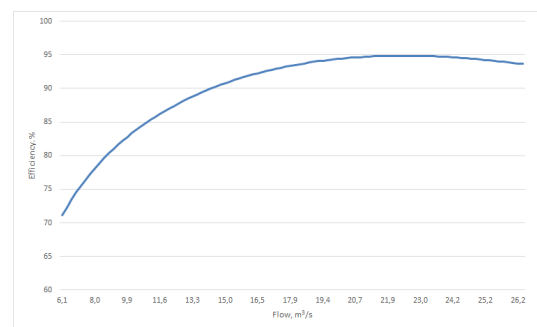


Figure 10. Turbine efficiency from look up table.

Figures 11, 12 show the dynamics of the inlet and outlet

pressure of the turbine for systems with surge tank and without. In the system with no surge tank, a significant pressure drop occurs. For the system with surge tank, on the other hand, the pressure oscillation is smooth (has less amplitude and magnitude), hence, the components of the system is less exposed to the harmful water hammer effect.

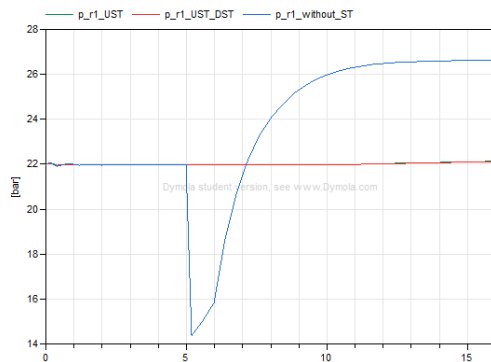


Figure 11. The turbine inlet pressure. Ramp-up test.

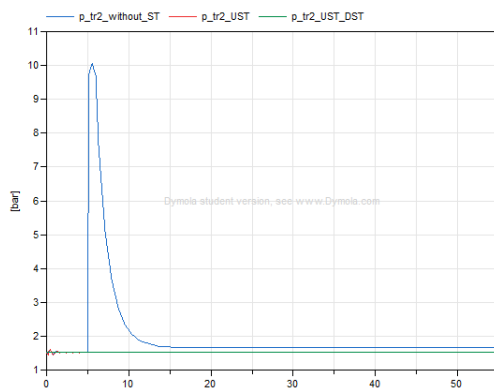


Figure 12. The turbine outlet pressure. Ramp-up test.

Figure 13 illustrates the dynamics of the outlet pressure of the turbine for hydropower system with one and two surge tanks to make a conclusion about feasibility of additional installation of a downstream surge tank. In the system with only upstream surge tank, the amplitude of the pressure oscillation is higher than in the system with additional downstream surge tank. Furthermore, the oscillations are smoother in the second one.

4 Conclusions

In this paper, a detailed overview of hydropower system components was given. A case study from the literature including a Francis turbine was used. The paper presents a case study hydropower system, with models implemented in Modelica. In this paper, a mechanistic model of the turbine based on the Euler equations was introduced, with dimensions computed using A-lab (McClimans et al., 2000). The turbine model based on the Euler equations was compared to a table look-up model. The influence of the surge tanks on the transients of the system was illustrated. The

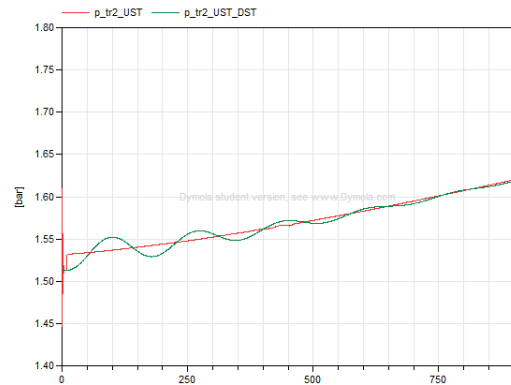


Figure 13. The turbine outlet pressure (cases with only upstream surge tank and both upstream and downstream surge tanks). Step-test.

developed model may not be suitable for analysis of cavitation, since neglecting compressibility and elasticity in water/pipes filters out some pressure transients. The research contributes in refining a case study for hydropower systems, and in emphasizing the usefulness of mechanistic turbine models.

References

- H. Brekke. *Hydraulic turbines. Design, Erection and Operation*. 2001.
- IEA. Technology Roadmap. Hydropower, 2012. Technical report, International energy agency, Paris Cedex, France, 2012.
- A. Kjoelle. *Hydropower in Norway. Mechanical equipment. Survey*. NTNU Norwegian University of Science and Technology, 2001.
- B. Lie and L. Vytvytskyi. *Modeling of Dynamic Systems. Lecture notes*. USN, 2016.
- B. Lie, L. Vytvytskyi, and C. Agu. Modeling of dynamic systems. project fm 1015. USN, 2016.
- T.A. McClimans, J. Pietrzak, V. Huess, N. Kliem, and B.O. Johannessen. A comparison of laboratory and numerical simulations of the ocean circulation in the skagerrak. *Cont. Shelf Res.*, 20:941–974, 2000.
- Ch. Nicolet. *Hydroacoustic modelling and numerical simulation of unsteady operation of hydroelectric systems*. Doctor of science dissertation, EPFL Swiss Federal Institute of Technology in Lausanne, ALcublens (Lausanne), Switzerland, 2007.
- Ch. Nicolet, B. Greiveldinger, J.-J. HÅlrou, B. Kawkabani, P. Allenbach, J.-J. Simond, and F. Avellan. High order modeling of hydraulic power plant in islanded power network. *IEEE Transaction on Power Systems*, 22(4):1870–1892, 2007.
- S.B. Valaamo. *Transient Modelling of Hydropower Plants*. Master thesis, NTNU Norwegian University of Science and Technology, Trondheim, Norway, 2016.

L. Vytvytskyi and B. Lie. Comparison of elastic vs. inelastic penstock model using openmodelica. *International Conference of Scandinavian Simulation Society, SIMS 2017*, 58, 2016.

D. Winkler, H.M. Thoresen, I. Andreassen, M.A.S. Perera, and B.R. Sharefi. Modelling and optimisation of deviation in hydro power production. *Modelica*, pages 1–10, 2011.

Appendix A. Parameters of the simulation

Reservoir

Initial height	48 m
Walls angle	20 deg
Bed width	100 m
Length	500 m
Friction factor	8e-4

Intake

Height	25 m
Length	2000 m
Diameter i&o	5 m

Penstock

Height	210 m
Length	450 m
Diameter i&o	4 m

Turbine

Diameter of the inlet pipe	1.73 m
Turbine blade inlet radius	2.02/2 m
Turbine blade outlet radius	1.5/2 m
Radius of the guide vane susp. circle	2.23/2 m
Width of turbine/blades inlet	0.259 m
Width of turbine/blades outlet	1.5/4 m
r_v	0.9 m
r_Y	1 m
R_Y	2.5 m
Hydraulic friction loss coefficient	1e5
β_1	112 deg
β_2	163.2 deg

Discharge

Height	5 m
Length	2000 m
Diameter i&o	4.5 m

Tail

Initial height	10 m
Bed width	100 m
Length	500 m
α	1145.9 deg
Friction factor	8e-4

Numerical Calculation of Stresses in Helical Cable Elements subject to Cable Bending and Twisting

Magnus Komperød¹

¹Technological Analyses Centre, Nexans Norway AS, Norway, magnus.komperod@nexans.com

Abstract

Calculating the mechanical stresses in cable elements is essential for analyzing the cable's mechanical properties and fatigue properties. This paper derives numerical calculations of the stresses in helical cable elements for cables subject to bending- and twisting loads. The numerical calculations are compared to analytical approximations from the scientific literature. The former gives higher accuracy, and discloses behaviors and coupling effects that are not captured by the latter. These favorable properties combined with easy implementation, no risk of convergence issues, and very short CPU time, make the numerical calculations a very attractive alternative to the analytical approximations.

Keywords: Applied Numerical Analysis; Cross Section Analysis; Differential Geometry; Power Umbilical; Subsea Power Cable; Umbilical.

1 Introduction

Mechanical analyses of subsea power cables, umbilicals, and power umbilicals establish the relationships between the cables' physical loads and the corresponding mechanical stresses in the cable elements. The physical loads are typically axial cable tension, cable bending curvature, cable twist, and hydrostatic pressure from the surrounding seawater. Physical loads also include the internal pressure inside umbilical tubes. Figure 1 shows an example of an umbilical.

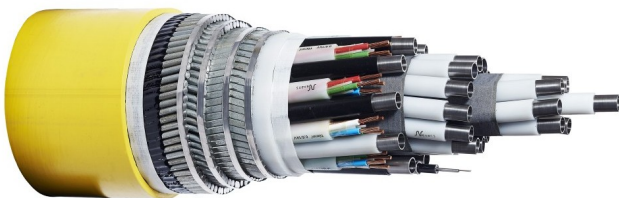


Figure 1. Umbilical with helical tubes, helical electric and fiber optic signal cables, and helical armor wires.

tion on how the cables will behave during manufacturing, transportation, installation, and operation. Further, the analyses conclude how large physical loads the cable can withstand without the risk of being compromised. Also, the results of these analyses are the basis for subsequent analyses that study the interactions between the cables and their surroundings, including the cables' expected fatigue lives.

Mechanical cable analyses date back to at least half a century ago, with publications written in the 1960s and 1970s still being highly relevant today, such as Lutchansky (1969) and Knapp (1979). Over the later decades the field has matured through improved modeling and by including new considerations in the analyses. Also, some validations against physical testing have been performed, but scientific publications on this topic are unfortunately very sparse. Among the published papers on physical testing are Maioli (2015), Tarnowski (2015), Ekeberg and Dhaigude (2016), Dhaigude and Ekeberg (2016), Jordal et al. (2017), and Komperød et al. (2017).

Like for most other fields of science and engineering, the increased performance and reduced cost of computers over the last decades have strongly influenced mechanical cable analyses. Today, there are several software tools specialized for mechanical analyses of cables and similar structures, such as CableCAD, Helica, UFLEX2D, and UFLEX3D. The author presented a comparison between UFLEX2D simulations and analytical calculations in Komperød (2014).

Also general purpose finite element software tools, such as Abaqus, ANSYS, and COMSOL, are used for analyzing cables' mechanical properties. Several papers have been published on this topic, for example Tjahjanto et al. (2017), which present interesting results on fatigue stresses of helical power phases in a three-phases power cable based on finite element simulations.

Although the field of mechanical cable analyses have matured by the efforts of engineers and scientists over several decades, it is constantly being challenged by the desire of installing and operating cables in ever deeper waters, in lower temperatures, and in harsher weather conditions. This calls for more accurate analyses, for more thorough validation against physical testing, and for inclusion of new considerations in the analyses work, such as cables' sensitivity to the ambient temperature.

The present paper aims to give a contribution to the

The mechanical cable analyses give essential informa-

work of improving and extending mechanical cable analyses. The paper derives numerical calculations of the cable elements' stresses and strains subject to cable bending and twisting. Similar results have been presented in the scientific literature using analytical calculations, see for example Kebabze (2000), Sødahl et al. (2010), and Skeie et al. (2012). As such analyses result in difficult mathematical problems, the analytical calculations are simplified, typically through linearizations, until the simplified problem can be solved within reasonable efforts. However, as shown by the author in Komperød (2017), these simplifications give less accurate results and abandon some interesting information.

The work presented in this paper is a continuation of the work presented by the author in Komperød (2017). From the author's point of view, mechanical cable analyses based on numerical solutions of first principle models is an attractive compromise between simplified analytical solutions and complex finite element analyses using advanced software tools. The numerical solution is easy to implement, gives high accuracy, and is efficient in terms of CPU time. The author's preliminary results also indicate that the nature of the numerical calculations make them suitable for parallel processing, which is necessary for taking full advantage of modern computers.

The calculated element stresses will in future works be used to establish the cable's capacity (allowed combinations of axial cable tension and cable bending curvature) and its expected fatigue life. Also, the element stresses and strains give the cable's strain energy, from which the cable's axial stiffness, torsion stiffness, and bending stiffness can be derived.

2 Nomenclature

Table 1 presents the nomenclature used in this paper. Subscript is a shorthand notation for discretization steps. For example f_{-2} means $f(x - 2h)$, where the nominal value x is understood from the context. The notation $\|\cdot\|$ means the 2-norm, i.e. the length of a vector.

3 Assumptions and Simplifications

The mathematical derivation of this paper is subject to the following assumptions and simplifications:

1. The cable is assumed to have constant bending curvature and constant twist angle along its length.
2. Helical cable elements are assumed to follow a loxodromic curve during cable bending. This means that if the cable element initially follows a thin, helical curve painted on the beneath cable sheath, the cable element will cover the painted curve also after cable bending. Dhaigude and Ekeberg (2016), Ekeberg and Dhaigude (2016), and Tjahjanto et al. (2017) present results from physical tests and finite element simulations which conclude that this assumption holds.

Table 1. Nomenclature.

\vec{b}	Binormal vector [-].
E	E-modulus [Pa].
G	Shear modulus [Pa].
h	Discretization step [m].
L	Pitch length [m].
l	Cable length parameter [m].
\vec{n}	Normal vector [-].
\vec{p}	Vector from center of the element to the point to calculate stresses [m].
p^r	Radial component of \vec{p} [m].
p^s	Surface component of \vec{p} [m].
R	Pitch radius [m].
\vec{r}	Parameterization vector of helical cable element [m].
s	Cable element length parameter [m].
\vec{T}	Tangent vector [-].
\vec{t}	Unit-length tangent vector [-].
\vec{u}	Unit-length radial vector [-].
\vec{v}	Unit-length surface vector [-].
α	Pitch angle [rad].
β	Helical cable element's angular position at $l = 0$ [rad].
$\gamma_{ut}, \gamma_{vt}, \gamma_{\psi t}$	Shear strain in helical cable element [-].
ϵ_{tt}	Axial strain in helical cable element [-].
κ	Cable bending curvature [m^{-1}].
κ^h	Helical cable element's local curvature [m^{-1}].
$\vec{\kappa}^h$	Helical cable element's local curvature vector [m^{-1}].
κ^r	Radial component of $\vec{\kappa}^h$ [m^{-1}].
$\Delta\kappa^r$	Difference in κ^r relative to zero-load [m^{-1}].
κ^s	Surface component of $\vec{\kappa}^h$ [m^{-1}].
σ_{tt}	Axial stress in helical cable element [Pa].
σ_{vm}	von Mises stress in helical cable element [Pa].
$\tau_{ut}, \tau_{vt}, \tau_{\psi t}$	Shear stress in helical cable element [Pa].
φ	Cable twist [rad/m].
φ^h	Helical cable element's local torsion [m^{-1}].
$\Delta\varphi^h$	Difference in φ^h relative to zero-load [m^{-1}].

3. The stress calculations assume the helical cable ele-

ments to follow a linear stress vs. strain relationship.

4. Axial tension and compression in the cable elements are not included in the calculations.
5. Friction / shear forces between cable elements is neglected.

4 Parameterization of Helical Cable Elements

The purpose of the present paper is to calculate the stresses and strains of helical cable elements subject to cable bending and cable twisting. These calculations depend on the elements' local curvature and local torsion, which in turn depend on a parameterization of the cable elements' paths in the three-dimensional space.

A parameterization is a function $\mathbb{R} \rightarrow \mathbb{R}^3$ which describes a curve in a three dimensional space in terms of a scalar variable. Lutchansky (1969) presents a parameterization of a helical cable element in a bent cable under the assumption that the element follows a loxodromic curve. The author of the present paper provides a similar, but not identical, parameterization in Komperød (2017). The latter parameterization has later been improved by including cable twist. Also, the location of origin of the coordinate system has been improved to give the parameterization better numerical properties. The result is the following parameterization, which will be used in the present paper:

$$\vec{r}(l) = [x(l), y(l), z(l)], \quad (1)$$

$$x(l) = \frac{1}{\kappa} (\cos(\kappa l) - 1) + R \cos\left(\left(\frac{2\pi}{L} + \varphi\right)l + \beta\right) \cos(\kappa l),$$

$$y(l) = R \sin\left(\left(\frac{2\pi}{L} + \varphi\right)l + \beta\right),$$

$$z(l) = \left[\frac{1}{\kappa} + R \cos\left(\left(\frac{2\pi}{L} + \varphi\right)l + \beta\right)\right] \sin(\kappa l).$$

In Eq. 1, the scalar cable length parameter l expresses the progress of the helical cable element in the three-dimensional space. The angle β is the element's orientation in the cable cross section at $l = 0$. The cable curvature κ and the cable twist φ are the cable's deformations due to external loads. The pitch length L and the pitch radius R express the helical cable element's geometry relative to the cable's cross section center. The parameterization follows the common convention in the industry: Positive L means right lay-angle of the helical cable element, while negative L means left lay-angle. Usually, successive cable layers have alternating left vs. right lay-angles. The pitch radius R is always positive.

The angles of Eq. 1 have important practical interpretations: The angle $((2\pi/L + \varphi)l + \beta)$ expresses the helical element's revolution around the cross section center. The angle κl expresses the cable's progress along a virtual circle with radius $1/\kappa$. The center of the virtual circle is in the point $(-1/\kappa, 0, 0)$.

The parameterization presented in Eq. 1 is not defined for $\kappa = 0$, because κ occurs in the denominator. The practical interpretation of $\kappa = 0$ is that the cable is straight (not bent). Taking the limit $\kappa \rightarrow 0$ gives

$$\lim_{\kappa \rightarrow 0} \vec{r}(l) = \left[\lim_{\kappa \rightarrow 0} x(l), \lim_{\kappa \rightarrow 0} y(l), \lim_{\kappa \rightarrow 0} z(l) \right], \quad (2)$$

$$\begin{aligned} \lim_{\kappa \rightarrow 0} x(l) &= \lim_{\kappa \rightarrow 0} \frac{1}{\kappa} (\cos(\kappa l) - 1) \\ &\quad + \lim_{\kappa \rightarrow 0} R \cos\left(\left(\frac{2\pi}{L} + \varphi\right)l + \beta\right) \cos(\kappa l) \\ &= R \cos\left(\left(\frac{2\pi}{L} + \varphi\right)l + \beta\right), \end{aligned}$$

$$\lim_{\kappa \rightarrow 0} y(l) = R \sin\left(\left(\frac{2\pi}{L} + \varphi\right)l + \beta\right),$$

$$\begin{aligned} \lim_{\kappa \rightarrow 0} z(l) &= \lim_{\kappa \rightarrow 0} \left[\frac{1}{\kappa} + R \cos\left(\left(\frac{2\pi}{L} + \varphi\right)l + \beta\right) \right] \sin(\kappa l) \\ &= l. \end{aligned}$$

Evaluating the limits in Eq. 2 results in two zero-over-zero expressions, which can easily be evaluated through MacLaurin series expansions of $\cos(\kappa l)$ and $\sin(\kappa l)$, or by using L'Hopital's rule.

The parameterization in Eq. 2 is the parameterization of a helix. This result was expected, because a helical cable element follows a helix curve when the cable is straight. When doing analytical calculations based on the parameterization, the limit $\kappa \rightarrow 0$ can be used. For numerical calculations, however, $\kappa = 0$ must be considered a special case, resulting in a parameterization with a piecewise function, i.e. \vec{r} is defined by Eq. 2 for $\kappa = 0$, and by Eq. 1 otherwise. Whether very small, but non-zero, absolute values of κ may result in numerical difficulties has not been studied by the author and is beyond the scope of this paper.

5 Calculating Curvature of Helical Cable Element

This section establishes the relationship between the external cable loads in terms of cable bending curvature, κ , and cable twist, φ , and the helical cable element's local curvature vector, $\vec{\kappa}^h$, where the superscript h means "helical element". This vector is essential for subsequent calculation of the element's stress, which is the final goal of this

paper. The derivation in this section is a brief modification of the author's derivation in Komperød (2017).

The tangent vector \vec{T} of the parameterized curve \vec{r} is defined as

$$\vec{T} \stackrel{\text{def}}{=} \frac{d\vec{r}}{dl}, \quad (3)$$

and the unit-length tangent vector \vec{t} is defined as

$$\vec{t} \stackrel{\text{def}}{=} \frac{\vec{T}}{\|\vec{T}\|}. \quad (4)$$

The definition of curvature from the field of differential geometry is

$$\kappa^h \stackrel{\text{def}}{=} \left\| \frac{d\vec{t}}{ds} \right\|, \quad (5)$$

where

$$ds \stackrel{\text{def}}{=} \|\vec{r}'\|. \quad (6)$$

However, for the subsequent calculations of the cable element stresses, it is insufficient to know the curvature as a scalar like it is defined in Eq. 5; also its direction must be known. Hence, for the purpose of mechanical analyses, it is more useful to define the curvature *vector* as

$$\vec{\kappa}^h \stackrel{\text{def}}{=} \frac{d\vec{t}}{ds}. \quad (7)$$

Because \vec{r} is parameterized in terms of l , not s , it is convenient to write the curvature vector as

$$\begin{aligned} \vec{\kappa}^h &= \frac{dl}{ds} \frac{d\vec{t}}{dl} \\ &= \frac{1}{\|\vec{T}\|} \frac{d\vec{t}}{dl}, \end{aligned} \quad (8)$$

where Eqs. 3 and 6 have been used.

A parameterization of the cable's cross section center can be obtained by setting $R = 0$ in Eqs. 1 and 2. In other words; the cross section center is considered as a helical cable element with zero pitch radius. Hence, a unit vector \vec{u} pointing from the physical cable element towards the cable's cross section center can be expressed as

$$\vec{u} \stackrel{\text{def}}{=} \frac{\left(\vec{r}(l)|_{R=0} \right) - \vec{r}(l)}{\left\| \left(\vec{r}(l)|_{R=0} \right) - \vec{r}(l) \right\|}. \quad (9)$$

Taking the dot product between \vec{T} and \vec{u} shows that these vectors are orthogonal. Because \vec{t} and \vec{T} are parallel, \vec{t} and \vec{u} are then orthonormal vectors. Hence, defining \vec{v} as

$$\vec{v} \stackrel{\text{def}}{=} \vec{t} \times \vec{u}, \quad (10)$$

gives that \vec{t} , \vec{u} , and \vec{v} are an orthonormal set of local basis vectors for \mathbb{R}^3 .

As \vec{t} is a unit length vector, its derivative $d\vec{t}/dl$ is normal to \vec{t} (please refer to Pressley (2012) p. 11 for proof). Hence, the curvature vector can be expressed as a linear combination of the two other basis vectors. That is

$$\vec{\kappa}^h = \kappa^r \vec{u} + \kappa^s \vec{v}, \quad (11)$$

for some real scalars κ^r and κ^s . Because \vec{u} and \vec{v} are orthonormal, κ^r and κ^s are easily found by

$$\kappa^r = \vec{\kappa}^h \bullet \vec{u}, \quad (12)$$

$$\kappa^s = \vec{\kappa}^h \bullet \vec{v}. \quad (13)$$

Hence, the vector $[0, \kappa^r, \kappa^s]$ expresses the curvature vector $\vec{\kappa}^h$ in the local Cartesian coordinate system defined by the basis vectors \vec{t} , \vec{u} , and \vec{v} .

6 Calculating Torsion of Helical Cable Element

The curvature derived in the previous section expresses the change in the direction of the tangent vector, \vec{t} , of the helical cable element. The physical interpretation is that the element bends locally. The present section considers torsion, which expresses how the two other local basis vectors, \vec{u} and \vec{v} , rotate in the plane normal to the tangent vector \vec{t} . This interprets into local twisting of the cable element.

The terms "curvature" and "torsion" are used both in the mathematical field of differential geometry and in mechanical cable analyses as in the present paper. Curvature and torsion are defined almost similarly in these two fields, but there is one important difference: Both fields define curvature and torsion based on a local Cartesian coordinate system in which the tangent vector \vec{t} is the first of the three basis vectors. However, differential geometry defines the two other basis vectors as

$$\vec{n} \stackrel{\text{def}}{=} \frac{\frac{d\vec{t}}{ds}}{\left\| \frac{d\vec{t}}{ds} \right\|}, \quad (14)$$

$$\vec{b} \stackrel{\text{def}}{=} \vec{t} \times \vec{n}. \quad (15)$$

Hence, the difference is that differential geometry defines the second basis vector to be in the direction of the derivative of the tangent vector, while in cable analyses the second basis vector is defined to point in the direction from

the cable element towards the cable's cross section center. In both fields the third vector is the cross product of the two other vectors.

When the cable is straight (not bent), the helical cable element has the parameterization of a helix. It can be shown that in this case \vec{n} points from the cable element towards the cable's cross section center. Hence, \vec{n} and \vec{u} coincide, which imply that also \vec{b} and \vec{v} coincide.

Differential geometry defines the torsion as

$$\varphi^h \stackrel{\text{def}}{=} -\vec{n} \bullet \frac{d\vec{b}}{ds}. \quad (16)$$

In cable analyses the torsion is defined similarly as

$$\varphi^h \stackrel{\text{def}}{=} -\vec{u} \bullet \frac{d\vec{v}}{ds}. \quad (17)$$

Again, Eqs. 16 and 17 give the same results if the cable is straight, while the results may be very different when the cable is bent. The definition of Eq. 17 will be used in this paper.

Because \vec{u} and \vec{v} are orthogonal, i.e. $\vec{u} \bullet \vec{v} = 0$, it follows that

$$\frac{d}{ds} (\vec{u} \bullet \vec{v}) = \frac{d\vec{u}}{ds} \bullet \vec{v} + \vec{u} \bullet \frac{d\vec{v}}{ds} = 0, \quad (18)$$

$$\frac{d\vec{u}}{ds} \bullet \vec{v} = -\vec{u} \bullet \frac{d\vec{v}}{ds}. \quad (19)$$

Hence, the torsion of the helical cable element can alternatively be written as

$$\varphi^h = \frac{d\vec{u}}{ds} \bullet \vec{v}. \quad (20)$$

Similar as for the curvature, because \vec{r} is parameterized in term of l , not s , it is convenient to write the torsion as

$$\begin{aligned} \varphi^h &= \frac{dl}{ds} \frac{d\vec{u}}{dl} \bullet \vec{v} \\ &= \frac{1}{\|\vec{T}\|} \frac{d\vec{u}}{dl} \bullet \vec{v}. \end{aligned} \quad (21)$$

7 Numerical Calculations

The two previous sections derive expressions for the curvature and the torsion of a helical cable element. The present section provides numerical calculations to evaluate these expressions. The numerical results will be used in the subsequent calculations of the element's mechanical stresses.

To numerically evaluate the derivatives, the finite difference method is used with a centered, second-order stencil. That is, the derivatives are approximated by

$$\frac{df}{dx} = \frac{f_1 - f_{-1}}{2h} + \mathcal{O}(h^2). \quad (22)$$

In Komperød (2017), the author argued that fourth order accuracy is necessary to achieve sufficient accuracy. However, the present paper provides an improved parameterization of the helical cable element's path, \vec{r} . This allows smaller discretization steps, h , which makes second order accuracy sufficient.

For each value of l to evaluate the curvature and torsion, the following calculations are performed:

1. The parameterization vector \vec{r} is evaluated for $l - 2h$, $l - h$, l , $l + h$, and $l + 2h$. That is, \vec{r}_{-2} , \vec{r}_{-1} , \vec{r}_0 , \vec{r}_1 , and \vec{r}_2 are calculated based on Eq. 1 and Eq. 2.
2. The tangent vector \vec{T} is calculated for $l - h$, l , and $l + h$ using the definition of Eq. 3 and the numerical differentiation of Eq. 22. I.e.

$$\vec{T}_i = \frac{\vec{r}_{i+1} - \vec{r}_{i-1}}{2h}, \quad i \in \{-1, 0, 1\}. \quad (23)$$

3. The length of the tangent vector, $\|\vec{T}\|$, is calculated for $l - h$, l , and $l + h$.
4. The unit length tangent vector is calculated for $l - h$, l , and $l + h$ using Eq. 4. That is,

$$\vec{t}_i = \frac{\vec{T}_i}{\|\vec{T}_i\|}, \quad i \in \{-1, 0, 1\}. \quad (24)$$

5. The curvature vector is calculated at l using Eq. 8 in combination with the numerical differentiation of Eq. 22, i.e.

$$\vec{\kappa}_0^h = \frac{\vec{t}_1 - \vec{t}_{-1}}{2h} \frac{1}{\|\vec{T}_0\|}. \quad (25)$$

6. The vector \vec{u} is calculated for $l - h$, l , and $l + h$.
7. The vector \vec{v} is calculated for l using Eq. 10. That is,

$$\vec{v}_0 = \vec{t}_0 \times \vec{u}_0. \quad (26)$$

8. The curvature components κ^r and κ^s are calculated using Eqs. 12 and 13, i.e.

$$\kappa_0^r = \vec{\kappa}_0^h \bullet \vec{u}_0, \quad (27)$$

$$\kappa_0^h = \vec{\kappa}_0^h \bullet \vec{v}_0. \quad (28)$$

9. The torsion are calculated using Eq. 21 and the numerical differentiation of Eq. 22, which gives

$$\varphi_0^h = \frac{(\vec{u}_1 - \vec{u}_{-1}) \bullet \vec{v}_0}{2h} \frac{1}{\|\vec{T}_0\|}. \quad (29)$$

8 The Zero-Load-Zero-Stress Assumption

A common assumption in mechanical cable analyses is to assume that all cable elements have zero stress when the cable is subject to no external loads. This means that residual stresses from the production process and other operations are neglected. Hence, the helical cable elements' curvature and torsion when the cable is at rest are used as zero-references for calculating the elements' strains and stresses.

When the cable is at rest, the radial component of the helical cable elements' curvature is

$$\kappa^r = \frac{4\pi^2 R}{4\pi^2 R^2 + L^2}. \quad (30)$$

The surface component of the curvature, κ^s , is zero when the cable is at rest. The torsion of the helical element is

$$\varphi^h = \frac{2\pi L}{4\pi^2 R^2 + L^2}. \quad (31)$$

It simplifies the subsequent calculations to define changes in curvature and torsion relative to the relaxed values as

$$\Delta\kappa^r = \kappa^r - \frac{4\pi^2 R}{4\pi^2 R^2 + L^2}, \quad (32)$$

$$\Delta\varphi^h = \varphi^h - \frac{2\pi L}{4\pi^2 R^2 + L^2}, \quad (33)$$

where κ^r and φ^h are the numerical values calculated in the previous section. Because κ^s is zero when the cable is at rest, there would be to no avail to introduce a corresponding notation for this variable.

9 Analytical Approximations from the Scientific Literature

The author is not familiar with other scientific publications that calculate helical cable elements' curvature and torsion numerically, except for the author's own paper Komperød (2017). However, there are several publications on analytical approximations of these values. It is then of interest to compare the analytical and numerical approaches. The analytical approximations of Skeie et al. (2012) and Keadze (2000) will be used for comparison in this paper.

Skeie et al. (2012) and Keadze (2000) use the pitch angle, α , instead of the pitch length, L . The pitch angle is defined as

$$\alpha = \arctan\left(\frac{2\pi R}{L}\right). \quad (34)$$

The derivation of Skeie et al. (2012) results in these formulas

$$\Delta\kappa^r = \cos^4(\alpha) \cos\left(\frac{2\pi}{L}l + \beta\right) \kappa \quad (35)$$

$$+ 2\cos^3(\alpha) \sin(\alpha) \varphi,$$

$$\kappa^s = -\cos(\alpha)(1 + \sin^2(\alpha)) \sin\left(\frac{2\pi}{L}l + \beta\right) \kappa, \quad (36)$$

$$\Delta\varphi^h = -\cos^3(\alpha) \sin(\alpha) \cos\left(\frac{2\pi}{L}l + \beta\right) \kappa \quad (37)$$

$$+ \cos^2(\alpha) \cos(2\alpha) \varphi.$$

Keadze (2000) provides these formulas

$$\Delta\kappa^r = \cos(\alpha) \cos\left(\frac{2\pi}{L}l + \beta\right) \kappa \quad (38)$$

$$+ 2\cos^3(\alpha) \sin(\alpha) \varphi,$$

$$\kappa^s = -\sin\left(\frac{2\pi}{L}l + \beta\right) \kappa, \quad (39)$$

$$\Delta\varphi^h = -\sin(\alpha) \cos\left(\frac{2\pi}{L}l + \beta\right) \kappa \quad (40)$$

$$+ \cos^2(\alpha) \sin^4(\alpha) \varphi.$$

Eqs. 35-40 are adapted to fit the notation and the orientation of the helical element used in this paper.

10 Example 1

This section compares the numerical calculations derived in this paper with the formulas of Skeie et al. (2012) and Keadze (2000). The geometry of the helical cable element used in the example is given in Table 2.

Table 2. Geometry of helical cable element used in Examples 1 and 2.

Property	Value
Pitch length, L [m]	5.0
Pitch radius, R [m]	0.20
Initial angle, β [rad]	0.00

The analytical and numerical approaches will be compared for the three load scenarios given in Table 3. Hence,

the first scenario is twist only, the second scenario is curvature only, while the third scenario is both curvature and twist. Figures 2, 3, and 4 show the curvatures $\Delta\kappa^r$ and κ^s , and the twist $\Delta\varphi^h$, plotted against the cable length parameter l for load scenarios #1, #2, and #3, respectively.

Table 3. Load scenarios used in Examples 1 and 2.

Scenario	κ [m^{-1}]	φ [rad/m]
#1	0.00	3.49×10^{-2}
#2	0.20	0.00×10^{-2}
#3	0.20	3.49×10^{-2}

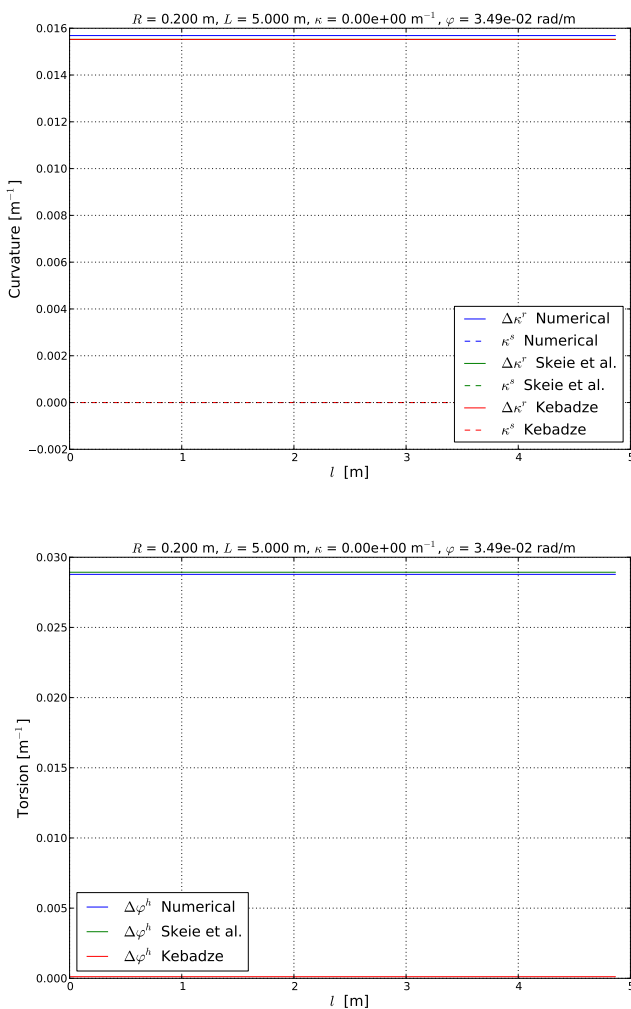


Figure 2. Curvatures $\Delta\kappa^r$ (upper), κ^s (upper), and torsion $\Delta\varphi^h$ (lower) for load scenario #1 given by Tables 2 and 3.

Figure 2 represents load scenario 1, which is the twist-only case. The figure shows that twisting the cable adds offsets to $\Delta\kappa^r$ and $\Delta\varphi^h$, while the graphs remain horizontal, straight lines. The curvature κ^s does not change at all, i.e. it remains at zero. These results are expected, because after twisting the cable, the helical elements still have the

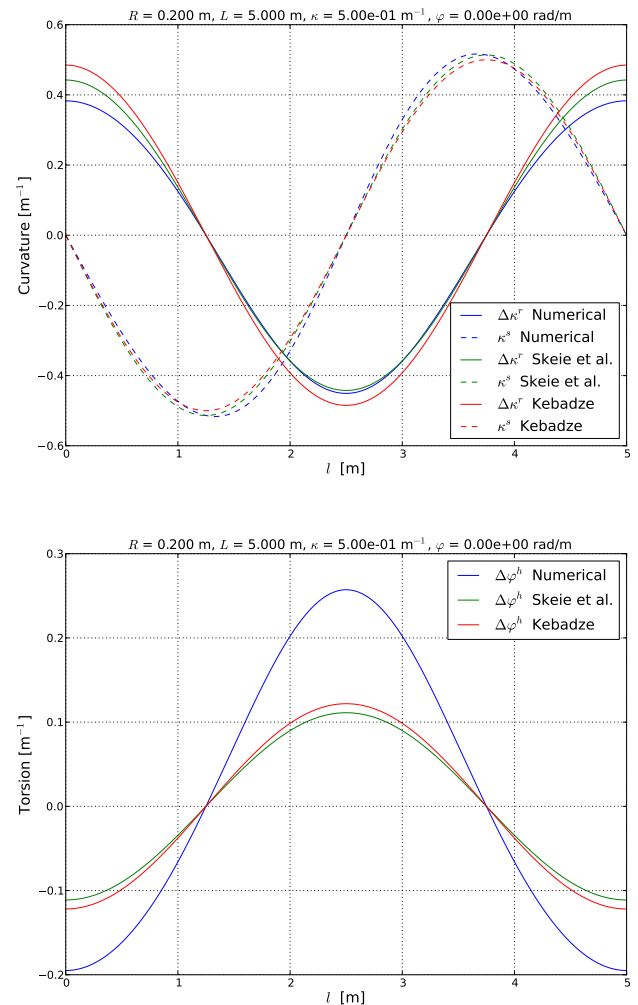


Figure 3. Curvatures $\Delta\kappa^r$ (upper), κ^s (upper), and torsion $\Delta\varphi^h$ (lower) for load scenario #2 given by Tables 2 and 3.

shapes of helices, which are known to have constant κ^r and φ^h over the length l , and zero κ^s .

For load scenario #1 the numerical calculation derived in this paper and the approximation of Skeie et al. (2012) are similar to the extent that they can hardly be distinguished to the resolution of Figure 2. Keadze (2000) give the same result for κ^s as the two other approaches, and also very similar result for $\Delta\kappa^r$. For $\Delta\varphi^h$, Keadze (2000) gives very different results. This can also be seen by comparing the second row of Eq. 37 and the second row of Eq. 40. The latter has the factor $\sin^4(\alpha)$ which is very small for realistic pitch angles. It is not known to the author whether this is Keadze's actual result or whether it is a typo in an otherwise excellent PhD thesis.

Load scenario #2, i.e. the curvature-only case, is shown in Figure 3. While twist adds offsets to the graphs, curvature induces sinusoidal-like oscillations around zero for $\Delta\kappa^r$, κ^s , and $\Delta\varphi^h$. As seen from Eqs. 35-40, the formulas of Skeie et al. (2012) and Keadze (2000) are perfect sinusoidals, while Figure 3 shows that the numerical ap-

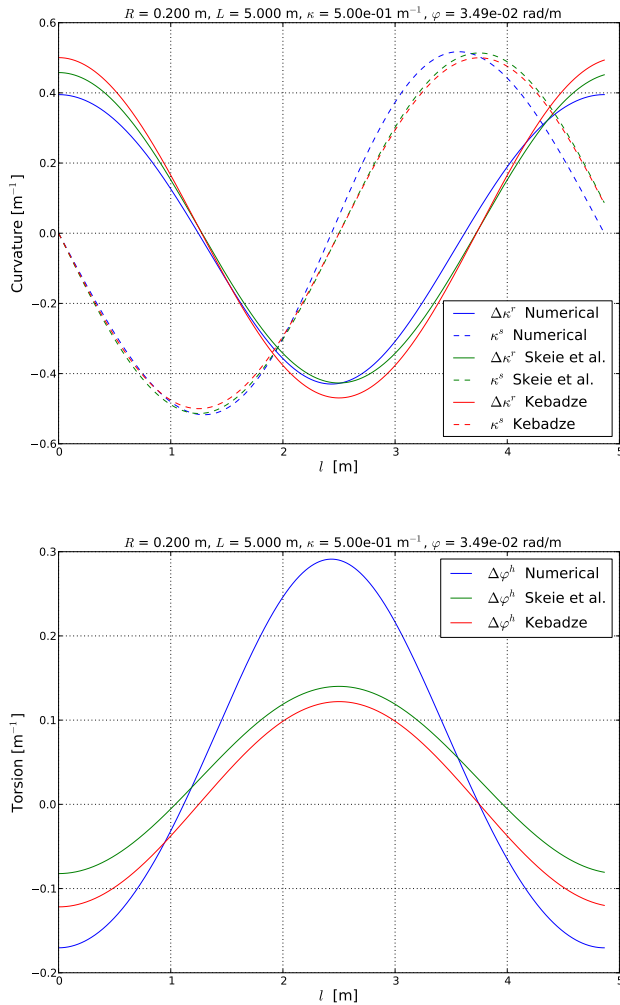


Figure 4. Curvatures $\Delta\kappa^f$ (upper), κ^s (upper), and torsion $\Delta\phi^h$ (lower) for load scenario #3 given by Tables 2 and 3.

proach produces graphs that differ somewhat from true sinusoids.

The most distinct observation in Figure 3 is the difference in amplitude for $\Delta\phi^h$ between the numerical calculation and the two analytical approximations. The former gives an amplitude that is roughly twice as large as the latter two. To the author's understanding, the difference is caused by an oversimplification in the analytical approximations: Skeie et al. (2012) parameterize the helical cable element in s , which is defined by Eq. 6, but simplify by introducing an approximation equivalent to

$$s = \frac{l}{\cos(\alpha)}, \quad (41)$$

which is exact only for $\kappa = 0$. In words this means that the analytical approximation neglects that the element is elongated in the cable's outer arc of bending and compressed in the inner arc. In the notation of the present paper this corresponds to simplifying Eq. 4 to

$$\vec{t} = \vec{T} \cos(\alpha). \quad (42)$$

After doing the same simplification in the numerical calculation, the result of load scenario #2 becomes as shown in Figure 5. As seen from the figure, there is then quite good agreement between the numerical calculation and the analytical approximations. Hence, this comparison supports that the difference in the lower subplot of Figure 3 is caused by the oversimplification in the analytical approximations.

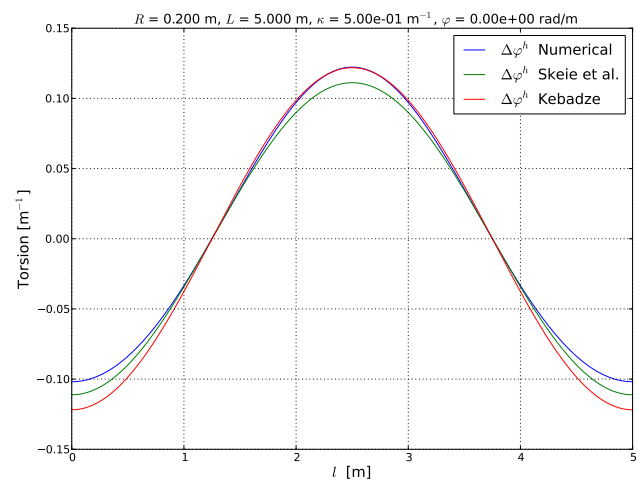


Figure 5. Torsion $\Delta\phi^h$ for load scenario #2 given after simplifying Eq. 4 to Eq. 42.

Load scenario #3, which is shown in Figure 4, demonstrates a coupling effect between the cable bending curvature, κ , and the cable twist, ϕ , which is only captured by the numerical calculation: When the cable is twisted, the curvatures and the torsion are still periodic, but with a period that is somewhat different from L , i.e. somewhat different from 5.0 m in the figure. In other words; twisting the cable increases or decreases the spatial frequency of the curvature oscillations and the torsion oscillation. The analytical approximations inherently fail to include this effect, because they are linearized in both κ and ϕ .

11 Calculating Mechanical Stresses

The previous sections derive numerical calculations of local curvature and local torsion of helical cable elements, and show that there are some differences between the numerical calculations and the analytical approximations presented by Skeie et al. (2012) and by Keadze (2000). The present section shows how to calculate the elements' strains and stresses from the local curvature and the local torsion. There is full agreement between the numerical approach and the analytical approaches for how to calculate the strains and the stresses, once the curvature and the torsion have been established.

The problem of interest is to calculate the axial strain, ϵ_{tt} , the axial stress, σ_{tt} , the shear strains, γ_{ut} and γ_{vt} , the shear stresses, τ_{ut} and τ_{vt} , and the von Mises stress, σ_{vm} , at a specified point in the helical cable element's cross section. Let \vec{p} be a vector from the helical cable element's cross section center to the specified point defined in the local orthonormal basis \vec{t} , \vec{u} , and \vec{v} . Because \vec{t} is normal to the element's cross section plane, while \vec{p} lies in this plane, \vec{p} has at most two nonzero components. Hence, \vec{p} is on the form

$$\vec{p} = [0, p^r, p^s]. \quad (43)$$

The axial strain, ϵ_{tt} , is the negative dot product between the curvature vector and the \vec{p} vector where both are in reference to the orthonormal basis \vec{t} , \vec{u} , and \vec{v} , i.e.

$$\begin{aligned} \epsilon_{tt} &= -[0, \Delta\kappa^r, \kappa^s] \bullet [0, p^r, p^s] \\ &= -\Delta\kappa^r p^r - \kappa^s p^s. \end{aligned} \quad (44)$$

The axial stress, σ_{tt} , is the axial strain multiplied by the E-modulus, which gives

$$\begin{aligned} \sigma_{tt} &= E\epsilon_{tt} \\ &= -E(\Delta\kappa^r p^r + \kappa^s p^s). \end{aligned} \quad (45)$$

The shear strains are calculated as

$$\gamma_{ut} = -\Delta\phi^h p^s, \quad (46)$$

$$\gamma_{vt} = \Delta\phi^h p^r. \quad (47)$$

The corresponding shear stresses are then

$$\begin{aligned} \tau_{ut} &= G\gamma_{ut} \\ &= -G\Delta\phi^h p^s, \end{aligned} \quad (48)$$

$$\begin{aligned} \tau_{vt} &= G\gamma_{vt} \\ &= G\Delta\phi^h p^r. \end{aligned} \quad (49)$$

In mechanical cable analyses, it is often not necessary to know γ_{ut} and γ_{vt} as individual components. This leads to an alternative approach: Replace the local Cartesian coordinate system \vec{t} , \vec{u} , and \vec{v} with a cylindrical coordinate system, where \vec{t} is the cylinder's length direction, and \vec{u} , and \vec{v} are replaced by polar coordinates. The shear stress necessary for the analyses can then be expressed by

$$\gamma_{\psi t} = \Delta\phi^h \sqrt{p^{r2} + p^{s2}}, \quad (50)$$

where ψ is the argument of the polar coordinate system and the square root expression is its magnitude. The stress is then

$$\begin{aligned} \tau_{\psi t} &= G\gamma_{\psi t} \\ &= G\Delta\phi^h \sqrt{p^{r2} + p^{s2}}. \end{aligned} \quad (51)$$

The format of Eqs. 50 and 51 is suitable for calculating the von Mises stress and the strain energy.

The axial stress and the shear stresses discussed in this section gives the following expression for the von Mises stress

$$\sigma_{vm} = \sqrt{\sigma_{tt}^2 + 3\tau_{\psi t}^2}, \quad (52)$$

where σ_{tt} and $\tau_{\psi t}$ are given by Eqs. 45 and 51, respectively.

12 Example 2

This example continues Example 1 by calculating stresses as derived in the previous section for the geometry given in Table 2 and the load scenarios given in Table 3. In addition to these data, the helical element's cross section geometry and material properties must be given. Assume a 10×3 mm rectangular steel armor wire, where the stresses at the corner in the first quadrant, i.e. along the positive \vec{u} and the positive \vec{v} , are to be calculated. The \vec{p} vector and the material properties are as given in Table 4.

Table 4. The \vec{p} vector and the material properties used in Example 2.

Property	Value
p^r [m]	1.5×10^{-3}
p^s [m]	5.0×10^{-3}
E-modulus, E [Pa]	2.0×10^{11}
Shear modulus, G [Pa]	7.5×10^{10}

Figure 6 shows the calculated stress for load scenarios #1 (upper), #2 (middle), and #3 (lower). As expected from Example 1, the axial stress and the shear stress are quite similar to sinusoids when the cable is bent, and straight lines otherwise.

13 Further Work

The results presented in this paper are part of a larger work to develop a framework for numerical analyses of cables' and umbilicals' mechanical properties and fatigue properties. The next step is to develop numerical calculations for cables' axial stiffness, torsion stiffness, and bending stiffness. Developing the numerical analyses is part of Nexans Norway's continuous work on improving the accuracy of

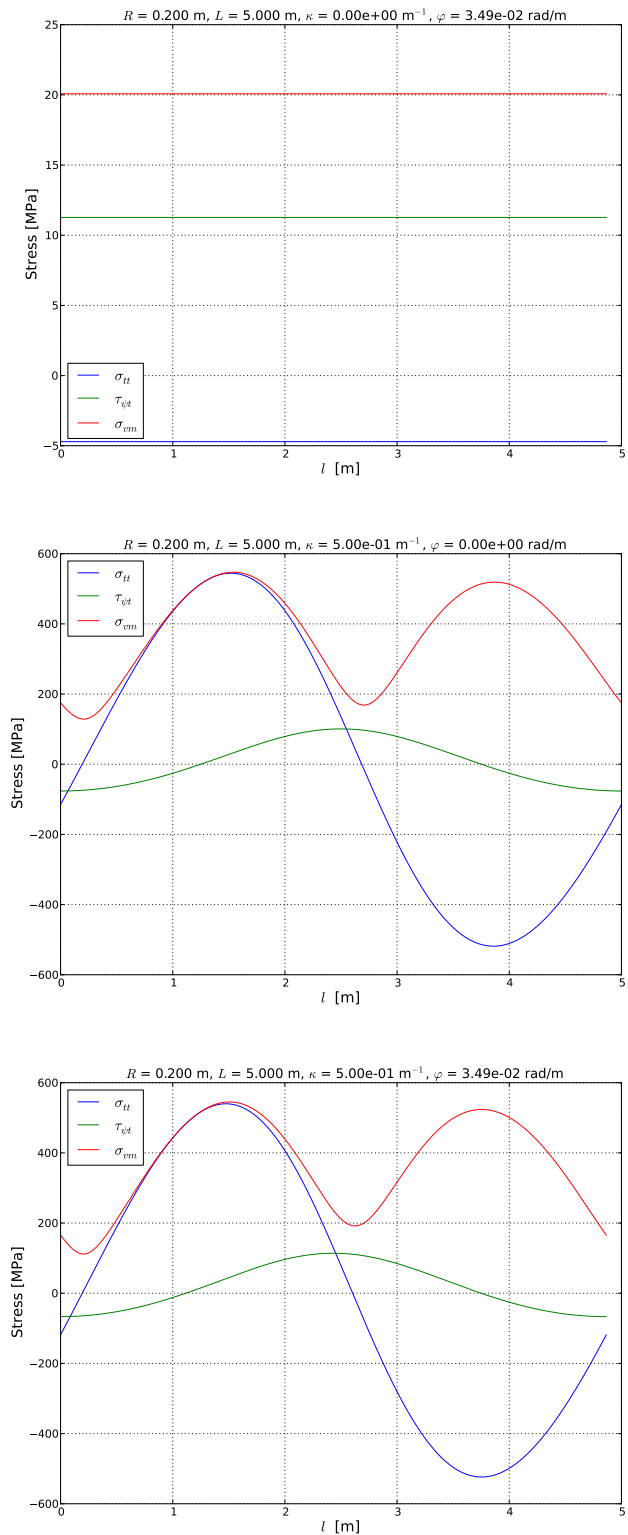


Figure 6. Numerical calculations of axial stress, σ_{tt} , shear stress, $\tau_{\psi t}$, and von Mises stress, σ_{vm} for load scenarios #1 (upper), #2 (middle), and #3 (lower).

the company’s analyses and physical testing, which is essential for installing and operating cables and umbilicals in ever deeper waters, lower temperatures, and harsher

weather conditions.

14 Conclusion

This paper derives numerical calculations of local curvature, local torsion, axial stress, shear stress, and von Mises stress for helical elements in cables and umbilicals subject to bending loads and twisting loads.

The numerical calculations disclose behaviors that analytical approximations from the scientific literature fail to identify. The numerical calculations also identified an erroneous approximation done by the analytical approaches, which probably is caused by an oversimplification.

The numerical calculations are simple to implement and do not depend on any iteration process that could cause convergence issues. The calculations are also very fast in terms of CPU time. From the author’s point of view, the numerical approach is a very attractive alternative to the analytical approximations, because it gives increased accuracy and deeper insight without any significant disadvantages.

References

- M. M. Dhaigude and K. I. Ekeberg. Validation of the loxodromic bending assumption using high-quality stress measurements - high tension case. In *Proceedings of the Twenty-sixth International Ocean and Polar Engineering Conference (ISOPE 2016)*, Rhodes, Greece, 2016.
- K. I. Ekeberg and M. M. Dhaigude. Validation of the loxodromic bending assumption using high-quality stress measurements. In *Proceedings of the Twenty-sixth International Ocean and Polar Engineering Conference (ISOPE 2016)*, Rhodes, Greece, 2016.
- L. Jordal, R. Slora, E. Vermeer, and M. Komperød. A novel bending stiffness rig for identification of subsea cables’ and umbilicals’ sensitivity to temperature under sinusoidal curvature oscillations. In *Proceedings of the Twenty-seventh International Ocean and Polar Engineering Conference (ISOPE 2017)*, San Francisco, California, USA, 2017.
- E. Keadze. *Theoretical modelling of unbonded flexible pipe cross-sections*. PhD thesis, South Bank University, 2000.
- R. H. Knapp. Derivation of a new stiffness matrix for helically armoured cables considering tension and torsion. *International Journal for Numerical Methods in Engineering*, 14:515 – 529, 1979.
- M. Komperød. Deriving analytical axisymmetric cross section analysis and comparing with FEM simulations. In *Proceedings of the 55th Conference on Simulation and Modelling (SIMS 2014)*, Aalborg, Denmark, 2014.
- M. Komperød. Calculating arc length and curvature of helical elements in bent cables and umbilicals using Fourier series. In *Proceedings of the 36th International Conference on Ocean, Offshore and Arctic Engineering (OMAE 2017)*, Trondheim, Norway, 2017.

- M. Komperød, J. I. Juvik, G. Evenset, R. Slora, and L. Jordal. Large-scale tests for identifying the nonlinear, temperature-sensitive, and frequency-sensitive bending stiffness of the NordLink cable. In *Proceedings of the 36th International Conference on Ocean, Offshore and Arctic Engineering (OMAE 2017)*, Trondheim, Norway, 2017.
- M. Lutchansky. Axial stress in armor wires of bent submarine cables. *Journal of Engineering Industry*, 91(3):687 – 693, 1969.
- P. Maioli. Bending stiffness of submarine cables. In *Proceedings of the 9th International Conference on Insulated Power Cables (Jicable '15)*, 2015.
- A. Pressley. *Elementary differential geometry - 2nd edition*. Springer-Verlag London Limited, 2012.
- N. Sødahl, G. Skeie, O. Steinkjær, and A. J. Kalleklev. Efficient fatigue analysis of helix elements in umbilicals and flexible risers. In *Proceedings of the 29th International Conference on Ocean, Offshore and Arctic Engineering (OMAE 2010)*, Shanghai, China, 2010.
- G. Skeie, N. Sødahl, and O. Steinkjer. Efficient fatigue analysis of helix elements in umbilicals and flexible risers: Theory and applications. *Journal of Applied Mathematics*, 2012.
- J. Tarnowski. Improved method of determining bending stiffness of underground cables. In *Proceedings of the 9th International Conference on Insulated Power Cables (Jicable '15)*, 2015.
- D. D. Tjahjanto, A. Tyrberg, and J. Mullins. Bending mechanics of cable cores and fillers in a dynamic submarine cable. In *Proceedings of the 36th International Conference on Ocean, Offshore and Arctic Engineering (OMAE 2017)*, Trondheim, Norway, 2017.

Online Drilling Fluid Flowmetering in Open Channels with Ultrasonic Level Sensors using Critical Depths

Khim Chhantyal Håkon Viumdal Saba Mylvaganam

Faculty of Technology, Natural Sciences, and Maritime Sciences, University College of Southeast Norway,
{khim.chhantyal,hakon.viumdal,saba.mylvaganam}@usn.no

Abstract

In drilling operations, non-Newtonian drilling fluid is continuously circulated in a closed loop. One of the ways to monitor and regulate drilling operations is by accurately measuring the flow rate of circulating drilling fluid before entering and after returning from the wellbore. The circulating fluid flows in an open channel on the return path from the wellbore. This work investigates the use of Venturi constriction to estimate the non-Newtonian fluid flow in an open channel. Based on the specific energy principle, a relation between volumetric flow rate and critical depth is developed, which is used to estimate the flow rate based on the measured critical depth. To measure a critical depth for a given flow rate, it is necessary to locate a critical depth position in the Venturi flume. In this study, the critical depth position is located using specific energy diagram (at a minimum specific energy within the Venturi constriction) and Froude Number approach (at a Froude Number equals to 1). Based on the identified critical depth, the flow conditions (subcritical, critical or supercritical) along the Venturi flume are observed. The location of the critical depth in the Venturi section is found by performing experiments at 350 [kg/min] flow rate of the fluid. Further, the developed critical depth flow model is tested for randomly varying flow rates (250-500 [kg/min]) with the identified critical depth location. The flow estimations of the model were within the acceptable limit. However, it is found that the estimates for 350 [kg/min] are comparatively more accurate, which proves that the critical depth and critical depth position depends on the flow rate and rheological properties.

Keywords: open channel Venturi flume, non-Newtonian flow, critical depth, ultrasonic scanning of open channel flow

1 Introduction

Open channel flow is a flow of fluid in conduct with a free surface. Examples of open channel flow are rivers, irrigation ditches, canals, storm and sanitary sewer systems, industrial waste applications, sewage treatment plants, transportation of non-Newtonian slurries, etc. In this work, a non-Newtonian drilling fluid flow in the open channel is studied.

The drilling fluids used in the oil & gas industries are

non-Newtonian, which helps:

- to keep the bottom-hole pressure within a pressure window of acceptable margins to prevent kicks and their losses into down-hole environment,
- to lubricate the drill bit, and
- to remove swiftly the cuttings and debris from down-hole due to their high viscous nature.

In drilling operations, the drilling fluid is continuously pumped down to wellbore through the drill pipe and is circulated through the annulus back to the surface where the flow is conducted in an open channel.(Caenn et al., 2011)

One way of maintaining the stability of bottom-hole pressure is by monitoring and regulating the drilling fluid flow rate. An early indication of wellbore instability can be detected using delta flow method, which is based on the difference between inflow and outflow measurements of drilling fluid while circulating the fluid, (Maus et al., 1979; Speers and Gehrig, 1987; Orban et al., 1987; Orban and Zanker, 1988; Schafer et al., 1992; Lloyd et al., 1990). Therefore, it is important to measure inflow and outflow of drilling fluid accurately. It is convenient to measure inflow accurately, as drilling fluids flowing in have known rheological properties with negligible impurities. In literature (Orban et al., 1987; Orban and Zanker, 1988; Schafer et al., 1992), flow meters like conventional pump stroke counter, rotatory pump speed counter, magnetic flow meter, ultrasonic Doppler flow meter, and Coriolis mass flow meter can be used to measure the inflow. However, it is difficult to accurately measure the outflow as the returning fluid contains rock cuttings, formation gases, and formation liquids. In literature (Orban et al., 1987; Orban and Zanker, 1988; Schafer et al., 1992), flow meters like standard paddle meter, ultrasonic level meter, a prototype rolling float meter, magnetic flow meter, and Venturi flow meter can be used to measure the outflow. In recent years, Rainer Haldenwang and his research group has performed several open channel flow studies in different cross-sectional shapes, (Burger et al., 2010, 2014; Kabwe et al., 2017). Our study focuses on the use of Venturi flow meter in an open channel for drilling fluid flow measurement.

2 System Description

A flow loop is available at University College of Southeast Norway (USN), Porsgrunn Campus for the study of drilling fluid flow through an open channel Venturi flume. The flow loop consist of a trapezoidal cross-sectional open channel with Venturi constriction as shown in Figure 1 and Figure 2. The flume can be inclined upto 2 degrees angle to the horizontal. There are three adjustable ultrasonic level sensors (LT-15, LT-17, and LT-18) above the flume for flow depth measurements at different section of the flume. Different model-drilling fluids are available for testing purposes. For this study, a water-based non-Newtonian shear thinning fluid with a density of 1153 kg/m^3 and viscosity of approximately $23 - 100 \text{ cP}$ for corresponding shear rates of $500 - 1 \text{ s}^{-1}$ is used. A centrifugal pump is used to circulate model-drilling fluids in the flow loop through the open channel.

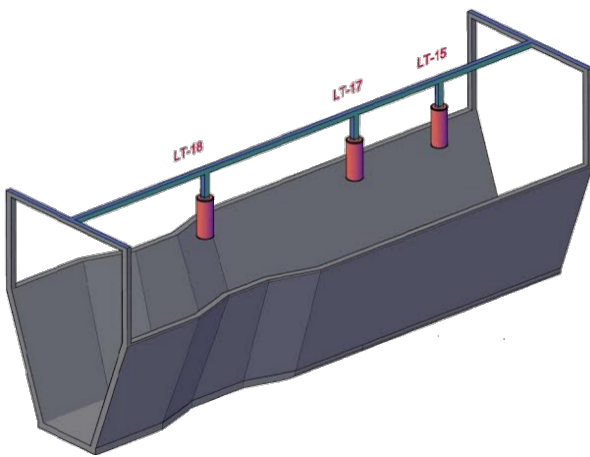


Figure 1. An open channel with Venturi constriction and three ultrasonic level sensors (LT-15, LT-17, and LT-18). (Chhantyal et al., 2016)

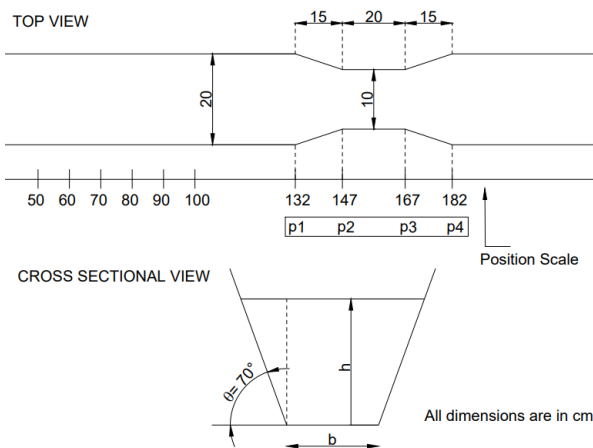


Figure 2. Top and cross sectional view of open channel Venturi flume with the position scale in centimetres. The Venturi constriction is shown in three sections with positions p1-p2 as converging section, positions p2-p3 as throat section, and p3-p4 as diverging section.

3 Methods

For a steady and incompressible fluid flow, the total energy remains constant along the horizontal flow conduit. The Bernoulli flow principle gives the energy equation of the flow as,

$$P + \rho gz + \frac{\rho v^2}{2} = \text{constant} \quad (1)$$

where P is applied pressure, ρ is fluid density, g is acceleration due to gravity, z is elevation, and v is average fluid velocity.

Dividing Equation 1 by specific weight ($\gamma = \rho g$) gives specific energy equation as in Equation 2.

$$E_s = h + z + \frac{v^2}{2g} \quad (2)$$

where h is fluid depth.

If the bottom surface of the conduit is considered as the datum, we can use $z = 0$ and Equation 2 becomes,

$$E_s = h + \frac{v^2}{2g} \quad (3)$$

where E_s is the specific energy of fluid and is dependent on fluid depth and velocity of the fluid.

In open channel flow, the surface or profile of fluid flow is studied using Hydraulic Grade Line (HGL) and Energy Grade Line (EGL), which are defined by Equation 4 and Equation 5 respectively.

$$HGL = h \quad (4)$$

$$EGL = h + \frac{v^2}{2g} \quad (5)$$

Further using $Q = v \cdot A$, Equation 3 can be rewritten as,

$$E_s = h + \frac{(Q/A)^2}{2g} \quad (6)$$

where Q is volumetric flow rate, and A is the cross-sectional area. For a trapezoidal channel, the cross-sectional area is $A = h(b + hcot\theta)$ where b is the bottom width of the channel and θ is the slope angle of the channel walls shown in Figure 2. Hence, the Equation 6 becomes,

$$E_s = h + \frac{Q^2}{2gh^2(b + hcot\theta)^2} \quad (7)$$

Using Equation 7, a specific energy diagram showing the relation between specific energy (E_s) vs. flow depth (h) can be developed for a given flow rate. From the specific energy diagram, different flow conditions (subcritical, critical, or supercritical) can be identified. For every value of given flow rate, there is a corresponding associated critical depth, h_c . Flow with a depth greater than the critical depth is a subcritical flow and flow with a

depth less than the critical depth is a supercritical flow. In subcritical flow, the potential energy component is large and in supercritical flow, the kinetic energy component is large. Whereas, the critical depth is a position having the minimum specific energy for the given flow rate in the specific energy diagram. Hence, the critical depth can be identified by equating the first derivative of Equation 7 to zero.

$$\frac{dE_s}{dh} = 0, \text{ for } h = h_c \quad (8)$$

Using Equation 7 and Equation 8 with several mathematical simplifications, the flow rate and the critical depth relation can be obtained as in Equation 9,

$$Q = \left[\frac{gh_c^3(b + h_c \cot \theta)^3}{b + 2h_c \cot \theta} \right]^{1/2} \quad (9)$$

In addition, Froude Number can be used to identify the critical depth. The dimensionless Froude Number for shallow fluid flow is given as the ratio of flow inertia to the wave velocity as in Equation 10,

$$Fr = \frac{v}{\sqrt{g(A/B)}} \quad (10)$$

where Fr is Froude Number and B is the free surface width. For $Fr < 1$ flow is subcritical flow, $Fr > 1$ flow is supercritical flow, and for $Fr \approx 1$ flow is critical flow.

For detail study on open channel flow energy principles, refer to (Featherstone and Nalluri, 1982; Chaudhry, 2007).

4 Results

To study the flow profile and identify the critical depth, the model-drilling fluid is circulated at five different flow rates ($Q = 275, 300, 350, 400, 450$ [kg/min]) in 12 different experimental set-ups. In each experimental set-up, the three ultrasonic level measurements are uniquely positioned along the Venturi-flume. As a result, 36 different flow depths are logged for each flow rate. These flow depths are used to locate critical depth along the Venturi constriction. Finally, the randomly varying flow rates are estimated using the critical depth.

4.1 Flow Profile Study

To study the flow profile, 36 different flow depths at the flow rate of 350 [kg/min] are fitted using an Artificial Neural Network (ANN) based polynomial. Thus obtained ANN based polynomial model for flow depth along the Venturi flume is further used to plot Hydraulic Grade Line (HGL) and Energy Grade Line (EGL) as shown in Figure 3. The HGL shows the steady upstream depth and is gradually reducing as the fluid flows through the constriction. EGL represents the total energy head available for the fluid at given flow rate. Within the constriction, EGL has a convex shape with a minimum specific energy, which represents the critical depth.

4.2 Specific Energy Diagram

Figure 4a shows a specific energy diagram within the Venturi constriction for the flow rate of 350 [kg/min]. Locating the minimum specific energy in the specific energy diagram, critical fluid depth is identified for the given flow rate. Any flow with flow depth greater than identified critical depth is subcritical flow and flow with a depth less than the critical depth is supercritical flow as shown in Figure 4a.

To identify the position of critical depth along the Venturi throat section, specific energy vs. position is plotted as shown in Figure 4b. The minimum specific energy is obtained around 156 [cm] position, which lies within the throat section of the Venturi constriction.

4.3 Froude Number Study

Froude Number is used to identify different flow conditions and the position of critical depth as shown in Figure 5. The flow is subcritical with $Fr < 1$, critical with $Fr = 1$, and supercritical with $Fr > 1$ as indicated in Figure 5. Tracking the corresponding position for $Fr = 1$, the critical depth is around 156 [cm] position in the throat section of the Venturi constriction.

4.4 Critical Depth Flow Model

The volumetric fluid flow can be estimated based on the critical depth using the Equation 9. In the context of this study, the flow rate is randomly varied and the critical depth is measured at 156 [cm] position using an ultrasonic level sensor. Figure 6 shows the comparison of estimates of critical depth flow model against the randomly varying mass flow rate setpoints. The original ultrasonic level measurements are very noisy. So, the moving average filter with last 10 samples is used to filter the noise to some extent. Both of the flow estimates with and without filtering are presented in Figure 6. The filtered estimates seem to be less noisy compared to the unfiltered estimates. However, the Mean Absolute Percentage Error (MAPE) is slightly better for unfiltered estimates.

In Figure 6, it can be seen that the estimates are comparatively much accurate for the flow rate of 350 [kg/min]. It is because the position of critical depth measurement is chosen based on the critical depth position of 350 [kg/min] flow rate. The critical depth and position of critical depth are dependent on the flow rate and rheological properties of the fluid.

Figure 7a shows the specific energy diagram of fluid flow along the Venturi constriction at different flow rates. It can be observed that with the increase in fluid flow rate, the specific energy and critical depth of the fluid increases. The primary reason for this is the increases in fluid volume. The possible secondary reason is the reduction in the viscosity of the fluid as flow rate increases for the shear thinning model-drilling fluid.

Figure 7b shows the specific energy vs. position plot in the throat section of Venturi constriction. It can be observed that the minimum specific energy point is

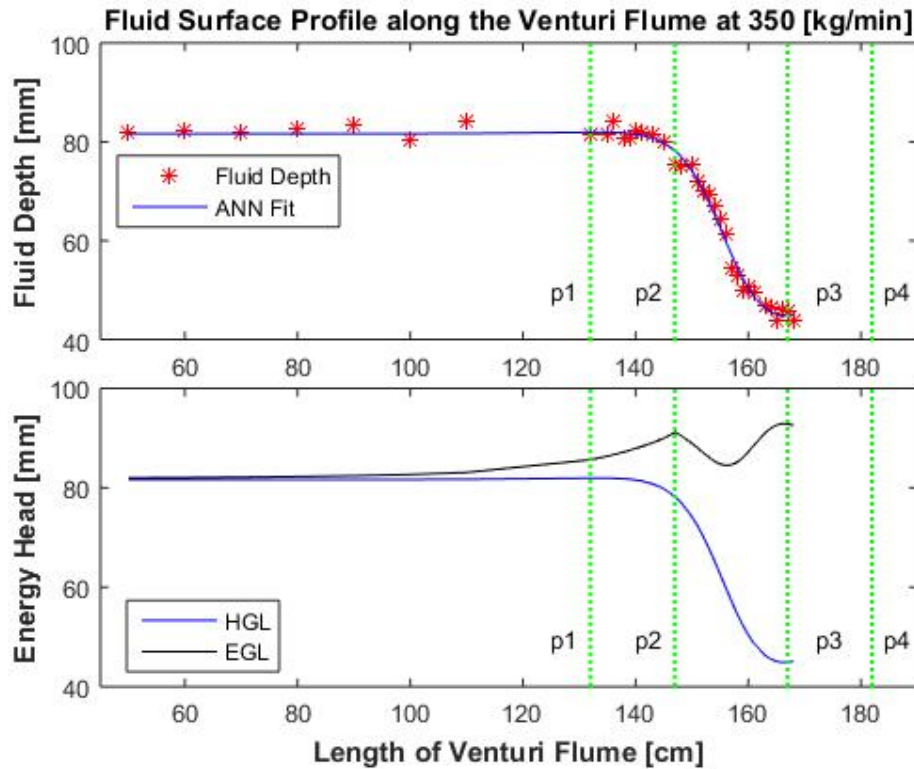


Figure 3. a) Experimental ultrasonic flow depth measurements with an Artificial Neural Network based polynomial fit. b) The Hydraulic Grade Line and Energy Grade Line along the Venturi flume at the flow rate of 350 [kg/min]. The green dotted lines indicate the different sections of Venturi constriction according to Figure 2.

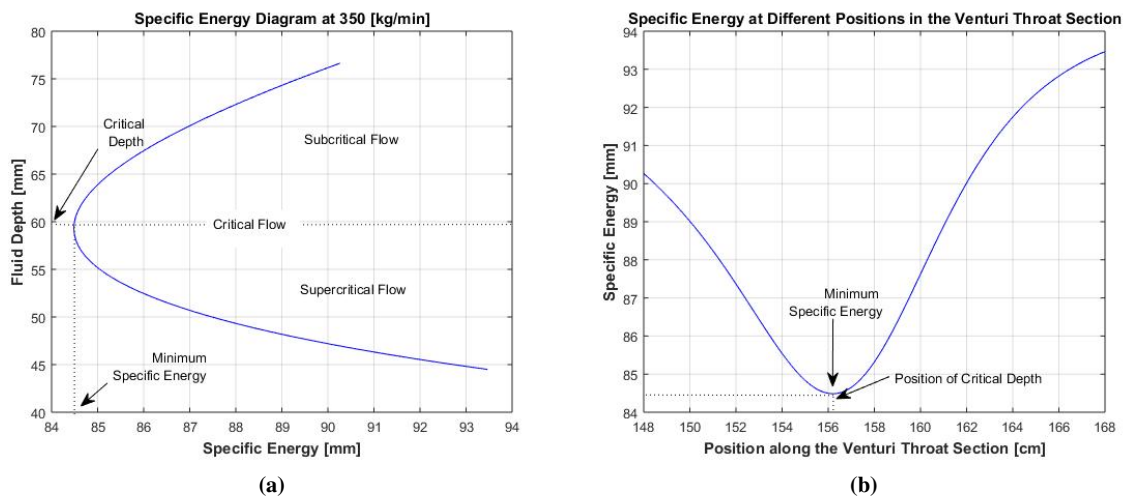


Figure 4. a) Specific energy diagram at the flow rate of 350 [kg/min] showing critical depth (at minimum specific energy point) and different flow conditions. b) Specific energy vs. position diagram showing the exact critical depth position in the Venturi constriction.

slightly shifting towards the end of the throat as the flow rate increases, giving different critical depth position for different flow rates. It is due to the momentum of the fluid flowing through the Venturi constriction. The higher flow rate fluid will flow faster within the fixed cross-section of Venturi flume, providing extra momentum as the flow rate increases.

5 Conclusion

In this work, one of the applications of open channel flow in the field of drilling operations is investigated. In drilling operations, non-Newtonian fluid is circulated in a closed loop from the mud tank, into the bottom-hole and back to the mud tank. The return flow is an open channel flow

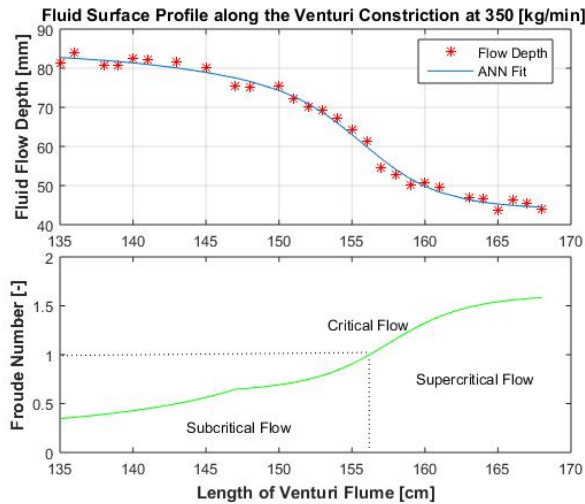


Figure 5. a) Experimental ultrasonic flow depth measurements with an Artificial Neural Network based polynomial fit. b) Froude number along the Venturi constriction showing critical depth position and different flow conditions at the flow rate of 350 [kg/min].

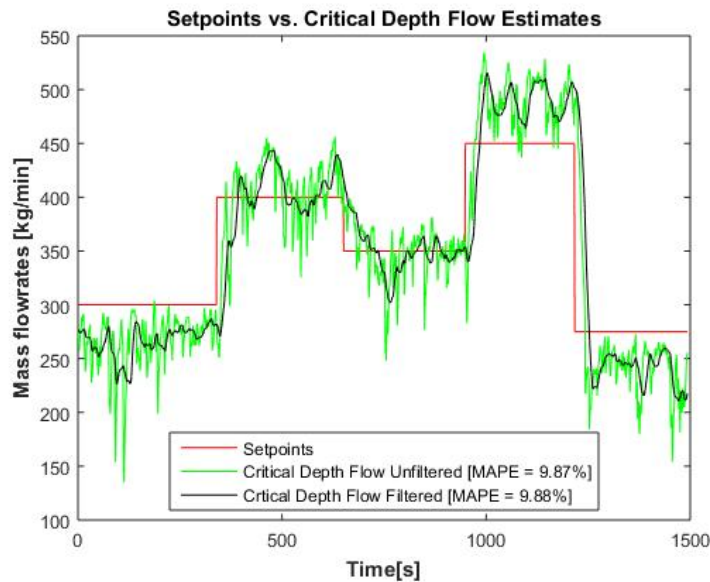


Figure 6. The comparison of estimated flow rates using critical depth (with or without filter) against the randomly varying setpoints based on Mean Absolute Percentage Error (MAPE).

and there is a need for accurate return flow for safe and efficient drilling operations. The study investigates the use of Venturi constriction in the return flow to estimate the flow rates based on the critical depth measurements using the test flow loop available at USN.

For the measurement of critical depths, specific energy diagram and Froude Number approaches are used to locate the critical depth position along the Venturi constriction. Using specific energy diagram, critical depth and critical depth position for a given flow rate are identified at the location of minimum specific energy. Using Froude Number, critical depth position is identified for the Fr value equal to 1. In both approaches, different flow conditions: subcritical flow, critical flow, and supercritical flow along the Venturi flume are observed with respect to

the critical depth. Further, a critical depth flow model is derived from specific energy equation, which can estimate flow rate for measured critical depth.

The detailed study is performed for 350 [kg/min] flow rate with the critical depth at 156 [cm] position in the throat section of Venturi constriction. For randomly varying flow rates, the estimates of critical depth flow model with critical depth position at 156 [cm] are compared with the setpoints. The comparison result shows that the estimates are within the acceptable limits. However, the estimates are more accurate for 350 [kg/min] flow as the critical depth position for 350 [kg/min] is chosen for critical depth measurement.

To investigate the effect of flow rates on critical depth, specific diagram for different flow rates are studied.

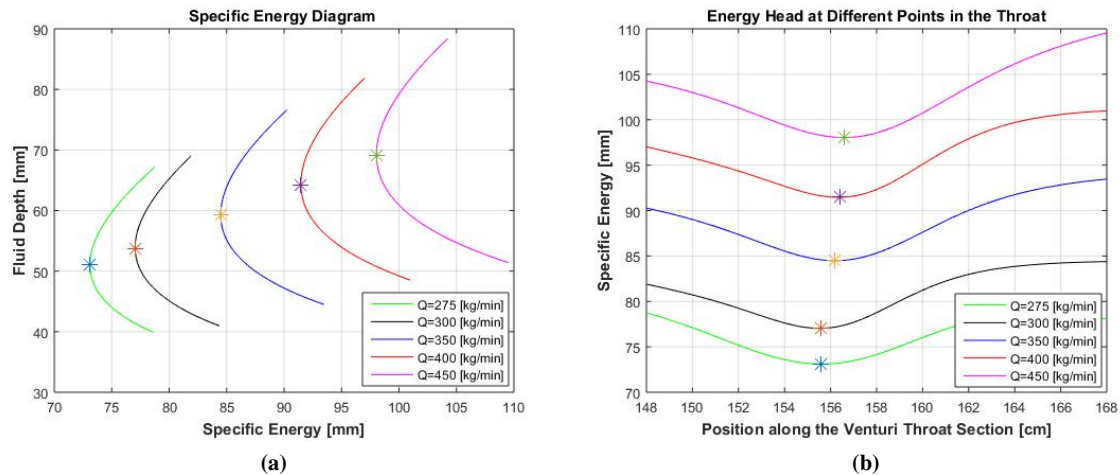


Figure 7. a) Specific energy diagram at different flow rates. b) Specific energy vs. position diagram at different flow rates. The asterisk signs with different colors indicate the point of minimum specific energy at different flow rates.

The study shows that as the flow rate increases the specific energy increases, critical depth increases, and the critical depth position shifts towards the end of the throat section. The changes are due to the increase in fluid flow momentum and change in rheological properties.

We foresee the future efforts in comparing and investigating specific energy diagrams of different model-drilling fluids at different flow rates to analyse the relation between critical depth and rheological properties.

Acknowledgement

The Ministry of Education and Research of the Norwegian Government is funding Khim Chhantyal's Ph.D. studies at USN. We acknowledge the collaboration with and support from STATOIL for providing open channel Venturi rig dedicated for flow studies of different Newtonian and non-Newtonian fluids.

References

- JH Burger, R Haldenwang, and NJ Alderman. Laminar and turbulent flow of non-newtonian fluids in open channels for different cross-sectional shapes. *Journal of Hydraulic Engineering*, 141(4):04014084, 2014.
- Johan Burger, Rainer Haldenwang, and Neil Alderman. Laminar non-newtonian open channel flow: investigating velocity, wall shear stress and fluid depth. BHR Group, 2010.
- Ryen Caenn, Henry CH Darley, and George R Gray. Composition and properties of drilling and completion fluids. chapter 1, pages 7–16. Gulf professional publishing, Waltham, USA, 2011.
- M Hanif Chaudhry. *Open-channel flow*. Springer Science & Business Media, 2007.
- Khim Chhantyal, Håkon Viumdal, Saba Mylvaganam, and Minh Hoang. Flow rate estimation using dynamic artificial neural network with ultrasonic level measurements. In *The 9th Eurosim congress on modelling and simulation, Oulu, Finland*. Eurosim, 2016.
- RE Featherstone and Chandra Nalluri. Civil engineering hydraulics: essential theory with worked examples. chapter 8, pages 185–248. Collins, 1982.
- Christine Kabwe, Rainer Haldenwang, Veruscha Fester, and Raj Chhabra. Transitional flow of non-newtonian fluids in open channels of different cross-sectional shapes. *Journal of the Brazilian Society of Mechanical Sciences and Engineering*, pages 1–19, 2017.
- GM Lloyd, DJ Bode, HV Nickens, SG Varnado, et al. Practical application of real-time expert system for automatic well control. In *SPE/IADC Drilling Conference*. Society of Petroleum Engineers, 1990.
- LD Maus, JD Tannich, and WT Ilfrey. Instrumentation requirements for kick detection in deep water. *Journal of Petroleum Technology*, 31(08):1–029, 1979. doi:doi.org/10.2118/7238-PA.
- JJ Orban and KJ Zanker. Accurate flow-out measurements for kick detection, actual response to controlled gas influxes. In *SPE/IADC Drilling Conference*. Society of Petroleum Engineers, 1988. doi:10.2118/17229-MS.
- JJ Orban, KJ Zanner, and AE Orban. New flowmeters for kick and loss detection during drilling. In *SPE Annual Technical Conference and Exhibition*. Society of Petroleum Engineers, 1987. doi:10.2118/16665-MS.
- DM Schafer, GE Loeppke, DA Glowka, DD Scott, and EK Wright. An evaluation of flowmeters for the detection of kicks and lost circulation during drilling. In *SPE/IADC Drilling Conference*. Society of Petroleum Engineers, 1992. doi:10.2118/23935-MS.
- JM Speers and GF Gehrig. Delta flow: An accurate, reliable system for detecting kicks and loss of circulation during drilling. *SPE Drilling Engineering*, 2(04):359–363, 1987. doi:10.2118/13496-PA.

Structural Analysis of the Casings in Deep Geothermal Wells

Gunnar Skúlason Kaldal^{1,2}, Magnús Þ. Jónsson¹, Halldór Pálsson¹, Sigrún Nanna Karlsdóttir¹

¹Faculty of Industrial Engineering, Mechanical Engineering and Computer Science, University of Iceland, Hjarðarhagi 2-6, 107 Reykjavík, Iceland

²ÍSOR – Iceland GeoSurvey, Grensásvegi 9, 108 Reykjavík, Iceland

Abstract

With recent increasing interest in drilling deep geothermal wells in order to produce from higher enthalpy heat sources than before, the strength of the casing becomes one of the most limiting factors. Casing failures include collapse or partial collapse (bulges) and tensile ruptures if wells are allowed to cool down or are killed by pumping water into them. Structural impact of large temperature and pressure changes remains one of the challenges to be solved for utilization of deep geothermal wells. Thermal expansion of materials, degradation of structural properties at elevated temperatures, corrosion and cyclic loads are of particular concern as well as determining how many thermal cycles casings can go through before failure occurs. A nonlinear structural finite-element model of the cased section of high temperature geothermal well is presented and discussed here. The purpose of the model is to evaluate the structural integrity of casings when subjected to large temperature and pressure loads. The model can be used further to evaluate well designs and material selections for deep geothermal wells.

Keywords: Casings, structural analysis, finite-element method, thermal loads, deep drilling

*email: gsk@isor.is

Introduction

This paper provides an overview of structural modeling of casings in high temperature geothermal wells. Structural integrity of high temperature geothermal wells is important for utilization and safety concerns on the surface. During each drilling phase, steel casings are run in hole and cemented externally, until the last phase where the production section of the well is drilled. This is done to control wells during drilling, seal off unwanted feed-zones and the last casing, the production casing, acts as a pipe allowing the geothermal fluid (water and/or steam) to flow to the surface. In most cases, a perforated liner is placed in the production section to avoid formation collapse. Above the liner is the cased section of the well, which is a layered structure of multiple cemented casings. The structure is initially relatively cold, i.e. during drilling and cementing, compared to the hot conditions during production of

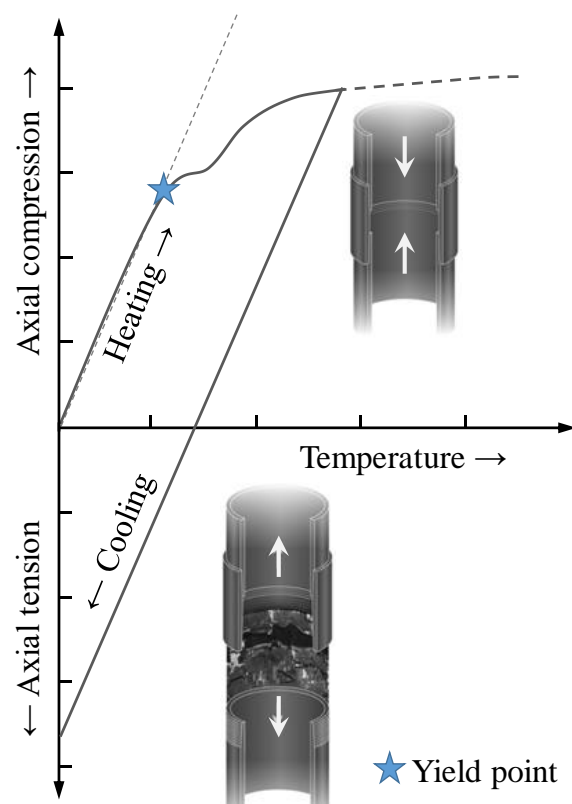


Figure 1. Concept diagram describing how plastic strain that forms in axial compression can result in axial tension during cooling. Adopted from a diagram by (Rahman & Chilingarian, 1995).

(two-phase or pure) steam. As cement sets and hardens after cementing jobs for each casing, its temperature distribution down the well provides initial conditions for subsequent thermal stresses that form as the well warms up. In high-temperature geothermal wells ($T > 200^{\circ}\text{C}$ at 1000 m depth) stresses which generate due to thermal expansion driven by the temperature change between an initially cold well to a producing well, typically reach beyond the yield point of the commonly used casing material, API (American Petroleum Institute) grade K55. As stresses go past the yield strength, plastic permanent strains are produced in the casings. Depending on the magnitude of these plastic strains, some wells, specially the hotter ones, cannot be cooled down again without causing casing failure. In such cases, plastic strains that build up in axial compression (hot well) lead to axial tensile load when the casing cools down again. Figure 1 illustrates this phenomenon, where plastic strains created in compression lead to high tensile stresses when the casing cools down again. Casing failure of tensile rupture of the casing normally occurs in the casing near couplings (first thread groove) or in the threads themselves. In casing design, guidelines acknowledge that axial tension leads to reduced collapse resistance of casings. However, as standards are developed for the oil & gas industry where casings are anchored at the casing shoe with cement and not cemented over their full length as in geothermal wells, failures as a result axial compressive loads are assumed to be on the form of Euler buckling (or helical buckling) where the casing string buckles laterally. Casings in geothermal wells have no means to displace laterally due to the cement support, instead high compressive stresses and strains are formed which can as with tension reduce their collapse resistance.

The Finite-Element Method (FEM) models shown in this paper have been created to evaluate stresses and strains in casings due

to pressure and temperature changes in wells.

Load history of casings

Casings are cold-drawn seamless steel pipes. Thickness tolerance of such pipes is -12.5% (API, 2005), meaning that for a 9 5/8" 47 lb/ft casing that is specified with thickness of 12 mm, it may be 12 mm on one side and 10.5 mm on the other. Heat treatments are used to relieve residual stresses present in the material due to non-uniform cooling during manufacturing. Residual stresses and non-circular geometry (ovality, eccentricity and wall thickness irregularity) can significantly lower the collapse resistance of casings. Material properties, i.e. yield strength and shape of the stress-strain curve, and residual stresses also affect collapse resistance (ISO/TR, 2007).

While casings are run-in-hole, the highest axial tensile stress occurs at the topmost coupling, which essentially holds up the whole casing string before it is cemented. Buoyancy and friction between the casing, centralizers and the wellbore lower the axial force on top.

Thermal stresses form in casings as wells warm up, which magnitudes are controlled by the temperature difference ΔT at each location as well as the (time dependent) thermal gradient through the layered casing structure. The initial conditions are different between wells, and depend on formation temperature, feed zones that are closed off with cement, cooling from drilling and the time the well has been cooled. In many cases, depending on feed zones, drilling time, etc., wells heat up faster downhole as the formation temperature increases with depth. In cases where the cement sets at such temperature conditions, the highest ΔT (from cementing conditions to production) is uppermost in the well. This does however not mean that the highest compressive stresses form at the wellhead. At the surface there is freedom for displacement, both because of the design of the wellhead, if it includes an expansion spool, and due to less

restricted displacement as the surface can displace upwards. Wellheads are known to move upwards as wells warm-up, sometimes called wellhead growth. This is in some cases very evident during discharge initiation, where the temperature uppermost in the well changes quickly, whereas deeper in the well lower ΔT is seen. When drilling has been problematic and the wellbore has been cooled for a long period, ΔT can be similar at the wellhead and deeper in the well, as the cement sets before the well heats up. The positive side of higher setting temperatures is that less stresses form during production. The down side is that if cement sets at too high temperature, cooling due to further drilling can de-bond the casing from the cement as it contracts, creating a micro-annulus.

As discussed in the introduction, compressive stresses form in the casing as the well warms up and plastic strains form in the most common material used, API grade K55. Using the next higher grade L80 postpones the problem and plastic strains will occur as well. Using the specified minimum yield strength of K55 and L80, 379 MPa and 552 MPa (API, 2005), onset of plastic strains is at around 150°C and 200°C, for K55 and L80, respectively (using a thermal expansion coefficient of 13 $\mu\text{m}/(\text{m}^\circ\text{C})$ and Young's modulus of 205 GPa). This however does not tell the whole story as stress-strain characteristics can influence collapse resistance. For a work hardening material such as K55 it has been shown that the API collapse equation applies only for small axial tensile stresses and that the measured collapse resistance is significantly higher than those predicted by the API equation (Maruyama, et al., 1990). They show that due to the work hardening characteristics of grade K55 casing, it may be superior to higher-grade casing for thermal well service where high residual axial tensile stresses may be present.

Field study and FEM analysis

In this study, wellhead displacement monitoring during discharge initiation is

used to validate a FEM model of the cased section of a high-temperature geothermal well (Kaldal, et al., 2015). Figure 2 shows temperature and elevation measurement locations on the wellhead of well HE-46, located in Sleggjubeinsdalur near Hellisheiði power plant.

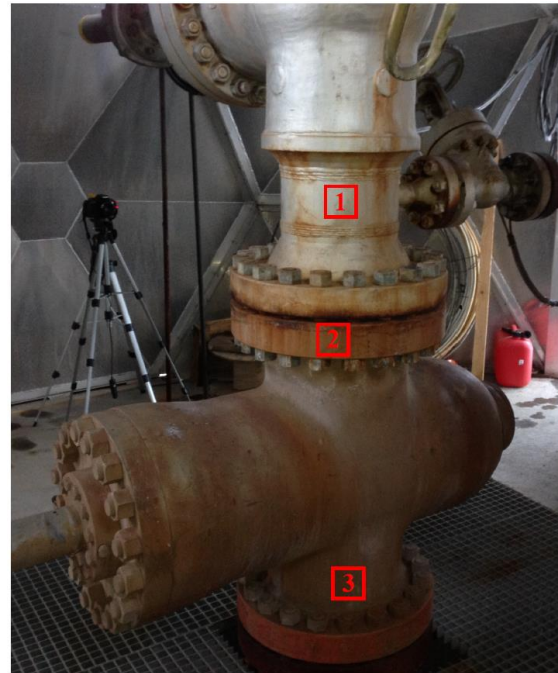


Figure 2. Locations for temperature measurements during discharge initiation of well HE-46, located in Sleggjubeinsdalur near Hellisheiði power plant. Location [2] shows where elevation measurements were taken for the wellhead.

The ANSYS Parametric Design Language (APDL) is used to construct the models. Included are temperature dependent material properties, including stress-strain curves for casing materials, for determining formation of plastic strain, and thermal expansion coefficients. Other material properties include; Young's modulus, Poisson's ratio, density, thermal conductivity, specific heat and compressive strength of cement. Kinematic hardening material model is used for the casings and the compressive strength of cement is included by using a bi-linear material model.

Boundary conditions of the model are at the rock formation outer boundary and bottom where displacements are constrained. Initial conditions of the rock formation is the

estimated formation temperature and cementing temperature distribution for all casings, which need to be defined for each specific case. Transient thermal analyses include load steps such as cooling due to drilling, thermal recovery where wells heat-up over a period of weeks to months, discharge initiation, discharge and well shut-in. Initial conditions for the structural modeling are the formation overburden pressure and residual axial load in casings from casing run-in. Transient thermal results are then used as temperature load in the structural analysis, where displacements, stresses and strains (elastic and permanent plastic strain) are analyzed.

Results

Wellhead displacement

Wellhead measurements, i.e. temperature, pressure and elevation changes during discharge initiation were taken for several wells including the case studied here, well HE-46.

Temperature changes, shown in Figure 3, are similar for two separate discharges, conducted in years 2011 and 2013. Wellhead pressure, measured for the 2011 discharge, is initially 37.5 bar-g and after discharge initiation (at 13:16 o'clock on graph), it lowers and stabilizes at 18 bar-g. In 2013 the wellhead pressure was initially 48 bar and after discharge initiation it stabilized at 16 bar-g.

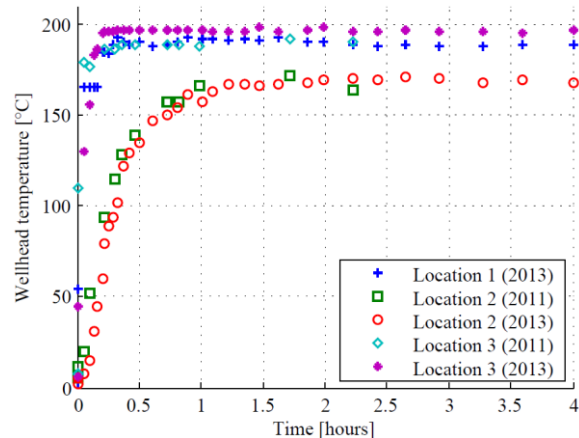


Figure 3. Temperature during discharge initiation of well HE-46, measurement locations are shown in Figure 2 (Kaldal, et al., 2012) (Kaldal, et al., 2015).

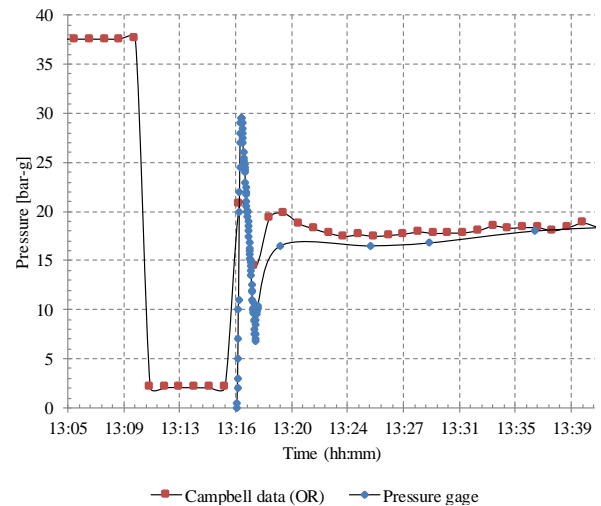


Figure 4. Wellhead pressure changes during discharge initiation (well opened at time 13:16). Campbell data (taken at 1 min intervals) shows initial pressure of 37.5 bar-g. Note that lowering in pressure in Campbell data before discharge is due to closing of control valve and both pressure gauges are behind it (Kaldal, et al., 2012) (Kaldal, et al., 2015).

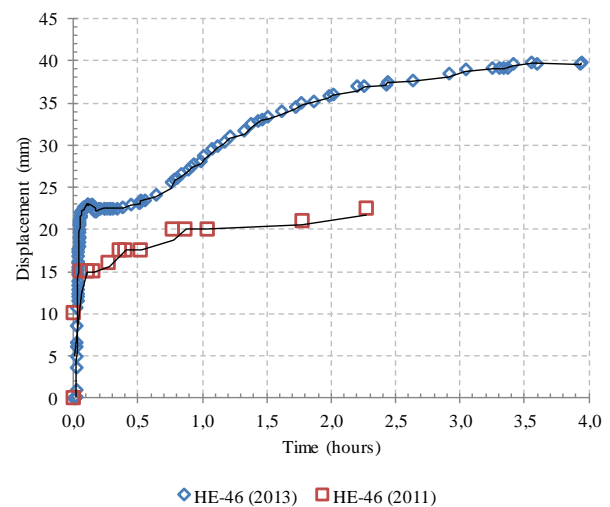


Figure 5. Measured displacement of the wellhead of two separate discharges of well HE-46 in years 2011 and 2013 (Kaldal, et al., 2012) (Kaldal, et al., 2015).

Measured wellhead displacements for the two separate discharges, shown in Figure 5, differ by 15 mm after 2 h of discharge. In 2013, wellhead displacement measured 37 mm and in 2011, it was 22 mm, in both cases after 2 h of discharge.

FEM results

During installation while casings are run in hole, wells are kept full of water or mud and the casing is filled with water. Depending on the situation, a buoyancy force and friction counteracts the casing's self weight. The largest tensile forces should occur at the top of the casing that hangs in the well. A buttress-threaded connection (BTC) is modeled. Assuming no buoyancy or friction, i.e. casing hanging in air, stresses forms in the threads of the connections as is shown in Figure 6.

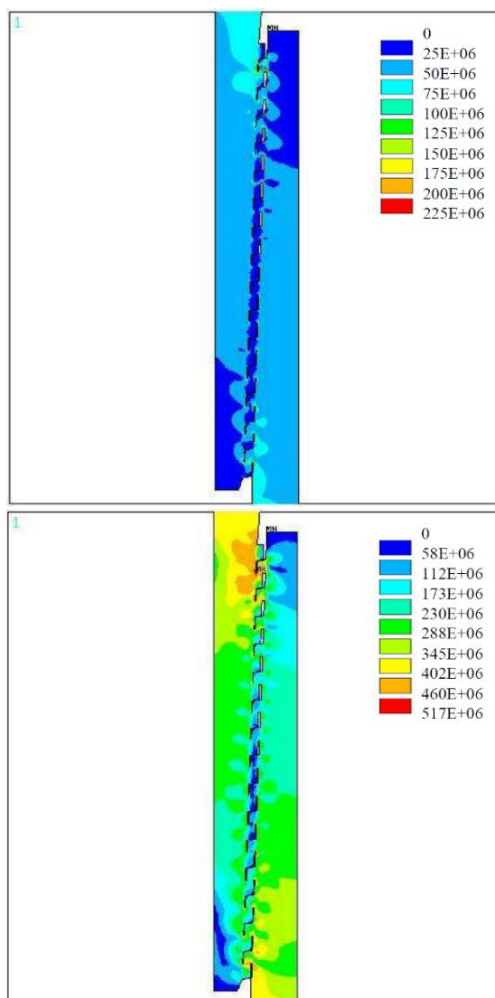


Figure 6. Von Mises stress (Pa) of buttress threaded connection (BTC) during installation assuming 700 m (top) and 5000 m (bottom) casing hanging from the connection in free in air. For API K55 grade casings the minimum yield strength is 379 MPa (API, 2005).

Two cases are taken, conventional 700 m casing and extreme 5000 m casing, assuming 9 5/8" 47 lb/ft casing. In the

former, the stresses are below yield of any API casing grade, but for the latter, stresses above yield occur in the area of the casing where the first threads are located. This implies a risk zone of casing failure due to axial tension.

After drilling, and warm-up, wells are flow tested. A simulation of flow test of well HE-46 results in wellhead displacement of 30 mm after 2 hours of discharge, whereas the measured value was at 36 mm (Figure 7). The modeled wellhead displacement, shown in Figure 8, shows that the production casing slides slightly inside the wellhead due to thermal expansion.

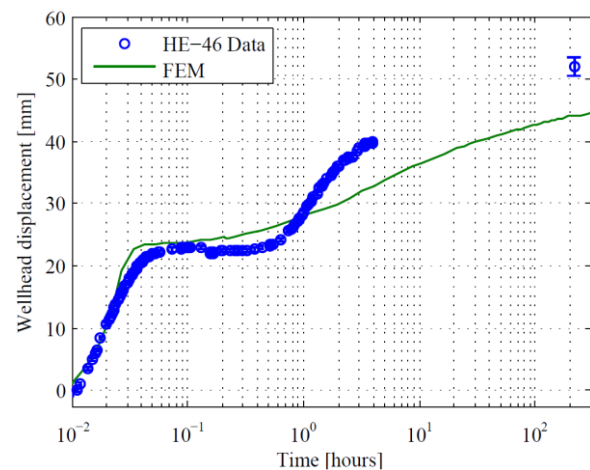


Figure 7. Measured displacement during discharge (2013 data) and modeled displacement in green (Kaldal, et al., 2015).

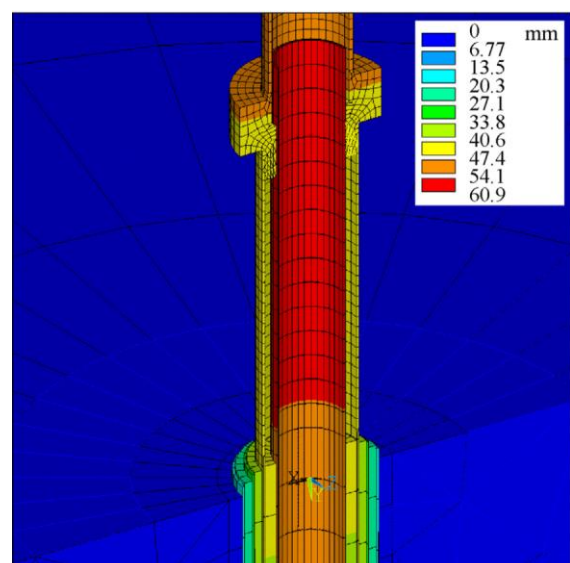


Figure 8. Modeled wellhead displacement due to thermal expansion of casings, also shown in Figure 7 (Kaldal, et al., 2015).

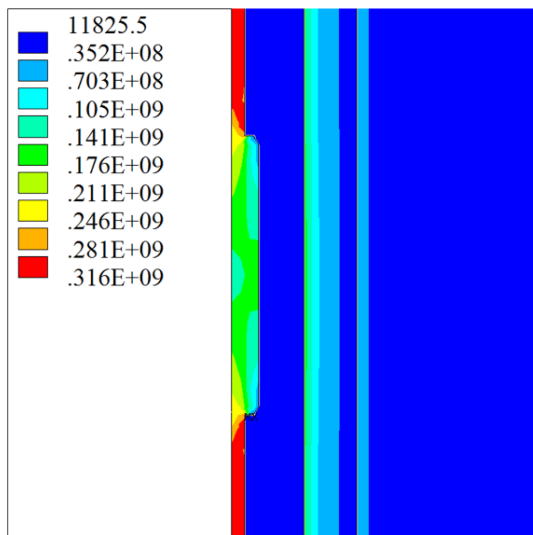


Figure 9. Modeling of casings during discharge shows high compressive stresses forming near couplings, which anchor the casing in the cement (Kaldal, et al., 2015).

Deeper in the well, where the casings are more constrained than at the surface,

discharge initiation results in compressive stresses forming due to thermal expansion as the well heats up. Figure 9 shows compressive stresses in the production casing near a simplified connection, illustrating how the casing is anchored at the couplings in the cement. In this case, the treads are not modeled and therefore lower stresses are seen in the coupling.

Modeling shows high stresses forming in the cement at these anchoring locations as the production expands. Figure 10 shows modeling of stresses near the uppermost coupling of the production casing as it displaces upwards. Stresses above the compressive strength (27 MPa) of the cement occurs at the top of the coupling. After the compressive strength is reached, the cement deforms according to its defined bi-linear material curve, explaining higher stresses.

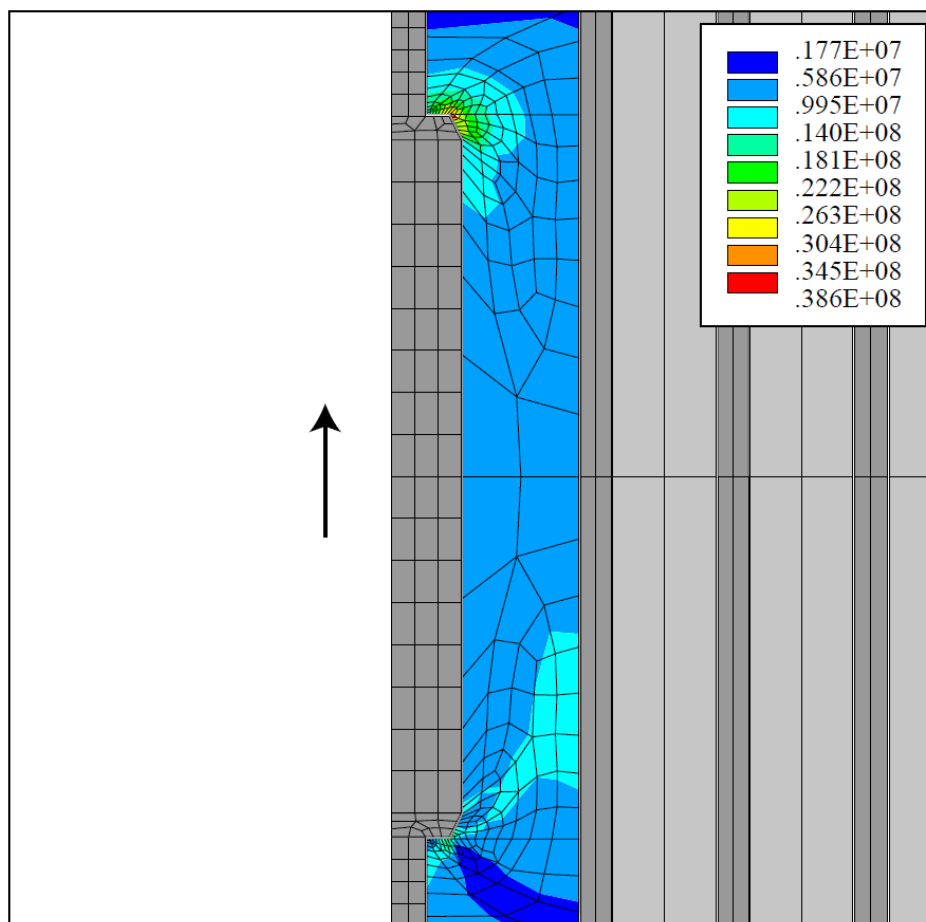


Figure 10. As wells heat up, high stresses develop in cement near the couplings that anchor the thermally expanding production casing in the cement (casings and simplified coupling shown in dark gray and external concrete shown in gray).

Modeling of casing collapse due to annular pressure, i.e. due to expansion of water in cement/annulus during discharge, shows that cement support has vital effect on the casing's collapse form (Figure 11). Casings without cement support collapse completely, but with the support the collapse is less severe. A small defect is included on the external surface of the casing for introducing instability to the model to allow buckling. Figure 12 shows that the collapse resistance of the uncemented casing is much less than that of the cemented casing.

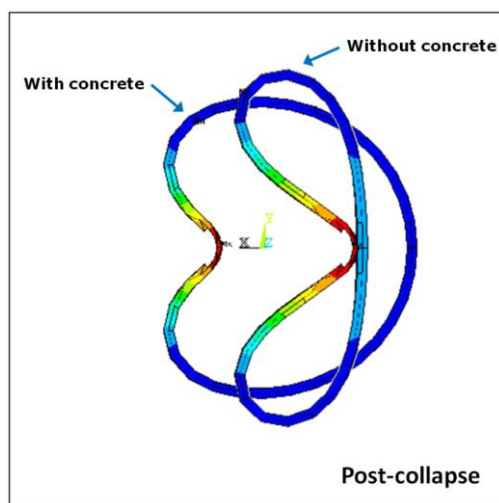


Figure 11. Collapse form of casing with and without external cement structural support (Kaldal, et al., 2013).

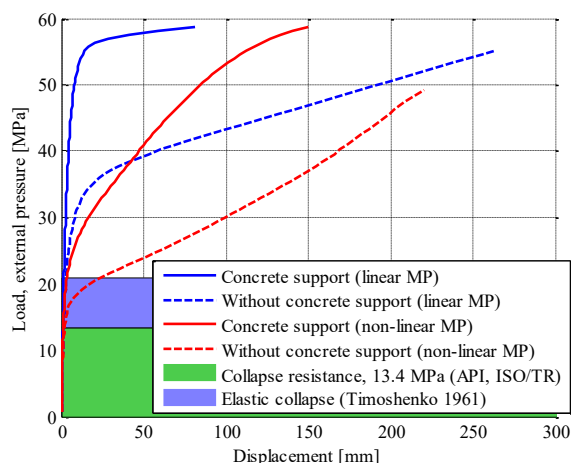


Figure 12. Modeled collapse of casings shows increased collapse resistance with cement structural support (Kaldal, et al., 2013).

Discussion

Measurements of wellhead displacement during discharge initiation was used to validate results from a FEM model of the cased section of a high-temperature geothermal well. Although temperature monitoring of well HE-46 showed similar values, two separate discharges (two years apart) show different outcome in wellhead displacement. The cause of this unclear, but many factors could influence the displacement, e.g. T and P wellbore conditions can be different although wellhead conditions are similar, constraints of the wellhead might be different as two years are between measurements, the wellhead might be less constrained in the latter case due to cement cracking near the top.

In FEM analysis of threaded casing/coupling connection, the highest stresses occur in the area of the casing where the first threads are located. Casing failures of tensile ruptures have been seen at this location in wells that were quenched by pumping cold water into them. In another case, in well IDDP-1 in Iceland, where premium connections were used, the threads of the casing were swept off due to high shear force in the threads.

The models show that the casings are anchored at the couplings that stand out into the cement. Therefore, higher stresses are seen in the cement nearby couplings.

According to the FEM results, collapse resistance of casings increases when cement is present in the annulus, and the collapse form is less severe than for non-cemented casings, that completely collapse together.

Conclusions

Nonlinear FEM structural modeling of casings in high-temperature geothermal wells was presented. As most wells experience temperature change that leads to thermal stresses above the yield strength of casing materials commonly used, API grades K55, L80 and T95, plasticity needs to be considered. This is addressed by

defining nonlinear material stress-strain curves, and using multilinear kinematic hardening material model. Modeling such as this requires knowledge about the structure, its initial conditions and loads in the form of temperature and pressure changes. Load history is therefore important, to fully understand the structure's response to loads. For drilling deeper wells to challenging pressures and temperatures and assuring a lasting well, the structural design needs to be carefully considered to include all aspects of the design. Including material challenges of strength reduction at elevated temperatures, thermal expansion, corrosion and embrittlement, wellhead pressure class. Modeling such as shown here provides an excellent tool for evaluating stresses and strains for future well designs.

Acknowledgement

This PhD work was financially supported by the University of Iceland research fund, the Technology Development Fund at RANNIS - The Icelandic Centre for Research, the Innovation Center Iceland, Landsvirkjun Energy Research Fund, and GEORG - Geothermal Research Group. Their support is greatly appreciated. The authors would like to thank Reykjavik Energy, HS Orka, Landsvirkjun, Iceland Drilling, ÍSOR - Iceland GeoSurvey, Mannvit and the Innovation Center Iceland for providing data and useful discussion and information for the work presented here.

References

API, 2005. *API Standard 5CT (ISO 11960:2004) Specification for Casing and Tubing*. 8th ed. Washington: American Petroleum Institute.

ISO/TR, 2007. *ISO/TR 10400, Petroleum and natural gas industries - equations and calculations for the properties of casing, tubing, drill pipe and line pipe used as*

casing or tubing. Geneva: ISO copyright office.

Kaldal, G. S., Jonsson, M. T., Palsson, H. & Karlsdottir, S. N., 2012. *Thermal and Structural Analysis of the Casings in a High Temperature Geothermal Well During Discharge*. s.l., Thirty-Seventh Workshop on Geothermal Reservoir Engineering, Stanford University, Stanford, California, January 30 - February 1, 2012.

Kaldal, G. S., Jonsson, M. T., Palsson, H. & Karlsdottir, S. N., 2013. *Collapse analysis of the casing in high temperature geothermal wells*. Stanford, California, s.n.

Kaldal, G. S., Jonsson, M. T., Palsson, H. & Karlsdottir, S. N., 2015. *Structural Analysis of Casings in High Temperature Geothermal Wells in Iceland*. Melbourne, Australia, World Geothermal Congress 2015.

Kaldal, G. S., Jonsson, M. T., Palsson, H. & Karlsdottir, S. N., 2015. Structural modeling of the casings in high temperature geothermal wells. *Geothermics*, Volume 55, pp. 126-137.

Kaldal, G. S., Jonsson, M. T., Palsson, H. & Karlsdottir, S. N., 2016. Structural modeling of the casings in the IDDP-1 well: Load history analysis. *Geothermics*, pp. 1-11.

Maruyama, K. et al., 1990. An Experimental Study of Casing Performance Under Thermal Cycling Conditions. *SPE*, pp. 156-164.

Rahman, S. S. & Chilingarian, G. V., 1995. *Casing design theory and practice*. Amsterdam - Lausanne - New York - Oxford - Shannon - Tokyo: Elsevier.

Modeling and simulation in the design process of a prosthetic foot

Heimir Tryggvason¹ Felix Starker² Christophe Lecompte² Fjóla Jónsdóttir¹

¹School of Engineering and Natural Sciences, University of Iceland, Iceland, {het11,fj}@hi.is
Össur hf, Iceland, fstarker@ossur.com, clecompte@ossur.com

Abstract

The design process of prosthetic feet largely depends on an iterative process of prototyping and user testing. As resources for reliable and repeatable user testing are limited, modeling and simulated testing of the design is a positive addition to this process to support further design development between prototyping.

The key goal of prosthetic foot design is to mimic the function of the lost limb. A passive spring and damper system can imitate the behavior of an ankle for low level activity, e.g. walking at slow to normal speeds and relatively gentle ascents/descents. In light of this, a variety of constant stiffness prosthetic feet are available on the market that serve their users well. However, when walking at a faster pace and ascending/descending stairs, the function of the physiological ankle is more complex and the muscular activity contributes to the stride in different ways.

One of the challenges in prosthetic device design is to achieve the appropriate range of stiffness of the arrangement of joints and spring elements for different tasks, as well as varying loading of the prosthetic device. This calls for an adaptive mechanism that mimics the stiffness characteristics of a physiological foot by applying real-time adaptive control that changes the stiffness reactively according to user's needs. The goal of this paper is to define the stiffness characteristics of such a device through modeling.

A finite element model was made for a well-received prosthetic foot design. The model was then validated by mechanical measurements of the actual product. We further enhanced the model to include a secondary spring/dampener element to provide added flexibility and damping of the ankle joint movement. Reactive control of the secondary element allows the simulated prosthetic foot to adapt the ankle joint to imitate the behavior of the physiological ankle during different activities and in different phases of the gait cycle.

1 Introduction

The goal of all prosthetic design is to mimic as closely as possible the actual physiological look, function and feel of the replaced body part. A real foot and ankle joint

is a complex system of muscles, sinews and ligaments, whose functionality is challenging to replicate. Many current prosthetic feet are mechanical designs with fixed spring and dampening characteristics, optimized for rather slow gait on a level surface (Hansen, 2004). However, such devices are not optimal for many everyday tasks, such as ascending and descending stairs, walking on uneven terrain and running. Higher ankle joint stiffness is required when walking rapidly or running, while a softer spring provides more comfort when walking slowly and places less strain on the residual limb. Changing prosthetics or making frequent manual adjustments is cumbersome. Adaptive prosthetics that suit a range of activities provide a better quality of life for the user. The human ankle and limb adapts dynamically to the terrain and variations in pace (Jin, 2016; Hunter, 2010). This calls for feet that have real-time variable stiffness.

Research on human legs and gait have produced many different designs of prosthetic feet. They can be divided into three main categories: conventional feet, energy storing feet and motor powered feet. A conventional foot is a solid ankle cushioning heel, which does not follow a normal gait pattern. Energy storing feet, such as Vari-Flex® and Pro-Flex® are made of a layered carbon-fiber composite that extends from the amputees' residual limb and aims to provide natural progression through the stages of normal gait. The stiffness of the foot, and its response to load, may be controlled via the thickness profile of the foot, as well as its shape. Additionally, a spring may be introduced to the structure to provide further shock absorption. In the third category are powered active prosthetic ankles, such as bionic ankle-foot prosthesis (Herr, 2012; Au, S., 2008) and the Proprio® foot. The Proprio foot is an adaptive prosthetic device for low to moderately active below-knee amputees that mimics natural foot motion. Quasi-passive feet (Williams, 2009; Jin, 2016; Li, 2006) are a further evolution in prosthetics design, whose goal is to adapt more closely to the users' needs.

Determining the optimal characteristics of a prosthetic foot in the design phase is still a process of trial and error and relies highly on the prosthetic users' feedback during real life tests. Our approach is to use

mechanical testing and finite element (FE) analysis to optimize the stiffness characteristics of a prosthetic foot. The Pro-Flex® prosthetic foot by Össur, Iceland was selected for the analysis as it is a popular example of a passive prosthetic design. The mechanical characteristics were determined using a dynamic test machine, according to ISO 16955. The standardized testing can be viewed as a step between simulations and real life user tests that provides consistent results and a less complex way of understanding and improving the characteristics of prosthetic feet. A model was constructed in the commercial finite element software ANSYS, whose purpose is to serve as a framework for experimenting with different material behavior, as well as additional elements, to improve the characteristics of the prosthetic design. Both static and dynamic simulations were carried out. The simulation results were validated by comparison with the measured mechanical characteristics. The modeled results were found to accurately match the experimental ones, in terms of deformation of the carbon fiber spring blades, as well as the resulting anterior and posterior forces and ankle moments. The finite element (FE) model was used to explore several variations of the foot design, including varying spring stiffness and dampener elements. The end goal is to use this model to experiment with actively controlled elements that adapt dynamically to the users' needs.

2 The Subject Prosthetic Foot

The Pro-Flex®, Cat. 5, size 27 was selected as a prosthetic foot model for this study; see Figure 1. One of the features of the design is a mechanical pivot within the composite springs, allowing for a defined ankle rotation. A mechanical link element is located posterior, connecting the midfoot spring with the pyramid adapter that is attached to the user's leg.

To change the stiffness characteristics of this foot the mechanical link seems as an ideal part as it influences both the rotation around the pivot and interacts with the mid blade spring.

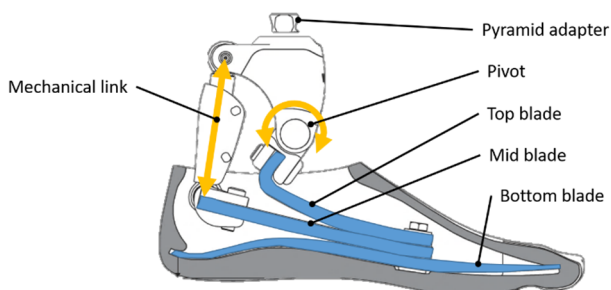


Figure 1: Schematic of the prosthetic foot model used for all tests (Pro-Flex® Össur).

3 Methodology

Subject based data is highly variable and the prosthetic user continuously adapts its motion profile. The approach for this study is to use a combination of mechanical testing and finite element analysis as described schematically in Figure 2. Mechanical testing of an actual prosthetic is first carried out. A simulation model is constructed and the prosthetics characteristics as obtained by testing, used to parametrize and validate the model. After completion of this first validation, the foot model is modified by introducing non-linear materials, e.g. spring and damper, to a specific section of the prosthesis to allow for an altered foot performance. The optimized models will later on be transferred into physical prototypes and finally fit to prosthetic users.

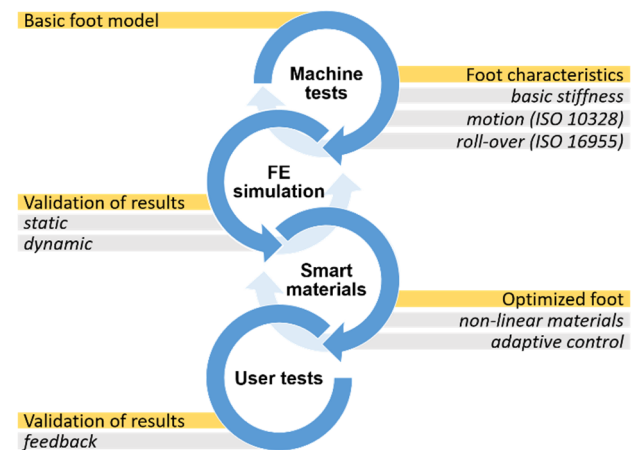


Figure 2: The methodologic approach for validating the simulation model of a prosthetic foot.

The basic foot model is setup by investigating the isolated stiffness characteristics of the carbon fiber spring blades for heel and toe by an internal standardized test procedure (basic stiffness). ISO 10328 a simplified dynamic endurance test is used as a first validation. In addition, ISO 16955 is used to simulate more realistic a complete heel to toe roll-over of the foot.

Current works investigate the links between actual user experience and these standardized tests. Hence, if the simulation model closely matches the mechanical testing, we can conclude that the model is capable of accurately describing the actual prosthetic users' experience.

4 Mechanical Testing

Stiffness evaluation of the foot sample was performed with a uniaxial tension and compression test machine (M350-10CT, Testomatic, UK) with linear displacement and constant speed of 300 mm/min. The foot sample is rigidly connected to the machine and set

under 15° angle for the heel and 15° respectively for the toe test. With 36 mm of set displacement, a resulting vertical force of 610 ± 35 N was measured for the toe. Respectively, a 12 mm set displacement resulted in 923 ± 45 N for the heel spring, measured throughout 40 samples. The variation between samples is due to variations in the carbon fiber blade production.

The mechanical testing of the prosthetic foot took place with two approaches. ISO 10328 is used for endurance testing and has a simplified setup with a prosthetic foot connected rigidly to the machine frame. Two pistons are compressing heel and toe with a defined phase shift and applying the dynamic load at a defined angle (-15° heel and $+20^\circ$ toe), see Figure 3.

Although ISO 10328 is valid for strength testing, deformation and motion data cannot be linked to prosthetic user experience due to the limited rigid setup.

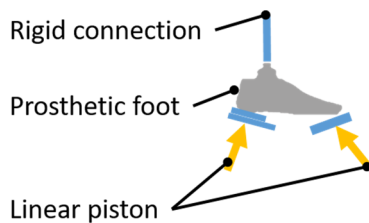


Figure 3: Schematic of the static loading according to ISO 10328.

Therefore, a second test was carried out with a modified test machine (Shore Western, USA) to evaluate the characteristics of the prosthetic foot under dynamic loading conditions, including swing phase according to ISO 16955; see Figure 4.

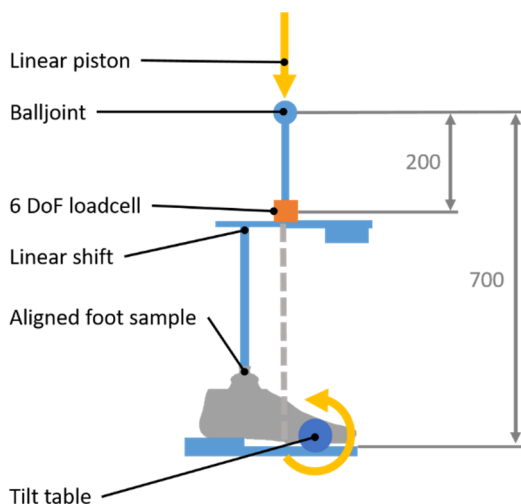


Figure 4: Schematic of the dynamic loading according to ISO 16955.

For this study, the focus is on the heel-to-toe roll-over test, applying a dynamic force of 824 N maximum, synchronized to a rotational motion ranging from -20° to $+40^\circ$ angle during 0.6 s of stance phase; see Figure

5. The foot suspension is achieved by a ball joint with low spring force (14 N) to reset the foot during swing phase. Hence, the foot is capable of rolling and deforming freely under the set load profile.

Several sensors capture the forces, the resulting torque and the displacement within the prosthetic leg. The horizontal rotational tilt table is in constant displacement control, as well as the linear piston pushing on the prosthetic foot. The force is adjusted by a PI-loop controller with the force profile as feedback signal; see Figure 5.

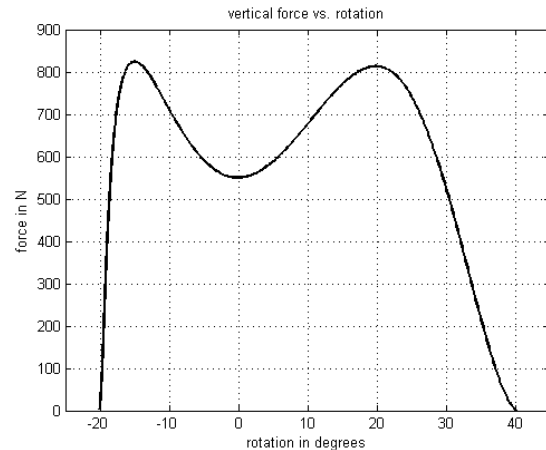


Figure 5: Input data (vertical force vs. the rotation of the tilt table) for the test machine.

5 Finite Element Model

A 3D FE model was built and simulated in Ansys WB; see Figure 6. In the FE model, the carbon blades are modeled as flexible surface bodies and assigned a layer element designating the buildup of the carbon layers; thickness, layer angle and material of the different layers in the section. Each part is also assigned an orientation element to designate the orientation of the carbon layers. The material properties used for modeling the carbon fiber blades are a combination of values provided by the supplier of the pre-preg carbon fibers and measurements made on carbon fiber plates prepared in a production line.

All other parts of the foot are simplified to four rigid bodies in the model, that is, main body (Pyramid adapter), mechanical link and two blade clamps. These are made of aluminum alloy and steel and are considered stiff enough to neglect deformation. The three joints between the rigidly modeled bodies have a rotational degree of freedom about an axis, at each connection of the mechanical link and at the pivot connection of the top blade to the main body. The connection between the three flexible surface bodies and connection of the clamps to the top and middle blade are modeled with contact elements in the area of the bolted clamping. These contact areas are the most sensitive attribute of the model where contact stiffness affects the

deformation of the flexible blades and therefore the overall quasi stiffness of the modelled foot.

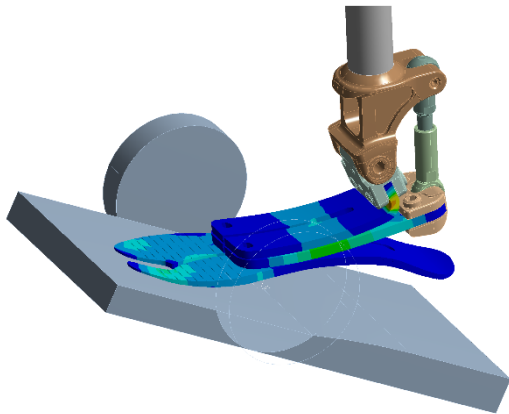


Figure 6: 3D view of the FE model of the Pro-Flex in ISO16955 test simulation, showing equivalent stresses in flexible parts.

The force reaction in the mechanical link goes from compression to tension, transitioning from heel-strike to toe-off. The maximum tension in the mechanical link is roughly three times the ground reaction force at maximum force on the fore-foot. Hence, effects of changes to the function of the link will influence the gait more after mid-stance than at heel-strike.

This originally rigid link allows for a superimposed spring and damping characteristics altering the

rotational stiffness of the foot during roll-over. The modelling of the test procedure is aimed at investigating the effects of changed function in this connection to approach a more desirable overall effect in the response of the foot.

Initial validation of the FE model was done by simulating the ISO 10328 test on the foot assembly. Force values were acquired from remote displacement boundary condition on a rigid plate at the appropriate angle on both toe and heel of the foot model. The resulting quasi stiffness on toe and heel then compared to measured values from the mechanical testing. Free frictional sliding contact was defined between elements on the sole blade and the rigidly defined plate to ensure correct rollover on the sole blade for the ramped displacement.

Furthermore, simulation was done to validate the model against the ISO 16955 test procedure. The tilt table and linear shift geometry was modeled as rigid bodies and a transient structural analysis performed with test machine input data as boundary conditions for the simulation; see Figure 7. For this simulation, the contact between tilt table and sole blade is defined as fully rough, with no slippage allowed. Values from the simulation are compared to test machine output data, that is, the vertical displacement of the ball joint, the force reaction and the moment at knee level.

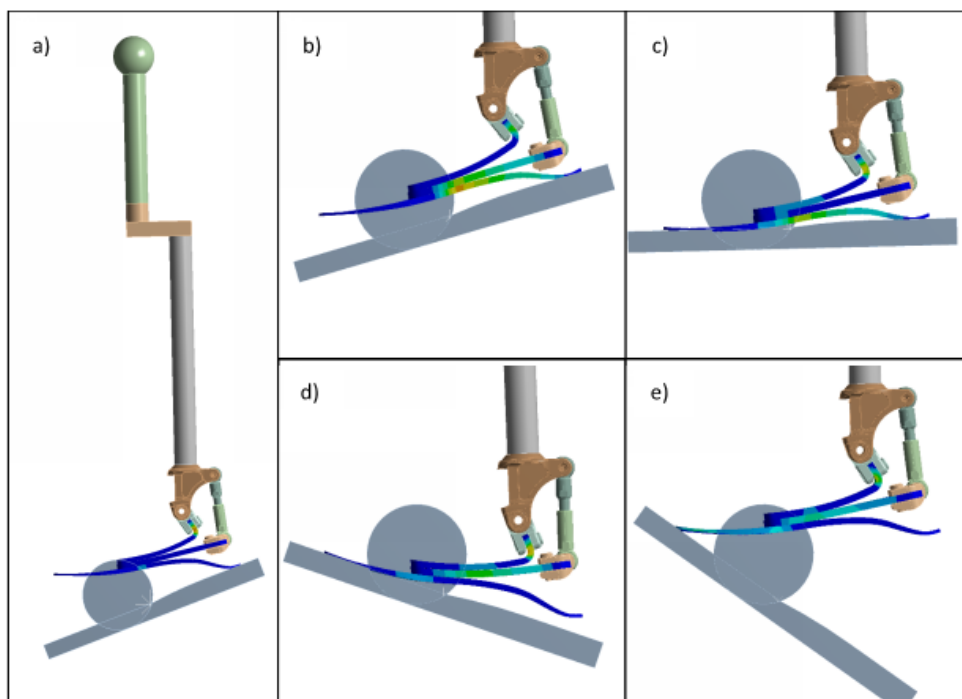


Figure 7: Transient simulation of the ISO 16955 test procedure for a 600 ms loop. a) Showing full model at early heel-strike, at 10 ms. b) Mid heel strike at max. vertical force, 150 ms. c) Mid-stance, at 300 ms. d) Right after heel-off, at 450 ms. e) Before Toe-off at 575 ms.

6 Model Validation

The machine test according to ISO 16955 and simulation showed comparable results during a full roll-over of the prosthetic sample, as shown in Figure 8. For the initial set parameters of the load vs. rotation profile, an accuracy of better than $\pm 1\%$ of the maximum force value of 824 N was achieved at the given stance phase time of 600 ms.

The resulting moment, measured at 500 mm above the tilt table, which represents the position of the knee joint, see figure 4, showed similar characteristic curves. The transition of the foot from the deformed heel to toe occurred at the same angle, which shows similar motion of the overall foot. A slight deviation of the resulting moment, especially after -15° to -2° , was found.

The quasi stiffness calculated by the vertical force divided by the vertical displacement showed high correlation until late stance (26° to 40°) where the foot only rests on the very toe-end of the bottom blade. Peak values for both knee moment and stiffness ranged within $\pm 2\%$ of the peak value.

The overall correlation between measurements and simulation are within required parameters for a valid comparison and valuation of shifts in the curves as the function of the mechanical link is changed.

7 Design Enhancements

The basic foot model as described above, was extended, allowing experimentation with the effects of modifying design elements. This work focuses on substituting a spring and dampener element for the rigid mechanical link shown in figure_1. Our hypothesis is that a translational link allows for a greater range of motion that can give increased comfort for the amputee. The results of the modeling of the enhanced design are shown in Figure 9. Initial parameters for spring stiffness and dampening for the translational joint are chosen as a moderate change for controlled adjustment steps towards a modified function i.e. a relatively high spring constant and low damping coefficient. ($k = 200 \text{ kN/m}$, $c = 10 \text{ kN s/m}$).

The input vertical force vs. plate angle profile for both the simulation and the test machine remains constant. Therefore, it can be assumed that all following data such as knee moment and quasi-stiffness is comparable to the initial comparison test. The sagittal moment at the knee transitions later from heel to toe. Resulting peak moment at late stance can be reduced by 15%. The quasi stiffness curve shows similar characteristics with a reduced peak stiffness at heel strike of 8% and a softer late stance. This can be explained by the higher range of motion in the pivot within the prosthetic foot model and a deflection of the spring and damper system the foot motion is altered. The

foot performs in late stance softer compared to the foot with a rigid link.

Comparing all data shows that the modified prosthetic foot does not evenly change its stiffness as it would by using softer carbon fiber spring blades. The spring-damper system in combination with the carbon fiber springs alters the overall transition and mechanical behavior of the foot which is well received during stair ambulation, when walking over slopes or at slow walking speeds.

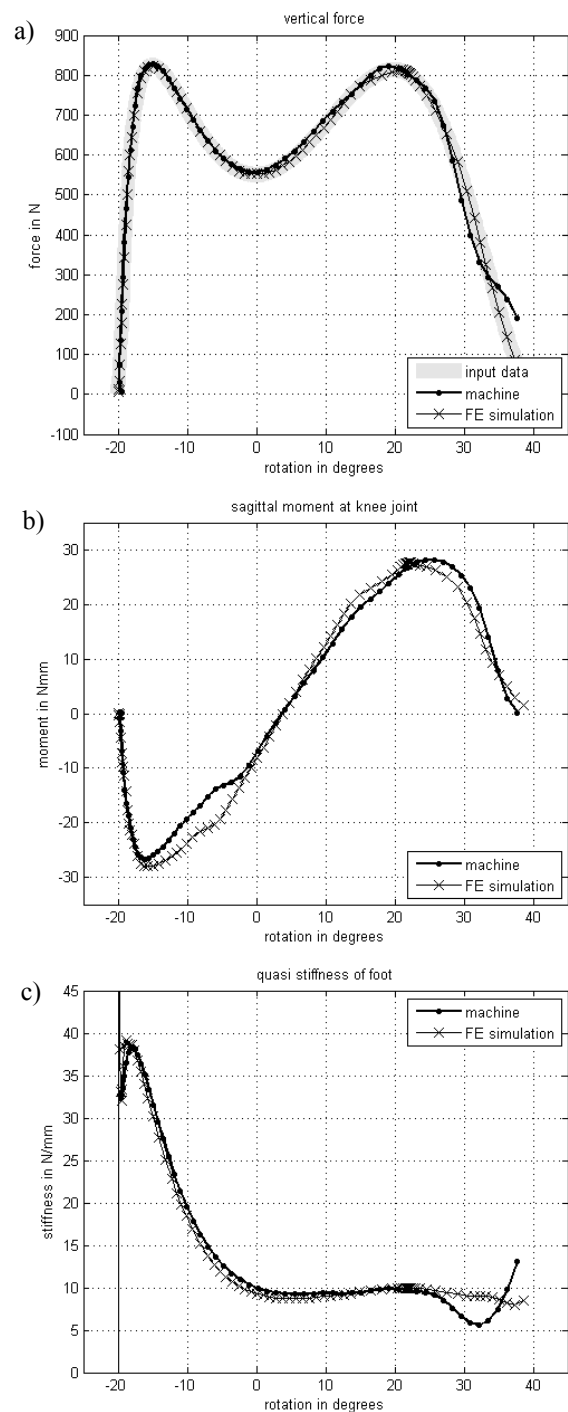


Figure 8: Results for the original Pro-Flex®. Measurements of the 16955-test machine in comparison

to the simulation a) vertical force vs. rotation angle or the plate b) knee moment c) quasi stiffness.

This alteration is less favorable for higher activity levels, e.g. walking at higher pace and running. The function needed in the link is to allow the flexibility at slower speeds but reduce it at higher speed.

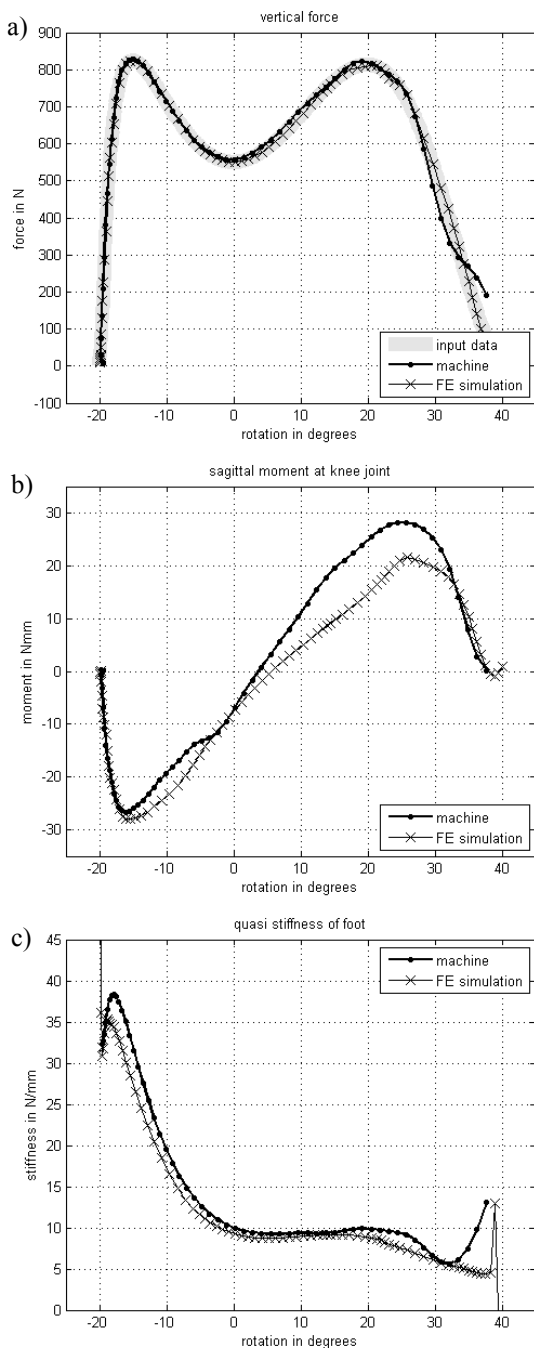


Figure 9: Comparison between measurements of the 16955-test machine and the simulation of a modified model a) vertical force vs. rotation angle or the plate b) knee moment c) quasi stiffness

Beside the overall good correlation of the results with the presented approach, minor offset and differences can

be explained by the absence of the effects of a cosmetic foot cover within the simulation. The foot cover provides a softer heel strike with a smooth transition towards midstance. At late stance, the foot cover elongates the foot by transitioning the load from the carbon fiber bottom blade to the elastic toes. All these effects can directly be examined in the comparison figures.

Apart from this the foot is under minimal unwanted sliding conditions, during the machine test, especially when the load is removed of the sample during late stance. Throughout this, each sensor, actuator and data acquisition of the machine causes a potential error that is by calibration assured to be below 1 % of the full signal, nevertheless a range of uncertainty remains. Altogether, this clearly points out that the simulated approach shows equivalent results and by this is highly suitable for further improvements of the prosthetic foot design and too evaluate the stiffness characteristics.

8 Conclusions

The study has shown that the standardized test procedure can be simulated and modifications to the model show anticipated shifts in function. Further work is aimed at modeling the desired shift in function of the mechanical link for different displacement rates and design of a functional link.

Ongoing research has to prove the links between these mechanical characteristics and different groups or the individual amputees. Nevertheless, the FE simulation model showed high correlation with the machine test results. Some differences can be explained by the use of a cosmetic cover within the machine test to allow for a defined friction. The FE model seems highly capable to optimize the application of new non-linear function in the foot. Comparison and interpretation of simulation results against standardized test machines is more practical than to traditional gait data. Further studies have to connect prototypes to the user experience and close the methodological development loop.

Acknowledgements

This work is funded by the Technology Development Fund, Rannís, Iceland.

References

- Ahmadkhanlou F., Zite, J. and Washington, G., 2007, "A magnetorheological fluid-based controllable active knee brace", *Smart Structures and Materials Proc. SPIE 6171* pp. 148-56.
- Au, S., Berniker, M. and Herr, H., 2008, "Powered ankle-foot prosthesis to assist level-ground and stair-descent gaits", *Neural Networks, Vol. 21*, pp. 654-666.
- C. Li, M. Tokuda, J. Furusho, K. Koyanagi, S. Morimoto, Y. Hashi-moto, A. Nakagawa, and Y. Akazawa, 2006, "Research and development of the intelligently controlled

- prosthetic ankle joint,” in Proc. IEEE Int. Conf. Mechatronics and Automation, Luoyang, China, pp.1114-1119.
- Deffenbaugh, B. W., Herr, H. M., Pratt, G. A. and Wittig, M. B., 2004, “Electronically controlled prosthetic knee” US Patent Specification 6,764,520.
- Gudmundsson, K. H., Jonsdottir, F. and Thorsteinsson, F., 2010, “Geometrical optimization of a magneto-rheological rotary brake in a prosthetic knee”, *Smart Materials and Structures*, Vol. 19, 035023.
- Hansen, A. H., Childress, D. S., Miff, S. C., Gard, S. A. and Mesplay, K. P., 2004, “The human ankle during walking: Implications for design of biomimetic ankle prosthesis”, *Journal of Biomechanics*, Vol. 37, pp. 1467-1474.
- Herr, H. M. and Grabowski, A. M., 2012, “Bionic ankle-foot prosthesis normalizes walking gait for persons with leg amputation”, *Proc. R. Soc. B.*, Vol. 279, pp. 457-464.
- Herr, H., and Wilkenfeld, A., 2003, “User-adaptive control of a magnetorheological prosthetic knee. *Industrial Robot: An International Journal*, Vol. 30, pp. 42-55.
- Hunter, L. C., Hendrix, E. C., & Dean, J. C., 2010, “The cost of walking downhill: Is the preferred gait energetically optimal?”, *Journal of Biomechanics*, 43(10), pp.1910-1915.
- ISO/TC 168 Prosthetics and orthotics. (2016). ISO 10328:2006 Prosthetics -- Structural testing of lower-limb prostheses -- Requirements and test methods. ISO. Retrieved from: <https://www.iso.org/standard/36413.html>
- ISO/TS 16955:2016 Prosthetics - Quantification of physical parameters of ankle foot devices and foot units. (2016). Retrieved from: <https://www.iso.org/standard/69821.html>
- Jin, L., Adamczyk, P. G., Roland, M., & Hahn, M. E. (2016). “The effect of high- and low-damping prosthetic foot structures on knee loading in the uninvolved limb across different walking speeds”, *Journal of Applied Biomechanics*, Vol. 32(3), pp. 233–240.
- Williams, R. J., Hansen, A. H. and Gard, S. A., 2009, “Prosthetic ankle-foot mechanism capable of automatic adaptation to the walking surface”, *J. Biomech. Eng.*, Vol. 131, pp. 035002-1-7.
- URL: <http://www.ansys.com>
- URL: <http://www.ossur.com/prosthetic-solutions>